Mathematical Problems in Engineering

Advanced Control and Optimization with Applications to Complex Automotive Systems

Guest Editors: Hui Zhang, Hamid Reza Karimi, Xinjie Zhang, and Junmin Wang

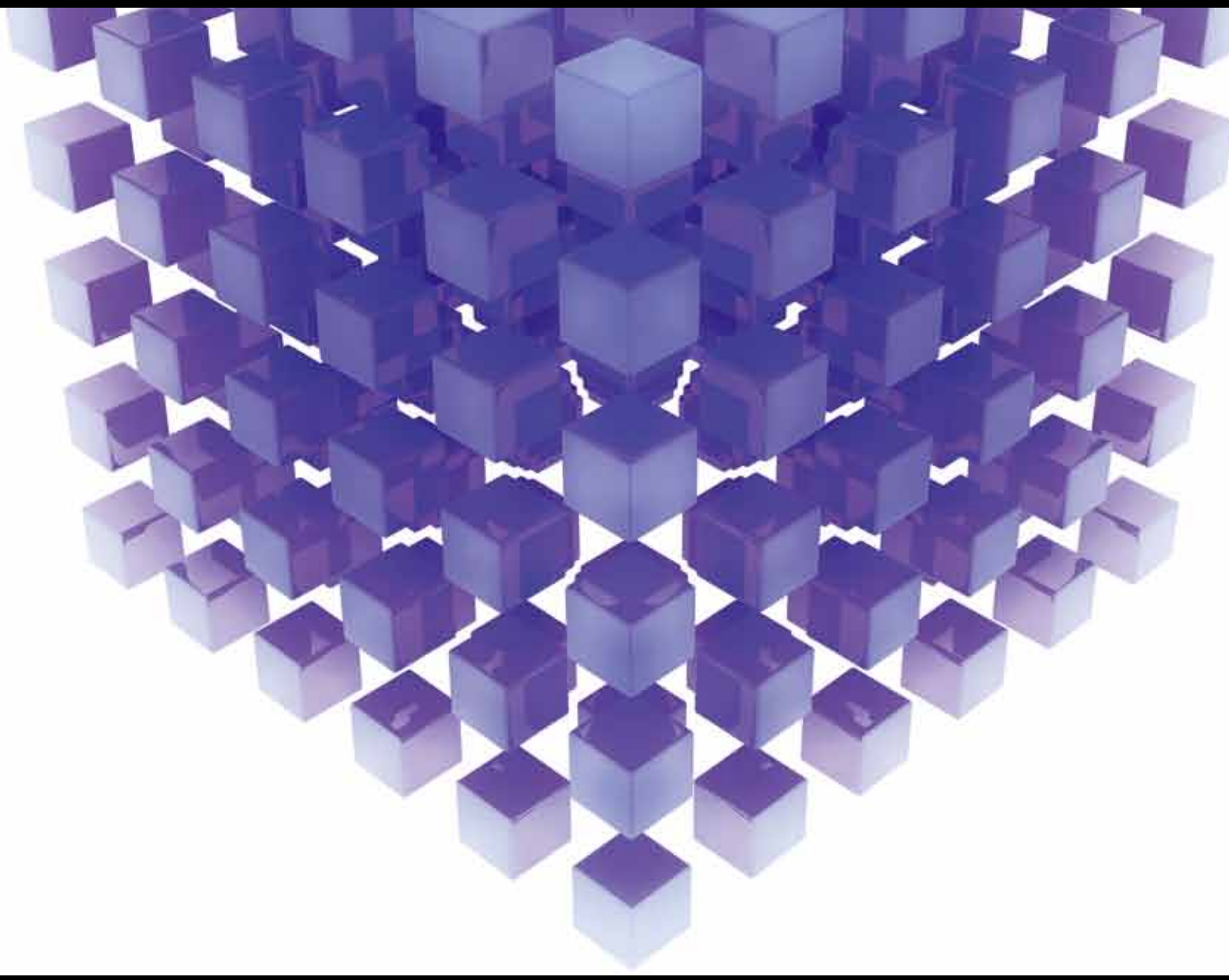

Advanced Control and Optimization with Applications to Complex Automotive Systems

Mathematical Problems in Engineering

Advanced Control and Optimization with Applications to Complex Automotive Systems

Guest Editors: Hui Zhang, Hamid Reza Karimi, Xinjie Zhang, and Junmin Wang

Editorial Board

Contents

A Frequency Compensation Algorithm of Four-Wheel Coherence Random Road, Jun Feng, Xinjie Zhang, Konghui Guo, Fangwu Ma, and Hamid Reza Karimi
Volume 2013, Article ID 986584, 12 pages

Finite Frequency Vibration Control for Polytopic Active Suspensions via Dynamic Output Feedback, Yifu Zhang, Gongdai Liu, Pinchao Wang, and Hamid Reza Karimi
Volume 2013, Article ID 598489, 12 pages

Hindawi Publishing Corporation
Mathematical Problems in Engineering
Volume 2014, Article ID 183580, 3 pages
http://dx.doi.org/10.1155/2014/183580

Editorial

Advanced Control and Optimization with Applications to Complex Automotive Systems

Hui Zhang,[1,2] Hamid Reza Karimi,[3] Xinjie Zhang,[4] and Junmin Wang[2]

[1] *Scientific Research Academy, Shanghai Maritime University, Shanghai 201306, China*
[2] *Department of Mechanical and Aerospace Engineering, The Ohio State University, Columbus, OH 43210, USA*
[3] *Department of Engineering, Faculty of Engineering and Science, University of Agder, 4898 Grimstad, Norway*
[4] *State Key Laboratory of Automotive Simulation and Control, Jilin University, Changchun 130022, China*

Correspondence should be addressed to Hui Zhang; huizhang285@gmail.com

Received 16 January 2014; Accepted 16 January 2014; Published 14 April 2014

With increasing and tightening requirements on the control and optimization performance, the traditional control and optimization strategies may not qualify in many application problems. To meet the challenges and requirements, advanced control and optimization methodologies should be employed or developed. Here, the advanced control and optimization denote the ones which, in principle, can best achieve the objectives in the presence of nonlinearities, highly interactivities, or newly emerged operating circumstances. As the advanced control and optimization will provide a basis for the design and operation of practical systems, these advanced techniques would result in substantial and sustainable benefits.

The overall aims of this special issue are twofold: (1) to provide an up-to-date overview of the research directions in the advanced control and optimization; (2) to illustrate how to formulate problems from automotive systems and develop suitable theory to solve the corresponding problems. Of particular interest the papers in this special issue are devoted to the development of advanced control and optimization including network control, nonlinear model predictive control, dynamic programming, and integral programming, with applications to complex automotive systems including vehicle dynamics and control, combustion and emission control, and vehicle integration and optimization, for instance. Topics in this special issue include, but are not limited to: (1) network analysis and protocol optimization, (2) fast nonlinear model predictive control and optimization, (3) advanced vehicle dynamics and control, (4) intelligent systems and mobility, (5) advanced vehicle integration and optimization, (6) robust and optimal control, and (7) information constraints and faults.

We have solicited considerable submissions to this special issue worldwide from control engineers and researchers, automotive engineers and researchers, electric engineers and researchers, and mathematics scientists. After a stringent peer review process, 37 submissions have been accepted, which covers electrified vehicles, vehicle dynamics and powertrain control, road information and vibration attenuation, control and optimization theory and applications, and networks and autonomous vehicles.

The electrification has been the consistent topic almost since the birth of the traditional engine-powered vehicles. In particular, recently, the electrification process has been enhanced due to the requirements on the fuel economy and emissions. In the work entitled "*Experimental study on communication delay of powertrain system of plug-in hybrid electric vehicles*" by D. Wang et al., a mathematical model of the vehicle system with delay is established. An experimental platform is developed to test the communication delays and identify the established mathematical model. In another work entitled "*A study on control strategy of regenerative braking in the hydraulic vehicle based on ECE regulations*" by T. Liu et al., the regenerative braking strategy is investigated for hydraulic hybrid vehicles. The simulation results validate the effectiveness and the application perspective of the proposed

strategy. C. B. Regaya et al. develop a scheme of simultaneous estimation of rotor resistance and the rotor speed of an induction motor in the paper "*Electric drive control with rotor resistance and rotor speed observers based on fuzzy logic.*" Two adaptive observers using fuzzy logic are designed and the optimal control gain is determined by a simple algorithm. A control strategy named least square support vector machines inverse control is proposed for a three-phase induction motor for electric vehicle in "*A high-performance control method of constant V/f-controlled induction motor drives for electric vehicles*" by L. Chen et al. A modified particle swarm optimization is used to determine the optimal parameters. In the work entitled "*Resident plug-in electric vehicle charging modeling and scheduling mechanism in the smart grid*" by P. Han et al., a distribution grid profile model with plug-in electric vehicle charging power is developed to study the resident charging effects on the distribution grid. The real data is used to identify the model and a queuing-theory-based scheduling mechanism is explored. The energy management problem for plug-in series-parallel hybrid electric bus is addressed in "*Global optimal energy management strategy research for a plug-in series-parallel hybrid electric bus by using dynamic programming*" by H. He et al. Employing the dynamic programming for the optimization, the fuel economy is improved by 53.7% compared with the corresponding conventional bus.

As the vehicle may be driven at a high speed especially on an highway, the vehicle dynamics and control such as the lateral and longitudinal dynamics is extremely important. In the paper entitled "*Optimal slip ratio based fuzzy control of acceleration slip regulation for four-wheel independent driving electric vehicles*" by G. Yin et al., an acceleration slip regulation algorithm is proposed for four-wheel independent driving electric vehicles. The utilized control method is the fuzzy logic control. It infers from the comparison that the vehicle driving stability and safety are both improved. R. Wang et al. study the motion control of four-wheel independently driven electric vehicles in "*Motion control of four-wheel independently actuated electric ground vehicles considering tire force saturations.*" The hierarchy controller consists of a high-level one and a low-level one. The high-level controller is used to generate the virtual control efforts to track the desired vehicle model. And the low-level one is to do the control allocation. R. He et al. analyze the braking performance for eddy current and electrohydraulic hybrid brake system in the work named "*Brake performance analysis of ABS for eddy current and electrohydraulic hybrid brake system.*" The intelligent control is employed to the integrated vehicle dynamics in the work "*Nonlinear analysis and intelligent control of integrated vehicle dynamics*" by C. Huang et al. The nonlinearity is also analyzed. For the clutch shifting investigation, there are four papers from two research groups: "*Research on shifting control method of positive independent mechanical split path transmission for the starting gear*" by J. Xi et al., "*Research on conflict decision between shift schedule and multienergy management for PHEV with automatic mechanical transmission under special driving cycles*" by J. Xi and Y. Chen, "*Fuzzy determination of target shifting time and torque control of shifting phase for dry dual clutch transmission*" by Z. Zhao et al., and "*Sliding mode variable structure control and real-time optimization of dry dual clutch transmission during the vehicle's launch*" by Z. Zhao et al. Though the main topic is similar, these four papers have different investigation points and different contributions inside.

The demands on the vehicle ride comfort are receiving more and more attention. The future direction is to improve and modify the passive suspension systems. Active suspension and semiactive suspension are two alternative options. The active suspension system is designed in "*Static output-feedback control for vehicle suspensions: a single-step linear matrix inequality approach*" by J. Rubio-Massegu et al. The employed control law is the static output-feedback control. It is well known that the optimal feedback gain of the static output feedback control is difficult to be determined. The authors propose a novel noniterative algorithm to derive the feedback gain. The finite-frequency control is used in "*Finite frequency vibration control for polytopic active suspensions via dynamic output feedback*" by Y. Zhang et al. for the active suspension design. Compared with the traditional entire-frequency optimization, the solution is improved a lot. The ride height adjusting controller design problem is investigated in "*Dynamic ride height adjusting controller of ECAS vehicle with random road disturbances*" by X. Xu et al. The variable structure control technique can be seen in this paper. In the paper entitled "*Considering variable road geometry in adaptive vehicle speed control*" by X. Yan et al., the road geometry is involved in the vehicle speed control. The adaptive vehicle speed controller is designed by using the Hamilton-Jacobi Inequality. In the work named "*Adaptive real-time estimation on road disturbances properties considering load variation via vehicle vertical dynamics*" by W. Yu et al., a Kalman filter is employed to estimate the road disturbance. Moreover, the recursive least-squares estimation is employed to estimate the sprung mass. The key contribution is to categorize the road condition into six special ranges which can be applied to the suspension control. J. Cao et al. investigate the driver model in the paper "*A driver modeling based on the preview-follower theory and the jerky dynamics.*" Simulation results carried out via CarSim show the advantages and the effectiveness of the proposed model. In the work entitled "*A frequency compensation algorithm of four-wheel coherence random road*" by J. Feng et al., the authors aim to deal with the different road power spectral densities between left and right wheels. A frequency compensation algorithm is proposed to compensate for the difference. Q. Yang et al. design the vehicle suspension with an adaptive optimization approach in the work "*An adaptive metamodel-based optimization approach for vehicle suspension system design.*"

The control and optimization theory has obtained a lot of witness during the past decade owing to the requirements of the emerging applications. In the work entitled "*Collision-free and energy-saving trajectory planning for large-scale redundant manipulator using improved PSO*" by M. Jin and D. Wu, the particle swarm optimization (PSO) algorithm is modified to overcome the drawbacks of the original algorithm. In the work entitled "*Actuator saturation constrained fuzzy control for discrete stochastic fuzzy systems with multiplicative noises*" by W.-J. Chang et al, the discrete-time fuzzy systems with

multiplicative noises are investigated. Sufficient conditions are derived to guarantee the stability of the closed-loop nonlinear stochastic systems subject to actuator saturation. J. Asprion et al. summarize the optimization problem in Diesel engines in the work "*Optimal control of diesel engines: numerical methods, applications, and experimental validation*." In the work entitled "*Optimization problem for physical design automation*", the physical design automation is optimized in the directions of area and interconnect length. A hybrid evolutionary algorithm is applied on the problem. B. Wang et al. develop a novel controller for integrated electric parking brake system in the paper "*Slide mode control for integrated electric parking brake system*." The sliding mode controller is applied to control the clamping force such that vehicle is parked firmly. The stability and the H_∞ performance of switched systems with time-varying delays are investigated by C. Qin et al. in the paper "*Robust stability and H_∞ stabilization of switched systems with time-varying delays using delta operator approach*." Numerical examples show the effectiveness of the proposed design method. In the paper entitled "*Quality-related process monitoring based on total kernel PLS model and its industrial application*" by K. Peng et al., the adaptively of projection to latent structure is enhanced. In addition, the proposed method is applicable for nonlinear systems. In the paper entitled "*Peak power demand and energy consumption reduction strategies for trains under moving block signalling system*" by Q. Gu et al., two novel approaches named service headway braking and extending stopping distance interval are developed, in which the restarting times of the trains are staggered and the traction periods are reduced.

The network control and autonomous vehicles are two promising topics which are not isolated from each other. In the work entitled "*Spatial path following for AUVs using adaptive neural network controllers*" by J. Zhou et al., the path following for autonomous vehicles is studied. Both ocean current and the systemic variations are considered. Observers are designed to observe the ocean current which is treated as the external disturbance. The uncertain parameters are also estimated. The bilateral control is studied in "*Stability problem of wave variable based bilateral control: influence of the force source design*" by D. Tian et al. The influence of the time delay is considered. Experimental test results validate the developed theory. X. Gu et al. study the trajectory planning of multiple unmanned combat aerial vehicles in the paper "*A virtual motion camouflage approach for cooperative trajectory planning of multiple UCAVs*." Simulation experiments are provided to show the performance of the proposed approach. A path planning method for unmanned air vehicles is developed in the paper "*Efficient UAV path planning with multiconstraints in a 3D large battlefield environment*" by W. Zhan et al. The proposed method has the capacity to find the optimal trajectory between two points. Experimental test results are also offered. For the CAN-network-induced delay, D. Wang et al. proposed the delay model of average online delay in the work entitled "*Modeling and analysis of online delay of nonperiodic CAN message*." The actual delays among several CAN nodes are measured to validate the developed model. As the CAN bus has been widely used in industry, the developed model can be employed to improve the control performance. The game theoretic approach is used to deal with the distributed localization problem in "*On distributed localization for road sensor networks: a game theoretic approach*" by J. Jia et al. Several techniques are also provided to enhance the convergence speed of the algorithm. In the work entitled "*Optimal ascent guidance for air-breathing launch vehicle based on optimal trajectory correction*" by X. Lu et al., based on the optimal trajectory correction, an optimal guidance algorithm is proposed for air-breathing launch vehicle which is a nonlinear system.

Acknowledgments

This special issue provides an up-to-date research progress in the area of advanced control and optimization with applications to complex vehicle systems such as the ground vehicle and underwater vehicles. We really appreciate all the authors for contributing submissions to the special issue. Meanwhile, we also would like to acknowledge all the anonymous reviewers for the voluntary work. In addition, special thanks are due to the China Postdoctoral Science Foundation (2012M520028), the National Natural Science Foundation of China (51205155, 61374213), and the National Basic Research Program of China (973 Program) (2011CB711201) for supporting authors' research.

Hui Zhang
Hamid Reza Karimi
Xinjie Zhang
Junmin Wang

Hindawi Publishing Corporation
Mathematical Problems in Engineering
Volume 2014, Article ID 809642, 15 pages
http://dx.doi.org/10.1155/2014/809642

Research Article

Optimal Solution for VLSI Physical Design Automation Using Hybrid Genetic Algorithm

I. Hameem Shanavas[1,2] and R. K. Gnanamurthy[3]

[1] *Anna University, Chennai, India*
[2] *MVJ College of Engineering, Bangalore 560067, India*
[3] *SKP Engineering College, Tiruvannamalai, Tamilnadu 606611, India*

Correspondence should be addressed to I. Hameem Shanavas; hameemshan@gmail.com

Received 30 July 2013; Revised 15 November 2013; Accepted 17 November 2013; Published 9 April 2014

Academic Editor: Hamid Reza Karimi

In Optimization of VLSI Physical Design, area minimization and interconnect length minimization is an important objective in physical design automation of very large scale integration chips. The objective of minimizing the area and interconnect length would scale down the size of integrated chips. To meet the above objective, it is necessary to find an optimal solution for physical design components like partitioning, floorplanning, placement, and routing. This work helps to perform the optimization of the benchmark circuits with the above said components of physical design using hierarchical approach of evolutionary algorithms. The goal of minimizing the delay in partitioning, minimizing the silicon area in floorplanning, minimizing the layout area in placement, minimizing the wirelength in routing has indefinite influence on other criteria like power, clock, speed, cost, and so forth. Hybrid evolutionary algorithm is applied on each of its phases to achieve the objective. Because evolutionary algorithm that includes one or many local search steps within its evolutionary cycles to obtain the minimization of area and interconnect length. This approach combines a hierarchical design like genetic algorithm and simulated annealing to attain the objective. This hybrid approach can quickly produce optimal solutions for the popular benchmarks.

1. Introduction

Physical design automation has been an active area of research for atleast three decades. The main reason is that physical design of chips has become a crucial and critical design task today due to the enormous increase of system complexity and the future advances of electronic circuit design and fabrication. Most commonly used high-level synthesis tools allow the designers to automatically generate huge systems simply by just changing a few lines of code in the functional specification. Nowadays, the open source codes simulated in open source software can automatically be converted to hardware description codes, but the automatically generated codes are not optimized ones. Synthesis and simulation tools often cannot hold with the complexity of the entire system under development. Every time designers want to concentrate on typical parts of a system to upgrade the speed of the design cycle. Thus the present state-of-the-art design technology requires a better solution for the system with fast and effective optimization [1]. Moreover, fabrication and packing technology makes the demand for increasing smaller feature sizes and augmenting the die dimensions possible to allow a circuit for accommodating several millions of transistors; however, logical circuits are restricted in their size and in the number of external pin connections.

So the technology requires partitioning of a system into manageable components by arranging the circuit blocks without wasting empty spaces. The direct implementation of large circuit without going for optimization will occupy large area. Hence the large circuit is necessary to split into small subcircuits. This will minimize the area of the manageable system and the complexity of the large system. When the circuit is partitioned, the connection between two modules or say partitions should be minimum. It is a design task by applying a hierarchical algorithmic approach to solve typical combinatorial optimization problems like dividing a large

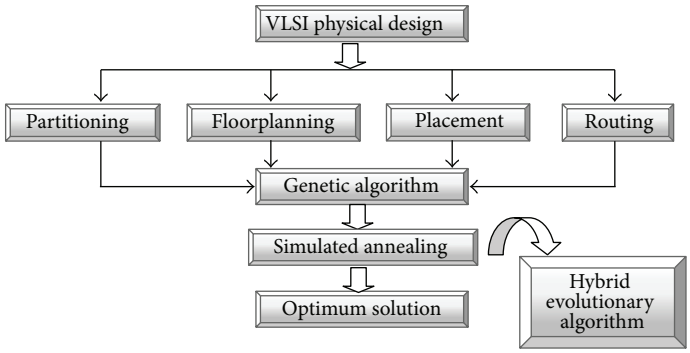

Figure 1: Design flow for the proposed approach.

circuit system into smaller pieces. Figure 1 shows the design flow for the proposed approach.

The method of finding block positions and shapes with minimizing the area objective is referred to as floorplanning. The input to the floorplanning is the output of system partitioning and design entry. Floorplanning paves the way to predict the interconnect delay by estimating the interconnect length. This is achieved because both interconnect delay and gate delay decrease as feature size of the circuit chips is scaled down—but at different rates. The goals of floorplanning are to (a) arrange the blocks on a chip, (b) decide the location of input and output pads, (c) decide the location and number of the power pads (d) decide the type of power distribution, and (e) decide the location and type of clock distribution.

Placement is much more suited to automation than floorplanning. The goal of a placement tool is to arrange all the logic cells with the flexible blocks on a chip. Ideally, the objectives of placement are to (a) minimize all the critical net delays, (b) make the chips as dense as possible, (c) guarantee the router can complete the routing step, (d) minimize power dissipation, and (e) minimize cross-talk between signals. The most commonly used objectives are (a) minimizing the total estimated interconnect length, (b) meeting the timing requirement for critical nets, and (c) minimizing the interconnect congestion.

Once the floorplanning of the chip and the logic cells within the flexible blocks placement are completed, then it is time to make the connection by routing the chip. This is still a hard problem that is made easier by dividing into smaller problems. Routing is usually split into global routing followed by the detailed routing. Global routing is not allowed to finalize the connections; instead it just plans the connections to achieve in a better way. There are two types of areas to global route: one inside the flexible blocks and another between the blocks. The global routing step determines the channels to be used for each interconnect. Using this information the detailed router decides the exact location and layers for each interconnect. The objectives are to minimize the total interconnect length and area and minimize the delay of critical paths [2]. Figure 15 shows the overall area minimized using hybrid evolutionary algorithm.

When the physical design components like partitioning, floorplanning, placement, and routing are combined and optimized in terms of area, then the cost increasing criteria like power and clock speed of each module can be controlled, and these subobjective criteria can also be optimized to a further extent. In the last three decades many interchanging methods have been used which also resulted in local optimum solutions. And later some of the mathematical approaches were also introduced with some heuristics models which resulted in better result but they have their own advantage and disadvantage. Since lots of solutions are possible for this kind of problem, hence stochastic optimization techniques are commonly utilized. Till today many techniques have been proposed like global search algorithm (GSA) which combines the local search algorithm (LSA) to produce a better result.

Global optimization technique like genetic algorithm (GA) which captured the context of generation from biological system had been used for physical design problems like circuit partitioning, floorplanning, placement, and routing. Genetic algorithm has been applied to several problems, which are based on graph because the genetic analogy can be most easily applied to any kind of problems. Lots of researchers have proposed their theories to minimize the feature size of the circuit using GA. Theodore Manikas and James Cain proposed that GA requires more memory but it takes less time than simulated annealing [3]. Sipakoulis et al. confessed that number of enhancements like crossover operator mutation or choosing different fitness functions can still be made to achieve optimal solutions [4]. This means that theory of GA still provides chances for new developments that can help in finding new optimal solutions for physical design problems. This work proposes hybrid evolutionary algorithm to solve the graph physical design component problems. This method includes several genetic algorithm features, namely, selecting population, performing crossover of the selected chromosomes, and if necessary mutation to get better stable solutions. This work tried to hybrid two evolutionary algorithms like genetic algorithm and simulated annealing to overcome the disadvantage of one another. Such type of algorithms with general iterative heuristic approach are called hybrid evolutionary algorithms or memetic algorithm in common.

This work addresses the problem of circuit partitioning with the objective of reducing delay, circuit floorplanning

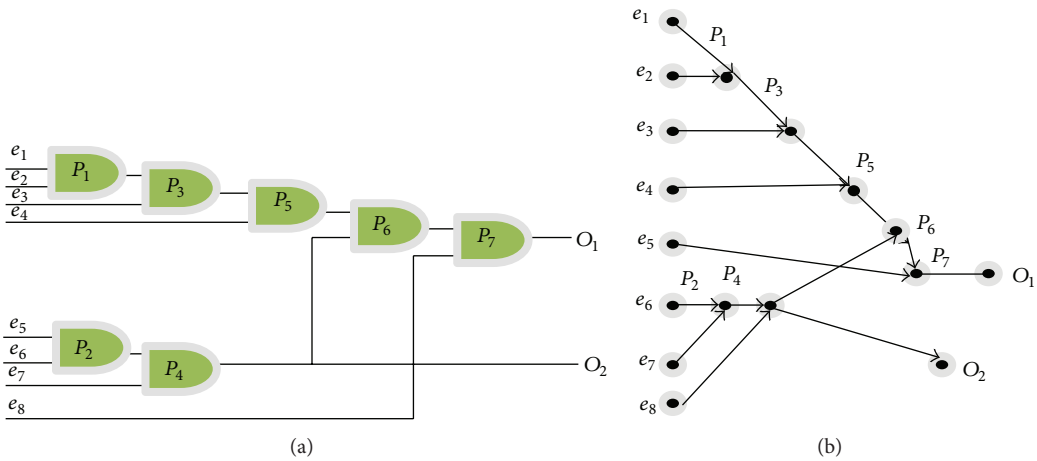

Figure 2: (a) Model circuit, (b) graphical representation of circuit.

with the objective of reducing area, placement with the objective of minimizing the layout area, and routing with the objective of minimizing the interconnect length. The main objective of area optimization and interconnect length reduction can be achieved by incorporating hybrid evolutionary algorithm (HEA) in VLSI physical design components.

2. Graphical Representation of Physical Design Components

2.1. Partitioning. Circuit partition will reduce big circuits into small subcircuits and result in a better routing area for the layout. Circuit partitioning problem belongs to the class of NP-hard optimization problems [5]. To measure connectivity, it is necessary to get help from the mathematics of graph theory. Figure 2 states this problem can be considered as a graph partitioning problem where each modules (gates, logic cells, etc.) are taken as vertices (nodes or points) and the connection between two logic cells represents the edges [6].

The algorithm starts with n gates placed on the graph as n vertex, and an initial population has to be chosen as the different permutations of various vertices of the given graph. Given is an unweighted connected graph $G = (V, E)$ on set of vertices V and edges E. Let $n \geq 2$ be a given integer and find a partition $P_1, P_2, P_3, \ldots, P_j$ set of vertices V such that

(i) $G_i = (V_i, E_i)$, for all values $i = 1, 2, 3, \ldots, k$, are connected.

2.2. Floorplanning. A module B is a rectangle of height H_B, width W_B, and area A_B. A super module consists of several modules, also called a subfloorplan. A floorplan for n modules consists of an enveloping rectangle R subdivided by horizontal lines and vertical lines into n nonoverlapping rectangles. Each rectangle must be large enough to accommodate the module assigned to it. In the given problem, a set of hard modules and outline constraints are provided. The modules inside the given outline have freedom to move [7, 8]. A feasible packing is in the first quadrant such that all the modules inside the outline should not duplicate and overlap each other. The objective is to construct a feasible floorplan R such that the total area of the floorplan R is minimized and simultaneously satisfies floorplanning constraint. Given is a set of modules to a specified number of cluster satisfying the predescribed properties. To solve the floorplanning problem, first construct a network graph, and then run the given algorithm to get the solution. The graph consists of two kinds of vertices like horizontal and vertical. The network graph $G = (V, E)$ has to be constructed. "$*$" represents vertical slicing of blocks. "+" represents horizontal slicing of blocks.

2.3. Placement. To position the components of the circuit in general-cell and standard-cell placement, such that the layout area is minimized, the area used here comprises the area used by the circuit components and the area needed for wiring the circuit components. The placement problem can be mainly classified into two, one dimensional packing problem and the other connection cost optimization problem. The packing problem is concerned about fitting a number of cells with different sizes and shapes tightly into a rectangular chip. Given is a set of modules $M_1, M_2, \ldots, M_n$ and set of k interconnects $N_1, N_2, \ldots, N_k$. When meeting the objective of the placement, it can also help to obtain the nonoverlapping package of all the modules which achieves some optimization objective such as minimizing the area of package and the interconnection length as shown in Figure 5.

Horizontal constraint is as follows.

If $(A, B) = (\ldots x \ldots y \ldots, x \ldots y \ldots)$ block y is at the right side of the block x.

Vertical constraint is as follows.

If $(A, B) = (\ldots x \ldots y \ldots, y \ldots x \ldots)$ block y is at the below side of the block x.

(1) Consider $V = \{S_h\} \cup \{T_h\} \cup \{y_i \mid i = 1, \ldots, M\}$, where y_i corresponds to the block, S_h is the source node representing the left boundary, and T_h is the target node representing the right boundary.

(2) Consider $E = \{(S_h, y_i) \mid i = 1, \ldots, M\} \cup \{(y_i, T_h) \mid i = 1, \ldots, N\} \cup \{(y_i, y_j) \mid \ldots y_i \ldots y_j\}$.

If existing edge (y_i, y_{i+1}), edge (y_{i+1}, y_{i+2}), and edge (y_i, y_{i+2}), then (y_i, y_{i+2}) is omitted.

(3) Vertex weight equals the width of the block y_i but zero for S_h and T_h, similarly to the vertical constraint graph (VGH) as shown in Figure 6.

Vertical constraint graph $G_v(V, E)$ is constructed for Figure 5 using "above" constraint and the height of each block. The corresponding constraint graphs $G_h(V, E)$ and $G_v(V, E)$ are as shown in Figures 6 and 7. Both $G_h(V, E)$ and $G_v(V, E)$ are vertex-weighted acyclic graphs so longest path algorithm can be applied to find the x and y coordinates of each block. The coordinates of the block coordinate of the lower left corner of the block.

Based on "left of" constraint of (A, B), a directed and vertex-weighted graph $G_h(V, E)$ (V: vertex set, E: edge set), called the horizontal-constraint graph (HCG), is constructed.

2.4. Routing. The classical approach in routing is to construct an initial solution by using constructive heuristic algorithms. A final solution is then produced by using iterative improvement techniques. A small modification is usually accepted if that makes reduction in cost; otherwise, it will be rejected. Constructive heuristic algorithms produce an initial solution from scratch. It takes a very small amount of computation time compared to iterative improvement algorithms and provides a good starting point for them (SM91). However, the solution generated by constructive algorithms may be far from optimal. Thus, an iterative improvement algorithm is performed next to improving the solution.

Although iterative improvement algorithms can produce a good final solution, the computation time of such algorithms is also large. Therefore, a hierarchical approach in the form of multilevel clustering is utilized to reduce the complexity of the search space. A bottom-up technique gradually clusters cells at several levels of the hierarchy. At the top level a genetic algorithm is applied where several good initial solutions are injected in to the population.

A local search technique with dynamic hill climbing capability is applied to the chromosomes to enhance their quality. The system tackles some of the hard constraints imposed on the problem with intermediate relaxation mechanism to further enhance the solution quality.

This problem is a particular example of graph partitioning problem. In general algorithms like exact and approximation run in polynomial time but do not exist for graph partitioning problems. This makes the necessity to solve the problem using heuristic algorithms. Genetic algorithm is a heuristic technique and the best choice that seeks to imitate the behavior of biological reproduction and its capability to collectively solve the given problem. GA can provide several alternative solutions to the optimization problem, which are considered as individuals in a population. These solutions are coded as binary strings, called chromosomes. The initial population is constructed randomly. These individuals are evaluated using partitioning by specific fitness function. GA then uses these individuals to produce a new generation of hopefully better solutions. In each generation, two of the individuals are selected probabilistically as parents, with the selection probability proportional to their fitness. Crossover is performed on these individuals to generate two new individuals, called offspring, by exchanging parts of their structure. Thus each offspring inherits a combination of features from both parents. The next step is mutation. An incremental change is made to each member of the population, with a small probability. This ensures that GA can explore new features that may not be in the population yet. It makes the entire search space reachable, despite the finite population size. The basic foundation of the algorithm is to represent each vertex in the graph as a location that can represent a logic gate and a connection is represented by an edge.

3. Global Optimization Using GA

Genetic algorithms are optimization strategies that imitate the biological evolution process. A population of individuals representing different problem solutions is subjected to genetic operators, such as selection, crossover, and mutation, that are derived from the model of evolution. Using these operators the individuals are steadily improved over many generations and eventually the best individual resulting from this process is presented as the best solution to the problem.

Consider the graph $G = (V, E)$ with vertex $|v| = u$ and in integer $1 < k < n/4$. Initialize a randomly generated population P of k elements. Population P has 1 to k elements. Assume each parent p_1 to p_k belong to the population P. Perform two point crossover for p_a and p_b from population P using the fitness function $(f) = k \cdot M(p)/n$, where $M(p)$ is the number of node of partition with maximum cardinality among n partitions. Assume $P_a(I)$ and $P_b(I)$ are the children from p_a and p_b, respectively. If $P_a(I)$ has not satisfied the fitness ($P_a(I)$ is not in I) then choose p_a randomly from $j > i$. Swap $P_a(i)$ and $P_a(j)$. Copy the first element k elements of p_a in q_1, q_3. If $P_b(I)$ has not satisfied the fitness ($P_b(I)$ is not in I) then choose p_b randomly from $h > k$. Swap $P_b(h)$ and $P_b(i)$. Copy the first element k elements of p_b in q_2, q_4. Create two vectors L, L' with $2(n - k)$ elements. If (j mod 2 = 1) then $L(i) = P_a[k + (j + 1)/2]$ and $L'(i) = P_b[k + (j + 1)/2]$, else $L(j) = P_a[k + (j + 1)/2]$ and $L'(j) = P_b[k + (j + 1)/2]$. Check the fitness of $L(i)$, $L'(i)$, $L(j)$, and $L'(j)$. If $L(i)$ is not in q_1, then copy $L'(i)$ in q_1 and $L(i)$ in q_2. If $L(j)$ is not in q_3, then copy $L'(j)$ in q_3 and $L(j)$ in q_4. Repeat the process again with $L(i)$ and $L(j)$, $L'(i)$ and $L'(j)$ to get new offspring. The new offsprings can have more fitness value or less fitness value depending upon the parents. Less fitness offspring can be discarded then to reduce the number of cycles. In this work, the pure genetic algorithm is combined with simulated annealing to produce the optimal result. The algorithm starts with the initial random population generation. It is essential to set the initial population, number of generation, crossover type, and mutation rate. First step of the genetic algorithm starts with the selection process; the selection process is based on the fitness function through which the chromosomes were selected from the crossover. Crossover is the reference point

for the next generation population. The crossover technique used in genetic algorithm is one-point crossover, two-point crossover, cut and splice crossover, uniform crossover, half uniform crossover, and so forth, depending upon the necessity. After crossover the mutation process, to maintain the genetic diversity from one generation to next generation. In this mutation the genetic sequence will be changed from its original sequence by generating a random variable for each bit sequence. After the mutation offspring with fitness are placed in the new population for further iteration. The next step is to apply the local optimization algorithm in between this genetic algorithm as told before; the local optimization is applied in three ways which are mentioned below: (a) before the crossover, (b) after the crossover, and (c) before and after the crossover.

Exhaustive Hybridization. Few solutions are selected from the final generation and improved using local search. Figure 16 shows simulated results for final generation.

Intermediate Hybridization. After a predetermined number of iterations by GA, local search is applied to few random individuals. This is done to have a better solution than the local maxima. This work deals with intermediate memetic algorithm.

3.1. Creation of Initial Population. The initial population is constructed from randomly created routing structures, that is, individuals. First, each of these individuals is assigned a random initial row number y_{ind}. Let $S = \{s_1, \ldots, s_i, \ldots, s_k\}$ be the set of all pins of the channel which are not connected yet and let $T = \{t_1, \ldots, t_j, \ldots, t_l\}$ be the set of all pins having at least one connection to other pin. Initially $T = 0$. A pin $S_i \in S$ is chosen randomly among all elements in S. If T contains pins $\{t_u, \ldots, t_j, \ldots, t_v\}$ (with $1 \le u < v \le l$) of the same net, a pin t_j is randomly selected among them. Otherwise, a second pin of the same net is randomly chosen from S and transferred into T. Both pins (s_i, t_j) are connected with a so-called random routing. Then s_i is transferred into T. The process continues with the next random selection of $s_i \in S$ until $S = 0$. The creation of the initial population is finished when the number of completely routed channels is equal to the population size $|P_c|$. As a consequence of our strategy, these initial individuals are quite different from each other and scattered all over the search space.

3.2. Populations and Chromosomes. In GA based optimizations a set of trial solutions are assembled as a population. The parameter set representing each trial solution or individual is coded to form a string or chromosome and each individual is assigned a fitness value by evaluation of the objective function. The objective function is to only link between the GA optimizer and the physical problem.

3.3. Calculation of Fitness. The fitness of the individual in partitioning is based on the delay of the module. The fitness of the individual is given by weighted evaluations of maximum delay (D). D_a identifies a particular subgraph, D_m is a predetermined maximum value, and D_f is the weighting factor. Delay can be measured using the difference between final time and initial time. The sum of the weighting factors equals one. The complete fitness function for partitioning is given in the following:

$$D_p = \left\{ \frac{D_a}{D_m} > 1, \frac{D_a}{D_m} \le 1, \frac{D_a}{D_m} * D_f \right\}, \tag{1}$$

$$\text{Total Delay} = \sum_{P=1}^{M} Dp. \tag{2}$$

Assuming an individual is fully feasible and meets constraints, the value of $D_p \le 1$, with smaller values being better.

At the beginning, a set of Polish expressions is given for floorplanning. It is denoted as P, randomly generated expression to compose a population. The fitness for floorplanning of the individual is based on the area of the module. Area of a block can be calculated by the general formula $A = LW$, where L stands for length of the module and W stands for width of the module:

$$\text{Total Area} = \sum_{f=1}^{M} Af. \tag{3}$$

The fitness of the individual is given by weighted evaluations of maximum area (A). A_a identifies a particular subgraph, A_m is a predetermined maximum value, and A_f is the weighting factor. The sum of the weighting factors equals one. The complete fitness function floorplanning is given in the following:

$$G_f = \left\{ \frac{A_a}{A_m} > 1, \frac{A_a}{A_m} \le 1, \frac{A_a}{A_m} * A_f \right\}. \tag{4}$$

The fitness $F(p)$ of each individual $p \in P$ is calculated to assess the quality of its routing structure relative to the rest of the population P. The selection of the mates for crossover and the selection of individuals which are transferred into the next generation are based on these fitness values. First, two functions $F_1(p)$ and $F_2(p)$ are calculated for each individual $p \in P$ according to

$$F_1(p) = \frac{1}{n_{\text{row}}}, \tag{5}$$

where n_{row} = number of rows of p, and

$$F_2(p) = \frac{1}{\sum_{i=1}^{n_{\text{ind}}} \left(l_{\text{acc}}(i) + a * l_{\text{opp}}(i) \right) + b * v_{\text{ind}}}, \tag{6}$$

where $l_{\text{acc}}(i)$ = net length of net i of net segments according to the preferred direction of the layer, $l_{\text{opp}}(i)$ = net length of net i of net segments opposite to the preferred direction of the layer, a = cost factor for the preferred direction, n_{ind} = number of nets of individual p, v_{ind} = number of vias of individual p, and b = cost factor for vias.

The final fitness $F(p)$ is derived from $F_1(p)$ and $F_2(p)$ in such a way that the area minimization, that is, the number

of rows, always predominates the net length and the number of vias. After the evaluation of $F(p)$ for all individuals of the population P these values are scaled linearly as described in order to control the variance of the fitness in the population.

In placement the cells present in the module are connected by wire. The estimation of interconnect length required for connection is calculated by

$$I_L = \sum_{I>j} w_{i,j} \left(\left(x_i - x_j \right)^2 + \left(y_i - y_j \right)^2 \right), \tag{7}$$

where $w_{i,j}$ is the weight of the connection between cell x and y, $(x_i - x_j)$ is the distance between two cells in X direction, and $(y_i - y_j)$ is the distance between two cells in Y direction.

Interconnect length of each net in the circuit is estimated during Steiner tree and then total Interconnect length is computed by adding the individual estimates:

$$\text{Cost} = \sum_{L=1}^{M} I_L, \tag{8}$$

where I_L is the interconnect length estimation for net i and M denotes total number of nets in circuit.

3.4. Parents. Following this initialization process, pairs of individuals are selected (with replacement) from the population in a probabilistic manner weighted by their relative fitness and designated as parents.

3.5. Children. A pair of offspring, or children, are then generated from the selected pair of parents by the application of simple stochastic operators. The principle operators are crossover and mutation. Crossover occurs with a probability of pcross (typ. 0.6–0.8) and involves the random selection of a crossover site and combining the two parent's genetic information. The two children produced share the characteristics of the parents as a result of these recombination operators. Other recombination operators are sometimes used, but crossover is the most important. Recombination (e.g., crossover) and selection are the principle way that evolution occurs in a GA optimization.

3.6. Mutation. Mutation introduces new and unexplored points into the GA optimizer's search domain. Mutation randomly changes the genetic makeup of the population. Mutation is much less important than recombination and occurs with a probability pmutation (typ. 0.05) which is much less than pcross.

3.7. New Generation. Reproduction consisting of selection, recombination, and mutation continues until a new generation is created to replace the original generation. Highly fit individuals, or more precisely highly fit characteristics, produce more copies of themselves in subsequent generation resulting in a general drift of the population as a whole towards an optimal solution point. The process can be terminated in several ways: threshold on the best individual (i.e., the process stops when an individual has an error less than some amount E), number of generations exceeds a preselected value, or some other appropriate criteria. A simple genetic algorithm must be able to perform five basic tasks: encode the solution parameters in the form of chromosomes, initialize a starting point population, evaluate and assign fitness values to individuals in the population, perform reproduction through the fitness weighted selection of individuals from the population, and perform recombination and mutation to produce members of the next generation [8–14].

4. Local Optimization Using SA

After a prescribed number of iterations by evolutionary algorithm local search algorithm is applied to few random individuals to have better solution. But simulated annealing algorithm is not a local search algorithm. Local search methods are iterative algorithms that tend to enhance solution by stepwise improvement and make an attempt to reach optimum solutions. SA is being used in this work. More often results in suboptimal solutions by trapping themselves in local minima/maxima. The simplest form of local search is repetitively flipping elements in a solution resulting in a gain in the objective function. Eventually local minima will be reached, whereby flipping any element in the solution will result in loss of object. Although these algorithms are simple, there have been many complex improvements for CAD tools which involve large dynamic memory and linked list usages. For refining the solution obtained by GA, the local search (LS) is applied. This can be used before crossover or after crossover; it can also be used for parents selection and used before or after mutation to increase the number of fitness variables (Algorithm 1).

5. Optimization by Simulated Annealing

Simulated annealing algorithm is applied for local search process since SA is not a local search algorithm. Here simulated annealing method is performed on finally generated offspring to improve the fitness. This method is called intermediate MA.

Simulated annealing is a stochastic computational method for finding global extrema to large optimization problems. It was first proposed as an optimization technique by Kirkpatrick et al. in 1983 [15] and Cerny in 1984 [16]. The optimization problem can be formulated by describing a discrete set of configurations (i.e., parameter values) and the objective function to be optimized. The problem is then to find a vector that is optimal. The optimization algorithm is based on a physical annealing analogy. Physical annealing is a process in which a solid is first heated until all particles are randomly arranged in a liquid state, followed by a slow cooling process. At each (cooling) temperature enough time is spent for the solid to reach thermal equilibrium, where energy levels follow a Boltzmann distribution. As temperature decreases the probability tends to concentrate on low energy states. Care must be taken to reach thermal equilibrium prior to decreasing the temperature. At thermal

```
Begin
   Initialize population P;
   For i := 1 To size of (P) Do
         Individual := P_i;
         Individual := Local_Search(Individual);
   Repeat Until (terminate = True) Do
      For i := 1 To #recombination Do
         Select two parents i_a, i_b ∈ P randomly;
         i_c := Recombination(i_a, i_b);
         i_c := Local Search(i_c);
   Add individual i_c to P;
   P := Select (P);
   If (P) converged Then
         For i := 1 To size of (P), i != index(Best) Do
         Individual := P_i
   Individual := Local_Search(Mutate(Individual));
End
```

Algorithm 1

equilibrium, the probability that a system is in a macroscopic configuration with energy is given by the Boltzmann distribution. The behavior of a system of particles can be simulated using a stochastic relaxation technique developed by Metropolis et al. [17]. The candidate configuration for the time is generated randomly. The new candidate is accepted or rejected based on the difference between the energies associated with states. The condition to be accepted is determined by

$$p = \frac{p_r}{p_q} = \frac{\exp\left(-E_j - E_i\right)}{K_t} > 1. \tag{9}$$

Given a current state i of the solid with energy level E_i, generate a subsequent state j randomly (by small perturbation).

Let E_j be the energy level at state j.

(i) If $E_j - E_i \leq 0$, then accept state j as the current state.

(ii) If $E_j - E_i > 0$, then accept state j with the probability $\exp(-E_j - E_i)/K_t$.

K_t where k is the Boltzmann constant.

One feature of the Metropolis way of simulated annealing algorithm is that a transition out of a local minimum is always possible at nonzero temperature. Another evenly interesting property of the algorithm is that it performs a kind of adaptive divide and conquer approach. Gross features of the system appear at higher temperatures; fine features develop at lower temperatures. For this application, it used the implementation by Ingber [18]. Each solution corresponds to a state of the system. Cost corresponds to the energy level. Neighborhood corresponds to a set of subsequent states that the current state can reach. Control parameter corresponds to temperature.

5.1. Partitioning Based on Simulated Annealing. The basic procedure in simulated annealing is to start with an initial partitioning and accept all perturbations or moves which result in a reduction in cost. Moves that result in a cost increase are accepted. The probability of accepting such a move decreasing with the increase in cost and also decreasing in later stages of the algorithm is given in (11). A parameter T, called the temperature, is used to control the acceptance probability of the cost-increasing moves. Simulated annealing algorithm for partitioning the modules will be described here. The cells are partitioned using simulated annealing so as to minimize the estimated interconnect length. There are two methods for generating new configurations from the current configuration [19]. Either a cell is chosen randomly and placed in a random location on the chip or two cells are selected randomly and interchanged. The performance of the algorithm was observed to depend upon r, the ratio of displacements to interchanges. Experimentally, r is chosen between 3 and 8. A temperature-dependent range limiter is used to limit the distance over which a cell can move. Initially, the span of the range limiter is twice the span of the chip. In other words, there is no effective range limiter for the high temperature range. The span decreases logarithmically with the temperature. Temperature span is given in the following:

$$\begin{aligned} L_{W_V}(T) &= L_{W_V}(T_i)\left[\frac{\log T}{\log T_i}\right], \\ L_{W_H}(T) &= L_{W_H}(T_i)\left[\frac{\log T}{\log T_i}\right], \end{aligned} \tag{10}$$

where T is the current temperature, T_i is the initial temperature, and $L_{W_V}(T_i)$ and $L_{W_H}(T_i)$ are the initial values of the vertical and horizontal window spans $L_{W_V}(T)$ and $L_{W_H}(T)$, respectively.

The wirelength cost C is estimated using the semiperimeter method, with weighting of critical nets and independent weighting of horizontal and vertical wiring spans for each net:

$$C = \sum_{\text{nets } i} \left[x(i)\, W_H(i) + y(i)\, W_V(i)\right], \tag{11}$$

where $x(i)$ and $y(i)$ are the vertical and horizontal spans of the net i's bounding rectangle and $W_H(i)$ and $W_V(i)$ are the weights of the horizontal and vertical wiring spans. When critical nets are assigned a higher weight, the annealing algorithm will try to place the cells interconnected by critical nets close to each other. Independent horizontal and vertical weights give the user the flexibility to prefer connections in one direction over the other. The acceptance probability is given by $\exp(-\Delta C/T)$, where ΔC (i.e., $E_i - E_j$) is the cost increase and T is the current temperature. When the cost increases, or when the temperature decreases, the acceptance probability (9) gets closer to zero. Thus, the acceptance probability $\exp(-\Delta C/T)$ less than random (0, 1) (a random number between 0 and 1) is high when ΔC is small and when T is large. At each temperature, a fixed number of moves per cell is allowed. This number is specified by the user. The higher the maximum number of moves, the better the results obtained. However, the computation time increases rapidly. There is a recommended number of moves per cell as a function of the problem size in. For example, for a 200-cell and 3000-cell circuit, 100 and 700 moves per cell are recommended, respectively.

The annealing process starts at a very high temperature, for example, $T_i = 4{,}000{,}000$, to accept most of the moves. The cooling schedule is represented by $T_i + 1 = a(T)$, where $a(T)$ is the cooling rate parameter and is determined experimentally. In the high and low temperature ranges, the temperature is reduced rapidly (e.g., $a(T) \approx 0.8$). However, in the medium temperature range, the temperature is reduced slowly (e.g., $a(T) \approx 0.95$). The algorithm is terminated when T is very small, for example, when $T < 0.1$. Within each temperature range the number of moves has been built experimentally. Once the number of moves is set, fix the particular move for the remainder of the scheduling.

5.2. Floorplanning Based on Simulated Annealing. This section describes an optimal floorplanning on simulated annealing algorithm. Assume that a set of modules is given and each module can be implemented in a finite number of ways, characterized by its width and height. Some of the important issues in the design of a simulated annealing optimization problem are as follows:

(1) the solution space,

(2) the movement from one solution to another,

(3) the cost evaluation function.

The branch cells correspond to the operands and the internal nodes correspond to the operators of the Polish expression. Figure 3 shows the floorplan module. A binary tree can also be constructed from a Polish expression by using a stack as shown in Figure 4. The simulated annealing algorithm moves from one Polish expression to another. A floorplan may have different slicing tree representations. For example, the tree in Figure 4 represents the given floorplan in Figures 8, 9, and 10. There is a one-to-one correspondence between a floorplan and its normalized Polish expression. But this leads to a larger solution space and some bias towards floorplans with multitree representations, since they have more chances to be visited in the annealing process. Assume three types of movement are defined to move from one floorplan to another. They operate on the Polish expression representation of the floorplan [20].

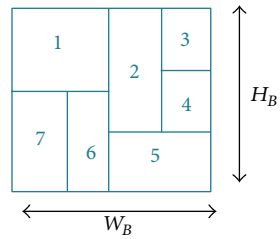

Figure 3: Floorplan module.

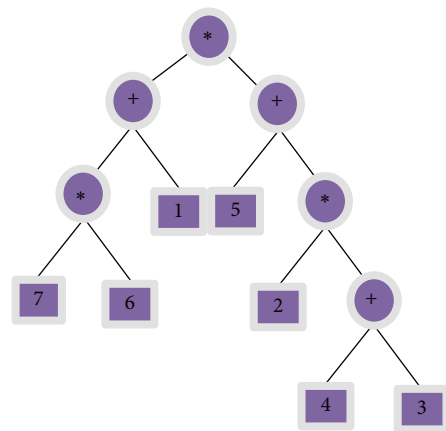

Polish expression: 76∗1+43+2∗5+∗

Figure 4: Graph representation of the given floorplan module.

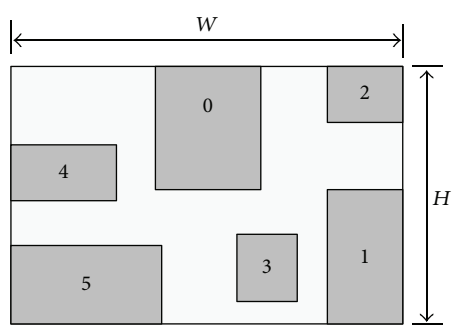

Figure 5: Placement module.

Condition 1. Exchange two operands when there are no other operands in between ($67 * 1 + 34 + 2 * 5 + *$).

Condition 2. Complement a series of operators between two operands ($67 + 1 * 34 * 2 + 5 * +$).

Condition 3. Exchange adjacent operand and operator if the resulting expression is a normalized Polish expression ($67 + 43 * +25 * 1 + *$).

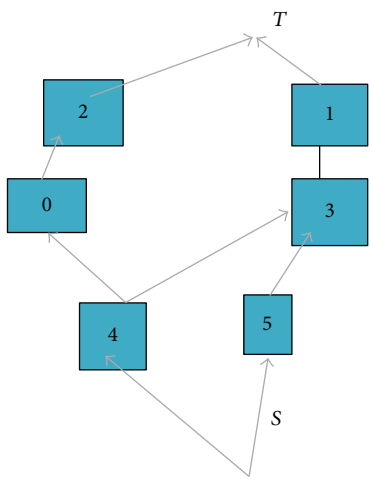

Figure 6: Vertical constraint graph (VGH) for the given block $G_v(V, E)$.

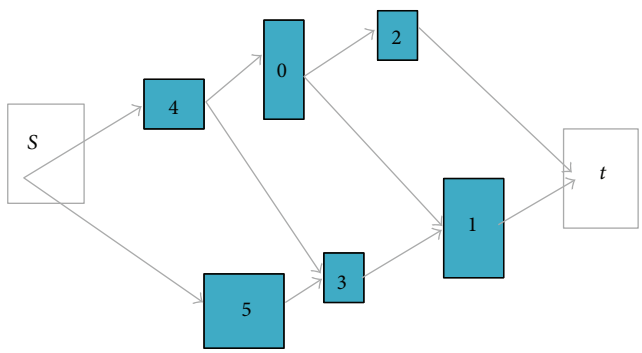

Figure 7: Horizontal constraint graph (HGH) for the given block $G_h(V, E)$.

It is obvious that the movements will generate only normalized Polish expressions. Thus, in effect, the algorithm moves from one floorplan to another. Starting from an arbitrary floorplan, it is possible to visit all the floorplans using the movement. If some floorplans cannot be reached, there is a danger of losing some valid floorplans in the solution. Starting from any floorplan, the modules can move to the floorplan based on the given conditions. The cost function is a function of the floorplan or equivalently the Polish expression. There are two components for the cost function, area and wirelength. The area of a sliceable floorplan can be computed easily using the floorplan sizing algorithm [21]. The wirelength cost can be estimated from the perimeter of the bounding box of each net, assuming that all terminals are located on the center of their module. In general, there is no universally agreed upon method of cost estimation. For simulated annealing, the cost function is best evaluated easily because thousands of solutions need to be examined. Figures 8, 9, and 10 show a series of movements which lead to a solution. We have implemented the exponential function for the accept method.

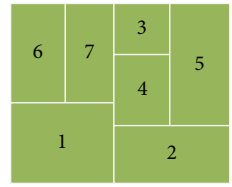

Figure 8: Condition 1 $(67 * 1 + 34 + 2 * 5 + *)$.

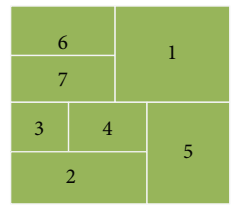

Figure 9: Condition 2 $(67 + 1 * 34 * 2 + 5 * +)$.

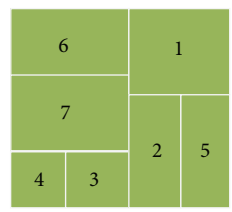

Figure 10: Condition 3 $(67 + 43 * +25 * 1 + *)$.

5.3. Placement Based on Simulated Annealing. Simulated annealing algorithm mimics the annealing process used to gradually cool molten metal to produce high quality metal structures:

(i) initial placement improved by iterative swaps and moves,

(ii) accept swaps if they improve the cost,

(iii) accept swaps that degrade the cost under some probability conditions to prevent the algorithm from being trapped in a local minimum and can reach globally optimal solution given enough time.

The advantage of using SA are open cost function, wirelength cost, and timing cost. Along with the advantage it also has its disadvantage of slowness. The purpose of our algorithm is to find a placement of the standard cells such that the total estimated interconnection cost is minimized. The algorithm for placement if divide into four principal components [22].

5.3.1. Initial Configuration. Initially the circuit decomposed into individual cells and found out the input and output cells for each cell.

Then it starts the annealing procedure by placing the cells on the chip randomly. And finally it calculates the total area of the circuit and places the cells accordingly so that they are placed at equal distances from each other.

Table 1: Partitioning optimization of GA compared with hybrid algorithm.

Circuit	GA			Hybrid		
	Delay (ps)	T (s)	Best (s)	Delay (ps)	T (s)	Best (s)
S1196	396	375	373	301	184	134
S1238	475	397	365	408	187	160
S1494	614	1228	1040	585	616	427
S2091	302	94	32	225	616	16
S3330	571	2096	2074	533	470	994
S5378	587	2687	2686	590	1078	1100

Table 2: Floorplanning optim of GA compared with hybrid algorithm.

Circuit	Number of blocks	GA		Hybrid	
		Wirelength	CPU time	Wirelength	CPU time
xerox	10	33.56	30	32.06	26
Ami33	33	35.44	30	34.39	24
apte	9	25.48	30	24.23	22
Ami49	49	63.55	175	58.33	150
hp	11	28.46	45	27.54	60

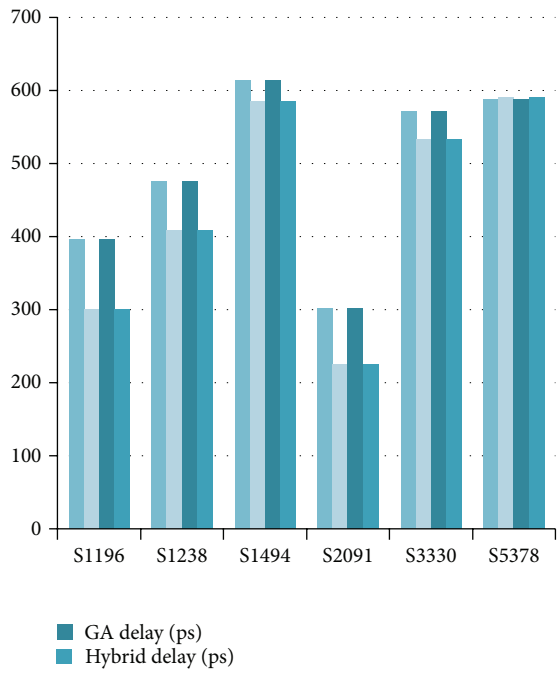

Figure 11: Comparison of GA delay and hybrid delay.

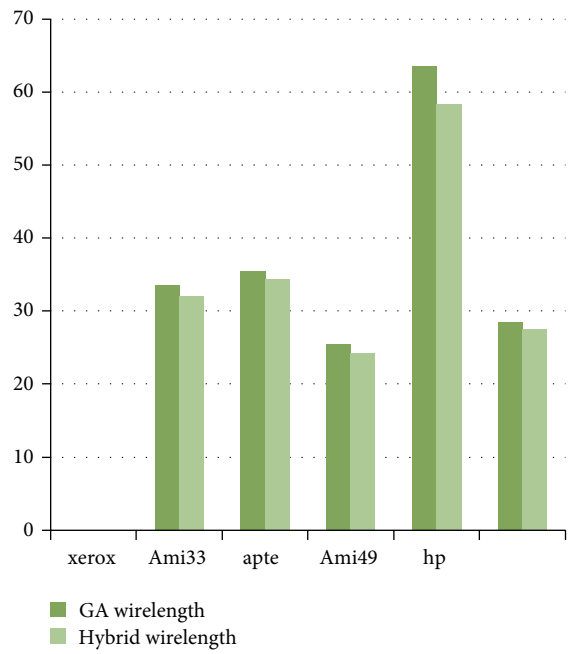

Figure 12: Comparison of GA wirelength and hybrid wirelength.

Since the cells are placed randomly, thus the distances between them and the length of their interconnection will be huge. Next the algorithm uses three different functions to get the optimal placement for the chip.

5.3.2. Move Generation Function. To generate a new possible cell placement, the algorithm uses two strategies:

(a) move a single cell randomly to a new location on the chip,

(b) swap the position of two cells. This algorithm uses both the strategies randomly. 50% of the move generation is done through random move (a) and the rest of the generation is done through swapping (50%).

5.3.3. Cost Function. The cost function in algorithm is comprised of two components:

$$C = C_1 + C_2. \tag{12}$$

Table 3: Placement optim of SA compared with hybrid algorithm.

Circuit	GA			Hybrid		
	Cells	Nets	Final interconnect length	Cells	Nets	Final interconnect length
apte	9	97	590.6	9	77	475.4
xerox	10	203	1038	10	171	1145
hp	11	83	365	11	68	283
Ami33	33	123	278.5	33	112	324
Ami49	49	408	2077	49	368	345

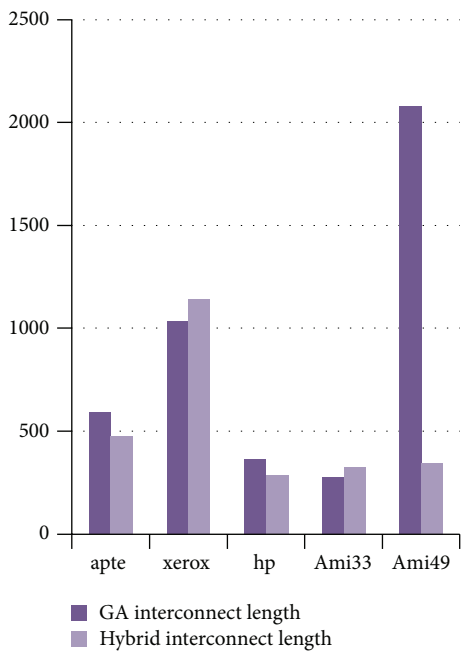

Figure 13: Comparison of GA interconnect length and hybrid.

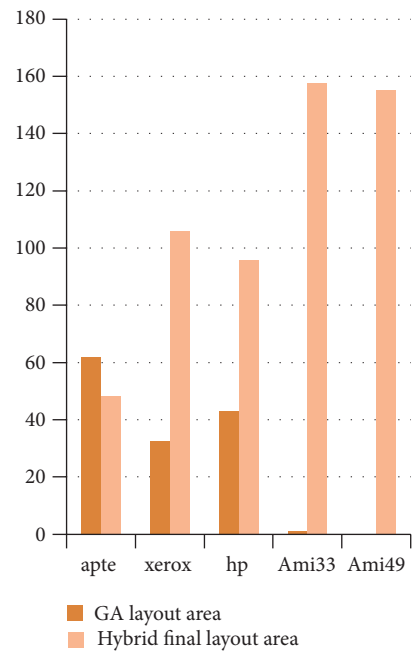

Figure 14: Comparison of GA layout area and hybrid.

C_1 is a measure of the total estimated wirelength. For any cell, we find out the wire-length by calculating the horizontal and the vertical distance between it and its out cell:

$$C_1 = \sum_{i=\text{cell}1}^{n} \sum_{j=\text{out cell}}^{n} \left(d_{hij} + d_{vij}\right), \tag{13}$$

where the summation is taken over all the cells in a circuit. When a cell is swapped it may so happen that two cells overlap with each other. Let Oij indicate the overlap between two cells. Clearly this overlap is undesirable and should be minimized. In order to penalize the overlap severely we square the overlap so that we get larger penalties for overlaps:

$$C_2 = \sum_{i!=i} (Oij)^2. \tag{14}$$

In (14) C_2 denotes the total overlap of a chip. Thus when we generate a new move we calculate the cost function for the newly generated move. If we find that the new move has a cost less than the previous best move, we accept it as the best move. But if we find a solution that is nonoptimal, we do not reject it completely. We define an Accept function which is the probabilistic acceptance function. It determines whether to accept a move or not. We have implemented an exponential function for the accept method. We are accepting a noncost optimal solution because we are giving the annealing schedule a chance to move out of a local minimum which it may have hit. For example, if a certain annealing schedule hits point B (local minima) and if we do not accept a noncost optimal solution, then the annealing cannot reach the global minima. By using the accept function we are giving the annealing schedule a chance to get out of the local minima. As a nature of the accept function used by us, the probability of accepting noncost optimal solution is higher at the beginning of the annealing schedule. As temperature decreases, so does the probability of accepting noncost optimal solutions, since the perturbations of a circuit are higher at higher temperatures than lower temperatures.

5.4. Routing Based on Simulated Annealing. Let p_α and p_β be copies of the mates and p_γ be their descendant.

Table 4: Routing optim of SA compared with hybrid algorithm.

Circuit	GA			Hybrid		
	Cells	Nets	Final layout area	Cells	Nets	Final layout area
apte	9	97	61.8	9	77	48.012
xerox	10	203	32.6	10	171	106.054
hp	11	83	42.9	11	68	95.862
Ami33	33	123	1.23	33	112	157.690
Ami49	49	408	—	49	368	155.24

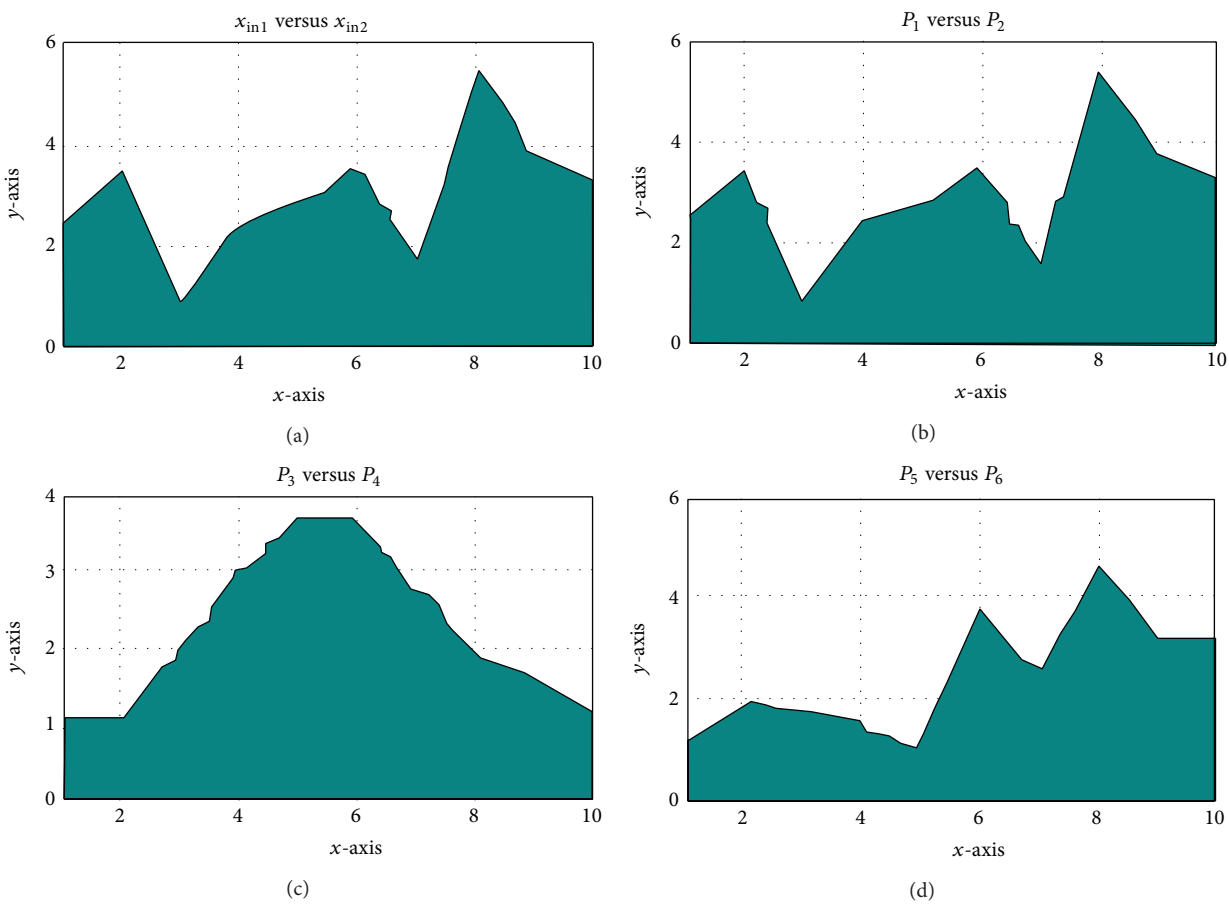

Figure 15: Overall area minimized using hybrid evolutionary algorithm.

First, a cut column x_c is randomly selected with $1 \leq x_c < x_{\text{ind}}$, where x_{ind} represents the number of columns of the individuals. The individual $p_\alpha(p_\beta)$ transfers the routing structure to p_γ which is located to the left (right) of the cut column x_c and not touched by x_c. Assume that the part of p_α (or p_β) which has to be transferred into p_γ contains rows not occupied by any horizontal segments. Then the row number of p_α (or p_β) is decremented by deleting this row until no empty row is left. The initial row number $y_{\text{ind}\gamma}$ of p_γ is equal to the maximum of $(y_{\text{ind}\alpha}, y_{\text{ind}\beta})$. The mate which now contains fewer rows than p_γ is extended with additional row(s) at random position(s) before transferring its routing structure to p_γ.

The routing of the remaining open connections in p_γ is done in a random order by our random routing strategy. If the random routing of two points does not lead to a connection within a certain number of extension lines, the extension lines are deleted and the channel is extended at a random position y_{add} with $1 \leq y_{\text{add}} \leq y_{\text{ind}\gamma}$. If the repeated extension of the channel also does not enable a connection, p_γ is deleted entirely and the crossover process starts again with a new random cut column x_c applied to p_α and p_β. This process of creating p_γ is finished with deleting all rows in p_γ that are not used for any horizontal routing segment [23, 24].

Reduction strategy simply chooses the P_c fittest individuals of $(P_c \upsilon P_n)$ to survive as P_c into the next generation.

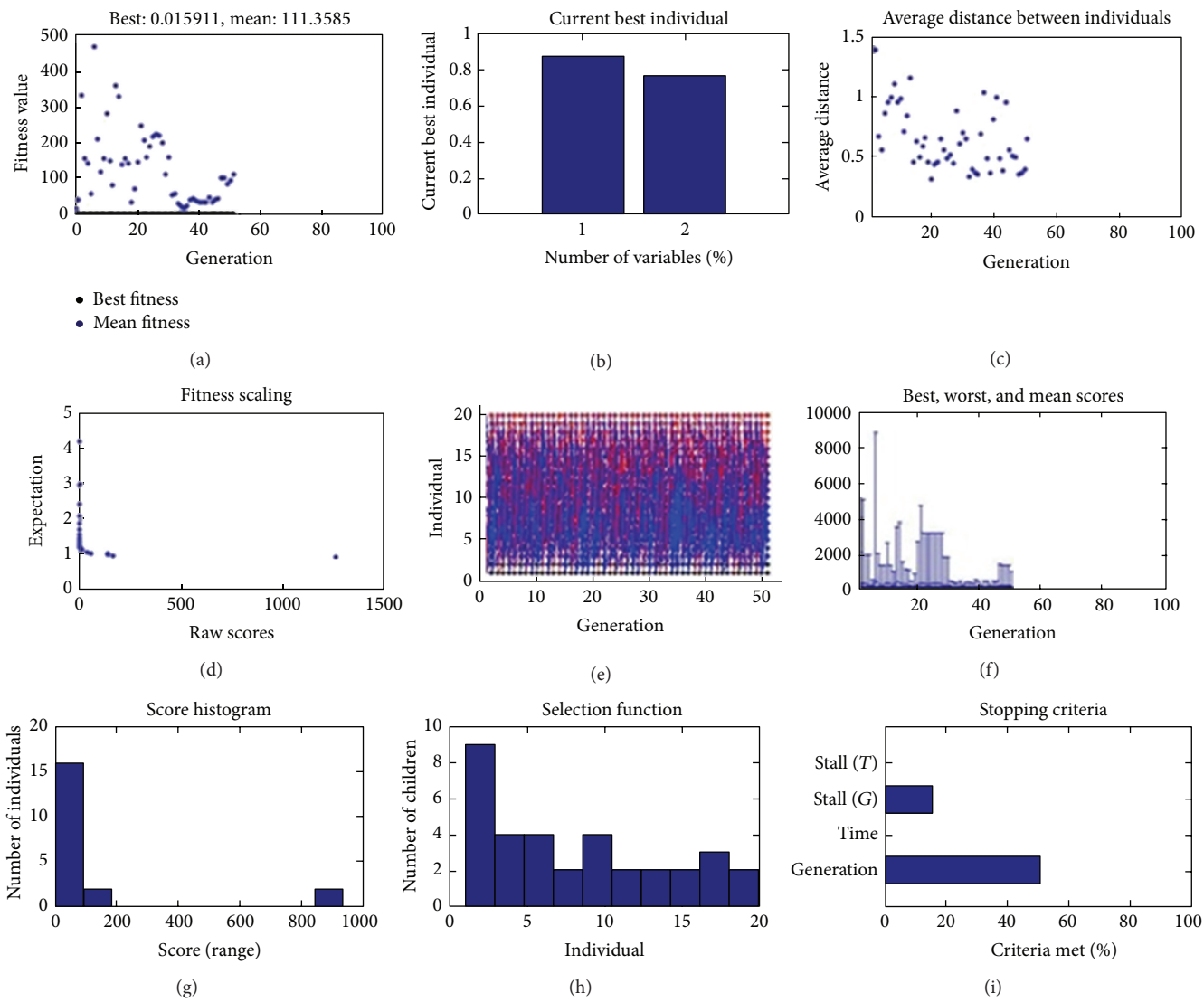

Figure 16: Simulated results for final generation.

The selection strategy is responsible for choosing the mates among the individuals of the population P_c.

According to the terminology of our selection strategy is actually stochastic sampling with replacement. That means any individual $p_i \in p_c$ is selected with a probability

$$F(p_i) = \frac{1}{\sum_{p \in p_c} F(p)}. \tag{15}$$

The two mates needed for one crossover are chosen of each other. An individual may be independently selected any number of times in the same generation.

6. Experimental Results

This work compares the performance of combined physical design automation tool for different benchmarks of physical design components. This iterative heuristic technique involves the combination of GA and SA. This work measures the speed of execution time of all levels on an average of 45% when compared to simple genetic algorithm. The objective of individual physical design components is discussed below as results. The results in this section were obtained by the simulation of each individual element of physical design components using general iterative heuristic approach. The experiments were executed on the Intel Core i3 processor with the clock speed of 3.3 Ghz machine which runs in Windows XP.

6.1. Partitioning. Delay (ps) is the delay of the most critical path. T (s) is the total run time, and best (s) is the execution time in seconds for reaching the best solution. Thus the objective of area minimization can be achieved by reducing the delay in circuit partitioning (see Table 1 and Figure 11).

6.2. Floorplanning. In floorplanning, wirelength and CPU time are compared. This heuristic approach can reduce

the wirelength on an average of 0.5 mm when compared with fast simulated annealing. When the wirelength gets reduced, obviously the area for floorplan will also get reduced (see Table 2 and Figure 12).

6.3. Placement. The initial population is generated to evaluate the fitness function. Based on that fitness parents were selected for the crossover; after this process the normal mutation and inversion operation take place. In addition to this process for each subpopulation local search is applied to refine the fitness of each individual to get the optimal solution. The cells describe the number of elements in the circuits, nets describe the interconnection (see Table 3 and Figure 13).

6.4. Routing. The method is also surprisingly fast, even when compared to tools that perform pattern routing. Improving routing congestion is significant concern for large and dense designs. If routing fails, the design team must modify the placement or possibly increase the chip size to introduce additional routing resources. In fixed-die design, if there is additional space available, the impact of increased routing area will generally be limited to increased wirelength and power consumption. If additional space is not available, routing failure may increase the cost of a design substantially. The results obtained for the popular benchmarks reduce the final interconnect length (see Table 4 and Figure 14).

7. Conclusion

By reducing the wirelength, cost of very large scale integrated chip manufacturing can be reduced. This paper explores the advantage of memetic algorithm which can be proven to be 45% faster than the simple software genetic algorithm by reducing the delay and area in partitioning and floorplanning, respectively, that would indefinitely reduce the wirelength. In hybrid approaches, local search techniques explore the solution space close to the sample points by applying specialized heuristics. When including problem specific knowledge during creation of individual, like in our approach, it is possible to identify unfavourable or redundant partial solutions and consider only the most promising ones. Therefore, each individual in our hybrid genetic algorithms encodes a set of high quality solutions, the best of which is a local optimum. The implementation of multiobjective in the algorithm enables getting the near optimal solution. After a predetermined number of iterations by GA, local search is applied to few random individuals to get the optimal solution by simulated annealing. In the future the performance of the algorithm has to be tested on different benchmarks.

Conflict of Interests

The authors declare that there is no conflict of interests regarding the publication of this paper.

References

[1] I. H. Shanavas and R. K. Gnanamurthy, "Wirelength minimization in partitioning and floorplanning using evolutionary algorithms," *VLSI Design*, vol. 2011, Article ID 896241, 9 pages, 2011.

[2] M. J. S. Smith, *Application Specific Integrated Circuits*, Pearson Education, Asia, 2004.

[3] W. Theodore Manikas and T. James Cain, "Genetic algorithms vs simulated annealing: a comparison of approaches for solving the circuit partitioning problem," Tech. Rep. 96-101, The University of Pittsburgh, 1996, http://www.ee.utulsa.edu/~tmanikas / Pubs/gasa-TR-96-101.pdf.

[4] G. Ch. Sipakoulis, I. Karafyllidis, and A. Thanailkis, "Genetic partition and placement for VLSI circuits," in *Proceedings of 6th IEEE conference on Electronics Circuits and Systems*, vol. 3, pp. 1647–1650, 1999.

[5] M. R. Garey and Johnson, *Computers and Intractability: A Guide to Theory of NP-Completeness*, Freeman, San Francisco, Calif, USA.

[6] C. J. Augeri and H. H. Ali, "New graph-based algorithms for partitioning VLSI circuits," in *Proceedings of the IEEE International Symposium on Cirquits and Systems*, vol. 6, pp. V-521–V-524, May 2004.

[7] S. N. Adya and I. L. Markov, "Fixed-outline floorplanning through better local search," in *Proceedings of the IEEE International Conference on: Computer Design: VLSI in Computers and Processors (ICCD '01)*, pp. 328–334, Austin, Tex, USA, September 2001.

[8] Y.-C. Chang, Y.-W. Chang, G.-M. Wu, and S.-W. Wu, "B∗-trees: a new representation for non-slicing floorplans," in *Proceedings of the 37th Design Automation Conference (DAC '00)*, pp. 458–463, June 2000.

[9] M. Tang and X. Yao, "A memetic algorithm for VLSI floor planning," *IEEE Transactions on Systems, Man, and Cybernetics*, vol. 37, no. 1, pp. 62–69, 2007.

[10] N. Xu, F. Huang, and Z. Jiang, "A fast algorithm for VLSI building block placement," in *Proceedings of the IMACS Multiconference on "Computational Engineering in Systems Applications" (CESA '06)*, pp. 2157–2160, Beijing, China, October 2006.

[11] M. Burstein and R. Pelavin, "Hierarchical wire routing," *IEEE Transactions on Computer-Aided Design of Integrated Circuits and Systems*, vol. 2, no. 4, pp. 223–234, 1983.

[12] A. Cincotti, V. Cuttelo, and M. Pavone, "Graph partitioning using genetic algorithms with OPDX," in *Proceedings of IEEE on World Congress on Computational Intelligence*, pp. 402–406, May 2002.

[13] I. Hameem Shanavas and R. K. Gnanamurthy, "Evolutionary algorithmical approach on VLSI Floorplanning problem," *International Journal of Computer Theory and Engineering*, vol. 1, no. 4, pp. 461–464.

[14] N. Sherwani, *Algorithms for VLSI Physical Design Automation*, Kluwer Academic Publishers, Boston, Mass, USA, 1999.

[15] S. Kirkpatrick, C. D. Gelatt Jr., and M. P. Vecchi, "Optimization by simulated annealing," *Science*, vol. 220, no. 4598, pp. 671–680, 1983.

[16] V. Cerny, "Thermodynamical approach to the traveling salesman problem: an efficient simulation algorithm," *Journal of Optimization Theory and Applications*, vol. 45, no. 1, pp. 41–45, 1985.

[17] N. Metropolis, A. W. Rosenbluth, M. N. Rosenbluth, A. H. Teller, and E. Teller, "Equation of state calculations by fast

computing machines," *The Journal of Chemical Physics*, vol. 21, no. 6, pp. 1087–1092, 1953.

[18] L. Ingber, "Very fast simulated re-annealing," *Mathematical and Computer Modelling*, vol. 12, no. 8, pp. 967–973, 1989.

[19] K. Sivasundari, P. Subbaraj, and P. S. Kumar, "An effective memetic algorithm for VLSI partitioning problem," in *Proceedings of the IET-UK International Conference on Information and Communication Technology in Electrical Sciences (ICTES '07)*, pp. 667–670, December 2007.

[20] C. K. Wong and M. Sarrafzadeh, *An Introduction to VLSI Physical Design*, The Mcgraw Hill Companies, 1996.

[21] S. Venkatraman, P. Subbaraj, and P. SivaKumar, "Hybrid algorithm for Vlsi floorplanning problem," in *International Conference on VLSI and Signal Processing (ICVSP '08)*, Chennai, India, March 2008.

[22] T. Kapilachander, P. Subbaraj, and P. SivaKumar, "An effective memetic algorithm for Vlsi placement problem," in *International Conference on VLSI and Signal Processing (ICVSP '08)*, Chennai, India, March 2008.

[23] I. H. Shanavas and R. K. Gnanamurthy, "Application metaheuristic technique for solving VLSI global routing problem," in *Proceedings of the International Conference on Advances in Recent Technologies in Communication and Computing (ARTCom '09)*, pp. 915–917, October 2009.

[24] P. Subbaraj, P. SivaKumar, and Pandiraj, "Memetic algorithm for solving channel routing problems," in *International Conference on VLSI and Signal Processing (ICVSP '08)*, Chennai, India, March 2008.

Hindawi Publishing Corporation
Mathematical Problems in Engineering
Volume 2014, Article ID 597092, 12 pages
http://dx.doi.org/10.1155/2014/597092

Research Article

Efficient UAV Path Planning with Multiconstraints in a 3D Large Battlefield Environment

Weiwei Zhan, Wei Wang, Nengcheng Chen, and Chao Wang

State Key Laboratory of Information Engineering in Surveying, Mapping and Remote Sensing, Wuhan University, 129 Luoyu Road, Wuhan 430079, China

Correspondence should be addressed to Chao Wang; c.wang@whu.edu.cn

Received 12 October 2013; Revised 6 January 2014; Accepted 6 January 2014; Published 26 February 2014

Academic Editor: Xinjie Zhang

This study introduces an improved A^* algorithm for the real-time path planning of Unmanned Air Vehicles (UAVs) in a 3D large-scale battlefield environment to solve the problem that UAVs require high survival rates and low fuel consumption. The algorithm is able to find the optimal path between two waypoints in the target space and comprehensively takes factors such as altitude, detection probability, and path length into account. It considers the maneuverability constraints of the UAV, including the safety altitude, climb rate, and turning radius, to obtain the final flyable path. Finally, the authors test the algorithm in an approximately 2,500,000 square meter area containing radars, no-fly zones, and extreme weather conditions to measure its feasibility, stability, and efficiency.

1. Introduction

With the development of various modern high-maneuverability air defense weapons and increasingly perfected air defense system, the capability of vehicles to break through enemy defenses at medium and high altitudes has decreased. Modern military low-altitude penetration is primarily performed by UAVs. The key lies in the path planning for UAVs [1]. Research in this area has been ongoing for many years, and several algorithms were developed for this problem.

The artificial potential field method was developed by Khatbi to plan the trajectory for the robots. This algorithm is intelligible in its mathematical description and has been widely used for real-time obstacle avoidance and smooth trajectory control [2]. However, the method has its inherent limits when applied to UAV path planning [3]; for example, in complex mountainous terrains, there are often multiple obstacles near the target point; it would result in a greater repulsion than attraction for the UAV. Thus, the UAV cannot reach the target [4]. Some researchers hoped to establish a unified potential function to solve this problem [5]; unfortunately, it still requires regular obstacle to avoid huge calculation requirements, which is nearly intolerable for real-time path planning.

Some researchers have attempted to find the solution in intelligent optimization algorithms, such as genetic algorithm (GA) [6, 7] and ant colony algorithm (ACA) [8, 9]. The former has good global searching maneuverability and can quickly find all of the solutions without falling into local optimal [7]. The latter is highly robust and good at searching for better solution [8], and their experimental results present the feasibility to solve this problem. However, these algorithms have common limits that are difficult to avoid in solving large-scale UAV path planning problems. For example, genetic algorithm is weak for local search with low efficiency in the later periods and easily reaches premature convergence [6]. Ant colony algorithm is sensitive to the initial parameters. An inappropriate setting decreases the search rate and yields poor results [9]. Furthermore, the real-time path planning of UAVs requires high efficiency and accuracy; these algorithms may not be proper solutions.

Graph search algorithms have been developed to find the optimal trajectory between two nodes on connected graphs. The greatest advantage of these algorithms, including Dijkstra, Bellman-Ford, and A^* algorithms, is their straightforward implementation and low computational cost to get the optimal path, which makes it the most suitable method in theory [1]. The A^* solver is one of the most widely used

algorithms among them. It was developed to analyze more effectively the domain in order to avoid distributed obstacles, which is largely applicable to robotics, space exploration, and video games [10]. Though maturely used in 2D graph searching, the A^* algorithm still faces some challenges in the UAV path planning in a 3D complex battlefield environment [11, 12], and previous research results may have problems as follows: (1) most experimental space was simple artificial topographies. The obstacles were few and regular, and complex threats such as radars and extreme weather conditions were not considered [13–15]; therefore, they did not verify their feasibility, efficiency, and convergence in large-scale complex space. (2) Some path planning is essentially performed in a 2D plane [16–18]. Some researchers use 2D spatial partitioning methods, like Voronoi map, to divide the target space into several sections to construct connected network graph. (3) The algorithms did not obtain a flyable path; most searching results are break lines or smoothing curves [14–17]. The maneuverability of the UAV, including the turning radius, safety altitude, climb rate, minimum step size, and fuel consumption, should be considered to get a flyable path, which is a fundamental difference from general robot path planning.

In light of the limitations above, the paper proposed an improved A^* algorithm for the UAV path planning in a 3D large-scale battlefield. This space is composed of real terrain data, radars, no-fly zones, and extreme weather conditions. The algorithm considers terrain following, threat avoidance, and fuel consumption to obtain a flyable path that follows the maneuverability constraints of a UAV. Meanwhile, an assessment algorithm was designed to evaluate the final path. Finally, the algorithm was compared with ACA and GA to present its advantage.

2. Materials and Methods

2.1. Modeling of the Battlefield Environment. The target space in this paper consists of a DEM map and battlefield plot information. Because the modeling methods for the former are very mature, this paper focuses on modeling the plot information, which includes radars, no-fly zones, and extreme weather.

Radars have been widely used to detect the UAVs in modern air defense system. This paper does not treat radar like a normal obstacle but build a detection probability model, which distinguishes this research from most previous studies [19]. The process for computing the detection probability at any point in the target space is essentially the inverse of the radar equation and pattern function [20]. This value is calculated as follows.

(1) From the target point and radar antenna's location, calculate the pitch angle, θ, and use the antenna pattern formula (1) to calculate the pattern function value $F(\theta)$ as follows:

$$F(\theta) = e^{-2.78\theta^2/\theta_B^2}. \tag{1}$$

(2) Calculate the range from the target point to the radar center $R(\theta)$, and determine the maximum radar detection range $R_{\max}$. Consider

$$R(\theta) = R_{\max} * \sqrt{F(\theta)}. \tag{2}$$

(3) Invert the radar equation and the minimum SNR formula to determine the radar detection probability. The radar equation is shown in

$$R_{\max} = \sqrt[4]{\frac{P_{\text{av}} G^2 T_m \lambda^2 \sigma}{(4\pi)^3 k T_0 F_n t B [S/N]_{\min} L}}, \tag{3}$$

where P_{av} is the average transmitted power, G is the antenna gain, λ is the wavelength, σ is the radar cross section, k is the Boltzmann constant, T_m is the pulse recurrence period, t is the pulse length, T_0 is the absolute temperature in K, F_n is the noise figure of the receiver, B is the noise bandwidth of the receiver, L is the system loss factor, and $[S/N]_{\min}$ is the minimum SNR based on single pulse detection, which is defined as follows:

$$\begin{aligned} \left[\frac{S}{N}\right]_{\min} &= A + 0.12AB + 1.7B, \\ A &= \ln\left[\frac{0.62}{P_f}\right], \\ B &= \ln\left[\frac{P_d}{1 - P_d}\right], \end{aligned} \tag{4}$$

where P_d is the detection probability, and P_f is the false alarm probability. We can obtain the detection probability P_d from formulas (3) and (4).

(4) Because modern radar normally adopts the standard of "M detections in N scans" [20], the detection probability, P, of any point must satisfy the following formula:

$$p_d = \sum_{M}^{N} \frac{N!}{K!\,(N-K)!} p^K (1-p)^{N-K}. \tag{5}$$

This formula is nonlinear, so we can use the more efficient Newton iteration method [21] to determine the radar detection probability at any point in the target space.

Furthermore, we should also consider the influence of the terrain on the signal propagation; see Figure 1. Point O is the center of the radar antenna. If AB is the first mountain section, the area below BC is a blind zone because the beam is blocked by AB, and the final detection region in this section is the blue area between OABCDO. Figure 2 shows the radar coverage area ignoring the effect of terrain, while Figure 3 shows the real detection area. The real detection probability at any point is given by the following:

$$p = \begin{cases} \text{Newton}\left(p_d(x, y, z)\right), & (x, y, z) \in Z_R, \\ 0, & (x, y, z) \notin Z_R, \end{cases} \tag{6}$$

where Z_R is the radar coverage and Newton is the Newton iteration method.

Extreme weather, including thunderstorms, blizzards, hails, hazes, and strong airstreams, poses a significant threat to the flight of UAVs. The climate threat model is divided into 2D and 3D zones based on its sphere of action. The former are described using a closed curve $\{P_i(x, y)\}$, where x and y represent the longitude and latitude, respectively,

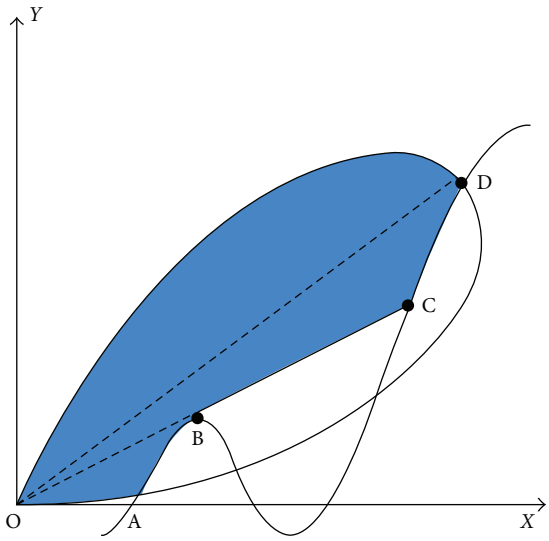

Figure 1: Radar signal propagation graph.

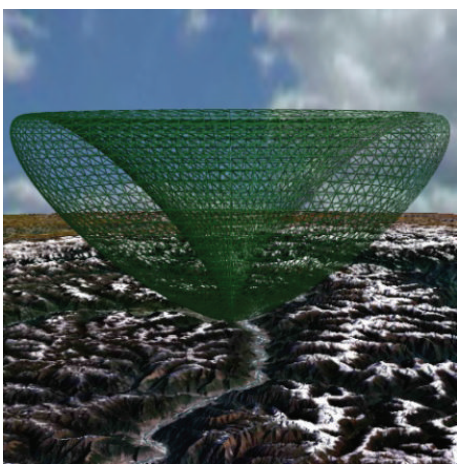

Figure 2: Sector radar coverage.

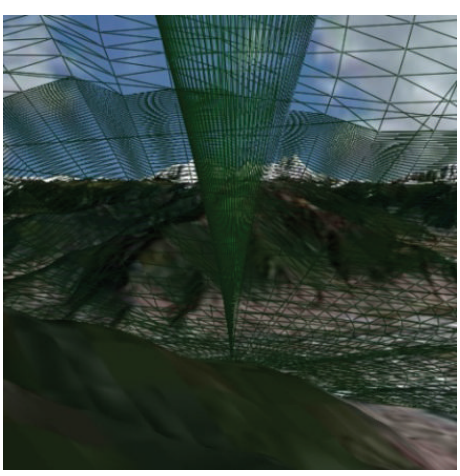

Figure 3: Terrain influence on radar coverage.

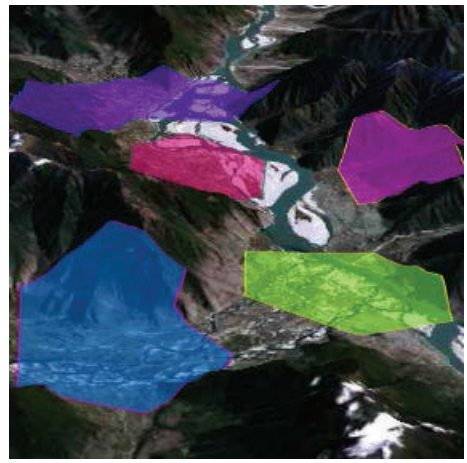

Figure 4: 2D climate threat model.

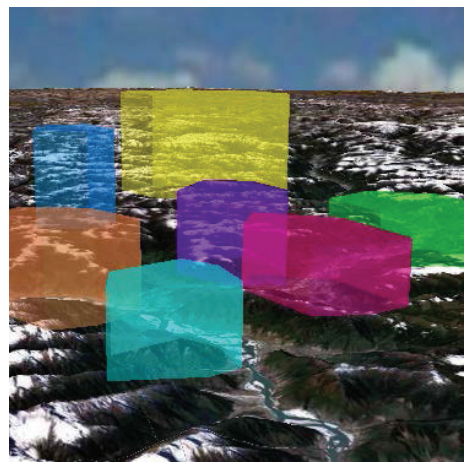

Figure 5: 3D climate threat model.

and are shown in Figure 4. The latter are described using polygonal prisms $(\{P_i(x, y)\}, H_{\min}, H_{\max})$. $H_{\min}$ and $H_{\max}$ are the altitude limits, respectively, and are shown in Figure 5. No-fly zones are described similarly to the 2D climate model.

2.2. Path Planning Strategies

2.2.1. Target Space Partition. The 3D area described by the DEM and DOM is a continuous raster space; therefore, there is no node-edge graph network present in traditional path searching, and spatial partitioning can solve this problem.

Some researchers used a Voronoi diagram to partition the space at a certain altitude [22]. Because UAVs change altitude during flight, this method is only applicable to certain flight missions in flat areas with small section changes at different altitudes. However, for mountainous terrain, this method cannot obtain a valuable optimal path. In addition, some researchers tried to use regular 3D boxes for the space partitioning [14]. It means that there are at least 26 nodes to expand during the searching process, which requires a large amount of time and memory to obtain an optimal solution, especially, in large space. This paper recommends a 2.5D

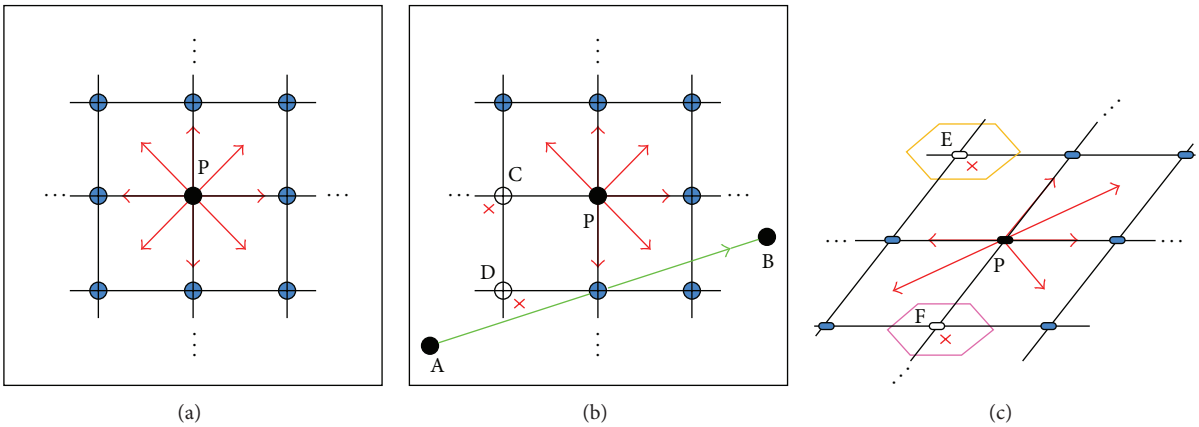

Figure 6: Space partition model.

partition model to solve this problem. The model is actually a surface partition model, which logically divides the DEM data into a series of independent rectangular grids in some accuracy. The terrain information in a grid is represented by its center. Each center point records the longitude, latitude, and altitude, as shown in Figure 6(a). The centers form a routing network needed in the routing process. This model has only 8 directions to expand for each node, which makes it more efficient than the 3D grid partition method.

To further improve the convergence rate and efficiency of the algorithm, some researchers recommend considering the maneuverability constraints of UAVs [14, 17], including the minimum step size and turning radius, in nodes expansion. Satisfying the minimum step size requirement means increase of the grid size, which does improve the search speed to some degree, but it causes an excessive loss of terrain details and may greatly decrease the accuracy of the searching result. Considering the limits to the UAV's speed, slope, and turning angle may decrease expansion directions, but some global optimal nodes may be missed due to the fact that the grid points are not the final waypoints. However, this method can be applied in local searching to filter out directions that the angle to the global direction is too large (e.g., >150°) as shown in Figure 6(b). In addition, this method can also filter out nodes in the no-fly zone and extreme climate threat as shown in Figure 6(c).

2.2.2. Initial Path Based on the Improved A^* Algorithm. The A^* algorithm cost function should be defined to evaluate the cost of the expansion nodes and obtain the node-edge list of the optimal path. The function is as follows:

$$f(n) = g(n) + h(n), \tag{7}$$

where n is the node being expanded, $g(n)$ is the actual cost to from the initial node to node n, and $h(n)$ is the estimated cost from node n to the target node. The heuristic function $g(n)$ is the main factor affecting the search result, and a reference formula was made [23] to plan a terrain following path. Consider

$$J = \int_0^{t_f} \left(\omega_1 c_t^2 + \omega_2 h^2 + \omega_3 f_{\mathrm{TA}}\right) dt, \tag{8}$$

where c_t is the distance from a specified route, h is the altitude, f_{TA} is the threat value, and ω_1, ω_2, and ω_3 are their weights, respectively.

This heuristic function may have some problems when applied to the subject of this paper. First, c_t is a relative distance, but h is an absolute altitude, and they have differing magnitudes. The distance to the center of the threat, f_{TA}, is positively correlated with the cost function, and the lower this value is the better it is. However, c_t and h run counter to this value, which makes it not easy to assign a reasonable weight to each factor. Second, the threat of radar should be measured as a probability rather than a relative distance. Thus, it is several orders of magnitude lower than the other factors and the function would be too insensitive to ω_1, ω_2, and ω_3, which makes finding three values to develop a meaningful cost function for determining the optimal path difficult.

To solve the above problems, the cost function is improved as follows:

$$J(n) = \sum_1^n \left(\omega_1 c_i + \omega_2 p_i + \omega_3 h_i\right). \tag{9}$$

In this formula, c_i is the surface distance from node i to node $i-1$, which is the penalty for the route length. p_i is the detection probability between nodes i and $i-1$ and is aimed at increasing the survival rate of the UAV. h_i is the weighted average altitude between nodes i and $i-1$.

These three cost function factors all push in the same direction; that is, the solution requires a reduced route length, altitude, and detection probability. However, these factors are not on the same magnitude, and the penalty factors should be normalized. The key to adopting a 0-1 scale is to determine the maximum and minimum values for each factor. We cannot directly determine the maximum and minimum distance because it varies for each route segment

due to the salient relief; however, regardless of the real or artificial terrain data, the maximum and minimum altitude is either already known or can be calculated from the data. Once $h_{\max}$ and $h_{\min}$ are determined, we can find the max and min of c_i; see as shown in Figure 7. Consider

$$c_{\max} = \sqrt{\Delta d^2 + (h_{\max} - h_{\min})^2} * (n_i - 1),$$
$$c_{\min} = \sqrt{d_i^2 - \Delta h_i^2}, \tag{10}$$

where $n_i = \lceil \sqrt{d_i^2 - \Delta h_i^2}/\Delta d \rceil$ is the number of interpolation points between nodes i and $i-1$ and d_i, Δh_i, and Δd are the Euclidean distance, altitude difference, and sampling interval, respectively.

p_i is the radar detection probability between nodes i and $i-1$ and should be considered as the sum of all radars in the space. The corresponding formula is shown as follows:

$$p_i = \sum_{i}^{m} p(R_i) - \sum_{1\le i\le j\le m}^{m} p(R_i R_j) + \sum_{1\le i\le j\le k\le m}^{m} p(R_i R_j R_k) - \cdots + (-1)^m p(R_1 R_2 \cdots R_m), \tag{11}$$

where $p(R_j)$ is the weighted average probability of detection by the jth radar between nodes i and $i-1$ for n_i interpolation points; the detection probability of each interpolation point can be calculated from formula (6). The normalization of these three factors is shown as follows:

$$C_i = \frac{(c_i - c_{\min})}{(c_{\max} - c_{\min})},$$
$$H_i = \frac{(h_i - h_{\min})}{(h_{\max} - h_{\min})}, \tag{12}$$
$$P_i = p_i.$$

Formula (13) is the new cost function using these normalizations. In this formula, $\omega_1 + \omega_2 + \omega_3 = 1$. Because the route length, altitude, and detection probability were normalized, the user can more directly assign the respective weights according to the planning objective. Consider

$$g(n) = \sum_{1}^{n} (\omega_1 C_i + \omega_2 H_i + \omega_3 P_i). \tag{13}$$

In formula (7), $h(n)$ was defined as the Euclidean distance from node n to the target point, which helps node n to approach the target point. Consider

$$h(n) = \frac{(d_n - d_{\min})}{(d_{\max} - d_{\min})}. \tag{14}$$

In this formula, d_n, $d_{\max}$, and $d_{\min}$ are the Euclidean, maximum, and minimum distances from node n to the target point as calculated using a similar formula to (10). However, it is worth mentioning that the sampling interval, ΔD, is generally greater than Δd to increase the efficiency of $h(n)$.

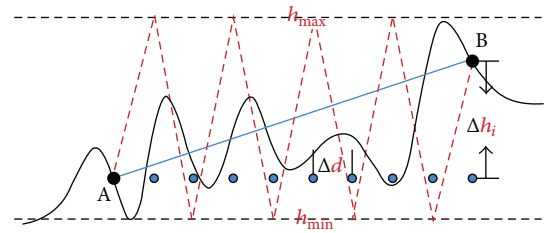

Figure 7: Computation of $c_{\max}$ and $c_{\min}$.

Once the target space and cost function are set, the standard A^* path searching process can begin. Open and closed lists were defined to store the expanded nodes, which were implemented with the minimum binary heap and linear lists to increase the efficiency.

Furthermore, to compare the searching result in different parameters, formula (15) is designed to evaluate the final path as follows:

$$V = \varepsilon_1 \frac{(C - C_{\min})}{(C_{\max} - C_{\min})} + \varepsilon_2 \frac{(H - H_{\min})}{(H_{\max} - H_{\min})} + \varepsilon_3 P, \tag{15}$$

where C is the route length, H is the mean altitude, and P is the detection probability. $C_{\max}$ and $H_{\max}$ are the maximum of C and H, respectively, and $C_{\min}$ and $H_{\min}$ are the minimum. ε_1, ε_2, and ε_3 are the weights of C, H, and P. Similar to the formula of $g(n)$, a smaller value of V indicates a better path.

2.2.3. The Path Optimization Algorithms. The search results from Section 2.2.2 may not satisfy the UAV maneuverability constraints, such as minimum step size, turning radius, turning angle, climb rate, and safety altitude. Therefore, a series of algorithms are developed to obtain the final flyable path.

The minimum step size and turning radius are constraints on the top view. The former requires the length of each route segment to be above a certain value $S_{\min}$, while the latter requires every segment to be long enough for two continuous turns; therefore, we have to compress the initial route. To satisfy the two constraints, in this paper, the FFP algorithm is used for the data compression [24], and the longest rectilinear trend can be furthest preserved to avoid frequent turning of the UAV. In addition, the turning angle constraint requires every segment angle to be below a critical value, $C_{\min}$. A potential field algorithm can be developed to solve this problem [5]. As UAVs cannot fly along a broken line, some researchers recommend various curve smoothing methods such as the B-spline curve [25]. However, these methods obviously conflict with the minimum step size constraint. In fact, UAVs generally turn by escribing or flyby [26].

The climb rate and safety altitude are constraints on the vertical view. UAVs tend to maintain posture without frequent turns or climbs. If the altitude of two waypoints, A and B, is different, the UAV does not fly directly from A to B but first climbs to O from A at a certain climb rate before flying horizontally to B as shown in Figure 8. The safety altitude is the minimum distance from the ground to ensure safe flight. Because of various factors, like strong turbulence and automatic-control error, a UAV usually deviates from the

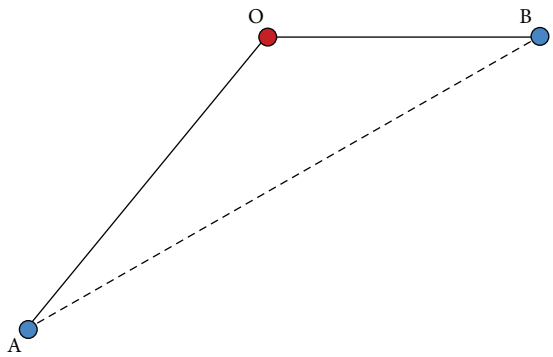

Figure 8: UAV climbing model.

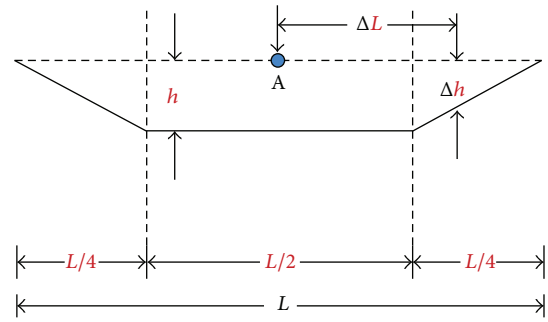

Figure 9: Route safety altitude model.

predefined path. Therefore, the algorithm should consider the safety altitude across the entire deviation area. This area is the safety corridor of the path, and its mathematical model is shown in Figure 9 [26]. This corridor is divided into the primary and secondary areas with the former providing the entire safety altitude h and the latter providing safety between 0 and h. The safety altitude, Δh, at any point is calculated as follows:

$$\Delta h = h * \left(1 - 2 * \frac{\Delta L}{L}\right), \tag{16}$$

where h is the safety altitude, ΔL is the distance between the target point and the predefined path, and L is the width of the safety corridor.

Based on the mathematic models above, we propose the following algorithm to meet the safety altitude constraint between waypoint A and waypoint B.

(1) Divide AB into AO and OB, and O is the level-flight point calculated from the climb rate at A.

(2) Calculate the minimum signed altitude difference, ΔH_1, for the OB segment. Begin the spatial interpolation for OB to obtain a series of interpolated points, $\{P_i\}$. Divide the cross section of P_i into a primary area and two secondary areas, and calculate the corresponding minimum signed heights. Consider

$$(\Delta H_1)_i = \min\left(\min\left(h_B - \Delta h - h_j\right), \min\left(h_B - h - h_k\right)\right), \tag{17}$$

where $(\Delta H_1)_i$ is the minimum signed height difference for cross section P_i, h_B is the altitude of the OB segment, h is the entire safety altitude, Δh is the safety altitude of the secondary areas as calculated from formula (16), h_j is the altitude of the interpolation point j in the primary area, and h_k is the altitude of the interpolation point k in the secondary area. The minimum $(\Delta H_1)_i$ value can be obtained by traversing $\{P_i\}$.

(3) Calculate the minimum signed height difference, ΔH_2, of the AO segment. First, get the interpolation points, $\{Q_i\}$, between AO by spatial interpolation, and the minimum signed height difference for cross section i of Q_i is calculated by

$$(\Delta H_2)_i = \min\left(\min\left(h_i - \Delta h - h_j\right), \min\left(h_i - h - h_k\right)\right), \tag{18}$$

where $h_i = h_A + AO * (h_O - h_A)/AQ_i$, and ΔH_2 can be calculated by traversing $\{Q_i\}$.

(4) Adjust the altitude of O and B to $h_B + \Delta H_1$ and the altitude of A to $h_A + \Delta H_2$. Create a radial through A using the climb rate and calculate the intersection with OB, which is the new level-flight point O.

3. Results and Discussion

The test space was about 2,500,000 Km^2 between Linzhi in Tibet and Chengdu in Sichuan province and was constructed with SRTM terrain and LANDSAT image data in 30 m accuracy. The area is a mountainous district that can verify the feasibility and adaptability of the algorithms in this paper. The algorithms were developed with C# and Direct 3D, and they have been successfully used for a 3DGIS platform, Gaea Explorer [27]. The hardware environment was as follows: CPU: Intel Core2 Duo E8200, memory: Kinston 1 G, video card: ATI Radeon HD 2600 XT.

To prove the feasibility of the algorithms in this paper, we developed the parameters in Table 1. Before searching, we defined the UAV parameters in Table 2.

In Figure 10, (a) shows the initial search result, (b) shows the compression results, (c) shows the smoothing results, (d) shows the results that consider the climb rate, (e) shows the safety corridor result, (f) shows the results that consider the safety altitude, and both (g) and (h) show the local features of the safety corridor from the top and front views, respectively. To prove the safety of the final path, we calculated the profile at $\pm L/4$ and $\pm L/2$, as shown in Figure 11. From these results, we determined that the algorithms were effective for low-altitude UAV path planning.

In Table 3, four experimental groups were designed to show the adaptability, convergence, and efficiency of the algorithm at various distances and grid sizes. Table 4 shows the parameters to evaluate the final path, where H_{aver} is the average altitude of the starting point and target point.

Table 1: The algorithm parameters.

Starting point (°, °, M)	Target point (°, °, M)	Surface distance (KM)	Grid size (°)	$\omega_1 : \omega_2 : \omega_3$
93.832779	94.372746			
29.127954	29.31984	59.783	0.01	1 : 2 : 1
2949.2	2923.6			

Table 2: UAV maneuverability parameters.

Speed (KM/H)	Slope (°)	Climb rate (M/S)	Turning method	Safety altitude (M)	Safety corridor width (NM)
300	20	120	Escribing	300	2

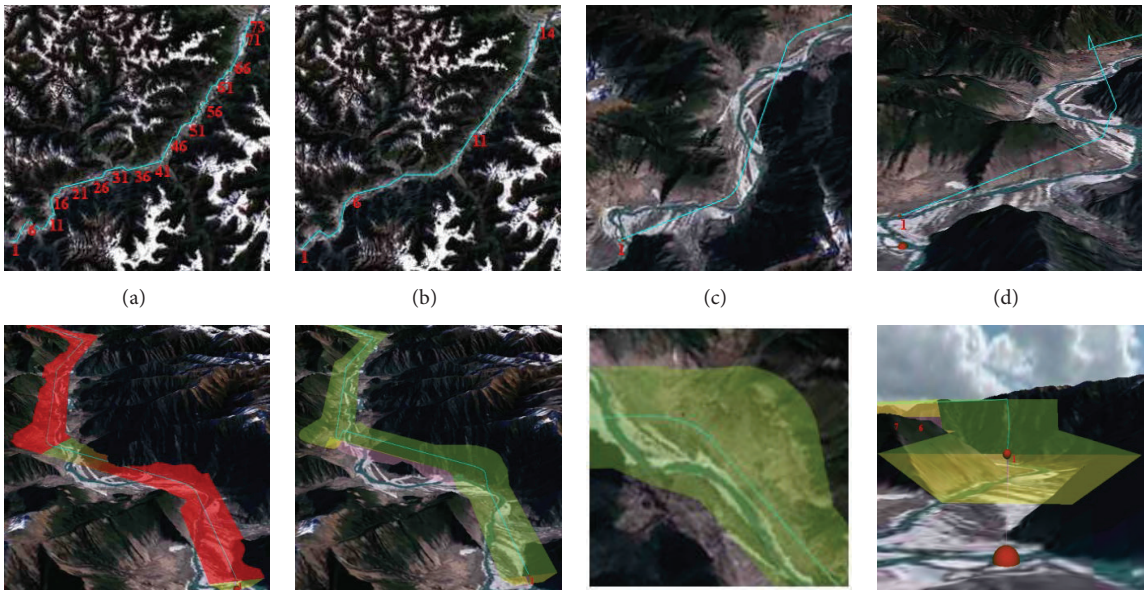

Figure 10: Algorithms results.

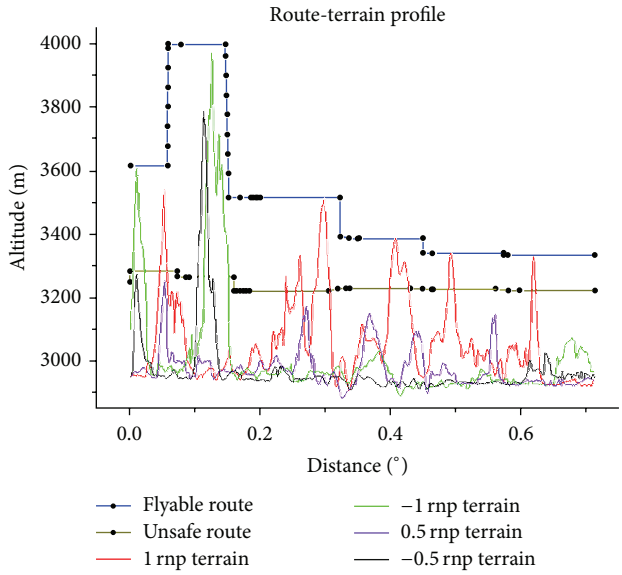

Figure 11: Route-terrain profile.

Table 3: Four control groups.

Starting point (°, °, M)	Target point (°, °, M)	Surface distance (KM)	Grid size (°)	$\omega_1 : \omega_2 : \omega_3$
93.832779	94.372746		0.005	
29.127954	29.31984	59.783	0.01	
2949.2	2923.6		0.02	
90.739257	94.835207		0.005	
29.292307	29.506482	419.073	0.01	
3606.3	2915.5		0.02	1 : 2 : 1
87.631027	94.816805		0.005	
29.130563	29.463092	729.349	0.01	
3985.1	2914.9		0.02	
93.562434	105.587785		0.005	
29.168065	30.119375	1236.916	0.01	
2976.5	399.4		0.02	

Table 4: Assessment parameters.

Minimum length (KM)	Maximum length (KM)	Minimum altitude (M)	Maximum altitude (M)	$\varepsilon_1 : \varepsilon_2 : \varepsilon_3$
Surface distance	2 ∗ surface distance	H_{aver}	4500	1 : 1 : 1

Table 5 shows that the algorithm can quickly determine the optimal path for various distances and grid sizes, which means that the algorithm is stable, convergent, and efficient. The time cost is proportional to the distance and inversely proportional to the grid size. Furthermore, the assessment value is smaller when the space partition grid is 0.01° rather than 0.005° or 0.02°.

To present the influence on the searching result of the changes of $\omega_1 : \omega_2 : \omega_3$, the four groups in Table 4 were compared at the ratio of the weight factors ω_1, ω_2, and ω_3 being equal to 2 : 1 : 1, 1 : 2 : 1, or 1 : 1 : 1. The result in Table 6 shows that the time cost is proportional to the weight of the route length and inversely proportional to the weight of the route altitude. A higher weight of the length results in faster approach to the target point, but the UAVs would be more likely to be detected by enemies because higher nodes may be chosen in nodes extension. Considering the survival rate of the UAVs, a higher weight of the altitude may be more reasonable, and it was seemingly backed up by Table 6, which shows that the assessment value is the smallest when the weight ratio is 1 : 2 : 1 rather than 1 : 1 : 1 or 2 : 1 : 1.

Figures 12(a)–12(d) show the results of the four comparison groups at a grid size of 0.01° and a weight ratio of 1 : 2 : 1.

We created a battlefield environment of approximately 2,500,000 Km^2, as shown in Figure 13, to demonstrate the algorithm's adaptability and convergence for large-scale complex situations including no-fly zones, extreme weather, and radars.

Table 7 shows the search results for the four groups at a grid size of 0.01°. The results prove that the algorithm is stable and convergent even for a complex battlefield environment. By comparing with the results shown in Table 4, we can see that the search time and route altitude increased slightly. Figure 14(a) shows the searching results for the first group; Figure 14(b) shows the local features. The other images are the results for the other three groups. These results indicate that the algorithm can effectively avoid no-fly zones and extreme weather while automatically searching for blind zones in radars network to accomplish a low-altitude penetration.

To present the advantages of the algorithm in solving the problem, we compared it with the ACA and the GA using the same parameters as in Table 3. The grid size is 0.001, and the iteration of ACS and GA is 2000.

The comparison results in Table 8 show that our algorithm has greater advantage in time efficiency than the other two algorithms, especially, in large scales, which is quite important in real-time path planning. On the surface, the advantage in the searching result is not so obvious, but the stability and convergence to get the optimal path still have comparative preponderance.

4. Conclusions

An improved A^* algorithm was developed for the path planning in large-scale 3D battlefields. The paper recommended a 2.5D spatial partition method for the 3D raster space, proposed a probability calculation model for radars network, and improved the A^* cost function to get an optimum route by considering the route length, the altitude, and the detection probability. A series of path optimization algorithms were developed to follow the maneuverability constraints of UAVs to obtain a final flyable path, and an assessment algorithm was designed to evaluate the path. The experimental results show that the improved A^* algorithm is stable, convergent, and efficient, and the comparison with ACA and GA shows its great advantage.

However, some issues should be further discussed. First, it is not so clear to quantify the planning goal to the optimal parameters, which is the key focus of decision makers. It was indicated that a comparatively good result was obtained at a grid size of 0.01° and a weight ratio of 1 : 2 : 1, but it is not easy to determine the exact optimal value of them. Table 6 presents

Table 5: The comparison results.

Assessment value	Route length (KM)	Detection probability	Mean altitude (M)	Total calculation time (S)		
				Initial path	Compress and smoothen	Altitude adjusting
0.133043	60.4	0	3542.2	0.012	0.169 0.121	0.036
0.129928	60.611	0	3528.9	0.004	0.129 0.086	0.039
0.207789	59.932	0	3907.2	0.002	0.104 0.065	0.037
0.346597	487.291	0	4347.6	3.19	4.462 0.941	0.331
0.207219	441.867	0	3963.8	0.271	1.51 0.952	0.287
0.395662	427.289	0	4707.4	0.086	1.138 0.774	0.278
0.450168	853.568	0	4689.2	9.916	13.063 2.693	0.454
0.273318	805.585	0	4201.2	0.543	3.268 2.241	0.484
0.328756	778.665	0	4414.6	0.068	2.202 1.684	0.45
0.323873	1591.054	0	3615.2	44.584	52.065 6.538	0.788
0.27795	1521.588	0	3385.6	3.63	11.488 6.915	0.943
0.294937	1399.922	0	3808.5	0.79	7.251 5.763	0.698

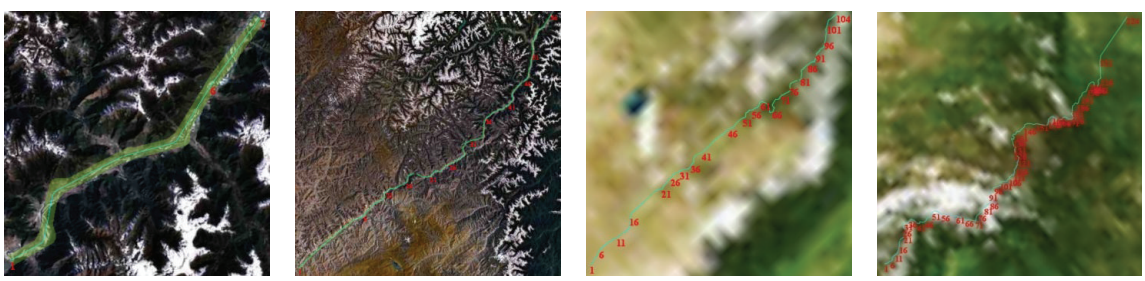

(a) (b) (c) (d)

Figure 12: Algorithms results at grid size of 0.01°.

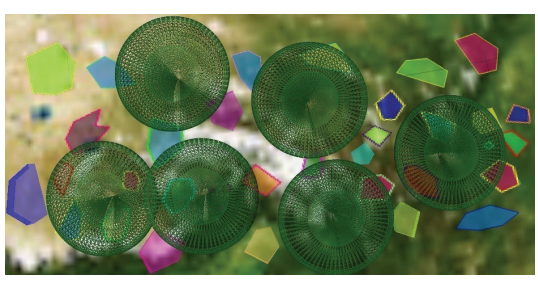

Figure 13: 3D battlefield environment.

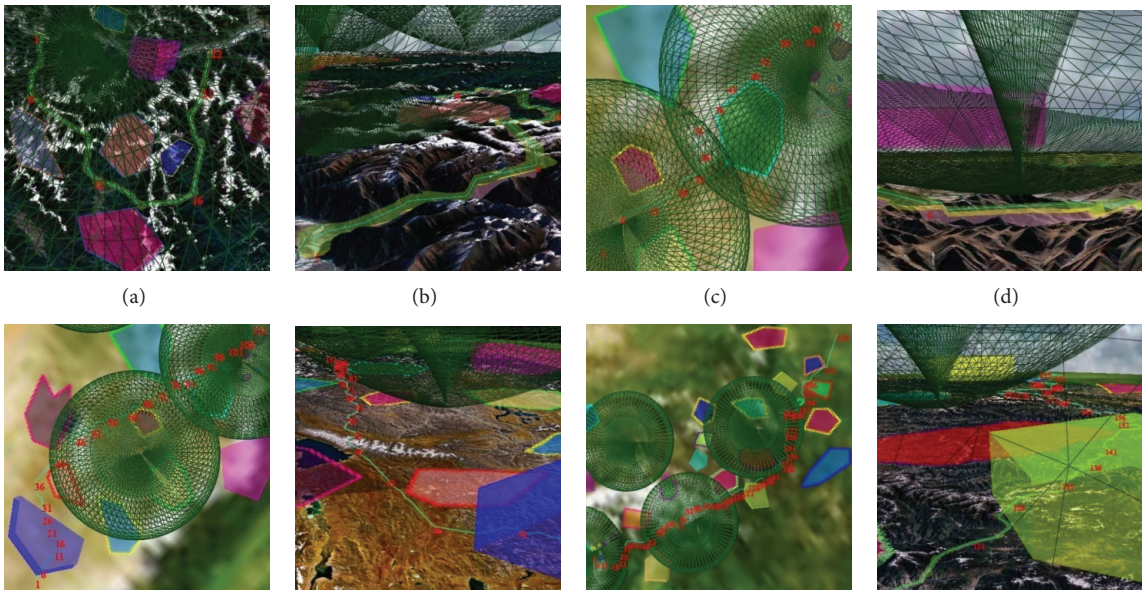

(a) (b) (c) (d)

(e) (f) (g) (h)

Figure 14: Algorithms results for the 3D battlefield environment.

Table 6: The comparison of different weights.

Assessment value	Route length (KM)	Detection probability	Mean altitude (M)	Total calculation time (S)		
				Initial path	Compress and smoothen	Altitude adjusting
0.189288	58.95	0	3846.1	0.004	0.132 0.091	0.037
0.130927	60.611	0	3528.9	0.004	0.129 0.086	0.039
0.27982	59.201	0	4264.2	0.003	0.135 0.084	0.042
0.379233	413.297	0	4687.7	0.103	1.121 0.764	0.254
0.207394	441.867	0	3963.8	0.271	1.51 0.952	0.287
0.436574	423.076	0	4872.4	0.088	1.364 0.983	0.293
0.413541	751.683	0	4720.5	0.261	2.316 1.643	0.412
0.273318	805.585	0	4201.2	0.543	3.268 2.241	0.484
0.482125	769.564	0	4910.8	0.179	2.58 1.875	0.526
0.285577	1342.626	0	3856.8	1.327	6.137 4.112	0.698
0.27795	1521.588	0	3385.6	3.63	11.488 6.915	0.943
0.310799	1398.655	0	3942.2	1.158	7.743 5.371	1.214

Table 7: The results in the battlefield environment.

Waypoints number	Route length (KM)	Detection probability	Mean altitude (M)	Total calculation time (S)		
				Initial path	Compress and smoothen	Altitude adjusting
22	143.436	0.0019	3953.1		0.483	
				0.093	0.308	0.082
71	513.648	0.0023	4655.4		2.361	
				0.77	1.264	0.327
111	865.65	0.0017	5133.7		6.048	
				2.732	2.871	0.445
215	1592.591	0.0011	3750.4		19.146	
				11.998	6.127	1.021

Table 8: Comparison results of different algorithms.

Algorithm type	Assessment value	Route length (KM)	Detection probability	Mean altitude (M)	Total calculation time (S)		
					Initial path	Compress and smoothen	Altitude adjusting
Improved A^*	0.130927	60.611	0	3528.9		0.129	
					0.004	0.086	0.039
ACS	0.133615	61.678	0	3513.6		90.715	
					110.265	110.265	110.265
GA	0.134115	59.898	0	3562.5		110.265	
					110.142	0.092	0.031
Improved A^*	0.207394	441.867	0	3963.8		1.51	
					0.271	0.952	0.287
ACS	0.231413	446.073	0	4041.3		1396.646	
					1394.478	1.957	0.211
GA	0.223132	450.576	0	3997.2		1769.705	
					1766.738	2.732	0.235
Improved A^*	0.273318	805.585	0	4201.2		3.268	
					0.543	2.241	0.484
ACS	0.27901	793.658	0	4236.3		3652.089	
					3643.819	7.717	0.553
GA	0.285504	799.532	0	4248.3		2944.994	
					2931.554	12.793	0.647
Improved A^*	0.27795	1521.588	0	3385.6		11.488	
					3.63	6.915	0.943
ACS	0.280544	1496.949	0	3463.5		11541.301	
					10848.625	31.539	1.137
GA	0.297615	1588.795	0	3398.7		7645.141	
					7570.303	73.15	1.688

that the path is better when the value of $\omega_1 : \omega_2 : \omega_3$ is $1:2:1$ rather than $1:1:1$ or $2:1:1$, but the assessment still depends on the parameters in Table 4.

Second, since the final path cannot be directly obtained by the A^* process as mentioned in Section 2.2.1., the searching result after the optimization process may no longer be the optimal solution. Although we adjusted the algorithms to locally optimize the route segments, globally optimizing the entire path is still to be solved.

Finally, the comparison of the improved A^* algorithm with ACA and GA shows its great superiority in time efficiency, but the advantage is not so obvious in the planning result, and more iterations of ACA or GA may even obtain better result than A^* algorithm. However, considering the

internal limitations of the latter, like their stability (sensitive to initial parameters), convergence, and efficiency, they need to be further studied to be used in the UAV path planning.

Conflict of Interests

The authors declare that there is no conflict of interests regarding the publication of this paper.

Acknowledgments

This work was supported by Grants from the National Basic Research Program of China (973 Program) (no. 2011CB707101), the National High Technology Research and Development Program of China (863 Program) (nos. 2011AA010500 and 2013AA01A608), the National Key Projects (2013ZX07503-001), and the National Nature Science Foundation of China (NSFC) Program (no. 2010CDB08403). The authors appreciate the support and help from both the Air Defense Commanding Troops and their research centers.

References

[1] B. M. Sathyaraj, L. C. Jain, A. Finn, and S. Drake, "Multiple UAVs path planning algorithms: a comparative study," *Fuzzy Optimization and Decision Making*, vol. 7, no. 3, pp. 257–267, 2008.

[2] S. S. Ge and Y. J. Cui, "Dynamic motion planning for mobile robots using potential field method," *Autonomous Robots*, vol. 13, no. 3, pp. 207–222, 2002.

[3] Y. Koren and J. Borenstein, "Potential field methods and their inherent limitations for mobile robot navigation," in *Proceedings of the IEEE International Conference on Robotics and Automation*, vol. 2, pp. 1398–1404, Sacramento, Calif, USA, April 1991.

[4] D. P. Horner and A. J. Healey, "Use of artificial potential fields for UAV guidance and optimization of WLAN communications," in *Proceedings of the IEEE/OES Autonomous Underwater Vehicles*, pp. 88–95, June 2004.

[5] J. Ruchti, R. Senkbeil, J. Carroll, J. Dickinson, J. Holt, and S. Biaz, "UAV collision avoidance using artificial potential fields," Tech. Rep. #CSSE11-03, 2011.

[6] F. C. J. Allaire, M. Tarbouchi, G. Labonté, and G. Fusina, "FPGA implementation of genetic algorithm for UAV real-time path planning," *Journal of Intelligent and Robotic Systems*, vol. 54, no. 1–3, pp. 495–510, 2009.

[7] D. M. Pierre, N. Zakaria, and A. J. Pal, "Master-slave parallel vector-evaluated genetic algorithm for unmanned aerial vehicle's path planning," in *Proceedings of the 11th International Conference on Hybrid Intelligent Systems (HIS '11)*, pp. 517–521, Malacca, Malaysia, December 2011.

[8] M. A. P. Garcia, O. Montiel, O. Castillo, R. Sepúlveda, and P. Melin, "Path planning for autonomous mobile robot navigation with ant colony optimization and fuzzy cost function evaluation," *Applied Soft Computing*, vol. 9, no. 3, pp. 1102–1110, 2009.

[9] A. Jevtić, D. Andina, A. Jaimes, J. Gomez, and M. Jamshidi, "Unmanned aerial vehicle route optimization using ant system algorithm," in *Proceedings of the 5th International Conference on System of Systems Engineering (SoSE '10)*, pp. 1–6, Loughborough, UK, June 2010.

[10] http://theory.stanford.edu/~amitp/GameProgramming/index.html.

[11] R. Samar and A. Rehman, "Autonomous terrain-following for unmanned air vehicles," *Mechatronics*, vol. 21, no. 5, pp. 844–860, 2011.

[12] J. Benton, S. S. Iyengar, W. Deng, N. Brener, and V. S. Subrahmanian, "Tactical route planning: new algorithms for decomposing the map," in *Proceedings of the 7th International Conference on Tools with Artificial Intelligence*, pp. 268–277, Herndon, Va, USA, November 1995.

[13] R. J. Szczerba, P. Galkowski, I. S. Glickstein, and N. Ternullo, "Robust algorithm for real-time route planning," *IEEE Transactions on Aerospace and Electronic Systems*, vol. 36, no. 3, pp. 869–878, 2000.

[14] H. Cao, N. E. Brener, and S. S. Iyengar, "3D large grid route planner for the autonomous underwater vehicles," *International Journal of Intelligent Computing and Cybernetics*, vol. 2, no. 3, pp. 455–476, 2009.

[15] M. G. H. Bell, "Hyperstar: a multi-path Astar algorithm for risk averse vehicle navigation," *Transportation Research B*, vol. 43, no. 1, pp. 97–107, 2009.

[16] L. de Filippis, G. Guglieri, and F. Quagliotti, "Path planning strategies for UAVS in 3D environments," *Journal of Intelligent & Robotic Systems*, vol. 65, no. 1–4, pp. 247–264, 2012.

[17] M. Jun and R. D'Andrea, "Path planning for unmanned aerial vehicles in uncertain and adversarial environments," in *Cooperative Control: Models, Applications and Algorithms*, vol. 1, pp. 95–110, Springer, New York, NY, USA, 2003.

[18] L. de Filippis, G. Guglieri, and F. Quagliotti, "A minimum risk approach for path planning of UAVs," *Journal of Intelligent & Robotic Systems*, vol. 61, no. 1–4, pp. 203–219, 2011.

[19] V. Roberge, M. Tarbouchi, and G. Labonte, "Comparison of parallel genetic algorithm and particle swarm optimization for real-time UAV path planning," *IEEE Transactions on Industrial Informatics*, vol. 9, no. 1, pp. 132–141, 2013.

[20] M. I. Skolnik, *Radar Handbook*, McGraw-Hill Professional, New York, NY, USA, 1991.

[21] S. Abbasbandy, "Improving Newton-Raphson method for nonlinear equations by modified Adomian decomposition method," *Applied Mathematics and Computation*, vol. 145, no. 2-3, pp. 887–893, 2003.

[22] Y. V. Pehlivanoglu, "A new vibrational genetic algorithm enhanced with a Voronoi diagram for path planning of autonomous UAV," *Aerospace Science and Technology*, vol. 16, no. 1, pp. 47–55, 2012.

[23] S. J. Asseo, "Terrain following/terrain avoidance path optimization using the method of steepest descent," in *Proceedings of the IEEE National Aerospace and Electronics Conference (NAECON '88)*, vol. 3, pp. 1128–1136, Dayton, Ohio, USA, May 1988.

[24] G. Chen and L. Li, "An optimized algorithm for lossy compression of real-time data," in *Proceedings of the IEEE International Conference on Intelligent Computing and Intelligent Systems (ICIS '10)*, pp. 187–191, Xiamen, China, October 2010.

[25] K. Yang and S. Sukkarieh, "3D smooth path planning for a UAV in cluttered natural environments," in *Proceedings of the IEEE/RSJ International Conference on Intelligent Robots and Systems (IROS '08)*, pp. 794–800, Nice, France, September 2008.

[26] U.S. Department of Transportation Federal Aviation Administration, "Standard for required navigation performance (RNP) approach procedures with special aircraft and aircrew authorization required," June 2005.

[27] http://www.gaeaway.com/html.asp?type=20&page=2.

Hindawi Publishing Corporation
Mathematical Problems in Engineering
Volume 2014, Article ID 207826, 9 pages
http://dx.doi.org/10.1155/2014/207826

Research Article

Electric Drive Control with Rotor Resistance and Rotor Speed Observers Based on Fuzzy Logic

C. Ben Regaya, A. Zaafouri, and A. Chaari

Unit C3S, High National School of Engineers of Tunis (ESSTT), University of Tunis, 5 Avenue Taha Hussein, BP 56, 1008 Tunis, Tunisia

Correspondence should be addressed to C. Ben Regaya; chiheb_ben_regaya@yahoo.fr

Received 10 September 2013; Revised 19 November 2013; Accepted 19 November 2013; Published 16 February 2014

Academic Editor: Hui Zhang

Many scientific researchers have proposed the control of the induction motor without speed sensor. These methods have the disadvantage that the variation of the rotor resistance causes an error of estimating the motor speed. Thus, simultaneous estimation of the rotor resistance and the motor speed is required. In this paper, a scheme for estimating simultaneously the rotor resistance and the rotor speed of an induction motor using fuzzy logic has been developed. We present a method which is based on two adaptive observers using fuzzy logic without affecting each other and a simple algorithm in order to facilitate the determination of the optimal values of the controller gains. The control algorithm is proved by the simulation tests. The results analysis shows the characteristic robustness of the two observers of the proposed method even in the case of variation of the rotor resistance.

1. Introduction

Induction motors are broadly used in industrial applications and the majority of power in the world is currently consumed by them. They are used because of their benefits compared to other types of rotating electrical machines, such as robustness, reliability, and reduced maintenance [1]. Many methods of control presented in the literature have been proposed to circumvent the problem of variation of the rotor resistance for the indirect field-oriented controlled induction machines, which can change with time due to ohmic heating [2]. Among these methods, we can mention the adaptive control using an adaptive scheme of the rotor resistance [3, 4], identification of rotor resistance based on Lyapunov stabilization theory [5], and estimator based on fuzzy logic [6–8]. In these studies, estimation and adaptation mechanisms have been used with the sole aim to correct the rotor resistance used as a reference value in the calculation of the slip frequency. To know the exact position of the rotor flux, the estimation block of the slip angular speed will be used by the control algorithm. Following the research done in this field shows that the performance of the control for the induction motor drive depends heavily on the precision with which the motor parameters are known in particular the rotor resistance. Its mismatch affects significantly the open loop slip estimator and degrades the performance of the speed control, especially when the machine is loaded [3–6].

In addition to the adaptive control of the vector control with rotor resistance adaptation, other works have proposed the speed sensorless control [9–14]. The elimination of speed sensors has become an inevitable task to guarantee the high performance control and operating reliability, not only because the sensors increase the cost and complexity of machines, but also the measures are stained by the noise that affects the robustness of control, especially in hostile environments. Various technical controls without speed sensor were presented in this research, such as adaptive speed observer [9], MRAS speed estimator [10, 11], fuzzy logic speed observer [12], and backstepping and sliding mode speed observer [13, 14].

A variation of the rotor resistance will cause an error of estimating the rotor speed [3]. To overcome this drawback, simultaneous estimation of the motor speed and the rotor resistance is required [15, 16]. In this paper, a solution based on the theory of the fuzzy logic is developed. The method will allow the estimation of rotor resistance and reinject it in the

control loop in order to guarantee the decoupling between the torque and flux dynamics. This solution will guarantee a good estimation of the slip frequency even in the case of variations in the rotor resistance. For the speed estimation we have used the model reference adaptive system MRAS observer which is based on fuzzy logic. Therefore, we have two observers which use fuzzy logic without interacting with each other. This paper presents the steps to be followed for the development of simultaneous estimation of the rotor resistance and rotor speed using two types of observer based on fuzzy logic.

First we are going to present the mathematical model of the induction motor in Section 2. Section 3 is dedicated to present the indirect field-oriented control technique. Then we are going to describe the steps of designing the fuzzy logic observer of the rotor resistance. The fuzzy logic MRAS speed estimation and the algorithm to determine the optimal values of the controller gains are developed in Section 5. Finally, simulations are presented in the last section using Matlab environment with some comments to conclude this work.

2. Induction Motor Modeling

The mathematical model of the induction motor can be described in the reference frame connected to the rotating field as follows [5, 12]

$$\frac{d}{dt}\begin{bmatrix} i_s \\ \phi_r \end{bmatrix} = \begin{bmatrix} A_{11} & A_{12} \\ A_{21} & A_{22} \end{bmatrix}\begin{bmatrix} i_s \\ \varphi_r \end{bmatrix} + \begin{bmatrix} B_1 \\ 0 \end{bmatrix} v_s, \qquad i_s = C\begin{bmatrix} i_s \\ \varphi_r \end{bmatrix}, \tag{1}$$

where

$i_s = [i_{sd} \;\; i_{sq}]^T$: stator current,

$\phi_r = [\varphi_{rd} \;\; \varphi_{rq}]^T$: rotor flux,

$v_s = [v_{sd} \;\; v_{sq}]^T$: stator voltage,

$A_{11} = -((R_s/\sigma L_s) + (R_r(1-\sigma)/\sigma L_r))I - \omega_s J$,

$A_{12} = (L_m/\sigma L_s L_r)[(R_r/L_r)I - \omega_r J]$,

$A_{21} = (L_m/\tau_r)I$, $A_{22} = (\omega_s - \omega_r)J - (1/\tau_r)I$, $B_1 = (1/\sigma L_s)I$,

$C = [I \;\; 0_{2\times 2}]$, $I = \begin{bmatrix} 1 & 0 \\ 0 & 1 \end{bmatrix}$, $J = \begin{bmatrix} 0 & -1 \\ 1 & 0 \end{bmatrix}$,

R_r, R_s: stator and rotor resistance,

L_s, L_r: stator and rotor self-inductance,

L_m: mutual inductance,

σ: leakage coefficient,

τ_r: rotor time constant,

ω_s: stator angular frequency,

ω_r: motor angular velocity (electric angle).

The electromagnetic torque developed by the machine is expressed by

$$T_{\text{em}} = \frac{3}{2}\frac{L_m n_p}{L_r}\left(\varphi_{rd} i_{sq} - \varphi_{rq} i_{sd}\right). \tag{2}$$

3. Indirect Field-Oriented Control of Induction Motor Drive (IFOC)

Two recommended techniques for controlling the induction motor with high performance have been presented in the literature. The first one is called direct field-oriented control (DFOC) and the second one is the indirect field-orientated control (IFOC) [1]. In order to optimize the performance of the induction motor and reduce the sensitivity of the stability of the device for controlling the variation of rotor resistance, we will use the indirect field-oriented control technique. The main objective of this control strategy is, as in DC machines, to independently control the torque and the flux; this is done by using a d-q rotating reference frame synchronously with the rotor flux space vector [2, 3]. In ideal field-oriented control, the rotor flux linkage axis is forced to align with the d-axes, and it follows that

$$\varphi_{rq} = \frac{d}{dt}\varphi_{rq} = 0, \qquad \varphi_{rd} = \varphi_r. \tag{3}$$

Applying the result of (3), the torque equation becomes analogous to the DC machine and can be described as follows:

$$T_{\text{em}} = \frac{3}{2}\frac{L_m n_p}{L_r}\varphi_{rd} i_{sq}. \tag{4}$$

The relationship of mechanical speed and the angular velocity of rotating reference frame d-q is given by the following equation:

$$\omega_s = \frac{L_m R_r}{L_r \varphi_{rd}} i_{sq} + n_p \omega_r. \tag{5}$$

4. Strategy for Estimating the Rotor Resistance Using Fuzzy Logic Method

From (1), in steady-state the dynamic of the rotor fluxes can be expressed as follows:

$$\varphi_{rd} = \frac{R_r L_m}{L_r}\left(\frac{L_r}{R_r} i_{sd} + \frac{L_r^2}{R_r^2 L_m}(\omega_s - \omega_r)\varphi_{rq}\right), \qquad \varphi_{rq} = \frac{R_r L_m}{L_r}\left(\frac{L_r}{R_r} i_{sq} - \frac{L_r^2}{R_r^2 L_m}(\omega_s - \omega_r)\varphi_{rd}\right). \tag{6}$$

By replacing φ_{rd}, φ_{rq} with expressions (1), (6) becomes

$$\varphi_{rd} = \frac{(L_m R_r/L_r)\left((R_r/L_r) i_{sd} + (\omega_s - \omega_r)\; i_{sq}\right)}{(R_r/L_r)^2} + (\omega_s - \omega_r)^2, \qquad \varphi_{rq} = \frac{(L_m R_r/L_r)\left((R_r/L_r) i_{sq} - (\omega_s - \omega_r) i_{sd}\right)}{(R_r/L_r)^2} + (\omega_s - \omega_r)^2. \tag{7}$$

The angular velocity is expressed as follows:

$$(\omega_s - \omega_r)^* = \omega_g^* = \frac{R_r^* i_{sq}^*}{L_r^* i_{sd}^*}, \tag{8}$$

where $(*)$ means reference.

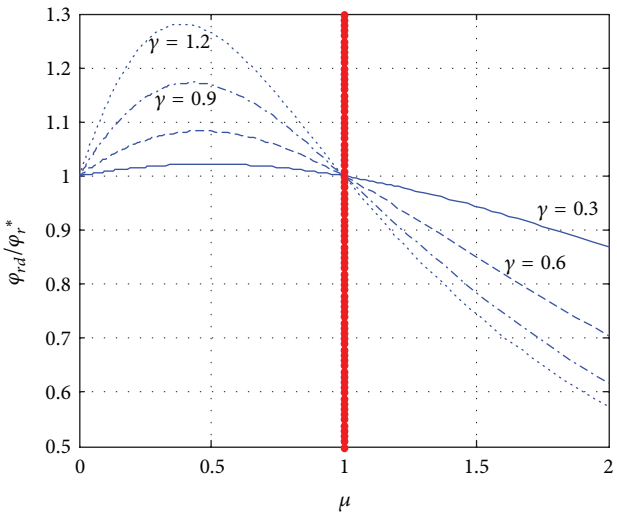

Figure 1: Effect of variation of the rotor resistance on the shape of the direct flux.

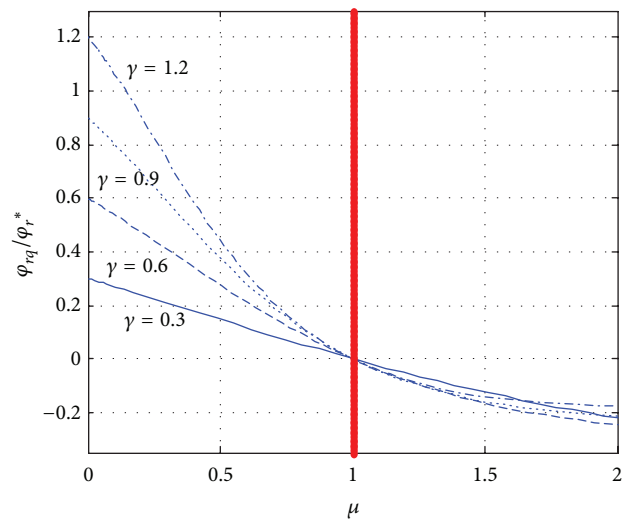

Figure 2: Effect of variation of the rotor resistance on the shape of the quadratic flux.

So the expressions of flux along the two axes become

$$\varphi_r^* = \varphi_{rd}^* = L_m i_{sd}^*, \qquad \varphi_{rq}^* = 0. \tag{9}$$

Equation (9) is considered as a reference model for the mechanism of adjusting the rotor resistance by fuzzy logic. Assuming that the rotor resistance changes from its nominal value R_{rn} to $R_{rn} + \Delta R_r$ and k_{Rr} is the factor for this variation we get

$$k_{Rr} = \frac{R_r}{R_{rn}} = \frac{1}{\mu}, \tag{10}$$

with $\mu = R_{rn}/R_r$.

By replacing the expression of μ in (7) we will have

$$\varphi_{rd} = \frac{L_m i_{sd} + L_m i_{sd}\mu\gamma^2}{1 + (\mu\gamma)^2}, \qquad \varphi_{rq} = \frac{L_m i_{sd}\gamma(1-\gamma)}{1 + (\mu\gamma)^2}, \tag{11}$$

with $\gamma = i_{sq}/i_{sd}$.

Finally, the flux components can be expressed in terms of the reference flux for an ideal decoupling as follows:

$$\frac{\varphi_{rd}}{\varphi_r^*} = \frac{1 + \mu\gamma^2}{1 + (\mu\gamma)^2}, \qquad \frac{\varphi_{rq}}{\varphi_r^*} = \frac{\gamma(1-\gamma)}{1 + (\mu\gamma)^2}. \tag{12}$$

Figures 1 and 2 show the shape of φ_{rd}/φ_r^* and φ_{rq}/φ_r^* as a function of μ, and the vertical line in color red represents the ideal orientation of the rotor flux.

γ is a parameter that reflects the power of the induction motor. The vertical line is the ideal orientation of the flux. We identify changes in flux along the two axes of the rotating frame d-q as follows:

$$\Delta\varphi_{rd} = \varphi_r^* - \varphi_{rd}, \qquad \Delta\varphi_{rq} = -\varphi_{rq}. \tag{13}$$

According to Figures 1 and 2 we can see that

(i) for $\mu > 1$, there is reduced flux along the two axes,

(ii) for $\mu < 1$, there is increased flux along the two axes.

According to (9), we can write

(i) for $\mu > 1$, $\Delta\varphi_{rd} > 0$ and $\Delta\varphi_{rq} > 0$,

(ii) for $\mu < 1$, $\Delta\varphi_{rd} < 0$ and $\Delta\varphi_{rq} < 0$.

Since $\mu = R_{rn}/R_r$, so we can write the rules of the adaptive fuzzy logic mechanism of the rotor resistance R_r as follows:

(i) for $\mu > 1 \Leftrightarrow R_r < R_{rn}$, we have $\Delta\varphi_{rd} > 0$ and $\Delta\varphi_{rq} > 0$,

(ii) for $\mu < 1 \Leftrightarrow R_r > R_{rn}$, we have $\Delta\varphi_{rd} < 0$ and $\Delta\phi_{rq} < 0$.

The block diagram of the fuzzy logic adaptation mechanism used in our simulation is given in Figure 3.

The estimated fluxes $\widehat{\varphi}_{rd}$ and $\widehat{\varphi}_{rq}$ can be obtained by measuring the currents and stator voltages. First we will estimate the stator flux using the following equations:

$$\begin{bmatrix} \varphi_{sd} \\ \varphi_{sq} \end{bmatrix} = \begin{bmatrix} \cos(\theta_s) & \sin(\theta_s) \\ -\sin(\theta_s) & \cos(\theta_s) \end{bmatrix} \begin{bmatrix} \varphi_{s\alpha} \\ \varphi_{s\beta} \end{bmatrix}, \tag{14}$$

with

$$\varphi_{\alpha s} = \int (v_{s\alpha} - R_s i_{s\alpha})\, dt, \qquad \varphi_{\beta s} = \int (v_{s\beta} - R_s i_{s\beta})\, dt. \tag{15}$$

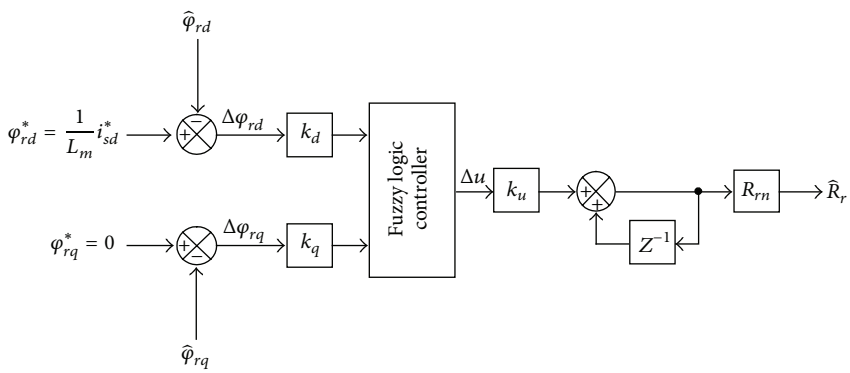

Figure 3: Block diagram of the adaptation mechanism of rotor resistance using fuzzy logic.

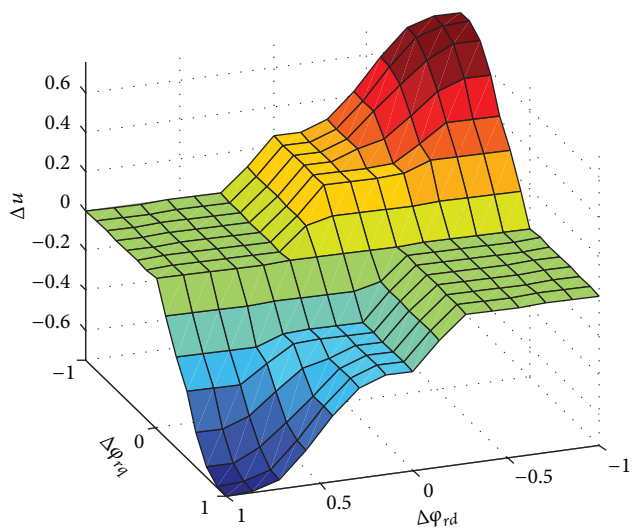

Figure 4: Variation law of fuzzy controller for the rotor resistance.

Then we can calculate the estimated flux by the following equation:

$$\begin{bmatrix} \widehat{\varphi}_{rd} \\ \widehat{\varphi}_{rq} \end{bmatrix} = \begin{bmatrix} \frac{L_r}{L_m} & 0 \\ 0 & \frac{L_r}{L_m} \end{bmatrix} \begin{bmatrix} \varphi_{sd} \\ \varphi_{sq} \end{bmatrix} - \begin{bmatrix} \frac{L_r L_s \sigma}{L_m} & 0 \\ 0 & \frac{L_r L_s \sigma}{L_m} \end{bmatrix} \begin{bmatrix} i_{sd} \\ i_{sq} \end{bmatrix}. \tag{16}$$

When choosing the linguistic value it should be taken into account that the control must be robust and time of calculation adopted by the fuzzy controller should not be high to not slow down the process [6, 7]. In this proposed method linguistic value of 5 is chosen which gives 25 rules.

For fuzzification, we have chosen triangular fuzzification and for deffuzzification the centroid deffuzzification method is used in the proposed method. The universe of discourse is common to all fuzzy variables ($\Delta\varphi_{rd}$, $\Delta\varphi_{rq}$, and Δ_u) and is divided into seven fuzzy sets (NB, NM, NS, ZE, PS, PM, and PB) with triangular membership functions.

In terms of numerical values, the behavior of this mechanism is characterized by action law shown in Figure 4. Indeed, for each pair of input values (Table 1)the mechanism generates a variation of the control law (Δu), which corresponds to the increase or decrease of the rotor resistance.

Table 1: Fuzzy control rules for calculating Δu.

$\Delta\varphi_{rq}$	$\Delta\varphi_{rd}$						
	NB	NM	NS	ZE	PS	PM	PB
NB	PB	PM	PS	PS	ZE	ZE	ZE
NM	PM	PS	PS	PS	ZE	ZE	ZE
NS	PS	PS	PS	PS	ZE	ZE	ZE
ZE	ZE	ZE	ZE	ZE	ZE	ZE	ZE
PS	ZE	ZE	ZE	NS	NS	NS	NS
PM	ZE	ZE	ZE	NS	NS	NS	NM
PB	ZE	ZE	ZE	NS	NS	NM	NB

5. Fuzzy Logic MRAS Speed Observer Design

In this section we will present the different steps to design the fuzzy logic MRAS speed observer. This method consists in comparing the output of both estimators. The first one

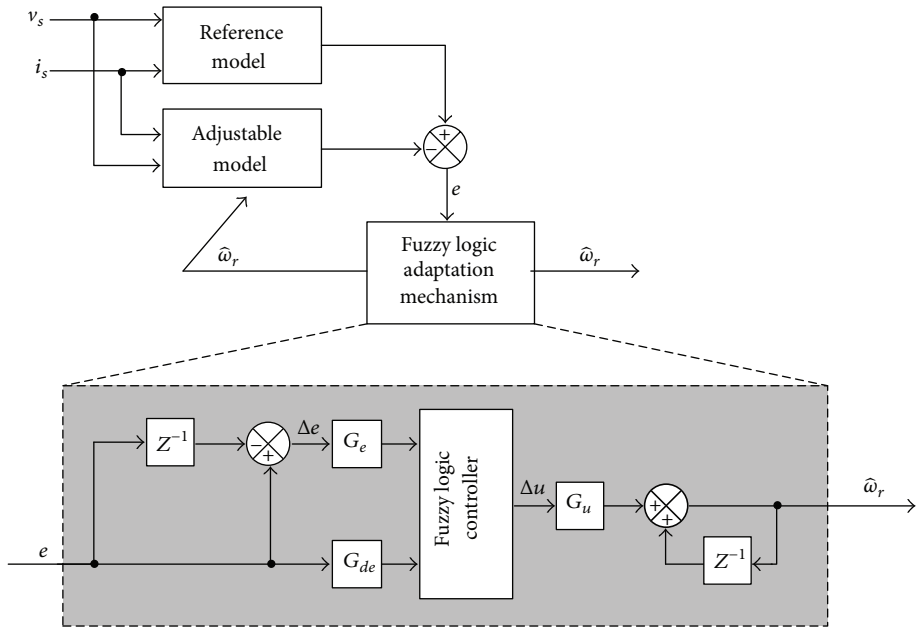

Figure 5: Block diagram of the fuzzy logic MRAS speed observer.

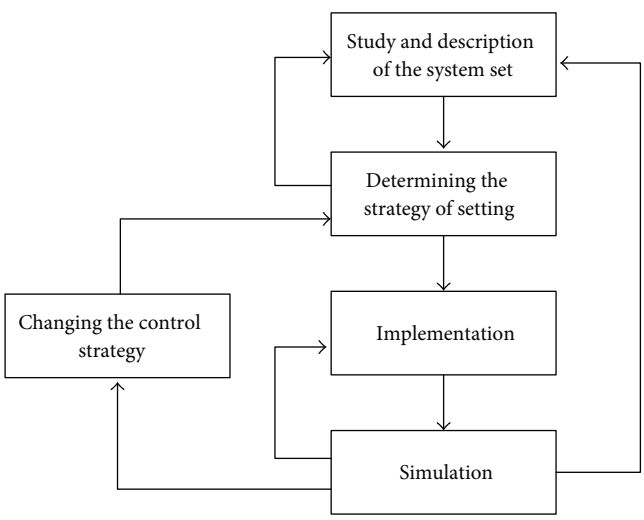

Figure 6: The steps for designing a fuzzy logic controller.

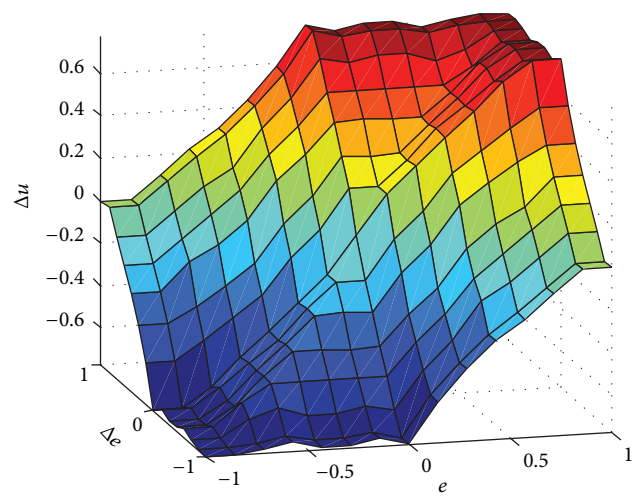

Figure 7: Variation law of fuzzy controller for MRAS speed observer.

is called the reference model which is independent of the quantity to estimate, and the second is the adjustable model [10]. The error between the two estimators of the observing rotor flux is injected in an adaptation mechanism which can generate the value of ω_r as a way to minimize the error of flux.

The mechanism of adaptation is a fuzzy logic controller; the block diagram of the MRAS speed observer and the structure of the controller is shown in Figure 5.

The reference model is expressed by using the stator voltages and stator currents. Their components are expressed in a stationary frame when the flux components are generated. The reference value of the rotor flux components is described by the following equation [3]:

$$\begin{aligned} \frac{d}{dt}\varphi_{rd} &= \frac{L_r}{L_m}\left(v_{sd} - R_s i_{sd} - \sigma L_s \frac{d}{dt} i_{sd}\right), \\ \frac{d}{dt}\varphi_{rq} &= \frac{L_r}{L_m}\left(v_{sq} - R_s i_{sq} - \sigma L_s \frac{d}{dt} i_{sq}\right). \end{aligned} \tag{17}$$

The adaptive model describes the rotor equation and the rotor flux according to the d-q axes which are expressed as a

function of the rotor speed and the stator currents. From (1), the adaptive model is described by the following equations:

$$\begin{aligned} \frac{d}{dt}\widehat{\varphi}_{rd} &= -\frac{R_r}{L_r}\widehat{\varphi}_{rd} - \widehat{\omega}_r\widehat{\varphi}_{rq} + \frac{L_m R_r}{L_r} i_{sd}, \\ \frac{d}{dt}\widehat{\varphi}_{rq} &= -\frac{R_r}{L_r}\widehat{\varphi}_{rq} + \widehat{\omega}_r\widehat{\varphi}_{rd} + \frac{L_m R_r}{L_r} i_{sq}. \end{aligned} \tag{18}$$

From (17) and (18), the adaptation mechanism can be designed to generate the estimated speed value which is used to minimize the error between the estimate and reference fluxes. The error between reference model and adjustable model e is minimized by a fuzzy logic controller which generates the estimated speed. This signal e is given by the following expression:

$$e = \varphi_{rq}\widehat{\varphi}_{rd} - \varphi_{rd}\widehat{\varphi}_{rq}. \tag{19}$$

For the design of a fuzzy regulator we must, first, study the system to adjust and make an adequate description. It is not a proper analysis to establish a mathematical model. We must rather explore the behavior of the controlled system vis-à-vis changes in the control variable and determine measurable quantities characteristic of dynamic behavior. The description may make use of linguistic variables and must be accompanied by a definition of membership functions [12]. Then we move on to determining the control strategy that includes the fuzzification, inference, and deffuzzification. After implementation, most often on a PC or microprocessor software or hardware with processor autographed (specific processors for the fuzzy logic), testing the installation is usually necessary to change the control strategy interactively in several steps in order to find proper behavior. This change is highlighted by Figure 6, since it is an important step in the design of a fuzzy set.

The quality of adjustment depends not only on the rules but also on the choice of values with which the input and output variables are multiplied. To define the values of G_e, G_{de}, and G_u we use the following algorithm.

Step 1. Set the gains values of G_e, G_{de}, and G_u (in our case $G_e = 1$, $G_{de} = 1$, and $G_u = 1$).

Step 2. If the error <1%, go to Step 7.

Step 3. Adjust G_e.

Step 4. If the error >10%, go to Step 3.

Step 5. Adjust G_{de} and G_u.

Step 6. If the error >1%, go to Step 5.

Step 7. End of algorithm.

The establishment of rules defining the output results from operating expertise. For our application, we used the basic rules given in Table 2, which stems from expertise and is based on the operating principle of the bang-bang that offers very good results. The latter is organized in the form of a decision table. The inference method used is the method (Max-Min) since it is easy to implement. The following table shows the rules that correspond to these reflections.

Table 2: Table fuzzy control rules Δu.

$e/\Delta e$	NB	NS	ZE	PS	PB
NB	NB	NB	NB	NS	ZE
NS	NB	NB	NS	ZE	PS
ZE	NB	NS	ZE	PS	PB
PS	NS	ZE	PB	PB	PB
PB	ZE	PS	PB	PB	PB

In the proposed method each variable of the fuzzy logic controller has five triangular membership functions. The fuzzy sets used in the proposed method are NB: Negative Big, NS: Negative Small, ZE: Zero Equal, PS: Positive Small, and PB: Positive Big. The variation law of fuzzy controller for MRAS speed observer is shown in Figure 7.

6. Simulation Results and Discussion

The performances of the proposed solution are evaluated using Matlab-Simulink. A dynamic three-phase induction motor model with speed and rotor resistance observer was built to emulate behavior of the motor. The three-phase induction motor parameters are given in Table 3. Figure 8 shows the architecture of the vector control algorithm incorporating the fuzzy logic MRAS speed observer and rotor resistance fuzzy logic observer.

Figure 9 shows the effect of sudden change on the shape of direct and quadratic flux. At $t = 2$ s we introduced a 50% increase of the rotor resistance. Just at the moment of variation (Figure 9(a)) the orientation of the fluxes is lost, which has a negative effect on the control. Using an estimate of the rotor resistance by the fuzzy logic guarantees the orientation of flux (Figure 9(b)).

Figure 10 shows the evolution of the real and estimated rotor resistance. When increasing the value of the rotor resistance, the fuzzy controllers calculate the new value and inject it into the control loop to ensure decoupling between the flux and torque dynamics.

Figure 11 shows the effect of a slow change of the rotor resistance on the flux behavior. Without adaptation it is clear that we will lose the direction of flux (Figure 11(a)). However, with rotor resistance adaptation we can keep the orientation of the flux (Figure 11(b)).

Figure 12 shows the response of the fuzzy controller for a slow variation of rotor resistance; the estimated and actual rotor resistances are almost the same.

Figure 13 represents the reference, estimated, and actual speed. This figure illustrates the speed system response under a load torque of 10 Nm applied at $t = 0.5$ s; the reference speed is increased from zero to its rated value 157 rd/s. The motor reaches its steady state after 0.4 s. At $t = 1$ s, we applied a slow increase of 50% of the value of the rotor resistance and a change in the reference speed at $t = 1.5$ s. The real and estimated speed are nearly similar and the difference between

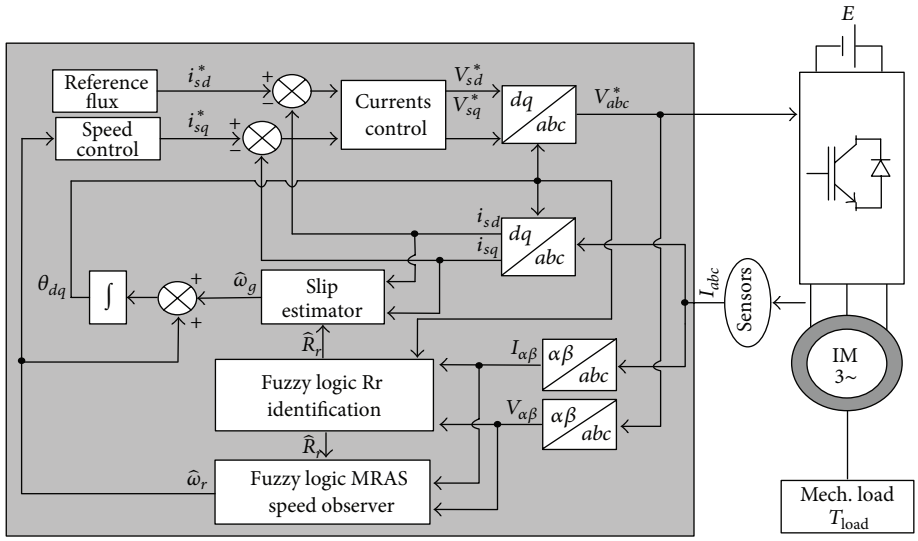

FIGURE 8: Block diagram of the vector control including speed and rotor resistance fuzzy logic observer.

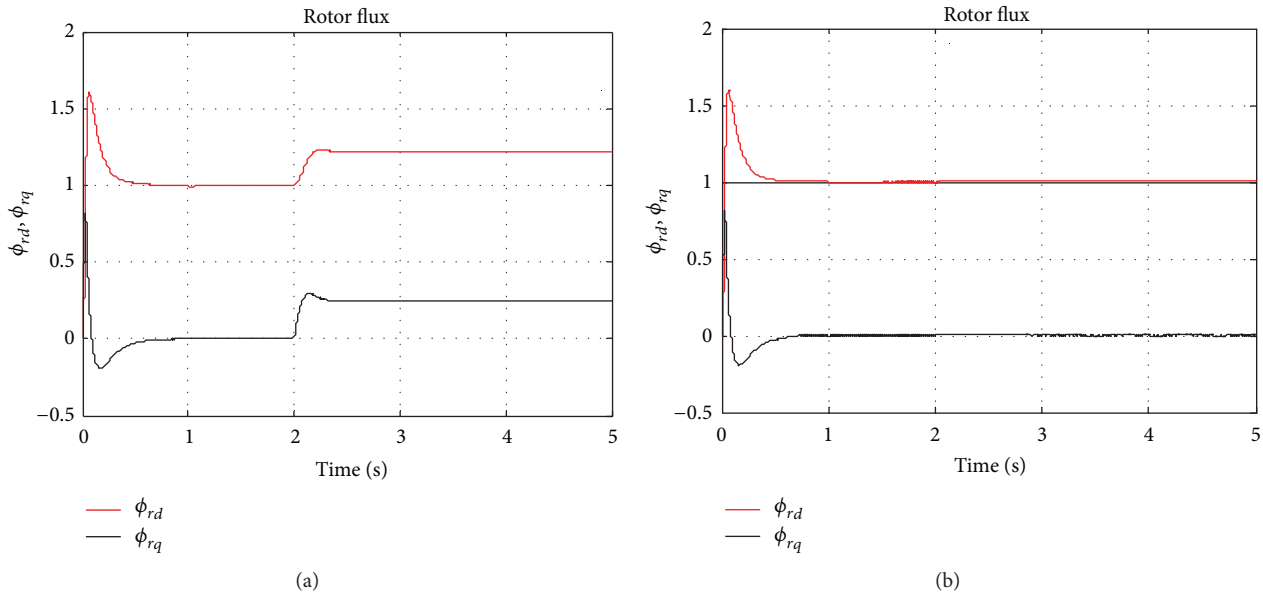

FIGURE 9: Simulated results with sudden change of the rotor resistance with and without adaptation: (a) without adaptation and (b) with adaptation.

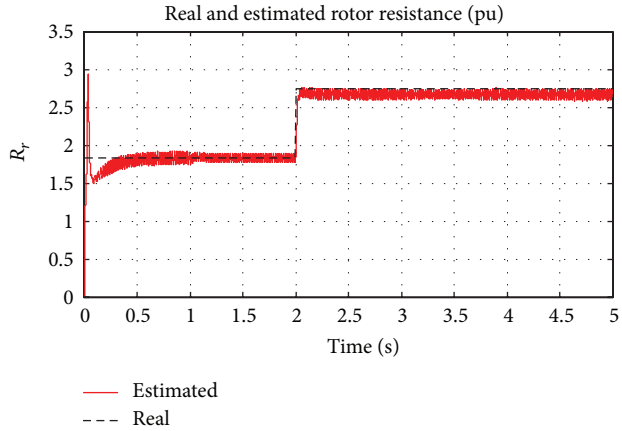

FIGURE 10: Tracking of the rotor resistance by fuzzy logic controller (case: sudden change).

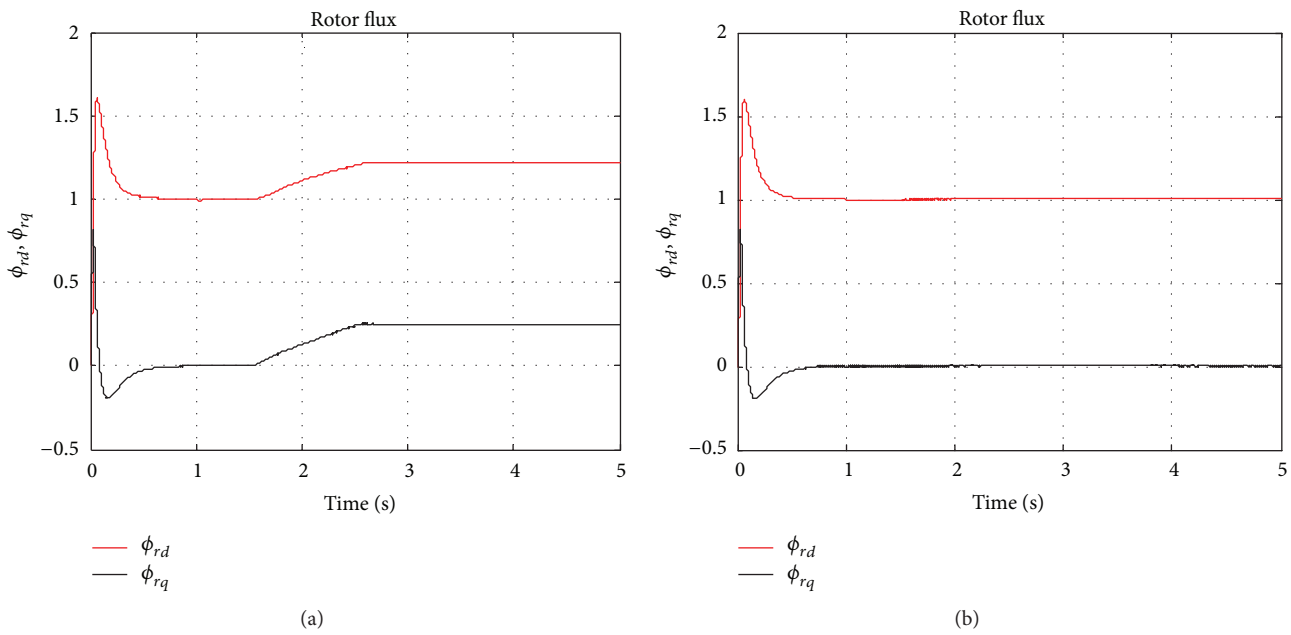

Figure 11: Simulated results with slow change of the rotor resistance with and without adaptation: (a) without adaptation, and (b) with adaptation.

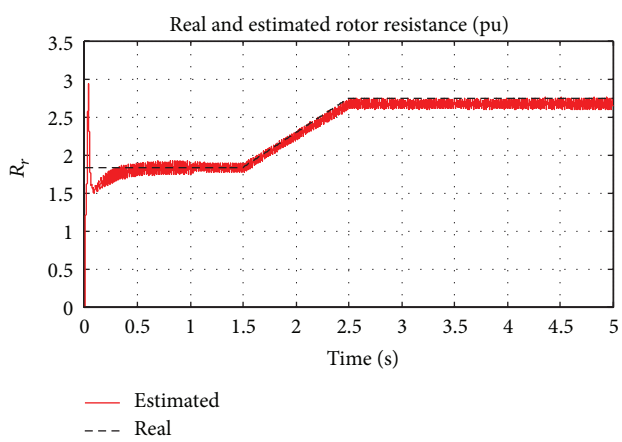

Figure 12: Tracking of the rotor resistance by fuzzy logic controller (case: slow change).

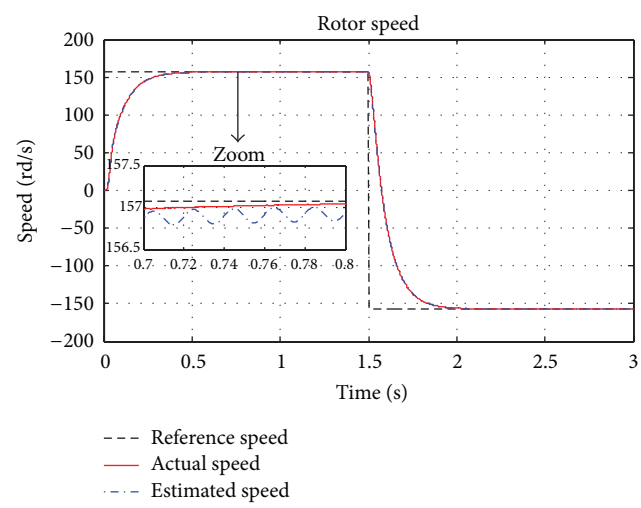

Figure 13: Simulation result of the fuzzy logic MRAS speed observer.

Table 3: Parameters of induction motor.

Designation	Notations	Rating values
Stator resistance	R_s	2.3 Ω
Rotor resistance	R_r	1.83 Ω
Stator self-inductance	L_s	261 mH
Rotor self-inductance	L_r	261 mH
Mutual inductance	L_m	245 mH
Moment of inertia	J	0.03 kgm^2
Friction coefficient	f	0.002 Nm
Number of poles	n_p	2
Rated voltage	V_{sn}	220 V

them is better shown in Figure 14 which does not exceed 1% of the nominal value.

7. Conclusion

To sum up we say that this paper presents a method to estimate the rotor resistance for induction machines based on the theory of fuzzy logic. A standard IFOC without speed sensor has been used for the induction machine based on the same theory to design a MRAS speed observer. The modeling approach proposed for both observers makes a high-performance control strategy to be used with induction

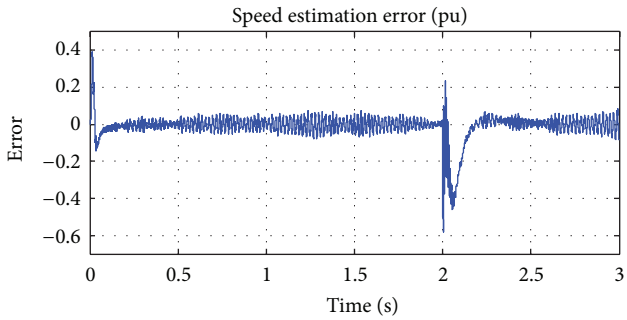

Figure 14: Error between real and estimated speed.

motor drive system. The drive system has been simulated with adaptive mechanisms to identify the values of rotor resistance and rotor speed based on fuzzy logic. The different simulation results have shown that the designed fuzzy logic observer has realized a good dynamic and performance for motor monitoring even in the case of the rotor resistance variation. The efficacity of the speed sensorless of the IFOC with rotor resistance is proved by extensive simulation results. The IFOC, the speed observer, and the rotor resistance observer described in the previous sections are to be implemented in the future work on a digital processor (DSP) to validate the proposed scheme.

Conflict of Interests

The authors declare that there is no conflict of interests regarding the publication of this paper.

References

[1] C. B. Regaya, A. Zaafouri, and A. Chaari, "Speed sensorless indirect field-oriented of induction motor using two type of adaptive observer," in *Proceedings of the International Conference on Electrical Engineering and Software Applications (ICEESA '13)*, pp. 1–5, Hammamet, Tunisia, March 2013.

[2] F. Farhani, C. B. Regaya, A. Zaafouri, and A. Chaari, "Electric drive control: multi-level optimization efficiency," in *Proceedings of the 4th International Renewable Energy Congress (IREC '12)*, pp. 894–898, Sousse, Tunisia, December 2012.

[3] C. B. Regaya, F. Farhani, A. Zaafouri, and A. Chaari, "Comparison between two methods for adjusting the rotor resistance," *International Review on Modelling & Simulations*, vol. 5, no. 2, pp. 938–944, 2012.

[4] A. Savoia, C. M. Verrelli, M. Mengoni, L. Zarri, A. Tani, and D. Casadei, "Adaptive flux observer for induction machines with on-line estimation of stator and rotor resistances," in *Proceedings of the 15th International Power Electronics and Motion Control Conference (EPE/PEMC '12)*, pp. LS7b-1.3-1–LS7b-1.3-6, Novi Sad, Serbia, September 2012.

[5] G. Shuqiu and L. Zhongli, "Induction motor vector control based on adaptive identification of rotor resistance," in *Proceedings of the International Conference on Control Engineering and Communication Technology (ICCECT '12)*, pp. 145–148, Liaoning, China, December 2012.

[6] Y. Miloud and A. Draou, "Fuzzy logic based rotor resistance estimator of an indirect vector controlled induction motor drive," in *Proceedings of the 28th Annual Conference of the IEEE Industrial Electronics Society (IECON '02)*, vol. 2, pp. 961–966, Sevilla, Spain, November 2002.

[7] H. Zhang, Y. Shi, and J. Wang, "Observer-based tracking controller design for networked predictive control systems with uncertain Markov delays," *International Journal of Control*, vol. 86, no. 10, pp. 1824–1836, 2013.

[8] H. Zhang, Y. Shi, and A. S. Mehr, "On H-infinity filtering for discrete-time takagi-sugeno fuzzy systems," *IEEE Transactions on Fuzzy Systems*, vol. 20, no. 2, pp. 396–401, 2012.

[9] H. Kubota, I. Sato, Y. Tamura, K. Matsuse, H. Ohta, and Y. Hori, "Regenerating-mode low-speed operation of sensorless induction motor drive with adaptive observer," *IEEE Transactions on Industry Applications*, vol. 38, no. 4, pp. 1081–1086, 2002.

[10] H. M. Kojabadi, L. Chang, and R. Doraiswami, "A MRAS-based adaptive pseudoreduced-order flux observer for sensorless induction motor drives," *IEEE Transactions on Power Electronics*, vol. 20, no. 4, pp. 930–938, 2005.

[11] T. Orlowska-Kowalska and M. Dybkowski, "Improved MRAS-type speed estimator for the sensorless induction motor drive," *COMPEL: The International Journal for Computation and Mathematics in Electrical and Electronic Engineering*, vol. 26, no. 4, pp. 1161–1174, 2007.

[12] A. A. Adam and K. Gulez, "Fast response adaptive fuzzy logic controller for sensorless direct torque control of PMSM with minimum torque ripple," *COMPEL: The International Journal for Computation and Mathematics in Electrical and Electronic Engineering*, vol. 27, no. 2, pp. 534–550, 2008.

[13] R. P. Vieira, C. C. Gastaldini, R. Z. Azzolin, and H. A. Grundling, "Discrete-time sliding mode speed observer for induction machine drives," in *Proceedings of the 11th Brazilian Power Electronics Conference (COBEP '11)*, pp. 213–218, Natal, Brazil, September 2011.

[14] D. Traoré, J. de Leon, and A. Glumineau, "Sensorless induction motor adaptive observer-backstepping controller: experimental robustness tests on low frequencies benchmark," *IET Control Theory and Applications*, vol. 4, no. 10, pp. 1989–2002, 2010.

[15] D. P. Marčetić and S. N. Vukosavić, "Speed-sensorless AC drives with the rotor time constant parameter update," *IEEE Transactions on Industrial Electronics*, vol. 54, no. 5, pp. 2618–2625, 2007.

[16] A. Larabi and M. S. Boucherit, "Robust speed-sensorless induction motor with the rotor time constant adaptation," in *Proceedings of the International Conference on Electrical Systems for Aircraft, Railway and Ship Propulsion (ESARS '10)*, Bologna, Italy, October 2010.

Hindawi Publishing Corporation
Mathematical Problems in Engineering
Volume 2014, Article ID 347490, 19 pages
http://dx.doi.org/10.1155/2014/347490

Research Article

Fuzzy Determination of Target Shifting Time and Torque Control of Shifting Phase for Dry Dual Clutch Transmission

Zhiguo Zhao, Haijun Chen, and Yunyun Yang

School of Automotive Studies, Tongji University, Shanghai 201804, China

Correspondence should be addressed to Haijun Chen; chenhaijun312240@sina.com

Received 19 September 2013; Revised 5 November 2013; Accepted 5 November 2013; Published 11 February 2014

Academic Editor: Hui Zhang

Based on the independently developed five-speed dry dual clutch transmission (DDCT), the paper proposes the torque coordinating control strategy between engine and two clutches, which obtains engine speed and clutch transferred torque in the shifting process, adequately reflecting the driver intention and improving the shifting quality. Five-degree-of-freedom (DOF) shifting dynamics model of DDCT with single intermediate shaft is firstly established according to its physical characteristics. Then the quantitative control objectives of the shifting process are presented. The fuzzy decision of shifting time and the model-based torque coordinating control strategy are proposed and also verified by simulating under different driving intentions in up-/downshifting processes with the DCT model established on the MATLAB/Simulink. Simulation results validate that the shifting control algorithm proposed in this paper can not only meet the shifting quality requirements, but also adapt to the various shifting intentions, having a strong robustness.

1. Introduction

To improve Automatic Transmissions' shifting quality, the following measures are usually taken: (1) the timely and effective intervening of engine, namely, the decreasing torque request signal, is given by Transmission Control Unit to Engine Electronic Control Unit in the up- or downshifting process to cut off the fuel injection or delay the response of ignition advance angle, thus obtaining a reduced torque transmitted by hydraulic torque converter; (2) the switch of hydraulic torque converter's working state, that is, the hydraulic torque converter, transfers from "locking" state to "unlocking" state to realize hydraulic transmission in the shifting process; (3) the adjusting of engaging pressure, which means actively adjusting the pressure of main oil line in different conditions according to the engine load change to ensure the shifting feel; (4) the working sequence's match of wet clutch in planetary transmission and brake, thus avoiding shifting overlapping and power interruption; (5) the adoption of shifting actuator equipped with electromagnetic valve and buffer valve. Compared with the AT, the torsion damper in clutch driven plate of dry dual clutch transmission cannot absorb the whole shifting impact without the aid of hydraulic torque converter, thus deteriorating the shifting feel. Meanwhile, the shifting process completely depends on the switch of dual clutches' working state and engine torque active control. Once emerging the torque's inappropriate coordination between the dual clutch and engine, the power interruption, power cycle and large torque fluctuations of transmission output shaft would appear which not only directly influence the shifting comfort, but also cause the shock and vibration of transmission system thus reducing the longevity of drive components. Therefore, the control of shifting process becomes a difficult and key point of DDCT control.

Guo et al. [1] established a two-DOF shifting dynamics model and studied the fuzzy control of DCT shifting process. Considering the inertia, damping, and stiffness of transmission components, Zhang et al. established a five-DOF shifting dynamics model [2, 3]. Goetz et al. [4, 5] and Qin et al. [6] divided the shifting process into torque phase which is used for the torque switch of dual clutch and inertia phase which is used to realize the synchronization of engine speed and clutch target speed. Besides, by controlling the throttle opening and the ignition advance angle, the engine speed was actively controlled to accelerate and ease the synchronization.

Niu et al. [7] divided the upshifting process into five phases, namely, low gear operation phase, low gear torque phase, inertial phase, high gear torque phase, and high gear operation phase. Models of these phases were established with EASY5 software and the simulation of DCT shifting process was studied as well. However, the studies are only qualitative analysis, and the dual clutches' engaging extent varying with time of the dual clutch is not given quantitatively. Wu and Zhan [8] and Zhao et al. [9, 10] obtained the optimal engaging curves of dual clutch by using the linear quadratic optimal control and robust control theory, which provides the theoretical basis for the engineering application of dual clutch coordination control. However, the designing and solving of quadratic optimal control and robust control are difficult to be applied online in the DCT complex shifting process.

Thus based on the independently developed five-speed DDCT, five-DOF shifting dynamics models of DDCT with single intermediate shaft are established. According to the requirements of shifting quality, the quantitative control objectives of the shifting process are proposed. Based on the analysis of torque and speed characteristics of engine and dual clutch during the shifting process, the fuzzy time decision and the model-based torque coordinating control strategy are produced to solve the problem of torque coordination control of dual clutch and engine.

2. Five-Speed Dry DCT Dynamics Equations

2.1. Five-Speed Dry DCT Dynamic Model. The five-speed dry DCT described in the paper is a complex system, which is made up of dry dual clutch and its actuator, four synchronizers and their actuators, single intermediate shaft, and gear transmission mechanism. In order to study the dynamics characteristics of single clutch in the starting process and develop relevant coordinating control strategy, the following assumptions should be made before modeling:

(1) both wheels' moment of inertia and vehicle's translational weight are converted into the transmission output shaft. The engine output shaft and the input shaft and intermediate shaft and output shaft of the transmission are regarded as rigid body with distributed parameters, concentrated inertia, and friction damping;

(2) neglect the clutch actuator's and synchronizers' dynamics, as well as the heat fade of the clutch;

(3) neglect the elasticity between bearing and its block, as well as the elasticity and gap in gear engagement. The established five-speed dry DCT dynamics model after simplification is shown in Figure 1. The relevant parameters and variables are defined in the notation.

2.2. Shifting Dynamics Equations for Five-Speed Dry DCT. In essence, the shifting process of DCT is to switch the working state of dual clutch; that is, the previously engaged clutch disengages and the previously disengaged clutch engages at the same time. Among them, the working process of disengaged and engaged clutch can be divided into three phases (taking the engaging of clutch as an example) as shown in Table 1.

Table 1: Three phases in shifting process.

Three phases in shifting process	Main function
Zero torque transfer phase	Quickly eliminating the vacant distance
Sliding friction phase	Torque and speed coordinating
Clutch fully engaged phase	Stable operation

Zero Torque Transfer Phase. The vacant distance between the driving plate and driven plate is quickly eliminated.

Sliding Friction Phase. The clutch driving plate and driven plate begin to engage and transfer torque, and the torque is gradually increased until the synchronization of the driving plate and driven plate speed.

Clutch Fully Engaged Phase. The transmission is operating in certain gear stably.

Due to the small effect of clutch engaging and disengaging speed in zero torque transferred phase and clutch fully engaged phase on the shifting quality, the attention is only focused on torque coordinating control in sliding friction phase in the paper.

To further analyze the sliding friction phase, this phase is generally divided into torque phase and initial phase [6]. The torque phase is used for the torque switch of dual clutch and the inertia phase is used to realize the synchronization of engine speed and clutch target speed.

2.2.1. Shifting Dynamics Model of DCT in Sliding Friction Phase. Taking the shifting from 1st to 2nd gear speed as an example, in the DCT sliding friction phase, there exists a torque overlap between two clutches to transfer engine torque to the drive wheels, namely, T_{c1} decreases and T_{c2} increases gradually with the clutch 1 disengaging and, meanwhile, clutch 2 engaging little by little. It should be noted that the power cycle may occur in the DCT shifting phase, so the direction of clutch torque is determined by the sign of the error of the clutch driving and driven plate speed. Finally the shifting dynamics model of DCT in sliding friction phase can be obtained by its dynamic analysis:

$$\begin{gathered}
I_e\dot{\omega}_e = T_e - \operatorname{sgn}(\omega_e - \omega_{c1})\, T_{c1} - \operatorname{sgn}(\omega_e - \omega_{c2})\, T_{c2} - b_e\omega_e, \\
I_{c1}\dot{\omega}_{c1} = \operatorname{sgn}(\omega_e - \omega_{c1})\, T_{c1} - T_{mc1} - b_{c1}\omega_{c1}, \\
(I_{c2} + I_{g2})\,\dot{\omega}_{c2} = \operatorname{sgn}(\omega_e - \omega_{c2})\, T_{c2} - T_{mc2} - b_{c2}\omega_{c2}, \\
(I_m + I_{g1})\,\dot{\omega}_m = T_{c1m} + T_{c2m} - T_{sm} - b_m\omega_m, \\
I_s\dot{\omega}_s = T_{ms} - T_f - b_s\omega_s,
\end{gathered} \tag{1}$$

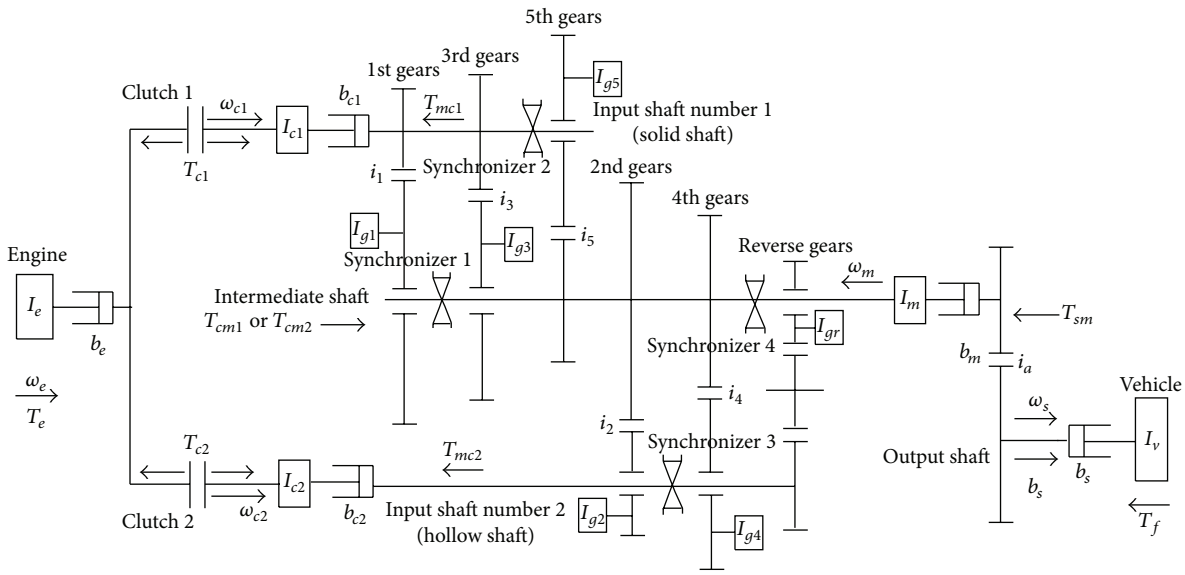

Figure 1: Five-speed dry DCT dynamics model.

where

$$T_{c2} = \begin{cases} \dfrac{2}{3}\left(\dfrac{R_0^3 - R_1^3}{R_0^2 - R_1^2}\right)\mu_2 F(x_2), & \omega_{c2} \le \omega_e, \\ T_{c2}^L, & \omega_{c2} = \omega_e, \end{cases}$$

$$T_e = f(\alpha, \omega_e), \qquad T_{c1m} = T_{mc1} i_1 \eta,$$

$$T_{c2m} = T_{mc2} i_2 \eta, \qquad T_{ms} = T_{sm} i_a \eta,$$

$$T_f = \left(\frac{C_d A}{21.15} v^2 + mg\sin\theta + mg\cos\theta f + \delta m \frac{dv}{dt}\right) R_w \tag{2}$$

$$v = \omega_s R_w,$$

$$\delta = 1 + \frac{1}{m}\frac{I_{c1} i_1^2 i_a^2 + I_m i_a^2 + I_s + I_v}{r^2},$$

where sgn is symbolic function, and its expression is

$$\operatorname{sgn}(\omega_e - \omega_{ci}) = \begin{cases} 1, & \omega_e \ge \omega_{ci}, \\ -1, & \omega_e < \omega_{ci}, \end{cases} \quad i = 1, 2. \tag{3}$$

Assume that

$$\omega_m = \omega_s i_a = \frac{\omega_{c1}}{i_1} = \frac{\omega_{c2}}{i_2}. \tag{4}$$

So the five-DOF model shown in (1) can be simplified to the following two-DOF model:

$$I_e \dot{\omega}_e = T_e - \operatorname{sgn}(\omega_e - \omega_{c1}) T_{c1} - \operatorname{sgn}(\omega_e - \omega_{c2}) T_{c2} - b_e \omega_e,$$

$$I_s^{\text{equ}} \dot{\omega}_s = \operatorname{sgn}(\omega_e - \omega_{c1}) T_{c1} K_{c1} + \operatorname{sgn}(\omega_e - \omega_{c2}) T_{c2} K_{c2} - T_f - b_s^{\text{equ}} \omega_s, \tag{5}$$

where I_s^{equ}, b_s^{equ} are the equivalent moment of inertia and rotating viscous damping coefficient, respectively; K_{c1}, K_{c2} are magnification factors of the torque transferred by clutch 1 and clutch 2, respectively, both of which are equivalently converted to the transmission output shaft; that is,

$$I_s^{\text{equ}} = I_s + (I_m + I_{g1}) i_a^2 \eta + I_{c1} i_1^2 i_a^2 \eta^2 + (I_{c2} + I_{g2}) i_2^2 i_a^2 \eta^2,$$

$$b_s^{\text{equ}} = b_s + b_m i_a^2 \eta + b_{c1} i_1^2 i_a^2 \eta^2 + b_{c2} i_2^2 i_a^2 \eta^2,$$

$$K_{c1} = i_1 i_a \eta^2,$$

$$K_{c2} = i_2 i_a \eta^2. \tag{6}$$

2.2.2. Dynamics Model of DCT In-Gear Stable Operation Phase. Still taking the shifting from 1st to 2nd gear speed as an example, the speed of engine is equal to that of the engaged clutch driven plate before and after the shifting process. Based on this constrain, dynamics model of DCT in-gear stable operation can be obtained from (6). The dynamics model of DCT in 1st speed gear stable operation is

$$I_s^{\text{equ1}} \dot{\omega}_s = T_e K_{e1} - T_f - b_s^{\text{equ1}} \omega_s. \tag{7}$$

The dynamics model of DCT in 2nd speed gear stable operation is

$$I_s^{\text{equ2}} \dot{\omega}_s = T_e K_{e2} - T_f - b_s^{\text{equ2}} \omega_s, \tag{8}$$

where I_s^{equ1}, I_s^{equ2} are equivalent moment of inertia in 1st and 2nd gear speed in stable operation, respectively; b_s^{equ1}, b_s^{equ2} are equivalent rotating viscous damping coefficient in 1st and 2nd gear speed in stable operation, respectively; K_{e1}, K_{e2} are the magnification factors of the torque output by engine in 1st and 2nd gear speed in stable operation, respectively, both of

which are equivalently converted to the transmission output shaft; that is,

$$\begin{aligned} I_s^{\text{equ1}} &= I_s + \left(I_m + I_{g1}\right) i_a^2 \eta + \left(I_{c1} + I_e\right) i_1^2 i_a^2 \eta^2 \\ &\quad + \left(I_{c2} + I_{g2}\right) i_2^2 i_a^2 \eta^2, \\ I_s^{\text{equ2}} &= I_s + \left(I_m + I_{g1}\right) i_a^2 \eta + I_{c1} i_1^2 i_a^2 \eta^2 + \left(I_{c2} + I_{g2} + I_e\right) i_2^2 i_a^2 \eta^2, \\ b_s^{\text{equ1}} &= b_s + b_m i_a^2 \eta + \left(b_{c1} + b_e\right) i_1^2 i_a^2 \eta^2 + b_{c2} i_2^2 i_a^2 \eta^2, \\ b_s^{\text{equ2}} &= b_s + b_m i_a^2 \eta + b_{c1} i_1^2 i_a^2 \eta^2 + \left(b_{c2} + b_e\right) i_2^2 i_a^2 \eta^2, \\ K_{e1} &= i_1 i_a \eta^2, \\ K_{e2} &= i_2 i_a \eta^2. \end{aligned} \tag{9}$$

It should be noted that the dynamic characteristics of the synchronizer are not considered in the dynamics model above for its small effect on shifting quality. That means the 2nd speed gear has already been engaged before the shifting process and the 1st speed gear is still engaging after the shifting process. In addition, the shifting dynamics model of DCT in other speed gears can be obtained in the similar method of the shifting from 1st speed gear to 2nd speed gear.

3. Objectives of Shifting Control and Shifting Process Analysis

3.1. Shifting Quality. The Shock intensity and sliding friction work are usually used to evaluate the shifting quality. And the Shock intensity in the sliding friction phase can be expressed as

$$j = \frac{r}{i_a I_s} \frac{dT_{ms}}{dt} = \frac{r}{i_a I_s} \left(i_1 \frac{dT_{c1}}{dt} + i_2 \frac{dT_{c2}}{dt} \right). \tag{10}$$

It can be noticed from (10) that the Shock intensity j is proportional to the derivative of the transmission output torque T_{ms}; meanwhile T_{ms} is determined by the torque transferred by clutch 1 and clutch 2. Therefore, in theory, if the torque transferred by the dual clutch satisfies a certain relationship, namely, $dT_{ms}/dt = 0$, the total output torque remains constant. That means the Shock intensity j remains constant zero and no impact produced in the shifting process.

The Shock intensity is as follows at the moment when the clutch driving plate speed and driven plate speed is synchronized:

$$\begin{aligned} j &= \frac{i_1 i_a r}{\Delta t} \left[\dot{\omega}_{c1}\left(t^+\right) - \dot{\omega}_{c1}\left(t^-\right) \right] \\ &= \frac{i_1 i_a r}{\Delta t} \frac{I_e}{I_e + I_{c1}^{\text{equ}}} \left[\dot{\omega}_e\left(t^-\right) - \dot{\omega}_{c1}\left(t^-\right) \right], \end{aligned} \tag{11}$$

where $\dot{\omega}_{c1}(t^-)$, $\dot{\omega}_{c1}(t^+)$ are the angular acceleration of clutch driven plate before and after the moment when the speed is synchronous; $\dot{\omega}_e(t^-)$ is the angular acceleration of engine output shaft before the moment when the speed is synchronous; t is the moment when the clutch driving plate speed and driven plate speed are synchronous; Δt is the sampling time of angular acceleration, whose value is determined by the longitudinal vibration frequency range that human body can withstand, taking $\Delta t = 20$ ms in the paper [11].

Equation (11) obviously shows that, in order to reduce the impact of clutch driving and driven plate, it is necessary to minimize the difference of angular acceleration between them at the synchronous moment.

The sliding friction work in the shifting phase can be expressed as

$$L = \int_{t_0}^{t_f} \left(T_{c1} \left|\omega_e - \omega_{c1}\right| + T_{c2} \left|\omega_e - \omega_{c2}\right| \right) dt, \tag{12}$$

where t_0, t_f are the moment when the shifting begins and ends, respectively.

Compared with the DCT starting process, the shifting time of DCT is shorter and the sliding friction work is less. Meanwhile, the sliding friction work is proportional to the shifting time approximately, so the shifting time can represent the slipping friction work generated during the shifting process. In this paper, the shifting time thus is regarded as the measure of slipping friction work, which means if the shifting time is within a reasonable range, the sliding friction work is acceptable. The domestic and international research shows that the shifting time of DCT is generally controlled within 0.5 to 0.8 s [12].

3.2. Objectives of Shifting Control. Based on the analysis of the shifting quality, the following quantitative shifting control objectives are obtained.

(1) Shifting without impact: during the entire shifting phase, the acceleration of the vehicle remains constant and the Shock intensity is identically equal to zero. Namely, $a = a^{\text{Init}}$ and $j \equiv 0$, where a^{Init} is the vehicle acceleration in the shifting beginning moment.

(2) Reasonable shifting time: the shifting time needs to be shortened and satisfy $t \in [0.5, 0.8]$ under the condition of meeting the driver's intention and vehicle and road conditions.

(3) Avoid the power cycle: it should be ensured that the engine speed is greater than or equal to the dual clutch driven plate speeds in sliding friction phase at the same time: $\omega_e \geq \omega_{c1}$ and $\omega_e \geq \omega_{c2}$.

4. Shifting Fuzzy Time Strategy and Torque Coordinating Control

The slip friction process control in the shifting process, as shown in Figure 4, can be specialized as first, according to the intention of the driver, vehicle states, and road conditions, the target shifting time is obtained through the fuzzy reasoning (including the torque phase time and the inertia phase time); second, the online genetic algorithm is adopted to optimize the torque phase time and inertial phase time; then the target speed of engine and the target angular acceleration of the two

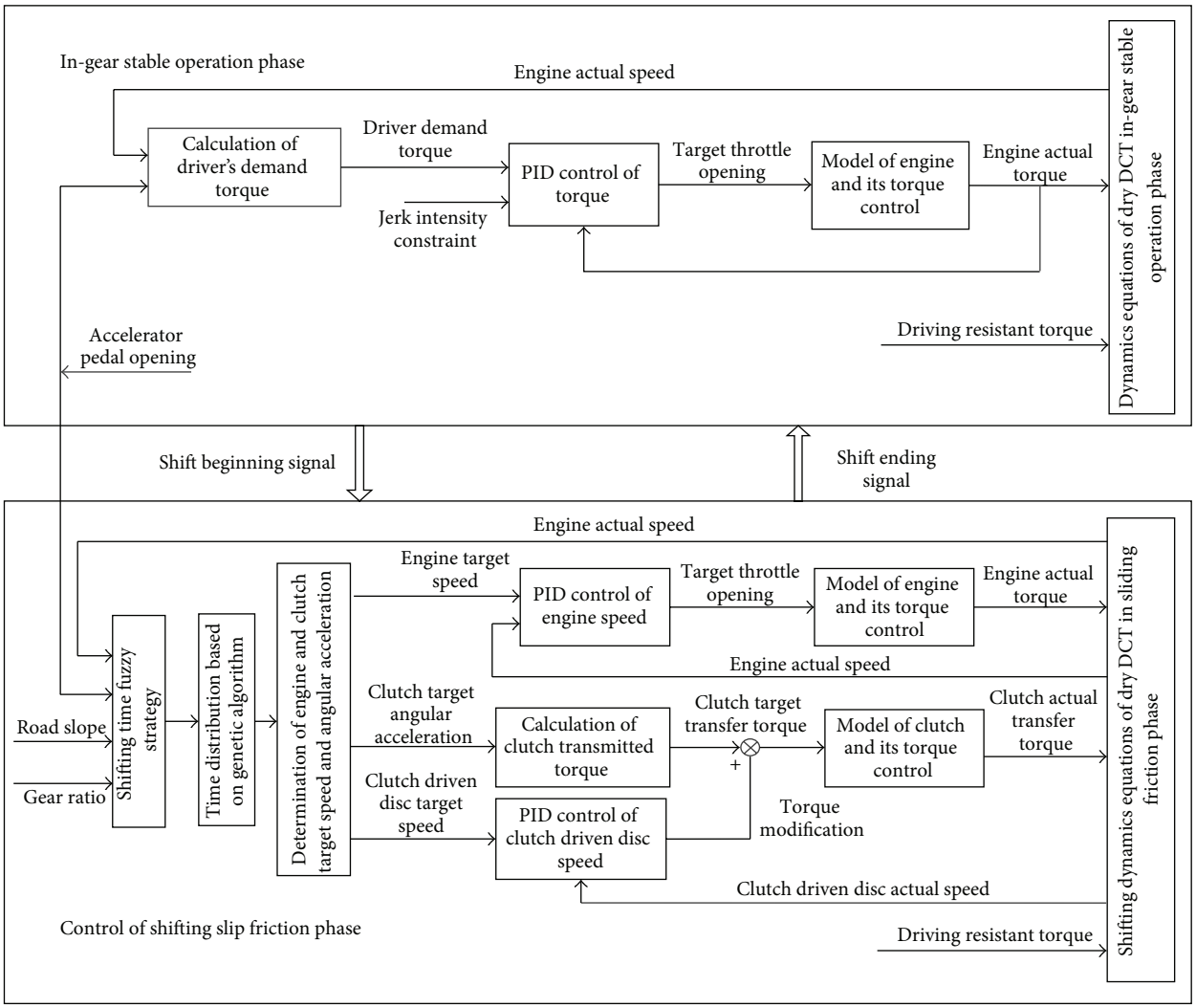

Figure 2: Shifting process control block diagram.

clutch driven plates are determined in the shifting process based on the shifting control quantitative targets; finally, the engine demand torque and the two clutches transmitted torque are calculated through the engine closed-loop control and model-based torque control.

"Shifting starting signal" in Figure 2 is determined by shifting schedule, and "shifting completing signal" refers to the speed synchronization signal of the engine and the clutch driven plate in upshifting process; meanwhile, it refers to the signal that the clutch separates and its torque becomes zero in downshifting process.

4.1. Target Shifting Time Fuzzy Determination

4.1.1. The Influence Factors of Shifting Time. Shifting time is affected and restricted by the factors as follows.

(1) Throttle opening and its changing rate: a relative big throttle opening and its changing rate indicate a shorter desired shifting time and vice versa; it means a longer desired shifting time.

(2) Engine output torque: the smaller the engine output torque is, the worse its load-carrying capacity is. And thus the clutch engaging process should slow down to avoid the flameout of the engine at the expense of shifting time. And when the engine output torque is relatively large, it accelerates the engaging process to shorten the shifting time.

(3) Transmission ratio changes before and after shifting: the greater the ratio changes before and after the shifting mean the bigger the vehicle longitudinal acceleration and dynamic load in the shifting process. To improve the shifting quality, slowing down the clutch engaging speed and extending the shifting time are required. Therefore, the shifting time from 1st speed gear to 2nd speed gear should be longer than from 2nd to 3rd.

(4) Road slope: the bigger the uphill road slope is, the smaller the engine backup power is. At this moment, a quick engagement would undoubtedly render a large shifting impact and may also lead to engine flameout.

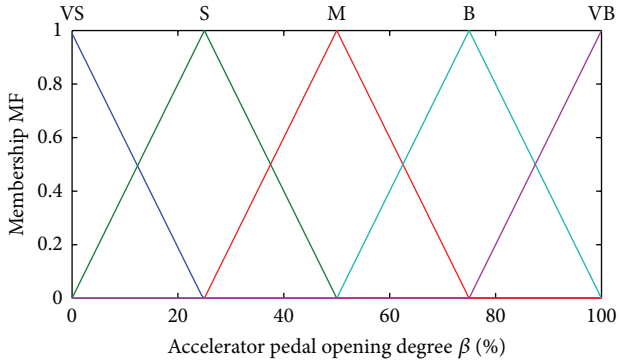

(a) Accelerator pedal opening degree membership function

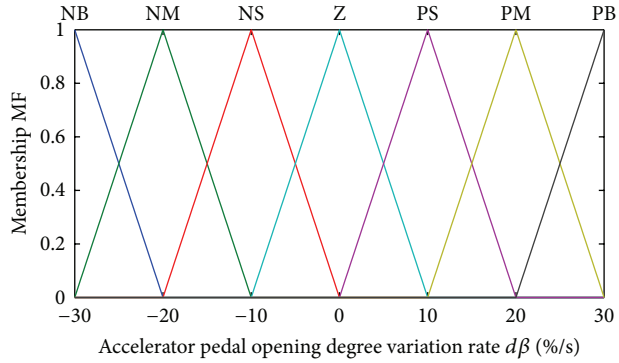

(b) Accelerator pedal opening degree variation rate membership function

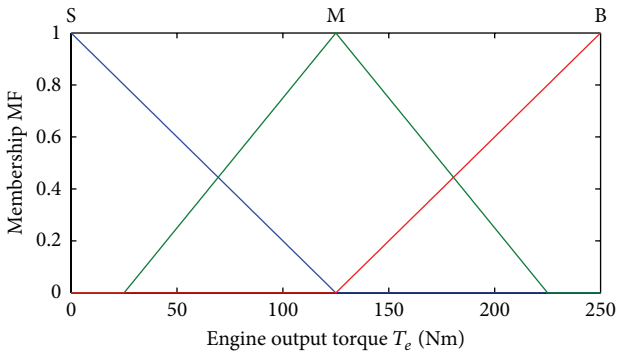

(c) Engine output torque membership function

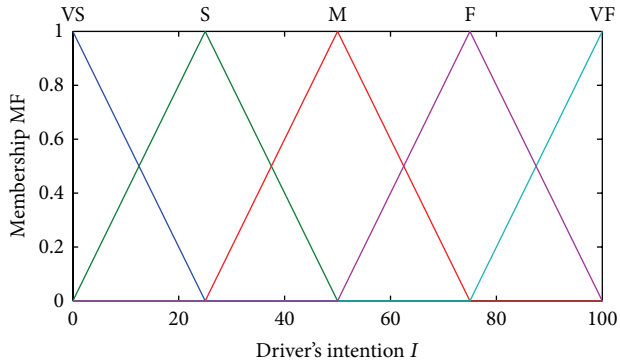

(d) Driver's intention membership function

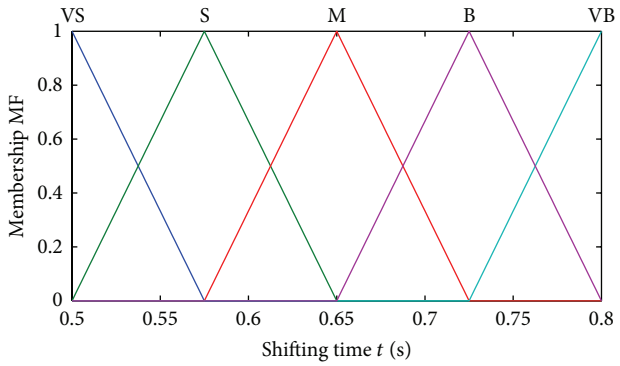

(e) Shifting time membership function

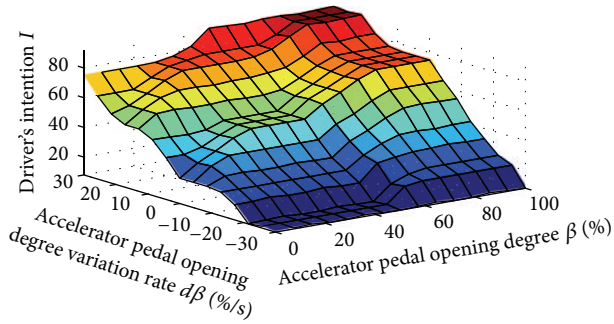

(f) Fuzzy controller input-output relationship of driver's intention

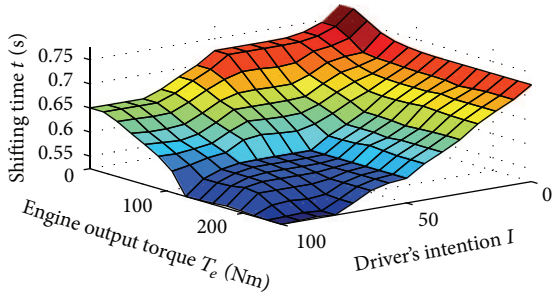

(g) Fuzzy controller input-output relationship of shifting time

Figure 3: Input and output membership functions and relations of shifting time fuzzy controller.

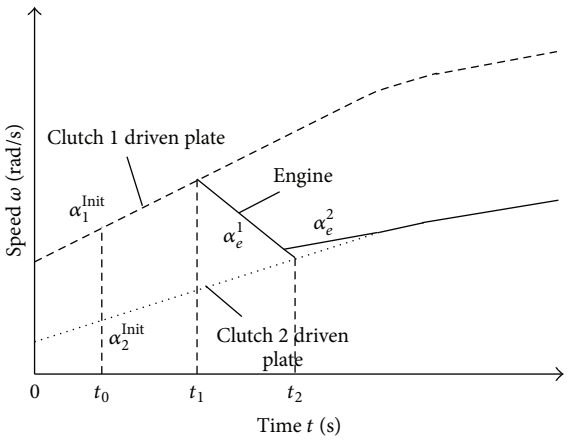

Figure 4: Target speed sketch map when upshifting.

Thus, the shifting time should be extended as the road gradient increases.

4.1.2. Shifting Time Fuzzy Reasoning [13]. Target shifting time should be determined by considering the combined effect of the above factors. However, in view of the realization, road slope is not taken into account. Besides, in order to overcome the shortcomings of large data store under multivariate [14], hierarchical fuzzy reasoning is adopted to determine the target shifting time. Firstly, the driver's intention is reasoned fuzzily by the accelerator pedal opening β and its variation rate $\dot{\beta}$, and then the target shifting time is obtained by fuzzy reasoning, according to the driver's intention I and engine target torque I_e^{ref}.

(1) Input language variable values and domains: accelerator pedal opening $\beta \in$ {very small (VS), small (S), middle (M), big (B), very big (VB)}; its domain is [0~100]; its membership function is shown in Figure 3(a).

Accelerator pedal opening variation rate $\dot{\beta} \in$ {negative big (NB), negative middle (NM), negative small (NS), zero (Z), positive small (PS), positive middle (PM), positive big (PB)}; its domain is [−50~50]; its membership function is shown in Figure 3(b).

Engine output torque $T_e \in$ {small (S), middle (M), big (B)}; its domain is [0~250]; its membership function is shown in Figure 3(c).

(2) Output language variable values and domains: driver's intention $I \in$ {very slow (VS), slow (S), middle (M), fast (F), very fast (VF)}; as for abstract quantity, its domain is [0~100]; its membership function is shown in Figure 3(d).

Shifting time $t \in$ {very small (VS), small (S), middle (M), big (B), very big (VB)}; its domain is {0.5~0.8}; its membership function is shown in Figure 3(e).

Its membership function is shown in Figure 3(b).

(3) Fuzzy reasoning rules table and mapping relationship between input and output variables: driver's intention fuzzy reasoning rules and mapping relationship surfaces between input and output variables are shown in Tables 2 and 3 and Figure 3(f), respectively. Shifting time fuzzy reasoning rules mapping relationship surfaces between input and output variables are shown in Table 4 and Figure 3(g), respectively.

Table 2: Driver's intention fuzzy reasoning rules table (upshifting).

Accelerator pedal opening	Accelerator pedal opening variation (%/s^2)						
	NB	NM	NS	Z	PS	PM	PB
VS	VS	VS	VS	S	M	M	F
S	VS	VS	S	M	M	F	F
M	VS	VS	S	M	M	F	VF
B	VS	S	M	F	F	VF	VF
VB	VS	S	M	F	F	VF	VF

Table 3: Driver's intention fuzzy reasoning rules table (downshifting).

Accelerator pedal opening	Accelerator pedal opening variation rate (%/s^2)						
	NB	NM	NS	Z	PS	PM	PB
VS	VS	VS	VS	S	M	M	F
S	VS	VS	S	M	M	F	F
M	VS	VS	S	M	M	F	VF
B	VS	S	M	F	F	VF	VF
VB	VS	S	M	F	F	VF	VF

Table 4: Shifting time fuzzy reasoning rules table.

Engine output torque T_e	Accelerator pedal opening degree β/%				
	VS	S	M	F	VF
S	VB	B	B	M	M
M	B	M	S	S	VS
B	B	M	S	VS	VS

4.1.3. Time Distribution Based on Genetic Algorithm. The time distribution strategy between torque phase and inertial phase is based on genetic algorithm.

According to driving condition, vehicle condition, and road condition, the time amount of torque phase and inertial phase in the shifting process has been already determined, but the specified time distribution between them is still needed. What is more important is that the time distribution between the two phases determines the values of sliding friction work and impact degree and thus influences the shifting feeling. Focused on this problem, the real-time time distribution strategy between torque phase and inertial phase based on genetic algorithm is proposed in the following paper. The time variables $t_1 - t_0$ and $t_2 - t_1$ are obtained by minimizing the sliding friction work in the process from t_0 to t_2.

The fitness function is determined as follows.

During the period of t_0 to t_2, only clutch 2 produces sliding friction work. In view of this, the sliding friction calculating equation is as follows:

$$\begin{aligned} W_{\min} &= \int_{t_0}^{t_2} \left(T_{c2} \left|\omega_e^{\text{ref}} - \omega_{c2}^{\text{ref}}\right|\right) dt \\ &= \int_{t_0}^{t_1} \left(T_{c2} \left|\omega_e^{\text{ref}} - \omega_{c2}^{\text{ref}}\right|\right) dt \\ &\quad + \int_{t_0}^{t_2} \left(T_{c2} \left|\omega_e^{\text{ref}} - \omega_{c2}^{\text{ref}}\right|\right) dt. \end{aligned} \tag{13}$$

The quality of each solution is evaluated by the fitness function. The bigger the fitness function is, the better is the quality of the solution, therefore the genetic algorithm fitness function can be determined as follows:

$$\text{fitness} = \frac{1}{W_{\min}}. \tag{14}$$

The optimization variable is t_1 (where $t_0 < t_1 < t_2$). According to the principle of genetic algorithm, the optimal variable t_1 can be obtained after a certain amount of iterative computation, and then the torque phase and inertial phase time are obtained which are $t_1 - t_0$ and $t_2 - t_1$, respectively.

It is noteworthy that it is hard to guarantee the real-time adopting the online genetic algorithm, but the genetic algorithm has the characteristic of fast convergence on starting search. This paper has been verified by offline simulation and a superior optimal result will be obtained after a certain amount of iterative computation and thus by this way can resolve the problem of genetic algorithm online optimization which is hard to guarantee its real-time performance.

4.2. The Target Speed and the Angular Acceleration Determination. To the realization of "no impact shifting," the clutch 1 and clutch 2 driven plate in shifting process should maintain a constant angular acceleration. Combined with the shifting process characteristics described and the shifting time determined previously, the target speed curves of engine and clutch can be further obtained.

4.2.1. Upshifting Speed and Angular Acceleration Determination. Target speed in upshifting process is shown in Figure 4, where t_0 is the shifting start time; t_1 is the torque phase ending time; t_2 is the traditional inertial phase ending time; α_1^{Init}, α_2^{Init} are the driven plate angular accelerations of clutch 1 and clutch 2 at the shifting beginning moment; α_e^1 is engine target angular acceleration in the first stage of inertia phase; α_e^2 is engine target angular acceleration in the slip friction stage of inertia phase.

From "no impact shifting" principle, the following equation can be obtained:

$$\alpha_1 = \alpha_1^{\text{Init}}, \qquad \alpha_2 = \alpha_2^{\text{Init}}. \tag{15}$$

In this equation, α_1, α_2 are the driven plate target angular accelerations of clutch 1 and clutch 2 in shifting process.

According to the "reduce or avoid power cycle" control target, in torque phase of upshifting process as shown in Figure 4, engine target speed should be bigger than or equal to clutch 1 driven plate target speed. For the convenience of calculation, assume that the two speeds are equal; that is,

$$\omega_e = \omega_{c1}. \tag{16}$$

As depicted in Figure 4, the whole shifting time should be the sum of the torque phase time and the inertia phase time; that is,

$$t = t_2 - t_0. \tag{17}$$

The method to confirm the shifting time t has been given in details in previous section. According to the pre-established time ratio of torque phase and inertial phase, the value of $(t_1 - t_0)$ and $(t_2 - t_1)$ can be determined. Based on the target angular acceleration and shifting time, the engine target speed at the moment t_1 and the driven plate target speed of clutch 2 at the moment t_2 can be obtained:

$$\begin{aligned} \omega_e(t_1) &= \alpha_1^{\text{Init}}(t_1 - t_0) + \omega_e(t_0), \\ \omega_{c2}(t_2) &= \alpha_2^{\text{Init}} t + \omega_{c2}(t_0). \end{aligned} \tag{18}$$

Here, $\omega_e(t_0)$, $\omega_{c2}(t_0)$ are the speed of engine and clutch 2 driven plate at shifting start moment.

To meet the requirement of speed synchronization, in the first stage of inertial phase, engine target angular acceleration is

$$\alpha_e^1 = \frac{[\omega_e(t_1) - \omega_{c2}(t_2)]}{(t_2 - t_1)}. \tag{19}$$

To reduce the vehicle impact in the synchronization moment, the microslip friction stage is introduced to the inertia phase. The purpose of this phase is to accelerate the speed of the engine output shaft in order to make the angular acceleration between the engine output shaft and the clutch 2 driven plate as close as possible

$$\alpha_e^2 = \delta\alpha_2. \tag{20}$$

In this equation, the value of δ is within $[0, 1]$. The bigger δ is, the smaller the angular acceleration deviation between engine and clutch 2 driven plate is at the synchronization moment. Besides, the impact will be smaller, but the synchronization time will increase. And vice versa a shorter synchronization time is needed but higher angular acceleration deviation and the impact. Therefore, it needs to weigh the effect of impact and the shifting time when choosing δ.

In addition, in upshifting process, microslip friction stage begins when the following constrain is met:

$$(\omega_e - \omega_{c2}) \le \omega_{\text{Const}}. \tag{21}$$

In this equation, ω_{Const} is the speed deviation threshold.

Different values of δ and ω_{Const} will render the change of target curves in microslide friction stage, so the introduction of microslip friction can get relatively smaller impact by sacrificing a certain shifting time.

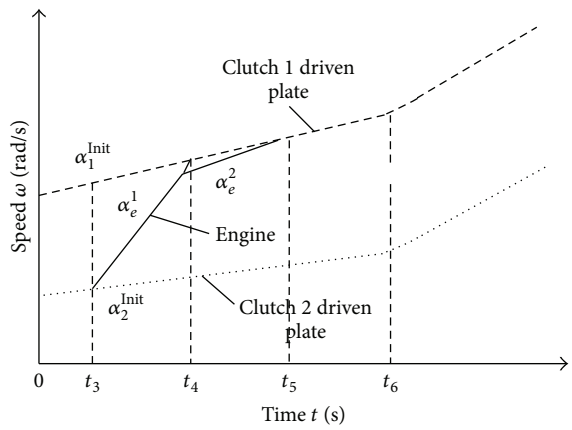

Figure 5: Target speed sketch map when downshifting.

4.2.2. Speed and Angular Acceleration Determination in the Downshifting Process. The target speed of downshifting process is shown in Figure 5; t_3 is the shifting start time; t_4 is the inertial phase ending time; t_5 is the torque phase start time; t_6 is the torque phase ending time.

Similar to upshifting process, in downshifting process, driven plate target angular accelerations of clutch 1 and clutch 2 and the engine target speed in torque phase can also be obtained from (15) and (16).

The engine target speed at the moment t_3 and the driven plate target speed of clutch 2 at the moment t_4 are as follows:

$$\omega_e(t_3) = \omega_{c2}(t_3), \qquad \omega_{c1}(t_4) = \alpha_2^{\text{Init}}(t_4 - t_3) + \omega_{c1}(t_3). \tag{22}$$

The engine target angular acceleration in the first stage of inertial phase is

$$\alpha_e^1 = \frac{[\omega_{c1}(t_4) - \omega_e(t_3)]}{(t_4 - t_3)}. \tag{23}$$

The engine target angular acceleration in slip friction stage of inertial phase is

$$\alpha_e^2 = \delta\alpha_1. \tag{24}$$

In downshifting process, microslip friction stage begins when the following constrain is met:

$$(\omega_{c1} - \omega_e) \le \omega_{\text{Const}}. \tag{25}$$

4.3. The Target Torque Determination

4.3.1. Engine Target Torque Determination. The PID control can be adopted to realize the closed-loop tracking of engine speed after the determination of engine target torque in the shifting process. The engine target torque is expressed as

$$\begin{gathered} e = \omega_e^{\text{Tar}} - \omega_e, \\ \alpha = K_P e + K_I \int e\,dt + K_D \frac{de}{dt}, \qquad T_e = f(\alpha, \omega_e), \end{gathered} \tag{26}$$

where ω_e^{Tar}, ω_e are the target and actual speed of engine respectively; K_P, K_I, K_D are proportional, integral, and differential coefficients in the PID control of engine speed; α is the engine throttle opening.

4.3.2. The Calculation of Model-Based Target Torque Transferred by Clutch. After obtaining the target angular speed of engine and clutch's driven plate, the target torque transferred by clutch in the shifting process can be calculated as follows based on DCT dynamical model.

(1) Torque Phase in Upshifting Process. As shown in Figure 2, clutch 1's torque gradually declines to zero, while clutch 2's torque rises up synchronously in this phase. Provided that the shifting time t has been predetermined and the time taken by torque phase and inertial phase is the same, the target torque of clutch 1 and clutch 2 can be gained based on the dynamics model expressed in (5):

$$\begin{gathered} T_{c1} = T_{c1}^{\text{Init}} - \int_{t_0}^{t_1} \frac{T_{c1}^{\text{Init}}}{(t_1 - t_0)} d\tau, \\ T_{c2} = \frac{I_s^{\text{equ}}\alpha_2/i_2 i_a + T_f + b_s^{\text{equ}}\omega_s - T_{c1}K_{c1}}{K_{c2}}, \end{gathered} \tag{27}$$

where T_{c1}^{Init} is the torque transfer by clutch 1 at the starting moment of shifting.

(2) Inertial Phase in Upshifting Process. The torque transfer by clutch 1 has already declined to zero in this phase; meanwhile, as for clutch 2, the torque remains constant; that is,

$$T_{c1} = 0, \qquad T_{c2} = \frac{I_s^{\text{equ}}\alpha_2/i_2 i_a + T_f + b_s^{\text{equ}}\omega_s - T_{c1}K_{c1}}{K_{c2}}. \tag{28}$$

(3) Inertial Phase in Downshifting Process. As the inertial phase in upshifting process, the torque transfer by clutch 1 and clutch 2 is as follows:

$$T_{c1} = 0, \qquad T_{c2} = \frac{I_s^{\text{equ}}\alpha_2/i_2 i_a + T_f + b_s^{\text{equ}}\omega_s - T_{c1}K_{c1}}{K_{c2}}. \tag{29}$$

(4) Torque Phase in Downshifting Process. As the torque phase in upshifting process, the torque transfer by clutch 1 and clutch 2 is as follows:

$$\begin{gathered} T_{c1} = \frac{I_s^{\text{equ}}\alpha_1/i_1 i_a + T_f + b_s^{\text{equ}}\omega_s - T_{c2}K_{c2}}{K_{c2}}, \\ T_{c2} = T_{c2}^{\text{Init}} - \int_{t_5}^{t_6} \frac{T_{c1}^{\text{Init}}}{(t_6 - t_5)} d\tau, \end{gathered} \tag{30}$$

where T_{c2}^{Init} is the torque transfer by clutch 2 at the zero hour of torque phase.

4.3.3. The Modification of Desired Torque Transfer by Clutches. Considering that the above-mentioned desired torque is obtained based on DCT dynamics model, in the practical application, however, factors such as response characteristics of clutch actuator, parameter variation, and external disturbance ought to be fully taken into account. Thus a torque close-loop modification is applied, as expressed by the following equations:

$$T_{ci}^{c} = T_{ci}^{o} + \Delta T_c, \quad i = 1, 2, \tag{31}$$

where T_{ci}^{o} is clutch's desired torque obtained from the model, T_{ci}^{c} is the modified clutch torque, and ΔT_c is the torque modification in close-loop, as defined by the following equations:

$$\begin{gathered} e = \omega_c^{\mathrm{Tar}} - \omega_c, \\ \Delta T_c = k_p e + k_i \int e\, dt + k_d \frac{de}{dt}, \end{gathered} \tag{32}$$

where ω_c^{Tar}, ω_c are the desired and actual speeds of clutch driven plate, respectively; k_p, k_i, k_d are proportional, integral and differential coefficients in the PID control of clutch driven plate speed, respectively.

5. Simulation Analysis and Results

Based on the DCT dynamics model, fuzzy shifting time decision, and torque coordinating control strategies, the simulation model of shifting control in DCT vehicles is established on MATLAB/Simulink software platform and the upshifting and downshifting process are simulated and analyzed, respectively.

5.1. Simulation Analysis of Upshifting Process. In terms of upshifting process, the simulation is analyzed from three aspects: driver different shifting intentions, different speed gears shifting, and open-plus-closed-loop speed control of clutch driven plate.

5.1.1. Driver Different Shifting Intentions. Driver different shifting intentions can be reflected by the throttle opening. In the case of shifting from 1st speed gear to 2nd speed gear, the corresponding simulation results of shifting process under throttle openings of 20% and 50% are shown in Figure 6.

As shown in Figure 6(a), the engine and clutch have a higher rotate speed, a higher angular acceleration, and a shorter shifting time (0.6064 s, excluding the microsliding phase) under 50% throttle opening in comparison to a 20% throttle opening (0.7162 s); Besides, the angular acceleration deviation factor δ is 0.4 in both working conditions. With 50% throttle opening clutch 2 angular acceleration is higher, so the microsliding time is shorter and the fast shifting demands can be better satisfied under large throttle opening.

Figure 6(b) illustrates that the Shock intensity is 0 under two conditions for adopting the nonimpact shifting principle. But the vehicle Shock intensity at the synchronizing moment is relatively larger, even slightly exceeding the required standard (10 m/s^3) due to the corresponding larger acceleration deviation under a 50% throttle opening. To dig the reason more detail, the current engine torque needs to meet the driver's demand torque after synchronization. However, during this process, the Shock intensity is proportional to the changing rate of engine output torque. Thus, a larger throttle opening leads to a larger torque changing rate and a larger Shock intensity.

In Figure 6(c), the peak Shock intensity has already exceeded the maximum limitation under the 50% throttle opening. A solution to the problem is to increase angular acceleration deviation factor δ at the sacrifice of shifting time at the synchronizing moment. As shown in Figure 6(c), the shifting time increases from 1.152 s to 1.24 s and accordingly the Shock intensity declines to the required range at the synchronizing moment after increasing δ.

As shown in Figure 6(d), compared with 20% throttle opening. The driver demands larger torque in the whole shifting process under 50% throttle opening. In addition, as the vehicle transmission ratio decreases, the clutch is required to transmit a relatively larger torque in order to realize the nonimpact shifting process. However, the engine output torque finally breaks away from the constraint of TCU torque requirements after engagement, restoring to the demanded torque level.

Figure 6(e) illustrates that a larger friction work is generated under 50% throttle opening, which is mainly caused by larger speed and torque differences between driving and driven plate (as shown in Figure 6(a) and Figure 6(d), resp.).

The variation of vehicle speed under two working conditions can be seen in Figure 6(f).

5.1.2. The Shifting Process between Different Speeds. To validate the fact that a large transmission ratio switch theoretically takes a longer shifting time, it is necessary to simulate the shifting process from 1st to 2nd and 3rd to 4th, as described in Figure 7. The simulation is performed under 30% throttle opening and 0.4 angular acceleration deviation factor. Moreover, for convenience, different initial speeds of engine and clutch driven plate are set according to different working conditions and the shifting process is enabled after 0.4 s and the delayed period is used for the engagement of the synchronizer.

Figure 7(a) shows the comparison of shifting time from 1st to 2nd and 3rd to 4th speed gear upshifting process, which takes 0.6738 s and 0.6052 s, respectively. Besides, in the process of 3rd to 4th speed gear upshifting, the initial angular acceleration should be smaller, so it needs to reduce speed deviation threshold value in (20) otherwise a too small desired angular acceleration will be generated during microsliding phase and the shifting time is prolonged.

Figure 7(b) shows a comparison in terms of Shock intensity in shifting process of 1st to 2nd and 3rd to 4th with the same angular acceleration deviation factor δ (0.4). In the process of 3rd to 4th speed gear, the angular acceleration of clutch driven plate is relatively smaller which also means a smaller angular speed deviation between engine and clutch driven plate at the synchronizing moment. No doubt that the vehicle Shock intensity is also smaller. After synchronizing, the Shock intensity, however, is mainly determined by

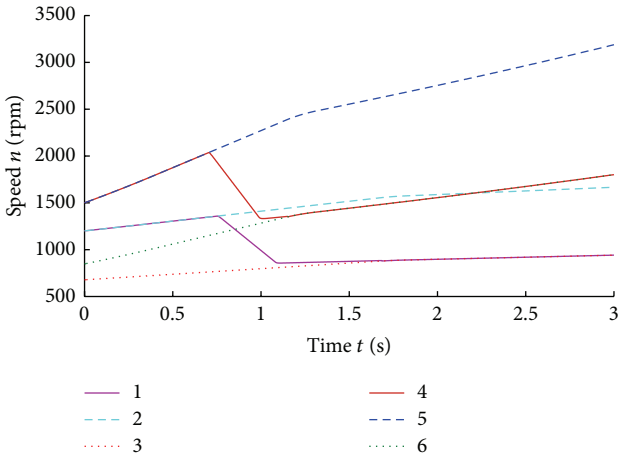

(a) The speeds of engine and clutch driven plate (1: 20% throttle opening engine speed, 2: 20% throttle opening clutch 1 driven plate speed, 3: 20% throttle opening clutch 2 driven plate speed, 4: 50% throttle opening engine speed, 5: 50% throttle opening clutch 1 driven plate speed, and 6: 50% throttle opening clutch 2 driven plate speed)

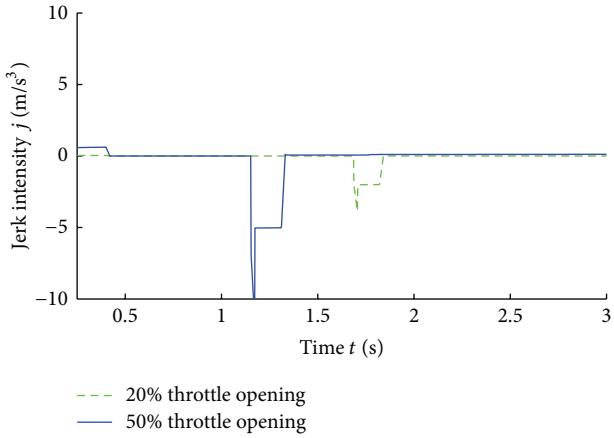

(b) Jerk intensity

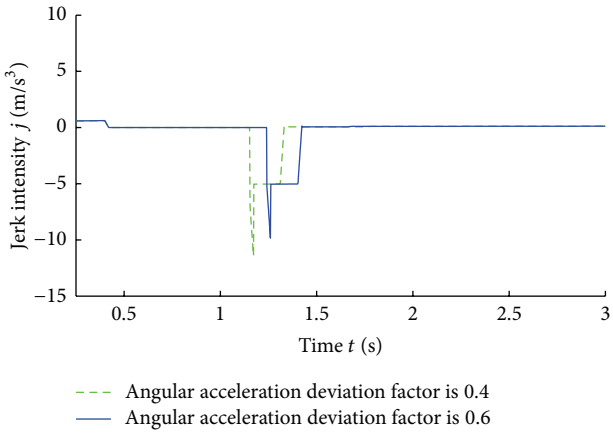

(c) The influences of different angular acceleration deviation factors on Jerk intensity under 50% throttle opening

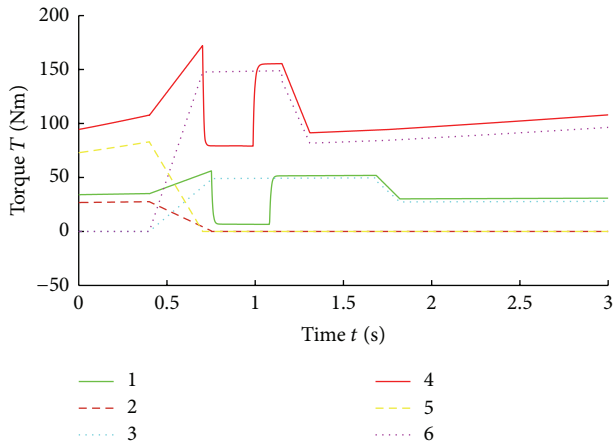

(d) The torque transferred by engine and clutch (1: 20% throttle opening engine torque, 2: 20% throttle opening clutch 1 torque, 3: 20% throttle opening clutch 2 torque, 4: 50% throttle opening engine torque, 5: 50% throttle opening clutch 1 torque, and 6: 50% throttle opening clutch 2 torque)

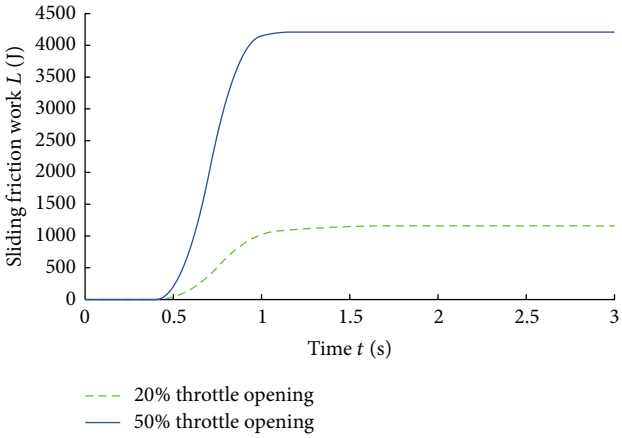

(e) Sliding friction work

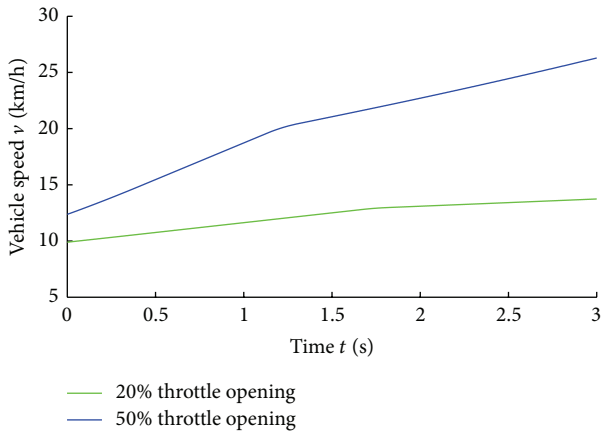

(f) Vehicle speed

Figure 6: Simulation results of driver different shifting intentions.

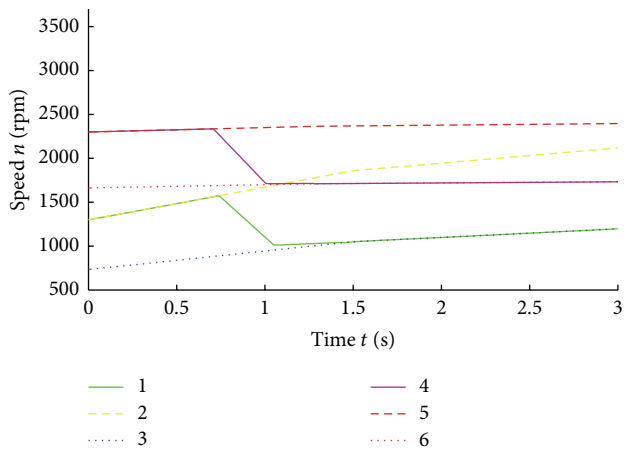

(a) Speeds of engine and clutch driven plate (1: engine speed during 1st to 2nd gear, 2: clutch 1 driven plate speed during 1st to 2nd gear, 3: clutch 2 driven plate speed during 1st to 2nd gear, 4: engine speed during 3rd to 4th gear, 5: clutch 1 driven plate speed during 3rd to 4th gear, and 6: clutch 2 driven plate speed during 3rd to 4th gear)

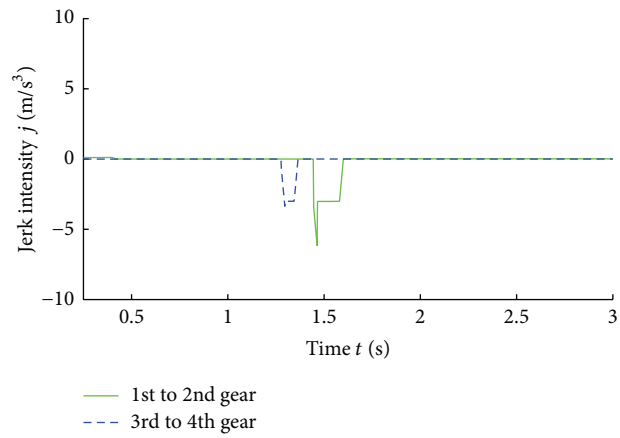

(b) Jerk intensity

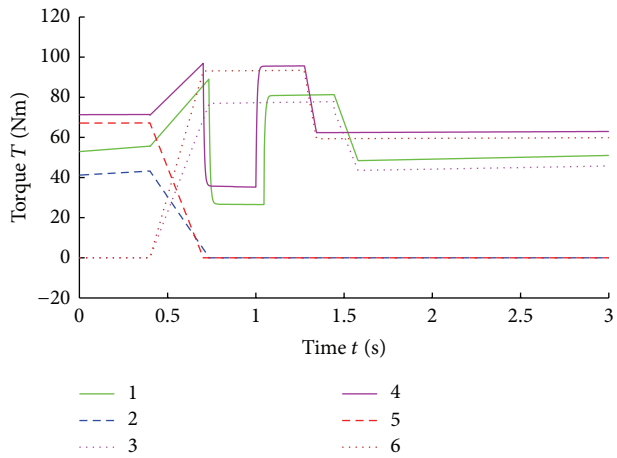

(c) Torque transferred by engine and clutch (1: engine torque during 1st to 2nd gear, 2: clutch 1 driven plate torque during 1st to 2nd gear, 3: clutch 2 driven plate torque during 1st to 2nd gear, 4: engine torque during 3rd to 4th gear, 5: clutch 1 driven plate torque during 3rd to 4th gear, and 6: clutch 2 driven plate torque during 3rd to 4th gear)

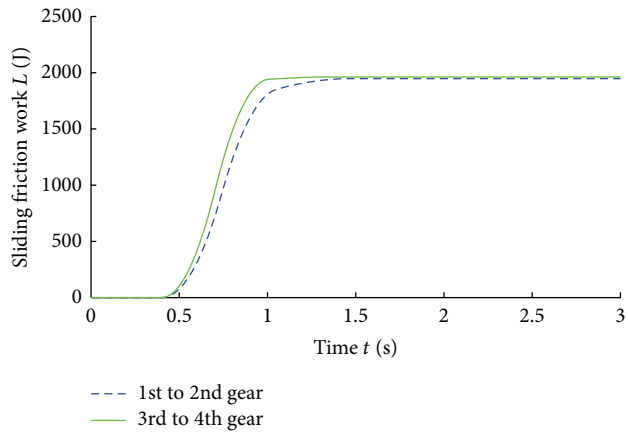

(d) Sliding friction work

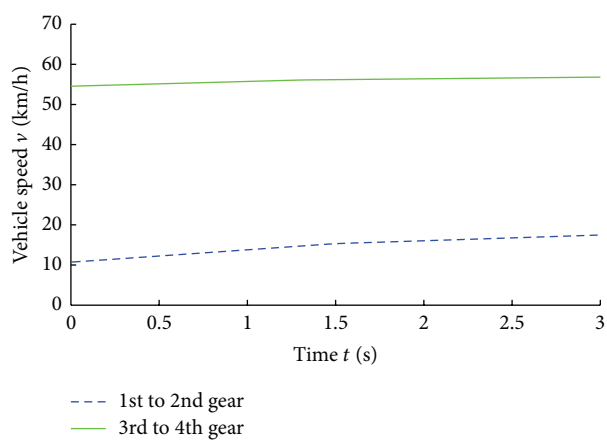

(e) Vehicle speed

Figure 7: Simulation results in different speed shifting.

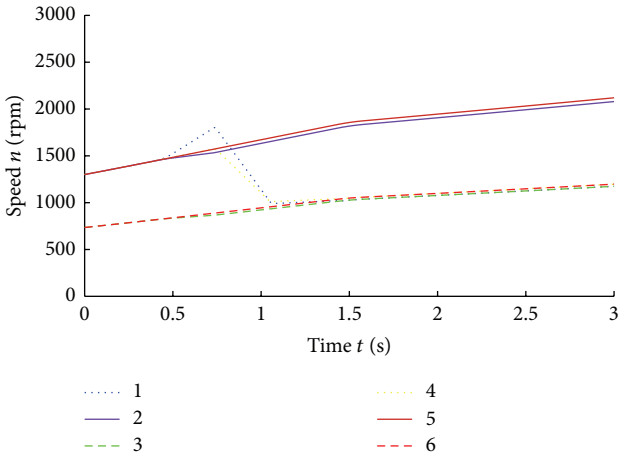

(a) Speeds of engine and clutch driven plate (1: engine speed in open-loop control, 2: clutch 1 driven plate speed in open-loop control, 3: clutch 2 driven plate speed in open-loop control, 4: engine speed after closed-loop modification, 5: clutch 1 driven plate speed after closed-loop modification, and 6: clutch 2 driven plate speed after closed-loop modification)

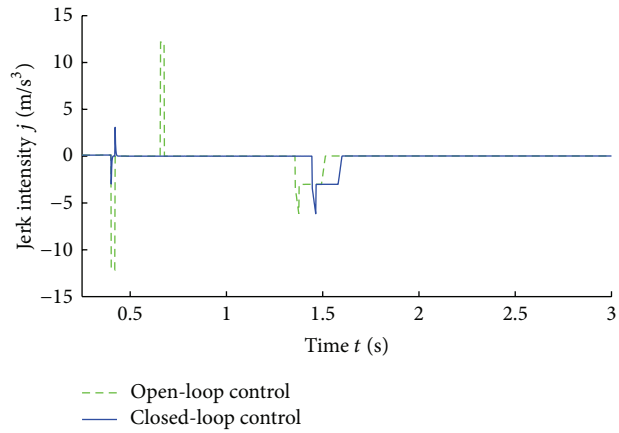

(b) Jerk intensity

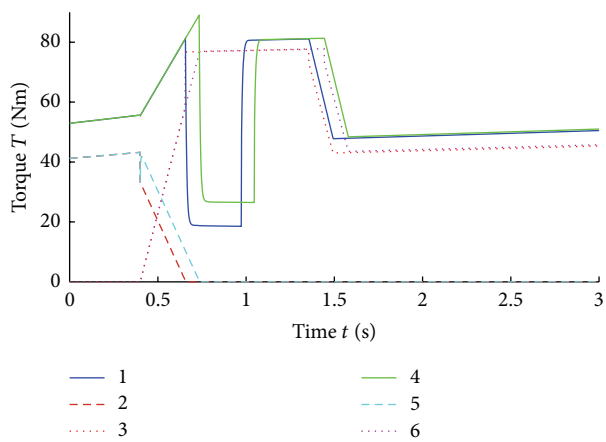

(c) Torque of engine and clutch (1: engine torque in open-loop control, 2: clutch 1 torque in open-loop control, 3: clutch 2 torque in open-loop control, 4: engine torque after closed-loop modification, 5: clutch 1 torque after closed-loop modification, and 6: clutch 2 torque after closed-loop modification)

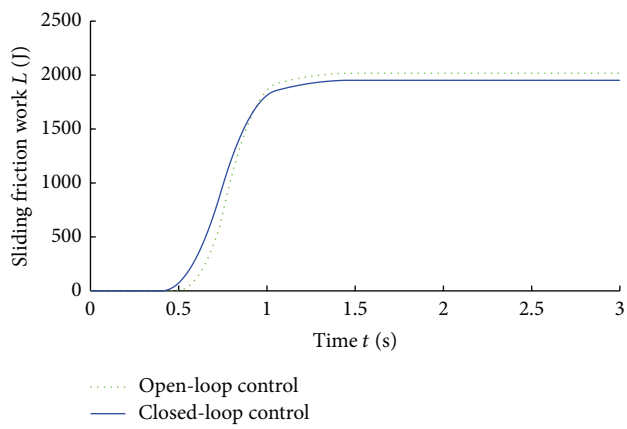

(d) Sliding friction work

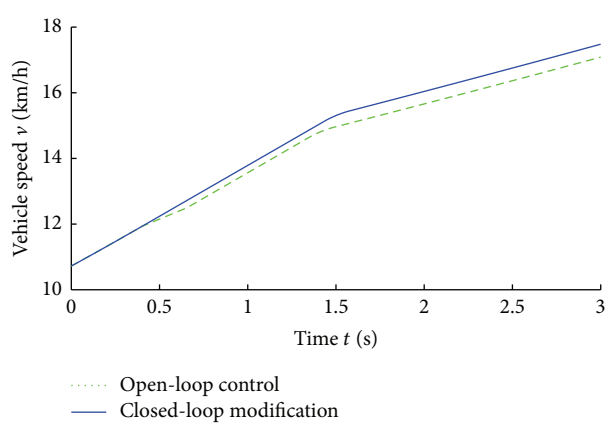

(e) Vehicle speed

Figure 8: The influence of clutch torque hysteresis on control effect.

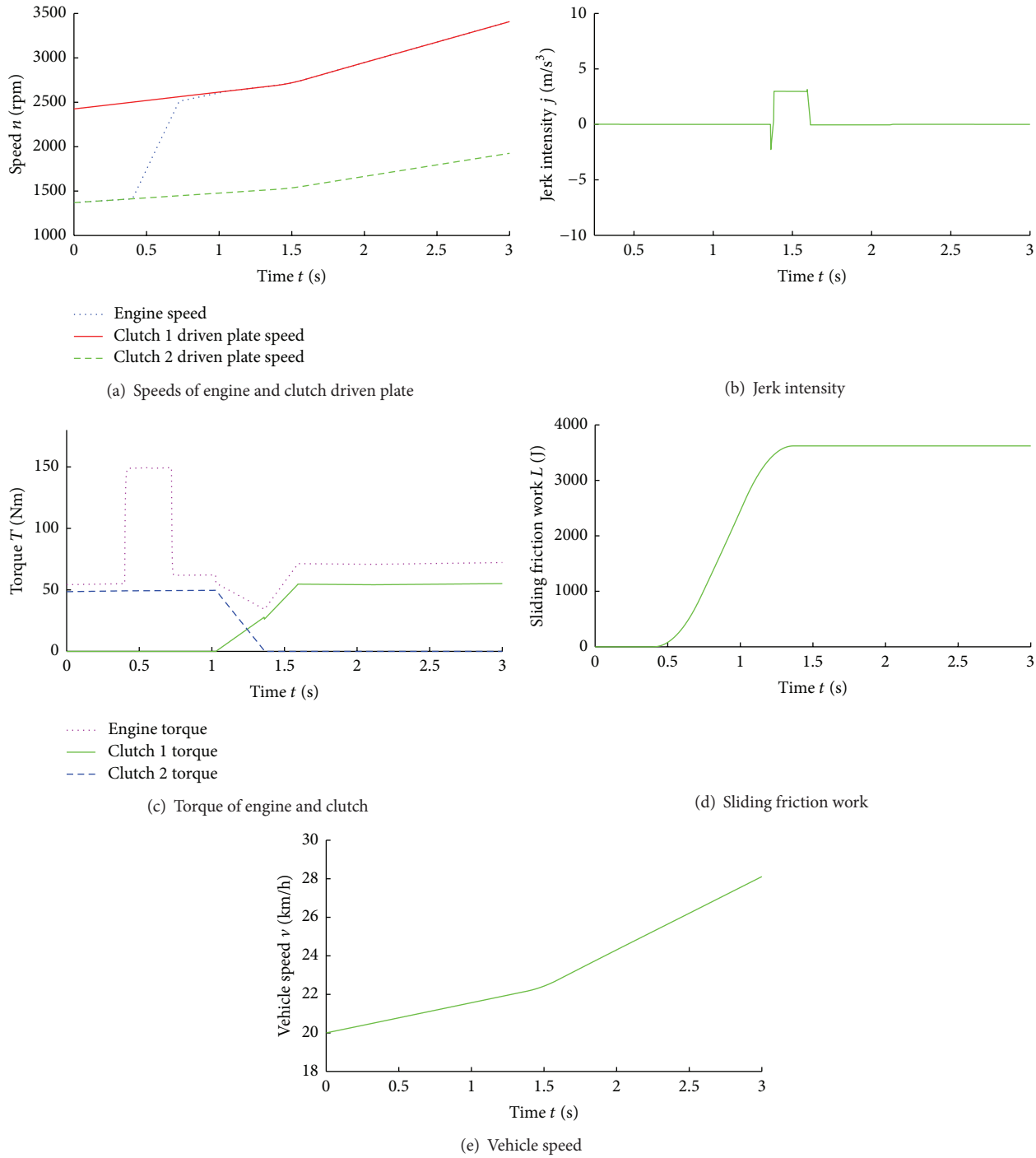

Figure 9: Simulation results of shifting from 2nd to 1st speed gear downshifting process.

the changing rates of engine torque, so the Shock intensity holds the same value in both processes, as depicted in Figure 7(b).

A shorter time is needed in the shifting from 3rd to 4th speed gear upshifting process in comparison with the shifting from 1st to 2nd as described in Figure 7(c).

As shown in Figure 7(d), the approximately equal friction work is generated. It is mainly because the speed and torque differences between clutch driving and driven plates are almost the same in the two working conditions.

Figure 7(e) describes a relatively stable speed variation, which has no large raised or depressed curves during the shifting process in both working conditions. It indicates a smooth riding performance.

5.1.3. The Influence of Clutch Actuator's Hysteresis. Suppose that the torque transfer by clutch 2 has a 0.1 s delay. Under this circumstance, the open-loop control and closed-loop modification of speeds are separately simulated and analyzed,

Figure 10: Five-speed dry DCT real vehicle chassis dynamometer test.

as depicted in Figure 8. Similarly, the attention is mainly focused on the hysteresis influence of clutch torque in torque phase.

As expressed in Figure 8(a), the existence of clutch 2 actuator's hysteresis decreases engine load-torque, which accounts for the engine speed's sharp rise in open-loop control; Moreover, because of the transmission torque reduction, the accelerations of clutch 1 and clutch 2 driven plates decrease accordingly. The influence of clutch 2 actuator's hysteresis, however, can be totally eliminated by adopting closed-loop modification.

As depicted in Figure 8(b), clutch 2 actuator's torque hysteresis also causes the variation of vehicle acceleration, which gives reasons for the large vehicle Shock intensity at the beginning of torque phase and after torque phase. The Shock intensity can be narrowed in a relatively small range by introducing closed-loop modification, which consequently increases the shifting-fell and riding comfort a lot.

As shown in Figure 8(c), at the beginning of torque phase, the torque clutch 2 transfer has a 0.1 s delay, therefore inducing the speed variation of clutch 2's driven plate, which can only be compensated by decreasing control accuracy and effect. The use of closed-loop modification, however, basically removes the torque hysteresis, restoring clutch 2's actual torque to its original value.

Figure 8(d) illustrates the friction work generated under two types of control methods is similar. That is because the existence of the hysteresis of clutch 2's actuator, to some extent, decreases the actual transferred torque, but meanwhile, the speed error between driving and driven plates is enlarged. So the gross friction work varies hardly.

Figure 8(e) shows the vehicle speed. Due to the existence of torque hysteresis transferred by clutch, the introducing of closed-loop modification control is advantageous for the control accuracy and the shifting feeling of vehicle.

5.2. Simulation of Down Shifting Process. As the up and downshifting process is similar, a brief simulation is shown in terms of shifting from 2nd to 1st speed gear downshifting process with the assumptions of 30% throttle opening and 20 km/h initial vehicle speed, which is depicted in Figure 9.

As shown in Figures 9(a) and 9(c), the downshifting process begins at 0.4 s, which starts with an inertia phase. In this phase clutch 1 transmits zero torque while clutch 2 gradually slips to the sliding-friction-position and transmits an invariant torque. Meanwhile, in order to be synchronized rapidly between engine and clutch 1, the engine torque needs be actively adjusted. As the speed differences between engine and clutch 1 driven plate reach a certain threshold, it turns to microsliding friction stage. The engine torque decreases and the angular acceleration of engine output shaft reduces correspondingly, which can guarantee a minor angular acceleration error of the clutch 1 driven plate at the synchronizing moment. After that, a torque phase is followed. In this phase, clutch 2 transmits a gradually declined torque, while clutch 1 transmits a rising torque. The torque changing rule of clutch meets a certain relationship, which ensures the vehicle has a constant acceleration. In the end, the engine output torque gradually comes to the driver demand; therefore the vehicle acceleration is varied slowly.

Figures 9(a), 9(b), and 9(e) indicate that the Shock intensity maintains zero in the downshifting process, though vibrating a little at the synchronizing moment, which satisfies the required standard. In addition, the shifting time is comparatively rational. With a small friction power, it can be completely accepted. The vehicle speed varies smoothly and the shifting comfort is also comparatively well.

The simulation analysis of upshifting and downshifting process illustrates that the proposed model-based torque coordinating control strategy can not only satisfy each index of the shifting quality, but also well adapt to driver shifting intentions and different speed gears shifting. Besides, the control strategy can solve the control error caused by the clutch actuator's hysteresis and external disturbance efficiently. To some degree, the system has a good robustness.

6. The Dry DCT Real Vehicle Chassis Dynamometer Test

Based on the simulation result, the MAP related to starting control strategy of DCT real vehicle is recalibrated. The real dry DCT vehicle chassis dynamometer test is performed based on NEDC after completing development of the DCT software. The test picture and NEDC test results are shown in Figures 10 and 11, respectively.

Figures 11(e) and 11(i) shows that, in the continuous shifting process of DCT vehicle under the NEDC driving condition, the impact degree is $j \leq 10\,\mathrm{m/s^3}$ and the shifting time remains less than 0.8 s, which prove that the proposed shifting control strategy can ensure the shifting smoothness and realize the fast and reliable shifting. Moreover, making an analysis of Figures 11(g), 11(h), 11(i), 11(j), 11(k), and 11(l), a conclusion can also be drawn that each speed gear and its synchronizer strictly satisfy the transmission relationship expressed in Figure 1, and depending on the switch of dual clutches' position, the five-speed dry DCT accomplishes the shifting process when the target gear synchronizer is already preengaged in advance.

As can be seen from Figures 12(a)–12(c), when the vehicle shifts from 1st gear to 2nd gear with a less than 50% throttle opening, the shifting time is 0.74 s and Jerk intensity is below

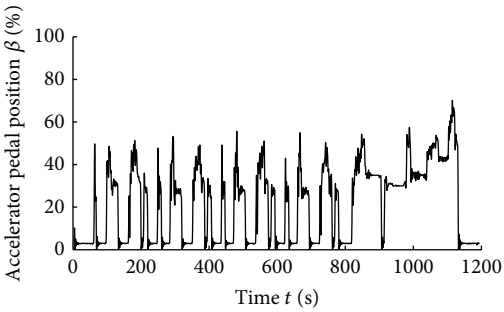

(a) Throttle opening

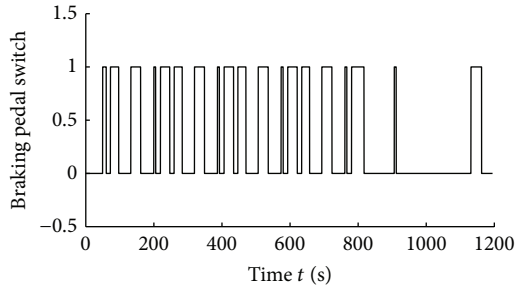

(b) Braking pedal switch

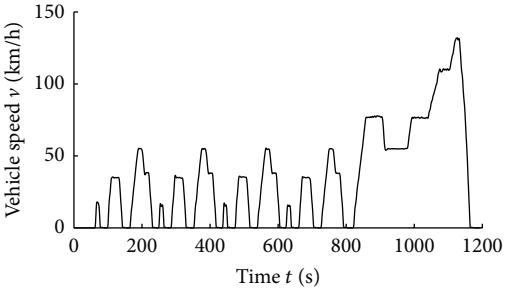

(c) Vehicle speed

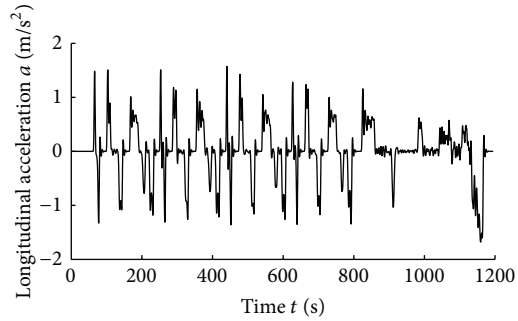

(d) Longitudinal acceleration

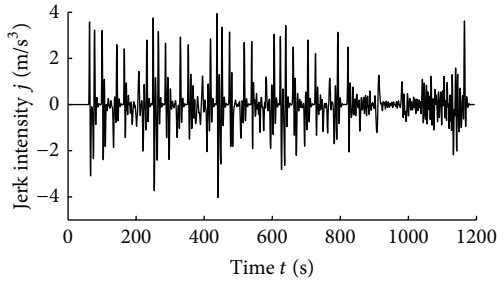

(e) Jerk intensity

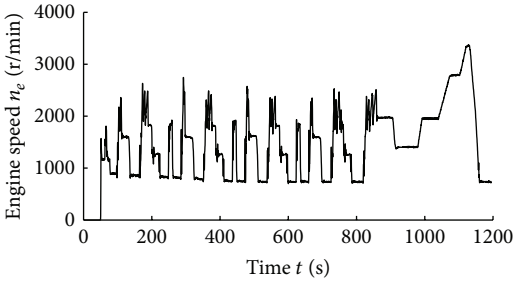

(f) Engine speed

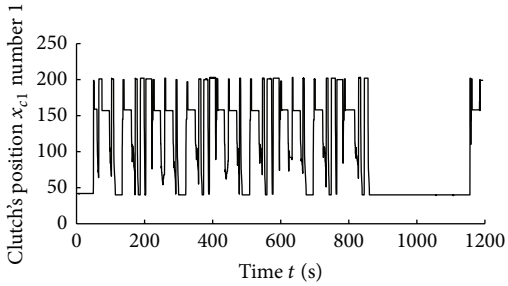

(g) Clutch's position number 1

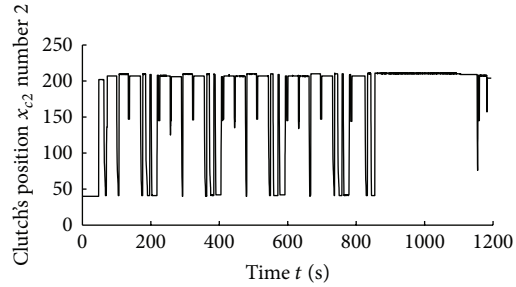

(h) Clutch's position number 2

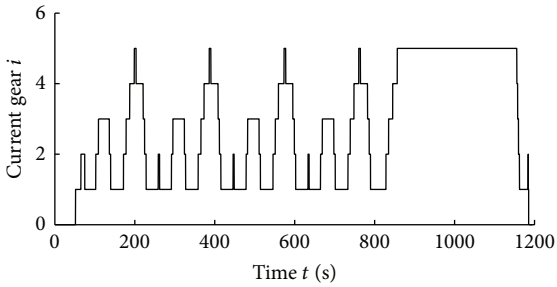

(i) Current gear

Figure 11: Continued.

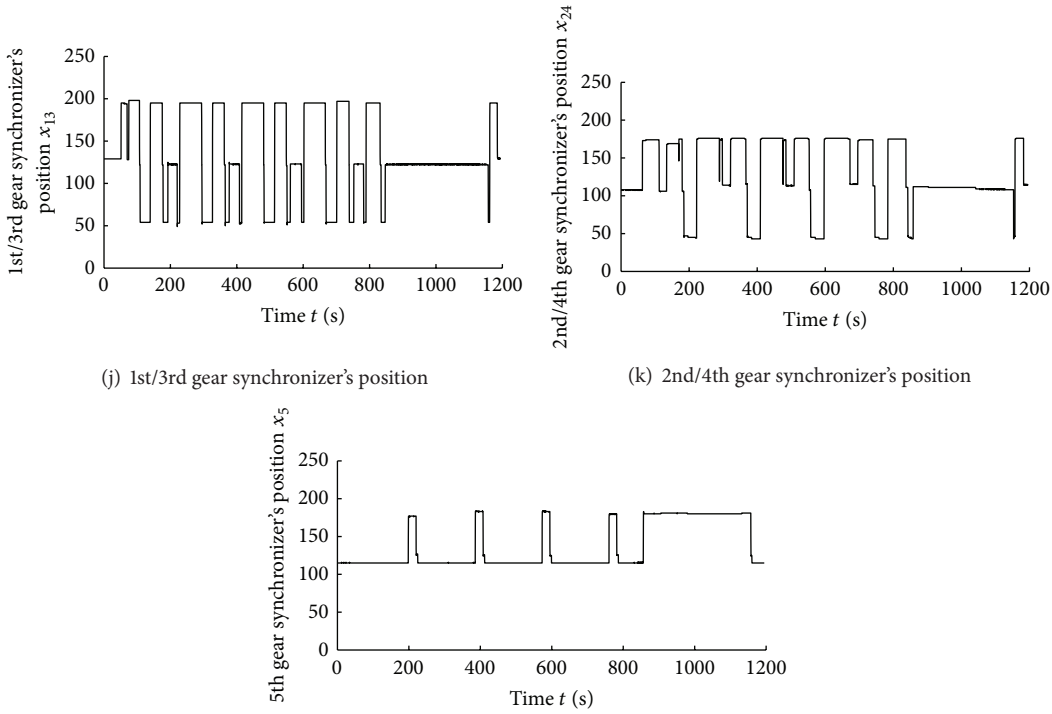

(j) 1st/3rd gear synchronizer's position

(k) 2nd/4th gear synchronizer's position

(l) 5th gear synchronizer's position

Figure 11: DCT sample vehicle revolving drum test based on NEDC.

6 m/s^3; thus the shifting quality is effectively guaranteed. Besides, the trend of engine speed as shown in Figure 12(d) is consistent with the upshifting characteristic described in Figure 4 and the simulation result in Figure 6(a), which validate the effectiveness of the proposed control strategies.

7. Conclusions

Consider the following.

(1) The control objectives of the shifting process are proposed. Based on the analysis of torque and speed characteristics of engine and dual clutches during the shifting process, the fuzzy time decision and the model-based torque coordinating control strategy are proposed. The shifting quality of prototype car with DCT has been simulated under different driving conditions on the Matlab/Simulink software platform. Experimental results show that the shifting control strategy proposed in this paper can not only meet the shifting quality requirements and adapt to the various shifting conditions, but also effectively reduce the control error caused by the factors such as the hysteresis of clutch actuator and external interferences. Besides, the shifting control strategy has strong robustness.

(2) The five-speed dry DCT real vehicle chassis dynamometer test based on NEDC illustrates that the dry DCT can realize power shifting and improve shifting quality, thus the effectiveness and feasibility of fuzzy time decision and the model-based torque control strategy are valuable.

Notation

I_e: Equivalent moment of inertia of engine crankshaft (including flywheel) and clutch driving plate

I_{c1}: Equivalent moment of inertia of clutch 1 driven plate, transmission input shaft number 1 (solid part), and relevant odd number gears

I_{c2}: Equivalent moment of inertia of clutch 2 driven plate, transmission input shaft number 2 (hollow part), and its relevant even number speed gears

I_m: Equivalent moment of inertia of transmission intermediate shaft and its relevant gears final drive driving part

I_s: Equivalent moment of inertia of final drive driven part, differential gears, axle shafts, wheels, and complete vehicle, which are equally converted into transmission output shaft

b_e: Rotating viscous damping coefficient of engine output shaft

b_{c1}: Rotating viscous damping coefficient of transmission input shaft number 1

b_{c2}: Rotating viscous damping coefficient of transmission input shaft number 2

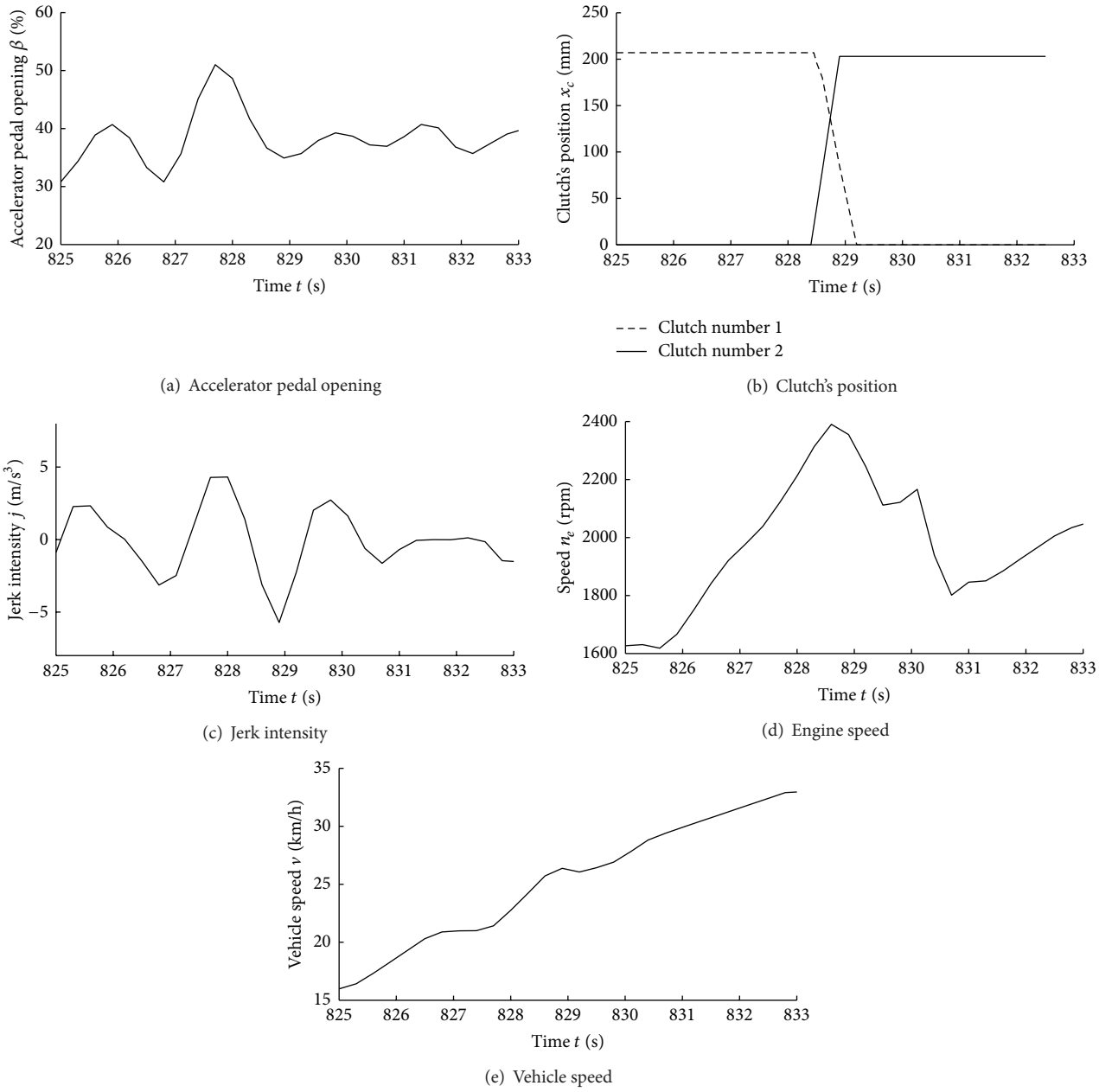

(a) Accelerator pedal opening

(b) Clutch's position

(c) Jerk intensity

(d) Engine speed

(e) Vehicle speed

Figure 12: 1st to 2nd gear shifting process under suburban driving condition.

b_m: Rotating viscous damping coefficient of transmission intermediate shaft
b_s: Equivalent rotating viscous damping coefficient of axle shafts and wheels, which are equally converted into transmission output shaft
ω_e: Angular speed of engine crankshaft
ω_{c1}: Angular speed of clutch 1 driven plate (or transmission input shaft number 1)
ω_{c2}: Angular speed of clutch 2 driven plate (or transmission input shaft number 2)
ω_m: Angular speed of transmission intermediate shaft
ω_s: Angular speed of transmission output shaft
ω_w: Angular speed of wheels, which are equally converted into transmission output shaft
T_e: Engine output torque
T_f: Driving resistance torque which is equally converted into transmission output shaft
T_{c1}, T_{c2}: Transfer torque of clutch 1 and clutch 2
T_{cm1}, T_{cm2}: Torque of transmission input shafts number 1 and number 2 acting on intermediate shaft
T_{mc1}, T_{mc2}: Torque of transmission intermediate shaft reacting on input shafts number 1 and number 2
I_{g1}, I_{g3}, I_{gr}: Moments of inertia of 1st, 3rd, and reverse driven gears

I_{g2}, I_{g4}, I_{g5}: Moments of inertia of 2nd, 4th, and 5th driving gears
$i_1 \sim i_5, i_a$: Forward gear ratios and final drive ratio
r: The radius of wheel
α: Engine throttle position
$f(\alpha, \omega_e)$: Engine output torque nonlinear function
η: Transmission efficiency of transmission shafts and final drive
μ_1, μ_2: Kinetic friction coefficient among friction plates of clutch 1 and clutch 2
R_0, R_1: Internal and external radius of friction plates of clutch
x_1, x_2: Displacement of clutch 1 and clutch 2
$F(x_1), F(x_2)$: Positive pressure function of pressure plate of clutch 1 and clutch 2
T_{c1}^L, T_{c2}^L: Transfer torque after full engaging of clutch which is determined by the engine torque, speed, and vehicle resistance torque
m: Mass of vehicle
g: Acceleration of gravity
f: Rolling resistance coefficient
v: Vehicle velocity
C_d: Wind drag coefficient
A: Windward area
θ: Slope angle
δ: Correction coefficient of rotating mass.

Conflict of Interests

The authors declare that there is no conflict of interests regarding the publication of this paper.

References

[1] X. X. Guo, C. Fu, F. Cheng et al., "Modeling and simulation research of dual clutch based on fuzzy control," SAE Paper 2007-01-3754, 2007.

[2] M. Kulkarni, T. Shim, and Y. Zhang, "Shift dynamics and control of dual-clutch transmissions," *Mechanism and Machine Theory*, vol. 42, no. 2, pp. 168–182, 2007.

[3] Y. Zhang, X. Chen, X. Zhang, H. Jiang, and W. Tobler, "Dynamic modeling and simulation of a dual-clutch automated lay-shaft transmission," *Journal of Mechanical Design, Transactions of the ASME*, vol. 127, no. 2, pp. 302–307, 2005.

[4] M. Goetz, M. C. Levesley, and D. A. Crolla, "Integrated powertrain control of gearshiftings on twin clutch transmissions," SAE Paper 2004-01-1637, 2004.

[5] M. Goetz, M. C. Levesley, and D. A. Crolla, "Dynamics and control of gearshifts on twin-clutch transmissions," *Automobile Engineering*, vol. 219, no. 8, pp. 951–963, 2005.

[6] D.-T. Qin, Y.-S. Zhao, J.-J. Hu, and M. Ye, "Analysis of shifting control for dry dual clutch system," *Journal of Chongqing University*, vol. 32, no. 9, pp. 1016–1022, 2009.

[7] M. K. Niu, X. H. Cheng, B. Z. Gao et al., "A study on shifting characteristics of dual clutch transmission," *Automotive Engineering*, vol. 6, no. 4, pp. 453–459, 2004.

[8] G. Q. Wu and D. M. Zhan, "A research on the way of clutch actuation during DCT upshifting based on optimality theory," *Automotive Engineering*, vol. 31, no. 3, pp. 258–261, 2009.

[9] Y. T. Li, Z. G. Zhao, and T. Zhang, "Research on optimal control of twin clutch engagement pressure for dual clutch transmission," *China Mechanical Engineering*, vol. 21, no. 12, pp. 1496–1501, 2010.

[10] Z. G. Zhao and J. H. Qiu, "H_∞ robust control for twin clutches of DCT during vehicle's starting and shifting processes," *China Mechanical Engineering*, vol. 23, no. 6, pp. 745–751, 2012.

[11] A. L. Ge and J. Q. Wu, "Research on optimizing engaged-schedule of clutch," *Automotive Engineering*, vol. 10, no. 2, pp. 54–65, 1988.

[12] Y. G. Liu, *Study on Integrated Control of Passenger Vehicles Equipped With Dual Clutch Transmission*, Chongqing University, Chongqing, China, 2010.

[13] J. Zhu, *Fuzzy Control and System Theory*, Machinery Industry Press, Beijing, China, 2005.

[14] H. Zhang, Y. Shi, and A. Saadat Mehr, "On H_∞ filtering for discrete-time takagi-sugeno fuzzy systems," *IEEE Transactions on Fuzzy Systems*, vol. 20, no. 2, pp. 396–401, 2012.

Hindawi Publishing Corporation
Mathematical Problems in Engineering
Volume 2014, Article ID 286538, 21 pages
http://dx.doi.org/10.1155/2014/286538

Research Article

Optimal Control of Diesel Engines: Numerical Methods, Applications, and Experimental Validation

Jonas Asprion,[1] Oscar Chinellato,[2] and Lino Guzzella[1]

[1] *Institute for Dynamic Systems and Control, ETH Zurich, Sonneggstraße 3, 8092 Zurich, Switzerland*
[2] *FPT Motorenforschung AG, Schlossgasse 2, 9320 Arbon, Switzerland*

Correspondence should be addressed to Jonas Asprion; jonas.asprion@alumni.ethz.ch

Received 6 October 2013; Revised 20 November 2013; Accepted 20 November 2013; Published 5 February 2014

Academic Editor: Hui Zhang

In response to the increasingly stringent emission regulations and a demand for ever lower fuel consumption, diesel engines have become complex systems. The exploitation of any leftover potential during transient operation is crucial. However, even an experienced calibration engineer cannot conceive all the dynamic cross couplings between the many actuators. Therefore, a highly iterative procedure is required to obtain a single engine calibration, which in turn causes a high demand for test-bench time. Physics-based mathematical models and a dynamic optimisation are the tools to alleviate this dilemma. This paper presents the methods required to implement such an approach. The optimisation-oriented modelling of diesel engines is summarised, and the numerical methods required to solve the corresponding large-scale optimal control problems are presented. The resulting optimal control input trajectories over long driving profiles are shown to provide enough information to allow conclusions to be drawn for causal control strategies. Ways of utilising this data are illustrated, which indicate that a fully automated dynamic calibration of the engine control unit is conceivable. An experimental validation demonstrates the meaningfulness of these results. The measurement results show that the optimisation predicts the reduction of the fuel consumption and the cumulative pollutant emissions with a relative error of around 10% on highly transient driving cycles.

1. Introduction

Optimal control of diesel engines becomes increasingly important. More stringent emission regulations [1, 2] require the exploitation of the remaining potential of reducing the emissions, not only in stationary operation but also especially during transients [3, 4]. Simultaneously, the fuel consumption has to be minimised for economic and environmental reasons.

The classical approach to parameterise an engine control unit (ECU) is to first derive stationary lookup maps. Subsequently, transient corrections are added to these static maps, and heuristic feedforward parts are included. This approach, which relies mainly on engineering experience, leads to a highly iterative procedure when transient driving cycles need to be considered. With the increasing complexity of modern engine systems, it becomes difficult for the calibration engineer to conceive all the cross couplings between the many actuators. A high demand for test-bench time results. Furthermore, each new calibration of an engine requires this manual procedure to be executed again. Particularly for heavy-duty engines, which are usually employed in a variety of applications, a fast and partially automated calibration process is desirable.

Model-based approaches and mathematical optimisation tools provide the means for such an automation. For example, during the calibration of the ECU, the static lookup maps need to be optimised. This optimisation can be performed directly on the engine [5], or mathematical models may be used in place of the physical engine [6–8]. An overview of modelling principles suitable for this approach can be found in [9]. The information about the driving cycle to be considered may be included by a weighting of the operating range of the engine. This weighting matrix represents the time during which the engine is operated at a certain engine speed and load torque. Alternatively, a few relevant operating points can be identified, and the optimisation is restricted to those points [10, Chapter 7]. Identifying the parameters

of a feedback controller can also be cast as an optimisation problem. Again, the solution can be obtained directly on the engine [11] or by a model-based approach [12]. Adaptive methods aim to automatically improve the engine calibration during normal operation [13].

Dynamics may be incorporated either online by model-predictive control [14–16] or offline by an optimisation of the control-trajectories over a representative driving profile. The solution of such optimal control problems (OCPs), which in the past were also obtained directly on the engine [17], provides implications for well-suited control structures [18–21]. The optimal control profiles with the corresponding fuel consumption and pollutant emissions can be used as a benchmark to disclose scenarios in which the performance of the actual control system is suboptimal. An analysis of these cases provides guidelines for the improvement of the control structure, the feedforward control, and the reference-trajectory generation. Another way of utilising the results from optimal control is to use this data to train function approximators such as artificial neural networks [22, 23].

In the literature referenced, it is stated that due to the complexity of the system, OCPs for diesel engines can only be solved over short time horizons of around 3 s to 10 s. Alternatively, model simplifications such as a quasistationary treatment are performed. However, to derive implications for a suitable control structure or to train function approximators, optimal solutions over long time horizons are required, based on a detailed, fully dynamic engine model. Transient driving cycles, which are used during the homologation procedure and thus emulate a representative operation scenario of the engine, are typically 20 to 30 minutes long.

This paper presents the means to calculate such optimal solutions. The optimisation-oriented modelling of diesel engines is summarised and extended to engines with exhaust-gas recirculation (EGR) in Section 2.2. Subsequently, the problem formulation is detailed, and the numerical optimisation methods are described in Sections 2.3–2.6. The presentation of the results is subdivided into three parts. First, the performance of the numerical methods is analysed in Section 3.1 and, subsequently, two case studies illustrate how the results from the optimisation can be utilised in Section 3.2. Finally, the experimental validation provided in Section 3.3 demonstrates the meaningfulness and the soundness of the approach.

A reader interested in the engineering aspects of the problem may focus on Sections 2–2.2, 2.6, and 3.2. Conversely, a reader interested in the details of the optimisation method and its performance may concentrate on Sections 2.3–2.5 and 3.1.

Throughout the text, the derivative with respect to time is denoted by $\dot{x} = dx/dt$, whereas $\overset{*}{x}$ designates a flow. Lower and upper bounds are denoted by $\underline{x}$ and $\overline{x}$, and $\hat{x}$ indicates a reference value. Bold-face symbols such as $\mathbf{x}$ or $\mathbf{X}$ represent vectors and matrices, respectively. The abbreviations and symbols are summarised in the nomenclature section at the end of the text, except for the specific notation used in Sections 2.4 and 2.5.

Table 1: Main data of the engines used.

Engine		A	B
Displ. volume V_d	(l)	8.7	3.0
Cylinders n_{cyl}	(—)	6	4
Bore/stroke	(mm)	117/135	96/104
Compression ratio	(—)	15.8	17.6
EGR		—	High pressure
Rated power	(kW)	300 (1,650 rpm)	130 (2,900 rpm)
Max. torque	(Nm)	1,720 (1,200 rpm)	420 (1,400 rpm)

2. Materials and Methods

This section introduces the engines used and presents all methods required for the optimal control of diesel engines. The numerical framework for optimal control as well as the engine model is implemented in MATLAB 2013b (MathWorks, Natick, MA, USA), running under 64bit Windows 8. All computations are performed on a laptop computer with an Intel Core i7-2760QM CPU running at a clock speed of 2.40 GHz.

2.1. Engines. The relevant data of the two engines considered here are provided in Table 1. Engine A is a heavy-duty engine which is used in on-road and off-road applications. It does not have an EGR system but relies on a selective catalytic-reduction system (SCR) to reduce the engine-out NO_x emissions to the level imposed by the legislation. Engine B is a light-duty engine that is used mainly in light commercial vehicles. It has an EGR system but no SCR. Both engines are equipped with a common-rail injection system and a diesel particulate filter (DPF). The soot emissions are low enough such that no active regeneration of the DPF is necessary. The optimisation thus has to maintain a similar level of soot emissions and should not produce large instantaneous soot peaks.

2.2. Engine Modelling. During an optimisation, a vast number of model evaluations are performed. Either the model function itself is evaluated, for example, during static calibration or when employing simultaneous methods for optimal control [24], or a forward simulation of the model is used, for example, for parametric studies or in the context of shooting methods for optimal control [25, Sections 3.2–3.4]. Therefore, the model has to be simple to enable a fast execution. In both cases described, partial derivatives need to be calculated as well. If only standard mathematical operations are used, automatic differentiation is applicable, which enables a fast and accurate evaluation of partial derivatives [26, 27].

Besides being computationally efficient, models apt for optimisation have to be smooth and quantitatively accurate, capture all relevant qualitative trends, and provide plausible extrapolation. These properties qualify the model itself or its simulation as an "accurate and consistent function generator" [25, Section 3.8]. As a fundamental requirement, the model outputs have to be predicted using the control signals, known parameters, and the ambient conditions only. Ideally,

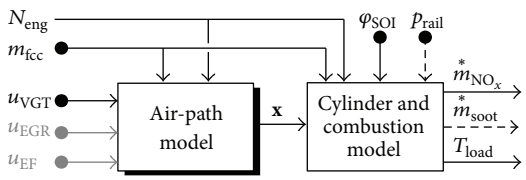

Figure 1: Structure of the engine model. The model for the engine with EGR does include the grey signals, but not the dashed ones.

the model can be identified using a small set of measurements in order not to cancel the reduction of test-bench time gained by the application of model-based approaches. If the model is able to predict the effects induced by influences that can hardly be excited on the test bench, its value for parametric studies is further enhanced.

Optimisation-oriented models are thus classified between control-oriented and phenomenological models [28, 29]. The former only capture the trends relevant to control while being as simple as to be implementable on the ECU. Due to the presence of feedback control, the quantitative accuracy is of minor importance, and the models have to be valid only in a region around the setpoints of the controller. In contrast, phenomenological models are used to perform predictive parametric studies or to analyse specific effects. Since a high execution speed is not critical, a single model evaluation typically takes from a few seconds up to several hours [30]. Due to their complexity, such models often suffer from error propagation [31, 32].

2.2.1. The Model Used. An optimisation-oriented model for a diesel engine without EGR is presented in [29, 33]. A classical mean-value model for the air path is extended by thermal models for the intake and the exhaust manifolds. Physics-based setpoint-relative models are used for the combustion efficiency, the in-cylinder processes, and the NO_x emissions. However, since all setpoint maps are replaced by polynomials, the model is smooth and apt for algorithmic differentiation. The models for the fuel consumption and the NO_x emissions capture the influence of the air-path state, the injection pressure, and the injection timing, that is, the start of injection (SOI). The modelling errors are in the range of 0.6% and 5%, respectively. For the soot emissions, the simple model described in [34] is used. It captures the effects of the injection pressure and the air-to-fuel ratio (AFR).

Figure 1 illustrates the general structure of the model. Only the air path is modelled as a dynamic system, whereas all phenomena occurring in the cylinders are assumed to be instantaneous processes. The state variables $\mathbf{x}$ of the air path are inputs to this static part of the model. The exhaust-gas aftertreatment system (ATS) is included in the model only as a flow restriction in the air path. The engine-out emissions are limited directly in the optimisation problem.

2.2.2. Extension to EGR. Several submodels need to be added or adapted for an engine with EGR. The dynamics in the intake manifold comprise balances for the mass, the energy, and the burnt-gas fraction. The corresponding differential equations read

$$\frac{dp_{IM}}{dt} = \frac{R\kappa}{V_{IM}}\left(\dot{m}_{CP}\vartheta_{IC} + \dot{m}_{EGR}\vartheta_{EGR} - \dot{m}_{cyl}\vartheta_{IM}\right), \tag{1a}$$

$$\frac{d\vartheta_{IM}}{dt} = \frac{R\vartheta_{IM}}{p_{IM}V_{IM}c_v}\left[c_p\left(\dot{m}_{CP}\vartheta_{IC} + \dot{m}_{EGR}\vartheta_{EGR} - \dot{m}_{cyl}\vartheta_{IM}\right) - c_v\vartheta_{IM}\left(\dot{m}_{CP} + \dot{m}_{EGR} - \dot{m}_{cyl}\right)\right], \tag{1b}$$

$$\frac{dx_{BG,IM}}{dt} = \frac{R\vartheta_{IM}}{p_{IM}V_{IM}}\left(\dot{m}_{EGR}\left(x_{BG,EM} - x_{BG,IM}\right) - x_{BG,IM}\dot{m}_{CP}\right). \tag{1c}$$

The burnt-gas fraction in the exhaust gas is

$$x_{BG,EM} = \frac{x_{BG,IM}\cdot\dot{m}_{cyl} + (1+\sigma_0)\cdot\dot{m}_{fuel}}{\dot{m}_{cyl} + \dot{m}_{fuel}}, \tag{2}$$

where $\sigma_0 \approx 14.5$ is the stoichiometric AFR.

The mass-flow through the EGR valve is modelled by a simplified flow function for compressible fluids [1, Section 2.3.5]:

$$\dot{m}_{EGR} = A_{EGR}\cdot\frac{p_{EM}}{\sqrt{R\cdot\vartheta_{EM}}}\cdot\Psi\left(\frac{p_{EM}}{p_{IM}}\right), \tag{3a}$$

$$\Psi(\Pi) = \sqrt{\frac{2}{k_\Pi\cdot\Pi}\cdot\left(1 - \frac{1}{k_\Pi\cdot\Pi}\right)}, \tag{3b}$$

$$A_{EGR} = k_{EGR,1}\cdot u_{EGR} + k_{EGR,2}\cdot u_{EGR}^{k_{EGR,e}}. \tag{3c}$$

The factor $k_\Pi \approx 1.04$ accounts for flow phenomena that change the effective pressure ratio over the EGR valve. The model for the EGR cooler has the same structure as the intercooler model presented in [33].

An exhaust flap (EF) is installed directly after the turbine. Its purpose is to choke the flow of exhaust gas such that the pressure in the exhaust manifold increases. This higher back-pressure enables higher EGR mass-flows. The EF is modelled by a factor that reduces the effective opening area of the ATS:

$$x_{EF} = 1 - k_{EF,1}\cdot u_{EF}^{k_{EF,2}}. \tag{4}$$

Due to the lower oxygen concentration when EGR is applied, the combustion efficiency is slightly reduced. The factor

$$\eta_{\xi_{O_2}} = 1 - a_{\xi_{O_2}}\left(N_{eng}, m_{fcc}\right)\cdot\left\|\xi_{O_2} - \hat{\xi}_{O_2}\right\|^{b_{\xi_{O_2}}} \tag{5a}$$

is appended as an additional multiplicative efficiency reduction. The reference oxygen mass-fraction before the combustion, $\hat{\xi}_{O_2}$, as well as the exponential factor $b_{\xi_{O_2}}$ are scalar parameters. The efficiency reduction is a function of the engine operating point:

$$a_{\xi_{O_2}} = a_0 + a_1\cdot N_{eng} + a_2\cdot m_{fcc}. \tag{5b}$$

The ignition-delay model also has a multiplicative structure. The additional correction factor

$$\tau_{\xi_{O_2}} = 1 - k_{\text{lin}} \cdot \left(\xi_{O_2} - \widehat{\xi}_{O_2}\right) - k_{\text{quad}}\left(N_{\text{eng}}, m_{\text{fcc}}\right) \cdot \left(\xi_{O_2} - \widehat{\xi}_{O_2}\right)^2 \tag{6a}$$

is introduced, where the coefficient of the second-order term is again a function of the engine operating point:

$$k_{\text{quad}} = k_{\text{quad},0} + k_{\text{quad},1} \cdot N_{\text{eng}} + k_{\text{quad},2} \cdot m_{\text{fcc}} + k_{\text{quad},3} \cdot N_{\text{eng}}^2 + k_{\text{quad},4} \cdot m_{\text{fcc}}^2 + k_{\text{quad},5} \cdot N_{\text{eng}} \cdot m_{\text{fcc}}. \tag{6b}$$

The NO_x model inherently accounts for the change of the temperature and of the composition of the intake air by the EGR. However, since the combustion speed is changed by the reduced oxygen availability, a smaller region in the cylinder reaches a temperature that is sufficiently high for thermal NO_x formation. This effect is found to depend on the engine speed and therefore the factor

$$x_{O_2} = \xi_{O_2}^{k_{O_2} \cdot N_{\text{eng}}} \tag{7}$$

is applied to the formation volume in the original NO_x model [29]. The effect of the EGR, which reduces the NO_x emissions by a factor of up to 18, is predicted by the model with an average magnitude of the relative error of 8%.

The simple soot model that is suitable for engine A does not yield plausible results for engine B with EGR. Therefore, no model for the soot emissions is used. In the OCP, the corresponding limit is replaced by a lower bound on the AFR.

2.3. Numerical Optimal Control. A general formulation of an OCP reads

$$\min_{\mathbf{x}(\cdot),\mathbf{u}(\cdot)} \quad \int_0^T L\left(\mathbf{x}(t), \mathbf{u}(t), \boldsymbol{\pi}(t)\right) dt \tag{8a}$$

$$\text{s.t.} \quad \dot{\mathbf{x}}(t) - \mathbf{f}\left(\mathbf{x}(t), \mathbf{u}(t), \boldsymbol{\pi}(t)\right) = 0, \quad t \in [0, T], \tag{8b}$$

$$\int_0^T \mathbf{g}\left(\mathbf{x}(t), \mathbf{u}(t), \boldsymbol{\pi}(t)\right) dt - \widehat{\mathbf{g}} \leq 0, \tag{8c}$$

$$\mathbf{c}\left(\mathbf{x}(t), \mathbf{u}(t), \boldsymbol{\pi}(t)\right) \leq 0, \quad t \in [0, T], \tag{8d}$$

$$\underline{\mathbf{x}}(t) \leq \mathbf{x}(t) \leq \overline{\mathbf{x}}(t), \quad t \in [0, T], \tag{8e}$$

$$\underline{\mathbf{u}}(t) \leq \mathbf{u}(t) \leq \overline{\mathbf{u}}(t), \quad t \in [0, T]. \tag{8f}$$

The goal is to find trajectories for the state variables $\mathbf{x}(t)$ and the control inputs $\mathbf{u}(t)$ that minimise the integral cost (8a) while satisfying the dynamics of the system (8b), the integral inequality constraints (8c), and the time-variable path constraints (8d). (The integral cost L is called a Lagrange term. Every differentiable end cost, also called a Mayer term, can be replaced by an equivalent Lagrange term. The latter is to be preferred from a numerical point of view [25, Section 4.9].) The simple bounds (8e) and (8f) represent the actuator ranges, mechanical limits, and fixed initial or end conditions. The system has n_x state variables, that is, $\mathbf{x}, \mathbf{f}, \underline{\mathbf{x}}, \overline{\mathbf{x}} \in \mathbb{R}^{n_x}$, and there are n_u control inputs to the system, $\mathbf{u}, \underline{\mathbf{u}}, \overline{\mathbf{u}} \in \mathbb{R}^{n_u}$. Several time-variable parameters $\boldsymbol{\pi} \in \mathbb{R}^{n_\pi}$ may be present. Finally, there are n_g integral constraints and n_c path constraints, that is, $\mathbf{g}, \widehat{\mathbf{g}} \in \mathbb{R}^{n_g}$, and $\mathbf{c} \in \mathbb{R}^{n_c}$, respectively.

The most common approaches to tackle continuous-time OCPs are outlined in Figure 2. The top level is inspired by [35]. Partial overviews are provided in [36–38], and [39] presents a brief historical outline. Solving the Hamilton-Jacobi-Bellman equation, which is a partial differential equation subject to the model equations, is practicable only for a system with few state variables and control inputs. Similar to its discrete-time equivalent, dynamic programming, it suffers from the curse of dimensionality for larger systems. Likewise, the indirect approach can hardly be applied to large and complex problems. If the first-order optimality conditions can be derived analytically, still a two-point boundary-value problem (BVP) needs to be solved. The dynamics of the costate variables however are ill-conditioned, and it is impossible to derive a good initial guess for the general case.

Direct methods start by discretising the full OCP. A finite-dimensional, constrained nonlinear optimisation problem results. This type of problem is termed nonlinear program (NLP). Due to the performance and the robustness of current NLP solvers, this approach is a means to an efficient numerical solution of large-scale, complex OCPs.

Within direct methods, two main approaches exist. The *sequential* approach, also called *single shooting*, discretises only the control inputs, and a forward simulation is used to evaluate the model. Although this method is simple to implement, the resulting NLP is highly nonlinear and sensitive [25, Sections 3.3 and 3.4], which limits the length of the time horizon. Furthermore, consistent derivatives have to be available for the solution of the NLP [25, Section 3.8], which requires the use of custom ODE solvers. Finally, instabilities of the model can lead to a failure of the ODE solver and thus a premature termination of the optimisation.

The alternative to the sequential approach is to discretise the state trajectories along with the control inputs. The entire continous-time problem is "transcribed" into a large but extremely sparse NLP, which fully includes the discretised state trajectories. No forward simulation is performed, and the model ODEs are only satisfied after the solution of the NLP. This *simultaneous* optimisation and simulation resolves the problems encountered by the sequential approach. One drawback is that the accuracy of the solution of the ODEs is coupled to the discretisation of the control inputs. An iterative mesh refinement may be necessary to obtain a sufficiently accurate solution. A recent overview of simultaneous approaches is provided in [24, 40], while [41] unveils the beginnings of these methods.

2.3.1. Direct Collocation. Collocation methods are a family of integration schemes often used for the direct transcription of OCPs [42–47]. In contrast to other Runge-Kutta schemes, they represent the state trajectories on each integration interval as polynomials and thus provide a continuous solution.

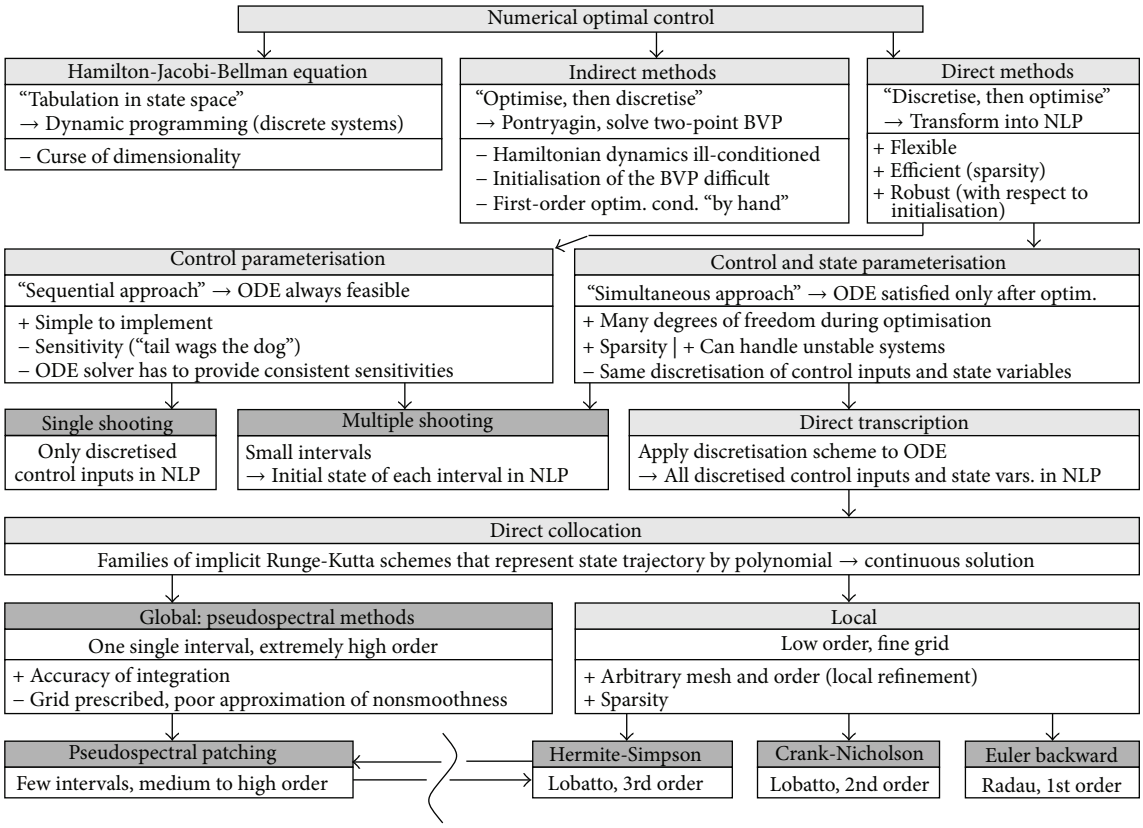

Figure 2: Overview of the most prominent methods for the numerical solution of optimal control problems.

The method chosen here is the family of Radau collocation schemes [48]. It provides stiff accuracy and stiff decay (or L-stability) [48], [49, Section 3.5]. L-stable schemes approximate the true solution of a stiff system when the discretisation is refined. Furthermore, the integral and the differential formulations of Radau collocation are equivalent [47]. This property is necessary to construct a consistent transcription of the OCP at hand.

Historically, two different branches of direct collocation methods evolved, which is indicated in Figure 2. On the one hand, low-order methods originated from the forward simulation of ODEs. A step-size adaptation is used to compensate for the low order. On the other hand, *pseudospectral methods* originally evolved in the context of partial differential equations within fluid dynamics. In their purest form, these methods do not subdivide the time horizon into intervals but represent the state variables as single high-order polynomials. The order of these polynomials may be increased to achieve a higher accuracy. In the context of direct collocation, these two branches can be cast in a unified framework that allows for an arbitrary order on each collocation interval. Nowadays, approaches that selectively refine the step size and the collocation order represent the state of the art [50, 51].

2.3.2. Nonlinear Programming. Before the equations for direct collocation and the structure of the resulting NLP are derived, the fundamentals of solving NLPs are summarised. This outline enables the interpretation of the performance of different solvers on the problem at hand. Neither completeness is claimed nor a proper mathematical foundation is followed. Several textbooks on the subject are available, for example, [52, 53].

An NLP is formulated as

$$\min_{\boldsymbol{\omega}} \quad F(\boldsymbol{\omega}) \tag{9a}$$

$$\text{s.t.} \quad \mathbf{g}(\boldsymbol{\omega}) = 0, \quad \mathbf{g} \in \mathbb{R}^{n_g}, \tag{9b}$$

$$\mathbf{h}(\boldsymbol{\omega}) \leq 0, \quad \mathbf{h} \in \mathbb{R}^{n_h}. \tag{9c}$$

By the introduction of the Lagrangian function

$$\mathscr{L}\left(\boldsymbol{\omega}, \boldsymbol{\lambda}_g, \boldsymbol{\lambda}_h\right) := F(\boldsymbol{\omega}) + \boldsymbol{\lambda}_g^T \mathbf{g}(\boldsymbol{\omega}) + \boldsymbol{\lambda}_h^T \mathbf{h}(\boldsymbol{\omega}), \tag{10}$$

the first-order necessary conditions for the NLP (9a)–(9c), also known as the Karush-Kuhn-Tucker (KKT) conditions, become

$$\nabla_{\boldsymbol{\omega}} \mathscr{L}\left(\boldsymbol{\omega}^*, \boldsymbol{\lambda}_g^*, \boldsymbol{\lambda}_h^*\right) = 0, \tag{11a}$$

$$\nabla_{\boldsymbol{\lambda}_g} \mathscr{L}\left(\boldsymbol{\omega}^*, \boldsymbol{\lambda}_g^*, \boldsymbol{\lambda}_h^*\right) = \mathbf{g}\left(\boldsymbol{\omega}^*\right) = 0, \tag{11b}$$

$$\nabla_{\boldsymbol{\lambda}_h} \mathscr{L}\left(\boldsymbol{\omega}^*, \boldsymbol{\lambda}_g^*, \boldsymbol{\lambda}_h^*\right) = \mathbf{h}\left(\boldsymbol{\omega}^*\right) \leq 0, \tag{11c}$$

$$\boldsymbol{\lambda}_h^* \geq 0, \tag{11d}$$

$$\lambda_{h,i}^* \cdot h_i(\boldsymbol{\omega}^*) = 0, \quad i = 1, \ldots, n_h. \tag{11e}$$

The matrix of the first partial derivatives of all constraints is called the Jacobian. The second-order sufficient conditions require the Hessian of the Lagrangian, $\nabla_{\boldsymbol{\omega}}^2 \mathscr{L}(\boldsymbol{\omega}, \boldsymbol{\lambda}_g, \boldsymbol{\lambda}_h)$, projected on the null-space of the Jacobian, to be positive definite. This projection is termed the "reduced Hessian."

Equality-constrained problems can be solved by applying Newton's method to the nonlinear KKT conditions. After some rearrangements, one obtains the KKT system

$$\begin{pmatrix} \nabla F(\boldsymbol{\omega}_k) \\ \mathbf{g}(\boldsymbol{\omega}_k) \end{pmatrix} + \begin{bmatrix} \nabla_{\boldsymbol{\omega}}^2 \mathscr{L}(\boldsymbol{\omega}_k, \boldsymbol{\lambda}_{g,k}) & \nabla \mathbf{g}(\boldsymbol{\omega}_k) \\ \nabla \mathbf{g}(\boldsymbol{\omega}_k)^T & 0 \end{bmatrix} \cdot \begin{pmatrix} \boldsymbol{\omega} - \boldsymbol{\omega}_k \\ \boldsymbol{\lambda}_g \end{pmatrix} = 0, \tag{12}$$

which is solved during each Newton iteration k. The solution of the quadratic program (QP)

$$\min_{\mathbf{p}} \quad \frac{1}{2}\mathbf{p}^T \nabla_{\boldsymbol{\omega}}^2 \mathscr{L}(\boldsymbol{\omega}_k, \boldsymbol{\lambda}_{g,k})\mathbf{p} + \nabla F(\boldsymbol{\omega}_k)^T \mathbf{p} \tag{13a}$$

$$\text{s.t.} \quad \nabla \mathbf{g}(\boldsymbol{\omega}_k)^T \mathbf{p} + \mathbf{g}(\boldsymbol{\omega}_k) = 0, \tag{13b}$$

with $\mathbf{p} = \boldsymbol{\omega} - \boldsymbol{\omega}_k$, is equivalent to the solution of (12). Applying Newton's method to the KKT conditions thus can be interpreted as *sequential quadratic programming* (SQP).

To ensure progress from remote starting points, two different *globalisation strategies* are used. The *line search* approach first defines a direction and searches along this direction until an acceptable step length is found. The most popular search direction is the *Newton direction* defined by (12) or (13a) and (13b). In contrast, the *trust-region* approach defines a region, for example, a ball, around the current point in which a model for F—usually also a quadratic approximation—is assumed to be reliable. The trust-region radius is adjusted by assessing the model accuracy observed over the last step. In proximity of the solution, both approaches reduce to the standard Newton iteration on the KKT conditions, which exhibits quadratic convergence.

Quasi-Newton Approximations. In the KKT system (12) or the QP (13a) and (13b), the exact Hessian of the Lagrangian can be replaced by a quasi-Newton (QN) approximation. This substitution is possible since the current Lagrange multipliers $\boldsymbol{\lambda}_{g,k}$ only occur implicitly in the Hessian itself. The basic idea is to utilise the curvature information obtained along the NLP iterations to construct an approximation of the exact Hessian. The most prominent method is the limited-memory BFGS update [54], named after its discoverers C. G. Broyden, R. Fletcher, D. Goldfarb, and D. F. Shanno. This update preserves the positive definiteness of a usually diagonal initialisation.

Inequality Constraints. To solve inequality-constrained (IC) problems, two fundamentally different approaches are used nowadays. On the one hand, the idea of SQP can be extended to the IC case. These methods model (9a)–(9c) as an IC QP at each iteration. The search direction $\mathbf{p}_k$ for a line search is thus the solution of the QP

$$\min_{\mathbf{p}} \quad \frac{1}{2}\mathbf{p}^T \nabla_{\boldsymbol{\omega}}^2 \mathscr{L}(\boldsymbol{\omega}_k, \boldsymbol{\lambda}_{g,k}, \boldsymbol{\lambda}_{h,k})\mathbf{p} + \nabla F(\boldsymbol{\omega}_k)^T \mathbf{p} \tag{14a}$$

$$\text{s.t.} \quad \nabla \mathbf{g}(\boldsymbol{\omega}_k)^T \mathbf{p} + \mathbf{g}(\boldsymbol{\omega}_k) = 0, \tag{14b}$$

$$\nabla \mathbf{h}(\boldsymbol{\omega}_k)^T \mathbf{p} + \mathbf{h}(\boldsymbol{\omega}_k) \leq 0. \tag{14c}$$

On the other hand, *interior-point* (IP) methods penalise the violation of the ICs by a logarithmic barrier function. The problem

$$\min_{\boldsymbol{\omega}} \quad F(\boldsymbol{\omega}) - \tau \sum_{i=1}^{n_h} \log(-h_i) \tag{15a}$$

$$\text{s.t.} \quad \mathbf{g}(\boldsymbol{\omega}) = 0, \tag{15b}$$

is solved, while the barrier parameter τ is decreased iteratively. The solution for one value is used to initialise the next iteration.

Both approaches to handle IC problems exhibit some advantages but also suffer from specific drawbacks. The main difference is that, within an SQP method, the structure of the QP approximation changes from iteration to iteration, whereas for IP methods, this structure is invariant. As a consequence, an IP method can afford to derive a good factorisation of the KKT system once to ensure a fast calculation of the Newton steps. Direct solvers for large, sparse linear systems are readily available. In contrast, an SQP method relies on a QP solver that detects the set of active ICs for the current QP approximation by itself. This solver thus has to deal with a constantly changing problem structure, which is usually handled by updates of the initial factorisation.

This difference is closely related to the two basic approaches to solve the KKT system. On the one hand, the full-matrix approach relies on a direct, symmetric indefinite factorisation of the KKT matrix. In this context, various software packages are available, for example, MA27/57/97 [55], MUMPS [56], or PARDISO [57]. On the other hand, the decomposition approach calculates and updates the null-space basis matrix. However, for large sparse problems, the reduced Hessian is much denser than the Hessian itself. Since dense linear algebra has to be applied to the reduced system, this approach is only computationally efficient when the number of the degrees of freedom is small.

The most important points concerning the advantages and the drawbacks of the SQP and IP methods are stated next [58].

(i) It is difficult to implement an exact-Newton SQP method. The main pitfalls are the nonconvexity of the QP subproblems when the exact Hessian is used and that SQP methods often rely on custom-tailored linear algebra. The latter limits the flexibility of those algorithms to adopt the latest developments in software and hardware technology.

(ii) IP methods are most efficient when relying on the exact second derivatives. Furthermore, they usually

converge in fewer inner iterations, even for very large problems, and may utilize the latest "off-the-shelf" linear algebra software.

(iii) Applying IP solvers to the QPs in an SQP framework had limited success because they are hard to warm-start [25, Section 4.13]. In short, an IP solver, which follows a central path and approaches the constraint surface orthogonally, faces sensitivity problems when forced to step onto the solution path perpendicularly.

NLP Solvers Used. The following list characterises the NLP solvers used here.

SNOPT 7.2 [59], a proprietary solver implementing an SQP algorithm based on a decomposition approach (LU factorisation) and a line-search globalisation. It cannot use exact second derivatives but relies on a BFGS update.

IPOPT 3.11.0 [60], an open-source solver implementing a primal-dual IP method using a line-search globalisation. As linear solver, MUMPS [56] with METIS preordering [61] is used. IPOPT provides a BFGS update but can also exploit the exact second derivatives.

WORHP 1.2-2533 [62]. This solver tackles the QPs within an SQP framework by an IP solver that can be efficiently warm-started. A line-search globalisation and various partitioned BFGS updates are implemented. The default linear solver MA97 is used. WORHP is free for academic use.

KNITRO 8.0 [63], a proprietary solver that provides three algorithms, namely, an SQP trust-region method and two IP methods. The latter rely either on a direct solver and a line search or on a projected conjugate-gradient (CG) method to solve trust-region subproblems. Exact and QN methods are implemented.

2.3.3. Direct Collocation of Optimal Control Problems. Radau collocation represents the state $x(t)$ of the scalar ODE $\dot{x} = f(x)$ on the interval $[t_0, t_f]$ as a polynomial, say of degree s. The time derivative of this polynomial is then equated to the values of f at s collocation points $t_0 < \tau_1 < \tau_2 \cdots < \tau_N = t_f$. The left boundary $\tau_0 = t_0$ is a noncollocated point. The notation $x_j := x(\tau_j)$ is adopted. The resulting system of equations reads

$$\begin{pmatrix} \dot{x}_1 \\ \dot{x}_2 \\ \vdots \\ \dot{x}_s \end{pmatrix} \approx \underbrace{[\mathbf{d}_0, \widetilde{\mathbf{D}}]}_{=:\mathbf{D}} \cdot \begin{pmatrix} x_0 \\ x_1 \\ x_2 \\ \vdots \\ x_s \end{pmatrix} \stackrel{!}{=} \begin{pmatrix} f(x_1) \\ f(x_2) \\ \vdots \\ f(x_s) \end{pmatrix}. \tag{16}$$

Each of these s equations (index i) is a sum of linear terms and one nonlinear term:

$$d_{0,i} \cdot x_0 + \sum_{j=1}^{s} \widetilde{D}_{ij} \cdot x_j - f(x_i) = 0. \tag{17}$$

The collocation nodes are defined as the roots of Legendre polynomials and have to be computed numerically [64, Section 2.3]. Lagrange interpolation by barycentric weights is used to calculate the differentiation matrix $\mathbf{D}$ along with the vector of quadrature weights $\mathbf{w}$ [65]. Here, the step length $h = t_f - t_0$ is assumed to be included in $\mathbf{D}$ and $\mathbf{w}$. The latter is used to approximate the definite integral of a function $g(t)$ as $\int_{t_0}^{t_f} g(t)dt \approx \sum_{j=1}^{s} w_j g(\tau_j)$.

The collocation naturally extends to a system of ODEs; that is, $\dot{\mathbf{x}} = \mathbf{f}(\mathbf{x})$. To simplify the notation, the state variables are assumed to be stacked in a row vector; that is, $\mathbf{x}, \mathbf{f} \in \mathbb{R}^{1\times n_x}$. Equation (16) becomes a matrix equation in $\mathbb{R}^{s\times n_x}$:

$$\mathbf{D} \cdot \begin{bmatrix} \mathbf{x}_0 \\ \mathbf{X} \end{bmatrix} = \mathbf{F}(\mathbf{X}), \tag{18}$$

where the rows of $\mathbf{X}$ and $\mathbf{F}$ correspond to one collocation point each. In turn, the columns of $\mathbf{X}$ and $\mathbf{F}$ represent one state variable and its corresponding right-hand side at all collocation points.

When the OCP (8a)–(8f) is transcribed, all functions and integrals have to be discretised consistently. Here, $k = 1, \ldots, m$ integration intervals $[t_{k-1}, t_k]$ are used with $0 = t_0 < t_1 \cdots < t_m = T$. The collocation order s_k can be different for each interval. Summing up the collocation points throughout all integration intervals results in a total of $M = l(m, s_m)$ discretisation points. The "linear index" l thereby corresponds to collocation node i in interval k:

$$l := l(k, i) = i + \sum_{\alpha=1}^{k-1} s_\alpha. \tag{19}$$

The following NLP results:

$$\min_{\mathbf{x},\mathbf{u}} \quad \sum_{l=1}^{M} W_l \cdot L(\mathbf{x}_l, \mathbf{u}_l) \tag{20a}$$

$$\text{s.t.} \quad \mathbf{D}^{(k)} \cdot \begin{bmatrix} \mathbf{X}^{(k-1)}_{s_{k-1},\cdot} \\ \mathbf{X}^{(k)} \end{bmatrix} - \mathbf{F}\left(\mathbf{X}^{(k)}, \mathbf{U}^{(k)}\right) = 0, \quad k = 1, \ldots, m, \tag{20b}$$

$$\sum_{l=1}^{M} W_l \cdot \mathbf{g}(\mathbf{x}_l, \mathbf{u}_l) - \widehat{\mathbf{g}} \le 0, \tag{20c}$$

$$\mathbf{c}(\mathbf{x}_l, \mathbf{u}_l) \le 0, \quad l = 1, \ldots, M. \tag{20d}$$

The simple bounds (8e) and (8f) are imposed at each discretisation point and are not restated here. The vector of the "global" quadrature weights $\mathbf{W}$ results from stacking the vectors of the quadrature weights $\mathbf{w}^{(k)}$ of each interval k after removing the first element, which is zero.

The Lagrangian of the NLP (20a)–(20d) is the sum of the objective (20a) and all constraints (20b), (20c), and (20d), which are weighted by the Lagrange multipliers $\boldsymbol{\lambda}$. To simplify the notation, the Lagrange multipliers are grouped according to the problem structure. The $n_x \cdot s_k$ multipliers for the discretised dynamic constraints on each integration interval

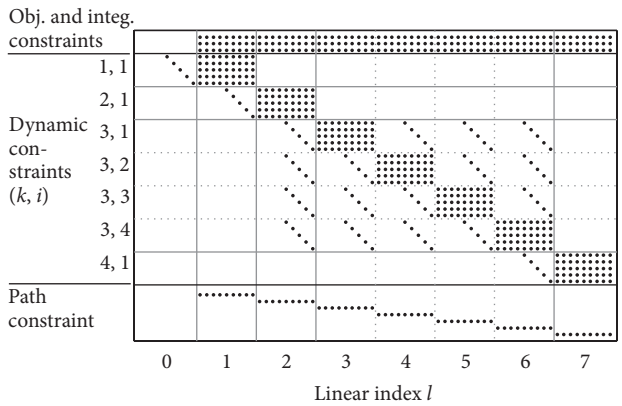

Figure 3: Sparsity structure of the Jacobian of the NLP resulting from the transcription of a continuous-time OCP by Radau collocation. Four collocation intervals are used, all with collocation order 1 except for the third interval which is of order 4. Characteristically for Radau collocation, the zeroth point only contributes linearly to the first dynamic constraint of the first interval. The variables at each discretisation point are ordered as $(\mathbf{u}_l^T, \mathbf{x}_l^T)^T$.

k are denoted by $\boldsymbol{\lambda}_d^{(k)}$, the n_g multipliers for the integral inequalities are stacked in $\boldsymbol{\lambda}_g$, and the n_c multipliers for the path constraints at each discretisation point l are gathered in the vector $\boldsymbol{\lambda}_{c,l}$.

The Lagrangian can be separated in the primal variables $\boldsymbol{\omega}_l = \boldsymbol{\omega}_i^{(k)} := (\mathbf{x}_i^{(k)}, \mathbf{u}_i^{(k)})$. The element Lagrangian $\mathscr{L}_i^{(k)}$ at collocation node l reads

$$\begin{aligned}\mathscr{L}_i^{(k)} &= W_l \cdot L(\boldsymbol{\omega}_l) \\ &\quad + \mathbf{x}_i^{(k)} \cdot \left(\sum_{j=1}^{N_k} \widetilde{D}_{ji}^{(k)} \boldsymbol{\lambda}_{d,j}^{(k)} + \delta_i^{(k)} \sum_{j=1}^{N_{k+1}} d_{0,j}^{(k+1)} \boldsymbol{\lambda}_{d,j}^{(k+1)} \right) \\ &\quad - \mathbf{f}\left(\boldsymbol{\omega}_i^{(k)}\right) \boldsymbol{\lambda}_{d,i}^{(k)} + W_l \cdot \boldsymbol{\lambda}_g^T \mathbf{g}(\boldsymbol{\omega}_l) + \boldsymbol{\lambda}_{c,l}^T \mathbf{c}(\boldsymbol{\omega}_l).\end{aligned} \tag{21}$$

The Lagrangian of the full NLP is obtained by summing these element Lagrangians. The Hessian of the Lagrangian thus is a perfect block-diagonal matrix with uniformly sized square blocks of size $(n_u + n_x)$.

Similarly, the Jacobian of the objective function and the constraints exhibits a sparse structure. Figure 3 provides an example. Exploiting the fact that only the derivatives of the model functions at each discretisation point are required to construct all derivative information of the NLP is crucial for an efficient solution [66]. In fact, the least number of model evaluations possible and thus a perfect sparsity exploitation are achieved by this procedure. Shared-memory parallel computing can be applied to further speed up the model evaluations, and a sparse matrix format has to be used in order not to be restricted by memory limitations for large problems.

The KKT system (12) is constructed from the Hessian of the Lagrangian and the Jacobian of the constraints. Therefore, it is very sparse in the case of direct collocation, and direct solvers are able to efficiently solve this linear system of equations.

2.4. Mesh Refinement. The idea of an iterative mesh refinement is to first solve a coarse approximation of the continuous-time OCP. This solution is used to identify regions where the discretisation needs refinement. Step-size refinement for relatively low-order collocation is considered here, and, consistently, the error is estimated by the local truncation error. For Radau collocation, a more detailed analysis of the convergence of the transcribed problem towards the continuous one is provided in [46].

The truncation error $\boldsymbol{\tau}$ is of order $s + 1$:

$$\mathbf{x} = \mathbf{x}^{(1)} + \boldsymbol{\tau}^{(1)}, \tag{22a}$$

$$\boldsymbol{\tau}^{(1)} = \mathbf{c} \cdot h^{s+1}. \tag{22b}$$

Here, $\mathbf{x}$ denotes the state at the end of the interval, that is, $\mathbf{x} := \mathbf{x}(t_k + h)$, and $\mathbf{x}^{(p)}$ is its approximation using p integration steps. The factors $\mathbf{c}$ depend on the model function $\mathbf{f}$ and therefore are not constant. However, over the time horizon of one integration step, assuming a constant value of $\mathbf{c}$ is reasonable. (Another common assumption is that the solution has a "memory" and thus $c_{i,k+1}/c_{i,k} \approx c_{i,k}/c_{i,k-1}$. In step-size control for ODE solvers, the two models may be combined [48].)

By subdivision of the interval into p equal steps, a more accurate approximation of the exact solution is obtained:

$$\mathbf{x} = \mathbf{x}^{(p)} + \boldsymbol{\tau}^{(p)}, \tag{23a}$$

$$\boldsymbol{\tau}^{(p)} = p \cdot \mathbf{c} \cdot \left(\frac{h}{p}\right)^{s+1} = \frac{\mathbf{c} \cdot h^{s+1}}{p^s} = \frac{\boldsymbol{\tau}^{(1)}}{p^s}. \tag{23b}$$

By equating the exact solution $\mathbf{x}$ in (22a) and (23a), with $p = 2$, an estimate for the absolute and the relative truncation error of the original approximation is obtained:

$$\boldsymbol{\tau}^{(1)} \approx \frac{\mathbf{x}^{(2)} - \mathbf{x}^{(1)}}{1 - 2^{-s}}, \qquad \widetilde{\tau}_i^{(1)} = \frac{\tau_i^{(1)}}{x_i^{(1)}}, \quad \text{for } i = 1, \ldots, n_x. \tag{24}$$

For the refined approximation, the estimate

$$\widetilde{\tau}_i^{(p)} \approx \frac{\tau_i^{(p)}}{x_i^{(1)}} \approx \frac{1}{p^s} \cdot \frac{\tau_i^{(1)}}{x_i^{(1)}} = \frac{\widetilde{\tau}_i^{(1)}}{p^s} \tag{25}$$

results. The magnitude of this relative error has to be smaller than the desired relative tolerance ε_{rel}. Solving for p yields the state-variable individual step refinement

$$p_i = \left\lceil k \cdot \left(\frac{\left|\widetilde{\tau}_i^{(1)}\right|}{\varepsilon_{\text{rel}}} \right)^{1/s} \right\rceil. \tag{26}$$

The "safety margin" k ensures that the desired tolerance is met on the new grid. The final step refinement is chosen as the maximum among all p_i.

In the context of optimal control, a value of $k < 1$ may be convenient. Since again an OCP is solved on the new grid, the control inputs may change. Thus, the exact solution of the ODEs as well as the error of the approximation changes. Due to this changing nature of the problem, it may be advantageous to refine the grid in multiple cautious iterations instead of trying to enforce the desired accuracy by a single refinement step.

2.5. Regularisation. In continuous-time OCPs, singular arcs are defined as time intervals over which the Hamiltonian becomes affine in at least one control input. (The Hamiltonian is the continuous-time equivalent of the Lagrangian. It can be shown that the KKT conditions of the transcribed problem are equivalent to the continuous first-order necessary conditions for optimality [45, 67].) On singular arcs, the optimal solution thus is not defined by the first-order optimality conditions, and the second-order sufficient conditions are not strictly satisfied since the second derivatives are zero. In indirect methods, a workaround is to consider time derivatives of the Hamiltonian of increasing order until the singular control input appears explicitly [68].

The presence of singular arcs introduces problems when a direct method is chosen to numerically solve the OCP. A good overview is provided in [69, Section 4.5]. Loosely spoken, the better the continuous problem is approximated, the more exactly the singular nature of the problem is revealed. Thus, a fine discretisation of the problem may lead to unwanted effects. Namely, spurious oscillations can be observed along singular arcs. This behaviour is intensified whenever the solution follows trajectory constraints.

In [69, Section 4.5], a method based on the "piecewise derivative variation of the control" is proposed to regularise the transcribed singular OCPs. Thereby, the square of the difference in the slope of each control input in two neighbouring intervals, that is, the local curvature, is added to the objective as a penalty term. The regularisation term for a scalar control input u is

$$L_{\text{reg}}(u_{\cdot}) := c_M \cdot \dot{\text{Var}}^2_{t_N}(u_{\cdot}) = c_M \cdot \frac{1}{2}\sum_{l=3}^{M-1} \left|s_{l+1} - s_l\right|^2, \quad (27)$$

where $s_l = (u_l - u_{l-1})/(t_l - t_{l-1})$ is its slope in interval l. The summation starts at $l = 3$ since the first point is not a collocation point in Radau methods and thus the control input at this point does not have a meaning and is usually excluded from the NLP. The factor c_M is chosen as

$$c_M := \frac{c_{\text{reg}}}{(M-3)(M-1)^2}. \quad (28)$$

The term $(M - 3)$ accounts for the number of summation terms, whereas $(M - 1)^2$ is an approximation of the average step size of the discretisation grid. This formulation scales the regularisation term according to the resolution of the transcription, such that the influence of the user-specified parameter c_{reg} is invariant with respect to a mesh refinement.

The solution of the regularised problem converges to the solution of the original problem for an increasingly fine resolution. It is further shown in the original literature that c_M goes to zero fast enough as $M \to \infty$ such as to ensure that the regularisation term stays bounded.

2.6. Optimal Control of Diesel Engines. The OCP of diesel engines can be cast in the form of the general OCP (8a)–(8f). The objective is to minimise the cumulative fuel consumption; that is, $L = \overset{*}{m}_{\text{fuel}}$ in (8a). The dynamic constraints (8b) represent the air-path model. The control inputs comprise the air-path actuators, the fuel injected per cylinder and combustion cycle, as well as the signals that control the combustion, namely, the start of injection (SOI) and the injection pressure delivered by the common-rail system. The engine speed, its time derivative, and the desired load torque are introduced as time-variable parameters. Therefore, in the most general case, the vectors of the state variables, the control inputs, and the time-variable parameters read

$$\mathbf{x} = \begin{pmatrix} p_{\text{IM}} \\ p_{\text{EM}} \\ \omega_{\text{TC}} \\ p_1 \\ p_4 \\ \vartheta_{\text{IM}} \\ x_{\text{BG,IM}} \\ \vartheta_{\text{EMC}} \\ \vartheta_{\text{IMC}} \end{pmatrix}, \quad \mathbf{u} = \begin{pmatrix} u_{\text{VGT}} \\ u_{\text{EGR}} \\ u_{\text{EF}} \\ m_{\text{fcc}} \\ \varphi_{\text{SOI}} \\ p_{\text{rail}} \end{pmatrix}, \quad (29)$$

$$\boldsymbol{\pi} = \begin{pmatrix} N_{\text{eng}} \\ \dot{N}_{\text{eng}} \\ \widehat{T}_{\text{load}} \end{pmatrix}.$$

The fuel mass-flow is simply $\overset{*}{m}_{\text{fuel}} = m_{\text{fcc}} \cdot N_{\text{eng}}/120 \cdot n_{\text{cyl}}$. The cumulative pollutant emissions are limited by the integral inequality constraints (8c); that is, $\mathbf{g} = (\overset{*}{m}_{\text{NO}_x}, \overset{*}{m}_{\text{soot}})^T$. The absolute limits $\widehat{\mathbf{g}}$ are calculated from the desired brake-specific values by multiplication with the integral of the nonnegative segments of the engine power $P_{\text{eng}} = N_{\text{eng}} \cdot \pi/30 \cdot \widehat{T}_{\text{load}}$. The desired load torque is imposed as a lower bound by a path constraint; that is, $\widehat{T}_{\text{load}}(t) - T_{\text{load}}(t) \leq 0$ for all t. The rationale for this formulation and a detailed description are provided in [70].

The simple bounds (8e) and (8f) represent various constraints. First, the physical actuator ranges need to be respected. The fuel mass is limited from below by zero and from above by the maximum injection quantity allowed for the engine at hand. Second, mechanical limits are imposed on several state variables such as the maximum turbocharger speed and maximum pressures and temperatures in the intake and exhaust manifolds. Finally, some of the control inputs are limited to a region in which the model is known to deliver plausible results. However, these limits are found not to be active at the optimal solution.

To initialise the OCP, a feedforward simulation of the model is performed. The control signals recorded during a test-bench run using a preseries ECU calibration are used. This initialisation is crucial in order not to obtain an infeasible QP in the first NLP iteration.

2.6.1. Engines with and without EGR. For engine A, which does not have an EGR system, the four state variables from p_1 to $x_{\text{BG,IM}}$, as well as the two control inputs u_{EGR} and u_{EF}, are not present in the model. Conversely, the full state and control vectors presented in (29) are required to represent the air path of engine B. However, since no satisfactory soot

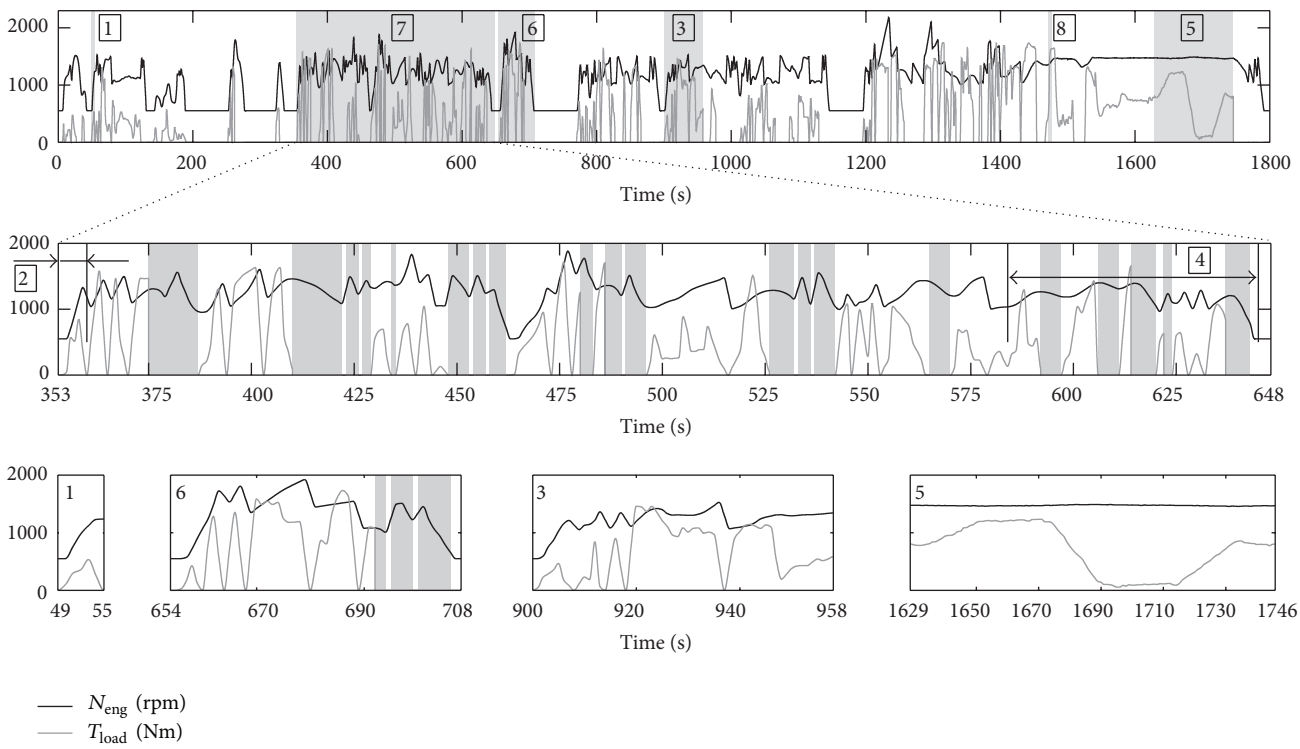

Figure 4: The full WHTC (top), with the individual test cases used in this paper indicated by the shaded areas. The test cycles are shown in the middle and bottom plots, scaled for engine A. Here, the shaded areas indicate drag phases. Test cycles 2 and 4 are contained within cycle 7. The detailed plot of test cycle 8, scaled for engine B, is provided in the left-hand plot in Figure 11.

model could be derived for this engine, the integral constraint for this emission species is not included in the problem formulation. To account for the most prominent influence on the soot emissions, the AFR is limited by the additional path constraint $\lambda_{\mathrm{AFR,min}} - \lambda_{\mathrm{AFR}}(t) \leq 0$ for all t.

The rail pressure defines a tradeoff between the soot emissions and the NO_x emissions. If the rail pressure is too low, the combustion is slow and incomplete, which causes high soot emissions. Conversely, this slow and cool combustion leads to less thermal NO_x formation. The negative effect of a low rail pressure on the combustion efficiency is almost outweighed by the reduced power consumption of the high-pressure pump of the common-rail system. Thus, if the soot emissions are not modelled and limited, there is no tradeoff for the rail pressure and the optimisation would always set it to its lower bound. For this reason, the rail pressure is excluded as a control input to the model for engine B. Instead, the values defined by the calibration map are used.

Dynamic Loops. For the engine with EGR, the optimisation terminates prematurely for all problem instances tested. Either the QP subproblem of some outer iteration is infeasible or the algorithm just diverges. The reason is the additional dynamic loop introduced by the EGR system. It interacts with the dynamic loop of the turbocharger and thus introduces a high degree of nonlinearity to the dynamic system. A similar observation is reported in [71], and the authors propose to break the loops and to apply a homotopy to close them again.

For the problem at hand, a more straightforward solution is implemented. The control inputs and the state variables are restricted to a small "stability region" around the initial trajectories. After solving this problem, the resulting trajectories are used as the new initial guess, and the stability region is relocated around these trajectories. This procedure is repeated until the solution lies entirely inside the current stability region. An SQP method is able to efficiently solve this sequence of related problems; see Section 3.1.2.

2.6.2. Driving Cycle and Test Cases. Various segments of the World-Harmonized Transient Cycle (WHTC) [72] are used as test cases. This driving profile prescribes the engine speed and the load torque over time. (For passenger cars and light commercial vehicles, a trajectory for the vehicle speed is usually prescribed. From this speed profile, an operating-point trajectory for the engine can be calculated by means of a vehicle emulation [73].) Figure 4 displays the full WHTC as well as the segments used here. Since the profile demands values for the engine speed and the load torque at each second only, shape-preserving cubic splines are used for the interpolation. Compared to a linear interpolation, this method smoothes the operating-point trajectory, which improves the numerical properties of the resulting OCP.

The shaded areas in the middle and bottom plots of Figure 4 indicate drag phases. During these intervals, the injection is cut off and the engine is motored at the prescribed

Table 2: Performance of the NLP solvers on test cycle 1, number of outer iterations, and overall time required for the solution (in brackets). For the discretisation with order 5*, a piecewise-constant control was imposed by additional linear constraints. This variant imitates multiple shooting by resolving the state variables finer than the control inputs. The last row is the pure pseudospectral method. Symbols used are h (length of collocation intervals), s (collocation order), n_{NLP} (number of NLP variables), n_{DOF} (degrees of freedom in the NLP), and QN/EN (quasi/exact Newton method). For WORHP, only the exact Newton method is shown. For the IP method using a direct solver in KNITRO (KN-IPDIR), only the QN method could solve the problem, which is shown here. The IP-CG method always performed worse and thus is not shown. An accuracy of 10^{-6} is requested with respect to optimality and feasibility. If this accuracy was not achieved within 200 iterations, the optimisation was terminated, which is indicated by italic script. Bold script indicates the fastest solution for each case.

h	s	c_{reg}	n_{NLP}	n_{DOF}	SNOPT	IPOPT, QN	IPOPT, EN	WORHP	KN-SQP, QN	KN-SQP, EN	KN-IPDIR
0.25	1	0	225	61	**20 (3.5)**	39 (6.4)	13 (4.5)	18 (6.7)	66 (11.3)	58 (29.6)	54 (7.8)
0.25	3	10	657	190	69 (15.2)	40 (9.9)	**15 (9.8)**	18 (11.9)	151 (49.0)	65 (64.9)	70 (19.3)
0.25	5*	0	1,089	60	**23 (7.1)**	30 (10.7)	15 (14.3)	21 (23.2)	136 (82.2)	112 (167.5)	137 (86.8)
3.00	15	1	279	78	42 (6.8)	62 (10.2)	**12 (4.8)**	21 (8.5)	*200 (43.8)*	*200 (107.1)*	*144 (32.3)*
6.00	30	0	279	80	154 (27.0)	82 (21.9)	**28 (10.7)**	27 (13.7)	*200 (45.9)*	*200 (118.2)*	*200 (45.9)*

speed. The individual test cases are characterised in the following list.

(1) Short, simple cycle used for first tests of the algorithms and for illustration purposes.

(2) Short segment with a singular arc. The effect of the regularisation is illustrated on this cycle.

(3) Longer, realistic driving profile, but without drag phases.

(4) Longer, realistic driving profile with many drag phases. The presence of motored phases renders the OCP more inhomogeneous and thus more difficult to be solved. Together with cycle 3, this test cycle is used to assess the convergence properties of the various algorithms.

(5) Long test cycle which is easy to be solved since almost no transients occur. The cycle is periodic; that is, it ends at the same operating point as it starts with. By a repetition of the cycle, large-scale OCPs can be constructed that retain the complexity of the single cycle.

(6) Longer, realistic cycle that is used for the experimental validation.

(7) Long, realistic cycle that is used for the experimental validation as well as for the identification of a causal control structure in Section 3.2.1.

(8) A single load step at almost constant engine speed used for the parametric study in Section 3.2.2.

3. Results and Discussion

The results are subdivided into three sections. The first one analyses crucial numerical aspects and states the conclusions that can be drawn from these tests. The second part covers the engineering aspect by presenting various ways of utilising the optimal solutions. The last section describes the experimental validation of the methodology, which indicates that all findings presented in this paper accurately transfer to the real engine.

3.1. Numerical Aspects. First, the results from all tests performed are presented. Based on these data, conclusions are drawn on what discretisation approach is suitable for the problem at hand and which numerical methods are preferable to solve the resulting NLPs.

3.1.1. Test Results. All NLP solvers introduced in Section 2.3.2 are tested for their convergence behaviour and their computational performance when applied to problems of varying complexity and size. Moreover, the basic effects of mesh refinement and regularisation are analysed.

Convergence Behaviour. Table 2 summarises the performance of all NLP solvers on the short, simple test cycle 1. Different discretisation approaches are tested, from first-order collocation to the pseudospectral method. The regularisation parameter c_{reg} is chosen for each case individually such that a smooth solution results. For the solver WORHP, only the exact Newton method is applied. None of the partitioned BFGS updates yields satisfactory results for the problem at hand.

Table 3 provides the same data for the more realistic test cycles 3 and 4. All methods implemented in KNITRO were not able to solve any of the problem instances to the required tolerance within 200 outer iterations. Therefore, this data is not shown. Similarly, IPOPT is most efficient with respect to the number of iterations and the solution time when the exact second derivatives are provided. The QN variant did not converge within 200 iterations for any of the tests on cycle 4.

The first and second partial derivatives of the model functions, from which the KKT matrix of the NLP is constructed, are calculated by forward finite differences (FFD). The convergence behaviour of the NLP solvers is not improved when more accurate derivatives are calculated by algorithmic differentiation (AD). Even the exact Newton methods require the same number of iterations when using AD instead of FFD. Therefore, AD is advantageous only if an implementation is available that is faster than FFD. All implementations of AD for Matlab tested, namely, ADiMat [74], ADMAT 2.0 (Cayuga Research, Waterloo, ON, Canada), INTLAB V6 [75], and the open-source implementation [76], are found to be at least a factor of 1.6 slower than FFD when

Table 3: Performance of the NLP solvers on test cycles 3 (top) and 4 (bottom). Only the exact Newton methods are shown for IPOPT and WORHP. The regularisation is chosen individually for all discretisation variants such that smooth control-input trajectories are obtained.

h	s	c_{reg}	n_{NLP}	n_{DOF}	SNOPT	IPOPT	WORHP
0.25	1	0	2,097	666	35 (29.9)	**16 (26.4)**	24 (54.5)
0.40	3	20	3,924	1,256	37 (114.8)	**19 (61.1)**	24 (108.1)
0.25	5*	10	10,449	669	**24 (114.5)**	17 (153.6)	33 (338.9)
3.00	15	10	2,574	822	51 (120.8)	**18 (39.0)**	28 (69.7)
9.60	47	30	2,547	810	179 (554.6)	*200 (544.4)*	**26 (92.7)**
58.0	282	30	2,547	791	*200 (5,495.5)*	26 (448.2)	**24 (433.7)**
0.25	1	0	2,205	450	**45 (29.7)**	28 (46.7)	37 (117.4)
0.40	3	500	4,113	1,199	114 (311.5)	**29 (89.0)**	49 (196.5)
0.25	5*	30	10,989	617	**66 (386.1)**	76 (680.2)	33 (405.8)
3.00	15	200	2,709	790	197 (331.8)	*25*[a] *(65.2)*	**41 (104.5)**
10.1	50	200	2,709	768	*200 (659.9)*	**36 (92.3)**	58 (204.2)
61.0	300	300	2,709	797	*200 (6,219.3)*	*30*[a] *(2,493.7)*	**30 (781.6)**

[a] A segmentation error crashed the optimisation at that iteration.

the first and second partial derivatives of the model functions are calculated.

Large-Scale Performance. Test cycle 5 is repeated multiple times to construct a problem of increasing size that retains the same complexity. Therefore, the performance of the NLP solvers when applied to large problems can be assessed independently of their general convergence behaviour. First-order collocation on a uniform grid with a step size of 0.25 s is used, and the cycle is repeated 1 to 6 times. NLPs with around 4,000 to 25,000 variables result.

The main observations are summarised next. All solvers require a similar number of iterations to solve the differently sized problems. Even the QN methods perform well for the large-scale problems. Therefore, their poor performance on the more difficult test cases is not induced by the size of the problem to be solved, but rather by its complexity and nonlinearity.

The number of model evaluations per iteration is proportional to the number of discretisation points and thus to the size of the NLP. Therefore, the time required to solve the KKT system or to perform updates of a decomposition directly defines the computational performance of the solvers for large-scale problems. The time required for the (re)factorisations and for the dense algebra on the reduced problem in SNOPT grows with a power of about 2.5 with respect to the problem size. All other solvers work on the full but sparse KKT system and exhibit an approximately linear runtime. The proportionality factor between runtime and problem size differs by a factor of 3 from the QN method of IPOPT (fastest) to the exact Newton method in WORHP (slowest). In WORHP, the linear solver has to recalculate or update the indefinite factorisation of the KKT system at the beginning of each outer iteration.

For the full-matrix approaches just described, the fraction of the overall solution time required for the model evaluations, which are performed in parallel on four cores, is between 40% (KNITRO) and 70% (IPOPT). For SNOPT, this fraction is below 1% for large problems.

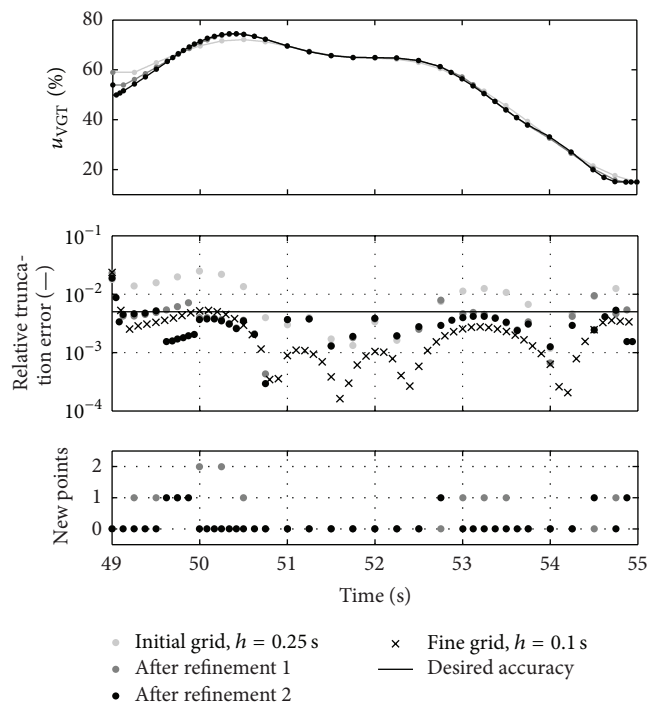

Figure 5: Mesh refinement on test cycle 1. First-order collocation is used, and the initial step size is 0.25 s. Two refinements are performed with $k = 0.5$ and $k = 1$, respectively.

Mesh Refinement. Figure 5 illustrates the effect of the mesh refinement on test cycle 1. First-order collocation is used, and a relative tolerance of $5 \cdot 10^{-3}$ is requested for the ODE solution. This accuracy is achieved by a uniform discretisation with a step size of 0.1 s. WORHP requires 21 iterations and 13.8 s for the solution of the resulting NLP.

When mesh refinement is applied, an initial step size of 0.25 s is used and two refinements are performed. The three solution runs of the coarse initial problem and the two refined problems require 17, 6, and 5 iterations and a total

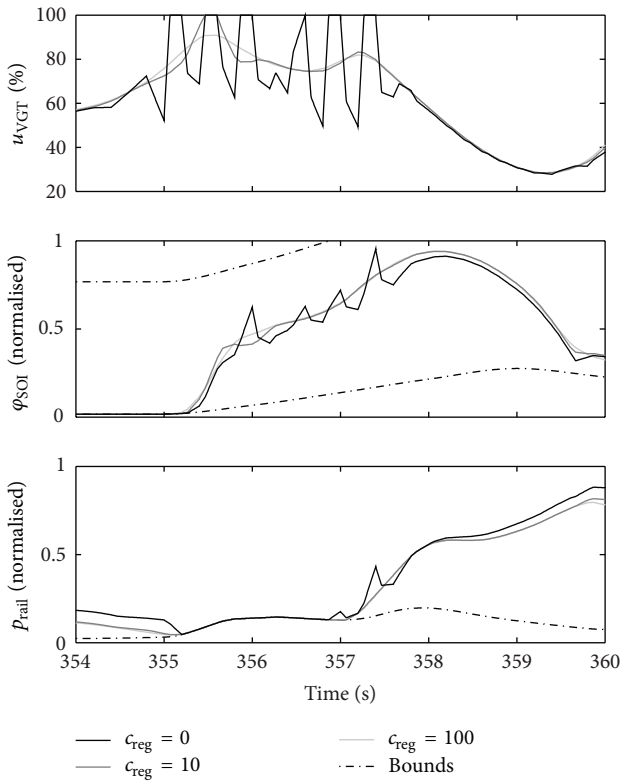

Figure 6: Regularisation of the control inputs, test cycle 2. The fuel consumption is reduced by 2.676% by the nonregularised solution and by 2.567% when a regularisation with $c_{reg} = 100$ is applied. Normalised signals are shown for reasons of confidentiality. A higher value of φ_{SOI} indicates an earlier injection.

of 11.0 s. After the second refinement, the desired accuracy is achieved, and the problem is discretised into 45 intervals only, as compared to the 60 intervals of the uniform discretisation.

When this procedure is applied to test cycle 7, the solution time is reduced from 2609 to 1015 s (or from around 43 to 17 minutes). IPOPT requires 3234 s to solve the uniformly discretised test cycle 7. However, in contrast to the SQP method implemented in WORHP, IPOPT is not able to exploit the good initialisation of the refined problems. In fact, the solution of the initial and the first refined problems requires the same time as the one-off solution of the uniformly discretised problem.

Regularisation. Figure 6 shows the optimal trajectories of the control inputs when a second-order collocation on a uniform grid with 0.2 s step size is applied to test cycle 2. As to be expected, oscillations occur mainly in the region where the trajectory constraint for the rail pressure is active. The fuel consumption and the pollutant emissions predicted by the optimisation are checked by an accurate forward simulation, which yields the same results. For a finer discretisation, faster oscillations result. Also when only the state variables are resolved more accurately, the oscillations persist.

Consequently, an oscillatory solution actually is optimal. Possibly, the gas-exchange losses are slightly reduced by the oscillations of the pressure in the exhaust manifold induced by the oscillations of the VGT. At the same time, the intake pressure is hardly affected due to the slow dynamics of the turbocharger. Therefore, the air mass-flow remains the same and the soot emissions do not increase.

Since a fast oscillating actuation of the mechanical actuators is not sustainable, regularisation has to be applied. As Figure 6 shows, the regularisation does not change the general shape of the solution. In particular, the solution is identical in the nonsingular regions. Furthermore, the loss in fuel efficiency when requiring a smooth solution is negligible.

3.1.2. Discussion. On the simple test case 1, all discretisations and all methods to solve the resulting NLPs seem to work reasonably well. However, especially the QN methods converge faster for a local discretisation than for the pseudospectral approach. The trust-region method implemented in KNITRO always gets stuck at a small trust radius and thus converges only slowly towards the optimum. The line-search globalisation thus seems to be preferable for the problem at hand.

When more meaningful driving profiles such as test cycles 3 and 4 are considered, the QN methods become less efficient also for local discretisation schemes. Surprisingly, SNOPT still manages to solve most problem instances in less than 200 iterations. As the complexity and the problem size increase, the SQP method implemented in WORHP becomes more reliable and consistent than the IP method of IPOPT.

The pseudospectral approach yields a denser NLP as indicated in Figure 3. Although the Hessian of the Lagrangian is still block diagonal, the Jacobian of the constraints does not retain a near-diagonal shape. The decomposition performed by SNOPT as well as the direct linear solvers of the full-matrix approaches become disproportionally slow when the collocation order is increased but the problem size is not changed.

Combined with the effectiveness of a step-size refinement, local discretisation schemes seem to be preferable for the problem at hand. A local discretisation enables a finer resolution of the problem only where necessary, and an SQP solver is able to exploit the good initialisation of the refined problem. Conversely, the pseudospectral method can only increase the order of the collocation polynomial and thus always refines the approximation of the problem over the full time horizon.

Summarising these findings, a full-matrix approach for the solution of the KKT system utilising a direct linear solver should be combined with an exact Newton SQP method and a line-search globalisation. (The effect of the choice of the merit function or a filter was analysed, too. No unique trend could be observed that favours one approach. The problem at hand thus seems not to be susceptible to the Maratos effect [53, Section 15.5].) WORHP implements such a method, and in fact this solver is found to perform well on all test cases, as well as to adapt to large problems best. A relatively low-order collocation scheme and an iterative step-size refinement combine well with this type of NLP solver. Only for small problems arising, for example, in receding horizon control, a decomposition approach and a QN method such as those implemented in SNOPT prove to be more efficient.

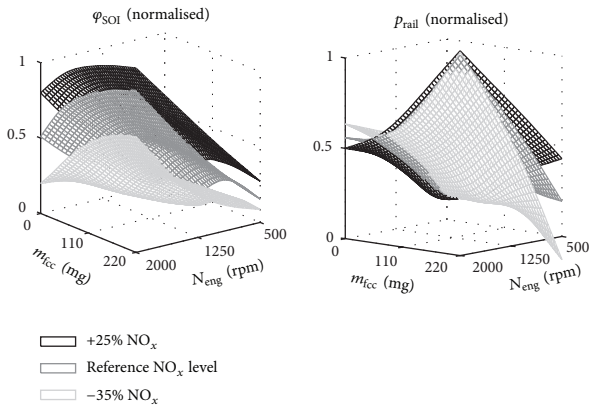

Figure 7: Maps obtained from the optimal control-trajectories and different NO_x levels relative to the one resulting from the current ECU calibration. Normalised signals are shown for reasons of confidentiality.

3.2. Engineering Aspects. Two ways of utilising the results from optimal control are proposed. On the one hand, the optimal solution may be used to identify all maps and even the control parameters of an entire feedback-control structure. On the other hand, control strategies for transient operation can be derived from parametric studies. The latter is illustrated by a case study in which the NO_x emissions of the engine with EGR have to be reduced over a load increase.

Another option is the repeated solution of a receding-horizon OCP online on the ECU. However, in contrast to model-predictive feedback control, where linear models may be used that are valid only around the reference maps [16], the full nonlinear model would have to be considered. Despite the application of custom-tailored algorithms, already the simpler optimisation problems encountered within model-predictive control are difficult to be solved in realtime due to the limited computational power and memory provided by the ECU [77]. Therefore, an online optimisation is not a feasible option at this time.

3.2.1. Model-Based Engine Calibration. Throughout this section, engine A is considered. From the solution of the OCP over a sufficiently long time horizon such as test case 7, implications for the control structure can be derived [34]. The optimal trajectories of the control inputs defining the combustion, that is, the SOI and the rail pressure, can be represented accurately by static maps over the engine operating range. The same finding applies to the boost pressure. Although these quantities might be chosen freely over time by the optimisation, values that can be scheduled over the engine speed and the injected fuel mass result. If a quasistationary representation of the air path is used, a static feedforward map for the VGT position is obtained from the solution of the corresponding OCP.

Two applications of these findings are presented here. First, the maps for the combustion-related control inputs can be derived for different emission levels. The maps for the SOI and the rail pressure for three different NO_x levels are shown in Figure 7. These maps can be parameterised by the requested emission level. On the ECU, the maps could be shifted adaptively, depending on the current performance of the ATS or according to the current driving situation.

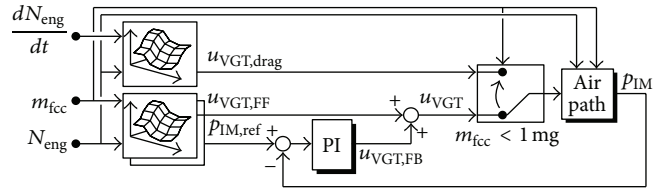

Figure 8: Structure of the boost-pressure controller.

The second application is the implementation of a feedback controller for the boost pressure based on the maps for the boost pressure and the static optimal VGT position. The former serves as reference to be tracked by the controller, and the latter is used as feedforward control signal. Figure 8 shows the structure of the control system. During drag phases, a pure feedforward control is applied. The map for the VGT position during motored operation is spanned by the engine speed and its derivative and is identified using the optimal data from the last 2 seconds of each drag phase [70]. Along with this controller defining the VGT position, the maps presented in Figure 7 are used for the SOI and the rail pressure.

The PI controller for the VGT position is implemented as

$$u_{\mathrm{VGT,FB}} = k_p \cdot e_{p_{\mathrm{IM}}}(t) + \frac{k_i}{10} \cdot \int_0^t e_{p_{\mathrm{IM}}}(\tau)\, d\tau, \qquad (30)$$

with $e_{p_{\mathrm{IM}}} = 10^{-4} \cdot (p_{\mathrm{IM}} - p_{\mathrm{IM,ref}})$. The scaling factors are used to provide a similar magnitude of the two controller parameters. A classical anti-reset windup scheme [78] is applied to handle actuator saturation and the purely feedforward operation during drag phases.

The optimal values for the two PI parameters, which are not scheduled over any quantity, may be obtained automatically. Here, a brute-force approach is proposed. The parameters are varied on a reasonable grid, and a forward simulation of the model is performed for all combinations. Figure 9 displays the results. The NO_x emissions are rather insensitive with respect to the choice of the PI parameters. Similarly, the soot emissions increase rapidly only if a too slow feedback controller is used. In this case, the boost-pressure buildup lags behind during load increases, resulting in low AFRs. An aggressive controller yields the lowest fuel consumption. However, the control signal overshoots and oscillates for this parameter set. Therefore, the parameter set which yields the closest representation of the optimal control-input trajectory is chosen.

The performances of the reference controller currently implemented, the optimal solution, and the fully causal control system derived from the optimal solution are illustrated in Figure 10. The causal controller is able to closely reproduce the optimal solution. Note that this causal control system is identified by a fully automated procedure requiring only the stationary measurement data for the identification of the engine model as input.

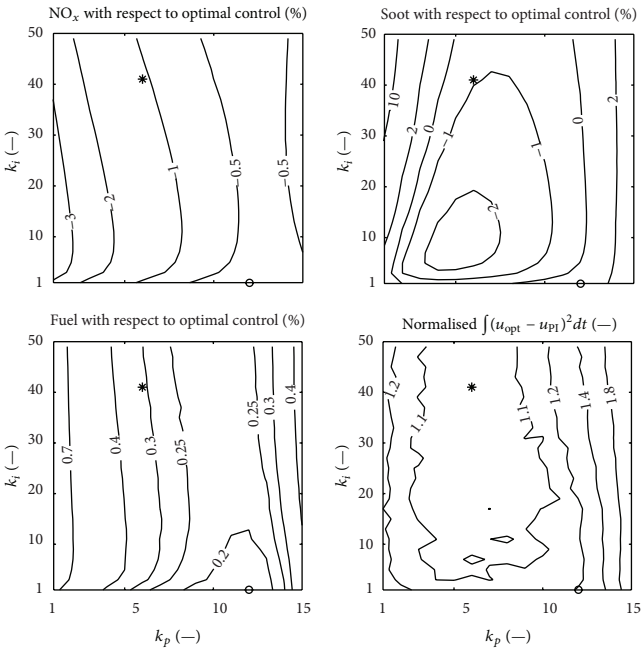

Figure 9: Selection of the parameter values for the PI controller. The circle indicates the fuel-optimal pair, while the asterisk denotes the values that result in the closest possible approximation of the optimal control-input trajectory.

3.2.2. Optimal Transient NO$_x$-Reduction Strategy. Several control inputs that define a tradeoff between the fuel consumption and the NO$_x$ emissions are present on engine B. The EGR valve controls the flow of exhaust gas into the intake manifold. The burnt gas in the intake mixture is inert and reduces the temperature of the combustion zones in the cylinders, which in turn reduces the thermal NO$_x$ formation. Conversely, the combustion becomes less efficient. The exhaust flap (EF) can be closed to increase the pressure difference over the EGR valve. A higher EGR mass-flow results, and also higher gas-exchange losses have to be overcome. Finally, a retardation of the injection yields a less efficient combustion and less NO$_x$ emissions.

Particularly during transient operation, it is difficult to derive a control strategy that reduces the NO$_x$ emissions to a desired level while maintaining the lowest possible fuel consumption. For a load increase, the additional constraint of a lower limit on the AFR has to be honoured in order not to produce large peaks of soot emissions. It is shown how optimal control can be used to derive a general control strategy. The single load step of test case 8 is considered; see the left-hand plot of Figure 11.

The following procedure is applied. First, optimal trajectories for the VGT and the SOI are derived while keeping the EGR valve closed and the EF fully open. This solution is used as reference for a successive reduction of the NO$_x$ emissions. For each desired level of the NO$_x$ emissions, the minimum fuel consumption is calculated by solving the corresponding OCP, with all four control inputs as free variables. Each resulting pair of cumulative NO$_x$ emissions and fuel consumption is plotted in the right-hand plot of Figure 11. The resulting line defines the optimal tradeoff, that is, the Pareto front, between the NO$_x$ emissions and the fuel consumption for the load step under consideration.

Figure 12 shows the corresponding control-input trajectories. The following control strategy can be derived. The optimisation does not close the EF at any point. Therefore, this is the least efficient way to reduce the NO$_x$ emissions and should be avoided. During the load increase, the VGT as well as the EGR valve needs to be closed such that the AFR stays above the lower limit, which is chosen at 1.4 here. A feedforward part based on the gradient of the torque demand could be derived from the solution of the OCP. Finally, the higher NO$_x$ emissions during the load step can be compensated by a transient shift of the SOI and a higher EGR rate during the stationary operation before and after the step.

By extending this case study to a more representative, longer time horizon, sufficient information could be collected to derive an overall controller calibration as presented for engine A in Section 3.2.1.

3.3. Experimental Validation. In order to validate the results from the dynamic optimisation on the engine test bench, three critical points have to be resolved. First, the control signals have to be transmitted to the ECU and the test-bench brake synchronously and sufficiently fast. A master process writes all signals to a shared memory section of the automation system at a frequency of 100 Hz. Using the iLinkRT protocol developed by AVL (AVL List GmbH, Graz, Austria) and ETAS (ETAS GmbH, Stuttgart, Germany), the control signals are transferred to an ETAS ES910.3 prototyping and interface module at the same frequency. This module immediately transfers the updated values to the ECU using the ETK interface (ETAS). Simultaneously, an additional process transfers the desired engine speed from the shared memory section to the controller (SPARC by HORIBA Ltd., Kyoto, Japan) of the test-bench dynamometer (HORIBA HD 700 LC). To this end, the proprietary OpenSIM CAN message protocol by HORIBA is used, which ensures a time-synchronous transfer at 100 Hz. These CAN messages, as well as all relevant signals of the ECU, are recorded at their natural sampling rate by INCA (ETAS), which runs on a host computer.

The second problem consists in obtaining meaningful and comparable results. When the engine is operated using the ECU, limits such as an operating-point dependent AFR limit are respected. Furthermore, a feedback controller is used to follow the desired load torque, resulting in deviations of up to 3%. Therefore, the engine does not exactly produce the torque desired by the driving cycle. In addition, the optimal solution has to provide the same braking torque during drag phases that results from the current control strategy implemented on the ECU. For these reasons, the effective torque delivered by the engine during a normal run is prescribed during the optimisation. Note that this different torque demand causes the change in the predicted fuel savings as compared to the values provided in the description of Figure 10. During

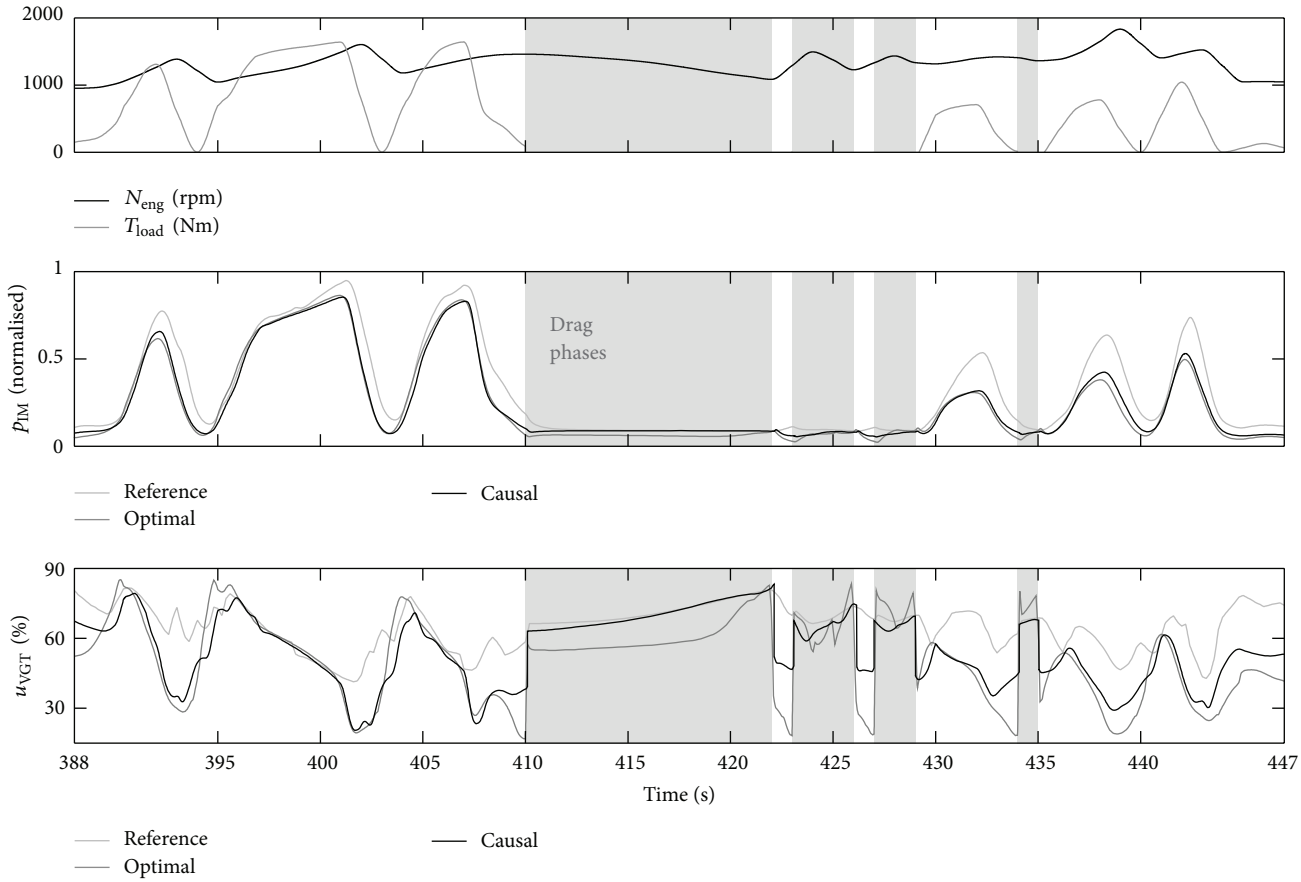

Figure 10: Comparison of the reference (the current ECU calibration), the optimal, and the causal control derived from the optimal solution. Results from a simulation of the model over a segment of test cycle 7 are shown. All three cases produce the same cumulative pollutant emissions. The optimal solution saves 2.21% fuel and the causal one 1.91%. Normalised signals are shown for reasons of confidentiality.

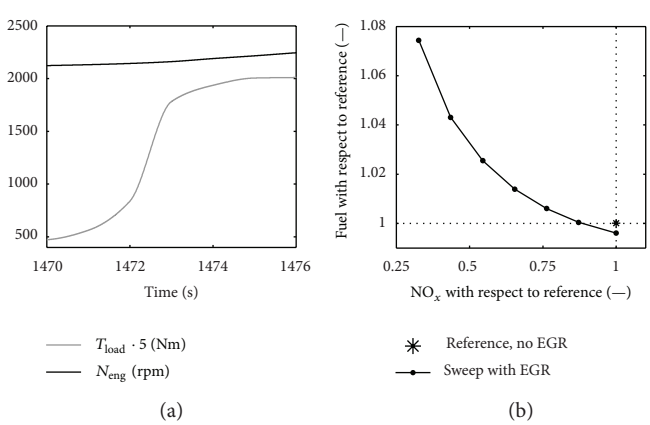

Figure 11: The driving profile of test case 8, scaled for engine B (a), and the optimal fuel-NO_x tradeoff for engine B over this cycle (b).

the validation run, the optimised control inputs are prescribed directly, and no bounds are applied.

Finally, the ECU does not inject exactly the amount of fuel demanded by the corresponding control signal. In fact, the injector maps are identified for a narrow operating region and the ECU estimation becomes increasingly inaccurate for larger deviations of the combustion-related control inputs from the current calibration. Contrarily, the model is identified using data recorded by an accurate external fuel scale. Therefore, the torque produced by the engine deviates from the desired one by up to 7%. To resolve this mismatch, a correction is applied after the first validation run. The fuel injection is updated according to a Willans approximation [1, Section 2.5.1]. The net torque is modelled as a time-variable, affine function of the fuel mass:

$$T_{\text{load}}(t) = \eta_W(t) \cdot m_{\text{fcc}}(t) - T_0\left(N_{\text{eng}}(t), p_{\text{EM}}(t) - p_{\text{IM}}(t)\right). \tag{31}$$

The loss torque T_0 is the sum of the friction, the inertia, and the gas-exchange work. The former two contributions are estimated using the corresponding submodels of the engine model, whereas the latter is estimated from the pressure difference over the engine measured during the first validation run.

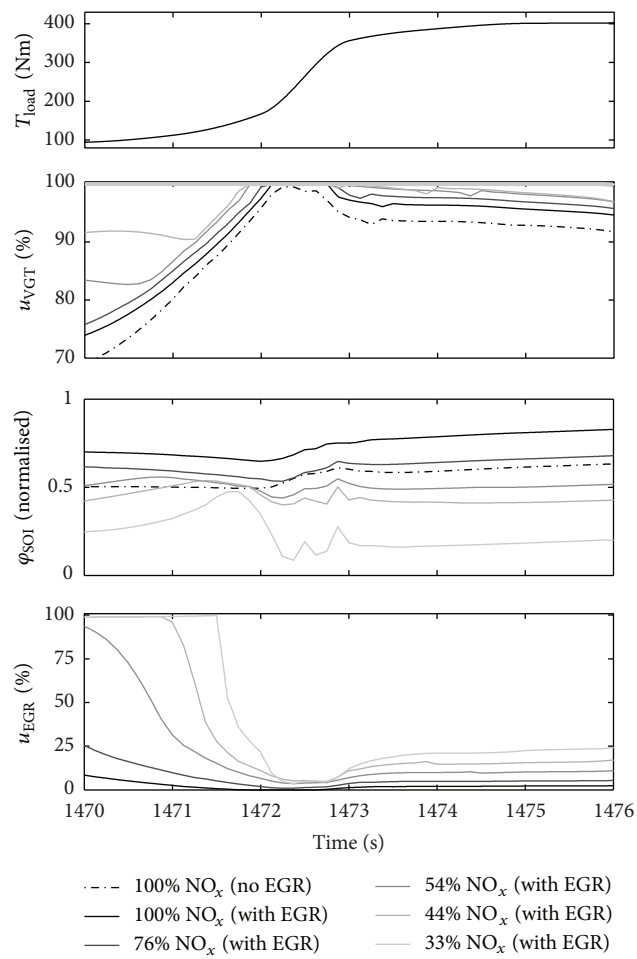

Figure 12: Control-input trajectories for the fuel-NO_x tradeoff depicted in the right-hand plot of Figure 11. The EGR valve is closed at 0%. The exhaust flap remains fully open for all cases and thus is not shown. Normalised signals are shown for reasons of confidentiality. A higher value of φ_{SOI} indicates an earlier injection.

The model is identified using the fuel mass prescribed for the first run, m_{fcc}, and the resulting torque T_{load}. Therefore, the updated fuel injection is calculated by

$$m_{fcc,NEW}(t) = m_{fcc}(t) \cdot \frac{\widehat{T}_{load}(t) - T_0(t)}{T_{load}(t) - T_0(t)}. \tag{32}$$

After the correction, the deviation of the torque produced by the engine from the desired load torque hardly ever exceeds 1%.

3.3.1. Results. For each of the two test cycles 6 and 7, two OCPs were solved. The first one required the emissions to remain at the level of the current engine calibration (I). The second one allowed a prescribed increase of the NO_x emissions (II). This increase is larger for test cycle 6 since for cycle 7 already high brake-specific (BS) NO_x emissions result from the current calibration. By performing this variation, not only the quantitative accuracy of the model is assessed, but also its ability to reproduce the tradeoff between fuel savings and NO_x emissions is evaluated.

Table 4: Results of the experimental validation. The changes relative to the values measured for the current engine calibration are shown.

Test cycle/OCP	6/I	6/II	7/I	7/II
Fuel				
Predicted	−1.28%	−2.85%	−1.52%	−2.49%
Measured	−0.85%	−2.39%	−1.42%	−2.50%
NO_x				
Predicted	0%	25%	0%	10%
Measured	−1.05%	21.27%	−3.64%	8.31%

For test cycle 6, the measurement is repeated 5 times for each set of control inputs to assess the reproducibility of the measurement. The maximum deviation of any of the 5 measurements from the average of all of them is used as a measure. For the BS fuel consumption, this deviation is 0.09%, and for the cumulative BS NO_x emissions, the figure is 0.64%. Based on this high reproducibility, the longer test cycle 7 was only measured once for each set of control-input trajectories.

Table 4 summarises the results from the experimental validation. On test cycle 6, the prediction overestimates the fuel savings but manages to predict the NO_x emissions accurately. An interesting quantity is the factor that describes by how much the NO_x emissions increase for a desired reduction of the fuel consumption:

$$k_{ntf} = -\frac{\Delta m_{NO_x}}{m_{NO_x,ref}} \cdot \frac{m_{fuel,ref}}{\Delta m_{fuel}}. \tag{33}$$

As can be extracted from the data in Table 4, the model predicts a factor of 15.9 when comparing cases I and II. The measured factor is 14.5.

On test cycle 7, the fuel savings are predicted accurately by the model. However, the increase of the NO_x emissions is underestimated. This shift of the model accuracy is due to the fact that the engine is operated in different operating regions on the two cycles. Cycle 6 comprises high-power operating points to the largest extent, whereas cycle 7 prescribes a low-power profile. For cycle 7, the predicted and the measured values of the NO_x-to-fuel factor k_{ntf} are 10.3 and 11.1, respectively.

Figure 13 shows the opacity of the exhaust gas measured for the reference and the two optimal solutions. As predicted by the model, the overall level remains the same and thus no active regeneration of the DPF becomes necessary. Furthermore, most instantaneous peaks are even slightly reduced.

4. Conclusion

A self-contained set of tools and numerical methods for the efficient solution of optimal control problems for diesel engines are presented. This framework enables the calculation of optimal trajectories of the control inputs over long driving profiles. These solutions provide sufficient information to derive complete dynamic engine calibrations. This

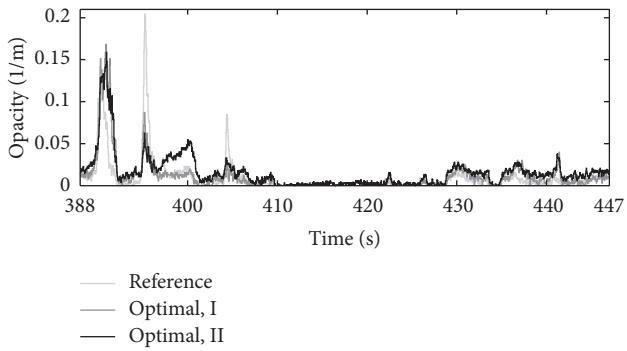

Figure 13: Opacity of the exhaust gas measured for the reference and the two optimal solutions. The same segment of test cycle 7 as in Figure 10 is shown.

fully automated model-based approach is illustrated for an engine without EGR. For an engine with EGR, it is shown how optimal control can be utilised to develop a control strategy that provides an optimal transient fuel-NO_x tradeoff. An experimental validation indicates that these findings accurately transfer to the real engines.

Further work should focus on a more detailed model for the soot emissions and on the analysis of the singular arcs occurring in the optimal solutions. The time-resolved control inputs could be replaced by the parameters of a prescribed control structure in the OCP. The simultaneous nature of the solution process would be preserved, but an optimal controller calibration could be obtained directly. From an engineering point of view, the exhaust-gas aftertreatment system should be included in the model to optimise the interaction between this system and the engine.

Nomenclature

Abbreviations and Indices

AD: Algorithmic differentiation
AFR: Air-to-fuel ratio
ATS: Aftertreatment system
BG: Burnt gas
BS: Brake-specific
BVP: Boundary-value problem
CG: Conjugate gradient
CP: Compressor
cyl: Cylinder
DPF: Diesel particulate filter
ECU: Engine control unit
EF: Exhaust flap
EGR: Exhaust-gas recirculation
EM(C): Exhaust manifold (casing)
eng: Engine
FB, FF: Feedback, feedforward
fcc: Fuel per cylinder and cycle
FFD: Forward finite differences
IC: Intercooler, inequality-constrained
IM(C): Intake manifold (casing)
IP: Interior point
KKT: Karush-Kuhn-Tucker
lin: linear
NLP: Nonlinear program (or programming)
ntf: NO_x-to-fuel
OCP: Optimal control problem
ODE: Ordinary differential equation
opt: Optimal
QN: Quasi-Newton
QP: Quadratic program (or programming)
quad: Quadratic
ref: Reference
SCR: Selective catalytic-reduction system
SOI: Start of injection
SQP: Sequential quadratic programming
TC: Turbocharger
VGT: Variable-geometry turbine
WHTC: World-Harmonized Transient Cycle.

Latin Symbols

A: Area
a, b: Generic model parameters
c: Specific heat, path constraint
$\mathbf{D}$: Differentiation matrix
e: Control error
f: Dynamic model function
F: Objective of a generic NLP
g: Integrand of a cumulative constraint
h: Step size, inequality constraint of a generic NLP
k: Generic model parameter
$L, \mathscr{L}$: Integrand of the objective, Lagrangian
M: Total number of collocation points
m: Mass, number of collocation intervals
n: Number
N: Rotational speed (rpm)
p: Pressure, QP step
R: Gas constant
s: Order of the collocation polynomial
T: Torque, time interval
t: Time
u: Control input
V: Volume
w, W: Quadrature weights
x: State variable, fraction.

Greek Symbols

η: Efficiency
λ: Lagrange multiplier, AFR
ξ: Mass fraction
Π: Pressure ratio
π: Time-varying parameter
τ: Barrier parameter, collocation points
φ: Crank angle
Ψ: Flow function
ω: Rotational speed (rad/s), generic NLP variable.

Conflict of Interests

The authors declare that there is no conflict of interests regarding the publication of this paper.

Acknowledgment

This work was partially funded by the Swiss Innovation Promotion Agency CTI under Grant no. 10808.1 PFIW-IW.

References

[1] L. Guzzella and C. H. Onder, *Introduction to Modeling and Control of Internal Combustion Engine Systems*, Springer, Berlin, Germany, 2nd edition, 2010.

[2] C. Rakopoulos and E. Giakoumis, *Diesel Engine Transient Operation*, Springer, London, UK, 2009.

[3] M. Lindgren and P.-A. Hansson, "Effects of transient conditions on exhaust emissions from two non-road diesel engines," *Biosystems Engineering*, vol. 87, no. 1, pp. 57–66, 2004.

[4] J. R. Hagena, Z. S. Filipi, and D. N. Assanis, "Transient diesel emissions: analysis of engine operation during a tip-in," SAE Technical Paper 2006-01-1151, 2006.

[5] J. F. Cassidy, "A computerized on-line approach to calculating optimum engine calibrations," SAE Technical Paper 770078, 1977.

[6] M. Hafner and R. Isermann, "Multiobjective optimization of feedforward control maps in engine management systems towards low consumption and low emissions," *Transactions of the Institute of Measurement and Control*, vol. 25, no. 1, pp. 57–74, 2003.

[7] C. Atkinson, M. Allain, and H. Zhang, "Using model-based rapid transient calibration to reduce fuel consumption and emissions in diesel engines," SAE Technical Paper 2008-01-1365, 2008.

[8] M. Guerrier and P. Cawsey, "The development of model based methodologies for gasoline IC engine calibration," SAE Technical Paper 2004-01-1466, 2004.

[9] I. Brahma, M. C. Sharp, and T. R. Frazier, "Empirical modeling of transient emissions and transient response for transient optimization," SAE Technical Paper 2009-01-1508, 2009.

[10] E. Alfieri, *Emissions-controlled diesel engine [Ph.D. thesis]*, ETH Zurich, 2009.

[11] A. de Risi, P. Carlucci, T. Donateo, and A. Ficarella, "A combined optimization method for common rail diesel engines," in *American Society of Mechanical Engineers, Internal Combustion Engine Division (Publication) ICE*, vol. 38, pp. 243–250, 2002.

[12] J. Wahlström, L. Eriksson, and L. Nielsen, "Controller tuning based on transient selection and optimization for a diesel engine with EGR and VGT," SAE Technical Paper 2008-01-0985, 2008.

[13] A. A. Malikopoulos, D. N. Assanis, and P. Y. Papalambros, "Real-time self-learning optimization of diesel engine calibration," *Journal of Engineering for Gas Turbines and Power*, vol. 131, no. 2, Article ID 022803, 2009.

[14] H. J. Ferreau, G. Lorini, and M. Diehl, "Fast nonlinear model predictive control of gasoline engines," in *Proceedings of the IEEE International Conference on Control Applications (CCA '06)*, pp. 2754–2759, Munich, Germany, October 2006.

[15] H. J. Ferreau, P. Ortner, P. Langthaler, L. del Re, and M. Diehl, "Predictive control of a real-world Diesel engine using an extended online active set strategy," *Annual Reviews in Control*, vol. 31, no. 2, pp. 293–301, 2007.

[16] L. del Re, P. Ortner, and D. Alberer, "Chances and challenges in automotive predictive control," in *Automotive Model Predictive Control*, chapter 1, pp. 1–22, Springer, Berlin, Germany, 2010.

[17] A. R. Dohner, "Optimal control solution of the automotive emission-constrained minimum fuel problem," *Automatica*, vol. 17, no. 3, pp. 441–458, 1981.

[18] Y. Urano, Y. Nakano, H. Takada, and M. Sugita, "Optimization technique for transient emission reduction of heavy duty diesel engine," SAE Technical Paper 2005-01-1099, 2005.

[19] A. Westlund and H. E. Angström, "Fast physical emission predictions for offline calibration of transient control strategies," SAE Technical Paper 2009-01-1778, 2009.

[20] C. Ericson, B. Westerberg, I. Odenbrand, and R. Egnell, "Characterisation and model based optimization of a complete diesel engine/SCR system," SAE Technical Paper 2009-01-0896, 2009.

[21] M. Benz, M. Hehn, C. H. Onder, and L. Guzzella, "Model-based actuator trajectories optimization for a diesel engine using a direct method," *Journal of Engineering for Gas Turbines and Power*, vol. 133, no. 3, Article ID 032806, 2011.

[22] R. Omran, R. Younes, J. C. Champoussin, D. Fedeli, F. Masson, and N. Guerrassi, "Genetic algorithm for dynamic calibration of engine's actuators," SAE Technical Paper 2007-01-1079, 2007.

[23] R. Omran, R. Younes, and J.-C. Champoussin, "Optimal control of a variable geometry turbocharged diesel engine using neural networks: applications on the ETC test cycle," *IEEE Transactions on Control Systems Technology*, vol. 17, no. 2, pp. 380–393, 2009.

[24] S. Kameswaran and L. T. Biegler, "Simultaneous dynamic optimization strategies: recent advances and challenges," *Computers and Chemical Engineering*, vol. 30, no. 10–12, pp. 1560–1575, 2006.

[25] J. T. Betts, *Practical Methods for Optimal Control and Estimation Using Nonlinear Programming*, vol. 19, Society for Industrial and Applied Mathematics (SIAM), Philadelphia, Pa, USA, 2nd edition, 2010.

[26] L. B. Rall, *Automatic Differentiation: Techniques and Applications*, vol. 120 of *Lecture Notes in Computer Science*, Springer, Berlin, Germany, 1981.

[27] A. Griewank and A. Walter, *Evaluating Derivatives: Principles and Techniques of Algorithmic Differentiation*, Society for Industrial and Applied Mathematics (SIAM), Philadelphia, Pa, USA, 2nd edition, 2008.

[28] C. Quérel, O. Grondin, and C. Letellier, "State of the art and analysis of control oriented NO_x models," SAE Technical Paper 2012-01-0723, 2012.

[29] J. Asprion, O. Chinellato, and L. Guzzella, "A fast and accurate physics-based model for the NO_x emissions of Diesel engines," *Applied Energy*, vol. 103, pp. 221–233, 2013.

[30] E. G. Pariotis, G. M. Kosmadakis, and C. D. Rakopoulos, "Comparative analysis of three simulation models applied on a motored internal combustion engine," *Energy Conversion and Management*, vol. 60, pp. 45–55, 2012.

[31] G. A. Weisser, *Modelling of combustion and nitric oxide formation for medium-speed DI diesel engines: a comparative evaluation of zero- and three-dimensional approaches [Ph.D. thesis]*, ETH Zurich, 2001.

[32] A. Schilling, A. Amstutz, C. H. Onder, and L. Guzzella, "A real-time model for the prediction of the NO_x emissions in DI diesel engines," in *Proceedings of the IEEE International Conference on Control Applications (CCA '06)*, pp. 2042–2047, Munich, Germany, October 2006.

[33] J. Asprion, O. Chinellato, and L. Guzzella, "Optimisation-oriented modelling of the NO_x emissions of a Diesel engine," *Energy Conversion and Management*, vol. 75, pp. 61–73, 2013.

[34] J. Asprion, O. Chinellato, C. H. Onder, and L. Guzzella, "From static to dynamic optimisation of Diesel-engine control," in *Proceedings of the 52nd IEEE Conference on Decision and Control*, Florence, Italy, December 2013.

[35] M. Diehl, H. G. Bock, H. Diedam, and P.-B. Wieber, "Fast direct multiple shooting algorithms for optimal robot control," in *Fast Motions in Biomechanics and Robotics*, M. Diehl and K. Mombaur, Eds., vol. 340 of *Lecture Notes in Control and Information Sciences*, pp. 65–93, Springer, Berlin, Germany, 2006.

[36] J. T. Betts, "Survey of numerical methods for trajectory optimization," *Journal of Guidance, Control, and Dynamics*, vol. 21, no. 2, pp. 193–207, 1998.

[37] A. V. Rao, "A survey of numerical methods for optimal control," *Advances in the Astronautical Sciences*, vol. 135, pp. 497–528, 2009.

[38] B. A. Conway, "A survey of methods available for the numerical optimization of continuous dynamic systems," *Journal of Optimization Theory and Applications*, vol. 152, no. 2, pp. 271–306, 2012.

[39] R. W. H. Sargent, "Optimal control," *Journal of Computational and Applied Mathematics*, vol. 124, no. 1-2, pp. 361–371, 2000.

[40] L. T. Biegler, "An overview of simultaneous strategies for dynamic optimization," *Chemical Engineering and Processing*, vol. 46, no. 11, pp. 1043–1053, 2007.

[41] G. Bashein and M. Enns, "Computation of optimal controls by a method combining quasi-linearization and quadratic programming," *International Journal of Control*, vol. 16, pp. 177–187, 1972.

[42] L. T. Biegler, "Solution of dynamic optimization problems by successive quadratic programming and orthogonal collocation," *Computers and Chemical Engineering*, vol. 8, no. 3-4, pp. 243–247, 1984.

[43] D. Tieu, W. R. Cluett, and A. Penlidis, "A comparison of collocation methods for solving dynamic optimization problems," *Computers and Chemical Engineering*, vol. 19, no. 4, pp. 375–381, 1995.

[44] A. L. Herman and B. A. Conway, "Direct optimization using collocation based on high-order Gauss-Lobatto quadrature rules," *Journal of Guidance, Control, and Dynamics*, vol. 19, no. 3, pp. 592–599, 1996.

[45] D. A. Benson, G. T. Huntington, T. P. Thorvaldsen, and A. V. Rao, "Direct trajectory optimization and costate estimation via an orthogonal collocation method," *Journal of Guidance, Control, and Dynamics*, vol. 29, no. 6, pp. 1435–1440, 2006.

[46] S. Kameswaran and L. T. Biegler, "Convergence rates for direct transcription of optimal control problems using collocation at Radau points," *Computational Optimization and Applications*, vol. 41, no. 1, pp. 81–126, 2008.

[47] D. Garg, M. Patterson, W. W. Hager, A. V. Rao, D. A. Benson, and G. T. Huntington, "A unified framework for the numerical solution of optimal control problems using pseudospectral methods," *Automatica*, vol. 46, no. 11, pp. 1843–1851, 2010.

[48] E. Hairer and G. Wanner, "Stiff differential equations solved by Radau methods," *Journal of Computational and Applied Mathematics*, vol. 111, no. 1-2, pp. 93–111, 1999.

[49] J. C. Butcher, *Numerical Methods for Ordinary Differential Equations*, John Wiley & Sons, Chichester, UK, 2003.

[50] C. L. Darby, W. W. Hager, and A. V. Rao, "Direct trajectory optimization using a variable low-order adaptive pseudospectral method," *Journal of Spacecraft and Rockets*, vol. 48, no. 3, pp. 433–445, 2011.

[51] C. L. Darby, W. W. Hager, and A. V. Rao, "An *hp*-adaptive pseudospectral method for solving optimal control problems," *Optimal Control Applications & Methods*, vol. 32, no. 4, pp. 476–502, 2011.

[52] J. F. Bonnans, J. C. Gilbert, C. Lemaréchal, and C. A. Sagastizábal, *Numerical Optimization: Theoretical and Practical Aspects*, Springer, Berlin, Germany, 2nd edition, 2006.

[53] J. Nocedal and S. J. Wright, *Numerical Optimization*, Springer Series in Operations Research and Financial Engineering, Springer, New York, Second edition, 2006.

[54] D. C. Liu and J. Nocedal, "On the limited memory BFGS method for large scale optimization," *Mathematical Programming*, vol. 45, no. 3, pp. 503–528, 1989.

[55] "The HSL mathematical software library," http://www.hsl.rl.ac.uk.

[56] "MUMPS homepage," http://graal.ens-lyon.fr/MUMPS.

[57] "PARDISO homepage," http://www.pardiso-project.org .

[58] P. E. Gill and E. Wong, "Sequential quadratic programming methods," in *Mixed Integer Nonlinear Programming*, J. Lee and S. Leyffer, Eds., vol. 154 of *The IMA Volumes in Mathematics and Its Applications*, pp. 147–224, Springer, New York, NY, USA, 2012.

[59] P. E. Gill, W. Murray, and M. A. Saunders, "SNOPT: an SQP algorithm for large-scale constrained optimization," *SIAM Review*, vol. 47, no. 1, pp. 99–131, 2005.

[60] A. Wächter and L. T. Biegler, "On the implementation of an interior-point filter line-search algorithm for large-scale nonlinear programming," *Mathematical Programming*, vol. 106, no. 1, pp. 25–57, 2006.

[61] "METIS—serial graph partitioning and fill-reducing matrix ordering," http://glaros.dtc.umn.edu/gkhome/metis/metis/overview.

[62] C. Büskens and D. Wassel, "The ESA NLP solver WORHP," in *Modeling and Optimization in Space Engineering*, G. Fasano and J. D. Pintér, Eds., vol. 73 of *Optimization and Its Applications*, pp. 85–110, Springer, New York, NY, USA, 2013.

[63] R. H. Byrd, J. Nocedal, and R. A. Waltz, "KNITRO: an integrated package for nonlinear optimization," in *Large-Scale Nonlinear Optimization*, vol. 83 of *Nonconvex Optimization and Its Applications*, pp. 35–59, Springer, New York, NY, USA, 2006.

[64] C. Canuto, M. Y. Hussaini, A. Quarteroni, and T. A. Zang, *Spectral Methods: Fundamentals in Single Domains*, Springer, Berlin, Germany, 2006.

[65] J.-P. Berrut and L. N. Trefethen, "Barycentric Lagrange interpolation," *SIAM Review*, vol. 46, no. 3, pp. 501–517, 2004.

[66] M. A. Patterson and A. V. Rao, "Exploiting sparsity in direct collocation pseudospectral methods for solving optimal control problems," *Journal of Spacecraft and Rockets*, vol. 49, pp. 364–377, 2012.

[67] J. R. Cloutier and C. N. D'Souza, "Unification of the direct and indirect approaches to optimal control," AIAA Meeting Papers Archive 481 AIAA-92-4529-CP, 1992.

[68] H. P. Geering, *Optimal Control with Engineering Applications*, Springer, Berlin, Germany, 2007.

[69] A. L. Schwartz, *Theory and implementation of numerical methods based on Runge-Kutta integration for solving optimal control problems [Ph.D. thesis]*, University of California, Berkeley, Calif, USA, 1996.

[70] J. Asprion, C. H. Onder, and L. Guzzella, "Including drag phases in numerical optimal control of Diesel engines," in *Proceedings of the 7th IFAC Symposium on Advances in Automotive Control*, Tokyo, Japan, 2013.

[71] S. Gros, M. Zanon, and M. Diehl, "A relaxation strategy for the optimization of airborne wind energy systems," in *European Control Conference (ECC '13)*, Zurich, Switzerland, 2013.

[72] E. G. Giakoumis and A. I. Alafouzos, "Comparative study of turbocharged diesel engine emissions during three different transient cycles," *International Journal of Energy Research*, vol. 34, no. 11, pp. 1002–1015, 2010.

[73] T. Ott, C. Onder, and L. Guzzella, "Hybrid-electric vehicle with natural gas-diesel engine," *Energies*, vol. 6, pp. 3571–3592, 2013.

[74] C. H. Bischof, H. M. Bücker, A. Vehreschild, and J. Willkomm, *Automatic Differentiation for Matlab (ADiMat)*, MATLAB-Day, Aachen, Germany, 2012.

[75] S. M. Rump, "Verification methods: rigorous results using floating-point arithmetic," *Acta Numerica*, vol. 19, pp. 287–449, 2010.

[76] M. Fink, "Automatic differentiation for Matlab," 2007, http://www.mathworks.com/matlabcentral/fileexchange/15235.

[77] G. Stewart, F. Borrelli, J. Pekar, D. Germann, D. Pachner, and D. Kihas, "Toward a systematic design for turbocharged engine control," in *Automotive Model Predictive Control*, chapter 14, pp. 211–230, Springer, Berlin, Germany, 2010.

[78] M. V. Kothare, P. J. Campo, M. Morari, and C. N. Nett, "A unified framework for the study of anti-windup designs," *Automatica*, vol. 30, no. 12, pp. 1869–1883, 1994.

Hindawi Publishing Corporation
Mathematical Problems in Engineering
Volume 2014, Article ID 965157, 9 pages
http://dx.doi.org/10.1155/2014/965157

Research Article

An Adaptive Metamodel-Based Optimization Approach for Vehicle Suspension System Design

Qinwen Yang,[1] Jin Huang,[2] Gang Wang,[1] and Hamid Reza Karimi[3]

[1] *College of Mechanical and Vehicle Engineering, Hunan University, Changsha, Hunan 410082, China*
[2] *School of Software, Tsinghua University, Beijing 100084, China*
[3] *Department of Engineering, Faculty of Engineering and Science, University of Agder, 4898 Grimstad, Norway*

Correspondence should be addressed to Jin Huang; huangjin@tsinghua.edu.cn

Received 8 October 2013; Accepted 21 November 2013; Published 4 February 2014

Academic Editor: Hui Zhang

The performance index of a suspension system is a function of the maximum and minimum values over the parameter interval. Thus metamodel-based techniques can be used for designing suspension system hardpoints locations. In this study, an adaptive metamodel-based optimization approach is used to find the proper locations of the hardpoints, with the objectives considering the kinematic performance of the suspension. The adaptive optimization method helps to find the optimum locations of the hardpoints efficiently as it may be unachievable through manually adjusting. For each iteration in the process of adaptive optimization, prediction uncertainty is considered and the multiobjective optimization method is applied to optimize all the performance indexes simultaneously. It is shown that the proposed optimization method is effective while being applied in the kinematic performance optimization of a McPherson suspension system.

1. Introduction

The suspension K&C characteristics have directly effects on vehicle handling and riding performances and thus gain much effort and are of great importance in vehicle development. With bush uncertainty and mechanical flexibility, it is very difficult to predict sensitivity of hardpoints locations in the kinematic performance of a suspension system as they are highly nonlinear and coupled [1, 2]. Traditional chassis developing, which benefits from the development of modern virtual prototyping technology, can now do system design effectively through some techniques, like the DOE (design of experiment) technique, as well as other experience-based attempts [3–5]. However, the mechanism of the suspension system is designed by trial and error based on the designer's experiences and intuition, which will be time-consuming in finding a sufficiently good solution since a lot of attempts may be needed in doing virtual prototyping simulations. A featured optimization technique may be useful to give guidance through the design process.

The performance index of a suspension system is a function of the maximum and minimum values over the parameter interval [6, 7]. Thus, it is impossible to apply directly a well-developed optimization algorithm based on gradient information. It can be very difficult to evaluate the analytical design sensitivity of the hardpoints locations because the deviation is defined by using the maximum and minimum values over the parameter interval. Metamodeling techniques, which were initially developed as "surrogates" of the expensive simulation process for improving the overall computation efficiency and quality [8], are useful in such a field. Metamodel-based methods in vehicle design area mainly focused on FEM related problems [9]. Much work has been done in suspension design area, most of which focused on complex structural related area. The authors in [10] studied a mechanical analysis of a suspension optimal design for suspension system based on reliability analyses, taking into consideration tolerances and grafting a reliability analysis that applied the mean-value first order method with tolerance optimization. Choi et al. recently studied

optimal design for automotive suspension systems based on reliability analyses for enhancing kinematics and compliance characteristics; they performed reliability optimization with the single-loop single-variable method by using the results from a deterministic optimization as initial values. The robust design problem was solved with 1700 analyses for 15 design variables and four random constants [11]. Recently, researches on applying metamodel-based optimization techniques to the K&C performance design of vehicle suspension systems were tried and gained reasonable good results. Kang et al. introduced a robust suspension system design approach, which takes into account the kinematic behaviors influenced by bush compliance uncertainty, using a sequential approximation optimization technique. The robust design problem has 18 design variables and 18 random constants with uncertainty [12]. After then, the team proposed a so-called target cascading method for the robust design optimization process of suspension system for improving vehicle dynamic performances [13]. The design target of the system is cascaded from a vehicle level to a suspension system level. The design problem structure of suspension system is defined as a hierarchical multilevel design optimization, and the design problem for each level is solved using the robust design optimization technique based on a metamodel. The researches above opened the way for doing suspension system optimization by using metamodel-based techniques with their effectiveness tested, which motivated us to further research along the direction. However, the former research neither considered optimizing several objectives simultaneously to make them stable in comparable intervals, nor gave the searching guidance for each design parameter in accelerating the convergence of objective parameters.

In this paper, we employ a new adaptive metamodel-based optimization approach for guiding suspension system design in determining appropriate hardpoints locations. The following characteristics distinguish the approach from other metamodel-based applications in suspension system design. (1) As we have several vehicle performance related parameters to be optimized, adaptive weighting factors are used for multiobjective optimization to ensure that all the objectives are optimized simultaneously. (2) For each iteration of the adaptive optimization, both predicted mean value and prediction standard deviation are considered in case of the system converging to the wrong optimum values. (3) We select kriging method as it is more accurate and efficient than other metamodeling methods in solving highly nonlinear problems. (4) The optimization approach provides the possible trends in selecting hardpoints locations for optimizing the system performances. We organize the paper in the following manner. Section 2 introduces the engineering requirements for the optimization problem in suspension system design. Section 3 presents the methodology of adaptive metamodel-based optimization considering modeling uncertainty. The application of adaptive optimization method in suspension system is given in Section 4. Section 5 compares the results of proposed adaptive metamodel-based optimization considering modeling uncertainty and the regular adaptive metamodeling approach. At last, Section 6 summarizes the contents of this research.

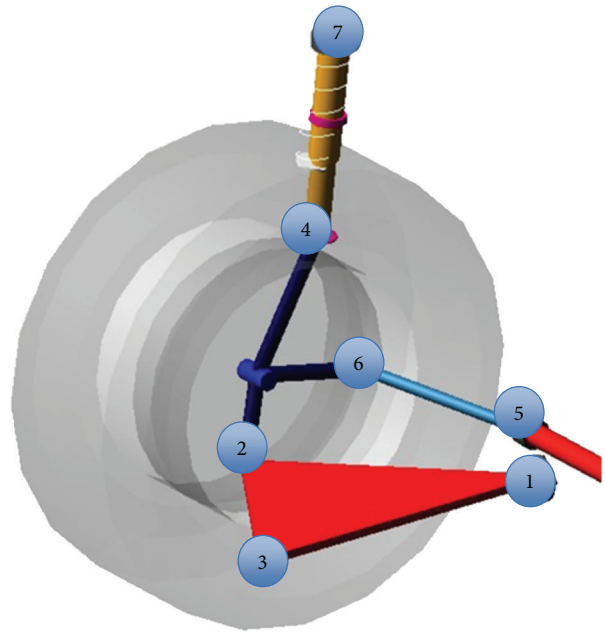

Figure 1: The kinematic structural model of a McPherson suspension system.

2. Optimization Problem in Suspension System

In multibody dynamics point of view, a suspension system can be classified into several groups according to the mechanical joints. In this study, we take McPherson type suspension system in consideration, which is sensitive to the kinematic performance. Figure 1 shows a kinematic structure model of a McPherson suspension system. Major components include the strut, the lower control arm, the tie rod, and the knuckle. Connections between individual components are spherical, revolute, and universal joints, as well as compliance elements such as springs, dampers, and bushings. The design purpose of this study is to determine the locations of the hardpoints according to the system kinematic performances, without considering the elastic deformations of the rigid components except for compliance elements. The commercial software ADAMS, which can easily get the suspension system performance, is employed for modeling and analyzing the suspension system.

The kinematic characteristics of the system include the positions of the fixed points of the suspension system. To achieve optimal solution for suspension system, designing a good kinematic performance is the first step and we thus carry out kinematic optimization of the suspension system in this study. For that purpose, the chosen suspension performance indexes are the deviations in the camber angle, the caster angle, the kingpin incline angle, and the toe angle during the wheel stroke. Camber angle is the angle between the vertical axis of the wheels used for steering and the vertical axis of the vehicle when viewed from the front or rear. It is defined as positive when the top of the wheel moves to the outside. The camber angle alters the handling

qualities of a suspension system; in particular, a negative camber angle improves grip when cornering. Caster angle is the angular displacement from the vertical axis of the suspension of a steered wheel in a vehicle, measured in the longitudinal direction. It is the angle between the pivot line (in a car, an imaginary line that runs through the center of the upper ball joint to the center of the lower ball joint) and vertical line. On most modern designs, the kingpin is set at an angle relative to the true vertical line, which is the kingpin inclination angle, as viewed from the front or back of the vehicle. The angle has an important effect on the steering, making it tend to return to the straight ahead or center position. Toe angle is the symmetric angle that each wheel makes with the longitudinal axis of the vehicle, as a function of static geometry and kinematic and compliant effects. The toe angle change plays an important role in determining the apparent transient oversteer or understeer. Positive toe is the front of the wheel pointing in towards the centerline of the vehicle. Negative toe is the front of the wheel pointing away from the centerline of the vehicle. Large errors will have a negative effect on the behavior of the chassis when braking or accelerating.

In suspension system design, the locations of hardpoints are the most important influencing factors that determine the system kinematic performances. Although engineers obtained some experiences on adjusting the locations of the hardpoints, much effort is still needed on trying different trials. Furthermore, all the geometric parameters of suspension system are coupled, which make finding the influence of the hardpoints locations on the system performances a more tough work, not mentioning there are several objectives to be determined. In this study, while determining the locations of the key hardpoints, we select the important characteristics, that is, the variations of the camber angle, the caster angle, the kingpin incline angle and the toe angle, for the objectives since they are related much to the kinematic performance. An adaptive metamodel-based optimization approach will be proposed in the next section considering modeling uncertainties.

3. Adaptive Metamodel-Based Optimization Method

3.1. Metamodeling Method. In metamodeling, the relationship between a vector of input parameters, $\mathbf{x}$, and an output parameter, Y, can be formulated as

$$Y = \widehat{f}(\mathbf{x}) + \varepsilon, \tag{1}$$

where Y is a random output variable, $\widehat{f}(\cdot)$ is the approximated relationship, and ε is the error of metamodel due to the uncertainty introduced by the metamodeling method. Many different metamodels, such as multivariate polynomial, radial basis function (RBF), and kriging, can be used to build the approximation relationship $\widehat{f}(\cdot)$. In metamodeling, first m sample data $(\mathbf{x}_i, y_i)$ $(i = 1, 2, \ldots, m)$ are collected to build $\widehat{f}(\cdot)$. When an input point $\mathbf{x_0}$ is given, the metamodel can then be used to predict the output Y_0 using

$$Y_0 = \widehat{f}(\mathbf{x}_0). \tag{2}$$

Among various metamodeling schemes, kriging method is often selected due to its high accuracy and efficiency for solving nonlinear problems [14]. Kriging method was originated from the geostatistics community [15] and used by Sacks et al. [16] for modeling computer experiments. Kriging method is based on the assumption that the true system response, Y, can be modeled by

$$Y = \sum_{i=0}^{m} \beta_i f_i(\mathbf{x}) + Z(\mathbf{x}), \tag{3}$$

where $f_i(\cdot)$ is a regression function, β_i is the coefficient for $f_i(\cdot)$, $m+1$ is the number of regression functions, and $Z(\cdot)$ is the stochastic process with zero mean and covariance defined by

$$\operatorname{Cov}\left(\mathbf{Z}(\mathbf{x}_j), \mathbf{Z}(\mathbf{x}_k)\right) = \sigma^2 R_{jk}\left(\boldsymbol{\theta}, \mathbf{x}_j, \mathbf{x}_k\right), \tag{4}$$

where σ^2 is the process variance, $R_{jk}(\cdot)$ is the correlation function, and $\boldsymbol{\theta}$ is a vector with coefficients to be determined.

For ordinary kriging, the linear part of (3) is usually assumed to be a constant, whereas the correlation function $R_{jk}(\boldsymbol{\theta}, \mathbf{x}_j, \mathbf{x}_k)$ is generally formulated as

$$R_{jk}\left(\boldsymbol{\theta}, \mathbf{x}_j, \mathbf{x}_k\right) = \prod_{i=1}^{p} Q\left(\theta_i, x_{ji}, x_{ki}\right), \tag{5}$$

where p is the dimension of $\mathbf{x}$, x_{ji} is the ith component of $\mathbf{x}_j$, x_{ki} is the ith component of $\mathbf{x}_k$, and $Q(\cdot)$ is usually assumed to be Gaussian as

$$\begin{gathered} Q\left(\theta_i, x_{ji}, x_{ki}\right) = \exp\left(-\theta_i d_i^2\right), \\ d_i = \left|x_{ji} - x_{ki}\right|. \end{gathered} \tag{6}$$

The linear predictor of kriging method can be formulated as

$$\widehat{g}(\mathbf{x}) = \mathbf{c}^T(\mathbf{x})\,\mathbf{y}, \tag{7}$$

where $\mathbf{c}^T(\cdot)$ is the coefficient vector and $\mathbf{y}$ is the vector of the observations at the sample sites $(\mathbf{x}_1, \ldots, \mathbf{x}_n)$

$$\mathbf{y} = \left[y(\mathbf{x}_1) \;\cdots\; y(\mathbf{x}_n)\right]^T. \tag{8}$$

Through minimizing the prediction variance σ_t^2:

$$\sigma_t^2 = E\left[\left(\widehat{g}(\mathbf{x}) - Y\right)^2\right] \tag{9}$$

concerning the coefficient vector $\mathbf{c}^T(\mathbf{x})$, the best linear unbiased predictor (BLUP) is solved as [17]

$$\widehat{g}(\mathbf{x}) = \mathbf{r}^T\mathbf{R}^{-1}\mathbf{y} - \left(\mathbf{F}^T\mathbf{R}^{-1}\mathbf{r} - \mathbf{f}\right)^T\left(\mathbf{F}^T\mathbf{R}^{-1}\mathbf{F}\right)^{-1}\left(\mathbf{F}^T\mathbf{R}^{-1}\mathbf{y}\right), \tag{10}$$

where

$$\mathbf{r} = \left[R\left(\boldsymbol{\theta}, \mathbf{x}_1, \mathbf{x}\right) \ \cdots \ R\left(\boldsymbol{\theta}, \mathbf{x}_n, \mathbf{x}\right)\right]^T,$$
$$\mathbf{R} = \begin{bmatrix} R\left(\boldsymbol{\theta}, \mathbf{x}_1, \mathbf{x}_1\right) & \cdots & R\left(\boldsymbol{\theta}, \mathbf{x}_1, \mathbf{x}_n\right) \\ \cdots & \cdots & \cdots \\ R\left(\boldsymbol{\theta}, \mathbf{x}_n, \mathbf{x}_1\right) & \cdots & R\left(\boldsymbol{\theta}, \mathbf{x}_n, \mathbf{x}_n\right) \end{bmatrix},$$
$$\mathbf{F} = \begin{bmatrix} f_0\left(\mathbf{x_1}\right) & \cdots & f_0\left(\mathbf{x_n}\right) \\ \cdots & \cdots & \cdots \\ f_m\left(\mathbf{x_1}\right) & \cdots & f_m\left(\mathbf{x_n}\right) \end{bmatrix}^T, \tag{11}$$
$$\mathbf{f} = \left[f_0\left(\mathbf{x}\right) \ \cdots \ f_m\left(\mathbf{x}\right)\right]^T.$$

The coefficients in $\boldsymbol{\theta}$ can be obtained by using maximum likelihood estimation as [17]

$$\min_{\theta} \psi\left(\boldsymbol{\theta}\right) = \left|\mathbf{R}\right|^{1/n} \sigma^2, \tag{12}$$

where $|\mathbf{R}|$ is the determinant of $\mathbf{R}$ and σ is obtained by generalized least squares fit as [17]

$$\widehat{\sigma}^2 = \frac{1}{n-m-1}\left(\mathbf{y} - \mathbf{F}\boldsymbol{\beta}^*\right)^T \mathbf{R}^{-1}\left(\mathbf{y} - \mathbf{F}\boldsymbol{\beta}^*\right), \tag{13}$$

where $\boldsymbol{\beta}^*$ is the vector with coefficients achieved from generalized least squares fit and is calculated by

$$\boldsymbol{\beta}^* = \left(\mathbf{F}^T\mathbf{R}^{-1}\mathbf{F}\right)^{-1}\mathbf{F}^T\mathbf{R}^{-1}\mathbf{y}. \tag{14}$$

When metamodeling is used for solving specific problems, collection of sample data in specific parameter space, rather than the whole parameter space, is then required to improve the quality and efficiency. This issue is critical when expensive or extensive experiments/simulations are required to collect the sample data. Since the relationship is unknown at the beginning, initial samples are usually collected to build the initial metamodel. This developed metamodel is then used to identify the input parameters that have the best potential to lead to the expected output result. Due to the errors of the metamodel, the actual output obtained from experiment/simulation is usually different from the expected one. The previously obtained metamodel is subsequently updated to improve its quality using the new pair of input-output data. The method to iteratively modify the metamodel through an iterative sampling process is called adaptive metamodeling.

3.2. Adaptive Metamodel-Based Optimization. When adaptive metamodeling is used for optimization, the optimization process can be referred to as adaptive metamodel-based optimization [8]. The detailed algorithm for adaptive metamodel-based optimization is introduced here and we call it adaptive optimization in later parts of the paper. First the m initial samples with input parameters $\mathbf{x}_i$ $(i = 1, 2, \ldots, m)$ and output parameter Y_i $(i = 1, 2, \ldots, m)$ are collected to build the metamodel:

$$Y = f_m\left(\mathbf{x}\right). \tag{15}$$

Based on the metamodel relationship f_m, we can identify the potential input parameters $\mathbf{x}^*$ that lead to the minimum output parameter through optimization:

$$\min_x f_m\left(\mathbf{x}\right). \tag{16}$$

The optimization result of $\mathbf{x}^*$ is then selected as the vector of input parameters for the $(m+1)$th sample $\mathbf{x_{m+1}}$. The output Y_{m+1} corresponding to the $\mathbf{x_{m+1}}$ is subsequently obtained through experiment or simulation. The new pair of data, $(\mathbf{x_{m+1}}, Y_{m+1})$, together with all the previously collected sample data are used to update the metamodel into a new relationship f_{m+1}:

$$Y = f_{m+1}\left(\mathbf{x}\right). \tag{17}$$

The process of identifying the potential optimal input parameters, obtaining the output parameter through experiment/simulation, and updating the metamodel is continued iteratively until the optimization criteria are satisfied.

3.3. Adaptive Optimization considering Modeling Uncertainty. In the process of adaptive optimization, the prediction uncertainty of the developed metamodel would influence the accuracy of the predicted optimum. Minimizing the f_m directly to find the optimal input parameters may not lead to good convergence for output parameters. The dual response surface methodology is a powerful tool for simultaneously optimizing the mean and the variance of responses to tackle the problem of misleading [18]. Lin and Tu [19] gave a dual response surface method using the mean squared error (MSE) approach as follows:

$$\min_x \mathrm{MSE} = \left(\widehat{\omega}_\mu - T\right)^2 + \widehat{\omega}_\sigma^2, \tag{18}$$

where $\widehat{\omega}_\mu$ is the predicted response value, T is the target value, and $\widehat{\omega}_\sigma$ is the prediction standard deviation. Following the format of (18), the objective function for our adaptive optimization can be defined as follows:

$$\min_x \mathrm{MSE} = \left(f_m\left(\mathbf{x}\right) - T\right)^2 + \sigma(\mathbf{x})^2. \tag{19}$$

The optimization result of $\mathbf{x}^*$ is then selected as the vector of input parameters for the $(m+1)$th sample $\mathbf{x_{m+1}}$. The output Y_{m+1} corresponding to the $\mathbf{x_{m+1}}$ is subsequently obtained through experiment or simulation. The new pair of data, $(\mathbf{x_{m+1}}, Y_{m+1})$, together with all the previously collected sample data are used to update the metamodel into a new relationship f_{m+1}, as shown in (17).

We will formulate the specific problem for McPherson suspension system using the adaptive metamodel-based optimization considering prediction uncertainty in the coming section.

4. Adaptive Optimization considering Modeling Uncertainty in McPherson Suspension

To investigate the performance of the designated suspension system, a classic McPherson suspension system is modeled

in ADAMS, as shown in Figure 2. The classic parallel wheel travel suspension system analysis can be employed to do system analysis. Vertical bound and rebound of 50 mm are used. By changing the locations of each hardpoint, the corresponding change of kinematic characteristics can be obtained.

In this study, we take the locations of the 7 key hardpoints labeled in Figure 1 as variables, 3 variables at each hardpoint, that is, the coordinates of the hardpoint along axes x, y and z of the vehicle coordinate. Therefore we have 21 variables (v1–v21) for the designated suspension system. Table 1 listed the 21 variables versus the hardpoint coordinate.

For the kinematic characteristics, as stated in Section 2, we choose the camber angle, the caster angle, the kingpin incline angle, and the toe angle as the objective parameters to be designed and optimized. For McPherson suspension system, small variations of the four estimate angles surely are more acceptable. Thus, we choose the four optimization objectives to be the minimum deviations of the four angles versus wheel travel from rebound −50 mm to bound 50 mm.

We thus have 21 design variables as input parameters and 4 optimum objectives as output parameters. The optimization problem is clearly highly nonlinear and coupled on the input variables. We thus employ the metamodeling method for the optimal design. We clearly have several optimization objectives; the usual way that people deal with multiobjective optimization problems is assigning weighting factors to each objective and then adding them to build a single objective. However, the predefined weighting factors may not be proper for the whole process of optimization. In our work, we only assign the same value to the weighting factors for the output parameters in the initial samples. Adaptive weighting factors are used in the process of adaptive optimization, which is carried out as follows:

$$Y_i = w_1 Y_{1i} + w_2 Y_{2i} + \cdots + w_r Y_{ri} \qquad i = 1, \ldots, m, \tag{20}$$

where r is the number of output parameters and m is number of initial samples. The m initial samples with input parameters $\mathbf{x}_i$ $(i = 1, 2, \ldots, m)$ and output parameter Y_i $(i = 1, 2, \ldots, m)$ are collected to build the metamodel and obtain the new group of input parameters using (19).

The initial metamodel is built on the data generated from Latin hypercube sampling [20], which has the following advantages: (1) its sample mean has a relatively smaller variance compared with simple random sampling, (2) it can be used for generating design points when the number of input variables is large and a great many runs are required, and (3) it is cheap in computing and easy for implementation compared with other more complex sampling methods. By using ADAMS batch processing tools, the initial sets samples can easily be obtained. With the built initial metamodel, the adaptive optimization method introduced in Section 3.3 can be used.

The 4 output parameters corresponding to the new group of input parameters are subsequently obtained through simulations. The weighting factors w_i are adjusted using (21) and the value of Y_{M+1} is calculated using (22). The larger the Y_{iM} is, the larger weighting factor will be assigned to it in order to minimize all the output parameters at the same time. Consider

$$w_i^{M+1} = \frac{|Y_{iM}|}{|Y_{1M}| + |Y_{2M}| + \cdots + |Y_{rM}|} \qquad i = 1, \ldots, r; \quad M = 50, \ldots N-1, \tag{21}$$

where $M+1$ is the number of samples for each iteration in the process of adaptive optimization, and N is the total sample size. Consider

$$Y_{M+1} = w_1^{M+1} Y_{1M} + w_2^{M+1} Y_{1M} + \cdots + w_r^{M+1} Y_{rM}. \tag{22}$$

The new pair of data, $(\mathbf{x_{M+1}}, Y_{M+1})$, together with all the previously collected sample data are used to update the metamodel into a new relationship. The optimization process is stopped when the change of the objective function in several consecutive iterations is less than a predefined value, or the maximum number of iterations is reached.

As there are 4 output parameters as optimizing objectives for our suspension system, (23) is used to transform the multiobjective optimization into single objective optimization.

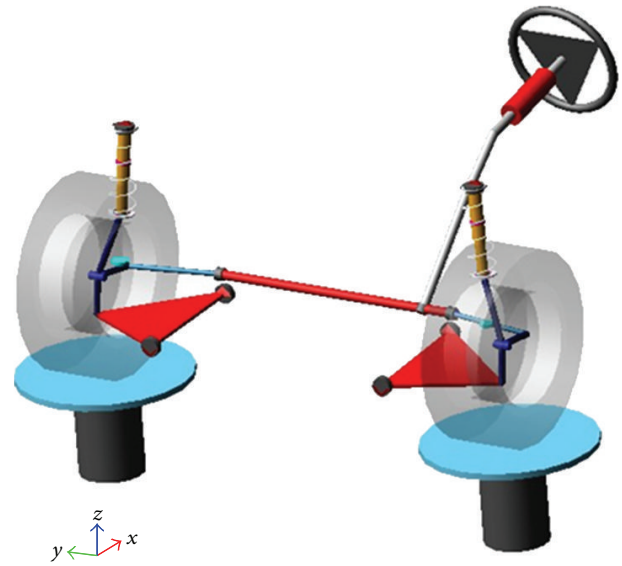

Figure 2: ADAMS model of the McPherson suspension system.

Table 1: The key hardpoints and corresponding variables.

Number	Hardpoint name	Coordinates	Variables
1	LCA_front	x, y, z	$v1, v2, v3$
2	LCA_outer	x, y, z	$v4, v5, v6$
3	LCA_rear	x, y, z	$v7, v8, v9$
4	Struct_lwr	x, y, z	$v10, v11, v12$
5	Tierod_inner	x, y, z	$v13, v14, v15$
6	Tierod_outer	x, y, z	$v16, v17, v18$
7	Top_mount	x, y, z	$v19, v20, v21$

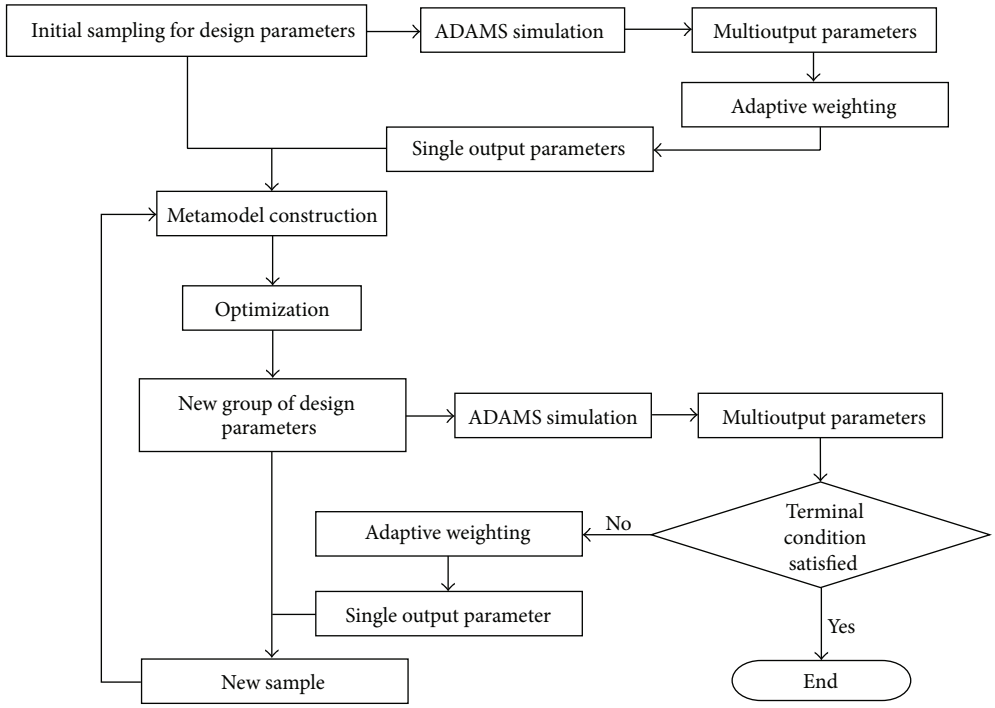

Figure 3: Flowchart of the proposed adaptive multiobjective optimization approach.

The adaptive weighting factors are obtained from (21). The design objective is to minimize Y as in

$$Y = w_1 Y_{\text{camber}} + w_2 Y_{\text{caster}} + w_3 Y_{\text{kingpin}} + w_4 Y_{\text{toe}}. \quad (23)$$

The flowchart for the adaptive optimization process is given in Figure 3.

5. Comparisons and Analysis of the Optimization Results

The number of the initial sample is selected as 50 to build the initial metamodel. 50 initial samples may not be enough for a metamodeling problem with 21 variables; however, due to the cost consideration in engineering design, we just initially choose 50 samples and gradually add new samples during the design process. Based on the initial metamodel, more trails are sampled sequentially and adaptively to approach the optimum value. When the total sample size reaches 100, the values of the output parameters are generally stable. We analyze each of the 4 output parameters individually every time while we update the metamodel. For this high dimensional (21D input) problem, 100 samples may not be enough to reach the optimum value. However, we can evaluate its effectiveness through its convergent trend. The optimization results are shown in Figure 4. The value of the objective function is well converged and the variations of the 4 output parameters are generally stable.

The 4 types of curves with "•", "×", "+", and "o" indicate the camber angle variation, the caster angle variation, the kingpin incline angle variation, and the toe angle variation. The trail distributions from 1 to 50 are obtained from Latin hypercube sampling in the whole design space for building the initial metamodel. From Figure 4, we can see that corresponding to the same design interval (−50, 50), the variation interval for the camber angle, the caster angle, the kingpin incline angle, and the toe angle are (0, 2.5), (0, 4.5), (0, 1.5), and (0, 4.5). While adaptive optimization is applied for the trails from 51 to 100, the variation intervals decrease and the curves become smooth. The adaptive weighting factors help

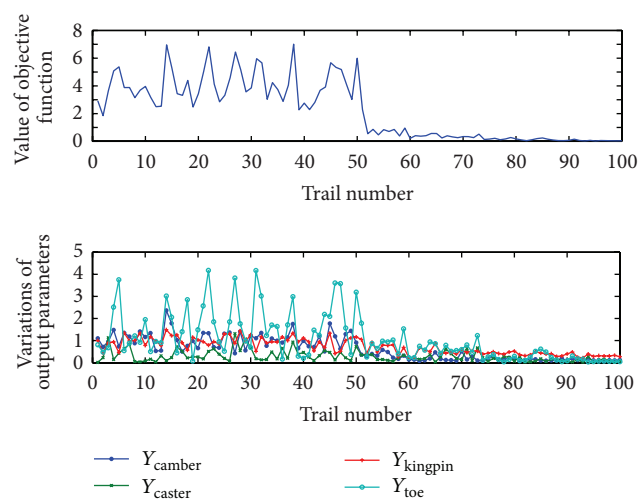

Figure 4: Adaptive optimization results.

Table 2: The initial and optimized hardpoints coordinates.

Variables	Initial	Optimized
$v1, v2, v3$	160, −410, 265	195.7, −381, 234
$v4, v5, v6$	−80, −710, 165	−95, −710.6, 213
$v7, v8, v9$	190, −395, 185	190.6, −366, 166
$v10, v11, v12$	50, −630, 530	64.6, −622, 531.3
$v13, v14, v15$	155, −440, 355	130, −391.2, 305
$v16, v17, v18$	210, −700, 240	219.5, −749, 290
$v19, v20, v21$	7.5, −603.8, 850	35.2, −642, 873.6

the output parameters with different variation intervals converge to the same variation interval (0, 0.33). It can be seen from Figure 4 that our method succeeds in optimizing the 4 output parameters simultaneously while the value of the objective function is well converged. Table 2 listed the initial and the optimized hardpoints locations for the suspension system. We have chosen the 100th sample as the optimized result.

As to the regular adaptive optimization, prediction standard deviation is not considered in the process of the optimization, and the objective function is usually defined as in (16). We used the same 50 initial samples to build the initial metamodel and then apply the objective function given in (16) to search the subsequent 50 samples. We compare the mean output values of the last 5 samples for each of the 4 output parameters from optimization objective functions defined by (19) and (16), as shown in Table 3. The mean output values are compared by a ratio, α, representing how much the adaptive optimization method considering uncertainty is better than the regular adaptive optimization method. Here,

$$\alpha = \frac{\mathrm{Var}_{\mathrm{mean}} - \mathrm{Var}_{\mathrm{mean(un)}}}{\mathrm{Var}_{\mathrm{mean(un)}}}, \tag{24}$$

where $\mathrm{Var}_{\mathrm{mean}}$ indicates the mean output value in the last 5 iterations from regular adaptive optimization method, and $\mathrm{Var}_{\mathrm{mean(un)}}$ gives the mean output value in the last 5 iterations from adaptive optimization method considering the modeling uncertainty.

From Table 3, we could see that the adaptive optimization method with consideration of modeling uncertainty performs better. The adaptive optimization performs better up to 81.11% for all the four output parameters. The reason should be that the number of sample points is far from sufficient to build an accurate metamodel, especially at the very beginning. Thus the optimization result based on the built metamodel only considering predicted mean value may not converge to the right direction. With the prediction standard deviation being considered at the same time, the inaccuracy of the metamodel can be compensated to some extent to approach the right direction.

What is interesting is that the approach can illustrate a suggested trend that the hardpoints should be moved over to. Figure 5 shows the approximate trends that the hardpoints tierod inner and tierod outer stay around during

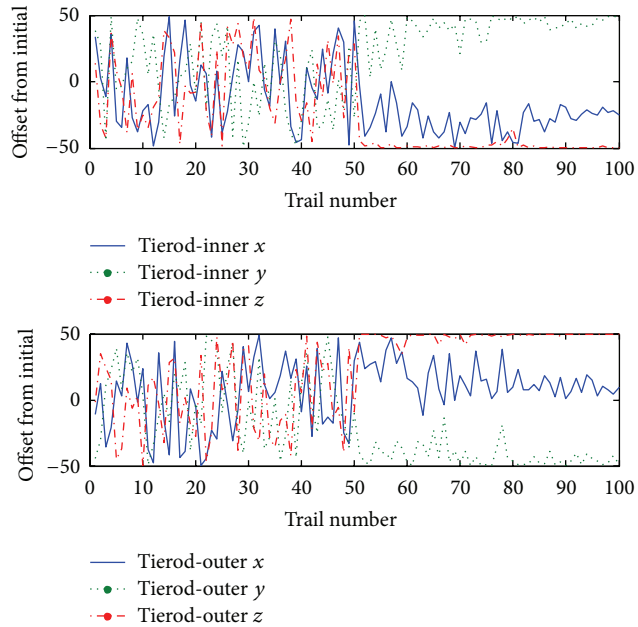

Figure 5: The evolution trend of the hardpoint tierod inner and tierod outer.

the optimization procedure, and other hardpoints perform similarly. From this figure, it can be seen that the 3 coordinate values for each input parameter tend to change in a smaller interval rather than change in the original design interval (−50, 50). This result from our research can help to reduce the design space in the process of adaptive optimization, in order to greatly improve the optimization efficiency, which would be especially significant for higher dimensional problems.

The apparent result that the optimization procedure can achieve is reducing the variation of the design objectives. Figure 6 gives the variations of the camber angle, the caster angle, the kingpin incline angle, and the toe angle, versus the wheel travel for the optimized trail number 100 and the initial trail during the parallel suspension travel analysis. We can see that the optimized data significantly reduced the variation of the camber angle, the kingpin incline angle, and the toe angle, while also slightly reducing the caster angle. This shows the effectiveness of the proposed approach on guiding to search for the optimized solution for kinematic performance design of vehicle suspension systems. Other related parameters can be considered in a similar way.

6. Conclusion

This study introduced adaptive metamodel-based optimization considering modeling uncertainty to optimize the kinematic performance of a McPherson suspension system. The optimization design problem is of 21 input parameters and 4 output parameters. The multioutput optimization in the McPherson suspension system is transformed to a single output optimization problem using adaptive weighting factors.

Table 3: Comparison between adaptive optimization considering modeling uncertainty and regular adaptive optimization.

Optimization objective function	Camber angle variation	Caster angle variation	Kingpin angle variation	Toe angle variation
Adaptive optimization considering modeling uncertainty	0.1056	0.0916	0.3044	0.0577
Regular adaptive optimization	0.1616	0.1585	0.4717	0.1045
α	53.03%	73.03%	54.96%	81.11%

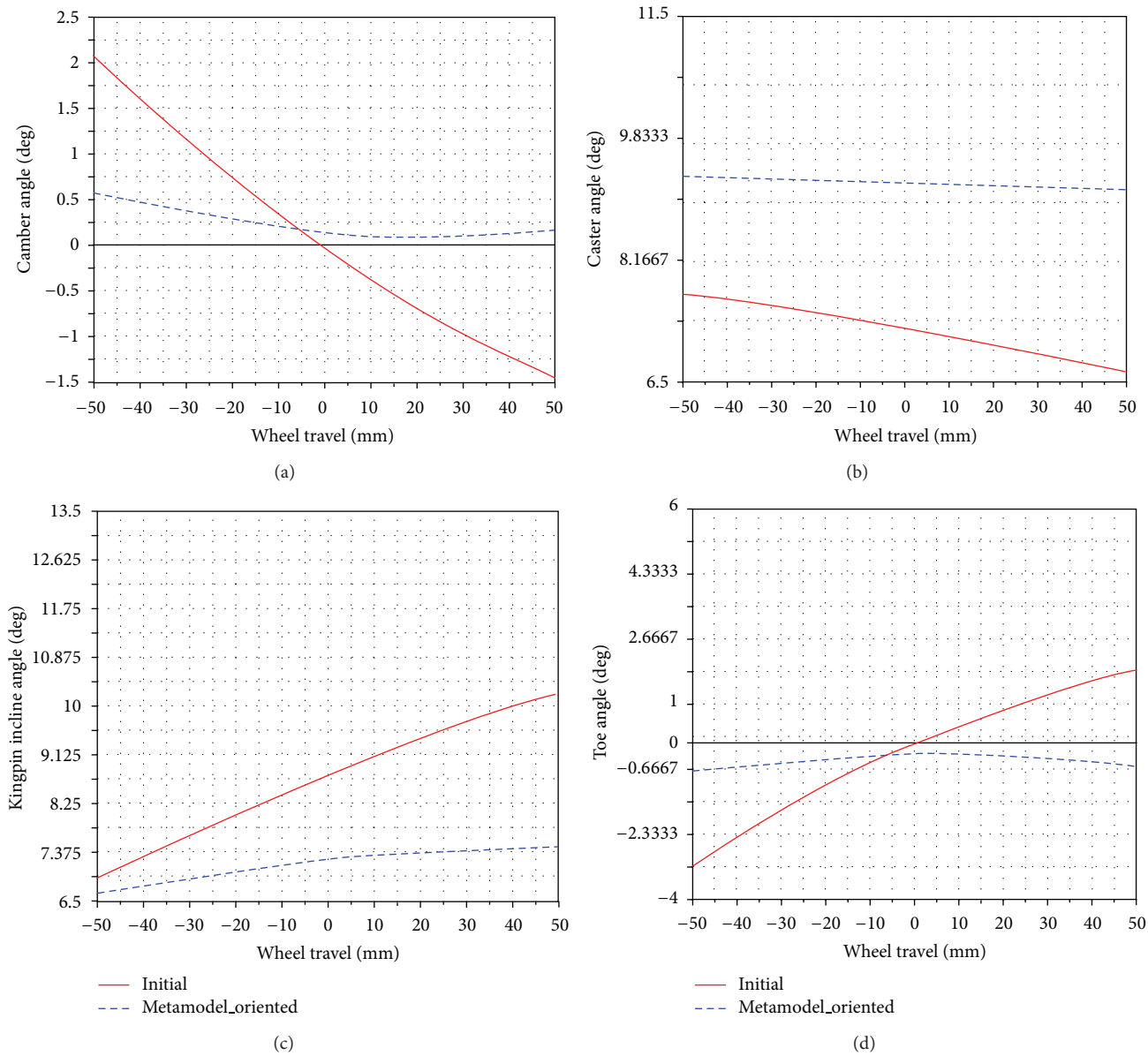

Figure 6: The variation of camber angle, caster angle, kingpin incline angle, and toe angle versus wheel travel before and after the optimization.

50 initial samples and 50 sequential trails are generated to analyze the convergent trend of the objective parameters. It shows that the proposed optimization method provided a set of relatively good results of the 4 output objective parameters simultaneously for the 50 sequential trails. Possible optimal design trends of the hardpoints are given as the trail goes on. Comparisons showed that the adaptive metamodel-based optimization method considering modeling uncertainty worked better than general adaptive metamodel-based optimization for the suspension design problem.

Conflict of Interests

The authors declare that there is no conflict of interests regarding the publication of this paper.

Acknowledgment

This work is supported by NSFC Grant no. 11302074.

References

[1] M. Blundell and D. Harty, *The Multibody Systems Approach to Vehicle Dynamics*, Maple-Vail, Kirkwood, NY, USA, 2004.

[2] M. Zapateiro, F. Pozo, H. R. Karimi, and N. Luo, "Semiactive control methodologies for suspension control with magnetorheological dampers," *IEEE/ASME Transactions on Mechatronics*, vol. 17, no. 2, pp. 370–380, 2012.

[3] H. Li, X. Jing, and H. R. Karimi, "Output-feedback-based H_∞ control for active suspension systems with control delay," *IEEE Transactions on Industrial Electronics*, vol. 61, no. 1, pp. 436–446, 2013.

[4] H. Zhang, Y. Shi, and A. S. Mehr, "Robust H_∞ PID control for multivariable networked control systems with disturbance/noise attenuation," *International Journal of Robust and Nonlinear Control*, vol. 22, no. 2, pp. 183–204, 2012.

[5] R. Wang, H. Zhang, and J. Wang, "Linear parameter-varying controller design for four-wheel independently actuated electric ground vehicles with active steering systems," *IEEE Transactions on Control Systems Technology*, 2013.

[6] Z. Shuai, H. Zhang, J. Wang, and J. Li, "Combined AFS and DYC control of four-wheel-independent-drive electric vehicles over CAN network with time-varying delays," *IEEE Transactions on Vehicular Technology*, 2013.

[7] H. Zhang, J. Wang, and Y. Shi, "Robust H_∞ sliding-mode control for Markovian jump systems subject to intermittent observations and partially known transition probabilities," *Systems & Control Letters*, vol. 62, no. 12, pp. 1114–1124, 2013.

[8] G. G. Wang and S. Shan, "Review of metamodeling techniques in support of engineering design optimization," *Journal of Mechanical Design, Transactions of the ASME*, vol. 129, no. 4, pp. 370–380, 2007.

[9] P. Zhu, Y. Zhang, and G.-L. Chen, "Metamodel-based lightweight design of an automotive front-body structure using robust optimization," *Proceedings of the Institution of Mechanical Engineers D*, vol. 223, no. 9, pp. 1133–1147, 2009.

[10] H. H. Chun, S. J. Kwon, and T. Tak, "Reliability based design optimization of automotive suspension systems," *International Journal of Automotive Technology*, vol. 8, no. 6, pp. 713–722, 2007.

[11] B.-L. Choi, J.-H. Choi, and D.-H. Choi, "Reliability-based design optimization of an automotive suspension system for enhancing kinematic and compliance characteristics," *International Journal of Automotive Technology*, vol. 6, no. 3, pp. 235–242, 2005.

[12] D. O. Kang, S. J. Heo, and M. S. Kim, "Robust design optimization of the McPherson suspension system with consideration of a bush compliance uncertainty," *Proceedings of the Institution of Mechanical Engineers D*, vol. 224, no. 6, pp. 705–716, 2010.

[13] D. O. Kang, S. J. Heo, M. S. Kim, W. C. Choi, and I. H. Kim, "Robust design optimization of suspension system by using target cascading method," *International Journal of Automotive Technology*, vol. 13, no. 1, pp. 109–122, 2012.

[14] D. Zhao and D. Xue, "A comparative study of metamodeling methods considering sample quality merits," *Structural and Multidisciplinary Optimization*, vol. 42, no. 6, pp. 923–938, 2010.

[15] G. Matheron, "Principals of geostatistics," *Economic Geology*, vol. 58, no. 8, pp. 1246–1266, 1963.

[16] J. Sacks, W. J. Welch, T. J. Mitchell, and H. P. Wynn, "Design and analysis of computer experiments," *Statistical Science*, vol. 4, no. 4, pp. 409–435, 1989.

[17] S. N. Lophaven, H. B. Nielsen, and J. Søndergaard, "DACE: A Matlab Kriging Toolbox, Version 2.0," Tech. Rep. IMMREP-2002-12, Technical University of Denmark, Kongens Lyngby, Denmark, 2002.

[18] R. Ding, D. K. J. Lin, and D. Wei, "Dual-response surface optimization: a weighted MSE approach," *Quality Engineering*, vol. 16, no. 3, pp. 377–385, 2004.

[19] D. K. J. Lin and W. Tu, "Dual response surface optimization," *Journal of Quality Technology*, vol. 27, no. 1, pp. 34–39, 1995.

[20] M. D. McKay, R. J. Beckman, and W. J. Conover, "A comparison of three methods for selecting values of input variables in the analysis of output from a computer code," *Technometrics*, vol. 21, no. 2, pp. 239–245, 1979.

Hindawi Publishing Corporation
Mathematical Problems in Engineering
Volume 2014, Article ID 494731, 18 pages
http://dx.doi.org/10.1155/2014/494731

Research Article

Sliding Mode Variable Structure Control and Real-Time Optimization of Dry Dual Clutch Transmission during the Vehicle's Launch

Zhiguo Zhao, Haijun Chen, and Qi Wang

School of Automotive Studies, Tongji University, Shanghai 201804, China

Correspondence should be addressed to Zhiguo Zhao; zhiguozhao@tongji.edu.cn

Received 19 September 2013; Revised 5 November 2013; Accepted 5 November 2013; Published 2 February 2014

Academic Editor: Hui Zhang

In order to reflect driving intention adequately and improve the launch performance of vehicle equipped with five-speed dry dual clutch transmission (DCT), the issue of coordinating control between engine and clutch is researched, which is based on the DCT and prototype car developed independently. Four-degree-of-freedom (DOF) launch dynamics equations are established. Taking advantage of predictive control and genetic algorithm, target tracing curves of engine speed and vehicle velocity are optimally specified. Sliding mode variable structure (SMVS) control strategy is designed to track these curves. The rapid prototyping experiment and test are, respectively, conducted on the DCT test bench and in the chassis dynamometer. Results show that the designed SMVS control strategy not only effectively embodies the driver's intention but also has strong robustness to the vehicle parameter's variations.

1. Introduction

Based on the automated mechanical transmission (AMT), if remodelling its transmission mechanism (including input shaft, positions of gear pairs, and intermediate shaft) and adding a set of dry friction clutch and corresponding actuator, dry dual clutch transmission (DCT) can be constructed. The problem of traction interruption, while gear shifting, can also be resolved effectively through the coordinating control between two clutches and engine. So, the quality of shifting and the power performance of vehicle can also be improved.

As to the launch process of vehicle equipped with dry DCT, single or double clutches can be adopted to launch. Launching with double clutches aims at balancing the sliding friction work of twin clutches and lengthening their service life [1, 2], but dual clutches participation mode can easily lead to power cycling inside the DCT, so its feasibility requires further investigation. By contrast, when single clutch is involved, the launch dynamics model and control logic of DCT are the same as the AMT's, because the launch modelling and controlling of vehicle equipped with AMT have been studied widely and profoundly. Two degree-of-freedom (DOF) dynamics model has been set up and the optimal clutch engaging control law via minimum principle has been founded [3, 4]. Quadratic optimal launch controller has been designed and equivalent damping of AMT transmission has also been taken into account [5, 6]. Six-DOF launch dynamics equations and clutch's hydraulic actuator model have been established. The corresponding model's parameters have been also obtained through experiments [7]. Five-DOF launch model has been established and simplified, and engine speed decoupling control strategy has also been put forward [8]. In addition, fuzzy logic control method for the launching process of AMT based on experience has been studied largely and fuzzy input variables could be the accelerator pedal opening and its changing rate [9], or the deviation and its changing rate between engine speed and target speed related to accelerator pedal [10], or the rotary speed difference between clutch driving plate and driven plate [11]. Generally, output variables could be clutch engaging speed; genetic algorithm has been further used to optimize the fuzzy rule set [12]. Moreover, in the aspect of launch control for vehicle

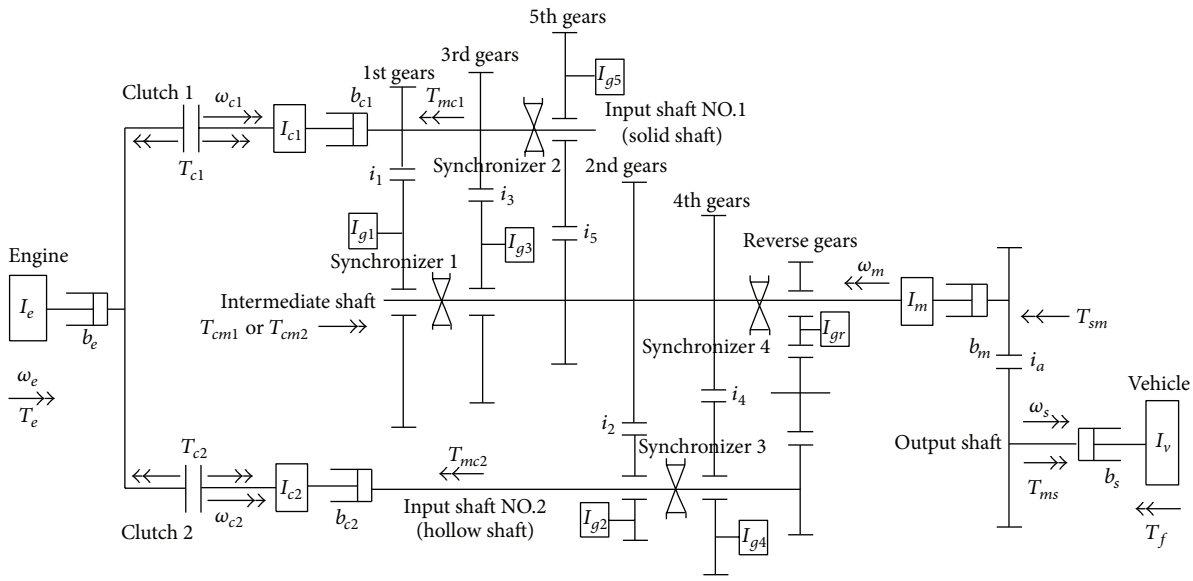

Figure 1: Five-speed dry DCT dynamic model.

equipped with DCT, clutch optimal engaging control law has been introduced by utilizing minimum principle and synthetically taking shock intensity, sliding friction work, and engine output torque into consideration [13]. Linear quadratic optimal control has been applied to simulate clutch engaging pressure in the launching process [14, 15]. Launch fuzzy intelligent control algorithm has been designed and optimized by using accelerator pedal opening and its changing rate, clutch relative slip rate and engine speed difference to describe the driving intention, clutch engaging states and engine working condition, respectively [16]. Comparatively, double-layer fuzzy intelligent control architecture has been presented by setting up clutch engaging fuzzy control rules and real car chassis dynamometer test has been conducted [17].

But the above stated studies only focus on the control of clutch engaging control rules, rarely taking consideration of the issue of coordinating control between engine and clutch during the vehicle's launch process and let alone the qualification of driver's intention.

Taking the factors such as driver's intention, engine condition, clutch state, and shock intensity into account, the issue of coordinating control between engine and clutch is investigated in the paper, which is based on the DCT and prototype car developed independently. Four degrees of freedom (DOF) launch dynamics equations are established. The computational formulas of engine speed and clutch transfer torque in the launching process have also been quantified and given. Taking advantage of predictive control and genetic algorithm, target tracing curves of engine speed and vehicle velocity are optimally specified. Sliding mode variable structure (SMVS) control strategy has been designed to track these curves. Based on the Matlab/Simulink software platform and the hardware-in-the-loop test bench, the launch performance of prototype car equipped with dry DCT has been simulated under different driving conditions, and the rapid prototyping experiment and test are, respectively, conducted on the DCT test bench and in the chassis dynamometer.

2. Mathematical Models

2.1. Five-Speed Dry DCT Dynamic Model. The five-speed dry DCT described in the paper is made up of dry dual clutch module and its actuator, four synchronizers and their actuators, and single intermediate shaft gear transmission mechanism. In order to study the dynamic characteristic of single clutch in the launching process and develop relevant coordinating control strategy, the following assumptions should be made before modeling (1) Both wheels' moment of inertia and vehicle's translation quality are converted into the transmission output shaft. The engine output shaft and the input shaft, intermediate shaft, and output shaft of transmission are regarded as rigid body with distributed parameters and concentrated inertia, and the friction damping loss is considered, respectively (2) The dynamic process of the clutch actuator and the synchronizers, as well as the heat fade of the clutch are not the focus of this paper. (3) Neglect the elasticity between bearing and its block, as well as the elasticity and gap in gear engagement. Finally the established dynamic model of five-speed dry DCT after simplification is shown in Figure 1.

In Figure 1, parameters and variables are defined as follows:

I_e: equivalent moment of inertia of engine crankshaft (including flywheel) and clutch driving plate;

I_{c1}: Equivalent moment of inertia of clutch 1 driven plate, transmission NO.1 input shaft (solid part), and relevant odd number gears;

I_{c2}: equivalent moment of inertia of clutch 2 driven plate, transmission NO.2 input shaft (hollow part) and its relevant even number speed gears;

I_m: equivalent moment of inertia of transmission intermediate shaft, its relevant gears, and final drive driving part;

I_s: equivalent moment of inertia of final drive driven part, differential gears, axle shafts, wheels, and complete vehicle, which are equally converted into transmission output shaft;

I_{g1}, I_{g3}, I_{gr}: moment of inertia of 1st, 3rd, and reverse driven gears;

I_{g2}, I_{g4}, I_{g5}: moment of inertia of 2nd, 4th, and 5th driving gears;

$i_1 \sim i_5, i_a$: forward gear ratios and final drive ratio;

b_e: rotating viscous damping coefficient of engine output shaft;

b_{c1}: rotating viscous damping coefficient of transmission NO.1 input shaft;

b_{c2}: rotating viscous damping coefficient of transmission NO.2 input shaft;

b_m: rotating viscous damping coefficient of transmission intermediate shaft;

b_s: equivalent rotating viscous damping coefficient of axle shafts and wheels, which are equally converted into transmission output shaft;

ω_e: angular speed of engine crankshaft;

ω_{c1}: angular speed of clutch 1 driven plate (or transmission NO.1 input shaft);

ω_{c2}: angular speed of clutch 2 driven plate (or transmission NO.2 input shaft);

ω_m: angular speed of transmission intermediate shaft;

ω_s: angular speed of transmission output shaft;

T_e: engine output torque;

T_{c1}, T_{c2}: transfer torque of clutch 1 and clutch 2;

T_{cm1}, T_{cm2}: torque of NO.1 and NO.2 input shafts acting on intermediate shaft;

T_{mc1}, T_{mc2}: torque of intermediate shaft reacting on NO.1 and NO.2 input shafts;

T_f: driving resistance torque which is equally converted into transmission output shaft.

2.2. Dynamics Equations for Five-Speed Dry DCT. DCT can use 1st speed gear or 2nd speed gear to start. Take 1st speed gear launch for example. Assuming that the engine is already operating in idle state, the synchronizer 1 firstly engages to the left gear (1st gear). Because the synchronizer engaging process does not belong to the research focus in this paper, the detailed analysis of synchronizer is neglected. After the engagement of synchronizer, the clutch 1 begins to engage to transmit the torque from the engine side until the end of launching process. During the launch process, clutch 1 gets through four phases.

Free Stroke Eliminating. It is to eliminate the vacant distance between the clutch driving and driven plates.

Slipping Friction before Half-Engaging. The clutch begins to engage but the transmitted torque cannot overcome the vehicle resistance to move the vehicle.

Sliding Friction after Half-Engaging. The clutch is further engaged and the torque transmitted by clutch is able to force the vehicle to move.

Full-Engaging after Synchronizing. The engaging process and the launching process finish.

The first two phases have a small effect on the launching quality and therefore the main research attention is focused in the last two phases, especially the third phase.

The four-DOF dynamics equations on the phase of slipping friction after half-engaging can be expressed as follows:

$$\begin{aligned} I_e\dot{\omega}_e &= T_e - T_{c1} - b_e\omega_e, \\ I_{c1}\dot{\omega}_{c1} &= T_{c1} - T_{mc1} - b_{c1}\omega_{c1}, \\ \left(I_m + I_{g1} + I_{g2}i_2^2\eta + I_{g4}i_4^2\eta + I_{g5}i_5^2\eta\right)\dot{\omega}_m &= T_{c1m} - T_{sm} - b_m\omega_m, \\ I_s\dot{\omega}_s &= T_{ms} - T_f - b_s\omega_s, \end{aligned} \tag{1}$$

where $T_e = f(\alpha, \omega_e), T_{cm1} = T_{mc1}i_1\eta, T_{ms} = T_{sm}i_a\eta, v = \omega_s R_W$

$$T_{c1} = \begin{cases} \dfrac{2}{3}\left(\dfrac{R_0^3 - R_1^3}{R_0^2 - R_1^2}\right)\mu_1 F(x_1) & \omega_{c1} \le \omega_e, \\ T_{c1}^L & \omega_{c1} = \omega_e, \end{cases} \tag{2}$$

$$T_f = \left(\frac{C_d A}{21.15}v^2 + mg\sin\theta + mg\cos\theta f + \delta m\frac{dv}{dt}\right)R_W, \tag{3}$$

$$\delta = 1 + \frac{1}{m}\frac{I_{c1}i_1^2 i_a^2 + I_m i_a^2 + I_s + I_v}{R_W}. \tag{4}$$

Among above formulas, α is engine throttle opening. $f(\alpha, \omega_e)$ denotes nonlinear function of engine output torque. η is transmitting efficiency of transmission shafts as well as final drive. μ_1 is kinetic friction coefficient among friction plates of clutch 1. R_0, R_1 are internal and external radius of friction plates of clutch 1. x_1 is opening of clutch 1. $F(x_1)$ denotes positive pressure function of pressure plate of clutch 1. T_{c1}^L is transfer torque after full-engaging of clutch. m is vehicle mass. g is gravity acceleration. f is rolling resistance coefficient. v is vehicle velocity. C_d is wind drag coefficient. A is windward area. θ is road slope. δ is conversion coefficient of rotating mass. R_W is radius of wheel.

For the sake of easily designing the controller, further assumptions about motional relationship among the input, intermediate, and output shafts of transmission should meet the equations $\omega_s i_a i_1 = \omega_m i_1 = \omega_{c1}$. Then the DCT dynamic model in Figure 1 can be simplified as that in Figure 2.

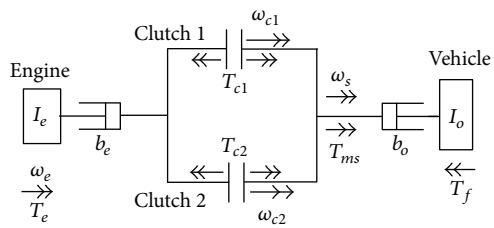

Figure 2: DCT dynamics model after simplification.

Simplify formula (1), and then some two-DOF dynamics equations are obtained:

$$\begin{aligned} I_e\dot{\omega}_e + b_e\omega_e &= T_e - T_{c1}, \\ I_o\dot{\omega}_s + b_o\omega_s &= T_{c1}i_e - T_f, \end{aligned} \tag{5}$$

where parameters are defined as follows:

$$\begin{aligned} i_e &= i_a i_1 \eta^2 \\ I_o &= I_s + \left(I_m + I_{g1}\right) i_a^2\eta + I_{c1}i_1^2 i_a^2\eta^2 + I_{g2}i_2^2 i_a^2\eta^2 \\ &\quad + I_{g4}i_4^2 i_a^2\eta^2 + I_{g5}i_5^2 i_a^2\eta^2, \\ b_o &= b_s + b_m i_a^2\eta + b_{c1}i_1^2 i_a^2\eta^2. \end{aligned} \tag{6}$$

When the clutch is fully engaged, $T_{c1} = T_{c1}^L$. He clutch transmitted torque T_{c1} is only determined by engine output torque and driving resistance, which satisfies:

$$T_{c1} = \frac{I_o\left(T_e - b_e\omega_e\right) + \left(T_f + b_o\omega_s\right) I_e i_1 i_a}{I_o + I_e i_e i_1 i_a}. \tag{7}$$

When the clutch is fully engages, the vehicle is launched in certain gear. In this sense, formula (5) can still be further simplified as a single-DOF dynamics equation:

$$I_d\dot{\omega}_s + b_d\omega_s = T_e i_e - T_f, \tag{8}$$

where

$$\begin{aligned} I_d &= I_s + \left(I_m + I_{g1}\right) i_a^2\eta + \left(I_{c1} + I_e\right) i_1^2 i_a^2\eta^2 \\ &\quad + I_{g2}i_2^2 i_a^2\eta^2 + I_{g4}i_4^2 i_a^2\eta^2 + I_{g5}i_5^2 i_a^2\eta^2, \\ b_d &= b_s + b_m i_a^2\eta + \left(b_{c1} + b_e\right) i_1^2 i_a^2\eta^2. \end{aligned} \tag{9}$$

Synthesizing formulas (5) and (8), the DCT launch dynamic model after eliminating the null distance of clutch can be seen as a hybrid model, namely including a two-DOF sliding friction model and a single-DOF stably operated model. The switching condition between the two models is $\omega_e = \omega_{c1}$. The controller will be designed on the basis of this hybrid model in the following.

3. Coordinating Control and Real-Time Optimization for Dry DCT

3.1. Launch Control Objectives. The control objectives of dry DCT in the launching process are as follows:

(1) reflect the driver's intention adequately to let the driver have different driving feel according to accelerator pedal opening and its changing rate;

(2) under the condition of meeting the requirements of shock intensity and sliding friction work, to decrease the slipping friction work as much as possible and guarantee the launch comfort (shock intensity is 10 m/s^3 in German standard [18]);

(3) take the effect of launching on engine's working state into account to avoid the flameout of the engine in the launching process.

3.2. Launch Controller Design Architecture. A layered architecture of launching control is used as shown in Figure 3. The upper layer controller is applied to determine the optimal clutch transfer torque and engine target speed (or torque), while the lower one is used to implement a servocontrol of clutch torque and a closed-loop control of engine torque (or speed). The upper controller can further be divided into two parts according to the activation order: the sliding control before the speed synchronization and engaging control after the speed synchronization. The sliding control is aiming at the sliding friction after half-engaging phase and also the core of the launching control. Based on the two-DOF model during the sliding phase, the driving intention, the closed-loop control of engine speed and clutch torque, and can be realized. Relatively, based on the single-DOF model, the engaging control is for the full-engaging after synchronizing phase and to make the clutch engage completely as quickly as possible and prevent engaged clutch plates from falling into sliding state again due to the change of engine output torque. Meanwhile, engine output torque is adjusted to match the demand torque. Even though the driving and driven plates are already synchronized, the launch controller does not send out an accomplishment signal. Only if the engine output torque is equal to the demand torque, it sends out the signal.

3.3. Launch Sliding Friction Process Control. The inputs of launch slipping friction process control include accelerator pedal opening, engine speed, wheel speed, and so forth. The outputs contain Clutch 1 target engaging pressure and engine demand torque. They would be realized through the sliding mode variable structure tracing control algorithm.

(1) Determine target control variables. The target control variables include engine target speed and vehicle target shock intensity. The engine target speed should be proportional to the accelerator pedal opening and its changing rate in order to partially reflect the driver's intention. Taking engine target speed and vehicle target shock intensity as measuring index of driver's intention, the DCT launch controller can be designed without considering the concrete physical characteristics of clutch actuators, thus improving the generality of launch controller.

(2) Target tracing controller design. Based on simplified models of engine and transmission, sliding mode variable

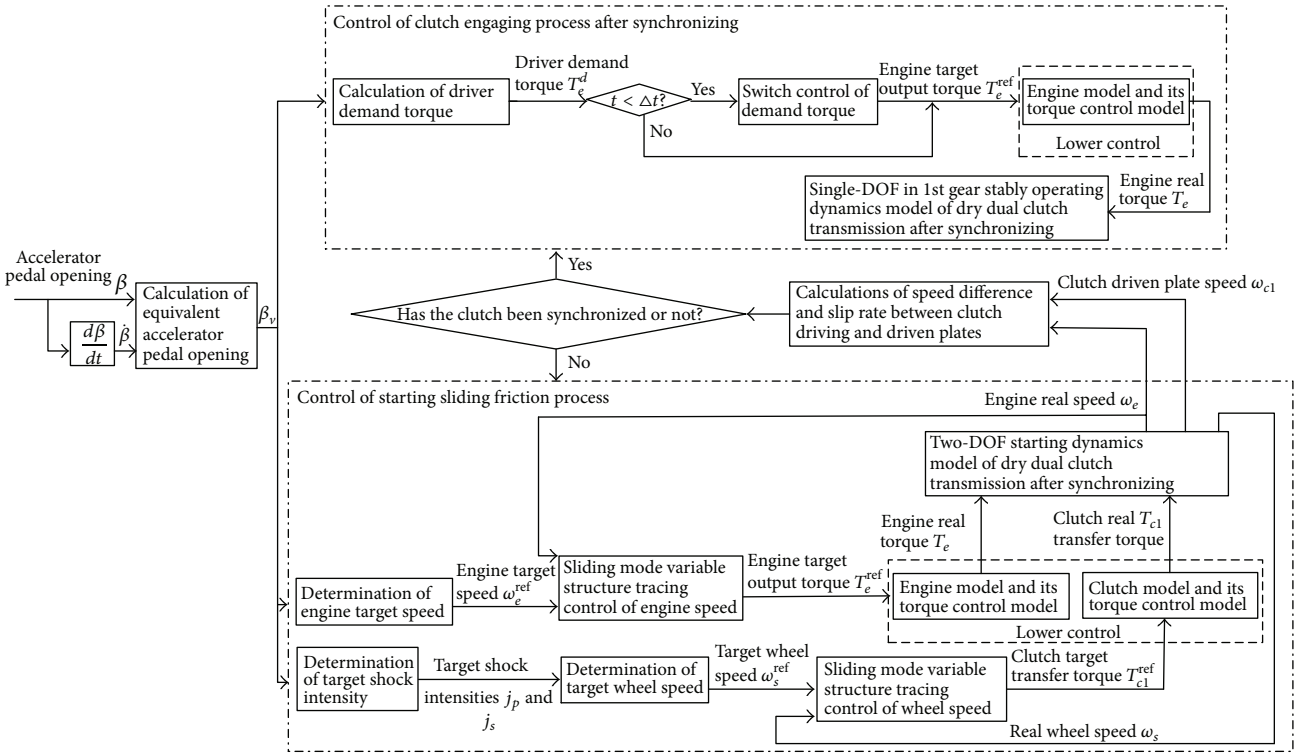

Figure 3: Design architecture of launch controller.

structure controller is designed to track engine target speed and vehicle target shock intensity.

3.3.1. Determining Method of Engine Target Speed. The principles of determining engine target speed are as follows.

(1) In order to avoid the stalling of engine and attrition of clutch due to overhigh speed, the target speed is not less than the engine idle speed (set as 800 r/min) and is limited to a maximum value (set as 2000 r/min) as well.

(2) Within optional limits of target speed, on one hand, the target speed changes along with the variation of accelerator pedal opening and its changing rate, and it can ensure that engine has enough output power to meet the launch demands under different conditions. On the other hand, the selected target speed can make the engine work in an economic area.

(3) When the difference between engine real speed and clutch driven plate speed is more than the setting threshold value $\Delta\omega$ and the clutch sliding friction time is less than the time variable t_p, the engine target speed will coordinate with the accelerator pedal opening and its changing rate. If the condition is reverse, the target speed will be fixed as synchronous speed $\omega_e(t_s)$, namely, the speed when engine and clutch driven plate are at the moment of synchronizing. The calculation of engine target speed ω_e^{ref} is shown in Figure 4 and Formula (10). The engine output characteristic can be seen in Figure 15. Consider

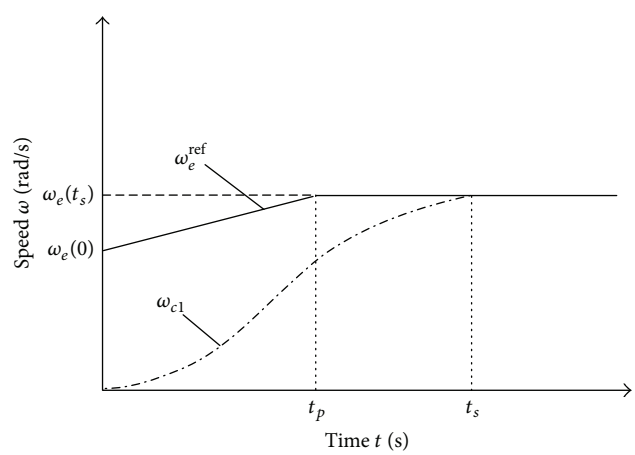

Figure 4: Determination of engine target speed.

$$\omega_e^{ref} = \begin{cases} \dfrac{\omega_e(t_s) - \omega_e(0)}{t_p} t + \omega_e(0) & (\omega_e - \omega_{c1}) \geq \Delta\omega,\ t < t_p, \\ \omega_e(t_s) & \text{other}, \end{cases} \quad (10)$$

where $\omega_e(t_s)$ and $\omega_e(0)$, respectively, denote engine target speed postsynchronizing and idle speed. t_p is linearly increasing time of engine speed. t_s is time elapsed until clutch driving

Table 1: Engine synchronous target speed.

Equivalent accelerator pedal opening β_v/%	Engine synchronous target speed $\omega_e(t_s)$/(r/min)
0~10	1000
10~20	1000
20~30	1100
30~40	1200
40~50	1300
50~60	1400
60~70	1500
70~80	1600
80~90	1700
90~100	2000

and driven plates are synchronized. $\Delta\omega$ is set threshold value of the difference between clutch driving and driven plates.

In order to reflect the driver's intention easily and determine $\omega_e(t_s)$, equivalent accelerator pedal opening β_v is introduced to synthesize the information of accelerator pedal opening and its changing rate. The relationship between β_v and $\omega_e(t_s)$ is shown in Table 1.

Consider

$$\beta_v(t) = \beta(t) + k\dot{\beta}(t), \tag{11}$$

where $\beta(t)$ is real value of accelerator pedal opening. $\dot{\beta}(t)$ is changing rate of accelerator pedal opening. k is weight index and must be determined according to the practice to guarantee the $\beta_t(t)$ falling into the scope of [0–100].

3.3.2. Determining Method of Target Shock Intensity in the Launching Process. The launch target shock intensity not only reflects the driver's intention, but also guarantees that the intensity is in a reasonable extent. The friction process is divided into three parts in [19], which qualitatively elaborated control key points when a vehicle was launched and its clutch driving and driven plates were synchronizing. In [20], the shock intensity while the clutch driving and driven plates were synchronizing is derived, which showed that it is proportional to the difference between engine acceleration and acceleration of clutch driven plate at the instant of presynchronization. That is

$$\dot{\omega}_c(+) - \dot{\omega}_c(-) = \frac{I_e}{I_e + I_{ca}}\left[\dot{\omega}_e(-) - \dot{\omega}_c(-)\right], \tag{12}$$

where $\dot{\omega}_c(-)$, $\dot{\omega}_c(+)$ denote accelerations of clutch driven plate at the instant of presynchronization and post- synchronization. $\dot{\omega}_e(-)$ is engine acceleration at the instant of presynchronization. I_{ca} is moment of inertia of complete vehicle and its transmission system, which are equally converted to clutch driven plate.

Suppose that the transmission system is rigid; namely, $\ddot{v} = \ddot{\omega}_s R_W = \ddot{\omega}_c i_1 i_a R_W$. The shock intensity of vehicle can be equally converted into the shock intensity of clutch driven plate. Consider Formula (12). If the difference between engine acceleration and acceleration of clutch driven plate is zero, the shock intensity will be zero at the moment of synchronizing. The condition is called no-impact synchronizing condition. As the engine target speed is determined in preceding passage, namely, the rotary speed difference is less than the threshold value $\Delta\omega$ or the elapsed time of sliding friction process is more than the time variable t_p, the engine speed remains constant as the same as synchronous target speed. So the engine acceleration is zero. For the sake of no-impact at the moment of synchronizing, the speed of clutch driven plate should be equal to the target speed and its acceleration should be zero.

Table 2: Driver's intention.

Launch mode	Slow	Moderate	Abrupt
Equivalent accelerator pedal opening β_v/%	0~20	20~50	50~100
Target shock intensity j_p/(m/s^3)	0.5	1.5	2.5

The authors divide the launch sliding friction process into three phases, determine the target shock intensity in different phases, and obtain related target vehicle acceleration and target vehicle velocity via integral. It is shown in Figure 5.

Phase One. During the time slot $0 \sim t_p$, the target shock intensity j_p is positive. It changes along with the equivalent acceleration, which reflects the driver's intention. As the particularity of creeping launch,that is, the clutch driving and driven plates should maintain slipping state during the whole launching process without considering their speed synchronization. In view of this, creeping launch is out of consideration in this paper. Therefore, on the basis of equivalent accelerator pedal opening and engine output torque capacity, driver's intention is divided into three categories [3, 6], which is shown in Table 2.

Phase Two. During the time slot $t_p \sim t_s$, the target shock intensity j_p is negative. The main goal is to lower the vehicle acceleration, so that the speed and acceleration of clutch driven plate stay the same as the engine's at the moment of synchronizing in order to realize no-impact synchronizing. The values are synchronous target speed and zero, respectively. Theoretically, different values are selected according to different target shock intensity in Phase One. However, considering that clutch driving plate and its driven plate are approaching to synchronize, the target shock intensity j_s is set as a constant value in order to accelerate the engaging speed and decrease the total sliding friction work in the launching process. Equations can be established as follows:

$$\begin{gathered} j_p t_p + j_s\left(t_s - t_p\right) = 0, \\ 0.5 j_p t_p^2 + j_p t_p\left(t_s - t_p\right) + 0.5 j_s\left(t_s - t_p\right)^2 = \omega\left(t_s\right) R_W, \end{gathered} \tag{13}$$

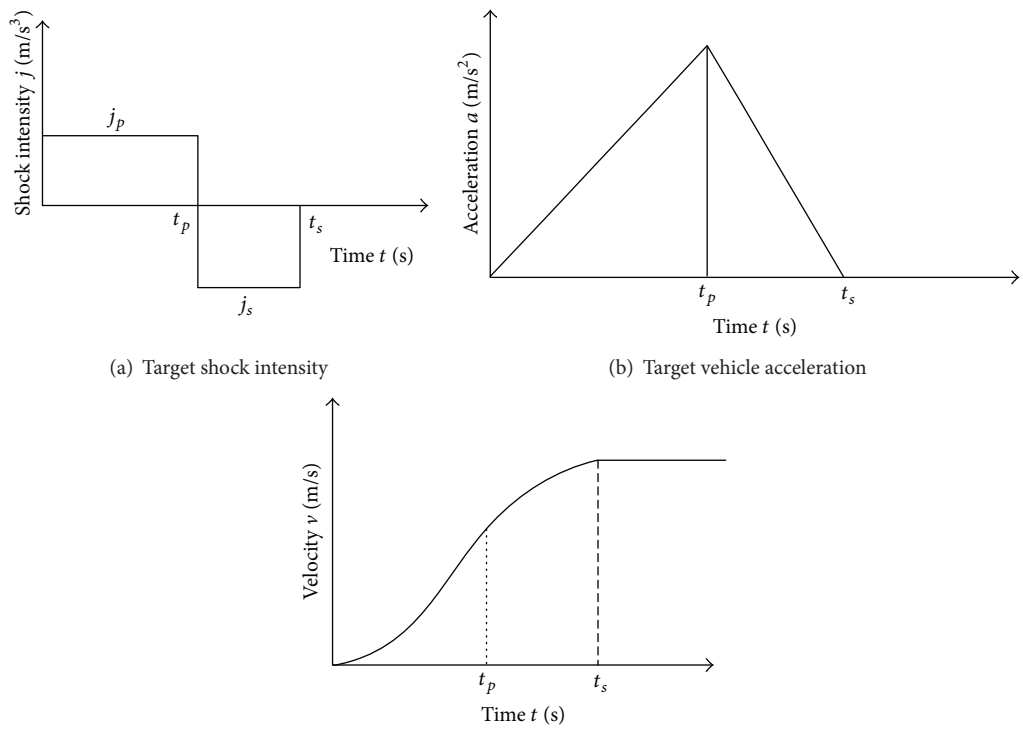

(a) Target shock intensity

(b) Target vehicle acceleration

(c) Target vehicle velocity

Figure 5: Target curves in the launching process.

where j_p is target shock intensity in phase one of sliding friction process, j_s is target shock intensity in Phase Two of sliding friction process. $\omega(t_s)$ is speed of clutch driven plate at time t_s, namely, the synchronous target speed.

By solving formula (13), the following can be obtained:

$$t_p = \sqrt{\frac{\omega(t_s) R_W}{\left(0.5 j_p - 0.5 j_p^2 / j_s\right)}},$$
$$t_s = t_p \left(1 - \frac{j_p}{j_s}\right). \tag{14}$$

According to equivalent accelerator pedal opening at the initial moment of sliding friction process, the synchronous target speed and target shock intensity in Phase One can be obtained by looking up Tables 1 and 2, respectively. Based on above values t_p and t_s, the target speed of clutch 1 in the sliding friction process will be listed in the following through the integral of j_p and j_s twice:

$$\omega_s^{\text{ref}} = \int_0^{t_s} \int_0^{t_s} \frac{j}{R_W} dt,$$
$$\omega_{c1}^{\text{ref}} = \omega_s^{\text{ref}} i_1 i_a. \tag{15}$$

Note that both t_p and t_s are measured in a coordinate system whose origin is the initial moment of sliding friction process.

Phase Three. During the time slot over t_s, clutch driving plate and its driven part are already synchronized, and DCT model is switched from sliding friction model to 1st speed gear stably operated model. So the control of sliding friction makes no sense any more. In order to meet the requirement of no-impact synchronizing, the target acceleration is set as zero and the target speed is constant.

3.3.3. Rolling Determination of Target Value and Genetic Optimization of Shock Intensity. The determining method of engine target speed and launch target shock intensity stated above can ensure no stalling of engine and ride comfort of vehicle in the launching process and partially reflect the driver's intention, but some shortages also exist as follows.

(1) Engine synchronizing target speed and target shock intensity in Phase One are only based on equivalent accelerator pedal opening at the initial moment of sliding friction process, without considering the whole sliding friction process. The transformation of equivalent accelerator pedal opening obviously does not accord with the fact.

(2) Neglect the sliding friction work in the launching process when determining the target speed.

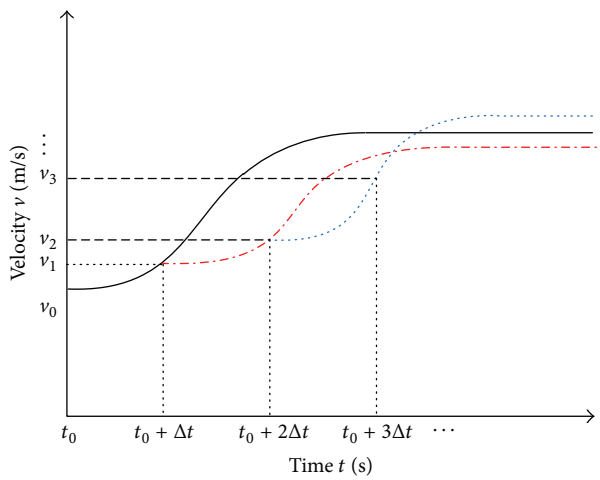

FIGURE 6: Schematic diagram of the rolling calculation of launch target vehicle velocity.

In order to overcome the above shortages, predictive control thoughts are used to optimize the target curves online. It means that during a time slot (namely, at an optimizing step), these variables, such as $\omega_e(t_s)$, t_p, t_s, and j_p can be obtained by minimizing the sliding friction work on the basis of the equivalent accelerator pedal opening and vehicle velocity. And then the target curves can also be obtained.

Determination of Rolling Algorithm of Target Vehicle Velocity. The target vehicle velocity curve is recalculated in a time interval Δt. Both vehicle velocity and acceleration are not equal to 0 at every calculation moment. Figure 6 shows that v_0, v_1, v_2, and v_3 represent the target vehicle velocities at these moments of t_0, $t_0 + \Delta t$, $t_0 + 2\Delta t$, and $t_0 + 3\Delta t$, respectively.

Figure 7 shows the calculation method of target vehicle velocity in a certain time. According to the condition of no-impact synchronizing, formula (13) can be rewritten as:

$$\begin{gathered} a(t_0) + j_p t_p + j_s(t_s - t_p) = 0, \\ v(t_0) + a(t_0)t_p + \frac{1}{2}j_p t_p^2 + (\alpha(t_0) + j_p t_p)(t_s - t_p) \\ + \frac{1}{2}j_s(t_s - t_p)^2 = \omega(t_s)R_W, \end{gathered} \tag{16}$$

where t_0 is optimizing moment, $\alpha(t_0)$ denotes vehicle acceleration at the optimizing moment, $v(t_0)$ denotes vehicle velocity at the optimizing moment, and $\omega_e(t_s)$ denotes synchronous target revolving speed, which updates its value at every optimizing step according to virtual accelerator pedal signal by looking up Table 1.

In a word, firstly at every optimizing step, synchronous target rotary speed $\omega_e(t_s)$ and target shock intensity are obtained by looking up Tables 1 and 2 according to the current equivalent accelerator pedal opening. Secondly solve (16) and get the latest values of t_p, t_s. Finally according to formula (15), we get the target vehicle velocity in the launching process.

The rolling determining method of engine target speed resembles the above description. According to (10), following formula can be obtained:

$$\omega_e^{\text{ref}} = \begin{cases} \dfrac{\omega_e(t_s) - \omega_e(0)}{t_p}t + \omega_e(0), & (\omega_e - \omega_{c1}) \geq \Delta\omega, \\ & t_0 < t < (t_0 + t_p), \\ \omega_e(t_s), & \text{other}. \end{cases} \tag{17}$$

Determination of Optimal Algorithm of Target Shock Intensity. The target shock intensity stated above is obtained by looking up Tables. But it does not ensure that the target curve is optimal. It is discussed below how to determine j_p and j_s through genetic algorithm and real-time optimization. In the time slot $t_0 \sim t_0 + t_s$, the predictive sliding friction work is

$$\begin{gathered} W = \int_{t_0}^{t_0+t_s} \widehat{T}_{c1}(\omega_e^{\text{ref}} - \omega_{c1})\,dt, \\ \widehat{T}_{c1} = \frac{I_o\dot{\omega}_s^{\text{ref}} + b_o\omega_s^{\text{ref}} + mgR_W\mu}{i_a i_1 \eta^2}, \end{gathered} \tag{18}$$

where $\widehat{T}_{c1}$ is estimated clutch transfer torque. If $|T_{c1} - \widehat{T}_{c1}| < \varepsilon$, estimated value $\widehat{T}_{c1}$ replaces real value T_{c1}, and target shock intensities j_p and j_s can be obtained by minimizing the sliding friction work. The selected fitness function based on genetic algorithm is the reciprocal of predictive sliding friction work:

$$F = \frac{1}{W}. \tag{19}$$

The optimizing process of parameters j_p and j_s can be seen in Figure 8.

3.3.4. Design of Sliding Mode Variable Structure Tracing Controller. Based on the design of previous details, the target vehicle velocity and target engine speed are already obtained in the launch sliding friction process. However, whether it can track accurately or not, depends on the performance of launch controller completely. Considering immeasurable driving resistance, a kind of sliding mode variable structure control algorithm with interference rejection has been put forward in the paper, which aims at tracking engine speed and wheel speed accurately.

Regardless of the influence of temperature and slip speed difference on clutch friction coefficient μ_1, the relationship between pressure F_1 of the clutch pressure plate and its transfer torque is determined uniquely, when the internal and external radius of friction plates are given. For the sake of easy description, clutch transfer torque is used to describe the clutch engaging law in the following.

Tracing Control of Wheel Speed. On the basis of launch dynamics equations of DCT transmission system (referring to Formula (5)), supposing $x_1 = \theta_s$, $x_2 = \omega_s$, there is:

$$\begin{gathered} \dot{x}_1 = x_2, \\ \dot{x}_2 = \frac{i_e}{I_o}T_{c1} - \frac{b_0}{I_0}x_2 - \frac{T_f}{I_0}. \end{gathered} \tag{20}$$

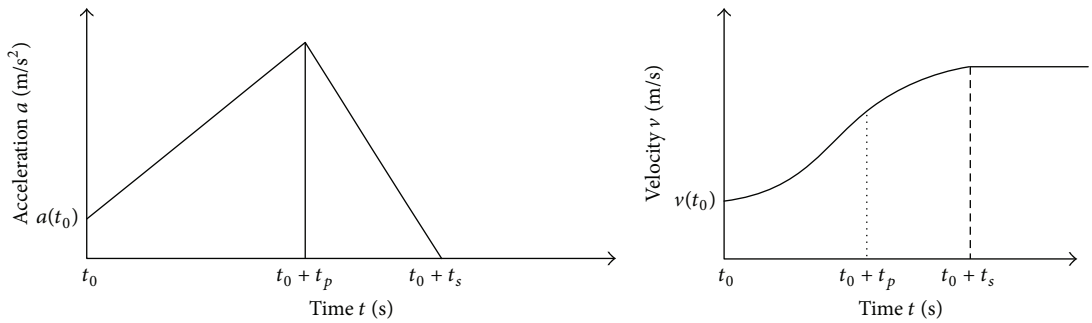

(a) Target acceleration (b) Target vehicle velocity

Figure 7: Calculation schematic diagram of target vehicle velocity at time t_0.

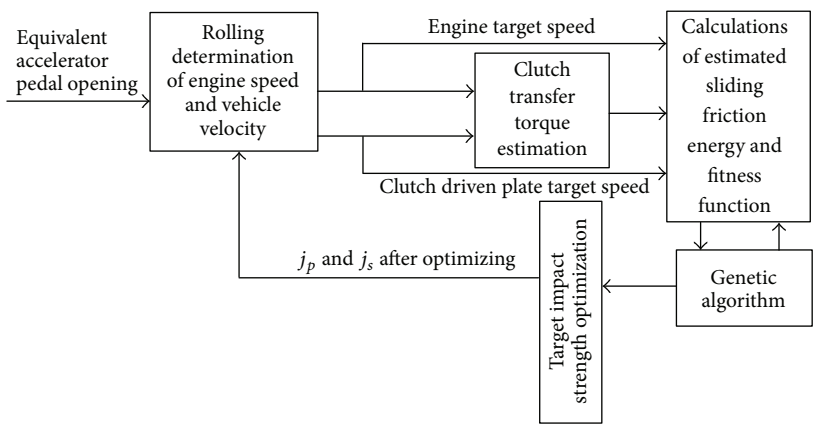

Figure 8: Optimizing process of target shock intensity.

Supposing that $e_1 = x_r - x_1$, $e_2 = \dot{x}_r - x_2$, $u_1 = T_{c1}$, where x_r is the expectation of x_1, there is

$$\begin{bmatrix} \dot{e}_1 \\ \dot{e}_2 \end{bmatrix} = \begin{bmatrix} 0 & 1 \\ 0 & -\dfrac{b_0}{I_0} \end{bmatrix} \begin{bmatrix} e_1 \\ e_2 \end{bmatrix} + \begin{bmatrix} 0 \\ -\dfrac{i_e}{I_0} \end{bmatrix} u_1 + \begin{bmatrix} 0 \\ f_2 \end{bmatrix} + \begin{bmatrix} 0 \\ f_3 \end{bmatrix}, \quad (21)$$

where $f_2 = \ddot{x}_r + (I_0/b_0)\dot{x}_r$, which is measurable interference, and $f_3 = T_f/I_0$, which is immeasurable interference related to the driving resistance.

In order to reduce the gain of sliding mode variable structure, it should contract the upper and lower boundaries of interference as much as possible. According to the computational formula of driving resistance, the rolling resistance is regarded as a part of measurable interference; namely, measurable interference f_2 can be rewritten as

$$f_2' = \ddot{x}_r + \frac{I_0}{b_0}\dot{x}_r + \frac{mgf}{b_0}. \quad (22)$$

And the immeasurable interference f_3 can be rewritten as

$$f_3' = \frac{T_f}{I_0} - \frac{mgf}{b_0}. \quad (23)$$

The switching function is designed as

$$s = c_1 e_1 + c_2 e_2, \quad (24)$$

where $c_1 > 0$, $c_2 > 0$. Take the approaching rate:

$$\dot{s} = -k \cdot s - d \cdot g(s) + c_2 f_3', \quad (25)$$

where $d > |c_2 f_3'|$,

$$g(s) = \begin{cases} \operatorname{sgn}(s) & |s| \geq \dfrac{\pi}{2p} \\ \sin(p \cdot s) & |s| < \dfrac{\pi}{2p} \end{cases} \quad p > 0. \quad (26)$$

While it is $p \to \infty$, $g(s) \to \operatorname{sgn}(s)$. The control input u_1 is calculated via the formula below:

$$u_1 = \frac{I_0}{c_2 i_e}\left[k \cdot s + d \cdot g(s) + e_2\left(c_1 - c_2\frac{b_0}{I_0}\right) + c_2 f_2'\right]. \quad (27)$$

Tracing Control of Engine Speed. Because engine model is a double-input (T_e and T_{c1})-single-output (ω_e) model and clutch transfer torque T_{c1} is available in use of wheel speed tracing controller stated previously, T_{c1} is a measurable interference of engine model. Based on the rotation dynamics of crankshaft (refer to Formula (5)), we can suppose that

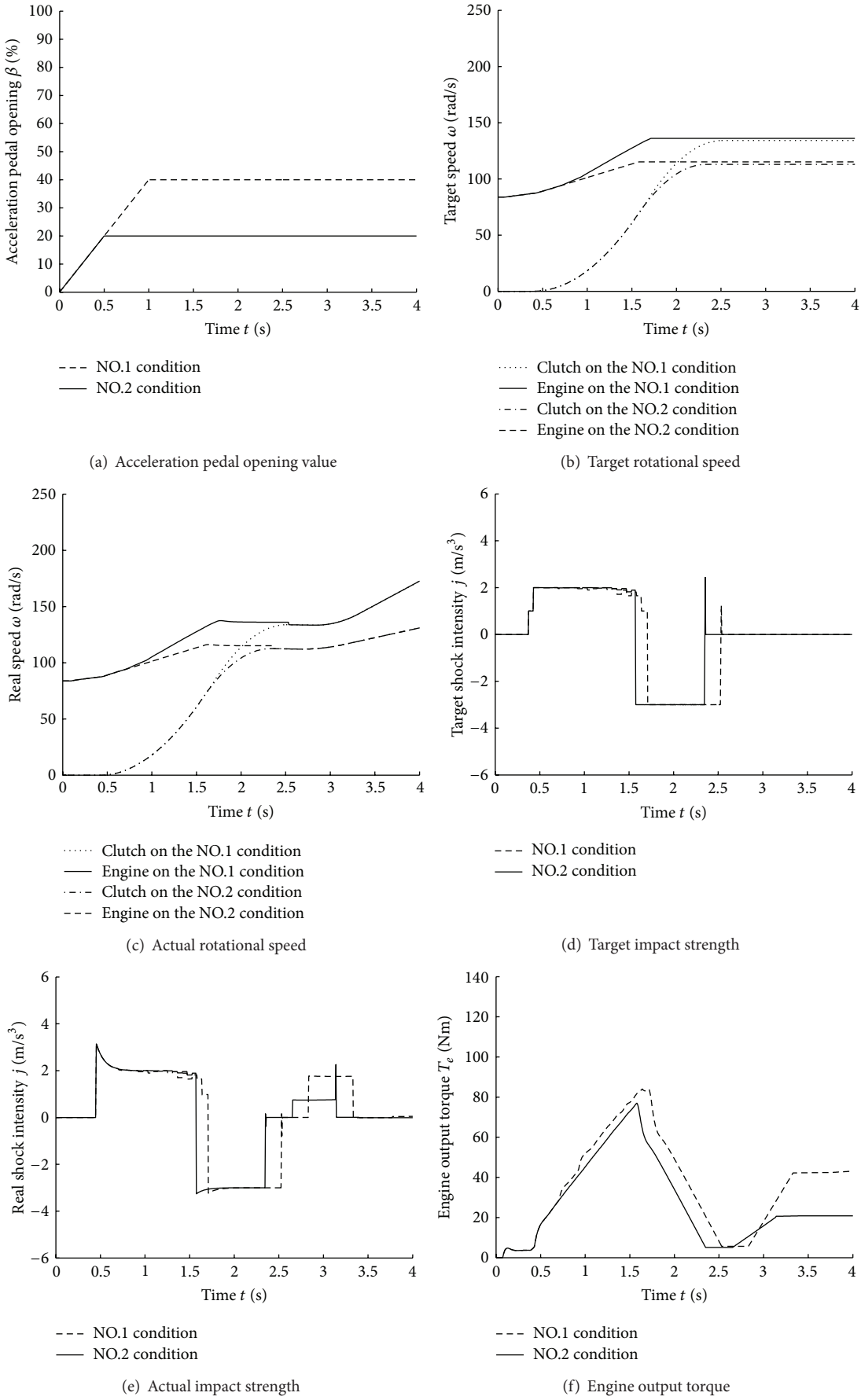

Figure 9: Continued.

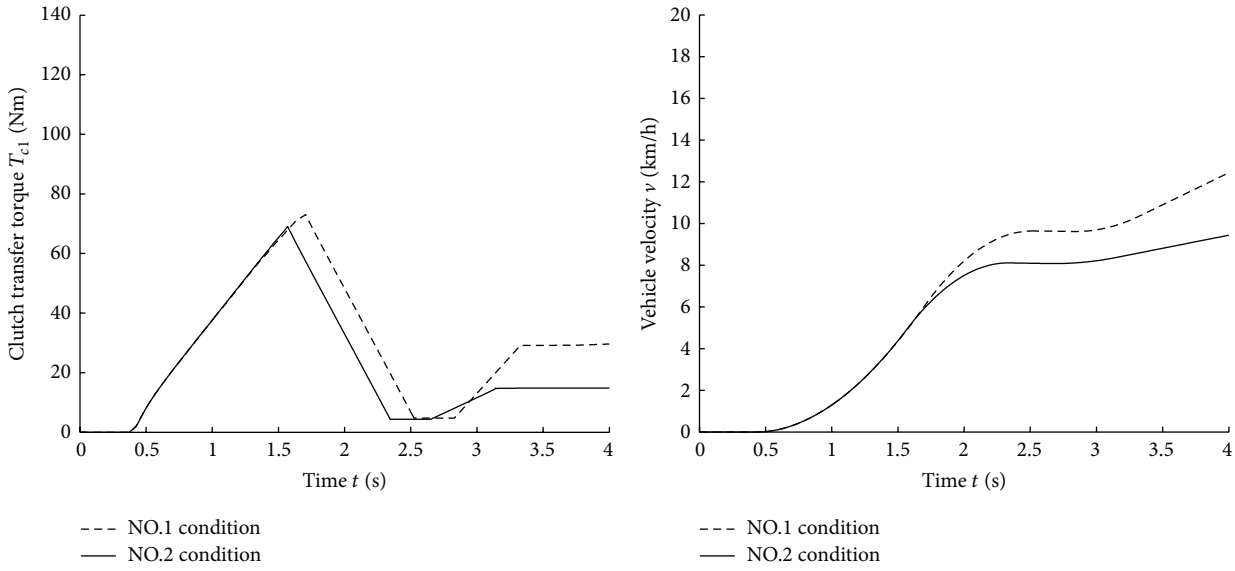

(g) Clutch transfer torque (h) Vehicle velocity

Figure 9: Simulation results of launch performance.

$x_{1e} = \theta_e$, $\dot{x}_{1e} = \dot{\theta}_e = \omega_e$, $e_{1e} = x_{re} - x_{1e}$, $e_{2e} = \dot{x}_{re} - x_{2e}$, where x_{re} is the expectation of θ_e; namely,

$$\begin{bmatrix} \dot{e}_{1e} \\ \dot{e}_{2e} \end{bmatrix} = \begin{bmatrix} 0 & 1 \\ 0 & -\dfrac{b_e}{I_e} \end{bmatrix} \begin{bmatrix} e_{1e} \\ e_{2e} \end{bmatrix} + \begin{bmatrix} 0 \\ -\dfrac{1}{I_e} \end{bmatrix} u_2 + \begin{bmatrix} 0 \\ f_{2e} \end{bmatrix}, \tag{28}$$

where $u_2 = T_e$, $f_{2e} = (T_{c1}/I_e) + \ddot{x}_{re} + (b_e/I_e)\dot{x}_{re}$, which are measurable interferences.

The switching function is designed as

$$s_e = c_{1e}e_{1e} + c_{2e}e_{2e}, \tag{29}$$

where $c_{1e} > 0$, $c_{2e} > 0$. Take the approaching rate:

$$\dot{s}_e = -k_e \cdot s_e - d_e \cdot g(s_e), \tag{30}$$

where $d_e > |c_{2e}f_{2e}|$,

$$g(s) = \begin{cases} \operatorname{sgn}(s), & |s| \geq \dfrac{\pi}{2p_e}, \\ \sin(p_e \cdot s), & |s| < \dfrac{\pi}{2p_e} \end{cases} \quad p > 0. \tag{31}$$

The control output u_2 is calculated via the following formula:

$$u_2 = \frac{I_e}{c_2}\left[k_e \cdot s_e + d_e \cdot g(s_e) + e_{2e}\left(c_{1e} - c_{2e}\frac{b_e}{I_e}\right) + c_{2e}f_{2e}\right]. \tag{32}$$

3.4. Switching Control of Engine Demand Torque in the Engaging Process after Synchronizing. When engine speed and clutch driven plate speed approach to synchronizing and reach set threshold values according to switching conditions, DCT launch models switch over; namely, the two-DOF sliding friction model transforms into the single-DOF 1st speed gear stable operated model. At the moment, the controller of sliding friction process does not work any longer. And switching controller of demand torque begins to work, which is in charge of converting engine torque into driver demand torque. It satisfies

$$T_e^d = T_e^L + K_e t, \tag{33}$$

$$K_e = \left(\frac{T_e^d - T_e^L}{\Delta t}\right), \tag{34}$$

wherein T_e^L is real engine torque at the switching moment of DCT launch models, T_e^d is driver demand torque, K_e is changing slope of engine torque, and Δt is switching time elapsed of demand torque.

In order to meet the requirement of vehicle shock intensity in the switching process, Δt has a minimum value. According to the 1st speed gear stably operated model (formula (8)), shock intensity is proportional to the changing rate of engine torque regardless of driving resistance and friction damping. That is

$$j = \frac{i_e R_W}{I_d}\dot{T}_e. \tag{35}$$

According to the requirement of shock intensity in the launching process, namely, $j \leq 10\,\mathrm{m/s^3}$, the upper limited value of changing rate of engine torque can be calculated. The minimum time elapsed in the switching process of torque also can be obtained on the basis of formula (33).

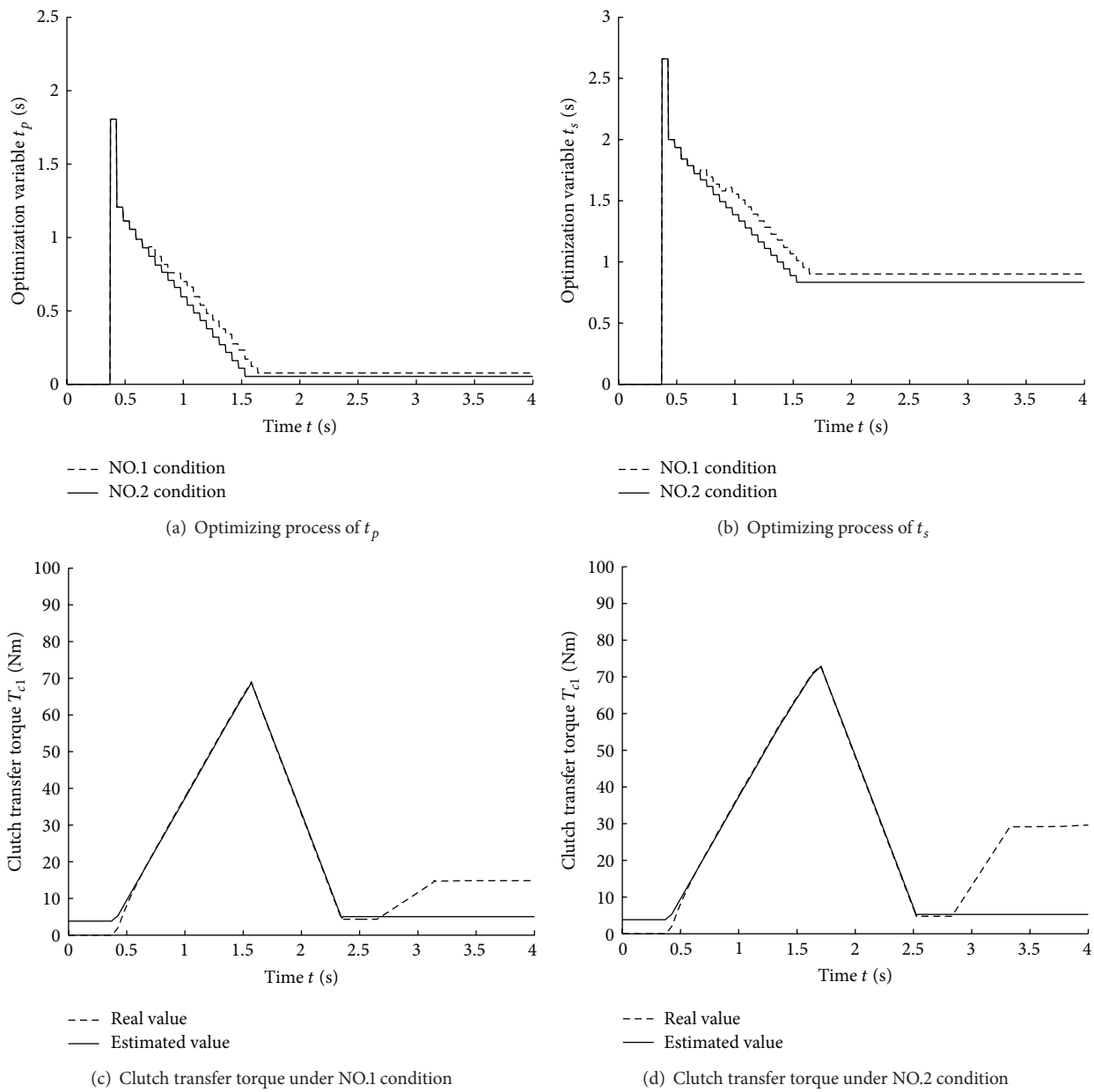

(a) Optimizing process of t_p

(b) Optimizing process of t_s

(c) Clutch transfer torque under NO.1 condition

(d) Clutch transfer torque under NO.2 condition

Figure 10: Comparisons of results of rolling optimization under NO.1 and NO.2 condition.

Similarly, according to the two-DOF launch model (Formula (5)) in the launch sliding friction process, we know that vehicle shock intensity in the sliding friction process is proportional to the changing rate of clutch transfer torque regardless of driving resistance and friction damping. So there is

$$j = \frac{i_e R_W}{I_0} \dot{T}_{c1}. \tag{36}$$

4. Simulation Results and Analysis

Based on the previously established dynamic model of dry DCT and its launch controller, the launch simulation model of vehicle equipped with dry DCT is built on the Matlab/simulink software platform. Immediately, the performance of vehicle is simulated under typical launch condition. The detailed parameters of adopted DCT can be seen in the appendix.

Figure 9 and Table 3 demonstrate simulation results of launch condition, which are defined as that the changing rate of accelerator pedal angle is constant and that the final values are different. It means that changing rate of accelerator is $0.4\,\mathrm{s}^{-1}$ and that the final values are 20% and 40% respectively. Relatively, they are called NO.1 and NO.2 conditions respectively, which are shown in Figure 9(a). Compared with NO.4 condition (it reaches the final value at 1 s), NO.3 condition requires a slower launch process.

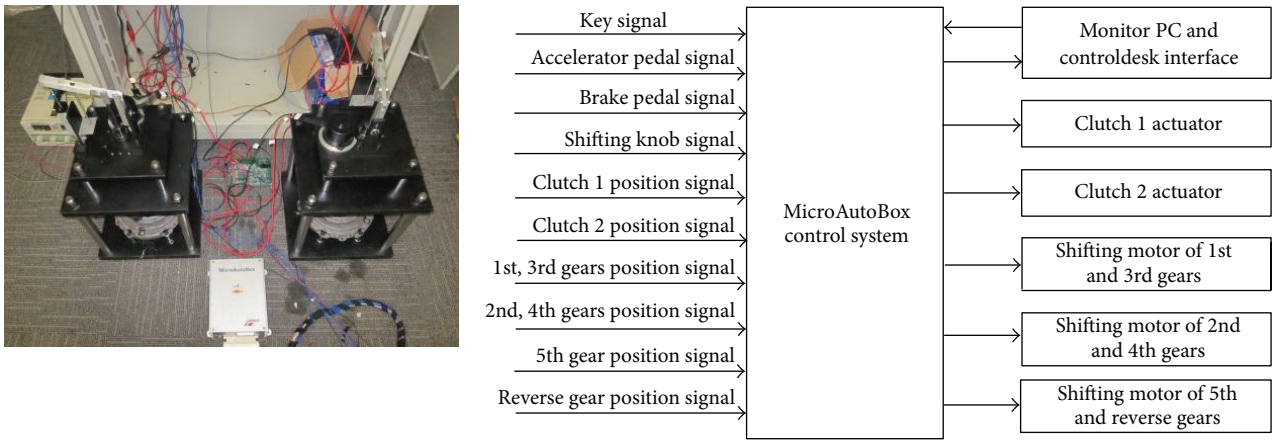

(a) Photo of dry DCT test bench

(b) Interfaces of DCT prototyping controller

Figure 11: DCT test bench and prototyping controller.

Table 3: Comparisons of simulated results of NO.1 and NO.2 conditions.

Working condition	NO.1	NO.2
Time elapsed when clutch driving and driven plates are synchronized t_s/s	2.355	2.535
Vehicle velocity when clutch driving and driven plates are synchronized v/(km/h)	8.1052	9.6367
Time elapsed when the demand torque switch over $(t_s + \Delta t)$/s	3.14	3.33
Vehicle velocity when the demand torque switch over v/(km/h)	8.3558	10.371
Total slipping friction work W/J	3739.9	4767.3
Time elapsed for launch t/s	3.14	3.33

In Figures 9(b), 9(c), and 9(g) and Table 3, both the synchronizing moment of clutch driving and driven plates and the switching finishing moment under NO.1 condition are earlier than that of NO.2 working condition. At any moment, vehicle velocity is quite little under NO.1 condition. So it can be concluded that the designed launch controller can reflect the driving intention. In Figures 9(d) and 9(e), launch impact strengths are less than 10 m/s^3, which meet the demands. In Figures 9(f) and 9(g), engine output and clutch transfer torque can also be divided into five parts.

Figures 10(a) and 10(b) demonstrate optimal time variables t_p and t_s calculated at every rolling optimization. The total optimizing frequency is 22 under NO.1 condition, while the time elapsed is 1.53 s at the last optimization. Relatively, the total optimizing frequency is 24 times under NO.2 condition, while the time elapsed is 1.64 s at the last optimization. Figures 10(c) and 10(d) show that estimated value of T_{c1} is quite approaching to its real value in the launch sliding friction process. It ensures that sliding friction is least in the launching process to some degree.

5. Rapid Prototyping Experiments for Dry DCT in the Launching Process

5.1. Five-Speed Dry DCT Transmission Actuator. In order to shorten the development cycle of dry DCT control system and test the real-time property and effectiveness of sliding mode variable structure control algorithm as well, the research group has established a dry DCT test bench (shown in Figure 11(a)) and used MicroAutoBox1401 of dSPACE Corporation as prototype controller. Some models are set up, such as five-speed dry DCT vehicle models (including engine mean value model, DCT model, and vehicle longitudinal dynamics model) and DCT control strategy model. The rapid prototyping experiments are conducted at the same time.

The interfaces of dry DCT prototype controller are shown in Figure 11(b). Before testing, calibrate the signals of sensors firstly and test the working performance of actuator motor driving units and actuator mechanisms in an open loop in order to ensure the reliability of hardware system. Secondly, test and verify the coordinating control strategy of clutch torque in a closed-loop. Thirdly, conduct the rapid prototyping experiments of sliding mode variable structure upper coordinating control strategy after proving its effectiveness and calibrating relative control parameters.

5.2. Results and Analysis of Rapid Prototyping Tests. By means of making use of RTI1401 toolbox offered by dSPACE Corporation, defining input signal pins such as accelerator pedal signal, brake pedal signal, and contacting with the previously designed DCT launch upper control module, the upper controller can be established.

The launch trigger signal is defined as follows: when the current speed gear is 1st speed gear, the brake pedal signal is zero (in loose state). The accelerator pedal opening is more than or equal to 3%. A trigger signal for preselecting 2nd speed gear is delayed 0.5 s after the launch is finished.

The trigger signal of shifting 1st speed gear to the 2nd one can be defined as follows: when the vehicle velocity is bigger

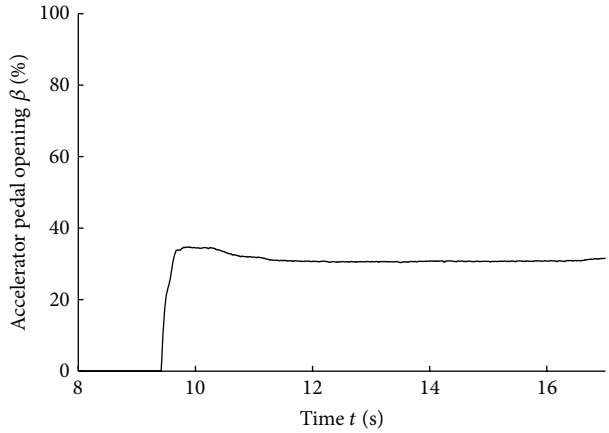

(a) Acceleration pedal opening

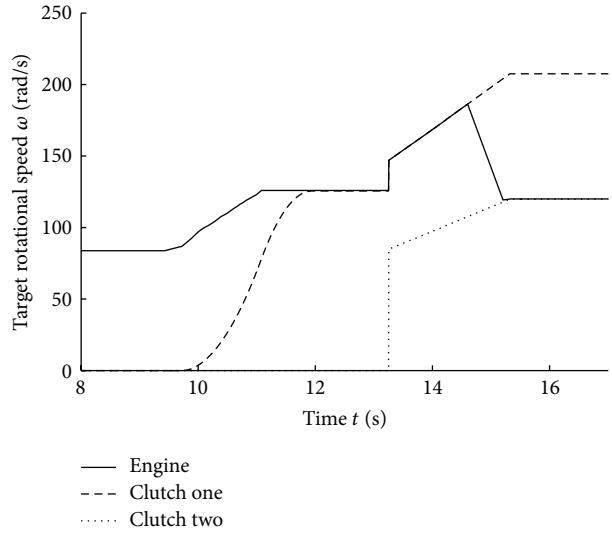

(b) Target rotational speed

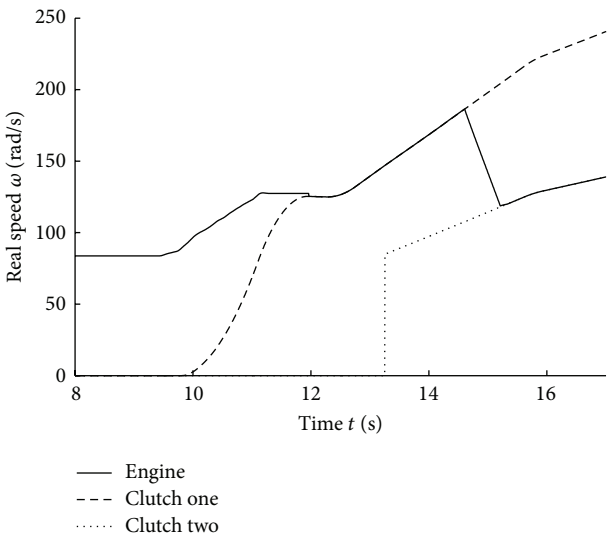

(c) Real rotational speed

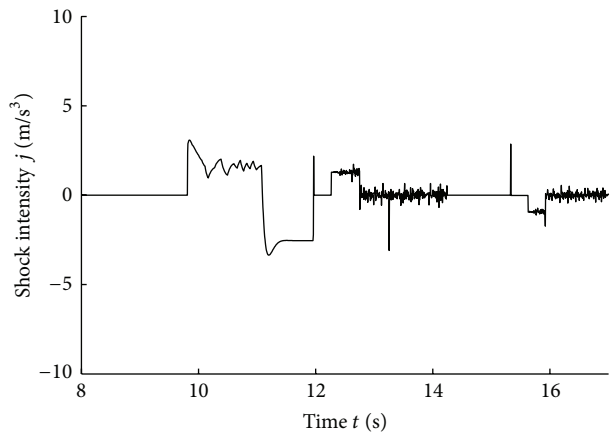

(d) Shock intensity

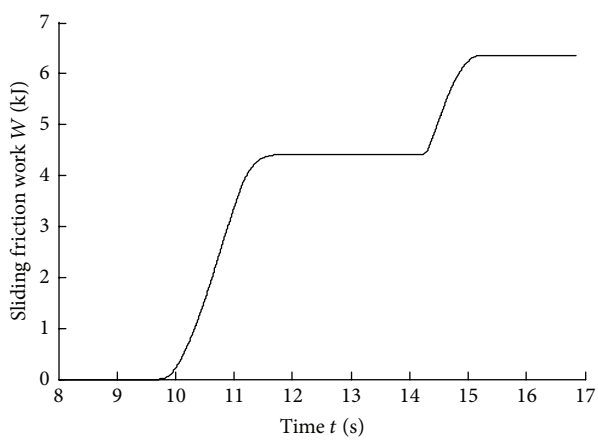

(e) Sliding friction work

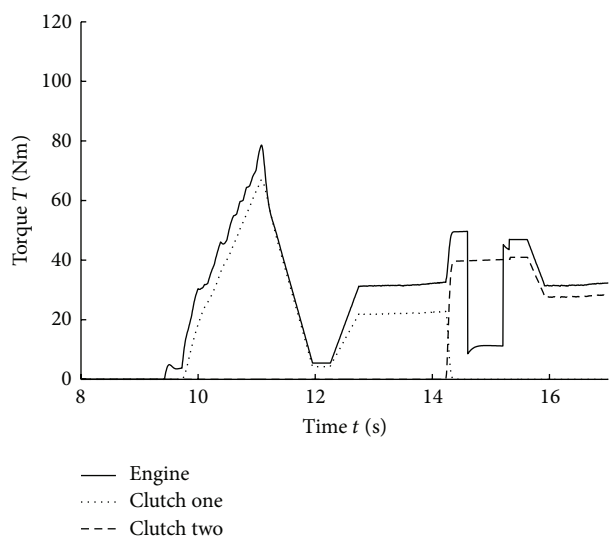

(f) Torque

Figure 12: Continued.

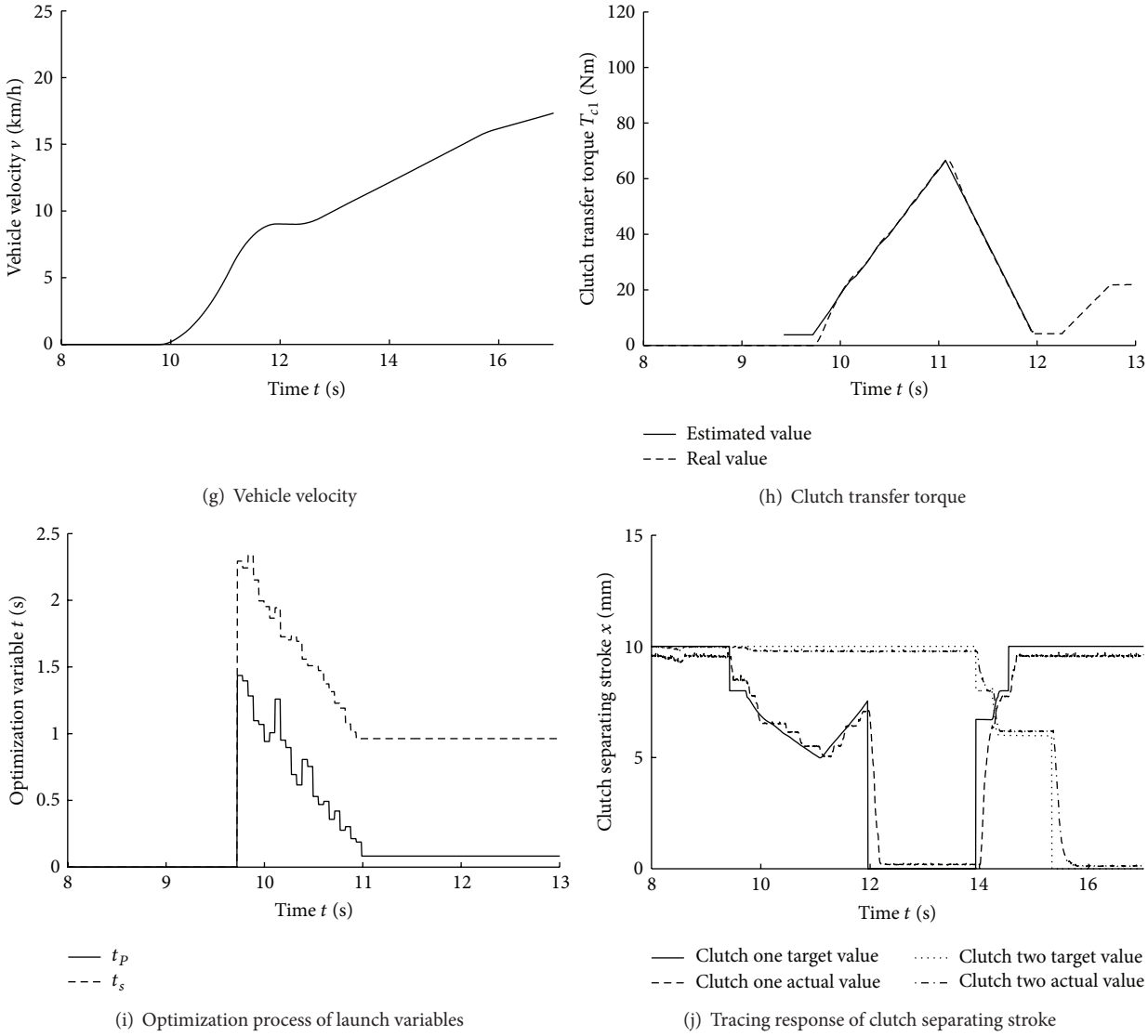

(g) Vehicle velocity

(h) Clutch transfer torque

(i) Optimization process of launch variables

(j) Tracing response of clutch separating stroke

Figure 12: Rapid prototyping experiment results of launch and shifting from the 1st gear to the 2nd one.

Figure 13: Photo of real car chassis dynamometer test.

Table 4: Rapid prototyping experiment results of dry DCT in the launching process.

Launch moment t_0/s	9.425
Synchronizing moment of launch clutch 1 driving and driven plates $(t_0 + t_s)$/s	11.96
Vehicle velocity at the synchronizing moment of clutch 1 v/(km/h)	9.029
Switching finishing moment of launch demand toque $(t_0 + t_s + \Delta t)$/s	12.74
Vehicle velocity at the switching finishing moment of demand toque v/(km/h)	9.498
Total sliding friction work W/J	4416
Rolling optimization frequency of time variable	24
Time elapsed for launch t/s	3.315

than the 1st to 2nd gear shifting speed 12 km/h and the target gear is 2nd gear.

The rapid prototyping experiment results of upper controller are demonstrated in Figure 12 and Table 4. It can be seen that the performance indexes of shock intensity and sliding friction work meet the standard demands in

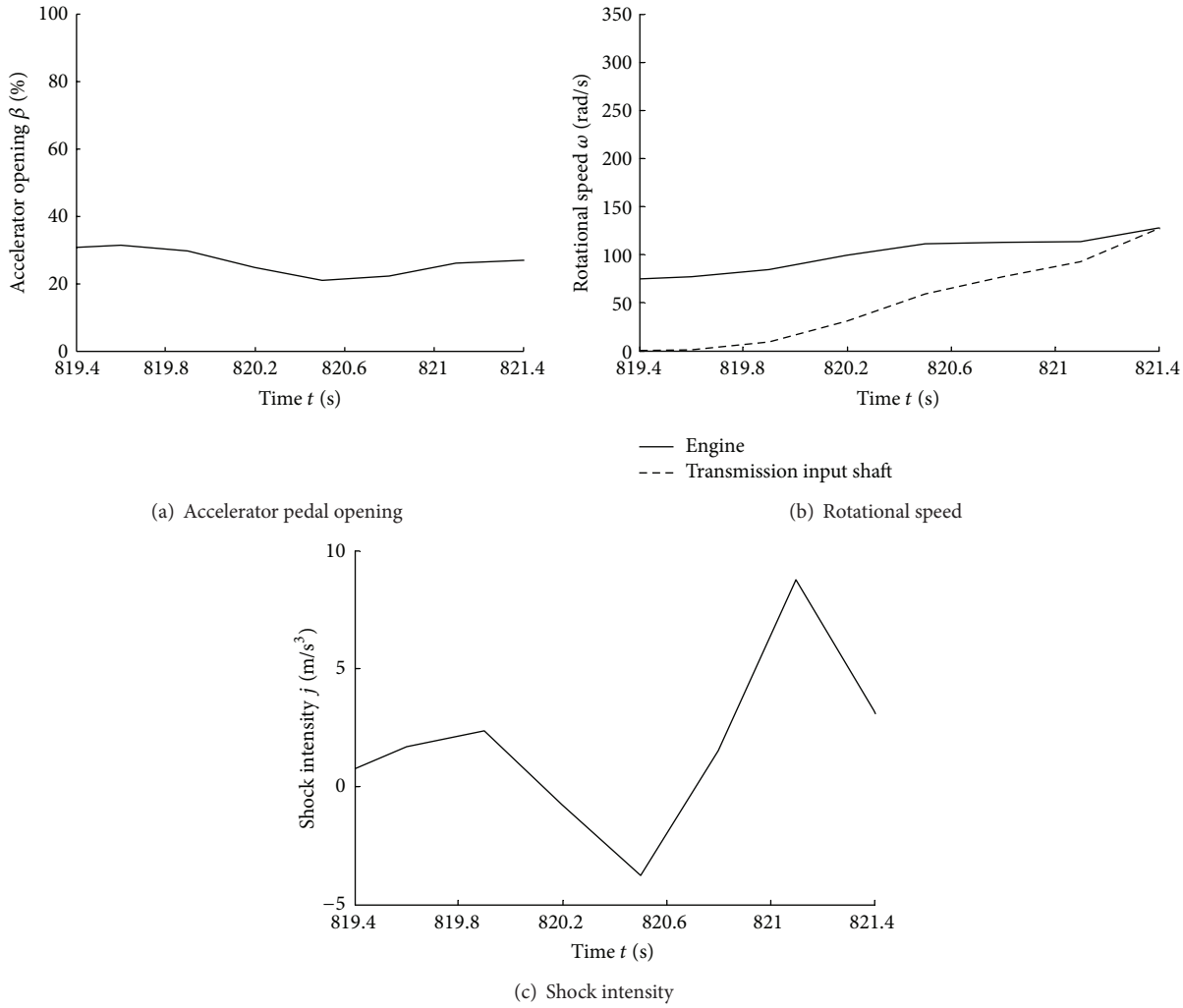

(a) Accelerator pedal opening

(b) Rotational speed

(c) Shock intensity

Figure 14: Results of dry DCT prototype car chassis dynamometer test.

the launching process and that results of rapid prototyping experiments coincide with simulated results. It is also proved that the stated sliding mode variable structure dry DCT upper controller can meet the requirement of real-time control based on real-time optimization.

6. Chassis Dynamometer Test of Real Car Equipped with Dry DCT

After rapid prototyping experiments, the independently developmental five-speed dry DCT control unit is used to replace the MicroAutoBox1401 rapid prototype controller. On the basis of simulation and bench test results, the corresponding MAP of prototype car equipped with dry DCT is recalibrated. After DCT software is developed, the real car chassis dynamometer test is conducted. The test photo is shown in Figure 13.

The results of launch test can be seen in Figure 14. The experiment results demonstrate that on the basis of sliding mode variable structure upper coordinating control strategy, the developed dry DCT control software not only reflects the launch riding comfort of vehicle, but also reflects the variation of driver's intention.

As can been seen from Figure 14, under the proposed launching strategies, the vehicle is launched within 2 s and the shock intensity is below 10 m/s^3. Besides, when the accelerator pedal opening is increasing, the corresponding shock intensity is relatively larger, which is consistent with the control strategies. Compared with the rapid prototyping tests, the results obtained in the chassis dynamometer test are also consistent, thus validating the effectiveness of the proposed control strategies.

7. Conclusion

The four-DOF launch dynamics model of five-speed dry DCT is established. After simplifying the model, two-DOF sliding friction model and single-DOF in-gear operation model are obtained, which provide a basis for the design and control

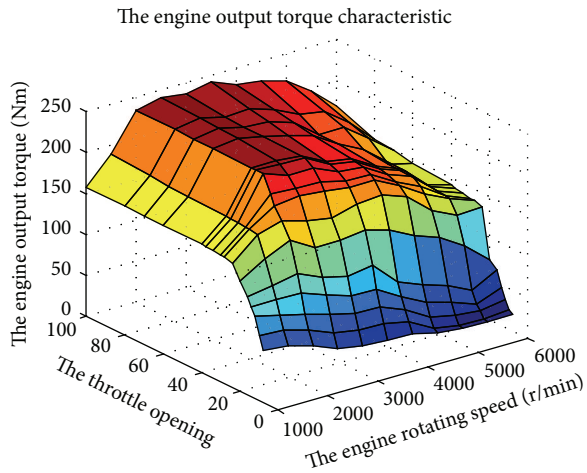

Figure 15

Table 5: The parameters of adopted DCT.

Parameters	Value
I_e	0.273 kg·m^2
I_{c1}	0.014 kg·m^2
I_{c2}	0.014 kg·m^2
I_m	0.01 kg·m^2
I_s	147.0392 kg·m^2
I_{g1} ~I_{g5}	0.005 kg·m^2
I_{gr}	0.005 kg·m^2
i_1 ~i_5	3.615, 2.042, 1.257 0.909, 0.714
i_a	3.895
b_e	0.01
b_{c1}	0.01
b_{c2}	0.01
b_m	0.01
b_s	0.01
m	1550 kg
f	0.0137
g	9.8 m/s^2
A	2.095 m
C_d	0.293
R_w	0.308 m
η	0.92
R_0	0.228 m
R_1	0.15 m

of launch controller. Driver's intention is reflected by using engine speed and vehicle shock intensity. Taking advantage of the idea of predictive control and genetic algorithm, the tracing curves of engine speed and vehicle target velocity are determined by rolling optimization online. The sliding mode variable structure controller (SMVS) is designed. Launch simulating model is built on the MATLAB/Simulink software platform for the dry DCT. the launch rapid prototyping experiment is conducted. Simulation and experiment results show that the designed SMVS coordinating controller can effectively reflect the driver's intention and improve the vehicle's launch performance. Furthermore, chassis dynamometer test result of DCT prototype car also shows that the proposed SMVS launch coordinating control strategy is effective and feasible.

Appendices

A. The Engine Output Characteristics (Map)

See Figure 15.

B. The Parameters of Adopted DCT in This Paper

See Table 5.

Conflict of Interests

The authors declare that there is no conflict of interests regarding the publication of this paper.

References

[1] D. Qin, Y. Liu, J. Hu, and R. Chen, "Control and simulation of launch with two clutches for dual clutch transmissions," *Chinese Journal of Mechanical Engineering*, vol. 46, no. 18, pp. 121–127, 2010.

[2] D. Qin and Q. Chen, "Universal clutch starting control of AMT/DCT automatic transmission based on optimal control," *Chinese Journal of Mechanical Engineering*, vol. 47, no. 12, pp. 85–91, 2011.

[3] C. Sun and J. Zhang, "Optimal control applied in automatic clutch engagements of vehicles," *Chinese Journal of Mechanical Engineering*, vol. 17, no. 2, pp. 280–283, 2004.

[4] Q.-H. Chen, D.-T. Qin, and X. Ye, "Optimal control about AMT heavy-duty truck starting clutch," *China Journal of Highway and Transport*, vol. 23, no. 1, pp. 116–121, 2010.

[5] F. Garofalo, L. Glielmo, L. Iannelli et al., "Optimal tracking for automotive dry clutch engagement," in *Proceedings of the International Federation of Automatic Control (IFAC '02)*, pp. 367–372, 2002.

[6] I. A. Amir, D. T. Qin, and J. J. Liu, "A control strategy on launch up a vehicle with AMT," *Information Technology Journal*, vol. 4, no. 2, pp. 140–145, 2005.

[7] G. Lucente, M. Montanari, and C. Rossi, "Modelling of an automated manual transmission system," *Mechatronics*, vol. 17, no. 2-3, pp. 73–91, 2007.

[8] A. Serrarens, M. Dassen, and M. Steinbuch, "Simulation and control of an automotive dry clutch," in *Proceedings of the 2004 American Control Conference (AAC '04)*, pp. 4078–4083, July 2004.

[9] C. H. Yu, H. Y. Chen, and H. R. Ding, "A study on fuzzy control of AMT clutch in launch phase," *Automotive Engineering*, vol. 27, no. 4, pp. 423–426, 2004.

[10] Z. Qi, Q. Chen, and A. Ge, "Fuzzy control of the AMT vehicle's starting process based on genetic algorithm," *Chinese Journal of Mechanical Engineering*, vol. 37, no. 4, pp. 8–24, 2001.

[11] M. Yong, D. Y. Sun, D. T. Qin et al., "Research on partial fuzzy control of car clutch in launch phase," *Automotive Technology*, vol. 12, pp. 12–15, 2008.

[12] H. Kong, F. Ren, and Y. M. Ren, "Application of the genetic algorithm to optimizing fuzzy control strategy in the vehicle's launch process," *Journal of Hefei University of Technology*, vol. 32, no. 1, pp. 21–23, 2009.

[13] M. X. Wu, J. W. Zhang, T. L. Lu et al., "Research on optimal control for dry dual-clutch engagement during launch," *Journal of Automobile Engineering*, vol. 224, no. 6, pp. 749–763, 2010.

[14] G. Q. Wu and D. M. Zhan, "A research on the way of clutch actuation during DCT upshift based on optimality theory," *Automotive Engineering*, vol. 31, no. 3, 2009.

[15] Y. Li, Z. Zhao, and T. Zhang, "Research on optimal control of twin clutch engagement pressure for dual clutch transmission," *China Mechanical Engineering*, vol. 21, no. 12, pp. 1496–1501, 2010.

[16] W. Yang, Q. Chen, G. Wu, and D. Qin, "Starting control strategy for dual clutch transmission based on intelligent control and the performance simulation," *Chinese Journal of Mechanical Engineering*, vol. 44, no. 11, pp. 178–185, 2008.

[17] Y. Liu, D. Qin, H. Jiang, and Y. Zhang, "A systematic model for dynamics and control of dual clutch transmissions," *Journal of Mechanical Design, Transactions of the ASME*, vol. 131, no. 6, pp. 0610121–0610127, 2009.

[18] Y. S. Zhao, *Integrated control of dual clutch transmission system [M.S. thesis]*, Chongqing University.

[19] H.-O. Liu, H.-Y. Chen, H.-R. Ding, and Z.-B. He, "Adaptive clutch engaging process control for automatic mechanical transmission," *Journal of Beijing Institute of Technology*, vol. 14, no. 2, pp. 170–174, 2005.

[20] F. Garofalo, L. Glielmo, L. Iannelli et al., "Smooth engagement for automotive dry clutch," in *Proceedings of the IEEE Control Systems Society Conference*, vol. 1, pp. 529–534, 2001.

Hindawi Publishing Corporation
Mathematical Problems in Engineering
Volume 2014, Article ID 748974, 15 pages
http://dx.doi.org/10.1155/2014/748974

Research Article

A Virtual Motion Camouflage Approach for Cooperative Trajectory Planning of Multiple UCAVs

Xueqiang Gu, Lincheng Shen, Jing Chen, Yu Zhang, and Wanpeng Zhang

College of Mechatronic Engineering and Automation, National University of Defense Technology, Changsha, Hunan 410073, China

Correspondence should be addressed to Jing Chen; chenjing00100@sina.com

Received 22 August 2013; Revised 28 November 2013; Accepted 1 December 2013; Published 22 January 2014

Academic Editor: Xinjie Zhang

This paper investigates cooperative trajectory planning of multiple unmanned combat aerial vehicles (multi-UCAV) in performing autonomous cooperative air-to-ground target attack missions. By integrating an approximate allowable attack region model, several constraint models, and a multicriterion objective function, the problem is formulated as a cooperative trajectory optimal control problem (CTOCP). Then, a virtual motion camouflage (VMC) for cooperative trajectory planning of multi-UCAV, combining with the differential flatness theory, Gauss pseudospectral method (GPM), and nonlinear programming, is designed to solve the CTOCP. In particular, the notion of the virtual time is introduced to the VMC problem formulation to handle the temporal cooperative constraints. The simulation experiments validate that the CTOCP can be effectively solved by the cooperative trajectory planning algorithm based on VMC which integrates the spatial and temporal constraints on the trajectory level, and the comparative experiments illustrate that VMC based algorithm is more efficient than GPM based direct collocation method in tackling the CTOCP.

1. Introduction

Nowadays, it is an active research area to perform autonomous cooperative air-to-ground target attack (CA/GTA) missions using multiple unmanned combat aerial vehicles (multi-UCAV) [1]. However, compared with single UCAV planning and coordinated formation control problems [2], new technical challenges in the CA/GTA missions are emerging. The cooperative trajectory planning is one of the key challenging technologies, due to its high dimensionality, severe equality and inequality constraints involved, and the requirement of spatial-temporal cooperation of multi-UCAV.

Recently, various algorithms have been developed to solve this cooperative trajectory planning problem [3, 4], including artificial neural network methods [5], sample-based planning methods [6], maneuver automation (MA) [7], and optimal control methods. There is no doubt that the optimal control theory is the most natural framework for this type of problem with dynamic constraints [8]. However, the rapid solution to optimal control problems (OCPs) for complicated nonlinear systems, such as UCAVs, is a challenging task [9]. Analytical solutions are seldom available or even possible. As a result, one usually resorts to numerical techniques [3]. The techniques can be classified into two general types, namely, indirect and direct methods. Indirect methods [10] solve the OCPs by formulating the first-order optimality conditions, applying Pontryagin's Maximum Principle and nonlinear programming (NLP) to tackle the resulting two-point boundary value problem numerically. Direct methods [11], on the other hand, are devoted to reduce the OCPs to finite-dimensional NLP problems by discretization and parameterization of subsets of the state and control vectors and then are solved by developed optimizers. As one of direct methods, Gauss pseudospectral method (GPM) is applied widely and efficiently in the trajectory optimization field [12–14], due to its advantages of fewer parameters and higher precision in the calculation procedure. However, the method to achieve the trajectory planning for a single vehicle or cooperative multivehicle required a high computational load. To reduce the computational complexity, the inverse dynamics methods [15, 16] and differential flatness theory (DFT) based methods [17–20] are introduced. Compared to pseudospectral methods, these methods can use any models

and any performance indexes and transform the OCP into a low dimensional NLP problem. However, they are still time-consuming. Particularly, when the number of the vehicles is too large, the computational cost will be unacceptable. For this purpose, the virtual motion camouflage (VMC) algorithm [21–23] is introduced into this work. Inspired by the biological motion known as the motion camouflage, the VMC algorithm can dramatically reduce the problem dimension and the computational cost. Some numerical simulations [22–24] suggest that its computational speed could be much faster than the pseudospectral methods. Motivated by these advantages, this paper employs virtual motion camouflage approach to develop cooperative trajectory planning algorithms.

For the cooperative trajectory planning of multi-UCAV, the objective is to generate dynamically feasible trajectories for UCAVs, which can guide them to the goals in the shortest time or distance, without collisions with obstacles or each other. To date, a number of theories and techniques have been developed to accomplish the cooperative tasks, including several collision avoidance techniques and time adjustment strategies [17, 25–30]. Bollino and Lewis [25] addressed the optimal path planning of UAVs in obstacle-rich environments and proposed a collision-free path planning for multi-UAV using optimal control techniques and pseudospectral methods. Kuwata and How [26] presented a cooperative distributed robust trajectory optimization approach, using RH-MILP with independent dynamics but coupled objectives and hard constraints. To improve the convergence rate, the virtual motion camouflage method was applied to the cooperative electronic combat air vehicles (ECAVs) [27] and unmanned aerial vehicle (UAV) formation control [28]. Reference [27] described how an interesting bioinspired motion strategy can be used to design real-time trajectories for cooperative electronic combat air vehicles. The constant speed motion camouflage law was developed to derive the feasible condition of a constant speed ECAVs and PT coherent mission, and its feasibility conditions were found. Reference [28] proposed a divide and conquer hierarchical approach in three levels to solve the UAV formation flight trajectory plan problem considering dynamics, state, and control variable inequality and equality constraints. These approaches mentioned above could generate collision-free trajectories, but the temporal cooperation was ignored. In contrast, Lian [17] introduced a differential flatness theory (DFT) based method to optimally formulate the cooperative path planning for multiagent dynamical systems considering spatial and temporal constraints. McLain and Beard [29] proposed the coordination variables (CV) and coordination function (CF) based strategy to achieve cooperative timing among teams of vehicles by coordinating the velocity and path length of each vehicle. But these approaches failed to deal with the dynamics constraints of vehicles, and the generated paths were not always flyable and smooth. Kaminer et al. [30] presented a general framework for coordinated control problem of multiple autonomous agents. On the basis of decoupling space and time in the problem formulation, it reduced the number of optimization parameters and made it easy to implement optimization in real time. However, the time coordination lays in the path following and the design of control laws in path following algorithms was much more difficult. Although the previous investigations have described several valuable strategies in the cooperative path planning, these methods cannot tackle the point-to-region cooperative trajectory planning for CA/GTA missions directly, which needs to integrate both the spatial and temporal constraints on the trajectory level.

To address the problems mentioned previously, a novel cooperative trajectory planning method for multi-UCAV in performing the CA/GTA missions is presented in this paper. Firstly, some constraints including individual and cooperative constraints are modeled. Particularly, an approximate allowable attack region is built for the critical terminal constraints. Then, after the multicriterion objective function is constructed, the cooperative trajectory planning problem is formulated as a cooperative trajectory optimal control problem (CTOCP). Owing to the temporal constraints, a notion of the virtual time is introduced and the VMC problem is reformulated in the virtual time domain. Inspired by VMC, DFT, and GPM algorithms, a new cooperative trajectory planning algorithm in an optimal control framework is proposed. The proposed approach is demonstrated by two typical CA/GTA examples, and the comparative experiments between GPM and VMC are carried out. The results show that the proposed approach is feasible, effective, and efficient.

The rest of the paper is organized as follows. In Section 2, the integrated model is set up. In Section 3, the problem is formulated as a CTOCP followed by a multicriteria objective function. Section 4 develops a novel cooperative trajectory planning algorithm based on virtual motion camouflage in virtual time domain, which can solve the problem efficiently. Section 5 presents several numerical examples, and finally the conclusions and future works are outlined in Section 6.

2. Modeling

2.1. Aircraft Model. The kinematic and dynamic model of vehicles is needed in the cooperative trajectory planning of multi-UCAV. In this work, a team of N_v homogeneous UCAVs is considered, each of which is described by the kinematic and dynamic model according to a full-blown three-degree of freedom (3-DOF) model as follows [31]:

$$\begin{gathered}\dot{x} = V\cos\gamma\cos\psi, \qquad \dot{y} = V\cos\gamma\sin\psi, \qquad \dot{z} = V\sin\gamma,\\ \dot{V} = g\left(n_x - \sin\gamma\right), \qquad \dot{\gamma} = \frac{g}{V}\left(n_z\cos\mu - \cos\gamma\right),\\ \dot{\psi} = \frac{g}{V\cos\gamma}n_z\sin\mu,\end{gathered} \tag{1}$$

where x, y, and z are the aircraft coordinates, that is, longitude, latitude, and height, V is the aircraft velocity, γ is the flight-path angle, ψ is the heading angle, μ is the roll angle, g is the gravity acceleration, and n_x and n_z are the longitudinal and normal components of the load factor, respectively.

For the optimal control problem, the state vector $\mathbf{x}$ and control vector $\mathbf{u}$ can be defined as

$$\mathbf{x} = \left\{ (x, y, z, V, \gamma, \psi) \mid \begin{array}{c} z_{\min} \le z \le z_{\max} \\ V_{\min} \le V \le V_{\max} \\ \gamma_{\min} \le \gamma \le \gamma_{\max} \\ \psi_{\min} \le \psi \le \psi_{\max} \end{array} \right\} \in \mathbf{X} \subset \mathbb{R}^6,$$
$$\mathbf{u} = \left\{ (\mu, n_x, n_z) \mid \begin{array}{c} \mu_{\min} \le \mu \le \mu_{\max} \\ n_{x,\min} \le n_x \le n_{x,\max} \\ n_{z,\min} \le n_z \le n_{z,\max} \end{array} \right\} \in \mathbf{U} \subset \mathbb{R}^3. \tag{2}$$

2.2. Allowable Attack Region Model. For the point-to-region trajectory planning problem, the allowable attack regions (AARs) of targets are defined as the areas where weapon delivery operations can be effectively performed by UCAVs. Therefore, in order to plan accurate and optimal attack trajectories, the AARs and the delivery parameters need to be obtained. The AARs of the ith target TAR_i, denoted as $R(\mathrm{TAR}_i)$, are such sets of all feasible release states that TAR_i can be effectively attacked whenever the aircraft belongs to those state sets. When n_v ($n_v \ge 2$) UCAVs are assigned to attack the same target TAR_i cooperatively, there will be n_v AARs in $R(\mathrm{TAR}_i)$; that is, $R(\mathrm{TAR}_i) = \bigcup_j^{n_v} \mathrm{AAR}_j$. Each AAR_j can be formulated as an abstract 6-dimensional space [32]:

$$\mathrm{AAR}_j = \{x, y, z, V, \gamma, \psi\} \subset \mathbb{R}^6. \tag{3}$$

Obviously, AAR_j is a high-dimensional nonlinear space, which is difficult to handle. By presetting an appropriate weapon release speed $\widehat{V}_r$ and the flight-path angle $\widehat{\gamma}_r$ based on estimating the weapon impact effects and destruction requirements to the target and predetermining release heading $\widehat{\psi}_r$, AAR_j can be reduced to a 3-dimensional space as

$$\mathrm{LAR}_{\mathrm{sp}}^j \left(\mathrm{TAR}_i, \left[\widehat{V}_r, \widehat{\gamma}_r\right]\right) = \left\{ \left(x, y, z, \widehat{V}_r, \widehat{\gamma}_r, \widehat{\psi}_r\right) \mid \begin{array}{l} (x, y, z) \in \mathrm{LAR}_{\mathrm{sp}}^j \left(\mathrm{TAR}_i, \left[\widehat{V}_r, \widehat{\gamma}_r, \widehat{\psi}_r\right]\right) \\ \widehat{\psi}_r = \text{azimuth of } \mathrm{TAR}_i \text{ relative to position } (x, y, z) \end{array} \right\}. \tag{4}$$

In the point-to-region trajectory planning, weapon delivery points (WDPt) as terminals of trajectories need to be included in the AARs, that is, meeting terminal constraints [33]. The formula can be denoted as $\mathrm{WDPt}_j \in \mathrm{AAR}_j$; that is,

$$\left|x_A^j - x_f^j\right| \le \Delta x, \qquad \left|y_A^j - y_f^j\right| \le \Delta y, \qquad \left|z_A^j - z_f^j\right| \le \Delta z, \tag{5}$$

where (x_A^j, y_A^j, z_A^j) are the coordinates of the center of the AAR_j, (x_f^j, y_f^j, z_f^j) are the coordinates of WDPt_j, and $(\Delta x, \Delta y, \Delta z)$ are the thresholds of errors.

2.3. No-Fly Zone Model. In the battlefield environment, the no-fly zone (NFZ) is an area where vehicles are not permitted to fly over, due to the presence of military restrictions (e.g., armed enemies and the missile killing range), the physical obstacles (e.g., mountains and buildings within the natural and urban environment, resp.), and civil restrictions mainly due to safety reasons (e.g., densely populated areas and severe weather condition zones).

It is complex and unnecessary to describe a NFZ's exact shape and size. In this work, the p-norm method [34] is used to mathematically model the shapes of the NFZs, given by

$$h(x, y, z) = \left\| \left(\frac{x - x_c}{k_1 + b_s}, \frac{y - y_c}{k_2 + b_s}, \frac{z - z_c}{k_3 + b_s} \right) \right\|_p^p - k_4^p, \tag{6}$$

$$\|(x, y, z)\|_p = \left(|x|^p + |y|^p + |z|^p\right)^{1/p}, \quad p \in \mathbf{N}, \tag{7}$$

where (x_c, y_c, z_c) indicates the location of the geometric center of the NFZ, $h(x, y, z)$ is the distance between a point (x, y, z) and the boundary of the NFZ, while $k_1 \sim k_4$ are the constant parameters chosen to define the size of the NFZ, and b_s represents the width of a safe buffer which can effectively expand the NFZ boundary by an amount that accounts for the size of the vehicle and improve the robustness of plans. By varying parameters $(p, k_1 \sim k_4)$, one can easily model a number of generic shapes (see Figure 1). And any NFZ can be approximately modeled by fitting one of those shapes around it.

Accordingly, the above NFZs can be expressed by the following path constraints in the OCP formulation as

$$h_n(x, y, z) \ge 0, \quad n = 1, 2, \ldots, N_{\mathrm{NFZ}}, \tag{8}$$

where h_n represents the nth NFZ and N_{NFZ} is the total of NFZs. However, (8) is not well scaled. If a large p is chosen or the vehicle is far from the NFZ, $h_n(x, y, z)$ can produce very large numbers; hence, for computational efficiency, the path constraint is scaled by the natural logarithm function as follows:

$$h_n(x, y, z) = \ln\left(\frac{1}{(k_4^n)^{p_n}} \left(\left(\frac{x - x_c^n}{k_1^n + b_s} \right)^{p_n} + \left(\frac{y - y_c^n}{k_2^n + b_s} \right)^{p_n} + \left(\frac{z - z_c^n}{k_3^n + b_s} \right)^{p_n} \right) \right) \ge 0. \tag{9}$$

2.4. Cooperative Constraint Model. In order to make the UCAVs arrive in the AARs of targets safely in an expected

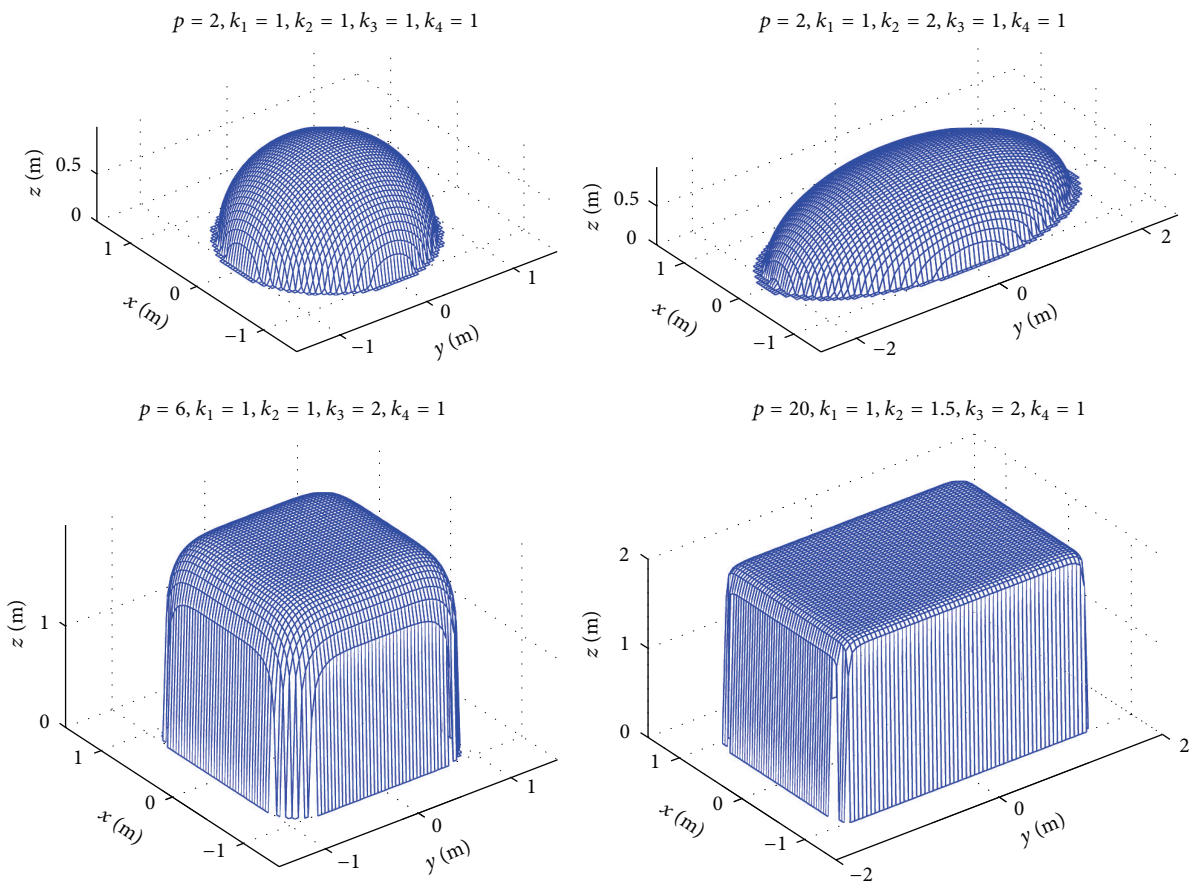

Figure 1: Several shapes generated from (6).

time sequence, cooperative trajectories should satisfy the following constraints.

2.4.1. Spatial Constraints. During the mission, multi-UCAV should maintain a safe distance to guarantee them not to collide with each other. The model can be denoted as

$$\left\|\boldsymbol{\rho}^j(t_i) - \boldsymbol{\rho}^k(t_i)\right\|_2 \geq \max\left(d^j_{\text{safe}}, d^k_{\text{safe}}\right), \quad \forall j \neq k, \quad j,k = 1,2,\ldots,N_v, \tag{10}$$

where $\boldsymbol{\rho}^j(t_i) = \{x^j(t_i), y^j(t_i), z^j(t_i)\}$ is the spatial position of each UCAV$_j$ at the time t_i, d^j_{safe} is the predetermined minimum safety radius of UCAV$_j$ (based on the vehicle size, maneuver agility, etc.), and N_v is the total of UCAVs.

2.4.2. Temporal Constraints. The temporal constraints include the simultaneous arrival constraint and sequencing constraint, which are described as

$$t^j_f + \Delta_{jk} - t^k_f \leq 0, \quad \forall j \neq k, \quad j,k = 1,2,\ldots,N_v, \tag{11}$$

where t^j_f is the terminal time of each UCAV$_j$ and Δ_{jk} is the arrival interval between UCAV$_j$ and UCAV$_k$. For the simultaneous arrival constraint, $\Delta = 0$, and for the sequencing constraint, Δ is the plus fixed quantity. Equation (11) is of the general form $f_T(t^1_f, \ldots, t^{N_v}_f) \leq 0$.

3. Problem Formulation

3.1. Objective Function. The objective function of the entire team is a sum of each individual cost, which is a multicriterion objective function, and each criterion could compete with each other as follows:

$$J = \min \sum_{j=1}^{N_v} J^j = \min \sum_{j=1}^{N_v} \left(w^j_t J^j_t + w^j_p J^j_{\text{prd}} + w^j_r J^j_{\text{rob}}\right), \tag{12}$$

and the criterions can be, respectively, defined as

$$J^j_t = \int_t dt = t^j_f - t^j_0, \tag{13}$$

$$J^j_{\text{prd}} = \int_t \text{PRD}^j(t) = \int_t \left(1 - \prod_{r=1}^{n_r}\left(1 - P^j_d(t,r)\right)\right), \tag{14}$$

$$J^j_{\text{rob}} = \int_t R^j(t) = \int_t \sum_{n=1}^{N_{\text{NFZ}}} w^{n,j}_r \left(e^{e^{-h_n}} - 1\right), \tag{15}$$

where t_0^j and t_f^j denote the initial and terminal time of UCAV_j. The first term, J_t^j, denotes the total fight time of UCAV_j. The second term, J_{prd}^j, denotes the detection-probability of the n_r-radar system to UCAV_j at the time t, which describes the threat risk criterion of UCAV_j as follows:

$$\mathrm{PRD}^j(t) = 1 - \prod_{r=1}^{n_r}\left(1 - P_d^j(t,r)\right), \tag{16}$$

where $P_d^j(t,r)$ is the model of the radar detection probability between the trajectory point of UCAV_j at the time t and the rth radar [35]. The final term, J_{rob}^j, guarantees the robustness of the vehicle collision avoidance against the model imprecision, disturbing in the battlefield and operating errors that could otherwise cause vehicles to collide with obstacles or other vehicles. The robustness cost is defined as

$$R^j(t) = \sum_{n=1}^{N_{\mathrm{NFZ}}} w_r^{n,j}\left(e^{e^{-h_n}} - 1\right), \tag{17}$$

where $w_r^{n,j}$ are weights that are incremented to increase the maneuver robustness when the trajectory of a vehicle passes in close proximity to an obstacle or another vehicle, which can be chosen by the method presented by Hurni et al. [36].

As can be seen, the individual objective function J^j is defined by the weighted sum of the three separate running cost terms with appropriate weighting factors w_t^j, w_p^j, and w_r^j. The three criteria (13)–(15) represent different physical meanings, and they are difficult to be compared directly. Hence the selection of these weighting factors is a skilled technique. In the experimentations, the multi-objective fuzzy optimization method proposed by Wang et al. [37] is employed. The method includes two main steps: (a) normalizing each single objective function and (b) solving the membership function about each criterion by using fuzzy distribution function.

3.2. Cooperative Trajectory Planning Problem Formulation. After establishing the above models, the cooperative trajectory planning problem is formulated in this section. The problem under consideration is a cooperative scheme, consisting of N_v homogeneous UCAVs. According to the system equations (1), the general form of the system for UCAV_j is given by

$$\dot{\mathbf{x}}^j(t) = f^j\left[\mathbf{x}^j(t), \mathbf{u}^j(t), t\right], \quad j = 1, \ldots, N_v. \tag{18}$$

As stated above, to obtain optimal or suboptimal cooperative trajectories, the cooperative trajectory planning for the CA/GTA missions can be formulated as a cooperative trajectory optimal control problem (CTOCP).

Problem 1 (CTOCP). Find the trajectories, which drive the system from given initial conditions to desired final conditions over time horizons $[t_0, t_f]$, while the cooperative objective function is minimized as

$$\begin{aligned}\min \quad J &= \sum_{j=1}^{N_v} J^j(\mathbf{x}, \mathbf{u}) \\ &= \sum_{j=1}^{N_v}\left[w_t^j\left(t_f^j - t_0^j\right) + w_p^j\int_{t_0^j}^{t_f^j}\left(1 - P_d^j(t,r)\right)dt \right. \\ &\quad \left. + w_r^j\int_{t_0^j}^{t_f^j}\sum_{n=1}^{N_{\mathrm{NFZ}}} w_r^{n,j}\left(e^{e^{-h_n}} - 1\right)dt\right],\end{aligned} \tag{19}$$

subject to the system equation (18) and the boundary constraints (i.e., the initial and terminal states (5))

$$\begin{aligned}&\Phi\left[\mathbf{x}^j\left(t_0^j\right), \mathbf{u}^j\left(t_0^j\right), t_0^j, \mathbf{x}^j\left(t_f^j\right), \mathbf{u}^j\left(t_f^j\right), t_f^j\right] = 0, \\ &\qquad \forall j = 1, 2, \ldots, N_v,\end{aligned} \tag{20}$$

and several inequality and equality constraints, the individual and cooperative constraints, including the state and control vectors (2) and (9)–(11), are denoted as

$$\begin{aligned}&\delta^j\left[\mathbf{x}^j(t), \mathbf{u}^j(t), t\right] \le 0, \\ &\varphi^j\left[\mathbf{x}^j(t), \mathbf{u}^j(t), \mathbf{x}^k(t), \mathbf{u}^k(t), t\right] \le 0, \\ &f_T^j\left(t_f^j, t_f^k\right) \le 0, \quad \forall j \ne k, \ j, k = 1, 2, \ldots, N_v.\end{aligned} \tag{21}$$

4. Virtual Motion Camouflage Based Cooperative Trajectory Planning

To tackle the cooperative trajectory planning for CA/GTA missions, an efficient virtual motion camouflage based planning method is proposed for numerically solving the CTOCP, which combines with the benefits of several other classical trajectory generation techniques, including DFT, GPM, and NLP. Correspondingly, this task contains three primary steps. The first is to determine outputs by VMC and DFT in the virtual time domain, such that the dynamics system can be mapped to a lower-dimensional output space. Then, GPM is used to discretize the outputs. Finally, the system is transformed into a NLP problem and the sequential quadratic programming (SQP) is used to solve the NLP to minimize the cost and subject to constraints in output space.

4.1. Virtual Motion Camouflage and Problem Formulation in the Output Space

4.1.1. Virtual Motion Camouflage. Inspired by mating hoverflies, Srinivasan and Davey [38] described a new form of the stealth strategy which is the so-called motion camouflage (MC). MC involves two moving objects, a prey and an aggressor, and occurs when the aggressor conceals its motion

(i.e., maintains a constant bearing in the prey's coordinates), except the inevitable size change, as viewed by the moving prey. Here the MC concept is introduced into the optimal trajectory planning and is called virtual motion camouflage (VMC) [21–23] because the "prey" is a virtual one. In the VMC framework, the aggressor trajectory (i.e., the aggressor position vector) $\boldsymbol{\rho}_a(t) \in \mathbb{R}^{n_a}$ is confined by the virtual prey trajectory (VPT) $\boldsymbol{\rho}_p(t) \in \mathbb{R}^{n_a}$, the selected reference point $\boldsymbol{\rho}_{\text{ref}}(t) \in \mathbb{R}^{n_a}$, and the path control parameter (PCP) $\nu(t) \in \mathbb{R}$ as follows:

$$\boldsymbol{\rho}_a(t) = \boldsymbol{\rho}_{\text{ref}} + \nu(t)\left(\boldsymbol{\rho}_p(t) - \boldsymbol{\rho}_{\text{ref}}\right). \tag{22}$$

The reference point is considered fixed over time, so the derivatives of the trajectory can be described as

$$\begin{aligned}\dot{\boldsymbol{\rho}}_a(t) &= \dot{\nu}(t)\left(\boldsymbol{\rho}_p(t) - \boldsymbol{\rho}_{\text{ref}}\right) + \nu(t)\dot{\boldsymbol{\rho}}_p(t),\\ \ddot{\boldsymbol{\rho}}_a(t) &= \ddot{\nu}(t)\left(\boldsymbol{\rho}_p(t) - \boldsymbol{\rho}_{\text{ref}}\right) + \nu(t)\ddot{\boldsymbol{\rho}}_p(t) + 2\dot{\nu}(t)\dot{\boldsymbol{\rho}}_p(t).\end{aligned} \tag{23}$$

From [23], it can be known that when the proposed VMC suboptimal trajectory design method is used, the complexity of the problem can be reduced by $(n_{sv} + m_{cv})$ times from the collocation method or n_{sv} times from the differential inclusion, where n_{sv} and m_{cv} are the numbers of the state variables and the control variables. In VMC framework, if the dimension of the position vector $\mathbf{x}_a(t)$ is one (i.e., $n_a = 1$), the dimension of the problem is the same as that of the differential inclusion method. Otherwise, when $n_a > 1$, the reference point can be fixed or regarded as a parameter to be optimized, whereas VPT can be predefined or predetermined by the initial and terminal conditions of the aggressor trajectory. Thus, the dimension of the problem is lowered from n_a to one, such that the solving speed can increase.

4.1.2. VMC Problem Formulation in Virtual Time Domain. Obviously, the time factor of trajectories is an argument of the state and control. To deal with temporal constraints and achieve the time cooperation of multi-UCAV, the time along the trajectories should be considered separately. Therefore, the independent intermediate variable (called virtual time here, $\bar{t} \in [0, 1]$) is introduced and described as

$$\bar{t} = \frac{(t - t_0)}{(t_f - t_0)}, \tag{24}$$

such that the trajectories can be generated in the virtual time domain from $\bar{t}_0 = 0$ to $\bar{t}_f = 1$.

For UCAVs, which are required to take off at the same time, it can be assumed that the initial time of all UCAVs is zero ($t_0 = 0$). Thus, the terminal time t_f can be written as $t_f = t/\bar{t}$. That is, t_f denotes the ratio between the true time variable and the newly defined virtual time variable. To coordinate the arrival time of all UCAVs, the terminal time can be defined as an argument to be optimized in the dynamical system, designated as T_f. Then, the following relationship between the virtual time domain and true time domain can be obtained for an arbitrary variable χ as follows:

$$\begin{aligned}\chi'(\bar{t}) &= \frac{d\chi(t)}{d\bar{t}} = \frac{T_f d\chi(t)}{dt} = T_f\dot{\chi}(t),\\ \chi''(\bar{t}) &= \frac{d\chi'(\bar{t})}{d\bar{t}} = \frac{T_f d\chi'(\bar{t})}{dt} = \frac{T_f d\left(T_f\dot{\chi}(t)\right)}{dt} = T_f^2\ddot{\chi}(t).\end{aligned} \tag{25}$$

Particularly, the derivative of the speed variable can be denoted as

$$\begin{aligned}V(\bar{t}) &= \sqrt{(x')^2 + (y')^2 + (z')^2}\\ &= T_f\sqrt{\dot{x}^2 + \dot{y}^2 + \dot{z}^2} = T_f V(t),\end{aligned} \tag{26}$$

where the superscript "$'$" represents the derivative with respect to the virtual time.

According to (18) and (24), the system equations can be rearranged as

$$\begin{aligned}\mathbf{x}'^j(\bar{t}) &= T_f\dot{\mathbf{x}}^j(t) = T_f f^j\left[\mathbf{x}^j(t), \mathbf{u}^j(t), t\right]\\ &= g^j\left[\mathbf{x}^j(\bar{t}), \mathbf{u}^j(\bar{t}), T_f^j\right],\\ T_f'^j &= 0, \quad j = 1, \ldots, N_v.\end{aligned} \tag{27}$$

Hence, the Problem 1 can be reformulated in virtual time domain (VTD) as follows.

Problem 2 (CTOCP-VTD). Minimize the cooperative objective function (19) of all UCAVs represented with respect to the new independent variable $\bar{t}$ as

$$\begin{aligned}\min \quad J &= \sum_{j=1}^{N_v} J^j\left(\mathbf{x}, \mathbf{u}, T_f^j\right)\\ &= \sum_{j=1}^{N_v}\left[w_t^j T_f^j + w_p^j\int_0^1 \text{PRD}^j(\bar{t})\,d\bar{t}\right.\\ &\qquad \left. + w_r^j\int_0^1 R^j(\bar{t})\,d\bar{t}\right],\end{aligned} \tag{28}$$

subject to the system equations (27), and the boundary constraints (20), written as

$$\phi\left[\mathbf{x}^j(0), \mathbf{u}^j(0), \mathbf{x}^j(1), \mathbf{u}^j(1), T_f^j\right] = 0, \tag{29}$$

Meanwhile satisfying the inequality and equality constraints (21) and additional temporal constraints as follows:

$$\begin{aligned}&\delta^j\left[\mathbf{x}^j(\bar{t}), \mathbf{u}^j(\bar{t}), T_f^j\right] \le 0,\\ &\varphi^j\left[\mathbf{x}^j(\bar{t}), \mathbf{u}^j(\bar{t}), \mathbf{x}^k(\bar{t}), \mathbf{u}^k(\bar{t}), T_f^j, T_f^k\right] \le 0,\\ &f_T^j\left(t_f^j, t_f^k\right) \le 0, \quad \forall j \ne k,\ j, k = 1, 2, \ldots, N_v.\end{aligned} \tag{30}$$

From (1), it can be clearly known that the dynamics system under consideration is a higher-dimensional space system. Due to the complexity in solving this type of the problem, the VMC based method is used to lower the system dimension and the state and control vectors can be related by the differential flatness theory based method [39]. In this system, the state vector $\mathbf{x} \in \mathbb{R}^6$ can be separated into two parts: the trajectory position (e.g., spatial trajectory) $\boldsymbol{\rho}_a = [x, y, z] \in \mathbb{R}^3$ and the corresponding state rate $\boldsymbol{\rho}_r = [V, \psi, \gamma] \in \mathbb{R}^3$, by which the trajectory position in virtual time domain and the terminal time T_f can be defined as the flat output vector

$$\vartheta = \left[\boldsymbol{\rho}_a(\bar{t}), T_f\right] = \left[x(\bar{t}), y(\bar{t}), z(\bar{t}), T_f\right]^T. \tag{31}$$

Thus, the original state vector $\mathbf{x}$ and control vector $\mathbf{u}$ can be recovered from the flat outputs and their derivatives as

$$\begin{aligned} \mathbf{x} &= \alpha\left(\vartheta, \vartheta', \vartheta''\right) = \alpha\left(\boldsymbol{\rho}_a, \boldsymbol{\rho}_a', \boldsymbol{\rho}_a'', T_f\right), \\ \mathbf{u} &= \beta\left(\vartheta, \vartheta', \vartheta''\right) = \beta\left(\boldsymbol{\rho}_a, \boldsymbol{\rho}_a', \boldsymbol{\rho}_a'', T_f\right). \end{aligned} \tag{32}$$

According to (1), the relation of the state vector and control vector in the VTD is described as follows:

$$\begin{aligned} V &= \sqrt{(x')^2 + (y')^2 + (z')^2}, \\ \psi &= \arctan\left(\frac{y'}{x'}\right), \\ \gamma &= \arctan\left(\frac{z'}{\sqrt{(x')^2 + (y')^2}}\right), \\ n_x &= \frac{V'}{\left(T_f^2 g\right)} + \sin\gamma, \\ n_z &= \frac{\sqrt{\left(V\gamma' + T_f^2 g\cos\gamma\right)^2 + \left(V\psi'\cos\gamma\right)^2}}{T_f g}, \\ \mu &= \arctan\left(\frac{V\psi'\cos\gamma}{\left(V\gamma' + T_f^2 g\cos\gamma\right)}\right). \end{aligned} \tag{33}$$

In the VMC framework, the trajectory position $\boldsymbol{\rho}_a$ can be defined as the aggressor position vector. As described above, the state and the control variables of the dynamics system can be recovered from the flat outputs. Hence, according to (22), these variables are also functions of the PCP, the predefined virtual prey motion, the reference point, and their corresponding derivatives. Once the predefined virtual prey motion and the reference point are selected, the system of cooperative trajectory planning of UCAVs, including the objective function and the constraints, is mapped to a lower-dimensional output space (here, the dimension is one). Obviously, the dynamic constraints of this system (27) can be automatically satisfied. Therefore, the Problem 2 can be redefined as follows.

Problem 3 (CTOCP-VTD in the output space). Consider

$$\begin{aligned} \min \quad J(v) &= \sum_{j=1}^{N_v} J^j\left(v^j\right) \\ &= \sum_{j=1}^{N_v}\Big[\left(v^j, v'^j, \ldots, T_f^j\right) \\ &\qquad + \int_0^1 f^j\left(v^j, v'^j, \ldots, \bar{t}\right) d\bar{t}\Big] \\ \text{s.t.} \quad & \phi^j\left[v^j(0), v^j(1), T_f^j\right] = 0, \\ & \delta^j\left(v^j, v'^j, \ldots,\right) \le 0, \\ & \varphi^j\left(v^j, v'^j, \ldots, v^k, v'^k, \ldots\right) \le 0, \\ & f_T^j\left(t_f^j, t_f^k\right) \le 0, \ \forall j \ne k, \ j, k = 1, 2, \ldots, N_v. \end{aligned} \tag{34}$$

4.2. Collocation Using Gauss Pseudospectral Method. In order to solve the Problem 3 through a NLP algorithm, the PCP history $v(\bar{t})$ should be discretized into $c = 0, 1, \ldots, N_c$, $N_c + 1$ nodes, with $v_0 = v(\bar{t}_0)$ and $v_{N_c+1} = v(\bar{t}_{N_c+1})$. In this paper, GPM is selected as the discretization method [12], which is an orthogonal collection method where the collocation points are the Legendre-Gauss (LG) points. Similar to other pseudospectral methods, a finite basis of global interpolating polynomials is used to approximate the state and control space at a set of discretization nodes in the GPM and then the optimal control equations can be transformed into nonlinear algebra equations, such that the OCP can be solved by a NLP algorithm.

The standard interval considered here is denoted as $\tau \in [-1, 1]$. By using a linear transformation, the virtual time $\bar{t}$ can be expressed as a function of τ via

$$\bar{t} = \frac{\left[\left(\bar{t}_f - \bar{t}_0\right)\tau + \left(\bar{t}_f + \bar{t}_0\right)\right]}{2} = \frac{(\tau + 1)}{2}. \tag{35}$$

Let $\tau_1 < \cdots < \tau_{N_c}$ be collocation points in $(-1, 1)$ and $\tau_0 = -1, \tau_f = 1$. The time history of the approximated PCP at the N_c LG points is given by

$$v(\tau) \approx \bar{v}(\tau) = \sum_{c=0}^{N_c} v(\tau_c) L_c(\tau), \tag{36}$$

where $v(\tau_c)$ is an approximant at the node τ_c and the base function $L_c(\tau)$ is the Lagrange interpolating polynomial of degree N_c, expressed as

$$L_c(\tau) = \prod_{l=0,\, l \ne c}^{N_c} \frac{\tau - \tau_l}{\tau_c - \tau_l}, \quad c = 0, 1, \ldots, N_c, \tag{37}$$

satisfying the isolation property

$$L_c(\tau_l) = \delta_{cl} = \begin{cases} 1, & c = l, \\ 0, & c \ne l. \end{cases} \tag{38}$$

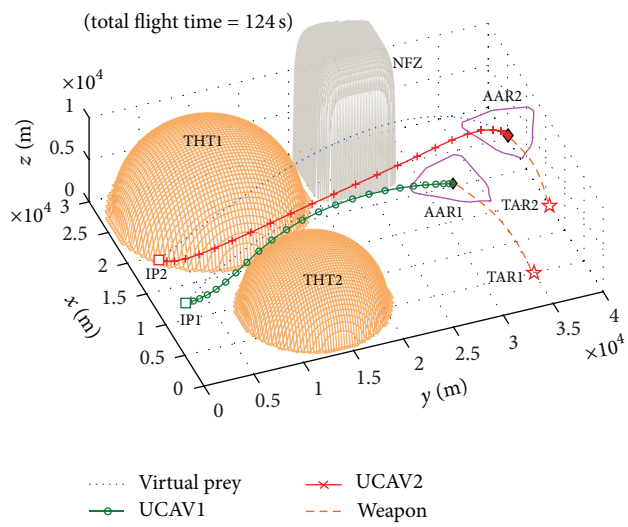

FIGURE 2: Two collision-free UCAV trajectories with arriving simultaneously.

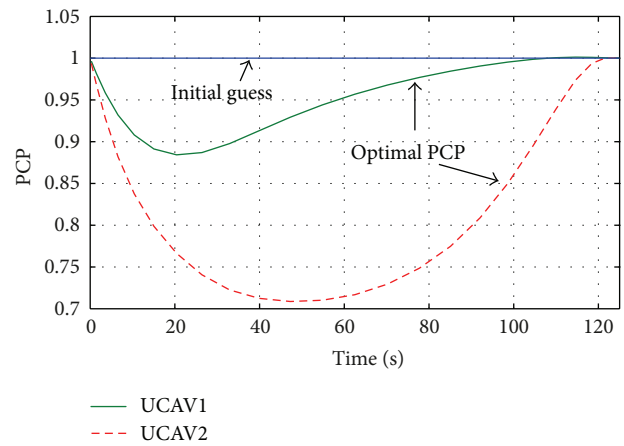

FIGURE 3: PCP histories of two UCAVs.

And the endpoint can be approximated according to the following formula:

$$v(\tau_f) \approx \bar{v}(\tau_f) = \bar{v}(\tau_0) + \frac{\bar{t}_f - \bar{t}_0}{2} \times \sum_{c=1}^{N_c} w_c f[\bar{v}(\tau_c), \tau_c], \tag{39}$$

where τ_c $(c = 1, \ldots, N_c)$ are the LG points and the variables ω_c are the LG weights given by

$$w_c = \int_{-1}^{1} L_c(\tau)\, d\tau. \tag{40}$$

The derivative of the state can be approximated as the exact derivative of the interpolating polynomial. Evaluating the derivative at the LG points results in

$$\begin{aligned} v'(\tau_l) \approx \bar{v}'(\tau_l) &= \sum_{c=0}^{N_c} v(\tau_c) L_c'(\tau_l) \\ &= \sum_{c=0}^{N_c} v(\tau_c) D_{lc}, \quad l = 1, \ldots, N_c, \end{aligned} \tag{41}$$

where $\mathbf{D} = [D_{lc}] \in \mathbb{R}^{N_c \times (N_c+1)}$ is a differential matrix and can be offline determined as

$$\begin{aligned} D_{lc} &= \sum_{k_1=0}^{N_c} \frac{\prod_{k_2=0, k_2 \neq c, k_1}^{N_c} (\tau_l - \tau_{k_2})}{\prod_{k_2=0, k_2 \neq c}^{N_c} (\tau_c - \tau_{k_2})}, \\ & l = 1, \ldots N_c, \quad c = 0, \ldots, N_c. \end{aligned} \tag{42}$$

The discretized states and controls satisfying the vehicle dynamics can be computed by ensuring that equation

$$\sum_{c=0}^{N_c} v(\tau_c) D_{lc} - \frac{\bar{t}_f - \bar{t}_0}{2} f[v(\tau_l), \tau_l] = 0, \quad l = 1, \ldots, N_c. \tag{43}$$

As described above, the continuous OCP can be transformed to the discretized NLP problem. The parameters to be optimized are the PCP nodes $\mathbf{v} = [v_c]_{c=0,1,\ldots N_c+1}$. When the prey motion $\boldsymbol{\rho}_{p,c}$ is equal to the aggressor motion $\boldsymbol{\rho}_{a,c}$ for $c = 0, N_c + 1$, one can assume that $v_0 = v_{N_c} = 1$, so the boundary conditions are no longer considered. And the discretized NLP problem can be denoted as follows.

Problem 4 (CTP-NLP). Its standard form is denoted as

$$\begin{aligned} \min\ J(\mathbf{v}) &= \sum_{j=1}^{N_v} J^j(\mathbf{v}^j) \\ &= \sum_{j=1}^{N_v} \Bigg[\Phi^j\left[\mathbf{v}^j, T_f^j\right] \\ &\qquad + \frac{\bar{t}_f - \bar{t}_0}{2} \sum_{c=1}^{N_c} f^j\left(\mathbf{v}^j, T_f^j\right) \omega_c \Bigg] \\ \text{s.t.}\quad & \delta_l^j\left[\mathbf{v}^j\right] \leq 0, \quad l = 1, \ldots, N_c, \\ & \varphi^j\left[\mathbf{v}^j, \mathbf{v}^k\right] \leq 0, \\ & f_T^j\left(t_f^j, t_f^k\right) \leq 0, \quad \forall j \neq k,\ j, k = 1, 2, \ldots, N_v, \end{aligned} \tag{44}$$

where $v^j = [v_c^j]_{c=1,\ldots N_c}$ is the vector form of the discretized PCP.

Then the resulting Problem 4 can be solved through well-developed algorithms, such as the SQP algorithm. In this paper, TOMLAB/SNOPT software toolbox is chosen due to its advantages on solution effectiveness for the large-scale NLP problems [40].

4.3. Convergence and Initial Guess. As analyzed in [41], the GPM exhibits global convergence properties in many

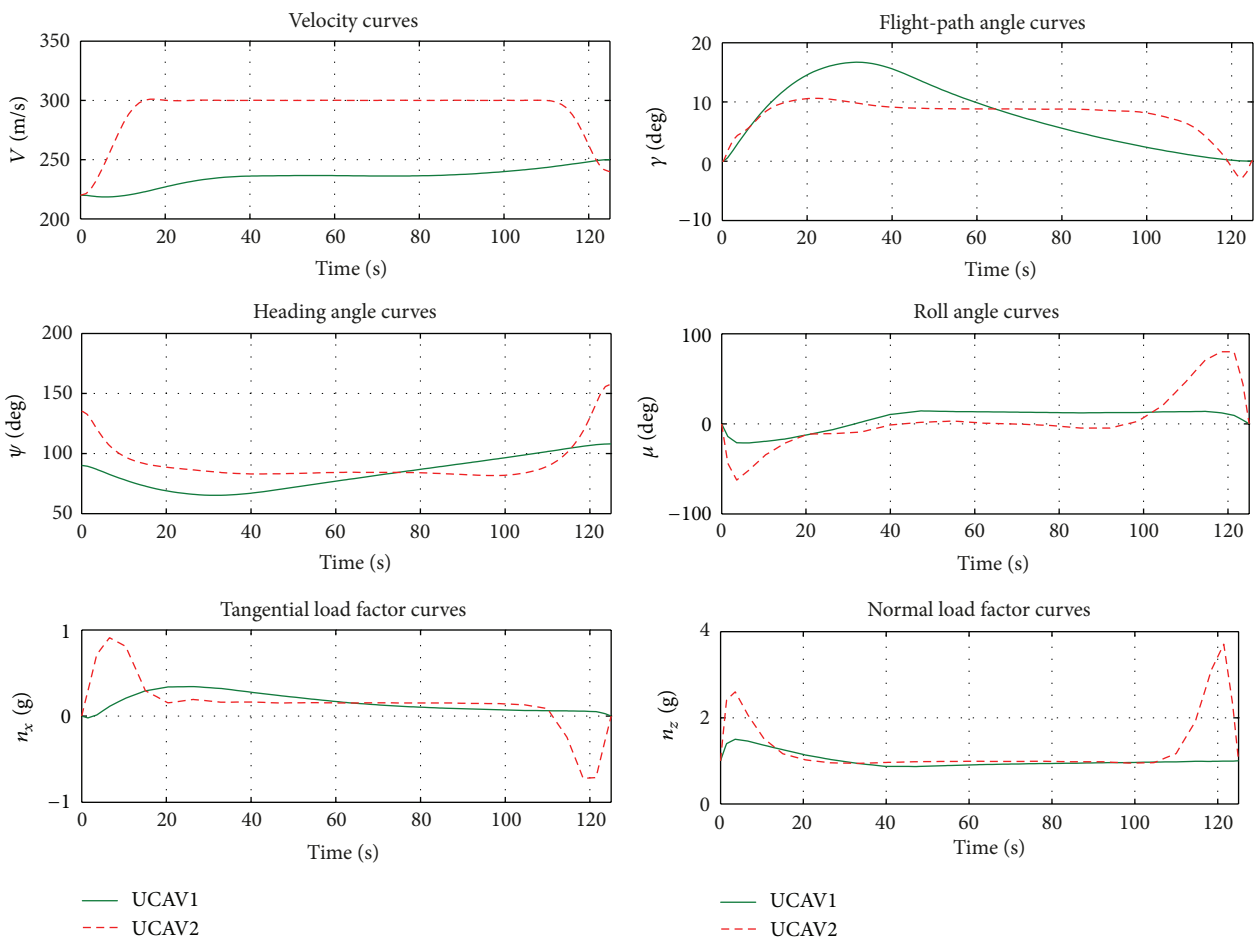

Figure 4: Example 1—state and control time histories of two UCAVs.

applications. In addition, the convergence of the virtual motion camouflage has been proved by Xu et al. [21, 23], in which [23] showed that if the problem was only one-dimensional, the VMC based trajectory design method could converge to the optimal solution, but when the problem was multi-dimensional and highly nonlinear, the result might be suboptimal in the full solution space, and [21] showed that the VMC framework together with the pseudospectral discretization method could converge to the optimal solution.

By Introducing elastic programming concept and some advances in both mathematical programming techniques and pseudospectral methods, Ross and Gong [42] designed a guess-free trajectory optimization algorithm. These advances have the effect of eliminating the guessing problem in the trajectory optimization, which has been used in the current GPM algorithm. In the proposed VMC method, the motion of the virtual prey and a reference point are guessed. However, both of them have direct physical relation to the problem. Typically the virtual prey motion is selected according to the boundary conditions and a proper guess is not a difficult task [23]. In this paper, the trivial guess for the reference point can be the initial point (IP), and an initial guess of $v_c = 1$ is chosen for $c = 1, \ldots, N_c$. The virtual prey motion is defined as a 2-order curve, determined by the initial and terminal conditions.

5. Numerical Examples

The basic ideas presented in this paper are illustrated in the following three examples. The specific vehicle platform used in simulations is the Storm shadow UCAV. Its relevant parameters are all taken from [43], summarized in Table 1.

The experimental test environment is a rectangle area of $30 \times 40\,\text{km}^2$, as shown in Figure 2, where the NFZ1 caused by the severe weather condition is modeled as a cuboid with infinite altitude, and the NFZs caused by enemy threats are modeled as two hemispheres, denoted as THT1 and THT2. According to Figure 1, the shape parameters can be set as follows: for the NFZ1, $k_1 = k_2 = k_3 = k_4 = 1$, $p = 2$, and the length of a side is set as 8 km; for THT1 and THT2, $k_1 = k_2 = k_4 = 1$, $k_3 = 2$, $p = 6$, and the radius of the threats can be set as 7 km and 9 km, respectively. In order to avoid contact, a safe buffer b_s ($b_s = 200$ m) is added around the outside edge of each obstacle/threat boundary. All the results presented below are generated using TOMLAB/SNOPT software toolbox on a

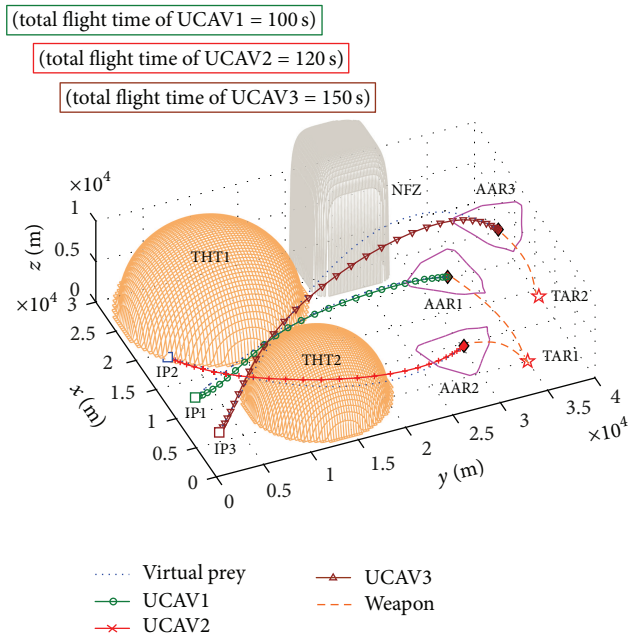

Figure 5: Three collision-free UCAV trajectories with arriving in sequence.

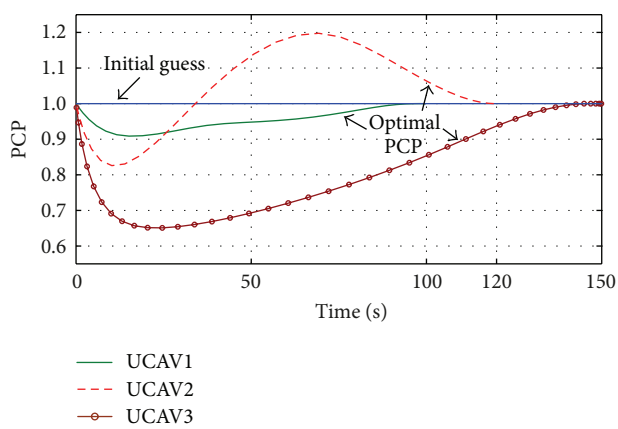

Figure 6: Path control parameter histories of three UCAVs.

2.4 GHz CPU and 2 G RAM computer running Windows XP and MATLAB R2009b. Table 2 summarizes the parameters used in the algorithm. To simplify the problem, the same weight coefficients for the objective function of each UCAV are set, and it is assumed that the target assignment is already completed before.

5.1. Example 1: Cooperative Trajectories of Two UCAVs Arriving Simultaneously. In this example, two UCAVs cooperatively attack two stationary ground targets while avoiding a series of static obstacles/threats detected and collision with each other en route and meeting aircraft dynamical constraints, especially simultaneous arrival constraint. UCAV1 and UCAV2 start at each initial point, that is, IP1 (10, 2, 2) km and IP2 (17, 2, 2) km. Then they fly into the AARs of

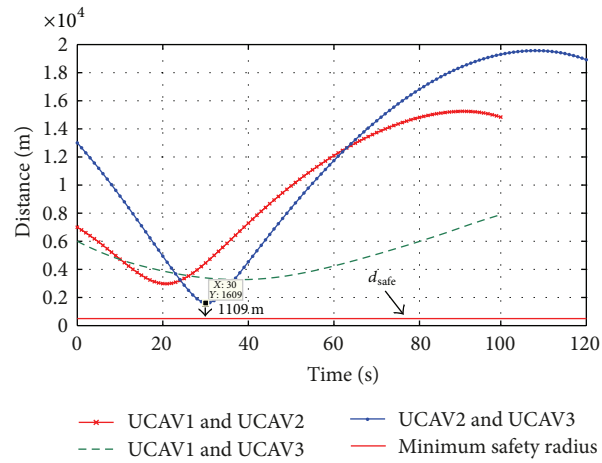

Figure 7: Distance between each pair of UCAVs.

two targets, TAR1 (4, 34, 0) km and TAR2 (13, 40, 0) km, respectively. The initial remaining three states and control inputs of each UCAV are preset as $\boldsymbol{\rho}_{r,0}^1 = (V_0^1, \gamma_0^1, \psi_0^1) = (220\,\text{m/s}, 0^\circ, 90^\circ)$, $\boldsymbol{\rho}_{r,0}^2 = (V_0^2, \gamma_0^2, \psi_0^2) = (220\,\text{m/s}, 0^\circ, 140^\circ)$, and $\mathbf{u}_0^1 = \mathbf{u}_0^2 = (\mu_0, n_{x,0}, n_{z,0}) = (0^\circ, 0\,\text{g}, 1\,\text{g})$, and the terminal remaining three states of each UCAV are predetermined as $\boldsymbol{\rho}_{r,f}^1 = (\widehat{V}_f^1, \widehat{\gamma}_f^1, \widehat{\psi}_f^1) = (250\,\text{m/s}, 0^\circ, 110^\circ)$ and $\boldsymbol{\rho}_{r,f}^2 = (\widehat{V}_f^2, \widehat{\gamma}_f^2, \widehat{\psi}_f^2) = (250\,\text{m/s}, 0^\circ, 160^\circ$. In VMC framework, the reference point $\boldsymbol{\rho}_{\text{ref}}$ for each UCAV is presumed as its IP, and the virtual prey path is predefined as a 2-order curve, determined by the initial and terminal conditions.

Figure 2 shows the overall collision-free attack trajectories of two UCAVs, whose total flight time is equal, equaling to 124 s. It means that two UCAVs arrive simultaneously. As can be seen from Figure 2, along the resulting smooth trajectories, the UCAVs can avoid collision with all obstacles, threats, and the other en route and then successfully fly into the AARs (fuchsin areas) to perform weapon delivery missions. In addition, the approximate weapon trajectories are drawn to illustrate the attack process. The PCP histories of two UCAVs are shown in Figure 3, which are smooth and lie in the range from 0 to 1. And the time histories of the UCAVs' states (V, γ, ψ) and control inputs (μ, n_x, n_z) are shown in Figure 4. It is clear that the constraints on these variables, especially the cooperative constraints, are all satisfied (see Tables 1 and 2), which means that the resulting trajectories are feasible and safe.

5.2. Example 2: Cooperative Trajectories of Multi-UCAV Arriving in Sequence. In this example, three UCAVs attack two stationary ground targets cooperatively. The only additional requirement is that the UCAVs arrive at their AARs in sequence rather than simultaneously, and the intervals between UCAVs are set to 20 s and 30 s, respectively, denoted as $\Delta_{12} = 20\,\text{s}$ and $\Delta_{23} = 30\,\text{s}$. The coordinates of the initial points IP1, IP2 and two targets TAR1, TAR2 are the same with those in Example 1, and the third initial point is

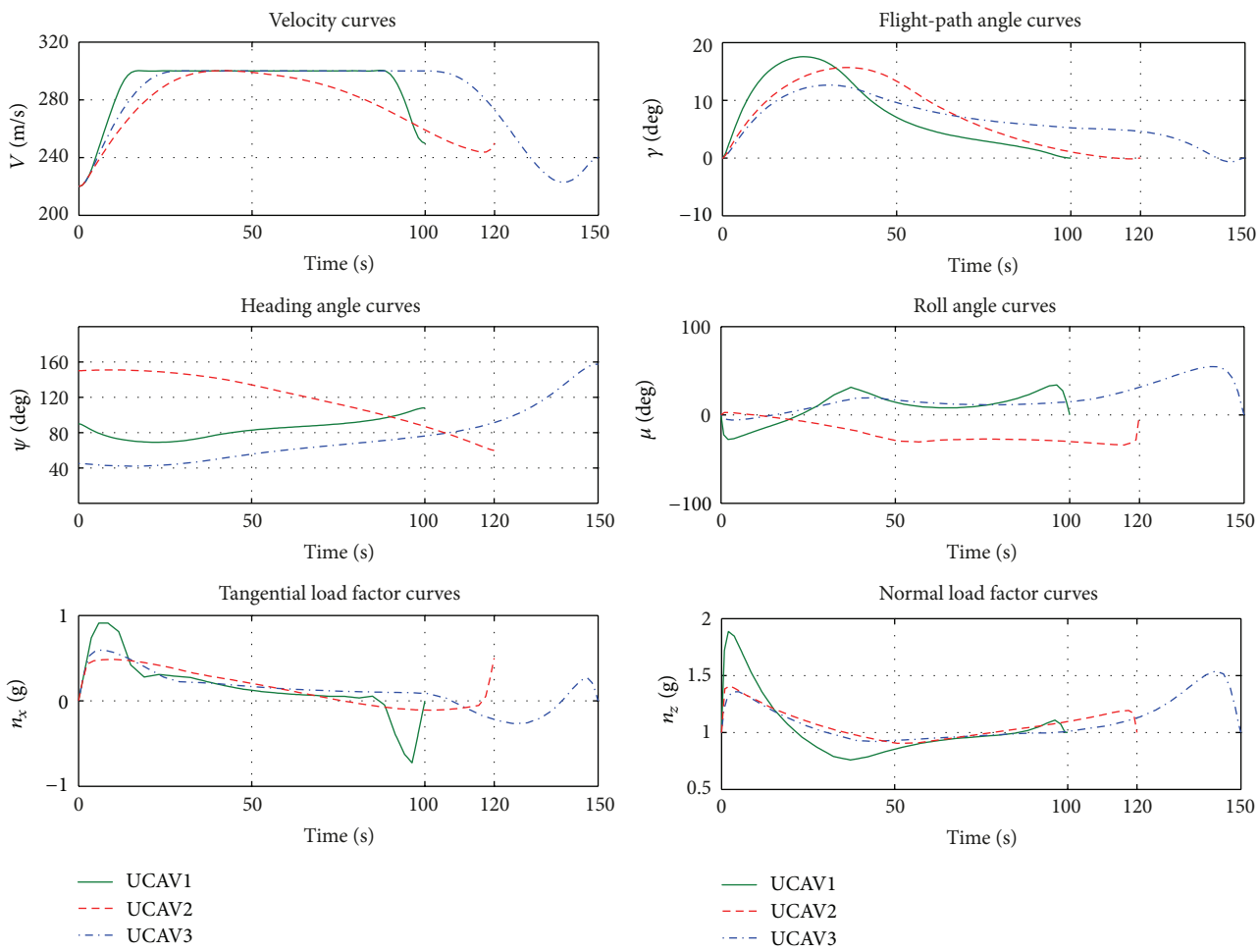

Figure 8: Example 2—state and control time histories of three UCAVs.

IP3 (4, 2, 2) km. The result of the previously finished target assignment is that the UCAV1 and UCAV2 attack TAR1 and UCAV3 attacks the other one. The initial remaining three states and control inputs of the UCAV3 are preset as $\boldsymbol{\rho}_{r,0}^3 = (V_0^3, \gamma_0^3, \psi_0^3) = (220\,\text{m/s}, 0^\circ, 45^\circ)$ and $\mathbf{u}_0^3 = (\mu_0, n_{x,0}, n_{z,0}) = (0^\circ, 0\,\text{g}, 1\,\text{g})$, and the terminal remaining three states of the UCAV3 are predetermined as $\boldsymbol{\rho}_{r,f}^3 = (\widehat{V}_f^3, \widehat{\gamma}_f^3, \widehat{\psi}_f^3) = (220\,\text{m/s}, 0^\circ, 160^\circ)$. In VMC framework, the reference point and the virtual prey path are predetermined, using the same strategy as the one in Example 1.

The overall collision-free attack trajectories of multi-UCAV are shown in Figure 5, and the total flight time of three UCAVs is 100 s, 120 s, and 150 s, respectively. It can be clearly demonstrated that UCAVs can avoid all obstacles or threats and successfully fly into the AARs in sequence to perform the weapon delivery. The PCP histories of three UCAVs are shown in Figure 6. And Figure 7 shows the distance between each pair of UCAVs. From it, one can find that the minimum distance between each UCAV is more than the minimal safety radius of d_{safe} ($d_{\text{safe}} = 500\,\text{m}$); that is, the UCAVs can avoid collision with each other en route. Figure 8 shows the time histories of the UCAVs' states (V, γ, ψ) and control inputs (μ, n_x, n_z). Obviously, the resulting trajectories are feasible and safe, since all the constraints listed in Tables 1 and 2 are satisfied.

Table 1: State and control constraints of UCAVs.

Item	Minimum value	Maximum value
Flight altitude (m)	$z_{\min} = 200$	$z_{\max} = 8\,000$
Airspeed (m/s)	$V_{\min} = 60$	$V_{\max} = 300$
Flight-path angle (deg)	$\gamma_{\min} = -89$	$\gamma_{\max} = 89$
Roll angle (deg)	$\mu_{\min} = -80$	$\mu_{\max} = 80$
Tangential load factor (g)	$n_{x,\min} = -0.725$	$n_{x,\max} = 0.91$
Normal load factor (g)	$n_{z,\min} = -3.2$	$n_{z,\max} = 8$
Roll angle rate (deg/s)	$\dot{\mu}_{\min} = -30$	$\dot{\mu}_{\max} = 30$
Rate of change of tangential load factor (g/s)	$\dot{n}_{x,\min} = -0.2$	$\dot{n}_{x,\max} = 0.2$
Rate of change of normal load factor (g/s)	$\dot{n}_{z,\min} = -2$	$\dot{n}_{z,\max} = 2$

Table 2: Parameter values for the algorithm.

Item	Parameter	Value
Minimum safety radius (m)	d_{safe}	500
Weighting factors of the objective function	w_t	0.3
	w_p	0.4
	w_r	0.3
Weighting factors of the robust subobjective	w_r^1	0.5
	w_r^2	0.3
	w_r^3	0.2
Safe buffer of NFZs (m)	b_s	200

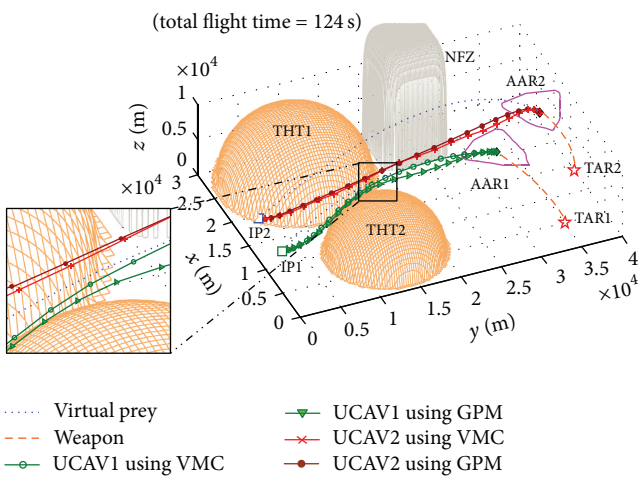

Figure 9: Comparison of two collision-free UCAV trajectories with arriving simultaneously.

In order to validate the convergence rate of VMC based algorithm in cooperative trajectory planning for multi-UCAV further, the comparative experiments are carried out with different numbers of UCAVs (N_v is set as 1, 2, 3, 5, 8, and 10, resp.) and the same number of nodes ($N_c = 20$). The performance comparison of multi-UCAV is summarized in Table 3. As can be seen clearly, along with the increase of the number of UCAVs, the average planning time is rising at a slow rate, which is acceptable for the preplanning applications. Particularly, for one UCAV, the average planning time is 2.21 s. When the number of UCAVs increases to 10, the average planning time increases by only more than quadruple of that for one UCAV, which is 9.62 s.

5.3. Comparison between VMC Based Method and GPM Based Direct Collocation Method. To further evaluate the performance of the proposed algorithm, a recently developed optimal trajectory generation method, GPM based direct collocation method, is used for comparison, which is basically converting the original optimal control problem to a NLP problem via the GPM directly. In the following comparative experiments, Example 1 is simulated again using the two algorithms, respectively, performed on the same desktop with different numbers of nodes (N_c is set as 10, 15, 20, and 30, resp.). All the results are presented below.

Table 3: Performance comparison with the increase of the number of UCAVs.

Number of UCAVs (N_v)	Number of optimization variables	Average planning time (s)	Ratio of the planning time (%)
1	$(20 \times 1 + 1) \times 1 = 21$	2.21	—
2	$(20 \times 1 + 1) \times 2 = 42$	2.83	128.05
3	$(20 \times 1 + 1) \times 3 = 63$	3.32	150.23
5	$(20 \times 1 + 1) \times 5 = 105$	4.93	223.08
8	$(20 \times 1 + 1) \times 8 = 168$	7.70	348.42
10	$(20 \times 1 + 1) \times 10 = 210$	9.62	435.29

Figures 9 and 10 show the comparative solutions attained by using the GPM and VMC based methods, respectively. It can be seen that the trajectories and the state and control time histories of these two algorithms are similar. The detailed performance comparison is summarized in Table 4. With comparison, when the number of nodes increases, the number of optimization variables in GPM is much more than VMC. As a result, the computational speed of VMC is more than an order of magnitude faster than GPM, while the optimization performance has only small loss.

In order to compare the convergence rate and analyze the impacts of the number of UCAVs on the computation time between VMC and GPM further, the comparative experiment is run multiple times with different numbers of UCAVs (N_v is set as an integer from 1 to 10, resp.) and the same number of nodes ($N_c = 20$). Figure 11 shows the change of the average planning time required to solve the optimization problem as the number of UCAVs increases. It can be seen that the increase of the number of UCAVs results in an exponential increase of the required computation time for GPM. In contrast, the computation time for VMC based algorithm increases slowly. When the number of UCAVs increases to 10, the number of the optimization variables for GPM is up to 1810. However, for VMC, the number is only 210. Since the required computation time strongly depends on the number of optimization variables, the computational time required by VMC is more than an order of magnitude less than that required by GPM. Maybe it can be concluded that the larger the number of UCAVs is, the more obvious the advantage of VMC to GPM is.

6. Conclusions

This paper is devoted to explore the cooperative collision-free trajectory planning for multiple UCAVs in performing the CA/GTA missions. The main contributions of the paper are as follows. Firstly, the cooperative trajectory planning problem under consideration is mathematically formulated as a cooperative trajectory optimal control problem (CTOCP). In order to consider the weapon delivery constraints, an

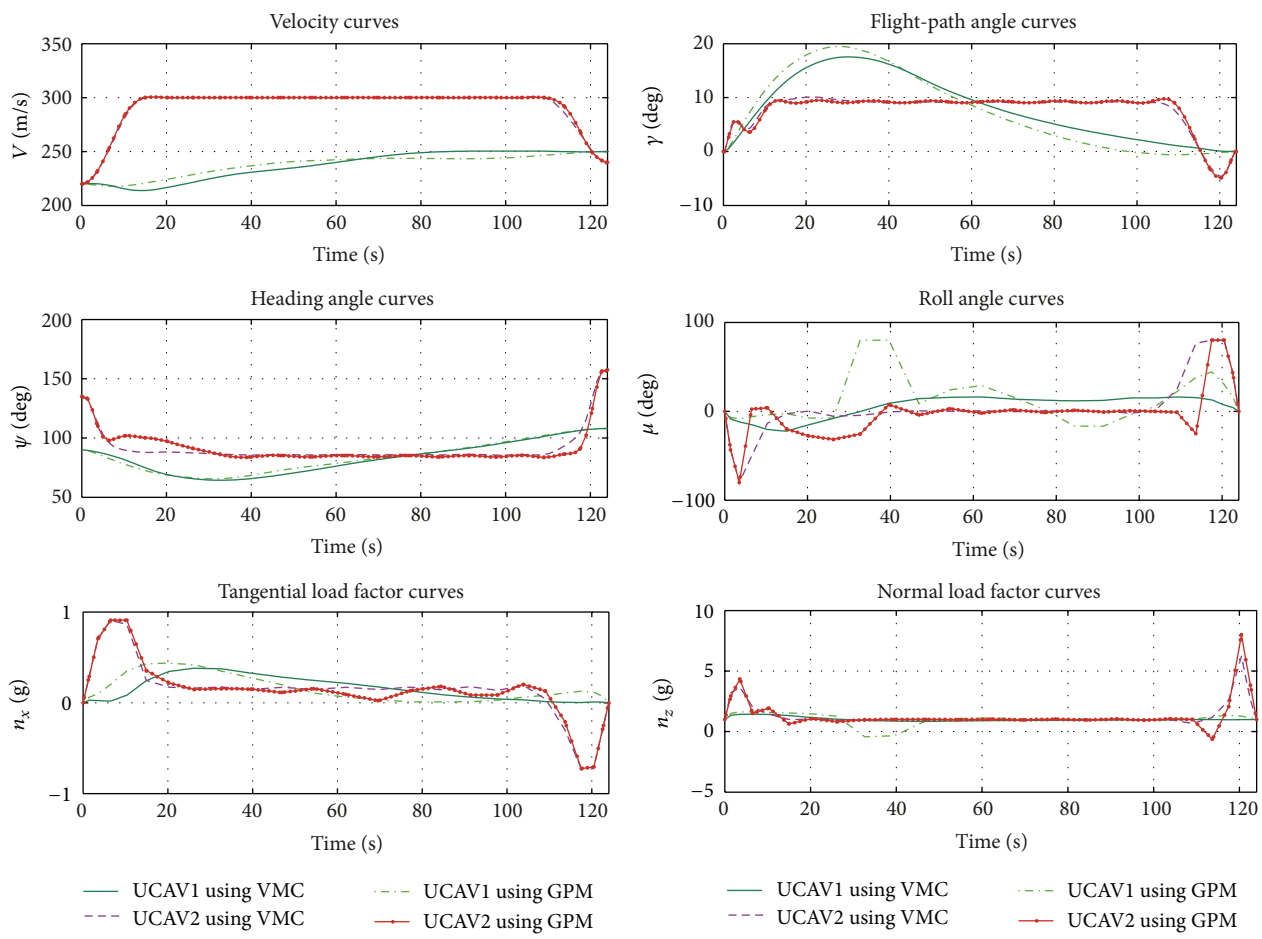

Figure 10: Comparison of state and control time histories.

Table 4: Comparison between GPM and VMC for Example 1.

Method	N_c	Number of optimization variables	Objective function value	Average planning time (s)	Ratio of the planning time (%)
GPM	10	$(10 \times 9 + 1) \times 2 = 182$	1.776	12.31	—
	15	$(15 \times 9 + 1) \times 2 = 272$	1.731	16.28	—
	20	$(20 \times 9 + 1) \times 2 = 362$	1.698	20.31	—
	30	$(30 \times 9 + 1) \times 2 = 542$	1.705	28.67	—
VMC	10	$(10 \times 1 + 1) \times 2 = 22$	1.851	2.23	18.12
	15	$(15 \times 1 + 1) \times 2 = 32$	1.840	2.46	15.11
	20	$(20 \times 1 + 1) \times 2 = 42$	1.769	2.83	13.93
	30	$(30 \times 1 + 1) \times 2 = 62$	1.731	3.18	11.09

approximate allowable attack region model is proposed and integrated into the problem formulation. Secondly, a particular virtual motion camouflage approach combining with differential flatness theory, Gauss pseudospectral method, and nonlinear programming is used to develop the trajectory planner for solving CTOCP. The advantages of this method are that it can automatically satisfy all boundary conditions and use any models and any performance indexes, does not require numerical integration of differentiation of the state equations, and transforms the OCP into a NLP problem of very low dimension. Finally, in order to handle the temporal constraints, the notion of the virtual time is introduced into the virtual motion camouflage approach to realize the spatial-temporal cooperation.

The proposed approach is validated by numerical examples. The results show that the approach is able to generate both feasible and near-optimal attack trajectories with meeting the spatial and temporal constraints very efficiently.

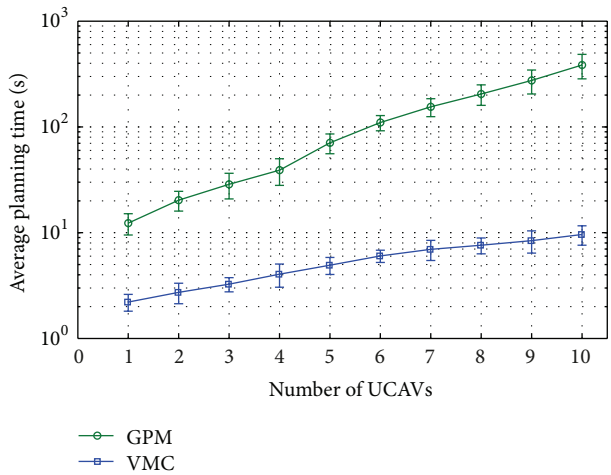

Figure 11: Comparison between GPM and VMC with the increase of the number of UCAVs.

Moreover, the convergence rate and average planning time of the method and optimality of the generated trajectories are evaluated via a detailed comparison with GPM based direct collocation method. The results show that the computational speed of virtual motion camouflage approach is more than an order of magnitude faster than GPM, at small loss of optimality.

For the future work, we will analyze some uncertain factors in the true battlefield environment and carry out the research on the real-time cooperative trajectory planning. For the presence of a larger number of UCAVs, we will make further efforts to exploit more efficient trajectory planning algorithm and improve the time cooperative strategy. Moreover, we will try to study another important aspect about how to plan in the opposability battlefield environment.

Conflict of Interests

The authors declare that there is no conflict of interests regarding the publication of this paper.

Acknowledgments

Great thanks are due to the editor for helpful comments and the reviewers for their valuable suggestions and comments on the revision of the paper. This work was supported by the Science and Technology on Electro-Optic Control Laboratory of China (no. 20125188006).

References

[1] R. M. Murray, "Recent research in cooperative control of multi-vehicle systems," *Journal of Dynamic Systems, Measurement and Control*, vol. 129, no. 5, pp. 571–583, 2007.

[2] M. Fu and J. Jiao, "A hybrid approach for coordinated formation control of multiple surface vessels," *Mathematical Problems in Engineering*, vol. 2013, Article ID 794284, 8 pages, 2013.

[3] J. T. Betts, "Survey of numerical methods for trajectory optimization," *Journal of Guidance, Control, and Dynamics*, vol. 21, no. 2, pp. 193–207, 1998.

[4] C. Goerzen, Z. Kong, and B. Mettler, "A survey of motion planning algorithms from the perspective of autonomous UAV guidance," *Journal of Intelligent and Robotic Systems*, vol. 57, no. 1–4, pp. 65–100, 2010.

[5] J. F. Horn, E. M. Schmidt, B. R. Geiger, and M. P. DeAngelo, "Neural network-based trajectory optimization for unmanned aerial vehicles," *Journal of Guidance, Control, and Dynamics*, vol. 35, no. 2, pp. 548–562, 2012.

[6] S. Karaman and E. Frazzoli, "Sampling-based algorithms for optimal motion planning," *The International Journal of Robotics Research*, vol. 30, no. 7, pp. 846–894, 2011.

[7] P. Narayan, P. Meyer, and D. Campbell, "Embedding human expert cognition into autonomous UAS trajectory planning," *IEEE Transaction on Cybernetics*, vol. 43, no. 2, pp. 530–543, 2013.

[8] Q. Gong, L. R. Lewis, and I. M. Ross, "Pseudospectral motion planning for autonomous vehicles," *Journal of Guidance, Control, and Dynamics*, vol. 32, no. 3, pp. 1039–1045, 2009.

[9] H. Liu, S. Chen, L. Shen et al., "An integrated multi-criterion hp-Adaptive pseudospectral method for direct optimal control problems solving," *Mathematical Problems in Engineering*, vol. 2012, Article ID 760890, 22 pages, 2012.

[10] K. Yang, S. Sukkarieh, and Y. Kang, "Adaptive nonlinear model predictive path tracking control for a fixed-wing unmanned aerial vehicle," in *Proceedings of the AIAA Guidance, Navigation, and Control Conference and Exhibit*, Chicago, Ill, USA, August 2009.

[11] O. A. Yakimenko, Y. Xu, and G. Basset, "Computing short-time aircraft maneuvers using direct methods," in *Proceedings of the AIAA Guidance, Navigation and Control Conference and Exhibit*, Honolulu, Hawaii, USA, August 2008.

[12] D. Benson, *A Gauss pseudospectral transcription for optimal control [Dissertation for the doctoral degree]*, Massachusettes Institute of Technology, Cambridge, Mass, USA, 2005.

[13] M. Soler, A. Olivares, and E. Staffetti, "Hybrid optimal control approach to commercial aircraft trajectory planning," *Journal of Guidance, Control, and Dynamics*, vol. 33, no. 3, pp. 985–991, 2010.

[14] J. Li, H. An, H. Zhu et al., "Geometric pseudospectral method on SE(3) for rigid-body dynamics with application to aircraft," *Mathematical Problems in Engineering*, vol. 2013, Article ID 595086, 16 pages, 2013.

[15] A. Verma and J. L. Junkins, "Inverse dynamics approach for real-time determination of feasible aircraft reference trajectories," in *Proceedings of the 24th Atmospheric Flight Mechanics Conference*, 1999.

[16] R. G. Drury, "Performance of NLP algorithms with inverse dynamics for near-real time trajectory generation," in *Proceedings of the AIAA Guidance, Navigation, and Control Conference*, Portland, Ore, USA, 2011.

[17] F.-L. Lian, "Cooperative path planning of dynamical multi-agent systems using differential flatness approach," *International Journal of Control, Automation and Systems*, vol. 6, no. 3, pp. 401–412, 2008.

[18] A. Chamseddine, Y. Zhang, C. A. Rabbath et al., "Trajectory planning and peplanning strategies applied to a quadrotor unmanned aerial vehicle," *Journal of Guidance, Control, and Dynamics*, vol. 35, no. 5, pp. 1667–1671, 2012.

[19] X. Gu, Y. Zhang, S. Chen et al., "Cooperative trajectory planning for multi-UCAV performing air-to-ground target attack missions," *Advanced Materials Research*, vol. 718-720, pp. 1329–1334, 2013.

[20] X. Gu, Y. Zhang, J. Chen et al., "Real-time cooperative trajectory planning using differential flatness approach and B-splines," *Applied Mechanics and Materials*, vol. 333-335, pp. 1338–1343, 2013.

[21] Y. Xu, "Analytical solutions to spacecraft formation-flying guidance using virtual motion camouflage," *Journal of Guidance, Control, and Dynamics*, vol. 33, no. 5, pp. 1376–1386, 2010.

[22] Y. Xu and G. Basset, "Sequential virtual motion camouflage method for nonlinear constrained optimal trajectory control," *Automatica*, vol. 48, no. 7, pp. 1273–1285, 2012.

[23] Y. Xu, "Virtual motion camouflage and suboptimal trajectory design," in *Proceedings of the AIAA Guidance, Navigation, and Control Conference*, pp. 555–571, August 2007.

[24] Y. Xu and G. Basset, "Pre and post optimality checking of the virtual motion camouflage based nonlinear constrained subspace optimal control," in *Proceedings of the AIAA Guidance, Navigation, and Control Conference and Exhibit*, Chicago, Ill, USA, August 2009.

[25] K. P. Bollino and L. R. Lewis, "Collision-free multi-UAV optimal path planning and cooperative control for tactical applications," in *Proceedings of the AIAA Guidance, Navigation and Control Conference and Exhibit*, Honolulu, Hawaii, USA, August 2008.

[26] Y. Kuwata and J. P. How Sr., "Cooperative distributed robust trajectory optimization using receding horizon MILP," *IEEE Transactions on Control Systems Technology*, vol. 19, no. 2, pp. 423–431, 2011.

[27] Y. Xu and G. Basset, "Virtual motion camouflage based phantom track generation through cooperative electronic combat air vehicles," *Automatica*, vol. 46, no. 9, pp. 1454–1461, 2010.

[28] Y. Xu, M. Xin, and J. Wang, "Unmanned aerial vehicle formation flight via a hierarchical cooperative control approach," in *Proceedings of the AIAA Guidance, Navigation, and Control Conference*, Portland, Ore, USA, 2011.

[29] T. W. McLain and R. W. Beard, "Coordination variables, coordination functions, and cooperative-timing missions," *Journal of Guidance, Control, and Dynamics*, vol. 28, no. 1, pp. 150–161, 2005.

[30] I. Kamlner, O. Yakimenko, V. Dobrokhodov et al., "Coordinated path following for time-critical missions of multiple UAVs via $\mathscr{L}1$ adaptive output feedback controllers," in *Proceedings of the AIAA Guidance, Navigation, and Control Conference*, pp. 915–948, August 2007.

[31] B. L. Stevens and F. L. Lewis, *Aircraft Control and Simulation*, John Wiley & Sons, New York, NY, USA, 2003.

[32] Y. Zhang, J. Chen, and L. Shen, "Hybrid hierarchical trajectory planning for a fixed-wing UCAV performing air-to-surface multi-target attack," *Journal of Systems Engineering and Electronics*, vol. 23, no. 4, pp. 256–264, 2012.

[33] X. Gu, Y. Zhang, N. Wang et al., "Robust multi-objective optimization based on NSGA-II for UCAV weapon delivery," in *Proceedings of the 4th International Conference on Intelligent Human-Machine Systems and Cybernetics*, 2012.

[34] L. P. R. Lewis, *Rapid motion planning and autonomous obstacle avoidance for unmanned vehicles [M.S. thesis]*, Naval Postgraduate School, Monterey, Calif, USA, 2006.

[35] E. Besada-Portas, L. de la Torre, J. M. de la Cruz, and B. de Andrés-Toro, "Evolutionary trajectory planner for multiple UAVs in realistic scenarios," *IEEE Transactions on Robotics*, vol. 26, no. 4, pp. 619–634, 2010.

[36] M. A. Hurni, P. Sekhavat, M. Karpenko, and I. M. Ross, "A pseudospectral optimal motion planner for autonomous unmanned vehicles," in *Proceedings of the American Control Conference (ACC '10)*, pp. 1591–1598, Baltimore, Md, USA, July 2010.

[37] Y. Wang, T. Wei, and X. Qu, "Study of multi-objective fuzzy optimization for path planning," *Chinese Journal of Aeronautics*, vol. 25, no. 1, pp. 51–56, 2012.

[38] M. V. Srinivasan and M. Davey, "Strategies for active camouflage of motion," *Proceedings of the Royal Society B*, vol. 259, no. 1354, pp. 19–25, 1995.

[39] M. Fliess, J. Levine, P. Martin, and P. Rouchon, "Flatness and defect of non-linear systems: introductory theory and examples," *International Journal of Control*, vol. 61, no. 6, pp. 1327–1361, 1995.

[40] K. Holmström, A. O. Göran, and M. M. Edvall, *USer'S Guide For TOMLAB /SNOPT*, Department of Mathematics and Physics, Mälardalen University, Västerås, Sweden, 2008.

[41] S. Chen, H. Liu, J. Chen et al., "Penetration trajectory planning based on radar tracking features for UAV," *Aircraft Engineering and Aerospace Technology*, vol. 85, no. 1, pp. 62–71, 2013.

[42] I. M. Ross and Q. Gong, "Guess-free trajectory optimization," in *Proceedings of the AIAA/AAS Astrodynamics Specialist Conference and Exhibit*, Honolulu, Hawaii, USA, August 2008.

[43] "Storm shadow UCAV performance," 2001, http://www.aerospaceweb.org/design/ucav/main.shtml.

Hindawi Publishing Corporation
Mathematical Problems in Engineering
Volume 2014, Article ID 832864, 15 pages
http://dx.doi.org/10.1155/2014/832864

Research Article

Nonlinear Analysis and Intelligent Control of Integrated Vehicle Dynamics

C. Huang, L. Chen, H. B. Jiang, C. C. Yuan, and T. Xia

School of Automobile and Traffic Engineering, Jiangsu University, Zhenjiang 212013, China

Correspondence should be addressed to L. Chen; chenlong@163.com

Received 24 September 2013; Revised 2 December 2013; Accepted 2 December 2013; Published 21 January 2014

Academic Editor: Hui Zhang

With increasing and more stringent requirements for advanced vehicle integration, including vehicle dynamics and control, traditional control and optimization strategies may not qualify for many applications. This is because, among other factors, they do not consider the nonlinear characteristics of practical systems. Moreover, the vehicle wheel model has some inadequacies regarding the sideslip angle, road adhesion coefficient, vertical load, and velocity. In this paper, an adaptive neural wheel network is introduced, and the interaction between the lateral and vertical dynamics of the vehicle is analyzed. By means of nonlinear analyses such as the use of a bifurcation diagram and the Lyapunov exponent, the vehicle is shown to exhibit complicated motions with increasing forward speed. Furthermore, electric power steering (EPS) and active suspension system (ASS), which are based on intelligent control, are used to reduce the nonlinear effect, and a negotiation algorithm is designed to manage the interdependences and conflicts among handling stability, driving smoothness, and safety. Further, a rapid control prototype was built using the hardware-in-the-loop simulation platform dSPACE and used to conduct a real vehicle test. The results of the test were consistent with those of the simulation, thereby validating the proposed control.

1. Introduction

When a car is travelling at a high speed, a slight variation of the steering could result in a crash. Moreover, steering instability is primarily caused by the lateral force acting on the steering wheels, which is particularly affected by the sideslip angle [1]. When a vehicle navigates a large radius curve, the change in the sideslip angle is small and linearly related to the change in the lateral force. However, for high lateral accelerations, the wheel characteristic is nonlinear and the lateral force varies nonlinearly, thereby reducing the steering stability [2]. Under these complex conditions and the accompanying uncertainties, there are variations in the vertical load and lateral force acting on the wheel, as well as the longitudinal force of the vehicle. It is therefore necessary to develop an effective nonlinear model and employ more accurate processes such as the use of a neural network model and the sliding mode to achieve control requirements [3–5].

Currently, vehicle dynamics is mostly studied by means of nonlinear dynamics. For example, Wu and Sheng [6] established the phase plane of the sideslip angle and the rate at which it changes, which afforded a better method for the quantitative determination of the stability region. However, the method is limited by the simplified wheel model and cannot be theoretically used to determine the state and analyze the trend of the vehicle outside the stable area. Inagaki et al. [7] also studied the phase plane of the turning kinetic energy and forward kinetic energy and proposed a method for interpreting experimental observations and the results of quantitative analyses. However, the application of his method is also limited.

Shi et al. [8] established the potential energy function for the major parameters of a vehicle such as the sideslip angle of the wheel, steering wheel angle, and vehicle speed. In addition, he conducted qualitative and quantitative analyses to determine the steering stability region of a vehicle. Yang et al. [9] used the nonlinear dynamical center manifold theory to simplify a high-dimensional system to a one-dimensional center manifold system and theoretically analyzed the phenomenon of bifurcated limit cycles. He pointed out that saddle node bifurcation occurs with increasing speed and front wheel angle.

Liu et al. [10] developed a nonlinear steering model of a front wheel drive vehicle, analyzed the Hopf bifurcation of the system, and confirmed that if the front wheel is periodically perturbed, chaotic motion would be produced in the system. Chang [11] created the bifurcation diagram of steer-by-wire vehicles for certain parameter ranges and used it to obtain the periodic and chaotic motions of the system. He proposed a chaotic feedback controller for steering the vehicle.

Ono et al. [12] analytically showed that the heading angle of a vehicle would be unstable if the heading speed exceeds a critical value. Beyond the critical speed, the vehicle may spin and possibly topple. Furthermore, Chang and Lin [13] used the bifurcation Lyapunov exponent to analyze complicated motions and offered detailed explanations of the topology change that occurs in the solutions of the mathematical model of a lateral system. A feedback controller of a linear lateral system has also been proposed and implemented in the steering system to enable the escape of a vehicle from the unstable domain, thereby preventing spinning and improving safety [14].

The steering and suspension are two important subsystems of the chassis of a vehicle, and both directly affect the overall vehicle performance, including handling stability, driving smoothness, and safety. The two systems are coupled and interact with each other. The suspension causes significant variations in the vertical force acting on the wheel, whereas the steering affects the lateral force, which in turn affects the overall lateral dynamics [15].

Studies have been conducted on the integrated control of electric power steering (EPS) and active suspension system (ASS) for complex nonlinear time-varying vehicle dynamics. The lateral and vertical dynamics of the vehicle were evaluated using different indexes, control strategies, and wheel dynamics. According to the linear superposition principle, if the lateral and vertical dynamics are separately controlled, the determined comprehensive properties would not be accurate. Over the past few years, diverse intelligent control strategies for integrated control have been proposed. March and Shim [16] developed an integrated control system for active front wheel steering and normal force control and used fuzzy logic to improve the vehicle handling. Yoshimura and Emoto [17] also used fuzzy logic and skyhook dampers to develop a steering and suspension system of a half car model subjected to irregular excitation by the surface of the road. Other techniques have been applied to the design of vehicle chassis control, such as sliding mode control and adaptive control [18–20]. More recently, the H_∞ approach was used to produce promising designs of a vehicle chassis controller [21–25].

Chen et al. [26] developed a full car dynamic model that integrates EPS and ASS and used it to design a random suboptimal control strategy based on output feedback for integrated EPS and ASS control. Wang et al. [27] determined the structural parameters and used them to obtain the controller parameters by means of a simulated annealing algorithm. Furthermore, for simultaneous optimization, the major mechanical parameters of the EPS and ASS and some of the controller parameters were used as design variables, and the comprehensive dynamic performance of the automobile was selected as the target function. An EPS, ASS, and rule-based central controller that supervised and coordinated the subsystems were designed based on the coupling relationships between the steering and suspension systems.

In the present study, a fuzzy control method was used to reduce the nonlinear effect, and a coordination mechanism was introduced to manage the interdependences and conflicts among handling stability, driving smoothness, and safety. Moreover, computer simulations were used to validate the bifurcation and chaotic motions implied by the integrated nonlinear differential equations that describe the vehicle dynamics. Finally, to conduct a real vehicle test, a rapid control prototype was built using the hardware-in-the-loop simulation platform dSPACE. The results of the test were consistent with those of the simulation, thereby validating the proposed control.

2. Integrated Vehicle Dynamics

2.1. Vehicle Model. To develop the vehicle dynamics model based on the steering working condition, the effect of the ground tangential force on the cornering properties of the wheel and the aerodynamics were ignored, as shown in Figure 1.

During the steering process of the vehicle, the effect of the roll angle and yaw velocity on changes in the sideslip angle cannot be ignored. The equations of motion of the vehicle were therefore derived by taking the effect of the roll angle into consideration and are as follows:
lateral movement of the vehicle:

$$mv\left(\dot{\beta}+\gamma\right)-m_s h_s\ddot{\phi}=S_1+S_2+S_3+S_4, \tag{1}$$

yaw movement of the vehicle:

$$I_\gamma\dot{\gamma}=l_f\left(S_1+S_2\right)-l_r\left(S_3+S_4\right), \tag{2}$$

vertical movement of the vehicle:

$$m_s\ddot{z}_2=F_{21}+F_{22}+F_{23}+F_{24}, \tag{3}$$

pitching movement of the vehicle:

$$I_\theta\dot{\theta}=l_r\left(F_{21}+F_{22}\right)-l_f\left(F_{23}+F_{24}\right), \tag{4}$$

roll movement of the vehicle:

$$I_\phi\ddot{\phi}=m_s v\left(\dot{\beta}+\gamma\right)h_s+m_s g h_s\phi+\left(F_{21}+F_{23}-F_{22}-F_{24}\right)d, \tag{5}$$

vertical movement of the unsuspended mass:

$$m_{li}\ddot{z}_{li}=k_{li}\left(z_{oi}-z_{li}\right)-F_{2i},\quad (i=1,2,3,4). \tag{6}$$

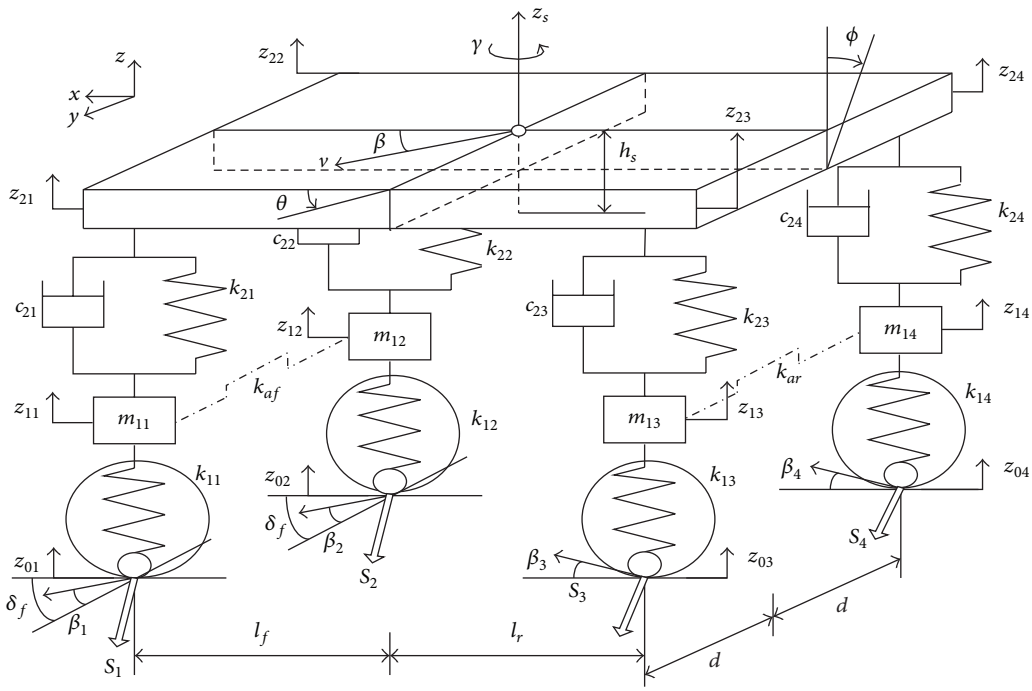

Figure 1: Vehicle dynamics model.

Taking into consideration the effect of the stabilizer bar on the inclination angle of the vehicle body, the resultant force of the suspension is given by the following:

$$\begin{aligned}
F_{21} &= k_{21}(z_{11}-z_{21})+c_{21}(\dot{z}_{11}-\dot{z}_{21})-\frac{k_{af}}{2d}\left(\phi-\frac{z_{11}-z_{12}}{2d}\right),\\
F_{22} &= k_{22}(z_{12}-z_{22})+c_{22}(\dot{z}_{12}-\dot{z}_{22})-\frac{k_{af}}{2d}\left(\phi-\frac{z_{11}-z_{12}}{2d}\right),\\
F_{23} &= k_{23}(z_{13}-z_{23})+c_{23}(\dot{z}_{13}-\dot{z}_{23})-\frac{k_{ar}}{2d}\left(\phi-\frac{z_{13}-z_{14}}{2d}\right),\\
F_{24} &= k_{24}(z_{14}-z_{24})+c_{24}(\dot{z}_{14}-\dot{z}_{24})-\frac{k_{ar}}{2d}\left(\phi-\frac{z_{13}-z_{14}}{2d}\right).
\end{aligned} \tag{7}$$

When the pitch angle θ and inclination angle ϕ are in the minor range, the following approximations can be obtained:

$$\begin{aligned}
z_{21} &= z_s - l_f\theta - d\phi,\\
z_{22} &= z_s - l_f\theta + d\phi,\\
z_{23} &= z_s + l_r\theta + d\phi,\\
z_{24} &= z_s + l_f\theta - d\phi.
\end{aligned} \tag{8}$$

2.2. Wheel Model. When a real vehicle is traveling on a nonflat road, the effect of the road on the wheel varies, which makes it necessary to obtain a dynamic model that is adaptable to environmental changes. The adaptive neural network (ANN) is more appropriate and is as follows:

$$T = \{F_y\} = \mathrm{NN}\left\{\begin{bmatrix} \alpha \\ P \\ v \\ F_z \\ F_{y(n-1)} \end{bmatrix}\right\}. \tag{9}$$

ANN includes the input layer, hidden layer, and output layer. The input layer contains five variables, namely, the sideslip angle of the wheel α, the wheel pressure P, the vertical load F_z, the velocity v, and the lateral force of the previous step $F_{y(n-1)}$. The hidden layer is composed of several nonlinear transfer functions, whereas the output layer is composed of a single variable, which is the lateral force acting on the wheel, F_y.

The input of the neuron in the hidden layer of the network is given by

$$\theta_j(k) = \sum_{i=1}^{m} w_{ij} p_i(k); \quad j = 1, 2, \ldots, 8; \; m = 5. \tag{10}$$

The relationship between the input and output of the hidden layer is given by the following sigmoid function, which is an expression of the output of the neuron in the hidden layer:

$$\xi_j(k) = f\left[\theta_j(k)\right]; \quad j = 1, 2, \ldots, 8. \tag{11}$$

Figure 2: Analytical tire contact system.

The output layer consists of one neuron, the input function of which is as follows:

$$\varsigma_l(k) = \sum_{j=1}^{n} v_{jl}\xi_j(k); \quad l = 1;\ n = 8. \tag{12}$$

The relationship between the input and output of the output layer is given by the following sigmoid function:

$$I_l = f\left[\varsigma_l(k)\right]; \quad l = 1. \tag{13}$$

Let us assume that the inclination angles of the left- and right-side wheels are equal and that the inclination angles of the front and rear wheels can be expressed as

$$\begin{aligned} \alpha_1 = \alpha_2 &= \delta_f - \beta - \frac{l_f\gamma}{v} + E_f\phi, \\ \alpha_3 = \alpha_4 &= \frac{l_r\gamma}{v} - \beta + E_r\phi. \end{aligned} \tag{14}$$

For our experiments, we used a 165/65R13 Radial Tyre (Hankooktire). The equipments used for the experiments included a Vehicle Tyre Road Rotating Test Stand (Figure 2) and a T-8050 Tyre Road Contacting Pressure Analysis System (US Tekscan Company).

Based on the characteristics of the Magic formula model, a comparative analysis of the fitting performances of the adaptive and Magic formula models was conducted using experimental tire data for different loads and with the assumption of steady working conditions, namely, a wheel speed of 20 km/h and inflation pressure of 250 kPa (Figure 3). As shown in the figure, the adaptive model produces a better fit of the experimental data. In the case of the Magic formula, because the trigonometric function is used as the base function, the fitting curve is only close to and crosses the experimental data. Moreover, there are distortions in the approximation of the lateral force.

3. Nonlinear Analysis of Lateral and Vertical Vehicle Dynamics

3.1. Coupled Mechanism. Figure 4 is a diagram of the interaction between the suspension and steering systems. The double lines in the figure indicate the basic and direct actions; the solid lines indicate the indirect effect of its functions; and the dashed lines indicate the constraints. When an increase in the gain of one of either the suspension or steering system is used to improve the performance of the system, the indirect effect on the performance of the other system is also significantly increased. For example, if the roll stiffness of the suspension is increased, the roll angle would decrease, resulting in a weakening of the under steer characteristics and an increase in the yaw velocity gain, which in turn deteriorates the yaw response characteristics.

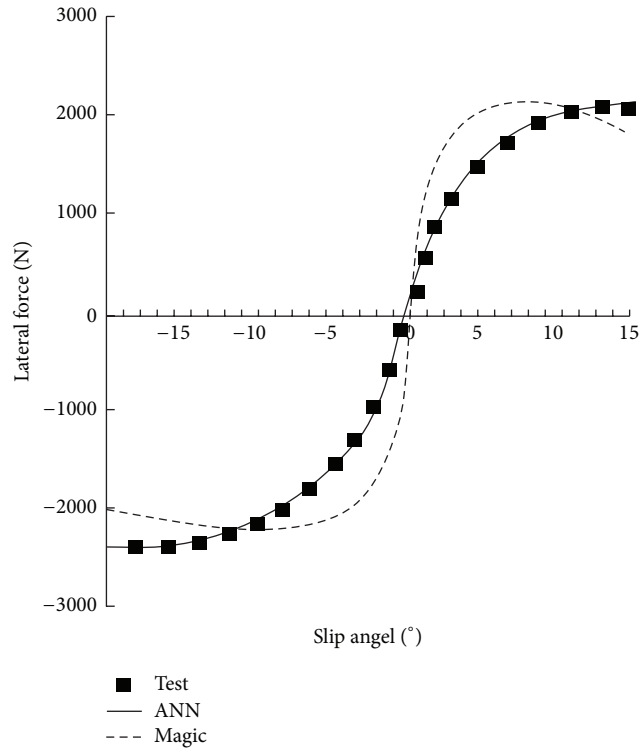

Figure 3: Model fitting.

It can be seen from (1)–(6) that the steering of a vehicle affects the roll of the body by laterally accelerating it, which in turn affects the motion of the suspension subsystem. The vertical force acting on the wheel changes significantly, which affects the vertical motion. The wheel model (see (9)) shows that this causes additional changes in the lateral force acting on the wheel, which in turn affects the overall lateral dynamics. This indicates that there are intercoupling and interaction between the steering and suspension systems of the vehicle.

3.2. Nonlinear Computation. An analytical solution of the nonlinear dynamic system of a coupled neural network is extremely cumbersome, which makes its actual application difficult. It is thus necessary to obtain an approximate solution by a numerical method, that is, to convert the differential differential equation to a differential equation. In this study, Matlab/Simulink was used to develop a simulation model, the calculation flow of which is shown in Figure 5. The model

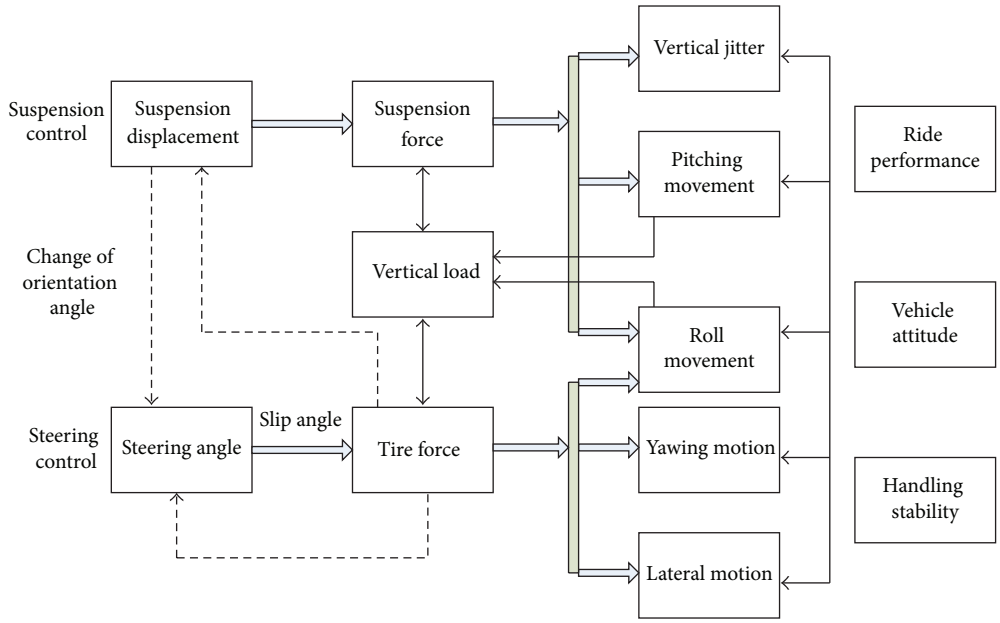

Figure 4: Interaction between the suspension and steering systems.

Table 1: Vehicle parameters.

Parameter	Value
Kerb weight/kg	900
Maximum total weight/kg	1330
Unsprung mass (front/rear)/kg	35/33
Front axle weight (empty/full)/kg	540/640
Wheel base/mm	2335
Front axle-centred distance/mm	955
Rear axle-centred distance/mm	1380
Front/rear wheel tread/mm	1360/1355
Vehicle body length/width/height/mm	3400/1575/1670
Wheel model/mm	165/65R13

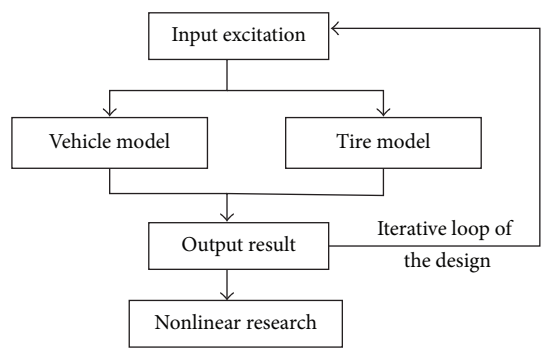

Figure 5: Calculation flowchart.

parameters were chosen with reference to those of a real vehicle and are given in Table 1.

The maximum Lyapunov exponent method and the phase plane method are the major methods used to examine the nonlinear system in this paper. In mathematics, the Lyapunov exponent characterizes the rate of separation of infinitesimally close trajectories. Quantitatively, the rate at which two trajectories separated by δZ_0 in a phase space diverge (provided the divergence can be treated using its linearized approximation) is given by

$$|\delta Z(t)| \approx e^{\lambda t} |\delta Z_0|. \tag{15}$$

The rate of separation may be different for different orientations of the initial separation vector. Thus, there is a spectrum of Lyapunov exponents, the number of which is equal to the dimensionality of the phase space. The largest exponent is commonly referred to as the maximal Lyapunov exponent (MLE) because it determines the predictability for a dynamic system. A positive MLE is usually considered as an indication that the system is chaotic (provided some other conditions are met, e.g., the compactness of the phase space). It should be noted that an arbitrary initial separation vector would typically have a component in the direction of the MLE, and the exponential growth rate would obliterate the effect of the other exponents over time.

The maximal Lyapunov exponent is defined as follows:

$$\lambda = \lim_{t \to \infty} \lim_{\delta Z_0 \to 0} \frac{1}{t} \ln \frac{|\delta Z(t)|}{|\delta Z_0|}. \tag{16}$$

The limit δZ_0 ensures the validity of the linear approximation at any time.

When computing the maximal Lyapunov exponent, the time series should be reconstructed to determine the closest point $V_{j'}$ for every point V_j.

The separation interval is defined as follows:

$$\omega = \frac{\max(\tau_i)}{\Delta t}; \quad i = 1, 2, \ldots, M. \tag{17}$$

It is assume that $d_j(0)$ is the distance between V_j and its closest point $V_{j'}$; that is,

$$d_j(0) = \left\| V_j - V_{j'} \right\|, \quad \left| j - j' \right| > \omega. \tag{18}$$

For every point V_j in the phase space, the distance to its closest point after the forward evolution in the ith step is calculated using

$$d_j(i) = \left\| V_{j+1} - V_{j+i'} \right\|, \tag{19}$$

where $i = J_0, J_{0+1}, \ldots, N$.

Assuming that the closest point of V_j diverges at the rate of the Lyapunov exponent, namely, $d_j(i) = d_j(0) \times e^{\lambda(i\Delta t)}$, the logarithm on both sides is used to obtain $\ln d_j(i) = \ln d_j(0) + \lambda(i\Delta t)$. The least square method is then used to fit the curve of $\ln d_j(i)$ relative to $i\Delta t$ to obtain the maximal Lyapunov exponent λ_1:

$$\lambda_1 = \frac{[i \times y(i)]}{\sum i^2}, \tag{20}$$

where $y(i) = (\sum_{j=1}^{p} \ln d_j(i))/(p\Delta t)$ and p is the number of nonzero $d_j(i)$.

A phase plane is a visual display of certain characteristics of certain types of differential equations. However, a coordinate plane is a plane whose axes represent two state variables such as (x, y), (q, p), or any other pair of variables. It is a two-dimensional case of the general n-dimensional phase space and can be used to determine the stability or otherwise of the dynamics.

3.3. Analysis of Results. The yaw angle rate γ of the chassis is the riding and visual evaluation index of the driver during steering. It is therefore necessary to study the dynamic behavior of γ to explain a variety of phenomena and evaluate the stability and control of the steering process.

In the bifurcation diagram (Figure 6), as the velocity v increases, γ initially maintains a single stable period. When v reaches 15 km/h, γ suddenly becomes chaotic. As v further increases to 45 km/h, γ suddenly changes to a period-4 motion. After another short period of stability, γ enters the chaotic state again and finally converges to a period-1 motion with further increase in v.

Figure 7 shows that when v increases from zero, λ begins at a negative value and continuously fluctuates as the absolute value of v increases. λ is zero when $v = 15$ km/h and subsequently becomes positive, which indicates that the system becomes chaotic. This shift corresponds to the change of γ from a period-1 motion to the chaotic state (Figure 6). As v increases from 15 to 50 km/h, λ fluctuates, alternating increasing from and decreasing back to zero. When v is 25 or 40 km/h, λ assumes a local maximum value. These local maximums correspond to regions in which the attractors are densely distributed in Figure 6. As v approaches 50 km/h, λ changes rapidly and assumes a global minimum value. In the bifurcation diagram in Figure 6, the attractors maintain the four-period stable state, after which the chaotic state is reentered. When $v = 65$ km/h, λ assumes another maximum value, which is the global maximum and corresponds to a narrow strip of densely distributed chaotic attractors in Figure 6. Subsequently, λ gradually decreases and the chaotic attractors correspondingly decrease in density and become increasingly narrow in scope. The attractors are narrowest at $v = 80$ km/h, at which point λ is zero, after which it increases again. When $v = 95$ km/h, λ assumes another local maximum. However, when v exceeds 95 km/h, λ continuously decreases. The Lyapunov exponent tends to negative infinity with continuous thinning of the chaotic attractors and convergence to a stable fixed point in the bifurcation diagram (Figure 6).

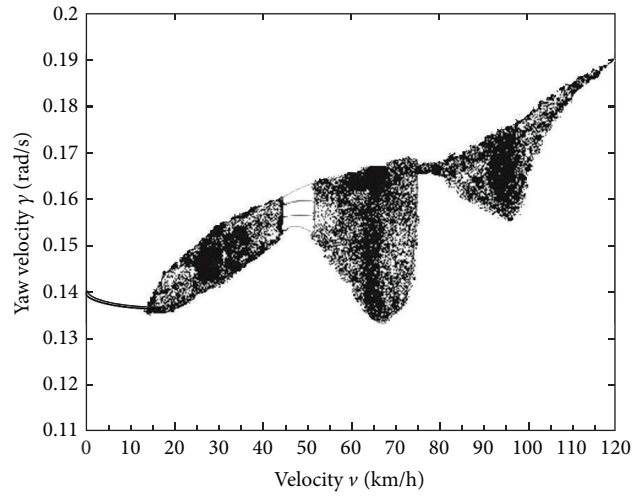

Figure 6: Bifurcation diagram.

Table 2: Description of control mode.

Identification	Rule	Working condition
1	$c_2 \wedge c_3 \wedge c_5$	Assist
2	$c_1 \wedge c_5$	Damping
3	$c_2 \wedge c_6$	Aligning

4. Intelligent Control for Chaotic State

4.1. EPS Based on Fuzzy Control. The input signals and system state are specified by $S = \{s_1, s_2, s_3, s_4\}$, where s_1 is the steering wheel torque, s_2 is the velocity, s_3 is the wheel steering angle, and s_4 is the motor current. The environment is categorized into three working conditions, namely, assist, damping, and aligning (see Tables 2 and 3 for the criteria for determining the working condition).

The schedule of the fuzzy rules is based on the working condition. In the assist condition, a seamless velocity assist mode is employed using a velocity range of 0–200 km/h and intervals of 20 km/h. For each velocity, the assist provided

Table 3: Conditions of EPS hybrid control system.

Identification	Logical expression
c_1	$T_d < T_{d,0}$
c_2	$\neg c_1$
c_3	$u_{\text{vehicle}} < u_{\text{vehicle,max}}$
c_4	$\neg c_4$
c_5	$\theta_h \dot{\theta}_h > 0$
c_6	$\neg c_5$

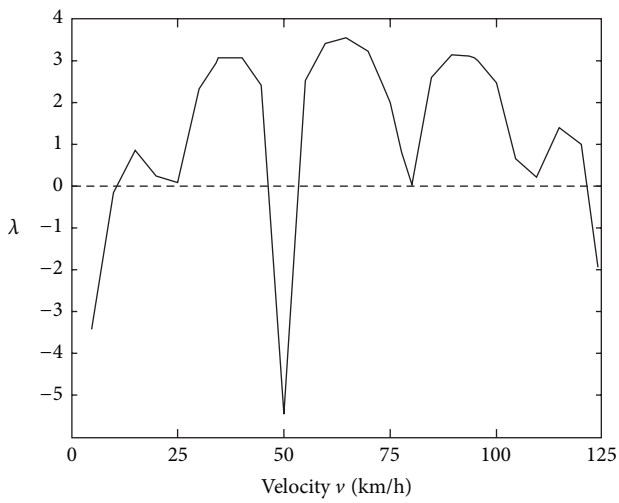

Figure 7: Lyapunov exponent diagram.

by the motor can be divided into three segments, which are as follows. When the steering wheel input torque is in the range of 0-1 Nm, there is a boosting dead zone and no assist is provided by the motor. When the input torque is in the range of 1–6 Nm, there is an assist zone. When the torque is beyond this range, there will be a 6 Nm assist saturated zone. The four parameters used for designing linear assist are the steering wheel input torque $T_{d,0}$ at the beginning of the assist, the maximum steering wheel input torque $T_{d,\max}$, the motor current maximum value $I_{t,\max}$, and the coefficient $k(v)$. The characteristics of the designed linear assist and its function expressions are as shown in Figure 8:

$$I_t = \begin{cases} 0, & |T_d| \le T_{d,0}, \\ k(v)\, f(T_d - T_{d,0}), & T_{d,0} \le |T_d| \le T_{d,\max}, \\ I_{t,\max}, & |T_d| \ge T_{d,\max}. \end{cases} \tag{21}$$

Based on the requirements and objectives, the aligning condition is composed of two parts. One is the aligning control, the major function of which is the provision of necessary assist for easy steering of the wheel back to the central position. In this process, the aligning control functions as a PI adjuster for adjusting the target steering wheel position θ and the actual steering wheel variance e_h, outputting the control voltage and allowing the motor to bring the steering wheel back to the central position:

$$V_{\text{mr}l} = -\left(K_p e_h + K_i \int e_h \mathrm{d}t\right). \tag{22}$$

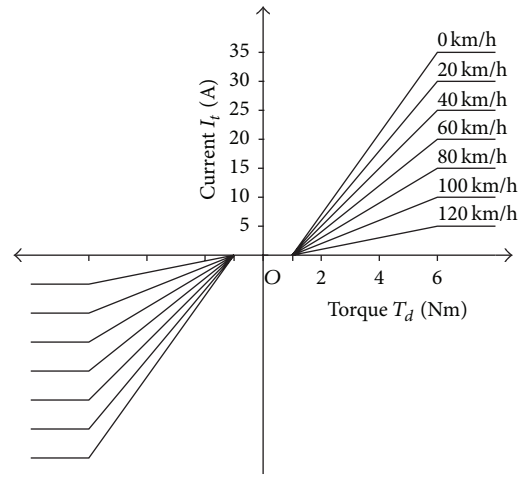

Figure 8: Characteristics of a linear assist.

The other part is damping control, the major function of which is to bring the vehicle back to the central position and avoid the shimmy events under the damping condition. During this process, a certain control voltage is generated based on the angular velocity of the aligning process, which produces a certain damping torque in the motor. The quicker the steering wheel spins, the higher the control voltage generated and the larger the damping torque is. Conversely, the slower the steering wheel spins, the smaller the damping torque is. The steering wheel alignment speed can therefore be adjusted by adjusting the damping coefficient:

$$V_{\text{mr}h} = -K_d \dot{e}_h. \tag{23}$$

The alignment control and the damping control can be integrated in one PID returning control algorithm. Moreover, by adjusting the coefficient, alignments that produce different effects can be obtained as expressed by the following:

$$V_{\text{mr}} = -\left(K_p e_h + K_i \int e_h \mathrm{d}t + K_d \dot{e}_h\right). \tag{24}$$

In the damping condition, the operation status of the system is determined by the value of the deviation $|e_d|$, and timely adjustment is made to the structure of the controller. The controlling rules are as follows:

$$\begin{aligned} &\text{IF } e_d > +e_{d,\max} \text{ THEN } K_{d,\text{PWM},m} = +K_{d,\text{PWM},\max}, \\ &\text{IF } e_d \le -e_{d,\max} \text{ THEN } K_{d,\text{PWM},m} = -K_{d,\text{PWM},\max}. \end{aligned} \tag{25}$$

The input variable e and the rate of change of the deviation ec are determined by computing the deviation between the actual current in the current booster motor and the target current, to carry out fuzzy query using the fuzzy rules and to query the fuzzy matrix table. The parameters k_p, k_i, and k_d controlled by the PID are then adjusted for adaptation (see Table 4 and Figure 9).

4.2. ASS Based on Fuzzy Control. In the external state $P = \{p_1, p_2, p_3, p_4, p_5\}$, p_1 is the vertical acceleration $\ddot{Z}_s$, p_2 is the

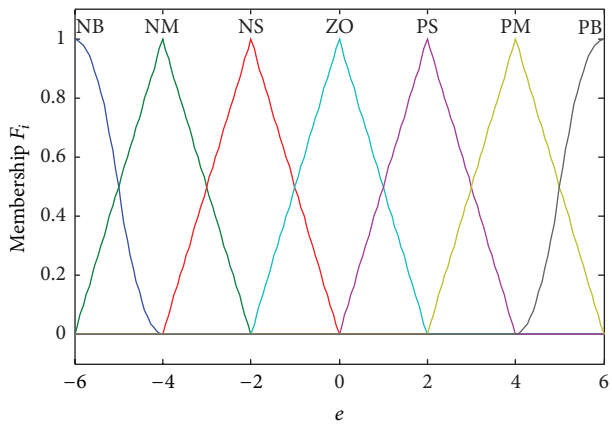

Figure 9: Membership function of variable e.

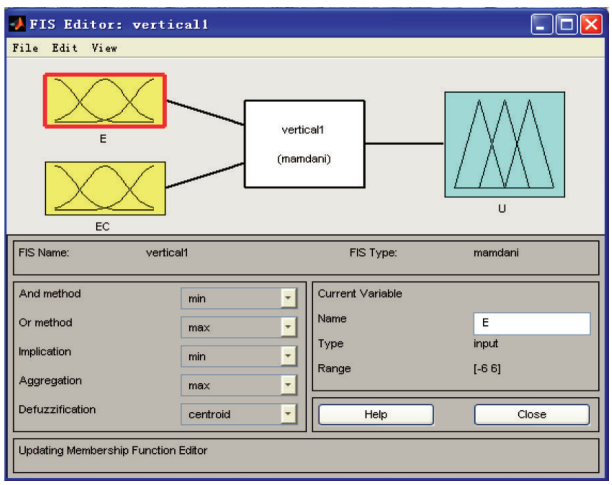

Figure 10: Fuzzy controller interface in Matlab/Simulink.

Table 4: Fuzzy rule table.

ec / e	NB	NM	NS	ZO	PS	PM	PB
NB	PB	PB	PM	PM	PS	ZO	ZO
NM	PB	PB	PS	ZO	NS	ZO	NS
NS	PM	PM	PM	PS	ZO	NS	NS
ZO	PM	PM	PS	ZO	NS	NM	NM
PS	PS	PS	ZO	NS	NS	NM	NM
PM	PS	PS	ZO	NS	NM	NM	NB
PB	ZO	ZO	NM	NM	NM	NB	NB

pitching angular speed of the vehicle $\dot{\theta}$, p_3 is the vehicle body roll angular speed $\dot{\theta}$, p_4 is the suspension dynamic deflection f_d, and p_5 is the wheel vertical acceleration $\ddot{Z}_t$.

To rank the changing amplitudes of p_1, p_2, p_3, p_4, and p_5 based on their values and achieve selective control (using the belief rules) of $\ddot{Z}_s$, $\dot{\phi}$, f_d, and $\ddot{Z}_t$ by combining the operation condition of the wheel angel with the velocity signal, the

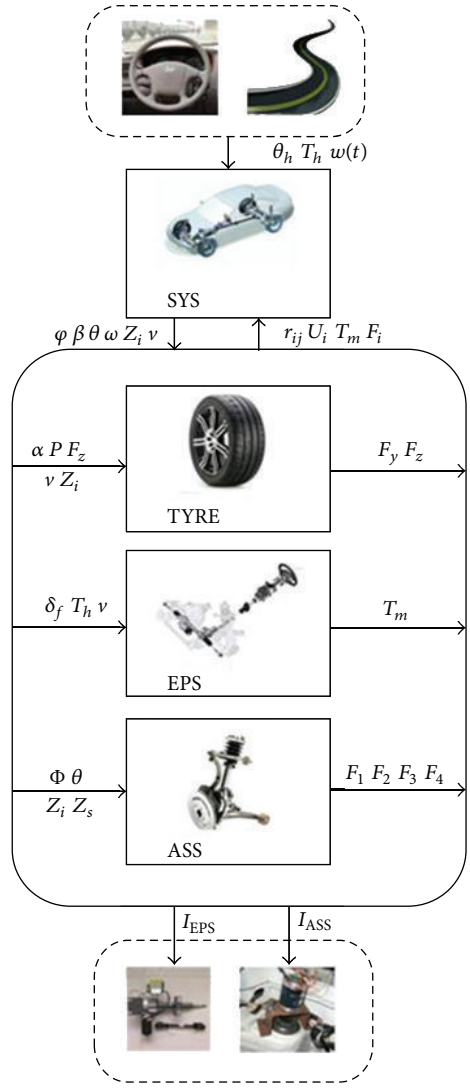

Figure 11: Schematic diagram.

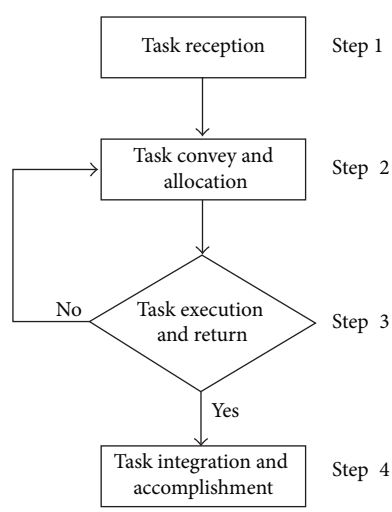

Figure 12: State flow of the controlling strategy.

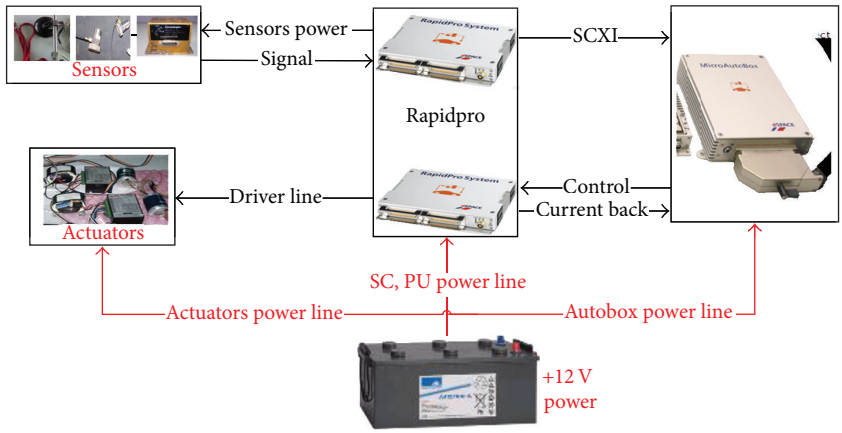

FIGURE 13: Rapid control system.

FIGURE 14: Entire control loop.

following control rules are used together with (24)-(25):

Steering $\rightarrow$ $\dot{\theta} \cap \dot{\phi} \cap \ddot{Z}_s$ $\rightarrow$ "stability",

Medium and low speed $\rightarrow$ $\ddot{Z}_s \cap f_d$ $\rightarrow$ "comfort",

High speed $\rightarrow$ $\dot{\phi} \cap \ddot{Z}_t \cap \ddot{Z}_s$ $\rightarrow$ "safety".

The fuzzy logic system can be described as follows:

$$\begin{aligned} &\text{if } x_1(t) = F_{1j}, \quad x_2(t) = F_{2j}, \ldots, x_n(t) = F_{nj}, \\ &\text{then } y_j(t) = G_j \quad (j = 1, 2, \ldots, 4). \end{aligned} \tag{26}$$

In this formula, $x = (x_1, x_2, \ldots, x_n)^T$ and y are the language variables; F_{ij} $(i = 1, 2, \ldots, n)$ and G_j are the fuzzy sets; and l is the number of rules. The output is

$$f(x) = \frac{\sum_{l=1}^{m} y_l \left[\prod_{i=1}^{n} \mu_{F_{ij}}(x)\right]}{\sum_{l=1}^{m} \left[\prod_{i=1}^{n} \mu_{F_{ij}}(x)\right]}, \tag{27}$$

where $\mu_{F_{ij}}$ is the membership function of the fuzzy set of F_{ij}:

$$F_i = \sum_{j=1}^{m} \left(\min f\left(x_j\right)\right), \quad i = 1, 2, 3, 4 \tag{28}$$

s.t. If "stability" $\rightarrow$ $x_1 = \dot{\theta}$, $x_2 = \dot{\phi}$, $x_3 = \ddot{Z}_s$,

If "comfort" $\rightarrow$ $x_1 = \ddot{Z}_s$, $x_2 = f_d$,

If "safety" $\rightarrow$ $x_1 = \dot{\phi}$, $x_2 = \ddot{Z}_t$, $x_3 = \ddot{Z}_s$.

The fuzzification and defuzzification processes of the fuzzy control of this study were designed using the fuzzy logic toolbox in MATLAB/Simulink (see Figure 10).

4.3. Negotiation Algorithm for Intelligent Control. Figure 11 shows a control strategy for vehicle integrated chassis control. Because it is difficult to directly determine the interrelations between EPS and ASS, the controller was designed using four parts as follows: TYRE, EPS-, ASS, and SYS. The inputs are the road noise w(t), steering wheel angle θ_h, and steering wheel torque T_h, and the outputs are the controlled current I_{ASS} powered by ASS and the controlled current I_{EPS} powered by EPS.

The logical process of the negotiation algorithm is as follows (see Figure 12):

input: road noise w(t), steering wheel angle θ_h, and steering wheel torque T_h,

output: the controlled current I_{ASS} powered by ASS, and the controlled current I_{EPS} powered by assist motors.

Step 1 (task reception). Categorize the operation conditions into steering control, suspension control, and coordination control based on the external input w(t), θ_h, and T_h. For steering control and suspension control, the operation conditions can be determined within the capacity limitations of the single EPS and ASS, which would initiate the corresponding agent and at the same time notify that the agent has been occupied by the operation conditions and should stop receiving new operation conditions until the completion and return of the current condition. However, if the current operation condition fails to accomplish the process by a single attempt, it means that it is beyond its capacity. The operation condition would thus be rejected and would return to the rank for allocation to others.

Step 2 (task convey and allocation). With the whole vehicle model, after obtaining signals $\beta, \omega, \theta, \varphi, Z_i$ for the vehicle

(a) Speed sensors installed on the vehicle

(b) Test car

(c) Gyroscope

(d) Data acquisition box

Figure 15: Main parts of the test and control systems.

body and making reference to the values for the velocity v and the rotation angle δ_f for the front wheels, the system would make a timely definition for employment and the proportion of the vague weights. Based on the planned working conditions allocation strategy, the target is subcategorized into several subtargets for the respective accomplishment.

Step 3 (task execution and return). After receiving orders for the subtargets, the EPS receives signals for the steering wheel torque T_h and velocity v and then uploads a set of solutions for the steering wheel assist and orientation. Regarding the ASS, after receiving the order for the subtargets, it receives the signals θ, Φ, Z_s, and Z_i for the vehicle body and uploads a set of solutions for the orientation of F_i powered by the suspension.

Step 4 (task integration and accomplishment). The controller coprocesses all the subsystems collected during the sequences of vague relational weights as follows:

input: the proposals for a_{EPS} and a_{SAS} at the negotiation of turn $j(x^{(j)}, y^{(j)})$; utility value V_{j-1},

output: the proposals for a_{EPS} and a_{SAS} at the negotiation of turn $j+1(x^{(j+1)}, y^{(j+1)})$.

(1) Compute $V_j(x^{(j)}, y^{(j)})$.

(2) If $V_j(x^{(j)}, y^{(j)}) \leq V_{j-1}(x^{(j-1)}, y^{(j-1)})$, then the negotiation is a failure; if $V_j(x^{(j)}, y^{(j)}) > V_{j-1}(x^{(j-1)}, y^{(j-1)})$, then the negotiation is a success and is followed by a return to the negotiation results $(x^{(j)}, y^{(j)})$.

(3) Compute the concession $Rs = V_j(x^{(j)}, y^{(j)}) - V_{j-1}(x^{(j-1)}, y^{(j-1)})/\text{N}$ to generate $V_{j+1} = V_j(x^{(j)}, y^{(j)}) - Rs$, and return to a_{EPS} and a_{SAS} for a new proposal $(x^{(j+1)}, y^{(j+1)})$.

(4) Output the proposal.

Using the above task integration, the return results for the entire operation condition can be obtained to output the controlled current I_{ASS} powered by the suspension and the steering force-controlled current I_{EPS}.

5. Road Test and Result

5.1. Test Device and System. The tests were performed using the control system shown in Figure 13. It comprises a rapid control module, an actuator system, and a sensor system. The SC unit is used for communication between the sensor system and the main controller unit, whereas the PU is used for communication between the actuators and the main controller unit. The 1401/1505/1507 MicroAutoBox is used as the main controller unit. In the actuator and dSPACE system, an input power of 12 V was obtained from the car battery. The vehicle state was determined using an arm position sensor, gyroscopes, a vehicle speed sensor, and a data acquiring box. The entire control loop shown in Figure 14 is closed by the driver. The main parts of the control and test systems are shown in Figure 15.

5.2. Road Test. To validate the control, a step input road and various S-shaped operation conditions were used to perform

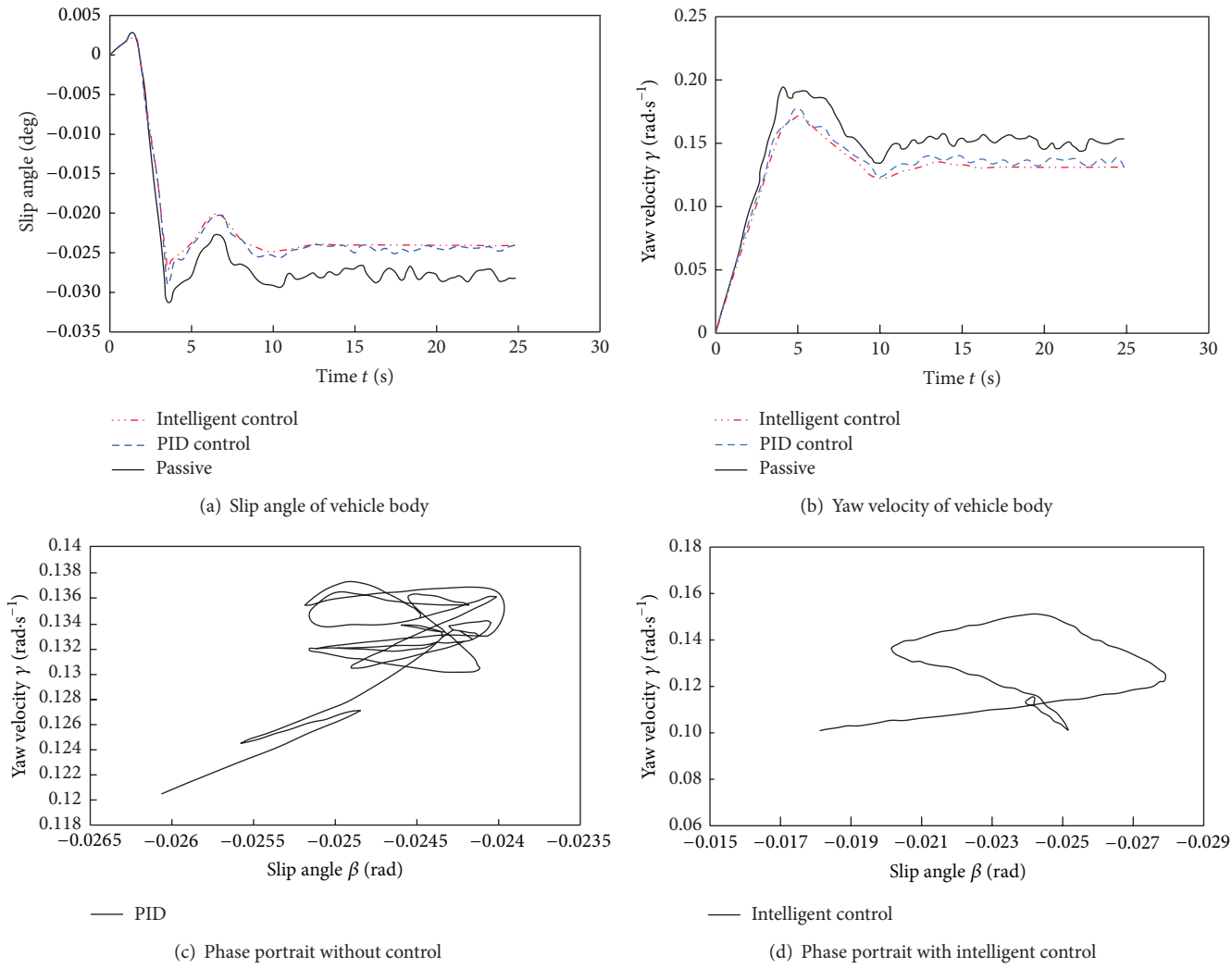

Figure 16: Vehicle results for angle step steering input.

joint simulations for different speeds of a passive and active vehicle, respectively. The test vehicle was equipped with the original passive suspension system and then with the active suspension system with chaos control.

5.2.1. Angle Step Steering Input Operation Conditions. A simulation analysis of the angle step steering input operation conditions can be used to illustrate the improved status of the ASS achieved by stabilizing the handling of the vehicle.

5.2.2. Simulation of the S-Shaped Operation Condition. The road surface was simulated using a vehicle speed of 30 ± 2 km/h. The primary variables that were measured during the simulation were the steering wheel turning angle, steering wheel torque, and velocity of the vehicle.

5.2.3. Angle Step Steering Input Operation Conditions on a Pulse Road. A simulation analysis of the angle step steering input operation conditions on a pulse road can be used to illustrate the improved status achieved by stabilizing the handling and ride comfort of the vehicle. The operation condition used for the simulation consisted of a velocity of 120 km/h (33 m/s) and front wheel steering angle of 6°. For a dry asphalt road, when the vehicle arrived at the 130 m point after 4 s, the front and rear axle wheels were excited by the pulse of the road with an amplitude of 5 cm.

5.3. Discussion. Figures 16(a) and 16(b) show that the intelligent control applied to ASS + EPS effectively reduced the first resonance of the slip angle and the yaw velocity. It produced better results than a passive suspension system and traditional PID control for ASS+EPS, especially for angle step steering. Although the performance of intelligent control and traditional PID control in the steady state are very close, the former afforded steady operation and produced little noise.

Meanwhile, it can be seen from the phase portraits in Figures 16(c) and 16(d) that the vehicle lateral dynamic runs along elliptic orbits when the intelligent controller is applied but exhibits chaotic behavior when the traditional PID controller is applied. Moreover, the oscillation peaks

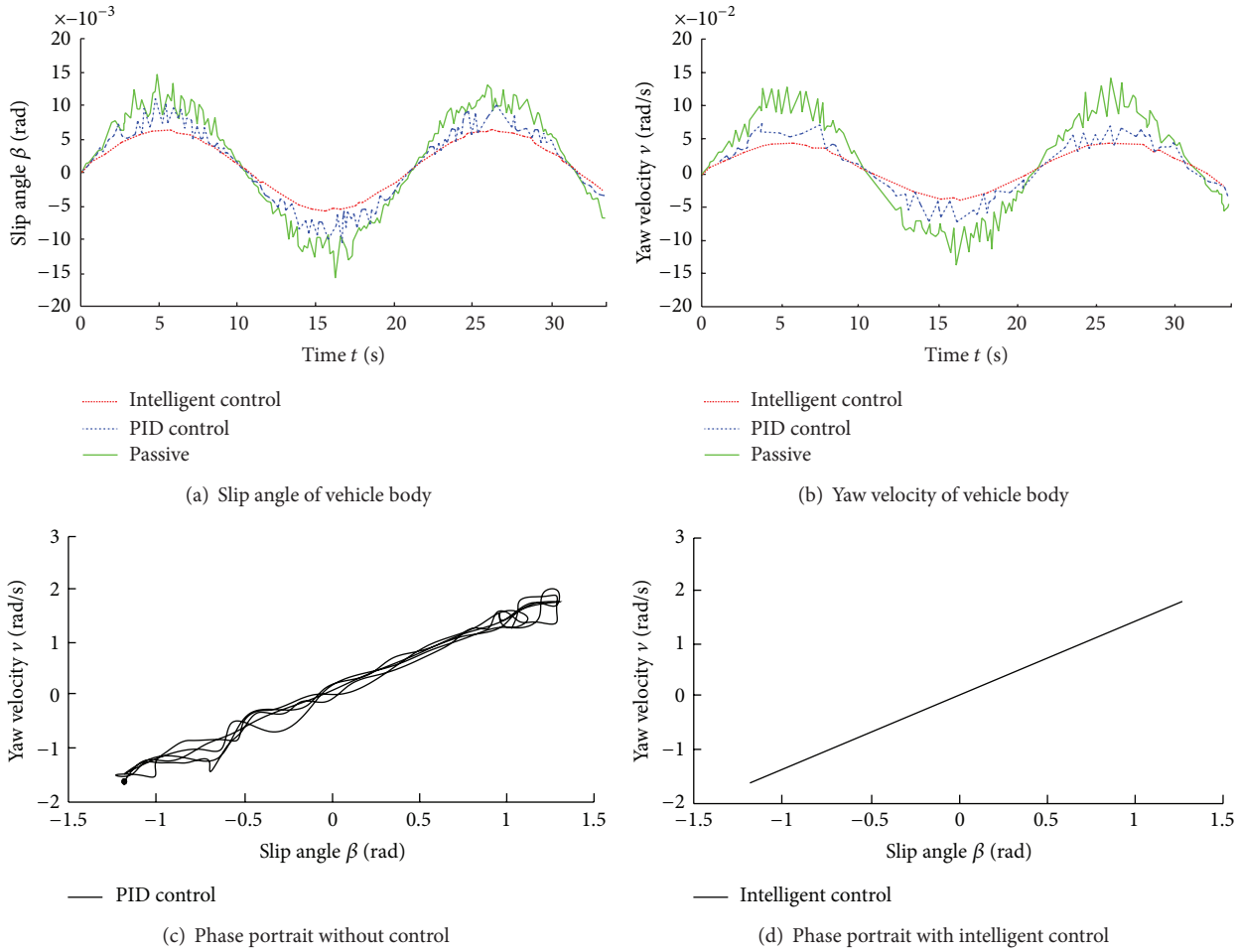

Figure 17: Vehicle results for S-shaped input.

produced by the irregularities are also significantly weakened. This indicates that the proposed control method can be effectively used to suppress chaotic behavior.

Under the S-shaped operation condition, the slip angle and yaw velocity when the intelligent controller is applied are significantly better than the others as shown in Figures 17(a) and 17(b). The parameters also exhibit greater linearity in the phase portrait for the intelligent controller (Figure 17(d)) but disorder for the PID controller (Figure 17(c)). This also shows that the proposed control method can be effectively used to suppress chaotic behavior.

In Table 5, the intelligent control was proposed to make the Lyapunov exponents of the closed-loop system negative and thereby eliminate chaos from the related system. From these table and figures, it can be concluded that the chaotic oscillators were controlled and the performance of the vehicle and its lateral dynamic were improved.

It can be seen from Figures 18(a) and 18(b) that when the vehicle is unevenly excited by the pulse road, the intelligent control significantly improves the vertical acceleration of the vehicle and the yaw velocity speed amplitude of the vibration. However, the effects of the control in the vertical direction controlled by traditional PID are slightly lower (the acceleration amplitude in the vertical direction is about 1 m/s^2). This is because, in the traditional integrated control system, vertical control and other performance indicators are considered in a single frame, and the amplitude of the controlling force is obtained from the optimal weight acting against the generalized suspension force. The same situation occurs during the pitching movement of the vehicle as shown in Figure 18(c). It should be noted that during the transfer

Table 5: Lyapunov exponents for road test.

Measurement points			Lyapunov exponents
Slip angle	Step input	PID control	1.89
		Intelligent control	−0.55
	Snake input	PID control	2.29
		Intelligent control	−0.23
Yaw velocity	Step input	PID control	3.18
		Intelligent control	−0.16
	Snake input	PID control	5.16
		Intelligent control	−1.66

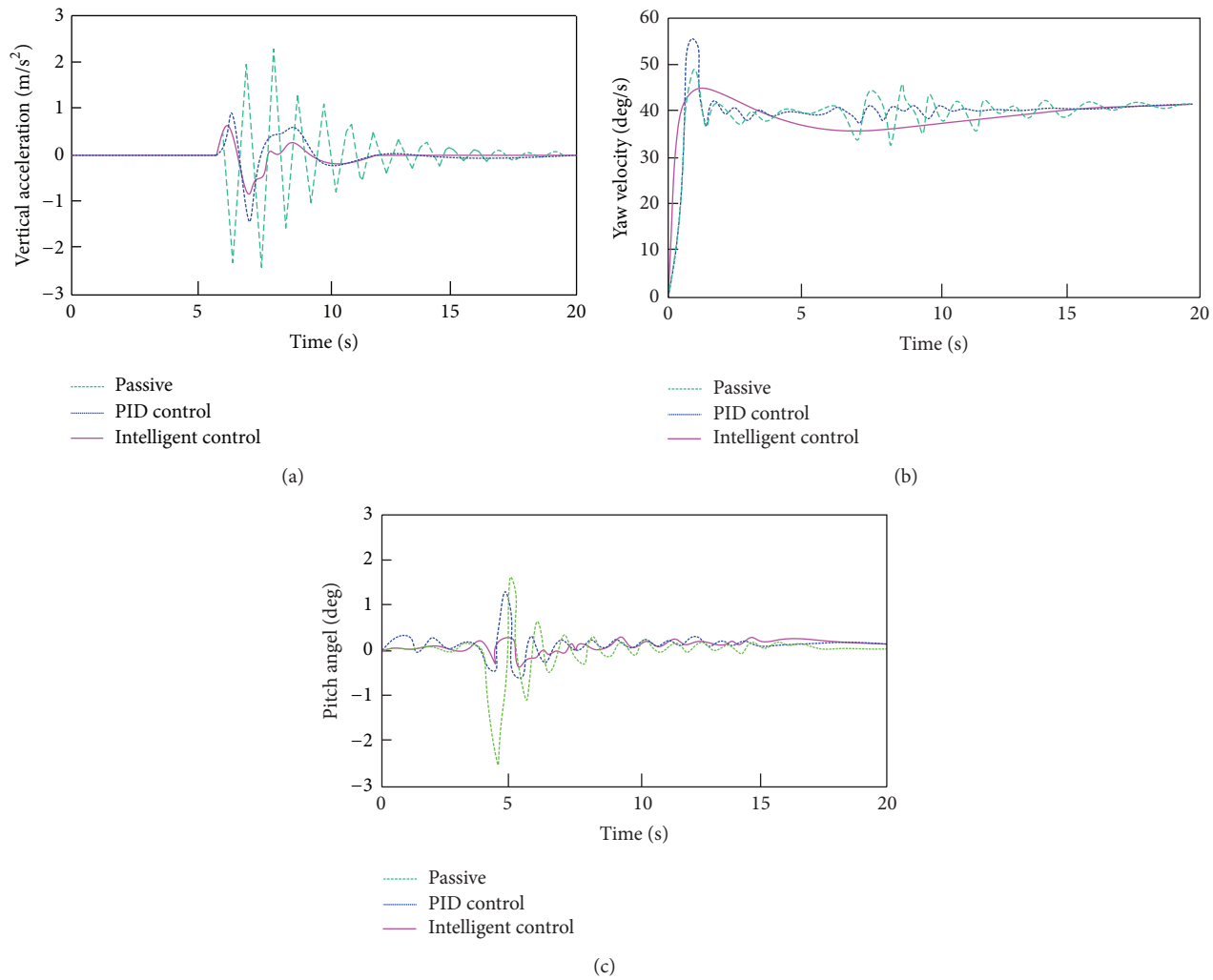

Figure 18: Results for step-pulse road.

from the step angle to the input, the entire vehicle has a stable roll angle of about 2° and the process lasts for about 4 s. The uneven excitation of the pulse road significantly affects the roll movement when the vertical load on the wheels changes the yaw and lateral forces, whereas this is not the case for traditional PID control. The negotiation algorithm can compensate for this by continuous negotiation among the different indicators. Moreover, the uneven pulse excitation of the road surface had almost no effect on the manipulation of the vehicle, which also reflects the robustness of the control strategy.

6. Conclusion

In this paper, we considered the coupling mechanism of advanced vehicle integration, as well as adaptive neural network of the vehicle wheels. By nonlinear analysis such as the use of bifurcation diagram and the Lyapunov exponent, it was shown that the lateral dynamics of the vehicle was characterized by complicated motions with increasing forward speed. Electric power steering and active suspension system based on intelligent control were used to reduce the nonlinearity, and a negotiation algorithm was designed to manage the interdependences and conflicts among handling stability, driving smoothness, and safety. The results of rapid control prototyping confirmed the feasibility of the proposed control method. By comparing the time response diagrams, phase portraits, and Lyapunov exponents for different operation conditions, we observed that the slip angle and yaw velocity of the lateral dynamics entered a stable domain and the chaotic motions were successfully suppressed. It was also shown that the safety was significantly improved. Under the angle step steering input operation conditions on the pulse road, the proposed intelligent control significantly improved the ride comfort and handling stability. The uneven pulse excitation of the road surface had almost no effect on the manipulation of the vehicle. Future work will focus on optimizing and

improving the robustness of the control and the information constraints and faults of the integrated vehicle dynamics.

Nomenclature

m, m_s: Qualities of the vehicle and the suspension, respectively
v: Velocity
$\beta, \dot{\beta}$: Slip angle and slip angular speed, respectively
h_s: Height of the center of gravity of the vehicle under roll condition
$\phi, \dot{\phi}, \ddot{\phi}$: Roll angle, roll angular speed, and roll angular acceleration of the vehicle, respectively
S_i: Lateral force on four wheels
I_γ: Rotary inertia of the vehicle
$\gamma, \dot{\gamma}$: Yaw rate and yaw acceleration, respectively
L_f, l_r: Distances from the front and rear wheels to the center of the body, respectively
$z_s, \dot{z}_s, \ddot{z}_s$: Vertical displacement, vertical velocity, and vertical acceleration of the vehicle body, respectively
F_{2i}: Composite force exerted by the suspension on the vehicle body
I_θ, I_φ: Pitching rotary inertia and roll rotary inertia of the vehicle, respectively
d: 1/2 of the track
m_{li}: Unsuspended mass
k_{li}: Stiffness of the wheels
z_{0i}: Displacement of the road
$z_{1i}, \dot{z}_{1i}, \ddot{z}_{1i}$: Vertical displacement, vertical velocity, and vertical acceleration of the unsuspended mass
k_{af}, k_{ar}: Stiffness of the stabilizer bar angle of the front and rear suspensions, respectively
k_{2i}: Stiffness of the suspension
c_{2i}: Damping coefficient of the suspension
$z_{2i}, \dot{z}_{2i}, \ddot{z}_{2i}$: Vertical displacement, vertical velocity, and vertical acceleration of the suspended mass, respectively
k_{af}, k_{ar}: Stiffness of the stabilizer rods of the front and rear suspensions, respectively
$\theta_j(k)$: Input of the jth neuron of the hidden layer
$p_i(k)$: Output of the input layer
w_{ij}: Weight of the connection between the input and hidden layers
ξ_j: Output of the jth neuron of the hidden layer
v_{jl}: Weight of the connection between the hidden and output layers
I_l: Output of the neuron of the output layer
α_1, α_2: Inclination angles of the left-side and right-side wheels of the front axle, respectively
α_3, α_4: Inclination angles of the left-side and right-side wheels of the rear axle, respectively
λ: Lyapunov exponent
$V_{\mathrm{mr}l}$: Returning control voltage of the motor
θ_h: Angle of the steering wheel
e_h: Deviation between the target and actual steering angles
K_p: Proportionality coefficient
K_i: Integral coefficient
$V_{\mathrm{mr}h}$: Returning control voltage of the motor
K_d: Integral coefficient
V_{mr}: Aligning control voltage of the motor
$e_d = I_{d,m,t} - I_{d,m}$: Deviation between the target and actual damping currents
$I_{d,m,t}$: Armature current for the target damping torque
$e_{d,\max}$: Maximum deviation between the target and actual damping currents
$K_{d,\mathrm{PWM},m}$: PWM duty ratio corresponding to e_d
$K_{d,\mathrm{PWM},\max}$: PWM duty ratio corresponding to $e_{d,\max}$.

Conflict of Interests

The authors declare that there is no conflict of interests regarding the publication of this paper.

Acknowledgments

This project was supported by the National Natural Science Foundation of China (Grant No. 50875112, 51305167), the Ph.D. Programs Foundation of the Ministry of Education of China (Grant no. 20093227110013, 20103227120011), the Jiangsu Municipal Natural Science Foundation (Grant no. BK2010337), and the Natural Science Foundation of Higher Education of Jiangsu (Grant no. 09KJA580001).

References

[1] H. Glaser, "Electronic stability program ESP," in *Audi Press Presentation*, pp. 9–13, 1996.

[2] X. Peng, X. Meng, K. Guo, D. Lu, and Y. Xie, "Experimental study of cornering properties of a tire on an icy and a dry pavement," *Chinese Journal of Mechanical Engineering*, vol. 40, no. 7, pp. 24–28, 2004.

[3] H. B. Pacejka, E. Bakker, and L. Nyborg, "Tyre modeling for use in vehicle dynamics studies," SAE Paper 870421, 1987.

[4] Y. L. Zhou and M. Chen, "Sliding mode control for NSVs with input constraint using neural network and disturbance observer," *Mathematical Problems in Engineering*, vol. 2013, Article ID 904830, 12 pages, 2013.

[5] B. L. Tian, W. R. Fan, Q. Zong, J. Wang, and F. Wang, "Adaptive high order sliding mode controller design for hypersonic vehicle with flexible body dynamics," *Mathematical Problems in Engineering*, vol. 2013, Article ID 357685, 11 pages, 2013.

[6] G. Wu and Y. Sheng, "Review on the application of chaos theory in automobile nonlinear system," *Chinese Journal of Mechanical Engineering*, vol. 46, no. 10, pp. 81–87, 2010.

[7] S. Inagaki, I. Kshiro, and M. Yamamoto, "Analysis on vehicle stability in critical cornering using phase-plane method," in *Proceedings of the International Symposium on Advanced Vehicle Control*, Tsukuba-shi, Japan, 1994.

[8] S. Shi, Z. Mao, H. Xiang, and X. Wang, "Nonlinear analysis methods of vehicle cornering stability," *Chinese Journal of Mechanical Engineering*, vol. 43, no. 10, pp. 77–81, 2007.

[9] X. Yang, Z. Wang, W. Peng, and S. Zhu, "Analysis on lateral dynamic stability and bifurcation of vehicle periodic steering under critical condition," *Journal of Highway and Transportation Research and Development*, vol. 43, no. 11, pp. 145–149, 2009.

[10] Z. Liu, G. Payre, and P. Bourassa, "Nonlinear oscillations and chaotic motions in a road vehicle system with driver steering control," *Nonlinear Dynamics*, vol. 9, no. 3, pp. 281–304, 1996.

[11] S.-C. Chang, "On controlling a chaotic vehicle dynamic system by using dither," *International Journal of Automotive Technology*, vol. 8, no. 4, pp. 467–476, 2007.

[12] E. Ono, S. Hosoe, H. D. Tuan, and S. Doi, "Bifurcation in vehicle dynamics and robust front wheel steering control," *IEEE Transactions on Control Systems Technology*, vol. 6, no. 3, pp. 412–420, 1998.

[13] S. Chang and H. Lin, "Study on controlling chaos of permanent magnet synchronous motor in electric vehicles," *International Journal of Vehicle Design*, vol. 58, no. 2, pp. 387–398, 2012.

[14] Z. Zhang, K. T. Chau, and Z. Wang, "Analysis and control of chaos for lateral dynamics of electric vehicles," in *Proceedings of the International Conference on Electrical Machines and Systems (ICEMS '11)*, pp. 1–6, Beijing , China, 2011.

[15] J. D. Lozoya-Santos, R. Morales-Menendez, and R. A. R. Mendoza, "Control of an automotive semi-active suspension," *Mathematical Problems in Engineering*, vol. 2012, Article ID 218106, 21 pages, 2013.

[16] C. March and T. Shim, "Integrated control of suspension and front steering to enhance vehicle handling," *Proceedings of the Institution of Mechanical Engineers D*, vol. 221, no. 4, pp. 377–391, 2007.

[17] T. Yoshimura and Y. Emoto, "Steering and suspension system of a half car model using fuzzy reasoning and skyhook dampers," *International Journal of Vehicle Design*, vol. 31, no. 2, pp. 229–250, 2003.

[18] A. Alleyne, "A comparison of alternative intervention strategies for unintended roadway departure (URD) control," *Vehicle System Dynamics*, vol. 27, no. 3, pp. 157–186, 1997.

[19] T. Gordon, M. Howell, and F. Brandao, "Integrated control methodologies for road vehicles," *Vehicle System Dynamics*, vol. 40, no. 1–3, pp. 157–190, 2003.

[20] Q. Qu and J. Zu, "Variable structure model following control of four-wheel-steering vehicle," *International Journal of Vehicle Design*, vol. 37, no. 4, pp. 291–310, 2005.

[21] P. Gaspar, I. Szaszi, and J. Bokor, "Design of robust controllers for active vehicle suspension using the mixed μ synthesis," *Vehicle System Dynamics*, vol. 40, no. 4, pp. 193–228, 2003.

[22] S.-S. You, H.-S. Choi, H.-S. Kim, T.-W. Lim, and S.-K. Jeong, "Active steering for intelligent vehicles using advanced control synthesis," *International Journal of Vehicle Design*, vol. 42, no. 3-4, pp. 244–262, 2006.

[23] H. Zhang, Y. Shi, and A. S. Mehr, "On H_∞ filtering for discrete-time Takagi—sugeno fuzzy systems," *IEEE Transactions on Fuzzy Systems*, vol. 20, no. 2, pp. 396–401, 2012.

[24] H. Zhang, Y. Shi, and B. Mu, "Optimal H_∞-based linear-quadratic regulator tracking control for discrete-time Takagi—sugeno fuzzy fystems with preview actions," *Journal of Dynamic Systems, Measurement, and Control*, vol. 135, Article ID 044501, pp. 1–5, 2013.

[25] H. Zhang, Y. Shi, and M. Liu, "H_∞ step tracking control for networked discrete-time nonlinear systems with integral and predictive actions," *IEEE Transactions on Industrial Informatics*, vol. 9, no. 1, pp. 337–345, 2013.

[26] W. Chen, H. Xiao, L. Liu, and J. W. Zu, "Integrated control of automotive electrical power steering and active suspension systems based on random sub-optimal control," *International Journal of Vehicle Design*, vol. 42, no. 3-4, pp. 370–391, 2006.

[27] Q. Wang, W. Jiang, W. Chen, and J. Zhao, "Simultaneous optimization of mechanical and control parameters for integrated control system of active suspension and electric power steering," *Chinese Journal of Mechanical Engineering*, vol. 44, no. 8, pp. 67–72, 2011.

Hindawi Publishing Corporation
Mathematical Problems in Engineering
Volume 2014, Article ID 386174, 10 pages
http://dx.doi.org/10.1155/2014/386174

Research Article

A High-Performance Control Method of Constant V/f-Controlled Induction Motor Drives for Electric Vehicles

Long Chen, Xiaodong Sun, Haobin Jiang, and Xing Xu

Automotive Engineering Research Institute, Jiangsu University, Zhenjiang 212013, China

Correspondence should be addressed to Xiaodong Sun; xdsun@ujs.edu.cn

Received 21 September 2013; Revised 12 December 2013; Accepted 12 December 2013; Published 21 January 2014

Academic Editor: Hui Zhang

A three-phase induction motor used as a propulsion system for the electric vehicle (EV) is a nonlinear, multi-input multi-output, and strong coupling system. For such a complicated model system with unmeasured and unavoidable disturbances, as well as parameter variations, the conventional vector control method cannot meet the demands of high-performance control. Therefore, a novel control strategy named least squares support vector machines (LSSVM) inverse control is presented in the paper. Invertibility of the induction motor in the constant V/f control mode is proved to confirm its feasibility. The LSSVM inverse is composed of an LSSVM approximating the nonlinear mapping of the induction motor and two integrators. The inverse model of the constant V/f-controlled induction motor drive is obtained by using LSSVM, and then the optimal parameters of LSSVM are determined automatically by applying a modified particle swarm optimization (MPSO). Cascading the LSSVM inverse with the induction motor drive system, the pseudolinear system can be obtained. Thus, it is easy to design the closed-loop linear regulator. The simulation results verify the effectiveness of the proposed method.

1. Introduction

Nowadays, some serious problems such as environment depravation and air pollution are becoming more and more serious, due to the rapid development of the global economy. Electric vehicles (EVs), including fuel cell-powered vehicle and hybrid electric vehicles, are being currently researched and their practicalities are increasingly capturing many countries' eyes, since they are a way to solve these problems that are tied to exhaust gas-emission and energy-saving issues [1–3].

By converting electrical energy into mechanical energy, a motor can propel a vehicle [4, 5]. Compared with the combustion engines, the motors have some main advantages in terms of power density, conversion efficiency, low-speed torque characteristics, and so on [6–9]. In addition, when the motor operates in the braking mode, it can convert the mechanical energy back to electrical energy [10, 11]. Aforementioned characteristics of the motors make the electric drive more energy efficient, more powerful, and more compact. With the rapid development of power electronics, information technology, and the revolution in motor control, the EV technologies are being quickly progressed. Among EV key technologies, selection of a suitable drive, optimum design of the motor topologies, and optimal control strategies are the major factors [12, 13].

In general, permanent-magnet synchronous motors (PMSMs) have been popular in EV traction applications, but some problems have recently arisen. One of the key issues is that the cost of rare earth materials, such as neodymium, has sharply increased in the past years [14–16]. Therefore, the induction motors are drawing attention as a promising alternative to PMSMs [17]. The induction motors have many characteristics, such as firm structure, small model, ruggedness, light capacity, low price, and the ability to operate in the extended high speed. Moreover, with the growth of power electronic technology and microprocess technology, high-speed induction motors driven by changeable frequency have many merits on aspects of reliability, low maintenance, low cost, craftwork, and so on [18–20]. So induction motor drive systems play an increasingly important role in driving EV. With the background, our study revisits and renews this old technology, aiming at high-performance control of the induction motor drives in EV applications.

The mature control method of induction motor drives is the vector control, which has been widely implemented in

electric drives [21, 22]. However, since the rotor flux angle of the induction motor is not directly measurable, vector control of an induction motor is more difficult than that of a PMSM. In addition, another issue in electrical drives is system sensitivity to inaccuracy and changes of motor parameters [23, 24]. Since the vector control systems are very sensitive to such inaccuracies, some parameters of the induction motor drives should be estimated online, and a more robust control structure is required. Therefore, some intelligent control methods, such as fuzzy control [25, 26], sliding mode control [27–29], adaptive control [30, 31], neural network control [32, 33], and other advanced control methods [34–36], are adopted for the induction motor drives. These approaches only improve different aspects of the control performance of induction motor drives. Thus, how to enhance the satisfying dynamic behavior of the induction motor drive for EVs further is very urgent.

The aim of this paper is to propose a novel control scheme based on least squares support vector machines (LSSVM) inverse for the constant V/f-controlled induction motor drive system for EVs. The mathematic model of the induction motor drive is presented, and a reversible analysis of such system is also performed. Based on the analysis, speed control of the induction motor drive based on LSSVM inverse system method is proposed. The method is combined by LSSVM, which has the abilities of learning and function approximation and the adaptation capacity of system parameter variations, and the inverse system method which can realize the linearization of complex nonlinear system [37, 38]. The LSSVM is used to identify the inverse model of the constant V/f-controlled induction motor drive system, and a modified particle swarm optimization (MPSO) algorithm is adopted to optimize the kernel parameter and regularization parameter of the LSSVM. Consequently, a composite pseudolinear system is completed by constructing LSSVM inverse and combining it with the original system. Then the linear control techniques can be applied to design control system to achieve the high performance control of the original nonlinear system. Finally, the simulation testing research is studied using this method, and the control effect is satisfying.

2. Mathematic Model and Reversible Analyses

For current-followed SPWM inverter of the induction motor, when the nonlinear and time delay of the inverter, magnetic saturation, and iron loss of the induction motor are ignored, the state equation is described as a 6-order nonlinear model in still α-β coordinates:

$$\begin{aligned}
\frac{d\omega_r}{dt} &= \frac{n_p}{J}\left(T_e - T_L\right) = \frac{n_p^2}{J}\left(\psi_{s\alpha} i_{s\beta} - \psi_{s\beta} i_{s\alpha}\right) - \frac{n_p}{J} T_L, \\
\frac{d\psi_{s\alpha}}{dt} &= V\cos\theta_1 - R_s i_{s\alpha}, \\
\frac{d\psi_{s\beta}}{dt} &= V\sin\theta_1 - R_s i_{s\beta}, \\
\frac{di_{s\alpha}}{dt} &= \frac{R_r}{L_sL_r - L_m^2}\psi_{s\alpha} + \frac{L_r}{L_sL_r - L_m^2}\omega_r\psi_{s\beta} - \frac{R_rL_s + L_rR_s}{L_sL_r - L_m^2} i_{s\alpha} \\
&\quad - \omega_r i_{s\beta} + \frac{L_r}{L_sL_r - L_m^2} V\cos\theta_1, \\
\frac{di_{s\beta}}{dt} &= \frac{R_r}{L_sL_r - L_m^2}\psi_{s\beta} - \frac{L_r}{L_sL_r - L_m^2}\omega_r\psi_{s\alpha} - \frac{R_sL_r + L_sR_r}{L_sL_r - L_m^2} i_{s\beta} \\
&\quad + \omega_r i_{s\alpha} + \frac{L_r}{L_sL_r - L_m^2} V\sin\theta_1, \\
\frac{d\theta_1}{dt} &= \omega_1,
\end{aligned} \tag{1}$$

where ω_1 and ω_r are synchronous angle frequency and rotate speed, respectively. $i_{s\alpha}$ and $i_{s\beta}$ are stator currents in α-β coordinates, respectively. $\psi_{s\alpha}$ and $\psi_{s\beta}$ are stator flux linkage in α-β coordinates, respectively. T_r is rotor time constant. L_m is mutual inductance. n_p is the number of pole pairs. L_s and L_r are stator inductance and rotor inductance, respectively. R_s and R_r are stator resistance and rotor resistance, respectively. T_e and T_L are electromagnetic torque and load torque, respectively. θ_1 is angle between the space voltage vector and the α axis. V is the amplitude of the space voltage vector.

Given the state variable

$$\mathbf{x} = \left[\omega_r, \psi_{s\alpha}, \psi_{s\beta}, i_{s\alpha}, i_{s\beta}, \theta_1\right]^T = \left[x_1, x_2, x_3, x_4, x_5, x_6\right]^T \tag{2}$$

and the input variable

$$\mathbf{u} = \left[V, \omega_1\right]^T = \left[u_1, u_2\right]^T, \tag{3}$$

the output is the ω_r, so

$$\begin{aligned}
\dot{\mathbf{x}} &= f(\mathbf{x}, \mathbf{u}) \\
&= \begin{bmatrix}
\frac{n_p^2}{J}\left(x_2x_5 - x_3x_4\right) - \frac{n_p}{J}T_L \\
u_1\cos x_6 - R_s x_4 \\
u_1\sin x_6 - R_s x_5 \\
\frac{R_r}{L_sL_r - L_m^2}x_2 + \frac{L_r}{L_sL_r - L_m^2}x_1x_3 - \frac{R_rL_s + L_rR_s}{L_sL_r - L_m^2}x_4 \\
-x_1x_5 + \frac{L_r}{L_sL_r - L_m^2}u_1\cos x_6 \\
\frac{R_r}{L_sL_r - L_m^2}x_3 - \frac{L_r}{L_sL_r - L_m^2}x_1x_2 - \frac{R_sL_r + L_sR_r}{L_sL_r - L_m^2}x_5 \\
+x_1x_4 + \frac{L_r}{L_sL_r - L_m^2}u_1\sin x_6 \\
u_2
\end{bmatrix}, \\
\mathbf{y} &= h(\mathbf{x}) = x_1 = \omega_r.
\end{aligned} \tag{4}$$

When the induction motor is operating in the constant V/f control mode, we can obtain the following expression:

$$V = k\omega_1, \tag{5}$$

where $k = \sqrt{3/2}\cdot(220\cdot\sqrt{2})/(2\cdot\pi\cdot 50) = ((\sqrt{3}\cdot 220)/(2\cdot\pi\cdot 50))$ is the proportion coefficient of frequency voltage.

So

$$u_1 = ku_2. \tag{6}$$

In order to analyze the reversibility of the induction motor, the output formula should be differentiated until the input variable is visualized firstly. According to expression (11), the following expressions can be deduced:

$$y^{(1)} = x^{(1)} = \frac{n_p^2}{J}\left(x_2x_5 - x_3x_4\right) - \frac{n_p}{J}T_L, \tag{7}$$

$$\begin{aligned} y^{(2)} &= \frac{n_p^2}{J}\left(x_2\dot{x}_5 + \dot{x}_2x_5 - x_3\dot{x}_4 - \dot{x}_3x_4\right) \\ &= \frac{n_p^2}{J}\left[x_2\left(\frac{R_r}{L_sL_r - L_m^2}x_3 - \frac{L_r}{L_sL_r - L_m^2}x_1x_2 \right.\right. \\ &\qquad - \frac{R_sL_r + L_sR_r}{L_sL_r - L_m^2}x_5 + x_1x_4 \\ &\qquad \left. + \frac{L_r}{L_sL_r - L_m^2}ku_2\sin x_6\right) \\ &\qquad + \left(ku_2\cos x_6 - R_sx_4\right)x_5 \\ &\qquad - x_3\left(\frac{R_r}{L_sL_r - L_m^2}x_2 \right. \\ &\qquad + \frac{L_r}{L_sL_r - L_m^2}x_1x_3 \\ &\qquad - \frac{R_rL_s + L_rR_s}{L_sL_r - L_m^2}x_4 - x_1x_5 \\ &\qquad \left. + \frac{L_r}{L_sL_r - L_m^2}ku_2\cos x_6\right) \\ &\qquad \left. - \left(ku_2\sin x_6 - R_sx_5\right)x_4\right], \end{aligned} \tag{8}$$

$$\begin{aligned} \frac{\partial y^{(2)}}{\partial u_2} &= \frac{n_p^2}{J}\left[x_2\frac{L_r}{L_sL_r - L_m^2}k\sin x_6 + k\cos x_6x_5 \right. \\ &\qquad \left. - x_3\frac{L_r}{L_sL_r - L_m^2}k\cos x_6 - k\sin x_6x_4\right] \\ &= \frac{n_p^2}{J}\left[\frac{L_rk}{L_sL_r - L_m^2}\left(x_2\sin x_6 - x_3\cos x_6\right) \right. \\ &\qquad \left. + k\left(\cos x_6x_5 - \sin x_6x_4\right)\right]. \end{aligned} \tag{9}$$

Since $x \in \mathbf{\Omega} = \{x \in R^6 : (L_rk/(L_sL_r - L_m^2))(x_2\sin x_6 - x_3\cos x_6) + k(x_5\cos x_6 - x_4\sin x_6) \neq 0\}$, the inverse of system is existent. According to implicit function theorem, the inverse system can be written as

$$u = \xi\left(x, y, \dot{y}, \ddot{y}\right). \tag{10}$$

3. Basic Conception of LSSVM

As an interesting variant of the standard support vector machines (SVM), least squares support vector machines (LSSVM) have been proposed by Suykens and Vandewalle for solving pattern recognition and nonlinear function estimation problems [39, 40]. Here, we simply present the basic principle of LSSVM. Considering a given training set $\{\mathbf{x}_i, \mathbf{y}_i\}_{i=1}^l$, with input data $\mathbf{x}_i \in \mathbf{R}^n$ and output data $\mathbf{y}_i \in \mathbf{R}$, in feature space, the regression model takes the form

$$f(\mathbf{x}) = \mathbf{w}^T\mathbf{\Phi}(\mathbf{x}) + b, \tag{11}$$

where the nonlinear mapping $\mathbf{\Phi}(\cdot) : \mathbf{R}^n \to \mathbf{R}^H$ maps the input data into a higher dimensional feature space, $\mathbf{w} \in \mathbf{R}^H$ is a weight vector of the same dimension as the feature space, and b is a threshold. Then the following optimization problem for the LSSVM is formulated:

$$\begin{aligned} \min \quad & J(\mathbf{w}, \xi) = \frac{1}{2}\|\mathbf{w}\|^2 + \frac{1}{2}\gamma\sum_{i=1}^l \xi_i^2 \\ \text{subject to} \quad & \mathbf{y}_i = w^T\mathbf{\Phi}(x_i) + b + \xi_i, \end{aligned} \tag{12}$$

where ξ is approximation error at the instant i, J is a loss function, and γ is an adjustable constant which determines penalties for estimation errors.

The corresponding Lagrange function is described as

$$\mathbf{L}(\mathbf{w}, b, \boldsymbol{\xi}, \boldsymbol{\alpha}) = J(\mathbf{w}, \boldsymbol{\xi}) - \sum_{i=1}^l \alpha_i\left[\mathbf{w}^T\mathbf{\Phi}(\mathbf{x}_i) + b + \boldsymbol{\xi}_i - \mathbf{y}_i\right], \tag{13}$$

where $\boldsymbol{\alpha} = (\alpha_1, \alpha_2, \alpha_3, \ldots, \alpha_l)^T$ is a vector with the Lagrange multipliers.

According to the optimization conditions by Karush-Kuhn-Tucker, the optimal values can be found by setting the derivatives of the Lagrange function equal to zero:

$$\begin{aligned} \frac{\partial \mathbf{L}}{\partial \mathbf{w}} &= 0 \longrightarrow \mathbf{w} = \sum_{i=1}^l \alpha_i\mathbf{\Phi}(x_i), \\ \frac{\partial \mathbf{L}}{\partial b} &= 0 \longrightarrow \sum_{i=1}^l \alpha_i = 0, \\ \frac{\partial \mathbf{L}}{\partial \xi_i} &= 0 \longrightarrow \alpha_i = \gamma\xi_i, \quad i = 1, 2, \ldots, l, \\ \frac{\partial \mathbf{L}}{\partial \alpha_i} &= 0 \longrightarrow \mathbf{w}^T\mathbf{\Phi}(\mathbf{x}_i) + b + \xi_i - \mathbf{y}_i = 0. \end{aligned} \tag{14}$$

Then the optimization problem can be rewritten as

$$\begin{bmatrix} 0 & \mathbf{1}_{l\times 1}^T \\ \mathbf{1}_{l\times 1} & \mathbf{\Omega} + \gamma^{-1}\mathbf{I} \end{bmatrix}\begin{bmatrix} b \\ \boldsymbol{\alpha} \end{bmatrix} = \begin{bmatrix} 0 \\ \mathbf{y} \end{bmatrix}, \tag{15}$$

where $\mathbf{y} = [y_1, y_2, y_3, \ldots, y_l]^T$, $\mathbf{1}_{l\times 1} = [1, 1, \ldots, 1]^T$, $\mathbf{I} = \mathrm{diag}[1, 1, \ldots, 1]$, $\mathbf{\Omega} = \{\Omega_{ij}\}_{l\times l}$, $\Omega_{ij} = \mathbf{\Phi}^T(\mathbf{x}_i) \cdot \mathbf{\Phi}(\mathbf{x}_j)$, $i = 1, 2, \ldots, l$.

According to Mercer's condition, there is kernel function $K(\mathbf{x}_i, \mathbf{x}) = \mathbf{\Phi}^T(\mathbf{x}_i) \cdot \mathbf{\Phi}(\mathbf{x})$, which causes such LSSVM model

$$f(\mathbf{x}) = \sum_{i=1}^l \boldsymbol{\alpha}_iK(\mathbf{x}_i, \mathbf{x}) + b, \tag{16}$$

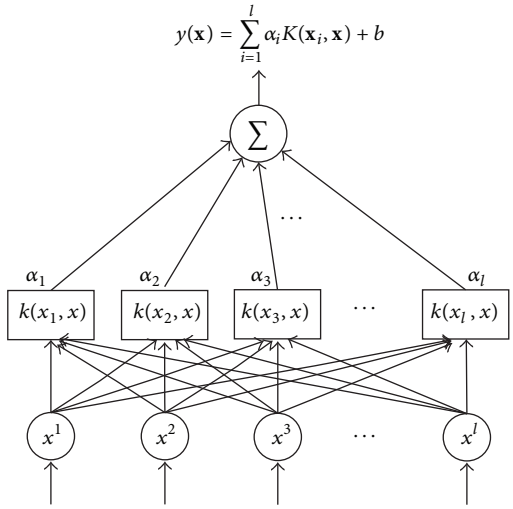

Figure 1: Structure of least squares support vector machine.

where $\boldsymbol{\alpha}$ and b are obtained by solving (7). In this paper, we will focus on RBF kernel function which corresponds to

$$K(\mathbf{x}_i, \mathbf{x}) = \exp\left(\frac{-|\mathbf{x}_i - \mathbf{x}|^2}{2\sigma^2}\right), \tag{17}$$

where σ is the kernel parameter. The structure of the LSSVM is shown in Figure 1.

4. MPSO-Based Parameters Optimization for LSSVM

4.1. MPSO. Particle swarm optimization (PSO), a novel evolutionary computation technique, was proposed by Kennedy and Eberhart in 1995 [41–43]. It is inspired by social behavior of bird flocking and fish schooling and has been found to be robust in solving nonlinear optimization problems. Compared with other stochastic approaches, PSO can generate solutions of high quality with relative shorter calculation time and has more stable convergence features. In the original PSO algorithm, particles flying through the search space are affected by two factors: one is the best position ever found of the individual, and another is the best position of the group.

The position and velocity of ith individual (called particle) in d-dimensional search space can be represented as $\mathbf{u}_i = [u_{i1}, u_{i2}, \ldots, u_{id}]$ and $\mathbf{v}_i = [v_{i1}, v_{i2}, \ldots, v_{id}]$, respectively. The local best of the ith particle can be denoted as $\mathbf{p}_i = [p_{i1}, p_{i2}, \ldots, p_{id}]$ and the global best found so far can be denoted as $\mathbf{p}_g = [p_{g1}, p_{g2}, \ldots, p_{gd}]$. Then, at each iteration, the new positions and velocities of each particle can be calculated as shown in the following formulas:

$$\begin{aligned}\mathbf{v}_i(k+1) = {} & \omega \mathbf{v}_i(k) + c_1 r_1 \left(\mathbf{p}_i(k) - \mathbf{u}_i(k)\right) \\ & + c_2 r_2 \left(\mathbf{p}_g(k) - \mathbf{u}_i(k)\right),\end{aligned} \tag{18}$$

$$\mathbf{u}_i(k+1) = \mathbf{u}_i(k) + \mathbf{v}_i(k), \tag{19}$$

where $i = 1, 2, \ldots, m$. m is the number of particles. k is the number of current iteration. $\mathbf{u}_i(k)$ is the position of ith particle at iteration k. $\mathbf{p}_i(k)$ is the best local position of ith particle at iteration k. $\mathbf{p}_g(k)$ is the best global position of all particles at iteration k. $\mathbf{v}_i(k)$ is the velocity of ith particle at iteration k. r_1 and r_2 are random variables drawn from a uniform distribution in the range $[0, 1]$ to provide a stochastic weight of the different components participating in the particle velocity definition. c_1 and c_2 are two acceleration constants regulating the relative velocities with respect to the best global and local positions, respectively. ω is the inertia weight used as a tradeoff between global and local exploration capabilities of the swarm. Let the inertia weight be a high value $\omega_{\max}$ in the early evolution and linearly decrease to $\omega_{\min}$ at the maximal number of iterations. Its mathematical representation can be described as

$$\omega = \omega_{\min} + \frac{n_{\max} - n}{n_{\max}} \left(\omega_{\max} - \omega_{\min}\right), \tag{20}$$

where $n_{\max}$ is the maximal number of iterations and n is the current number of iterations.

In order to overcome the limitation that basic PSO was not convergent because of the maximum speed parameters and big acceleration constants (c_1, c_2), Clerc introduced the shrinkage factor η. This approach can ensure that the PSO algorithm convergent during the search process. So, in this paper, we apply the MPSO method with shrinkage factor η to optimize the LSSVM's parameters. Then the mathematical representations of PSO algorithm given in (18) can be changed to

$$\begin{aligned}\mathbf{v}_i(k+1) = \eta \Big(& \omega \mathbf{v}_i(k) + c_1 r_1 \left(\mathbf{p}_i(k) - \mathbf{u}_i(k)\right) \\ & + c_2 r_2 \left(\mathbf{p}_g(k) - \mathbf{u}_i(k)\right)\Big),\end{aligned} \tag{21}$$

where

$$\eta = \frac{2}{\left|2 - \varphi - \sqrt{\varphi^2 - 4\varphi}\right|}, \quad \varphi = c_1 + c_2 > 4. \tag{22}$$

Aiming at the regularization parameter γ and kernel parameter σ which are needed to be optimized, choose mean square root error (RMSE) of the LSSVM as shown in (14) as the fitness function $f(\cdot)$ of the MPSO:

$$f(\mathbf{u}) = f(\gamma, \sigma) = E_{\text{RMSE}} = \sqrt{\frac{1}{l}\sum_{i=1}^{l}\left(\mathbf{y}_i - \hat{\mathbf{y}}_i\right)^2}, \tag{23}$$

where $\mathbf{y}_i$ and $\hat{\mathbf{y}}_i$ are real value and model output one, respectively. The minimization of the fitness function can be seen as a mechanism to guarantee a reasonable choice of the optimized parameters (γ, σ).

4.2. Procedure of LSSVM's Parameters Optimization Using MPSO. The steps of the MPSO-LSSVM estimation are summarized as follows.

Step 1. Generate training and test samples sets, and normalize the data.

Step 2. Initialize the parameters of MPSO. The values of the parameters are as follows: $m = 60$, $d = 2$, $n_{\max} = 500$, $c_1 = c_2 = 2.05$, $\omega_{\max} = 0.9$, and $\omega_{\min} = 0.4$.

Step 3. Generate an initial swarm of size m. Set the best position of each particle with its initial position; that is, $\mathbf{p}_i = \mathbf{u}_i$ $(i = 1, 2, \ldots, m)$.

Step 4. Set to zero the velocity vectors $\mathbf{v}_i$ $(i = 1, 2, \ldots, m)$ that are associated with the m particles.

Step 5. For each candidate particle $\mathbf{u}_i$ $(i = 1, 2, \ldots, m)$, train an LSSVM estimator on the corresponding training set and with the estimation of γ and σ that are conveyed by $\mathbf{u}_i$. Then, compute its fitness function $f(\mathbf{u}_i)$.

Step 6. Update the velocity of each particle using (21). To perform the update, the best global position $\mathbf{p}_g$ is selected. $\mathbf{p}_g$ is chosen as the position exhibiting the minimal value of the considered fitness function over all explored trajectories. In detail, compare each particle's current fitness value $f(\mathbf{u}_i)$ with the fitness value of its best local position $f(\mathbf{p}_i)$. If $f(\mathbf{u}_i) < f(\mathbf{p}_i)$, let $\mathbf{p}_i = \mathbf{u}_i$. And compare the current fitness value $f(\mathbf{u}_i)$ with the fitness value of the best globe position $f(\mathbf{p}_g)$. If $f(\mathbf{u}_i) < f(\mathbf{p}_g)$, let $\mathbf{p}_g = \mathbf{u}_i$.

Step 7. Update the position of each particle by means of (19). In the event of a particle flying beyond the predefined boundary of the search space, set the position of the particle at the space boundary and reverse its search direction by means of multiplying its velocity vector by −1.

Step 8. If $n_{\max} \geq 500$ or RMSE $< 1 \times 10^{-3}$, output the optimal parameter values; else return to Step 5.

5. LSSVM Inverse Control

From the mathematical model of the constant V/f-controlled induction motor described as (2), it can be seen that the induction motor drive system is a nonlinear and strong coupling system. Therefore, it is very difficult to get the accurate analytic expression described in (10). To effectively solve this thorny problem, an LSSVM is employed to identify the inverse model of the constant V/f-controlled induction motor drive system, since the LSSVM has the ability of approaching an arbitrary nonlinear function with satisfactory accuracy. The proposed LSSVM inverse consists of an LSSVM approximating the nonlinear mapping (10) and two integrators charactering its dynamic behaviors. In view of the principle of the LSSVM regression and the control principle of the inverse system scheme, we can easily obtain the whole implementation steps of the LSSVM inverse control scheme for the induction motor drive system for EVs.

Step 1. A superposition of the random signals and constant is chosen as the input excitation signal. The original induction motor drive system is adequately excited, and then we can obtain its static and dynamic performance. We not only need the static data of the constant V/f-controlled induction motor drive system but also need the dynamic ones for the LSSVM learning the inverse model of the constant V/f-controlled induction motor. Consequently, the complete inverse model of induction motor drive system can just be gotten. During the measuring process, because there are various random noises jamming and the error of measurement devices themselves, there are generally some errors between measured values and real ones. In order to effectively overcome these disadvantages, the 2-order filters are used for adopting data. Note that the variation period of the given speed signal must be chosen properly; otherwise the practical system cannot follow the given signal. In this paper, the variation period of the all kinds of given signal is set at 10 s and the sampling period of speed is set at 0.1 s. The whole operation time is 200 s and 2000 sampled data are obtained.

Step 2. By using precise seven-point algorithm, the 1-order and 2-order offline derivative of speed output response can be obtained. Therefore, the training sample sets $\{\mathbf{x}_i, u\}$ $(i = 1, 2, \ldots, l, l = 1000)$ can be formed by chosing from original sampling period equidistantly, where, $\mathbf{x} = [y^{(2)}, y^{(1)}, y] = [\omega_r^{(2)}, \omega_r^{(1)}, \omega_r]$ and $u = \omega_1$ are, respectively, the input data and the expected output data of the LSSVM which learns the inverse model of the constant V/f-controlled induction motor drive system. Figure 2 shows the collected training data.

Step 3. According to the MPSO optimization procedure mentioned aforementioned, the best values of LSSVM parameters are $\gamma = 950$ and $\sigma = 2.6$, and its RMSE (i.e., the fitness function) is equal to 3.421×10^{-3}. Through learning the LSSVM with training sample sets, the corresponding input vector coefficient α_i (where the zero coefficients are also included in the formula) and threshold value b can be obtained. Therefore, in view of the current input $\mathbf{x}$, the output of the αth-order inversion can be identified as

$$\mathbf{u}(\mathbf{x}) = \sum_{i=1}^{d} \boldsymbol{\alpha}_i \left(\boldsymbol{\Phi}^T(\mathbf{x}_i) \cdot \boldsymbol{\Phi}(\mathbf{x})\right) + b = \sum_{i=1}^{d} \boldsymbol{\alpha}_i K(\mathbf{x}_i, \mathbf{x}) + b. \quad (24)$$

Step 4. By combining the LSSVM inverse with the induction motor drive system, a 2-order compound system, named pseudolinear system, can be obtained as shown in Figure 3. The input and output linearization of the original constant V/f-controlled induction motor drive system is achieved. Although the relationship between input and output of the compound system is linear, there are still some nonlinear factors in the system. Therefore, the compound system is not an ideal linear system and is called the pseudolinear system. Since the compound system is an open-loop unstable system and various uncertainties are existing in practical applications, the additional closed-loop controller should be designed. In this paper, the proportional integral (PI) controller is designed for the closed-loop controller. Figure 4 shows the whole control diagram of LSSVM inverse for the induction motor drive system.

6. Simulation Test Research

The parameters of the induction motor are $P_e = 5$ KW, $R_s = 5.35\,\Omega$, $R_r = 4.85\,\Omega$, $L_s = 0.41$ H, $L_r = 0.46$ H, $L_m = 0.47$ H, and $J = 0.0018$ kg·m^2. Rated speed is 1600 r/min.

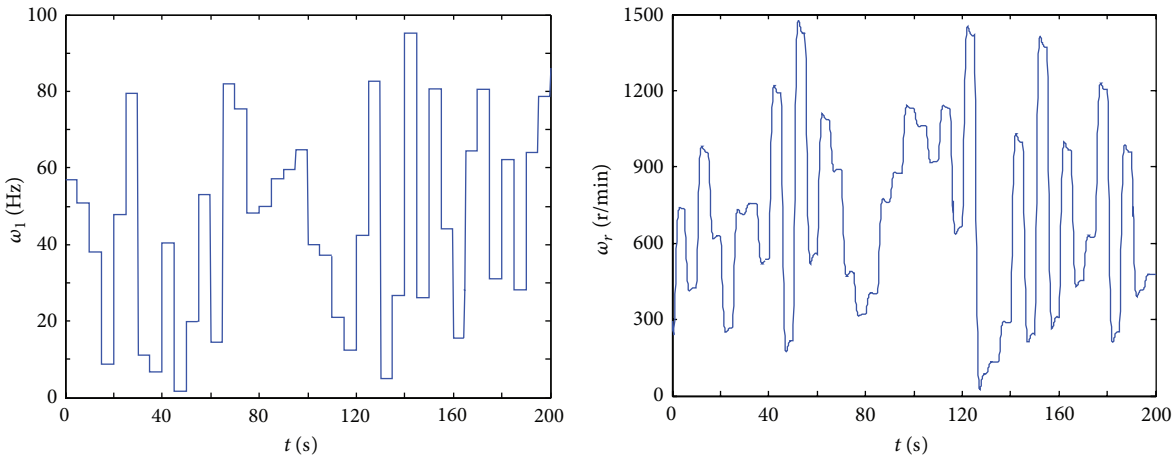

(a) ω_1 (b) ω_r

Figure 2: Collected training data.

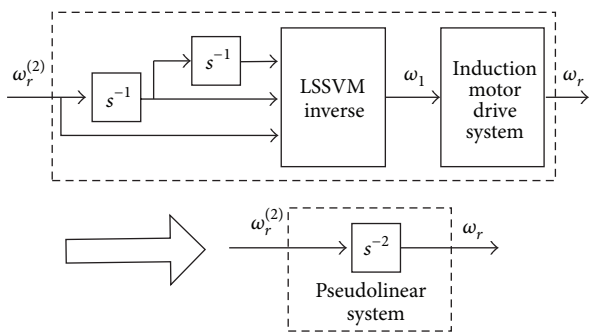

Figure 3: Diagram of pseudolinear system.

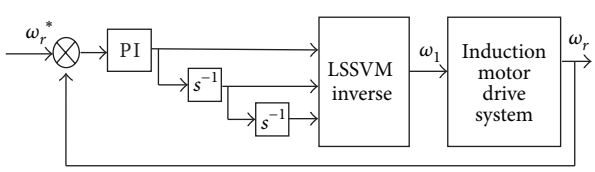

Figure 4: Control diagram of LSSVM inverse control.

6.1. Predicted Result Comparison of the Inverse Model. The remaining 1000 groups of data from the whole sample data sets are chosen and then adopted for testing sample to compare the predicted performance of the inverse model. To effectively test the performance of the inversion, the mean square root of error (E_{RMSE}) and maximal absolute error (E_{MAXE}) are considered as

$$E_{\mathrm{RMSE}} = \sqrt{\frac{1}{l}\sum_{i=1}^{l}(\mathbf{y}_i - \hat{\mathbf{y}}_i)^2},$$
$$E_{\mathrm{MAXE}} = \max_{i=1}^{l} \left|\mathbf{y}_i - \hat{\mathbf{y}}_i\right|, \tag{25}$$

where $i = 1, 2, \ldots, l$ and $\mathbf{y}_i$ and $\hat{\mathbf{y}}_i$ are real and predicting values.

Table 1: Comparison of predicting results of E_{RMSE}, E_{MAXE}, and t.

	E_{RMSE}	E_{MAXE}	t/s
Standard SVM	0.0091	0.0073	60. 472
Standard LSSVM	0.0053	0.0042	23. 193
MPSO-LSSVM	$1.306e-04$	$7.616e-04$	11.178

In order to verify the predicted performance of the LSSVM inversion with the MPSO algorithm (MPSO-LSSVM), the standard SVM and LSSVM are utilized for the training sample to develop the inversion of the constant V/f-controlled induction motor drive system. The CPU runtime (t/s) and the corresponding key performance indicators (E_{RMSE} and E_{MAXE}) of the models are listed in Table 1. From Table 1, it can be seen that the generalization ability and predicted precision of MPSO-LSSVM inversion is superior to the standard SVM and LSSVM inversion.

6.2. Simulation Results Analysis. The constant V/f-controlled induction motor drive system under the control schemes of the proposed method and vector control are simulated using Matlab/Simulink.

Case 1 (performance comparison of speed startup response without load disturbances). In this case, Figures 5 and 6 are, respectively, the simulation results of speed startup response curves in the case of rated load with the proposed method and vector control. The dashed and solid lines are, respectively, the reference value and practical one. Compared with the speed response with vector control, the speed response under LSSVM inverse control has a shorter settling time and much smaller overshoot and steady-state error. The corresponding performance index of the speed response is shown in Table 2. From Figures 5 and 6 and Table 2, we can see that the constant V/f-controlled induction motor drive system has a better speed-adjusting performance by using the proposed method.

Case 2 (performance comparison of tracking triangular wave without load disturbances). In this case, Figures 7 and 8

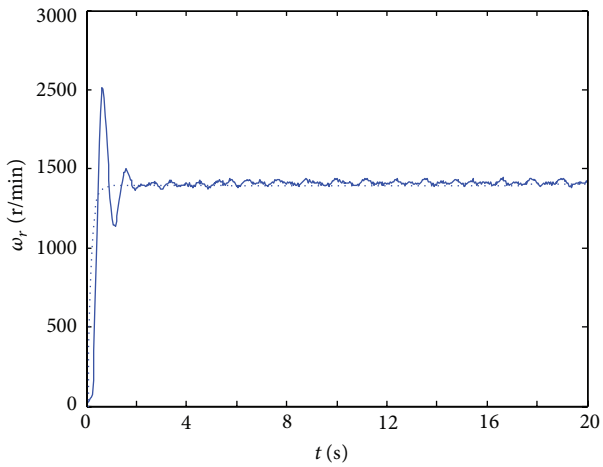

Figure 5: Speed startup response curves in the case of rated load with vector control method.

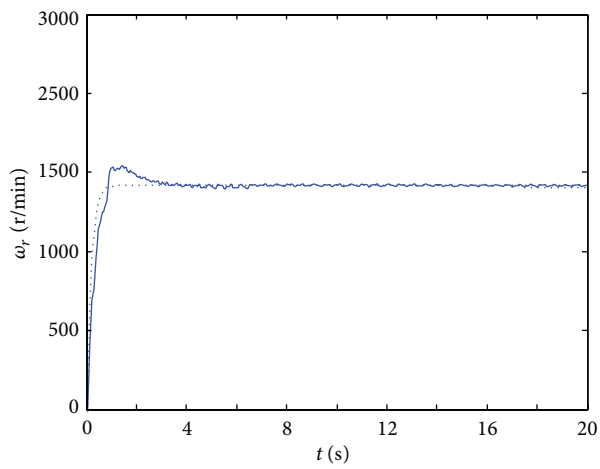

Figure 6: Speed startup response curves in the case of rated load with the proposed control method.

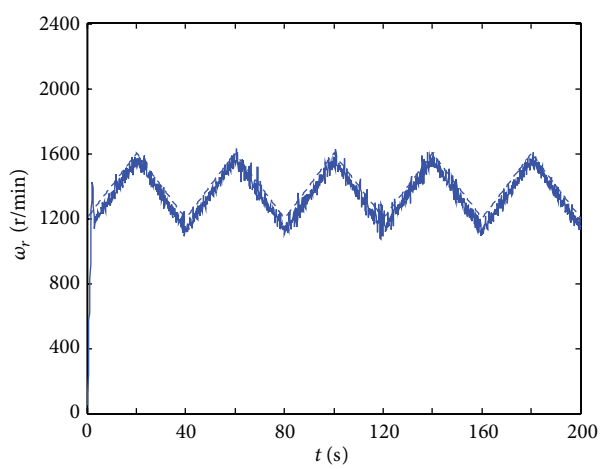

Figure 7: Response of tracking triangle curves in the case of rated load with vector control method.

Table 2: Speed performance comparison in the case of rated load.

	Settling time	Overshoot	Steady-state error
Proposed method	1.4 s	7.33%	0.56
Vector control method	2 s	32.62%	6.83

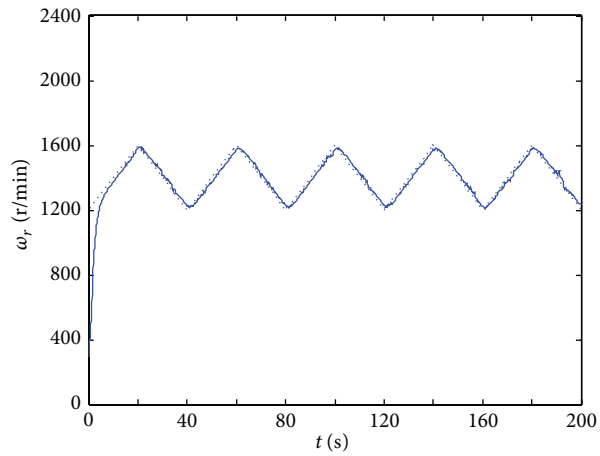

Figure 8: Response of tracking triangle curves in the case of rated load with proposed control method.

show, respectively, the simulation results of tracking triangular wave in the case of rated load with LSSVM inverse control and vector control methods. In Figures 7 and 8, the amplitudes of the triangular waves are all between 1200 r/min and 1600 r/min, and the dashed and the solid lines are, respectively, the given motor input signals and response curves. From Figures 7 and 8, we can see that, by adopting LSSVM inverse control method, the setting time of the constant V/f-controlled induction motor drive system is shorter, and its dynamic performance is also better. Additionally, the response curve can more accurately and quickly track the given motor input signal, and the control accuracy can be improved form 86% to 96%.

Case 3 (performance comparison with rotor resistance variation). Of all the motor parameters, the rotor resistance has the greatest impact on the control performance of the motor drive system. In this case, a random variable is added to the rated value of the motor rotor resistance, and its amplitude is not more than 10% of the rated resistance value. The comparison results of the proposed LSSVM inverse control and the vector control methods in the case of rotor resistance variation and without load disturbances are shown in Figures 9 and 10, respectively. From Figures 9 and 10, it can be seen that, compared with the vector control method, the LSSVM inverse scheme has a smoother speed curve with almost no overshoot. In addition, by adopting the proposed LSSVM inverse method, the relative steady error can be reduced from 12% to 4%.

Case 4 (performance comparison with load disturbances). To compare the capacity of being insensitive to the load torque variation of the proposed LSSVM inverse control and the vector control schemes, the simulation comparison

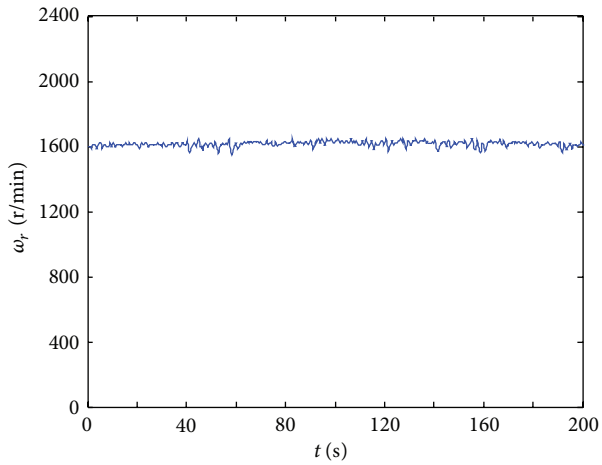

Figure 9: Speed response curves in the case of rotor resistance variation with vector control method.

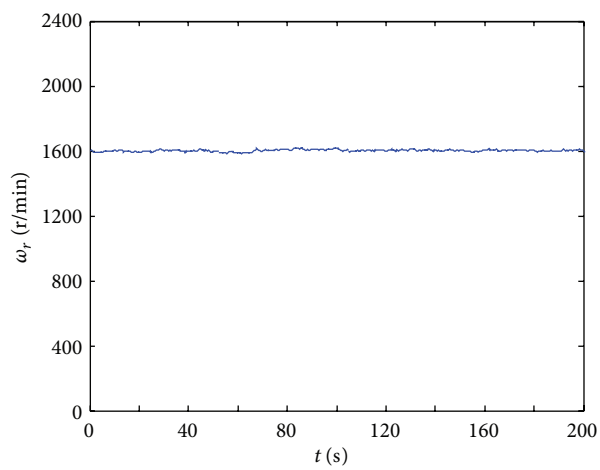

Figure 10: Speed response curves in the case of rotor resistance variation with the proposed control method.

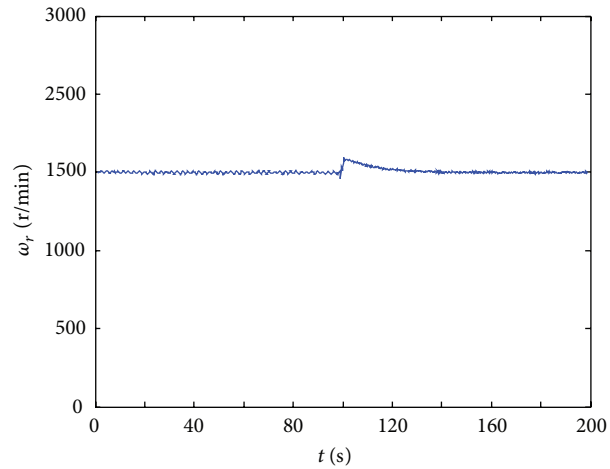

Figure 11: Speed response curves in the case of load disturbance with vector control method.

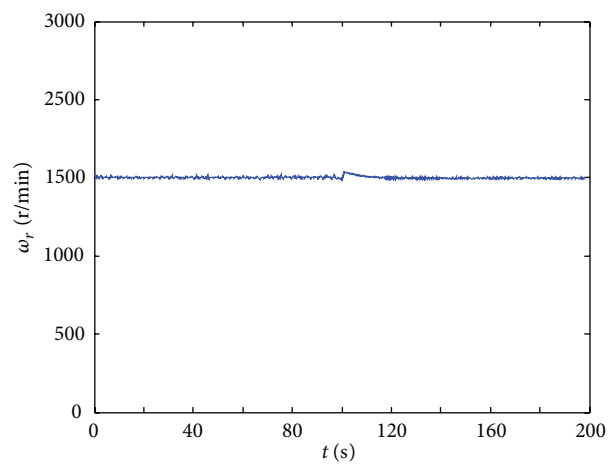

Figure 12: Speed response curves in the case of load disturbance with the proposed control method.

was also carried out under sudden load disturbance impact. When the constant V/f-controlled induction motor drive system is running at steady state of 1600 r/min, a sudden load torque disturbance was applied at 100 s and removed immediately, and the simulation results of speed response curves during the sudden application and removal of the load disturbance are shown in Figures 11 and 12. From Figures 11 and 12, it can be seen that the speed response by using the proposed method recovers faster when the load torque disturbance was added and removed. We can see that the proposed method can effectively attenuate the speed deviation caused by load disturbances and has a shorter recovery time. Moreover, from Figures 11 and 12, we can see that the control accuracy can be improved form 90% to 97% by using the proposed method. Therefore, it obviously suggests that the constant V/f-controlled induction motor drive system has better robustness performance compared with the vector control method and that the LSSVM inverse method possesses a good adaptation and a much better dynamic performance against load disturbance.

7. Conclusion

This paper aims at how to further improve the performance of the induction motor drive system used in EVs widely. The design and implementation procedure of a control scheme named LSSVM inverse control for a high-performance induction motor drive system for the traction purpose of EVs has been investigated. According to the characteristic of the constant V/f control mode, the mathematic model of the induction motor drive system is deduced and an inverse system model suitable for the constant V/f control mode is also obtained. Based on these, the LSSVM inverse control method is applied to control the induction motor drive system. The simulation test results testify that the proposed method is feasible and it can realize the high performance control of the induction motor drive system. It also offers a new method for the control of the induction motor drive system.

Conflict of Interests

The authors declare that there is no conflict of interests regarding the publication of this paper.

Acknowledgments

This work was supported by the National Natural Science Foundation of China under Project 51305170 and 51105177, the National New Energy Vehicle Industry Technological Innovation Plan of China (Chery Plug-in Hybrid Vehicle Industrialization Development Project), the National High Tech Research and Development Plan of China under Project SS2012AA111401, the National Science Foundation of Jiangsu Province of China under Project BK20130515 and BK20131255, the China Postdoctoral Science Foundation funded project under Project 2012M521012, the Professional Research Foundation for Advanced Talents of Jiangsu University under Project 12JDG057 and 11JDG047, and a Project Funded by the Priority Academic Program Development of Jiangsu Higher Education Institutions under Project 201106.

References

[1] K. Nam, S. Oh, H. Fujimoto, and Y. Hori, "Estimation of sideslip and roll angles of electric vehicles using lateral tire force sensors through RLS and kalman filter approaches," *IEEE Transactions on Industrial Electronics*, vol. 60, pp. 988–1000, 2013.

[2] S. Kelouwani, K. Agbossou, Y. Dubee, and L. Boulon, "Fuel cell plug-in hybrid electric vehicle anticipatory and real-time blended-mode energy management for battery life preservation," *Journal of Power Sources*, vol. 221, pp. 406–418, 2013.

[3] C. C. Chan, "The state of the art of electric and hybrid vehicles," *Proceedings of the IEEE*, vol. 90, no. 2, pp. 247–275, 2002.

[4] Z. Mei and J. Chen, "Modified motor vehicles travel speed models on the basis of curb parking setting under mixed traffic flow," *Mathematical Problems in Engineering*, vol. 2012, Article ID 351901, 14 pages, 2012.

[5] Y. Zhou, J. Lian, T. Ma, and W. Wang, "Design for motor controller in hybrid electric vehicle based on vector frequency conversion technology," *Mathematical Problems in Engineering*, vol. 2010, Article ID 627836, 13 pages, 2010.

[6] J. Vittek and S. Ryvkin, "Decomposed sliding mode control of the drive with interior permanent magnet synchronous motor and flexible coupling," *Mathematical Problems in Engineering*, vol. 2013, Article ID 680376, 17 pages, 2013.

[7] W. Chen, Y. Wu, R. Du, Q. Chen, and X. Wu, "Speed tracking and synchronization of a dual-motor system via second order sliding mode control," *Mathematical Problems in Engineering*, vol. 2013, Article ID 919837, 10 pages, 2013.

[8] J. He and C. Zhang, "A design method for fault reconfiguration and fault-tolerant control of a servo motor," *Mathematical Problems in Engineering*, vol. 2013, Article ID 647571, 6 pages, 2013.

[9] H. Zhang, Y. Shi, and A. Saadat Mehr, "Robust static output feedback control and remote PID design for networked motor systems," *IEEE Transactions on Industrial Electronics*, vol. 58, no. 12, pp. 5396–5405, 2011.

[10] A. Emadi, Y. J. Lee, and K. Rajashekara, "Power electronics and motor drives in electric, hybrid electric, and plug-in hybrid electric vehicles," *IEEE Transactions on Industrial Electronics*, vol. 55, no. 6, pp. 2237–2245, 2008.

[11] K. T. Chau, C. C. Chan, and C. Liu, "Overview of permanent-magnet brushless drives for electric and hybrid electric vehicles," *IEEE Transactions on Industrial Electronics*, vol. 55, no. 6, pp. 2246–2257, 2008.

[12] Z. Q. Zhu and D. Howe, "Electrical machines and drives for electric, hybrid, and fuel cell vehicles," *Proceedings of the IEEE*, vol. 95, no. 4, pp. 746–765, 2007.

[13] K. M. Rahman, B. Fahimi, G. Suresh, A. V. Rajarathnam, and M. Ehsani, "Advantages of switched reluctance motor applications to EV and HEV: design and control issues," *IEEE Transactions on Industry Applications*, vol. 36, no. 1, pp. 111–121, 2000.

[14] A. Akrad, M. Hilairet, and D. Diallo, "Design of a fault-tolerant controller based on observers for a PMSM drive," *IEEE Transactions on Industrial Electronics*, vol. 58, no. 4, pp. 1416–1427, 2011.

[15] T. D. Batzel and K. Y. Lee, "Electric propulsion with sensorless permanent magnet synchronous motor: implementation and performance," *IEEE Transactions on Energy Conversion*, vol. 20, no. 3, pp. 575–583, 2005.

[16] C.-F. Huang, J.-S. Lin, T.-L. Liao, C.-Y. Chen, and J.-J. Yan, "Quasi-sliding mode control of chaos in permanent magnet synchronous motor," *Mathematical Problems in Engineering*, vol. 2011, Article ID 964240, 10 pages, 2011.

[17] S. A. Taher and M. Malekpour, "A novel technique for rotor bar failure detection in single-cage induction motor using FEM and MATLAB/SIMULINK," *Mathematical Problems in Engineering*, vol. 2011, Article ID 620689, 14 pages, 2011.

[18] M. Zeraoulia, M. E. H. Benbouzid, and D. Diallo, "Electric motor drive selection issues for HEV propulsion systems: a comparative study," *IEEE Transactions on Vehicular Technology*, vol. 55, no. 6, pp. 1756–1764, 2006.

[19] T. F. Podlesak, D. C. Katsis, P. W. Wheeler, J. C. Clare, L. Empringham, and M. Bland, "A 150-kVA vector-controlled matrix converter induction motor drive," *IEEE Transactions on Industry Applications*, vol. 41, no. 3, pp. 841–847, 2005.

[20] D. Diallo, M. E. H. Benbouzid, and A. Makouf, "A fault-tolerant control architecture for induction motor drives in automotive applications," *IEEE Transactions on Vehicular Technology*, vol. 53, no. 6, pp. 1847–1855, 2004.

[21] P. Wójcik and M. P. Kaźmierkowski, "Simple direct flux vector control with space vector modulation for pwm inverter fed induction motor drive," *Przeglad Elektrotechniczny*, vol. 86, no. 2, pp. 60–64, 2010.

[22] C. Chakraborty and Y. Hori, "Fast efficiency optimization techniques for the indirect vector-controlled induction motor drives," *IEEE Transactions on Industry Applications*, vol. 39, no. 4, pp. 1070–1076, 2003.

[23] Y.-S. Jeong and J.-Y. Lee, "Parameter identification of an induction motor drive with magnetic saturation for electric vehicle," *Journal of Power Electronics*, vol. 11, no. 4, pp. 418–423, 2011.

[24] S. Cheng, P. Zhang, and T. G. Habetler, "An impedance identification approach to sensitive detection and location of stator turn-to-turn faults in a closed-loop multiple-motor drive," *IEEE Transactions on Industrial Electronics*, vol. 58, no. 5, pp. 1545–1554, 2011.

[25] M. E. H. Benbouzid, D. Diallo, M. Zeraoulia, and F. Zidani, "Active fault-tolerant control of induction motor drives in EV and HEV against sensor failures using a fuzzy decision system," *International Journal of Automotive Technology*, vol. 7, no. 6, pp. 729–739, 2006.

[26] P. Khatun, C. M. Bingham, N. Schofield, and P. H. Mellor, "Application of fuzzy control algorithms for electric vehicle antilock braking/traction control systems," *IEEE Transactions on Vehicular Technology*, vol. 52, no. 5, pp. 1356–1364, 2003.

[27] A. Nasri, A. Hazzab, I. K. Bousserhane, S. Hadjeri, and P. Sicard, "Fuzzy-sliding mode speed control for two wheels electric vehicle drive," *Journal of Electrical Engineering and Technology*, vol. 4, no. 4, pp. 499–509, 2009.

[28] A. B. Proca, A. Keyhani, and J. M. Miller, "Sensorless sliding-mode control of induction motors using operating condition dependent models," *IEEE Transactions on Energy Conversion*, vol. 18, no. 2, pp. 205–212, 2003.

[29] H. Zhang, J. Wang, and Y. Shi, "Robust H_∞ sliding-mode control for Markovian jump systems subject to intermittent observations and partially known transition probabilities," *Systems & Control Letters*, vol. 62, no. 12, pp. 1114–1124, 2013.

[30] B. Tabbache, A. Kheloui, and M. E. H. Benbouzid, "An adaptive electric differential for electric vehicles motion stabilization," *IEEE Transactions on Vehicular Technology*, vol. 60, no. 1, pp. 104–110, 2011.

[31] F. R. Salmasi, T. A. Najafabadi, and P. J. Maralani, "An adaptive flux observer with online estimation of dc-link voltage and rotor resistance for VSI-Based induction motors," *IEEE Transactions on Power Electronics*, vol. 25, no. 5, pp. 1310–1319, 2010.

[32] F.-J. Lin, Y.-C. Hung, J.-C. Hwang, I.-P. Chang, and M.-T. Tsai, "Digital signal processor-based probabilistic fuzzy neural network control of in-wheel motor drive for light electric vehicle," *IET Electric Power Applications*, vol. 6, no. 2, pp. 47–61, 2012.

[33] B. Singh, P. Jain, A. P. Mittal, and J. R. P. Gupta, "Torque ripples minimization of DTC IPMSM drive for the EV propulsion system using a neural network," *Journal of Power Electronics*, vol. 8, no. 1, pp. 23–34, 2008.

[34] H. Zhang, Y. Shi, and M. Liu, "H-infinity step tracking control for networked discrete-time nonlinear systems with integral and predictive actions," *IEEE Transactions on Industrial Informatics*, vol. 9, pp. 337–345, 2013.

[35] H. Zhang, Y. Shi, and J. Wang, "Observer-based tracking controller design for networked predictive control systems with uncertain Markov delays," *International Journal of Control*, vol. 86, pp. 1824–1836, 2013.

[36] W. Li, Y. Xu, and H. Li, "Robust $l_2 - l_\infty$ filtering for takagi-sugeno fuzzy systems with norm-bounded uncertainties," *Discrete Dynamics in Nature and Society*, vol. 2013, Article ID 979878, 8 pages, 2013.

[37] J. A. K. Suykens, J. Vandewalle, and B. De Moor, "Optimal control by least squares support vector machines," *Neural Networks*, vol. 14, no. 1, pp. 23–35, 2001.

[38] T. Van Gestel, J. A. K. Suykens, D.-E. Baestaens et al., "Financial time series prediction using least squares support vector machines within the evidence framework," *IEEE Transactions on Neural Networks*, vol. 12, no. 4, pp. 809–821, 2001.

[39] Z. Y. Han, Y. Liu, J. Zhao, and W. Wang, "Real time prediction for converter gas tank levels based on multi-output least square support vector regressor," *Control Engineering Practice*, vol. 20, pp. 1400–1409, 2012.

[40] X. B. Chen, J. Yang, J. Liang, and Q. L. Ye, "Recursive robust least squares support vector regression based on maximum correntropy criterion," *Neurocomputing*, vol. 97, pp. 63–73, 2012.

[41] I. C. Trelea, "The particle swarm optimization algorithm: convergence analysis and parameter selection," *Information Processing Letters*, vol. 85, no. 6, pp. 317–325, 2003.

[42] M. Clerc and J. Kennedy, "The particle swarm-explosion, stability, and convergence in a multidimensional complex space," *IEEE Transactions on Evolutionary Computation*, vol. 6, no. 1, pp. 58–73, 2002.

[43] H. Yoshida, K. Kawata, Y. Fukuyama, S. Takayama, and Y. Nakanishi, "A Particle swarm optimization for reactive power and voltage control considering voltage security assessment," *IEEE Transactions on Power Systems*, vol. 15, no. 4, pp. 1232–1239, 2000.

Hindawi Publishing Corporation
Mathematical Problems in Engineering
Volume 2014, Article ID 540624, 8 pages
http://dx.doi.org/10.1155/2014/540624

Research Article

Resident Plug-In Electric Vehicle Charging Modeling and Scheduling Mechanism in the Smart Grid

Peng Han, Jinkuan Wang, Yinghua Han, and Yan Li

School of Information Science and Engineering, Northeastern University, Shenyang 110819, China

Correspondence should be addressed to Jinkuan Wang; wjk@mail.neuq.edu.cn

Received 18 October 2013; Accepted 10 December 2013; Published 2 January 2014

Academic Editor: Hui Zhang

With the development of smart grid and the increase of global resident Plug-In Electric Vehicle (PEV) market in the near future, the interaction between limited distribution grid capacity and uncontrollable PEV charging loads can lead to violations of local grid restrictions. And the proper model charging scheduling mechanism is the key to assess and satisfy various resident charging requirements and help in optimizing utility utilization. In this paper, the distribution grid profile model with PEV charging power is firstly constructed for the purpose of studying resident PEV charging impact on the distribution grid. To better reflect the actual impact of PEVs, we use real data on driving behaviors, vehicle characteristics, and electricity loads to generate our model. Furthermore, an improved queuing-theory-based scheduling mechanism is proposed, the distribution grid communication structure and the algorithm are illustrated, and computer simulations are demonstrated to verify their performance. The results show that the proposed scheduling mechanism will enhance the distribution grid flexibility to meet various charging requirements while maximizing the grid capacity.

1. Introduction

The smart grid represents a new paradigm in electrical power distribution and management. Incorporating advanced two-way communications and distributed computing capabilities, smart grid is emerging power grids that enhance control, efficiency, reliability, and safety. The resident Plug-In Electric Vehicle (PEV) is a motor vehicle that can be recharged by plugging in the house electricity source [1]. With zero greenhouse gas emission and a readily available energy source, PEV offers a promising alternative for residents as a new mean of transportation. The National Electromobility Development Plan, proposed by the German Federal Government in August 2009, predicts one million electric vehicles on German roads by 2020 [2]. And current estimations state that only by 2015 there would be more than 3 million electric vehicles on roads all around the world [3].

While this is a huge step forward for electric vehicles and emissions reduction, it will also cause a huge demand for electricity. Considering that the PEV batteries are sizeable and uncoordinated loads, the large-scale adoption of PEVs will significantly increase the power grid load especially in the peak load hours. And the coincidence between peaks of PEV charging load and non-PEV load will require massive investments in generation, transmission, and distribution [4, 5]. Moreover, since PEV adoption is initially expected to cluster in residential communities where the demand for PEVs is strongest [6], those PEVs will increase the potential for negative distribution system impacts, and the charging power may overload transformers and sap much needed distribution capacity, causing severe grid fluctuations and blackouts while degrading power grid efficiency [7].

On the other side, due to the PEVs' high battery capacities and high charging powers to store massive electricity at off-peak hours, they may serve as ideal actors for demand side management (DSM) and can maximize the yield of electricity supplied by renewable sources such as PV panels [8]. And the development of smart grid and AMI techniques enables utilities in many countries to adopt various price strategies or regulations, for example, time-of-use (TOU) tariff, to shift the PEVs charging requests [9]. However, the increasing penetration of resident PEVs brings various quality-of-service

Table 1: PEV types and key parameters.

PEV types[a]	Prototypes	Key parameters			
		Battery capacity	Charge power	Max range	Market share
Auto	Nissan LEAF	24 kWh	6.6 kW	73 mL	49.9%
SUV	AMP and Jeep Cherokee	37.6 kWh	6.5 kW	80 mL	19.4%
Pick-up	Smith Newton	80 kWh	8 kW	50 mL	18.2%
Truck	Smith Edison	36 kWh	6 kW	60 mL	8.2%

[a]2009 National Household Travel Survey.

(QoS) requirements [10]. Moreover, if it goes without the proper charging scheduling management, the large charging activities that have been shifted to the night by price strategies will also bring night high-peak hours to the grid [11].

Considering all the facts above, in order to maintain the reliability of the power system, the appropriate model for evaluating and predicting PEV charging activity impact toward smart grid must be designed, and a proper PEV charging scheduling mechanism is critical for maintaining the grid safety and PEV charging efficiency. Several recent works currently are undergoing the effort to optimize the PEV charging activity. Asad et al. [12] adopted sensor web service to manage the charging activity, but the algorithm considers few parameters and is not practical. Callaway and Hiskens proposed a hysteresis-based control strategy in [13] to charge PEV intermittently, but that strategy will cause obvious oscillations due to charging synchrony. Taheri and Entriken proposed a clustering algorithm in [14] to consider future demands of vehicles in a fleet, and in their algorithm each vehicle's charging schedule is instantly determined as it connects to the grid; therefore, the scheduling process is not dynamic and lacks flexibility. Baek et al. in [15] put forward a queuing model for PEV charging systems; however, the proposed M/M/Inf model does not quite match the real PEV charging scenario in the smart grid.

Although a number of papers in this field have established the benefits of optimizing PEV charging activities, the PEV charging model in the smart grid has not been practically and clearly demonstrated; therefore, the real-time impact of PEVs on the distribution grid has yet to be fully explored. Moreover, considering the limited computational capabilities of smart grid terminals in the residential area, a relatively low complexity scheduling mechanism is preferred. Therefore, this paper proposed a resident PEV charging model based on the driving data from National Household Travel Survey (NHTS), 2009 [16]. The real-time grid profile data of the utility are also imported into this model to get the impact of charging activity. Based on the model this paper illustrates the communication structure of the distribution grid, and an improved queuing-theory-based scheduling algorithm is proposed, which would work to coordinate PEVs charging activity with the consideration of both distribution grid safety and the various PEV charging requirements. The simulation shows that the proposed mechanism can improve the ability of the distribution grid to better respond to the resident PEV charging demand while improving the reliability of the grid system.

The rest of this paper is organized as follows. Section 2 illustrates the communication structure of the smart grid with the adoption of PEVs, analyses the resident PEV charging activity, and proposes the model in the distribution grid. The charging activity impact of the PEV is demonstrated with the proposed model. Section 3 analyses scheduling using queuing theory and proposes the improved scheduling mechanism. The simulation is presented and discussed in Section 4 to inspect its effectiveness; then the paper concludes in Section 5.

2. PEV Charging Activity Analysis and Modeling

2.1. Key Parameters Analysis of PEV Charging Activity. Considering the fact that resident PEVs will be a major smart grid application [17], the key parameters that affect the power grid are the PEV types, resident driving habits, the distribution grid load profile, and PEV market.

(1) PEV Types. PEV type determines the vehicle's charging power P_c and battery capacity C. Based on the 2009 NHTS database, the resident vehicles can mainly be classified by the following four types: auto, sport utility vehicle (SUV), pickup, and truck. To model the impact of PEV charging activities, we selected four PEV prototypes, respectively, for each type, and their key parameters are shown in Table 1. Nissan LEAF [18] is the latest version of pure electric autos in the market, and the electric Cherokee [19] developed by AMP and Jeep is an ideal substitution for ordinary SUV, while the Newton Pickup and Edison Truck produced by Smith [20] have been widely used in US transportation business.

(2) Resident Driving Habits. Driving habits of the drivers influence the charging start time T_s and duration T_l directly, where T_s is mainly determined by the home-arrival time, and T_l depends on the daily driving range together with the battery capacity and charging power. Given the assumption that the resident driving habits stay unchanged and PEVs will get recharged immediately when arriving home, the two-dimensional conditional probability distribution diagram between daily range and home-arrival time on weekdays and weekends is constructed based on the statistical data in NHTS 2009. The two distribution diagrams are illustrated in Figures 1 and 2. As can be observed, the majority of PEVs should be charged between 15:00–20:00 on the weekdays and 18:00–23:00 on the weekends, and the daily ranges are mostly within 50 miles.

(3) Distribution Grid Load Profile. The PEV charging load will superimpose directly onto the real-time distribution

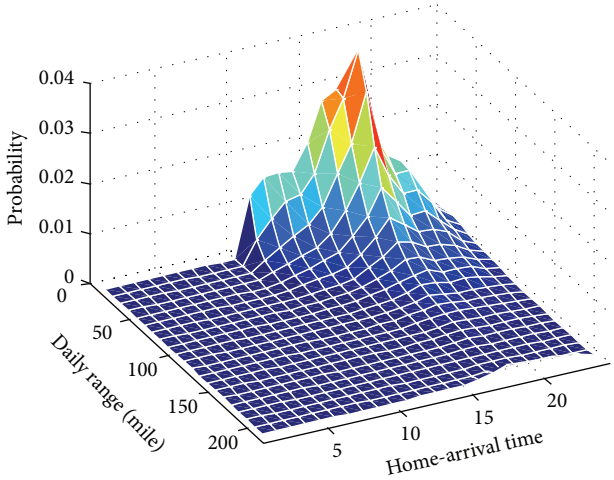

FIGURE 1: Conditional probability distribution diagram in weekdays.

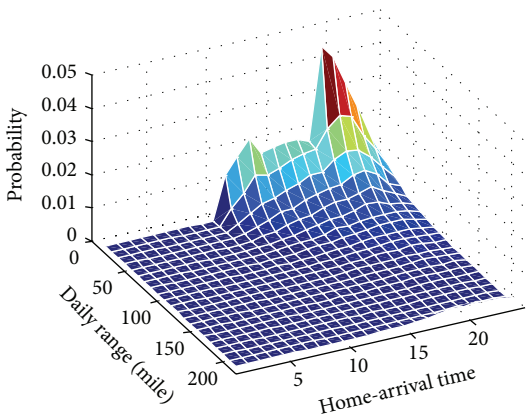

FIGURE 2: Conditional probability distribution diagram in weekends.

grid load curve $P_G(t)$. And therefore the available power for PEV charging activities depends on the original grid load profile P_{load} and the distribution grid capacity P_{all}, that is, the maximum power allowance. In this paper, the electricity grid load profile consults the real load of the Electric Reliability Council of Texas (ERCOT) [21]. ERCOT is an isolated electrical system operator that manages the flow of electric power to 23 million customers in Texas; this paper calculates the average power consumption on the hour and interpolates the hourly data into continuous power profile $P_G(t)$. Considering that the large-scale PEV data is not presently available, the paper reasonably assumes a residential community with one-ten-thousandth of Texas population, and all houses in this community are equipped with the smart meters. Provided that the residential consumption ratio θ of Texas electricity is 37.6% [22], the residential community original grid load profile P_{load} can be calculated from the function:

$$P_{\text{load}} = \frac{P_G(t)\,\theta e}{E}, \quad 0 \le t < 24, \tag{1}$$

where e is the population of the proposed residential community, which is supposed to be 2300 as one-ten-thousand of the population of Texas E. Given that the ERCOT capacity is 83000 MW, the community distribution grid capacity P_{all} is assumed to be 3000 kW.

(4) PEV Market. The number of PEVs N on a certain area depends on its population e, vehicles ownership ratio R, and the PEV penetration ratio μ. Due to the NHTS 2009, the vehicles ownership ratio R is 74%. Therefore, given the 2300-population residential community, the vehicle amount is about 1702.

2.2. PEV Charging Activity Modeling. Considering the charging activity from the ith PEV, the charging time duration T_{li} can be calculated from the function:

$$T_{li} = \frac{l_i C_i}{K_i P_{ci} \rho}, \tag{2}$$

where l_i is the driving miles, C_i is the battery capacity, K_i is the maximum range, P_{ci} is the charging power, and ρ is the charging efficiency. Provided the PEV charging start time, the charging end time T_{ei} can be calculated by the function:

$$T_{ei} = T_{si} + T_{li}. \tag{3}$$

Without the loss of generality, the arrival time of the PEV in this paper is regarded to be a nonstationary Poisson process [23], and the probability distribution function of K new-arrival charging PEVs in each hour is the function:

$$P(X = k) = \frac{e^{-\lambda_t} \lambda_t^k}{k!}, \tag{4}$$

where λ_t is the expectation of hourly new-arrival charging PEVs, and it can be calculated from the function:

$$\lambda_t = \lambda_f e R \mu, \tag{5}$$

where λ_f is the piecewise function of PEV charging time hourly fractions on weekdays and weekends, which can be derived from Figures 1 and 2. Therefore, considering the proposed community with all the above parameters, the real power load on the distribution grid when adopted with PEVs P_{real} can be expressed in the function:

$$P_{\text{real}} = P_{\text{load}} + \sum_{i=1}^{R} P_{ci} \left[u(t - T_{ei}) - u(t - T_{si}) \right], \quad 0 \le P_{\text{real}} \le P_{\text{all}}, \tag{6}$$

where $u(t)$ is the step function.

2.3. PEV Charging Impact Simulation. Based on the proposed model, the simulation of PEV charging impact to the electricity grid is demonstrated in Figure 3. The PEV penetration ratio is set to be 0.4. The thin and thick dashed red wave represents the power of original distribution grid load P_{load} in summer weekdays and weekends, and the dotted line in

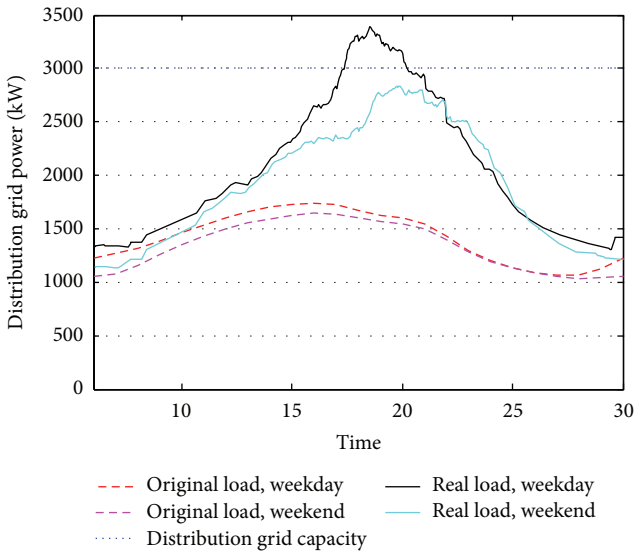

Figure 3: PEV charging activity impact without the proper management.

3000 kW is the distribution grid capacity. The thin and thick solid lines denote the distribution grid load P_{real} which includes the addup of PEV charging power.

As is indicated in Figure 3, the PEV charging activity without proper management conducts a severe grid fluctuation. The power profile caused by mass PEV charging activity significantly reshapes the original grid load power profile and enlarges the peak time as well as the peak value. Due to the coincidence of the night charging activities, the charging load around 20:00 p.m. rises to the distribution grid capacity, which might cause critical accidents in reality. However, the load after midnight is nearly unchanged, which denotes that the power generation in the night is not well utilized. In order to maximize the grid utilization to support the future growth of PEV market without investing heavily in upgrading existing grid capacity, the PEV charging activity scheduling mechanism should be developed.

3. PEV Charging Activity Scheduling Mechanism

3.1. Distribution Grid Communication Structure. In this paper, it is assumed that most of the PEVs owners in the proposed community have been interested in participating in utility scheduling by charging or discharging their PEVs. And therefore a proper communication structure based on the smart grid is necessary to enable the utility's scheduling instruction and the PEV owners' timely response. Considering a PEV-adopted distribution grid system, we can identify three main communication network components between resident houses and distribution station: wide area network, neighborhood area network, and home area network.

As is demonstrated in Figure 4, in order to achieve the scheduling, each resident PEV should be monitored and powered by a smart meter in the house of the PEV owner. The smart meter is an intelligent device that manages the power supply of the home area network (HAN) in the smart grid, and the control of the house owner or utility will be performed by the predeployed smart sockets. Smart meters in a certain area, for example, a residential community, can form a neighborhood area network (NAN) through wireless mesh networks, power line communication (PLC), or Ethernet and handle the last-mile connectivity from the smart meters located on the edge of the power grid to the grid data collectors. Each data collector coordinates a large number of houses and manages the communication between a group of residents and an electric distribution utility, collecting smart meter data and transferring the utility instruction and information through wide area network (WAN), and the public wired (solid line) and wireless (dashed line) communication networks with a ubiquitous reach are critical elements of successful WAN communication.

3.2. Queuing-Theory-Based Scheduling Algorithm. There are currently no standard algorithms on regulating PEV charging activity in the smart grid. Although several proposed sophisticated management mechanisms relying on real-time high-speed communications could allow distribution circuits to run at nearly full capacity, the cost-effectiveness would then compromise due to the sophisticated mechanism, and complex negotiation between the resident and the utility may result in an unsuccessful outcome [24]. Considering the realistic scenario of the smart grid in the near future, scheduling algorithm based on relatively low computing complexity should be more appropriate. They can be easily deployed in smart meters and other smart devices; meanwhile their communications require relatively few network resources to manage hundreds of PEV charging activities in a certain area. Queuing theory is adopted in a widespread manner for analyzing and optimizing stochastic problems, as they provide a range of benefits in scheduling the available resource to maximize the need of consumers with low computing complexity, which is suitable for the low-cost and low-power smart sockets and can be well applied in smart meters.

There are many different queuing regulations for different circumstances, which follow a different scheduling algorithm and have their own advantages and disadvantages. first-come first-served (FCFS) is the basic scheduling algorithm for PEV charging in many grids and charging stations. The main process of scheduling mechanism with FCFS algorithm is illustrated in Figure 5(a). If the grid is in peak hours when new PEV arrives and there is no available power for charging, the PEV will be suspended and regulated by the FCFS queuing regulation which places all PEVs in a queue and charges them in the order that they arrive in. And as soon as the available distribution grid power is sufficient for the headmost PEV in the queue, the FCFS algorithm will automatically trigger the charging process of that vehicle.

Due to its low complexity and fairness of the service, the FCFS scheduling has been considered as a possible strategy in scheduling the PEV charging activity in the smart grid [15]. However, this method cannot distinguish PEV charging requests with urgency. In order to satisfy the various

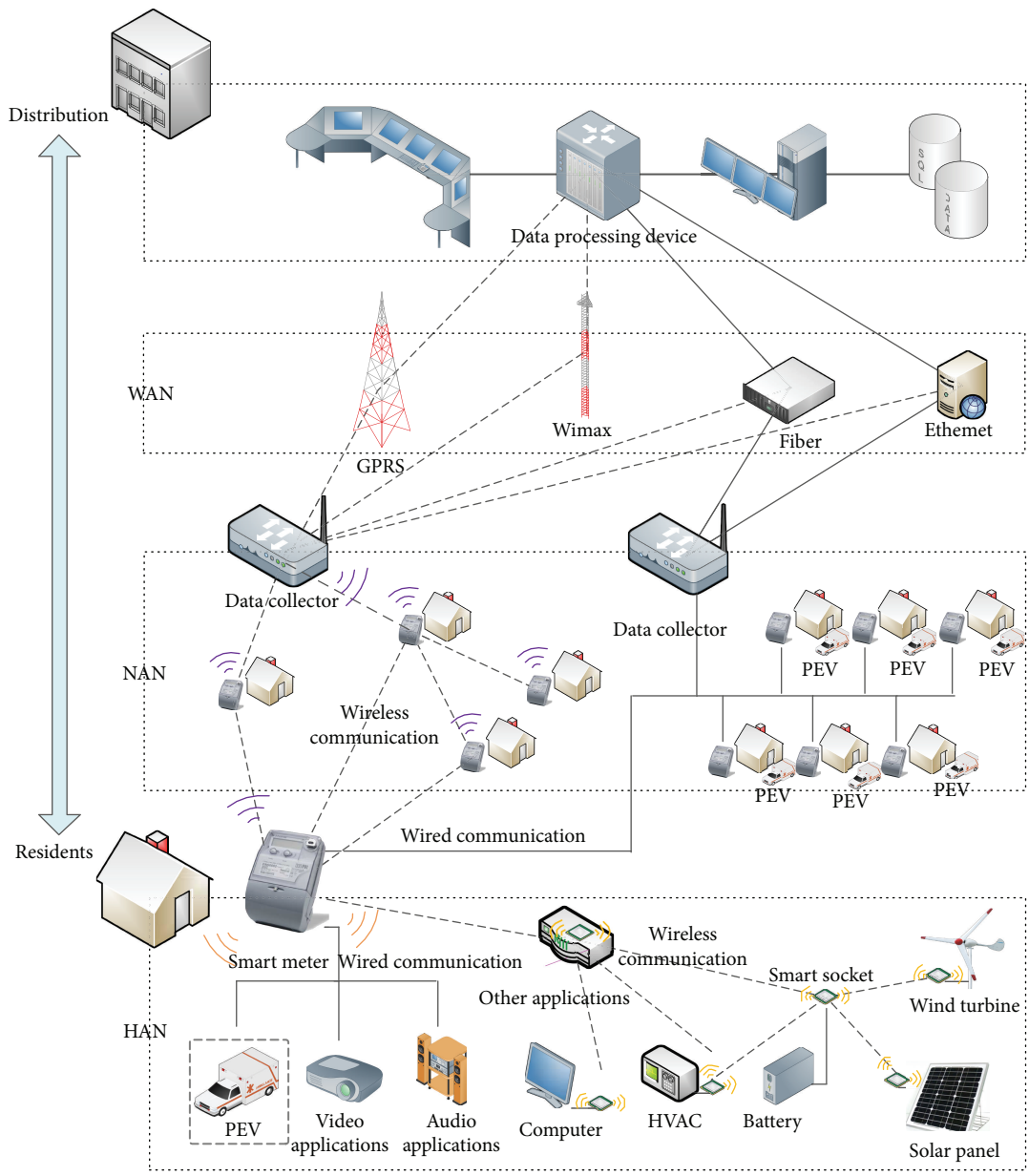

Figure 4: Distribution grid communication structure.

charging requirements brought by the increasing penetration of PEVs, this paper proposes an improved queuing-theory-based dynamic scheduling algorithm that assigns each PEV with different priority levels, with which the schedule queue can be considered as a soft real-time system comprising mainly aperiodic tasks [25, 26]. Therefore, the PEV priority is assigned based on the slack time of each process, which is defined in the function:

$$T_{ki} = T_{di} - T_{si} - T_{li}, \tag{7}$$

where T_{di} is the allowable latest charging finish time and can be calculated by the function:

$$T_{di} = T_{pi} - T_{si}, \tag{8}$$

where T_{pi} is the resident-preset charging duration time through smart meters, and it reflects the resident charging urgency. The main process of dynamic scheduling algorithm is illustrated in Figure 5(b).

4. Computer Simulation

4.1. Simulation Platform and Configuration. The computer simulation is demonstrated based on the proposed model in order to verify the performance of the proposed scheduling mechanism. Considering that the PEV charging events of a certain area form a typical discrete event process, the ExtendSim software is adopted as the simulation platform to establish the proposed model. ExtendSim is advanced simulation software with powerful constructs and unlimited hierarchical

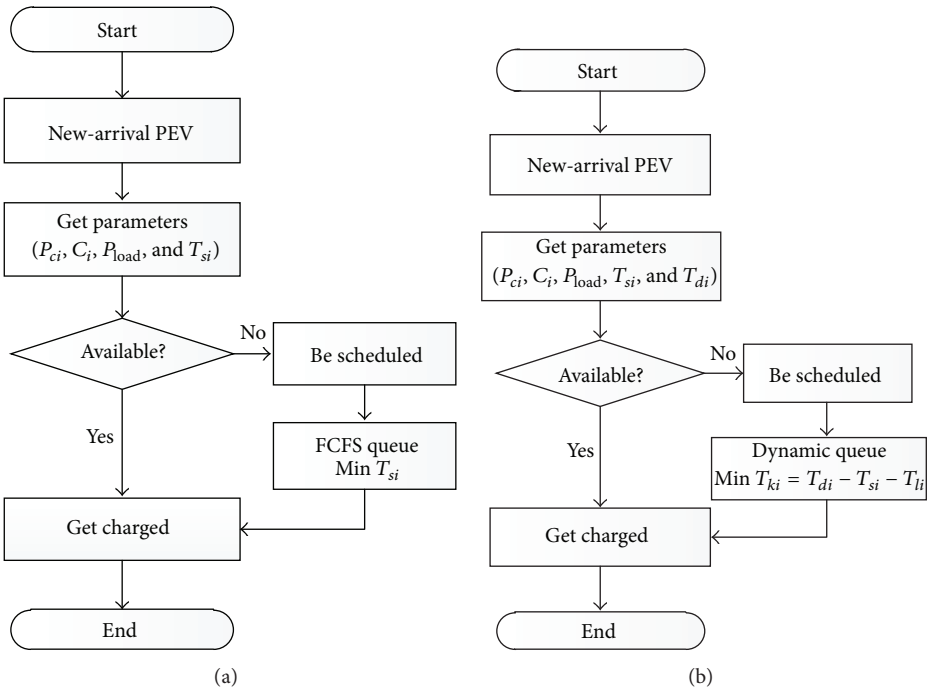

Figure 5: Main process of scheduling mechanisms.

Table 2: Key parameters of the simulation.

Population	Vehicle owner	PEV penetration ratio	Charging efficiency	Power capacity	Power threshold
2300	1702	0.4	0.833	3000 kW	2400 kW

structure for modeling complex discrete event processes [27], which is especially suitable for the modeling the dynamic PEV charging queuing process and multiple scheduling algorithms. Meanwhile, the features of the ExtendSim also make the constructed model flexible and extensible for more complex situations in the future study.

In order to compare the performance of the proposed algorithms as well as the FCFS, the main simulation parameters including the resident population, PEV types and specification, and the driving habit of the proposed residential community keep the same as those in Section 2, where the key parameters are listed in Table 2. And in order to represent the charging PEVs with high, middle, and low urgency, T_{pi} in the simulation is preset to be 1 h, 3 h, and 6 h with the probability of 0.3, 0.3, and 0.4.

With the simulation parameters added and modules connected in the ExtendSim platform, the main simulation structure of the proposed model is shown in Figure 6, where the scheduling algorithms are programmed in function modules marked with a black block in the figure.

4.2. Simulation Result and Discussion. A series of computer simulations are conducted based on the above conditions. Figure 7 shows P_{real} with the FCFS algorithm and the proposed algorithm, in which group 1 and group 2 denote the P_{real} profiles in weekdays and weekends.

Compared with P_{real} in Figure 3, electricity grid and the two PEV charging scheduling algorithms both enjoy a stable charging load in charging peak hours. And the performance of the two algorithms is similar to each other. The reshaped electricity grid load power profiles are safely limited under the 2400 kW threshold. Moreover, the power valley after midnight is largely filled up, and therefore the PAR is reduced. In order to examine the proposed scheduling algorithm in satisfying the PEV owners' requirements, the comparable simulation between the FCFS scheduling and the proposed scheduling is illustrated in Figure 8, in which the thin and thick solid lines denote the FCFS and proposed algorithms performance in weekdays and dashed lines are their performance in weekends.

Compared to the traditional FCFS scheduling, the proposed scheduling algorithm gives the PEV with smaller slack time T_{ki} higher priorities; therefore, it has relatively higher on-time ratio, which helps to insure the charging of urgent PEV owners. The key parameters in the simulations have been listed in Table 3. It can be observed that the proposed algorithm has similar average queue length, maximum queue length, and average wait time. However, to ensure residents charging urgency requirements, it regulates residents with low urgency requirements with relatively longer wait time. Therefore, the maximum wait time of the proposed algorithm in weekdays and weekends is larger than FCFS, but the whole on-time rate is guaranteed. Moreover, in the simulation

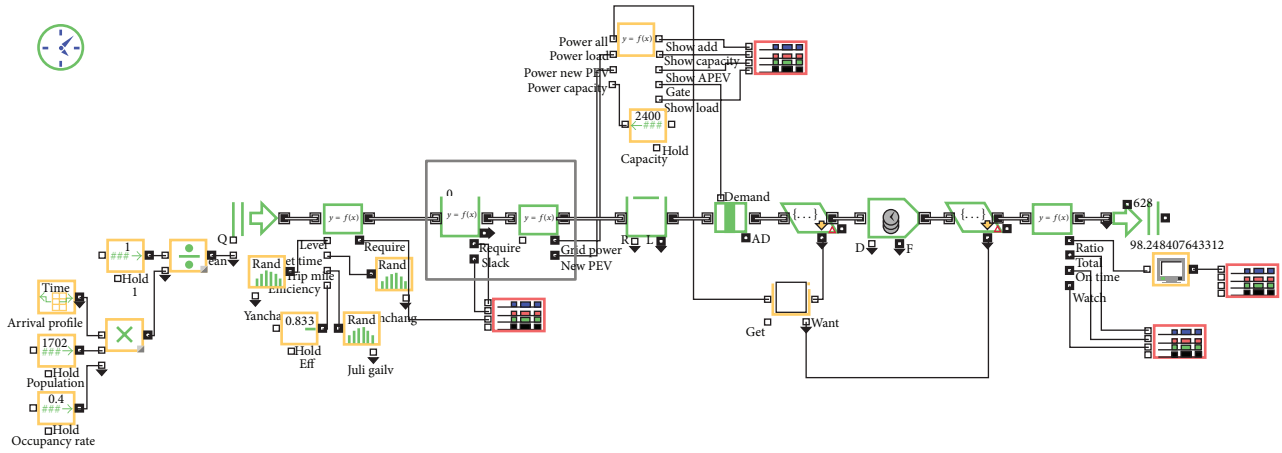

Figure 6: Main simulation structure of the proposed model.

Table 3: FCFS and proposed algorithm performance analysis.

	Key parameters				
Algorithm	On-time rate	Ave. queue	Max. queue	Ave. wait	Max. wait
FCFS weekdays	64.39	47.85	239	2.14 h	3.85 h
Proposed weekdays	98.24	47.87	244	2.15 h	5.88 h
FCFS weekends	85.82	14.35	108	0.65 h	1.49 h
Proposed weekends	100.00	13.29	98	0.60 h	3.30 h

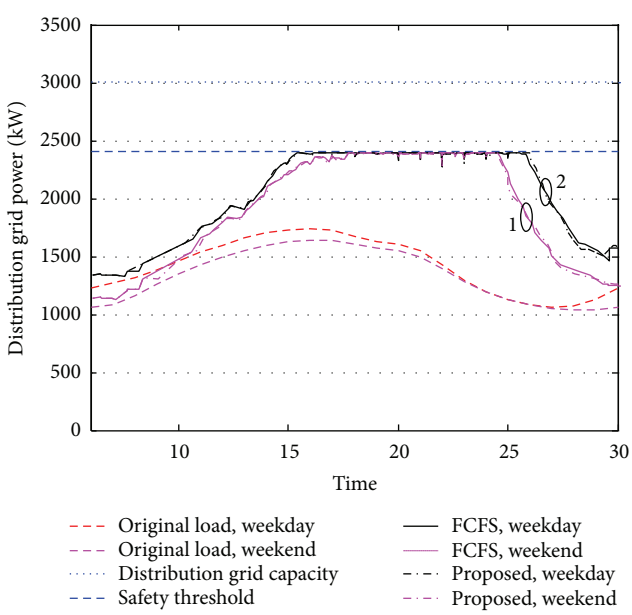

Figure 7: PEV charging impact with FCFS and proposed algorithm.

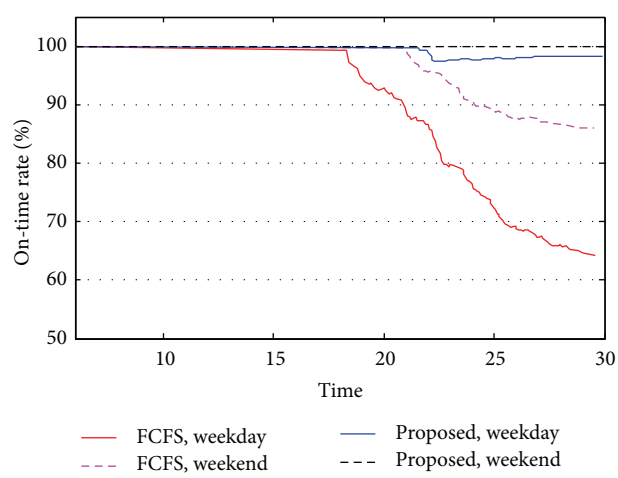

Figure 8: On-time ratio comparison.

most of night-coming PEVs are served before 06:00 a.m. the next day, which denotes the proposed charging algorithm's efficiency in maintaining the electricity grid safety as well as satisfying the PEV owner charging requirements.

In practice, the proposed scheduling can be adopted with dynamic electricity prices; therefore, the idle PEV owners are encouraged to preset a larger T_{di} for an electricity bill discount, while urgent PEV owners can get charged in advance at a cost of high bills. It should be noted that due to the fact that PEV is owned mostly by residential consumers, in this analysis it is assumed that the proposed charging mechanism is associated with home charging for simplicity. Nevertheless, in case it becomes necessary to account for the charging at public locations, the proposed scheduling and dispatch methods would still be properly applied as well.

5. Conclusions

The paper proposes a new PEV charging activity model and develops a queuing-theory-based mechanism to schedule the

PEV charging in order to maximize the utilization of excess distribution circuit capacity while keeping the probability of a distribution grid load profile negligible. The proposed scheduling algorithm shows preferable performance in alleviating the charging impact. And by adopting the mechanism, the limited available power in high-peak load times is well utilized, the significant peak load is reduced, and the various charging requirements are largely satisfied. Due to its simplicity and flexibility, the model can be easily facilitated for grid system adopting vast amounts of PEVs.

Conflict of Interests

The authors declare that there is no conflict of interests regarding the publication of this paper.

Acknowledgments

This work is supported by the National Natural Science Foundation of Hebei, China, under Grant no. 201202073. The authors would sincerely show their appreciation to the editor and the anonymous reviewers for their invaluable comments.

References

[1] E. Ungar and K. Fell, "Plug in, turn on, and load up," *IEEE Power and Energy Magazine*, vol. 8, no. 3, pp. 30–35, 2010.

[2] German Federal Government, *National Electromobility Development Plan Executive Summary*, German Federal Government, Berlin, Germany, 2009.

[3] Pike Research, Investment in electric vehicle IT systems to total $5.1 billion by 2015, http://www.pikeresearch.com/newsroom/smart-grid-investment-to-total-200-billion-worldwide-by-2015.

[4] J. T. Salihi, "Energy requirements for electric cars and their impact on electric power generation and distribution systems," *IEEE Transactions on Industry Applications*, vol. 9, no. 5, pp. 516–532, 1973.

[5] A. Y. Saber and G. K. Venayagamoorthy, "Plug-in vehicles and renewable energy sources for cost and emission reductions," *IEEE Transactions on Industrial Electronics*, vol. 58, no. 4, pp. 1229–1238, 2011.

[6] F. Ahmad, R. M. Hledik, A. Levy, and A. L. Madian, "Will smart prices induce smart charging of electric vehicles?" July 2011, http://www.smartgrid.gov/sites/default/files/doc/files/Will_Smart_Prices_Induce_Smart_Charging_Electric_Vehicles_201107.pdf.

[7] S. Ruthe, V. Schmutzler, and C. Rehtanz, "Study on V2G protocols against the background of demand side management," *Ibis*, vol. 11, pp. 33–44, 2011.

[8] W. Kempton and J. Tomić, "Vehicle-to-grid power fundamentals: calculating capacity and net revenue," *Journal of Power Sources*, vol. 144, no. 1, pp. 268–279, 2005.

[9] Y. Cao, S. Tang, C. Li et al., "An optimized EV charging model considering TOU price and SOC curve," *IEEE Transactions on Smart Grid*, vol. 3, no. 1, pp. 388–393, 2012.

[10] J. Gartner and C. Wheelock, "Electric vehicles?: 10 predictions for 2011," Tech. Rep., Pike Research, Boulder, Colo, USA, 2011.

[11] P. Fairley, "Speed bumps ahead for electric-vehicle charging," *IEEE Spectrum*, vol. 47, pp. 13–14, 2010.

[12] O. Asad, M. Erol-Kantarci, and H. Mouftah, "Sensor network web services for demand-side energy management applications in the smart grid," in *Proceedings of the IEEE Consumer Communications and Networking Conference (CCNC '11)*, pp. 1176–1180, Las Vegas, Nev, USA, January 2011.

[13] D. S. Callaway and I. A. Hiskens, "Achieving controllability of electric loads," *Proceedings of the IEEE*, vol. 99, pp. 184–199, 2011.

[14] N. Taheri and R. Entriken, "A dynamic algorithm for facilitated charging of plug-in electric vehicles," *Management Science*, pp. 1–16, 2011.

[15] S. J. Baek, D. Kim, S.-J. Oh, and J.-A. Jun, "A queuing model with random interruptions for electric vehicle charging systems," in *Proceedings of the IEEE International Conference on Consumer Electronics (ICCE '11)*, pp. 679–680, Las Vegas, Nev, USA, January 2011.

[16] US Department of Transportation, *Summary of Travel Trends: 2009 National Household Travel Survey*, Federal Highway Administration, Washington, DC, USA, 2012.

[17] J. Taylor, A. Maitra, M. Alexander, D. Brooks, and M. Duvall, "Evaluation of the impact of plug-in electric vehicle loading on distribution system operations," in *Proceedings of the IEEE Power and Energy Society General Meeting (PES '09)*, pp. 26–30, Calgary, Canada, July 2009.

[18] Nissan Leaf Electric Car, http://www.nissanusa.com/leaf-electric-car/index.

[19] AMP to electrify Jeep Grand Cherokee, http://news.carjunky.com/alternative_fuel_vehicles/Amp_Electric_Jeep_Grand_Cherokee.shtml.

[20] Smith Electric Vehicles, http://www.smithelectric.com/smith-vehicles/.

[21] FERC, Annual Electric Balancing Authority and Planning Area Report, http://www.ferc.gov/docs-filing/forms.asp#714.

[22] The Energy Report of Texas, http://www.window.state.tx.us/specialrpt/energy/.

[23] K. Turitsyn, N. Sinitsyn, S. Backhaus, and M. Chertkov, "Robust broadcast-communication control of electric vehicle charging," in *Proceedings of the IEEE International Conference on Smart Grid Communication*, pp. 4–6, Gaithersburg, Md, USA, 2010.

[24] M. Mültin, F. Allerding, and H. Schmeck, "Integration of electric vehicles in smart homes—an ICT-based solution for V2G scenarios," in *Proceedings of the IEEE PES Conference on Innovative Smart Grid Technologies*, pp. 16–20, Washington, DC, USA, 2011.

[25] M. Hwang, D. Choi, and P. Kim, "Least slack time rate first: an efficient scheduling algorithm for pervasive computing environment," *Journal of Universal Computer Science*, vol. 17, no. 6, pp. 912–925, 2011.

[26] A. K. Mok, *Fundamental design problems of distributed systems for the hard-real-time environment [Ph.D. thesis]*, Massachusetts Institute of Technology, Cambridge, Mass, USA, 1983.

[27] ExtendSim Advantages, http://www.extendsim.com/prods_advantage.html.

Hindawi Publishing Corporation
Mathematical Problems in Engineering
Volume 2013, Article ID 707953, 14 pages
http://dx.doi.org/10.1155/2013/707953

Research Article

Quality-Related Process Monitoring Based on Total Kernel PLS Model and Its Industrial Application

Kaixiang Peng,[1] Kai Zhang,[1] and Gang Li[2]

[1] *Key Laboratory for Advanced Control of Iron and Steel Process, School of Automation and Electrical Engineering, University of Science and Technology of Beijing, Beijing 100083, China*
[2] *Department of Automation, TNList, Tsinghua University, Beijing 100084, China*

Correspondence should be addressed to Kai Zhang; ustb.kaizhang@gmail.com

Received 5 October 2013; Accepted 31 October 2013

Academic Editor: Hui Zhang

Projection to latent structures (PLS) model has been widely used in quality-related process monitoring, as it can establish a mapping relationship between process variables and quality index variables. To enhance the adaptivity of PLS, kernel PLS (KPLS) as an advanced version has been proposed for nonlinear processes. In this paper, we discuss a new total kernel PLS (T-KPLS) for nonlinear quality-related process monitoring. The new model divides the input spaces into four parts instead of two parts in KPLS, where an individual subspace is responsible in predicting quality output, and two parts are utilized for monitoring the quality-related variations. In addition, fault detection policy is developed based on the T-KPLS model, which is more well suited for nonlinear quality-related process monitoring. In the case study, a nonlinear numerical case, the typical Tennessee Eastman Process (TEP) and a real industrial hot strip mill process (HSMP) are employed to access the utility of the present scheme.

1. Introduction

Multivariate statistic process monitoring (MSPM) is effective for detecting and diagnosing abnormal operating situations in many industrial processes, which helps by improve products' quality a lot. In MSPM, projection to latent structures (PLS) model pays more attention to quality-related faults while principal component analysis (PCA) considers all faults in a process [1–7]. The major advantage of PLS is its ability to capture the relations of a large number of highly correlated process variables and few quality variables. By building a PLS model on process variables and quality variables, the process data can be projected onto two low-dimension subspaces [1, 8]. Then some statistics can be calculated in these subspaces separately. It should be noted that PLS is a linear algorithm; thus, it performs well in linear or approximately linear data. However, when the process data have strong nonlinearity, PLS will give unsatisfactory results [8].

For many physical and chemical processes, the nonlinearity lying in the process data and quality data is too obvious to be neglected. To deal with this problem, many nonlinear PLS methods have been proposed [6, 9]. Generally, PLS can be improved by two ways for nonlinear cases, which are the modification of inner model and the modification of outer model, which reflects the relation between process variables and quality variables. A method called kernel projection to latent structures (KPLS) proposed by Rosipal and Trejo is developed successfully as a nonlinear PLS model [10]. In KPLS model, the original input data are transformed into a high-dimensional space via nonlinear mapping, and then a linear PLS model is created between the feature data and quality data [11–13]. KPLS takes the advantage over other nonlinear PLS approaches as it avoids the nonlinear optimization [14, 15]. In fact, it just uses the linear algorithm of PLS in the high-dimensional feature space.

In the aforementioned literature [16, 17], Li et al. revealed the geometric properties of PLS for process monitoring and compared monitoring policies based on various PLS, which indicates that the standard PLS model divides the measured space into two oblique subspaces. One includes the quality-related variations; another subspace contains the quality-unrelated variations. Two statistics are usually

utilized for fault detection separately [3, 18]. Although PLS-based methods work well in several cases, there are still some problems. In regular PLS, there are usually many components extracted from process variables $\mathbf{X}$ for predicting quality variables $\mathbf{Y}$. As a result, the PLS model is complex to interpret [16, 19–21]. These PLS components still include variations orthogonal to $\mathbf{Y}$ which have no contribution for predicting $\mathbf{Y}$. On the other hand, the $\mathbf{X}$-residuals from PLS model are not necessarily small in covariances. This makes the use of Q statistic on $\mathbf{X}$-residuals inappropriate. The KPLS model space decomposition is similar to PLS model, with the above-mentioned defects.

In order to improve the KPLS model, a new total kernel PLS (T-KPLS) is proposed for nonlinear quality-related process monitoring in this paper. First of all, we reveled and summarized the existing KPLS model and corresponding process monitoring techniques. Then T-KPLS is developed. The properties of the new model and the process monitoring strategies are discussed then. T-KPLS model can describe the nonlinear process according to quality data effectively and also give a further decomposition on the feature spaces in KPLS. Actually, besides nonlinearity, traditional MSPM approaches also possess the assumption that the processes operate under a Gaussian distribution and in a single mode. Also, increasing number of studies can be found in this area. However, due to the scope in this paper, these issues will be considered in the subsequent researches [14, 15, 22–25].

This paper is organized as follows. KPLS-related algorithm and process monitoring methods are introduced in Section 2. Section 3 proposes the algorithm of T-KPLS, discusses its properties, and constructs T-KPLS-based process monitoring policy. Section 4 provides a numerical simulation example and TEP benchmark to illustrate the feasibility of T-KPLS-based approaches. Furthermore, the new method is also implemented to a real industrial hot strip mill process in Section 5. Finally, this paper is concluded in Section 6.

Notation. The notation adopted in this paper is fairly standard. All vectors and matrices are presented in a bold fashion and written in a vector-matrix style. The symbols for scalars and functions are regularly formulated throughout this paper.

2. KPLS Model for Process Monitoring

2.1. KPLS Model. For a nonlinear process, the input matrix can be defined as $\mathbf{X} = [\mathbf{x}_1, \mathbf{x}_2, \ldots, \mathbf{x}_n]^T \in \Re^{n\times m}$, which consists of n samples with m process variables, and output matrix with p quality variables can be denoted by $\mathbf{Y} = [\mathbf{y}_1, \mathbf{y}_2, \ldots, \mathbf{y}_n]^T \in \Re^{n\times p}$. Define ϕ as a nonlinear map which maps the input vector from the original space into the feature space F, in which they are related linearly approximately. After the nonlinear map, the original input matrix $\mathbf{X}$ is changed to $\mathbf{\Phi} = [\phi(\mathbf{x}_1), \phi(\mathbf{x}_2), \ldots, \phi(\mathbf{x}_n)]^T \in \Re^{n\times M}$. Note that the dimensionality of the feature space M can be very large and even infinite. Define $\mathbf{K} \in \Re^{n\times n}$ as the kernel matrix to represent $\mathbf{\Phi}\mathbf{\Phi}^T$, where $\mathbf{K}_{ij} = K(\mathbf{x}_i, \mathbf{x}_j) = \langle \phi(\mathbf{x}_i), \phi(\mathbf{x}_j)\rangle$, $i, j = 1, 2, \ldots, n$, where $K(\cdot)$ is an inner product operator in feature space. With the kernel trick, one can avoid performing explicit nonlinear mapping [10]. Similar to PLS, KPLS algorithm sequentially extracts the latent vectors $\mathbf{t}$, $\mathbf{u}$ and the weight vectors $\mathbf{w}$, $\mathbf{q}$ from the $\mathbf{\Phi}$ and $\mathbf{Y}$ matrices [12]. To eliminate the mean effect, mean centering in the high-dimensional space is performed. In order to center the feature data to zero mean, the following preprocessing for normal training data is necessary [10, 12, 13]: $\mathbf{\Phi} = \mathbf{\Phi}_{\text{raw}} - \mathbf{1}_n\overline{\mathbf{\Phi}}_{\text{raw}}$, where $\mathbf{\Phi}_{\text{raw}}$ is the directly mapped matrix, $\overline{\mathbf{\Phi}}_{\text{raw}}$ denotes the mean of $\mathbf{\Phi}_{\text{raw}}$, and $\mathbf{1}_n$ represents the n-dimension column vector whose elements are all one. So the centered $\mathbf{K}$ can be calculated as follows:

$$\mathbf{K} = \left(\mathbf{I}_n - \left(\frac{1}{n}\right)\mathbf{1}_n\mathbf{1}_n^T\right)\mathbf{K}_{\text{raw}}\left(\mathbf{I}_n - \left(\frac{1}{n}\right)\mathbf{1}_n\mathbf{1}_n^T\right). \quad (1)$$

For a test sample $\mathbf{x}_{\text{new}} \in \Re^m$, the directly mapped feature vector is $\phi(\mathbf{x}_{\text{new}})_{\text{raw}} \in \Re^M$; then the inner product is calculated by $(\mathbf{K}_{\text{raw}}^{\text{new}})_i = \langle \phi(\mathbf{x}_i), \phi(\mathbf{x}_j)\rangle = K(\mathbf{x}_i, \mathbf{x}_{\text{new}})$. The centered vector $\phi(\mathbf{x}_{\text{new}})$ is $\phi(\mathbf{x}_{\text{new}}) = \phi(\mathbf{x}_{\text{new}})_{\text{raw}} - \overline{\mathbf{\Phi}}_{\text{raw}}^T$ and $\mathbf{K}_{\text{new}}$ are mean-centered as

$$\mathbf{K}_{\text{new}} = \left(\mathbf{I}_n - \left(\frac{1}{n}\right)\mathbf{1}_n\mathbf{1}_n^T\right)\left(\mathbf{K}_{\text{raw}}^{\text{new}} - \left(\frac{1}{n}\right)\mathbf{K}_{\text{raw}}\mathbf{1}_n\right). \quad (2)$$

The algorithm of KPLS modeling has been illustrated in Appendix A. After that, $\mathbf{\Phi}$ and $\mathbf{Y}$ can be represented as

$$\begin{aligned} \mathbf{\Phi} &= \widehat{\mathbf{\Phi}} + \mathbf{\Phi}_r = \mathbf{T}\mathbf{P}^T + \mathbf{\Phi}_r, \\ \mathbf{Y} &= \widehat{\mathbf{Y}} + \mathbf{Y}_r = \mathbf{T}\mathbf{Q}^T + \mathbf{Y}_r. \end{aligned} \quad (3)$$

Let $\mathbf{R} = \mathbf{\Phi}^T\mathbf{U}(\mathbf{T}^T\mathbf{K}\mathbf{U})^{-1} \in \Re^{M\times A}$; then

$$\mathbf{T} = \mathbf{\Phi}\mathbf{R}. \quad (4)$$

The derivation of (4) is presented in Appendix B.

The determination of kernel function $K(\cdot)$ is very important. According to Mercer's theorem, there exists a mapping into a space where a kernel function acts as a dot product if the kernel function is a continuous kernel of a positive integral operator. Hence, the necessary condition for the kernel function is to meet Mercer's theorem [10, 27]. A specific choice of kernel function implicitly determines the mapping $\mathbf{\Phi}$ and the feature space F. The most widely used kernel functions include Gaussian, polynomial, sigmoid function. In this study, the Gaussian kernel function is considered

$$K(x, y) = \exp\left(-\frac{\|x - y\|^2}{c}\right), \quad (5)$$

where the parameter c is the width of a Gaussian function. It plays a crucial role in process monitoring. In general, when c becomes large, the robustness of this model increases whereas the sensitivity decreases. Namely, false alarms decrease while missing alarms increase. In [28], Mika et al. proposed a method for determining c, which is widely utilized for KPLS-based nonlinear regression [29]. In this paper, first of all, we choose an appropriate false alarm rate level for normal training data (10% in this paper). Then c can be searched along with the component number A until that the KPLS model with A components acquired by cross validation presents a false alarm rates below the predefined level.

2.2. KPLS-Based Fault Detection. Usually T^2 and Q statistics are used in KPLS-based monitoring, where T^2 is for quality-related faults and Q for quality-unrelated faults. Given a new sample, the score $\mathbf{t}_{\text{new}}$ of $\phi(\mathbf{x}_{\text{new}})$ can be calculated as

$$\mathbf{t}_{\text{new}} = \mathbf{R}^T\phi(\mathbf{x}_{\text{new}}) = \left(\mathbf{U}^T\mathbf{K}\mathbf{T}\right)^{-1}\mathbf{U}^T\mathbf{K}_{\text{new}} \in \Re^A. \quad (6)$$

The residuals of $\phi(\mathbf{x}_{\text{new}})$ are represented as $\phi_r(\mathbf{x}_{\text{new}}) = \phi(\mathbf{x}_{\text{new}}) - \mathbf{P}\mathbf{t}_{\text{new}}$, which cannot be calculated directly. Further, two statistics T^2 and Q can be calculated [3, 19] as follows:

$$T^2 = \mathbf{t}_{\text{new}}^T\Lambda^{-1}\mathbf{t}_{\text{new}},$$
$$Q = \left\|\phi_r(\mathbf{x}_{\text{new}})\right\|^2, \quad (7)$$

where $\Lambda = (1/(n-1))\mathbf{T}^T\mathbf{T}$. Two kinds of control limits are given, respectively: $(A(n^2-1)/(n(n-A)))F_{A,n-A,\alpha}$ and $g\chi_{h^2,\alpha}$. $F_{A,n-A}$ is F-distribution with A and $n-A$ degrees of freedom. $g\chi_h^2$ is the χ^2-distribution with scaling factors g and h degrees of freedom [13]. Although $\phi(\mathbf{x}_{\text{new}})$ is unavailable, it is able to calculate Q by the kernel trick as follows:

$$Q = \phi^T(\mathbf{x}_{\text{new}})\phi(\mathbf{x}_{\text{new}}) - 2\mathbf{t}_{\text{new}}^T\mathbf{T}^T\mathbf{K}_{\text{new}} + \mathbf{t}_{\text{new}}^T\mathbf{T}^T\mathbf{K}\mathbf{T}\mathbf{t}_{\text{new}}, \quad (8)$$

where

$$\phi^T(\mathbf{x}_{\text{new}})\phi(\mathbf{x}_{\text{new}}) = 1 - \left(\frac{2}{n}\right)\sum_{i=1}^{n}\mathbf{K}_{\text{raw}}^{\text{new}}(i) + \left(\frac{1}{n^2}\right)\sum_{i=1}^{n}\sum_{j=1}^{n}\mathbf{K}_{\text{raw}}(i,j). \quad (9)$$

3. T-KPLS Model for Nonlinear Data

KPLS divides the feature space F into two subspaces. One is the principal space which is monitored by T^2, reflecting the major variation related to $\mathbf{Y}$. The other is the residual space which is monitored by Q, reflecting the variation unrelated to $\mathbf{Y}$. However, the principal part $\widehat{\mathbf{\Phi}}$ contains variations which do not affect output $\mathbf{Y}$ and is useless for predicting $\mathbf{Y}$. For the residual part $\mathbf{\Phi}_r$, as the objective of KPLS is to maximize the covariance between $\mathbf{\Phi}$ and $\mathbf{Y}$, it does not extract the variance of $\mathbf{\Phi}$ in a descending order. So the latter KPLS score may capture more variance in $\mathbf{\Phi}$ than the previous one. After the score vectors have been extracted, $\mathbf{Y}$ is best predicted, but the residual of $\mathbf{\Phi}$ may still contain the large variability. Therefore, it is not suitable to use Q statistic to monitor the residual part in KPLS. In this part, a T-KPLS model is proposed to improve the original KPLS model. Following that, the T-KPLS-based process monitoring strategy is established.

3.1. T-KPLS Model. The T-KPLS model is a further decomposition on the KPLS model. It can be thought as a postprocessing method to decompose the $\widehat{\mathbf{\Phi}}$ and $\mathbf{\Phi}_r$ further in KPLS. The detailed algorithm for T-KPLS can be found in Algorithm 1.

In step (4) of Algorithm 1, loading matrix $\mathbf{P}_o = \mathbf{\Phi}_o^T\mathbf{W}_o \in \Re^{M\times A_o}$, where $\mathbf{W}_o \in \Re^{n\times A_o}$ contains the scaled eigenvectors of $(1/n)\mathbf{\Phi}_o\mathbf{\Phi}_o^T$ corresponding to its A_o largest eigenvalues. In step (5), $\mathbf{P}_r = \mathbf{\Phi}_r^T\mathbf{W}_r \in \Re^{M\times A_r}$, where $\mathbf{W}_r \in \Re^{n\times A_r}$ are the scaled eigenvectors of $(1/n)\mathbf{\Phi}_r\mathbf{\Phi}_r^T$ corresponding to its A_r largest eigenvalues [27]. As $\phi(\cdot)$ is unknown, the algorithm in Algorithm 1 cannot be implemented intuitively, while the calculable steps are shown in Algorithm 2. In Algorithm 2,

$$\mathbf{K}_o = Z_y\mathbf{T}\mathbf{T}^T\mathbf{K}\mathbf{T}\mathbf{T}^TZ_y,$$
$$\mathbf{K}_r = \left(\mathbf{I}_n - \mathbf{T}\mathbf{T}^T\right)\mathbf{K}\left(\mathbf{I}_n - \mathbf{T}\mathbf{T}^T\right), \quad (10)$$

where $Z_y = \mathbf{I}_n - \mathbf{T}_y(\mathbf{T}_y^T\mathbf{T}_y)^{-1}\mathbf{T}_y$.

In T-KPLS model, we can model $\mathbf{\Phi}$ and $\mathbf{Y}$ as follows:

$$\mathbf{\Phi} = \mathbf{\Phi}_y + \mathbf{\Phi}_o + \mathbf{\Phi}_{rp} + \mathbf{\Phi}_{rr},$$
$$\mathbf{Y} = \mathbf{T}_y\mathbf{Q}_y^T + \mathbf{Y}_r. \quad (11)$$

The meanings of different sections of $\mathbf{\Phi}$ are listed in Table 1. Compared with KPLS, T-KPLS is clearer for describing $\mathbf{\Phi}$ and more suitable for monitoring different parts of $\phi(\mathbf{x})$. T-KPLS does not change the prediction ability of $\mathbf{Y}$, but it decomposes $\mathbf{\Phi}$ thoroughly supervised by $\mathbf{Y}$. $\mathbf{T}_y$ is the score of $\mathbf{\Phi}_y$ and completely related to $\mathbf{Y}$ from the original $\mathbf{T}$, whereas $\mathbf{T}_o$ is the score of $\mathbf{\Phi}_o$ and orthogonal to $\mathbf{Y}$ in original $\mathbf{T}$. $\mathbf{T}_r$ is the main part of $\mathbf{\Phi}_r$. $\mathbf{\Phi}_{rr}$ represents the residual of $\mathbf{\Phi}$ and the noise. Note that in the T-KPLS model, all the scores $\mathbf{T}_y$, $\mathbf{T}_o$, and $\mathbf{T}_r$ have their definite values. However, the loadings $\mathbf{P}_y$, $\mathbf{P}_o$, and $\mathbf{P}_r$ are unknown because of the uncertain map function ϕ.

In T-KPLS, the orthogonality among all score vectors holds. Meanwhile, $\mathbf{T}_o$ is orthogonal to output $\mathbf{Y}$. The proof is omitted, and one can refer to Zhou et al. [19].

Table 1: Meaning of different sections of $\mathbf{\Phi}$.

Section	Description
$\mathbf{\Phi}_y$	The $\mathbf{Y}$-related part of $\widehat{\mathbf{\Phi}}$ which is responsible for predicting $\mathbf{Y}$
$\mathbf{\Phi}_o$	The part of $\widehat{\mathbf{\Phi}}$ that is orthogonal to $\mathbf{Y}$ in original $\mathbf{T}$ of KPLS
$\mathbf{\Phi}_{rp}$	The principal part of $\mathbf{\Phi}_r$ which represents a large variation in $\mathbf{\Phi}_r$
$\mathbf{\Phi}_{rr}$	The residual part which is not excited in $\mathbf{\Phi}$

3.2. T-KPLS-Based Quality-Related Process Monitoring. In multivariate statistical process monitoring, two types of statistics are widely used for fault detection. One is the D statistic which calculates the Mahalanobis distance between new scores and the normal scores. The other is the Q statistic which represents the square predict error of the sample. As for T-KPLS, the similar statistics are constructed. After T-KPLS model is built from normal historical data, the new scores and residuals are calculated from the new sample. Then, the statistics are constructed with corresponding control limits for fault detection.

(1) Perform KPLS algorithm on $\mathbf{X}$ and $\mathbf{Y}$ to get the model described in (3)
(2) Run PCA on $\widehat{\mathbf{Y}}$ with A_y components, where $\widehat{\mathbf{Y}} = \mathbf{T}_y\mathbf{Q}_y^T$, $A_y = \operatorname{rank}(\mathbf{Q})$
(3) Define $\mathbf{\Phi}_y = \mathbf{T}_y\mathbf{P}_y^T$, where $\mathbf{P}_y^T = \left(\mathbf{T}_y^T\mathbf{T}_y\right)^{-1}\mathbf{T}_y^T\widehat{\mathbf{\Phi}}$, $\mathbf{P}_y \in \mathfrak{R}^{M\times A_y}$
(4) Run PCA on $\mathbf{\Phi}_o = \widehat{\mathbf{\Phi}} - \mathbf{\Phi}_y$, with A_o components, $A_o = A - A_y$, $\mathbf{\Phi}_o = \mathbf{T}_o\mathbf{P}_o^T$
(5) Perform PCA on $\mathbf{\Phi}_r$, with A_r components, where A_r is determined using PCA methods, $\mathbf{\Phi}_{rp} = \mathbf{T}_r\mathbf{P}_r^T$
(6) $\mathbf{\Phi}_{rr} = \mathbf{\Phi}_r - \mathbf{\Phi}_{rp} = \mathbf{\Phi}_r - \mathbf{T}_r\mathbf{P}_r^T$

Algorithm 1: T-KPLS algorithm for comprehension.

Obtain $\mathbf{K}$ and $\mathbf{Y}$

(1) After KPLS model: $\mathbf{T} = \mathbf{KU}(\mathbf{T}^T\mathbf{KU})^{-1}$
(2) Run eigenvector decomposition on $\widehat{\mathbf{Y}}$: $\mathbf{T}_y = \widehat{\mathbf{Y}}\mathbf{Q}_y = \mathbf{TQ}^T\mathbf{Q}_y$
(3) Perform eigenvector decomposition on $(1/n)\,\mathbf{K}_o$ to get the eigenvectors $\mathbf{W}_o$ with regard to its largest A_o eigenvalues. $\mathbf{T}_o = \mathbf{K}_o\mathbf{W}_o$
(4) Perform eigenvector decomposition on $(1/n)\,\mathbf{K}_r$ to get the eigenvectors $\mathbf{W}_r$ with regard to its largest A_r eigenvalues. $\mathbf{T}_r = \mathbf{K}_r\mathbf{W}_r$

Algorithm 2: T-KPLS algorithm for calculation.

Table 2: Monitoring statistics and control limits.

Statistic	Calculation	Control limit
T_y^2	$\mathbf{t}_{y\text{new}}^T\mathbf{\Lambda}_y^{-1}\mathbf{t}_{y\text{new}}$	$\dfrac{A_y\left(n^2-1\right)}{n\left(n-A_y\right)}F_{A_y,n-A_y,\alpha}$
T_o^2	$\mathbf{t}_{o\text{new}}^T\mathbf{\Lambda}_o^{-1}\mathbf{t}_{o\text{new}}$	$\dfrac{A_o\left(n^2-1\right)}{n\left(n-A_o\right)}F_{A_o,n-A_o,\alpha}$
T_r^2	$\mathbf{t}_{r\text{new}}^T\mathbf{\Lambda}_r^{-1}\mathbf{t}_{r\text{new}}$	$\dfrac{A_r\left(n^2-1\right)}{n\left(n-A_r\right)}F_{A_r,n-A_r,\alpha}$
Q_r	$\left\lVert\phi_{rr}\left(\mathbf{x}_{\text{new}}\right)\right\rVert^2$	$g\chi_{h,a}^2$

According to T-KPLS model, three score vectors can be calculated as follows:

$$\begin{aligned}\mathbf{t}_{y\text{new}} &= \Theta_y\mathbf{K}_{\text{new}} \in \mathfrak{R}^{A_y},\\ \mathbf{t}_{o\text{new}} &= \Theta_o\mathbf{K}_{\text{new}} \in \mathfrak{R}^{A_o},\\ \mathbf{t}_{r\text{new}} &= \Theta_r\mathbf{K}_{\text{new}} \in \mathfrak{R}^{A_r}.\end{aligned} \tag{12}$$

Motivated by total PLS- (T-PLS-) based methods [19], four fault detection indices are constructed in Table 2. The expression of Q_r can be calculated as follows:

$$Q_r = \phi^T\left(\mathbf{x}_{\text{new}}\right)\phi\left(\mathbf{x}_{\text{new}}\right) - \mathbf{K}_{\text{new}}^T\Omega_r\mathbf{K}_{\text{new}}. \tag{13}$$

The detailed expression of (12) and Q_r for calculation are shown in Appendix C.

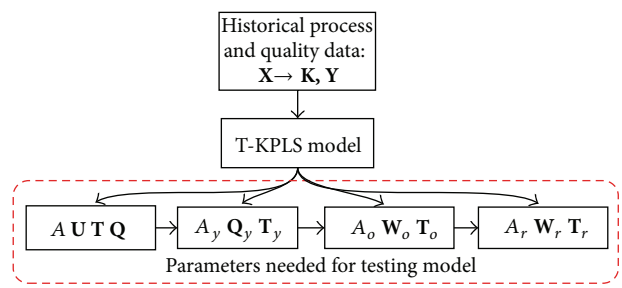

Figure 1: Training model T-KPLS-based monitoring.

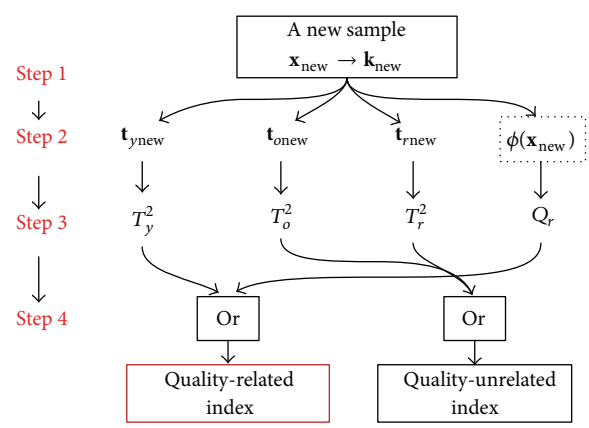

Figure 2: Flowchart of testing model for T-KPLS-based monitoring.

3.3. Model Implementation. Implementation of the T-KPLS-based quality-related detection scheme involves offline training model and online testing model. As sketched in Figure 1, the training model aims to obtain the model parameters. When all parameters are available, the schematic plot for a testing sample is sketched in Figure 2. The whole procedure involves four steps: the acquisition of online measurement, the calculation of all scores for the new sample, the acquirement of four detection indices, and the result for quality-related detection.

4. Case Study on Simulation Examples

In this section, two detailed simulation examples are carried out to demonstrate the advantage of T-KPLS.

4.1. Simulation on a Numerical Nonlinear Example. Firstly, a synthetic nonlinear numerical process without feedback is presented as follows:

$$\text{Process variable}: \begin{cases} \mathbf{x}_1 \sim \mathbf{N}(0,1), \quad \mathbf{x}_2 \sim \mathbf{N}(0,1), \\ \mathbf{x}_3 = \sin(\mathbf{x}_1) + e_1, \\ \mathbf{x}_4 = \mathbf{x}_1^2 - 3\mathbf{x}_1 + 4 + e_2, \\ \mathbf{x}_5 = \mathbf{x}_2^2 + \cos(\mathbf{x}_2^2) + 1 + e_3, \end{cases} \tag{14}$$

$$\text{Quality variable}: \mathbf{y} = \mathbf{x}_3^2 + \mathbf{x}_3\mathbf{x}_4 + \mathbf{x}_1 + \nu,$$

where $e_i \sim \mathbf{N}(0, 0.01^2)$ $(i = 1, 2, 3)$, $\nu \sim \mathbf{N}(0, 0.05^2)$, $\mathbf{N}(\mu, \sigma^2)$ means the normal distribution with mean μ and variance σ^2. From (14), it is obvious that the abnormal variation in $\mathbf{x}_1$ can cause the disturbances in $\mathbf{x}_3$ and $\mathbf{x}_4$, while $\mathbf{x}_2$ just influences $\mathbf{x}_5$. As quality variable $\mathbf{y}$ merely relates to $\mathbf{x}_1$, $\mathbf{x}_3$, and $\mathbf{x}_4$, so the fault in $\mathbf{x}_1$ will affect $\mathbf{y}$, while the fault in $\mathbf{x}_2$ cannot.

We used 200 samples generated from the above process as a training dataset. The faulty dataset with 400 samples was also generated according to the following faults:

(i) Fault 1: a step bias in $\mathbf{x}_2$ at 201st sample, $\mathbf{x}_2 = \mathbf{x}_2^* + f$,

(ii) Fault 2: a ramp change in $\mathbf{x}_2$ at 201st sample, $\mathbf{x}_2 = \mathbf{x}_2^* + (k - 200)f$,

(iii) Fault 3: a step bias in $\mathbf{x}_1$ at 201st sample, $\mathbf{x}_1 = \mathbf{x}_1^* + f$,

(iv) Fault 4: a ramp change in $\mathbf{x}_1$ at 201st sample, $\mathbf{x}_1 = \mathbf{x}_1^* + (k - 200)f$,

where $\mathbf{x}_1^*$, $\mathbf{x}_2^*$ are the normal values of $\mathbf{x}_1$ and $\mathbf{x}_2$, respectively, f is the magnitude for step bias and slope for ramp change, and k is the sample number. Then the faulty measurements of variable $\mathbf{x}_3$, $\mathbf{x}_4$, and $\mathbf{x}_5$ are generated by (14).

Training samples are applied to perform a KPLS model on $(\mathbf{X}, \mathbf{y})$. The width of Gaussian kernel $c = 100$ is kept for this simulation. The components number $\mathbf{A} = 2$ is determined using cross validation, which provides a good prediction of $\mathbf{y}$. Then T-KPLS model is constructed based on KPLS, where $A_y = 1$ for the single output, and $A_r = 1$ is chosen as the principal component unrelated to $\mathbf{y}$.

According to the descriptions of Faults 1 and 2, they are quality-unrelated faults. Let $f = 1$; the monitoring results with KPLS model (T^2 and Q) are plotted in Figure 3. It is observed that Fault 1 causes significant alarms in both two detection indices of KPLS. However, the alarms in T^2 chart are false alarms for indicating a $\mathbf{y}$-related fault. Thus, KPLS-based monitoring causes false alarms for this disturbance. T-KPLS-based monitoring for Fault 1 is depicted in Figure 4. Among the four detection indices, T_y^2 is kept under the control line, which gives correct result. Also T_r^2 and Q_r alarm tinily. Compared with KPLS, T-KPLS provides lower false alarm rates for Fault 1. Similarly, the detection results of Fault 2 with $f = 0.005$ using KPLS and T-KPLS are shown in Figures 5 and 6, respectively. It is shown that the results for Fault 2 is similar to that of Fault 1. Table 3 lists the false alarm rates under different fault magnitudes f. In all simulations, we repeat 100 times and make use of the mean for conviction. From Table 3, it is clear that T-KPLS-based method gives lower false alarm rates.

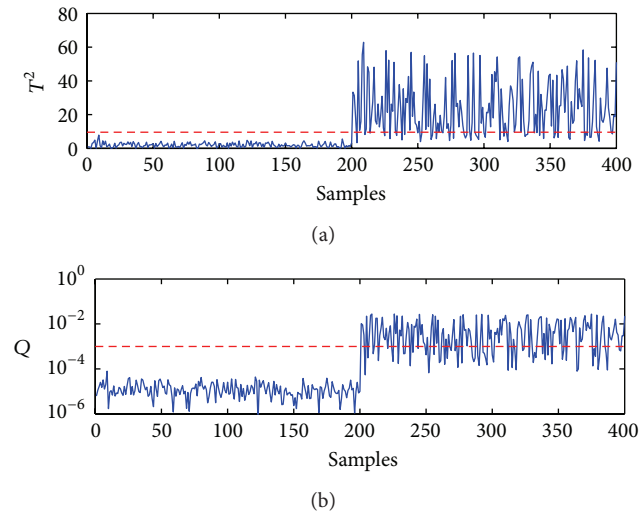

Figure 3: KPLS-based monitoring with 99% control limit when quality-unrelated Fault 1 occurs.

Table 3: False alarm rates of faults unrelated to $\mathbf{y}$ (%).

	Fault value (f)	KPLS (T^2)	T-KPLS (T_y^2)	T-KPLS (Q_r)	T-KPLS (T_y^2 or Q_r)
Fault 1	0.2	26.8	0	4.7	4.7
	0.4	31.7	0	11.6	11.6
	0.6	53.3	0	26.6	26.6
	0.8	77.2	0	43.3	43.3
Fault 2	0.002	24.5	0	8.3	8.3
	0.003	37.4	0	18.6	18.6
	0.004	44.5	0	27.8	27.8
	0.005	56.3	0	36.8	36.8

The predefined Faults 3 and 4 are quality-related. For Fault 3 with $f = 0.6$, KPLS-based method could detect this fault as shown in Figure 7. T-KPLS-based method performs sensitively in T_y^2, T_r^2, and Q_r in Figure 8. That is to say, the alarms in T^2 of KPLS are merely denoted by T_y^2 of T-KPLS. Thus, for this kind of fault, when the step magnitude is small enough, T-KPLS will work better than KPLS. For quality-related Fault 4 with $f = 0.005$, KPLS-based method cannot detect quality-related faults by T^2 as shown in Figure 9, while T-KPLS-based Q_r statistic detects the fault sensitively in Figure 10. It means that the variations leading $\mathbf{y}$ to abnormality occur in the residual space. The results of simulation on Faults 3 and 4 show that T-KPLS-based policy could improve the detection rates. Moreover, Table 4 lists the detection results which show that the quality-related fault can be detected by T-KPLS using T_y^2 and Q_r better.

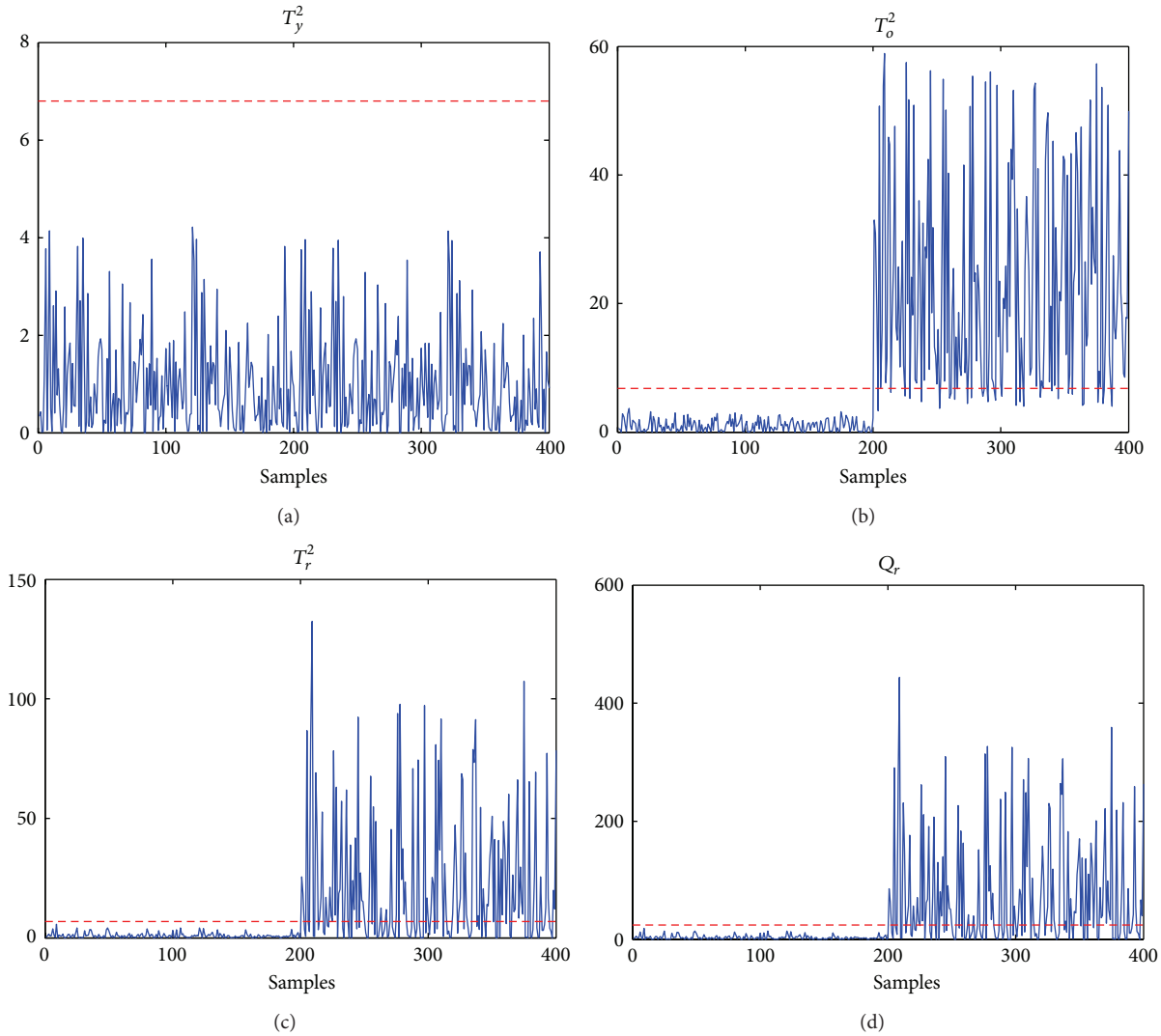

Figure 4: T-KPLS-based monitoring when quality-unrelated Fault 1 occurs.

Table 4: False detection rates of faults related to **y** (%).

	Fault value (f)	KPLS (T^2)	T-KPLS (T_y^2)	T-KPLS (Q_r)	T-KPLS (T_y^2 or Q_r)
Fault 3	0.2	63.6	80.5	57.3	83.6
	0.4	79.8	88.5	74.4	88.7
	0.6	90.3	99.2	86.3	99.2
	0.8	99.4	100	99.5	100
Fault 4	0.002	4.1	0	29.5	29.5
	0.003	4.3	0	43.1	43.1
	0.004	3.5	0	54.2	54.2
	0.005	4.6	0	62.1	62.1

4.2. Simulation on Tennessee Eastman Process

4.2.1. Tennessee Eastman Process. The Tennessee Eastman (TE) Process was provided by Eastman Chemical Company which is a realistic industrial process for evaluating different process control and monitoring technologies [16, 30]. The process has five major parts: a reactor, condenser, recycle compressor, liquid separator, and product stripper, and it involves eight components: A–H. The gaseous reactants A, C–E, and the inert B are fed to the reactor while the liquid products G and H are formed. The reactions in the reactor follow (15). The species F is a by-product. All reactions of this process are irreversible, exothermic, and approximately one-order with respect to the reactant concentrations. For detailed process description, one can refer to Lee et al. and Chiang et al. [30, 31]. The process used here is implemented under closed-loop control. All the training and testing datasets were generated by Chiang et al. and Lee et al., which can be openly downloaded in their website. The faults in the test dataset are introduced from the 160th sample. The TE process has been used as a benchmark process for evaluating process monitoring methods. Kano et al. applied PCA-based method for monitoring this process [32]. Russell et al. compared canonical vector analysis (CVA) and PCA-based technologies, while Lee et al. reviewed the results using both

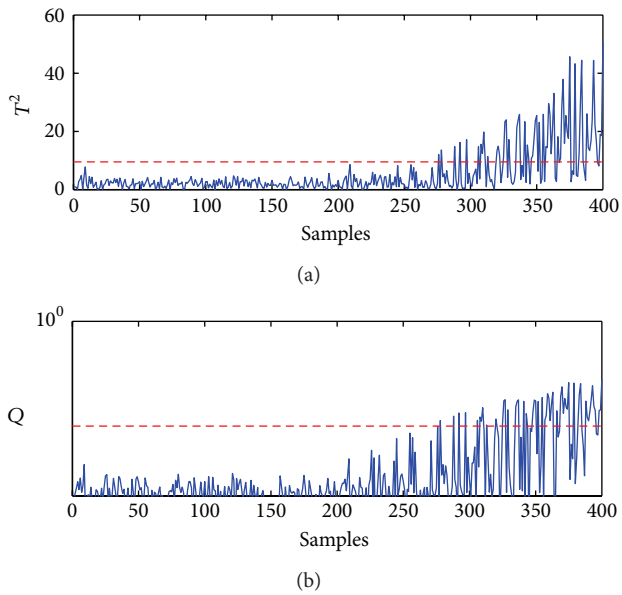

Figure 5: KPLS-based monitoring with 99% control limit when quality-unrelated Fault 2 occurs.

independent component analysis (ICA) and PCA for TEP [26, 30, 33]. Also, PLS-based monitoring policy has been utilized for quality-related fault detection [30]. In [31], Chiang et al. compared the fault detection and diagnosis method such as PCA, PLS, and Fisher discriminant analysis (FDA), according to the case study of TEP.

The TEP contains two blocks of variables: 12 manipulated variables and 41 measured variables. Process measurements are sampled with interval of 3 min, while nineteen composition measurements are sampled with time delays which vary from 6 min to 15 min. The time delay has a potentially critical impact on product quality control in this process, because the closed-loop control works when the next sample of quality variable is available [21]. Thus during this interval, the products are produced with uncontrolled quality. It also implies that the fault effect on product quality cannot be detected until next measurement sampled,

$$\begin{gathered} \mathrm{A}(\mathbf{g}) + \mathrm{C}(\mathbf{g}) + \mathrm{D}(\mathbf{g}) \longrightarrow \mathrm{G}(\mathrm{liq}), \\ \mathrm{A}(\mathbf{g}) + \mathrm{C}(\mathbf{g}) + \mathrm{E}(\mathbf{g}) \longrightarrow \mathrm{H}(\mathrm{liq}), \\ \mathrm{A}(\mathbf{g}) + \mathrm{E}(\mathbf{g}) \longrightarrow \mathrm{F}(\mathrm{liq}), \\ 3\mathrm{D}(\mathbf{g}) \longrightarrow 2\mathrm{F}(\mathrm{liq}); \end{gathered} \tag{15}$$

PLS and KPLS-based monitoring methods can detect the fault correlated to $\mathbf{Y}$, thus receiving wide applications in industrial cases. There are 21 predefined faults in TEP, in which 15 of them are known, denoted by IDV (1–15). IDV (1–7) are step changes in a process variable, for example, in the cooling water inlet temperature. IDV (8–12) are associated with an increase in the variability of some process variables. Fault 13 is a slow drift in the reaction kinetics. IDV (14–15) are associated with sticking valves [19, 20].

Table 5: Fault detection rate of TEP using T-PLS, KPLS, and T-KPLS (%).

Faults ID	Type	T-PLS	KPLS	T-KPLS
IDV(1)	Step	99.3	88.6	**99.7**
IDV(2)	Step	97.6	98.6	**99.6**
IDV(5)	Step	**99.5**	48.2	97.4
IDV(6)	Step	**99.8**	99.5	**99.8**
IDV(8)	Random variation	93.4	95.6	**97.3**
IDV(12)	Random variation	95.6	**99.8**	98.3
IDV(13)	Slow drift	95.3	96.4	**98.5**

Table 6: False alarm rates of TEP using T-PLS, KPLS, and T-KPLS (%).

Faults ID	Type	T-PLS	KPLS	T-KPLS
IDV(0)	—	**5.2**	8.6	5.9
IDV(3)	Step	**5.9**	9.8	**5.9**
IDV(4)	Step	33.5	25.3	**17.2**
IDV(9)	Step	5.3	8.2	**4.4**
IDV(11)	Random variation	32.3	32.7	**17.8**
IDV(14)	Random variation	12.4	22.7	**7.8**
IDV(15)	Slow drift	**5.3**	28.0	10.0

4.2.2. T-KPLS-Based Quality-Related Detection for TEP. In this case study, the component G in steam 9, that is, the 35th measured variable, is chosen as the output quality variable $\mathbf{y}$. The process variables $\mathbf{X}$ consist of measured variable 1–22 and manipulated variable 1–11. The detailed $\mathbf{X}$ and $\mathbf{y}$ are summarized by Li et al. [20]. We use 480 normal samples to build KPLS and T-KPLS model. The selection of kernel parameter c affects the detection results for this process significantly. According to the simulation results, the larger c is, the lower the false alarm rates and the higher the missing alarm rates will be. In this simulation, $c = 5000$ is chosen for the KPLS model. Eight principal components are kept according to cross validation. For T-KPLS, A_y is set to 1 because of the single quality variable, and $A_o = A - A_y = 7$, $A_r = 6$ are determined according to the KPCA-based method. TEP provides 21 faulty sample datasets, and each of them consists of 960 samples. Here, we apply 13 known fault sets to perform our simulation. First of all, these known faults should be divided into two groups including the quality-related faults and the quality-unrelated faults with the criteria proposed by Zhou et al. [19]. Here, the IDV (1, 2, 5, 6, 8, 12, 13) are related to quality variable $\mathbf{y}$; others are not. For comparison, the normal data set is also included in this simulation. As illustrated in Figures 11 and 12, the proposed approach with T_y^2 and Q_r can detect Fault 1 effectively, but show few false alarms for quality-unrelated Fault 3. The alarm for the quality-related fault is considered as an effective alarm, while the detection for quality-unrelated fault is thought to be a false alarm. Tables 5 and 6 list the fault detection rates and fault alarm rates of KPLS and T-KPLS. Also, the detection results by T-PLS [19] are cited in these two tables for comparison.

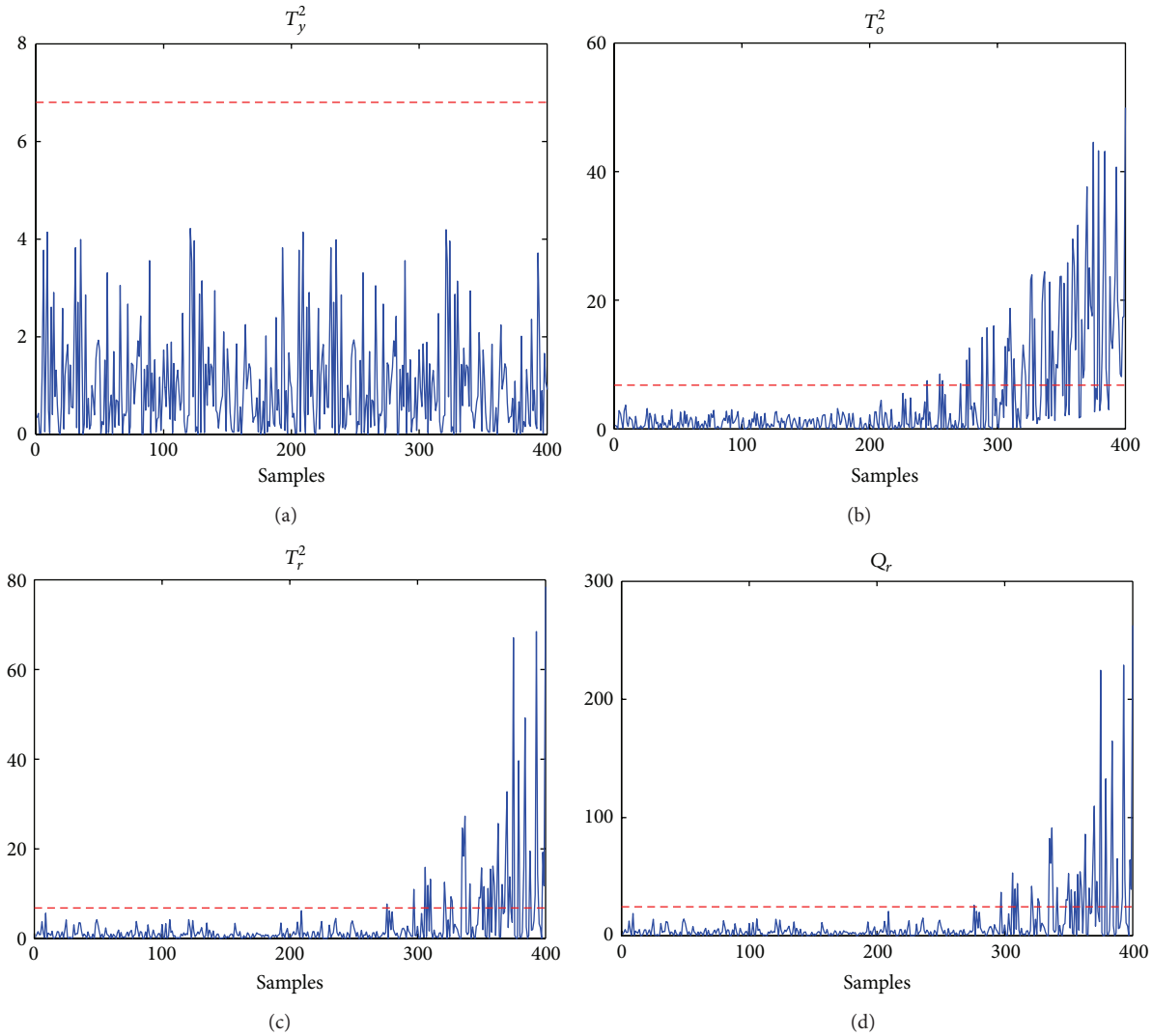

Figure 6: T-KPLS-based monitoring when quality-unrelated Fault 2 occurs.

From the detection results, it is observed that T-KPLS-based method gives a higher detection rate and lower false alarm rate than KPLS-based method. Compared with linear T-PLS, T-KPLS performs better in most cases. In Table 5, T-KPLS has higher detection rates in most cases. Meanwhile, T-KPLS gives lower false alarm rates in most cases as shown in Table 6. To sum up, T-KPLS is an improvement for KPLS, and it is effective to detect quality-related faults in nonlinear processes.

5. Application in Real Industrial Hot Strip Mill

Hot strip mill process (HSMP) is an extremely complex process in iron and steel industry. A schematic layout of the hot strip mill is illustrated in Figure 13 corresponding to the real industrial hot strip mill. According to Figure 13, the process generally consists of the following units: reheating furnaces, roughing mill, transfer table, crop shear, finishing mill, run-out table cooling, and coiler. The finishing mill has the most significant influence on the final thickness of steel strip, in which the controlled variables include average gap of the 7 finishing mill stands and work roll bending (WRB) force of the last 6 stands (WRB force of the first stand is not measured). The thickness and temperature of the strip after finishing rolling are around 850°C–950°C and 1.5–12.7 mm, respectively. As is well known from materials science, the kinetics of metallurgical transformations and the flow stress of the rolled steel strip are dominantly controlled by the temperature, which is mainly determined by the finishing temperature control (FTC).

The demand of dimensional precision, especially thickness precision of hot strip mill, has become stricter in recent years, which makes the improvement of thickness precision be a hot topic. In general, the thickness in exit of finishing mill is closely related to gap and rolling force and has little connection with bending force. In this paper, two classes of strips' manufacturing process are taken for this test with thicknesses, where their thickness targets are 3.95 mm and

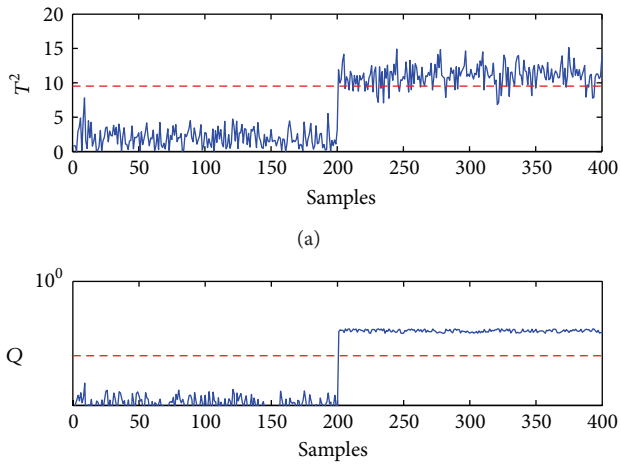

Figure 7: KPLS-based monitoring with 99% control limit when quality-related Fault 3 occurs.

Table 7: Process and quality variables in finishing mill.

Variable	Type	Description	Unit
1~7	Measured	F_i stand average gap, $i = 1, ..., 7$	mm
8~14	Measured	F_i stand total force, $i = 1, ..., 7$	MN
15~20	Measured	F_i stand work roll bending force, $i = 2, ..., 7$	MN
y	Quality	Finishing mill exit strip thickness	mm

2.70 mm, respectively. Based on historical dataset, the new proposed framework can be constructed with the measured process variables and quality variable which are listed in Table 7. In this case study, three kinds of frequently occurring faults are mainly studied, which are listed in Table 8, where all faults with the same duration time of 10 s are terminated artificially. In real circumstances, faults may occur in some driving units or sensors for measuring force, temperature, and gaps. Furthermore, malfunction of control loop in a single stand may also exist occasionally. To be summarized, three kinds of faults defined in control systems can all be found in finishing mill process. In this work, three typical faults separately selected from each type are chosen to support our study, which are tabulated in Table 8. Among all these faults, Fault 1 is a little quality-related; others are directly quality-related. Gaussian kernel parameter c affects detection results significantly. In this study, T-KPLS model is built, where $A = 8$ is determined according to cross validation, $A_y = 1$; because of the single output, $A_r = 10$ is obtained by KPCA-based method. In the model, $c_{\min} = 0$ and $c_{\max} = 10000$ are chosen, which yield an optimum $c = 7500$.

The results of thickness quality-related process monitoring are given by Table 9. As can be shown in Table 9, compared with PLS, KPLS, and T-PLS, T-KPLS-based method

Table 8: Typical faults in finishing mill.

No.	Description	Fault type	Quality related
1	Sensor fault of bending force measurement in F_5 stand	Sensor fault	No
2	Malfunction of hydraulic gap control loop in F_4 stand	Process fault	Yes
3	Actuator fault of cooling valve between F_2 and F_3 stands	Actuator fault	Yes

Table 9: Detection rate or false alarm rate for hot strip mill (%).

Fault No.	Type of detection	PLS (T^2)	KPLS (T^2)	T-PLS (T^2 or Q_r)	T-KPLS (T^2 or Q_r)
1	False alarm rate	0.104	0.117	0.366	**0.044**
2	Detection rate	0.998	**1.000**	**1.000**	**1.000**
3	Detection rate	0.656	0.870	0.900	**0.980**

just gives a little false alarm rate for quality-unrelated Fault 1, while for quality-related Fault 2 and 3, it presents higher detection rates, especially in Fault 3. In conclusion, T-KPLS is an appropriate enhancement for typical KPLS model, and it is effective to deal with the quality-related disturbances in real industrial processes.

Regarding HSMP, the following should be noted.

Remark 1. We clarify that the data considered about finishing mill process are acquired from real steel industrial field, namely, Ansteel Corporation, China. The faults occur occasionally and were eliminated manually.

Remark 2. In this implementation, only thickness has been concerned as the quality variable, whereas T-KPLS model can handle multioutput cases.

6. Conclusion

In this paper, the T-KPLS algorithm is proposed by further decomposing KPLS. The purpose of T-KPLS is to perform a further decomposition on the high dimension space induced by KPLS, which is more suitable for quality-related process monitoring. The process monitoring methods based on T-KPLS are developed to monitor the operating performance. Both theoretical analysis and simulation results show better performance of T-KPLS than KPLS. T-KPLS-based methods can give lower false alarm rates and missing alarm rates than KPLS-based methods in most simulated cases. However, there are still some problems needed to be considered in the modeling with T-KPLS, such as how to select an appropriate kernel function for a given process data and establish a framework for precisely choosing the kernel parameters. Due to the scope of this paper, further studies for these issues will be concerned in the future.

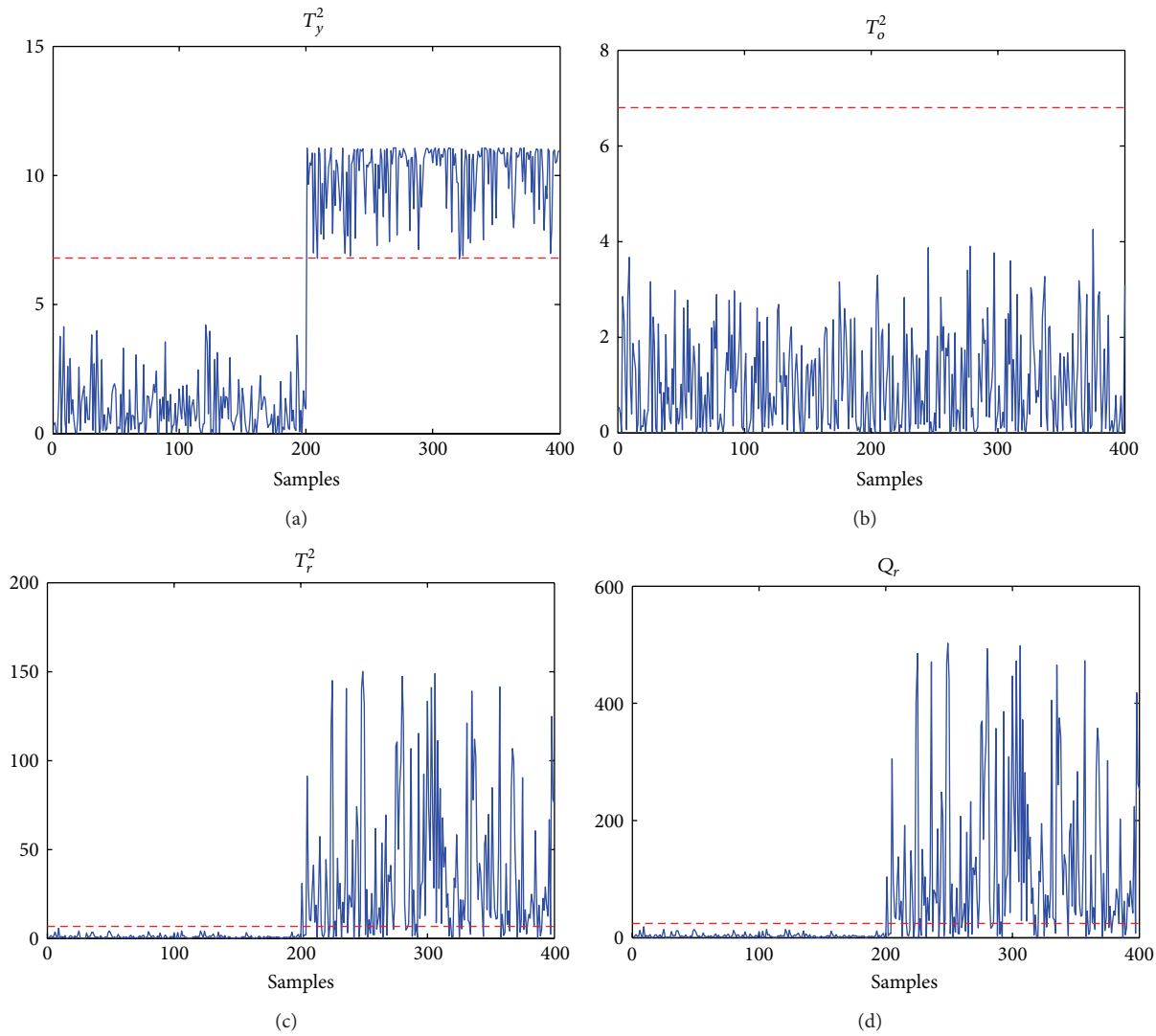

Figure 8: T-KPLS-based monitoring when quality-related Fault 3 occurs.

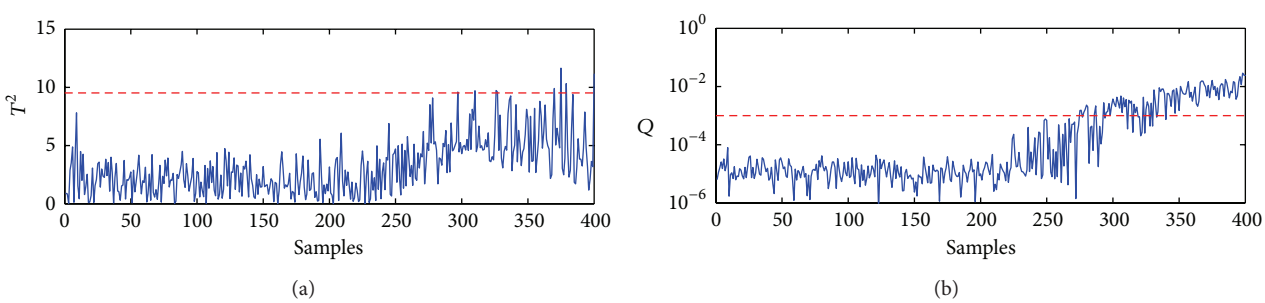

Figure 9: KPLS-based monitoring with 99% control limit when quality-related Fault 4 occurs.

Appendices

A. KPLS Algorithm

The nonlinear iterative KPLS algorithm is shown in Algorithm 3.

Based on Algorithm 3, the following equations hold:

$$\mathbf{P} = \mathbf{\Phi}^T\mathbf{T}, \qquad \mathbf{Q} = \mathbf{Y}^T\mathbf{T},$$
$$\mathbf{\Phi}_r = \left(\mathbf{I} - \mathbf{T}\mathbf{T}^T\right)\mathbf{\Phi}, \tag{A.1}$$
$$\mathbf{Y}_r = \left(\mathbf{I} - \mathbf{T}\mathbf{T}^T\right)\mathbf{Y},$$

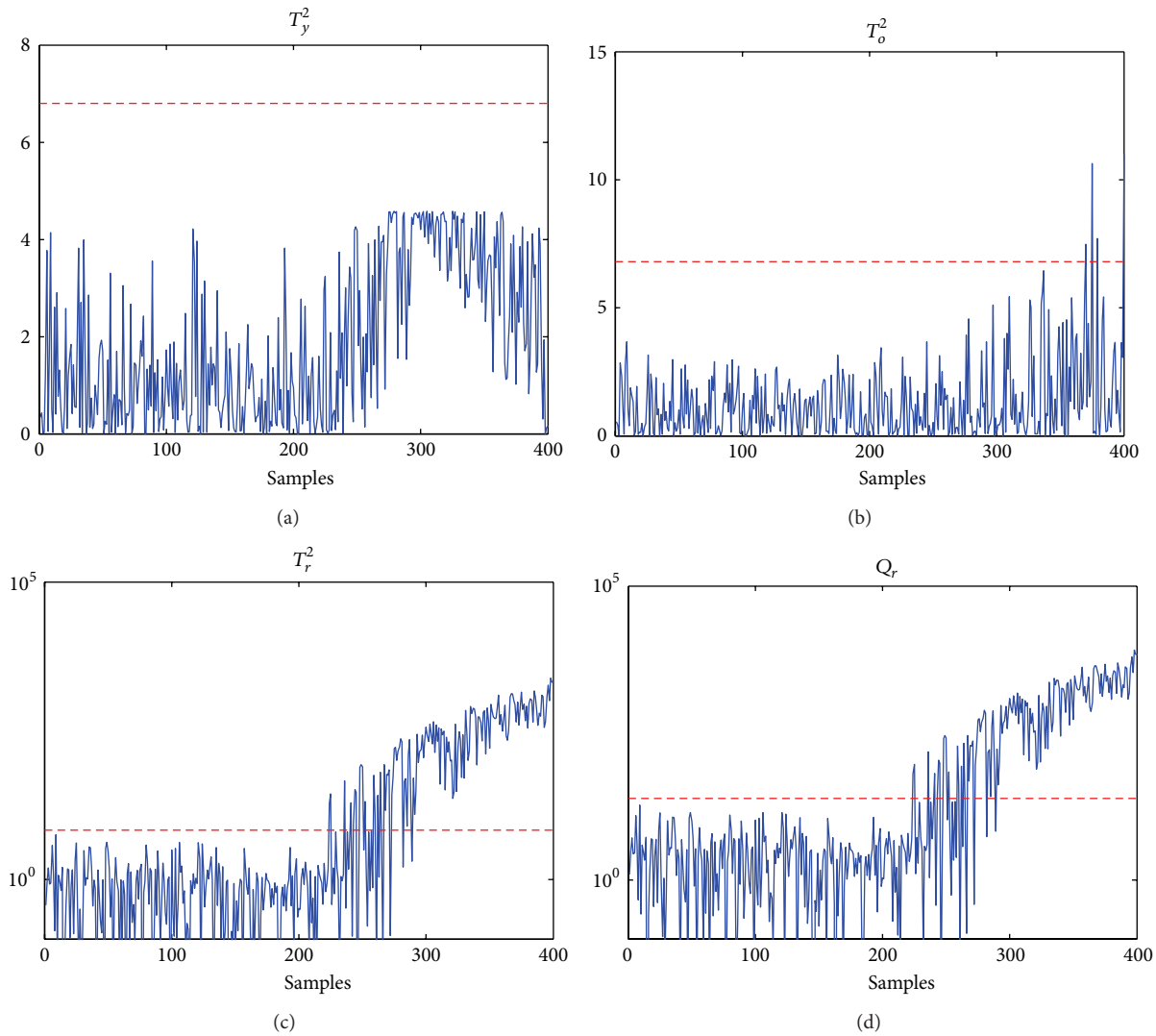

Figure 10: T-KPLS-based monitoring when quality-related Fault 4 occurs.

where $\mathbf{T} = [\mathbf{t}_1, \mathbf{t}_2, \ldots, \mathbf{t}_A] \in \Re^{n\times A}$ is the score matrix, and A is KPLS score number, obtained by cross validation [34]. $\mathbf{P} = [\mathbf{p}_1, \mathbf{p}_2, \ldots, \mathbf{p}_A] \in \Re^{m\times A}$, $\mathbf{Q} = [\mathbf{q}_1, \mathbf{q}_2, \ldots, \mathbf{q}_A] \in \Re^{p\times A}$ are the loadings matrices, and $\mathbf{\Phi}_r$, $\mathbf{Y}_r$ are the residuals matrices.

B. The Proof of $\mathbf{T} = \mathbf{\Phi R}$

First of all, setting $\mathbf{U} = [\mathbf{u_1 u_2} \cdots \mathbf{u_A}]$, $\mathbf{K_1} = \mathbf{K} = \mathbf{\Phi\Phi}^T$. According to the KPLS algorithm in Algorithm 3, the following equations hold:

$$\mathbf{t}_1 = \frac{\mathbf{K_1 u}_1}{\|\mathbf{K_1 u}_1\|} \Longrightarrow \mathbf{K_1 u}_1 = \mathbf{t}_1 \|\mathbf{K_1 u}_1\| = \mathbf{t}_1 C_{11},$$

$$\mathbf{t}_2 = \frac{\mathbf{K_2 u}_2}{\|\mathbf{K_2 u}_2\|} = \frac{\left(\mathbf{I} - \mathbf{t}_1\mathbf{t}_1^T\right)\mathbf{K_1 u}_2}{\left\|\left(\mathbf{I} - \mathbf{t}_1\mathbf{t}_1^T\right)\mathbf{K_1 u}_2\right\|}$$

$$\Longrightarrow \mathbf{K_1 u}_2 = \mathbf{t}_1\left(\mathbf{t}_1^T\mathbf{K_1 u}_2\right) + \mathbf{t}_2\left\|\left(\mathbf{I} - \mathbf{t}_1\mathbf{t}_1^T\right)\mathbf{K_1 u}_2\right\|$$

$$= \mathbf{t}_1 C_{12} + \mathbf{t}_2 C_{22},$$

$$\mathbf{t}_3 = \frac{\mathbf{K_3 u}_3}{\|\mathbf{K_3 u}_3\|} \Longrightarrow \mathbf{K_1 u}_3 = \mathbf{t}_1\left(\mathbf{t}_1^T\mathbf{K_1 u}_3\right) + \mathbf{t}_2\left(\mathbf{t}_2^T\mathbf{K_1 u}_3\right)$$

$$+ \mathbf{t}_3\left\|\left(\mathbf{I} - \mathbf{t}_1\mathbf{t}_1^T\right)\left(\mathbf{I} - \mathbf{t}_2\mathbf{t}_2^T\right)\mathbf{K_1 u}_3\right\|$$

$$= \mathbf{t}_1 C_{13} + \mathbf{t}_2 C_{23} + \mathbf{t}_3 C_{33}. \tag{B.1}$$

To sum up,

$$\mathrm{K}_1\mathbf{u}_A = \mathbf{t}_1 C_{1A} + \mathbf{t}_2 C_{2A} + \mathbf{t}_3 C_{3A} \cdots \mathbf{t}_A C_{AA}. \tag{B.2}$$

Then,

$$\mathbf{K}_1\mathbf{U} = \mathbf{TC}. \tag{B.3}$$

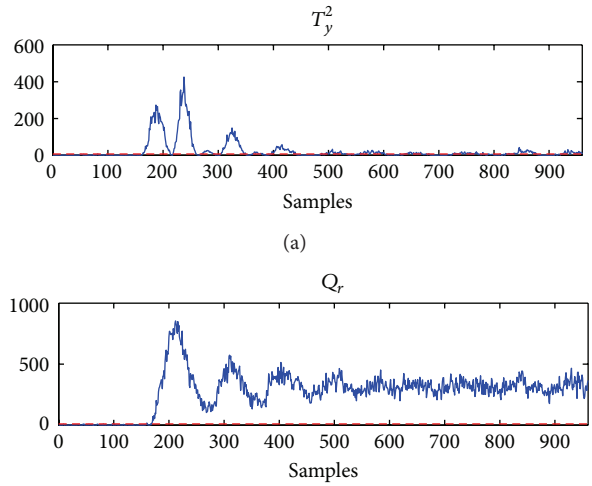

FIGURE 11: Detection of IDV (1) using T-KPLS (T_y^2 and Q_r). The dashed line represents the 99% control limit.

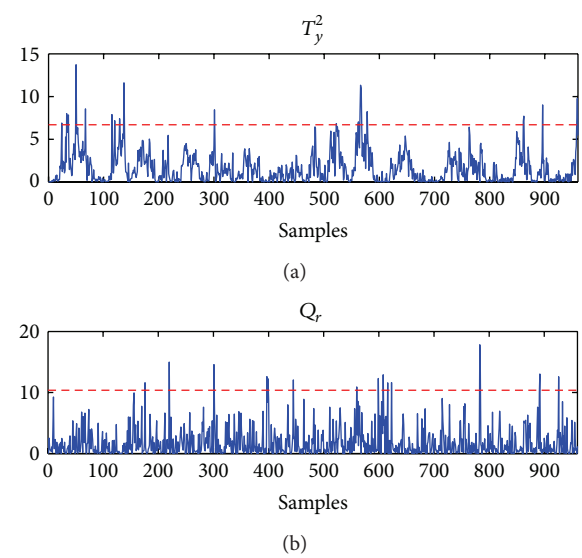

FIGURE 12: Detection of IDV (3) using T-KPLS (T_y^2 and Q_r). The dashed line represents the 99% control limit.

Here, $\mathbf{C} = \begin{bmatrix} C_{11} & C_{12} & C_{13} & \cdots & C_{1A} \\ & C_{22} & C_{23} & \cdots & \\ & & C_{33} & \cdots & \vdots \\ & & & \ddots & \\ & & & & C_{AA} \end{bmatrix}$ is a reversible upper triangle matrix. As $\mathbf{T}$ is a unit orthogonal matrix; namely, $\mathbf{T}^T\mathbf{T} = \mathbf{I}_A$, so $\mathbf{C} = \mathbf{T}^T\mathbf{K}_1\mathbf{U}$; then,

$$\mathbf{T} = \mathbf{K}_1\mathbf{U}\mathbf{C}^{-1} = \mathbf{K}_1\mathbf{U}\left(\mathbf{T}^T\mathbf{K}_1\mathbf{U}\right)^{-1} = \mathbf{\Phi}\mathbf{\Phi}^T\mathbf{U}\left(\mathbf{T}^T\mathbf{K}\mathbf{U}\right)^{-1}. \tag{B.4}$$

Thus $\mathbf{T} = \mathbf{\Phi}\mathbf{R}$ holds.

C. Calculations of Scores and Q_r

Motivated by the calculation in T-PLS model,

$$\begin{aligned}
\mathbf{t}_{y\text{new}} &= \mathbf{Q}_y^T\mathbf{Q}\mathbf{R}^T\phi\left(\mathbf{x}_{\text{new}}\right) \\
&= \mathbf{Q}_y^T\mathbf{Q}\left(\mathbf{U}^T\mathbf{K}\mathbf{T}\right)^{-1}\mathbf{U}^T\mathbf{K}_{\text{new}} = \Theta_y\mathbf{K}_{\text{new}}, \\
\mathbf{t}_{o\text{new}} &= \mathbf{P}_o^T\left(\mathbf{P}\mathbf{R}^T - \mathbf{P}_y\mathbf{Q}_y^T\mathbf{Q}\mathbf{R}^T\right)\phi\left(\mathbf{x}_{\text{new}}\right) \\
&= \mathbf{W}_o^T\mathbf{\Phi}_o\mathbf{\Phi}^T\mathbf{T}\mathbf{R}^T\phi\left(\mathbf{x}_{\text{new}}\right) \\
&\quad - \mathbf{W}_o^T\mathbf{\Phi}_o\mathbf{\Phi}^T\mathbf{T}\mathbf{T}^T\mathbf{T}_y\left(\mathbf{T}_y^T\mathbf{T}_y\right)^{-1}\mathbf{Q}_y^T\mathbf{Q}\mathbf{R}^T\phi\left(\mathbf{x}_{\text{new}}\right) \\
&= \mathbf{W}_o^T Z_y\mathbf{T}\mathbf{T}^T\mathbf{K}\mathbf{T}\left(\mathbf{U}^T\mathbf{K}\mathbf{T}\right)^{-1}\mathbf{U}^T\mathbf{K}_{\text{new}} \\
&\quad - \mathbf{W}_o^T Z_y\mathbf{T}\mathbf{T}^T\mathbf{K}\mathbf{T}\mathbf{T}^T\mathbf{T}_y\left(\mathbf{T}_y^T\mathbf{T}_y\right)^{-1} \\
&\quad \times \mathbf{Q}_y^T\mathbf{Q}\left(\mathbf{U}^T\mathbf{K}\mathbf{T}\right)^{-1}\mathbf{U}^T\mathbf{K}_{\text{new}} \\
&= \Theta_o\mathbf{K}_{\text{new}}, \\
\mathbf{t}_{r\text{new}} &= \mathbf{P}_r^T\left(\mathbf{I} - \mathbf{P}\mathbf{R}^T\right)\phi\left(\mathbf{x}_{\text{new}}\right) \\
&= \mathbf{W}_r^T\mathbf{\Phi}_r\phi\left(\mathbf{x}_{\text{new}}\right) - \mathbf{W}_r^T\mathbf{\Phi}_r\mathbf{P}\mathbf{R}^T\phi\left(\mathbf{x}_{\text{new}}\right) \\
&= \mathbf{W}_r^T\left(\mathbf{I} - \mathbf{T}\mathbf{T}^T\right)\mathbf{K}_{\text{new}} \\
&\quad - \mathbf{W}_r^T\left(\mathbf{I} - \mathbf{T}\mathbf{T}^T\right)\mathbf{K}\mathbf{T}\left(\mathbf{U}^T\mathbf{K}\mathbf{T}\right)^{-1}\mathbf{U}^T\mathbf{K}_{\text{new}} \\
&= \Theta_r\mathbf{K}_{\text{new}}.
\end{aligned} \tag{C.1}$$

The Q statistic for T-KPLS is as follows:

$$\begin{aligned}
Q_r &= \left\|\phi_{rr}\left(\mathbf{x}_{\text{new}}\right)\right\|^2 = \left\|\phi_r\left(\mathbf{x}_{\text{new}}\right) - \mathbf{P}_r\mathbf{t}_{r\text{new}}\right\|^2 \\
&= \phi_r^T\left(\mathbf{x}_{\text{new}}\right)\phi_r\left(\mathbf{x}_{\text{new}}\right) - 2\phi_r^T\left(\mathbf{x}_{\text{new}}\right)\mathbf{P}_r\mathbf{t}_{r\text{new}} \\
&\quad + \mathbf{t}_{r\text{new}}^T\mathbf{P}_r^T\mathbf{P}_r\mathbf{t}_{r\text{new}}.
\end{aligned} \tag{C.2}$$

The first part of Q_r is detailed in (8). And the second part is

$$\begin{aligned}
&\phi_r^T\left(\mathbf{x}_{\text{new}}\right)\mathbf{P}_r\mathbf{t}_{r\text{new}} \\
&\quad = \left(\phi\left(\mathbf{x}_{\text{new}}\right) - \mathbf{P}\mathbf{t}_{\text{new}}\right)^T\mathbf{\Phi}_r^T\mathbf{W}_r\mathbf{t}_{r\text{new}} \\
&\quad = \phi^T\left(\mathbf{x}_{\text{new}}\right)\mathbf{\Phi}_r^T\mathbf{W}_r\mathbf{t}_{r\text{new}} - \mathbf{t}_{\text{new}}^T\mathbf{P}^T\mathbf{\Phi}_r^T\mathbf{W}_r\mathbf{t}_{r\text{new}} \\
&\quad = \phi^T\left(\mathbf{x}_{\text{new}}\right)\mathbf{\Phi}^T\left(\mathbf{I} - \mathbf{T}\mathbf{T}^T\right)\mathbf{W}_r\mathbf{t}_{r\text{new}} \\
&\qquad - \mathbf{t}_{\text{new}}^T\mathbf{T}^T\mathbf{\Phi}\mathbf{\Phi}^T\left(\mathbf{I} - \mathbf{T}\mathbf{T}^T\right)\mathbf{W}_r\mathbf{t}_{r\text{new}} \\
&\quad = \mathbf{K}_{\text{new}}^T\left(\mathbf{I} - \mathbf{T}\mathbf{T}^T\right)\mathbf{W}_r\mathbf{t}_{r\text{new}} \\
&\qquad - \mathbf{t}_{\text{new}}^T\mathbf{T}^T\mathbf{K}\left(\mathbf{I} - \mathbf{T}\mathbf{T}^T\right)\mathbf{W}_r\mathbf{t}_{r\text{new}}.
\end{aligned} \tag{C.3}$$

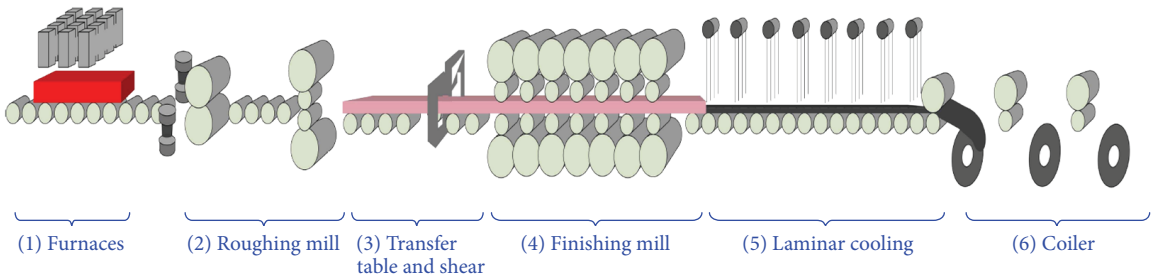

Figure 13: Schematic layout of the hot strip mill.

(1) Set $i = 1$, initialize $\mathbf{u}_i$ as the first column of $\mathbf{Y}_i$.
(2) $\mathbf{t}_i = \mathbf{\Phi}_i \mathbf{w}_i = \mathbf{K}_i \mathbf{u}_i$, where $\mathbf{w}_i = \mathbf{\Phi}_i^T \mathbf{u}_i$.
(3) Scale $\mathbf{t}_i$ to unit length, $\mathbf{t}_i = \mathbf{t}_i / \|\mathbf{t}_i\|$.
(4) $\mathbf{u}_i = \mathbf{Y}_i \mathbf{q}_i$, where $\mathbf{q}_i = \mathbf{Y}_i^T \mathbf{t}_i$.
(5) Scale $\mathbf{u}_i$ to unit length, $\mathbf{u}_i = \mathbf{u}_i / \|\mathbf{u}_i\|$.
Repeat (2)–(5) until $\mathbf{t}_i$ convergence.
(6) Deflate matrices $\mathbf{K}$, $\mathbf{Y}$ and $\mathbf{\Phi}$:

$$\mathbf{\Phi}_{i+1} = \left(\mathbf{I} - \mathbf{t}_i \mathbf{t}_i^T\right) \mathbf{\Phi}_i, \quad \mathbf{Y}_{i+1} = \left(\mathbf{I} - \mathbf{t}_i \mathbf{t}_i^T\right) \mathbf{Y}_i$$
$$\mathbf{K}_{i+1} = \left(\mathbf{I} - \mathbf{t}_i \mathbf{t}_i^T\right) \mathbf{K}_i \left(\mathbf{I} - \mathbf{t}_i \mathbf{t}_i^T\right).$$

(7) Set $i = i + 1$, loop to step (1), until $i > A$.

Algorithm 3: KPLS algorithm.

The last one is

$$\begin{aligned} &\mathbf{t}_{r\text{new}}^T \mathbf{P}_r^T \mathbf{P}_r \mathbf{t}_{r\text{new}} \\ &\quad = \mathbf{t}_{r\text{new}}^T \mathbf{W}_r^T \mathbf{\Phi}_r \mathbf{\Phi}_r^T \mathbf{W}_r \mathbf{t}_{r\text{new}} \\ &\quad = \mathbf{t}_{r\text{new}}^T \mathbf{W}_r^T \left(\mathbf{I} - \mathbf{T}\mathbf{T}^T\right) \mathbf{K} \left(\mathbf{I} - \mathbf{T}\mathbf{T}^T\right) \mathbf{W}_r \mathbf{t}_{r\text{new}}. \end{aligned} \tag{C.4}$$

By substituting $\mathbf{t}_{r\text{new}}$ with $\Theta_r \mathbf{K}_{\text{new}}$ and combining relevant parts, Q_r can be expressed as

$$Q_r = \phi^T(\mathbf{x}_{\text{new}}) \phi(\mathbf{x}_{\text{new}}) - \mathbf{K}_{\text{new}}^T \Omega_r \mathbf{K}_{\text{new}}. \tag{C.5}$$

Acknowledgements

This work was supported by national 973 projects under Grants 2010CB731800 and 2009CB32602 and by NSFC under Grants (61074084 and 61074085), China, and Beijing Key Discipline Development Program (no. XK100080537). We also appreciate the data support from Ansteel Corporation in Liaoning Province, China.

References

[1] S. J. Qin, "Statistical process monitoring: basics and beyond," *Journal of Chemometrics*, vol. 17, no. 8-9, pp. 480–502, 2003.

[2] B. M. Wise and N. B. Gallagher, "The process chemometrics approach to process monitoring and fault detection," *Journal of Process Control*, vol. 6, no. 6, pp. 329–348, 1996.

[3] J. F. MacGregor, C. Jaeckle, C. Kiparissides, and M. Koutoudi, "Process monitoring and diagnosis by multiblock PLS methods," *AIChE Journal*, vol. 40, no. 5, pp. 826–838, 1994.

[4] J. F. MacGregor and T. Kourti, "Statistical process control of multivariate processes," *Control Engineering Practice*, vol. 3, no. 3, pp. 403–414, 1995.

[5] T. Kourti, P. Nomikos, and J. F. MacGregor, "Analysis, monitoring and fault diagnosis of batch processes using multiblock and multiway PLS," *Journal of Process Control*, vol. 5, no. 4, pp. 277–284, 1995.

[6] G. Baffi, E. B. Martin, and A. J. Morris, "Non-linear projection to latent structures revisited (the neural network PLS algorithm)," *Computers and Chemical Engineering*, vol. 23, no. 9, pp. 1293–1307, 1999.

[7] S. Yin, S. Ding, A. Haghani, H. Hao, and P. Zhang, "A comparison study of basic data-driven fault diagnosis and process monitoring methods on the benchmark Tennessee Eastman process," *Journal of Process Control*, vol. 22, no. 9, pp. 1567–1581, 2012.

[8] S. Wold, N. Kettaneh-Wold, and B. Skagerberg, "Nonlinear PLS modeling," *Chemometrics and Intelligent Laboratory Systems*, vol. 7, no. 1-2, pp. 53–65, 1989.

[9] G. Baffi, E. B. Martin, and A. J. Morris, "Non-linear projection to latent structures revisited: the quadratic PLS algorithm," *Computers and Chemical Engineering*, vol. 23, no. 3, pp. 395–411, 1999.

[10] R. Rosipal and L. J. Trejo, "Kernel partial least squares regression in reproducing kernel Hillbert space," *Journal of Machine Learning Research*, vol. 2, pp. 97–123, 2001.

[11] Y. W. Zhang and Z. Y. Hu, "On-line batch process monitoring using hierarchical kernel partial least squares," *Chemical Engineering Research and Design*, vol. 89, no. 10, pp. 2078–2084, 2011.

[12] K. Kim, J. M. Lee, and I. B. Lee, "A novel multivariate regression approach based on kernel partial least squares with orthogonal signal correction," *Chemometrics and Intelligent Laboratory Systems*, vol. 79, no. 1-2, pp. 22–30, 2005.

[13] Y. W. Zhang, H. Zhou, S. J. Qin, and T. Y. Chai, "Decentralized fault diagnosis of large-scale processes using multiblock kernel partial least squares," *IEEE Transactions on Industrial Informatics*, vol. 6, no. 1, pp. 3–10, 2010.

[14] H. Zhang, Y. Shi, and M. Liu, "H1 step tracking control for networked discrete-time nonlinear systems with integral and predictive actions," *IEEE Transactions on Industrial Informatics*, vol. 9, no. 1, pp. 337–345, 2013.

[15] H. Zhang, Y. Shi, and B. Mu, "Optimal H1-based linear-quadratic regulator tracking control for discrete-time Takagi-Sugeno fuzzy systems with preview actions," *ASME Transactions, Journal of Dynamic Systems, Measurement, and Control*, vol. 135, Article ID 044501, 5 pages, 2013.

[16] G. Li, S. J. Qin, and D. H. Zhou, "Geometric properties of partial least squares for process monitoring," *Automatica*, vol. 46, no. 1, pp. 204–210, 2010.

[17] G. Li, S. J. Qin, and D. H. Zhou, "Output relevant fault reconstruction and fault subspace extraction in total projection to latent structures models," *Industrial and Engineering Chemistry Research*, vol. 49, no. 19, pp. 9175–9183, 2010.

[18] S. W. Choi and I. B. Lee, "Multiblock PLS-based localized process diagnosis," *Journal of Process Control*, vol. 15, no. 3, pp. 295–306, 2005.

[19] D. H. Zhou, G. Li, and S. J. Qin, "Total projection to latent structures for process monitoring," *AIChE Journal*, vol. 56, pp. 168–178, 2010.

[20] G. Li, C. F. Alcala, S. J. Qin, and D. Zhou, "Generalized reconstruction-based contributions for output-relevant fault diagnosis with application to the Tennessee Eastman process," *IEEE Transactions on Control Systems Technology*, vol. 19, no. 5, pp. 1114–1127, 2011.

[21] G. Li, S. J. Qin, Y. D. Ji, and D. H. Zhou, "Total PLS based contribution plots for fault diagnosis," *Acta Automatica Sinica*, vol. 35, no. 6, pp. 759–765, 2009.

[22] J. Yu and S. J. Qin, "Multimode process monitoring with bayesian inference-based finite Gaussian mixture models," *AIChE Journal*, vol. 54, no. 7, pp. 1811–1829, 2008.

[23] J. Yu, "Localized Fisher discriminant analysis based complex chemical process monitoring," *AIChE Journal*, vol. 57, no. 7, pp. 1817–1828, 2011.

[24] J. Yu, "A nonlinear kernel Gaussian mixture model based inferential monitoring approach for fault detection and diagnosis of chemical processes," *Chemical Engineering Science*, vol. 68, no. 1, pp. 506–519, 2012.

[25] H. Zhang, Y. Shi, and A. Saadat Mehr, "On H_∞ filtering for discrete-time takagi-sugeno fuzzy systems," *IEEE Transactions on Fuzzy Systems*, vol. 20, no. 2, pp. 396–401, 2012.

[26] E. L. Russell, L. H. Chiang, and R. D. Braatz, "Fault detection in industrial processes using canonical variate analysis and dynamic principal component analysis," *Chemometrics and Intelligent Laboratory Systems*, vol. 51, no. 1, pp. 81–93, 2000.

[27] H. J. Cho, J. Lee, S. W. Choi, D. Lee, and I. Lee, "Fault identification for process monitoring using kernel principal component analysis," *Chemical Engineering Science*, vol. 60, no. 1, pp. 279–288, 2005.

[28] S. Mika, B. Schölkopf, A. Smola, and K. R. Müller, "Kernel PCA and de-noising in feature spaces," *Advances in Neural Information Processing Systems*, vol. 11, pp. 536–542, 1999.

[29] R. D. Jia, Z. Z. Mao, Y. Q. Chang, and S. N. Zhang, "Kernel partial robust M-regression as a flexible robust nonlinear modeling technique," *Chemometrics and Intelligent Laboratory Systems*, vol. 100, no. 2, pp. 91–98, 2010.

[30] G. Lee, C. H. Han, and E. S. Yoon, "Multiple-fault diagnosis of the Tennessee Eastman process based on system decomposition and dynamic PLS," *Industrial and Engineering Chemistry Research*, vol. 43, no. 25, pp. 8037–8048, 2004.

[31] L. H. Chiang, E. L. Russell, and R. D. Braatz, "Fault diagnosis in chemical processes using Fisher discriminant analysis, discriminant partial least squares, and principal component analysis," *Chemometrics and Intelligent Laboratory Systems*, vol. 50, no. 2, pp. 243–252, 2000.

[32] M. Kano, S. J. Hasebe, I. Hashimoto, and H. Ohno, "A new multivariate statistical process monitoring method using principal component analysis," *Computers and Chemical Engineering*, vol. 25, no. 7-8, pp. 1103–1113, 2001.

[33] J. M. Lee, C. K. Yoo, and I. B. Lee, "Statistical monitoring of dynamic processes based on dynamic independent component analysis," *Chemical Engineering Science*, vol. 59, no. 14, pp. 2995–3006, 2004.

[34] S. Wold, "Cross-validatory estimation of the number of components In factor and principal components models," *Technometrics*, vol. 20, pp. 397–405, 1975.

Hindawi Publishing Corporation
Mathematical Problems in Engineering
Volume 2013, Article ID 952106, 10 pages
http://dx.doi.org/10.1155/2013/952106

Research Article

A Driver Modeling Based on the Preview-Follower Theory and the Jerky Dynamics

Jianyong Cao,[1,2] Hui Lu,[1] Konghui Guo,[1] and Jianwen Zhang[2]

[1] *School of Mechanical Engineering, Shanghai Jiaotong University, Shanghai 200240, China*
[2] *Shanghai Motor Vehicle Inspection Center, Shanghai 201805, China*

Correspondence should be addressed to Konghui Guo; guokonghui@gmail.com

Received 14 September 2013; Revised 15 November 2013; Accepted 17 November 2013

Academic Editor: Hui Zhang

Based on the preview optimal simple artificial neural network driver model (POSANN), a new driver model, considering jerky dynamics and the tracing error between the real track and the planned path, is established. In this paper, the modeling for the driver-vehicle system is firstly described, and the relationship between weighting coefficients of driver model and system parameters is examined through test data. Secondly, the corresponding road test results are presented in order to verify the vehicle model and obtain the information on drive model and vehicle parameters. Finally, the simulations are carried out via CarSim. Simulation results indicate that the jerky dynamics need to be considered and the proposed new driver model can achieve a better path-following performance compared with the POSANN driver model.

1. Introduction

Although the chassis control systems of a vehicle can improve vehicle dynamics performances, enhance active safety, and reduce driver load, they bring more challenges for the evaluation of vehicle performance, especially for the evaluation of handling and stability in terms of subjective sense [1, 2]. Previous studies [3, 4] reveal that the driver-vehicle-road closed-loop system works effectively when investigating the performances of vehicle handling and stability. In order to evaluate the handling quality of a vehicle and avoid potential risk in actual tests, the study on driver modeling is essential. This research field has drawn significant attention and several typical models have been carried out by many researchers in an early time. In 1953, Kondo [5] started with driver modeling in Japan. His research is based on the 2-wheel vehicle model on a straight line, running at a constant speed with side wind disturbances. In addition, McRuer and Jex [6] extended pilot models to road driver models by considering the factors of reaction time and inertial delay and a compensation driver model was presented. However, the preview characteristics of the driver were not taken into consideration in the studies. Macadam [7] established a driver model by using optimal preview closed-loop control in 1980. Moreover, the Preview-Follower theory [8] was proposed for the purpose of modeling the driver's path-following behaviors. The driver's behaviors were assumed based on the path-following theory in which the driver's operation always aims at minimizing the errors between the desired and actual vehicle trajectory [9]. With the development of intelligence technology, several artificial neural network driver models were proposed in order to accurately imitate human driving behaviors. For instance, Fujioka et al. [10] presented a NN driver model, in which the steering angle was mapped as a function of lateral deviation and heading angle. The model was trained by a human driver in a simulator environment. Neusser et al. [11] also proposed a neurocontroller for lateral vehicle guidance. This driver model was trained with measured human-driving data. In addition, Macadam and Johnson [12] constructed a two-layer neural network to represent driver steering behaviors. Sampled data collected by the sensors of an on-road car was employed to train the network. Guo et al. [13] proposed a preview optimal artificial neural network (ANN) driver model, whose training sample was

the ideal following path instead of experimental data. The global optimization of the closed-loop system was carried out in the training process of the network through the Genetic Algorithm. Further research showed that the weight factors of this artificial neural network could be calculated analytically through the Error Elimination Algorithm [14]. For the sake of simulating driver behaviors under some severe or critical scenarios, Edelmann et al. [15] presented a driver model for higher lateral accelerations. The driver model was able to perform a good tracking behavior even at higher lateral accelerations. Tracking accuracy was further enhanced by incorporating information on the change of curvature and the local curvature of vehicle motion in the prediction of anticipated vehicle positions. The above-mentioned models were established based on the driver's visual sensory inputs; kinesthetic (steering torque) or vestibular (lateral acceleration, yaw rate, and slip angle) sensory was not taken into account. Recently, some driver models were proposed in [16–18]; those models integrate both anticipatory and compensatory visual strategies and take into account both visual perception and kinesthetic perception. Little amount of the literature gives information on how vestibular information is used.

Many driver models have been established based on many kinds of modern control theories and methods. Unlike acceleration, velocity, and displacement of vehicle, the time derivative of acceleration (TDoA) of vehicle motion, which is used to show the vestibular information, has not been extensively studied in those studies. The TDoA, also referred to in the literature as jerk, is one of the parameters considered in vibration control [19] and comfort evaluation [20, 21]. It is a physical property that is felt by humans when a sudden change of motion occurs. Consequently, it is closely monitored for discomfort caused to a passenger in a vehicle. As a sudden change of motion occurs, the vehicle might drop into the boundary area of stability, and the tire forces are prone to sudden change. The driver response can be made according to the steering torque feedback and the jerk dynamics on the vehicle response to lateral force change. Thus, the optimal preview control driver model cannot achieve accurate vehicle performance, especially when the tires are in the sudden change conditions.

Hence, it is essential to consider the TDoA of vehicle motion in the preview-follower driver model. Based on the preview-follower driver modeling approach and ANN, a modified driver model considering the jerky dynamics is investigated. The drivers' behaviors are described with the parameters of preview and jerk characteristic. The steering angle is obtained according to the error between the real track and the planned path and modified by the jerky dynamics under lateral force mutation. This paper is organized as follows. A modified driver model is presented in Section 1. Internal vehicle model is built and simplified in Section 2. The parameters of driver and vehicle characteristics are analyzed and calculated according to the driving conditions in Section 3, where road tests are used to verify vehicle model and calculate the closed-loop system parameters. Numerical simulations are employed to verify the proposed driver model in Section 4. Conclusions are given in Section 7.

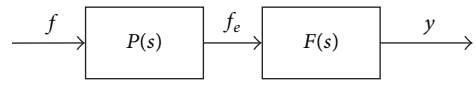

Figure 1: The diagram of preview-follower's structure.

2. Modeling of Driver-Vehicle System

Many driver models have been established to simulate the characteristics of driving behaviors on the desired trajectory. On the basis of the previous researches, the paper explores the driver model based on the combination of the preview-follower theory and the jerky dynamics.

2.1. Preview-Follower Theory. Preview-Follower theory describes the following properties in accordance with the future input information. The theory can be demonstrated generally with the following points.

(1) Since the drivers operation is a low frequency process under usual driving, the transfer function of the closed-loop system should always be 1 at low frequency range. That is, $P(s) \cdot F(s) \approx 1$. The theory is realized by a cascade system, which is composed of a preview and a follower. $P(s)$ and $F(s)$ denote the preview and follower transfer functions, respectively.

(2) Figure 1 shows the diagram of the preview-follower's structure, where y denotes the vehicle's actual lateral position and f and f_e denote the vehicle lateral position on the absolute and vehicle coordinate system, respectively [8].

2.2. Preview Optimal Simple Artificial Neural Network Driver Model. Generally, the behaviors of a qualified and excellent driver fit with the Preview-Follower theory. According to this knowledge, the preview optimal simple artificial neural network (POSANN) driver model is built in Figure 2.

In the preview module $P(s)$, the driver can acquire the effective road information f_e from target course f through preview process, whose transfer function is $e^{t_p s}$, in which t_p indicates the driver preview time for path following. The input f represents the function of the lateral displacement of the target course, and the output f_e indicates the lateral displacement of the target course at look-ahead point.

In the follower module $F(s)$, the driver uses the motion information of the vehicle to decide on the optimal steering wheel angle δ. However, since there are response delays of both human and vehicle, the real steering wheel angle of vehicle should be δ_{sw}. $w_1 \sim w_4$ are the ANN weight coefficients of f_e, lateral displacement y, lateral speed $\dot{y}$, and lateral acceleration $\ddot{y}$, respectively. Here, human factors are taken into account, which are expressed by the reaction delay of the driver with the transfer function $e^{-t_d s}$. In this transfer function, t_d is the lag of the driver's neural reaction system. $1/(1 + t_h s)$ reflects the inertial delay of the steering system.

2.3. A Modified ANN Driver Model with Jerky Dynamics. An unequivocal definition of the jerk as "the derivative of

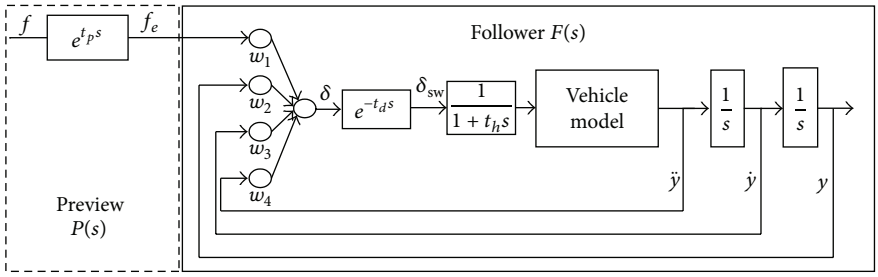

Figure 2: Preview optimal simple artificial neural network (POSANN) driver model.

acceleration with respect to time" was given by Melchior who justifies the use of the term by referring to the physiological sensation experienced by large changes in acceleration [22]. Jerk has been used by many researchers to quantify aggressive driving behavior [23]. Based on Newton's second law

$$F = ma, \tag{1}$$

both sides of (1) with respect to time are differentiated; it can be seen that

$$\frac{dF}{dt} = mj = m\left(\frac{\Delta a}{\Delta t}\right). \tag{2}$$

Thus, if the net external force is not constant, a system of constant mass will move with a jerk. That jerk is directly proportional to the time rate of change of the force and inversely proportional to the mass. Hence, the driver's sense of discomfort may rise rapidly whenever there is the unpredictable lateral acceleration. Considering the motion parallel to the y-axis, let j, a_y, v_y, and y be the y-components of the jerk, acceleration, velocity, and position, respectively. According to the expression,

$$j = \frac{a_2 - a_1}{t_2 - t_1} = \frac{\Delta a}{\Delta t} \ \left(\text{constant jerk}\right). \tag{3}$$

Equation (3) was rewritten, letting $a_1 = a_{y0}$ (the acceleration at $t = 0$, so $t_1 = 0$) and $a_2 = a_y$ (the acceleration at a time t, so $t_2 = t$). The average jerk equals the instantaneous jerk when the jerk is constant. So, (3) becomes

$$j = \frac{a_y - a_{y0}}{t - 0} \ \left(\text{constant jerk}\right), \tag{4}$$

so that

$$a_y = a_{y0} + jt \ \left(\text{constant jerk}\right). \tag{5}$$

The similarities between (5) and (6) are obvious

$$v_y = v_{y0} + a_y t \ \left(\text{constant acceleration}\right). \tag{6}$$

Consider the method(s) it uses to obtain

$$y = y_0 + v_y t + \frac{1}{2}a_y t^2 \ \left(\text{constant acceleration}\right). \tag{7}$$

It can use the same methods (integration, area under a curve, or whatever) to derive

$$v_y = v_{y0} + a_y t + \frac{1}{2}jt^2 \ \left(\text{constant jerk}\right). \tag{8}$$

It can be seen that it can move from a constant acceleration relationship to a constant jerk equation by replacing y by v_y, v_y by a_y, and a_y by j. With calculus and $v_y = dy/dt$, it is easy to obtain

$$y = y_0 + v_y t + \frac{1}{2}a_y t^2 + \frac{1}{6}jt^3 \ \left(\text{constant jerk}\right). \tag{9}$$

For the lateral motion of the vehicle, (9) was rewritten, letting $y = y(t + T)$ (the new position of vehicle, T is a period of look-ahead time), $y_0 = y(t)$ (the current lateral position of vehicle), $v_y = y'(t)$ (the current lateral speed of vehicle), $a_y = y''(t)$ (the current lateral acceleration of vehicle), and $j = y'''(t)$ (the jerk motion of the vehicle). Equation (9) becomes

$$y(t+T) = y(t) + Ty'(t) + \frac{T^2}{2}y''(t) + \frac{T^3}{6}y'''(t). \tag{10}$$

So, it is feasible to eliminate the error of trajectory caused by the variations of driving condition through compensation control of jerk characteristic between acceleration of present moment and previous moment. Based on the preview-follower driver modeling approach and ANN, this paper establishes the preview-compensation ANN (PCANN) driver model, which is shown in Figure 3. In this figure, $P(s)$, $F(s)$, and $C(s)$ are the transfer functions of the preview, follower, and jerk character, respectively.

The compensator $C(s)$ is introduced in order to simulate driver behaviors under lateral force disturbances. $C(s)$ contains compensation gain and internal model. It is noted that $C(s)$ will not be necessary unless there is transient and unpredictable vehicle motion. The relationship between the steering wheel change and the lateral acceleration change can be expressed as follows:

$$\Delta\delta = K\Delta\alpha = K\left(a_{yi} - a_{ym}\right). \tag{11}$$

In Figure 3, $\Delta\delta$ is the change of steering wheel. $\overline{\delta}_{sw}$ is the steering wheel angle. a_{yi} is the lateral acceleration of the previous moment. a_{ym} is the lateral acceleration $\ddot{y}$ of the present moment, which is the real response of vehicle under

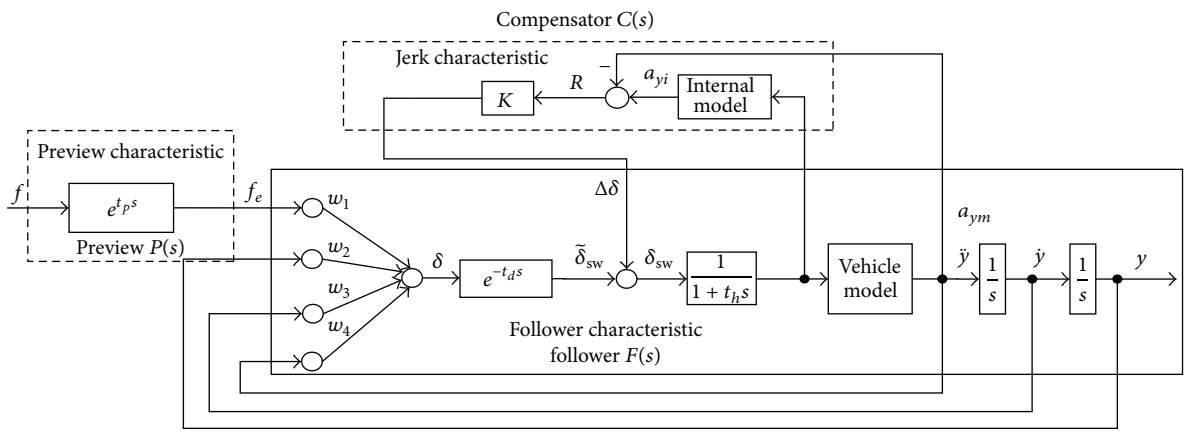

Figure 3: Block diagram of preview-compensation ANN driver model.

various operating conditions. $\Delta\alpha$ is the lateral acceleration change. K is the compensation gain. The internal model is the driver's recognition and understanding of the vehicle, which can be obtained through vehicle model linearization under the steady-state condition of the previous moment. It means that internal model can produce the same outputs for the same inputs with vehicle under the steady-state condition. To be specific, a_{yi} and a_{ym} cancel out each other, $\Delta\alpha = 0$ leads to $\Delta\delta = 0$ under the steady-state condition. In this case, it is unnecessary for the driver to compensate control since the vehicle is at lateral steady-state. When there are variations of the driving condition or the vehicle dynamic characteristics, the performances of vehicle and internal model cannot stay the same, indicating that the internal model cannot produce the same outputs for the same inputs with vehicle under lateral force disturbances. In this condition, a_{yi} is different from a_{ym}, $\Delta\alpha \neq 0$, and $\Delta\delta \neq 0$. The driver may have a feeling of discomfort and then $C(s)$ will be activated to make the necessary corrections for the steering wheel. The corrected steering wheel angle δ_{sw} is defined as follows:

$$\delta_{sw} = \overline{\delta}_{sw} + \Delta\delta. \tag{12}$$

If there are more differences between a_{yi} and a_{ym} that the driver can feel, more corrections of the steering wheel angle will be made.

3. Internal Vehicle Model

Research in the field of neuroscience has been undertaken in recent decades with the goal of understanding how humans plan and carry out physical motion tasks through the use of the central nervous system (CNS) and the neuromuscular system (NMS). Research in this area of neuroscience has increasingly pointed to the conclusion that the human CNS learns and stores multiple sets of "internal models" for use when interacting with the external world [24]. The internal model paradigm postulates that the CNS generates and stores models that represent the dynamics of the physical systems of interest to the CNS, allowing the CNS to then recall and use these models to predict the behavior of the dynamic system in question. Hence, the driver can predict the vehicle motion within the preview horizon and compensate the transient vehicle motion based on internal models according to vehicle state. The driver models were used in a linear 2-wheel vehicle model and rarely in the complex vehicle model. Keen proposed the derivation of a nonlinear driver steering controller using multiple linearized models of the vehicle dynamics and Model Predictive Control (MPC) theory [25]. In order to simulate the vehicle more accurately, the vehicle model is built up in CarSim. However, it is difficult to calculate the parameters of the driver model with the complex vehicle model directly. Therefore, the kinematic equations of a linear 2-wheel vehicle model are employed as a driver's internal vehicle model, by which the parameters of the driver model can be calculated. The corresponding transfer function of the internal vehicle can be represented as follows:

$$\begin{aligned} V(s) = \frac{\ddot{y}}{\delta_{sw}}(s) &= G_{ay}\frac{1 + T_{y1}s + T_{y2}s^2 + \cdots}{1 + T_1 s + T_2 s^2 + \cdots} \\ &\approx G_{ay}\frac{1}{1 + T_{q1}s + T_{q2}s^2}, \end{aligned} \tag{13}$$

where $V(s)$ is the transfer function from the vehicle lateral acceleration to steering wheel angle, G_{ay} is the vehicle lateral acceleration gain to steering wheel angle, T_1, T_2, T_{y1}, and T_{y2} are the parameters which present the vehicle's dynamic response property, and T_{q1} and T_{q2} can be calculated using T_1, T_2, T_{y1}, and T_{y2}, respectively.

Different vehicles lead to different second order systems. Based on step test data, the parameters (T_1, T_2, T_{y1}, and T_{y2}) of the second order system were identified by LSM (Least-Square Method) in this paper.

4. Parameters of Closed-Loop System

In this section, the parameters of closed-loop system are calculated with regard to the test data and road condition. Those parameters represent common behaviors of the driver and vehicle, including the preview time t_p, neural reaction time t_d, and inertial delay t_h of steering system. In a real world

application, most of those parameters are uncertain factors. The $H\infty$ control and robust control have been also paid considerable attention to eliminate the impact of uncertainty [26–28], According to some particular parameters values, we can obtain the weighting parameters of the driver model by the Error Elimination Algorithm. The meaning and features of each parameter will be described in detail in the following part.

4.1. Preview Time t_p. Preview time t_p can be considered mathematically as a negative delay time, which can compensate the delay characteristics of the driver and vehicle, and is one of the key parameters to express the characters of drivers. It relates not only to the driver's characteristic but also to the driving condition. The computational method of preview time was not given in the optimal preview control driver model under complicated operation conditions [29]. The preview time is set by a time constant, and the range of values selected for the general driver model is 0.5 to 2.0 s. The fixed preview time driver models have a good tracking reference trajectory when the speed of the vehicle is low and lateral motion is not in the nonlinear area. Under high speed, complex trajectory, and bounded constraint conditions, it is difficult to complete the driving tasks for the fixed preview time driver models. When the vehicle runs from a small curvature path into a big curvature path or the vehicle speed becomes faster, the driver may reduce the preview time instinctively. Hence, t_p is related to the curvature and vehicle speed. In the big curvature path and high speed, t_p is small, and vice versa. Define that the curvature of the follow path $y = f(x)$ is ρ and the speed is v_x. The preview time can be expressed as $t_p = f(v_x, \rho)$. The calculation schematic diagram of preview time is shown in Figure 4. In Figure 4, OXY and $O'X'Y'$ are the global coordinate system and vehicle coordinate system, respectively. The trajectory $y = f(x)$ in OXY can be transformed into $y' = g(x')$ in $O'X'Y'$. Whether the vehicle is safe within the range of preview or deviates from the planned trajectories is an important criterion for a driver after preview time t_p. The offset τ between the vehicle driving prediction route and the center of the path can be determined by the driver's characteristic, which is acceptance of course error for a driver. We can define the point of the maximum offset in the range of vision as the preview point of driver. When the offset reaches maximum value, which is constant for one driver, the driver will operate the steering wheel to reduce the offset and make vehicle run into a safe area. The preview distance L is defined from driver position to preview point. In Figure 4, $x_0' = \tau$ and $y_0' = L$. Since the radius of the desired path $R = 1/\rho$ is much larger than that of τ, $AB \approx R + \tau$. Because ABO' is a right-angled triangle, we can obtain that

$$\begin{aligned}\left(t_p * v_x\right)^2 &= L^2 = AB^2 - AO'^2 \\ &= (R+\tau)^2 - R^2 = 2 * R * \tau + \tau^2.\end{aligned} \tag{14}$$

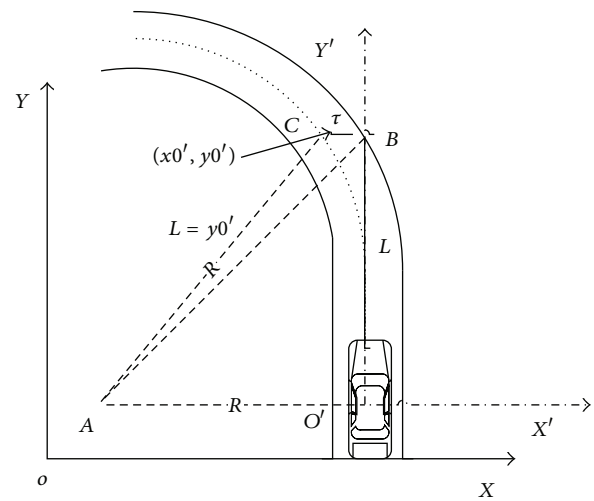

Figure 4: The calculation of preview time.

According to the previous equation, the preview time can be expressed as

$$t_p = \frac{\sqrt{2\tau/\rho + \tau^2}}{v_x}. \tag{15}$$

Through the above analysis, it has been seen that τ has an influence on the key parameter t_p. The value of τ can be measured through the road test as shown in Figure 4. t_p can be estimated based on (15).

4.2. Reaction Time t_d. The time gap between receiving information and operating the steering wheel is defined as the reaction time t_d, which reflects the response capacity and affects safe driving. The simple reaction time T is defined as the reaction time t_d without considering the driving conditions and complex driving behavior. T is a psychological, physical index and an innate character of humans, which is related to personal experience, proficiency, character, age, gender, and so on. The reaction time t_d may be influenced by the environment and driving conditions. Both road curvature and vehicle speed are the key factors of vehicle handling stability throughout the turn. Generally, the driver may be sensitive to large curvature and high speed, which will lead to the tension of the driver. For example, when the vehicle enters the corner, the curvature begins to increase and t_d will decrease, but on the contrary the curvature starts to decrease and t_d will increase. The same principles can be applied to vehicle speed; for instance, the reaction time decreases when vehicle accelerates. Curvature and speed affect the change of reaction time together. In brief, the relationship between t_d, curvature, and speed is a decreasing function [9], as follows:

$$t_d = T\left(ae^{1/v_x} + be^{-\rho}\right), \tag{16}$$

where ρ is curvature and a, b are the weight coefficients of curvature and speed, respectively. When one factor, curvature or speed, becomes the main status, its corresponding

coefficient is large which exercises an important influence on the reaction time. Meanwhile, the driver is sensitive to lateral acceleration while turning usually takes one lateral acceleration α_y as threshold value of discomfort feeling. There is a certain functional relation between curvature and speed, and the function is $\alpha_y \approx v_x^2/R$. If α_y is determined by the drivers' feeling, high speed directly corresponds to small curvature and t_d is mainly affected by speed, and vice versa. So the weight coefficients can be obtained as follows:

$$\frac{v_x^2}{R} \approx \frac{a}{b}, \qquad a + b = 1. \tag{17}$$

4.3. Inertial Delay t_h. This paper proposes the cross-correlation method to calculate the inertial delay t_h which is an important parameter between steering wheel and vehicle response. Generally, for single-input-single-output system, the signals of input and output are utilized to find out the largest cross-correlation and consequently calculate the time delay between input and output. In this paper, the cross-correlation R_{xy} between the steering wheel angle $x(t)$ and yaw rate $y(t + t_h)$ is achieved to calculate the inertial delay t_h, as shown in (18). The values of $x(t)$ and $y(t+t_h)$ are measured by the road tests, as shown in Figure 5. Consider the following:

$$R_{xy} = E\left[x(t)\, y(t + t_h)\right]. \tag{18}$$

In (19), the cross-correlation coefficient can be expressed as a function of t_h as follows:

$$\rho_{xy}(t_h) = \frac{R_{xy} - \mu_x \mu_y}{\sigma_x \sigma_y}, \tag{19}$$

where μ_x, μ_y are the arithmetic means of $x(t)$ and $y(t + t_h)$, respectively. σ_x, σ_y are the variances of $x(t)$ and $y(t + t_h)$, respectively. The curve of $\rho_{xy}(t_h)$ is shown in Figure 6. When $\rho_{xy}(t_h)$ reaches its largest value, t_h is equal to the steering system delay time t_h^*, as follows:

$$t_h^* = \left\{t_h \max\left(\rho_{xy}(t_h)\right), 0 < t_h < 2.0\right\}. \tag{20}$$

4.4. Weight Parameters of Driver Model. The closed-loop system should be an ideal low-frequency following system, which can meet the requirement as follows:

$$P(S) \cdot F(S) \approx 1. \tag{21}$$

That is to say, $F(s)^{-1}$, the inverse function of the follower, should be an approximation of $P(s)$.

The Taylor series expansions of $F(s)^{-1}$ and $P(s)$ are presented as follows:

$$F(s)^{-1} = F_0 + F_1 s + F_2 s^2 + F_3 s^3 + \cdots, \qquad P(s) = P_0 + P_1 s + P_2 s^2 + P_3 s^3 + \cdots. \tag{22}$$

If $F_i = P_i$ $(i = 0, 1, \ldots, n)$, $F(s)$ can be called "follower," which is compensated by the $C(s)$. Moreover, vehicle's motion

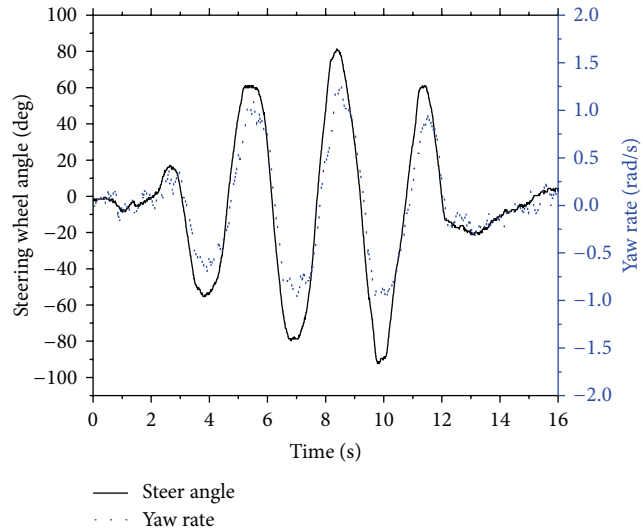

Figure 5: The relationship between steering wheel angle and yaw rate.

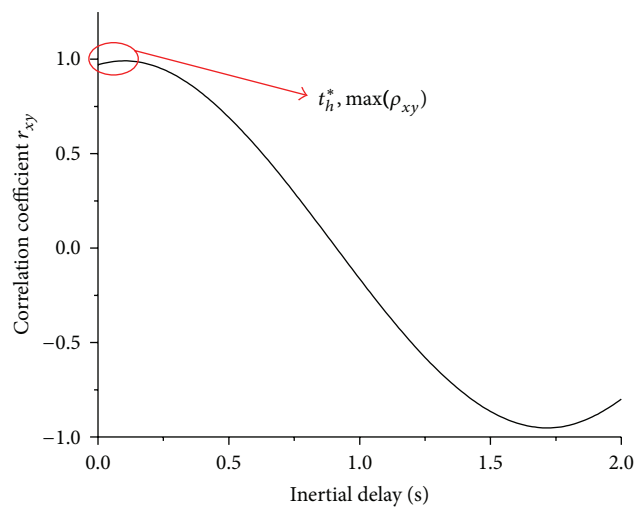

Figure 6: The relationship between the inertial delay and cross-correlation coefficient.

is a low-pass filter [13], so the high-frequency signals can be ignored, which leads to an ideal following system. By using the Error Elimination Analysis method, the weight parameters of the closed-loop system are obtained based on the driver's basic parameters and vehicle parameters. The weight parameters can be calculated as follows:

$$w_1 = 1, \qquad w_2 = -w_1, \qquad w_3 = -t_p, \qquad w_4 = k_0 - \frac{t_p^2}{2},$$

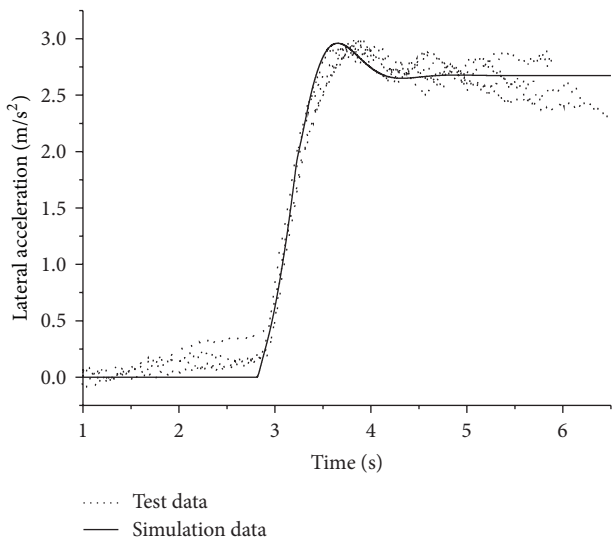

Figure 7: Result comparison for step input test.

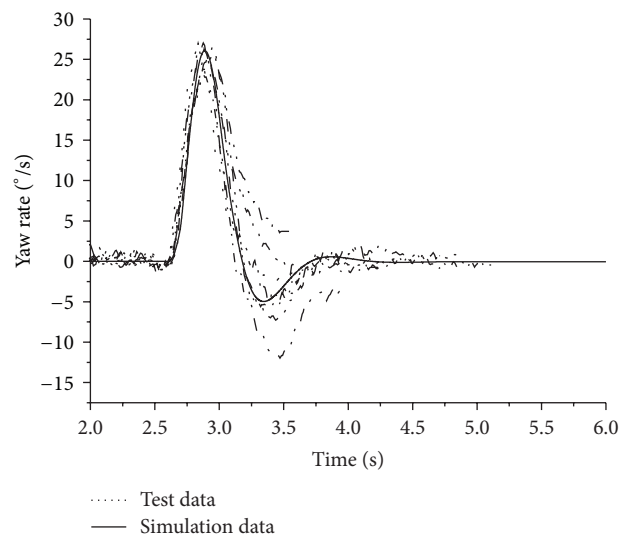

Figure 8: Result comparison for pulse input test.

$$K = \frac{t_p^3}{6} - k_0\left(T_{q1} + t_h + t_d\right),$$
$$k_0 = \frac{\left(t_p^4/24\right) - \left(t_d t_p^3/6\right)}{T_{q2} + t_h T_{q1} - t_d^2}. \tag{23}$$

5. Test Identification and Model Verification

In order to obtain the model parameters, a lot of experiments have been carried out using a small car as test vehicle. Furthermore, the vehicle model will be verified to ensure the effectiveness of vehicle model in simulations.

5.1. Vehicle Model Verification. The simulations are carried out in CarSim, in which complex vehicle model can be built up to operate in nonlinear region. The vehicle model is verified by comparing the simulations and test results. Two typical tests including step input and pulse input of steering wheel angle are presented and shown in Figures 7 and 8, respectively. From the figures it can be seen that the simulation results fit the test results well, indicating that the vehicle model can be used in simulation with sufficient accuracy.

5.2. Calculation of Model Parameters

(1) The Offset τ. Based on Section 4.1, the road tests are carried out to calculate the offset τ. Typical driver A is selected for road tests. Driver A is skilled and professional with high driving proficiency. In the tests, the initial positions of the steering wheel change and speed had been recorded when the driver saw the first bend and intended to enter the bend. The offset τ was calculated and the average of results is 0.843 m.

(2) Simple Reaction Time T. In order to get actual simple reaction time T of drivers, the tests are carried out in a proving ground, in which the environmental distraction can be eliminated. The test method is to record the procedure of simple stimuli-human reaction-execution behavior using a high-speed digital camera. The test system is composed of a test car, a camera, a signal lamp, and a data collector, as shown in Figure 9. The camera is Redlake Y3 high-speed digital camera, which can provide very high sample frequency up to 2000 fps. Eight men and one woman are selected to complete this test. During the test, each subject sits in the stationary vehicle and observes the signal light. Once the signal lamp is lighted, the subject should turn the steering wheel immediately. Meanwhile, the camera records the whole process of the steering wheel operation. The time difference from the time when the signal lamp is lighted to the time when the subject starts to turn the steering wheel is the simple reaction time T. Each subject should complete the test 10 times, and the average value of these data is taken as the final result. All test results are presented in Table 1.

Figure 9: Test system for simple reaction time T.

(3) Inertial Delay t_h. According to Figure 5, (19), and (20), the delay time of the steering system is determined by the maximum value of ρ_{xy}. When the value of the correlation

Table 1: Simple reaction time T of nine subjects (unit: ms).

Test number	Subjects								
	1	2	3	4	5	6	7	8	9
1	257	439	279	247	280	450	408	267	244
2	256	466	271	255	271	269	—	245	237
3	—	293	249	242	265	239	284	225	293
4	263	257	242	260	263	258	381	219	332
5	273	281	253	279	338	240	341	211	268
6	314	266	295	276	277	273	—	280	273
7	267	315	241	253	338	236	373	260	265
8	284	313	293	228	377	245	306	198	260
9	—	248	285	281	256	234	296	186	280
10	314	244	266	274	286	241	353	290	258
Average T	276	302	267	261	290	250	341	238	271

coefficient becomes the max value, $\rho_{xy} = 0.98727$, the value of the corresponding horizontal axis is inertial delay, $t_h = 0.12$ s.

6. Simulation Results and Analysis

In order to examine the influence of driver model with the jerky dynamics, the comparisons are made in several cases by simulations for the driver models with/without the compensator using the identified vehicle parameter. Here, taking the skilled driver A as an example, simulation tests are conducted in CarSim. Two emergency cases and results are described as follows.

Case 1. The vehicle runs at the speed of 40 km/h on a μ-split road without ABS, which has two different friction coefficients on the left/right sides of the road center line, that is, 0.2 and 0.5. After 2 s, braking is exerted till the vehicle stops completely. The lateral displacement and acceleration of vehicle are shown in Figures 10 and 11, respectively. POSANN driver model cannot achieve accurate path following, while the PCANN driver model produces better path-following performance, considering the y-coordinate error and the lateral acceleration error. The maximum position error is 0.936 m with the POSANN driver model. Meanwhile, the maximum error obtained with the PCANN driver model is 0.435 m, which is 46.5% of that of POSANN driver model. The maximum lateral acceleration error with the POSANN driver model is 2.83 m/s^2. Meanwhile, the corresponding error, 32.4% of that of the POASNN driver model, is 0.918 m/s^2 with the POSANN driver model. Obviously, it can be seen that the PCANN driver model of the driver A can reduce vehicle lateral responses effectively and make the vehicle recovering to the stable condition much more quickly than POSANN driver model.

Case 2. In order to simulate extreme working conditions, the double-lane change is carried out in CarSim, supposing that the vehicle runs at the speed of 80 km/h into the slippery road of $\mu = 0.2$, and the other conditions are under ideal conditions. The responses of lateral displacement and acceleration are shown in Figures 12 and 13, respectively.

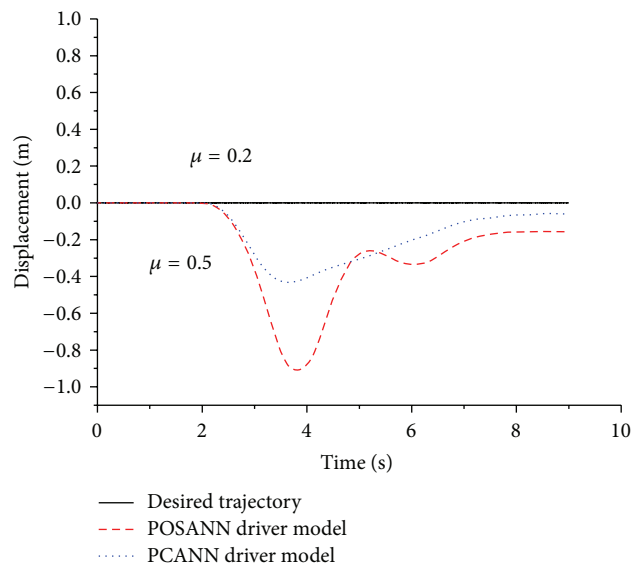

Figure 10: Comparison of lateral displacement.

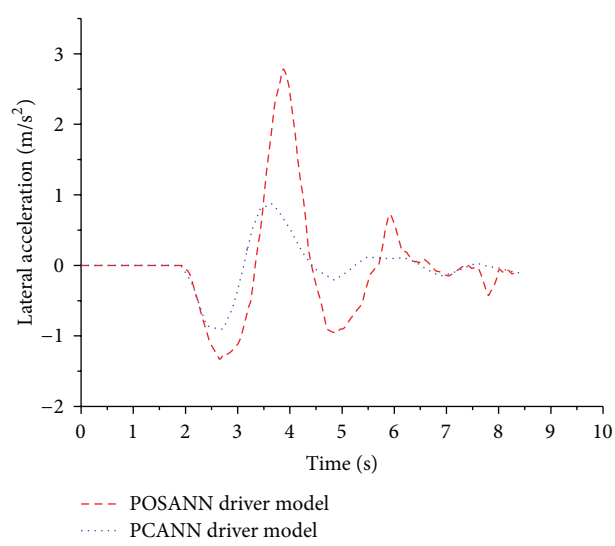

Figure 11: Comparison of lateral acceleration.

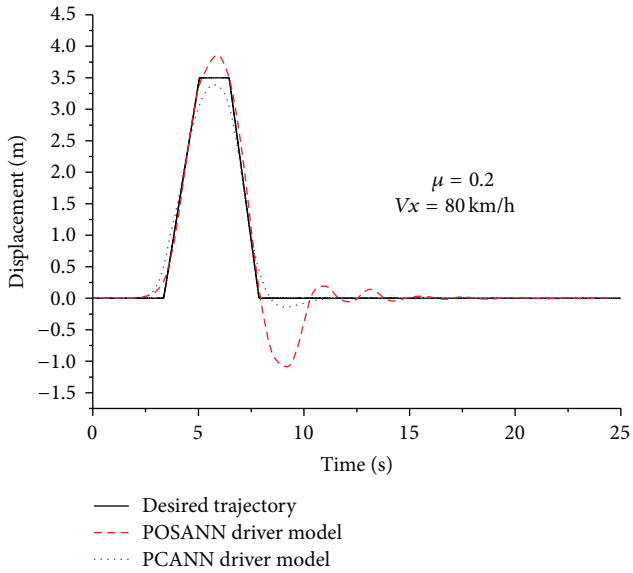

Figure 12: Comparison of lateral displacement.

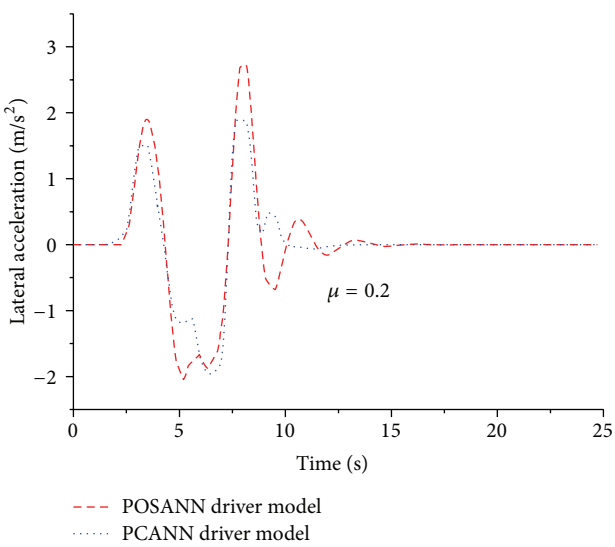

Figure 13: Comparison of lateral acceleration.

From these two figures, it can be obtained that the vehicle with the PCANN driver model has better performance of the lateral acceleration and the lateral displacement than that the POSANN driver model. The sway of the vehicle with the PCANN driver model is smaller than that the POSANN driver model. It is obvious that the PCANN driver model of driver A can adapt to environmental changes more rapidly.

The above results in two emergency cases show that compared with the POSANN driver model, the proposed PCANN driver model can adapt to the changes of road condition more quickly, implying that the driving compensation is very necessary especially in emergency cases for the driver. The compensator will exhibit more potential benefits when the road is worse.

7. Conclusion

A new POSANN-based driver model with compensator controller using the jerky dynamics is investigated. The compensator controller is built using linearized models of the nonlinear vehicle dynamics and vehicle current states to generate a steering corrected value for the POSANN driver model. The key model parameters reflecting the driving behaviors, such as preview time and reaction time, are calculated according to the test data which can vary with changes under operating conditions. The inertial delay of the steering system is obtained by the cross-correlation method, which is applied to eliminate random fluctuation of experimental data. Simulation results demonstrated that the proposed driver model can achieve better path-following performance than the POSANN driver model under critical maneuvering conditions. Furthermore, the driver model can be used effectively for representing driver steering control behaviors to some extent. Consequently, the proposed driver model presented in this study can be used in a closed-loop simulation and in the development of the vehicle's intelligent safety system.

Acknowledgments

The authors acknowledge the support of the research team of test technology on the active safety of automobile (2012-CX-04). The authors greatly appreciate the support of the National Natural Science Foundation of China (no. 51375299).

References

[1] Y. Kuriyagawa, H.-E. Im, I. Kageyama, and S. Onishi, "A research on analytical method of driver-vehicle-environment system for construction of intelligent driver support system," *Vehicle System Dynamics*, vol. 37, no. 5, pp. 339–358, 2002.

[2] D.-J. Zhuang, F. Yu, and Y. Lin, "Evaluation of a vehicle directional control with a fractional order PD$^{\mu}$ controller," *International Journal of Automotive Technology*, vol. 9, no. 6, pp. 679–685, 2008.

[3] C. Zong, K. Guo, and B. Li, "Theoretical prediction and comprehensive evaluation for vehicle handling stability," *Automotive Engineering*, vol. 23, no. 1, pp. 5–12, 2001.

[4] C. C. Macadam, "Understanding and modeling the human driver," *Vehicle System Dynamics*, vol. 40, no. 1–3, pp. 101–134, 2003.

[5] M. Kondo, "Directional stability (when steering is added)," *Journal of the Society of Automotive Engineers of Japan*, vol. 7, no. 5-6, p. 9, 1953.

[6] D. T. McRuer and H. R. Jex, "A review of quasi-linear pilot models," *IEEE Transactions on Human Factors in Electronics*, vol. 8, no. 3, pp. 231–249, 1967.

[7] C. C. MacAdam, "An optimal preview control for linear systems," *Journal of Dynamic Systems, Measurement and Control*, vol. 102, no. 3, pp. 188–190, 1980.

[8] K. Guo and P. S. Fancher, "Preview-follower method for modelling closed-loop vehicle directional control," in *Proceedings of the 19th Annual Conference on Manual Control*, pp. 159–186, Boston, Mass, USA, 1983.

[9] H. Ding, K. Guo, F. Wan, J. Cao, and Y. Tian, "An analytical driver model for arbitrary path following at varying vehicle speed," *International Journal of Vehicle Autonomous Systems*, vol. 5, no. 3-4, pp. 204–218, 2007.

[10] T. Fujioka, K. Nomura, N. Takubo, and D. H. Chung, "Driver model using neural network system," in *Proceedings of the 6th International Pacific Conference on Automotive Engingeering*, vol. 2, pp. 931–938, Seoul, Republic of Korea, November 1991.

[11] S. Neusser, J. Nijhuis, L. Spaanenburg, B. Hoefflinger, U. Franke, and H. Fritz, "Neurocontrol for lateral vehicle guidance," *IEEE Micro*, vol. 13, no. 1, pp. 57–66, 1993.

[12] C. C. Macadam and G. E. Johnson, "Application of elementary neural networks and preview sensors for representing driver steering control behaviour," *Vehicle System Dynamics*, vol. 25, no. 1, pp. 3–30, 1996.

[13] K. Guo, F. Pan, Y. Cheng, and H. Ding, "Driver model based on the preview optimal artificial neural network," in *Proceedings of the International Symposium on Advanced Vehicle Control (AVEC '02)*, Hiroshima, Japan, 2002.

[14] K. Guo, Y. Cheng, and H. Ding, "Analytical method for modeling driver in vehicle directional control," *Vehicle System Dynamics*, vol. 41, pp. 401–410, 2004.

[15] J. Edelmann, M. Plöchl, W. Reinalter, and W. Tieber, "A passenger car driver model for higher lateral accelerations," *Vehicle System Dynamics*, vol. 45, no. 12, pp. 1117–1129, 2007.

[16] C. Sentouh, P. Chevrel, F. Mars, and F. Claveau, "A sensorimotor driver model for steering control," in *Proceedings of the IEEE International Conference on Systems, Man and Cybernetics (SMC '09)*, pp. 2462–2467, San Antonio, Tex, USA, October 2009.

[17] C. Sentouh, P. Chevrel, F. Mars, and F. Claveau, "A human-centred approach of steering control modelling," in *Proceedings of the 21st International Association for Vehicle System Dynamics Symposium on Dynamics of Vehicles on Roads and Tracks*, Stockholm, Sweden, 2009.

[18] L. Saleh, P. Chevrel, F. Mars, J. F. Lafay, and F. Claveau, "Human-like cybernetic driver model for lane keeping," in *Proceedings of the 18th World Congress of the International Federation of Automatic Control (IFAC '11)*, pp. 4368–4373, Milan, Italy, September 2011.

[19] D. Hrovat and M. Hubbard, "A comparison between jerk optimal and acceleration optimal vibration isolation," *Journal of Sound and Vibration*, vol. 112, no. 2, pp. 201–210, 1987.

[20] C. Liu, D. C. Gazis, and T. W. Kennedy, "Human judgment and analytical derivation of ride quality," *Transportation Science*, vol. 33, no. 3, pp. 290–297, 1999.

[21] J. Förstberg, "Ride comfort and motion sickness in tilting trains: human responses to motion environments in train experiment and simulator experiments," Tech. Rep. no. TRITA-FKT 2000:28, Railway Technology, Department of Vehicle Engineering, Royal Institute of Technology, Stockholm, Sweden, 2000.

[22] S. H. Schot, "Jerk: the time rate of change of acceleration," *American Journal of Physics*, vol. 46, no. 11, pp. 1090–1094, 1978.

[23] O. Bagdadi and A. Várhelyi, "Jerky driving—an indicator of accident proneness?" *Accident Analysis and Prevention*, vol. 43, no. 4, pp. 1359–1363, 2011.

[24] M. Kawato, "Internal models for motor control and trajectory planning," *Current Opinion in Neurobiology*, vol. 9, no. 6, pp. 718–727, 1999.

[25] S. D. Keen and D. J. Cole, "Steering control using model predictive control and multiple internal models," in *Proceedings of the 8th International Symposium on Advanced Vehicle Control (AVEC '06)*, Taipei, Taiwan, 2006.

[26] H. Zhang, Y. Shi, and A. S. Mehr, "Robust non-fragile dynamic vibration absorbers with uncertain factors," *Journal of Sound and Vibration*, vol. 330, no. 4, pp. 559–566, 2011.

[27] R. Wang, H. Zhang, and J. Wang, "Linear parameter-varying controller design for four-wheel independently actuated electric ground vehicles with active steering systems," *IEEE Transactions on Control Systems Technology*, 2013.

[28] H. Zhang, Y. Shi, and M. Liu, "H_∞ step tracking control for networked discrete-time nonlinear systems with integral and predictive actions," *IEEE Transactions on Industrial Informatics*, vol. 9, no. 1, pp. 337–345, 2013.

[29] C. C. MacAdam, "Application of an optimal preview control for simulation of closed-loop automobile driving," *IEEE Transactions on Systems, Man and Cybernetics*, vol. 11, no. 6, pp. 393–399, 1981.

Hindawi Publishing Corporation
Mathematical Problems in Engineering
Volume 2013, Article ID 230576, 11 pages
http://dx.doi.org/10.1155/2013/230576

Research Article

Robust Stability and H_∞ Stabilization of Switched Systems with Time-Varying Delays Using Delta Operator Approach

Chen Qin,[1] Zhengrong Xiang,[1] and Hamid Reza Karimi[2]

[1] *School of Automation, Nanjing University of Science and Technology, Nanjing 210094, China*
[2] *Department of Engineering, Faculty of Engineering and Science, University of Agder, 4898 Grimstad, Norway*

Correspondence should be addressed to Zhengrong Xiang; xiangzr@mail.njust.edu.cn

Received 29 September 2013; Accepted 13 November 2013

Academic Editor: Hui Zhang

This paper considers the problems of the robust stability and robust H_∞ controller design for time-varying delay switched systems using delta operator approach. Based on the average dwell time approach and delta operator theory, a sufficient condition of the robust exponential stability is presented by choosing an appropriate Lyapunov-Krasovskii functional candidate. Then, a state feedback controller is designed such that the resulting closed-loop system is exponentially stable with a guaranteed H_∞ performance. The obtained results are formulated in the form of linear matrix inequalities (LMIs). Finally, a numerical example is provided to explicitly illustrate the feasibility and effectiveness of the proposed method.

1. Introduction

Switched systems are a kind of hybrid systems consisting of a set of discrete event dynamic subsystems or continuous variable dynamic subsystems and a switching rule which defines a particular subsystem working during a certain interval of time. Switched systems have numerous applications in network control systems [1], robot control systems [2], intelligent traffic control systems [3], chemical industry control systems [4], and many other areas [5, 6]. Many important achievements on stability and stabilization of switched systems have been developed [7–10]. It was shown in the literature that the average dwell time (ADT) method is a powerful tool to deal with the stability of switched systems.

The delta operator which is a novel approach with good finite word length performance under fast sampling rates has been investigated by many researchers due to their extensive applications [11–13], for instance, optimal filtering [14], signal processing [15], robust control [16], system identification [17], and so forth. As stated in [15], the standard shift operator was mostly adopted in the study of control theories for discrete-time systems. However, the dynamic response of a discrete system does not converge smoothly to its continuous counterpart when the sampling period tends to zero; namely, data are taken at high sampling rates. The delta operator method can solve the above problem. In addition, it was shown in [15] that delta operator requires smaller word length when implemented in fixed-point digital control processors than shift operator does. So far, some useful results on delta operator systems have been formulated in [18–21]. As is well known, time delay phenomena which often cause instability or undesirable performance in control systems are involved in a variety of real systems, such as chaotic systems, and hydraulic pressure systems [22]. In the past years, a mass of results on delta operator systems with time delay have appeared [23–27]. The delta operator is defined by

$$\delta x(t) = \begin{cases} \dfrac{dx(t)}{dt}, & T = 0, \\ \dfrac{(x(t+T) - x(t))}{T}, & T \neq 0, \end{cases} \tag{1}$$

where T is a sampling period. When $T \to 0$, the delta operator model will approach the continuous system before discretization and reflect a quasicontinuous performance [28].

It should be noted that external disturbances are generally inevitable, and the output will be subsequently affected by disturbances in the system. Some results on H_∞ control were

developed by many researchers to restrain the external disturbances [29–33]. The H_∞ control problem for a class of discrete systems was solved by using delta operator approach [34]. Low order sampled data H_∞ control using the delta operator was reported in the literature [35]. Robust H_∞ control for a class of uncertain switched systems using delta operator was investigated [36]. However, few results on the issues of robust stability and H_∞ controller design for delta operator switched systems with time-varying delay are presented, which motivates the present investigations.

In this paper, we concentrate our interest on investigating the stability and H_∞ controller design problems for delta operator switched systems with time-varying delay. The main contributions of this paper can be summarized as follows: (1) by constructing a new Lyapunov-Krasovskii functional candidate and using the average dwell time approach, an exponential stability criterion for the considered system is proposed and (2) a state feedback controller design scheme is developed such that the corresponding closed-loop system is exponentially stable with a guaranteed H_∞ performance.

The remainder of the paper is organized as follows. The formulation of the considered systems and some corresponding definitions and lemmas is given in Section 2. In Section 3, the exponential stability analysis and H_∞ control for the underlying system are developed. A numerical example is given to illustrate the feasibility and effectiveness of the proposed method in Section 4. Finally, concluding remarks are presented in Section 5.

Notations. $\|\cdot\|_2$ denotes the Euclidean norm. $\lambda_{\min}(\cdot)$ and $\lambda_{\max}(\cdot)$ denote the minimum and maximum eigenvalues of a matrix, respectively; A^T means the transpose of matrix A; R denotes the set of all real numbers; R^n represents the n-dimensional real vector space; $R^{m\times n}$ is the set of all $(m\times n)$-dimensional real matrices. The notation $A > 0(\geq 0)$ means that the matrix A is positive (nonnegative) definite; diag$\{\cdots\}$ refers to the block-diagonal matrix; I is the identity matrix of appropriate dimension. $l_2[k_0,\infty)$ stands for the space of square summable functions on $[k_0,\infty)$.

2. Problem Formulation

Consider the following delta operator switched system with time-varying delay:

$$\begin{gathered}\delta x(k) = \widehat{A}_{\sigma(k)}x(k) + \widehat{A}_{d\sigma(k)}x(k-\tau(k)) + D_{\sigma(k)}w(k),\\ z(k) = C_{\sigma(k)}x(k) + G_{\sigma(k)}w(k),\\ x(k_0+\theta) = \phi(\theta), \quad \theta = -\overline{\tau}, -\overline{\tau}+1,\ldots,0,\end{gathered} \tag{2}$$

where $x(k)\in R^n$ is the state vector, $z(k)\in R^l$ denotes the controlled output, and $w(k)\in R^w$ represents the disturbance input belonging to $l_2[k_0,\infty)$. k means the time $t = kT$ and $T > 0$ is the sampling period; k_0 is the initial instant. $\sigma(k) : [k_0,\infty) \to \underline{N} = \{1,2,\ldots,N\}$ is the switching signal with N being the number of subsystems. $\tau(k)$ is the time-varying delay satisfying $0 \leq \underline{\tau} \leq \tau(k) \leq \overline{\tau}$ for known constants $\underline{\tau}$ and $\overline{\tau}$. $\phi(\theta)$ is the discrete vector-valued initial function. C_i, D_i, and G_i are constant matrices with proper dimensions. $\widehat{A}_i$ and $\widehat{A}_{di}$ are uncertain real-valued matrices with appropriate dimensions and have the following form:

$$\left[\widehat{A}_i \quad \widehat{A}_{di}\right] = \left[A_i \quad A_{di}\right] + H_iF_i(k)\left[E_{ai} \quad E_{adi}\right], \tag{3}$$

where A_i, A_{di}, H_i, E_{ai}, and E_{adi} are known real constant matrices of suitable dimensions and $F_i(k)$ is an unknown time-varying matrix which satisfies

$$F_i^T(k)F_i(k) \leq I. \tag{4}$$

To obtain the main results, we first give some definitions and lemmas which will be essential in our later development.

Definition 1 (see [36]). Consider system (2) with $w(k) = 0$. It is said to be exponentially stable under a switching signal $\sigma(k)$ if, for the initial condition $x(k_0+\theta) = \phi(\theta)$, $\theta = -\overline{\tau}, -\overline{\tau}+1,\ldots,0$, there exist constants $\alpha > 0$ and $\beta > 0$ such that the solution $x(k)$ satisfies

$$\|x(k)\| \leq \alpha\|x(k_0)\|_c e^{-\beta(k-k_0)}, \quad \forall k \geq k_0, \tag{5}$$

where $\|x(k_0)\|_c = \sup_{-\overline{\tau}\leq k\leq 0}\|x(k_0+\theta)\|$.

Definition 2. For given $0 < \alpha < 1/T$ and $\gamma > 0$, system (2) is said to have an H_∞ performance level γ if there exists a switching signal $\sigma(k)$ such that the following conditions are satisfied:

(1) system (2) is exponentially stable when $w(k) = 0$;

(2) under the zero-initial condition, that is, $\phi(\theta) = 0$, $\theta = -\overline{\tau}, -\overline{\tau}+1,\ldots,-1,0$, system (2) satisfies

$$\begin{gathered}\sum_{k=k_0}^{\infty}(1-T\alpha)^{(k-k_0)}\|z(k)\|^2 \leq \gamma^2\sum_{k=k_0}^{\infty}\|w(k)\|^2,\\ \forall w(k)\in l_2[k_0,\infty).\end{gathered} \tag{6}$$

Definition 3 (see [37]). For any switching signal $\sigma(k)$ and any $k_2 > k_1 \geq 0$, let $N_{\sigma(k)}(k_1,k_2)$ denote the number of switching of $\sigma(k)$ over the interval $[k_1,k_2)$. For given $\tau_a > 0$ and $N_0 \geq 0$, if the inequality

$$N_{\sigma(k)}(k_1,k_2) \leq N_0 + \frac{k_2-k_1}{\tau_a} \tag{7}$$

holds, then the positive constant τ_a is called the average dwell time and N_0 is called the chattering bound. As commonly used in the literature, we choose $N_0 = 0$ in this paper.

Lemma 4 (see [20]). *For a given matrix* $S = \begin{bmatrix} S_{11} & S_{12}\\ S_{12}^T & S_{22}\end{bmatrix}$, *where* S_{11} *and* S_{22} *are square matrices, the following conditions are equivalent:*

(i) $S < 0$;

(ii) $S_{11} < 0$, $S_{22} - S_{12}^TS_{11}^{-1}S_{12} < 0$;

(iii) $S_{22} < 0$, $S_{11} - S_{12}S_{22}^{-1}S_{12}^T < 0$.

Lemma 5 (see [20]). *Let U, V, W, and X be real matrices of appropriate dimensions with X satisfying $X = X^T$; then, for all $V^TV \le I$,*

$$X + UVW + W^TV^TU^T < 0 \tag{8}$$

if and only if there exists a scalar ε such that

$$X + \varepsilon UU^T + \varepsilon^{-1}W^TW < 0. \tag{9}$$

Lemma 6 (see [28]). *For any time function $x(t)$ and $y(t)$, the following equation holds:*

$$\begin{aligned}\delta\left(x(t)\,y(t)\right) &= \delta\left(x(t)\right)y(t) + x(t)\,\delta\left(y(t)\right)\\ &\quad + T\delta\left(x(t)\right)\delta\left(y(t)\right),\end{aligned} \tag{10}$$

where T is the sampling period.

The objectives of the paper are (1) to find a class of switching signal $\sigma(k)$ such that system (2) is exponentially stable with a guaranteed H_∞ performance and (2) to determine a class of switching signal and design a state feedback controller $u(k) = K_{\sigma(k)}x(k)$ for the following delta operator switched system with time-varying delay:

$$\begin{aligned}\delta x(k) &= \widehat{A}_{\sigma(k)}x(k) + \widehat{A}_{d\sigma(k)}x(k-\tau(k))\\ &\quad + \widehat{B}_{\sigma(k)}u(k) + D_{\sigma(k)}w(k),\\ z(k) &= C_{\sigma(k)}x(k) + G_{\sigma(k)}w(k),\\ x(k_0+\theta) &= \phi(\theta), \quad \theta = -\overline{\tau}, -\overline{\tau}+1, \ldots, 0\end{aligned} \tag{11}$$

such that the corresponding closed-loop system is exponentially stable with a guaranteed H_∞ performance.

3. Main Results

3.1. Robust Stability Analysis. In this section, we will focus on the stability of system (2) with $w(k) = 0$.

Theorem 7. *For a given positive constant $0 < \alpha < 1/T$, if there exist scalars ε_i and positive definite symmetric matrices X_i and Q_i, $i \in \underline{N}$, with appropriate dimensions, such that*

$$\begin{bmatrix} E_i & A_{di}X_i & TX_iA_i^T & \varepsilon_iH_i & X_iE_{ai}^T\\ X_iA_{di}^T & -(1-T\alpha)^{(\overline{\tau}+1)}Q_i & TX_iA_{di}^T & 0 & X_iE_{adi}^T\\ TA_iX_i & TA_{di}X_i & -TX_i & \varepsilon_iTH_i & 0\\ \varepsilon_iH_i^T & 0 & \varepsilon_iTH_i^T & -\varepsilon_iI & 0\\ E_{ai}X_i & E_{adi}X_i & 0 & 0 & -\varepsilon_iI \end{bmatrix} < 0, \tag{12}$$

where $E_i = A_iX_i + X_iA_i^T + \alpha X_i + (1-T\alpha)(\overline{\tau} - \underline{\tau} + 1)Q_i$, then system (2) with $w(k) = 0$ is exponentially stable for any switching signal $\sigma(k)$ with the following average dwell time scheme:

$$\tau_a > \tau_a^* = -\frac{\ln\mu}{\ln(1-T\alpha)}, \tag{13}$$

where $\mu \ge 1$ satisfies

$$X_i \le \mu X_j, \quad Q_i \le \mu Q_j, \quad \forall i, j \in \underline{N}. \tag{14}$$

Proof. Choose the following Lyapunov-Krasovskii functional candidate for the ith subsystem

$$V_i(k) = V_{i1}(k) + V_{i2}(k) + V_{i3}(k), \quad \forall i \in \underline{N}, \tag{15}$$

where

$$\begin{aligned}V_{i1}(k) &= x^T(k)P_ix(k),\\ V_{i2}(k) &= T\sum_{s=k-\tau(k)}^{k-1}(1-T\alpha)^{(k-s)}x^T(s)S_ix(s),\\ V_{i3}(k) &= T\sum_{l=-\overline{\tau}+1}^{-\underline{\tau}}\sum_{s=k+l}^{k-1}(1-T\alpha)^{k-s}x^T(s)S_ix(s).\end{aligned} \tag{16}$$

Taking the delta operator manipulations of Lyapunov functional candidate $V_i(k)$ along the trajectory of system (2), by Lemma 6, we have

$$\begin{aligned}&\delta V_{i1}(k)\\ &= \delta\left(x^T(k)P_ix(k)\right)\\ &= \delta\left(x^T(k)P_i\right)x(k) + x^T(k)P_i\delta(x(k))\\ &\quad + T\delta\left(x^T(k)P_i\right)\delta(x(k))\\ &= \left(\widehat{A}_ix(k) + \widehat{A}_{di}x(k-\tau(k))\right)^TP_ix(k)\\ &\quad + x^T(k)P_i\left(\widehat{A}_ix(k) + \widehat{A}_{di}x(k-\tau(k))\right)\\ &\quad + T\left(\widehat{A}_ix(k) + \widehat{A}_{di}x(k-\tau(k))\right)^T\\ &\quad \times P_i\left(\widehat{A}_ix(k) + \widehat{A}_{di}x(k-\tau(k))\right)\\ &= x^T(k)P_i\widehat{A}_ix(k) + x^T(k)P_i\widehat{A}_{di}x(k-\tau(k))\\ &\quad + x^T(k)\widehat{A}_i^TP_ix(k) + x^T(k-\tau(k))\widehat{A}_{di}^TP_ix(k)\\ &\quad + Tx^T(k)\widehat{A}_i^TP_i\widehat{A}_ix(k) + Tx^T(k)\widehat{A}_i^TP_i\widehat{A}_{di}x(k-\tau(k))\\ &\quad + Tx^T(k-\tau(k))\widehat{A}_{di}^TP_i\widehat{A}_ix(k)\\ &\quad + Tx^T(k-\tau(k))\widehat{A}_{di}^TP_i\widehat{A}_{di}x(k-\tau(k))\\ &= \begin{bmatrix} x(k)\\ x(k-\tau(k))\end{bmatrix}^T\\ &\quad \times \begin{bmatrix} P_i\widehat{A}_i + \widehat{A}_i^TP_i + T\widehat{A}_i^TP_i\widehat{A}_i & P_i\widehat{A}_{di} + T\widehat{A}_i^TP_i\widehat{A}_{di}\\ \widehat{A}_{di}^TP_i + T\widehat{A}_{di}^TP_i\widehat{A}_i & T\widehat{A}_{di}^TP_i\widehat{A}_{di}\end{bmatrix}\\ &\quad \times \begin{bmatrix} x(k)\\ x(k-\tau(k))\end{bmatrix},\end{aligned} \tag{17}$$

$$\begin{aligned}
&\delta V_{i2}(k) \\
&= \frac{1}{T}\left(V_{i2}(k+1) - V_{i2}(k)\right) \\
&= \frac{1}{T}\left(T\sum_{s=k+1-\tau(k+1)}^{k+1-1}(1-T\alpha)^{(k+1-s)}x^T(s)S_ix(s)\right. \\
&\qquad \left. - T\sum_{s=k-\tau(k)}^{k-1}(1-T\alpha)^{(k-s)}x^T(s)S_ix(s)\right) \\
&\le -T\alpha\sum_{s=k-\tau(k)}^{k-1}(1-T\alpha)^{(k-s)}x^T(s)S_ix(s) \\
&\qquad + (1-T\alpha)x^T(k)S_ix(k) \\
&\qquad - (1-T\alpha)^{(\overline{\tau}+1)}x^T(k-\tau(k))S_ix(k-\tau(k)) \\
&\qquad + \sum_{s=k+1-\overline{\tau}}^{k-\underline{\tau}}(1-T\alpha)^{(k+1-s)}x^T(s)S_ix(s), \\
&\delta V_{i3}(k) \\
&= \frac{1}{T}\left(V_{i3}(k+1) - V_{i3}(k)\right) \\
&= \frac{1}{T}\left(T\sum_{l=-\overline{\tau}+1}^{-\underline{\tau}}\sum_{s=k+1+l}^{k-1+1}(1-T\alpha)^{(k+1-s)}x^T(s)S_ix(s)\right. \\
&\qquad \left. -T\sum_{l=-\overline{\tau}+1}^{-\underline{\tau}}\sum_{s=k+l}^{k-1}(1-T\alpha)^{(k-s)}x^T(s)S_ix(s)\right) \\
&= -T\alpha\sum_{l=-\overline{\tau}+1}^{-\underline{\tau}}\sum_{s=k+l}^{k-1}(1-T\alpha)^{(k-s)}x^T(s)S_ix(s) \\
&\qquad + (1-T\alpha)\left(\overline{\tau}-\underline{\tau}\right)x^T(k)S_ix(k) \\
&\qquad - \sum_{s=k+1-\overline{\tau}}^{k-\underline{\tau}}(1-T\alpha)^{(k+1-s)}x^T(s)S_ix(s).
\end{aligned} \tag{18, 19}$$

Combining (17)–(19), we have

$$\begin{aligned}
&\delta V_i(k) + \alpha V_i(k) \\
&= \begin{bmatrix} x(k) \\ x(k-\tau(k)) \end{bmatrix}^T \\
&\quad \times \begin{bmatrix} P_i\widehat{A}_i + \widehat{A}_i^TP_i + T\widehat{A}_i^TP_i\widehat{A}_i & P_i\widehat{A}_{di} + T\widehat{A}_i^TP_i\widehat{A}_{di} \\ \widehat{A}_{di}^TP_i + T\widehat{A}_{di}^TP_i\widehat{A}_i & T\widehat{A}_{di}^TP_i\widehat{A}_{di} \end{bmatrix} \\
&\quad \times \begin{bmatrix} x(k) \\ x(k-\tau(k)) \end{bmatrix} \\
&\quad + \alpha P_i + (1-T\alpha)\left(\overline{\tau}-\underline{\tau}+1\right)x^T(k)S_ix(k) \\
&\quad - (1-T\alpha)^{(\overline{\tau}+1)}x^T(k-\tau(k))S_ix(k-\tau(k)) \\
&\le \begin{bmatrix} x(k) \\ x(k-\tau(k)) \end{bmatrix}^T \Omega_i \begin{bmatrix} x(k) \\ x(k-\tau(k)) \end{bmatrix},
\end{aligned} \tag{20}$$

where

$$\Omega_i = \begin{bmatrix} P_i\widehat{A}_i + \widehat{A}_i^TP_i + \alpha P_i + (1-T\alpha)\times\left(\overline{\tau}-\underline{\tau}+1\right)S_i + T\widehat{A}_i^TP_i\widehat{A}_i & P_i\widehat{A}_{di} + T\widehat{A}_i^TP_i\widehat{A}_{di} \\ \widehat{A}_{di}^TP_i + T\widehat{A}_{di}^TP_i\widehat{A}_i & T\widehat{A}_{di}^TP_i\widehat{A}_{di} - (1-T\alpha)^{(\overline{\tau}+1)}S_i \end{bmatrix}. \tag{21}$$

Applying Lemma 4, we can obtain that $\Omega_i < 0$ is equivalent to

$$\begin{bmatrix} P_i\widehat{A}_i + \widehat{A}_i^TP_i + \alpha P_i + (1-T\alpha)\left(\overline{\tau}-\underline{\tau}+1\right)S_i & P_i\widehat{A}_{di} & T\widehat{A}_i^T \\ \widehat{A}_{di}^TP_i & -(1-T\alpha)^{(\overline{\tau}+1)}S_i & T\widehat{A}_{di}^T \\ T\widehat{A}_i & T\widehat{A}_{di} & -TP_i^{-1} \end{bmatrix} < 0. \tag{22}$$

Using diag $\{P_i^{-1} \quad P_i^{-1} \quad I\}$ to pre- and post-multiply both sides of (22), respectively, we have

$$\begin{bmatrix} \overline{E}_i & \widehat{A}_{di}P_i^{-1} & TP_i^{-1}\widehat{A}_i^T \\ P_i^{-1}\widehat{A}_{di}^T & -(1-T\alpha)^{(\overline{\tau}+1)}P_i^{-1}SP_i^{-1} & TP_i^{-1}\widehat{A}_{di}^T \\ T\widehat{A}_iP_i^{-1} & T\widehat{A}_{di}P_i^{-1} & -TP_i^{-1} \end{bmatrix} < 0, \tag{23}$$

where $\overline{E}_i = \widehat{A}_iP_i^{-1} + P_i^{-1}\widehat{A}_i^T + \alpha P_i^{-1} + (1-T\alpha)(\overline{\tau}-\underline{\tau}+1)P_i^{-1}S_iP_i^{-1}$.

Denote $Q_i = P_i^{-1}S_iP_i^{-1}$ and $X_i = P_i^{-1}$; then, substituting (3) into (23) and applying Lemmas 4 and 5, we obtain that (23) is equivalent to (12). Thus, from (12), we can easily obtain

$$\delta V_i(k) + \alpha V_i(k) \le 0. \tag{24}$$

It follows from (24) that

$$\begin{aligned} \delta V_i(k) &= \frac{V_i(k+1) - V_i(k)}{T} \le -\alpha V_i(k), \\ V_i(k+1) - V_i(k) &\le -\alpha_i T V_i(k), \\ V_i(k+1) &\le (1-\alpha T) V_i(k). \end{aligned} \tag{25}$$

Let $k_1 < \cdots < k_q$ denote the switching instants of $\sigma(k)$ over the interval $[k_0, k)$. Consider the following piecewise Lyapunov functional for system (2):

$$\begin{aligned} V(k) &= V_{\sigma(k)}(k) = V_{\sigma(k_p)}(k), \\ \forall k &\in \left[k_p, k_p+1\right), \quad p = 0, 1, \ldots, q. \end{aligned} \tag{26}$$

From (14), we obtain

$$V_{\sigma(k_p)}\left(k_p\right) \le \mu V_{\sigma(k_p^-)}\left(k_p^-\right), \quad p = 0, 1, \ldots, q. \tag{27}$$

It can be obtained from (24), (27), and Definition 3 that

$$\begin{aligned} V_{\sigma(k)}(k) &\le (1-T\alpha)^{(k-k_q)} V_{\sigma(k_q)}\left(k_q\right) \\ &\le \mu(1-T\alpha)^{(k-k_q)} V_{\sigma(k_q^-)}\left(k_q^-\right) \\ &\le \mu(1-T\alpha)^{(k-k_{q-1})} V_{\sigma(k_{q-1})}\left(k_{q-1}\right) \\ &\le \mu^2(1-T\alpha)^{(k-k_{q-1})} V_{\sigma(k_{q-1}^-)}\left(k_{q-1}^-\right) \\ &\le \cdots \\ &\le \mu^{N_{\sigma(k)}(k_0,k)}(1-T\alpha)^{(k-k_0)} V_{\sigma(k_0)}(k_0) \\ &\le \mu^{(k-k_0)/\tau_a}(1-T\alpha)^{(k-k_0)} V_{\sigma(k_0)}(k_0) \\ &= \left(\mu^{1/\tau_a}(1-T\alpha)\right)^{(k-k_0)} V_{\sigma(k_0)}(k_0). \end{aligned} \tag{28}$$

Considering the definition of $V_{\sigma(k)}(k)$, it yields that

$$V_{\sigma(k)}(k) \ge a\|x(k)\|^2, \tag{29}$$

$$V_{\sigma(k)}(k_0) \le b\|x(k_0)\|_c^2, \tag{30}$$

where

$$\begin{aligned} a &= \min_{i\in\underline{N}} \lambda_{\min}(P_i), \\ b &= \max_{i\in\underline{N}} \left\{\lambda_{\max}(P_i) + T\left(\overline{\tau}^2 - \overline{\tau}\underline{\tau} + \overline{\tau}\right)\lambda_{\max}(S_i)\right\}, \\ \|x(k_0)\|_c &= \sup_{-\overline{\tau}\le\theta\le 0} \|x(k_0+\theta)\|. \end{aligned} \tag{31}$$

Combining (29) and (30), we have

$$\|x(k)\|^2 \le \frac{b}{a}\left(\mu^{1/\tau_a}(1-T\alpha)\right)^{(k-k_0)}\|x(k_0)\|^2. \tag{32}$$

Therefore, system (2) with $w(k) = 0$ is exponentially stable under the average dwell time scheme (13).

The proof is completed. □

Remark 8. When $\mu = 1$ in (14), which leads to $X_i = X_j$, $Q_i = Q_j$, $\forall i, j \in \underline{N}$, and $\tau_a^* = 0$ by (13), system (2) has a common Lyapunov-Krasovskii functional and the switching signal can be arbitrary.

When $\tau(k) = 0$, system (2) with $w(k) = 0$ becomes the following system:

$$\begin{aligned} \delta x(k) &= \left(\widehat{A}_{\sigma(k)} + \widehat{A}_{d\sigma(k)}\right) x(k), \\ z(k) &= C_{\sigma(k)} x(k). \end{aligned} \tag{33}$$

Then we have the following corollary.

Corollary 9. *For a given positive constant $0 < \alpha < 1/T$, if there exist scalars ε_i and positive definite symmetric matrices X_i, $\forall i \in \underline{N}$, of appropriate dimensions, such that*

$$\begin{bmatrix} \left(A_i + A_{di}\right)X_i + X_i\left(A_i^T + A_{di}^T\right) + \alpha X_i & TX_i\left(A_i^T + A_{di}^T\right) & \varepsilon_i H_i & X_i\left(E_{ai}^T + E_{adi}^T\right) \\ T\left(A_i + A_{di}\right)X_i & -TX_i & \varepsilon_i T H_i & 0 \\ \varepsilon_i H_i^T & \varepsilon_i T H_i^T & -\varepsilon_i I & 0 \\ \left(E_{ai} + E_{adi}\right)X_i & 0 & 0 & -\varepsilon_i I \end{bmatrix} < 0, \tag{34}$$

then system (33) is exponentially stable for any switching signal $\sigma(k)$ with average dwell time scheme (13), where $\mu \ge 1$ satisfies

$$X_i \le \mu X_j, \quad \forall i, j \in \underline{N}. \tag{35}$$

3.2. H_∞ Performance Analysis. The following theorem gives sufficient conditions for the existence of an H_∞ performance level for system (2).

Theorem 10. *For given positive constants γ and $0 < \alpha < 1/T$, if there exist scalars ε_i and positive definite symmetric matrices X_i and Q_i, $i \in \underline{N}$, of appropriate dimensions, such that*

$$\begin{bmatrix} \Delta_i & A_{di}X_i & D_i & TX_iA_i^T & X_iC_i^T & \varepsilon_iH_i & X_iE_{ai}^T \\ X_iA_{di}^T & -(1-T\alpha)^{\overline{\tau}+1}Q_i & 0 & TX_iA_{di}^T & 0 & 0 & X_iE_{adi}^T \\ D_i^T & 0 & -\gamma^2 I & TD_i^T & G_i^T & 0 & 0 \\ TA_iX_i & TA_{di}X_i & TD_i & -TX_i & 0 & \varepsilon_iTH_i & 0 \\ C_iX_i & 0 & G_i & 0 & -I & 0 & 0 \\ \varepsilon_iH_i^T & 0 & 0 & \varepsilon_iTH_i^T & 0 & -\varepsilon_iI & 0 \\ E_{ai}X_i & E_{adi}X_i & 0 & 0 & 0 & 0 & -\varepsilon_iI \end{bmatrix} < 0, \tag{36}$$

where $\Delta_i = A_iX_i + X_iA_i^T + \alpha X_i + (1-T\alpha)(\overline{\tau} - \underline{\tau} + 1)Q_i$, then system (2) is exponentially stable with an H_∞ performance level γ for any switching signal $\sigma(k)$ with average dwell time scheme (13), where $\mu \geq 1$ satisfies (14).

Proof. Equation (12) in Theorem 7 can be directly derived from (36). Thus, system (2) is exponentially stable. We are now in a position to show the H_∞ performance of system (2).

Choosing the Lyapunov-Krasovskii functional candidate (15) and following the proof line of Theorem 7, we get

$$\begin{aligned} &\delta V_{i1}(k) \\ &= x^T(k)P_i\delta x(k) + (\delta x(k))^T P_i x(k) \\ &\quad + T(\delta x(k))^T P_i \delta x(k) \\ &= x^T(k)P_i\left(\widehat{A}_i x(k) + \widehat{A}_{di}x(k-\tau(k)) + D_i w(k)\right) \\ &\quad + \left(\widehat{A}_i x(k) + \widehat{A}_{di}x(k-\tau(k)) + D_i w(k)\right)^T P_i x(k) \\ &\quad + T\left(\widehat{A}_i x(k) + \widehat{A}_{di}x(k-\tau(k)) + D_i w(k)\right)^T \\ &\quad \times P_i\left(\widehat{A}_i x(k) + \widehat{A}_{di}x(k-\tau(k)) + D_i w(k)\right) \\ &= \begin{bmatrix} x(k) \\ x(k-\tau(k)) \\ w(k) \end{bmatrix}^T \widetilde{\Theta}_i \begin{bmatrix} x(k) \\ x(k-\tau(k)) \\ w(k) \end{bmatrix}, \end{aligned} \tag{37}$$

where

$$\widetilde{\Theta}_i = \begin{bmatrix} P_i\widehat{A}_i + \widehat{A}_i^TP_i + T\widehat{A}_i^TP_i\widehat{A}_i & P_i\widehat{A}_{di} + T\widehat{A}_i^TP_i\widehat{A}_{di} & P_iD_i + T\widehat{A}_i^TP_iD_i \\ \widehat{A}_{di}^TP_i + T\widehat{A}_{di}^TP_i\widehat{A}_i & T\widehat{A}_{di}^TP_i\widehat{A}_{di} & T\widehat{A}_{di}^TP_iD_i \\ D_i^TP_i + TD_i^TP_i\widehat{A}_i & TD_i^TP_i\widehat{A}_{di} & TD_i^TP_iD_i \end{bmatrix},$$

$$\begin{aligned} \delta V_{i2}(k) &\leq -T\alpha \sum_{s=k-\tau(k)}^{k-1} (1-T\alpha)^{(k-s)} x^T(s) S_i x(s) \\ &\quad + (1-T\alpha)x^T(k)S_ix(k) \\ &\quad - (1-\alpha T)^{(\overline{\tau}+1)} x^T(k-\tau(k)) S_i x(k-\tau(k)) \\ &\quad + \sum_{s=k+1-\overline{\tau}}^{k-\underline{\tau}} (1-T\alpha)^{(k+1-s)} x^T(s) S_i x(s), \\ \delta V_{i3}(k) &= -T\alpha \sum_{l=-\overline{\tau}+1}^{-\underline{\tau}} \sum_{s=k+l}^{k-1} (1-T\alpha)^{(k-s)} x^T(s) S_i x(s) \\ &\quad + (1-T\alpha)(\overline{\tau} - \underline{\tau}) x^T(k) S_i x(k) \\ &\quad - \sum_{s=k+1-\overline{\tau}}^{k-\underline{\tau}} (1-T\alpha)^{(k+1-s)} x^T(s) S_i x(s). \end{aligned} \tag{38}$$

It follows from (37)-(38) that

$$\begin{aligned} &\delta V_i(k) + \alpha V_i(k) + z^T(k)z(k) - \gamma^2 w^T(k)w(k) \\ &\quad = \delta V_i(k) + \alpha V_i(k) \\ &\qquad + (Cx(k) + Gw(k))^T (Cx(k) + Gw(k)) \\ &\qquad - \gamma^2 w^T(k)w(k) \\ &\quad = \begin{bmatrix} x(k) \\ x(k-\tau(k)) \\ w(k) \end{bmatrix}^T \Theta_i \begin{bmatrix} x(k) \\ x(k-\tau(k)) \\ w(k) \end{bmatrix}, \end{aligned} \tag{39}$$

where

$$\Theta_i = \begin{bmatrix} \Pi_i & P_i\widehat{A}_{di} + T\widehat{A}_i^TP_i\widehat{A}_{di} & P_iD_i + T\widehat{A}_i^TP_iD_i + C_i^TG_i \\ \widehat{A}_{di}^TP_i + T\widehat{A}_{di}^TP_i\widehat{A}_i & T\widehat{A}_{di}^TP_i\widehat{A}_{di} - (1-T\alpha)^{\overline{\tau}+1}S_i & T\widehat{A}_{di}^TP_iD_i \\ D_i^TP_i + TD_i^TP_i\widehat{A}_i + G_i^TC_i & TD_i^TP_i\widehat{A}_{di} & TD_i^TP_iD_i + G_i^TG_i - \gamma^2 I \end{bmatrix}, \tag{40}$$

$$\Pi_i = P_i\widehat{A}_i + \widehat{A}_i^TP_i + T\widehat{A}_i^TP_i\widehat{A}_i + \alpha P_i + (1-T\alpha)(\overline{\tau} - \underline{\tau} + 1)S_i + C_i^TC_i.$$

Applying Lemma 4, we can obtain that $\Theta_i < 0$ is equivalent to the following inequality:

$$\begin{bmatrix} P_i\widehat{A}_i + \widehat{A}_i^T P_i + \alpha P_i + (1-T\alpha)\left(\overline{\tau}-\underline{\tau}+1\right)S_i & P_i\widehat{A}_{di} & P_iD_i & T\widehat{A}_i^T & C_i^T \\ \widehat{A}_{di}^T P_i & -(1-T\alpha)^{\overline{\tau}+1}S_i & 0 & T\widehat{A}_{di}^T & 0 \\ D_i^T P_i & 0 & -\gamma^2 I & TD_i^T & G_i^T \\ T\widehat{A}_i & T\widehat{A}_{di} & TD_i & -TP_i^{-1} & 0 \\ C_i & 0 & G_i & 0 & -I \end{bmatrix} < 0. \tag{41}$$

Using diag $\{P_i^{-1} \quad P_i^{-1} \quad I \quad I \quad I\}$ to pre- and post-multiply both sides of (41), respectively, we have

$$\begin{bmatrix} M_i & \widehat{A}_{di}P_i^{-1} & D_i & TP_i^{-1}\widehat{A}_i^T & P_i^{-1}C_i^T \\ P_i^{-1}\widehat{A}_{di}^T & -(1-T\alpha)^{\overline{\tau}+1}P_i^{-1}S_iP_i^{-1} & 0 & TP_i^{-1}\widehat{A}_{di}^T & 0 \\ D_i^T & 0 & -\gamma^2 I & TD_i^T & G_i^T \\ T\widehat{A}_iP_i^{-1} & T\widehat{A}_{di}P_i^{-1} & TD_i & -TP_i^{-1} & 0 \\ C_iP_i^{-1} & 0 & G_i & 0 & -I \end{bmatrix} < 0, \tag{42}$$

where $M_i = \widehat{A}_iP_i^{-1} + P_i^{-1}\widehat{A}_i^T + \alpha P_i^{-1} + (1-T\alpha)(\overline{\tau}-\underline{\tau}+1)P_i^{-1}S_iP_i^{-1}$.

Set $Q_i = P_i^{-1}S_iP_i^{-1}$ and $X_i = P_i^{-1}$; then, substituting (3) into (42) and applying Lemmas 4 and 5, we can obtain that (42) is equivalent to (36).

Therefore, one has, for $k \in [k_p, k_{p+1})$,

$$V(k) \le (1-T\alpha)^{(k-k_p)}V_{\sigma(k_p)}\left(k_p\right) - \sum_{s=k_p}^{k-1}(1-T\alpha)^{(k-1-s)}\Lambda(s), \tag{43}$$

where $\Lambda(s) = T\|z(s)\|^2 - \gamma^2 T\|w(s)\|^2$.

Following the proof line of (28), we obtain

$$\begin{aligned} &V_{\sigma(k)}(k) \\ &\le \mu(1-T\alpha)^{(k-k_q)}V_{\sigma(k_q^-)}\left(k_q^-\right) \\ &\quad - \sum_{s=k_q}^{k-1}(1-T\alpha)^{(k-1-s)}\Lambda(s) \\ &\le \mu(1-T\alpha)^{(k-k_{q-1})}V_{\sigma(k_{q-1})}\left(k_{q-1}\right) \\ &\quad - \mu\sum_{s=k_{q-1}}^{k_q-1}(1-T\alpha)^{(k-1-s)}\Lambda(s) \\ &\quad - \sum_{s=k_q}^{k-1}(1-T\alpha)^{(k-1-s)}\Lambda(s) \\ &= \mu^{N_{\sigma(k)}(k_{q-1},k)}(1-T\alpha)^{(k-k_{q-1})}V_{\sigma(k_{q-1})}\left(k_{q-1}\right) \\ &\quad - \mu^{N_{\sigma(k)}(k_{q-1},k)}\sum_{s=k_{q-1}}^{k_q-1}(1-T\alpha)^{(k-1-s)}\Lambda(s) \\ &\quad - \sum_{s=k_q}^{k-1}(1-T\alpha)^{(k-1-s)}\Lambda(s) \\ &\le \cdots \\ &\le \mu^{N_{\sigma(k)}(k_0,k)}(1-T\alpha)^{(k-k_0)}V_{\sigma(k_0)}\left(k_0\right) \\ &\quad - \mu^{N_{\sigma(k)}(k_0,k)}\sum_{s=k_0}^{k_1-1}(1-T\alpha)^{(k-1-s)}\Lambda(s) \\ &\quad - \mu^{N_{\sigma(k)}(k_1,k)}\sum_{s=k_1}^{k_2-1}(1-T\alpha)^{(k-1-s)}\Lambda(s) \\ &\quad - \cdots - \sum_{s=k_q}^{k-1}(1-T\alpha)^{(k-1-s)}\Lambda(s) \\ &= \mu^{N_{\sigma(k)}(k_0,k)}(1-T\alpha)^{(k-k_0)}V_{\sigma(k_0)}\left(k_0\right) \\ &\quad - \sum_{s=k_0}^{k-1}\mu^{N_{\sigma(k)}(s,k)}(1-T\alpha)^{(k-1-s)}\Lambda(s). \end{aligned} \tag{44}$$

Under the zero initial condition, we get

$$0 \le -\sum_{s=k_0}^{k-1}\mu^{N_{\sigma(k)}(s,k)}(1-T\alpha)^{(k-1-s)}\Lambda(s). \tag{45}$$

Namely,

$$\sum_{s=k_0}^{k-1}\mu^{N_{\sigma(k)}(s,k)}(1-T\alpha)^{(k-s)}\|z(s)\|^2 \le \gamma^2\sum_{s=k_0}^{k-1}\mu^{N_{\sigma(k)}(s,k)}(1-T\alpha)^{(k-s)}\|w(s)\|^2. \tag{46}$$

Multiplying both sides of (46) by $\mu^{-N_{\sigma(k)}(k_0,k)}$ leads to

$$\sum_{s=k_0}^{k-1}\mu^{-N_{\sigma(k)}(k_0,s)}(1-T\alpha)^{(k-s)}\|z(s)\|^2 \le \gamma^2\sum_{s=k_0}^{k-1}\mu^{-N_{\sigma(k)}(k_0,s)}(1-T\alpha)^{(k-s)}\|w(s)\|^2. \tag{47}$$

From Definition 3 and (13), we have

$$\mu^{-N_{\sigma(k)}(k_0,s)} \le (1-T\alpha)^{s-k_0}. \tag{48}$$

Combining (47) and (48) leads to

$$\sum_{s=k_0}^{k-1}(1-T\alpha)^{(s-k_0)}(1-T\alpha)^{(k-s)}\|z(s)\|^2 \le \gamma^2\sum_{s=k_0}^{k-1}(1-T\alpha)^{(k-s)}\|w(s)\|^2. \tag{49}$$

Then, summing both sides of (49) from k_0 to ∞ leads to

$$\sum_{k=k_0}^{\infty}(1-T\alpha)^{(k-k_0)}\|z(k)\|^2 \le \gamma^2\sum_{k=k_0}^{\infty}\|w(k)\|^2. \tag{50}$$

According to Definition 2, we can conclude that the theorem is true.

The proof is completed. □

3.3. H_∞ Controller Design. In this section, a state feedback controller $u(k) = K_{\sigma(k)}x(k)$ will be designed for system (11) such that the corresponding closed-loop system (51) is exponentially stable and satisfies an H_∞ performance. Consider

$$\begin{aligned}\delta x(k) &= \left(\widehat{A}_{\sigma(k)} + \widehat{B}_{\sigma(k)}K_{\sigma(k)}\right)x(k) + \widehat{A}_{d\sigma(k)}x(k-\tau(k)) + D_{\sigma(k)}w(k),\\ z(k) &= C_{\sigma(k)}x(k) + E_{\sigma(k)}w(k),\\ x(k_0+\theta) &= \varphi(\theta), \quad \theta = -\overline{\tau}, -\overline{\tau}+1, \ldots, -1, 0,\end{aligned} \tag{51}$$

where K_i, $i \in \underline{N}$, are the controller gains to be determined. $\widehat{B}_i$ are uncertain real-valued matrices with appropriate dimensions and have the following form

$$\widehat{B}_i = B_i + H_iF_i(k)E_{bi}. \tag{52}$$

Theorem 11. *Consider system* (11). *For given positive constants γ and $0 < \alpha < 1/T$, if there exist scalars ε_i, positive definite symmetric matrices Q_i and X_i, and any matrices W_i, $i \in \underline{N}$, of appropriate dimensions, such that*

$$\begin{bmatrix} \Upsilon_i & A_{di}X_i & D_i & T(A_iX_i+B_iW_i)^T & X_iC_i^T & \varepsilon_iH_i & (E_{ai}X_i+E_{bi}W_i)^T \\ X_iA_{di}^T & -(1-T\alpha)^{\overline{\tau}+1}Q_i & 0 & TX_iA_{di}^T & 0 & 0 & X_iE_{adi}^T \\ D_i^T & 0 & -\gamma^2 I & TD_i^T & G_i^T & 0 & 0 \\ T(A_iX_i+B_iW_i) & TA_{di}X_i & TD_i & -TX_i & 0 & \varepsilon_iTH_i & 0 \\ C_iX_i & 0 & G_i & 0 & -I & 0 & 0 \\ \varepsilon_iH_i^T & 0 & 0 & \varepsilon_iTH_i^T & 0 & -\varepsilon_iI & 0 \\ (E_{ai}X_i+E_{bi}W_i) & E_{adi}X_i & 0 & 0 & 0 & 0 & -\varepsilon_iI \end{bmatrix} < 0, \tag{53}$$

where $\Upsilon_i = (A_iX_i + B_iW_i) + (A_iX_i + B_iW_i)^T + \alpha X_i + (1-T\alpha)(\overline{\tau}-\underline{\tau}+1)Q_i$, then under the state feedback controller

$$u(k) = K_{\sigma(k)}x(k), \qquad K_i = W_iX_i^{-1} \tag{54}$$

and the average dwell time scheme (13), *the closed-loop system* (51) *is exponentially stable with a prescribed H_∞ performance level γ, where $\mu \ge 1$ satisfies* (14).

Proof. Replacing $\widehat{A}_i$ in (36) with $\widehat{A}_i + \widehat{B}_iK_i$, we get

$$\Theta_i = \begin{bmatrix} \varphi_i & A_{di}X_i & D_i & TX_i(A_i+B_iK_i)^T & X_iC_i^T & \varepsilon_iH_i & X_i(E_{ai}+E_{bi}K_i)^T \\ X_iA_{di}^T & -(1-T\alpha)^{\overline{\tau}+1}Q_i & 0 & TX_iA_{di}^T & 0 & 0 & X_iE_{adi}^T \\ D_i^T & 0 & -\gamma^2 I & TD_i^T & G_i^T & 0 & 0 \\ T(A_i+B_iK_i)X_i & TA_{di}X_i & TD_i & -TX_i & 0 & \varepsilon_iTH_i & 0 \\ C_iX_i & 0 & G_i & 0 & -I & 0 & 0 \\ \varepsilon_iH_i^T & 0 & 0 & \varepsilon_iTH_i^T & 0 & -\varepsilon_iI & 0 \\ (E_{ai}+E_{bi}K_i)X_i & E_{adi}X_i & 0 & 0 & 0 & 0 & -\varepsilon_iI \end{bmatrix} < 0, \tag{55}$$

where $\varphi_i = (A_i+B_iK_i)X_i + X_i(A_i+B_iK_i)^T + \alpha X_i + (1-T\alpha)(\overline{\tau}-\underline{\tau}+1)Q_i$.

Denoting $W_i = K_iX_i$, (53) is directly obtained.

The proof is completed. □

We are now in a position to give an algorithm for determining K_i and τ_a^*.

Algorithm 12. Step 1. Input the system matrices.

Step 2. Choose the parameters $0 < \alpha < 1/T$ and $\gamma > 0$. By solving (53), one can obtain the solutions of ε_i, W_i, X_i, and Q_i.

Step 3. By (54), with the obtained W_i and X_i, one can compute the gain matrices K_i.

Step 4. Compute μ and τ_a^* by (13)-(14).

4. Numerical Example

Consider system (11) with parameters as follows:

$$\begin{gathered} A_1 = \begin{bmatrix} 0.5 & -0.7 \\ 0 & 0.4 \end{bmatrix}, \qquad A_{d1} = \begin{bmatrix} 0.2 & 0 \\ 0 & -0.4 \end{bmatrix}, \\ B_1 = \begin{bmatrix} 0.12 & 0 \\ 0.4 & -1 \end{bmatrix}, \qquad C_1 = \begin{bmatrix} 0.2 & -0.18 \end{bmatrix}, \\ D_1 = \begin{bmatrix} 0.01 \\ 0 \end{bmatrix}, \qquad G_1 = 0.01, \\ H_1 = \begin{bmatrix} 0.05 \\ -0.05 \end{bmatrix}, \qquad E_{a1} = \begin{bmatrix} -0.11 \\ 0.03 \end{bmatrix}^T, \\ E_{ad1} = \begin{bmatrix} 0.03 \\ -0.1 \end{bmatrix}^T, \qquad E_{b1} = \begin{bmatrix} 0.02 \\ -0.01 \end{bmatrix}^T, \\ A_2 = \begin{bmatrix} 1.2 & -1.3 \\ 1.2 & -0.8 \end{bmatrix}, \qquad A_{d2} = \begin{bmatrix} 0 & 0.3 \\ 0.1 & 0 \end{bmatrix}, \\ B_2 = \begin{bmatrix} -0.1 & 0 \\ 0 & 0.3 \end{bmatrix}, \qquad C_2 = \begin{bmatrix} 0.1 & -0.18 \end{bmatrix}, \\ D_2 = \begin{bmatrix} 0.02 \\ -0.01 \end{bmatrix}, \qquad G_2 = 0.05, \\ H_2 = \begin{bmatrix} 0.07 \\ -0.1 \end{bmatrix}, \qquad E_{a2} = \begin{bmatrix} 0.06 \\ -0.13 \end{bmatrix}^T, \\ E_{ad2} = \begin{bmatrix} 0.01 \\ -0.03 \end{bmatrix}^T, \qquad E_{b2} = \begin{bmatrix} -0.24 \\ 0.01 \end{bmatrix}^T, \\ F_1(k) = F_2(k) = \sin(k). \end{gathered} \tag{56}$$

Choosing $\overline{\tau} = 1$, $\underline{\tau} = 0$, $\alpha = 0.9$, $\gamma = 2$, and $T = 0.25$ and solving (53) in Theorem 11, we obtain

$$\begin{gathered} X_1 = \begin{bmatrix} 48.9936 & 28.9063 \\ 28.9063 & 57.2489 \end{bmatrix}, \\ Q_1 = \begin{bmatrix} 28.3482 & 16.5940 \\ 16.5940 & 39.3879 \end{bmatrix}, \\ X_2 = \begin{bmatrix} 7.7646 & 12.2103 \\ 12.2103 & 35.4768 \end{bmatrix}, \\ Q_2 = \begin{bmatrix} 4.3523 & 9.9187 \\ 9.9187 & 35.9927 \end{bmatrix}, \end{gathered} \tag{57}$$

and the state feedback gain matrices are as follows:

$$\begin{gathered} K_1 = \begin{bmatrix} -25.2606 & 14.3786 \\ -11.3117 & 7.9375 \end{bmatrix}, \\ K_2 = \begin{bmatrix} 24.9665 & -8.2606 \\ 16.0614 & -12.3235 \end{bmatrix}. \end{gathered} \tag{58}$$

According to (14), we have $\mu = 6.5134$. Then, from (13), we get $\tau_a > \tau_a^* = 7.3516$. Choosing $\tau_a = 7.5$, the simulation results are shown in Figures 1 and 2, where the initial conditions are $x(0) = \begin{bmatrix} -1 & 1 \end{bmatrix}^T$, $x(k) = \begin{bmatrix} 0 & 0 \end{bmatrix}^T$, and $k \in [-1, 0)$ and the exogenous disturbance input is $w(k) = 0.05e^{-0.5k}$. The switching signal with average dwell time $\tau_a = 7.5$ is shown in

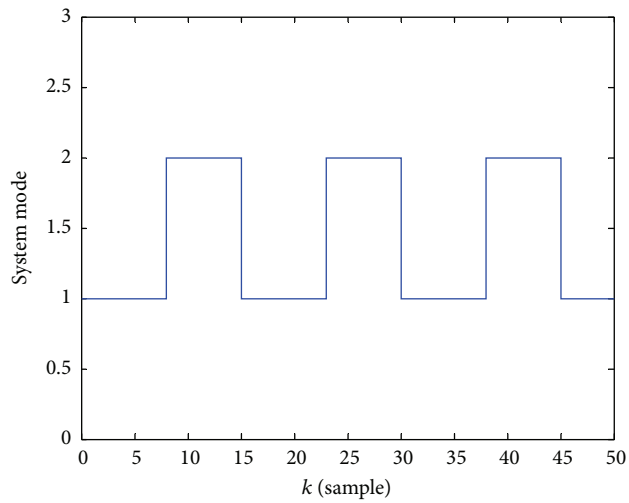

Figure 1: Switching signal.

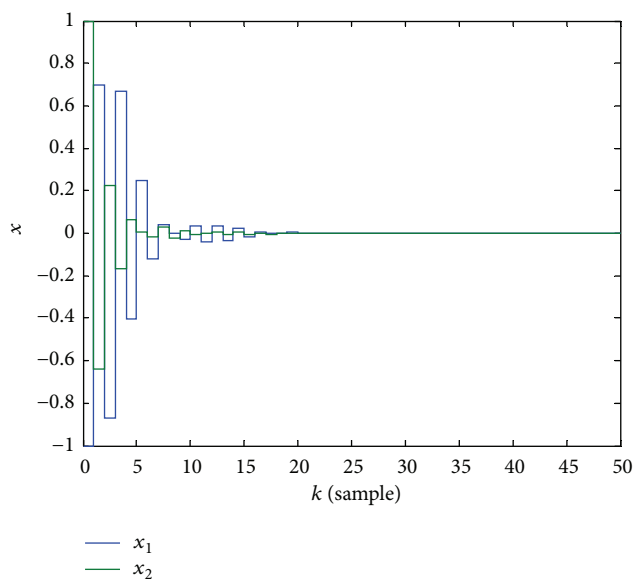

Figure 2: State responses of the closed-loop system.

Figure 1 and the state responses of the corresponding closed-loop system are given in Figure 2.

From Figures 1 and 2, it is easy to see that the designed controller can guarantee that the resulting closed-loop system is exponentially stable. This demonstrates the effectiveness of the proposed method.

5. Conclusions

In this paper, the robust stability and H_∞ controller design problems for time-varying delay switched system using delta operator approach have been investigated. By using the average dwell time approach and constructing a Lyapunov-Krasovskii functional candidate, sufficient conditions for the existence of a state feedback H_∞ controller are presented. Finally, a numerical example is given to illustrate the feasibility of the proposed approach. In our future work, we will study the problem of robust H_∞ filtering for delta operator switched systems with uncertainties and time-varying delays.

Conflict of Interests

The authors declare that there is no conflict of interests regarding the publication of this paper.

Acknowledgment

This work was supported by the National Natural Science Foundation of China under Grant no. 61273120.

References

[1] W. Zhang, M. S. Branicky, and S. M. Phillips, "Stability of networked control systems," *IEEE Control Systems Magazine*, vol. 21, no. 1, pp. 84–97, 2001.

[2] P. Varaiya, "Smart cars on smart roads: problems of control," *IEEE Transactions on Automatic Control*, vol. 38, no. 2, pp. 195–207, 1993.

[3] Y. B. Wang, Z. J. Han, and Z. W. Luo, "Opening study of intelligent transportation systems," *Control and Decision*, vol. 12, no. 1, pp. 403–407, 1997.

[4] B. Lennartson, M. Tittus, B. Egardt, and S. Pettersson, "Hybrid systems in process control," *IEEE Control Systems Magazine*, vol. 16, no. 5, pp. 45–56, 1996.

[5] B. E. Bishop and M. W. Spong, "Control of redundant manipulators using logic-based switching," in *Proceedings of the 36th IEEE Conference on Decision and Control (CDC '98)*, pp. 16–18, 1998.

[6] N. H. El-Farra and P. D. Christofides, "Coordinating feedback and switching for control of spatially distributed processes," *Computers and Chemical Engineering*, vol. 28, no. 1-2, pp. 111–128, 2004.

[7] J. P. Hespanha, "Uniform stability of switched linear systems: extensions of LaSalle's invariance principle," *IEEE Transactions on Automatic Control*, vol. 49, no. 4, pp. 470–482, 2004.

[8] J. P. Hespanha, D. Liberzon, D. Angeli, and E. D. Sontag, "Nonlinear norm-observability notions and stability of switched systems," *IEEE Transactions on Automatic Control*, vol. 50, no. 2, pp. 154–168, 2005.

[9] C. de Persis, R. de Santis, and A. S. Morse, "Nonlinear switched systems with state dependent dwell-time," in *Proceedings of the IEEE Conference on Decision and Control*, pp. 4419–4424, 2002.

[10] Z. Xiang and R. Wang, "Robust L_∞ reliable control for uncertain nonlinear switched systems with time delay," *Applied Mathematics and Computation*, vol. 210, no. 1, pp. 202–210, 2009.

[11] R. H. Middleton and G. C. Goodwin, *Digital Control and Estimation: A Unified Approach*, Prentice-Hall, New Jersey, NJ, USA, 1990.

[12] D. Zhang and C. Yang, "Delta-operator theory for feedback control system—a survey," *Control Theory & Applications*, vol. 15, no. 2, pp. 153–160, 1998.

[13] Z. Xiang, Q. Chen, and W. Hu, "Robust H_∞ control of interval systems using the delta operator," in *Proceedings of the 4th World Congress on Intelligent Control and Automation*, pp. 1731–1733, 2002.

[14] M. Salgado, R. Middleton, and G. C. Goodwin, "Connection between continuous and discrete Riccati equations with applications to Kalman filtering," *IEE Proceedings D*, vol. 135, no. 1, pp. 28–34, 1988.

[15] J. Wu, S. Chen, G. Li, R. H. Istepanian, and J. Chu, "Shift and delta operator realizations for digital controllers with finite word length considerations," *IEE Proceedings D*, vol. 147, no. 6, pp. 664–672, 2000.

[16] C. B. Soh, "Robust stability of discrete-time systems using delta operators," *IEEE Transactions on Automatic Control*, vol. 36, no. 3, pp. 377–380, 1991.

[17] R. Vijayan, H. V. Poor, J. B. Moore, and G. C. Goodwin, "A Levinson-type algorithm for modeling fast-sampled data," *IEEE Transactions on Automatic Control*, vol. 36, no. 3, pp. 314–321, 1991.

[18] S. Chen, R. H. Istepanian, J. Wu, and J. Chu, "Comparative study on optimizing closed-loop stability bounds of finite-precision controller structures with shift and delta operators," *Systems & Control Letters*, vol. 40, no. 3, pp. 153–163, 2000.

[19] W. Ebert, "Optimal filtered predictive control a delta operator approach," *Systems & Control Letters*, vol. 42, no. 1, pp. 69–80, 2001.

[20] Z. Xiang and R. Wang, "Robust H_∞ control for a class of uncertain switched systems using delta operator," *Transactions of the Institute of Measurement and Control*, vol. 32, no. 3, pp. 331–344, 2010.

[21] J. Gao, Z. Xiang, and G. Chen, "Study on robust control for uncertain switched systems using delta operator," *Computer Simulation*, vol. 29, no. 10, pp. 189–195, 2012.

[22] J.-P. Richard, "Time-delay systems: an overview of some recent advances and open problems," *Automatica*, vol. 39, no. 10, pp. 1667–1694, 2003.

[23] J. Qiu, Y. Xia, H. Yang, and J. Zhang, "Robust stabilisation for a class of discrete-time systems with time-varying delays via delta operators," *IET Control Theory & Applications*, vol. 2, no. 1, pp. 87–93, 2008.

[24] R. Wang, J. Xing, P. Wang, and Q. Yang, "Non-fragile observer design for nonlinear time delay systems using delta operator," in *Proceedings of the UKACC International Conference on Control (CONTROL '12)*, pp. 387–393, 2012.

[25] Z. Zhong, G. Sun, H. R. Karimi, and J. Qiu, "Stability analysis and stabilization of T-S fuzzy delta operator systems with time-varying delay via an input-output approach," *Mathematical Problems in Engineering*, vol. 2013, Article ID 913234, 14 pages, 2013.

[26] T. H. Lee, Z.-G. Wu, and J. H. Park, "Synchronization of a complex dynamical network with coupling time-varying delays via sampled-data control," *Applied Mathematics and Computation*, vol. 219, no. 3, pp. 1354–1366, 2012.

[27] H. Yang, Y. Xia, J. Qiu, and J. Zhang, "Filtering for a class of discrete-time systems with time-delays via delta operator approach," *International Journal of Systems Science*, vol. 41, no. 4, pp. 423–433, 2010.

[28] K. Premaratne, R. Salvi, N. R. Habib, and J. P. LeGall, "Delta-operator formulated discrete-time approximations of continuous-time systems," *IEEE Transactions on Automatic Control*, vol. 39, no. 3, pp. 581–585, 1994.

[29] G. Wei, G. Feng, and Z. Wang, "Robust H_∞ control for discrete-time fuzzy systems with infinite-distributed delays," *IEEE Transactions on Fuzzy Systems*, vol. 17, no. 1, pp. 224–232, 2009.

[30] H. Zhang, Y. Shi, and B. Mu, "Optimal H_∞-based linear-quadratic regulator tracking control for discrete-time Takagi-Sugeno fuzzy systems with preview actions," *Journal of Dynamic Systems, Measurement, and Control*, vol. 135, no. 4, Article ID 044501, 5 pages, 2013.

[31] H. Zhang, J. Wang, and Y. Shi, "Robust H_∞ sliding-mode control for Markovian jump systems subject to intermittent observations and partially known transition probabilities," *Systems & Control Letters*, vol. 62, no. 12, pp. 1114–1124, 2013.

[32] H. Zhang, Y. Shi, and M. Liu, "H_∞ step tracking control for networked discrete-time nonlinear systems with integral and predictive actions," *IEEE Transactions on Industrial Informatics*, vol. 9, no. 1, pp. 337–345, 2013.

[33] Z. Shuai, H. Zhang, J. Wang, J. Li, and M. Ouyang, "Combined AFS and DYC control of four-wheel-Independent-drive electric vehicles over CAN network with time-varying delays," *IEEE Transactions on Vehicular Technology*, no. 99, 2013.

[34] E. G. Collins Jr. and T. Song, "A delta operator approach to discrete-time H_∞ control," *International Journal of Control*, vol. 72, no. 4, pp. 315–320, 1999.

[35] B. Lennartson, R. Middleton, A.-K. Christiansson, and T. McKelvey, "Low order sampled data H_∞ control using the delta operator and LMIs," in *Proceedings of the 43th IEEE Conference on Decision and Control (CDC '04)*, vol. 4, pp. 4479–4484, 2004.

[36] X.-M. Sun, W. Wang, G.-P. Liu, and J. Zhao, "Stability analysis for linear switched systems with time-varying delay," *IEEE Transactions on Systems, Man, and Cybernetics B*, vol. 38, no. 2, pp. 528–533, 2008.

[37] J. P. Hespanha and A. S. Morse, "Stability of switched systems with average dwell-time," in *Proceedings of the 38th IEEE Conference on Decision and Control (CDC '99)*, pp. 2655–2660, 1999.

Hindawi Publishing Corporation
Mathematical Problems in Engineering
Volume 2013, Article ID 191574, 9 pages
http://dx.doi.org/10.1155/2013/191574

Research Article

Research on Shifting Control Method of Positive Independent Mechanical Split Path Transmission for the Starting Gear

JunQiang Xi,[1] JianMin Meng,[2] and HuiYan Chen[1]

[1] *Science and Technology on Vehicle Transmission Laboratory, Beijing Institute of Technology, Beijing 100081, China*
[2] *Patent Examination Cooperation Center of the Patent Office, SIPO, Beijing 100081, China*

Correspondence should be addressed to JunQiang Xi; xijunqiang@bit.edu.cn

Received 24 October 2013; Revised 21 November 2013; Accepted 21 November 2013

Academic Editor: Hui Zhang

To realize a smooth and quick shift of the positive independent mechanical split path transmission (PIMSPT) equipped with automatic shifting control system (ASCS), the research on the feasibility of improving shift quality by dynamic and cooperative controlling engine, steering clutches, and brakes has been conducted. The shifting control method suited to starting gear of PIMSPT has been proposed. The control method is based on control parameters, such as the driving shaft speed and its derivative. The control laws of steering clutches and brakes are presented during each gear and stage of shifting. Bench and road test results show that the proposed shifting control method can not only shorten the shift time, but also decrease the jerk of shifting effectively.

1. Introduction

During the straight driving process of a vehicle equipped with PIMSPT, power from the engine is transmitted through the shifting mechanism and steering mechanism. The splitting power is converged by planet gear trains on each side of the transmission and then outputs to driving wheels. Thus, the shifting mechanism only transmits part of the engine torque, which means that the torque transmitted by the shifting mechanism can be decreased. As a result, the power density of the transmission can be improved. So, the PIMSPT is widely used in many kinds of track vehicles in the world [1–3].

Figure 1 shows a schematic diagram of a PIMSPT and its power transmission path. We can see that the PIMSPT shares the same shifting components with the fixed shaft transmission, although its structure is very different from the latter. Because of the difference of the structures, both the driving shaft and the countershaft of the PIMSPT are rotating when the vehicle stops, which leads to longer shifting time of starting gear and causes more shifting noise. This paper takes the PIMSPT shown in Figure 1 as a research subject and conducts research on the shifting control method for starting gear.

2. Kinematics and Dynamics Analysis

2.1. Dynamic Model of Neutral Position. Assuming that the gear shift of transmission is in the neutral position before launching. First, we should separate the main clutch completely. The planetary carriers are static now. The driving shaft and the countershaft of the transmission are decelerated by the resistant torque produced by the oil. Considering the structure of the PIMSPT, we can set up the kinematic model and the dynamic model of the transmission in the condition that the steering clutches or steering brakes are engaged, according to their status on both sides.

2.1.1. Analysis of Steering Clutches Engagement. When the clutches on both sides are engaged, respectively, the counter shaft, steering clutches, and sun gear shaft can be regarded as a whole. And we can assume that the rotational inertia of counter shaft can be added to the sun gear shaft. The motion state of each transmission component can be seen in Figures 2 and 3.

In Figures 2 and 3, T_L, T_R represent the resistance imposed on each side of the planet carrier, respectively, and are caused

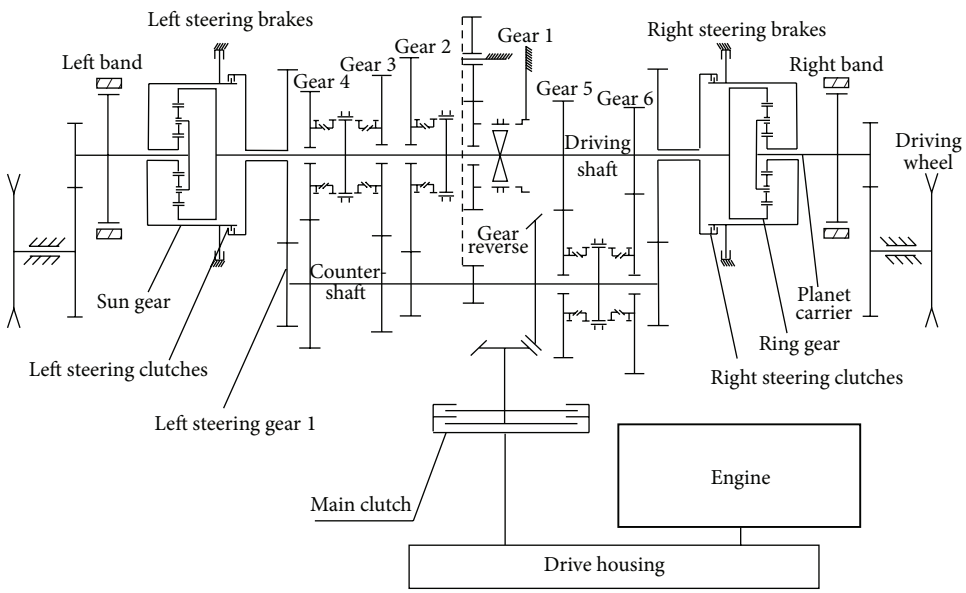

Figure 1: The structure of the PIMSPT and the transmit path of the power.

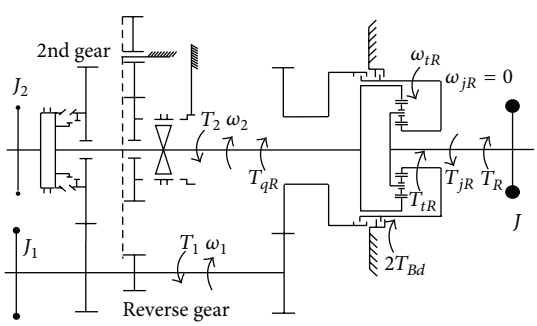

Figure 2: The diagram of dynamics analysis of the components of the gear box in the condition of the steering clutches engaged.

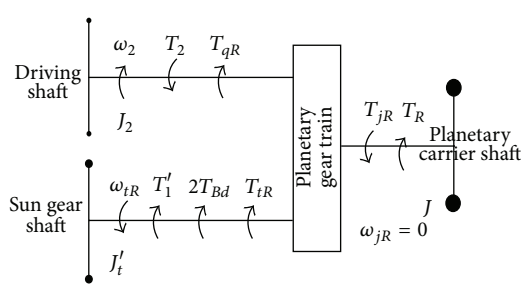

Figure 3: The diagram of equivalent kinematics and dynamics analysis of the components of the gear box in the condition of the steering clutches engaged.

by road resistance, N·m; ω_1, ω_2 represent the angular speed of the counter shaft and the driving shaft, respectively, rad/s; $\omega_{tL}\omega_{tR}$ represent the angular speed of the sun gears, rad/s; ω_{zL}, ω_{zR} represent the angular speed of the steering clutches, rad/s; J_1, J_2 represent the sum of the rotational inertia of the counter shaft and the driving shaft with some rotating components and the equivalent rotational inertia of the free gears on their own shaft, respectively, kg·m^2; J represents the rotational inertia converted to the planet carrier shaft due to the mass of vehicle, kg·m^2. J_t' represents the rotational inertia converted to the sun gear shaft by the counter shaft, $J_t' = i_z^2 J_1 + 2J_t + 2J_c$, kg·m^2, where J_t and J_c represent the rotational inertia of the sun gears and the steering clutch, respectively, kg·m^2. Because J_1, J_2 are much greater than J_t, J_c, we can assume that $J_t' = i_z^2 J_1$; T_1 and T_2 represent the resistance moment of the counter shaft and the driving shaft, respectively, N·m; T_{tR}, T_{qR}, and T_{jR} represent, respectively the resistance moment on the sun gear shaft, driving shaft, and the planet carrier forced by the planet gears, N·m; T_{Bd} represents the resistance moment on the sun gear shaft forced by the steering brakes of a single side, N·m; T_1' represents the resistance moment on the sun gear shaft by T_1, $T_1' = i_z T_1$, N·m; T_d represents the towing torque when the multiplate wet clutch is separating, N·m.

Establishing the equivalent kinetics equations of the sun gear shaft and the driving shaft according to the force analysis of Figure 3:

$$\begin{aligned} J_t' \dot{\omega}_{tR} &= T_{tR} + T_1' + 2T_{Bd}, \\ J_2 \dot{\omega}_2 &= T_{qR} - T_2. \end{aligned} \tag{1}$$

In (1), $\dot{\omega}_{tR}$, $\dot{\omega}_2$ represent the angular acceleration of the sun gear shaft and the driving shaft, respectively, rad/s^2. And $\dot{\omega}_R = \dot{\omega}_1 / i_z$, $\dot{\omega}_1$ represents the angular acceleration of the counter shaft, rad/s^2.

The speed and resistance moment of a single planetary gear set satisfy the following equations:

$$\begin{aligned} \omega_t + k\omega_q &= (1+k)\,\omega_j, \\ \dot{\omega}_t + k\dot{\omega}_q &= (1+k)\,\dot{\omega}_j, \\ T_t : T_q : T_j &= 1 : k : (1+k)\,. \end{aligned} \tag{2}$$

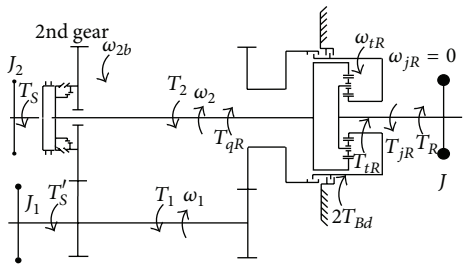

Figure 4: The diagram of kinematics and dynamics analysis of the components of the gear box before launching in the condition of the steering brakes engaged.

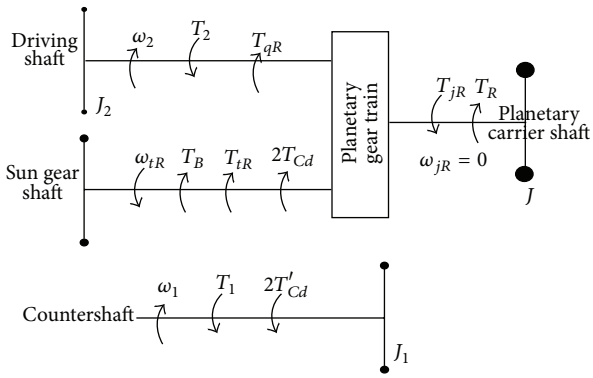

Figure 5: The diagram of the equivalent kinematics and the dynamics analysis of the components of the gear box before launching in the condition of the steering brakes engaged.

In (2), ω_t, ω_q, and ω_j represent the angular speed of the sun gear shaft, ring shaft, and the planet carrier, respectively, rad/s; $\dot{\omega}_t$, $\dot{\omega}_q$, $\dot{\omega}_j$ represent the angular acceleration of them, rad/s^2; and T_t, T_q, and T_j represent the resistance moment on them, N·m.

When $\omega_j = 0$, $\dot{\omega}_j = 0$, we can calculate the angular acceleration of the counter shaft and the driving shaft according to (1) and (2):

$$\begin{bmatrix} \dot{\omega}_1 \\ \dot{\omega}_2 \end{bmatrix} = \frac{-1}{J_2 + k^2 i_z^2 J_1} \begin{bmatrix} (ki_z)^2 & ki_z & 2k^2 i_z \\ ki_z & 1 & 2k \end{bmatrix} \begin{bmatrix} T_1 \\ T_2 \\ T_{Bd} \end{bmatrix}, \quad (3)$$

$$T_{jR} = \frac{1+k}{J_2 + k^2 i_z^2 J_1} \begin{bmatrix} -i_z J_2 & ki_z^2 J_1 & -2J_2 \end{bmatrix} \begin{bmatrix} T_1 \\ T_2 \\ T_{Bd} \end{bmatrix}. \quad (4)$$

2.1.2. Analysis of Steering Brakes Combination. When the steering brakes of both sides are engaged and the steering clutches of both sides are released, the counter shaft and the sun gears move independently. The motion state and stress state of each component are shown in Figures 4 and 5.

In Figures 4 and 5, T_{Cd} represents the towing torque of the steering clutches, N·m; T'_{Cd} represents the equivalent torque on the counter shaft by T_{Cd}, $T'_{Cd} = T_{Cd}/i_z$, N·m. T_B represents the braking torque on the sun gear shaft forced by the steering brakes, N·m.

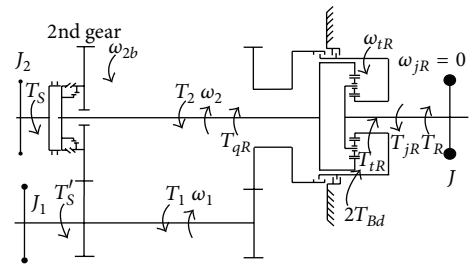

Figure 6: The diagram of the kinematics and dynamics analysis of the components of the gear box in the synchronizing stage of 2nd gear in the condition of the steering brakes being engaged.

Establishing the kinetics equations of the counter shaft, the driving shaft, and the sun gear shaft according to the force analysis of Figure 5,

$$\begin{aligned} J_1 \dot{\omega}_1 &= -T_1 - 2T'_{Cd}, \\ J_t \dot{\omega}_{tR} &= T_{tR} + T_B + 2T_{Cd}, \\ J_2 \dot{\omega}_2 &= T_{qR} - T_2. \end{aligned} \quad (5)$$

When $\omega_j = 0$, $\dot{\omega}_j = 0$, we can calculate the following results according to (2) and (5):

$$\begin{bmatrix} \dot{\omega}_1 \\ \dot{\omega}_2 \end{bmatrix} = -\begin{bmatrix} \dfrac{1}{J_1} & 0 & 0 & \dfrac{2}{i_z J_1} \\ 0 & \dfrac{1}{(J_2 + k^2 J_t)} & \dfrac{k}{(J_2 + k^2 J_t)} & \dfrac{2k}{(J_2 + k^2 J_t)} \end{bmatrix} \times \begin{bmatrix} T_1 \\ T_2 \\ T_B \\ T_{Cd} \end{bmatrix}, \quad (6)$$

$$T_{jR} = \frac{1+k}{J_2 + k^2 J_t} \begin{bmatrix} kJ_t & -J_2 & -2J_2 \end{bmatrix} \begin{bmatrix} T_2 \\ T_B \\ T_{Cd} \end{bmatrix}. \quad (7)$$

2.1.3. Analysis Conclusion. By comparing (3) with (6), we know that the angular speeds of the counter shaft and the driving shaft decrease faster when the main clutch is released and the steering brakes are engaged.

2.2. Dynamic Model of Shifting Process. Taking the shifting process of 2nd gear as an example, synchronizer is used during this shifting process. According to Figure 6, we know that when the vehicle is launching with 2nd gear, the synchronizer rotates in opposite direction to the 2nd gear and the angular speeds are ω_2 and $\omega_{2b} = \omega_1/i_2$, respectively. When they reach the same speed, the angular speed difference value of the synchronizer and the 2nd gear should be zero.

We divide the shifting process into two stages: synchronizer gap elimination and synchronizer working. And then we analyze the conditions of the steering clutches and the steering brakes of both sides when they are engaged. We have analyzed the former condition in Section 2.1.

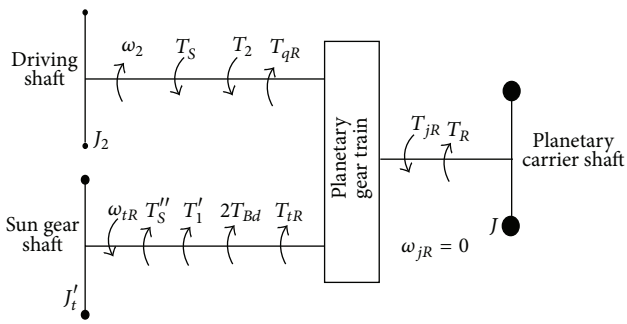

Figure 7: The diagram of the equivalent kinematics and dynamics analysis of the components of the gear box in the synchronizing stage of 2nd gear in the condition of steering brakes being engaged.

2.2.1. Analysis of Shifting Process in the Condition of Steering Clutches Engaged. Under the action of shifting force, there are equal and opposite torque on the friction cone of the synchronizer and the driving gear. The synchronizing torque on the driven gear in 2nd gear is transmitted to the counter shaft by the constant mesh gear of 2nd gear. The motion state and stress state of each component in this condition can be seen in Figure 6.

In Figures 6 and 7, T_s represents the torque on the synchronizer, N·m; T_s' represents the torque transmitted to the counter shaft, $T_s' = T_s/i_2$, N·m; T_s'' represents the equivalent torque on the sun gear shaft by T_s, $T_s'' = T_s i_z/i_2$, N·m. Other parameters have the same meaning as mentioned previously.

Establishing the kinetics equations of the sun gear shaft, driving shaft, and the sun gear shaft according to the force analysis of Figure 7,

$$J_t'\dot{\omega}_{tR} = T_{tR} + T_1' + 2T_{Bd} + T_s'', \tag{8}$$

$$J_2\dot{\omega}_2 = T_{qR} - T_2 - T_s. \tag{9}$$

According to (8) and (9), we can calculate the angular accelerations ($\dot{\omega}_{1t2}$, $\dot{\omega}_{2t2}$) of the counter shaft and the driving shaft during synchronization:

$$\begin{bmatrix} \dot{\omega}_{1t2} \\ \dot{\omega}_{2t2} \end{bmatrix} = \frac{-1}{J_2 + k^2 i_z^2 J_1} \times \begin{bmatrix} (ki_z)^2 & ki_z & k^2 i_z & ki_z + \dfrac{(ki_z)^2}{i_2} \\ ki_z & 1 & k & 1 + \dfrac{ki_z}{i_2} \end{bmatrix} \begin{bmatrix} T_1 \\ T_2 \\ 2T_{Bd} \\ T_s \end{bmatrix}. \tag{10}$$

When the angular acceleration is constant, the relation of the angular speed and the angular acceleration is as follows:

$$\dot{\omega} = \frac{(\omega_e - \omega_b)}{t}. \tag{11}$$

In (11), t represents the action time, s; ω_b represents the angular speed when the angular acceleration has a certain value, rad/s; and ω_e represents the angular speed when the angular acceleration stays zero, rad/s.

If ω_{1t0}, ω_{2t0} represent the angular speeds of the counter shaft and the driving shaft in t_0, then we can calculate the angular speeds (ω_{1t1}, ω_{2t1}) of them when the synchronization process begins.

According to (9), (10), and (11), the time of the stage before the synchronization process can be calculated, $t_{01} = t_1 - t_0$, $t_{12} = t_2 - t_1$. And we can also get the functional relationship of the synchronizing torque, the angular speeds of the counter shaft, and the driving shaft when synchronization begins and the synchronization time is

$$t_{01} = \begin{cases} \dfrac{(\omega_{1t0} - \omega_{1t1})\left(J_2 + k^2 i_z^2 J_1\right)}{\left[(ki_z)^2 T_1 + ki_z T_2 + 2k^2 i_z T_{Bd}\right]}, \\ \dfrac{(\omega_{2t0} - \omega_{2t1})\left(J_2 + k^2 i_z^2 J_1\right)}{(ki_z T_1 + T_2 + 2kT_{Bd})}, \end{cases} \tag{12}$$

$$t_{12} = \begin{cases} \omega_{1t1}\left(k^2 i_z^2 J_1 + J_2\right) \\ \quad \times \left[(ki_z)^2 T_1 + ki_z T_2 + 2k^2 i_z T_{Bd} \right. \\ \quad \left. + \left(ki_z + \dfrac{(ki_z)^2}{i_2}\right) T_s\right]^{-1}, \\ \dfrac{\omega_{2t1}\left(k^2 i_z^2 J_1 + J_2\right)}{\left[ki_z T_1 + T_2 + 2kT_{Bd} + (1 + ki_z/i_2) T_s\right]}, \end{cases} \tag{13}$$

$$T_s = \begin{cases} \dfrac{\left(k^2 i_z^2 J_1 + J_2\right)\omega_{1t1}}{\left[ki_z + (ki_z)^2/i_2\right] t_{12}} \\ \quad - \dfrac{1}{ki_z + (ki_z)^2/i_2} \begin{bmatrix} (ki_z)^2 & ki_z & 2k^2 i_z \end{bmatrix} \begin{bmatrix} T_1 \\ T_2 \\ T_{Bd} \end{bmatrix}, \\ \dfrac{\left(k^2 i_z^2 J_1 + J_2\right)\omega_{2t1}}{(1 + ki_z/i_2) t_{12}} \\ \quad - \dfrac{1}{(1 + ki_z/i_2)} \begin{bmatrix} k^2 i_z & 1 & 2k \end{bmatrix} \begin{bmatrix} T_1 \\ T_2 \\ T_{Bd} \end{bmatrix}. \end{cases} \tag{14}$$

Based on energy conservation law, the friction work produced in the process of synchronization can be calculated by the following:

$$W_s = \frac{1}{2} J_1 \omega_{1t1}^2 + \frac{1}{2} J_2 \omega_{2t1}^2 - (T_1 \omega_{1t1} + T_2 \omega_{2t1}) - \int_{t1}^{t2} 2T_{Bd}\omega_{1t1} dt. \tag{15}$$

In this equation, W_s represents the friction work of the synchronizer, J.

From (12), we know that the friction work of the synchronizer is directly proportional to the angular speed of the counter shaft and the driving shaft when the synchronization begins. Thus, the friction work can be reduced by reducing ω_{1t1} and ω_{2t1}. When the steering clutches of both sides are

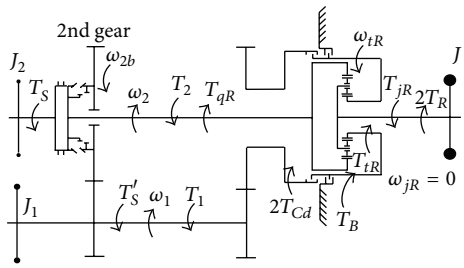

Figure 8: The diagram of the kinematics and dynamics analysis of the components of the gear box.

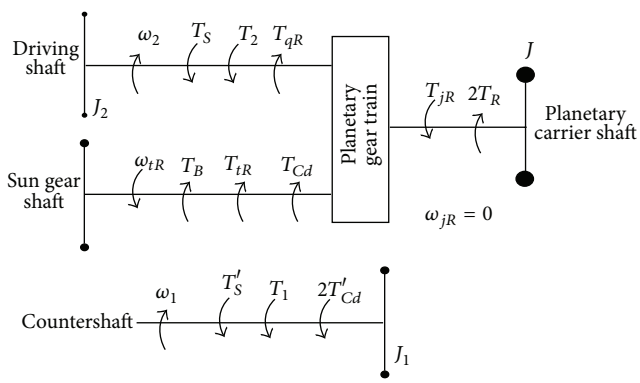

Figure 9: The diagram of the equivalent kinematics and dynamics analysis of the components of the gear box.

engaged, the synchronization torque and the slipping work can be reduced by extending the time before synchronization, but it will cause a longer shifting time.

2.2.2. Analysis of Shifting Process When Steering Brakes in Condition of Combination. When the steering brakes of both sides are engaged, the transitive relation between the counter shaft, and the sun gear is cut off. The motion state and stress state of each transmission component can be seen in Figure 8.

Establishing the kinetics equations of the counter shaft, the sun gear shaft and the driving shaft according to the force analysis of Figures 8 and 9, the angular speeds $(\dot{\omega}_{1t2}, \dot{\omega}_{2t2})$ of the counter shaft, and the driving shaft in this stage are calculated:

$$\begin{bmatrix} \dot{\omega}_{1t2} \\ \dot{\omega}_{2t2} \end{bmatrix} = -\begin{bmatrix} \frac{1}{J_1} & 0 & 0 & \frac{2}{i_z J_1} & \frac{1}{i_2 J_1} \\ 0 & \frac{1}{(J_2+k^2J_t)} & \frac{k}{(J_2+k^2J_t)} & \frac{2k}{(J_2+k^2J_t)} & \frac{1}{(J_2+k^2J_t)} \end{bmatrix} \times \begin{bmatrix} T_1 \\ T_2 \\ T_B \\ T_{Cd} \\ T_s \end{bmatrix}. \tag{16}$$

When the steering brakes are engaged, the synchronization time (t_{01}, t_{12}) of the beginning and ending stage can be calculated in a similar way. And we can also obtain the functional relationship of the synchronizing torque, the angular speed of the counter shaft and the driving shaft when the synchronization begins:

$$t_{01} = \begin{cases} \dfrac{(\omega_{1t0} - \omega_{1t1})}{(T_1/J_1 + 2T_{Cd}/i_z J_1)}, \\ \dfrac{(\omega_{2t0} - \omega_{2t1})\left(J_2 + k^2 J_t\right)}{(T_2 + kT_B + 2kT_{Cd})}, \end{cases} \tag{17}$$

$$t_{12} = \begin{cases} \dfrac{\omega_{1t1}}{[T_1/J_1 + 2T_{Cd}/(i_z J_1) + T_s/(i_2 J_1)]}, \\ \dfrac{\omega_{2t1}\left(J_2 + k^2 J_t\right)}{(T_2 + kT_B + 2kT_{Cd} + T_s)}, \end{cases} \tag{18}$$

$$T_s = \begin{cases} \dfrac{i_2 J_1 \omega_{1t1}}{t_{12}} - \begin{bmatrix} i_2 & \dfrac{2i_2}{i_z} \end{bmatrix} \begin{bmatrix} T_1 \\ T_{Cd} \end{bmatrix}, \\ \dfrac{\omega_{2t1}\left(J_2 + k^2 J_t\right)}{t_{12}} - \begin{bmatrix} 1 & k & 2k \end{bmatrix} \begin{bmatrix} T_2 \\ T_B \\ T_{Cd} \end{bmatrix}. \end{cases} \tag{19}$$

Based on energy conservation law, the fraction work produced in the process of synchronization can be calculated:

$$W_s = \frac{1}{2} J_1 \omega_{1t1}^2 + \frac{1}{2} J_2 \omega_{2t1}^2 - \left[T_1 \omega_{1t1} + (T_2 + T_B)\,\omega_{2t1}\right] - \int_{t1}^{t2} \left(\frac{2T_{Cd}\omega_{1t1}}{i_z}\right) dt. \tag{20}$$

When the steering brakes are engaged and the steering clutches are in combination condition, the influence on synchronizing torque and slipping work at the beginning of synchronization is the same, which is affected by the counter shaft and driving shaft's angular speeds and the synchronization time.

2.2.3. Comparison and Analysis of the Two Types of Shifting Processes. By comparing (12) with (17), it is obvious that when the angular speed of the counter shaft is the same as the angular speed (ω_{1t1}) of synchronization starting, the steering brakes in the engagement condition takes less time than the steering clutches in the engagement condition. Since $T_B \gg T_1 > T_2$, the angular speed of the driving shaft when the steering brakes are engaged is less than that in t_1, which is equivalent to reducing the speed difference of the initiative and passive parts of the synchronizer.

Comparing (14) with (19), the conclusion that the synchronizing torque in the steering brakes engaged condition is less than that in the steering clutches engaged condition when the synchronous time and the angular speed of the counter shaft are the same can be obtained.

Comparing (15) with (20), it is noticeable that the fraction work in the steering brakes engaged condition is less than that in the steering clutches engaged condition when the initial angular speeds of the counter shaft are the same (ω_{1t1}) in both conditions.

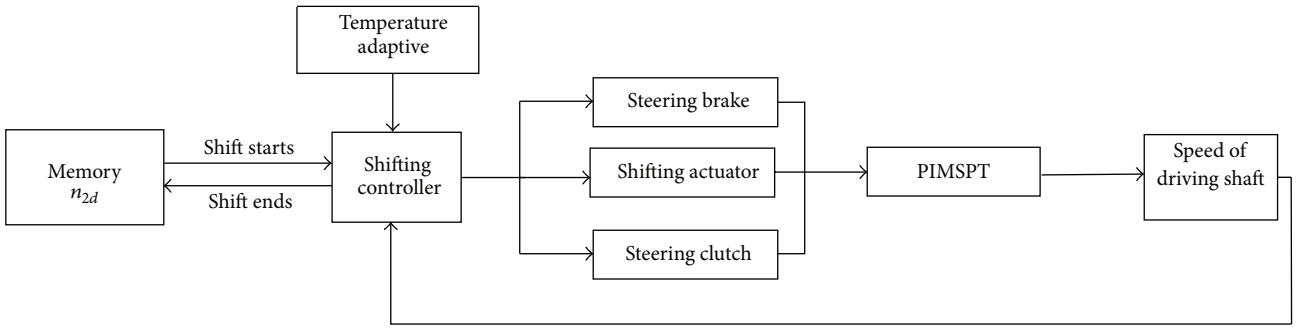

Figure 10: Diagram of control block of shifting into 1st gear.

To sum up, during the shifting process of starting gear, the shift time, the shift force, and the fraction work of the synchronizer can be reduced by breaking the steering brakes of both sides. As a result, the shift quality can be improved.

3. Shifting Control Method for Staring Gear

Aiming at optimizing the shifting control of an automatic mechanical transmission (AMT) used in vehicles, Yang et al. proposed a method of optimal shifting control based on pattern recognition and a learning algorithm [4]. Bóka et al. use a simple mechanical model to define the reduction of the speed difference between the synchronizers in order to obtain a smooth gear shifting [5]. Qi et al. analyze the principle of gear shifting in a hydraulic system and obtain an expert PID control to reduce the shifting vibration and time [6].

But the above researches and other relative researches [7–11] are only validated through simulation and limited to the traditional manual transmission which is not satisfied with the PIMSPT.

According to the analysis of Section 2, the requirements for steering clutch and brake control might be different depending on the different starting gears. So the shifting control strategies of two starting gears are introduced, respectively.

3.1. Shifting Control Strategy of First Gear

3.1.1. Selection of the Control Parameters. By controlling the steering brakes and imposing braking torque to the sun gear, the absolute value of the driving shaft angular velocity can be increased and the time of the driving shaft achieving ideal shifting rotation speed can be shortened. However, if the driving shaft rotation speed is too low during shifting, it may cause the sliding teeth sleeve to stop because the teeth of synchronization loop makes shifting difficult. Therefore, the key of the control process is to choose an appropriate shifting rotation speed of the driving shaft.

The driving shaft rotation speed and rotational acceleration can be used to describe the status and trend of driving shaft quickly and accurately, and they can be obtained by finite difference method. So, the driving shaft rotation speed and its derivative are used as the control parameters in the control process.

3.1.2. The Stage of Steering Brake Control. By imposing braking torque to the sun gear, the driving shaft rotation speed will slow down to an expected value with the control of the steering brakes. The value is inverse proportional to the temperature of transmission oil, and the relationship function can be calibrated by test. Due to the large reserve coefficient of brake, improper control might make the driving shaft rotation speed slow down to zero quickly. To address the issue and get a good performance, the incremental PD control can be adopted in the deceleration process. In the future, some advanced control methods such as robust control [12–14] can be applied.

3.1.3. The Stage of Shifting Control. This phase needs to control steering brakes and remove the braking torque imposed on the sun gear and meanwhile maintain the steering clutch separated. Steering clutch can be controlled to separate completely; at this time the sun gear of confluence planetary row is free. The planet carrier connects with the vehicle, and the degree of freedom of planetary row can be considered as one. When the sliding gear sleeve engages into the tooth, the driving shaft speed n_2 changes directly in response to the disturbance of the sun gear and it will not impact the vehicle. Therefore, steering clutch displacement is selected as a shift operation trigger in this stage.

The whole control process diagram is shown in Figure 10. The control process flow diagram is shown in Figure 11, $lst_{\text{disengage}}$ is the steering clutch displacement, tx is the shifting piston displacement, and $tx_{\min}$ is the piston displacement after shifting to 1st gear.

3.2. Shifting Control Strategy of Second Gear. When the gear shift is in the neutral position, the power flows as follows: by twice outer meshing between splitter gear and planetary gear of confluence planet row, the counter shaft transmits the torque to the driving shaft, making the driving shaft and the counter shaft rotate in the same direction, as shown in Figure 12A. However, after shifting to 2nd gear, the rotation of driving shaft and counter shaft is in the opposite direction, as shown in Figure 12C. The direction of rotation of each axis is as follows: rotation direction of counter shaft ω_1 and the sun gear planetary row ω_t must be the same, but they are the outer meshing and the direction of rotation is different; the steering clutch should be ensured that they are separated.

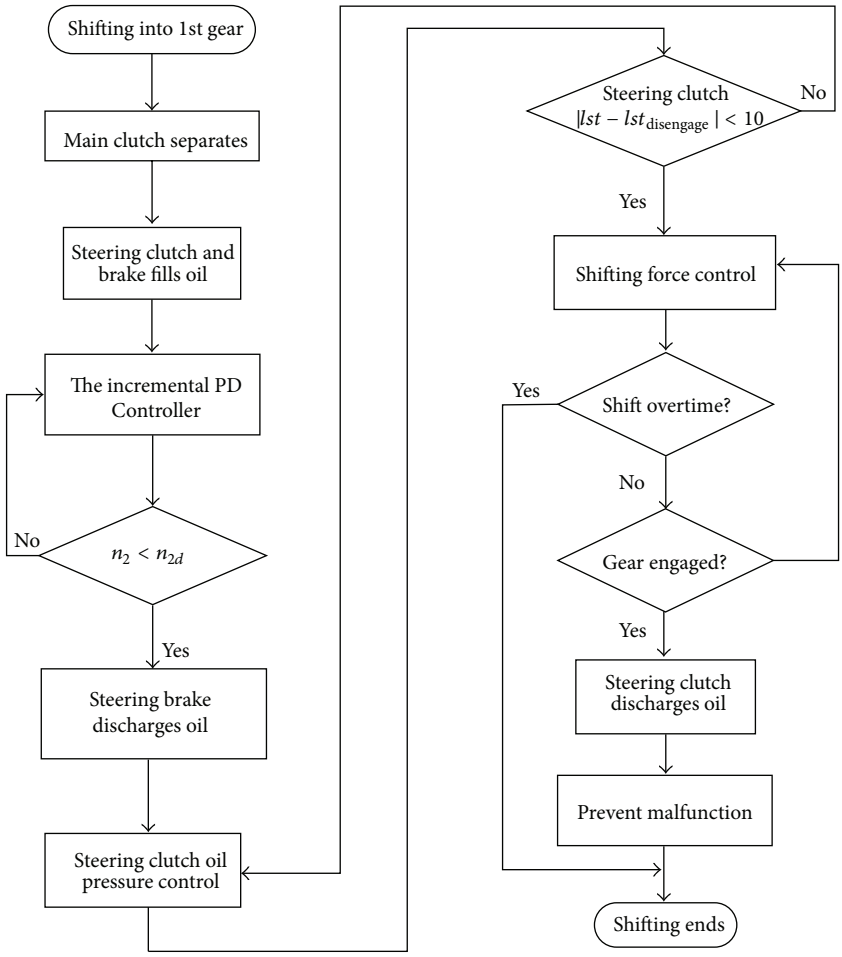

Figure 11: Diagram of control flow of shifting into 1st gear.

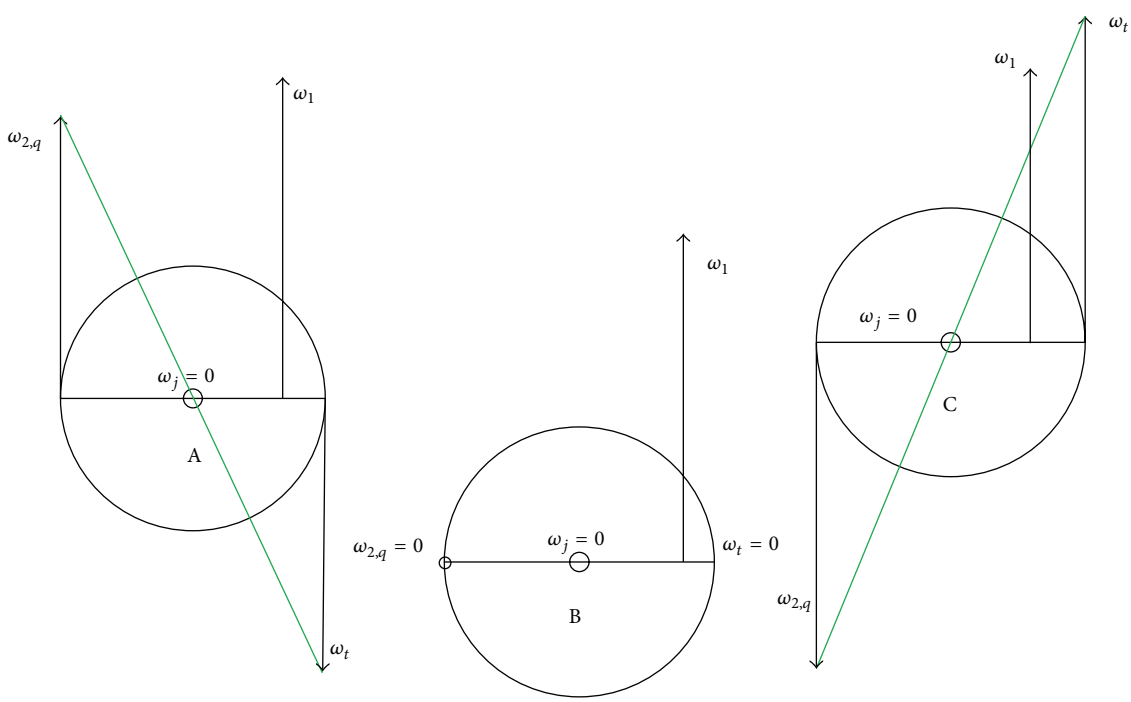

Figure 12: Three components velocity direction of planetary line schematic.

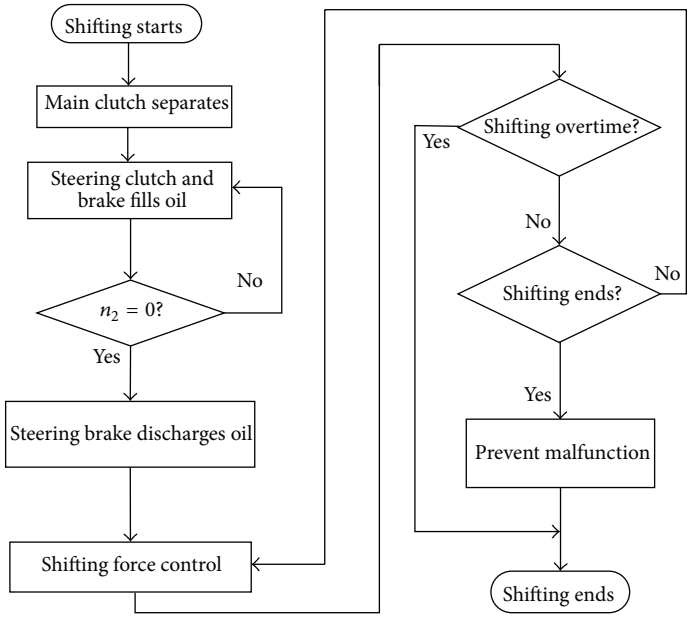

Figure 13: Diagram of control flow of shifting into 2nd gear.

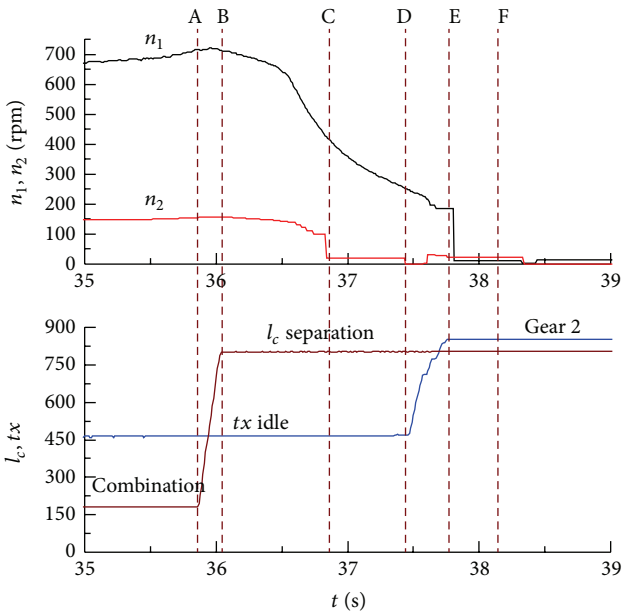

Figure 14: The shifting process with the controlling method.

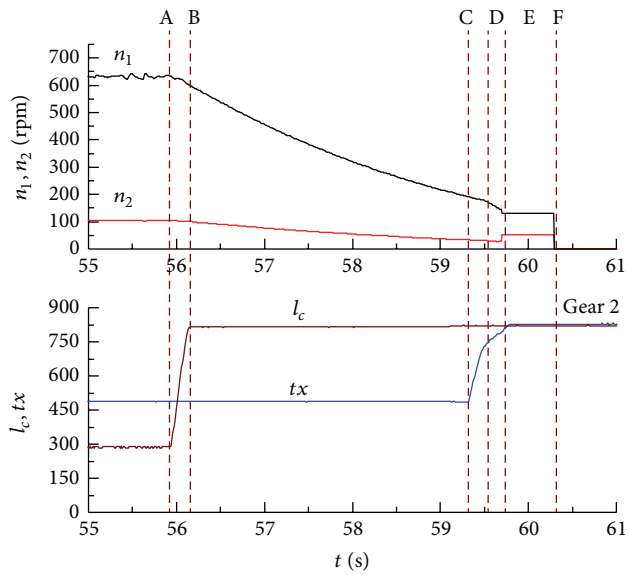

Figure 15: The shifting process without the controlling strategy.

When shifting to 2nd gear, the rotation direction of driving shaft (ring gear wheel) $\omega_{2,q}$ changes from A to C, and it must pass through the state B, as shown in Figure 12. In order to reduce the shifting time, steering clutch can be separated before shifting, and the maximum braking torque is imposed to the sun gear by controlling steering brake to make sure that the driving shaft speed is reduced to zero quickly, as shown in Figure 12B.

Then, a shifting action can be made after steering clutch separating completely. The diagram of control flow of shifting starting 2nd gear is shown in Figure 13.

4. Experimental Researches

The automatic shift control system for the PIMSPT was designed [15, 16]. Experiments of shifting process of 2nd gear are conducted with and without the strategy of controlling the steering clutches and steering brakes. The curves of the process can be seen in Figures 14 and 15.

In Figure 14, A~B represents the separating process of the main clutch; B~D represents the decline stage of the angular speed of driving shaft; B~C represents the response time of the control stage; D~E represents the oil charging stage of

hydrocylinder during shifting process and the stage of eliminating synchronizer gap; E~F represents the accomplishment of shifting action with synchronizer working.

In Figure 15, A~B represents the separating process of the main clutch; B~C represents the decline stage of the angular speeds of driving and counter shaft to a reasonable shift speed; C~E represents the oil charging stage of hydrocylinder during shift process and the stage of eliminating synchronizer gap; E~F represents the accomplishment of shifting action with synchronizer working.

Comparing Figure 14 with Figure 15, it is obvious that the stage E~F of Figure 14 parallels the stage D~E of Figure 15. From the figures, we can make a conclusion that when the shifting jerks are the same, the shifting time could be reduced over 50% by adopting the new shifting control strategy.

5. Conclusions

As the main clutch of the positive independent mechanical split path transmission is released, the speed of countershaft and driving shaft can be descended faster by controlling the steering clutches and brakes. Based on this mechanism, the shifting time can be shortened and the shifting jerk can be reduced as well with steering clutches and brakes control, which take the driving shaft speed as a closed-loop control parameter and can actively control the speed difference between the driving part and passive part of synchronizer. Subsequently, this control strategy has been approved with a road test of vehicle that it can improve the shift quality effectively.

References

[1] J.-M. Meng, J.-Q. Xi, H.-Y. Chen, and P. Gong, "Automatic shift technology for positive independent mechanical split path transmission," *Acta Armamentarii*, vol. 29, no. 1, pp. 2–5, 2008.

[2] J.-M. Meng, J.-Q. Xi, and H.-Y. Chen, "Automated shift mechanism applied to AMT system of positive independent mechanical split path transmission," *Transactions of Beijing Institute of Technology*, vol. 2, no. 2, pp. 108–112, 2009 (Chinese).

[3] Y.-Y. Chen, J.-Q. Xi, and H.-Y. Chen, "Optimal gear shift control strategy for positive independent mechanical split path transmission with automatic shift system," *Journal of Beijing Institute of Technology*, vol. 20, no. 3, pp. 387–393, 2011.

[4] Z. Yang, C. Cao, and Y. Su, "A method of optimal shift control based on pattern recognition and learning algorithm," in *Proceedings of the 4th World Congress on Intelligent Control and Automation*, vol. 2, pp. 955–959, Shanghai ,China, June 2002.

[5] G. Bóka, J. Márialigeti, L. Lovas, and B. Trencséni, "Face dog clutch engagement at low mismatch speed," *Periodica Polytechnica Transportation Engineering*, vol. 38, no. 1, pp. 29–35, 2010.

[6] S. Qi, C. Zhang, and H. Xie, "SOPC technology applied on automatic mechanical transmission control unit design," in *Proceedings of the IEEE/ASME International Conference on Mechatronic and Embedded Systems and Applications*, pp. 529–532, Qingdao, China, 2010.

[7] Z. Zhong, G. Kong, Z. Yu, X. Xin, and X. Chen, "Shifting control of an automated mechanical transmission without using the clutch," *International Journal of Automotive Technology*, vol. 13, no. 3, pp. 487–496, 2012.

[8] C. H. Yu and C. Y. Tseng, "Research on gear-change control technology for the clutchless automatic-manual transmission of an electric vehicle," *Journal of Automobile Engineering*, vol. 223, no. 9, pp. 1101–1108, 2013.

[9] H. Liu, Y. Lei, Z. Li, J. Zhang, and Y. Li, "Gear-shift strategy for a clutchless automated manual transmission in battery electric vehicles," *SAE International Journal of Commercial Vehicles*, vol. 5, no. 1, pp. 57–62, 2012.

[10] G. Lucente, M. Montanari, and C. Rossi, "Modelling of an automated manual transmission system," *Mechatronics*, vol. 17, no. 2-3, pp. 73–91, 2007.

[11] L. Glielmo, L. Iannelli, V. Vacca, and F. Vasca, "Gearshift control for automated manual transmissions," *Mechatronics*, vol. 11, no. 1, pp. 17–26, 2006.

[12] H. Zhang, Y. Shi, and J. Wang, "Observer-based tracking controller design for networked predictive control systems with uncertain Markov delays," *International Journal of Control*, vol. 86, no. 10, pp. 1824–1836, 2013.

[13] H. Zhang, Y. Shi, and M. Liu, "H_∞ step tracking control for networked discrete-time nonlinear systems with integral and predictive actions," *IEEE Transactions on Industrial Informatics*, vol. 9, no. 1, pp. 337–345, 2013.

[14] H. Zhang, Y. Shi, and A. Saadat Mehr, "Robust static output feedback control and remote PID design for networked motor systems," *IEEE Transactions on Industrial Electronics*, vol. 58, no. 12, pp. 5396–5405, 2011.

[15] J. Xi, H. Chen, and J. Meng, "Automatic mechanical transmission used for tracked vehicle equipped with fixed shaft transmission," Chinese Patent, China, CN101539200, 2009.

[16] J. Xi, J. Meng, and Y. Zhai, "The automatic shifting control for positive independent mechanical split path transmission system," Chinese Patent, China, CN101695903A, 2010.

Hindawi Publishing Corporation
Mathematical Problems in Engineering
Volume 2013, Article ID 640391, 9 pages
http://dx.doi.org/10.1155/2013/640391

Research Article

On Distributed Localization for Road Sensor Networks: A Game Theoretic Approach

Jie Jia, Guiyuan Zhang, Xingwei Wang, and Jian Chen

College of Information Science and Engineering, Northeastern University, Shenyang 110819, China

Correspondence should be addressed to Xingwei Wang; wangxw@mail.neu.edu.cn

Received 7 October 2013; Accepted 1 December 2013

Academic Editor: Xinjie Zhang

Road sensor network is an important part of vehicle networks system and is critical for many intelligent automobile scenarios, such as vehicle safety monitoring and transportation efficiency supporting. Localization of sensors is an active and crucial issue to most applications of road sensor network. Generally, given some anchor nodes' positions and certain pairwise distance measurements, estimating the positions of all nonanchor nodes embodies a nonconvex optimization problem. However, due to the small number of anchor nodes and low sensor node connectivity degree in road sensor networks, the existing localization solutions are ineffective. In order to tackle this problem, a novel distributed localization method based on game theory for road sensor networks is proposed in this paper. Formally, we demonstrate that our proposed localization game is a potential game. Furthermore, we present several techniques to accelerate the convergence to the optimal solution. Simulation results demonstrate the effectiveness of our proposed algorithm.

1. Introduction

A wireless sensor network (WSN) usually consists of a large number of static sensor nodes that organize themselves into multihop networks [1]. Sensor nodes are able to measure various parameters of the environment and transmit collected data to the sink node through multihop communication. Once the sink node received the sensed data, it processes and forwards it to the users. Roadways, which are mainly used for the transportation of people, are one of the typical application areas for WSNs. Recently, roadways equipped with intelligent sensor nodes have prompted the emergence of road sensor network, which is a new type of WSN and is considered as a promising solution to effectively enhance the driving safety and mobility [2]. Furthermore, the U.S. Department of Transportation (DOT) and many automobile companies (e.g., General Motors and Toyota) have started to apply the WSN technology to the Intelligent Transportation Systems (ITS) infrastructures [3–5]. In addition, the European Telecommunications Standards Institute (ETSI) has been making globally applicable standards for Intelligent Transportation Systems integrated with WSNs [6], in which sensor nodes are deployed on the roadways to monitor the road condition (e.g., road construction sites or obstacles) and to announce such condition to vehicles through vehicle-to-vehicle or infrastructure-to-vehicle communications.

Localization technology has become one of the key technologies of road sensor networks [7]. Firstly, node localization is crucial for potential location-aware applications of ITS, such as surveillance and target tracking. Secondly, node location is needed for geographic message forwarding, geographic hash tables, coverage control, energy conservation algorithms, and others [7–9]. Finally, security can also be enhanced by location awareness [10]. In wireless sensor networks, many localization approaches have been proposed. These algorithms can be classified into coarse- and fine-grained localization, respectively. The former relies on lower hardware but is less accurate, while the latter facilitates higher precision of position determination and may represent the most suitable ones. In these fine-grained localization techniques, only a fraction of the nodes, named as anchor nodes, are endowed with their exact coordinates through GPS or manual placement, while the remaining nodes, referred to as nonanchor nodes, are able to calculate their distances to nearby nodes through measurement-based techniques, such as received signal strength (RSS) [11], angle

of arrival (AoA) [12], or time of arrival (ToA) [13]. Hence, assuming that the coordinates of anchor nodes are known and obtaining pairwise distance measurements between nearby nodes, the fine-grained localization problem is to estimate the positions of all nonanchor nodes. It is important to recognize that this problem can be formulated as multivariable nonconvex optimization problem [14], which has proven to be rather difficult [15]. In response to a multivariable nonconvex optimization task, three different approaches have been presented, namely, multidimensional scaling (MDS) [16], semidefined programming (SDP) [17], and stochastic optimization [14, 18]. MDS, applied widely in data analysis, hinges on obtaining the relative coordinates of each node based on a starting distance matrix. On the other hand, SDP relaxes the original nonconvex optimization problem and obtains an approximate solution at a reduced computational effort. Since the relaxation may increase estimation error, additional refinements, such as gradient descent search procedures, are often employed to refine the initial solutions obtained by SDP [19]. Finally, the third class of techniques considers the heuristic optimization algorithms to efficiently solve the localization problem, such as simulated annealing (SA), genetic algorithms, or pareto archived evolution strategies (PAES). However, all these methods discussed above cannot be directly applied to road sensor networks, which is mainly because that these methods ignore two important characteristics in road networks. One is that; in road sensor networks, sensors are deployed with only a small number of anchor nodes; the other is that the localization estimation in road sensor networks should be executed in a distributed manner, and previous works using centralized localization may result in severe communication congestion and high computational complexity. Although some distributed fine-grained localization methods (e.g., distributed SDP [20] and distributed MDS [21]) have been proposed to improve network performance recently, however, existing distributed methods tend to have worse localization accuracy than centralized methods, which are further exacerbated by the fact that the number of anchor nodes is sufficiently small and the network connectivity degree is not sufficiently high. Hence, exploiting distributed localization algorithm with high localization accuracy guarantee is of great importance for road sensor networks.

In this work, we develop a computationally efficient and distributed localization method for road sensor network. The proposed method borrows the model from game theory, which is a mathematical tool, particularly useful in the network engineering field to model highly complex scenarios. This mathematical tool provides researchers with the ability to model individual or independent decision makers called "players." Every player interacts with other players and has an impact on their decisions. The dynamics of the localization, in which pure mathematical analysis has been met with limited success, closely resemble this observation. It has recently come to our attention that some works have also applied game theory for WSNs [22, 23]. In [22], the authors proposed a localization game in wireless sensor networks, where the two-player game model is used to assess the reliability of the node localization data, thus identifying the attacker node and enhancing the security of WSNs. In [23], the coalition game theory is applied to form coalitions, which can reduce communication costs and track mobile target. The major differences between their work and ours lie, however, in that, (i) in our work, we intend to achieve a fully distributed localization with high localization accuracy. We have given a theoretical proof on the fact that the localization game is a potential game; (ii) our distributed sensor localization algorithm is based on the above theoretical analysis and is hence theoretically founded; (iii) we have presented new methods to accelerate the convergence for the localization game.

The rest of the paper is organized as follows. Section 2 presents the assumptions, network model, and design considerations. A fully distributed localization scheme based on potential game is proposed in Section 3. Section 4 gives the simulation results, and Section 5 concludes our paper.

2. Network Model

In this section, we present our network model and basic assumptions. Consider a 2D road sensor network composed of N sensor nodes with position $p_i = (x_i, y_i) \in R^2$, $i = 1, \ldots, N$, where 1 to N_n ($N_n < N$) are nonanchor nodes to be localized and N_{n+1} to N are anchor nodes whose positions are known a priori. We adopt a simple disk model for network connectivity determination, and if the distance between nodes i and j, denoted by r_{ij}, is less than the physical communication range R_c, we say that nodes i and j are neighbor nodes, and thus can communicate and obtain a (noisy) distance measurement d_{ij} using some measurement technique (see Section 1), and it is represented as

$$d_{ij} = r_{ij} + e_{ij}, \tag{1}$$

where $r_{ij} = \|p_i - p_j\|$ represents the true distance between i and j ($\| \ \|$ denotes the norm-2 operator) and $e_{ij} = e_{ji}$ is the corresponding measurement error. The statistics on this measurement error depend on the ranging technique used in [24]. Considering that the RSS-based distance estimation can easily be achieved in most modern wireless systems, the measurement error model used in our paper is similar to [15, 18, 19], which are independent and follow a zero-mean Gaussian distribution with an unknown variance σ^2, $e_{ij} \sim N(0, \sigma_{ij}^2)$. Further, we assume range measurements are symmetric; that is, $d_{ij} = d_{ji}$, for all i, j.

Based on the above disk model, each node can easily determine which other nodes it can directly communicate with, and we define N_i as the neighbor set of node i, and it can be represented as

$$N_i = \left\{ j \in N, j \neq i : \left\| p_i - p_j \right\| \leq R_c \right\}. \tag{2}$$

Without loss of generality, we assume the position of nonanchor node $i \in \{1, \ldots, N_n\}$ that is estimated by the localization algorithm as $\widehat{p}_i = \{\widehat{x}_i, \widehat{y}_i\}$, so that the estimated

distance $d(\widehat{p}_i, \widehat{p}_j)$ between two neighbor sensors i and j can be calculated as

$$d\left(\widehat{p}_i, \widehat{p}_j\right) = \begin{cases} \left\|\widehat{p}_i - p_j\right\|, & \text{if } j \text{ is an anchor node,} \\ \left\|\widehat{p}_i - \widehat{p}_j\right\|, & \text{otherwise.} \end{cases} \tag{3}$$

The difference of d_{ij} and $d(\widehat{p}_i, \widehat{p}_j)$ is denoted by $\delta(\widehat{p}_i, \widehat{p}_j)$ and is determined as follows:

$$\delta\left(\widehat{p}_i, \widehat{p}_j\right) = \begin{cases} \left(d_{ij} - d\left(\widehat{p}_i, \widehat{p}_j\right)\right)^2, & \text{if nodes } i \text{ and } j \text{ are neighbors,} \\ 0, & \text{otherwise.} \end{cases} \tag{4}$$

If all the nonanchor nodes are localized accurately, $\delta(\widehat{p}_i, \widehat{p}_j)$ tends to 0. Obviously, the goal of the localization algorithm is to estimate the position of all nonanchor nodes as accurately as possible, and it can be defined as the following optimization problem:

$$\text{Min } U_{\text{Net}} = \sum_{i=1}^{N_n} \sum_{j \in N_i} \delta\left(\widehat{p}_i, \widehat{p}_j\right). \tag{5}$$

To this purpose, for any nonanchor node i, its own utility function can be defined as

$$\text{Min} \sum_{j \in N_i} \delta\left(\widehat{p}_i, \widehat{p}_j\right). \tag{6}$$

3. Distributed Localization Based on Game Theory

In this section, we firstly present the distributed localization scheme applying the game theory and then present the techniques that can be adopted to improve convergence speed. The main objective of such modeling is to achieve the precise localization using the mathematical analyses provided by the game theory framework.

In our algorithm, each nonanchor node is considered as a decision maker in the game. All the game players, denoted by $A = \{1, 2, \ldots, N_n\}$, have a common strategy space $\mathbf{S} = \{s_i\}$, for all $i \in A$. In this context, we map the estimated position as its chosen strategy, and the strategy of the player i is its estimated location $s_i = \{\widehat{x}_i, \widehat{y}_i\}$. The game profile is defined as the Cartesian product of the players' strategy vector, $\Psi = \times_{i \in A} s_i = s_1 \times s_2 \times \cdots \times s_{N_n}$. Note that a game profile includes one strategy for each player. Similarly, s_{-i} is defined as the strategy set chosen by all the other players except player i.

We assume that each player has a decision module to select its location based on its local information and observation. More specifically, we consider a practical scenario where each player only knows the information of its neighbors. Therefore, for each player, say i, the location $s_i = \{\widehat{x}_i, \widehat{y}_i\}$ should be selected to minimize the following:

$$U_i(\Psi) = U_i(s_i, s_{-i}) = \sum_{j \in N_i} \delta\left(\widehat{p}_i, \widehat{p}_j\right), \tag{7}$$

where $U_i(\Psi)$ is defined as the utility function of player $i \in A$.

From the network's perspective, it is desirable to obtain the optimum location selection Ψ^* which minimizes the network cost function given by

$$R(\Psi) = \sum_{i=1}^{N_n} \sum_{j \in N_i} \delta\left(\widehat{p}_i, \widehat{p}_j\right). \tag{8}$$

In order to achieve an optimal value for $U_i(\Psi)$, the players will negotiate and change their interdependent strategies in Ψ. Then, two important issues will arise: (i) whether they will ever reach a consensus, or a steady state, and (ii) if the steady state exists, whether the steady state of the game is also the precise localization of the whole network.

Definition 1 (Nash equilibrium, NE). A strategy $s^* \in \Psi$ is a NE if it satisfies

$$U_i(s^*) \le U_i\left(s_i', s_{-i}\right), \quad \forall s_i' \in S, \ \forall i \in A. \tag{9}$$

According to this definition, no player can benefit by deviating from its strategy if other players do not change theirs. In other words, this result guarantees an agreement for negotiations among all the players. However, no optimal outcome or fairness is intrinsically guaranteed. Nevertheless, we show that the sensor location game falls into the category of potential games, where the existence of Nash equilibrium can be established.

Definition 2 (potential game). A game is defined as a potential game in which a potential function P exists, such that

$$P(s_i, s_{-i}) - P\left(s_i', s_{-i}\right) = U_i(s_i, s_{-i}) - U_i\left(s_i', s_{-i}\right), \quad \forall i, \tag{10}$$

where s_i and s_i' are two arbitrary strategies.

Potential game is a specific type of games. And if a game is a potential one, there exists at least one pure strategy NE for such a game. Moreover, all NEs are either local or global optimal solutions of the potential function P.

Theorem 3. *Nonanchor node localization game is a potential game, and has a Nash equilibrium, which minimizes, either locally or globally, the following function:*

$$P(s_i, s_{-i}) = \frac{1}{2} * R(\Psi). \tag{11}$$

Proof. Without loss of generality, let us assume sensor node i is updating its location selection unilaterally, given the location selections of other sensors, that is, s_{-i}. For two feasible location selection strategies s_i and s_i', the performance difference for sensor node i is calculated as

$$U_i(s_i, s_{-i}) - U_i\left(s_i', s_{-i}\right) = \sum_{j \in N_i} \delta\left(\widehat{p}_i, \widehat{p}_j\right) - \sum_{j \in N_i} \delta\left(\widehat{p}_i', \widehat{p}_j\right). \tag{12}$$

We next rewrite the function P and obtain

$$\begin{aligned}
P(s_i, s_{-i}) &= \frac{1}{2} * \sum_{i=1}^{N_n} \sum_{j \in N_i} \delta(\widehat{p}_i, \widehat{p}_j) \\
&= \frac{1}{2} * \left(\sum_{j \in N_i} \delta(\widehat{p}_i, \widehat{p}_j) + \sum_{k \neq i, k=1}^{N_n} \sum_{j \in N_k} \delta(\widehat{p}_k, \widehat{p}_j) \right) \\
&= \frac{1}{2} * \left(\sum_{j \in N_i} \delta(\widehat{p}_i, \widehat{p}_j) \right. \\
&\qquad + \sum_{k \neq i, k=1}^{N_n} \left(\sum_{j \neq i, j \in N_k} \delta(\widehat{p}_k, \widehat{p}_j) \right. \\
&\qquad \left. \left. + \delta(\widehat{p}_k, \widehat{p}_i) \right) \right) \\
&= \frac{1}{2} * \left(\sum_{j \in N_i} \delta(\widehat{p}_i, \widehat{p}_j) + \sum_{k \neq i, k=1}^{N_n} \sum_{j \neq i, j \in N_k} \delta(\widehat{p}_k, \widehat{p}_j) \right. \\
&\qquad \left. + \sum_{k \neq i, k=1}^{N_n} \delta(\widehat{p}_k, \widehat{p}_i) \right).
\end{aligned} \tag{13}$$

According to (4), if nodes k and i are not neighbors, $\delta(\widehat{p}_k, \widehat{p}_i) = 0$; then we have

$$\begin{aligned}
\sum_{k \neq i, k=1}^{N_n} \delta(\widehat{p}_k, \widehat{p}_i) &= \sum_{k \in N_i} \delta(\widehat{p}_k, \widehat{p}_i) \\
&\quad + \sum_{k \neq i, k \notin N_i, k=1}^{N_n} \delta(\widehat{p}_k, \widehat{p}_i) = \sum_{k \in N_i} \delta(\widehat{p}_k, \widehat{p}_i).
\end{aligned} \tag{14}$$

And (13) can be rewritten as

$$\begin{aligned}
P(s_i, s_{-i}) &= \frac{1}{2} * \left(\sum_{j \in N_i} \delta(\widehat{p}_i, \widehat{p}_j) \right. \\
&\qquad + \sum_{k \neq i, k=1}^{N_n} \sum_{j \neq i, j \in N_k} \delta(\widehat{p}_k, \widehat{p}_j) \\
&\qquad \left. + \sum_{k \in N_i} \delta(\widehat{p}_k, \widehat{p}_i) \right) \\
&= \frac{1}{2} * \left(2 * \sum_{j \in N_i} \delta(\widehat{p}_i, \widehat{p}_j) \right. \\
&\qquad \left. + \sum_{k \neq i, k=1}^{N_n} \sum_{j \neq i, j \in N_k} \delta(\widehat{p}_k, \widehat{p}_j) \right) \\
&= \sum_{j \in N_i} \delta(\widehat{p}_i, \widehat{p}_j) \\
&\quad + \frac{1}{2} * \sum_{k \neq i, k=1}^{N_n} \sum_{j \neq i, j \in N_k} \delta(\widehat{p}_k, \widehat{p}_j).
\end{aligned} \tag{15}$$

Thus, the difference of function P with two strategies s_i and s_i' can be calculated as

$$\begin{aligned}
&P(s_i, s_{-i}) - P(s_i', s_{-i}) \\
&\quad = \sum_{j \in N_i} \delta(\widehat{p}_i, \widehat{p}_j) + \frac{1}{2} * \sum_{k \neq i, k=1}^{N_n} \sum_{j \neq i, j \in N_k} \delta(\widehat{p}_k, \widehat{p}_j) \\
&\qquad - \left(\sum_{j \in N_i} \delta(\widehat{p}_i', \widehat{p}_j) + \frac{1}{2} * \sum_{k \neq i, k=1}^{N_n} \sum_{j \neq i, j \in N_k} \delta(\widehat{p}_k, \widehat{p}_j) \right) \\
&\quad = U_i(s_i, s_{-i}) - U_i(s_i', s_{-i}).
\end{aligned} \tag{16}$$

□

Note that we utilize the property that when a single sensor node i switches its location strategy from s_i to s_i', the costs of other sensors that are not neighbors of i are unchanged. We stress that the above equation is valid for any i, s_i to s_{-i}. Therefore, the location selection game is an exact potential game with a potential function given by (11). It is worth noting that every Nash equilibrium in the location selection game, where no sensor node can improve its own performance by deviating unilaterally, corresponds to a local or global localization solution of the whole network. The existence of Nash equilibrium follows the results of [25].

By making use of NE and potential game, our localization approach can converge to an agreement among all players and this point is an efficient solution of the whole network. In the literature, there are two famous learning schemes that are used to converge to NE, namely, the best and better response techniques, expressed as follows:

$$\begin{aligned}
s_i^{t+1} &= \arg\min_{s \in S_i} U_i(\Psi) \\
&= \arg\min_{s \in S_i} \left(\sum_{j \in N_i, j \in N_n} \left(d_{ij} - \left\| s - s_j^t \right\| \right)^2 \right. \\
&\qquad \left. + \sum_{j \in N_i, j \notin N_n} \left(d_{ij} - \left\| s - p_j \right\| \right)^2 \right),
\end{aligned} \tag{17}$$

$$s_i^{t+1} = \begin{cases} s_i^{\text{rand}}, & \text{if } U_i(s_i^{\text{rand}}, s_{-i}) < U_i(s_i^t, s_{-i}), \\ s_i^t, & \text{otherwise.} \end{cases} \tag{18}$$

In the former scheme, for each player, during its turn to play, it searches its entire strategy space and selects the one that yields the best outcome considering all its neighbors' (including both neighbor anchor node and neighbor nonanchor node) strategies, as shown in (17). The primary drawback

of the best response is the computational complexity for resource constrained sensor nodes, which grows linearly with the cardinality of the strategy space. The latter scheme is an improvement of the former one, where at each step, the player updates its strategy as long as the randomly selected strategy s_i^{rand} yields a better utility $U_i(s_i^{\text{rand}}, s_{-i})$ than the previous one $U_i(s_i^t, s_{-i})$, as shown in (18). The dramatically reduced computation is the trade off with the convergence speed. Both the best response and the better response are guaranteed to converge to a NE in potential games [25]. However, the equilibrium may occur at the local optimum of the utility function, instead of the global optimum if there are multiple NEs. In this case, the system performance will be trapped in a suboptimal state and, since this is one instance of NE, no node will be able to increase its utility function by changing its strategy. Therefore, some response techniques should be designed to avoid being trapped in a local optimal state.

In our paper, the smoothed better response learning scheme [26] is applied, which can converge to the optimal NE with high probability. In this scheme, for each player i, during its turn to play, it selects a random strategy s_i^{rand} and keeps it with the probability of $p(s_i^{\text{rand}}, s_i^t)$, which can be expressed as

$$p\left(s_i^{\text{rand}}, s_i^t\right) = \frac{1}{1 + e^{(U_i(s_i^{\text{rand}}, s_{-i}) - U_i(s_i^t, s_{-i}))/\gamma}}, \tag{19}$$

where γ is the smoothing factor. Equation (19) is a function of the difference of the utility functions; if $U_i(s_i^{\text{rand}}, s_{-i}) < U_i(s_i^t, s_{-i})$, player i will change its strategies with high probability; otherwise, it will keep them with high probability. If only a small difference occurs, the player will select one of the strategies almost randomly. In this case, even though the players will be able to select a "worse" strategy or not to select a marginally "better" strategy, this uncertainty of the probability allows the players to move from a local optimum state and to start negotiating towards a new NE.

In addition, smoothing factor γ is responsible for controlling the trade-off between the algorithmic performance and convergence speed. The larger the smoothing factor is, the more extensive strategy search and slower convergence speed will be obtained. On the other hand, smaller γ represents more limited search and faster a convergence speed. In our simulations, we borrow the concept of temperature in simulated annealing [18], and γ is set to $10/t^2$, where t denotes the negotiation iterations. It is advisable that γ keeps deceasing as the negotiation iterates.

Due to the uneven sensor distribution, some nonanchor nodes with more neighbor anchors and larger neighbor connectivity may tend to converge faster than others. With the purpose of saving energy during negotiation, those nodes that are already accurately localized should be detected and deleted from the game as early as possible. Moreover, any time when a nonanchor node is considered to be localized, it should elevate as an anchor node and help to decide the strategy space for all its neighbor nonanchor nodes. In our paper, we further propose the following strategy space determination techniques for each player before game negotiation.

(i) If the player has three or more neighbor anchors, the estimate on the position of this sensor can be calculated by one of the existing algorithms for range based positioning, such as the one proposed in [27], and the player is elevated as an anchor node.

(ii) If the sensor has two neighbor anchors, its strategy space is set as the junctions of its neighbor anchors' communication circles.

(iii) If the sensor has one neighbor anchor, its strategy space is set as the communication circle of its neighbor anchor.

(iv) If the sensor has no neighbor anchor, its strategy space is set as the full target area.

In addition, after game negotiation, if the value of the utility function of one player is smaller than the prior given localization threshold, it may be precisely localized or localized with flip-ambiguity [15]. In order to avoid the flip-ambiguity during localization, only the value of the utility function achieved by the player is satisfactory in consecutive k times; the player is considered to be accurately localized. And then this player is elevated as an anchor node. Combined with the parameters and techniques associated with our localization game discussed above, the steps of the proposed localization algorithm are summarized in Algorithm **??**. For each player, its game framework involves a strategy space generation step, a negotiation step, and an anchor node elevation step, where only local communications are necessary in all steps.

In our algorithm, T is the maximum number of iterations for localization game and w_i records the number of consecutive game iterations that the ith node's utility function is no larger than Θ_h. Once $w_i \geq k$, node i is considered to be accurately localized and is elevated as an anchor node. It is obvious that, for these nodes elevated as anchor nodes, their game iterations are smaller than T, and their complexity is smaller than $O(n_c * T)$, where n_c is the average size of their neighbor sensor set. Therefore the time complexity of the whole network is $O(N_n * n_c * T)$.

4. Performance Evaluation

To evaluate the performance of the proposed algorithm, we introduce the mean localization error (MLE), which can be calculated by

$$\text{MLE} = \frac{1}{N_n}\sqrt{\sum_{i=1}^{N_n}\left\|\widehat{p}_i - p_i\right\|^2}. \tag{20}$$

4.1. Simulation in Regular Network. At first, 200 nonanchor nodes and 10 anchor nodes are randomly located in a 100 × 100 area network. The communication range is set to 15, the variance of measurement error e_{ij} is given by $\lambda^2 r_{ij}^2$, at first, λ is first set to 0, which means that the system is in an ideal situation, and there is no measurement error in distance calculation.

Figure 1(a) shows the initial distribution and the nonanchor nodes connecting with anchor nodes, where the anchors and the true locations of nonanchor nodes are shown by red asterisks and green circles. Figure 1(b) shows the final

```
set t = 0, s_i = {∅}, w_i = 0 (∀i ∈ A)
while t < T
  for each non-anchor node i ∈ A
   //solution space generation
   get posOfNeighborsandnumOfNeighborAnchor of i
   if numOfNeighborAnchor < 1
     set its straSpace as the target area
   else if numOfNeighborAnchor equals to 1
     set its straSpace as the communication circle of its anchor
   else if numOfNeighborAnchor equals to 2
   set its straSpace as the junctions of its neighbor anchors' communication circles
   else
        estimate the position of the player using existing localization algorithms
       A = A − {i};
       continue;
   end if
   // negotiation
   s_i^rand ← random strategy form its strategy space;
   if p(s_i^rand, s_i^t) ≥ random number from 0 to 1
     s_i^{t+1} ← s_i^rand
   else
     s_i^{t+1} ← s_i^t
   end if
   // anchor node elevation
   if U_i(s_i^{t+1}, s_{−i}) ≤ Θ_h
     w_i = w_i + 1;
     if w_i ≥ k
       Elevate node i as an anchor node
       A = A − {i};
   else
     w_i = 0
     t = t + 1
     end if
  end for
end while
```

Algorithm 1: Distributed localization algorithm based on potential game.

location results after 500th iterations, where the anchors and the true locations of nonanchor nodes are also shown by red asterisks and green circles, the estimated locations are shown by the plus, and the dashed lines quantize localization error. From the simulation results in Figure 1, we can make the following observations. (1) As can be observed in Figure 1(a), no more than 20 nodes have two anchor neighbors, and the other anchor nodes have less than one anchor neighbor. (2) Almost all the nonanchor nodes are accurately localized in our algorithm; only a few nodes are deviated from the true locations, as can be observed in Figure 1(b). This is mainly because of the nonuniqueness of these nodes' location in the network, where the flip-ambiguity problem is happening during localization game.

In Figure 2, we illustrate the negotiation process reaching the NE with different responses. In the best response, the player selects the strategy with the best utility function, which has fast convergence speed as expected, but it may generate suboptimal results when nodes find themselves trapped in a local optimum NE. In contrast, better response can obtain better results than the best response, but it needs many more iterations to converge. As the uncertainty is used in strategy selection, the SBR scheme has the best performance. And we also can find that, by adding the accelerating techniques in the localization game, both strategies can converge to the NE rapidly.

Since our approach is a range based technique, in a practical application, the measurement error has great influence on the localization accuracy. We further set communication radius as 15, 20, and 25 and compare the localization performance with different measurement error. Considering that the road sensor network is usually deployed in a typical outdoor environment, the measurement error is smaller than 0.1 in most cases [15]. Therefore, in our simulation, the range of λ is set from 0 to 0.2, and simulations with $\lambda > 0.2$ are not executed in our paper.

Figure 3 shows the MLE comparison with different communication radii and different λ. From Figure 3, we can draw the conclusion that (1) localization accuracy will be improved when the communication radius increases; this is

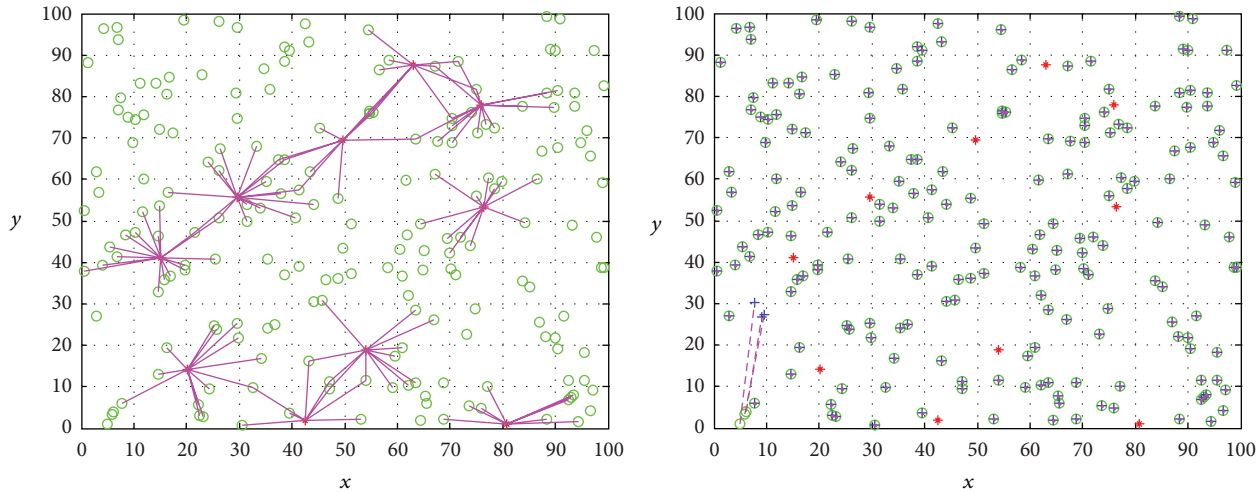

(a) Initial distribution (b) Final localization results

Figure 1: The initial distribution and final localization results.

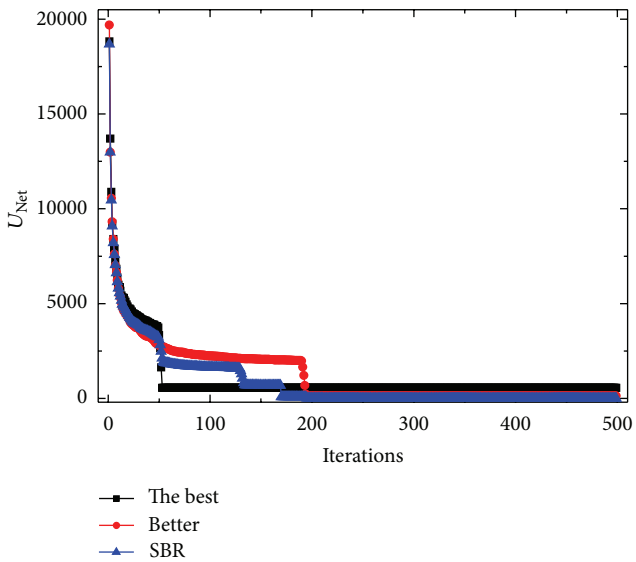

Figure 2: U_{Net} in different numbers of iterations.

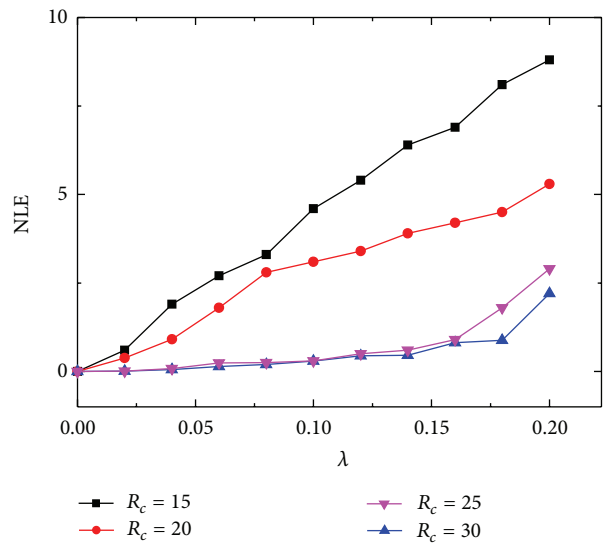

Figure 3: MLE comparison with different communication radii and different λ in regular networks.

mainly because the larger the communication radius is, the more node connectivity can be obtained, thus improving the localization performance; (2) localization error increases with the measurement error increases; (3) when the communication radius increases to 25 and 30, our work can work well for typical outdoor environment ($\lambda > 0.1$); (4) even when the measurement error is very large, our algorithm still works better, which demonstrates the effectiveness of the algorithm.

4.2. Simulation in Irregular Network. In a practical road sensor network deployment, it is most likely that the shape of the roadway is irregular due to the presence of physical obstacles. In Figure 4, we give an example of such a network, in particular, a C-shaped network, with 200 nonanchor nodes and 10 anchors.

Figure 5 shows the MLE comparison with different communication radii and different λ. From Figure 5, we can draw the conclusion that (1) localization error is more serious in irregular networks shapes than that in regular networks; (2) when the communication range is larger than 25, for about 60% of the scenarios, the localization error is less than 2, which demonstrates the robustness against distance estimation noise and irregular network shape.

4.3. Comparison with MDS-MAP and PAES. We further compare the performance obtained by our algorithm with those obtained by the PAES algorithm and MDS-MAP algorithm with the same network topologies, where the target area is set to $100 * 100$, R_c is set to 25, and λ is set to 0.1.

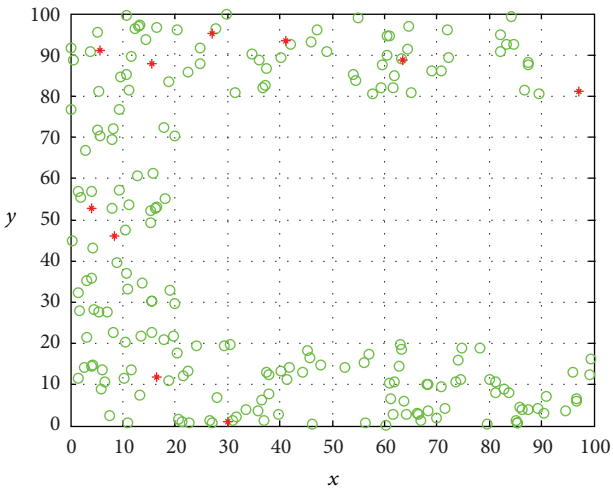

Figure 4: Irregular sensor distribution.

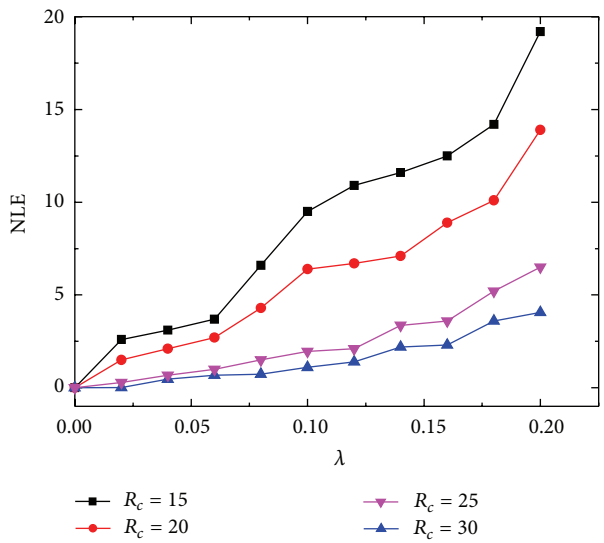

Figure 5: MLE comparison with different communication radii and different λ in irregular networks.

In each topology, the ratio of anchor nodes and nonanchor nodes is 0.1. Since our algorithm and PAES are running with the number of iterations, the maximum number iterations of these two algorithms is 1000, and any time the total utility function decreases to 0.5, the whole network is considered accurately localized and the total running time is calculated.

Table 1 shows the average localization error and computation time of the 6 network topologies with different numbers of sensor nodes. From Table 1, we can get some conclusions as follows: (1) our algorithm has a significantly shorter running time and localization error than MDS-MAP and PAES in most cases ($N_n \geq 100$), which is mainly because in our approach, its complexity scales as $O(N_n * n_c * T)$; (2) the time complexities of PAES and MDA-MAP are $O(N_n * N_n * T)$ and $O(N_n * n_c^3)$, as PAES takes a number of iterations much larger than n to converge; that is, $T \gg n$; PAES takes the longest computation time to converge; (3) when the number of deployed nodes is very small ($N_n \leq 50$), our algorithm has a slightly longer running time and localization error than MDS-MAP, which is mainly because when the number of sensors is very small, each nonanchor node has fewer neighbor sensors, and thus more nodes tend to be flipped during localization and more running time is used for convergence. Combined with our previous results on the localization error for different network shapes, our proposed localization algorithm is a very efficient and distributed method with excellent localization accuracy.

Table 1: Comparison of localization error and computation time.

N_n	Algorithm	NLE (m)	Computation time (s)
50	Game	6.18	0.07
	MDS-MAP	5.28	0.03
	PAES	7.61	0.59
100	Game	1.37	0.11
	MDS-MAP	6.25	0.18
	PAES	3.32	1.23
150	Game	0.32	0.17
	MDS-MAP	1.09	0.35
	PAES	1.05	2.1
200	Game	0.29	0.27
	MDS-MAP	3.57	0.62
	PAES	0.82	3.66
250	Game	0.32	0.33
	MDS-MAP	3.4	1.11
	PAES	0.68	4.7
300	Game	0.22	0.35
	MDS-MAP	3.47	1.7
	PAES	0.34	5.21

5. Conclusion

In this paper, we have proposed a potential game for distributed localization for road sensor networks using only local information. Our main contributions are as follows. First, we have transformed the optimal localization problem to a distributed potential game. Second, we have developed a negotiation-based localization algorithm using the properties of potential game. Furthermore, we have derived new methods to accelerate the localization algorithm in converging to optimal solutions. Extensive simulations demonstrate that our algorithm can quickly converge to the optimal solution and perform well even with a small number of anchor nodes and achieve better localization accuracy and efficiency than the existing algorithms.

Acknowledgments

This work is supported by the National Science Foundation for Distinguished Young Scholars of China under Grant no. 61225012 and no. 71325002; the National Natural Science Foundation of China under Grant no. 61173153 and no.

60903159; the Fundamental Research Funds for the Central Universities under Grant nos. N110404014, N110318001, N110204003, and N120104001; the Specialized Research Fund of the Doctoral Program of Higher Education for the Priority Development Areas under Grant no. 20120042130003; the Specialized Research Fund for the Doctoral Program of Higher Education under Grant no. 20110042110024; the China Postdoctoral Science Foundation funded project under Grant no. 20110491508 and no. 2012T50248.

References

[1] I. F. Akyildiz, W. Su, Y. Sankarasubramaniam, and E. Cayirci, "Wireless sensor networks: a survey," *Computer Networks*, vol. 38, no. 4, pp. 393–422, 2002.

[2] M. Shuai, K. Xie, M. Xiujun, and G. Song, "An on-road wireless sensor network approach for urban traffic state monitoring," in *Proceedings of the 11th International IEEE Conference on Intelligent Transportation Systems (ITSC '08)*, pp. 1195–1200, Beijing , China, December 2008.

[3] R. J. Weiland and L. B. Purser, "Intelligent transportation systems," in *Transportation in the New Millennium*, 2000, (030001).

[4] "Driving Today: Cars Talking to Cars," http://www.drivingtoday.com/partner/content/StudioOne/archive/feature/cars_talking_to_cars/index.html.

[5] Toyota Motor Corporation (TMC), "TMC Develops Onboard DSRC Unit to Improve Traffic Safety," http://www2.toyota.co.jp/en/news/09/09/0903.html.

[6] European Telecommunications Standards Institute (ETSI), "Intelligent Transportation Systems," http://www.etsi.org/WebSite/technologies/IntelligentTransportSystems.aspx.

[7] G. Mao, B. Fidan, and B. D. O. Anderson, "Wireless sensor network localization techniques," *Computer Networks*, vol. 51, no. 10, pp. 2529–2553, 2007.

[8] J. Jia, X. Wu, J. Chen, and X. Wang, "Exploiting sensor redistribution for eliminating the energy hole problem in mobile sensor networks," *EURASIP Journal on Wireless Communications and Networking*, vol. 2012, article 68, 2012.

[9] J. Jia, J. Chen, X. Wang, and L. Zhao, "Energy-balanced density control to avoid energy hole for wireless sensor networks," *International Journal of Distributed Sensor Networks*, vol. 2012, Article ID 812013, 10 pages, 2012.

[10] A. Vempaty, O. Ozdemir, K. Agrawal, H. Chen, and P. K. Varshney, "Localization in wireless sensor networks: byzantines and mitigation techniques," *IEEE Journal and Magazines*, vol. 61, no. 6, pp. 1495–1508, 2013.

[11] X. Li, "RSS-based location estimation with unknown pathloss model," *IEEE Transactions on Wireless Communications*, vol. 5, no. 12, pp. 3626–3633, 2006.

[12] A. Savvides, C.-C. Han, and M. B. Strivastava, "Dynamic fine-grained localization in ad-hoc networks of sensors," in *Proceedings of the 7th Annual International Conference on Mobile Computing and Networking*, pp. 166–179, July 2001.

[13] X. Li and K. Pahlavan, "Super-resolution TOA estimation with diversity for indoor geolocation," *IEEE Transactions on Wireless Communications*, vol. 3, no. 1, pp. 224–234, 2004.

[14] L. Doherty, K. S. J. Pister, and L. El Ghaoui, "Convex position estimation in wireless sensor networks," in *Proceedings of the 20th Annual Joint Conference of the IEEE Computer and Communications Societies*, pp. 1655–1663, Anchorage, Alaska, USA, April 2001.

[15] M. Vecchioa, R. L. López, and F. Marcellonib, "A two-objective evolutionary approach based on topological constraints for node localization in wireless sensor networks," *Applied Soft Computing*, vol. 15, no. 7, pp. 1891–1901, 2012.

[16] Y. Shang, W. Ruml, Y. Zhang, and M. Fromherz, "Localization from connectivity in sensor networks," *IEEE Transactions on Parallel and Distributed Systems*, vol. 15, no. 11, pp. 961–974, 2004.

[17] P. Biswas and Y. Ye, "Semidefinite programming for ad hoc wireless sensor network localization," in *Proceedings of the 3rd International Symposium on Information Processing in Sensor Networks (IPSN '04)*, pp. 46–54, April 2004.

[18] A. A. Kannan, G. Mao, and B. Vucetic, "Simulated annealing based wireless sensor network localization with flip ambiguity mitigation," in *Proceedings of the IEEE 63rd Vehicular Technology Conference (VTC '06)*, pp. 1022–1026, Melbourne, Australia, July 2006.

[19] P. Biswas, T.-C. Liang, K.-C. Toh, Y. Ye, and T.-C. Wang, "Semidefinite programming approaches for sensor network localization with noisy distance measurements," *IEEE Transactions on Automation Science and Engineering*, vol. 3, no. 4, pp. 360–371, 2006.

[20] P. Biswas, T.-C. Lian, T.-C. Wang, and Y. Ye, "Semidefinite programming based algorithms for sensor network localization," *ACM Transactions on Sensor Networks*, vol. 2, no. 2, pp. 188–220, 2006.

[21] J. A. Costa, N. Patwari, and A. O. Hero III, "Distributed weighted-multidimensional scaling for node localization in sensor networks," *ACM Transactions on Sensor Networks*, vol. 2, no. 1, pp. 39–64, 2006.

[22] N. Gatti, M. Monga, and S. Sicari, "A localization game in wireless sensor networks," in *Proceedings of the International Conference on Decision and Game Theory for Security*, pp. 168–179, 2010.

[23] B. Bejar, P. Belanovic, and S. Zazo, "Cooperative localisation in wireless sensor networks using coalitional game theory," in *Proceedings of the 18th European Signal Processing Conference*, pp. 1459–1463, 2010.

[24] S. M. Kay, *Fundamentals of Statistical Signal Processing: Estimation Theory*, Prentice-Hall, 1993.

[25] D. Monderer and L. S. Shapley, "Potential games," *Games and Economic Behavior*, vol. 14, no. 1, pp. 124–143, 1996.

[26] G. Arslan, M. F. Demirkol, and Y. Song, "Equilibrium efficiency improvement in MIMO interference systems: a decentralized stream control approach," *IEEE Transactions on Wireless Communications*, vol. 6, no. 8, pp. 2984–2993, 2007.

[27] S. Zhu and Z. Ding, "A simple approach of range-based positioning with low computational complexity," *IEEE Transactions on Wireless Communications*, vol. 8, no. 12, pp. 5832–5836, 2009.

Hindawi Publishing Corporation
Mathematical Problems in Engineering
Volume 2013, Article ID 819302, 8 pages
http://dx.doi.org/10.1155/2013/819302

Research Article

Motion Control of Four-Wheel Independently Actuated Electric Ground Vehicles considering Tire Force Saturations

Rongrong Wang,[1] Hamid Reza Karimi,[2] Nan Chen,[1] Guodong Yin,[1] and Jinxiang Wang[1]

[1] *School of Mechanical Engineering, Southeast University, Nanjing 211189, China*
[2] *Department of Engineering, Faculty of Engineering and Science, University of Agder, 4898 Grimstad, Norway*

Correspondence should be addressed to Rongrong Wang; wrr06fy@gmail.com

Received 26 September 2013; Accepted 17 November 2013

Academic Editor: Hui Zhang

A vehicle stability control approach for four-wheel independently actuated (FWIA) electric vehicles is presented. The proposed control method consists of a higher-level controller and a lower-level controller. An adaptive control-based higher-level controller is designed to yield the vehicle virtual control efforts to track the desired vehicle motions due to the possible modeling inaccuracies and parametric uncertainties. The lower-level controller considering tire force saturation is given to allocate the required control efforts to the four in-wheel motors for providing the desired tire forces. An analytic method is given to distribute the high-level control efforts, without using the numerical-optimization-based control allocation algorithms. Simulations based on a high-fidelity, CarSim, and full-vehicle model show the effectiveness of the control approach.

1. Introduction

Electric vehicles typically achieve greater fuel economy, lower emissions, and increased energy security than conventional internal combustion engine vehicles [1]. Four-wheel independently actuated (FWIA) electric vehicles employ four in-wheel (or hub) motors to actuate the four wheels, and thus the torque of each wheel can be controlled independently. The actuation flexibility of the FWIA electric vehicles together with the fast and precise torque responses of electric motors enhances the vehicle control strategies, such as the traction control system and direct yaw-moment control [2–4].

The actuators in a FWIA electric vehicle are more than those in a conventional vehicle. This actuator redundancy makes the FWIA electric vehicle control problem more challenging but rewarding. This paper considers the motion control problems of FWIA electric vehicles. Both the vehicle longitudinal speed and yaw motion are controlled. Many studies have been carried out on the vehicle control methods for improving the vehicle stability and maneuverability. Most of them nevertheless are designed for the conventional vehicle architectures [5–7], not for the FWIA electric vehicles. Sakai et al. [8] proposed a direct yaw-moment control system for a FWIA electric vehicle, a half-vehicle model which is a linear approximation of vehicle dynamics was used in the controller design, and only the vehicle lateral motion was controlled. A braking control method for electric vehicle was proposed in [9], and the studied vehicle was driven by independent front and rear motors. The vehicle stability problem was not considered either in the paper. A stability control method for four-wheel driven hybrid electric vehicle was proposed in [10]. The studied vehicle in this paper was driven by a front and a rear motor, and the rear motor with an electrohydraulic brake was used to generate the required torque split for yaw motion control. As a FWIA electric vehicle is equipped with four in-wheel motors to independently actuate the four wheels, the control problem in [10] is thus different from the one considered in this study.

In this paper, the tracking control problem [11–14] of a FWIA electric vehicle is studied. The proposed control system consists of a higher-level controller and a lower-level controller. Due to the possible modeling inaccuracies and vehicle parametric uncertainties, an adaptive controller is designed as the higher-level control to give the required virtual total ground forces and the force split between the left and right sides of the vehicle. The vehicle longitudinal

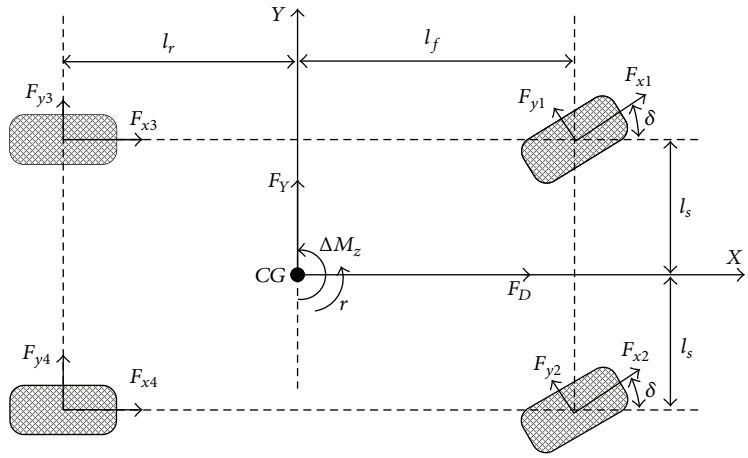

Figure 1: Schematic diagram of a vehicle planar motion model.

speed is controlled by the total ground forces while the yaw motion is compensated with the external yaw moment generated with the tire force difference between the two sides of the vehicle. The lower-level controller allocates the virtual ground forces from the higher-level controller to the four wheels. Control allocation algorithms are generally used to distribute the higher-level control signals to the lower-level actuators [15, 16]. As the control allocation algorithms usually require high computational costs, which may discourage their implementations in real time, an analytic solution of allocating the ground forces without using the numerical-optimization-based control allocation algorithms is given in this study. When the tire slip ratios become large and move into the unstable tire force region, the tire forces will be saturated and it may no longer be possible to fully transfer the desired tire force onto the road. What is more, locking/skidding wheels no longer provide any grip on the road and thus the cornering forces transferred to the ground will be limited. So the vehicle will be unsteerable if the tire slip ratios become too large. The constraints of the tire forces are also explicitly considered in the optimal solution.

The rest of the paper is organized as follows. System modeling is presented in Section 2. The proposed higher-level controllers are designed in Section 3. Tire force distribution design considering the tire force constraints is described in Section 4. Simulation results based on a high-fidelity, CarSim, full-vehicle model are provided in Section 5 followed by conclusive remarks.

2. System Modelling

Vehicle yaw control enhances the vehicle handling performance and maintains vehicle stability in cornering maneuvers [17]. When the vehicle yaw rate can be controlled to track the reference, the vehicle lateral speed and slip angle will be small [18]. A schematic diagram of a vehicle model is shown in Figure 1. If the vehicle longitudinal speed and yaw rate are controlled at the same time, the vehicle model can be expressed as

$$\begin{aligned}\dot{v}_x &= v_y r - \frac{C_a}{m} v_x^2 + \frac{1}{m}\sum_{i=1}^{2} F_{yi}\sin(\delta) + \frac{F_D}{m},\\ \dot{r} &= \frac{1}{I_z}\left(\sum_{i=1}^{2} F_{yi}\left(l_f\cos(\delta) + (-1)^i l_s \sin(\delta)\right) - \sum_{i=3}^{4} l_r F_{yi}\right)\\ &\quad + \frac{1}{I_z}\Delta M_z,\end{aligned} \tag{1}$$

where v_x and v_y are the vehicle longitudinal speed and lateral speed, respectively, r is the yaw rate, m is the mass of the vehicle, I_z is the yaw inertia, and C_a is the aerodynamic drag term. F_D is the total driving/braking forces in vehicle longitudinal direction, ΔM_z is the external yaw moment generated with the longitudinal tire force difference between the left and right side wheels, F_D and ΔM_z can be written as

$$\begin{aligned}F_D &= \sum_{i=1}^{2} F_{xi}\cos(\delta) + \sum_{3=1}^{4} F_{xi},\\ \Delta M_z &= \sum_{i=1}^{2} F_{xi}\left((-1)^i\cos(\delta) l_s + \sin(\delta) l_f\right)\\ &\quad + \sum_{i=3}^{4}(-1)^i l_s F_{xi}.\end{aligned} \tag{2}$$

The wheel slip angle is a function of the vehicle states and can be calculated as

$$\begin{aligned}\beta_{1,2} &= -\delta + \tan^{-1}\left(\frac{v_y + l_f r}{v_x \mp l_s r}\right),\\ \beta_{3,4} &= \tan^{-1}\left(\frac{v_y - l_r r}{v_x \mp l_s r}\right).\end{aligned} \tag{3}$$

The tire lateral forces are functions of the tire slip angles which can be calculated with the vehicle states, which indicates that the tire lateral forces in F_{yi} are also functions of the vehicle states. Denoting $x = [v_x \;\; v_y \;\; r]^T$, the vehicle model can be rewritten as

$$\begin{aligned} \dot{x}_1 &= f_1(x) + \frac{1}{m}u_1, \\ \dot{x}_2 &= f_2(x) + \frac{1}{I_z}u_2, \end{aligned} \tag{4}$$

where $u_1 = F_D$ and $u_2 = \Delta M_z$ are the control signals, $f_1(x) = v_y r - (C_a/m)v_x^2 + (1/m)\sum_{i=1}^{2} F_{yi}\sin(\delta)$, and $f_2(x) = (1/I_z)(\sum_{i=1}^{2} F_{yi}(l_f\cos(\delta) + (-1)^i l_s \sin(\delta)) - \sum_{i=3}^{4} l_r F_{yi})$.

The tire longitudinal slip ratio s_i is defined as the relative difference between the tire center speed and tire circumferential speed, and the tire slip ratio can be written as

$$s_i = \frac{\omega_i R - v_{xi}}{\max(v_{xi}, \omega_i R)}, \tag{5}$$

where ω_i is the tire longitudinal rotational speed of the ith wheel, R is the tire effective rolling radius, and v_{xi} are the speeds at the centers of the wheels and are given as

$$\begin{aligned} v_{x1,2} &= (v_x \mp l_s r)\cos\delta + (v_y + l_f r)\sin\delta, \\ v_{x3,4} &= v_x \mp l_s r. \end{aligned} \tag{6}$$

The vehicle states can be measured with the global positioning system (GPS) and inertia measurement unit (IMU) [19, 20]. The wheel speeds can be measured with wheel speed sensors. Thus, in this study, we assume all of the required signals to be known.

3. Higher-Level Controller Design

The proposed control system consists of a higher-level controller and a lower-level controller. The vehicle longitudinal speed is controlled by the total ground forces while the yaw rate is compensated with the external yaw moment. For the first channel of (4), the following controller

$$u_1^* = m(-f_1(x) + K_1 e_x + \dot{v}_{xr}), \tag{7}$$

with v_{xr} being the reference vehicle longitudinal speed and K_1 being a positive constant, can make the longitudinal speed tracking error, $e_x = v_{xr} - v_x$, converge to 0. However, $f_1(x)$ and the vehicle mass m may not be accurately obtained due to the modeling error and parameter uncertainties, and an adaptive controller is thus designed to yield the control signal u_1. The controller for the first channel is thus modified as

$$u_1 = \widehat{m}\left(-\widehat{f}_1(x) + K_1 e_x + \dot{v}_{xr}\right), \tag{8}$$

where $\widehat{f}_1$ and $\widehat{m}$ are the estimated values of $f_1(x)$ and m, respectively. If the following control law are used:

$$\dot{\widehat{f}}_1 = -\gamma_1 e_x, \qquad \dot{\widehat{m}} = e_x \gamma_2 u_1, \tag{9}$$

with γ_1 and γ_2 being positive constants, the longitudinal speed tracking error e_x can be bounded as

$$|e_x| = \sqrt{\frac{(f_{1\max} - f_{1\min})\left|\dot{f}_1\right|_{\max}}{K_1\gamma_1}}, \tag{10}$$

where $|\dot{f}_1|_{\max}$ is the upper boundary of $|\dot{f}_1|$ and $f_{1\max}$ and $f_{1\min}$ are the upper and lower boundaries of $f_1(x)$, respectively. Proof can be found in Appendix A. Note that by choosing sufficiently large γ_1 and K_1, the longitudinal speed tracking error e_x can be arbitrarily small.

The adaption law for $\widehat{f}_1$ and $\widehat{m}$ in (9) may cause the control signals grow out of the boundary. Thus the following control law modifications are introduced:

$$\begin{aligned} u_1 &= \widehat{m}\left(-\widehat{f}_1(x) + K_1 e_x + \dot{v}_{xr}\right), \\ \dot{\overline{f}}_1 &= -\gamma_1 e_x - \kappa_1\left(\overline{f}_1 - \widehat{f}_1\right), \\ \dot{\overline{m}} &= e_x \gamma_2 u_1 - \kappa_2(\overline{m} - \widehat{m}), \end{aligned} \tag{11}$$

where κ_1 and κ_2 are positive constants,

$$\begin{aligned} \widehat{f}_1 &= \begin{cases} \overline{f}_1 & \text{if } f_{1\min} \le \overline{f}_1 \le f_{1\max} \\ f_{1\min} & \text{if } \overline{f}_1 < f_{1\min} \\ f_{1\max} & \text{if } \overline{f}_1 > f_{1\max}, \end{cases} \\ \widehat{m} &= \begin{cases} \overline{m} & \text{if } m_{\min} \le \overline{m} \le m_{\max} \\ m_{\min} & \text{if } \overline{m} < m_{\min} \\ m_{\max} & \text{if } \overline{m} > m_{\max}, \end{cases} \end{aligned} \tag{12}$$

with $m_{\max}$ and $m_{\min}$ being the upper and lower bounds of m. The modified control law (11) for the first channel can still make the tracking error e_x be arbitrarily small. Proof can be found in Appendix B.

Similar to the controller design for the first channel, the control law for the second channel can be designed as

$$\begin{aligned} u_2 &= \frac{\widehat{I}_z}{l_s}\left(-\widehat{f}_2 + K_2 e_2 + \dot{r}_{\text{ref}}\right), \\ \dot{\overline{f}}_2 &= -\gamma_3 e_x - \kappa_3\left(\overline{f}_2 - \widehat{f}_2\right), \\ \dot{\overline{I}}_z &= e_2 \gamma_4 l_s u_2 - \kappa_4(\overline{m} - \widehat{m}), \end{aligned} \tag{13}$$

where $e_2 = r_{\text{ref}} - r$ is the yaw rate tracking error and γ_3, γ_4, κ_3, and κ_4 are positive constants,

$$\begin{aligned} \widehat{f}_2 &= \begin{cases} \overline{f}_2 & \text{if } f_{1\min} \le \overline{f}_2 \le f_{2\max} \\ f_{2\min} & \text{if } \overline{f}_2 < f_{2\min} \\ f_{2\max} & \text{if } \overline{f}_2 > f_{2\max}, \end{cases} \\ \widehat{I}_z &= \begin{cases} \overline{I}_z & \text{if } I_{z\min} \le \overline{I}_z \le I_{z\max} \\ I_{z\min} & \text{if } \overline{I}_z < I_{z\min} \\ I_{z\max} & \text{if } \overline{I}_z > I_{z\max}. \end{cases} \end{aligned} \tag{14}$$

Here, $f_{2\max}$ and $f_{2\min}$ are the upper and lower bounds of f_2, respectively. $I_{z\max}$ and $I_{z\min}$ are the upper and lower bounds of I_z, respectively.

4. Lower-Level Controller Design

When the higher-level controller signals are obtained, the lower-level controller operates the four in-wheel motors such that the control requirements from the higher-level controller can be satisfied. An analytic solution is given to distribute the higher-level control efforts without using the numerical-optimization-based control allocation algorithms.

The cost function for allocating the four tire forces can be defined as

$$J = \frac{1}{2}\left(F_x^T W F_x + (BF_x - u)^T Q (BF_x - u)\right), \tag{15}$$

where $Q = \mathrm{diag}[q_1 \;\; q_2]$, $W = \mathrm{diag}[w_1 \;\; w_2 \;\; w_3 \;\; w_4]$, $F_x = [F_{x1} \;\; F_{x2} \;\; F_{x3} \;\; F_{x4}]^T$, $u = [u_1, u_2]^T$ is the desired control effort given by the higher-level controller, and B is the control effectiveness matrix and can be written according to (2)

$$B = \begin{bmatrix} \cos(\delta) & \cos(\delta) & 1 & 1 \\ -\cos(\delta)\, l_s + \sin(\delta)\, l_f & \cos(\delta)\, l_s + \sin(\delta)\, l_f & -l_s & l_s \end{bmatrix}. \tag{16}$$

Based on (15), we have

$$\begin{aligned} \frac{\partial J}{\partial F_x} &= F_x^T W + F_x^T B^T Q B - B^T Q u \\ &= F_x^T \left(W + B^T Q B\right) - B^T Q u, \end{aligned} \tag{17}$$

$$H = \frac{\partial^2 J}{\partial^2 F_x} = W + B^T Q B. \tag{18}$$

As $W > 0$ and $B^T Q B \geq 0$, one can claim $H > 0$, which implies that the objective function J has a global minimum with the minimizing F_{x0} given by

$$F_{x0} = \left(W + B^T Q B\right)^{-1} B^T Q u. \tag{19}$$

It is known that the tire force may become saturated if a sufficiently large motor control signal is applied in some extreme cases such as hard brake on a low-μ road. Once the tire longitudinal force reaches its maximal value, further increasing of slip makes the tire work in the unstable range and the tire force will decrease quickly. So the constraints of the tire forces should be explicitly considered in the tire force allocation design. Note that a bigger weighting factor w_i in (15) for a wheel means that a smaller portion of the total torque is required from this wheel. So one can control a certain wheel to provide a larger or less portion of the total torque by selecting a smaller or bigger weighting factor for this wheel. The constraint violations of the tire forces can be discouraged by defining the weighting factors w_i in (15) as

$$w_i = \frac{w_0}{\left(1 - s_i^*\right)^{\kappa}}, \tag{20}$$

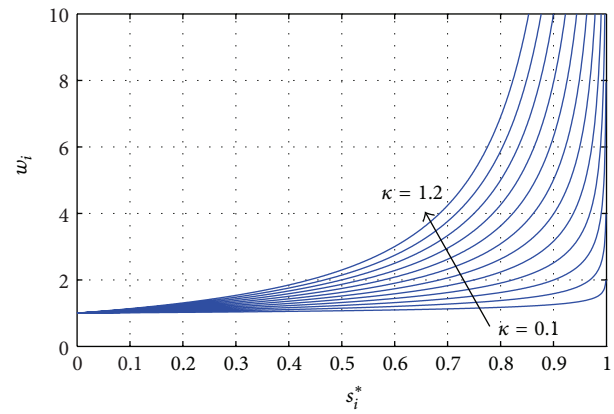

Figure 2: Weighting factor curves at different κ ($w_0 = 1$).

where w_0 is a positive constant, $\kappa > 0$ is a constant which is used to determine the shape of the weighting factor, and $s_i^* = s_i / s_i^{\mathrm{peak}}$ is the normalized tire slip ratio with s_i^{peak} corresponding to the maximum longitudinal forces of the ith tire. The curves of the weighting factor at different $\kappa > 0$ are plotted in Figure 2. When the slip ratio of a certain wheel reaches the s_i^{peak} which corresponds to the maximum longitudinal tire force, the weighting factor for this wheel will become large according to (20), which means that the required tire force from this wheel will become small; in this way the tire slip ratio can always be limited within the stable region. Based on the desired tire force calculated from (19), motor control signals can be generated such that the desired tire forces can be provided [21].

5. Simulation Results

Two simulation cases based on a high-fidelity, full-vehicle model constructed in CarSim were conducted. The vehicle parameters in the simulations were taken from an actual FWIA electric vehicle with in-wheel motors developed at the Ohio State University [21]. The desired vehicle yaw rate and speed can be generated from the drivers steering angle, accelerator/brake pedal positions. The vehicle reference model can be found in the literatures such as [22, 23].

5.1. J-Turn Simulation. In this simulation, the vehicle ran at a low-speed range. A counter-clockwise turn was introduced with the front wheel steering angle shown in Figure 3. We aim at controlling the vehicle such that the actual vehicle states can follow the references. The nominal vehicle mass was set to 800 kg in the simulation. As the designed controller does not depend on the actual vehicle parameters, we set the vehicle mass in the controller as 600 kg, which is different than the actual vehicle mass.

The generated external yaw moment with the tire force difference between two sides of the vehicle is shown in Figure 4. The vehicle yaw rate and vehicle speed are plotted in Figures 5 and 6, respectively. One can see from these two figures that both vehicle yaw rate and speed could be well

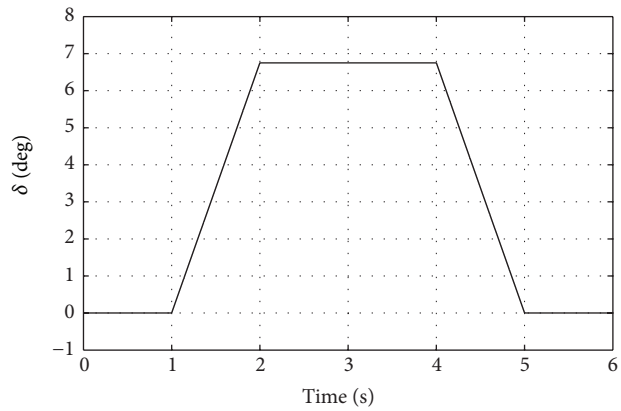

Figure 3: Front wheel steering angle in the J-turn simulation.

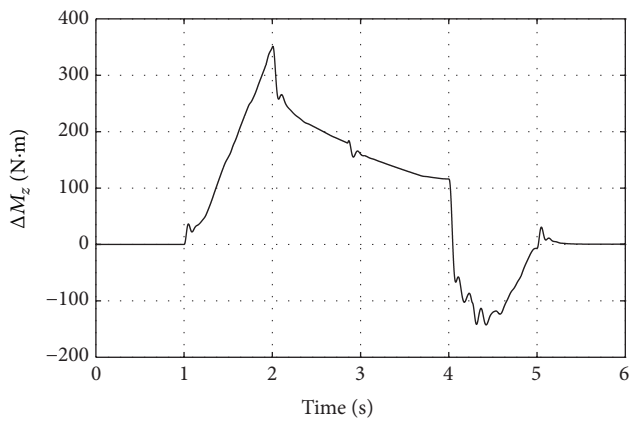

Figure 4: The generated external yaw moment in the J-turn simulation.

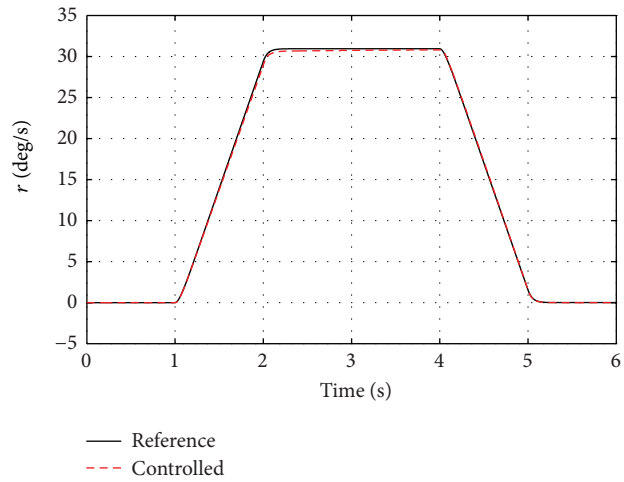

Figure 5: Vehicle yaw rates in the J-turn simulation.

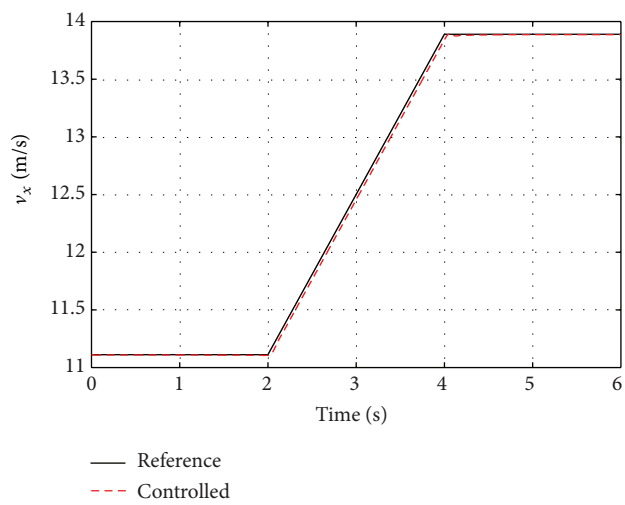

Figure 6: Vehicle speeds in the J-turn simulation.

controlled. Note that, in this simulation, a big steering angle was applied to the vehicle, and this steering angle could make the vehicle yaw rate reach up to 30 deg/s, which indicates that the proposed control method can control the vehicle well at extreme conditions.

5.2. Single-Lane Change. In the above simulation, we investigated the performance of the proposed controller in the cases where the vehicle runs on a high-μ road. In this simulation, the vehicle was controlled to make a single-lane change on a low-μ road. The tire-road friction coefficient was set as 0.2 and a big steering which would make the vehicle loss of stability was introduced at 2 s. The desired speed increased from 24.5 m/s to around 27.8 m/s in 6 seconds. The vehicle mass in the controller was set to 1000 kg, which is bigger than the actual vehicle mass.

The front wheel steering angle is shown in Figure 7. The generated yaw moment which regulated the vehicle yaw rate was plotted in Figure 8. The yaw rate control results are shown in Figure 9. To better show the effectiveness of the proposed control method, the yaw rate of an uncontrolled vehicle which ran on the same low-μ road was compared. One can see from Figure 9 that the yaw rate of the controlled vehicle could always follow the reference, while the yaw rate of the uncontrolled vehicle deviated from the reference when the front wheel steering angle became large. The yaw rate control results indicate that stability of the controlled vehicle was ensured. The vehicle longitudinal speeds are plotted in Figure 10. One can see again that the vehicle speed could be well controlled as well.

6. Conclusion

A vehicle stability control system for an FWIA electric vehicle is presented. The proposed adaptive control-based higher-level controller does not need the accurate vehicle parameters or tire force models but can still yield the desired control signals. An analytic solution considering tire force constraints is designed to allocate the required control efforts from the higher-lever controller to the four wheels. Simulations under various driving scenarios are carried out with a high-fidelity,

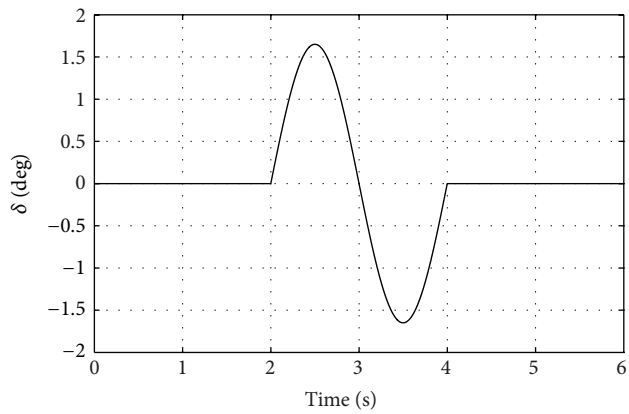

Figure 7: Front wheel steering angle in the single-lane change simulation.

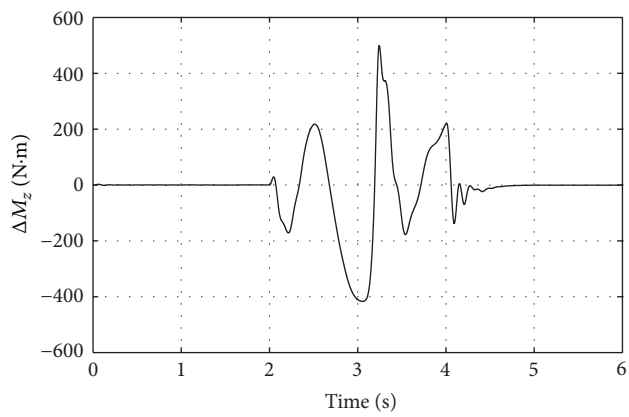

Figure 8: The generated external yaw moment in the single-lane change simulation.

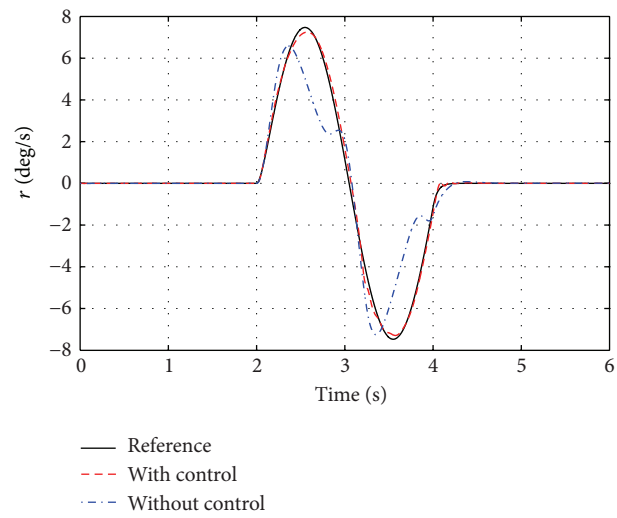

Figure 9: Vehicle yaw rates in the single-lane change simulation.

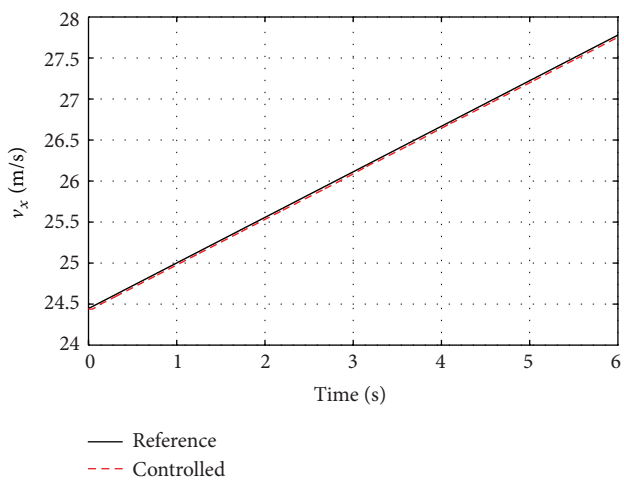

Figure 10: Vehicle longitudinal speeds in the single-lane change simulation.

CarSim, and full-vehicle model. Simulation results show the effectiveness of the proposed control approach.

Appendices

A.

By defining $\widetilde{m} = \widehat{m} - m$ and $\widetilde{f}_1 = \widehat{f}_1 - f_1$, the dynamics of the vehicle speed can be written as

$$\begin{aligned}\dot{v}_x &= f_1 + \frac{1}{m}u_1 \\ &= \left(\widehat{f}_1 - \widetilde{f}_1\right) + \frac{1}{m}(m + \widetilde{m})\left(-\widehat{f}_1 + K_1 e_1 \dot{v}_{rx}\right) \\ &= \left(\left(\widehat{f}_1 - \widetilde{f}_1\right) + \left(-\widehat{f}_1 + K_1 e_1 + \dot{v}_{rx}\right)\right) + \frac{\widetilde{m}}{m}u_1 \\ &= \left(-\widetilde{f}_1 + K_1 e_1 + \dot{v}_{rx}\right) + \frac{\widetilde{m}}{m}u_1,\end{aligned} \tag{A.1}$$

which means that the error dynamics of the first channel can be written as

$$\begin{aligned}\dot{e}_1 &= \dot{v}_{rx} - \dot{v}_x \\ &= -K_1 e_1 + \widetilde{f}_1 - \frac{\widetilde{m}}{m}u_1.\end{aligned} \tag{A.2}$$

Define the Lyapunov function candidate for this channel as

$$V_1 = \frac{1}{2}\left(e_1^2 + \frac{\widetilde{f}_1^2}{\gamma_1} + \frac{\widetilde{m}^2}{\gamma_2 m}\right), \tag{A.3}$$

whose time derivative can be expressed as

$$\begin{aligned}\dot{V}_1 &= e_1\dot{e}_1 - \frac{\tilde{f}_1\left(\dot{\hat{f}}_1 - \dot{f}_1\right)}{\gamma_1} + \frac{\tilde{m}\dot{\hat{m}}}{\gamma_2 m}\\ &= e_1\left(-K_1e_1 + \tilde{f}_1 - \frac{\tilde{m}}{m}u_1\right) - \frac{\tilde{f}_1\left(\dot{\hat{f}}_1 - \dot{f}_1\right)}{\gamma_1} + \frac{\tilde{m}\dot{\hat{m}}}{\gamma_2 m}\\ &= -K_1e_1^2 + \left(e_x\tilde{f}_1 + \frac{\tilde{f}_1\dot{\hat{f}}_1}{\gamma_1}\right) - \left(\frac{e_x\tilde{m}u_1}{m} - \frac{\tilde{m}\dot{\hat{m}}}{\gamma_2 m}\right) - \frac{\tilde{f}_1\dot{f}_1}{\gamma_1}.\end{aligned} \tag{A.4}$$

Assuming that the upper bound of $\hat{f}_1$ is the same as that for f_1, the update law (11) can make the time derivative of V_1 to be written as

$$\begin{aligned}\dot{V}_1 &= -K_1e_1^2 - \frac{\tilde{f}_1\dot{f}_1}{\gamma_1}\\ &\le -K_1e_1^2 - \frac{\left|\hat{f}_1 - f_1\right|\left|\dot{f}_1\right|}{\gamma_1}\\ &\le -K_1e_1^2 - \frac{\left(\hat{f}_{1\max} - f_{1\min}\right)\left|\dot{f}_1\right|_{\max}}{\gamma_1},\end{aligned} \tag{A.5}$$

where $|\dot{f}_1|_{\max}$ is the upper boundary of $|\dot{f}_1|$ and $f_{1\min}$ and $f_{1\max}$ are the upper and lower boundaries of f_1, respectively. The error can be bounded according to (10). The proof is completed.

B.

Redefine the Lyapunov function candidate (A.3) as

$$V_1 = \frac{1}{2}\left(e_1^2 + \frac{\left(\overline{f}_1 - f_1\right)^2 - \left(\overline{f}_1 - \hat{f}_1\right)^2}{\gamma_1} + \frac{(\overline{m} - m)^2 - (\overline{m} - \hat{m})^2}{m\gamma_2}\right). \tag{B.1}$$

Based on (12), the time derivative of the above Lyapunov function candidate is

$$\begin{aligned}\dot{V}_1 &= e_1\left(-K_1e_1 + \tilde{f}_1 - \frac{\tilde{m}}{m}u_1\right)\\ &\quad - \frac{\left(\tilde{f}_1 - f_1\right)\left(\dot{\tilde{f}}_1 - \dot{f}_1\right) - \left(\tilde{f}_1 - \hat{f}_1\right)\left(\dot{\tilde{f}}_1 - \dot{\hat{f}}_1\right)}{\gamma_1}\\ &\quad - \frac{(\tilde{m} - m)\left(\dot{\tilde{m}} - \dot{m}\right) - (\tilde{m} - \hat{m})\left(\dot{\tilde{m}} - \dot{\hat{m}}\right)}{\gamma_2 m}\\ &= -K_1e_1^2 + \left(\left(\gamma_1e_1\left(\hat{f}_1 - f_1\right) - \overline{f}_1\dot{f}_1 - f_1\dot{\overline{f}}_1 + f_1\dot{f}_1 + \overline{f}_1\dot{\hat{f}}_1 + \hat{f}_1\dot{\overline{f}}_1 - \hat{f}_1\dot{\hat{f}}_1\right) \times (\gamma_1)^{-1}\right)\\ &\quad + \frac{\gamma_2e_2(\hat{m} - m)u_1 - m\dot{\overline{m}} - \hat{m}\dot{\overline{m}} + \overline{m}\dot{\hat{m}} - \hat{m}\dot{\hat{m}}}{\gamma_2 m}\\ &= -K_1e_1^2\\ &\quad + \frac{\left(f_1 - \overline{f}_1\right)\dot{f}_1}{\gamma_1} + \frac{\left(\gamma_1e_1 + \dot{\hat{f}}_1\right)\left(\hat{f}_1 - f_1\right) + \left(\overline{f}_1 - \hat{f}_1\right)\dot{\hat{f}}_1}{\gamma_1}\\ &\quad + \frac{\left(\dot{\overline{m}} - e_1\gamma_2u_1\right)(\hat{m} - m) + (\overline{m} - \hat{m})\dot{\hat{m}}}{\gamma_2 m}.\end{aligned} \tag{B.2}$$

If $f_{1\min} \le \overline{f}_1 \le f_{1\max}$, the following holds

$$\hat{f}_1 = \overline{f}_1, \qquad \dot{\overline{f}}_1 = \gamma_1e_1. \tag{B.3}$$

And if $\overline{f}_1 < f_{1\min}$ or $\overline{f}_1 > f_{1\max}$, we have

$$\begin{aligned}&\dot{\hat{f}}_1 = 0,\\ &\left(\gamma_1e_1 + \dot{\overline{f}}_1\right)\left(\hat{f}_1 - f_1\right) = -\kappa_1\left(\overline{f}_1 - \hat{f}_1\right)\left(\hat{f}_1 - f_1\right) \le 0,\end{aligned} \tag{B.4}$$

which means the following always holds:

$$\frac{\left(\gamma_1e_1 + \dot{\hat{f}}_1\right)\left(\hat{f}_1 - f_1\right) + \left(\overline{f}_1 - \hat{f}_1\right)\dot{\hat{f}}_1}{\gamma_1} \le 0. \tag{B.5}$$

Similarly, one has

$$\frac{\left(\dot{\overline{m}} - e_1\gamma_2u_1\right)(\hat{m} - m) + (\overline{m} - \hat{m})\dot{\hat{m}}}{\gamma_2 m} \le 0, \tag{B.6}$$

so (B.2) can be rewritten as

$$\dot{V}_1 \le -K_1e_1^2 + \frac{\left(f_1 - \hat{f}_1\right)\dot{f}_1}{\gamma_1}. \tag{B.7}$$

Based on (20), one can see that if $\hat{f}_1$ tends to move out of its boundary $[f_{1\min}, f_{1\max}]$, the feedback term $-\kappa_1(\overline{f}_1 - \hat{f}_1)$ will pull $\overline{f}_1$ back to close to $\hat{f}_1$; thus $\overline{f}_1$ is also bounded. Thus, the modified control law given by (11) and (12) can also make e_1 arbitrarily small if sufficiently large γ_1 and K_1 are taken.

Conflict of Interests

The authors declare that there is no conflict of interests regarding the publication of this paper.

Acknowledgments

This paper was supported by National Science Foundation of China (51105074, 51205058, and 51375086), Foundation of State Key Laboratory of Mechanical Transmission (SKLMT-KFKT-201206), and by the Polish-Norwegian Research Programme operated by the National Centre for Research and 24 Development under the Norwegian Financial Mechanism 2009–2014 in the frame of Project Contract no. Pol-Nor/200957/47/2013.

References

[1] C. C. Chan, "The state of the art of electric, hybrid, and fuel cell vehicles," *Proceedings of the IEEE*, vol. 95, no. 4, pp. 704–718, 2007.

[2] J. Yamakawa, A. Kojima, and K. Watanabe, "A method of torque control for independent wheel drive vehicles on rough terrain," *Journal of Terramechanics*, vol. 44, no. 5, pp. 371–381, 2007.

[3] M. Shino and M. Nagai, "Independent wheel torque control of small-scale electric vehicle for handling and stability improvement," *JSAE Review*, vol. 24, no. 4, pp. 449–456, 2003.

[4] R. Wang and J. Wang, "Fault-tolerant control for electric ground vehicles with independently-actuated in-wheel motors," *Journal of Dynamic Systems, Measurement and Control*, vol. 134, no. 2, Article ID 021014, 2012.

[5] H. E. Tseng, B. Ashrafi, D. Madau, T. A. Brown, and D. Recker, "The development of vehicle stability control at Ford," *IEEE/ASME Transactions on Mechatronics*, vol. 4, no. 3, pp. 223–234, 1999.

[6] M. Canale, L. Fagiano, and V. Razza, "Vehicle lateral stability control via approximated NMPC: real-time implementation and software-in-the-loop test," in *Proceedings of the 48th IEEE Conference on Decision and Control held jointly with 2009 28th Chinese Control Conference (CDC/CCC '09)*, pp. 4596–4601, December 2009.

[7] M. Canale, L. Fagiano, M. Milanese, and P. Borodani, "Robust vehicle yaw control using an active differential and IMC techniques," *Control Engineering Practice*, vol. 15, no. 8, pp. 923–941, 2007.

[8] S. Sakai, H. Sado, and Y. Hori, "Motion control in an electric vehicle with four independently driven in-wheel motors," *IEEE/ASME Transactions on Mechatronics*, vol. 4, no. 1, pp. 9–16, 1999.

[9] N. Mutoh, Y. Hayano, H. Yahagi, and K. Takita, "Electric braking control methods for electric vehicles with independently driven front and rear wheels," *IEEE Transactions on Industrial Electronics*, vol. 54, no. 2, pp. 1168–1176, 2007.

[10] D. Kim, S. Hwang, and H. Kim, "Vehicle stability enhancement of four-wheel-drive hybrid electric vehicle using rear motor control," *IEEE Transactions on Vehicular Technology*, vol. 57, no. 2, pp. 727–735, 2008.

[11] H. Zhang, Y. Shi, and J. Wang, "Observer-based tracking controller design for networked predictive control systems with uncertain Markov delays," *International Journal of Control*, vol. 86, no. 10, pp. 1824–1836, 2013.

[12] R. Wang, H. Zhang, and J. Wang, "Linear parameter-varying controller design for four wheel independently-actuated electric ground vehicles with active steering systems," *IEEE Transactions on Control Systems Technology*, 2013.

[13] H. Zhang, Y. Shi, and J. Wang, "Observer-based tracking controller design for networked predictive control systems with uncertain Markov delays," *International Journal of Control*, vol. 86, no. 10, pp. 1824–1836, 2013.

[14] H. Zhang, Y. Shi, and A. Saadat Mehr, "Robust static output feedback control and remote PID design for networked motor systems," *IEEE Transactions on Industrial Electronics*, vol. 58, no. 12, pp. 5396–5405, 2011.

[15] J. Wang and R. G. Longoria, "Coordinated and reconfigurable vehicle dynamics control," *IEEE Transactions on Control Systems Technology*, vol. 17, no. 3, pp. 723–732, 2009.

[16] J. Tjoønnäs and T. A. Johansen, "Stabilization of automotive vehicles using active steering and adaptive brake control allocation," *IEEE Transactions on Control Systems Technology*, vol. 18, no. 3, pp. 545–558, 2010.

[17] Z. Shuai, H. Zhang, J. Wang, J. Li, and M. Ouyang, "Combined AFS and DYC control of four-wheel-independent-drive electric vehicles over CAN network with time-varying delays," *IEEE Transactions on Vehicular Technology*, 2013.

[18] H. Zhou and Z. Liu, "Vehicle yaw stability-control system design based on sliding mode and backstepping control approach," *IEEE Transactions on Vehicular Technology*, vol. 59, no. 7, pp. 3674–3678, 2010.

[19] S. Di Cairano and H. E. Tseng, "Driver-assist steering by active front steering and differential braking: design, implementation and experimental evaluation of a switched model predictive control approach," in *Proceedings of the 49th IEEE Conference on Decision and Control (CDC '10)*, pp. 2886–2891, December 2010.

[20] J. Wang, L. Alexander, and R. Rajamani, "Friction estimation on highway vehicles using longitudinal measurements," *Journal of Dynamic Systems, Measurement and Control*, vol. 126, no. 2, pp. 265–275, 2004.

[21] R. Wang, Y. Chen, D. Feng, X. Huang, and J. Wang, "Development and performance characterization of an electric ground vehicle with independently actuated in-wheel motors," *Journal of Power Sources*, vol. 196, no. 8, pp. 3962–3971, 2011.

[22] S. Horiuchi, K. Okada, and S. Nohtomi, "Improvement of vehicle handling by nonlinear integrated control of four wheel steering and four wheel torque," *JSAE Review*, vol. 20, no. 4, pp. 459–464, 1999.

[23] J. Y. Wong, *Theory of Ground Vehicles*, Wiley, New York, NY, USA, 3rd edition, 2001.

Hindawi Publishing Corporation
Mathematical Problems in Engineering
Volume 2013, Article ID 907056, 12 pages
http://dx.doi.org/10.1155/2013/907056

Research Article

Static Output-Feedback Control for Vehicle Suspensions: A Single-Step Linear Matrix Inequality Approach

Josep Rubió-Massegú,[1] Francisco Palacios-Quiñonero,[1] Josep M. Rossell,[1] and Hamid Reza Karimi[2]

[1] *Department of Applied Mathematics III, Universitat Politècnica de Catalunya (UPC), Avenue Bases de Manresa 61-73, Manresa 08242, Barcelona, Spain*
[2] *Department of Engineering, Faculty of Engineering and Science, University of Agder (UiA), 4898 Grimstad, Norway*

Correspondence should be addressed to Josep Rubió-Massegú; josep.rubio@upc.edu

Received 28 September 2013; Accepted 31 October 2013

Academic Editor: Hui Zhang

In this paper, a new strategy to design static output-feedback controllers for a class of vehicle suspension systems is presented. A theoretical background on recent advances in output-feedback control is first provided, which makes possible an effective synthesis of static output-feedback controllers by solving a single linear matrix inequality optimization problem. Next, a simplified model of a quarter-car suspension system is proposed, taking the ride comfort, suspension stroke, road holding ability, and control effort as the main performance criteria in the vehicle suspension design. The new approach is then used to design a static output-feedback H_∞ controller that only uses the suspension deflection and the sprung mass velocity as feedback information. Numerical simulations indicate that, despite the restricted feedback information, this static output-feedback H_∞ controller exhibits an excellent behavior in terms of both frequency and time responses, when compared with the corresponding state-feedback H_∞ controller.

1. Introduction

In recent decades, vehicle suspension systems have been attracting a growing interest. In particular, much research effort has been devoted to designing different kinds of passive, active, and semiactive vehicle suspensions using a wide variety of control strategies. Some relevant instances of control strategies used in this field are fuzzy control, optimal control, H_∞ control, gain scheduling, adaptive control, and model predictive control [1–5]. The development of these control strategies has been closely related to the emergence of computational tools and efficient numerical algorithms, which allow solving complex and sophisticated control problems in a reasonably short time.

When designing a feedback control system, the amount of information available for feedback purposes is an element of particular importance. In the ideal case that the entire state vector is available, many advanced state-feedback controller designs can be formulated as linear matrix inequality (LMI) optimization problems and efficiently computed using standard computational tools as those provided by the *MATLAB Robust Control Toolbox* [6]. In a more realistic situation, however, the complete state vector is rarely accessible and the available feedback information consists only in a reduced set of linear combinations of the states. In this context, static output-feedback control strategies are an excellent option to facilitate a simple implementation in practice.

From a computational perspective, static output-feedback controller designs lead to challenging problems. Typically, this kind of problems has been solved using multistep numerical algorithms such as those based on random search [7], or those consisting in iterative procedures [8–11]. In both cases, complex matrix equations or LMI optimization problems need to be solved at each step. To avoid the high computational cost associated with the multistep methods, some single-step strategies have also been proposed [12–15], which formulate the static output-feedback controller design in terms of a single LMI optimization problem. These

single-step methods are based on a proper transformation of the state variables and present the drawback of being highly problem-dependent, in the sense that a complete derivation of the LMI optimization problem must be carried out for most controller designs.

Recently, a new single-step strategy has been presented in [16], which can be applied to any control problem that admits an LMI-based state-feedback controller design. In this case, an LMI formulation to compute the output-feedback control gain matrix can be easily derived by means of a simple change of variables. The new design methodology is computationally effective, conceptually simple, and easy to implement. Moreover, it can be an excellent tool to design static output-feedback controllers in a wide variety of problems by taking advantage of the rich literature on LMI formulations for state-feedback controller design. Some preliminary works, with successful applications to the field of vibration control of large structures, can be found in [17–21].

The main objective of this paper is to explore the potential applicability of the new design methodology in the field of vehicle suspensions. Additionally, we are also interested in providing a clear and practical presentation of the main theoretical elements of the new approach, which we believe can be of general interest for control engineers in different fields. To this end, a static output-feedback H_∞ controller is designed for a simplified quarter-car suspension system. A state-feedback H_∞ controller is also designed, and it is used as a reference in the performance assessment. Moreover, the LMI formulation of the state-feedback design serves as a natural starting point to derive the LMI formulation for the output-feedback design.

The paper is organized as follows. In Section 2, the fundamental elements of the new strategy for static output-feedback controller design are summarily discussed. In Section 3, a suitable mathematical model for a quarter-car suspension system is provided, and the general ideas of Section 2 are applied to the particular case of H_∞ controller design. In Section 4, a static output-feedback H_∞ controller is designed for a particular quarter-car suspension system, and a suitable set of frequency and time responses are computed to assess the effectiveness of the proposed controller. Finally, in Section 5, some conclusions and future lines of research are briefly presented.

2. Theoretical Background

Let us consider a linear matrix inequality that depends on a symmetric positive-definite matrix $X \in \mathbb{R}^{n\times n}$, a matrix $Y \in \mathbb{R}^{m\times n}$, and possibly other scalar or matrix variables. Such an LMI can be written in the form:

$$X > 0, \qquad F(X, Y, \zeta) > 0, \tag{1}$$

where the vector $\zeta \in \mathbb{R}^{p\times 1}$ collects the free entries of the matrices distinct from X and Y, together with the remaining LMI variables, and F is a given affine map that makes the matrix inequality an LMI. This kind of LMI formulation is very common in practice and appears in a large number of state-feedback control problems [22]; some recent works can be found in [23–28]. More precisely, the LMI formulation (1) arises naturally in a wide variety of state-feedback controller designs, where the state control gain matrix $G \in \mathbb{R}^{m\times n}$ is explicitly given by

$$G = YX^{-1}, \tag{2}$$

where X is usually the inverse of a Lyapunov matrix or a scaling of it, and Y comes from a previous change of variables defined by

$$Y = GX. \tag{3}$$

Static output-feedback control problems can be seen as static state-feedback problems with the additional constraint that the state control gain matrix G admits a factorization of the form:

$$G = KC_y, \tag{4}$$

where $K \in \mathbb{R}^{m\times q}$ is the output control gain matrix and $C_y \in \mathbb{R}^{q\times n}$ is the observed-output matrix, which is assumed to be a given full row-rank matrix with $q < n$. Consequently, if a static state-feedback control problem can be formulated in terms of an LMI of the form (1) with the state gain matrix given in (2), then the corresponding static output-feedback version of the same control problem can be reduced to a nonconvex problem, consisting in finding matrices X, Y, and ζ satisfying

$$X > 0, \qquad F(X, Y, \zeta) > 0, \quad (X, Y) \in \mathscr{M}, \tag{5}$$

where $\mathscr{M}$ is the set of all pairs of matrices (X, Y) for which there exists an $m \times q$ matrix K satisfying

$$YX^{-1} = KC_y. \tag{6}$$

Recently, a systematic and easy-to-implement strategy to obtain feasible solutions of (5) has been proposed in [16]. This strategy considers an $n\times(n-q)$ matrix Q, whose columns are a basis of $\ker(C_y)$, and a matrix R defined by

$$R = C_y^{\dagger} + QL, \tag{7}$$

where L is a given $(n-q)\times q$ matrix and

$$C_y^{\dagger} = C_y^T\left(C_yC_y^T\right)^{-1} \tag{8}$$

is the *Moore-Penrose pseudoinverse* of C_y. Next, the following linear transformations are introduced:

$$X = QX_QQ^T + RX_RR^T, \qquad Y = Y_RR^T, \tag{9}$$

where $X_Q \in \mathbb{R}^{(n-q)\times(n-q)}$ and $X_R \in \mathbb{R}^{q\times q}$ are symmetric matrices and $Y_R \in \mathbb{R}^{m\times q}$ is an arbitrary matrix. The design of static output-feedback controllers is based on the following result.

Theorem 1 (see [16]). *If the matrix X in (9) is nonsingular, then X_R is also nonsingular and the matrix equation $YX^{-1} = KC_y$ holds with*

$$K = Y_R X_R^{-1}. \tag{10}$$

Moreover, X is positive-definite if and only if the matrices X_Q and X_R are both positive-definite.

This theorem provides a systematic methodology to obtain solutions of (5). Indeed, we only need to choose a suitable $(n-q)\times q$ matrix L in order to define $R = C_y^{\dagger} + QL$, and solve the following LMI with variables X_Q, X_R, Y_R, and ζ:

$$\begin{aligned} &X_Q > 0, \quad X_R > 0, \\ &F\left(QX_QQ^T + RX_RR^T, Y_RR^T, \zeta\right) > 0, \end{aligned} \tag{11}$$

which has been obtained from (1) by using the transformations (9), using also the fact that the condition $X > 0$ can be replaced by $X_Q > 0$ and $X_R > 0$. If a feasible solution to the LMI (11) is achieved by the matrices $\widetilde{X}_Q$, $\widetilde{X}_R$, $\widetilde{Y}_R$, and $\widetilde{\zeta}$ then, for the corresponding matrices $\widetilde{X}$, $\widetilde{Y}$ defined in (9) and the vector $\widetilde{\zeta}$ we obtain a feasible solution of (5) that, at the same time, satisfies the constraint (6) with the output gain matrix:

$$K = \widetilde{Y}_R \widetilde{X}_R^{-1}. \tag{12}$$

The main features of this strategy are its generality, conceptual simplicity, and ease of implementation. Moreover, it can also be applied to optimization problems of the form:

$$\begin{aligned} &\text{minimize} \quad h(X, Y, \zeta) \\ &\text{subject to} \quad X > 0, \quad F(X, Y, \zeta) > 0, \quad (X, Y) \in \mathscr{M}, \end{aligned} \tag{13}$$

where the objective function h is assumed to be linear. This kind of optimization problem arises when some performance criterion needs to be optimized. In this case, the optimization problem (13) can be transformed into the following LMI optimization problem with variables X_Q, X_R, Y_R, and ζ:

$$\begin{aligned} &\text{minimize} \quad \widehat{h}(X_Q, X_R, Y_R, \zeta) \\ &\text{subject to} \quad X_Q > 0, \quad X_R > 0, \\ &\qquad\qquad F\left(QX_QQ^T + RX_RR^T, Y_RR^T, \zeta\right) > 0, \end{aligned} \tag{14}$$

where the new objective function $\widehat{h}$ is defined as

$$\widehat{h}(X_Q, X_R, Y_R, \zeta) = h\left(QX_QQ^T + RX_RR^T, Y_RR^T, \zeta\right). \tag{15}$$

Clearly, given an optimal solution to the optimization problem (14), a corresponding triplet $(\widetilde{X}, \widetilde{Y}, \widetilde{\zeta})$ of matrices can be computed, which minimizes the objective function $h(X, Y, \zeta)$ on a set that satisfies all the constraints in (13). In particular, we will have $\widetilde{Y}\widetilde{X}^{-1} = KC_y$ with $K = \widetilde{Y}_R\widetilde{X}_R^{-1}$.

Remark 2. In general, the objective function h in (13) depends on the variables X, Y, and ζ. However, an objective function $h(\zeta)$ that only depends on ζ will be encountered in the following sections. In this case, we have $\widehat{h}(X_Q, X_R, Y_R, \zeta) = h(\zeta)$ and the corresponding LMI optimization problem (14) takes the simplified form:

$$\begin{aligned} &\text{minimize} \quad h(\zeta) \\ &\text{subject to} \quad X_Q > 0, \quad X_R > 0, \\ &\qquad\qquad F\left(QX_QQ^T + RX_RR^T, Y_RR^T, \zeta\right) > 0. \end{aligned} \tag{16}$$

Remark 3. For simplicity, positive semidefinite terms are not considered in the LMI (1). If necessary, this kind of terms can be easily included by adding a new matrix inequality of the form $F_0(X, Y, \zeta) \geq 0$.

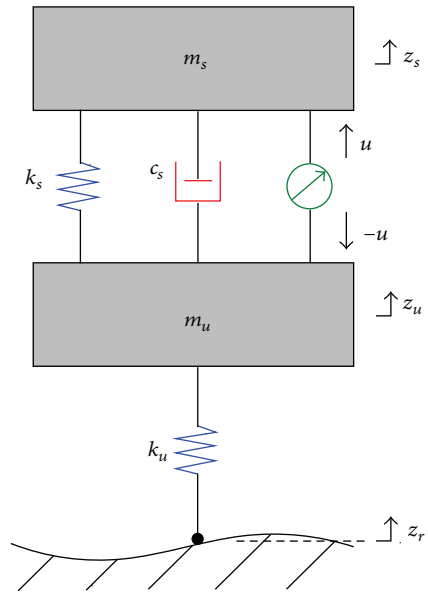

Figure 1: Quarter-car suspension model with active suspension.

3. Static Output-Feedback Control for Vehicle Suspensions

In this section, the general methodology introduced in Section 2 is applied to design an output-feedback H_∞ control system for a quarter-car suspension model. More precisely, in Section 3.1, a first-order state-space model for a quarter-car together with a suitable vector of controlled outputs are presented. An LMI formulation to compute static output-feedback H_∞ controllers is provided in Section 3.2.

3.1. Mathematical Model. Let us consider the quarter-car suspension model schematically depicted in Figure 1. The motion equations can be written as

$$\begin{aligned} m_s\ddot{z}_s(t) &= -c_s\left[\dot{z}_s(t) - \dot{z}_u(t)\right] - k_s\left[z_s(t) - z_u(t)\right] \\ &\quad + u(t), \\ m_u\ddot{z}_u(t) &= c_s\left[\dot{z}_s(t) - \dot{z}_u(t)\right] + k_s\left[z_s(t) - z_u(t)\right] \\ &\quad - k_u\left[z_u(t) - z_r(t)\right] - u(t), \end{aligned} \tag{17}$$

where m_s and m_u are the sprung and unsprung masses representing the chassis mass and wheel mass, respectively; k_s and c_s are, respectively, the stiffness and damping of the suspension system; k_u stands for the tire stiffness; $z_r(t)$ represents the vertical road displacement; $z_s(t)$ and $z_u(t)$ are the vertical displacements of the sprung and unsprung masses, respectively; and $u(t)$ is the active input of the suspension system. By defining the state variables

$$\begin{aligned} x_1(t) &= z_s(t), \qquad x_2(t) = z_u(t), \\ x_3(t) &= \dot{z}_s(t), \qquad x_4(t) = \dot{z}_u(t), \end{aligned} \tag{18}$$

a first-order state-space model in the form:

$$\dot{x}(t) = Ax(t) + Bu(t) + B_w w(t) \tag{19}$$

can be derived, where $x(t) = [x_1(t), x_2(t), x_3(t), x_4(t)]^T$ is the vector of states, $u(t)$ is the control input, $w(t) = z_r(t)$ is the road disturbance input, and the matrices A, B, and B_w are given by

$$\begin{aligned} A &= \begin{bmatrix} 0 & 0 & 1 & 0 \\ 0 & 0 & 0 & 1 \\ -\dfrac{k_s}{m_s} & \dfrac{k_s}{m_s} & -\dfrac{c_s}{m_s} & \dfrac{c_s}{m_s} \\ \dfrac{k_s}{m_u} & -\dfrac{k_s + k_u}{m_u} & \dfrac{c_s}{m_u} & -\dfrac{c_s}{m_u} \end{bmatrix}, \\ B &= \begin{bmatrix} 0 \\ 0 \\ \dfrac{1}{m_s} \\ -\dfrac{1}{m_u} \end{bmatrix}, \qquad B_w = \begin{bmatrix} 0 \\ 0 \\ 0 \\ \dfrac{k_u}{m_u} \end{bmatrix}. \end{aligned} \tag{20}$$

To define the vector of controlled outputs, we consider the ride comfort, suspension stroke, road holding ability, and the required control effort as main performance criteria in the vehicle suspension design. These criteria can be quantified using the sprung mass acceleration $\ddot{z}_s(t)$, the suspension deflection $z_s(t) - z_u(t)$, the tire deflection $z_u(t) - z_r(t)$, and the control force $u(t)$, respectively, and should be made as small as possible in order to have good vehicle suspension characteristics [29, 30]. Therefore, we consider the following vector of controlled outputs:

$$z(t) = \begin{bmatrix} \ddot{z}_s(t) \\ \alpha(z_s(t) - z_u(t)) \\ \beta(z_u(t) - z_r(t)) \\ \eta u(t) \end{bmatrix}, \tag{21}$$

where α, β, and η are adjustable weights that should manage the tradeoff between the above performance requirements. Using (17) to isolate the sprung mass acceleration, the controlled output $z(t)$ can be written as

$$z(t) = Cx(t) + Du(t) + D_w w(t) \tag{22}$$

with

$$\begin{aligned} C &= \begin{bmatrix} -\dfrac{k_s}{m_s} & \dfrac{k_s}{m_s} & -\dfrac{c_s}{m_s} & \dfrac{c_s}{m_s} \\ \alpha & -\alpha & 0 & 0 \\ 0 & \beta & 0 & 0 \\ 0 & 0 & 0 & 0 \end{bmatrix}, \\ D &= \begin{bmatrix} \dfrac{1}{m_s} \\ 0 \\ 0 \\ \eta \end{bmatrix}, \qquad D_w = \begin{bmatrix} 0 \\ 0 \\ -\beta \\ 0 \end{bmatrix}. \end{aligned} \tag{23}$$

3.2. Static Output-Feedback H_∞ Controller Design. Now, let us consider the system:

$$\begin{aligned} \dot{x}(t) &= Ax(t) + Bu(t) + B_w w(t), \\ z(t) &= Cx(t) + Du(t) + D_w w(t), \end{aligned} \tag{24}$$

where $x(t) \in \mathbb{R}^n$ is the state vector, $u(t) \in \mathbb{R}^m$ is the control input, $w(t) \in \mathbb{R}^r$ is the disturbance input, $z(t) \in \mathbb{R}^d$ is the controlled output, and A, B, B_w, C, D, and D_w are constant matrices with appropriate dimensions. Given a state-feedback controller:

$$u(t) = Gx(t) \tag{25}$$

with state gain matrix $G \in \mathbb{R}^{m\times n}$, the following closed-loop system results:

$$\begin{aligned} \dot{x}(t) &= A_G x(t) + B_w w(t), \\ z(t) &= C_G x(t) + D_w w(t), \end{aligned} \tag{26}$$

where

$$A_G = A + BG, \qquad C_G = C + DG. \tag{27}$$

For a given control gain matrix G, the H_∞-norm of the closed-loop system (26) is given by

$$\gamma_G = \|T_G\|_\infty = \sup_{\omega\in\mathbb{R}} \sigma_{\max}[T_G(j\omega)], \tag{28}$$

where $\sigma_{\max}[\cdot]$ denotes the maximum singular value and T_G is the transfer function from the disturbance input to the controlled output:

$$T_G(s) = C_G(sI - A_G)^{-1}B_w + D_w. \tag{29}$$

In the state-feedback H_∞ controller design approach, the objective is to obtain a controller of the form (25), which defines an asymptotically stable matrix A_G and, simultaneously, minimizes the corresponding H_∞-norm γ_G. According to the *Bounded Real Lemma* [22], for a given scalar $\gamma > 0$, the closed-loop state matrix A_G is asymptotically stable and $\gamma_G < \gamma$, if and only if there exists a symmetric positive-definite matrix $P \in \mathbb{R}^{n\times n}$ such that the matrix inequality

$$\begin{bmatrix} PA_G + A_G^T P & * & * \\ B_w^T P & -\gamma I & * \\ C_G & D_w & -\gamma I \end{bmatrix} < 0 \tag{30}$$

holds, where $(*)$ denotes the transposed entry. Pre- and postmultiplying both sides of (30) by the symmetric matrix $\mathrm{diag}[X, I, I]$ with $X = P^{-1}$, using the values of the matrices A_G, and C_G in (27), and introducing the new variable $Y = GX$, we arrive at the linear matrix inequality:

$$S(X,Y,\gamma) = \begin{bmatrix} AX + XA^T + BY + Y^TB^T & * & * \\ B_w^T & -\gamma I & * \\ CX + DY & D_w & -\gamma I \end{bmatrix} < 0. \tag{31}$$

The state-feedback H_∞ controller can then be effectively computed by solving the following LMI optimization problem:

$$\begin{aligned} &\text{minimize} \quad \gamma \\ &\text{subject to} \quad X > 0, \quad \gamma > 0, \quad S(X,Y,\gamma) < 0. \end{aligned} \tag{32}$$

If the optimization problem (32) attains an optimal value $\tilde{\gamma}$ for the matrices $\tilde{X}$ and $\tilde{Y}$, then the state gain matrix $G = \tilde{Y}\tilde{X}^{-1}$ defines a state-feedback controller $u(t) = Gx(t)$ with an asymptotically stable closed-loop state matrix A_G and an optimal H_∞-norm $\gamma_G = \tilde{\gamma}$.

Let us now consider the case of a static output-feedback controller:

$$u(t) = Ky(t), \tag{33}$$

where $K \in \mathbb{R}^{m\times q}$ is the observed-output gain matrix and $y(t) \in \mathbb{R}^q$ is the vector of observed outputs, which can be written as

$$y(t) = C_y x(t), \tag{34}$$

for a given full row-rank matrix $C_y \in \mathbb{R}^{q\times n}$ with $q < n$. From (33) and (34), we obtain

$$u(t) = KC_y x(t), \tag{35}$$

and consequently, the output-feedback controller (33) can be considered as a state-feedback controller with an associated state gain matrix $G_{\mathrm{of}} = KC_y$. Therefore, the design of a static output-feedback H_∞ controller leads to the optimization problem (32) with the additional constraint $YX^{-1} = KC_y$, which is a particular case of the optimization problem (13) with

$$\begin{gathered} \zeta = \gamma, \quad h(X,Y,\gamma) = \gamma, \\ F(X,Y,\gamma) = \mathrm{diag}\left[\gamma, -S(X,Y,\gamma)\right]. \end{gathered} \tag{36}$$

According to the discussion presented in Section 2, the following LMI optimization problem results:

$$\begin{aligned} &\text{minimize} \quad \gamma \\ &\text{subject to} \quad X_Q > 0, \quad X_R > 0, \quad \gamma > 0, \\ &\qquad S\left(QX_QQ^T + RX_RR^T, Y_RR^T, \gamma\right) < 0, \end{aligned} \tag{37}$$

where the matrix inequality $S(QX_QQ^T + RX_RR^T, Y_RR^T, \gamma) < 0$ takes the explicit form

$$\begin{bmatrix} AQX_QQ^T + QX_QQ^TA^T + ARX_RR^T + RX_RR^TA^T + BY_RR^T + RY_R^TB^T & * & * \\ B_w^T & -\gamma I & * \\ CQX_QQ^T + CRX_RR^T + DY_RR^T & D_w & -\gamma I \end{bmatrix} < 0. \tag{38}$$

If the optimization problem defined in (37) attains an optimal solution $\tilde{\gamma}$ for the matrices $\tilde{X}_Q$, $\tilde{X}_R$, and $\tilde{Y}_R$, then the output gain matrix $K = \tilde{Y}_R\tilde{X}_R^{-1}$ defines a static output-feedback controller $u(t) = Ky(t)$ with asymptotically stable matrix $A_{G_{\mathrm{of}}}$ and optimal H_∞-norm $\gamma_{G_{\mathrm{of}}} \le \tilde{\gamma}$, where $G_{\mathrm{of}} = KC_y$.

Remark 4. Note that the LMI optimization problem (37) allows us to design a static output-feedback H_∞ controller $u(t) = Ky(t)$ by solving a single LMI optimization problem. Moreover, the optimal value $\tilde{\gamma}$ provides an upper bound of the H_∞-norm corresponding to $G_{\mathrm{of}} = KC_y$. The actual value of $\gamma_{G_{\mathrm{of}}}$ can be obtained by maximizing the maximum singular value of the matrix $T_{G_{\mathrm{of}}}(j\omega)$, as indicated in (28). Alternatively, the value $\gamma_{G_{\mathrm{of}}}$ can also be computed by solving the LMI optimization problem:

$$\begin{aligned} &\text{minimize} \quad \gamma \\ &\text{subject to} \quad P > 0, \quad \gamma > 0, \quad \text{LMI (30)}. \end{aligned} \tag{39}$$

4. Numerical Results

In this section, the ideas presented in Section 3.2 are applied to design a static output-feedback H_∞ controller for the quarter-car suspension model described in Section 3.1. This output-feedback controller only uses the suspension deflection and the sprung mass velocity as feedback information. A state-feedback H_∞ controller is also computed to be taken as a reference in the performance assessment. Next, three different configurations are considered: (i) uncontrolled system, (ii) controlled system using the state-feedback H_∞ controller, and (iii) controlled system using the static output-feedback H_∞ controller. For these configurations, a brief discussion on the corresponding frequency responses is presented in Section 4.2. The time responses to an isolated bump as road disturbance are presented and discussed in Section 4.3. Finally, some closing remarks are provided in Section 4.4. All computations have been carried out with

the *MATLAB Robust Control Toolbox* [6], and the following particular values [29, 31]

$$m_s = 504.5\,\text{kg}, \qquad m_u = 62\,\text{kg}, \qquad k_s = 13100\,\text{N/m},$$
$$k_u = 252000\ \text{N/m}, \qquad c_s = 400\ \text{Ns/m}, \tag{40}$$

have been taken as parameters of the quarter-car suspension model in the controllers design and numerical simulations.

4.1. Controllers Design. Let us consider the quarter-car state-space model defined by (19), (20), and the parameter values given in (40). To design a state-feedback H_∞ controller

$$u(t) = G_{\text{sf}} x(t), \tag{41}$$

which uses the full state vector given in (18) as feedback information, we also consider the controlled output defined in (22), (23) and the following particular values of the weighting coefficients:

$$\alpha = 8, \qquad \beta = 10, \qquad \eta = 1.5 \times 10^{-3}. \tag{42}$$

By solving the LMI optimization problem given in (32), we obtain the state gain matrix:

$$G_{\text{sf}} = 10^3 \times \begin{bmatrix} 1.4733 & -5.0315 & -2.8818 & 0.1018 \end{bmatrix}, \tag{43}$$

with an associated H_∞-norm:

$$\gamma_{G_{\text{sf}}} = 528.32. \tag{44}$$

Now, as proposed in [29], let us assume that the available feedback information only includes the suspension deflection and the sprung mass velocity. In this case, the vector of observed outputs is

$$y(t) = \begin{bmatrix} z_s(t) - z_u(t) & \dot{z}_s(t) \end{bmatrix}^T, \tag{45}$$

which can be written in the form:

$$y(t) = C_y x(t), \tag{46}$$

where $x(t)$ is the state vector defined in (18), and

$$C_y = \begin{bmatrix} 1 & -1 & 0 & 0 \\ 0 & 0 & 1 & 0 \end{bmatrix} \tag{47}$$

is the observed-output matrix. To design a static output-feedback H_∞ controller

$$u(t) = Ky(t), \tag{48}$$

we compute the matrix

$$Q = \begin{bmatrix} 1 & 0 \\ 1 & 0 \\ 0 & 0 \\ 0 & 1 \end{bmatrix}, \tag{49}$$

whose columns are a basis of $\ker(C_y)$ and the matrix

$$R = \begin{bmatrix} \frac{1}{2} & 0 \\ -\frac{1}{2} & 0 \\ 0 & 1 \\ 0 & 0 \end{bmatrix}, \tag{50}$$

which can be obtained from (7) for the particular choice $L = 0$. By solving the LMI optimization problem (37) with the matrices Q and R given in (49), (50) and the same matrices A, B, B_w, C, D, and D_w used in the previous state-feedback controller design, we get the observed-output gain matrix:

$$K = 10^3 \times \begin{bmatrix} -0.3585 & -8.9459 \end{bmatrix}, \tag{51}$$

and an optimal γ-value:

$$\tilde{\gamma} = 551.03. \tag{52}$$

According to Remark 4 and the γ-value in (44), the H_∞-norm of the state gain matrix

$$G_{\text{of}} = KC_y \tag{53}$$

associated with the observed-output gain matrix K, satisfies

$$528.32 \le \gamma_{G_{\text{of}}} \le 551.03. \tag{54}$$

By setting $G = G_{\text{of}}$ in (30) and solving the optimization problem (39), the following value of $\gamma_{G_{\text{of}}}$ results:

$$\gamma_{G_{\text{of}}} = 532.74, \tag{55}$$

which is only a 0.84% greater than the optimal value $\gamma_{G_{\text{sf}}}$ achieved by the state-feedback H_∞ controller.

4.2. Frequency Response. In this subsection, we consider the frequency response for three different control configurations of the quarter-car suspension model: (i) uncontrolled system, (ii) controlled system using the state-feedback H_∞ controller defined in (41) and (43), and (iii) controlled system using the static output-feedback H_∞ controller defined in (45), (48), and (51). For these configurations, the frequency transfer functions from the road displacement $w(t)$ to the magnitudes used as performance criteria are displayed in Figure 2. Specifically, the frequency transfer functions from the road displacement $w(t)$ to the sprung mass acceleration $\ddot{z}_s(t)$ are presented in Figure 2(a), where the black dotted line corresponds to the uncontrolled system (denoted as *Passive* in the legend), the blue dashed line pertains to the state-feedback controller (denoted as *State-feedback* in the legend), and the red solid line corresponds to the static output-feedback controller (denoted as *Output-feedback* in the legend). The frequency transfer functions from the road displacement $w(t)$ to the suspension deflection $z_s(t) - z_u(t)$, tire deflection $z_u(t) - z_r(t)$, and control force $u(t)$ are displayed in Figures 2(b), 2(c), and 2(d), respectively, using the same line styles and colors.

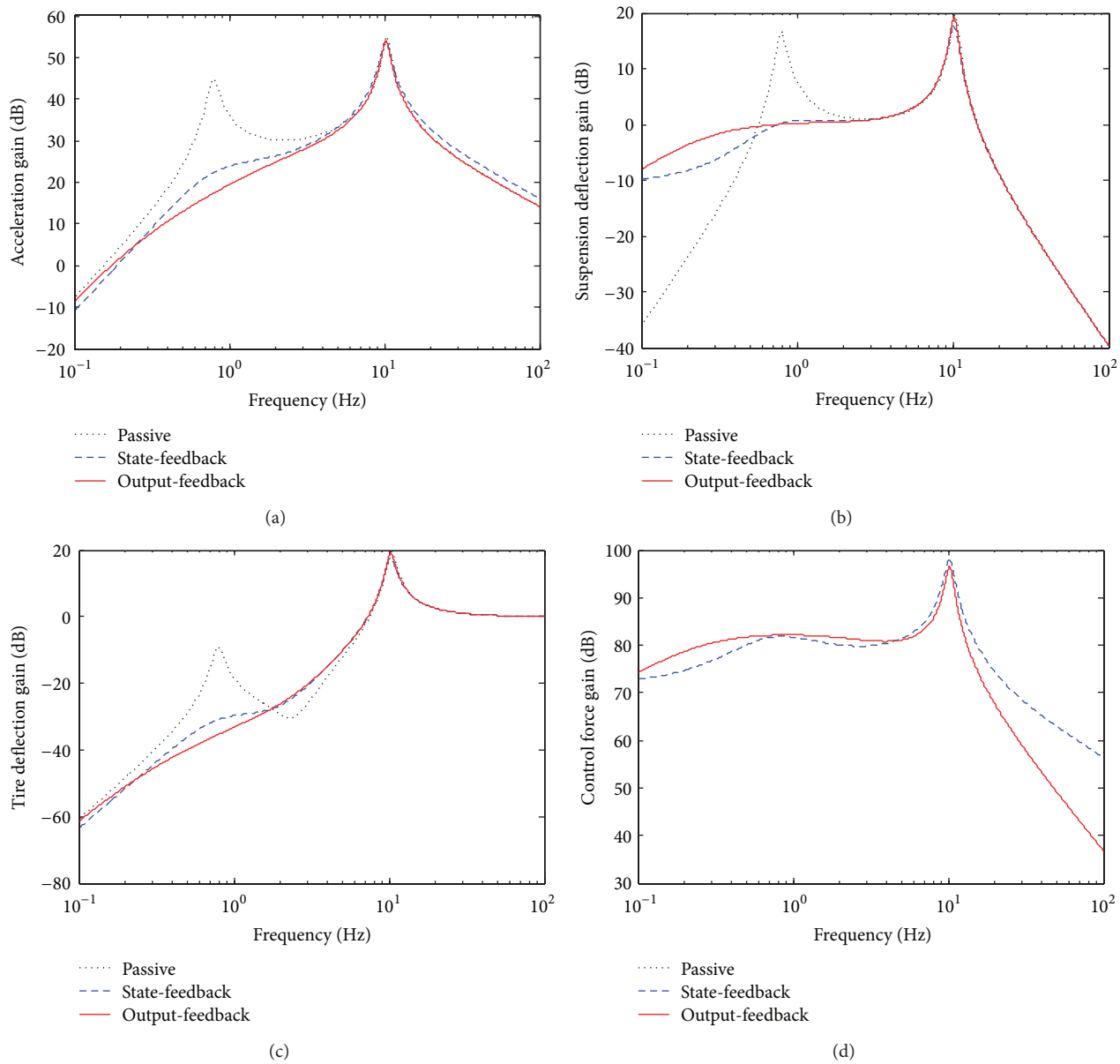

FIGURE 2: Frequency transfer functions from road displacement to (a) sprung mass acceleration, (b) suspension deflection, (c) tire deflection, and (d) control effort, corresponding to the passive (black dotted line), state-feedback (blue dashed line), and static output-feedback (red solid line) configurations.

Looking at the graphics in Figure 2(a), it can be appreciated that a significant improvement on ride comfort is provided by the state-feedback and output-feedback controllers when compared with the passive system, especially in the sensitive frequency range of 0–65 rad/s [32]. A closer look at the graphics corresponding to the active control configurations in Figures 2(a) and 2(d) also indicates that, in this case, the static output-feedback controller behaves slightly better than the state-feedback controller requiring, moreover, similar levels of control effort. Regarding the suspension deflection and tire deflection, the graphics in Figures 2(b) and 2(c) show that both active controllers provide a significant improvement near the natural frequency of the sprung mass mode:

$$f_s = \sqrt{\frac{k_s}{m_s}}, \tag{56}$$

which for our particular model takes the value $f_s = 5.1$ rad/s (0.81 Hz). It should be highlighted that, in the case of suspension deflection (Figure 2(b)), the passive control configuration exhibits the best behavior for frequencies inferior to 0.6 Hz. However, it should also be noted that in this case both active control configurations present negative dB-gains for frequencies below 0.6 Hz.

Remark 5. As indicated in [33], independently of the suspension type (passive or active), the frequency transfer function from road displacement to sprung mass acceleration has an invariant point at the wheel-hop frequency:

$$f_u = \sqrt{\frac{k_u}{m_u}}, \tag{57}$$

with magnitude k_u/m_s. This fact reveals the difficulty of improving the ride comfort for frequencies around f_u. For the parameter values in (40), we have a wheel-hop frequency of $f_u = 63.75$ rad/s (10.15 Hz) with a magnitude of $k_u/m_s = 499.50$ (53.97 dB). The existence of an invariant point also applies to the frequency transfer function from road displacement to suspension deflection at the rattle-space frequency:

$$f_r = \sqrt{\frac{k_u}{m_s + m_u}}, \tag{58}$$

which for the parameters in (40) takes the value $f_r = 21.10$ rad/s (3.36 Hz).

Remark 6. The graphics of frequency response in Figure 2 use the road displacement as disturbance input. For the sake of completeness, the graphics of frequency response using the road displacement velocity as disturbance input are presented in Figure 3. Note that the comments made to the graphics in Figure 2 also apply to this second set of graphics.

4.3. Time Response to a Bump Disturbance. To provide a more complete picture of the performance achieved by the proposed static output-feedback controller, in this subsection we present the time response of the quarter-car suspension system to a road disturbance. More precisely, we consider an isolated bump of the form:

$$z_r(t) = \begin{cases} \dfrac{H}{2}\left[1 - \cos\left(\dfrac{2\pi V}{L}t\right)\right] & \text{if } 0 \le t \le \dfrac{L}{V}, \\ 0 & \text{otherwise,} \end{cases} \tag{59}$$

where H and L are the bump height and length, respectively; and V is the vehicle velocity. The following particular values of the parameters [30]:

$$H = 0.1\,\text{m}, \qquad L = 5\,\text{m}, \qquad V = 12.5\,\text{m/s}, \tag{60}$$

have been used to conduct the numerical simulations. For this road disturbance, the magnitudes taken as performance criteria have been computed for the control configurations (i)–(iii) defined in Section 4.2, and the corresponding graphics are presented in Figure 4. In particular, the graphics in Figure 4(a) display the sprung mass acceleration $\ddot{z}_s(t)$ for the uncontrolled system (black dotted line), the controlled system with state-feedback controller (blue dashed line), and the controlled system with static output-feedback controller (red solid line). The graphics of suspension deflection $z_s(t) - z_u(t)$, tire deflection $z_u(t) - z_r(t)$, and control force $u(t)$ for these three control configurations are displayed in Figures 4(b), 4(c), and 4(d), respectively, using the same line styles and colors.

The graphics in Figures 4(a)–4(c) clearly show that a significant improvement in ride comfort, suspension deflection, and road holding ability is provided by the active controllers. It can also be appreciated that the static output-feedback controller achieves practically the same levels of vibrational response mitigation as the state-feedback controller. Moreover, the graphics in Figure 4(d) point out that there are no relevant differences between the levels of control effort required to operate the active controllers.

4.4. Closing Remarks. The numerical results obtained in this section indicate that the proposed static output-feedback H_∞ controller exhibits a remarkable performance in terms of both frequency and time responses when compared with the corresponding state-feedback H_∞ controller. In fact, from the point of view of H_∞ controller design, the values of the H_∞-norms in (44) and (55) show that the static output-feedback controller is practically optimal.

These outstanding numerical results are even more meaningful when considering some additional features of the new design methodology: (i) Generality: the proposed methodology can be applied to a wide variety of control problems, with the only requirement that the state-feedback version of the problem admits a standard LMI formulation. (ii) Conceptual simplicity: the ideas involved in the proposed change of variables are simple and transparent. As shown in Section 2, new LMI formulations for static output-feedback controller designs can be easily derived from existing state-feedback LMI formulations through a simple change of the LMI variables. (iii) Ease of implementation: the static output-feedback controller design is formulated in terms of LMI optimization problems, which can be directly solved using standard computational tools, as those provided by the MATLAB Robust Control Toolbox [6]. (iv) Computational efficiency: traditionally, static output-feedback gain matrices have been computed by means of multistep optimization algorithms that require solving complex matrix equations or LMI problems at each step. In contrast, in the new design methodology, the output-feedback gain matrix is computed by solving a single LMI optimization problem.

The property of computational efficiency deserves some additional considerations. As it is well known, the nonconvex nature of static output-feedback control problems makes them NP-hard [34, 35]. Consequently, heuristic strategies are commonly used to solve this kind of problems in a computationally effective way. These heuristic strategies can be based on a certain set of sufficient conditions for controller design or on sophisticated randomized algorithms. In any case, the design procedure depends critically on a suitable choice of certain parameters that, in principle, can take a wide range of possible values.

Obviously, the previous remark also applies to the new design strategy proposed in this paper, which requires a proper choice of the matrix L in (7) to define the change of variables (9). The output-feedback controller design presented in Section 4.1 has been carried out by taking L as a zero matrix, which leads to the simplified form $R = C_y^\dagger$

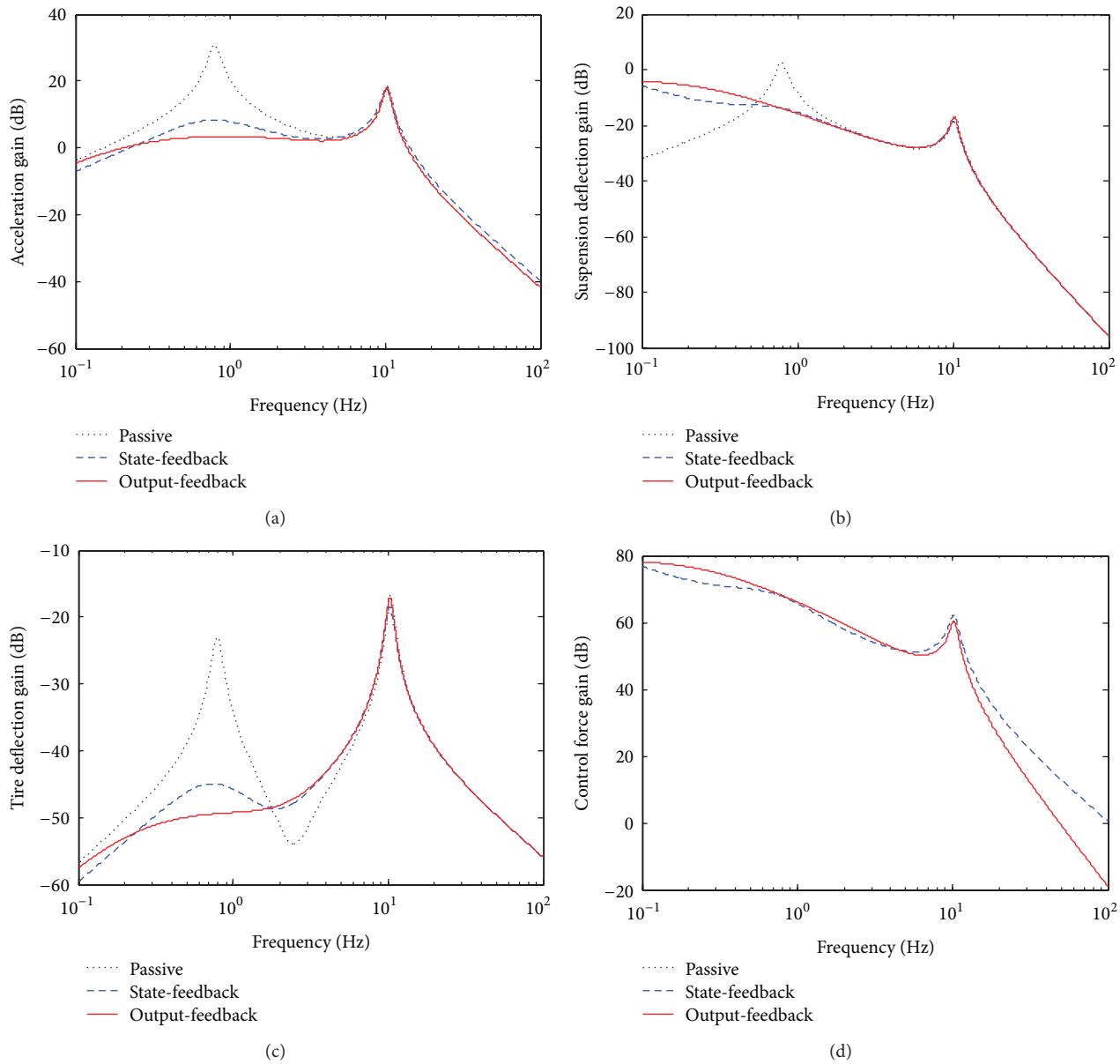

Figure 3: Frequency transfer functions from road displacement velocity to (a) sprung mass acceleration, (b) suspension deflection, (c) tire deflection, and (d) control effort, corresponding to the passive (black dotted line), state-feedback (blue dashed line), and static output-feedback (red solid line) control configurations.

in (7). The choice $L = 0$ has also been used recently in the field of vibration control of large structures with positive results [17–21]. However, it is worth pointing out that certain feasibility problems typically appear when applying the proposed methodology to the design of static output-feedback controllers for structural vibration control, and that ongoing investigations indicate that a suitable choice of the L matrix can play an important role in solving these feasibility issues.

5. Conclusions and Future Directions

In this work, a new strategy to design static output-feedback controllers for vehicle suspension systems has been presented. The proposed strategy is conceptually simple, easy to implement, and computationally efficient, and it can be applied to a wide variety of control problems, with the only requirement that the state-feedback version of the problem admits a standard LMI formulation. To illustrate the main elements of the new approach, a static output-feedback H_∞ controller has been designed for a simplified quarter-car suspension system. Numerical simulations show that the proposed static output-feedback H_∞ controller exhibits a remarkable behavior in terms of both frequency and time responses, when compared with the corresponding state-feedback H_∞ controller.

The main contribution of the paper is twofold: (i) to provide a clear and practical presentation of the main

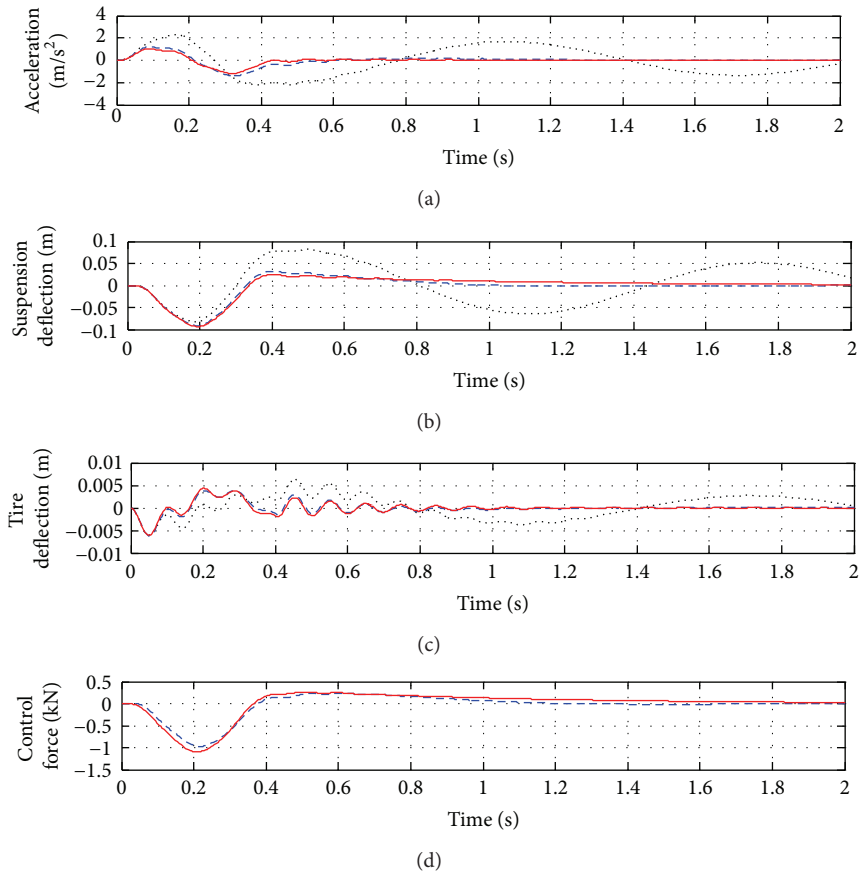

Figure 4: Time response to an isolated bump disturbance: (a) sprung mass acceleration, (b) suspension deflection, (c) tire deflection, and (d) control effort, corresponding to the passive (black dotted line), static state-feedback (blue dashed line), and static output-feedback (red solid line) control configurations.

theoretical elements of the new strategy for static output-feedback controller design and (ii) to show the practical relevance of the proposed design strategy in the field of automotive suspensions. Indeed, the positive results obtained for the quarter-car suspension system clearly indicate that more research effort should be invested in applying the new design methodology to more complex scenarios. Specifically, more complete physical models can be considered, as half or full car models, seat suspension systems, and human-body models [4, 36, 37]. More sophisticated control strategies should be also explored, as those including multiobjective designs with H_∞ and generalized H_2 control strategies, fuzzy control, advanced H_∞ control, or model predictive control [2, 3, 28, 36, 38–43], combined with different mathematical complexities as, for example, uncertainties, input and output constraints, actuation saturations, delays and actuator faults [23, 24, 26, 30, 36, 44–46], and also combined with actuator dynamics and road excitation models [39, 47].

Conflict of Interests

The authors declare that there is no conflict of interests regarding the publication of this paper.

Acknowledgments

This work was supported in part by the Spanish Ministry of Economy and Competitiveness under Grant DPI2012-32375/FEDER and by the Norwegian Center of Offshore Wind Energy (NORCOWE) under Grant 193821/S60 from the Research Council of Norway (RCN). NORCOWE is a consortium with partners from industry and science, hosted by Christian Michelsen Research.

References

[1] I. Fialho and G. J. Balas, "Road adaptive active suspension design using linear parameter-varying gain-scheduling," *IEEE Transactions on Control Systems Technology*, vol. 10, no. 1, pp. 43–54, 2002.

[2] H. Chen and C. W. Scherer, "An LMI based model predictive control scheme with guaranteed H_∞ performance and its application to active suspension," in *Proceedings of the American Control Conference (AAC '04)*, pp. 1487–1492, Boston, Mass, USA, July 2004.

[3] H. Du and N. Zhang, "Fuzzy control for nonlinear uncertain electrohydraulic active suspensions with input constraint," *IEEE Transactions on Fuzzy Systems*, vol. 17, no. 2, pp. 343–356, 2009.

[4] H. Li, H. Gao, and H. Liu, "Robust quantised control for active suspension systems," *IET Control Theory & Applications*, vol. 5, no. 17, pp. 1955–1969, 2011.

[5] R. S. Prabakar, C. Sujatha, and S. Narayanan, "Response of a quarter car model with optimal magnetorheological damper parameters," *Journal of Sound and Vibration*, vol. 332, no. 9, pp. 2191–2206, 2013.

[6] G. Balas, R. Chiang, A. Packard, and M. Safonov, *MATLAB Robust Control Toolbox User's Guide, Version 4.2*, The MathWorks, Inc., Natick, Mass, USA, 2012.

[7] R. Toscano, "A simple method to find a robust output feedback controller by random search approach," *ISA Transactions*, vol. 45, no. 1, pp. 35–44, 2006.

[8] D. D. Moerder and A. J. Calise, "Convergence of a numerical algorithm for calculating optimal output feedback gains," *IEEE Transactions on Automatic Control*, vol. 30, no. 9, pp. 900–903, 1985.

[9] Y.-Y. Cao, J. Lam, and Y.-X. Sun, "Static output feedback stabilization: an ILMI approach," *Automatica*, vol. 34, no. 12, pp. 1641–1645, 1998.

[10] J. Gadewadikar, F. L. Lewis, L. Xie, V. Kucera, and M. Abu-Khalaf, "Parameterization of all stabilizing H_∞ static state-feedback gains: application to output-feedback design," *Automatica*, vol. 43, no. 9, pp. 1597–1604, 2007.

[11] J.-E. Feng, J. Lam, P. Li, and Z. Shu, "Decay rate constrained stabilization of positive systems using static output feedback," *International Journal of Robust and Nonlinear Control*, vol. 21, no. 1, pp. 44–54, 2011.

[12] C. A. R. Crusius and A. Trofino, "Sufficient LMI conditions for output feedback control problems," *IEEE Transactions on Automatic Control*, vol. 44, no. 5, pp. 1053–1057, 1999.

[13] E. Prempain and I. Postlethwaite, "Static output feedback stabilisation with H_∞ performance for a class of plants," *Systems and Control Letters*, vol. 43, no. 3, pp. 159–166, 2001.

[14] G. I. Bara and M. Boutayeb, "Static output feedback stabilization with H_∞ performance for linear discrete-time systems," *IEEE Transactions on Automatic Control*, vol. 50, no. 2, pp. 250–254, 2005.

[15] M. Chaabane, F. Tadeo, D. Mehdi, and M. Souissi, "Robust admissibilization of descriptor systems by static output-feedback: an LMI approach," *Mathematical Problems in Engineering*, vol. 2011, Article ID 960981, 10 pages, 2011.

[16] J. Rubió-Massegú, J. M. Rossell, H. R. Karimi, and F. Palacios-Quiñonero, "Static output-feedback control under information structure constraints," *Automatica*, vol. 49, no. 1, pp. 313–316, 2013.

[17] J. Rubió-Massegú, F. Palacios-Quiñonero, and J. M. Rossell, "Decentralized static output-feedback H_∞ controller design for buildings under seismic excitation," *Earthquake Engineering and Structural Dynamics*, vol. 41, no. 7, pp. 1199–1205, 2012.

[18] F. Palacios-Quiñonero, J. Rubió-Massegú, J. M. Rossell, and H. R. Karimi, "Optimal passive-damping design using a decentralized velocity-feedback H_∞ approach," *Modeling, Identification and Control*, vol. 33, no. 3, pp. 87–97, 2012.

[19] F. Palacios-Quiñonero, J. Rubió-Massegú, J. M. Rossell, and H. R. Karimi, "Discrete-time static output-feedback semi-decentralized H_∞ controller design: an application to structural vibration control," in *Proceedings of the American Control Conference*, pp. 6126–6131, Montreal, Canada, 2012.

[20] F. Palacios-Quiñonero, H. R. Karimi, J. Rubió-Massegú, and J. M. Rossell, "Passive-damping design for vibration control of large structures," in *Proceedings of the 10th IEEE International Conference on Control and Automation*, pp. 33–38, Hangzhou, China, 2013.

[21] F. Palacios-Quiñonero, J. Rubió-Massegú, J. M. Rossell, and H. R. Karimi, "Vibration control for adjacent structures using local state information," *Mechatronics*, 2014.

[22] S. Boyd, L. El Ghaoui, E. Feron, and V. Balakrishnan, *Linear Matrix Inequalities in System and Control Theory*, vol. 15 of *SIAM Studies in Applied Mathematics*, SIAM, Philadelphia, Pa, USA, 1994.

[23] X. Yang, H. Gao, P. Shi, and G. Duan, "Robust H_∞ control for a class of uncertain mechanical systems," *International Journal of Control*, vol. 83, no. 7, pp. 1303–1324, 2010.

[24] A. Chen and J. Wang, "Delay-dependent L_2-L_∞ control of linear systems with multiple time-varying state and input delays," *Nonlinear Analysis: Real World Applications*, vol. 13, no. 1, pp. 486–496, 2012.

[25] F. Amato, R. Ambrosino, M. Ariola, and A. Merola, "Domain of attraction and guaranteed cost control for non-linear quadratic systems. Part 2: controller design," *IET Control Theory & Applications*, vol. 7, no. 4, pp. 565–572, 2013.

[26] Z. Gu, D. Yue, C. Peng, J. Liu, and J. Zhang, "Fault tolerant control for systems with interval time-varying delay and actuator saturation," *Journal of the Franklin Institute*, vol. 350, no. 2, pp. 231–243, 2013.

[27] P.-L. Liu, "State feedback stabilization of time-varying delay uncertain systems: a delay decomposition approach," *Linear Algebra and Its Applications*, vol. 438, no. 5, pp. 2188–2209, 2013.

[28] H. Xia, P. Zhao, L. Li, A. Wu, and G. Ma, "A novel approach to H_∞ control design for linear neutral time-delay systems," *Mathematical Problems in Engineering*, vol. 2013, Article ID 526017, 9 pages, 2013.

[29] H. Du, J. Lam, and K. Y. Sze, "Non-fragile output feedback H_∞ vehicle suspension control using genetic algorithm," *Engineering Applications of Artificial Intelligence*, vol. 16, no. 7-8, pp. 667–680, 2003.

[30] H. Chen and K.-H. Guo, "Constrained H_∞ control of active suspensions: an LMI approach," *IEEE Transactions on Control Systems Technology*, vol. 13, no. 3, pp. 412–421, 2005.

[31] P. K. S. Tam and W. Tan, "A direct composite H_∞ controller design for a two-time-scale active suspension system," in *Proceedings of the 22nd IEEE International Conference on Industrial Electronics, Control, and Instrumentation (IECON '96)*, vol. 3, pp. 1401–1405, Taipei, Taiwan, August 1996.

[32] I. J. Fialho and G. J. Balas, "Design of nonlinear controllers for active vehicle suspensions using parameter-varying control synthesis," *Vehicle System Dynamics*, vol. 33, no. 5, pp. 351–370, 2000.

[33] J. K. Hedrick and T. Butsuen, "Invariant properties of automotive suspensions," *Proceedings of the Institution of Mechanical Engineers, Part D: Journal of Automobile Engineering*, vol. 204, no. 1, pp. 21–27, 1990.

[34] V. Blondel and J. N. Tsitsiklis, "NP-hardness of some linear control design problems," *SIAM Journal on Control and Optimization*, vol. 35, no. 6, pp. 2118–2127, 1997.

[35] V. L. Syrmos, C. T. Abdallah, P. Dorato, and K. Grigoriadis, "Static output feedback—a survey," *Automatica*, vol. 33, no. 2, pp. 125–137, 1997.

[36] H. Gao, Y. Zhao, and W. Sun, "Input-delayed control of uncertain seat suspension systems with human-body model," *IEEE Transactions on Control Systems Technology*, vol. 18, no. 3, pp. 591–601, 2010.

[37] H. Du, W. Li, and N. Zhang, "Integrated seat and suspension control for a quarter car with driver model," *IEEE Transactions on Vehicular Technology*, vol. 61, no. 9, pp. 3893–3908, 2012.

[38] H. Zhang, Y. Shi, and A. S. Mehr, "Robust weighted H_∞ filtering for networked systems with intermittent measurements of multiple sensors," *International Journal of Adaptive Control and Signal Processing*, vol. 25, no. 4, pp. 313–330, 2011.

[39] L. C. Félix-Herrán, D. Mehdi, J. de J. Rodríguez-Ortiz, R. Soto, and R. Ramírez-Mendoza, "H_∞ control of a suspension with a magnetorheological damper," *International Journal of Control*, vol. 85, no. 8, pp. 1026–1038, 2012.

[40] H. Zhang, Y. Shi, and A. S. Mehr, "Robust H_∞ PID control for multivariable networked control systems with disturbance/noise attenuation," *International Journal of Robust and Nonlinear Control*, vol. 22, no. 2, pp. 183–204, 2012.

[41] J. Liu, Y. Hu, and Z. Lin, "State-feedback H_∞ control for LPV system using T-S fuzzy linearization approach," *Mathematical Problems in Engineering*, vol. 2013, Article ID 169454, 18 pages, 2013.

[42] H. Zhang, Y. Shi, and M. Liu, "H_∞ step tracking control for networked discrete-time nonlinear systems with integral and predictive actions," *IEEE Transactions on Industrial Informatics*, vol. 9, no. 1, pp. 337–345, 2013.

[43] H. Zhang, J. Wang, and Y. Shi, "Robust H_∞ sliding-mode control for markovian jump systems subject to intermittent observations and partially known transition probabilities," *Systems and Control Letters*, vol. 62, no. 12, pp. 1114–1124, 2013.

[44] S. Hu, D. Yue, Z. Du, and J. Liu, "Reliable H_∞ non-uniform sampling tracking control for continuous-time non-linear systems with stochastic actuator faults," *IET Control Theory & Applications*, vol. 6, no. 1, pp. 120–129, 2012.

[45] Y. Cui, K. Liu, Y. Zhao, and X. Wang, "Robust H_∞ control for a class of uncertain switched fuzzy time-delay systems based on T-S models," *Mathematical Problems in Engineering*, vol. 2013, Article ID 234612, 8 pages, 2013.

[46] X. Li, H. R. Karimi, and Z. Xiang, "Robust reliable control of uncertain discrete impulsive switched systems with state delays," *Mathematical Problems in Engineering*, vol. 2013, Article ID 197819, 8 pages, 2013.

[47] L.-X. Guo and L.-P. Zhang, "Robust H_∞ control of active vehicle suspension under non-stationary running," *Journal of Sound and Vibration*, vol. 331, no. 26, pp. 5824–5837, 2012.

Hindawi Publishing Corporation
Mathematical Problems in Engineering
Volume 2013, Article ID 617879, 12 pages
http://dx.doi.org/10.1155/2013/617879

Research Article

Considering Variable Road Geometry in Adaptive Vehicle Speed Control

Xinping Yan,[1] Rui Zhang,[1] Jie Ma,[1] and Yulin Ma[2]

[1] *Intelligent Transport Systems Research Center, Engineering Research Center for Transportation Safety (Ministry of Education), Wuhan University of Technology, Wuhan 430063, China*
[2] *Department of Automobile Engineering, Academy of Military Transportation, Tianjin 300161, China*

Correspondence should be addressed to Rui Zhang; zhangrui318@163.com

Received 2 September 2013; Revised 4 November 2013; Accepted 4 November 2013

Academic Editor: Hui Zhang

Adaptive vehicle speed control is critical for developing Advanced Driver Assistance Systems (ADAS). Vehicle speed control considering variable road geometry has become a hotspot in ADAS research. In this paper, first, an exploration of intrinsic relationship between vehicle operation and road geometry is made. Secondly, a collaborative vehicle coupling model, a road geometry model, and an AVSC, which can respond to variable road geometry in advance, are developed. Then, based on H_∞ control method and the minimum energy principle, a performance index is specified by a cost function for the proposed AVSC, which can explicitly consider variable road geometry in its optimization process. The proposed AVSC is designed by the Hamilton-Jacobi Inequality (HJI). Finally, simulations are carried out by combining the vehicle model with the road geometry model, in an aim of minimizing the performance index of the AVSC. Analyses of the simulation results indicate that the proposed AVSC can automatically and effectively regulate speed according to variable road geometry. It is believed that the proposed AVSC can be used to improve the economy, comfort, and safety effects of current ADAS.

1. Introduction

At present, Advanced Driver Assistance Systems (ADAS) has become a hotspot in intelligent transportation systems (ITS) research area. There are many ADAS that have been or are being developed, including Adaptive Cruise Control System (ACC), which regulates the speed with the target vehicle spacing [1], Intelligent Speed Adaptive System (ISA), which regulates the speed with speed limit signs and marking, and Lane Keeping Assist Systems (LKAS) and Lane Departure Warning System (LDWS) that maintain a safe lane position, the vehicle orientation and among others [2]. Such systems either regulate vehicle operation or even directly control vehicle speed according to road geometry, such as traffic signs, pavement, and sight distance.

The literature review indicates that variable road geometry is mainly presented as changing road shapes. Accident rate of rear-end collision and rollover are still high, especially for those "dangerous locations," such as long steep slopes, sharp curves, and irregular road surface. Several reasons contribute to this. On one hand, speeding and the inherent limitations of vehicular sensor system in vision, sensitivity, and delay are widespread. On the other hand, variable road geometry is commonly not considered within ADAS. This results in that ADAS equipped vehicles cannot comprehensively "know" the road ahead and therefore they cannot develop an "optimal" vehicle operation in response to variable road geometry. Related studies show that considering variable road geometry can effectively improve the safety, comfort, and economy of vehicle operation.

Vehicle speed control is an important part of ADAS. Typically, the traditional methods of speed control are static in that they mostly specify one speed limit for a given road condition (e.g., sharp curve or steep slope), regardless of the relative location of the vehicle and road features (e.g., the beginning or the ending portion of a curve or a slope). In order to precisely control the vehicle speed on variable road geometry, most researches focus on road

geometrical features extraction and estimation. As the road features, such as slope, curvature, bank angle, are not easy to get by vehicular sensors available, road features estimation mainly adopts direct observers such as Kalman, Luenberger, or other observers based on proportional-integral, fuzzy, and sliding mode control [3]. Moreover, recent studies tend to collect road and environment information within a limited distance ahead. However, the methods proposed above over-rely on online data acquisition and processing and unknown data that need to be predictable but by a high cost of measurement, which results in that the real time of algorithm cannot be achieved easily [4]. For these reasons, limited researches tried to explore adaptive speed control method on variable road geometry. With the development of Cooperative Vehicle Infrastructure Systems (CVIS), real-time and abundant information about vehicle inside and outside, especially road geometry information, can be obtained by GPS, GIS, mobile communications, digital map, and so forth, which can support the development of adaptive vehicle speed controller (AVSC) in order to respond to variable road geometry [5]. AVSC can collect road information of entire road features (e.g., a curve or a slope) and make more informative and comprehensive decisions in the control of vehicle speed.

The literature review indicates that few researches have been focused on AVSC considering variable road geometry. Németh and Gáspár [6] introduced road division into vehicle modeling and added appropriate weighting factor for the reference velocity in each road section. They used LPV/H_∞ control method to design a velocity tracking controller on the slope road. The controller cannot only adjust the speed quickly and effectively on the slope but also reduce the frequent operations of the vehicle actuator. For the platooning vehicle on the slope, Németh and Gáspár [7] also adopt the above idea, which still adopts LPV/H_∞ control method to design a velocity tracking controller for the leader and string stable controller for each vehicle in the platoon. However, the slope angle in these references is still taken as the external disturbance, and the cruise/platooning system is guaranteed just by LPV method to keep the robustness for the change of the slope angle and uncertain factors.

Kamal et al. [8, 9] designed an ecological driving system for running a vehicle on roads with up-down slopes. This ecological system makes full use of the road information obtained from digital road maps and proposed a nonlinear model predictive control method to derive the vehicle control inputs by road terrain, vehicle dynamics, and fuel consumption characteristics. They acquired the complete road feature data including slope angle and the rate of slope angle, developed a fuel consumption model, and designed the optimal speed controller. This method mainly starts with driving economy on a slope road, but it does not consider vehicle running on a curve road as well as its safety and comfort on variable road geometry. In addition, other researches usually take road features as external disturbances and used the weight factors to eliminate the influence of disturbances, or simply ignore these road geometrical features [10, 11].

In China, Wang and Ma [12] developed the vehicle speed and spacing model on a curve and/or a slope road. But these models are mainly suitable for macroscopic traffic flow simulation, and it is difficult to reflect the individual vehicle difference, that is, how vehicle regulates its own speed fitting in with variable road geometry. Zhang et al. [13] conducted a comprehensive research on ACC vehicles, such as driveline simplification, actuator design, acceleration switch, disturbance decoupling on the uncertainty parameters and nonlinear model, and fuel consumption analysis. Currently, they have done some researches on the ACC vehicle on a curve road to prevent vehicle from sideslip and rollover. Zhang combined ACC and Direct Yaw Control (DYC) together to put forward a curve coordinate controller, which not only can satisfy the longitudinal tracking for vehicles, but also can ensure the lateral stability of vehicles. However, in curve road, although the controller separates the ego and adjacent lanes effectively, it does not fundamentally consider the speed adaption on the curve road. In addition, there is rare report on AVSC on variable road geometry both at home and abroad.

Many control algorithms such as PID and LQ algorithms are required for online identification of controlled object, so precise mathematical model of object/process is essential by using these algorithms. However, the nonlinear, time varying and uncertain vehicle systems retrain the development of precise modeling of a vehicle. The approach used in this paper is the H_∞ optimization algorithm.

The study of H_∞ optimization algorithm has been of great interest, and many results can be found in the literature. To mention a few, the problem of filtering is investigated in [14–16], and the problem of model reduction is considered in [17]. The problem of the H_∞ step tracking control for discrete-time nonlinear systems is analyzed in [18–20]. The problem of robust static output feedback controls for networked control systems (NCSs) subject to network-induced delays and missing data are studied in [21]. Moreover, the H_∞ control has been also paid considerable attention and many results have been reported in automotive systems. For instance, lateral control of autonomy vehicle by using both H_∞ control and fuzzy control is studied in [22] to confirm that the control algorithm is feasible for practical application, and longitudinal control of electric vehicle by using H_∞ robust control is investigated in [23] to enhance the riding comfort and energy saving for vehicle constant speed cruise, especially in slope road. However, the road geometry features are used as disturbance or constant values to controller. To the best of the authors' knowledge, little cost function of H_∞ control has been developed by road geometry model. In this study, based on H_∞ Control Method and Hamilton-Jacobi Inequality (HJI) theory, a performance index is specified by a proposed cost function for the proposed AVSC, which can explicitly consider variable road geometry in its optimization process. The proposed AVSC is to make more informative and comprehensive decisions in the control of vehicle speed.

The rest of this paper develops as the following. After a literature review for adaptive speed control on variable road geometry is conducted, a collaborative vehicle coupling model and road geometrical model are presented in detail; an adaptive vehicle speed controller (AVSC) for variable road geometry consisting of upslope and a curve scenario

by using H_∞ and HJI method is described. And then simulation results are carried out and presented to illustrate the safety, comfort, and economy of the proposed AVSC. Finally, conclusions and further works are provided.

2. Methodology

Vehicle dynamic characteristics and road geometrical features are necessary in determining the risk behaviors of vehicle collision or rollover. Vehicle running on the slope needs to consider both vehicle dynamic parameters and road geometrical parameters, such as longitudinal acceleration, traction force, velocity, and slope angle. Vehicle running on the curve needs to consider lateral acceleration, yaw rate, steering wheel angle, and road curvature. Besides, a coupling relationship exists between longitudinal and lateral vehicle movements; a collaborative vehicle coupling model and road geometry model have been studied to accurately describe vehicle driving characteristics on the variable road geometry, thus improving the controller designed for AVSC.

2.1. Vehicle Coupling Model. The vehicle dynamics model with three degrees of freedom including longitudinal, lateral, and yaw motion can be developed by Newton's vector method. Besides, the operation conditions of vehicle usually need to fit in with different road geometries. So, the vehicle model should firstly consider the dynamic coupling between the lateral and longitudinal, followed by a full impact that road geometrical features have on the vehicle model. The model is referred to [24, 25] as shown below:

$$\begin{aligned}
\dot{v}_x &= a_1 v_x^2 + v_y\dot{\psi} + C_f\frac{v_y + l_f\dot{\psi}}{mv_x}\delta - \mu g + \frac{F - C_f\delta}{m},\\
\dot{v}_y &= -a_2\frac{v_y}{v_x} - \left(v_x + \frac{ka_3}{v_x}\right)\dot{\psi} + \frac{F - \mu\lambda\left(mg - k_L v_x^2\right) + C_f}{m}\delta,\\
\ddot{\psi} &= -a_4\frac{\dot{\psi}}{v_x} - a_3\frac{v_y}{v_x} + \frac{l_f}{I_z}\left(\frac{F - \mu\lambda\left(mg - k_L v_x^2\right) + C_f}{m}\delta\right),
\end{aligned} \tag{1}$$

where

$$\begin{aligned}
a_1 &= \frac{\mu k_L - k_D}{m},\\
a_2 &= \frac{\left(C_f + C_r\right)}{m},\\
a_3 &= \frac{\left(C_f l_f - C_r l_r\right)}{I_z},\\
a_4 &= \frac{\left(C_f l_f^2 + C_r l_r^2\right)}{I_z},\\
\lambda &= \frac{l_r}{l_f + l_r},\\
k &= \frac{I_z}{m},
\end{aligned} \tag{2}$$

and the vehicle parameters used are listed in Table 1.

In order to accurately define road geometrical features, such as slope, bank, and curvature, it is assumed that the orientation of the road surface is obtained from the horizontal position by a rotation around the vehicle's lateral axis equal to the slope angle θ_s and a subsequent rotation around the longitudinal axis equal to the bank angle θ_b. The slope angle and bank angle cause gravity components to appear in vehicle model, yielding

$$\begin{aligned}
\dot{v}_x &= a_1 v_x^2 + v_y\dot{\psi} + C_f\frac{v_y + l_f\dot{\psi}}{mv_x}\delta + \frac{F - C_f\delta}{m}\\
&\quad - \mu g\cos\theta_s \mp g\sin\theta_s,\\
\dot{v}_y &= -a_2\frac{v_y}{v_x} - \left(v_x + \frac{ka_3}{v_x}\right)\dot{\psi} + \frac{F - \mu\lambda\left(mg - k_L v_x^2\right) + C_f}{m}\delta\\
&\quad - g\cos\theta_s\sin\theta_b.
\end{aligned} \tag{3}$$

Then the road curvature is considered. As the road curvature and vehicle motion are not in the same coordinate system, the road curvature cannot be used directly by the vehicle model. Secondly, the bank angle is not easy to get, compared with road altitude and curvature got by digital map or other on board sensors. Last but not least, each lane of road has a certain width and an appropriate deviation is allowed in terms of the lateral motion of vehicle. So, a vehicle lateral deviation model is given here. In order to achieve a better ride comfort, the lateral deviation of the vehicle is defined as the lateral distance y_s from the mounting location of vehicle sensors to the road centerline, rather than the lateral distance y from the vehicle center of gravity (c.o.g) to the road centerline, as shown in Figure 1.

Assume that ψ_r is the angle between road centerline and the longitudinal axis of vehicle, and d_s is the horizontal distance between the road centerline and the vehicle longitudinal axis in radians. The approximate relationship between y_s, y and ψ_r is

$$\sin\psi_r = \frac{y_s - y}{d_s} \approx \psi_r, \tag{4}$$

where d_s is the horizontal distance to the sensor from c.o.g.

Time differentiating (4), we get

$$\begin{aligned}
\dot{y}_s &= \dot{y} + d_s\dot{\psi}_r,\\
\ddot{y}_s &= \ddot{y} + d_s\ddot{\psi}_r.
\end{aligned} \tag{5}$$

Table 1: Vehicle parameters.

Parameters	Description
m/kg	Total mass
I_z/kg·m^2	Yaw inertial
l_f/m	Distance from front axle to center of gravity
l_r/m	Distance from rear axle to center of gravity
C_f/N·rad^{-1}	Front cornering stiffness
C_r/N·rad^{-1}	Rear cornering stiffness
μ	Rolling friction coefficient
k_D/N·s^2·m^{-2}	Aerodynamic drag parameter
k_L/N·s^2·m^{-2}	Aerodynamic lift parameter
g/m·s^{-2}	Gravity acceleration
$F_{yf}F_{yr}$/N	Tire lateral force
$F_{xf}F_{xr}$/N	Tire longitudinal force
δ/rad	Steering wheel angle

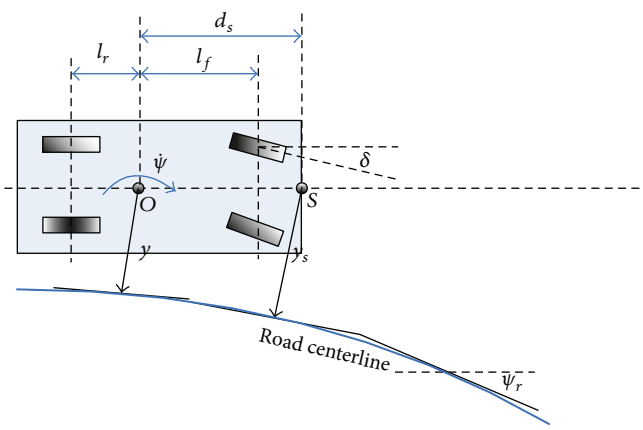

Figure 1: Vehicle lateral deviation model in terms of sensor space.

Let ψ_d be the yaw rotation of the road centerline with respect to the fixed earth frame, allowing us to write

$$\psi = \psi_r + \psi_d. \tag{6}$$

Time differentiating (6), we get

$$\begin{aligned} \dot{\psi}_r &= \dot{\psi} - \dot{\psi}_d, \\ \ddot{\psi}_r &= \ddot{\psi} - \ddot{\psi}_d, \end{aligned} \tag{7}$$

where $\dot{\psi}_d = Cv_x$; it should achieve an absolute desired yaw rate of Cv_x, for a vehicle follows a curve with road curvature C (radius of curvature $R = 1/C$).

Substituting ψ_r and its derivatives from (6) and (7) for (5), we get the vehicle lateral deviation model in the sensor space as

$$\begin{aligned} \dot{y}_s &= \dot{y} + d_s\left(\dot{\psi} - Cv_x\right), \\ \ddot{y}_s &= \ddot{y} + d_s\left(\ddot{\psi} - \ddot{\psi}_d\right). \end{aligned} \tag{8}$$

Consistent with the road conditions, it can be reasonably assumed that the roadway can be described by a series of curves that have a constant road curvature. Because the road curvature is piecewise continuous, it can be assumed that $\ddot{\psi}_d \approx 0$ [26].

In summary, according to the vehicle coupling model with regard to road geometrical features, on one hand, the vehicle still needs to overcome the action of gravity caused by the slope angle in the longitudinal control. On the other hand, the vehicle also needs to mitigate the change of deviation caused by the road curvature in the lateral control. In addition, it is necessary to analyze the speed performance caused by the changes of variable road geometries.

2.2. Road Geometry Model. According to road design rules, road geometry determines the direction and specific location of the route. Road geometry can reach the best combination by integrated design of the road shapes including horizon, vertical, and cross sections, which can meet not only driver visual and psychological requirements, but also vehicle dynamics and kinematics characteristics, thus reducing the driving work and improving the driving safety, comfort, and economy. Clothoid curves have been used for road geometry design in order to geometrically join a straight road to a curve road, or a straight road to a slope road [3, 27, 28]. Besides, vertical curves should be used to geometrically join an uphill and a downhill road. As the example of curve road, the main characteristic of a clothoid function is that its curvature is proportional to the length of the curve measured from its origin

$$C(l) = C_0 + C_1 \cdot l, \tag{9}$$

where C_0 and $C_1 = dC/dl$ are the curvature and rate of curvature of the road, respectively; l is the curve length.

Then, the heading direction $\varphi(l)$ is got by the first integral of the curvature

$$\varphi(l) = \varphi_0 + \int_0^l C(\tau)\,\mathrm{d}\tau = \varphi_0 + C_0 l + \frac{1}{2}C_1 l^2. \tag{10}$$

And the second integral represents the curve's longitudinal distance $x(l)$ and lateral distance $y(l)$

$$\begin{aligned} x(l) &= x_0 + \int_0^l \cos\varphi(\tau)\,\mathrm{d}\tau, \\ y(l) &= y_0 + \int_0^l \sin\varphi(\tau)\,\mathrm{d}\tau. \end{aligned} \tag{11}$$

Assuming $\sin\varphi \approx \varphi$, $\cos\varphi \approx 1$, (11) is rewritten as

$$\begin{aligned} x(l) &= x_0(l) + l, \\ y(l) &= y_0 + \varphi l + \frac{1}{2}C_0 l^2 + \frac{1}{6}C_1 l^3. \end{aligned} \tag{12}$$

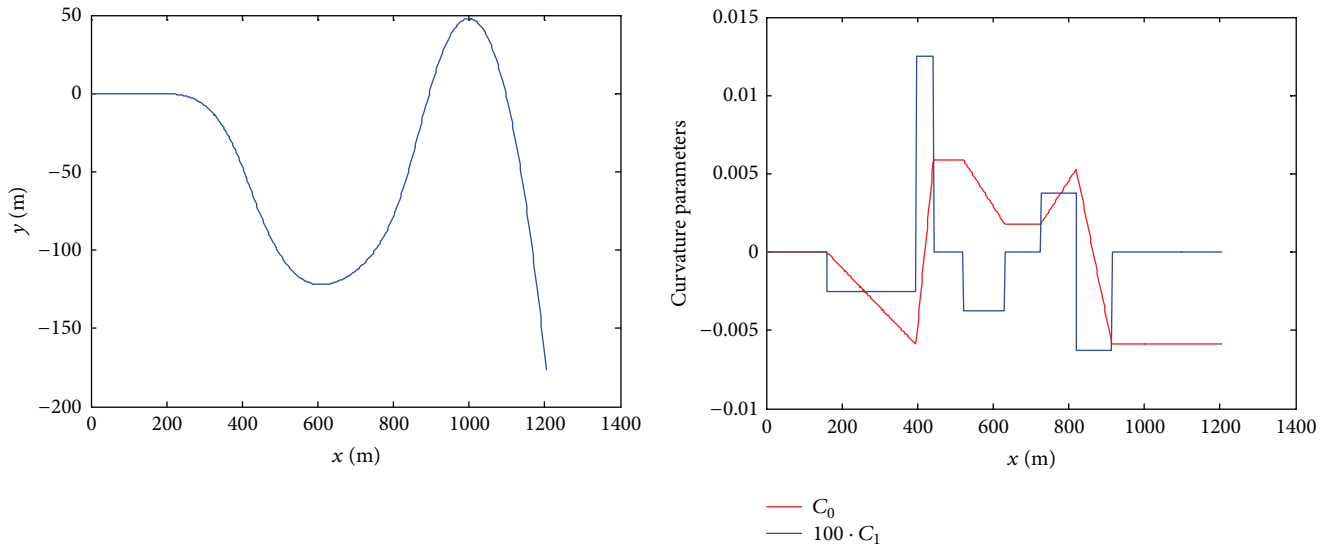

(a) Simulated curve road

(b) Curvature parameters

Figure 2: Simulated curve road with curvature parameters.

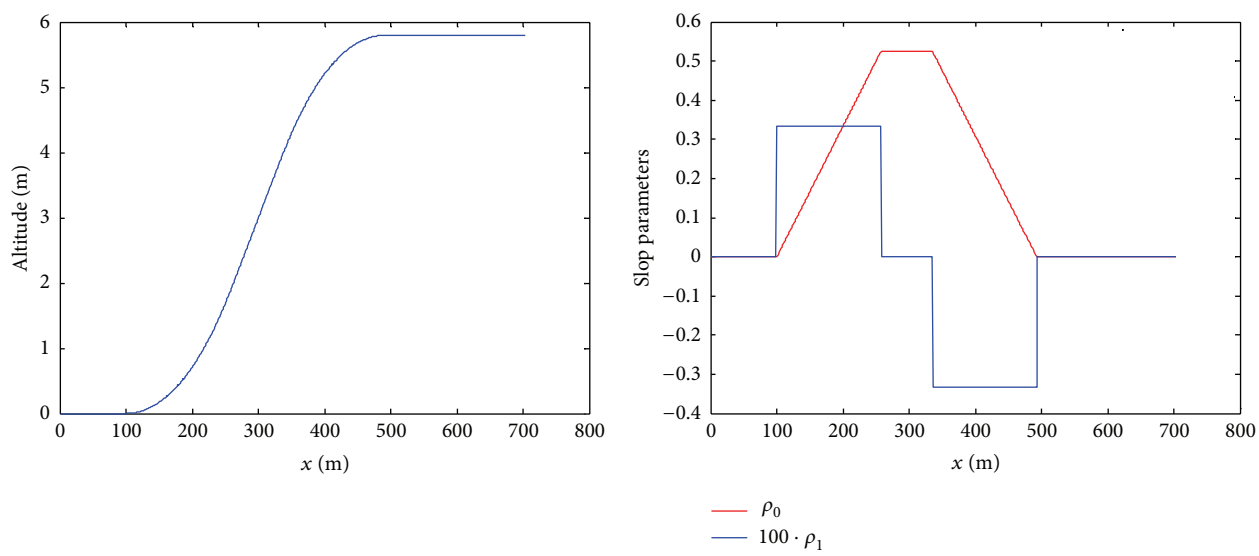

(a) Simulated slope road

(b) Slope parameters

Figure 3: Simulated slope road with slope parameters.

If $x_0(l) = 0$ leads to $x(l) = l$, the curve's lateral distance $y(x)$ and the head direction $\varphi(x)$ can be given as

$$\varphi(x) = \varphi_0 + C_0 x + \frac{1}{2} C_1 x^2,$$
$$y(x) = y_0 + \varphi x + \frac{1}{2} C_0 x^2 + \frac{1}{6} C_1 x^3. \tag{13}$$

Figure 2 gives a simulated curve road with curvature parameters C_0 and C_1 by this curve road model.

Similarly, in slope modeling, we can substitute the slope angle ρ_0 and its rate ρ_1 for C_0 and C_1, respectively, and also substitute the horizontal and vertical distance for the longitudinal and lateral distances, respectively, so the vertical distance $z(x)$ and the head direction $\varphi(x)$ also can be given as

$$\varphi(x) = \varphi_0 + \rho_0 x + \frac{1}{2} \rho_1 x^2,$$
$$z(x) = z_0 + \varphi x + \frac{1}{2} \rho_0 x^2 + \frac{1}{6} \rho_1 x^3. \tag{14}$$

Figure 3 gives a simulated slope road with slope parameters ρ_0 and ρ_1 by this curve road model.

Seen from road geometry model developed above, these road geometrical features, such as C_0 and C_1, or ρ_0 and

ρ_1, can represent the direction and location of a curve or a slope, and the derivation has shown a great deal of similitude between these road features and vehicle parameters, such as acceleration, velocity, and displacement. Hence, if the control system of vehicle makes full use of these road features and vehicle parameters, AVSC can be achieved.

3. AVSC Design

According to the collaborative vehicle coupling model and road geometry model, we combine (1), (3), and (8), yielding

$$\begin{aligned}\dot{v}_x &= a_1 v_x^2 + v_y\dot{\psi} + C_f\frac{v_y + l_f\dot{\psi}}{mv_x}\delta + \frac{F - C_f\delta}{m} \\ &\quad - \mu g\cos\theta_s \mp g\sin\theta_s, \\ \ddot{y}_s &= -(a_2 + d_s a_3)\frac{\dot{y}_s}{v_x} - \left(v_x + \frac{ka_3 - d_s(a_2 - a_4) - d_s^2 a_3}{v_x}\right)\dot{\psi} \\ &\quad + \left(1 + \frac{d_s l_f}{I_z}\right)\frac{F - \mu\lambda\left(mg - k_L v_x^2\right) + C_f}{m}\delta \\ &\quad - C\left(d_s a_2 + d_s^2 a_3\right).\end{aligned} \tag{15}$$

As the lateral deviation model needs lateral and yaw motion information, and both lateral and yaw motion share the same control input, the only two independent states have been controlled.

Assuming that brake, throttle, and steering dynamics are discounted, we make some transformation for inputs of state equation of the vehicle system

$$\begin{aligned}u_1 &= C_f\frac{v_y + l_f\dot{\psi}}{mv_x}\delta + \frac{F - C_f\delta}{m}, \\ u_2 &= \frac{F - \mu\lambda\left(mg - k_L v_x^2\right) + C_f}{m}\delta.\end{aligned} \tag{16}$$

Thus, we have only to design proper AVSC law to compute the inputs of the vehicle system F (δ, resp.) as the traction/braking force (the steering wheel angle, resp.).

Then, the collaborative vehicle coupling model and road geometry model can be got as a form of state

$$\begin{aligned}\dot{x}_1 &= a_1 x_1^2 + x_2 x_3 + u_1 - \mu g\cos\theta_s - g\sin\theta_s = f\left(x \;\; u_1 \;\; \theta_s\right), \\ \dot{x}_2 &= -(a_2 + a_3 d_s)\frac{x_2}{x_1} \\ &\quad - \left(x_1 + \frac{ka_3 - d_s(a_2 - a_4) - d_s^2 a_3}{x_1}\right)x_3 \\ &\quad + \left(1 + \frac{d_s l_f}{I_z}\right)u_2 - C\left(d_s a_2 + d_s^2 a_3\right) = f\left(x \;\; u_2 \;\; C\right).\end{aligned} \tag{17}$$

Among them $\mathbf{x}[x_1, x_2, x_3]$ is the state variables of vehicle control system, and $[x_1, x_2, x_3] = [v_x, v_y, \dot{\psi}]$, θ_s is the road slope angle, and C is the road curvature.

H_∞ control theory is to analyze the stability of a system in terms of energy dissipation. If a system is activated, its stored energy will be attenuated gradually with time. When it reaches the equilibrium state, its energy is at the minimum value, and we can say that the system is asymptotically stable. H_∞ method presents an objective function about tracking error or control cost and designs a suitable feedback controller so that the closed loop system is stable with the H_∞ norm of its transfer function minimum or less than a constant. Among them, the criterion of H_∞ method can be seen as a nonlinear optimal control problem considering the performance index below:

$$\min_u \int_0^\infty \left(\|u(t)\|^2 + L(x)\right)dt, \tag{18}$$

where L is the cost function, $L(x) \geq 0$, and $L(0) = 0$.

In this formulation, the cost function L is considered to have the following form:

$$L = \lambda_1\Phi_1 + \frac{\lambda_2}{2}\Phi_2^2 + \lambda_3\left[\frac{1}{2}(x_1 - v_d)^2\right], \tag{19}$$

where

$$\begin{aligned}\Phi_1 &= \begin{cases}\dfrac{\varphi x + (1/2)\rho_0 x^2 + (1/6)\rho_1 x^3}{x_1} & \text{slope} \\ \dfrac{\varphi x + (1/2)C_0 x^2 + (1/6)C_1 x^3}{x_1} & \text{curve}\end{cases} \\ \Phi_2 &= \begin{cases}a_x + g\sin\theta_s & \text{slope} \\ a_y + d_s\left(\ddot{\psi} - C\dot{x}_1\right) & \text{curve.}\end{cases}\end{aligned} \tag{20}$$

The cost function consists of three terms, each of which is multiplied by a constant weight λ_1, λ_2, and λ_3, respectively. The first term defines the cost in terms of speed changes caused by road geometrical features. In a curve road, it can be computed from (13) as $y(x)/x_1$ and setting $y_0 = 0$. In a slope road, it can be computed from (14) as $z(x)/x_1$ and setting $z_0 = 0$. The second term is the cost that corresponds to the longitudinal and lateral acceleration forces on the vehicle, respectively, considering the counteracting effect of gravitational force on the vehicle due to the road slope from (3) and that of yaw moment on the vehicle due to the road curvature from (8), respectively. The last term is the cost for not running at the given speed on the road v_d. The weights are chosen in such a way that the usual magnitudes of the cost terms are balanced with respect to others. Finally, the weights can be fine-tuned through observation of simulation results to maximize the performance of controller.

In order to derive the optimal control inputs, the Hamiltonian function is formed using (17)–(19) as follows:

$$H_i(x, p_i, \varphi_i, u_i) = p_i^T f(x, u_i, \varphi_i) + L_i(x, u_i), \tag{21}$$

where i is the different road geometry, such as slope or curve, p is costate, and φ is road geometrical features, such as slope angle θ_s or curvature C.

Let $f(x,u,\varphi) = f(x) + g(x)u + k(x)\varphi$, according to the Hamilton-Jacobi Inequality (HJI), if there is a non-negative function solution of $V(x)$ of C^r class ($r > 1$) satisfying

$$V_x(x) f(x) + \frac{1}{2} V_x(x) g(x) g^T(x) V_x^T(x) + \frac{1}{2} L(x) = 0. \tag{22}$$

Then the state feedback control law of C^{r-1} class can be obtained:

$$u = -g^T(x) V_x^T(x). \tag{23}$$

For this specific problem of deriving optimal control inputs, it is required to compute the following.

On a slope road

$$\begin{aligned} \frac{\partial H}{\partial \varphi} &= \frac{\partial}{\partial \varphi} H_i(x, p_i, \varphi_i, u_i) \\ &= \frac{\partial}{\partial \varphi}\left(p_i^T f(x, u_i, \varphi_i) + L_i(x, u_i)\right) \\ &= -p_2 g \cos\theta_s \dot{\theta}_s, \end{aligned} \tag{24}$$

$$\begin{aligned} \theta_s(l) &= \tan^{-1}\left(\frac{R_{\text{alt}}(l+\Delta l) - R_{\text{alt}}(l-\Delta l)}{2\Delta l}\right), \\ \frac{d}{dl}\theta_s(l) &= \left(\frac{\theta_s(l+\Delta l) - \theta_s(l-\Delta l)}{2\Delta l}\right), \end{aligned} \tag{25}$$

where R_{alt} is altitude of road and l is mileage, and these data can be obtained by digital map.

On a curve road

$$\begin{aligned} \frac{\partial H}{\partial \varphi} &= \frac{\partial}{\partial \varphi} H_i(x, p_i, \varphi_i, u_i) \\ &= \frac{\partial}{\partial \varphi}\left(p_i^T f(x, u_i, \varphi_i) + L_i(x, u_i)\right) \\ &= -p_2 d_s \dot{x}_1 C C_1, \end{aligned} \tag{26}$$

$$\begin{aligned} C &= \frac{1}{R}, \\ \dot{C} &= C_1, \end{aligned} \tag{27}$$

where R is curve radius and C_1 is a constant, and these also can be obtained by digital map or actual measurement.

Last but not least, the constraint of driving comfort also needs to be considered (changes of longitudinal acceleration and lateral acceleration within $\pm 2\,\text{m/s}^{-2}$, $\pm 0.05\,\text{g m/s}^{-2}$) in controller design. So, we can get

$$\dot{x}_{1,2} = \begin{cases} a_{\min} & (|\dot{x}_{1,2}| \le |a_{\min}|), \\ a_{\max} & (|\dot{x}_{1,2}| \ge |a_{\max}|). \end{cases} \tag{28}$$

Table 2: Vehicle parameters.

Parameters	Value
m/kg	2000
I_z/kg·m^2	3150
l_f/m	1.33
l_r/m	1.26
C_f/N·rad^{-1}	80000
C_r/N·rad^{-1}	80000
μ	0.02
k_D/N·s^2·m^{-2}	0.4
k_L/N·s^2·m^{-2}	0.005
g/m·s^{-2}	9.8
d_s/m	2
λ_1	230
λ_2	220
λ_3	8

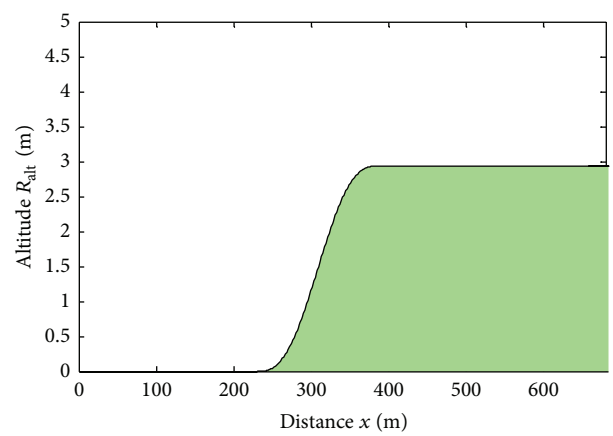

Figure 4: The simulation of the slope road.

4. AVSC Simulation

For the purpose of testifying the performance of designed AVSC, a series of simulation experiments combining the vehicle coupling model with the road geometry model are performed. The specific vehicle parameters are as shown in Table 2.

In simulation 1, a slope road is given first. The slope is shown in Figure 4, and its slope angle is calculated by (14) and (25), as shown in Figure 5.

Then, the AVSC simulation is made for this slope scenario. Assuming the initial speed v_d is 79.2 km/h (22 m/s), simulation lasts 30 s, and its sampling time is 0.05 s. First, the following two types of vehicle speed control, Adaptive Speed Control Driving (ASCD) and Constant Speed Driving

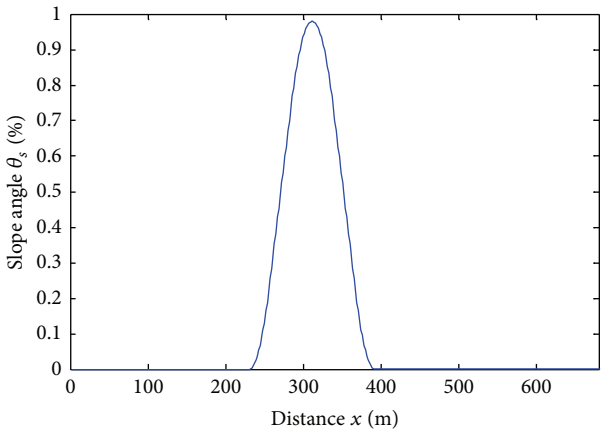

Figure 5: The calculation of the slope angle.

(CSD), are applied for a comparison analysis. CSD uses the information of the slope road to generate the control input so that the velocity remains constant, regardless of the changing of the slope. ASCD uses the proposed method in this paper to automatically regulate speed fitting in with the change of the slope road and, in this case, slope angle.

It can be seen from Figure 6(a) that with the vehicle entering slope with its initial speed, based on the defined cost function, the ASCD vehicle can reach the top of slope through an adaptive way with an operation profile of "pre-accelerating-post-decelerating." Despite that the speed of the ASCD vehicle should not have little ups and downs in the early stages of running on the slope, maybe something wrong in computation of the cost function, it has a good, smooth running performance on the whole slope. But the CSD vehicle keeps the speed unchanged at the cost of a very high control input, easily making the actuators in danger.

Figure 6(b) shows the traction/braking forces under two types of speed control for the slope scenario. The forces of the CSD vehicle change greatly when it runs on the slope, while the forces of the ASCD vehicle move gently over the slope, depending on the location of the vehicle. That is because the cost functions of the ASCD take the slope angle and its changing rate into account, that is, ρ_0 and ρ_1. Except for the final steady state, also seen in Figure 4(b), the forces of the ASCD remain stable for a period of time, due to the constraint of driving comfort from (28).

In addition, the performance of the two types of speed controllers is compared from the perspective of the control forces, which is calculated as the sum of absolute value of the entire traction/braking forces under the slope scenario ($\Sigma|F|$). As shown in Figure 6(c), the total force of the CSD vehicle is 692,280 N, while that for the ASCD vehicle is 374,800 N. Therefore, it can be concluded that under the same slope and initial speed condition, the AVSC applied in this paper can reduce the consumption of the control energy by 45.86%.

In simulation 2, the curve road is given. Road radius can be obtained from (29), and the curvature can be obtained from (13) and (25), as shown in Figure 7.

Then, the AVSC simulation is made for this curve scenario. Assuming the initial speed is 90 km/h (25 m/s), the simulation also lasts 30 s, and its sampling time is 0.05 s. Both ASCD and CSD vehicles are still applied via the curve road for a comparison analysis. Therefore,

$$R = \begin{cases} 0\,, & 0 \le x < 120, \\ 200, & 120 \le x < 120 + 25\pi, \\ 400, & 120 + 25\pi \le x < 120 + 100\pi, \\ 200, & 120 + 100\pi \le x < 120 + 125\pi, \\ 0, & x \ge 120 + 125\pi. \end{cases} \tag{29}$$

In Figure 8(a), the ASCD vehicle runs via a curve in the same way as it runs on a slope. Based on the defined cost function, the ASCD vehicle can decrease when approaching the curve and accelerate when it is going to leave the curve. However, although the CSD vehicle keeps a constant speed through the curve, it is easy to result in a risky behavior of collision or rollover. Figure 8(b) shows the steering angle under two types of speed control. The steering angle of the CSD vehicle changes greatly when it runs through the curve, as the very reason for rollover. While the steering angle of the ASCD vehicle is very small, only one tenth of that of the CSD vehicle. In addition, the lateral velocity and the yaw rate are also fitting in with the road curvature as shown in Figures 8(c) and 8(d), respectively. For Figure 8(e), the initial horizontal position in this simulation is 0.2 m, in terms of sensor space y_s, rather than y, and the ASCD vehicle can maintain the lateral deviation minimum when leaving the curve, while the CSD vehicle need not only turn sharply, but also have the deviation kept within ±0.2 m; thus it is difficult to meet the desired state.

In a summary, the ASCD vehicle can regulate the speed fitting in with the road geometrical features under AVSC design. Compared with the CSD vehicle, the ASCD vehicle has a proper, satisfactory performance of the longitudinal, lateral, and yaw control.

5. Conclusions and Future Works

A novel adaptive vehicle speed controller (AVSC) is presented in this paper. The AVSC proposed is developed based on a cost function and H_∞ control method and it is tested with a collaborative road geometrical model and vehicle coupling model. Both the developed collaborative model and the cost function of the AVSC consider variable road geometry and therefore are more accurate for simulating vehicle's performance. The proposed AVSC can regulate speed automatically fitting in with the changing road geometry; and has the advantages of improved safety, comfort, and economy.

Because the vehicle coupling model does not consider traction force and wheel angle, the simulations carried out in this paper only contain three state parameters as longitudinal velocity, lateral velocity, and yaw rate. In the future, the lateral deviation submodel used is mainly for lane changing and lane keeping purposes. A more realistic representation of acceleration, braking, and steering wheel operation still needs to be further studied in order to include traction/braking

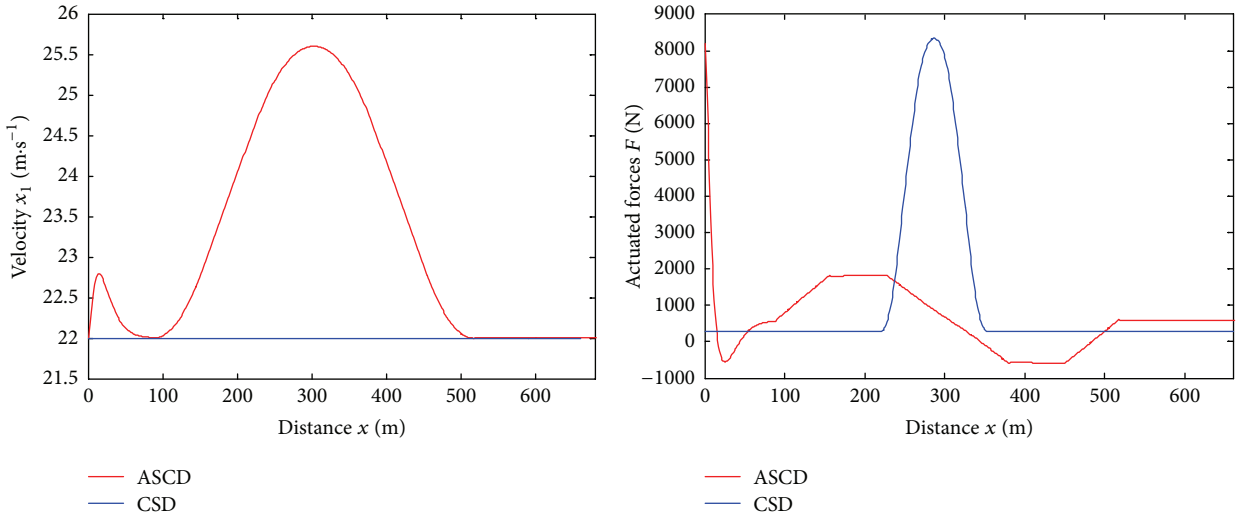

(a) Comparison of longitudinal velocity

(b) Comparison of traction/braking forces

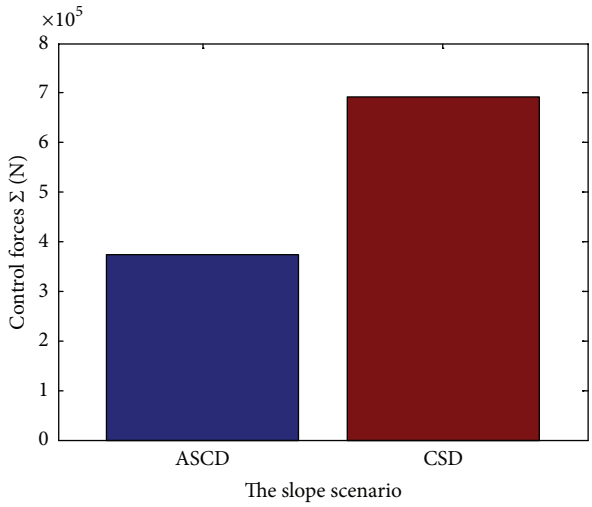

(c) Comparison of control forces

Figure 6: AVSC simulation on a slope road.

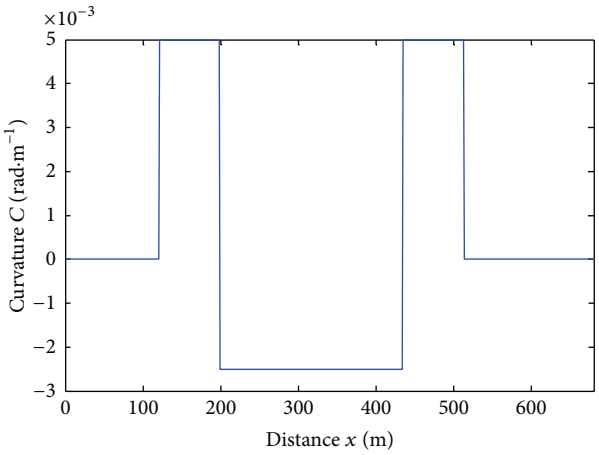

Figure 7: Road curvature.

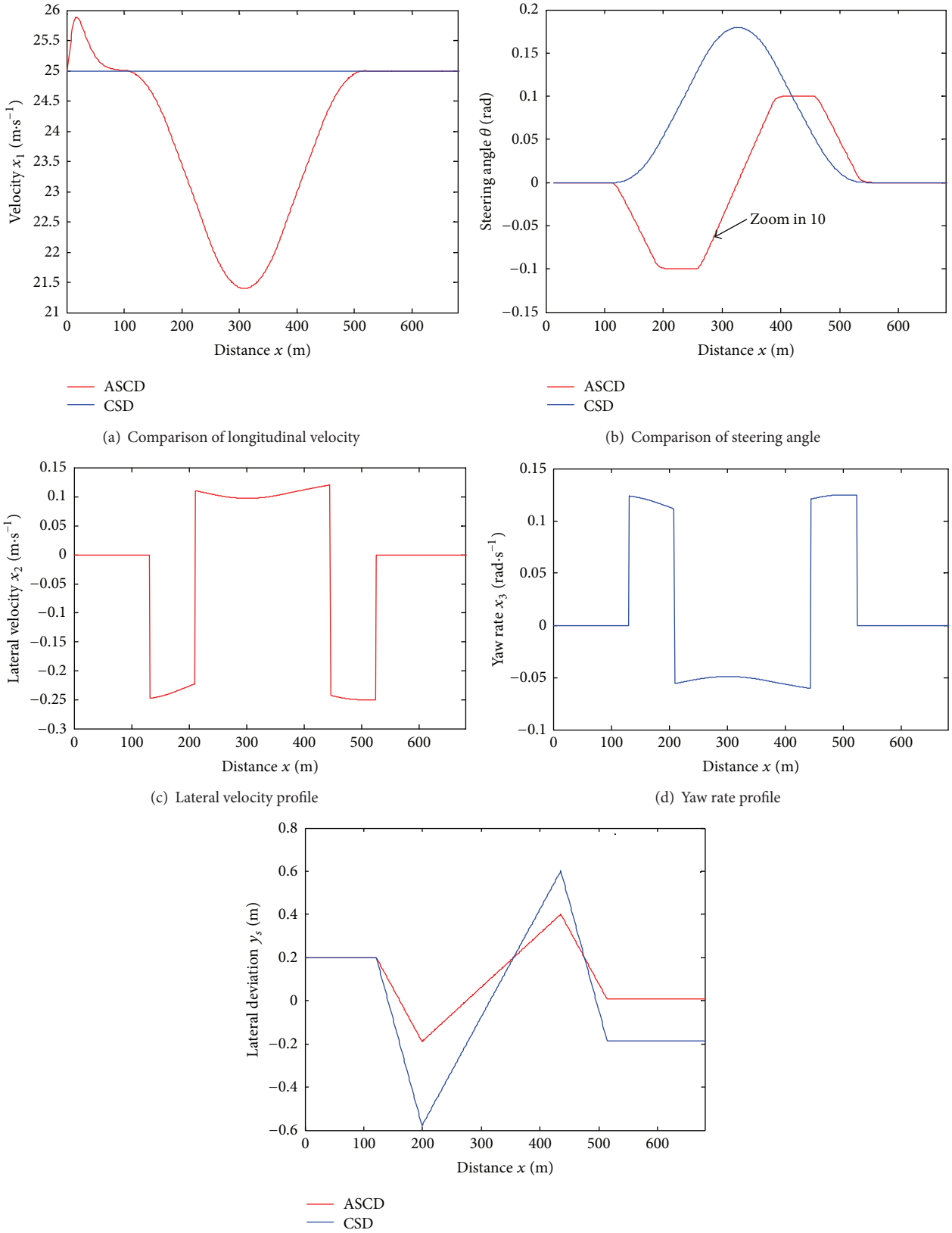

(a) Comparison of longitudinal velocity

(b) Comparison of steering angle

(c) Lateral velocity profile

(d) Yaw rate profile

(e) Comparison of lateral deviation

Figure 8: AVSC simulations via a curve road.

force and front wheel angle into the lateral deviation submodel.

Conflict of Interests

The authors declare that there is no actual or potential conflict of interests regarding the publication of this paper.

Acknowledgments

This study is supported by the National High-Tech R&D Program of China (863 Program) (no. 2011AA110402) and the National Natural Science Foundations of China (nos. 61203236 and 61174173).

References

[1] L. Xiao and F. Gao, "A comprehensive review of the development of adaptive cruise control systems," *Vehicle System Dynamics*, vol. 48, no. 10, pp. 1167–1192, 2010.

[2] J. Piao and M. McDonald, "Advanced driver assistance systems from autonomous to cooperative approach," *Transport Reviews*, vol. 28, no. 5, pp. 659–684, 2008.

[3] C. Lundquist and T. B. Schön, "Road geometry estimation and vehicle tracking using a single track model," in *Proceedings of the IEEE Intelligent Vehicles Symposium*, pp. 144–149, Eindhoven, The Netherlands, June 2008.

[4] L. Guo, X. H. Huang, B. Y. Liu, and B. Li, "Curved road detection based on roadway design model," *Journal of Transport Information and Safety*, vol. 3, no. 30, pp. 141–146, 2012.

[5] G. Toulminet, J. Boussuge, and C. Laurgeau, "Comparative synthesis of the 3 main European projects dealing with Cooperative Systems (CVIS, SAFESPOT and COOPERS) and description of COOPERS demonstration Site 4," in *Proceedings of the 11th International IEEE Conference on Intelligent Transportation Systems (ITSC '08)*, pp. 809–814, Beijing, China, December 2008.

[6] B. Németh and P. Gáspár, "Design of vehicle platoon control based on predicted road inclinations," in *Proceedings of the IEEE/ASME International Conference on Advanced Intelligent Mechatronics (AIM '11)*, pp. 265–270, Budapest, Hungary, July 2011.

[7] B. Németh and P. Gáspár, "Considering predicted road conditions in platoon control design," *Transportation Engineering*, vol. 39, no. 2, pp. 69–75, 2011.

[8] M. A. S. Kamal, M. Mukai, J. Murata, and T. Kawabe, "Ecological vehicle control on roads with up-down slopes," *IEEE Transactions on Intelligent Transportation Systems*, vol. 12, no. 3, pp. 783–794, 2011.

[9] M. A. S. Kamal, M. Mukai, J. Murata, and T. Kawabe, "Ecological driver assistance system using model-based anticipation of vehicle-road-traffic information," *IET Intelligent Transport Systems*, vol. 4, no. 4, pp. 244–251, 2010.

[10] J. E. Naranjo, C. Gonzalez, R. Garcia, and T. Pedro, "Cooperative throttle and brake fuzzy control for ACC stop & go maneuvers," *IEEE Transactions on Vehicular Technology*, vol. 56, no. 4, pp. 1623–1630, 2007.

[11] V. L. Bageshwar, W. L. Garrard, and R. Rajamani, "Model predictive control of transitional maneuvers for adaptive cruise control vehicles," *IEEE Transactions on Vehicular Technology*, vol. 53, no. 5, pp. 1573–1585, 2004.

[12] H. Wang and S. F. Ma, "Car-following model and simulation with curves and slopes," *China Civil Engineering Journal*, vol. 38, no. 11, pp. 106–111, 2005.

[13] D. Z. Zhang, K. Q. Li, and J. Q. Wang, "A curving ACC system with coordination control of longitudinal car-following and lateral stability," *Vehicle System Dynamics*, vol. 50, no. 7, pp. 1085–1102, 2012.

[14] X. J. Su, P. Shi, L. G. Wu, and Y. D. Song, "A novel approach to filter design for T-S fuzzy discrete-time systems with time-varying delay," *IEEE Transactions on Fuzzy Systems*, vol. 20, no. 6, pp. 1114–1129, 2012.

[15] W. B. Li, Y. Xu, and H. Z. Li, "Robust I2-I_∞ filtering for discrete-time Markovian jump linear systems with multiple sensor faults, uncertain transition probabilities and time-varying delays," *IET Signal Processing*, vol. 7, no. 8, pp. 710–719, 2013.

[16] H. Zhang, Y. Shi, and A. S. Mehr, "Robust weighted H_∞ filtering for networked systems with multiple sensor faults," in *Proceedings of the 8th World Congress on Intelligent Control and Automation (WCICA '10)*, pp. 1228–1233, Jinan, China, July 2010.

[17] X. J. Su, L. G. Wu, P. Shi, and Y. D. Song, "H_∞ model reduction of takagi-sugeno fuzzy stochastic systems," *IEEE Transactions on Systems, Man, and Cybernetics B*, vol. 42, no. 6, pp. 1574–1585, 2012.

[18] H. Zhang, Y. Shi, and M. X. Liu, "Step tracking control for networked discrete-time nonlinear systems with integral and predictive actions," *IEEE Transactions on Industrial Informatics*, vol. 9, no. 1, pp. 337–345, 2013.

[19] H. Zhang, Y. Shi, M. Q. Xu, and H. T. Cui, "Observer-based tracking controller design for networked predictive control systems with uncertain markov delays," in *Proceedings of the American Control Conference*, pp. 5682–5687, Montréal, Canada, June 2012.

[20] H. Zhang, Y. Shi, and B. X. Mu, "Optimal H_∞-based linear-quadratic regulator tracking control for discrete-time takagi-sugeno fuzzy systems with preview actions," *Journal of Dynamic Systems, Measurement, and Control*, vol. 135, pp. 044501-1–044501-5, 2013.

[21] H. Zhang, Y. Shi, and A. Saadat Mehr, "Robust static output feedback control and remote PID design for networked motor systems," *IEEE Transactions on Industrial Electronics*, vol. 58, no. 12, pp. 5396–5405, 2011.

[22] L. Chen, J. Wang, and N. Li, "H_∞ adaptive variable universe fuzzy control for autonomous vehicles," in *Proceedings of the 26th Chinese Control Conference (CCC '07)*, pp. 82–86, Zhangjiajie, China, July 2007.

[23] Y. Hou and Z. Liu, "An H2/H∞ robust control approach to electric vehicle constant speed cruise," in *Proceedings of the 30th Chinese Control Conference (CCC '11)*, pp. 2384–2389, Yantai, China, July 2011.

[24] R. Zhang, X. P. Yan, J. Ma, C. Z. Wu, and Y. L. Ma, "Design of intelligent vehicle speed adaption based on variable road geometry," in *Proceedings of the 2nd International Conference on Transportation Information and Safety*, pp. 1708–1714, Wuhan, China, June 2013.

[25] Y. L. Ma, Q. Wu, X. P. Yan, and R. Zhang, "The hardware-in-the-loop simulator: a mechatronic testbed for cooperative vehicles maneuvers," *International Journal of Intelligent Transportation Systems Research*, vol. 11, no. 1, pp. 11–22, 2013.

[26] S. Kumarawadu and T. T. Lee, "Neuroadaptive combined lateral and longitudinal control of highway vehicles using RBF networks," *IEEE Transactions on Intelligent Transportation Systems*, vol. 7, no. 4, pp. 500–512, 2006.

[27] H. Dahmani, M. Chadli, A. Rabhi, and A. El Hajjaji, "Vehicle dynamics and road geometry estimation using a Takagi-Sugeno fuzzy observer with unknown inputs," in *Proceedings of the IEEE Intelligent Vehicles Symposium (IV '11)*, pp. 272–277, Baden-Baden, Germany, June 2011.

[28] A. Hernandez-Gutierrez, J. I. Nieto, T. Bailey, and E. M. Nebot, "Probabilistic road geometry estimation using a millimetre-wave radar," in *Proceedings of the IEEE/RSJ International Conference on Intelligent Robots and Systems*, pp. 4601–4607, San Francisco, Calif, USA, September 2011.

Hindawi Publishing Corporation
Mathematical Problems in Engineering
Volume 2013, Article ID 208628, 8 pages
http://dx.doi.org/10.1155/2013/208628

Research Article

Collision-Free and Energy-Saving Trajectory Planning for Large-Scale Redundant Manipulator Using Improved PSO

Min Jin and Dan Wu

School of Information Science and Engineering, Hunan University, Changsha, Hunan 410082, China

Correspondence should be addressed to Min Jin; jinmin@hnu.edu.cn

Received 1 October 2013; Accepted 18 November 2013

Academic Editor: Hui Zhang

The large-scale boom system, such as the five-arm concrete pump truck with the arm length of 36–65 meters, usually operates in an unknown dynamic outdoor environment. The motion safety and the energy consumption are thus the two vital measurements to the effectiveness of the trajectory planning for the large-scale boom system. Due to the redundancy of the large-scale boom system and some drawbacks of the original particle swarm optimization (PSO) algorithm, an improved PSO algorithm is presented to solve the inverse kinematic problem of the redundant large-scale boom system. By the improved PSO algorithm, the energy-saving trajectory planning of the large-scale boom system that operates in a workspace without obstacles and with obstacles is optimized, which considers different important degrees of the subgoals, respectively. The optimal results from the simulation study and the practical application verify the effectiveness of the proposed planning strategy. At the same time, the performance of the improved strategy is compared with that of the traditional, and the superiority is further demonstrated.

1. Introduction

Owing to the agility of action, capability of obstacle avoidance, and excellent dynamic performance, redundant manipulators have attracted more and more attention and have been used widely in lots of fields, such as manufacturing and surgery. As they possess more degrees of freedom than those required to execute a given task, the inverse kinematics admit a number of solutions. Furthermore, when manipulator tasks are demanded in precision and diversity, these tasks' execution might make the design of a trajectory planning of the redundant manipulator difficult because of the nonlinearity of the dynamics and the coupling between axes. How to obtain an optimal solution for the inverse kinematics problem of redundant manipulators has become a research focus.

At present, there are mainly three methods, algebra method, geometrical method, and numerical iteration method, which are applied to the inverse kinematics of redundant manipulator [1–4]. Although these methods can solve the problem, they have their own disadvantage, respectively. Algebra method and geometrical method are only used to solve the simple redundant manipulators such as two-joint SCARA mechanical arm. The numerical iteration method can be utilized to obtain the solution for the intricate redundant manipulators, but the solution is unique and unreliable. Moreover, these methods only considered one object, namely, the end-effector of manipulator move from the initial position to the final desired precisely. The workspace obstacle avoidance is not discussed.

Aiming at this problem, many researchers made a lot of research. Han and Piu presented the Tank-Hopfield network and J function to plan the trajectory of the redundant robot, so that the desired end-effector trajectory is tracked closely, the workspace obstacles are avoided simultaneously [5]. McAvoy et al. utilized a genetic algorithm (GA) to optimize the point-to-point trajectory planning of kinematically redundant manipulators [6]. Peng and Wei proposed the ASAGA trajectory planning method of redundant manipulators by incorporating the GA and simulated annealing algorithm [7]. Although these methods can obtain a superior solution for the kinematic of redundant manipulator, when number of the parameters to be optimized is large and the parameters are highly correlated, they can use more computing time and degrade efficiency to search the global

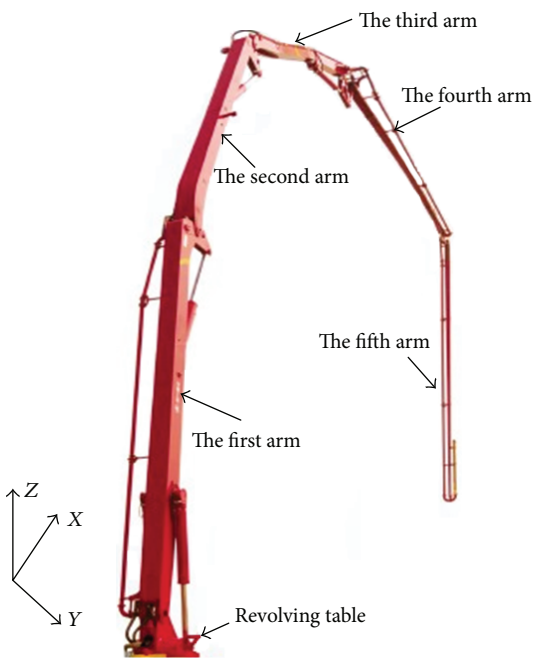

Figure 1: The boom system of concrete pump truck.

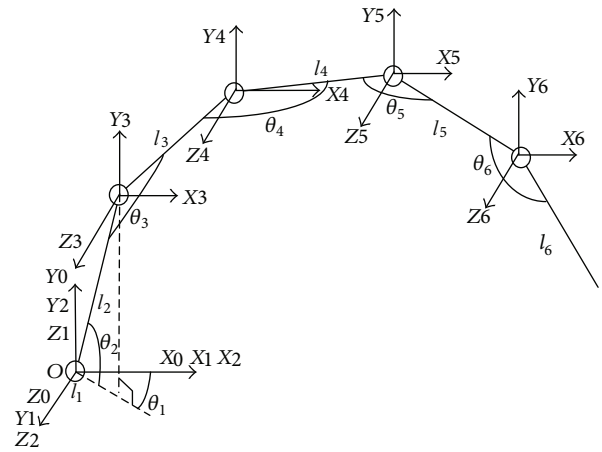

Figure 2: Geometry of a six-degrees-of-freedom of joint angles θ_i, $i = 1, 2, \ldots, 6$.

optimum solution. Furthermore, some vital characteristics of the redundant manipulator such as safety, energy consumption, and stability of the manipulator may not be considered.

The large-scale boom system of the five-arm concrete bump truck with the arm length of 36–65 meters is a representative 6-degree-of-freedom redundant manipulator. They usually operate in an unknown dynamic outdoor environment with overhead power transmission lines and field construction workers. Thus, the motion safety and the energy consumption are the two vital measurements to the effectiveness of trajectory planning for the large-scale boom system. In order to ensure the motion safety as well as reduce the energy consumption, an improved particle swarm optimization (PSO) algorithm which can overcome the drawbacks mentioned above is adopted to optimize the trajectory of the boom system in this paper.

The paper is organized as follows. The kinematic description of boom system of concrete pump truck is given in Section 2. Section 3 introduces the improved PSO algorithm. The PSO method is used to solve the inverse kinematic problem of the boom system in Section 4. Section 5 gives some cases study. The practical application is demonstrated in Section 6. The conclusion is drawn in Section 7.

2. Kinematic Description of Boom System of Five-Arm Concrete Pump Truck

Figure 1 shows the boom system of five-arm concrete pump truck with 6 degrees of freedom. It is composed of five arms and a revolving table. The revolving table is fixed to the frame foundation with the screws and revolves on the z axis. The five arms and the revolving table are connected in a series with five revolute joints and each arm is driven by the arm cylinder.

According to the characteristic of the framework of the boom system, the mechanism of the boom system and the coordinate system of each arm are displayed in Figure 2. It can be seen that the revolving table coordinate system and the first arm coordinate system are coincided with the reference coordinate system and the material outlet of boom system is set as the end coordinate system origin of the fifth arm. l_i $(i = 1, 2, \ldots, 6)$ denote the length of each arm, θ_i $(i = 1, 2, \ldots, 6)$ signifies the angle between the ith arm and the $(i-1)$th arm. Thereinto, l_1 and θ_1 are the length of revolving table and the angle between the first arm and the axis $X1$, respectively. For convenience, they are all set as 0; that is, the boom system becomes a planar five-bar linkages. Table 1 shows the kinematic parameters of each arm.

Utilizing these parameters the transformation matrixes [8] which describe the relative position and gesture between two adjacent arms can be obtained and described as follows.

$$A_0 = \begin{bmatrix} 1 & 0 & 0 & 0 \\ 0 & 0 & 1 & 0 \\ 0 & -1 & 0 & 0 \\ 0 & 0 & 0 & 1 \end{bmatrix}, \quad A_1 = \begin{bmatrix} c1 & 0 & s1 & 0 \\ s1 & 0 & -c1 & 0 \\ 0 & 1 & 0 & 0 \\ 0 & 0 & 0 & 1 \end{bmatrix},$$

$$A_2 = \begin{bmatrix} c2 & -s2 & 0 & l_1 c2 \\ s2 & c2 & 0 & l_1 s2 \\ 0 & 0 & 1 & 0 \\ 0 & 0 & 0 & 1 \end{bmatrix}, \quad A_3 = \begin{bmatrix} c3 & -s3 & 0 & -l_2 c3 \\ s3 & c3 & 0 & -l_{2s3} \\ 0 & 0 & 1 & 0 \\ 0 & 0 & 0 & 1 \end{bmatrix},$$

$$A_4 = \begin{bmatrix} c4 & -s4 & 0 & l_3 c4 \\ s4 & c4 & 0 & l_{3s4} \\ 0 & 0 & 1 & 0 \\ 0 & 0 & 0 & 1 \end{bmatrix}, \quad A_5 = \begin{bmatrix} c5 & -s5 & 0 & -l_4 c5 \\ s5 & c5 & 0 & -l_4 s5 \\ 0 & 0 & 1 & 0 \\ 0 & 0 & 0 & 1 \end{bmatrix},$$

$$A_6 = \begin{bmatrix} c6 & -s6 & 0 & -l_5 c6 \\ s6 & c6 & 0 & -l_5 s6 \\ 0 & 0 & 1 & 0 \\ 0 & 0 & 0 & 1 \end{bmatrix}, \tag{1}$$

Table 1: The kinematic parameters of each arm.

J_i	θ_i (°)	Interval (°)	α_{i-1} (°)	a_{i-1} (mm)	d_i (mm)
1	θ_1	0	−90	l_1	0
2	θ_2	[0, 90]	90	l_2	0
3	θ_3	[0, 180]	0	l_3	0
4	θ_4	[0, 180]	0	l_4	0
5	θ_5	[0, 200]	0	l_5	0
6	θ_6	[0, 240]	0	l_6	0

where A_i $(i = 0, 1, \ldots, 6)$ denotes the relative position and gesture pose of the ith arm to the $(i-1)$th arm, ci $(i = 1, 2, \ldots, 6)$ signifies $\cos(\theta_i)$, and si $(i = 1, 2, \ldots, 6)$ represents $\sin(\theta_i)$. Thus, the position and gesture of the end of the fifth arm can be expressed as

$$T_7 = A_0 A_1 A_2 A_3 A_4 A_5 A_6 = \begin{pmatrix} n_x & o_x & a_x & p_x \\ n_y & o_y & a_y & p_y \\ n_z & o_z & a_z & p_z \\ 0 & 0 & 0 & 1 \end{pmatrix}, \quad (2)$$

where

$$\begin{gathered} n_x = c1c23456, \qquad n_y = s23456, \\ n_z = -s1c23456 \\ o_x = -c1s23456, \qquad o_y = c23456, \\ o_z = s1s23456 \\ a_x = s1, \qquad a_y = 0, \qquad a_z = c1, \\ p_x = c1\left(l_5c23456 - l_4c2345 + l_3c234 - l_2c23 + l_1c2\right) \\ p_y = l_5s23456 - l_4s2345 + l_3s234 - l_2s23 + l_1s2 \\ p_z = s1\left(-l_5c23456 + l_4c2345 - l_3c234 + l_2c23 - l_1c2\right) \end{gathered} \quad (3)$$

in which $c1 = \cos(\theta_1)$, $s1 = \sin(\theta_1)$, $c12 = \cos(\theta_1 + \theta_2)$ and so on.

3. Review of Particle Swarm Optimization Algorithm and Improved PSO

3.1. Review of Particle Swarm Optimization Algorithm (PSO). Particle swarm optimization algorithm is a new entrant to the family of evolutionary algorithms, which is capable of mimicking the social behavior of birds flocking and fish schooling in search for food and proposed by Kennedy and Eberhart [9]. Its basic concept is that the potential solutions are flown through hyperspace and are accelerated towards better or more optimum solutions. The algorithm is described simply as follows.

Given a swarm of N particles in a D-dimension space, the ith particle which is a feasible solution in an optimal problem is represented by the position vector $x_i = (x_1^i, x_2^i, \ldots, x_D^i)$. The best previous solution which has been found is denoted by the particle $p_i = (p_1^i, p_2^i, \ldots, p_D^i)$, and the current group's best solution that is found by the neighborhood particles of the ith particle is signified by $g_i = (g_1^i, g_2^i, \ldots, g_D^i)$. The velocity of the ith particle is represented as $V_i = (v_1^i, v_2^i, \ldots, v_D^i)$. At the iteration step $t+1$, the position of the ith particle is updated by the following equations:

$$\begin{gathered} v_d^i(t+1) = w_0 v_d^i(t) + c_1 r_1 \left[p_d^i(t) - x_d^i(t)\right] \\ + c_2 r_2 \left[g_d^i(t) - x_d^i(t)\right], \\ x_d^i(t+1) = x_d^i(t) + v_d^i(t+1), \end{gathered} \quad (4)$$

where $i = 1, 2, \ldots, N$, $d = 1, 2, \ldots, D$. w_0, c_1 and c_2 are the positive constants, and r_1 and r_2 are two random parameters which belong to the interval [0, 1]. Thus, according to (4), the iterative process will continue warm by warm until the fittest solution is obtained.

3.2. Improved PSO. The original PSO has been applied to all kinds of engineering fields widely because of its robustness and fastness in solving the optimization problems, but it still has some difficulties in searching the overall optimal solution and improving the computational efficiency. Jiang et al. have analyzed the relationship between the convergence and parameter selection of the standard particle algorithm [10]. And many scholars have proposed some methods to improve the performance of the standard PSO algorithm [11–13]. Although these modified PSO algorithms have improved the global search ability of the particles, the computation burden is increased. In order to ensure the real-time control and intelligent work of the boom system, an improved PSO algorithm is introduced.

It is well known that the convergence property and performance of the standard PSO algorithm are influenced by many factors such as the selection of the nonnegative real parameter w, c_1 and c_2 [10]. Thereinto, the parameter w is called the inertia weight, which can adjust the velocity of the particle and enable the particle to search the new solution space. To enhance the particle's global search ability, the positive constant w is modified using the following equation:

$$w = w_0 \times \frac{1 + \cos\left(t/T_{\max}\right)}{2}, \quad (5)$$

where w_0 is the initial value and is set as 0.729, t is the tth iteration step, and $T_{\max}$ is the maximal iteration step number. And the maximal and minimal velocity of particles are set as

$$V_{\max} = \frac{X_{\max} - X_{\min}}{2}$$
$$V_{\min} = -V_{\max}, \tag{6}$$

where $X_{\max}$ and $X_{\min}$ are the maximal and minimal boundaries of the parameter space.

For the parameters c_1 and c_2 which is included in the second term and the third term on the right hand of (4), they represent the cognitive part of PSO which can enable the particle to change its velocity based on its own thinking and memory and the social part as the particle change its velocity based on the social-psychological adaptation of knowledge, respectively, and reflect the personal experience and the social experience of its own. When the personal and social experiences accumulated so far are overused the particle can be driven away from the local optimum. However, if they are not fully used, the convergence performance of the PSO algorithm is undermined. In addition, considering the working characteristic and environment of the of the boom system of the five-arm concrete pump truck, there can be a small number of local optimal solutions to the inverse kinematic problem. To make use of the personal experience and social experience of the particle and obtain the global optimal configuration of the boom system, the velocity of particle is updated by the following formula:

$$\begin{aligned} v_d^i(t+1) = {} & w v_d^i(t) + \left(\frac{1 - \left|p_d^i(t) - x_d^i(t)\right|}{x_d^{\max} - x_d^{\min}}\right)^2 \\ & \times r_1\left[p_d^i(t) - x_d^i(t)\right] + \left(\frac{1 - \left|g_d^i(t) - x_d^i(t)\right|}{x_d^{\max} - x_d^{\min}}\right)^2 \\ & \times r_2\left[g_d^i(t) - x_d^i(t)\right]. \end{aligned} \tag{7}$$

4. Trajectory Planning of Boom System Based on Improved PSO

Because of the redundancy and difference of working requirement and environment, the improved PSO algorithm is adopted to solve the inverse kinematic problem of the boom system when the concrete pump truck work. The calculation procedure is shown in Figure 3.

Assumed that the initial position of the material outlet of the boom system is represented by the vector $P_{\text{ini}} = [p_x^{\text{ini}}, p_y^{\text{ini}}, p_z^{\text{ini}}]$, the initial joint angle is denoted by the vector $\theta^{\text{ini}} = [\theta_0^{\text{ini}}, \theta_1^{\text{ini}}, \ldots, \theta_5^{\text{ini}}]$, the desired position and desired joint angle are represented by two vectors $P_{\text{goal}} = [p_x^{\text{goal}}, p_y^{\text{goal}}, p_z^{\text{goal}}]$, and $\theta^{\text{goal}} = [\theta_0^{\text{goal}}, \theta_1^{\text{goal}}, \ldots, \theta_5^{\text{goal}}]$, respectively. The fitness function is designed according to the desired goal. All constraints and criteria are translated into penalty functions to be minimized and that are defined in the sequel. Consider the following:

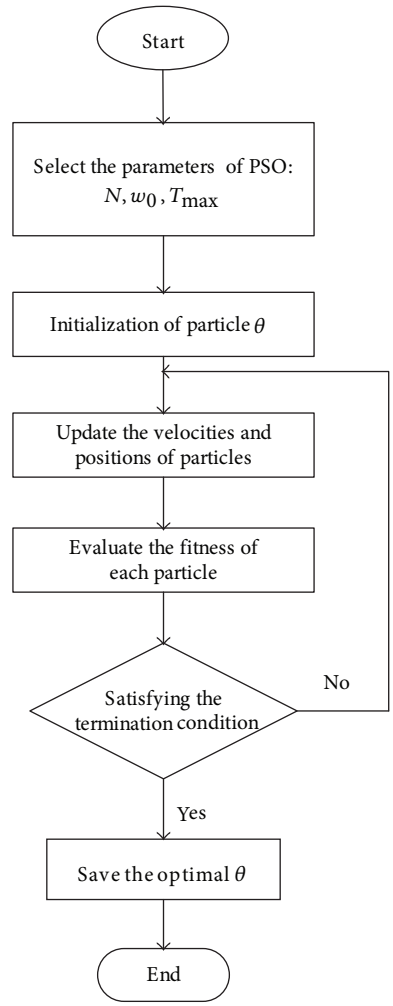

Figure 3: The flowchart of the PSO.

(1) In order to reduce the loss of energy, when material outlet move from the initial position P_{ini} to the desired position P_{goal}, according to the characteristic of the boom system the variation of joint angle should be minimized.

$$f_1(\theta) = \sum_{i=0}^{5} \frac{1}{(i+1)} \times \left[\text{abs}\left(\theta_i^{\text{goal}} - \theta_i^{\text{ini}}\right)\right]. \tag{8}$$

(2) For working convenience of boom system, the variation orientation of angle between two adjacent links should be concurrent; namely, the configuration of the boom system is flexible, the objective function can be described by the following the function:

$$f_2(\theta) = \sum_{i=1}^{5} \lambda_i \left[\theta_i(t+1) - \theta_i(t)\right]^2, \tag{9}$$

where t and $t+1$ are two consecutive sampling instants, and

$$\lambda_i = \begin{cases} t^{1/2} & \text{if } (\theta_{i+1} - \theta_i)(\theta_i - \theta_{i-1}) < 0 \\ 1 & \text{otherwise,} \end{cases} \quad i = 2, \ldots, 4. \tag{10}$$

(3) In order to avoid tilt of the concrete pump truck because of self-weight, the gravity center of the boom system should be close to the revolving table; namely,

$$f_3(\theta) = \max(\theta_1). \tag{11}$$

(4) In order to avoid obstacle, the displacements between obstacle and each end points of all links should be maximized, and there is no interference between each link and the obstacle. The function can be represented as follows:

$$f_4(\theta) = \max(d_i) \quad i = 1, \ldots, 6, \tag{12}$$

where d_i represents the displacement between obstacle and the ith end point.

(5) In order to ensure that the material outlet of boom system can get to the desired final position P_{goal}, the positional error P_{error} is defined as follows:

$$P_{\text{error}} = \sqrt{\left(p_x^{\text{goal}} - p_x^c\right)^2 + \left(p_y^{\text{goal}} - p_y^c\right)^2 + \left(p_z^{\text{goal}} - p_z^c\right)^2}, \tag{13}$$

where $P_c = (p_x^c, p_y^c, p_z^c)$ is the current position of material outlet of boom system.

Thus, the fitness function F_{fitness} is defined as follows:

$$F_{\text{fitness}} = P_{\text{error}} + \alpha_i f_i(\theta), \tag{14}$$

where $0 < \alpha_i < 1$ denotes a weight factor which is used to represent the importance degree of different subgoals.

5. Simulation Study

Given that the length of the arm of the boom system is $l_0 = 0$, $l_1 = 10$, $l_2 = 9$, $l_3 = 9$, $l_4 = 9$, $l_5 = 9$, respectively. The initial joint angle is $\theta_0^{\text{ini}} = [0, 60^\circ, 150^\circ, 150^\circ, 162^\circ, 150^\circ]$. The desired position is set as $P_{\text{goal}} = [30, 20, 0]$. Utilizing the PSO method mentioned above, the inverse kinematic problem of the redundant boom system in a workspace with obstacles and without obstacles is solved. In addition, the number of particles is set as $N = 40$, the maximal number of iteration step is set as $T_{\max} = 150$, and the positive constants are set as $w_0 = 0.729$, $c_1 = 1.49$ and $c_2 = 1.49$, respectively.

5.1. Improved PSO Performance in a Workspace without Obstacles. Generally speaking, the boom system of concrete pump truck usually works in a workspace without obstacles. Under different work conditions, when the performance of concrete pump truck considered is different, the attitude of the boom system can be different. In order to enable the boom system to work better, three different configurations of the boom system are optimized in this paper.

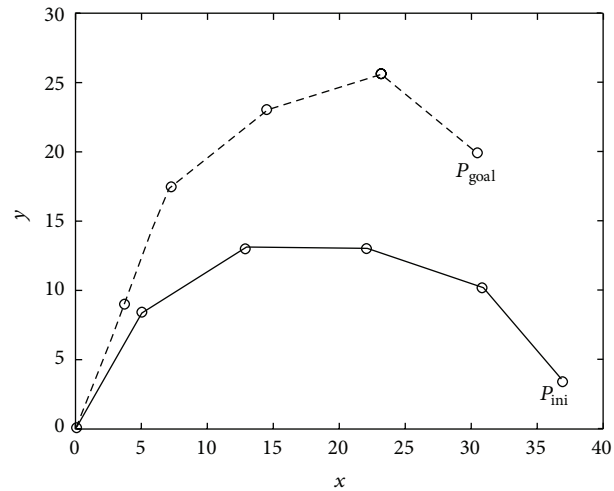

Figure 4: The configuration with the minimal loss of energy.

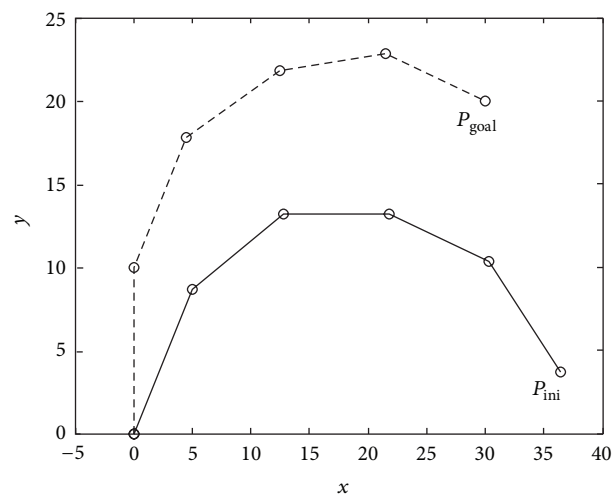

Figure 5: The configuration with the tilt-avoidance.

When the outlet of the boom system move to the desired position and the different subgoals are also considered preferentially, the configuration of the boom system is different. Figure 4 shows the optimal configuration with the minimal loss of energy. Figure 5 displays the optimal configuration with the tilt-avoidance. The optimal configuration which has considered all the subgoals is shown in Figure 6.

From Figure 4 it can be seen that when the loss of energy of the concreter pump truck is considered precedently the flexibility of the boom system is not optimal. The solution corresponding to the configuration in Figure 5 can avoid the tilt effectively, and the flexibility is superior, but the loss of energy is the maximal. The solution corresponding to the configuration in Figure 6 is the best, which consider, all the

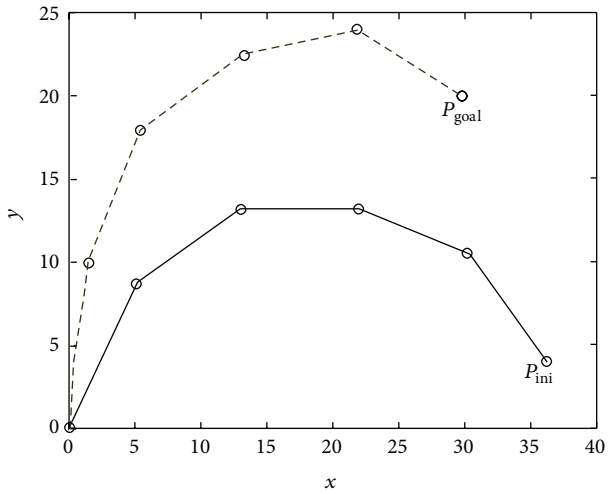

Figure 6: The optimal configuration of boom system.

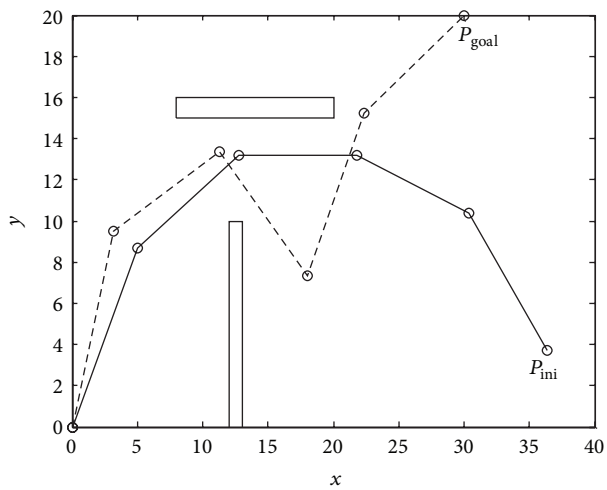

Figure 7: The configuration in a workspace with two obstacles.

performance such as the loss of the energy, tilt-avoidance, and flexibility.

In addition, from these figures it can be drawn that the improved PSO can optimize the multigoal trajectory planning problem. In other words, according to the different performance requirements of the boom system considered, the optimal configuration of the boom system, which considers different degree of different subgoal, can be obtained by the improved PSO algorithm effectively.

5.2. Improved PSO Performance in a Workspace with Obstacles. Considering two obstacles in the workspace, for a given initial configuration some arms of the boom system locate between two obstacles, the final configuration result of the boom system obtained by the improved PSO algorithm is shown in Figure 7. It can be seen that the boom system can work safely and the material outlet can move to the desired position accurately. But the flexibility of boom system is bad.

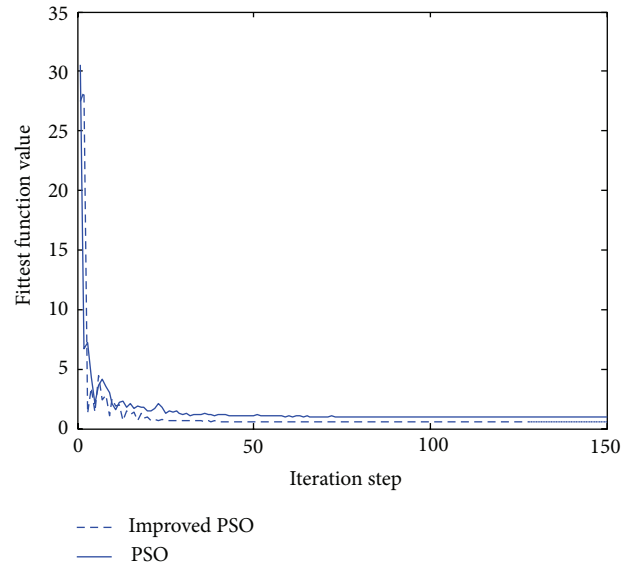

Figure 8: The optimization process obtained by the improved PSO and PSO.

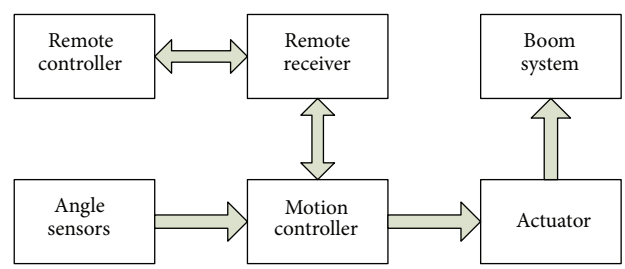

Figure 9: The flowchart of control system of the boom system.

At the same time, it is also demonstrated that the improved PSO can solve the inverse kinematic problem with obstacle-avoidance.

5.3. Comparison Analysis of Improved PSO and PSO. In order to further illustrate the superiority of the improved PSO, the improved PSO algorithm and original PSO are used to solve the same inverse kinematic problem of the boom system in the workspace with the obstacle mentioned above. The optimal process obtained by these two algorithms is shown in Figure 8. From the figure, it can be seen that the convergence velocity of the improved PSO is quicker than that of the PSO and the solution is also better. All these have demonstrated that the performance of the improved PSO is superior to that of the PSO.

6. Practical Application

Figure 9 shows the flowchart of control system that makes the boom system of the concrete pump truck works intelligently. Utilizing the data which describes the position of the outlet of the boom system and is received by the remote receiver and emitted by the remote controller along with the signals

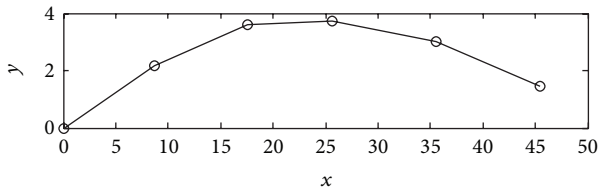

Figure 10: The schematic diagram of the boom system obtained theoretically.

that the angle sensors acquire, the motion controller uses the improved PSO algorithm to plan the configuration of the boom system. When the angles between two adjacent arms are obtained, the displacement increment of each cylinder is acquired by the geometrical relationship between the cylinder and two adjacent arms. Accordingly, the variation of hydraulic oil volume of each arm cylinder is obtained. And the driver current value is calculated by the proportion of variation of the oil volume to the current increment. Thus, the arm cylinder of the boom system is driven by the actuator and the outlet of the boom system can get to the desired position.

In order to verify the practicability of the control system that the improved PSO algorithm has been embedded in, an application test that plans the trajectory of the 46- meters five-arm boom system of concrete pump truck is done. In this test, the length of each arm is $l_1 = 9, l_2 = 9, l_3 = 8, l_4 = 10, l_5 = 10$, respectively. There is no obstacle in the workspace and all subgoals are considered. The initial position of the outlet is (10, 0, 0), namely, the boom system, is not opened up and the desired position is (45.5, 1.5, 0).

After running the control system, the schematic diagram obtained theoretically is shown in Figure 10. The joint angle obtained is $\theta^{\text{goal}} = [0^\circ_0, 14^\circ_1, 175^\circ_2, 172^\circ_2, 175^\circ_2, 175^\circ_2]$ and the obtained position of the outlet is (45.47, 1.46, 0). In practice, the final configuration of the boom system is displayed in Figure 10. The position of the outlet is (45.12, 1.25, 0). It is deviated from the desired goal in a sort. This is mainly attributed to the gravity of boom system and the calculation error, but it is still satisfied with the working requirements.

7. Conclusion

In this paper, an improved PSO algorithm is proposed to solve the multigoal trajectory planning problem of the redundant large-scale boom system of concrete pump truck. Because of the drawback of the original PSO such as the low convergence velocity and the inexact solution, an improved PSO is introduced.

Utilizing the improved PSO algorithm, the simulation result to the inverse kinematic problem which considers different performance requirements of the redundant boom system of concrete pump truck that works in a workspace without obstacles and with obstacles have been obtained. At the same time, the performance of the improved PSO is compared with that of the PSO. Furthermore, the improved PSO algorithm have been embedded in the controller and applied to the trajectory planning of the boom system of concrete pump truck. All results illustrate that the proposed strategy can plan a collision-free and energy-saving trajectory for the redundant large-scale boom system, and thus it has the practicability.

Conflict of Interests

The authors declare that there is no conflict of interests regarding the publication of this paper.

Acknowledgments

This work is supported by the National Scientific and Technological Achievement Transformation Project of China (Grant no. 201255), Electronic Information Industry Development Fund of China (Grant no. 2012407), and National Natural Science Foundation of China (Grant no. 61374172).

References

[1] D. Manocha and J. F. Canny, "Real time inverse kinematics for general 6R manipulators," in *Proceedings of the IEEE International Conference on Robotics and Automation*, pp. 383–389, Raleign, NC, USA, May 1992.

[2] R. Manseur and K. L. Doty, "Structural kinematics of 6-revolute-axis robot manipulators," *Mechanism and Machine Theory*, vol. 31, no. 5, pp. 647–657, 1996.

[3] B.-L. Lu and K. Ito, "Regularization of inverse kinematics for redundant manipulators using neural network inversions," in *Proceedings of the IEEE International Conference on Neural Networks*, pp. 2726–2731, December 1995.

[4] K. Li and Y. Zhang, "Fault-tolerant motion planning and control of redundant manipulator," *Control Engineering Practice*, vol. 20, no. 3, pp. 282–292, 2012.

[5] D. Han and C. S. Piu, "Collision-free motion planning for redundant robots using neural-network processing," *Engineering Applications of Artificial Intelligence*, vol. 10, no. 2, pp. 179–188, 1997.

[6] B. McAvoy, B. Sangolola, and Z. Szabad, "Optimal trajectory generation for redundant planar manipulators," in *Proceedings of the IEEE International Conference on Systems, Man and Cybernetics*, pp. 3241–3246, Nashville, Tenn, USA, October 2000.

[7] Y. Peng and W. Wei, "A new trajectory planning method of redundant manipulator based on adaptive simulated annealing genetic algorithm (ASAGA)," in *Proceedings of the International Conference on Computational Intelligence and Security (ICCIAS '06)*, pp. 262–265, Guangzhou, China, October 2006.

[8] Z. X. Cai and Robotics Tsinghua University Press, Beijing, China, 2002.

[9] J. Kennedy and R. Eberhart, "Particle swarm optimization," in *Proceedings of the IEEE International Conference on Neural Networks*, pp. 1942–1948, Perth, Australia, December 1995.

[10] M. Jiang, Y. P. Luo, and S. Y. Yang, "Stochastic convergence analysis and parameter selection of the standard particle swarm optimization algorithm," *Information Processing Letters*, vol. 102, no. 1, pp. 8–16, 2007.

[11] P. C. Fourie and A. A. Groenwold, "The particle swarm optimization algorithm in size and shape optimization," *Structural and Multidisciplinary Optimization*, vol. 23, no. 4, pp. 259–267, 2002.

[12] S. L. Ho, S. Yang, G. Ni, and H. C. Wong, "A particle swarm optimization method with enhanced global search ability for design optimizations of electromagnetic devices," *IEEE Transactions on Magnetics*, vol. 42, no. 4, pp. 1107–1110, 2006.

[13] G. Xu, J.-P. Qu, and Z.-T. Yang, "Improved adaptive particle swarm optimization algorithm," *Journal of South China University of Technology*, vol. 36, no. 9, pp. 6–10, 2008.

Hindawi Publishing Corporation
Mathematical Problems in Engineering
Volume 2013, Article ID 313197, 11 pages
http://dx.doi.org/10.1155/2013/313197

Research Article

Optimal Ascent Guidance for Air-Breathing Launch Vehicle Based on Optimal Trajectory Correction

Xuefang Lu, Yongji Wang, and Lei Liu

Key Laboratory of Ministry of Education for Image Processing and Intelligent Control, School of Automation, Huazhong University of Science and Technology, Wuhan 430074, China

Correspondence should be addressed to Yongji Wang; wangyjch@mail.hust.edu.cn

Received 14 October 2013; Revised 28 October 2013; Accepted 28 October 2013

Academic Editor: Hui Zhang

An optimal guidance algorithm for air-breathing launch vehicle is proposed based on optimal trajectory correction. The optimal trajectory correction problem is a nonlinear optimal feedback control problem with state inequality constraints which results in a nonlinear and nondifferentiable two-point boundary value problem (TPBVP). It is difficult to solve TPBVP on-board. To reduce the on-board calculation cost, the proposed guidance algorithm corrects the reference trajectory in every guidance cycle to satisfy the optimality condition of the optimal feedback control problem. By linearizing the optimality condition, the linear TPBVP is obtained for the optimal trajectory correction. The solution of the linear TPBVP is obtained by solving linear equations through the Simpson rule. Considering the solution of the linear TPBVP as the searching direction for the correction values, the updating step size is generated by linear search. Smooth approximation is applied to the inequality constraints for the nondifferentiable Hamiltonian. The sufficient condition for the global convergence of the algorithm is given in this paper. Finally, simulation results show the effectiveness of the proposed algorithm.

1. Introduction

The development of space technology has given rise to the expectation that launchers will become low cost and fully reusable. The launch vehicle with hypersonic air-breathing propulsion is considered to reduce the cost of payloads taken to the Earth's orbit. The air-breathing launch has inherent features that make it a candidate for future space transportation [1]. The impulse of air-breathing propulsion, which is approximately 3000 s [2], is significantly higher than that of a rocket (360 s). Air-breathing propulsion brings high impulse as well as strong nonlinear, coupling aerodynamic and thrust.

The traditional design category for ascent guidance is to drive an optimal nominal trajectory off-board. The guidance problem is then transformed into a tracking problem for the designed optimal nominal trajectory. The design of a trajectory could be formulated as a global optimization task [3]. The methods for numerical optimization of continuous dynamic systems could be termed "Hamiltonian" (indirect method) and "Transcription" (direct method) [4]. For the optimization problem with inequality constraints, smoothing approximation was considered in [5, 6]. A filled function approach for nonsmooth constrained global optimization was presented in [7]. Linear-quadratic optimization was implemented to optimal control in [8]. Direct and indirect optimization methods were implemented to the off-board trajectory optimization problem in previous literature. The numerical algorithms of trajectory optimization for vehicles were summarized and systematically analyzed in [9, 10]. A new concept of pseudocontrol sets to solve optimal control problems was proposed in [11]. This approach reduces the calculation cost by combining large-scale linear programming algorithms with discretization of the continuous system dynamics on small segments. An algorithm for multiobjective optimization was presented in [12]. Intelligent algorithms can also be used for trajectory optimization problems. The particle swarm optimization (PSO) method was implemented to the space trajectory optimization in [13]. The simulation results showed the effective of PSO in finding the optimal solution to the space trajectory optimization problems, with great numerical accuracy. Approximate numerical methods

of optimization were presented for multiorbit noncoplanar orbit transfers of low-thrust spacecraft in [14].

Many control methods were implemented to trajectory tracking guidance and control problem [15]. In the previous literature, many researchers focused on the robust control method [16, 17]. It has obtained successful application in the industry [18, 19]. For the networked control system, a H-infinity step tracking control method was presented in [20]. An adaptive fuzzy robust control for a class of nonlinear systems was proposed in [21]. An adaptive guidance law and off-board trajectory optimization for air-breathing launch vehicle were addressed in [22]. In that paper, the optimal control problem was solved using SQP method. And the adaptive guidance law was developed using a feedback loop based on a second-order rate controller for angle of attack. A robust state feedback guidance law was generated in real time using the indirect Legendre pseudospectral feedback method in [23]. In that paper, the guidance problem was converted into a trajectory state regulation problem which is a linear time varying system.

However, the accuracy of the trajectory tracking method is low with the disturbance and the modeling error. It lacks the autonomy and adaptability to cope with the non-nominal vehicle and mission conditions needed for future reusable launch vehicles [24]. To improve the performance and the accuracy of the guidance, the optimal guidance method generates the prospective trajectory by fast trajectory optimization on-board based on current flight state. This guidance method has become a research focus with the advance in on-board computation capability. Ping Lu used the indirect method to pose the trajectory optimization problem as a nonlinear two-point boundary value problem (TPBVP) in [25, 26]. From this model, the optimal thrust vector that satisfied the optimality condition was derived. A finite difference method was employed to solve the nonlinear TPBVP through numerical calculations. Similarly, a fast trajectory optimization for hypersonic air-breathing vehicles was presented in [27]. The indirect method was implemented for ascent trajectory optimization on-board considering the features of the air-breathing vehicle. Ping Lu's work is significant for the optimal ascent guidance. However, the TPBVP is nonlinear and nondifferentiable for the air breathing launch vehicle. It is difficult to solve the nonlinear and nondifferentiable TPBVP on-board in every guidance cycle. Using the direct method, a new guidance concept based on nonlinear programming (NLP) method was proposed in [24]. NLP-based guidance concepts appear advantageous over conventional methods because the on-board guidance algorithm allows a single algorithm to be implemented for different vehicles and missions. The optimal control problem was parameterized into a nonlinear programming problem that was solved by the gradient projection algorithm. In [28], the reference trajectory was updated for disturbance by an on-board algorithm that satisfied the real-time requirement. A new real-time guidance method derived from the optimality condition was proposed in [29]. In that paper, the simple guidance parameters were updated in real time. In [30], a guidance method was presented for online launcher ascent trajectory updating based on neural networks. In the paper, the utilization of a neural network approximation was used online during the ascent flight, with a training process performed off-line.

In this paper, we present an optimal guidance algorithm for air breathing launch vehicle based on optimal trajectory correction to reduce the on-board calculation cost. Considering the current vehicle state as the initial condition, the optimal trajectory correction problem is referred to as a nonlinear optimal control problem with state inequality constraints. For the real-time requirement of the on-board algorithm, the linear TPBVP is obtained for optimal trajectory correction by linearizing the optimality condition in this paper. The Simpson rule is applied to transform the linear TPBVP into linear equations. Considering the solution of the linear TPBVP as the searching direction for the correction values, the updating step size is generated by linear search. Smooth approximation is applied to the inequality constraints for the nondifferentiable Hamiltonian. The sufficient condition for the global convergence of the algorithm is given in this paper. Finally, simulation results for different cases of the modeling error show the effectiveness of the proposed algorithm. In summation, the main contributions of this paper are given as follows.

(1) We reduce the on-board calculation cost of the guidance method a lot. Comparing with the methods in previous literatures which solves nonlinear equations in every guidance cycle, the proposed guidance method in this paper solves linear equations once in every guidance cycle only.

(2) We obtain the relationship between the global convergence and the guidance cycle of the online algorithm. The sufficient condition of the global convergence of this algorithm is given.

The remainder of this paper is organized as follows. Section 2 presents the state normalized-energy differential equations of motion of the vehicle and the optimal control problem for optimal ascent guidance. Section 3 provides details on the optimal guidance algorithm. Section 4 presents an analysis of the global convergence of the proposed algorithm. Section 5 discusses the proposed differentiable approximation for Hamiltonian. Section 6 presents the simulations for the Generic Hypersonic Vehicle (GHV) model and scramjet engine. Section 7 presents the conclusion.

2. Problem Formulation

2.1. Ascent Dynamic. The formulation of motion of the air-breathing vehicle in the longitudinal plane is presented in this section. As shown in Figure 1, the thrust T, gravitation g, and the aerodynamic lift force L and drag force D are acting on the vehicle. The angle of attack α is the angle between the body axis and the vector of the velocity v. The flight path angle γ is the angle between the vector of the velocity v and the ground plane.

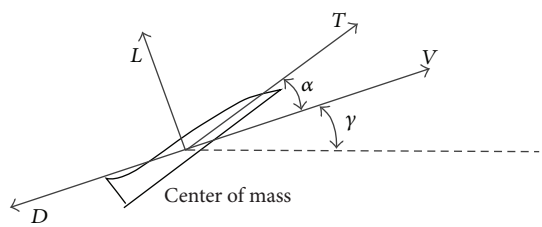

Figure 1: The forces acting on the vehicle.

The motion of the vehicle in the longitudinal plane can be described as follows:

$$\begin{aligned} \frac{dr}{dt} &= v\sin\gamma, \\ \frac{dv}{dt} &= \frac{T\cos\alpha - D}{m} - g\sin\gamma, \\ \frac{d\gamma}{dt} &= \frac{1}{v}\left[\frac{T\sin\alpha + L}{m}\cos\sigma - g\cos\gamma + \frac{v^2}{r}\cos\gamma\right], \\ \frac{dm}{dt} &= -\frac{T}{I_{\mathrm{sp}}}, \end{aligned} \tag{1}$$

where r, m, I_{sp}, and g are the altitude, weight of the vehicle, impulse, and gravity acceleration, respectively.

The lift force L and the drag force D are given as follows:

$$\begin{aligned} L &= \frac{1}{2}\rho v^2 S_{\mathrm{ref}} C_L\left(M_a, \alpha\right), \\ D &= \frac{1}{2}\rho v^2 S_{\mathrm{ref}} C_D\left(M_a, \alpha\right), \end{aligned} \tag{2}$$

where ρ and S_{ref} are the air density of the current altitude and the reference area respectively, C_L and C_D are the lift coefficient and the drag coefficient, respectively, which are the nonlinear functions of the angle of attack α and Mach number M_a. For the air-breathing engine, the thrust is given by

$$T = T\left(\rho, M_a, \alpha, \phi\right), \tag{3}$$

where T is the nonlinear function of ρ, α, M_a, and the throttle command ϕ.

In [25], the equations were normalized to reduce the numerical calculation error. Variable substitutions are applied as follows:

$$R = \frac{r}{r_0}, \qquad V = \frac{v}{\sqrt{g_0 r_0}}, \qquad g = \frac{g_0 r_0^2}{r^2}, \tag{4}$$

where r_0 and g_0 are Earth radius and the ground gravity acceleration, respectively. Considering the thrust T and aerodynamic forces as a composition of forces, we define the normalized accelerations a_T and a_L as follows:

$$a_T = \frac{T\cos\alpha - D}{mg_0}, \qquad a_L = \frac{T\sin\alpha + L}{mg_0}. \tag{5}$$

We define

$$\tau = \frac{t}{\sqrt{r_0/g_0}}. \tag{6}$$

The normalized equations of motion are obtained from (1), (4), (5), and (6) as follows:

$$\begin{aligned} \frac{dR}{d\tau} &= V\sin\gamma, \\ \frac{dV}{d\tau} &= a_T - \frac{\sin\gamma}{R^2}, \\ \frac{d\gamma}{d\tau} &= \frac{1}{V}\left[a_L + \left(V^2 - \frac{1}{R}\right)\left(\frac{\cos\gamma}{R}\right)\right], \\ \frac{dm}{d\tau} &= -\frac{T\sqrt{r_0}}{I_{\mathrm{sp}}\sqrt{g_0}}. \end{aligned} \tag{7}$$

The mission of ascent is to send the vehicle to the required final state which is denoted as (R_f, V_f, γ_f). Define normalized-energy E as follows:

$$E = \frac{V^2}{2} - \frac{1}{R}. \tag{8}$$

From (8) we obtain

$$\begin{aligned} \frac{dE}{d\tau} &= Va_T, \\ \frac{dR}{dE} &= \frac{\sin\gamma}{a_T}, \\ \frac{dV}{dE} &= \frac{1}{a_T V}\left[a_T - \frac{\sin\gamma}{R^2}\right], \\ \frac{d\gamma}{dE} &= \frac{1}{a_T V^2}\left[a_L + \left(V^2 - \frac{1}{R}\right)\left(\frac{\cos\gamma}{R}\right)\right], \\ \frac{dm}{dE} &= -\frac{T\sqrt{r_0}}{a_T V I_{\mathrm{sp}}\sqrt{g_0}}. \end{aligned} \tag{9}$$

The integration interval $[E_0, E_f]$ is fixed.

2.2. Optimal Feedback Control Problem for Ascent Guidance. In this section, the optimal feedback control problem for optimal ascent guidance is addressed. This problem differs from trajectory optimization off-board in that the initial state of the optimal control problem is obtained from the navigation system. We denote the state and the guidance command of the trajectory as

$$\begin{aligned} x(E) &= \left[R(E) \;\; V(E) \;\; \gamma(E) \;\; m(E)\right]^T, \\ u(E) &= \left[\alpha(E) \;\; \phi(E)\right]^T. \end{aligned} \tag{10}$$

With the feedback vehicle state xc_k obtained from navigation system, the optimal ascent guidance algorithm is used to

generate new reference trajectory $[x(E)\ \ u(E)]^T$ and output $u(E)$ from the following optimal control problem:

$$\begin{aligned} \min\quad & J = \phi\left(x\left(E_f\right)\right) + \int_{Ec_{k+1}}^{E_f} g(x,u)\,dE, \\ \text{s.t.}\quad & \dot{x} = f(x,u), \\ & x\left(Ec_k\right) = xc_k, \\ & W\left(x\left(E_f\right)\right) = 0, \\ & C(x,u) \le 0, \end{aligned} \tag{11}$$

where Ec_k is the normalized energy for current vehicle state xc_k.

3. Optimal Ascent Guidance Algorithm

In [25, 26], the optimal control problem was solved on-board in every guidance cycle. However, it is difficult to solve the nonlinear and nondifferentiable TPBVP on-board for air-breathing launch vehicles. In this section, we propose an optimal guidance algorithm. This guidance algorithm updates the reference trajectory $[x\ \ u]^T$ in every guidance cycle to deal with the unknown disturbance. For the current state xc_k of the kth guidance cycle, the optimal feedback control problem is transformed into a linear TPBVP problem using optimality condition linear approximation. The searching direction of the correction values d_k is obtained by solving the linear TPBVP. With the searching direction, the new reference trajectory is generated by linear search. For the kth guidance cycle, the trajectory update is performed as follows:

$$\left[x_{k+1}(E)\ \ u_{k+1}(E)\right]^T = \left[x_k(E)\ \ u_k(E)\right]^T + l_k d_k^T(E). \tag{12}$$

The initial reference trajectory $[x_0(E)\ \ u_0(E)]^T$ is derived from the off-board from trajectory optimization by direct method. The flow chart of the algorithm is shown in Figure 2. Figure 3 shows the time sequence of algorithm.

3.1. Linear Approximation for the Optimality Condition. In this section, we linearize the optimality condition for optimality trajectory updating. The optimal control problem (11) without inequality constraints is given as follows:

$$\begin{aligned} \min\quad & J = \phi\left(x\left(E_f\right)\right) + \int_{Ec_{k+1}}^{E_f} g(x,u)\,dE, \\ \text{s.t.}\quad & \dot{x} = f(x,u), \\ & x\left(Ec_k\right) = xc_k, \\ & W\left(x\left(E_f\right)\right) = 0. \end{aligned} \tag{13}$$

The Hamiltonian of (13) is given as follows:

$$H = g(x,u) + \lambda^T f(x,u), \tag{14}$$

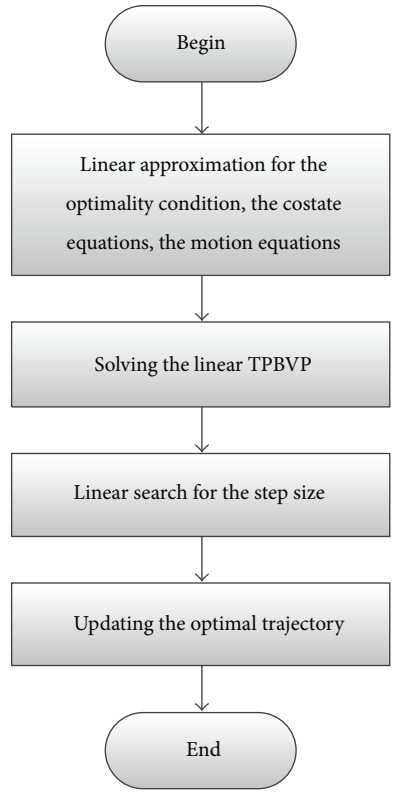

Figure 2: Flow chart of the optimal ascent guidance algorithm.

where λ is the costate vector. The state equations, costate equations, and optimality condition for the optimal control problem are given by

$$\begin{aligned} \dot{x} &= f(x,u), \\ \dot{\lambda} &= -\left(\frac{\partial H}{\partial x}\right)^T, \\ \frac{\partial H}{\partial u} &= 0. \end{aligned} \tag{15}$$

The initial and transversality conditions are given by

$$\begin{aligned} x\left(Ec_k\right) &= xc_k, \\ W\left(x\left(E_f\right)\right) &= 0, \\ \lambda\left(E_f\right) &= \left[\frac{\partial \phi}{\partial x\left(E_f\right)}\right]^T + \left[\varpi^T \frac{\partial W}{\partial x\left(E_f\right)}\right]^T. \end{aligned} \tag{16}$$

We denote the trajectory correction variables as follows:

$$\begin{bmatrix} \Delta x(E) \\ \Delta u(E) \\ \Delta\lambda(E) \end{bmatrix} = \begin{bmatrix} x(E) - x_k(E) \\ u(E) - u_k(E) \\ \lambda(E) - \lambda_k(E) \end{bmatrix}. \tag{17}$$

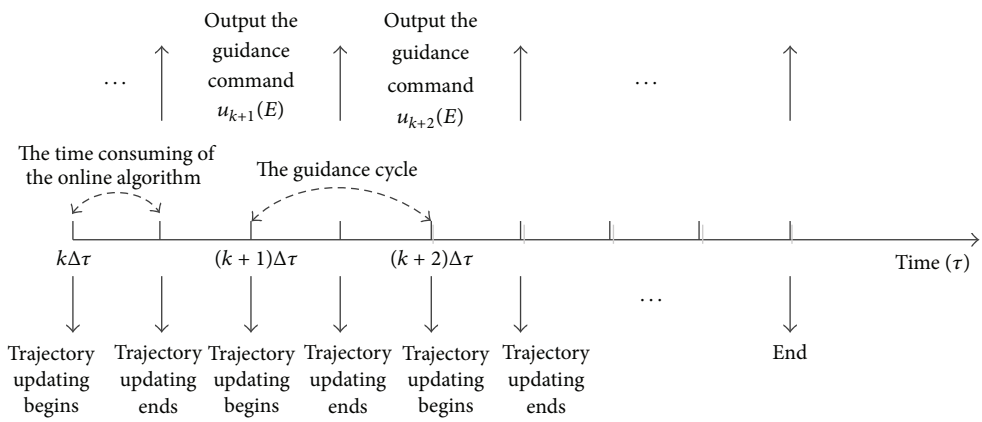

Figure 3: Time sequence of the optimal ascent guidance algorithm.

We denote that

$$\begin{aligned}
H_{ux}^k &= \frac{\partial^2\left(g+\lambda^T f\right)}{\partial u\partial x}\left(x_k,u_k,\lambda_k\right);\\
H_u^k &= \left[\frac{\partial H}{\partial u}(x_k,u_k,\lambda_k)\right]^T;\\
H_{uu}^k &= \frac{\partial^2\left(g+\lambda^T f\right)}{\partial u^2}\left(x_k,u_k,\lambda_k\right);\\
H_x^k &= \left[\frac{\partial H}{\partial x}(x_k,u_k,\lambda_k)\right]^T;\\
H_{xx}^k &= \frac{\partial^2\left(g+\lambda^T f\right)}{\partial x^2}\left(x_k,u_k,\lambda_k\right);\\
f_u^k &= \frac{\partial f}{\partial u}\left(x_k,u_k\right);\\
H_{xu}^k &= \frac{\partial^2\left(g+\lambda^T f\right)}{\partial x\partial u}\left(x_k,u_k,\lambda_k\right);\\
f_x^k &= \frac{\partial f}{\partial x}\left(x_k,u_k\right);\\
g_u^k &= \left[\frac{\partial g}{\partial u}(x_k,u_k)\right]^T;\\
g_x^k &= \left[\frac{\partial g}{\partial x}(x_k,u_k)\right]^T.
\end{aligned} \tag{18}$$

The first-order Taylor expansion of (15) on the old reference trajectory $[x_k \quad u_k \quad \lambda_k]^T$ is

$$\begin{aligned}
\left[\frac{\partial H}{\partial u}\right]^T &\approx H_u^k + H_{ux}^k\Delta x + H_{uu}^k\Delta u + \left(f_u^k\right)^T\Delta\lambda,\\
\dot\lambda &\approx -H_x^k - H_{xx}^k\Delta x - H_{xu}^k\left(x_k,u_k,\lambda_k\right)\Delta u - \left(f_x^k\right)^T\Delta\lambda,\\
\dot x &\approx f\left(x_k,u_k\right) + f_x^k\Delta x + f_u^k\Delta u.
\end{aligned} \tag{19}$$

The following equations are established:

$$\begin{aligned}
H_u^k + \left(f_u^k\right)^T\Delta\lambda &= g_u^k + \left(f_u^k\right)^T\lambda,\\
H_x^k + \left(f_x^k\right)^T\Delta\lambda &= g_x^k + \left(f_x^k\right)^T\lambda.
\end{aligned} \tag{20}$$

Substituting (20) into (19) yields

$$\begin{aligned}
\dot\lambda &= -g_x^k - H_{xx}^k\Delta x - H_{xu}^k\left(x_k,u_k,\lambda_k\right)\Delta u - \left(f_x^k\right)^T\lambda,\\
\Delta\dot x &= f_x^k\Delta x + f_u^k\Delta u - \dot x_k + f\left(x_k,u_k\right),\\
g_u^k &+ H_{ux}^k\Delta x + H_{uu}^k\Delta u + \left(f_u^k\right)^T\lambda = 0,\\
\Delta x\left(Ec_k\right) &+ \Delta x_k\left(Ec_k\right) = xc_k,\\
\frac{\partial W}{\partial x\left(E_f\right)}\Delta x\left(E_f\right) &+ W\left(x_k\left(E_f\right)\right) = 0,\\
\lambda\left(E_f\right) &= \left[\frac{\partial\phi}{\partial x\left(E_f\right)}\right]^T + \left[\varpi^T\frac{\partial W}{\partial x\left(E_f\right)}\right]^T.
\end{aligned} \tag{21}$$

This equation is a linear TPBVP about the variables $[\Delta x \quad \Delta u \quad \lambda]^T$. The linear TPBVP is solved using the Simpson rules in Section 6.

3.2. Backtracking Line Search for the Step Size. In this section, the step size l_k is determined by backtracking line search considering the solution of the linear TPBVP as the search direction. The penalty function for problem (13) is given by

$$\begin{aligned}
p_k = J(x,u) + \eta\Bigg\{&\left\|W\left(x_f\right)\right\| + \int_{Ec_k}^{E_f}\left\|f(x,u)-\dot x\right\|\\
&+ \left\|x\left(Ec_k\right) - xc_k\right\|\Bigg\},
\end{aligned} \tag{22}$$

where η is the penalty parameter satisfied $\eta > \max|\lambda|$. We denote

$$y = \begin{bmatrix} x_k \\ u_k \end{bmatrix}, \qquad d_k = \begin{bmatrix} \Delta x \\ \Delta u \end{bmatrix}, \tag{23}$$

where $[\Delta x \;\; \Delta u \;\; \lambda]^T$ is the solution of the linear TPBVP (21).

The minimizer of penalty function $p_k(x,u)$ corresponds to the solution of problem (11). Backtracking line search was used for large-scale nonlinear optimization problems in [31]. The step size l_k is determined by backtracking line search that satisfies

$$\begin{aligned} l_k = \; & \max\{l \in S : p_{k+1}(y_k + l d_k) \\ & \leq p_{k+1}(y_k) + l\varepsilon_1 \delta p_{k+1}(y_k, d_k)\}, \\ S = \; & \{l : l = \varepsilon_2{}^m, m = 0, 1, 2, \ldots\}, \end{aligned} \tag{24}$$

where $\varepsilon_1 \in (0,1)$, $\varepsilon_2 \in (0,1)$, and $\delta p_{k+1}(y_k, d_k)$ is the variational of the functional $p_{k+1}(y)$ caused by variational d_k of y on y_k. Considering d_k as the solution of (21), $\delta p_{k+1}(y_k, d_k) \leq 0$ is established. The new state and guidance command of the reference trajectory are generated as follows:

$$\begin{bmatrix} x_{k+1} \\ u_{k+1} \end{bmatrix} = \begin{bmatrix} x_k \\ u_k \end{bmatrix} + l_k \begin{bmatrix} \Delta x \\ \Delta u \end{bmatrix}. \tag{25}$$

4. The Global Convergence of the Algorithm

In [32, 33], the convergence of the off-board algorithm was analyzed. But the relationship between the global convergence and the guidance cycle τ has not been discussed for on-board optimization in the previous literatures. In this section, we state and prove the global convergence of the on-board algorithm proposed in the preceding section. The solution sequence $[x_k \;\; u_k]^T$ generated by the algorithm will converge to the solution of the feedback optimal control problem. Unlike off-board trajectory optimization, the initial condition of the feedback optimal control problem depends on the current state of the vehicle in real time. For the kth guidance cycle, the optimal feedback control problem is described as (13). The penalty function p_k for this feedback optimal control problem is given by (22). For the subsequent guidance cycle, the optimal feedback guidance problem is given by

$$\begin{aligned} \min \quad & J = W\left(x\left(E_f\right)\right) + \int_{Ec_{k+1}}^{E_f} g(x,u)\, dE, \\ \text{s.t.} \quad & \dot{x} = f(x,u), \\ & x\left(Ec_{k+1}\right) = xc_{k+1}, \\ & W\left(x\left(E_f\right)\right) = 0, \end{aligned} \tag{26}$$

where

$$Ec_{k+1} = Ec_k + \int_{\tau_k}^{\tau_k + \Delta\tau} \frac{dE}{d\tau} d\tau, \tag{27}$$

$\Delta\tau$ is the guidance cycle and xc_{k+1} is the new state of vehicle from navigation system at the time $\tau_k + \Delta\tau$. The penalty function for optimal problem (24) is given by

$$\begin{aligned} p_{k+1}(x,u) = \; & J(x,u) + \eta \left\| W\left(x_k\left(E_f\right)\right)\right\| \\ & + \eta \int_{Ec_{k+1}}^{E_f} \left\| f(x,u) - \dot{x}\right\| dE \\ & + \eta \left\| x\left(Ec_{k+1}\right) - xc_{k+1}\right\|. \end{aligned} \tag{28}$$

We define the entire penalty function as follows:

$$\begin{aligned} \tilde{p}_k(x,u) = \; & p_k(x,u) \\ & + \sum_{i=0}^{k-1} \int_{Ec_i}^{Ec_{i+1}} \left[\eta \left\| f(x_i,u_i) - \dot{x}_i\right\| + g(x_i,u_i)\right] dE. \end{aligned} \tag{29}$$

The entire penalty function $\tilde{p}_k(x,u)$ includes the penalty function on the whole integration interval $[E_0, E_f]$.

Theorem 1. *If the minimizer of $\tilde{p}_k(x_k,u_k)$ is exited, $g(x,u) \geq 0$, and $\Delta\tau$ is selected and satisfies*

$$\frac{\eta \left\| xc_{k+1} - xc_k - \int_{Ec_k}^{Ec_{k+1}} \dot{x}_k dE\right\|}{-\delta p_{k+1}(y_k, d_k)} < l_k \varepsilon_3, \tag{30}$$

where $\varepsilon_3 \in (0, \varepsilon_1)$. The solution sequence $[x_k \;\; u_k]^T$ generated from (24) will converge to the solution of the feedback optimal control problem.

Proof. From (22), (28), (29) and

$$x_k\left(Ec_{k+1}\right) = x_k\left(Ec_k\right) + \int_{Ec_k}^{Ec_{k+1}} \dot{x}_k dE \tag{31}$$

we can obtain that

$$\begin{aligned} & \tilde{p}_{k+1}(x_k,u_k) - \tilde{p}_k(x_k,u_k) \\ & \quad = \eta \left\| x_k\left(Ec_k\right) - xc_k \right. \\ & \qquad \left. - \left(xc_{k+1} - xc_k - \int_{Ec_k}^{Ec_{k+1}} \dot{x}_k dE\right)\right\| \\ & \qquad - \eta \left\| x_k\left(Ec_k\right) - xc_k\right\|. \end{aligned} \tag{32}$$

From (32), we obtain

$$\begin{aligned}
&\lim_{\Delta\tau\to 0}\left[\widetilde{p}_{k+1}\left(x_k,u_k\right)-\widetilde{p}_k\left(x_k,u_k\right)\right]=0,\\
&\lim_{f(x_k,u_k)-\dot{x}_k\to 0}\left[\widetilde{p}_{k+1}\left(x_k,u_k\right)-\widetilde{p}_k\left(x_k,u_k\right)\right]=0,
\end{aligned}\tag{33}$$

$$\begin{aligned}
&\widetilde{p}_{k+1}\left(x_k,u_k\right)-\widetilde{p}_k\left(x_k,u_k\right)\\
&\quad=\eta\left\{\left\|x_k\left(Ec_k\right)-xc_{k+1}+\int_{Ec_k}^{Ec_{k+1}}\dot{x}_k dE\right\|\right.\\
&\qquad\left.-\left\|x_k\left(Ec_k\right)-xc_k\right\|\right\}\\
&\quad\le\eta\left\{\left\|x_k\left(Ec_k\right)-xc_k\right\|\right.\\
&\qquad+\left\|xc_{k+1}-xc_k-\int_{Ec_k}^{Ec_{k+1}}\dot{x}_k dE\right\|\\
&\qquad\left.-\left\|x_k\left(Ec_k\right)-xc_k\right\|\right\}\\
&\quad=\eta\left\|xc_{k+1}-xc_k-\int_{Ec_k}^{Ec_{k+1}}\dot{x}_k dE\right\|.
\end{aligned}\tag{34}$$

From conditions (24) and (30), it is obtained that

$$\begin{aligned}
&\widetilde{p}_{k+1}\left(x_{k+1},u_{k+1}\right)\\
&\quad\le\widetilde{p}_{k+1}\left(x_k,u_k\right)+l_k\varepsilon_1\delta p_{k+1}\left(d_k\right)\\
&\quad=\widetilde{p}_k\left(x_k,u_k\right)+l_k\varepsilon_1\delta p_{k+1}\left(d_k\right)\\
&\qquad+\eta\left\{\left\|x_k\left(Ec_k\right)-xc_k\right.\right.\\
&\qquad\left.-\left(xc_{k+1}-xc_k-\int_{Ec_k}^{Ec_{k+1}}\dot{x}_k dE\right)\right\|\\
&\qquad\left.-\left\|x_k\left(Ec_k\right)-xc_k\right\|\right\}\\
&\quad\le\widetilde{p}_k\left(x_k,u_k\right)+\eta\left\|xc_{k+1}-xc_k-\int_{Ec_k}^{Ec_{k+1}}\dot{x}_k dE\right\|\\
&\qquad+l_k\varepsilon_1\delta p_{k+1}\left(y_k,d_k\right)\\
&\quad\le\widetilde{p}_k\left(x_k,u_k\right)+\eta\left\|xc_{k+1}-xc_k-\int_{Ec_k}^{Ec_{k+1}}\dot{x}_k dE\right\|\\
&\qquad+l_k\varepsilon_3\delta p_{k+1}\left(y_k,d_k\right)\\
&\quad<\widetilde{p}_k\left(x_k,u_k\right).
\end{aligned}\tag{35}$$

Thus, the sequence $\widetilde{p}_k(x_k,u_k)$, $k=1,2,3,\ldots$. is monotonically decreasing. Considering the existence of a minimizer, $\widetilde{p}_k(x_k,u_k)$ converges. Thus, the following equation is established:

$$\lim_{k\to\infty}\left(l_k\varepsilon_3\delta p_{k+1}\left(y_k,d_k\right)-l_k\varepsilon_1\delta p_{k+1}\left(y_k,d_k\right)\right)=0.\tag{36}$$

From (36), we derive

$$\lim_{k\to\infty}\left(l_k\delta p_{k+1}\left(y_k,d_k\right)\right)=0.\tag{37}$$

If $d_k\neq 0$, $[x_k\ \ u_k]^T$ is not the minimizer of penalty function, then $\delta p_{k+1}(y_k,d_k)\neq 0$. Considering that l_k is bounded away from zero, we derive

$$\begin{aligned}
&\lim_{k\to\infty}d_k=0,\\
&\lim_{k\to\infty}\delta p_{k+1}\left(y_k,d_k\right)=0,\\
&\lim_{k\to\infty}\left[\dot{x}_k-f\left(x_k,u_k\right)\right]=0,\\
&\lim_{k\to\infty}\left(\dot{\lambda}_k+H_x^k\right)=0,\\
&\lim_{k\to\infty}H_u^k=0.
\end{aligned}\tag{38}$$

Thus, the solution sequence $[x_k\ \ u_k]^T$ generated by the algorithm will converge to the solution of the optimal control problem. □

5. Smooth Approximation for Inequality Constraints

The nondifferentiable TPBVP from optimal control problem (11) with the inequality constraints brings difficulties for the proposed algorithm, which can only solve a smooth problem. Smooth approximations for nondifferentiable optimization problems have been studied in [5, 6, 34]. In this section we introduce the smooth approximation method for the inequality constraints. If the inequality constraint function is about the state and the guidance command

$$C\left(x,u\right)\le 0\tag{39}$$

the Hamiltonian for the optimal control problem (11) with inequality constraints (39) is given by

$$H=g\left(x,u\right)+\lambda^T f\left(x,u\right)+\mu\max\left\{C\left(x,u\right),0\right\}.\tag{40}$$

However, the Hamiltonian (40) is a nondifferentiable function, which brings difficulty for the proposed algorithm. For the smooth Hamiltonian approximation, a differentiable function is substituted for $\max\{C(x,u),0\}$. We denote the nondifferentiable function as follows:

$$\max\left\{0,y\right\}=\int_{-\infty}^{y}w\left(z\right)dz,\tag{41}$$

where $w(z)$ is the step function

$$w\left(z\right)=\begin{cases}1, & \text{if } z\ge 0,\\ 0, & \text{if } z<0.\end{cases}\tag{42}$$

Considering $s(z,a)$ as the approximation function of $w(z)$, the differentiable approximation to $\max\{0,y\}$ is obtained as

$$f_p\left(y,a\right)\approx\int_{-\infty}^{y}s\left(z,a\right)dz=y+\frac{1}{a}\operatorname{In}\left(1+e^{-ay}\right),\tag{43}$$

where $s(z,a)$ is Sigmoid function

$$s(z,a) = \frac{1}{1+e^{-az}}, \quad a > 0. \tag{44}$$

The Properties of $f_p(y,a)$, $a > 0$ are as follows [5]:

(1) $f_p(y,a)$ is n-times continuously differentiable for any positive integer n, with $\partial f_p(y,a)/\partial y = 1/(1+e^{-ay})$ and $\partial^2 f_p(y,a)/\partial y^2 = ae^{-ay}/(1+e^{-ay})^2$.

(2) $f_p(y,a)$ is strictly convex and strictly increasing on $\mathbb{R}$.

(3) $f_p(y,a) > \max\{0, y\}$.

(4) $\lim_{a\to\infty} f_p(y,a) = \max\{0, y\}$.

(5) $f_p(y,a) > f_p(y,a_1)$ for $a < a_1$, $y \in \mathbb{R}$.

Substituting (43) into (40), the following differentiable Hamiltonian approximation is obtained:

$$\widehat{H} = g(x,u) + \lambda^T f(x,u) + \mu\left[C + \frac{1}{a}\operatorname{In}\left(1+e^{-aC}\right)\right]. \tag{45}$$

If the inequality constraint function is a qth-order state variable inequality constraint given by

$$C(x) \le 0. \tag{46}$$

If p times derivatives of $C(x)$ are required before u appears explicitly in the result, the Hamiltonian with inequality constraints (46) is given by

$$H = g(x,u) + \lambda^T f(x,u) + \mu C^{(q)}, \tag{47}$$

where

$$\mu = 0 \quad \text{if } C < 0. \tag{48}$$

Considering the differentiable approximation to μ as follows:

$$\mu = \widehat{\mu} w(C) \approx \widehat{\mu}\frac{1}{1+e^{-aC}} \tag{49}$$

the following differentiable Hamiltonian approximation is obtained:

$$\widehat{H} = g(x,u) + \lambda^T f(x,u) + \widehat{\mu}\frac{1}{1+e^{-aC}}C^{(q)}. \tag{50}$$

With the differentiable Hamiltonian approximation, the inequality constraints are considered in the proposed guidance algorithm.

6. Simulation Results

6.1. Numerical Calculation Based on Linear TPBVP Discretization. In this section, the linear TPVBP is transformed into linear equations using the Simpson rule, which corresponds to the three-point Newton-Cotes quadrature rule. The Simpson rule for differential equation $dX/dE = y(E)$ is given by

$$\int_a^b y(E)\,dE = \frac{b-a}{6}\left[y(a) + 4y\left(\frac{a+b}{2}\right) + y(b)\right]. \tag{51}$$

From (51), we obtain

$$X(b) - X(a) = \frac{b-a}{6}\left[y(a) + 4y\left(\frac{a+b}{2}\right) + y(b)\right]. \tag{52}$$

We disperse the normalized energy E into N equal segments as $[E_0 \;\; E_1 \;\; \cdots \;\; E_N]$, with $E_0 = Ec_k$ and $E_N = E_f$. The differential equation $dX/dE = y(X,E)$ can be transformed into the following equation:

$$\begin{aligned} X(E_i) - X(E_{i-1}) &= \frac{E_i - E_{i-1}}{6}\Bigg[y(X_i, E_i) \\ &\quad + 4y\left(\frac{X_i + X_{i-1}}{2}, \frac{E_i + E_{i-1}}{2}\right) \\ &\quad + y(X_{i-1}, E_{i-1})\Bigg], \quad i = 1,2,3,\ldots,N. \end{aligned} \tag{53}$$

Based on (53), the linear TPBVP (21) can be transformed into linear equations described by

$$AX = B. \tag{54}$$

The linear equations can be solved by Gaussian elimination.

Finally, we can obtain the solution $\Delta x(E)$, $\Delta u(E)$, and $\lambda(E)$ of the linear TPBVP (21) from the solution of the linear equations through interpolating.

6.2. GHV Model. The proposed method is applied to the Generic Hypersonic Vehicle (GHV) to verify the effectiveness by flight simulation. In order to develop a complete set of aerodynamic coefficients, experimental longitudinal and lateral-directional aerodynamics were obtained for the GHV by using six Langley wind tunnels [35]. The aerodynamic database of the GHV is shown in [35]. The GHV model with scramjet propulsion system is used for the simulation, where $S_{\text{ref}} = 334.73\,\text{m}^2$ and the full-scale weight $m_{\text{ini}} = 110000\,\text{kg}$.

According to the characterization of scramjet propulsion system described in [2, 27], the development of the propulsion system begins with the following equation:

$$T = 0.5\phi I_{\text{sp}}(\phi, M_a)\,\rho v g_0 C_T(\alpha, M_a), \tag{55}$$

where ϕ is the throttle command which varies from 0 to 1. The coefficient C_T depends on α and M_a as follows:

$$C_T = -0.0012M_a\alpha^2 + 0.008\alpha + 1.4 - 0.1M_a. \tag{56}$$

The impulse I_{sp} is given by the following equation:

$$I_{\text{sp}} = -81M_a^2 + 1004M_a - 52 + 100\phi. \tag{57}$$

6.3. Simulation Results for Modeling and Initial State Error. Considering the high cost of the flight experimental test, researchers do flight numerical simulation, hardware-in-the-loop simulation and final flight experimental test to verify the guidance algorithm step by step. In this section, flight

Table 1: Initial and required final states of the vehicle.

r_{ini} (m)	v_{ini} (m/s)	γ_{ini} (deg)	r_{rf} (m)	v_{rf} (m/s)	γ_{rf} (deg)
20000	1000	0	35000	2000	0

numerical simulation results for the GHV with modeling error and initial state error are given to show the effectiveness of the proposed guidance algorithm. For the modeling error caused by the wind tunnel experimental test, the aerodynamic coefficients bias is considered in the flight simulation. The simulations end once the final normalized energy E_f is reached. The optimal guidance algorithm updates the trajectory every guidance cycle, which is 0.3 s. The initial and required final states of the air-breathing vehicle are shown in Table 1. The number of the discrete nodes $N = 10$. The dynamic pressure inequality constraint is given by

$$Q = \frac{1}{2}\rho v^2 \leq 140000 \text{ Pa}. \tag{58}$$

To assess the capability of the proposed algorithm to deal with disturbance, the aerodynamic coefficients bias and the initial state error in the simulations are given by following cases:

(1) $\Delta C_L = -0.1C_L$, $\Delta C_D = +0.1C_D$.
(2) $\Delta C_L = -0.1C_L$, $\Delta C_D = +0.1C_D$, $\Delta r_{\text{ini}} = +500$ m.
(3) $\Delta C_L = -0.1C_L$, $\Delta C_D = +0.1C_D$, $\Delta r_{\text{ini}} = -500$ m.
(4) $\Delta C_L = -0.1C_L$, $\Delta C_D = +0.1C_D$, $\Delta r_{\text{ini}} = +1000$ m.
(5) $\Delta C_L = -0.1C_L$, $\Delta C_D = +0.1C_D$, $\Delta r_{\text{ini}} = -1000$ m.

The simulation results of the optimal guidance algorithm are shown in Figures 4, 5, 6, 7, and 8. The altitude, velocity, flight path angle, angle of attack, and dynamic pressure are, respectively, shown in Figures 4 to 8. As expected, the final state is achieved under aerodynamic bias and initial state error. Figure 8 shows that the state inequality constraint is satisfied. The dynamic pressure is less than 140000 Pa for different cases.

Table 2 shows the terminal error and the fuel cost of the optimal guidance algorithm. The terminal accuracy is high for different cases. Moreover, the fuel cost of the optimal guidance algorithm is lower than that of the tracking guidance algorithm. A greater initial state error will result in more fuel savings. In summary, with lower fuel cost the results of the proposed optimal guidance algorithm satisfies all the equality and inequality constraints. The simulation results show the great potential for the final flight experimental test.

7. Conclusion

In this paper, we present an optimal guidance algorithm for air-breathing launch vehicle based on optimal trajectory correction. The proposed guidance algorithm corrects the reference trajectory in every guidance cycle to satisfy the optimality condition of the optimal feedback control problem.

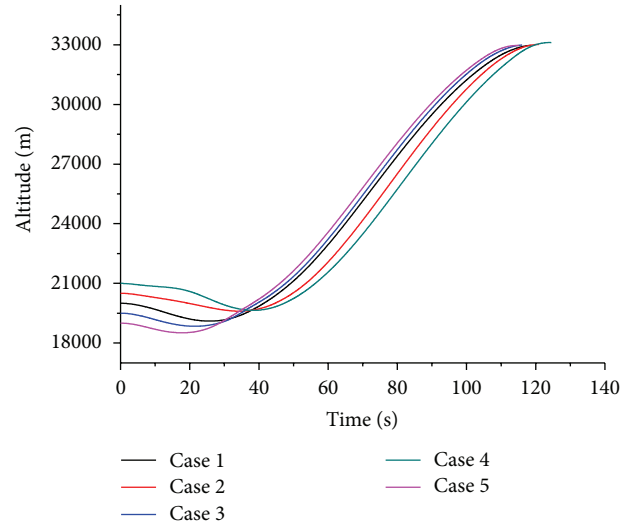

Figure 4: The altitude of the simulation results.

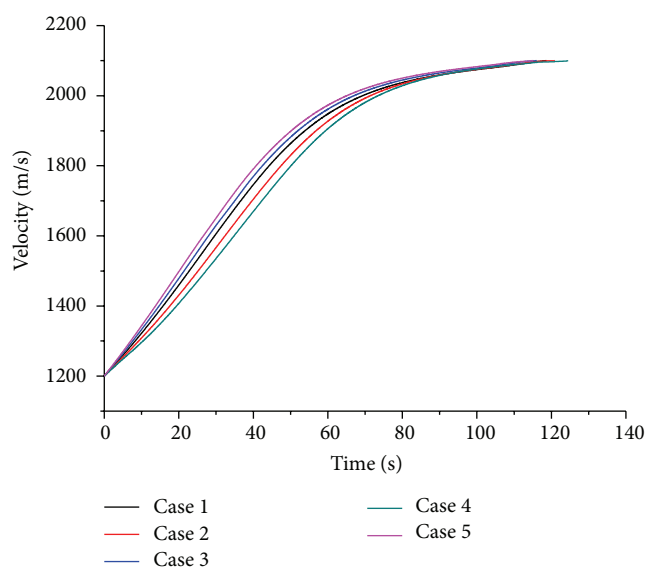

Figure 5: The velocity of the simulation results.

By linearizing the optimality condition, the linear TPBVP is obtained for optimal trajectory correction. The solution of the linear TPBVP is derived using the Simpson rule. The new trajectory is generated by a linear search for the step size of the solution. Smooth Hamiltonian approximation is implemented to the inequality constraints. The sufficiency condition for the global convergence of the guidance algorithm is given in this paper.

Finally, simulations for 5 different cases of modeling and initial state error are presented. Compared with the tracking guidance method, the simulation results prove the low fuel cost and high precision of the proposed optimal guidance method.

Table 2: The simulation results for optimal guidance algorithm.

Case	Δr_f (m)	Δv_f (m/s)	$\Delta \gamma_f$ (deg)	Fuel cost (kg)	Fuel cost (tracking method) (kg)
1	−28.20	0.136	0.20	4572.19	4574.62
2	8.59	−0.03	−0.15	4583.14	4628.39
3	−15.08	0.07	0.20	4584.74	4605.66
4	108.16	0.47	−0.23	4602.92	4776.00
5	−32.43	0.19	−0.16	4601.33	4688.94

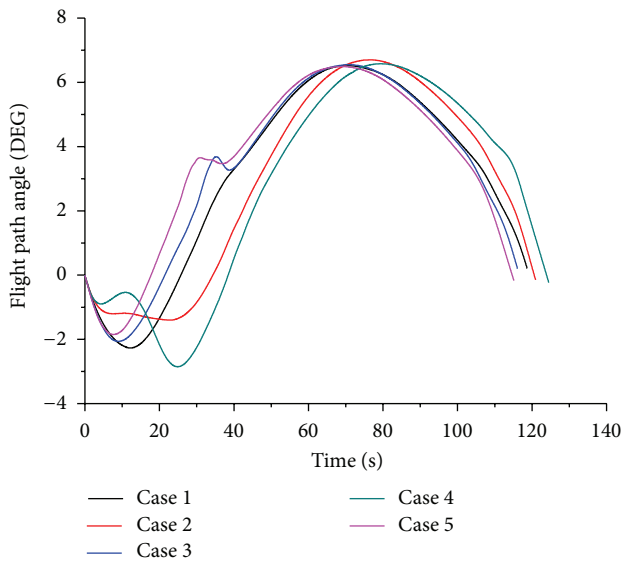

Figure 6: The flight path angle of the simulation results.

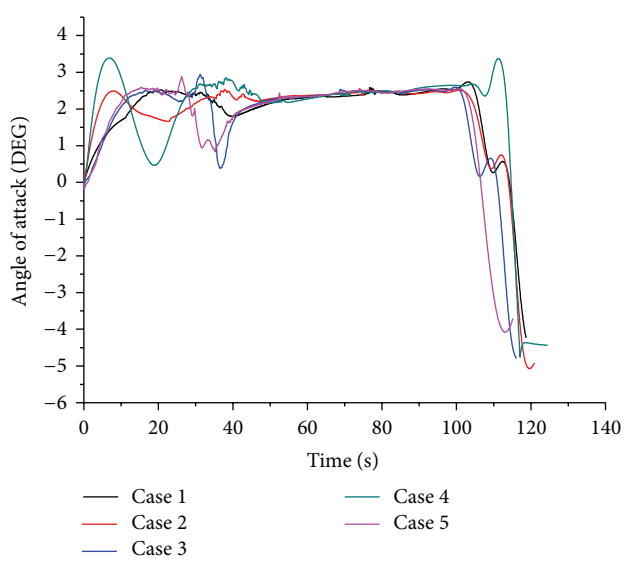

Figure 7: The angle of attack of the simulation results.

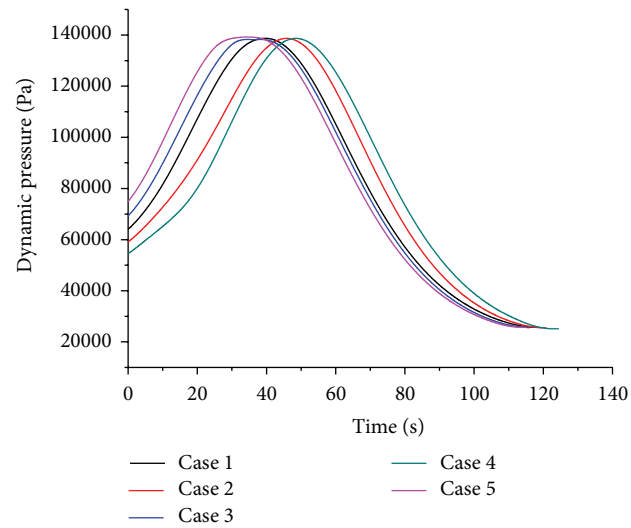

Figure 8: The dynamic pressure of the simulation results.

Acknowledgments

This work was supported in part by the National Nature Science Foundation of China nos. 61203081 and 61174079, Doctoral Fund of Ministry of Education of China no. 20120142120091, and Precision manufacturing technology and equipment for metal parts no. 2012DFG70640.

References

[1] H. J. Henry Jr. and C. H. McLellan, "Air-breathing launch vehicle for earth-orbit shuttle. New technology and development approach," *Journal of Aircraft*, vol. 8, no. 5, pp. 381–387, 1971.

[2] J. E. Corban, A. J. Calise, and G. A. Flandro, "Real-time guidance algorithm for aerospace plane optimal ascent to low earth orbit," in *Proceedings of the American Control Conference*, pp. 2475–2481, Pittsburgh, PA, USA, June 1989.

[3] C. H. Yam, D. D. Lorenzo, and D. Izzo, "Low-thrust trajectory design as a constrained global optimization problem," *Journal of Aerospace Engineering G*, vol. 225, no. 11, pp. 1243–1251, 2011.

[4] B. A. Conway, "A survey of methods available for the numerical optimization of continuous dynamic systems," *Journal of Optimization Theory and Applications*, vol. 152, no. 2, pp. 271–306, 2012.

[5] C. H. Chen and O. L. Mangasarian, "Smoothing methods for convex inequalities and linear complementarity problems," *Mathematical Programming*, vol. 71, no. 1, pp. 51–69, 1995.

[6] X. Chen, "Smoothing methods for nonsmooth, nonconvex minimization," *Mathematical Programming*, vol. 134, no. 1, pp. 71–99, 2012.

[7] W. Wang, Y. Shang, and Y. Zhang, "A filled function approach for nonsmooth constrained global optimization," *Mathematical*

Problems in Engineering, vol. 2010, Article ID 310391, 9 pages, 2010.

[8] L. I. Rozonoer, "Linear-quadratic optimization and some general hypotheses on optimal control," *Mathematical Problems in Engineering*, vol. 5, no. 4, pp. 275–289, 1999.

[9] J. T. Betts, "Survey of numerical methods for trajectory optimization," *Journal of Guidance, Control, and Dynamics*, vol. 21, no. 2, pp. 193–207, 1998.

[10] G. Q. Huang, Y. P. Lu, and Y. Nan, "A survey of numerical algorithms for trajectory optimization of flight vehicles," *Science China-Technological Sciences*, vol. 55, no. 9, pp. 2538–2560, 2012.

[11] Y. Ulybyshev, "Discrete pseudocontrol sets for optimal control problems," *Journal of Guidance, Control, and Dynamics*, vol. 33, no. 4, pp. 1133–1142, 2010.

[12] M. Vasile and F. Zuiani, "Multi-agent collaborative search: an agent-based memetic multi-objective optimization algorithm applied to space trajectory design," *Journal of Aerospace Engineering G*, vol. 225, no. 11, pp. 1211–1227, 2011.

[13] M. Pontani and B. A. Conway, "Particle swarm optimization applied to space trajectories," *Journal of Guidance, Control, and Dynamics*, vol. 33, no. 5, pp. 1429–1441, 2010.

[14] Y. P. Ulybyshev, "Optimization of low-thrust orbit transfers with constraints," *Cosmic Research*, vol. 50, no. 5, pp. 376–390, 2012.

[15] M. Chen, R. Mei, and B. Jiang, "Sliding mode control for a class of uncertain MIMO nonlinear systems with application to near-space vehicles," *Mathematical Problems in Engineering*, vol. 2013, Article ID 180589, 9 pages, 2013.

[16] H. Zhang, Y. Shi, M. Q. Xu, and H. T. Cui, "Observer-based tracking controller design for networked predictive control systems with uncertain markov delays," in *Proceedings of the American Control Conference*, pp. 5682–5687, 2012.

[17] H. Zhang and Y. Shi, "Robust H-infinity sliding-mode control for markovian jump systems subject to intermittent observations and partially known transition probabilities," *Systems & Control Letters*, vol. 62, no. 12, pp. 1114–1124, 2013.

[18] Z. Shuai, H. Zhang, J. Wang, J. Li, and M. Ouyang, "Combined AFS and DYC control of four-wheel-independent-drive electric vehicles over CAN network with time-varying delays," *IEEE Transactions on Vehicular Technology*, no. 99, p. 1, 2013.

[19] H. Zhang, Y. Shi, and A. Saadat Mehr, "Robust static output feedback control and remote PID design for networked motor systems," *IEEE Transactions on Industrial Electronics*, vol. 58, no. 12, pp. 5396–5405, 2011.

[20] H. Zhang, Y. Shi, and M. X. Liu, "H-infinity step tracking control for networked discrete-time nonlinear systems with integral and predictive actions," *IEEE Transactions on Industrial Informatics*, vol. 9, no. 1, pp. 337–345, 2013.

[21] X. J. Wang and S. P. Wang, "Adaptive fuzzy robust control for a class of nonlinear systems via small gain theorem," *Mathematical Problems in Engineering*, vol. 2013, Article ID 201432, 11 pages, 2013.

[22] V. Brinda, S. Dasgupta, and M. Lal, "Trajectory optimization and guidance of an air breathing hypersonic vehicle," in *Proceedings of the 14th AIAA/AHI International Space Planes and Hypersonics Systems Technologies Conference*, vol. 2, pp. 856–869, November 2006.

[23] B. Tian and Q. Zong, "Optimal guidance for reentry vehicles based on indirect legendre pseudospectral method," *Acta Astronautica*, vol. 68, no. 7-8, pp. 1176–1184, 2011.

[24] M. H. Gräßlin, J. Telaar, and U. M. Schöttle, "Ascent and reentry guidance concept based on NLP-methods," *Acta Astronautica*, vol. 55, no. 3–9, pp. 461–471, 2004.

[25] P. Lu and B. Pan, "Highly constrained optimal launch ascent guidance," *Journal of Guidance, Control, and Dynamics*, vol. 33, no. 2, pp. 404–414, 2010.

[26] P. Lu, H. Sun, and B. Tsai, "Closed-loop endo-atmospheric ascent guidance," in *Proceedings of the AIAA Guidance, Navigation, and Control Conference*, Monterey, Calif, USA, 2002.

[27] J. Oscar Murillo and P. Lu, "Fast ascent trajectory optimization for hypersonic air-breathing vehicles," in *Proceedings of the AIAA Guidance, Navigation, and Control Conference*, pp. 5–8, Toronto, Canada, 2010.

[28] M. Marrdonny and M. Mobed, "A guidance algorithm for launch to equatorial orbit," *Aircraft Engineering and Aerospace Technology*, vol. 81, no. 2, pp. 137–148, 2009.

[29] T. Yamamoto and J. Kawaguchi, "A new real-time guidance strategy for aerodynamic ascent flight," *Acta Astronautica*, vol. 61, no. 11-12, pp. 965–977, 2007.

[30] C. Filici and R. S. Sánchez Peña, "Online guidance updates using neural networks," *Acta Astronautica*, vol. 66, no. 3-4, pp. 477–485, 2010.

[31] P. T. Boggs, A. J. Kearsley, and J. W. Tolle, "A global convergence analysis of an algorithm for large-scale nonlinear optimization problems," *SIAM Journal on Optimization*, vol. 9, no. 4, pp. 833–862, 1999.

[32] S. Schlenkrich and A. Walther, "Global convergence of quasi-Newton methods based on adjoint Broyden updates," *Applied Numerical Mathematics*, vol. 59, no. 5, pp. 1120–1136, 2009.

[33] S. Schlenkrich, A. Griewank, and A. Walther, "On the local convergence of adjoint Broyden methods," *Mathematical Programming*, vol. 121, no. 2, pp. 221–247, 2010.

[34] S. Lian and L. Zhang, "A simple smooth exact penalty function for smooth optimization problem," *Journal of Systems Science & Complexity*, vol. 25, no. 3, pp. 521–528, 2012.

[35] S. Keshmiri, R. Colgren, and M. Mirmirani, "Development of an aerodynamic database for a generic hypersonic air vehicle," in *Proceedings of the AIAA Guidance, Navigation, and Control Conference*, pp. 3978–3998, San Francisco, Calif, USA, August 2005.

Hindawi Publishing Corporation
Mathematical Problems in Engineering
Volume 2013, Article ID 979384, 11 pages
http://dx.doi.org/10.1155/2013/979384

Research Article

Brake Performance Analysis of ABS for Eddy Current and Electrohydraulic Hybrid Brake System

Ren He,[1] Xuejun Liu,[1,2] and Cunxiang Liu[2]

[1] *School of Automotive & Traffic Engineering, Jiangsu University, Zhenjiang 212013, China*
[2] *Department of Automotive Engineering, Guangxi Vocational and Technical College of Communications, Nanning 530023, China*

Correspondence should be addressed to Xuejun Liu; gxlxj2000@tom.com

Received 24 September 2013; Revised 29 October 2013; Accepted 30 October 2013

Academic Editor: Hui Zhang

This paper introduces an eddy current and electro-hydraulic hybrid brake system to solve problems such as wear, thermal failure, and slow response of traditional vehicle brake system. Mathematical model was built to calculate the torque of the eddy current brake system and hydraulic brake system and analyze the braking force distribution between two types of brake systems. A fuzzy controller on personal computer based on LabVIEW and Matlab was designed and a set of hardware in the loop system was constructed to validate and analyze the performance of the hybrid brake system. Through lots of experiments on dry and wet asphalt roads, the hybrid brake system achieves perfect performance on the experimental bench, the hybrid system reduces abrasion and temperature of the brake disk, response speed is enhanced obviously, fuzzy controller keeps high utilization coefficient due to the optimal slip ratio regulation, and the total brake time has a smaller decrease than traditional hydraulic brake system.

1. Introduction

The electro-hydraulic antilock brake system (ABS) has already become the conventional equipment in commercial vehicles. However, as the increase of the engine power, the improvement of vehicle speed, and vehicle safety standard, traditional hydraulic ABS gradually presents many problems, such as the time delay in pressure building up, noise, squeal, brake pad wear, harmful friction dust, and braking system thermal failure due to its contact movement. Also, the poor braking performance at high speed needs enhancement. Thus, a new more powerful and stable braking system is required to ensure reliability and safety of vehicles.

In order to solve the problems of traditional hydraulic braking system, the eddy current brake system is a good choice; its features of rapid responding speed, contactless braking principle, perfect performance in high speed, and so forth have already been acknowledged by users but the eddy current brake system has some shortcoming, too. For example, it perhaps needs extra battery to provide electric current for electromagnetic coil when high brake torque needed. Otherwise, the poor brake ability in low speed is also a limitation to practical application.

How to make full use of the advantage of eddy current brake system and traditional hydraulic brake system and design an eddy current and electro-hydraulic hybrid brake system has become one of the important research directions in vehicle braking system. Many researchers have achieved lots of achievements in the past several decades. Desta invented an eddy current braking device which was equipped on the vehicle's transmission axle to assist hydraulic braking system [1]. Anwar and Zheng discussed antilock-braking algorithm for an eddy current-based brake-by-wire system and designed a nonlinear sliding-mode-type controller for slip regulation in a braking event [2, 3]. Gay presented a contactless magnetic brake for automotive applications; an integrated mechanism based on electromagnetic braking and hydraulic braking was described in his papers [4]. Performance evaluation of a hybrid electric brake system with a sliding mode controller was made by Song [5]; a configuration of hybrid system (HEBS) and mathematical model was built to evaluate the braking performance. He et al.

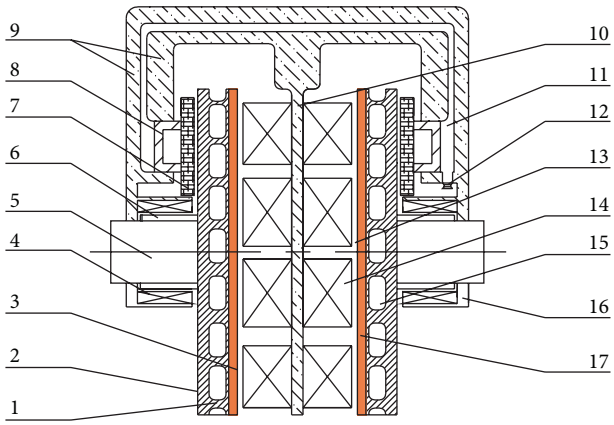

Figure 1: Structural diagram of hybrid brake system.

designed a composited braking system based on eddy current braking system and traditional hydraulic braking system. The experimental results proved that the composited braking system reduced braking distance obviously [6]. Lee and Park presented an ABS algorithm based on sliding mode control based on eddy current brake system, and the eddy current brake torque was derived from several aspects in the literature [7–10]. They mainly discussed the eddy current brake in high speed area.

In this paper, we propose a new conceptual hybrid braking system, and achieved the optimal combination of ECB and EHB. All of the research work, such as mathematical model building, controls strategy designing, and the hardware in the loop testing bench constructing, discusses about the structure of Figure 1. As illustrated in Figure 1, the hybrid system is composed of an eddy current braking system (ECB) and an electro-hydraulic braking system (EHB); the main parts of the system are hybrid brake disk (1), electromagnetic coil (14), copper layer (17), permanent magnet generator (4—stator coil, 6—permanent magnet, and 16—generator shell), bracket (9), hydraulic piston (8), and friction pad (7). Since the brake disk material is different for ECB and EHB, the brake disk of EHB should have good wear resistance; however, the brake disk of ECB should have good conductivity. Both of the ECB and EHB should have good heat dissipation performance. Therefore, through creative design to the mechanism of hybrid brake system, a new hybrid brake system has been developed. The advantage of this hybrid brake system is as follows.

(1) The brake disk of EHB utilizes outside face of the hybrid disk, the disk of ECB utilizes inner face of the hybrid disk, and the friction of EHB system will not influence ECB system, so the magnetic gap between electromagnetic coil and copper layers will not change forever and ECB system can keep its stability.

(2) Since different types of brake disks have different materiels, both the EHB and ECB can achieve the best performance by optimizing the design scheme themselves, respectively, in a whole unit.

(3) Permanent magnet generator, changing the kinetic energy of wheel into electricity, can supply power for ECB; the energy saving and environmental protection come true; this point will not be discussed in the paper.

(4) For both of the ECB and EHB have their braking merit, and the hybrid brake system can get all of the merits of the ECB system and EHB system, the whole performance of hybrid brake system is better than ECB or EHB separately.

In the work, we build several mathematical models; they are eddy current brake model, hydraulic brake model, brake disk model, and wheel force analysis model. Since the force distribution scheme is very important in hybrid ABS control strategy, these models are analysis tools for analyzing the braking force distribution between ECB and EHB. However, when we construct the hardware in the loop testing bench, a torque sensor is equipped to verify and modify theoretic value of brake torque.

The main objective of this hybrid control system is to maintain the wheel slip at an ideal value so that the tire can still generate lateral and steering forces as well as decrease the vehicle stopping distance; because the vehicle and tire model contain nonlinearities and uncertainties, a nonlinear control strategy based on the fuzzy theory was chosen for the slip ratio controlling. The paper presents a virtual fuzzy controller based on LabVIEW and Matlab to supervise ABS control strategy for eddy current and electro-hydraulic hybrid brake systems. On the testing bench, different types of braking system in the same road scenarios and different road scenarios were simulated to validate and analyze the hybrid brake system. The research result shows that the hybrid ABS has a better performance than traditional hydraulic brake system.

2. Hybrid Brake System Model

In order to analyze the braking force distribution between ECB and EHB, this work established four mathematical models as follows. These models mainly describe the relationship between brake torque, brake current, brake pressure, wheel speed, vehicle speed, and so forth.

2.1. Eddy Current Brake Model. Figure 2 shows the dimension parameter of ECB in hybrid brake system; according to Lee and Park [7], the eddy current brake torque can be expressed as

$$T_{bc} = T_i i^2 \omega, \tag{1}$$

where T_{bc} is the eddy current brake torque, i is the current of the coil, and ω is the angular velocity of the disk. The braking torque coefficient T_i is

$$T_i = \sigma_0 R_b^2 \left(\frac{\mu_0 N}{L}\right) SD, \tag{2}$$

where σ_0, μ_0, N, L, S, D, and R_b represent the electric conductivity, permeability of air, number of coil turns, air gap

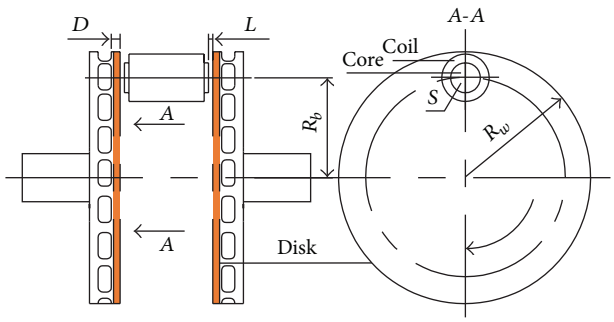

Figure 2: ECB parameters in the hybrid brake system.

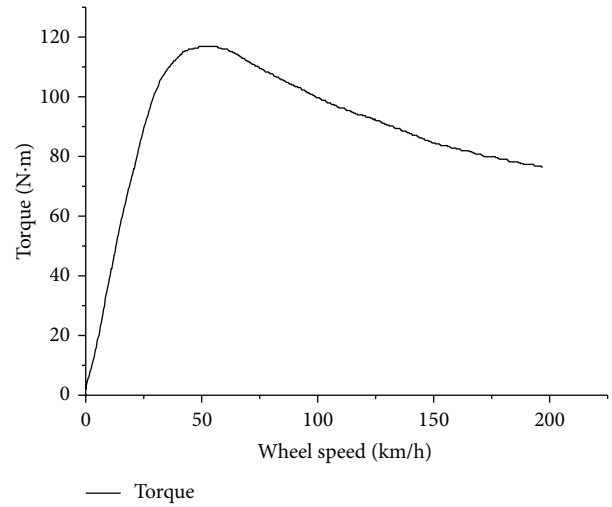

Figure 3: Torque versus rotor speed curve.

distance, cross-sectioned area of the core, the disk thickness, and the brake torque radius of the disk. However, because of the flux leakage, heat influences the disk. The coefficient T_i should be modified. According to Simeu and Georges [11],

$$T_i = \alpha C \sigma_0 R_b^2 \left(\frac{\mu_0 N}{L}\right) SD, \tag{3}$$

where α and C are the modified factors:

$$\alpha = 1 - \frac{1}{2\pi}\left[4\tan(\psi) + \psi \ln\left(1 + \frac{1}{\psi^2}\right) - \frac{1}{\psi}\ln\left(1 + \psi^2\right)\right],$$
$$C = 0.5\left[1 - \frac{AB}{\pi\left(1 + R_b/R_w\right)^2\left(R_w - R_b\right)^2}\right]. \tag{4}$$

Here, A and B are the width and height of the iron cross-sectioned area and $\psi = B/A$.

Formula (1) indicates that the brake torque is proportional to the speed of brake disk when the current is kept constant. But the proportional relationship is broken as the disk speed increases. Figure 3 shows the torque versus rotor speed relationship tested on the testing bench. When the electric current in the coil keeps constant, the electromagnetic brake torque is not always proportional to rotor speed. There is a peak value on the curve, and the abscissa of this peak value is a critical speed. When rotor speed surpasses critical speed, the torque and speed have an inverse proportional relation. It is because the electromagnetic field produced by eddy current influences the external magnetic field [12]. Hence, when rotor speed surpasses the critical speed, the eddy current brake torque can be expressed as

$$T_{bc} = \frac{2\widehat{T}i}{v_k/v + v/v_k},$$
$$\widehat{T} = \left(\sqrt{\left(\frac{c}{\zeta}\right)\frac{\pi}{4}R_b^2}\sqrt{\left(\frac{L}{R_b}\right)}\right)\frac{N}{L}, \tag{5}$$
$$v_k = \frac{2}{\mu_0}\sqrt{\left(\frac{1}{c\xi}\right)\frac{\rho}{D}}\sqrt{\frac{L}{R_b}},$$

where v, v_k, c, ξ, and ρ represent the speed of brake disk, critical speed, scale factor, scale coefficient, and resistivity of brake disk [13–15].

Since the ECB in the hybrid brake system has two brake disks, the eddy current brake torque should be as follows. When $v < v_k$:

$$T_{bc} = 2\left\{1 - \frac{1}{2\pi}\left[4\tan(\psi) + \psi\ln\left(1 + \frac{1}{\psi^2}\right) - \frac{1}{\psi}\ln\left(1 + \psi^2\right)\right]\right\} \times \left(0.5\left[1 - \frac{AB}{\pi\left(1 + R_b/R_w\right)^2\left(R_w - R_b\right)^2}\right]\right) \times \sigma_0 R_b^2\left(\frac{\mu_0 N}{L}\right) SD\, I^2\omega. \tag{6}$$

When $v > v_k$:

$$T_{bc} = \frac{2}{v_k/v + v/v_k}\left(\sqrt{\left(\frac{c}{\zeta}\right)\frac{\pi}{4}R_b^2}\sqrt{\left(\frac{L}{R_b}\right)}\right)\frac{N}{L}. \tag{7}$$

2.2. Brake Disk Model. The brake disk model describes relationship between pressure of wheel cylinder and brake torque.

According to Chen et al. [16], the empirical model of brake torque and pressure can be expressed as

$$T_{bh} = \frac{p_w \mu}{k_\mu},$$
$$\mu = 0.3 + 0.12\exp\left[-\left(1.2492 - 0.0029v - 0.0814p_w\right)\right], \tag{8}$$

where T_{bh} is brake torque, p_w is brake pressure, μ is friction coefficient, k_μ is calculation coefficient (2.099), and v is vehicle speed.

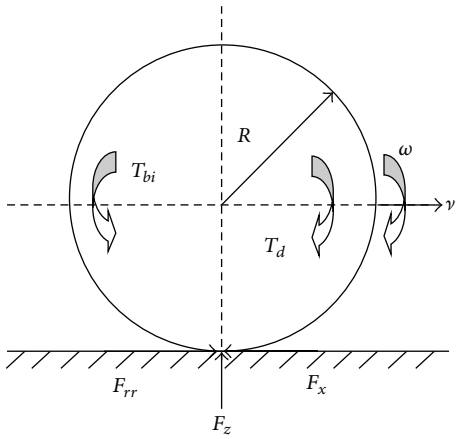

Figure 4: Wheel dynamics in braking.

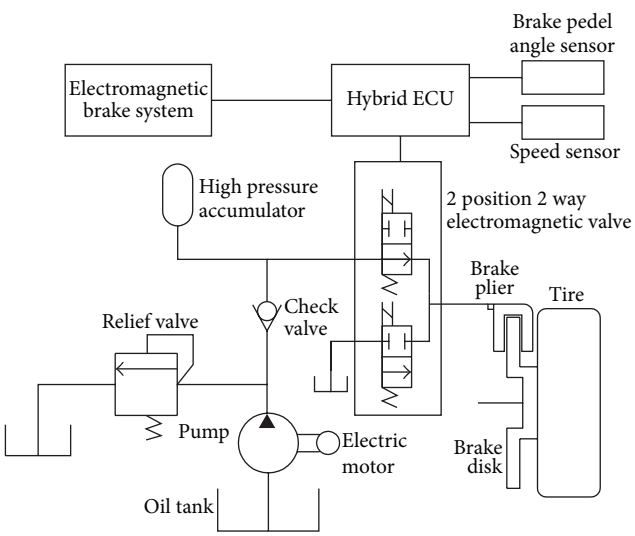

Figure 5: Hydraulic circuit diagram of EHB system.

2.3. Wheel Model. In order to analyze the performance of the hybrid brake system with varying torque characteristics, a vehicle wheel model is needed. It is assumed that vehicle lateral, vertical, roll, and yaw dynamics are negligible for the braking application. As shown in Figure 4, the wheel rotational dynamics are given by the following equation:

$$\sum M_y = T_{bi} - F_x R + F_{rr} R - T_d = -I_\omega \dot{\omega}, \qquad T_{bi} = T_{bc} + T_{bh}, \tag{9}$$

where T_{bi} is brake torque of ECB and EHB, T_{bc} is brake torque of ECB, T_{bh} is brake torque of EHB, F_x is longitudinal friction force at tire contact patch, F_{rr} is rolling resistance at tire contact patch, T_d is drive torque, I_ω is wheel rotational inertia, $\dot{\omega}$ is angular acceleration of wheel, R is wheel radius.

2.4. Hydraulic Brake Model. Figure 5 shows a hydraulic circuit diagram of EHB system; because the hydraulic brake system has too many circuits, solenoid and the other parts, it is difficult to establish an exact mathematical model to simulate and control the brake progress. In this work, an actual electronic hydraulic braking system which has hydraulic circuits, solenoid valve, and ECU has been utilized to simulate the brake progress. In the braking system, there is a high pressure accumulator to keep steady pressure. The hybrid ECU can control the brake pressure of wheel cylinder by opening or closing the electromagnetic valves. Hence, hybrid ECU can adjust brake pressure of the wheel cylinder easily. The key technique of the hydraulic brake system is to control the electromagnetic valve rapidly according to the slip ratio.

According to MK20-I type ABS hydraulic modulator [17], the model of the throttle characteristics is

$$\frac{dp_w}{dt} = \begin{cases} 35.7418(p_m - p_w)^{0.58} & \text{Pressure increase} \\ 0 & \text{Pressure holding} \\ -36.3714 p_w^{0.92} & \text{Pressure relief.} \end{cases} \tag{10}$$

3. The Control Strategy of Hybrid Brake System

The controller of hybrid brake system adopts nonlinear fuzzy strategy; when ABS works, fuzzy controller will track the optimal objective slip ratio and eliminate the tracking error [18, 19] in order to achieve a good steady-state response. As shown in Figure 6, the hybrid ABS controller will decide the driver's intention based on the feedback of the displacement and acceleration of the brake pedal sensor and then output calculated total torque gradually to objective brake torque. According to the analysis of braking force distribution between ECB and EHB, the torque proportion of ECB and EHB should be 1 : 1.5. As the process of braking torques increasing, the controller always detects slip ratio of wheels synchronously. If the slip ratio does not reach theoretic optimal value (0.2), the hybrid system was located in normal braking state, and the brake force is proportional to displacement of brake pedal. Once the slip ratio reaches 0.2, the controllers antilock control program will work. The basic control strategy of the hybrid brake system is to keep the hydraulic brake pressure at a stationary value when the slip ratio reaches 0.2 and keep the optimal slip ratio (0.2) by adjusting the current of ECB.

There are two input parameters and one output parameter in the fuzzy controller; one of the input parameters is difference value ($e(t)$):

$$e(t) = \lambda_f(t) - \lambda_r(t), \tag{11}$$

λ_f is objective slip ratio, λ_r is actual slip ratio.

The second input parameter is change rate ($\Delta e(t)$) of difference value:

$$\Delta e(t) = e(t) - e(t - T), \tag{12}$$

where $e(t)$ is sample at the moment of t, $e(t - T)$ is sample at the previous time $(t - T)$.

The output parameter of fuzzy controller is current change (i) of electromagnetic brake system. The difference

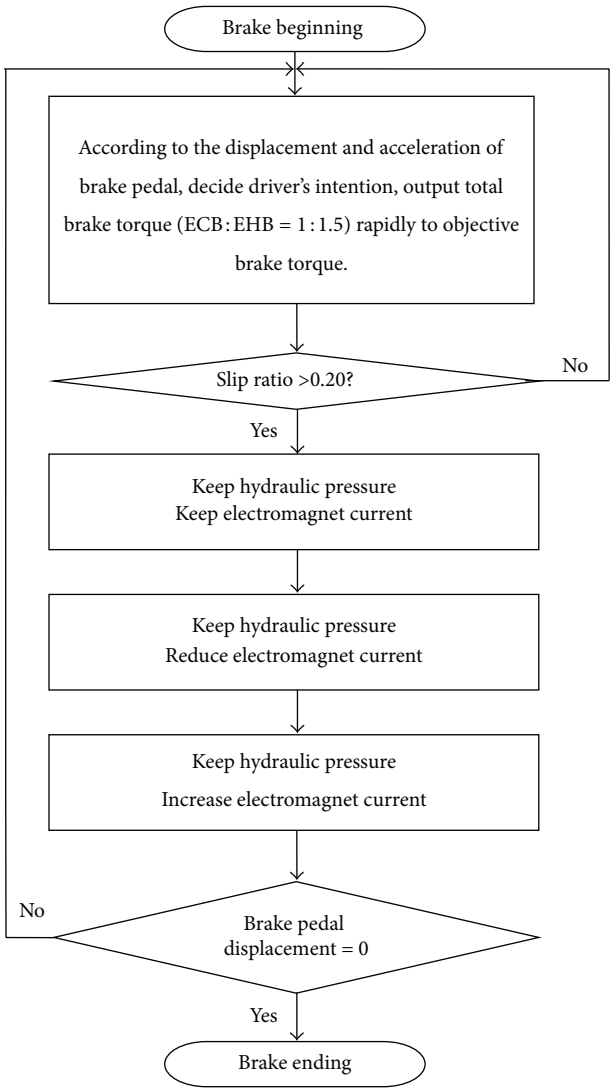

Figure 6: Control strategy of hybrid system.

value universe (E) is $[-6, 6]$, the change rate universe (EC) is $[-6, 6]$, and the current change universe (TU) is $[0, 40]$. The values are as follows [20]:

$$E = \{\text{NB NM NS NW Z PW PS PM PB}\},$$

$$EC = \{\text{NB NM NS Z PS PM PB}\},$$

$$TU = \{\text{NB NM NS NW Z PW PS PM PB}\}.$$

If the difference value is NB, the change rate value is NB. It indicates that the slip ratio now is very high and the eddy current brake torque should be reduced quickly. The output value of current is NB. However, if the difference value is PB, then the change rate value is PB. It indicates that the slip ratio now is very low and the eddy current brake torque should be increased quickly. The output value of current is PB. If the difference value is PW, then the change rate value is PS. It indicates that the slip ratio now is little bigger than the optimal value. At this moment, the eddy current brake torque should not be changed [21]. The output value of current is Z. The fuzzy control strategy rule is as shown in Table 1.

4. HILS System Design Based on LabVIEW and Matlab

Figure 7(a) is a sketch of the HILS system of ECB&EHB hybrid brake system. The hardware of the HILS system consists of hybrid brake system, sensor nets, driving device, battery, data acquisition board, personal computer, and so forth [22]. The software of the HILS system consists of Matlab mathematical operating progress of the hybrid brake model and the LabVIEW controlling program. The main role of software part is to define a brake system model and carry out the real-time simulation.

Figure 7(b) shows the interface of the hybrid brake system testing bench based on LabVIEW and Matlab [23]. In the model of data processing, by compiling the functions in the Math Library of Matlab C/C++ into dynamic-link library (DLL), the sharing function library for data processing was established. LabVIEW can compile the calculation method and control algorithm to control program by calling DLL easily.

Control commands of virtual controller in personal computer are sent via data acquisition board (USB-6341) and driving device to hybrid brake system. The brake pedal position sensor, wheel speed sensor, torque sensor, and other sensor signals are sent to virtual controller through sensor nets and data acquisition board. On the actual testing bench, two tires are used to simulate the driving wheel and road. The tire that simulates road can package different materials to adapt different road conditions. Torque sensor was equipped to test the torque of hybrid brake system.

The performance of the ABS HILS was developed and tested under the previous environments and conditions (Table 2) vehicle parameters are listed in Table 3. The target of the control program is to hold the desired slip ratio as 0.2.

5. Experimental Results and Discussion

In order to analyze the performance of the hybrid brake system, different type of brake systems (ECB, EHB, and ECB & EHB) experiment in the same road scenarios and different road scenarios (dry and wet asphalt roads) experiment have been made to validate the hybrid brake system on the testing bench.

5.1. Dry Asphalt Road Test. Dry asphalt road has high friction coefficient for braking system, approximately 0.8. Figure 8 shows the results of ECB, EHB, and ECB & EHB braking experiments on dry asphalt road. The initial velocity of vehicle is 100 Km/h. Figures 8(a), 8(c), and 8(e) show the time responses of the slip ratio tracking of the vehicle, and Figures 8(b), 8(d), and 8(f) show the velocity of vehicle decelerating by the ECB, EHB, and hybrid ECB & EHB systems.

When sudden stop action occurs, Figure 8(a) shows the slip ratio of ECB system is very low. When the wheel speed decreases, the brake torque of ECB reduces, too, and the slip

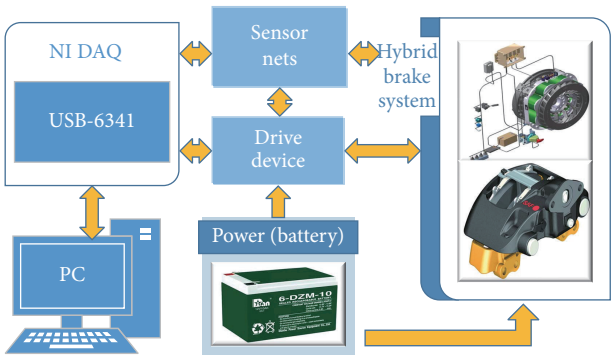

(a) Sketch for the HILS system

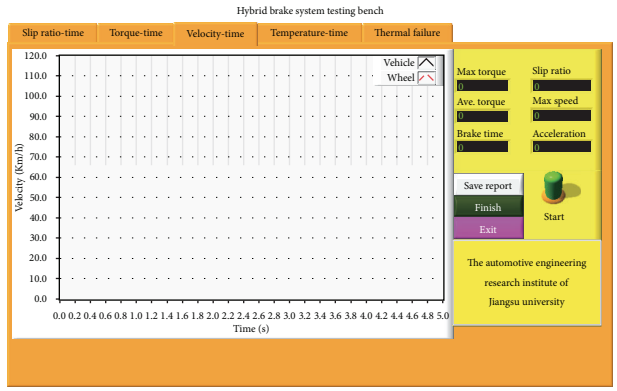

(b) Interface of the testing bench

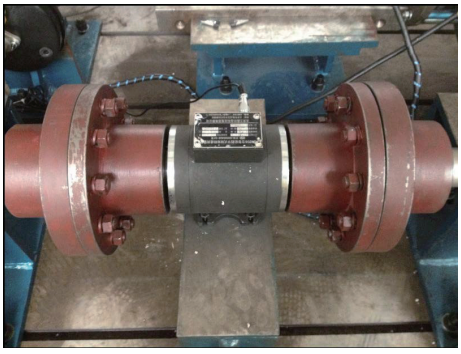

(c) Torque sensor of the testing bench

(d) Panorama of the testing bench

(e) Frequency transformer, Instrument, and Power

(f) Data acquisition board (USB-6341)

Figure 7: HILS system design based on LabVIEW and Matlab.

ratio of ECB cannot reach 0.2. Hence, the vehicle speed and wheel speed are approached to each other in Figure 8(b), and the curve is smoother than that of Figure 8(c). Due to the possible hydraulic impact, there is little abnormal fluctuation on the slip ratio curve of Figure 8(c). Figure 8(d) shows the difference between vehicle speed and wheel speed; it is a little big. Figures 8(e) and 8(f) show the slip ratio and speed curve of hybrid system. The slip ratio of EHB and hybrid ECB & EHB can stabilize at 0.20, but the hybrid system is more stable than EHB.

From the aspect of braking time, Figure 8(b) shows that ECB has a more rapid response than other brake systems. When brake action occurs, ECB responds immediately, but its wheel speed has no locking trend. Figure 8(d) shows that EHB has a slower response than other brake systems. It is almost delayed 0.3s comparing to ECB system. EHB has better brake effect than ECB; its wheel speed has obvious change, and the wheel keeps a critical condition of locking. The whole braking time only needs 5.1s. Because the ECB & EHB hybrid system has all of the merits of the ECB and EHB systems,

Table 1

TU					E				
	NB	NM	NS	NW	Z	PW	PS	PM	PB
EC									
NB	NB	NB	NM	NM	Z	NS	NS	NS	NS
NM	NB	NB	NS	NS	Z	NW	Z	Z	PW
NS	NB	NM	NW	NW	Z	Z	Z	PW	PS
Z	NM	NS	NW	NW	Z	Z	PW	PS	PM
PS	NS	NW	Z	Z	Z	PW	PW	PM	PM
PM	NW	Z	PW	PW	Z	PS	PS	PM	PB
PB	Z	Z	PS	PS	Z	PM	PM	PB	PB

Table 2: Hybrid brake system testing conditions.

Road	Condition	Friction	Velocity	Target slip ratio
Dry road	Dry asphalt	0.8	100 Km/h	0.2
Wet road	Wet asphalt	0.5	100 Km/h	0.2

Table 3: Vehicle parameters that were simulated on testing bench.

Vehicle parameters	Parameter value
Mass of the vehicle m/kg	1 300
Wheel effective rolling radius R/m	0.255
Wheel rotational inertia I_ω/(kg·m^2)	1.58/1.02

Figure 8(e) shows it has a rapid response to braking action, almost immediately. The wheel speed has an obvious variety. The wheel keeps a critical condition of locking, too. The wheel speed is more stable than EHB system; the whole braking time only needs 4.6 s.

5.2. Wet Asphalt Road Test. Wet asphalt road has a smaller friction coefficient than dry road, approximately 0.5. With the same initial braking velocity, Figures 9(a), 9(c), and 9(e) show the time responses of the slip ratio tracking of the vehicle, and Figures 9(b), 9(d), and 9(f) show the velocity of vehicle decelerating by the ECB, EHB, and hybrid ECB & EHB systems.

Figure 9(a) shows the slip ratio on wet road is a little bigger than that of Figure 8(a); the speed difference between wheel and vehicle on wet road is also much larger than that on dry road by comparing Figure 9(b) to Figure 8(b). The slip ratio and speed of EHB on wet road have not too much difference from Figures 9(c) and 9(d) to Figures 8(c) and 8(d). So the performance of EHB has little difference on dry and wet roads. The slip ratio and speed curves on wet road in Figures 9(e) and 9(f) present the same controlling trend as Figures 8(e) and 8(f); it indicates that the fuzzy controller has a robust control in hybrid brake system.

The braking time on wet road has similar results to dry road. ECB has a more rapid response than other brake systems, but its brake time reaches 13.2 seconds. EHB has a slower response than other brake systems; its whole braking time only needs 7 s. The ECB&EHB also has a rapid response to braking action; the whole braking time only needs 5.6 s.

6. Conclusions

In this paper, we discussed the brake performance analysis of ABS for ECB and EHB hybrid brake system. First, we designed a new conceptual hybrid braking system that achieved the optimal combination of ECB and EHB. Based on the structure of the hybrid brake system, mathematical model was built to calculate the torque character of ECB and EHB, and we analyzed the braking force distribution between two kinds of brake systems. Second, a fuzzy controller on personal computer based on Labview and Matlab was designed and hardware in the loop system was constructed to validate and analyze the performance of the hybrid brake system. Through lots of experiments on dry and wet asphalt road, as shown in Figure 10, the result indicates the following.

(1) The response of hybrid brake system is better than that of traditional hydraulic braking system. It enhances about 0.3 s more than hydraulic braking system.

(2) Due to the merits of the hybrid brake system and the best slip ratio regulation of fuzzy controller, the curve of slip ratio of hybrid brake system is more stable than EHB, and the ability to track objective slip ratio is better than that of EHB, too. Therefore, the adhesion utilization of hybrid brake system is bigger than that of EHB in the whole braking time.

(3) Comparing EHB, the total brake time of hybrid brake system reduces to 0.5 s at the speed of 100 Km/h on dry asphalt road and to 1.4 s on wet asphalt road.

(4) For the brake distribution of the contactless braking system (ECB), the abrasion, noise, harmful friction dust, and the risk of thermal failure in hybrid brake system were reduced obviously.

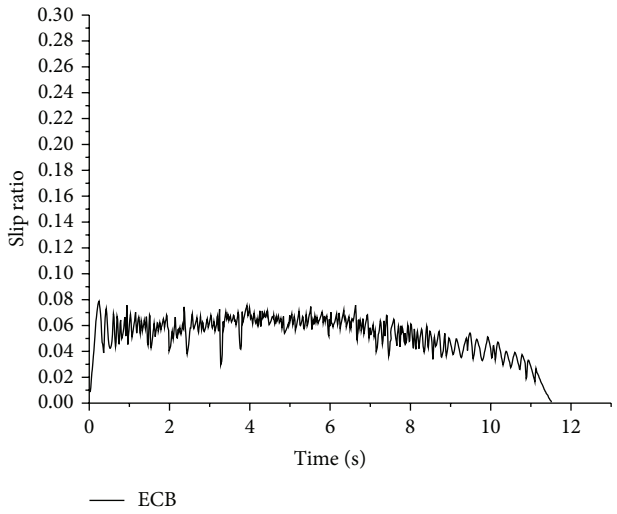

(a) Slip ratio of ECB

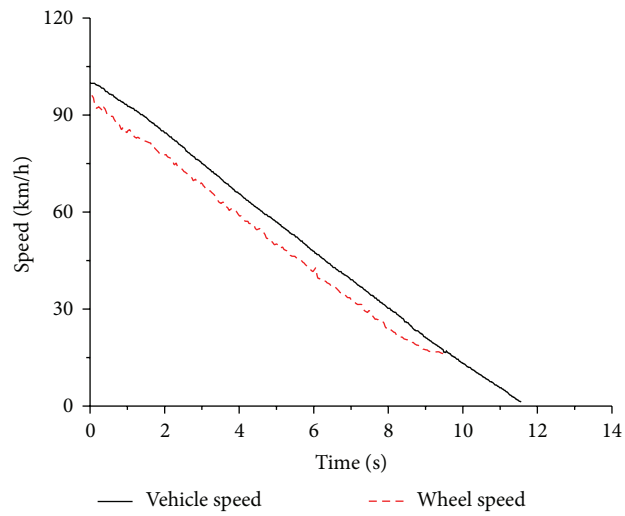

(b) Velocity of ECB

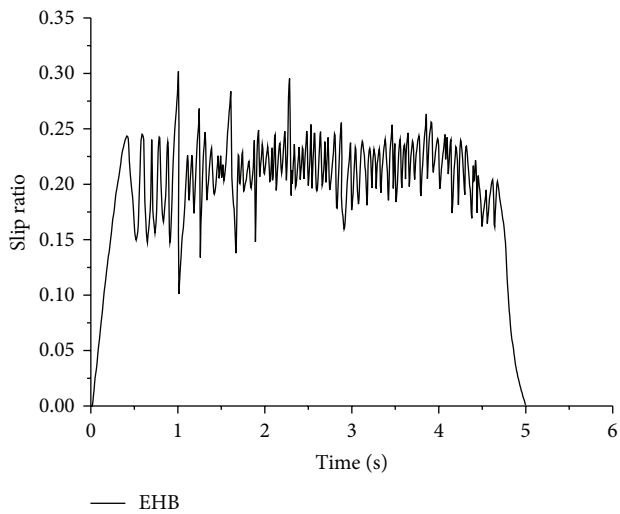

(c) Slip ratio of EHB

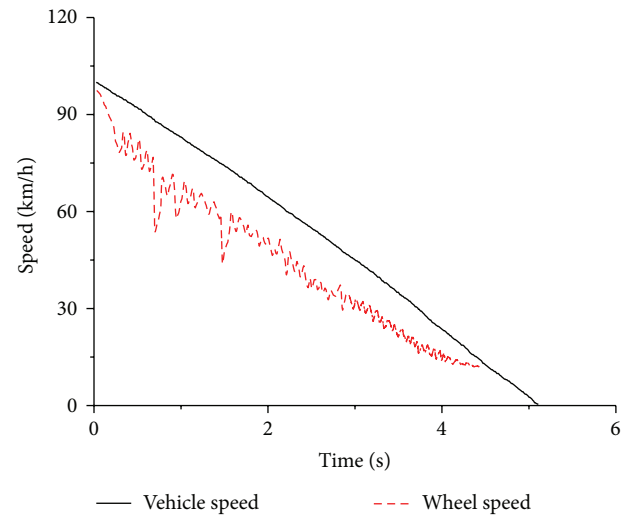

(d) Velocity of EHB

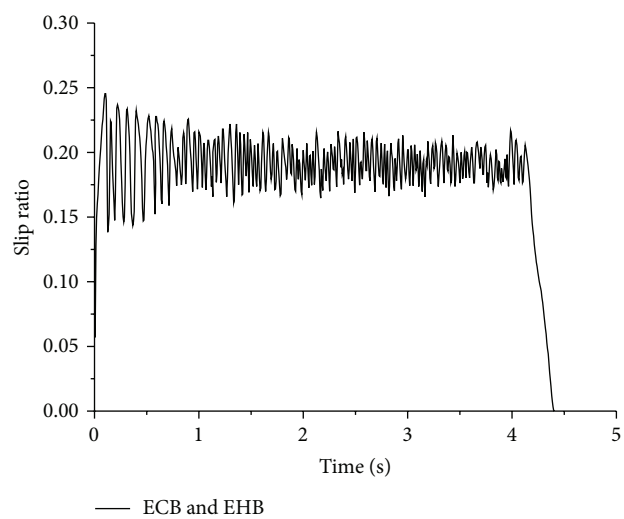

(e) Slip ratio of hybrid ECB and EHB

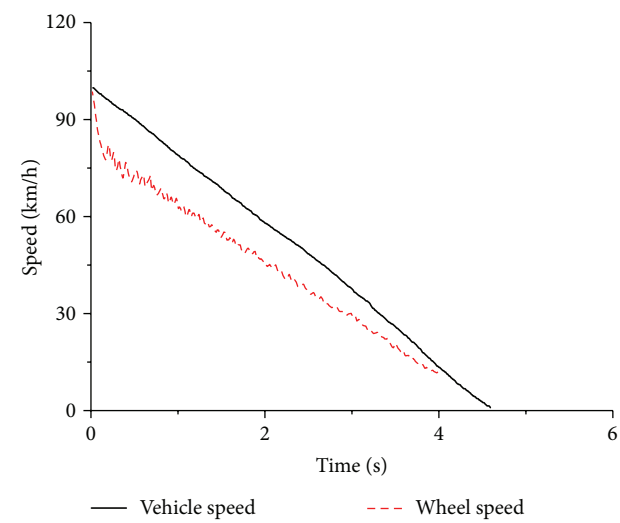

(f) Velocity of hybrid ECB and EHB

Figure 8: Results of ECB, EHB, and ECB & EHB braking experiments on dry asphalt road.

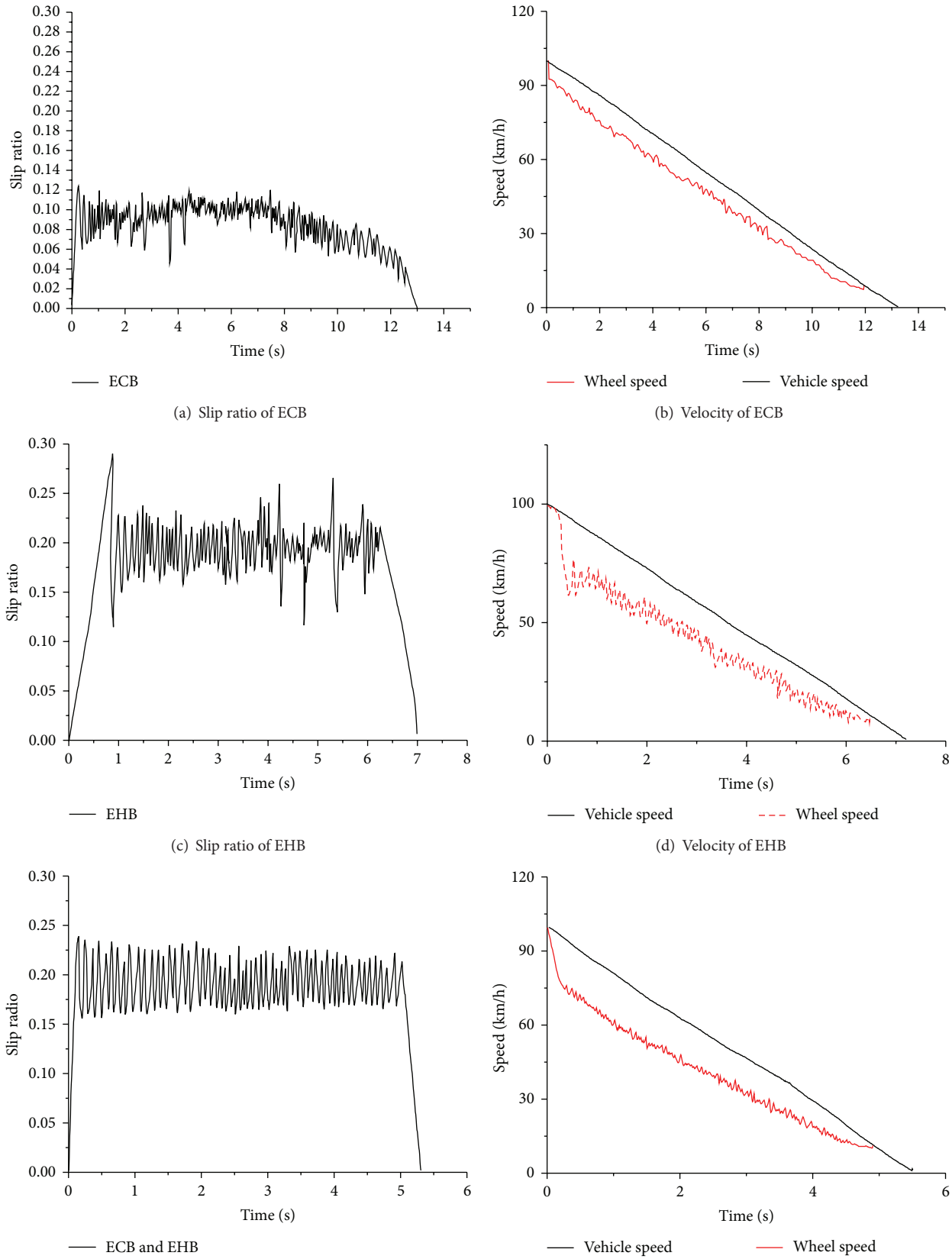

(a) Slip ratio of ECB

(b) Velocity of ECB

(c) Slip ratio of EHB

(d) Velocity of EHB

(e) Slip ratio of hybrid ECB and EHB

(f) Velocity of hybrid ECB and EHB

Figure 9: Results of ECB, EHB, and ECB & EHB braking experiments on wet asphalt roads.

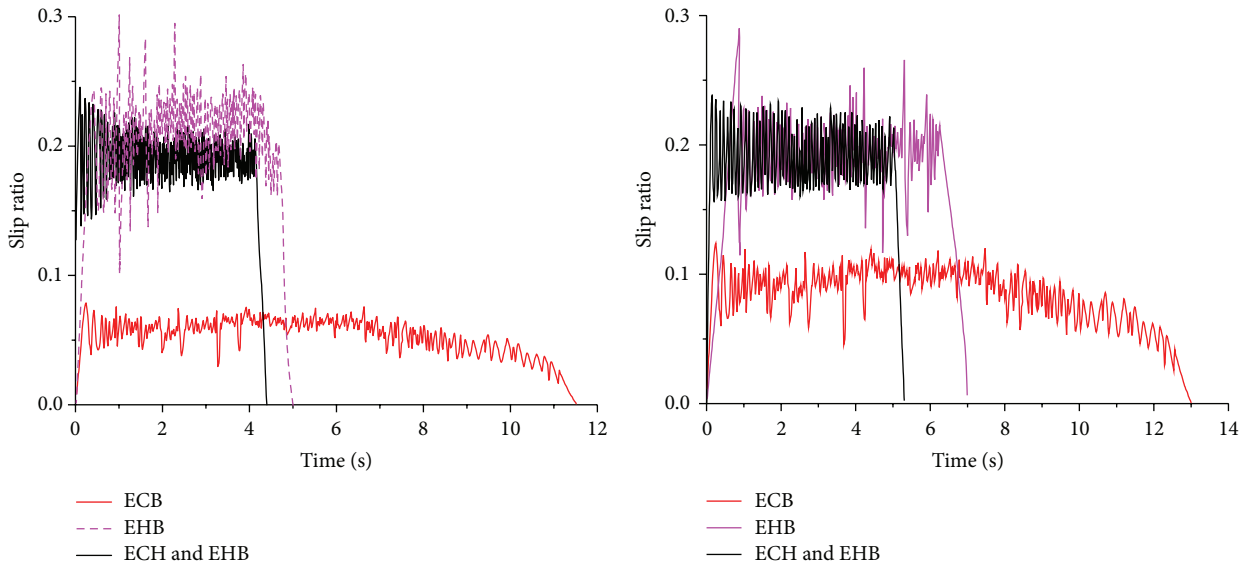

(a) Slip ratio comparison on dry asphalt road

(b) Slip ratio comparison on wet asphalt road

Figure 10: Slip comparison of ECB, EHB, and ECB & EHB on different road scenarios.

Conflict of Interests

The authors declare that there is no conflict of interests regarding the publication of this paper.

Acknowledgments

This work is supported by National Natural Science Foundation of China (no. 51275212), the 2012 Jiangsu Province Post-graduate Innovative Fund Project (CXZZ12_0664), and the 2012 Jiangsu Province Key Laboratory of Automotive Engineering (QC201203).

References

[1] G. G. Desta, "Eddy Current Brake System," 2004, US 6,698,554 B2.

[2] S. Anwar and B. Zheng, "An antilock-braking algorithm for an eddy-current-based brake-by-wire system," *IEEE Transactions on Vehicular Technology*, vol. 56, no. 3, pp. 1100–1107, 2007.

[3] S. Anwar and R. C. Stevenson, "Torque characteristics analysis of an Eddy current electric machine for automotive braking applications," in *Proceedings of the American Control Conference*, pp. 3996–4001, June 2006.

[4] S. E. Gay, *Contactless Magnetic Brake for Automotive Applications*, Texas A&M University, 2005.

[5] J. Song, "Performance evaluation of a hybrid electric brake system with a sliding mode controller," *Mechatronics*, vol. 15, no. 3, pp. 339–358, 2005.

[6] R. He, C. Liu, and N. Li, "Fuzzy control of the integrated system of electromagnetic brake and friction brake of car," *Journal of Mechanical Engineering*, vol. 46, no. 24, pp. 83–87, 2010.

[7] K. Lee and K. Park, "Optimal robust control of a contactless brake system using an eddy current," *Mechatronics*, vol. 9, no. 6, pp. 615–631, 1999.

[8] K. Lee and K. Park, "Modeling Eddy currents with boundary conditions by using Coulomb's law and the method of images," *IEEE Transactions on Magnetics*, vol. 38, no. 2, pp. 1333–1340, 2002.

[9] K. Lee Jr. and K. Park, "Modeling of the Eddy currents with the consideration of the induced magnetic flux," in *Proceedings of the IEEE Region 10th International Conference on Electrical and Electronic Technology*, pp. 762–768, August 2001.

[10] K. Lee and K. Park, "Contactless eddy current brakes for cars: United States," US6,286,637, 9.11, 2001.

[11] E. Simeu and D. Georges, "Modeling and control of an eddy current brake," *Control Engineering Practice*, vol. 4, no. 1, pp. 19–26, 1996.

[12] W. R. Swythe, "On eddy current in a rotating disk," *Transactions of the AIEE*, vol. 61, pp. 681–684, 1942.

[13] J. H. Wouterse, "Critical torque and speed of eddy current brake with widely separated soft iron poles," *IEE Proceedings B*, vol. 138, no. 4, pp. 153–158, 1991.

[14] O. Bottauscio, M. Chiampi, and A. Manzin, "Modeling analysis of the electromagnetic braking action on rotating solid cylinders," *Applied Mathematical Modelling*, vol. 32, no. 1, pp. 12–27, 2008.

[15] A. Younis, K. Karakoc, Z. Dong, E. Park, and A. Suleman, "Application of SEUMRE global optimization algorithm in automotive magnetorheological brake design," *Structural and Multidisciplinary Optimization*, vol. 44, no. 6, pp. 761–772, 2011.

[16] H. Chen, J. Song, T. Wang, and L. Ren, "Exponential function model of friction characteristics of a disc brake," *Transactions of the Chinese Society of Agricultural Machinery*, vol. 33, no. 5, pp. 79–83, 2002.

[17] D. Peng, Y. Zhang, C.-L. Yin, and J.-W. Zhang, "Combined control of a regenerative braking and antilock braking system for hybrid electric vehicles," *International Journal of Automotive Technology*, vol. 9, no. 6, pp. 749–757, 2008.

[18] H. Zhang, Y. Shi, and M. Liu, "H_∞ Step tracking control for networked discrete-time nonlinear systems with integral and

predictive actions," *IEEE Transactions on Industrial Informatics*, vol. 9, no. 1, pp. 337–345, 2013.

[19] Z. Shuai, H. Zhang, and J. Wang, "Combined AFS and DYC control of four-wheel-independent-drive electric vehicles over CAN network with time-varying delays," *IEEE*, 2013.

[20] C. Jun, "A study on robust control for anti-lock braking system," *Automotive Engineering*, vol. 1, pp. 17–22, 1998.

[21] L. Zhengdong, W. Man, and Y. Jianying, "Nonlinear robust control of a hypersonic flight vehicle using fuzzy disturbance observer," *Mathematical Problems in Engineering*, vol. 2013, Article ID 369092, 10 pages, 2013.

[22] L. Yi, S. Chen, and W. Jun, "A simulation study on fuzzy control of anti-lock characteristic of brake-by-wire system," *Journal of Highway and Transportation Research and Development*, vol. 10, pp. 124–127, 2006.

[23] W. Zhang, N. Ding, M. Chen, G. Yu, and X. Xu, "Development of a low-cost hardware-in-the-loop simulation system as a test bench for anti-lock braking system," *Chinese Journal of Mechanical Engineering*, vol. 24, no. 1, pp. 98–104, 2011.

Hindawi Publishing Corporation
Mathematical Problems in Engineering
Volume 2013, Article ID 216982, 11 pages
http://dx.doi.org/10.1155/2013/216982

Research Article

Slide Mode Control for Integrated Electric Parking Brake System

Bin Wang,[1] Xuexun Guo,[1] Chengcai Zhang,[1] Zhe Xiong,[1] Huan Xia,[1] and Jie Zhang[2]

[1] *Hubei Key Laboratory of Advanced Technology of Automotive Parts, Wuhan University of Technology, Wuhan 430070, China*
[2] *Wanxiang Group Technology Center, Hangzhou 310000, China*

Correspondence should be addressed to Xuexun Guo; guoxx@whut.edu.cn

Received 25 October 2013; Accepted 27 October 2013

Academic Editor: Hui Zhang

The emerging integrated electric parking brake (IEPB) system is introduced and studied. Through analyzing the various working stages, the stages switched IEPB system models are given with the consideration of the friction and system idle inertia. The sliding mode control (SMC) method is adopted to control the clamping force by the widely used motor angle and clamping force relationship method. Based on the characteristics of the state equations, two sliding surfaces are built to control the motor angle and current, respectively. And in every working stage, the control stability is guaranteed by choosing the control parameters based on Lyapunov theory and SMC reachability. The effectiveness of the proposed control system has been validated in Matlab/Simulink.

1. Introduction

Lots of strong points exist in X-by-wire systems, such as component number reduction, weight reduction, and performance improvement [1, 2]. Electronic parking brake (EPB) system is one kind of brake-by-wire systems, which generates the parking force by motor torque instead of the manual force. Hence, the EPB system can increase the vehicle cabin space, facilitate the parking process, and have potential function [3]. There are mainly two kinds of EPB: the first one generates the force by pulling down traditional parking cable, as seen in [3–9]. The second one is called integrated EPB (IEPB), which has the similar structure with the electromechanical brake [10–12] and hence it can offer numerous possibilities [13]. IEPB actuator is mounted on the traditional caliper. Through screw-nut structure, the rotating movement from the DC motor can be transformed to the rectilinear motion of the nut [14]. By the moving forward or backward of the nut, the braking force can be generated or released. Once the desired braking force is reached, the motor power can be cut off and the clamping force can be steady due to the screw-nut self-locking.

While IEPB system has been used in some advanced sedans [15, 16], there is very little published research. For EPB with traditional cables, Lee et al. studied the bang-bang [4], nonlinear P controllers [3, 6, 7] to control the clamping force and the controller stability is also analyzed in [3, 7]. The traditional EPB system models were built in [3–7]; however, motor friction and screw-nut system inertia were neglected. Actually, during the motor idle stage, the motor friction and the nut inertia have direct effects on the modeling precision. For IEPB system, due to the limited installation space and the high cost of force sensor, clamping force estimation methods based on the motor position have been proposed in [1, 10–12]. From the researches [10–12, 17], we know based on the angular displacement of the motor that the clamping force can be estimated precisely. However, few control methods that can track the desired motor angle precisely for electric parking brake system are shown in published researches. Especially, robust control, hardly guaranteed by the published control methods, is very important for vehicle safety system [18, 19]. Hence, the authors proposed the sliding mode control method based on the system characteristics to optimize the control precision and robustness [20–22].

The present authors have made much effort over a long time to research and develop EPB system [14, 23, 24]. And to the authors' best knowledge, little published research is about the IEPB system. The main contributions of this paper lie in three aspects. First, this is among the first attempts to develop a detailed system model for IEPB system. In particular, the state-switched system stages and also the motor and screw-nut friction model are considered seriously. Second, this is

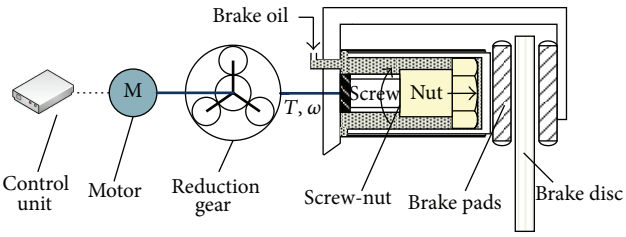

Figure 1: Structure of the IEPB system.

the first attempt to integrate a sliding mode control (SMC) method with EPB system. Through the SMC method, both the precision and robustness of IEPB system are improved apparently. Third, two sliding surfaces are designed to improve the control performance and the control system stability is studied based on Lyapunov theory and system reachability.

The rest of this paper is organized as follows. In the second section, principle and model of the state-dependent IEPB system, including the DC motor and screw-nut system as well as the clamping force, are given. The third section proposed the SMC control law with the proof of the control stability. The simulations and analyses of the proposed control system are shown in the fourth section, followed by the concluding remarks in the final section.

2. System Modeling

In this section, the system structure and system modeling will be presented. The IEPB is a system that locks the vehicle wheels steadily by controlling the motor when receiving the parking brake command. The structure of IEPB system is shown in Figure 1, including DC motor, reduction gears, screw-nut module, traditional brake pads, and disc.

2.1. DC Motor. In IEPB system, the final parking braking force is provided by the motor torque. As shown in Figure 1, motor torque is first transferred to the reduction gears for increasing the driven torque. The model of DC motor can be built as

$$\begin{aligned} U &= L_a \dot{i}_a + R_a i_a + K_{\text{emf}}\omega, \\ K_{\text{motor}} i_a &= J_m \dot{\omega}_m + T_F + T_G, \\ T_m &= K_{\text{motor}} i_a, \end{aligned} \tag{1}$$

where U is the motor voltage; L_a is the inductance; i_a is the motor current; R_a is the resistance; K_{emf} is the EMF constant; ω is the angular rate; T_m is motor torque; K_{motor} is motor constant; T_F is the friction torque, including the viscous friction, dynamical friction T_{FC}, and the maximum static friction $T_{F\max}$; T_G is the load torque; J_m is the moment of inertia of this system. Based on the Armstrong friction model [25], the friction torque of DC motor can be described as

$$T_F = T_{FC} + \left(T_{F\max} - T_{FC}\right) e^{-|\omega/\omega_s|^{\delta_s}} + b_v\omega, \quad (\omega \neq 0), \tag{2}$$

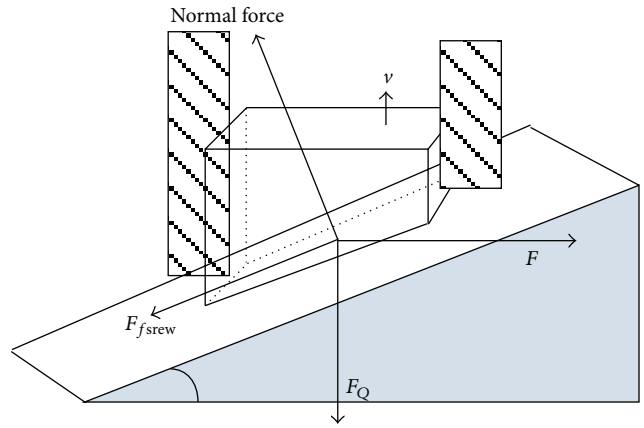

Figure 2: The equivalent structure of screw-nut.

where ω_s is the Stribeck velocity that describes the continuous decrease instead of the break point; δ_s is a coefficient for Stribeck friction.

For simplicity of the analysis, the friction torque can be written as

$$T_F = b_v\omega_m. \tag{3}$$

2.2. Screw-Nut System. In IEPBs, the nut can just move in the axial direction, secured against twisting; on the contrary, the screw can just rotate without moving forward or backward. When the screw rotates in counter-clockwise direction, the head will move forward to the left side in the axial direction. Figure 2 shows the equivalent structure of the screw-nut. The lower wedge denotes the screw while the upper one denotes the nut. Therefore, the relative motion for nut and screw can be seen as the nut is sliding along the slope with an angle inclination α [26–28].

According to the equivalent schematic diagram of screw-nut, the relationship between the screw torque T_L and F can be described as

$$\begin{aligned} N \cdot T_G &= T_L, \\ T_L &= F \cdot r, \end{aligned} \tag{4}$$

where N is the gear ratio between the motor and the IEPB actuator; r is the screw pitch radius; F is the equivalent force on the nut cross section shown in Figure 2. When the nut is moving on the screw, the friction force $F_{f\text{srew}}$ in the screw-nut system can be written as

$$F_{f\text{srew}} = F_{\text{coulomb}\_f} + \left(F_{\max\_f} - F_{\text{coulomb}\_f}\right) e^{-|v/v_s|^2} + c_v v, \tag{5}$$

where $F_{f\text{srew}}$ is the friction force of the screw-nut system; v_s is the Stribeck velocity; c_v is the viscous friction coefficient; $F_{\max\_f}$ is the maximum static friction; F_{coulomb_f} is the coulomb friction proportional to the normal force.

Due to the clearance existing between the nut and the brake disc, the nut needs to move forward first to clear this

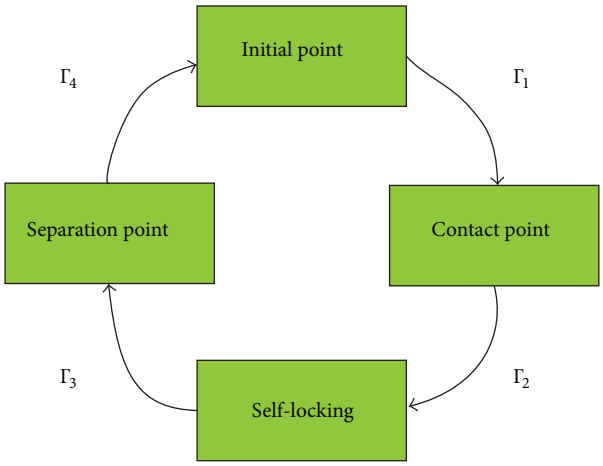

Figure 3: State switched screw-nut system.

gap. This status is named Γ_1 as shown in Figure 3 and it is obvious that there is no clamping force due to no contacting during Γ_1. However, in order to estimate the contact point precisely, the friction torque analysis in screw-nut system is still needed. Stages Γ_1 and Γ_4 have the similar dynamics equations though the speed direction is contrary. While Stages Γ_2 and Γ_3 have the similar dynamics equations, they have a contrary speed direction. Hence, for simplicity of the modeling process, only Γ_1 and Γ_2 are analyzed in this paper.

For Stages Γ_1. Due to no clamping force in Γ_1, the friction force can be written as

$$F \cdot \cos\alpha = F_{f\text{srew}}, \tag{6}$$

where α is the lead angle. When there is no contact, the F_{coulomb_f} can be ignored and the viscous friction is playing a leading role in (5). Substituting (3) and (4) into (6), it yields

$$\frac{c_v\dot{x}_{\text{nut}}}{\sin\alpha} + \frac{m\ddot{x}_{\text{nut}}}{\sin\alpha} = T_L \cdot \cos\alpha, \tag{7}$$

$$T_L = 2r \cdot \frac{c_v\dot{x}_{\text{nut}} + m_{\text{nut}}\ddot{x}_{\text{nut}}}{\sin 2\alpha}, \tag{8}$$

where m is the mass of the nut. The state equations for the IEPBs in Γ_1 can be presented as

$$\frac{d}{dt}\begin{bmatrix} i \\ \omega \\ \theta \end{bmatrix} = \begin{bmatrix} -\dfrac{R_a}{L_a}i - \dfrac{K_{\text{emf}}}{L_a}\omega + \dfrac{1}{L_a}U \\ \dfrac{K_{\text{motor}}i}{J_m} - \dfrac{b_v\omega}{J_m} - \dfrac{2r\left(c_v\dot{x}_{\text{nut}} + m_{\text{nut}}\ddot{x}_{\text{nut}}\right)}{J_m N \sin 2\alpha} \\ \omega \end{bmatrix}. \tag{9}$$

For Stages Γ_2. During the clamping stage Γ_2, based on the horizontal and perpendicular forces on the contact surface in Figure 2 and due to the much higher magnitude coulomb friction force, the friction force can be written as

$$F_{f\text{srew}} = \begin{cases} \dfrac{1}{r}T_L\cos\alpha - F_Q\sin\alpha & v = 0,\ \Delta F < F_{\max\_f} \\ F_{\max\_f}\,\text{sgn}\,(\Delta F) & v = 0,\ \Delta F \geq F_{\max\_f} \\ \mu_s \cdot \dfrac{T_L\sin\alpha + F_Q\cos\alpha r}{r} & v \neq 0, \end{cases} \tag{10}$$

where μ_s is the coulomb friction coefficient; F_Q is the axial load on the nut; ΔF is the external force, deciding the friction direction. Ignoring the little inertia effect of the nut mass during Γ_2 for simplifying modeling, according to Figure 2, the relationship between the screw torque T_L and the head load F_Q can be written as

$$T_L \cdot \frac{1}{r \cdot \tan\left(\alpha + \arctan\mu_s\right)} = F_Q + m_{\text{nut}}\ddot{x}_{\text{nut}}, \tag{11}$$

where m_{nut} is the mass of head and x_{nut} is the linear displacement of head.

According to (8)–(11), the T_L can be written as

$$T_L = \begin{cases} 2r \cdot \dfrac{c_v\dot{x}_{\text{nut}} + m_{\text{nut}}\ddot{x}_{\text{nut}}}{\sin 2\alpha} & \text{during } \Gamma_1 \\ \dfrac{F_Q + m_{\text{nut}}\ddot{x}_{\text{nut}}}{\sigma_1} & \text{during } \Gamma_2, \end{cases} \tag{12}$$

where

$$\sigma_n = \frac{1}{r \cdot \tan\left(\arctan\,\mu + \alpha\right)}. \tag{13}$$

2.3. Clamping Force Model. As shown in Figure 4, A_0, A_c, and A_1 are three points, namely, the nut initial point, nut contact point, and the system contact point, respectively. In clamping maneuver, the nut moves from point A_0 to point A_c and then pushes the pads to clamp the disc and then moves back to initial point A_0 during $\Gamma_{3,4}$. Line d_1 is the gap between the nut initial position A_0 and the piston position. Line d_2 is the total thickness of pad and piston and is a constant value under no pressure. To simplify analyses, the piston and pad are considered as an assembly and we assume no gap exists between the pad and piston. Line d_3 represents the gap between the friction pads to braking disc, which can be guaranteed by the seal groove mechanism. Line d_4 is not shown in Figure 4, since it is the deformation value. With the gap cleared, clamping force will be generated by the nut translational motion.

Nut rectilinear movement x_{nut} can be written as

$$x_{\text{nut}} = d_1 + d_3 + d_4. \tag{14}$$

Based on Newton's laws of motion, the clamping force can be written as

$$F_Q(t) = 2 \cdot \left(k_{\text{brake}} \cdot d_4(t) + b_{\text{brake}} \cdot \dot{d}_4(t)\right), \tag{15}$$

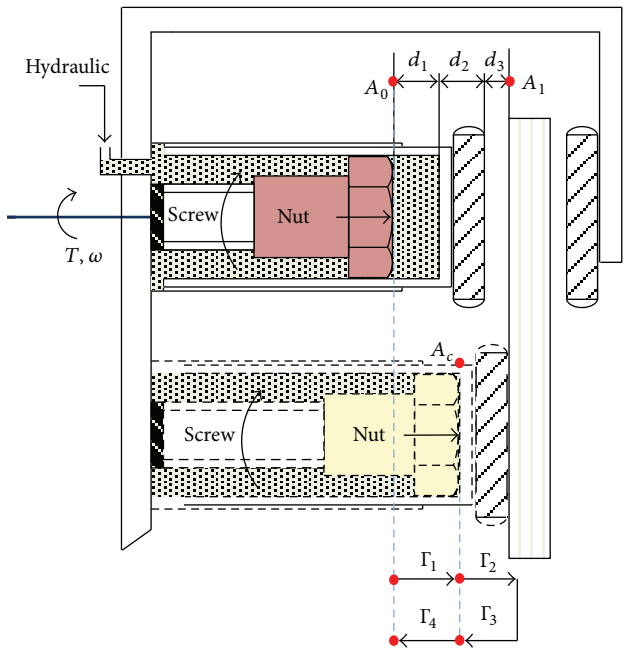

FIGURE 4: Schematic diagram of the IEPBs.

where b_{brake} is the damping coefficient and the overall stiffness of actuator k_{brake} can be calculated from each individual part [1]:

$$k_{\text{brake}} = \frac{1}{1/k_{\text{disk}} + 1/k_{\text{head}} + 2/k_{\text{pad}} + 1/k_{\text{caliper}}}, \tag{16}$$

where k_{brake} is stiffness coefficient of the brake system; k_{disk}, k_{head}, k_{pad}, and k_{caliper} are the stiffness coefficient of brake disc, nut, pad, and the caliper, respectively; θ_L is the angular displacement corresponding to the normal gap distance and is a constant value; θ is the total angular displacement, which can be described as

$$\frac{d_1 + d_3}{\theta_L} = \frac{p}{2\pi N}, \qquad \frac{x_{\text{nut}}}{\theta} = \frac{p}{2\pi N}, \tag{17}$$

$$d_4 = \frac{P}{2\pi N}\tilde{\theta}, \tag{18}$$

where $\tilde{\theta} = \left\{ \begin{smallmatrix} \theta-\theta_L, & \theta>\theta_L \\ 0, & \theta\le\theta_L \end{smallmatrix} \right.$ is the active angular displacement corresponding to the compression movement d_4 and p is the pitch of screw:

$$F_Q(t) = 2 \cdot \left(k_{\text{brake}} \cdot \frac{P}{2\pi N}\tilde{\theta} + b_{\text{brake}} \cdot \frac{P}{2\pi N}\dot{\tilde{\theta}} \right). \tag{19}$$

Based on (1) and (12)–(19), the state equations for the IEPBs in Γ_2 can be presented as

$$\frac{d}{dt}\begin{bmatrix} i \\ \omega \\ \theta \end{bmatrix} = \begin{bmatrix} -\dfrac{R_a}{L_a} i - \dfrac{K_{\text{emf}}}{L_a}\omega + \dfrac{1}{L_a}U \\ \dfrac{K_{\text{motor}} i}{J_m} - \dfrac{b_v \omega}{J_m} - \dfrac{p k_{\text{brake}}\tilde{\theta} + p b_{\text{brake}}\omega + m_{\text{head}} p\ddot{\theta}}{2 J_m \pi \sigma_1 N^2} \\ \omega \end{bmatrix}. \tag{20}$$

3. Control Design

Based on (15) and researches in [1, 3–7, 12], we know that the clamping force has a direct relationship with the motor angle. In this paper, a robust control system is designed to track the desired motor angle precisely and then to reach the desired force. Rearranging (9) into standard state space for stage Γ_1 yields

$$\frac{d}{dt}\begin{bmatrix} i \\ \omega \\ \theta \end{bmatrix} = A_{\Gamma_1}\begin{bmatrix} i \\ \omega \\ \theta \end{bmatrix} + B_{\Gamma_1} U, \tag{21}$$

where

$$A_{\Gamma_1} = \begin{bmatrix} -\dfrac{R_a}{L_a} & -\dfrac{K_{\text{emf}}}{L_a} & 0 \\ K_{\text{motor}}\xi & -(b_v + \psi)\xi & 0 \\ 0 & 1 & 0 \end{bmatrix}, \tag{22}$$

$$B_{\Gamma_1} = \begin{bmatrix} \dfrac{1}{L_a} \\ 0 \\ 0 \end{bmatrix}, \tag{23}$$

$$\psi = \frac{\text{rcp}}{\pi N^2 \sin 2\alpha}, \tag{24}$$

$$\xi = \frac{\pi N^2 \sin 2\alpha}{J_m \pi N^2 \sin 2\alpha + \text{rpm}_{\text{nut}}}. \tag{25}$$

Rearranging (20) into standard state space for state Γ_2 yields

$$\frac{d}{dt}\begin{bmatrix} i \\ \omega \\ \theta \end{bmatrix} = A_{\Gamma_2}\begin{bmatrix} i \\ \omega \\ \theta \end{bmatrix} + B_{\Gamma_2} U, \tag{26}$$

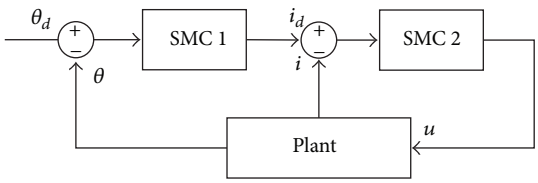

Figure 5: Schematic diagram of the SMC system.

where

$$A_{\Gamma_2} = \begin{bmatrix} -\dfrac{R_a}{L_a} & -\dfrac{K_{\text{emf}}}{L_a} & 0 \\ K_{\text{motor}}\varphi_n & -(b_v + \kappa_n)\varphi_n & -\delta_n\varphi_n \\ 0 & 1 & 0 \end{bmatrix}, \quad B_{\Gamma_2} = \begin{bmatrix} \dfrac{1}{L_a} \\ 0 \\ 0 \end{bmatrix}, \tag{27}$$

where

$$\kappa_n = \frac{p \cdot b_{\text{brake}}}{2\pi\sigma_n N^2}, \quad \delta_n = \frac{p \cdot k_{\text{brake}}}{2\pi\sigma_n N^2}, \quad \varphi_n = \frac{2\pi\sigma_n N^2}{2\pi\sigma_n J_m N^2 + m_{\text{head}} p}. \tag{28}$$

For all the dynamic stages Γ_{1-4}, the feedback can be chosen as

$$y = \begin{bmatrix} 0 & 0 & 1 \end{bmatrix} \begin{bmatrix} i \\ \omega \\ \theta \end{bmatrix}. \tag{29}$$

3.1. Control Law Design. The control robustness is very important [29], especially for braking system. In this part, a sliding mode control (SMC) design procedure for the state-switched IEPB system is presented, which mainly includes 2 steps: firstly, the design of the sliding surface; secondly, the design of the controller, by which the trajectory will be guided to sliding on the surface designed in step one. Note that the clamping force has a direct relationship with the angular displacement $\tilde{\theta}$ based on (18) and (19). From (21), (26), and (29), we know the control input u can just directly control the current; however, current i has a relationship with the angular displacement. Hence, we define two sliding surfaces as shown in Figure 5 for angular displacement control and current control, respectively.

These two sliding surfaces are defined as

$$s_1 = \dot{e}_1 + g e_1, \quad (g > 0), \qquad s_2 = i_d - i, \tag{30}$$

where s_1 and s_2 are two sliding surfaces for angular displacement and motor current and $e_1 = \theta_d^* - \theta$, g is a positive gain.

The corresponding control inputs can be written as

$$i_d = \begin{cases} H_{1,\Gamma_1}\,\text{sgn}(s_1) + \dfrac{s_1}{H_{1,\Gamma_1}}, & \text{during } \Gamma_1 \\ H_{1,\Gamma_2}\,\text{sgn}(s_1) + \dfrac{s_1}{H_{1,\Gamma_2}}, & \text{during } \Gamma_2, \end{cases} \tag{31}$$

$$u = \begin{cases} H_{2,\Gamma_1}\,\text{sgn}(s_2) + \dfrac{s_2}{H_{2,\Gamma_1}}, & \text{during } \Gamma_1 \\ H_{2,\Gamma_2}\,\text{sgn}(s_2) + \dfrac{s_1}{H_{2,\Gamma_2}}, & \text{during } \Gamma_2, \end{cases} \tag{32}$$

where $H_{i,\Gamma_j(i,j=1,2)}$ are the control parameters which need to be determined.

Remark 1. The current i_d is a virtual input to connect the desired angular displacement and the actual control input u.

Remark 2. If $H_{i,\Gamma_j(i,j=1,2)}$ is a very small value and $1/H_{i,\Gamma_j(i,j=1,2)}$ will be a large value, which can help reduce the chattering when the state trajectories are closing to the sliding surfaces and can also apply a higher gain for larger error.

Remark 3. $H_{i,\Gamma_j(i,j=1,2)}$ should be chosen to make the sliding surface satisfy the reachability condition as follows [20]:

$$\frac{1}{2}\frac{d}{dt}\left(s(t)^2\right) \le -\eta\,|s(t)|, \quad \eta > 0. \tag{33}$$

Theorem 4. *The SMC controller given in* (31) *is asymptotically stable if the gains are chosen as*

$$H_{1,\Gamma_1} > \frac{\eta_1 + |(b_v\xi + \psi\xi - g)\,\omega|}{K_{motor}\xi}, \qquad H_{1,\Gamma_2} > \frac{\eta + |(b_v + \kappa_n - g)\,\omega| + \delta_n\varphi_n\theta}{K_{motor}\varphi_n}. \tag{34}$$

Proof. Select a Lyapunov function candidate for s_1 as

$$V_1 = \frac{1}{2}{s_1}^2, \tag{35}$$

for stage Γ_1.

Substituting (21) and (22) into the first order derivative of (35) yields

$$\dot{V}_1 = \ddot{e}_1 + g\dot{e}_1 = -\left(\frac{d\omega}{dt} + g\omega\right) = (b_v\xi + \psi\xi - g)\,\omega - K_{\text{motor}} i\xi. \tag{36}$$

Based on Remark 3, we have

$$\frac{1}{2}\frac{d}{dt}\left(s_1(t)^2\right) \le -\eta_1\,|s_1(t)|, \quad \eta_1 > 0, \tag{37}$$

when $s_1 > 0$; substituting (31) and (36) into (37),we have

$$s_1\left[(b_v\xi + \psi\xi - g)\,\omega - K_{\text{motor}} i\xi\right] \le -\eta_1 s_1, \tag{38}$$

$$H_{1,s_1>0,\Gamma_1} > \frac{\eta_1 + (b_v\xi + \psi\xi - g)\,\omega}{K_{\text{motor}}\xi}, \tag{39}$$

when $s_1 < 0$; we have

$$s_1\left[\left(b_v\xi + \psi\xi - g\right)\omega - K_{\text{motor}}i\xi\right] \le -\eta_1 s_1, \tag{40}$$

$$H_{1,s_1<0,\Gamma_1} > \frac{\eta_1 - \left(b_v\xi + \psi\xi - g\right)\omega}{K_{\text{motor}}\xi}. \tag{41}$$

Hence, based on (39) and (41), the reachability can be satisfied if

$$H_{1,\Gamma_1} > \frac{\eta_1 + \left|\left(b_v\xi + \psi\xi - g\right)\omega\right|}{K_{\text{motor}}\xi}, \tag{42}$$

for stage Γ_2.

Substituting (27) into the first time derivative of (35), we have

$$\begin{aligned}\dot{V}_1 &= \ddot{e}_1 + g\dot{e}_1 = -\left(\frac{d\omega}{dt} + g\omega\right)\\ &= \left(b_v + \kappa_n - g\right)\omega + \delta_n\varphi_n\theta - K_{\text{motor}}\varphi_n i.\end{aligned} \tag{43}$$

According to Remark 3, the reachability needs to be satisfied,

$$\frac{1}{2}\frac{d}{dt}\left(s_1(t)^2\right) \le -\eta_1\left|s_1(t)\right|, \quad \eta_1 > 0, \tag{44}$$

when $s_1 > 0$; substituting (31) and (43) into (44),we have

$$\left(b_v + \kappa_n - g\right)\omega + \delta_n\varphi_n\theta - K_{\text{motor}}\varphi_n H_{1,\Gamma_2} < -\eta_1, \tag{45}$$

$$H_{1,s_1>0,\Gamma_2} > \frac{\eta_1 + \left(b_v + \kappa_n - g\right)\omega + \delta_n\varphi_n\theta}{K_{\text{motor}}\varphi_n}, \tag{46}$$

when $s_1 < 0$,

$$\left(b_v + \kappa_n - g\right)\omega + \delta_n\varphi_n\theta + K_{\text{motor}}\varphi_n H_{1,\Gamma_2} > \eta_1, \tag{47}$$

$$H_{1,s_1<0,\Gamma_2} > \frac{\eta_1 - \left(b_v + \kappa_n - g\right)\omega - \delta_n\varphi_n\theta}{K_{\text{motor}}\varphi_n}. \tag{48}$$

Hence, based on (46) and (48), the reachability can be satisfied if

$$H_{1,\Gamma_2} > \frac{\eta_1 + \left|\left(b_v + \kappa_n - g\right)\omega\right| + \delta_n\varphi_n\theta}{K_{\text{motor}}\varphi_n}. \tag{49}$$

□

Theorem 5. *The SMC controller given in* (32) *is asymptotically stable if the gains are chosen as*

$$H_2 \ge \eta L_a + R_a i_a + K_{\text{emf}}\omega, \tag{50}$$

which is the reaching condition for the sliding mode.

Note that due to the fact that Theorem 5 shares the same Lyapunov function with Theorem 4, the proof will not be presented here.

Table 1: IEPBs simulation parameters.

Motor (25–30°C)	R_a	0.465 Ω
	K_{emf}	9.947 mV/rad/sec
	K_{motor}	9.947 m-Nm/Amp
Reduction gear	Gear ratio	150 : 1
Screw-nut	Pitch	2 mm
	radius	5 mm

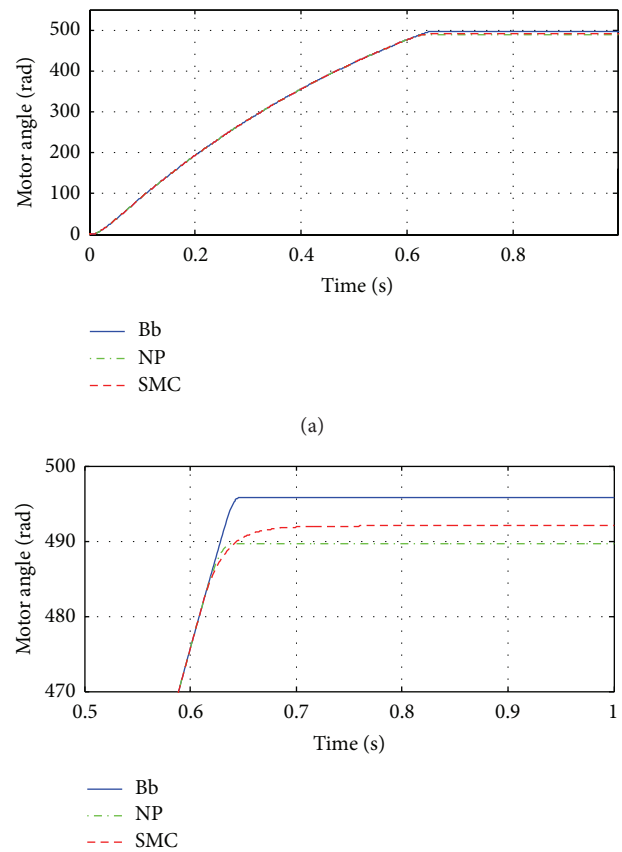

Figure 6: Comparison among three control laws ($\theta_d = 492$ rad). Bb: Bang-bang control. NP: nonlinear Proportion control. SMC: sliding mode control.

4. Simulations and Discussions

In this section, we will study the control performance of the proposed sliding mode control strategy by means of simulation examples. The system parameters and actuator parameters are given in Table 1. The proposed SMC control law is validated by simulation performed in Matlab/Simulink.

Figure 6 shows the target motor angle tracking performance between the Bang-bang control [4], nonlinear Proportion control [3, 7], and sliding mode control with the desired motor angle 492 rad. From Figure 6(a), it is obvious that before 0.6 sec, there is nearly no difference among these three controllers. From Figure 6(b), we can see that the Bang-bang controller leads to a steady state error of 5 rad though it

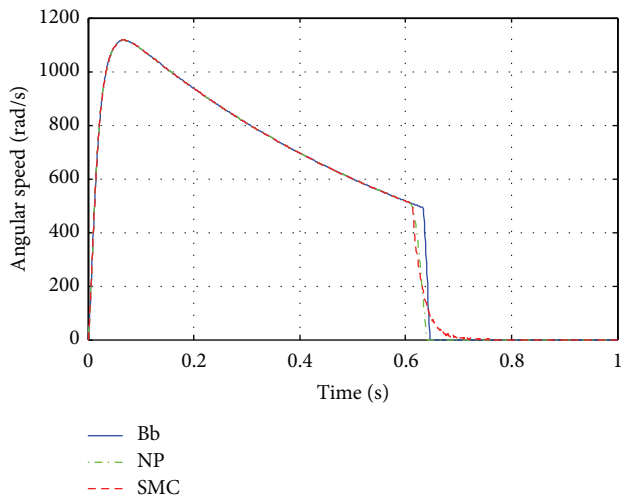

FIGURE 7: Motor speed comparisons among three control laws (θ_d = 492 rad).

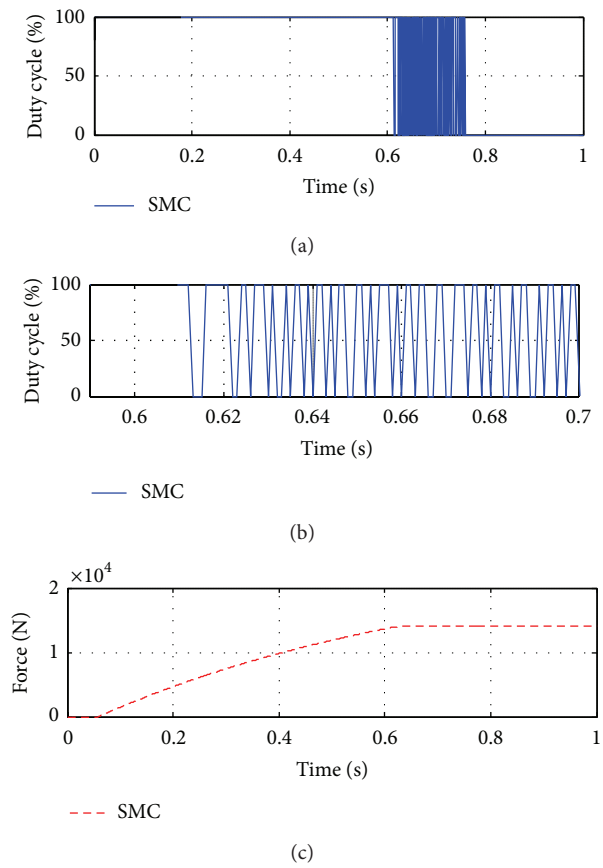

FIGURE 8: Duty cycle and clamping force under SMC (θ_d = 492 rad).

increases to the target first. The nonlinear P controller results in a negative error of 2 rad. In SMC, it is easy to notice that when the motor angle is closing to the target, the gradient is decreasing gradually due to the effects of sliding surfaces. And the SMC controller reaches the 492 rad precisely. Note that for common parking brake maybe the larger force may not lead to dangerous situations. However, IEPBs should have the ability to track the target precisely, because 1 rad angle error can cause hundreds of Newton force error, which may lead to serious condition during the dynamic braking maneuver. On the other hand, compared with the desired clamping force, a larger one can also lead to a releasing problem, since during the releasing mode, the motor needs to rotate contrarily. With the larger clamping force, it may result in a much higher motor current to rotate this nut.

Figure 7 shows the comparisons of three controllers. We can see that before 0.6 s these three speed curves are similar, while after 0.6 s the gradient of SMC speed curve changes due to the sliding surface effect. The NP speed curve gradient also changes based on the angle tracking error. For the bang-bang controller, only if the target 492 rad is reached, the control input will be changed. Hence, based on the analysis of Figure 7, it is easier to understand the motor angle curves in Figure 6.

Based on the analysis for Figures 6 and 7, we know the sliding mode control overmatches the other two control methods with respect to the tracking precision. From Figure 8, we will analyze the control input and the clamping force. In Figure 8(a), the duty cycle of control input is always 100 percent due to the large error before 0.6 s. While from the period 0.6 to 0.77 s shown also in Figure 8(b), it is obvious that the duty cycle is changing fast between 0 and 100 percent, since the trajectory is entering to the sliding surfaces. The clamping force is shown in Figure 8(c). And it can be seen, before 0.06 s, that the clamping force is zero while during the same period the motor angle is increasing to 47 rad as shown in Figures 8(c) and 6. That is because there is gap distance between the nut and the disc that need be cleared first to generate the clamping force.

In order to testify the control robustness with respect to the setpoint value, the desired motor angle is chosen as 300 rad. As can be seen in Figure 9(a), all of these three curves can increase to the value around the target 300 rad and hold steady. From Figure 9(b), it is obvious that the SMC curve reaches the target exactly, while the nonlinear P and Bang-bang have 6.2 rad and 13.6 rad error, respectively.

From Figure 10, we can see that after 0.35 s, the SMC speed curve converges to zero much more gently due to the sliding mode effect when compared with the other two curves. For nonlinear P controller, we can see that due to the nonlinear P control effect, the NP speed curve can change based on the angle error nonlinearly to improve the tracking performance compared with the bang-bang as seen in Figures 9 and 10.

From Figures 11(a) and 11(b), we can see the control input change. The duty cycle is constant 100 percent until 0.31 s. When entering into the sliding surface, the duty cycle of the voltage changes fast to make the trajectory converge to zero. Note that in Figure 11(b), during the period 0.31 s–0.34 s, the duty cycle is also zero. That is because in the first sliding surface $s_1 = \dot{e}_1 + ge_1$, the absolute value of angular speed is larger than the angle error, which results in the negative value of the sliding surface. Correspondingly, the duty cycle

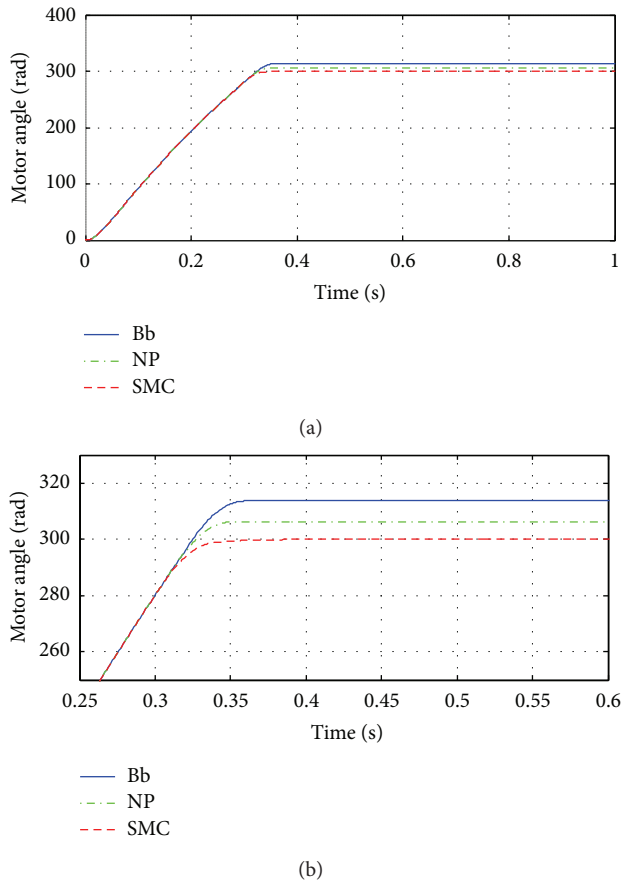

Figure 9: Comparison among three control laws ($\theta_d = 300$ rad).

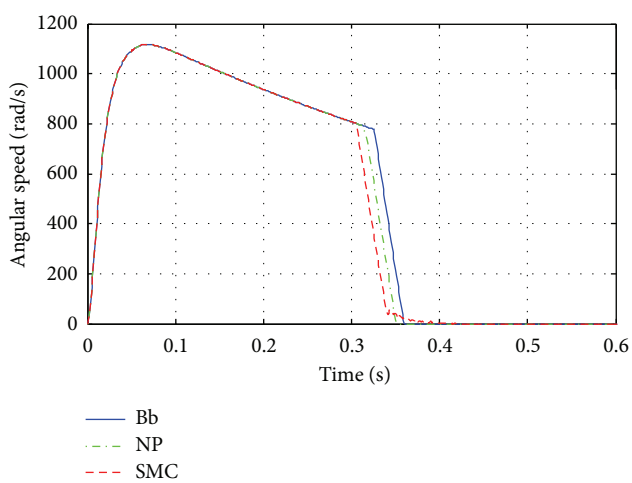

Figure 10: Motor speed comparisons among three control laws ($\theta_d = 300$ rad).

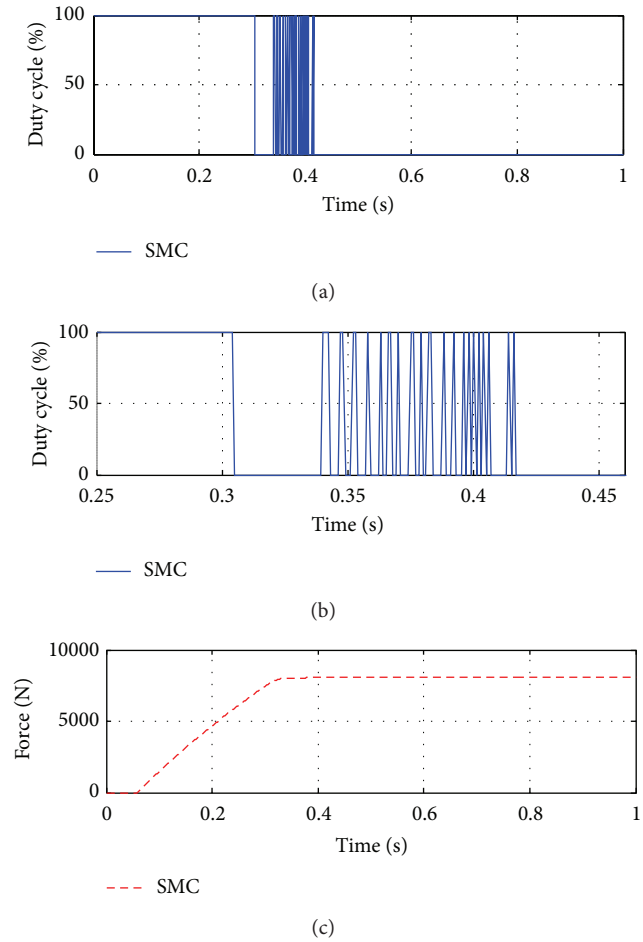

Figure 11: Duty cycle and clamping force under SMC ($\theta_d = 300$ rad).

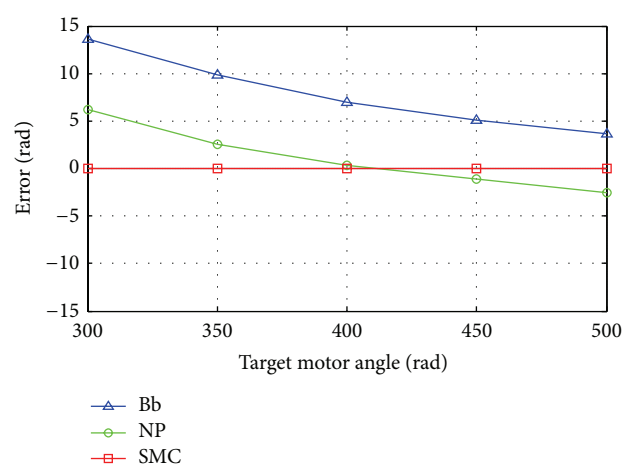

Figure 12: The motor angle errors with three controllers under various set-points.

will be the lowest value to attract the trajectory to zero from the negative orthant. Once the sliding surfaces $s_1 = 0$, $s_2 = 0$ are reached steadily, the motor power can be cut off. The corresponding clamping force is shown in Figure 11(c).

As can be seen in Figure 12, the values of the motor angle errors with three different controllers at each set-point are shown. The positive error implies the redundancy force while the negative erros means the insufficient displacement. Apparently, the SMC curve shows the best performance with no error during the whole targets. NP curve shows the best

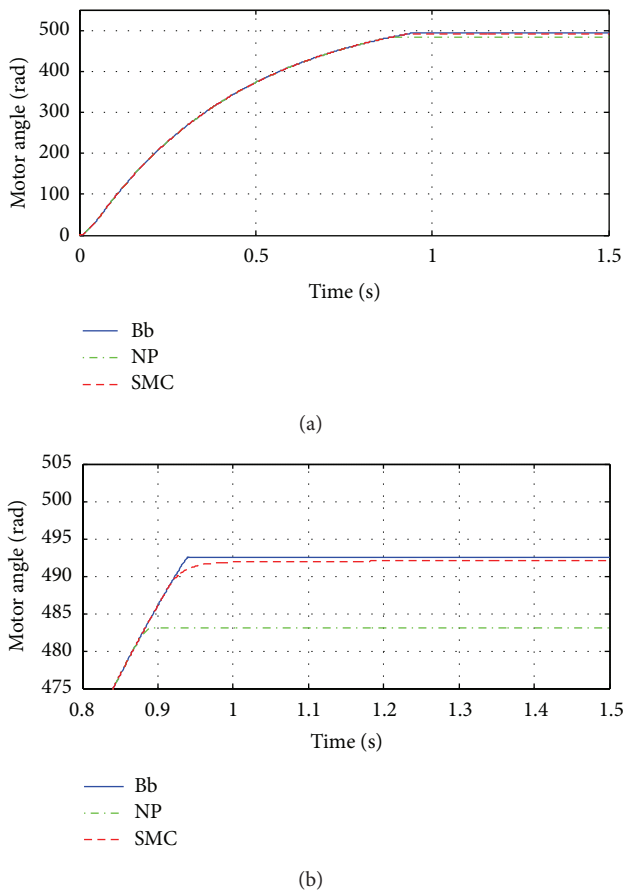

FIGURE 13: The motor angle errors with an increase in screw-nut friction coefficient (θ_d = 492 rad).

performance when the target is 400 rad, while on the other targets the absolute value of the error is increasing. The Bang-bang controller shows the worst performance in terms of the precision, while the error is converging to zero with the increase of the target angle. This good trend may result from the lower angular speed at the power cut-off point.

It is possible that due to the wear of the actuator or the external effects, the friction coefficient of screw-nut system changes. We still take the desired value 492 rad as an example to testify the robustness of these three controllers. The coefficient μ is assumed to change from 0.25 to 0.4 and the performance is shown in Figure 13. Apparently, the NP curve has a larger error, nearly 9 rad, compared with the desired value. Bang-bang shows a better performance with 0.5 rad error, since with the increase of the friction coefficient the angular speed will be lower than the normal status at cut-off point. The SMC curve shows a very good robustness with respect to the friction ratio change.

5. Conclusions

In this paper, a sliding mode control method is utilized to control the clamping force on an integrated electric parking brake system. The working stages are analyzed with a graphical description. By means of the working stages analyses, the stage-switched state-space equations are given with the consideration of friction and system inertia. Based on the system structure from the stage-switched state-space, two sliding surfaces are developed to control the current and angular displacement, respectively. A common Lyapunov function is constructed to guarantee the control system stability. And through the reachability of SMC system, the control gain is also given in this paper. Through these two sliding surfaces, the angle degree set-point can be reached robustly with the gains the scope of which is obtained in the stability section. In the simulation section, three control methods are compared. For each set-point, the Bang-bang controller can track the target but always with a positive error which decreases with the rising of the target displacement; the nonlinear Proportional controller widely used in some published papers can track the target with less error than Bang-bang controller; however, it shows a poor robustness with respect to the friction and set-point variation; the proposed SMC method can track the desired value precisely and robustly. For various set-points, the SMC can track the target value by changing the control input quickly, and under the gain boundary it shows a good robustness with respect to the friction and set-point variation. Based on the relationship between the motor angle and clamping force, the future work is studying the dynamic braking control by IEPBs actuators.

Appendix

Nonlinear P Control

A nonlinear clamping force control law using nonlinear P control theory for traditional EPB system was developed by Lee et al. [3–7]. The control input can be written as

$$u = \begin{cases} K_{p\_nl}|e|^{\alpha}, & \forall e > \delta > 0 \\ K_{p\_nl}\delta^{\alpha-1}, & \forall e \le \delta \\ u_{\min}, & \forall e < 0. \end{cases} \tag{A.1}$$

It applies high gain for small error and small gain for large error.

Nomenclature

b_v: Motor viscous friction coefficient
b_{brake}: Damping coefficient of IEPBs
d_1: Gap between the nut and piston
d_2: Total thickness of pad and piston
d_3: Gap between the friction pad and disc
E_b: Back-EMF voltage
F_f: Friction force
F_v: Screw-nut viscous friction coefficient
$F_{\max\_f}$: Maximum friction force
F_Q: Axial load force
i_a: Motor current
J_m: Moment of inertia
k_{brake}: Stiffness coefficient of the brake system
k_{disk}: Stiffness coefficient of brake disc
k_{head}: Stiffness coefficient of nut
k_{pad}: Stiffness coefficient of pad

k_{caliper}: Stiffness coefficient of and the caliper
K_{emf}: EMF constant
K_{motor}: Motor torque constant
L_a: Inductance
m_{nut}: Mass of nut
N: Gear ratio
R_a: Resistance
T_m: Motor torque
T_F: Motor friction torque
T_L: Screw torque
T_{FC}: Motor dynamic friction torque
$T_{F\max}$: Motor maximum static friction torque
u: Control input
U: Motor Voltage
x_{nut}: Linear displacement of nut
α: Screw lead angle
θ_L: Angular position corresponding to gap
θ: Total angular displacement
ω: Motor angular velocity
ω_s: Stribeck angular velocity
μ_s: Sliding friction coefficient.

Acknowledgments

This work is partially supported by the Fundamental Research Funds for the Central Universities (Grant no. 2012-JL-11), China Scholarship Council Funding (Grant no. 201306950040), and the Wanxiang Group.

References

[1] S. Ralf, R. Isermann, J. Böhm et al., "Clamping force estimation for a brake-by-wire actuator," SAE 1999-01-0482, 1999.

[2] E. A. Bretz, "By-wire cars turn the corner," *IEEE Spectrum*, vol. 38, no. 4, pp. 1–7, 2001.

[3] Y. O. Lee, Y. S. Son, and C. C. Chung, "Clamping force control for an electric parking brake system: switched system approach," *IEEE Transactions on Vehicular Technology*, vol. 62, no. 7, pp. 2937–2948, 2013.

[4] Y. O. Lee, M. Jang, W. Lee, C. W. Lee, C. C. Chung, and Y. S. Son, "Novel clamping force control for electric parking brake systems," *Mechatronics*, vol. 21, no. 7, pp. 1156–1162, 2011.

[5] M. Jang, Y. O. Lee, W. Lee, C. W. Lee, C. C. Chung, and Y. Son, "Novel clamping force control for electric parking brake systems," in *Proceedings of the 7th Asian Control Conference (ASCC '09)*, pp. 1588–1593, Hong Kong, China, August 2009.

[6] Y. O. Lee, C. W. Lee, H. B. Chung et al., "A nonlinear proportional controller for electric parking brake system," SAE 2007-01-3657, 2007.

[7] Y. O. Lee, C. W. Lee, C. C. Chung, Y. Son, P. Yoon, and I.-Y. Hwang, "Stability analysis of an Electric Parking Brake (EPB) systems with a nonlinear proportional controller," in *Proceedings of the 17th World Congress, International Federation of Automatic Control, IFAC*, pp. 14247–14253, Coex, South Korea, July 2008.

[8] C. W. Lee, H. B. Chung, Y. O. Lee, C. C. Chung, Y. S. Son, and P. Yoon, "Fault detection method for electric parking brake (EPB) systems with sensorless estimation using current ripples," *International Journal of Automotive Technology*, vol. 11, no. 3, pp. 387–394, 2010.

[9] K. Kondo and T. Watanabe, Parking brake control system US Patent 8296029 B2, 2012.

[10] S. Saric, A. Bab-Hadiashar, and R. Hoseinnezhad, "Clamp-force estimation for a brake-by-wire system: a sensor-fusion approach," *IEEE Transactions on Vehicular Technology*, vol. 57, no. 2, pp. 778–786, 2008.

[11] C. Line, C. Manzie, and M. Good, "Control of an electromechanical brake for automotive brake-by-wire systems with an adapted motion control architecture," SAE 2004-01-2050, 2004.

[12] C. Jo, S. Hwang, and H. Kim, "Clamping-force control for electromechanical brake," *IEEE Transactions on Vehicular Technology*, vol. 59, no. 7, pp. 3205–3212, 2010.

[13] R. Leiter, "Design and control of an electric parking brake," SAE 2002-01-2583, 2002.

[14] W. Bin, G. Xuexun, Z. Chengcai et al., "Simulation and experiment on electrical parking brake system," *Transactions of the Chinese Society for Agricultural Machinery*, vol. 44, no. 8, pp. 45–49, 2013.

[15] TRW, http://www.trw.com/braking_systems/electric_park_brake/epb.

[16] Mercedes Benz 216 Electric parking brake Control Units, http://www.micro-tronik.com/mercedes_benz_216_electric_parking_brake_(efb)_235.html.

[17] S. Saric, A. Bab-Hadiashar, and J. V. D. Walt, "Estimating clamp force for brake-by-wire systems: thermal considerations," *Mechatronics*, vol. 19, no. 6, pp. 886–895, 2009.

[18] H. Zhang, Y. Shi, and J. Wang, "Observer-based tracking controller design for networked predictive control systems with uncertain Markov delays," *International Journal of Control*, vol. 86, no. 10, pp. 1824–1836, 2013.

[19] H. Zhang, Y. Shi, and M. Liu, "H∞ step tracking control for networked discrete-time nonlinear systems with integral and predictive actions," *IEEE Transactions on Industrial Informatics*, vol. 9, no. 1, pp. 337–345, 2013.

[20] P. Kachroo and M. Tomizuka, "Chattering reduction and error convergence in the sliding-mode control of a class of nonlinear systems," *IEEE Transactions on Automatic Control*, vol. 41, no. 7, pp. 1063–1068, 1996.

[21] H. Zhang, J. Wang, and Y. Shi, "Robust H∞ sliding-mode control for Markovian jump systems subject to intermittent observations and partially known transition probabilities," *Systems & Control Letters*, vol. 62, no. 12, pp. 1114–1124, 2013.

[22] H. Zhang, Y. Shi, and A. Saadat Mehr, "Robust static output feedback control and remote PID design for networked motor systems," *IEEE Transactions on Industrial Electronics*, vol. 58, no. 12, pp. 5396–5405, 2011.

[23] J. Zhang, Y. Tong, X. Zi et al., "Electronic parking brake actuator with cable," Chinese Patent 201120276953.2.

[24] Y. Yong, W. Haotian, G. Xuexun et al., "Design of test bench of the electronic parking brake system," *Chinese Automobile Technology*, vol. 11, no. 1, pp. 40–45, 2012.

[25] H. Olsson, K. J. Åström, C. C. D. Wit, M. Gäfvert, and P. Lischinsky, "Friction models and friction compensation," *European Journal of Control*, vol. 4, no. 3, pp. 1–37, 1998.

[26] O. Vahid and F. Golnaraghi, *Friction-Induced Vibration in Lead Screw Drives*, Springer, New York, NY, USA, 2011.

[27] R. C. Juvinall and K. M. Marshek, *Fundamentals of Machine Component Design*, John Wiley & Sons, New York, NY, USA, 1999.

[28] O. Vahid, N. Eslaminasab, and M. F. Golnaraghi, "Friction-induced vibration in lead screw systems: mathematical modeling and experimental studies," *Transactions of the ASME*, vol. 131, no. 2, pp. 1–10, 2009.

[29] H. Zhang, Y. Shi, and A. S. Mehr, "Robust weighted H∞ filtering for networked systems with intermittent measurements of multiple sensors," *International Journal of Adaptive Control and Signal Processing*, vol. 25, no. 4, pp. 313–330, 2011.

Hindawi Publishing Corporation
Mathematical Problems in Engineering
Volume 2013, Article ID 732939, 9 pages
http://dx.doi.org/10.1155/2013/732939

Research Article

Actuator Saturation Constrained Fuzzy Control for Discrete Stochastic Fuzzy Systems with Multiplicative Noises

Wen-Jer Chang, Cheung-Chieh Ku, and Hao-Jie Liang

Department of Marine Engineering, National Taiwan Ocean University, Keelung 202, Taiwan

Correspondence should be addressed to Wen-Jer Chang; wjchang@mail.ntou.edu.tw

Received 18 August 2013; Revised 3 November 2013; Accepted 3 November 2013

Academic Editor: Hui Zhang

This paper deals with the fuzzy controller design problem for discrete-time Takagi-Sugeno (T-S) fuzzy systems with multiplicative noises. Using the Lyapunov stability theory and Itô formula, the sufficient conditions are derived to guarantee the stability of the closed-loop nonlinear stochastic systems subject to actuator saturation. Based on the Parallel Distributed Compensation (PDC) concept, the fuzzy controller can be obtained to stabilize the T-S fuzzy models with multiplicative noises by combining the same membership functions of plants and desired state feedback gains. In order to illustrate the availability and practicability of proposed fuzzy controller design approach, the numerical simulations for the nonlinear truck-trailer system are given to demonstrate the applications of this paper.

1. Introduction

In recent years, there has been an increasing interest in the fuzzy control of nonlinear systems. Some works have studied the stability and the stabilization of closed-loop fuzzy systems. Specially, these approaches are studied for the T-S fuzzy models which are described by a set of fuzzy "IF-THEN" rules with fuzzy sets in the antecedent and dynamic systems in the consequent part. The subsystems are considered as local linear models, the aggregation of which representing the nonlinear systems. Tanaka and Sugeno [1] presented sufficient conditions for the stability of T-S models. Applying the fuzzy modeling approach, many papers [2–4] have been proposed to investigate the controller design methods of nonlinear systems. According to the discrete T-S fuzzy models, the stability analysis and synthesis have been considered in [5–9]. Not only control schemes [5–8] but also filter design methods [9] have been proposed for nonlinear discrete-time systems via T-S fuzzy model. In general, the stochastic signals and random parameters may exist in the real systems. It is interesting to consider the stochastic behaviors for analyzing the stability of nonlinear stochastic systems. Recently, the T-S fuzzy system with multiplicative noise term [10–16] is structured for representing the nonlinear stochastic system. In [10, 11, 13, 15], the time delay phenomenon is considered in the control problem. Besides, the fuzzy filter design problem for nonlinear stochastic systems is studied in [12]. Different from the traditional additive noise, multiplicative noise is more practical since it allows the statistical description of the noise to be unknown a prior but depends on the control and state solution. Therefore, the T-S fuzzy model with multiplicative noises is considered in this paper to represent the nonlinear stochastic systems.

The presence of actuator saturation imposes additional constraints on the analysis and synthesis of control systems. Addressing actuator saturation has been well recognized to be practically imperative, yet it brings theoretically challenging. Physical capacity of the actuator is limited and the actuator saturation may severely degrade the performance of the closed-loop systems. The actuator saturation usually leads to a large overshoot, induces a limit cycle, and even makes the otherwise stable closed-loop system unstable. This is reflected in the large body of literature on linear and nonlinear systems in the presence of actuator saturation (see, e.g. [17–24]). Recently, some fuzzy control approaches for nonlinear systems subject to actuator saturation were investigated in [19–24]. Most of recent papers studied the fuzzy controller design problem of continuous-time nonlinear systems subject to actuator saturation. However, few papers [21] have been

proposed to investigate the similar problems for discrete nonlinear systems, especially for discrete nonlinear stochastic systems. In general, the saturation function is characterized in terms of convex hull of some linear combinations of linear function and saturation function [19]. However, the number of stability conditions increases dramatically with the number of control inputs. In [22], the saturation function is formulated inside a specific nonlinear saturation sector that provides less stability condition numbers. The saturation function formulated in [22] has not been employed to deal with the actuator saturation constrained control problem for the discrete-time T-S fuzzy model with multiplicative noises. Thus, the motivation of this paper is to discuss fuzzy control problem of discrete-time nonlinear stochastic system with multiplicative noises and actuator saturation. The actuator saturation function formulated in [22] is employed in this paper to design a stable fuzzy controller.

To deal with a performance constrained control problem for the nonlinear T-S fuzzy stochastic systems, a fuzzy controller design subject to actuator saturation is investigated in this paper. Based on the PDC concept [25], the fuzzy controller can be obtained by combining the same membership functions of plant and linear feedback gains of subsystems. Thus, the overall system input can be blended by these linear feedback gains. Usually, the sufficient conditions are derived into Linear Matrix Inequality (LMI) forms [26] which can be calculated by optimal convex algorithm [27] for finding a common definite matrix and feedback gains. According to the actuator saturation function formulated in [22], the contribution of this paper is to develop a PDC-based fuzzy controller design methodology for guaranteeing the stability of discrete-time T-S fuzzy models with multiplicative noises. In order to demonstrate the applicability and effectiveness of the proposed design approach, the fuzzy controller design problem of a truck-trailer system [28] subject to actuator saturation is discussed in this paper.

The organization of this paper is structured as follows. The structure of T-S fuzzy model with multiplicative noises is introduced in Section 2. In Section 3, a fuzzy controller design methodology is developed by using the concept of PDC and the Lyapunov stability criterion. Through applying the proposed fuzzy controller design approach, simulation results for the nonlinear stochastic truck-trailer systems are demonstrated in Section 4. Finally, some conclusions are proposed in Section 5.

2. System Descriptions and Problem Statements

The T-S fuzzy model is described by fuzzy IF-THEN rules, which represent local linear input-output relations of the nonlinear systems. This section outlines the mathematical model of the T-S fuzzy model with multiplicative noise for the discrete-time nonlinear stochastic systems. The i-th rule of T-S fuzzy model is introduced in the following form.

2.1. Plant Part

Rule i

$$\begin{aligned} &\text{IF} \quad z_1(k) \text{ is } M_{i1} \cdots \text{and } z_p(k) \text{ is } M_{ip} \\ &\text{THEN} \quad x(k+1) = \mathbf{A}_i x(k) + \mathbf{B}_i \overline{u}(k) \\ &\qquad + \left(\overline{\mathbf{A}}_i x(k) + \overline{\mathbf{B}}_i \overline{u}(k)\right) w(k), \end{aligned} \tag{1}$$

where $\mathbf{A}_i \in \mathbb{R}^{n\times n}$, $\mathbf{B}_i \in \mathbb{R}^{n\times m}$, $\overline{\mathbf{A}}_i \in \mathbb{R}^{n\times n}$, and $\overline{\mathbf{B}}_i \in \mathbb{R}^{n\times m}$ are constant matrices, $i = 1, 2, \ldots, r$ and r is the number of fuzzy rules, and $z_1(k), z_2(k), \ldots, z_p(k)$ are premise variables. Besides, $x(k) \in \mathbb{R}^n$ denotes the state vector, $\overline{u}(k) = \text{sat}(u(k)) \in \mathbb{R}^m$ denotes the saturating control input, and $w(k)$ is a scalar zero mean white noise with variance one.

In this paper, the saturating actuator is defined as follows:

$$\overline{u}_k(k) = \text{sat}(u_k) = \begin{cases} u_{kL} & \text{if } u_k < u_{kL} \\ u_k & \text{if } u_{kL} \le u_k \le u_{kH} \\ u_{kH} & \text{if } u_{kH} < u_k, \end{cases} \tag{2}$$

where $u_{kL} < 0 < u_{kH}$ and $k = 1, 2, \ldots, m$.

Given a pair of $(x(k), \overline{u}(k))$, the final output of the fuzzy system is inferred as follows:

$$\begin{aligned} &x(k+1) \\ &= \left(\sum_{i=1}^{r} \omega_i(z(k)) \right. \\ &\qquad \left. \times \left\{\mathbf{A}_i x(k) + \mathbf{B}_i \overline{u}(k) + \left(\overline{\mathbf{A}}_i x(k) + \overline{\mathbf{B}}_i \overline{u}(k)\right) w(k)\right\}\right) \\ &\quad \times \left(\sum_{i=1}^{r} \omega_i(z(k))\right)^{-1} \\ &= \sum_{i=1}^{r} h_i(z(k)) \left\{\mathbf{A}_i x(k) + \mathbf{B}_i \overline{u}(k) \right. \\ &\qquad \left. + \left(\overline{\mathbf{A}}_i x(k) + \overline{\mathbf{B}}_i \overline{u}(k)\right) w(k)\right\}, \end{aligned} \tag{3}$$

where $z(k) = [z_1(k) z_2(k) \cdots z_p(k)]^T$, $h_i(z(k)) = \omega_i(z(k)) / \sum_{i=1}^{r} \omega_i(z(k))$ and $\omega_i(z(k)) = \prod_{j=1}^{p} M_{ij}(z_j(k))$. Note that $h_i(z(k)) \ge 0$ and $\sum_{i=1}^{r} h_i(z(k)) = 1$.

Considering the saturating actuator, one can formulate the following inequality from relations of $\overline{u}_k(k)$ defined in (2):

$$\|u(k)\| \ge \|\overline{u}(k)\|. \tag{4}$$

The following inequality can be derived from the inequality (4) and Remark 1 of [22]:

$$\frac{1-\varepsilon}{2} \|u(k)\| \ge \left\|\overline{u}(k) - \frac{1+\varepsilon}{2} u(k)\right\|, \tag{5}$$

where $0 < \varepsilon < 1$. The sector parameter ε can be used to guarantee that the saturation map sat is inside the sector

$(\varepsilon, 1)$. The inequality (5) can be arranged by $u_{kH} \geq \varepsilon u_k$ and $u_{kL} \leq \varepsilon u_k$ as follows:

$$\frac{u_{kL}}{\varepsilon} \leq u_k \leq \frac{u_{kH}}{\varepsilon}, \qquad k = 1, 2, \ldots, m. \tag{6}$$

In this paper, one can find that if $u_{kH} = -u_{kL}$ is set, then one has

$$|u_k| \leq \frac{u_{kH}}{\varepsilon}. \tag{7}$$

Expanding the inequality (5), one can obtain the following inequality:

$$\begin{aligned} &\left(\overline{u}(k) - \frac{1+\varepsilon}{2} u(k)\right)^T \left(\overline{u}(k) - \frac{1+\varepsilon}{2} u(k)\right) \\ &\quad \leq \left(\frac{1-\varepsilon}{2}\right)^2 u^T(k)\, u(k). \end{aligned} \tag{8}$$

The inequality (8) is an important basis in the following derivations of this paper. According to the sector parameter ε, the state equation (3) can be rewritten as

$$\begin{aligned} x(k+1) &= \sum_{i=1}^{r} h_i(z(k)) \\ &\quad \times \left\{\mathbf{A}_i x(k) + \mathbf{B}_i \overline{u}(k) + \overline{\mathbf{A}}_i w(k)\, x(k) + \overline{\mathbf{B}}_i w(k)\, \overline{u}(k)\right\} \\ &= \sum_{i=1}^{r} h_i(z(k)) \left\{\mathbf{A}_i x(k) + \mathbf{B}_i \left(\frac{1+\varepsilon}{2}\right) u(k) \right. \\ &\qquad + \mathbf{B}_i \left(\overline{u}(k) - \frac{1+\varepsilon}{2} u(k)\right) \\ &\qquad + \overline{\mathbf{A}}_i w(k)\, x(k) + \overline{\mathbf{B}}_i w(k) \left(\frac{1+\varepsilon}{2}\right) u(k) \\ &\qquad \left. + \overline{\mathbf{B}}_i w(k) \left(\overline{u}(k) - \frac{1+\varepsilon}{2} u(k)\right)\right\}. \end{aligned} \tag{9}$$

Based on the PDC concept [25], the fuzzy controller can be proposed as follows.

2.2. Controller Part

Rule i

$$\begin{aligned} &\text{IF} \quad z_1(k) \text{ is } M_{i1} \cdots \text{and } z_p(k) \text{ is } M_{ip} \\ &\text{THEN} \quad u(k) = \mathbf{K}_i x(k) \quad \text{for } i = 1, 2, \ldots, r, \end{aligned} \tag{10}$$

where $\mathbf{K}_i \in \mathbb{R}^{m \times n}$ are constant feedback matrices. The output of PDC-based fuzzy controller (10) is determined by the summation

$$u(k) = \frac{\sum_{i=1}^{r} \omega_i(z(k)) \left(\mathbf{K}_i x(k)\right)}{\sum_{i=1}^{r} \omega_i(z(k))} = \sum_{i=1}^{r} h_i(z(k)) \left(\mathbf{K}_i x(k)\right). \tag{11}$$

By substituting (11) into (9), one can obtain the corresponding closed-loop system as follows:

$$\begin{aligned} x(k+1) &= \sum_{i=1}^{r} h_i(z(k)) \\ &\quad \times \left\{\mathbf{A}_i x(k) + \mathbf{B}_i \overline{u}(k) + \left(\overline{\mathbf{A}}_i x(k) + \overline{\mathbf{B}}_i \overline{u}(k)\right) w(k)\right\} \\ &= \sum_{i=1}^{r}\sum_{j=1}^{r} h_i(z(k))\, h_j(z(k)) \left\{\mathbf{A}_{ij} x(k) + \overline{\mathbf{A}}_{ij} w(k)\, x(k) \right. \\ &\qquad + \mathbf{B}_i \left(\overline{u}(k) - \frac{1+\varepsilon}{2} \mathbf{K}_j x(k)\right) \\ &\qquad + \overline{\mathbf{B}}_i w(k) \\ &\qquad \left. \times \left(\overline{u}(k) - \frac{1+\varepsilon}{2} \mathbf{K}_j x(k)\right)\right\}, \end{aligned} \tag{12}$$

where $\mathbf{A}_{ij} = \mathbf{A}_i + ((1+\varepsilon)/2)\mathbf{B}_i \mathbf{K}_j$ and $\overline{\mathbf{A}}_{ij} = \overline{\mathbf{A}}_i + ((1+\varepsilon)/2)\overline{\mathbf{B}}_i \mathbf{K}_j$. After arranging (12), the augmented system can be derived in the following form:

$$\begin{aligned} x(k+1) &= \sum_{i=1}^{r} h_i^2(z(k)) \\ &\quad \times \left\{\mathbf{A}_{ii} x(k) + \overline{\mathbf{A}}_{ii} w(k)\, x(k) \right. \\ &\qquad + \mathbf{B}_i \left(\overline{u}(k) - \frac{1+\varepsilon}{2} \mathbf{K}_i x(k)\right) \\ &\qquad \left. + \overline{\mathbf{B}}_i w(k) \left(\overline{u}(k) - \frac{1+\varepsilon}{2} \mathbf{K}_i x(k)\right)\right\} \\ &\quad + 2\sum_{i=1}^{r}\sum_{i<j}^{r} h_i(z(k))\, h_j(z(k)) \\ &\quad \times \left\{\frac{1}{2}\left(\left(\mathbf{A}_{ij} + \mathbf{A}_{ji}\right) x(k) + \left(\overline{\mathbf{A}}_{ij} + \overline{\mathbf{A}}_{ji}\right) w(k)\, x(k) \right.\right. \\ &\qquad + \left(\mathbf{B}_i \left(\overline{u}(k) - \frac{1+\varepsilon}{2} \mathbf{K}_j x(k)\right) \right. \\ &\qquad \left. + \mathbf{B}_j \left(\overline{u}(k) - \frac{1+\varepsilon}{2} \mathbf{K}_i x(k)\right)\right) \\ &\qquad + \left(\overline{\mathbf{B}}_i \left(\overline{u}(k) - \frac{1+\varepsilon}{2} \mathbf{K}_j x(k)\right) \right. \\ &\qquad \left.\left.\left. + \overline{\mathbf{B}}_j w(k) \left(\overline{u}(k) - \frac{1+\varepsilon}{2} \mathbf{K}_i x(k)\right)\right)\right)\right\}. \end{aligned} \tag{13}$$

Let an ellipsoid Ω_1 and a positive scalar function $V(x(k))$ be defined as follows, respectively:

$$\Omega_1 = \left\{x(k) \mid x^T(k)\mathbf{P}x(k) \le 1\right\}, \qquad V(x(k)) = x^T(k)\mathbf{P}x(k), \tag{14}$$

where $\mathbf{P} \in \mathbb{R}^{n\times n}$ denotes a positive definite matrix. The ellipsoid Ω_1, which is inside the domain of attraction, is said to be contractively invariant [19] if the following condition can be satisfied:

$$\Delta V(x(k)) < 0, \quad \forall x(k) \in \Omega_1 \setminus \{0\}. \tag{15}$$

From (7) and (11), the constraint $|u_k| \le u_{kH}/\varepsilon$ can be inferred as follows:

$$\left|\sum_{i=1}^{r} h_i(z(k))\left(\mathbf{K}_i^{(k)}x(k)\right)\right| \le \frac{u_{kH}}{\varepsilon}, \tag{16}$$

where $\mathbf{K}_i^{(k)}$ denotes the k-th row of $\mathbf{K}_i$. It is obvious that if (16) holds with $h_i(z(k)) = 1$, then one can define the following equation:

$$\Omega_2 = \left\{x(k) \mid x^T(k)\left(\mathbf{K}_i^{(k)}\right)^T\left(\mathbf{K}_i^{(k)}\right)x(k) \le \left(\frac{u_{kH}}{\varepsilon}\right)^2\right\}. \tag{17}$$

In this paper, it is required that $x(k) \in \Omega_1 \subset \Omega_2$; that is, Ω_1 is a subset of Ω_2. The equivalent condition for $x(k) \in \Omega_1 \subset \Omega_2$ can be represented as follows:

$$\left(\mathbf{K}_i^{(k)}\right)\mathbf{P}^{-1}\left(\mathbf{K}_i^{(k)}\right)^T \le \left(\frac{u_{kH}}{\varepsilon}\right)^2. \tag{18}$$

Considering the discrete-time T-S fuzzy model with multiplicative noises (1), the purpose of this paper is to find the solutions of PDC-based fuzzy controller (11) subject to actuator saturation defined in (2). Employing the Lyapunov stability criterion and Itô formula, the stability conditions are derived in the next section. Solving these stability conditions, the feedback gains $\mathbf{K}_i$ of PDC-based fuzzy controller (11) can be used to stabilize the discrete-time T-S fuzzy model with multiplicative noises (1) subject to the constraint of actuator saturation (2).

3. Stability Conditions Derivations and Fuzzy Controller Design

In this section, the stability conditions are derived for the closed-loop system (12) subject to actuator saturation (2). Before describing the stability conditions, the Lyapunov function is defined in the following equation which satisfies $x(0) \in \Omega_1 \subset \Omega_2$ and $x(k) \in \Omega_1 \subset \Omega_2$, for all $k \ge 0$:

$$V(x(k)) = x^T(k)\mathbf{P}x(k). \tag{19}$$

Based on the Lyapunov function (19), one can obtain the following theorem for analyzing the stability of augmented system (12).

Theorem 1. *Considering the actuator saturation* (2), *the closed-loop system* (12) *is asymptotically stable if there exist matrix* $\mathbf{Q} = \mathbf{Q}^T > 0$ *and feedback gains* $\mathbf{K}_i$ *such that*

$$\begin{bmatrix} -\mathbf{Q} & \mathbf{Q}\mathbf{A}_i^T + \mathbf{Y}_j^T\mathbf{B}_i^T & \mathbf{Q}\overline{\mathbf{A}}_i^T + \mathbf{Y}_j^T\overline{\mathbf{B}}_i^T \\ * & -\mathbf{Q} & 0 \\ * & * & -\mathbf{Q} \end{bmatrix} < 0 \tag{20}$$

$$\begin{bmatrix} \ell & \frac{1+\varepsilon}{2}\mathbf{Y}_i^{(k)} \\ * & \mathbf{Q} \end{bmatrix} \ge 0, \tag{21}$$

where $\mathbf{Q} = \mathbf{P}^{-1}$, $\mathbf{Y}_i = \mathbf{K}_i\mathbf{Q}$, $\mathbf{Y}_i^{(k)} = \mathbf{K}_i^{(k)}\mathbf{Q}$, *and* $\ell = ((1+\varepsilon)/2)^2(u_{kH}/\varepsilon)^2$ *and* $*$ *denotes the transposed element in the symmetric position.*

Proof. By choosing the Lyapunov function defined in (19), one can obtain

$$\Delta V(x(k)) = V(x(k+1)) - V(x(k)). \tag{22}$$

According to the Lyapunov function (19) and the closed-loop system (12), one can get

$$\begin{aligned}
&V(x(k+1)) \\
&\quad = x^T(k+1)\mathbf{P}x(k+1) \\
&\quad = \sum_{i=1}^{r}\sum_{j=1}^{r} h_i(z(k))h_j(z(k)) \\
&\qquad \times \Bigg\{\Bigg(\mathbf{A}_{ij}x(k) + \mathbf{B}_i\left(\overline{u}(k) - \frac{1+\varepsilon}{2}\mathbf{K}_jx(k)\right) \\
&\qquad\qquad + \overline{\mathbf{A}}_{ij}w(k)x(k) \\
&\qquad\qquad + \overline{\mathbf{B}}_iw(k)\left(\overline{u}(k) - \frac{1+\varepsilon}{2}\mathbf{K}_jx(k)\right)\Bigg)^T \\
&\qquad\quad \times \mathbf{P}\Bigg(\mathbf{A}_{ij}x(k) + \mathbf{B}_i\left(\overline{u}(k) - \frac{1+\varepsilon}{2}\mathbf{K}_jx(k)\right) \\
&\qquad\qquad + \overline{\mathbf{A}}_{ij}w(k)x(k) + \overline{\mathbf{B}}_iw(k) \\
&\qquad\qquad \times\left(\overline{u}(k) - \frac{1+\varepsilon}{2}\mathbf{K}_jx(k)\right)\Bigg)\Bigg\} \\
&\quad = \sum_{i=1}^{r} h_i^2(z(k)) \\
&\qquad \times \Bigg\{\Bigg(\mathbf{A}_{ii}x(k) + \mathbf{B}_i\left(\overline{u}(k) - \frac{1+\varepsilon}{2}\mathbf{K}_ix(k)\right)
\end{aligned}$$

$$
\begin{aligned}
&+\overline{\mathbf{A}}_{ii}x(k)+\overline{\mathbf{B}}_i\left(\overline{u}(k)-\frac{1+\varepsilon}{2}\mathbf{K}_ix(k)\right)\Bigg)^T\\
&\times\mathbf{P}\Bigg(\mathbf{A}_{ii}x(k)+\mathbf{B}_i\left(\overline{u}(k)-\frac{1+\varepsilon}{2}\mathbf{K}_ix(k)\right)\\
&\quad+\overline{\mathbf{A}}_{ii}x(k)+\overline{\mathbf{B}}_i\left(\overline{u}(k)-\frac{1+\varepsilon}{2}\mathbf{K}_ix(k)\right)\Bigg)\Bigg\}\\
&+2\sum_{i=1}^{r}\sum_{i<j}^{r}h_i(z(k))h_j(z(k))\\
&\times\Bigg\{\frac{1}{2}\Bigg(\mathbf{A}_{ij}x(k)+\mathbf{B}_i\left(\overline{u}(k)-\frac{1+\varepsilon}{2}\mathbf{K}_jx(k)\right)\\
&\quad+\mathbf{A}_{ji}x(k)+\mathbf{B}_j\left(\overline{u}(k)-\frac{1+\varepsilon}{2}\mathbf{K}_ix(k)\right)\\
&\quad+\overline{\mathbf{A}}_{ij}x(k)+\overline{\mathbf{B}}_i\left(\overline{u}(k)-\frac{1+\varepsilon}{2}\mathbf{K}_jx(k)\right)\\
&\quad+\overline{\mathbf{A}}_{ji}x(k)+\overline{\mathbf{B}}_j\left(\overline{u}(k)-\frac{1+\varepsilon}{2}\mathbf{K}_ix(k)\right)\Bigg)^T\\
&\times\mathbf{P}\Bigg(\frac{1}{2}\Bigg(\mathbf{A}_{ij}x(k)+\mathbf{B}_i\left(\overline{u}(k)-\frac{1+\varepsilon}{2}\mathbf{K}_jx(k)\right)\\
&\quad+\mathbf{A}_{ji}x(k)+\mathbf{B}_j\left(\overline{u}(k)-\frac{1+\varepsilon}{2}\mathbf{K}_ix(k)\right)\\
&\quad+\overline{\mathbf{A}}_{ij}x(k)+\overline{\mathbf{B}}_i\left(\overline{u}(k)-\frac{1+\varepsilon}{2}\mathbf{K}_jx(k)\right)\\
&\quad+\overline{\mathbf{A}}_{ji}x(k)+\overline{\mathbf{B}}_j\left(\overline{u}(k)-\frac{1+\varepsilon}{2}\mathbf{K}_ix(k)\right)\Bigg)\Bigg)\Bigg\}.
\end{aligned}
\tag{23}
$$

According to (8), (23), and the fact that $\mathbf{X}^T\mathbf{Y}+\mathbf{Y}^T\mathbf{X}\le\mathbf{X}^T\mathbf{X}+\mathbf{Y}^T\mathbf{Y}$, the inequality (22) can be arranged as follows:

$$
\begin{aligned}
&\Delta V(x(k))\\
&\le\sum_{i=1}^{r}\sum_{i<j}^{r}h_i(z(k))h_j(z(k))x^T(k)\\
&\times\Bigg\{\frac{1}{4}\Bigg(\mathbf{A}_{ij}^T\mathbf{P}\mathbf{A}_{ij}+\mathbf{A}_{ij}^T\mathbf{P}\mathbf{A}_{ji}+\mathbf{A}_{ji}^T\mathbf{P}\mathbf{A}_{ij}+\mathbf{A}_{ji}^T\mathbf{P}\mathbf{A}_{ji}\\
&\quad+\mathbf{A}_{ij}^T\mathbf{P}\mathbf{B}_i\left(\frac{1-\varepsilon}{2}\mathbf{K}_j\right)+\mathbf{A}_{ij}^T\mathbf{P}\mathbf{B}_j\left(\frac{1-\varepsilon}{2}\mathbf{K}_i\right)\\
&\quad+\mathbf{A}_{ji}^T\mathbf{P}\mathbf{B}_i\left(\frac{1-\varepsilon}{2}\mathbf{K}_j\right)+\mathbf{A}_{ji}^T\mathbf{P}\mathbf{B}_j\left(\frac{1-\varepsilon}{2}\mathbf{K}_i\right)\\
&\quad+\left(\frac{1-\varepsilon}{2}\mathbf{K}_j\right)^T\mathbf{B}_i^T\mathbf{P}\mathbf{A}_{ij}+\left(\frac{1-\varepsilon}{2}\mathbf{K}_j\right)^T\mathbf{B}_i^T\mathbf{P}\mathbf{A}_{ji}\\
&\quad+\left(\frac{1-\varepsilon}{2}\mathbf{K}_i\right)^T\mathbf{B}_j^T\mathbf{P}\mathbf{A}_{ij}+\left(\frac{1-\varepsilon}{2}\mathbf{K}_i\right)^T\mathbf{B}_j^T\mathbf{P}\mathbf{A}_{ji}\\
&\quad+\left(\frac{1-\varepsilon}{2}\mathbf{K}_j\right)^T\mathbf{B}_i^T\mathbf{P}\mathbf{B}_i\left(\frac{1-\varepsilon}{2}\mathbf{K}_j\right)\\
&\quad+\left(\frac{1-\varepsilon}{2}\mathbf{K}_j\right)^T\mathbf{B}_i^T\mathbf{P}\mathbf{B}_j\left(\frac{1-\varepsilon}{2}\mathbf{K}_i\right)\\
&\quad+\left(\frac{1-\varepsilon}{2}\mathbf{K}_i\right)^T\mathbf{B}_j^T\mathbf{P}\mathbf{B}_i\left(\frac{1-\varepsilon}{2}\mathbf{K}_j\right)\\
&\quad+\left(\frac{1-\varepsilon}{2}\mathbf{K}_i\right)^T\mathbf{B}_j^T\mathbf{P}\mathbf{B}_j\left(\frac{1-\varepsilon}{2}\mathbf{K}_i\right)\\
&\quad+\overline{\mathbf{A}}_{ij}^T\mathbf{P}\overline{\mathbf{A}}_{ij}+\overline{\mathbf{A}}_{ij}^T\mathbf{P}\overline{\mathbf{A}}_{ji}+\overline{\mathbf{A}}_{ji}^T\mathbf{P}\overline{\mathbf{A}}_{ij}+\overline{\mathbf{A}}_{ji}^T\mathbf{P}\overline{\mathbf{A}}_{ji}\\
&\quad+\overline{\mathbf{A}}_{ij}^T\mathbf{P}\overline{\mathbf{B}}_i\left(\frac{1-\varepsilon}{2}\mathbf{K}_j\right)+\overline{\mathbf{A}}_{ij}^T\mathbf{P}\overline{\mathbf{B}}_j\left(\frac{1-\varepsilon}{2}\mathbf{K}_i\right)\\
&\quad+\overline{\mathbf{A}}_{ji}^T\mathbf{P}\overline{\mathbf{B}}_i\left(\frac{1-\varepsilon}{2}\mathbf{K}_j\right)+\overline{\mathbf{A}}_{ji}^T\mathbf{P}\overline{\mathbf{B}}_j\left(\frac{1-\varepsilon}{2}\mathbf{K}_i\right)\\
&\quad+\left(\frac{1-\varepsilon}{2}\mathbf{K}_j\right)^T\overline{\mathbf{B}}_i^T\mathbf{P}\overline{\mathbf{A}}_{ij}+\left(\frac{1-\varepsilon}{2}\mathbf{K}_j\right)^T\overline{\mathbf{B}}_i^T\mathbf{P}\overline{\mathbf{A}}_{ji}\\
&\quad+\left(\frac{1-\varepsilon}{2}\mathbf{K}_i\right)^T\overline{\mathbf{B}}_j^T\mathbf{P}\overline{\mathbf{A}}_{ij}+\left(\frac{1-\varepsilon}{2}\mathbf{K}_i\right)^T\overline{\mathbf{B}}_j^T\mathbf{P}\overline{\mathbf{A}}_{ji}\\
&\quad+\left(\frac{1-\varepsilon}{2}\mathbf{K}_j\right)^T\overline{\mathbf{B}}_i^T\mathbf{P}\overline{\mathbf{B}}_i\left(\frac{1-\varepsilon}{2}\mathbf{K}_j\right)\\
&\quad+\left(\frac{1-\varepsilon}{2}\mathbf{K}_j\right)^T\overline{\mathbf{B}}_i^T\mathbf{P}\overline{\mathbf{B}}_j\left(\frac{1-\varepsilon}{2}\mathbf{K}_i\right)\\
&\quad+\left(\frac{1-\varepsilon}{2}\mathbf{K}_i\right)^T\overline{\mathbf{B}}_j^T\mathbf{P}\overline{\mathbf{B}}_i\left(\frac{1-\varepsilon}{2}\mathbf{K}_j\right)+\left(\frac{1-\varepsilon}{2}\mathbf{K}_i\right)^T\\
&\quad\times\overline{\mathbf{B}}_j^T\mathbf{P}\overline{\mathbf{B}}_j\left(\frac{1-\varepsilon}{2}\mathbf{K}_i\right)\Bigg)\Bigg\}x(k)-x^T(k)\mathbf{P}x(k)\\
&=\sum_{i=1}^{r}\sum_{i<j}^{r}h_i(z(k))h_j(z(k))x^T(k)\mathbf{P}\Theta_{ij}\mathbf{P}x(k),
\end{aligned}
\tag{24}
$$

where

$$
\begin{aligned}
\Theta_{ij}=\mathbf{P}^{-1}\Big(&\left(\mathbf{A}_i+\mathbf{B}_i\mathbf{K}_j\right)^T\mathbf{P}\left(\mathbf{A}_i+\mathbf{B}_i\mathbf{K}_j\right)\\
&+\left(\overline{\mathbf{A}}_i+\overline{\mathbf{B}}_i\mathbf{K}_j\right)^T\mathbf{P}\left(\overline{\mathbf{A}}_i+\overline{\mathbf{B}}_i\mathbf{K}_j\right)-\mathbf{P}\Big)\mathbf{P}^{-1}.
\end{aligned}
\tag{25}
$$

Using the Schur complement [26], the condition (20) is equivalent to $\Theta_{ij}<0$. Obviously, if the condition (20) of Theorem 1 is satisfied, then $\Delta V(x(k))<0$ can be obtained from (25). Therefore, the condition (20) is provided for guaranteeing the asymptotical stability of the closed-loop system (12). Additionally, using the Schur complement [26], the following relation can be obtained from (18):

$$
\begin{bmatrix}\ell_2 & \frac{1+\varepsilon}{2}\mathbf{Y}_i^{(k)}\\ * & \mathbf{Q}\end{bmatrix}\ge 0,
\tag{26}
$$

where $\mathbf{Y}_i^{(k)}=\mathbf{K}_i^{(k)}\mathbf{Q}$ and $\ell_2=((1+\varepsilon)/2)^2(u_{kH}/\varepsilon)^2$. Obviously, the inequality (26) is equivalent to the condition (21). Hence, if the condition (21) is satisfied, then (26) holds and the actuator saturation constraint is achieved. Therefore, if the conditions (20)-(21) are held, then the closed-loop system (12) is asymptotically stable subject to actuator saturation (2). □

Remark 2. In Theorem 1, the sufficient conditions (20) and (21) are derived into LMI problems that can be directly calculated via optimal convex algorithm [27]. In the conditions of Theorem 1, the variables $\mathbf{P}$ and $\mathbf{K}_i$ are needed to be found. With increasing the number of fuzzy rules, the number of inequality conditions is increasing such that the difficulty of finding the desired variables is also increased. Thus, the computational complexity of the proposed approach will be increased when the number of fuzzy rules is arisen. For reducing the computational complexity, the nonlinear system is recommended to be modeled by T-S fuzzy model as less fuzzy rules as possible.

Remark 3. The fuzzy control problem for discrete-time nonlinear systems subject to actuator saturation has been discussed in [21]. Based on the saturation function of [21], the number of stability conditions is increased dramatically when the number of control inputs is increased. For this reason, the authors of [22] propose a novel function to formulate actuator saturation such that the energy of controller can be limited in a specific nonlinear saturation sector. Referring to [22], the number of stability conditions is not increased when the number of control inputs is increased. Based on the actuator saturation described in [22], the stability conditions of fuzzy controller design are derived in Theorem 1 for the discrete-time nonlinear stochastic system with multiplicative noises.

The LMI stability conditions (20)-(21) have been derived in Theorem 1 to guarantee the stability of T-S fuzzy model with multiplicative noises subject to actuator saturation. In the following section, a truck-trailer system is proposed to demonstrate the application and usefulness of the proposed fuzzy controller design approach.

4. Numerical Simulations for the Control of Nonlinear Truck-Trailer Systems

Applying the proposed fuzzy controller design approach, the control problem subject to actuator saturation for a nonlinear discrete-time truck-trailer model [28] is studied in this section. The considered truck-trailer system is depicted in Figure 1. According to Figure 1, the dynamic equations of the nonlinear discrete-time truck-trailer system can be described as follows:

$$x_0(k+1) = x_0(k) + \frac{v \times \Delta t}{L_1} \tan(u(k)) \tag{27a}$$

$$x_1(k) = x_0(k) - x_2(k) \tag{27b}$$

$$x_2(k+1) = \frac{v \times \Delta t}{L_2} \sin(x_1(k)) + x_2(k) \tag{27c}$$

$$x_3(k+1) = x_3(k) + v \times \Delta t \times \cos(x_1(k)) \times \sin\left(\frac{x_2(k+1) + x_2(k)}{2}\right) \tag{27d}$$

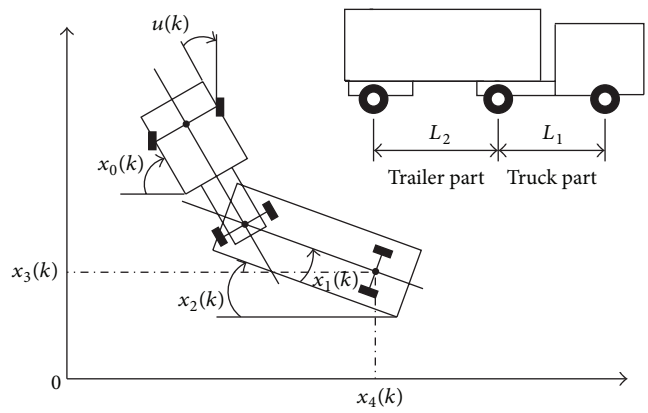

Figure 1: Nonlinear discrete-time truck-trailer system.

$$x_4(k+1) = x_4(k) + v \times \Delta t \times \cos(x_1(k)) \times \cos\left(\frac{x_2(k+1) + x_2(k)}{2}\right), \tag{27e}$$

where L_1 is length of truck (2.8 m); L_2 is length of trailer (5.5 m); Δt is sampling time (2.0 sec); v is constant speed of backing up (−1.0 m/sec); $x_0(k)$ is angle of truck; $x_1(k)$ is angle difference between truck and trailer; $x_2(k)$ is angle of trailer; $x_3(k)$ is vertical position of rear end of trailer; $x_4(k)$ is horizontal position of rear end of trailer; $u(k)$ is steering angle.

For the state $x_1(k)$, 90° and −90° correspond to two "jackknife" positions. The jackknife phenomenon cannot be avoided if the steering is not controlled during the backward movement. To succeed in the backing control, we need to avoid the jackknife phenomenon. The control purpose of this example is to back up a truck-trailer along straight line ($x_3 = 0$) without forward movements as shown in Figure 1; that is, $x_1(k) \to 0$, $x_2(k) \to 0$, and $x_3(k) \to 0$.

In this example, the multiplicative noise term is added into the system for describing the stochastic behaviors. Besides, it is assumed that $x_1(k)$ and $u(k)$ are always small values and the horizontal position motion $x_4(k)$ is not considered in this example. Therefore, one can represent and simplify the original model equation ((27a), (27b), (27c), (27d), and (27e)) as follows:

$$x_1(k+1) = \left(1 - \frac{v \times \Delta t}{L_2}\right) x_1(k) + \frac{v \times \Delta t}{L_1} u(k) + 0.01 \times \left(\left(1 - \frac{v \times \Delta t}{L_2}\right) x_1(k) + \frac{v \times \Delta t}{L_1} u(k)\right) w(k) \tag{28a}$$

$$x_2(k+1) = \frac{v \times \Delta t}{L_2} x_1(k) + x_2(k) + 0.01 \times \left(\frac{v \times \Delta t}{L_2} x_1(k) + x_2(k)\right) w(k) \tag{28b}$$

$$\begin{aligned} x_3(k+1) = {} & v \times \Delta t \times \sin\left(\frac{v \times \Delta t}{2L_2} x_1(k) + x_2(k)\right) \\ & + x_3(k) + 0.01 \\ & \times \left(v \times \Delta t \times \sin\left(\frac{v \times \Delta t}{2L_2} x_1(k) + x_2(k)\right)\right. \\ & \left. + x_3(k)\right) w(k), \end{aligned} \tag{28c}$$

where $w(k)$ is a scalar zero mean white noise with variance one.

Assume that $(v \times \Delta t/2L_2)x_1(k) + x_2(k)$ is operated between $(-\pi, +\pi)$. Then, the T-S fuzzy model representing the dynamics of the truck-trailer system ((28a), (28b), and (28c)) with multiplicative noise term can be described as follows.

Rule 1. IF $(v \times \Delta t/2L_2)x_1(k) + x_2(k)$ is about 0 THEN

$$x(k+1) = \mathbf{A}_1 x(k) + \mathbf{B}_1 \overline{u}(k) + \left(\overline{\mathbf{A}}_1 x(k) + \overline{\mathbf{B}}_1 \overline{u}(k)\right) w(k). \tag{29}$$

Rule 2. IF $(v \times \Delta t/2L_2)x_1(k) + x_2(k)$ is about $-\pi$ or π THEN

$$x(k+1) = \mathbf{A}_2 x(k) + \mathbf{B}_2 \overline{u}(k) + \left(\overline{\mathbf{A}}_2 x(k) + \overline{\mathbf{B}}_2 \overline{u}(k)\right) w(k), \tag{30}$$

where

$$\begin{gathered} \mathbf{A}_1 = \begin{bmatrix} 1 - \dfrac{v \times \Delta t}{L_2} & 0 & 0 \\ \dfrac{v \times \Delta t}{L_2} & 1 & 0 \\ \dfrac{v^2 \times \Delta t^2}{2L_2} & v \times \Delta t & 1 \end{bmatrix}, \\ \overline{\mathbf{A}}_1 = 0.01 \times \begin{bmatrix} 1 - \dfrac{v \times \Delta t}{L_2} & 0 & 0 \\ \dfrac{v \times \Delta t}{L_2} & 1 & 0 \\ \dfrac{v^2 \times \Delta t^2}{2L_2} & v \times \Delta t & 1 \end{bmatrix}, \\ \mathbf{A}_2 = \begin{bmatrix} 1 - \dfrac{v \times \Delta t}{L_2} & 0 & 0 \\ \dfrac{v \times \Delta t}{L_2} & 1 & 0 \\ \dfrac{\varphi \times v^2 \times \Delta t^2}{2L_2} & \varphi \times v \times \Delta t & 1 \end{bmatrix}, \\ \overline{\mathbf{A}}_2 = 0.01 \times \begin{bmatrix} 1 - \dfrac{v \times \Delta t}{L_2} & 0 & 0 \\ \dfrac{v \times \Delta t}{L_2} & 1 & 0 \\ \dfrac{\varphi \times v^2 \times \Delta t^2}{2L_2} & \varphi \times v \times \Delta t & 1 \end{bmatrix}, \\ \mathbf{B}_1 = \mathbf{B}_2 = \begin{bmatrix} \dfrac{v \times \Delta t}{L_1} \\ 0 \\ 0 \end{bmatrix}, \qquad \overline{\mathbf{B}}_1 = \overline{\mathbf{B}}_2 = 0.01 \times \begin{bmatrix} \dfrac{v \times \Delta t}{L_1} \\ 0 \\ 0 \end{bmatrix}, \end{gathered} \tag{31}$$

and φ is $10^{-2}/\pi$.

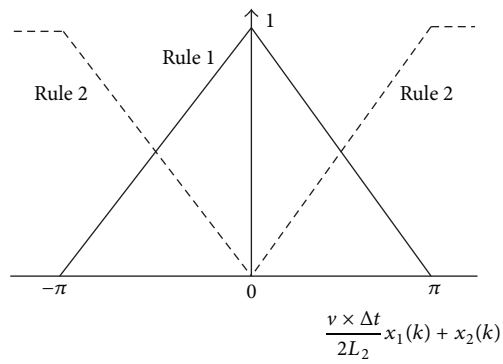

Figure 2: Membership function of $(v \times \Delta t/2L_2)x_1(k) + x_2(k)$.

The membership function is proposed in Figure 2. For applying the proposed fuzzy controller design technique, the parameters corresponding to actuator saturation are chosen as $u_{kH} = 1.5$ and $\varepsilon = 0.6$. Because there are two fuzzy rules in this T-S fuzzy model, three variables, that is, $\mathbf{P}$, $\mathbf{K}_1$, and $\mathbf{K}_2$, are needed to be found to satisfy (20) and (21). By using the LMI toolbox in MATLAB [27], the following feasible solutions can be solved:

$$\mathbf{P} = \begin{bmatrix} 1.0467 & -1.6144 & 0.2874 \\ -1.6144 & 3.7534 & -0.6673 \\ 0.2874 & -0.6673 & 0.2486 \end{bmatrix}. \tag{32}$$

Besides, the control gains are also obtained as follows:

$$\mathbf{K}_1 = \begin{bmatrix} 1.8985 & -2.0338 & 0.2439 \end{bmatrix}, \tag{33a}$$

$$\mathbf{K}_2 = \begin{bmatrix} 1.8589 & -1.7002 & 0.3022 \end{bmatrix}. \tag{33b}$$

Substituting the above control gains into (10), the PDC-based fuzzy controller can be obtained. Employing the obtained fuzzy controller (10) to drive the nonlinear discrete-time stochastic truck-trailer system ((28a), (28b), and (28c)), the simulation results of the state responses can be found in Figures 3, 4, and 5 with the initial conditions $x(0) = \begin{bmatrix} 88^\circ & 90^\circ & 3 \end{bmatrix}^T$. Besides, the responses of constrained control input are shown in Figure 6. From the simulation results, one can find that the nonlinear discrete-time stochastic truck-trailer system ((28a), (28b), and (28c)) is asymptotically stable and the actuator saturation constraint is achieved.

5. Conclusions

In this paper, the T-S fuzzy model with multiplicative noises was employed to represent the discrete-time nonlinear stochastic systems. According to the discrete-time T-S fuzzy model with multiplicative noises, the sufficient stability conditions have been derived subject to the actuator saturation constraints. Solving these sufficient stability conditions via LMI techniques, the PDC-based fuzzy controllers can be obtained. Applying the proposed fuzzy controller design approach, some systems represented by the discrete-time T-S fuzzy model with multiplicative noises can be protected

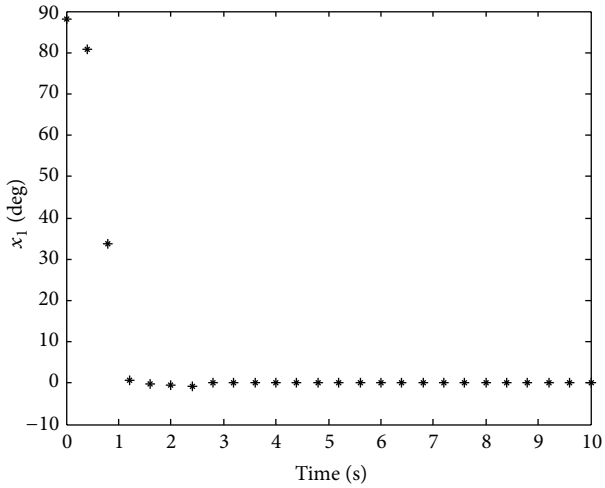

Figure 3: The angle difference $x_1(k)$ between truck and trailer.

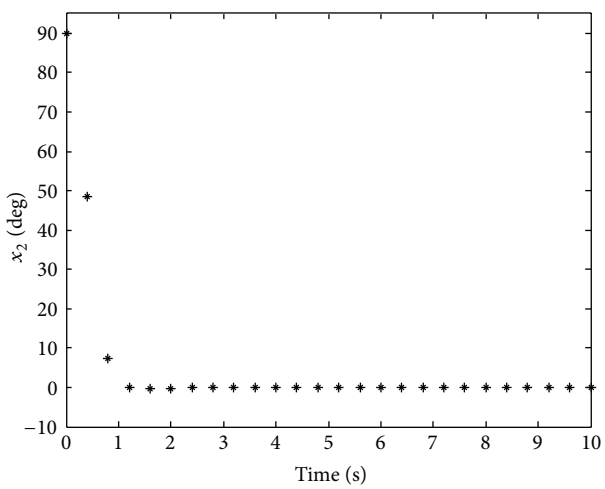

Figure 4: The angle $x_2(k)$ for trailer.

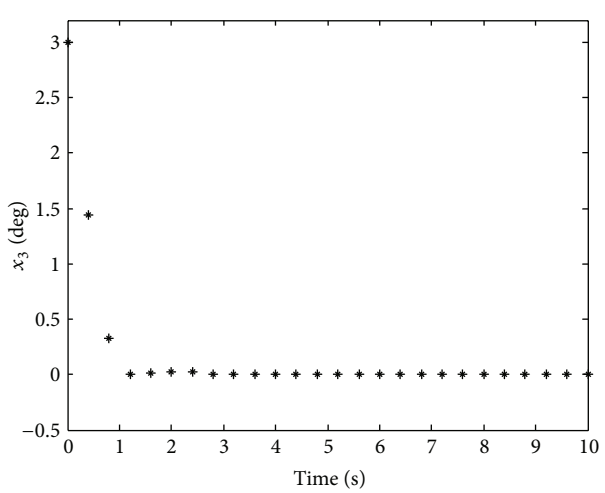

Figure 5: The vertical position of rear end $x_3(k)$ for trailer.

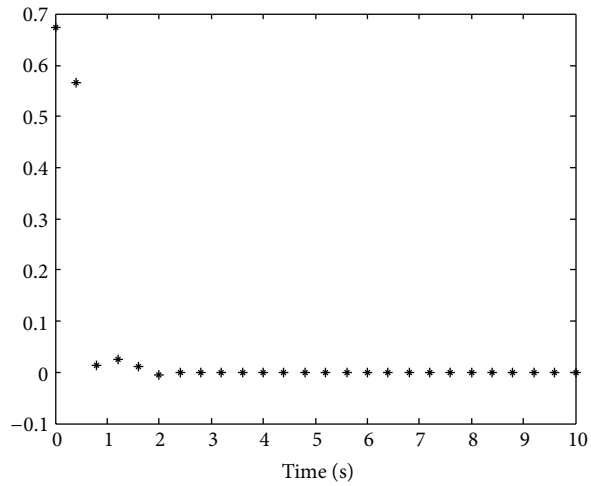

Figure 6: The constrained control input.

for avoiding the huge power into the precise system. Finally, a numerical simulation was provided to demonstrate the effectiveness and applicability of the proposed fuzzy control method.

References

[1] K. Tanaka and M. Sugeno, "Stability analysis and design of fuzzy control systems," *Fuzzy Sets & Systems*, vol. 45, no. 2, pp. 135–156, 1992.

[2] W.-J. Chang, W.-H. Huang, W. Chang, and C.-C. Ku, "Robust fuzzy control for continuous perturbed time-delay affine Takagi-Sugeno fuzzy models," *Asian Journal of Control*, vol. 13, no. 6, pp. 818–830, 2011.

[3] M. R. Soltanpour, B. Zolfaghari, M. Soltani, and M. H. Khooban, "Fuzzy sliding mode control design for a class of nonlinear systems with structured and unstructured uncertainties," *International Journal of Innovative Computing, Information and Control*, vol. 9, no. 7, pp. 2713–2726, 2013.

[4] W. H. Ho, S. H. Chen, and J. H. Chou, "Observability robustness of uncertain fuzzy-model- based control systems," *International Journal of Innovative Computing, Information and Control*, vol. 9, no. 2, pp. 805–819, 2013.

[5] W.-J. Chang, C. C. Ku, and W. Chang, "Analysis and synthesis of discrete nonlinear passive systems via affine T-S fuzzy models," *International Journal of Systems Science*, vol. 39, no. 8, pp. 809–821, 2008.

[6] W.-J. Chang, S.-S. Jheng, and C.-C. Ku, "Fuzzy control with robust and passive properties for discrete-time Takagi-Sugeno fuzzy systems with multiplicative noises," *Proceedings of the Institution of Mechanical Engineers*, vol. 226, no. 4, pp. 476–485, 2012.

[7] H. Zhang, Y. Shi, and M. Liu, "H_∞ step tracking control for networked discrete-time nonlinear systems with integral and predictive actions," *IEEE Transactions on Industrial Informatics*, vol. 9, no. 1, pp. 337–345, 2013.

[8] H. Zhang, Y. Shi, and B. Mu, "Optimal H_∞-based linear-quadratic regulator tracking control for discrete-time takagi-sugeno fuzzy systems with preview actions," *ASME, Journal of*

Dynamic System, Measurement, and Control, vol. 135, no. 4, pp. 044501-1–044501-5, 2013.

[9] H. Zhang, Y. Shi, and A. Saadat Mehr, "On H_∞ filtering for discrete-time takagi-sugeno fuzzy systems," *IEEE Transactions on Fuzzy Systems*, vol. 20, no. 2, pp. 396–401, 2012.

[10] X. Zhang, G. Lu, and Y. Zheng, "Stabilization of networked stochastic time-delay fuzzy systems with data dropout," *IEEE Transactions on Fuzzy Systems*, vol. 16, no. 3, pp. 798–807, 2008.

[11] H. Zhang, Y. Wang, and D. Liu, "Delay-dependent guaranteed cost control for uncertain stochastic fuzzy systems With multiple time delays," *IEEE Transactions on Systems, Man, and Cybernetics B*, vol. 38, no. 1, pp. 126–140, 2008.

[12] L. Wu and D. W. C. Ho, "Fuzzy filter design for Itô stochastic systems with application to sensor fault detection," *IEEE Transactions on Fuzzy Systems*, vol. 17, no. 1, pp. 233–242, 2009.

[13] L. Wu and W. X. Zheng, "L_2-L_∞ control of nonlinear fuzzy itô stochastic delay systems via dynamic output feedback," *IEEE Transactions on Systems, Man, and Cybernetics B*, vol. 39, no. 5, pp. 1308–1315, 2009.

[14] C.-C. Ku, P.-H. Huang, and W.-J. Chang, "Passive fuzzy controller design for nonlinear systems with multiplicative noises," *Journal of the Franklin Institute*, vol. 347, no. 5, pp. 732–750, 2010.

[15] W.-J. Chang, C.-C. Ku, and P.-H. Huang, "Robust fuzzy control for uncertain stochastic time-delay Takagi-Sugeno fuzzy models for achieving passivity," *Fuzzy Sets & Systems*, vol. 161, no. 15, pp. 2012–2032, 2010.

[16] W.-J. Chang, C.-C. Ku, and C.-H. Chang, "PDC and non-PDC fuzzy control with relaxed stability conditions for contintuous-time multiplicative noised fuzzy systems," *Journal of the Franklin Institute*, vol. 349, no. 8, pp. 2664–2686, 2012.

[17] B.-S. Chen and S. S. Wang, "The stability of feedback control with nonlinear saturating actuator: time domain approach," *IEEE Transactions on Automatic Control*, vol. 33, no. 5, pp. 483–487, 1988.

[18] W. J. Wang and B.-S. Chen, "Stability of large-scale systems with saturating actuators," *International Journal of Control*, vol. 47, no. 3, pp. 827–850, 1988.

[19] Y.-Y. Cao and Z. Lin, "Robust stability analysis and fuzzy-scheduling control for nonlinear systems subject to actuator saturation," *IEEE Transactions on Fuzzy Systems*, vol. 11, no. 1, pp. 57–67, 2003.

[20] W.-J. Chang and S.-M. Wu, "Continuous fuzzy controller design subject to minimizing control input energy with output variance constraints," *European Journal of Control*, vol. 11, no. 3, pp. 269–279, 2005.

[21] S. Lee, E. Kim, H. Kim, and M. Park, "Robust analysis and design for discrete-time nonlinear systems subject to actuator saturation via fuzzy control," *IEICE Transactions on Fundamentals of Electronics, Communications and Computer Sciences*, vol. E88-A, no. 8, pp. 2181–2191, 2005.

[22] C.-S. Tseng and B.-S. Chen, "H_∞ fuzzy control design for nonlinear systems subject to actuator saturation," in *Proceedings of the IEEE International Conference on Fuzzy Systems*, pp. 783–788, Canada, July 2006.

[23] X. Gao, M. Ma, and H. Chen, "Guaranteed cost tracking scheme for wheeled mobile robot with actuator saturations via T-S fuzzy model," in *Proceedings of the 5th International Conference on Fuzzy Systems and Knowledge Discovery (FSKD '08)*, pp. 85–89, Jinan, China, October 2008.

[24] T. Zhang, G. Feng, H. Liu, and J. Lu, "Piecewise fuzzy anti-windup dynamic output feedback control of nonlinear processes with amplitude and rate actuator saturations," *IEEE Transactions on Fuzzy Systems*, vol. 17, no. 2, pp. 253–264, 2009.

[25] K. Tanaka and H. O. Wang, *Fuzzy Control Systems Design and Analysis: A Linear Matrix Inequality Approach*, John Wiley & Sons, 2001.

[26] S. Boyd, L. El Ghaoui, E. Feron, and V. Balakrishnan, *Linear Matrix Inequalities in System and Control Theory*, SIAM, Philadelphia, Pa, USA, 1994.

[27] P. Gahinet, A. Nemirovski, A. J. Laub, and M. Chilali, *LMI Control Toolbox*, The MathWorks, Natick, Mass, USA, 1995.

[28] K. Tanaka and M. Sano, "Robust stabilization problem of fuzzy control systems and its application to backing up control of a truck-trailer," *IEEE Transactions on Fuzzy Systems*, vol. 2, no. 2, pp. 119–134, 1994.

Hindawi Publishing Corporation
Mathematical Problems in Engineering
Volume 2013, Article ID 517387, 8 pages
http://dx.doi.org/10.1155/2013/517387

Research Article

Research on Conflict Decision between Shift Schedule and Multienergy Management for PHEV with Automatic Mechanical Transmission under Special Driving Cycles

JunQiang Xi[1] and Yongdan Chen[2]

[1] *School of Mechanical Engineering, Beijing Institute of Technology, Beijing 100081, China*
[2] *China North Vehicle Research Institute, Beijing 100072, China*

Correspondence should be addressed to JunQiang Xi; xijunqiang@bit.edu.cn

Received 30 September 2013; Accepted 3 November 2013

Academic Editor: Hui Zhang

In order to satisfy the character of parallel hybrid electric vehicle (PHEV) in some special driving cycles, a collision decision problem between the shift decision and power split ratio is proposed. Based on a large amount of experimental data the optimal decisions are determined with evidential reasoning theory. The proposed decision strategy has been verified through real road test of Chongqing public transportation line 818 and the fuel economic improvement has also been achieved.

1. Introduction

The so-called special driving cycles of hybrid buses traveling refers primarily to climbing a big slope and/or rapid acceleration (or kickdown). A common feature in these cycles is the requirement of large drive torque to overcome road resistance or to provide additional acceleration. This is similar to the Boost function applied in some passenger cars. To provide short-term high torque in the traditional vehicles, in addition to extracting engine power, an increased gear ratio is used. But the engine cannot be overloaded due to existing self-sustaining measures; hence the torque response is slow. Thus in order to meet the requirement of large torque in a short time, traditional vehicles commonly use the method of power downshifting.

When parallel hybrid electric bus is faced with such special driving cycles, the traction motor of hybrid powertrain allows short-term overload. In this case there are two mutually exclusive decision-making options: (1) multienergy power spilt management and (2) gear changing. This leads to a task conflict, since both the decision-making schedules involve the motor control that is not feasible to realize simultaneously. Although the regulation of the Chinese urban road design code CJJ37-1990 states that "the maximum longitudinal limiting value is 9% in the urban road [1]," in some mountain cities (such as Chongqing etc.) it is 15%. This can be attributed to the influence of topographical factors, which implies that the bus often needs to climb a big slope and the up gradient will cause a deceleration of nearly 1.5 m/s^2.

If the shift operation occurs during this gradient climb and the time of torque interruption is 2 seconds, the speed will decrease by 10.8 km/h. This decrease in speed is difficult to be accepted in terms of ride comfort running performance. In addition, if the downshift operation is selected during the undulating road, there is a chance that automatic transmission might start the upshift operation as soon as a certain speed level is reached. This can bring forth the phenomenon of shift hunting (undesirable). Conversely, if multienergy power spilt management is selected to increase the motor drive torque in such a case then the shift hunting phenomenon can be avoided. Further study about the problems is required such as (1) whether the use of electrical energy is reasonable and (2) whether the maximization of the vehicle performance could be realized.

At present, many scholars have argued that the key to solve such problems is pattern recognition, so in-depth and

meticulous research has been conducted on pattern recognition [2, 3]. In the case of hybrid vehicles, even if obtaining information of the external pattern is available, the problem of making the optimal decision exists. Therefore, there is an urgent need to research on shift schedule and multi-energy power split management decision-making under special driving cycles for hybrid buses. This paper will study the problem of task conflict in hybrid buses while climbing big slope by applying the multiattribute decision-making theory.

2. Mathematical Description of Task Conflict under Special Driving Cycles

The decision-making process has to take into view the characteristics of hybrid buses' traveling road uncertainty, driving behavior randomness, and the dynamic nature of powertrain control. First of all, the problem of evaluation and decision-making must consider qualitative attributes. The so-called qualitative attribute judges the information of one vehicle properties, and the evaluation is not a specific value but a grade of linguistic assessment [4]. The collection of evaluation grades is given by

$$H = \{H_1, \ldots, H_n, \ldots, H_N\}, \tag{1}$$

where H_n assesses the grade of each attribute. To simplify the calculation, H_n is quantized in a certain scale [5] and $p(H_n)$ stands for the grade of H_n. The evaluation grades' range is limited in $[-1, 1]$ and will be quantized by

$$p\{H\} = [p(H_1), \ldots, p(H_n), \ldots, p(H_N)]^T. \tag{2}$$

A finite set of basic attributes are denoted by

$$E = \{e_1, \ldots, e_i, \ldots, e_L\}. \tag{3}$$

We assume that the weighting factor is

$$W = (w_1, \ldots, w_i, \ldots, w_L), \quad 0 \le w_i \le 1, \tag{4}$$

where w_i is the weight suited for the respective basic attribute e_i, which plays a key role in multiple attribute decision-making. The evaluation of each attribute e_i can be expressed as

$$S(e_i) = \{(H_n, \beta_{n,i}) \mid n = 1, \ldots, N\}, \quad \text{for } i = 1, \ldots, L, \tag{5}$$

where $\beta_{n,i}$ is the trust degree of correlation attribute and satisfies $\beta_{n,i} \ge 0$, $\sum_{n=1}^{N} \beta_{n,i} \le 1$. When $\sum_{n=1}^{N} \beta_{n,i} = 1$, $S(e_i)$ is called complete evaluation, when $\sum_{n=1}^{N} \beta_{n,i} < 1$, $S(e_i)$ is called incomplete evaluation.

For convenience, assume that only the evaluation of two-level attribute is considered, as is shown in Figure 1, define the vehicle performance y as a total attribute of the upper, $E = \{e_1, e_2, e_3, e_4, e_5, e_6, e_7, e_8, e_9\}$ as a basic attribute of the lower, and β_n as the trust degree of evaluation grade for total attribute y. Specifically, the evaluation grade is divided into six classes; they are, respectively, as follows:

$$H = \{H_1 (\text{worst}), H_2 (\text{poor}), H_3 (\text{average}), H_4 (\text{Good}), H_5 (\text{Excellent}), H_6 (\text{Top})\}. \tag{6}$$

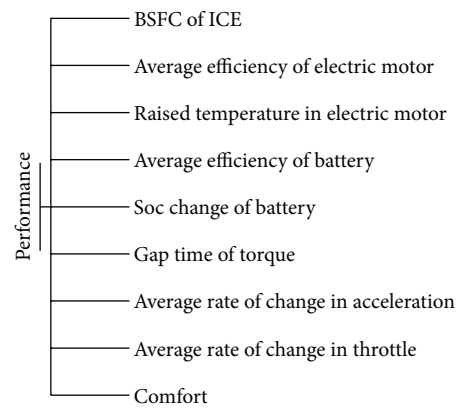

Figure 1: Evaluating hierarchy of Vehicular performance under special driving cycles.

According to the evaluation of expected vehicle performance of total attribute y under various decision-making, the final decision of multi-energy power spilt management under special driving cycles is obtained.

3. Data Acquisition of Basic Attribute for Hybrid Powertrain under Special Driving Cycles

In order to evaluate the multi-attribute decision-making for hybrid electric bus under typical special driving cycles, it is needed to collect the impacts on vehicle performance when gear changing and multi-energy power spilt management are applied, respectively, under the typical driving cycle and different vehicle states. Taking climbing a big slope condition as an example to explain the tests designed to obtain the performance parameters of the same type of hybrid buses in test venue, the specific test process is shown in Figure 2. The specified value of each test in the flowchart is shown in Table 1, and the recorded data is the basic attribute in Figure 1.

In order to ensure that the two strategies will be output of the same driving force on the vehicle, the motor output torque required in the test is decided by the difference between the output torque of low gear and current gear. The impact on vehicle performance after application of the shift schedule and multi-energy power split management strategy by the above-mentioned test under uphill condition is described by quantitative and qualitative data respectively.

Because of the uncertain factors which are brought about by the deviation of artificial control and the influence of external environment in the above-mentioned process, the test does not exactly match the actual operating conditions, and it causes uncertainty of the collected qualitative and quantitative data. A more effective method for this uncertainty is to synthesize the evidence (data) via Dempster-Shafer theory. The next section will introduce the Dempster-Shafer evidential reasoning approach.

Table 1: Related values in test process.

Category of specified value	Test value				
Slope (%)	5	10	13	16.7	—
SOC (%)	20	40	60	70	80
Vehicle speed passing slope bottom (km/h)	10	15	20	30	50
Throttle opening (%)	40	50	60	80	100

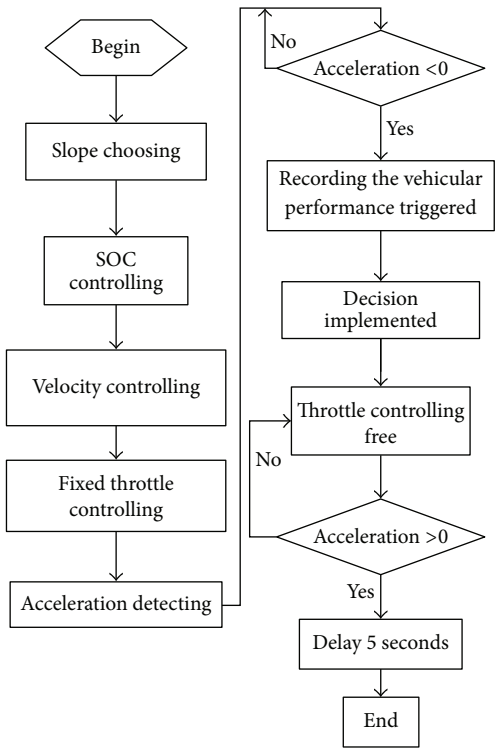

Figure 2: Multi-attribute data collecting flow under ramp condition.

4. Conflict Task Decision-Making Based on the Evidential Reasoning Approach

The evidential reasoning approach was first proposed by the University of Manchester, UK, Jian-Bo Yang in 1994; he first proposed a basic evidential reasoning model [6], which theoretical foundation is based on the Dempster-Shafer evidence theory as well as multi-attribute decision-making analysis framework [7].

4.1. Basic Concept of Dempster-Shafer Evidence Combination Theory. Evidence theory was first proposed by Dempster in 1967 and later was formally established on monograph "A Mathematical Theory of Evidence," which is published in 1976 by his student Shafer [8], known as the Dempster-Shafer evidence theory.

Define $\Theta = H$ as a frame of discernment; it is a collection of all possible results we can recognize about the hybrid bus performance, and the basic performance attributes of the vehicle are shown in Figure 1. The selection of them depends on our prior knowledge and experimental data, and the elements in the frame of discernment should be independent of each other [7]. The trust for proposition or decision-making based on some evidence is described by the mass function (basic probability assignment) [9]. The power set 2^{Θ} in the frame of discernment Θ constitutes a collection of all possible vehicular states. Trust degree is given to all propositions (including Θ) via mass function according to the obtained vehicular experimental data, which is the probability of separate appearance for similar vehicle state under different special driving cycles. Mass function is defined as the mapping of $m : 2^{\Theta} \rightarrow [0, 1]$

$$2^{\Theta} = \{\phi, \{\Theta_1\}, \ldots, \{\Theta_N\}, \{\Theta_1, \Theta_2\}, \ldots, \{\Theta_{N-1}, \Theta_N\}, \ldots, \{\Theta_{N-1}, \ldots, \Theta_N\}\} \tag{7}$$

and satisfies the next two conditions:

$$m(\phi) = 0, \qquad \sum_{A \in 2^{\Theta}} m(A) = 1, \tag{8}$$

where $\forall A \in \Theta$, $m(A)$ indicates the trust degree to proposition A; if $m(A) > 0$, then A is called focal element. For all of $A \neq \Theta$, if $m(\Theta) = 1$ and $m(A) = 0$, then it is called that m has not been assigned in any subsets but is the expression for the unknown information.

For any proposition, it could obtain two evidential functions by the mass function, which, respectively, are the belief function Bel and the plausibility function Pl and are defined as follows [10]:

$$\begin{aligned} \mathrm{Bel}(A) &= \sum_{\phi \neq B \subseteq A} m(B), \\ \mathrm{Pl}(A) &= 1 - \mathrm{Bel}(-A) = 1 - \sum_{B \subseteq -A} m(B), \end{aligned} \tag{9}$$

where $\mathrm{Pl}(A)$ indicates the degree of reliability or plausibility for A we can find. The sum of the trust function of a proposition and the trust function of its negative proposition does not necessarily equal to 1; that is,

$$\mathrm{Bel}(A) + \mathrm{Bel}(-A) \leq 1. \tag{10}$$

The feature for D-S evidence theory is more excellent than the past fusion theory because it is established on its description of incident. It is not a single point probability value which is described with the traditional probability theory, but it possesses the trust interval $[\mathrm{Bel}(A), \mathrm{Pl}(A)]$. $\mathrm{Bel}(A)$ indicates the support degree of the evidence to this proposition; plausibility function $\mathrm{Pl}(A)$ indicates the degree by which the evidence does not deny this proposition. It

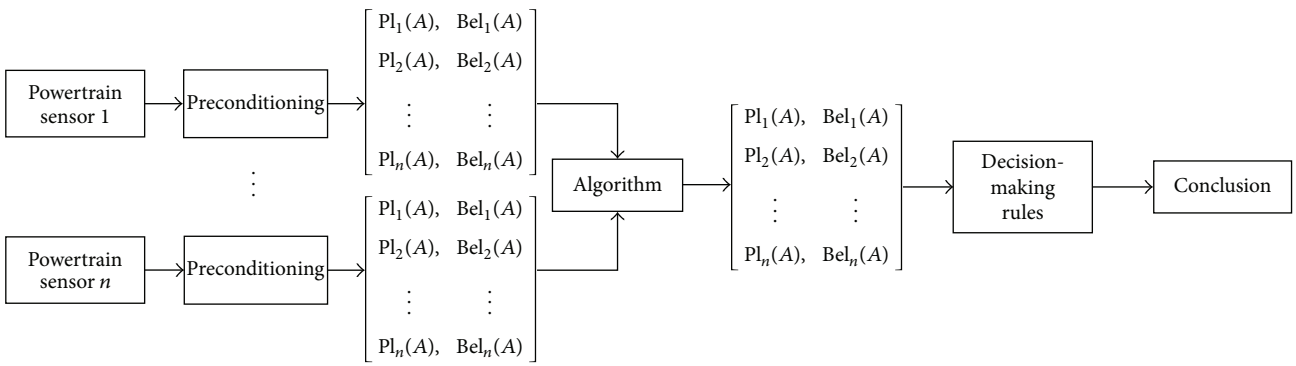

Figure 3: The specific processes with D-S.

indicates that the trust degree to proposition A is completely determinate when $\mathrm{Bel}(A) = \mathrm{Pl}(A)$ [11].

Reliability function of several independent pieces of evidence exists on the same frame of discernment in the actual application process, and they are not in complete conflict. Then joint reliability function of several pieces of evidence can be obtained by using Dempster evidence fusion rules, and such reliability function is called the direct sum of this evidence reliability function. A composite mass function could be obtained according to D-S fusion rules in consideration for mass function m_1 and m_2 of two different pieces of evidence:

$$\begin{aligned} (m_1 \oplus m_2)(A) &= \frac{1}{1-k} \sum_{B \cap C = A} m_1(B)\, m_2(C) \\ \text{where} \quad k &= \sum_{B \cap C = \phi} m_1(B)\, m_2(C), \end{aligned} \tag{11}$$

where k is conflicting belief which represents the level of conflict between the pieces of evidence. If the value of k is large, it illustrates that it has a greater conflict between the evidence. If $k = 1$, then it suggests that m_1 and m_2 is in total contradiction, and they cannot be combined. The coefficient $1/(1-k)$ is called normalization factor, which has the function to avoid assigning the probability of nonzero to the empty set ϕ in the evidence combination. In this decision-making system, the significance of the weights of conflict is that a big contradiction may exist in vehicle performance attribute, such as the interruption time of powertrain and change rate of vehicle acceleration.

In summary, at first, it needs to calculate, respectively, basic probability assignment function $m(A)$, reliability function $\mathrm{Bel}(A)$, and plausibility function $\mathrm{Pl}(A)$ of various evidence. Then, it is necessary to obtain basic probability assignment function, reliability function, and plausibility function by using evidence composition algorithm under the combined effect of all evidence. Lastly, a decision-making with maximum support degree under the effect of the combined evidence is selected by using certain decision-making rules, and specific processes are shown in Figure 3. Since hybrid powertrain is related to quantitative and qualitative evidence, the authors choose evidential reasoning approach to evaluate the decision-making.

4.2. Calculation Principle of Evidential Reasoning Approach. The evidential reasoning approach put forward by Yang and Sen has a good effect on solving multi-attribute decision-making problems which contain both quantitative index and qualitative index; the reliability matrixes based on Figure 3 and evidence combination rule are used to fuse the evaluation value of various index in the problem of multi-attribute decision-making. The model extends the decision-making matrix of the traditional problems, and it makes the traditional decision-making matrix to be divided into part of the quantitative index and part of qualitative index, whose evaluation value of qualitative index is extended from single value to a $N+1$ dimensional vector; every element in the $N+1$ dimensional vector is the experience judgment of confidence level in a linguistic evaluation degree for a evaluation index, that is, $\beta_{n,i}(A_l)$ [7].

Therefore, according to (2), total confidence level of the total attribute of a decision-making A_l could be described as follows:

$$S(y(A_l)) = \{(\Theta_n, \beta_n(A_l)), \ldots, (\Theta, \beta_\Theta(A_l))\}. \tag{12}$$

There are both accurate evaluation value of quantitative index and frame of discernment based on different qualitative index which is set to make the decision-making more accurate and more realistic in the practical application under the special driving cycles of hybrid vehicles; the method of inverting the evaluation value of quantitative index into confidence on the total frame of discernment is presented in [12]; the invert rules show as follows:

$$\begin{aligned} \gamma_{n,j} &= \frac{H_{j+1} - H_{n,i}}{H_{j+1} - H_j}, \qquad \left(H_j \le H_{n,i} \le H_{j+1}\right), \\ \gamma_{n+1,j} &= 1 - \gamma_{n,j}. \end{aligned} \tag{13}$$

where $\gamma_{n,j}$ $\gamma_{n+1,j}$, respectively, are the confidence on n and $n+1$ level for quantitative index.

Concretely speaking, evaluation grade $H_{n,i}$ for quantitative attribute is based on basic attribute (6), and it could be expressed as

$$H_{n,i} = \{(H_l, \gamma_{l,n}), l = 1, \ldots, N\}. \tag{14}$$

In addition, there are some uncertainties due to the different quantitative attribute, of driving cycles and vehicle states, for example, there is a significant difference of fuel consumption in different operating conditions:

$$S(e_i) = \left\{\left(H_j, p_j\right), j = 1, 2, \ldots, M_i\right\}, \tag{15}$$

where H_j refers to the possible value of e_i and p_j is the probability while the value of e_i is H_j, $\sum_{j=1}^{M_i} p_j \leq 1$; combining (13) and (15), we get

$$\widetilde{S}(e_i) = \left\{\left(H_j, \widetilde{\gamma}_{n,i}\right), n = 1, 2, \ldots, N\right\},$$
$$\widetilde{\gamma}_{n,i} = \begin{cases} \sum p_j \gamma_{n,j} \\ \sum p_j \gamma_{n,j} + \sum p_j \left(1 - \gamma_{n,j}\right) \\ \sum p_j \left(1 - \gamma_{n,j}\right). \end{cases} \tag{16}$$

In order to simplify the calculation, the quantitative conversion process can be described as

$$\mathbf{B}_i = \mathbf{A}_i \times \mathbf{R}_i \times \mathbf{p}_i, \tag{17}$$

where

$$\mathbf{A}_i = \begin{array}{c} \\ H_1 \\ H_2 \\ \vdots \\ H_N \end{array} \begin{array}{c} \begin{array}{cccc} H_{i,1} & H_{i,2} & \cdots & H_{i,M_i} \end{array} \\ \begin{bmatrix} 1 & 0 & \cdots & 0 \\ 0 & 1 & \cdots & 0 \\ \vdots & \vdots & \ddots & \vdots \\ 0 & 0 & \cdots & 1 \end{bmatrix} \end{array},$$
$$\mathbf{R}_i = \begin{bmatrix} \gamma_{1,1} & \gamma_{1,2} & \cdots & \gamma_{1,M_i} \\ \gamma_{2,1} & \gamma_{2,2} & \cdots & \gamma_{2,M_i} \\ \vdots & \vdots & \ddots & \vdots \\ \gamma_{N,1} & \gamma_{N,2} & \cdots & \gamma_{N,M_i} \end{bmatrix}, \tag{18}$$
$$\mathbf{p}_i = \begin{bmatrix} p_1 \\ p_2 \\ \vdots \\ p_{M_i} \end{bmatrix}.$$

4.3. Comprehensive Evaluation of Vehicle Performance Based on the Evidential Reasoning Approach. We can make final decision by obtaining the utility value of various propositions or decisions (that is comprehensive evaluation of vehicle performance) from the evidential reasoning approach. Assume that the utility value of evaluation grade H_n is indicated by $u(H_n)$. The expected utility $S(y(A_l))$ in (12) could be expressed as follows:

$$u\left(S\left(y\left(A_i\right)\right)\right) = \sum_{n=1}^{N} u\left(H_n\right) \beta_n\left(A_i\right). \tag{19}$$

It shows the evaluation for one decision scheme in nth grade of linguistic assessment in (2), but it cannot compare the quality relationship between several schemes through this equation. In order to compare and select schemes, it needs to transform the total confidence for each scheme A_l into the utility value as following "deterministic" [13]:

$$u\left(y\left(A_i\right)\right) = \sum_{n=1}^{N} \beta_n\left(A_i\right) \cdot u\left(H_n\right). \tag{20}$$

To calculate the utility value of the party A_l which is evaluated in the uncertain evaluation, Yang has defined three types of expected utility, which is the maximum utility u^+, the minimum utility u^-, and the average expected utility $\overline{u}$ [14] as

$$u^+\left(A_l\right) = \sum_{n=1}^{N-1} \beta_n\left(A_l\right) u\left(H_n\right) + \left(\beta_H\left(A_l\right) + \beta_N\left(A_l\right)\right) u\left(H_N\right), \tag{21}$$

$$u^-\left(A_l\right) = \left(\beta_1\left(A_l\right) + \beta_H\left(A_l\right)\right) u\left(H_1\right) + \sum_{n=2}^{N} \beta_n\left(A_l\right) u\left(H_n\right), \tag{22}$$

$$\overline{u}\left(A_l\right) = \frac{u^+\left(A_l\right) + u^-\left(A_l\right)}{2}. \tag{23}$$

Note that if $S(e_i)$ is complete evaluation, then $\beta_H(A_l) = 0$ and $u(S(y(A_l))) = u^+(A_l) = u^-(A_l) = \overline{u}(A_l)$. Two decision schemes A_l and A_k are taken into consideration; just when $u^-(A_l) > u^+(A_k)$, it could be thought that scheme A_l is better than A_k. When $u^-(A_l) = u^-(A_k)$ and $u^+(A_l) = u^+(A_k)$, then it could be concluded that scheme A_l is identical with A_k. This paper ranks decision-making schemes objectively through average utility, scheme A_l could be thought better than A_k just when $\overline{u}(A_l) > \overline{u}(A_k)$. Of course, in order to obtain reliable decision-making, it needs to improve the completeness of the original data to eliminate errors caused by the uncertainty of data.

5. An Instance for Decision-Making of Task Conflict

Table 1 shows that 500 groups of vehicle attribute data are collected under the uphill condition, to calculate the utility value of each group of test data which, respectively, applies different control strategies according to the evidential reasoning approach in Section 4. The following describes specifically the calculation process for evaluating the vehicle utility by using specific experimental data.

Hybrid bus drives in speed of 8 m/s with 3th gear on about 15% uphill during the test; the engine speed is about 1360 (r/min) and the vehicle is running in pure engine mode. According to the vehicle longitudinal dynamics calculation, the maximum acceleration that a vehicle can be provided is about 0.7 m/s^2, which means that the slope can be overcome is 7%. Now we face that the problem involving the choice of task conflict, and the current state in Table 2 contains the above describing vehicle state. To find the best match driving cycle collected in Section 2 by interpolation. The record of performance data relevant to the vehicle which, respectively, applies different decision-making schemes is shown in the column of decision-making scheme in

Table 2: Expected vehicle state parameters relevant to various decision-makings.

Attribute type	Definition of attribute	Current state	Decision-making schemes	
			Multi-energy power split management	Gear changing
Quantitative data	BSFC of ICE	204	$\{(202, 0.8), (208, 0.2)\}$	$\{(220, 0.9)\}$
	Raised of motor temperature	0	$\{(10, 0.8)\}$	$\{(0, 1)\}$
	Efficiency of motor	100	$\{(92, 0.9)\}$	$\{(100, 1)\}$
	SOC change of battery/%	0	$\{(2\%, 0.7)\}$	$\{(0, 1)\}$
	Gap time of torque	0	$\{(0.5, 0.9)\}$	$\{(1.7, 0.8)\}$
	Efficiency of battery	100	$\{(94, 0.7)\}$	$\{(100, 1)\}$
Qualitative estimate	Average rate of change in acceleration	W	$\{(G, 0.8), (A, 0.2)\}$	$\{(E, 0.6), (G, 0.4)\}$
	Average rate of change in throttle	P	$\{(E, 0.8), (G, 0.2)\}$	$\{(P, 0.6), (I, 0.4)\}$
	Comfort	A	$\{(E, 0.9), (G, 0.1)\}$	$\{(P, 0.7), (I, 0.3)\}$

Table 3: Expected state parameters after conversion relevant to various decision-making schemes.

Definition of attribute	Decision-making schemes	
	Multi-energy power split management	Gear changing GC
BSFC of ICE	$\{(G, 0.32), (E, 0.68)\}$	$\{(A, 0.9)\}$
Raised of motor temperature	$\{(G, 0.8)\}$	$\{(T, 1)\}$
Efficiency of motor	$\{(G, 0.72)\}$	$\{(T, 1)\}$
SOC change of battery/%	$\{(G, 0.7)\}$	$\{(T, 1)\}$
Gap time of torque	$\{(T, 0.9)\}$	$\{(P, 0.26)\}$
Efficiency of battery	$\{(G, 0.7)\}$	$\{(T, 1)\}$
Average rate of change in acceleration	$\{(G, 0.8), (A, 0.2)\}$	$\{(E, 0.6), (G, 0.4)\}$
Average rate of change in throttle	$\{(E, 0.8), (G, 0.2)\}$	$\{(P, 0.6), (A, 0.4)\}$
Comfort	$\{(E, 0.9), (G, 0.1)\}$	$\{(P, 0.7), (A, 0.3)\}$

Table 2; the specific form of recording values is {quantitative or qualitative data, confidence}.

All quantitative attributes can be expressed equivalently by using the conversion rules, to divide the engine fuel consumption rate into the following several levels according to engine universal performance characteristics map, which, respectively, are corresponding to (6):

$$\begin{aligned} H^1 &= \{H_{1,1}, H_{2,1}, H_{3,1}, H_{4,1}, H_{5,1}, H_{6,1}\} \\ &= \{270, 250, 220, 210, 200, 190\}. \end{aligned} \tag{24}$$

Similarly, the raised rate of motor temperature, motor efficiency, the change of battery SOC, and the power interruption time and battery efficiency can be equivalently expressed as

$$\begin{aligned} H^2 &= \{35, 25, 15, 10, 5, 0\}, \\ H^3 &= \{80, 85, 90, 94, 97, 100\}, \\ H^4 &= \{10, 6, 4, 2, 1, 0\}, \\ H^5 &= \{2, 1.8, 1.5, 1.2, 1, 0.5\}, \\ H^6 &= \{80, 85, 90, 94, 96, 100\}. \end{aligned} \tag{25}$$

For example, in the multi-energy power split management, the probability of engine BSFC $H_1 = 202$ is $p_1 = 0.8$, and for $H_1 = 208$ is $p_1 = 0.2$, by (13)

$$\begin{aligned} \gamma_{4,1} &= \frac{H_{5,1} - H_1}{H_{5,1} - H_{4,1}} = \frac{200 - 202}{200 - 210} = 0.2, \\ \gamma_{5,1} &= 1 - \gamma_{4,1} = 0.8, \\ \gamma'_{4,1} &= \frac{H_{5,1} - H_1}{H_{5,1} - H_{4,1}} = \frac{200 - 208}{200 - 210} = 0.8, \\ \gamma'_{5,1} &= 1 - \gamma'_{4,1} = 0.2. \end{aligned} \tag{26}$$

The final conversion result is

$$\begin{aligned} S(e_1(\mathrm{PSR})) &= \{(H_4, 0.48), (H_5, 0.52)\} \\ &= \{(G, 0.32), (E, 0.68)\}. \end{aligned} \tag{27}$$

The expected state parameters relevant to various decision-making are shown in Table 3 after finishing the conversion of quantitative attribute orderly.

Assume that all attributes have the same weight coefficient, which is $w_i = 1/9$ in (4); the evaluation result of these two decision-making under special driving cycles is obtained by using evidential reasoning iteration algorithm and D-S evidence combination rules, as shown in Table 4.

Table 4: Evaluation of whole performance for various decision-making schemes.

	Decision-making schemes	
	Multi-energy power split management	Gear changing
Performance evaluation	$\{(W, 0.2), (P, 0.1), (A, 0.4), (G, 0.8), (E, 0.2), (T, 0.3)\}$	$\{(W, 0.3), (P, 0.4), (A, 0.6), (G, 0.4), (E, 0.1), (T, 0.35)\}$

Table 5: Average utility and rank of the two decision-making schemes.

	Decision-making scheme	
	Gear changing	Multi-energy power split management
Rank of utility	0.8851	0.6615
	1	2

Evaluating the utility related to various decision-making schemes by using the recursive method based on the evaluation results of whole performance. Firstly, it needs the normalization process for the utilization of various evaluation grades, assuming that each grade has the same position of the utility. We could determine the utility of the two decision-making schemes by (19) and (23) (if the attribute information is complete in Table 2, then the maximum utility, minimum utility, and average utility of various decision-making are equal). To provide a direct basis for the solution of the two-task conflict, the rank of vehicular performance caused by the two decision-making can be determined based on utility value, as shown in Table 5. It can determine that gear changing is the optimal decision-making under this diving cycle for overcoming the load, which can make vehicular performance to be the optimal.

According to the above evaluation of calculating method, the best decision for 500 groups' typical experimental data under ramp condition is obtained via making corresponding software to select the driving cycle which is closest to the current vehicle state from 500 kinds of typical driving cycles by the method of interpolating selecting when the specific application and then to make decision according to the evaluation results. The results of Chongqing public transportation line 818 tests confirm that the proposed decision strategy is correct and effective, and fuel economy improvement has been achieved compared with applying the decision of gear changing or multi-energy power split management all the time for hybrid electric bus.

6. Conclusions

(1) One of the issues is associated with conflict decision between shift schedule and power management. This issue is addressed in this study for parallel hybrid electric vehicle (PHEV) under special driving cycle.

(2) Using the evidential reasoning approach based on Dempster-Shafer evidence combination theory, the evaluation system of whole performance for hybrid system under typical special driving cycles is established. The optimal decision table used for real-time applications is obtained.

(3) By calculating the instance, the interruption duration of hybrid power AMT shifting process plays a crucial role in the conflict decision-making. It is also necessary to put an in-depth and meticulous research on shifting process control. In order to reach at a point for reducing the time of shifting process significantly and improving vehicular comprehensive performance in the decision-making time of downshift under special driving cycles, a new technology for shift process control is proposed [15, 16].

Acknowledgment

This work was supported by the National High Technology Research and Development Program of China (Grant no. 2011AA11A252).

References

[1] W. Rui-lin and S. Jian-wu, *Urban Road Design*, China Communications Press, 2003.

[2] L. Qiao, M. Sato, K. Abe, and H. Takeda, "Self-supervised learning algorithm of environment recognition in driving vehicle," *IEEE Transactions on Systems, Man, and Cybernetics A*, vol. 26, no. 6, pp. 843–850, 1996.

[3] S.-I. Jeon, S.-T. Jo, Y.-I. Park, and J.-M. Lee, "Multi-mode driving control of a parallel hybrid electric vehicle using driving pattern recognition," *Journal of Dynamic Systems, Measurement and Control*, vol. 124, no. 1, pp. 141–149, 2002.

[4] A. D. Abdollahi, "An intelligent control strategy in a parallel hybrid vehicle," in *Proceedings of the IEEE Conference on Electric and Hybrid Vehicles (ICEHV '06)*, pp. 1–2, December 2006.

[5] M. Montazeri-Gh, A. Ahmadi, and M. Asadi, "Driving condition recognition for genetic-fuzzy HEV control," in *Proceedings of the 3rd International Workshop on Genetic and Evolving Fuzzy Systems (GEFS '08)*, pp. 65–70, March 2008.

[6] V.-N. Huynh and Y. Nakamori, "A satisfactory-oriented approach to multiexpert decision-making with linguistic assessments," *IEEE Transactions on Systems, Man, and Cybernetics B*, vol. 35, no. 2, pp. 184–196, 2005.

[7] J.-B. Yang and P. Sen, "General multi-level evaluation process for hybrid MADM with uncertainty," *IEEE Transactions on Systems, Man and Cybernetics*, vol. 24, no. 10, pp. 1458–1473, 2005.

[8] J.-B. Yang and M. G. Singh, "Evidential reasoning approach for multiple-attribute decision making with uncertainty," *IEEE Transactions on Systems, Man and Cybernetics*, vol. 24, no. 1, pp. 1–18, 1994.

[9] Z. Mi, *Research on Some Problems in the Multiple Attribute Decision Making Based on Evidential Reasoning Approach*, Hefei University of Technology, 2009.

[10] G. Shafer, *A Mathematical Theory of Evidence*, Princeton University Press, Princeton, NJ, USA, 1976.

[11] H. Jing-feng, *The Assessment Model and Implementation for Quality Performance*, Northwestern Polytechnical University, 2006.

[12] D. Thierry, *A k-Nearest Neighbor Classification Rule Based on Dempster-Shafer Theory*, Springer, New York, NY, USA, 2008.

[13] R. R. Yager, "On the dempster-shafer framework and new combination rules," *Information Sciences*, vol. 41, no. 2, pp. 93–137, 1987.

[14] J.-B. Yang and D.-L. Xu, "On the evidential reasoning algorithm for multiple attribute decision analysis under uncertainty," *IEEE Transactions on Systems, Man, and Cybernetics A*, vol. 32, no. 3, pp. 289–304, 2002.

[15] H. Zhang, J. Wang, and Y. Shi, "Robust H_∞ sliding-mode control for Markovian jump systems subject to intermittent observations and partially known transition probabilities," *Systems & Control Letters*, vol. 62, no. 12, pp. 1114–1124, 2013.

[16] H. Zhang, Y. Shi, and J. Wang, "Observer-based tracking controller design for networked predictive control systems with uncertain Markov delays," *International Journal of Control*, vol. 86, no. 10, pp. 1824–1836, 2013.

Hindawi Publishing Corporation
Mathematical Problems in Engineering
Volume 2013, Article ID 105298, 11 pages
http://dx.doi.org/10.1155/2013/105298

Research Article

Stability Problem of Wave Variable Based Bilateral Control: Influence of the Force Source Design

Dapeng Tian, Bao Zhang, Honghai Shen, and Jiaquan Li

Key Laboratory of Airborne Optical Imaging and Measurement, Changchun Institute of Optics, Fine Mechanics and Physics, Chinese Academy of Sciences, Changchun, Jilin 130033, China

Correspondence should be addressed to Dapeng Tian; d.tian@ciomp.ac.cn

Received 29 August 2013; Accepted 18 October 2013

Academic Editor: Hui Zhang

The wave variable has been proposed to achieve robust stability against the time delay in bilateral control system. However, the influence of the force source on the overall system is still not clear. This paper analyzes this problem and proposes a supplement to the stability analysis for wave variable based bilateral control. Based on the scattering theory, it is pointed out that the design of force source decides the passivity of the two-port network of slave robot. This passivity influences the stability of overall system. Based on the characteristic equation and small gain theorem, it is clear that inappropriate designed force source in encoding the wave variable destroys the stability in the presence of time delay. A wave domain filter makes up for the broken stability. The principle of this reparation is explained in this paper. A reference is also provided by the analysis to design the parameter of the wave domain filter. Experiments prove the correctness and validity.

1. Introduction

Bilateral control is investigated for the haptic communication, which expands the range of human beings' activities to perform complex tasks such as telesurgery, space, and undersea exploration [1–3]. There are two robots, the master and the slave, in the system. An operator manipulates the master robot. Meanwhile, the slave one tracks the position of the master and contacts the environment. The force generated from the contact is transmitted to the master side, which makes the operator able to feel the reaction effect from the environment [4]. Therefore, bilateral control makes teleoperation more effective [5].

In the bilateral control system, robust stability is the most important requirement [6]. However, the time delay that exists in the communication channels between the master and the slave always weakens and even destroys the stability [7, 8]. In modern applications of the bilateral control, the networks based on various communication protocols are employed as the communication lines. The network-induced delays, which may be constant, time-varying, or stochastic, packet dropouts, and disorder become the major constraints. In fact, the packet dropouts can be treated in a similar way to network-induced delay because the last received packet (delayed signal) can be used if the packet dropouts occur [9, 10]. Besides, the disordered data can be reordered via buffers, which also turns into the problem of delay. In the situation of long distance or complex network, for example, the Internet, the network-induced delay is inevitable. For normal network control system, robust control algorithms, for example, the H_∞ control, are discussed, which are very effective methods [11–13]. However, the feedback of a robot in the bilateral control system is the other robots, the human beings, and the environment, which means that the dynamics of such a system is more complex. Therefore, the delay of such a system must be specially considered.

To deal with the problem, many synthesis methods were investigated. For example, Natori et al. proposed the communication disturbance observer (CDOB) [14] and applied it in bilateral control system [15–17]. However, the performance of this method is weakened due to the mismatching of the model of slave robot. Besides, the transparency, that is, the index of the control performance, is not satisfying using this method [18]. The H_∞ control and the adaption control were also used to design the system with time delay [19]. However, the stability is limited by the situation of environment. Besides

these researches, the wave variable is one of the famous and the important methods [20], because it provides the system robust stability against arbitrary time delay.

The systemized wave variable method was proposed based on the scattering theory [21]. Then, a more physically motivated reformulation led to the development of wave theory [22], which provides a framework for designing and analyzing bilateral control system. From the proposition of wave variable method to present, many improvements were investigated. A modified Smith predictor was utilized in the wave variable framework [23]. A flexible design and analysis tool has been provided for two-channel teleoperation systems [24]. To avoid the so-called "wave reflection" phenomenon, which leads to the oscillatory behavior of the robots, two remedies have been utilized. One is the impedance matching procedure [22] and the other is the low pass filter in the wave domain [25]. To improve the transparency of wave variable based bilateral control, Aziminejad et al. proposed the idea that force feedback can be improved by designing the force source in encoding the wave variable. Specifically, the design of kinesthetic force-based (KFB) wave variable [26] that was also called directly reflective force wave variable was proposed [27].

On the wave variable methods, past analyses only focused on the passivity of the communication channels; however, they did not consider the overall system, because they assumed that the human-master, slave-environment pairs are passive. Besides, in some works, for example, the KFB method, all past experimental results are obtained with the employment of the wave domain filter. And the cutoff frequency is very low. Then, the stability of the overall system is questionable with high cutoff frequency or without the wave domain filter. There is still no work to point out that what is the influence of designing the force source in encoding the wave variable on the robust stability against time delay. Then, there are following questions.

(Q1) Does the design of force source in encoding the wave variable influence the system stability?

(Q2) What is the effect of the wave domain filter on improving the stability? And how to design the cutoff frequency of such a filter?

This paper answers the above questions and gives useful supplement to the process of designing a bilateral control system. The paper is organized as follows. In Section 2, problem formulation is given. The original wave variable based control and the KFB wave variable method are introduced as two specific situations. In Section 3, the stability of overall system is analyzed. In Section 4, experimental results are illustrated to prove the analysis. Finally, it is concluded in Section 5.

2. Problem Formulation

In this section, the problem of time delayed bilateral control system is described via a two-port network model. Then, the control objective is given by a hybrid matrix. Secondly, the algorithm of wave variable encoder is introduced. Finally, the problem of practice design that this paper focuses on is described.

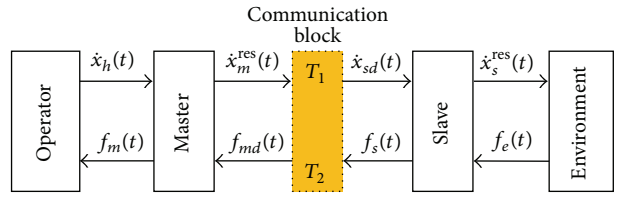

Figure 1: Two-port network model of the teleoperation system.

2.1. Control Objective by Two-Port Network Model of Teleoperation. The bilateral teleoperation system is depicted in Figure 1, where $\dot{x}_h(t)$, $\dot{x}_m^{\text{res}}(t)$, $\dot{x}_{sd}(t)$, $\dot{x}_s(t)$, $f_m(t)$, $f_{md}(t)$, $f_s(t)$ and $f_e(t)$, denote the human velocity, the master velocity response, the desired velocity for slave, the slave velocity response, the master force, the desired master force, the slave force, and environment force, respectively. Here, $f_h(t) = -f_m(t)$ means the human force, according to the law of action and reaction.

Such a system can be viewed as a series' cascade of one-port and two-port networks with an effort-flow pair, which is the force-velocity pair for teleoperation robots, being exchanged at each port. The relationship between the forces and velocities at all ports can be represented by the hybrid matrix H as follows:

$$\begin{bmatrix} f_1(t) \\ -\dot{x}_2(t) \end{bmatrix} = \underbrace{\begin{bmatrix} h_{11} & h_{12} \\ h_{21} & h_{22} \end{bmatrix}}_{H} \begin{bmatrix} \dot{x}_1(t) \\ f_2(t) \end{bmatrix}, \tag{1}$$

where the $f_1(t)$, $\dot{x}_1(t)$ pair and the $f_2(t)$, $\dot{x}_2(t)$ pair mean the force source and the velocity flow in each side of a two-port network, respectively [21].

The hybrid matrix describes the kinesthetic feedback between the input and output of a two-port network model. For the robot system, the hybrid matrix can be also used to describe the relationship between environment and human operator by choosing $f_1(t) = f_h(t)$, $f_2(t) = -f_e(t)$, $\dot{x}_1(t) = \dot{x}_m^{\text{res}}(t)$, and $\dot{x}_2(t) = \dot{x}_s^{\text{res}}(t)$.

Then, the control objective is to make $h_{11} = 0$, $h_{12} = 1$, $h_{21} = -1$, and $h_{22} = 0$ when there is no time delay, which means the motion tracking and action-reaction law of the forces as follows:

$$\dot{x}_m^{\text{res}}(t) - \dot{x}_s^{\text{res}}(t) = 0, \tag{2}$$

$$f_h(t) + f_e(t) = 0. \tag{3}$$

With the same initial states, $\dot{x}_m^{\text{res}}(0) = \dot{x}_s^{\text{res}}(0)$, (2) also means $x_m^{\text{res}}(t) - x_s^{\text{res}}(t) = 0$.

2.2. Wave Variable. According to the passivity theory, if the master and the slave two-port networks are both passive, the passivity of the communication channel means the system robust stability against arbitrary time delay.

The wave variable approach in bilateral control system stems from scattering theory and theoretically guarantees

stability under arbitrary time delay [24]. The wave variable encoding is described in Figure 2. Instead of directly transmitting the power signals $\dot{x}_m^{\text{res}}(t)$ and $f_s(t)$, the signals are encoded to the wave variables $u_m(t)$ and $v_s(t)$, which are given as follows:

$$u_m(t) = \frac{1}{\sqrt{2b}}\left[b\dot{x}_m^{\text{res}}(t) + f_{md}(t)\right],$$
$$v_s(t) = \frac{1}{\sqrt{2b}}\left[b\dot{x}_{sd}(t) - f_s(t)\right]. \tag{4}$$

These formulations are identical to the scattering formulation, with the only parameter b being the characteristic impedance of the transmission. The transmitted wave variables over the communication channel with time delay are given by the following:

$$u_s(t) = u_m(t - T_1), \qquad v_m(t) = v_s(t - T_2). \tag{5}$$

The reference signals on both sides of the channel are derived as the inverse transformation of the wave variables:

$$\begin{aligned} f_{md}(t) &= b\dot{x}_m^{\text{res}}(t) - \sqrt{2b}v_m(t) \\ &= f_s(t - T_2) + b\left[\dot{x}_m^{\text{res}}(t) - \dot{x}_{sd}(t - T_2)\right], \\ \dot{x}_{sd}(t) &= \frac{1}{b}\left[\sqrt{2b}u_s(t) - f_s(t)\right] \\ &= \dot{x}_m^{\text{res}}(t - T_1) + \frac{1}{b}\left[f_{md}(t - T_1) - f_s(t)\right]. \end{aligned} \tag{6}$$

With the wave variable encoding, the passivity of the communication block can be verified in time domain with zero initial energy storage. The passivity is confirmed if the output energy $E(t)$ of the communication block (7) is less than or equal to the input energy for all time:

$$E(t) = \int_0^t \left[\dot{x}_m^{\text{res}}(\tau) f_{md}(\tau) - \dot{x}_{sd}(\tau) f_s(\tau)\right] d\tau. \tag{7}$$

Obviously, the wave variable method ensures this relationship reasonable as follows:

$$\begin{aligned} E(t) &= \frac{1}{2}\int_0^t \left(u_m^T u_m - v_m^T v_m - u_s^T u_s + v_s^T v_s\right) d\tau \\ &= \frac{1}{2}\int_{t-T_1}^t u_m^T u_m d\tau + \frac{1}{2}\int_{t-T_2}^t v_s^T v_s d\tau \geq 0. \end{aligned} \tag{8}$$

In some past works, the fist-order low pass filters are introduced into the wave transmission to reduce the reflection of signals and improve the performance of the system as illustrated in Figure 2, which is called wave domain filter. However, the important effect of the wave domain filter on stability is not clear. Furthermore, the design principle of such filters is also not clear.

2.3. Wave Variable Based Applications

2.3.1. Original Wave Variable Based System. For the application of original wave variable, the force source $f_s(t)$ that participates in the wave variable encoding is designed as follows:

$$f_s(t) = K_v\left[\dot{x}_{sd}(t) - \dot{x}_s^{\text{res}}(t)\right] + K_p\int_0^t \left[\dot{x}_{sd}(\tau) - \dot{x}_s^{\text{res}}(\tau)\right] d\tau. \tag{9}$$

In this situation, the $f_s(t)$ is the control effect generated by the controller in the slave robot. K_v denotes the velocity gain and K_p denotes the position gain. The structure of this application method is described in Figure 3. Here, C_v is the velocity controller, which is a PI control as $C_v = K_p/s + K_v$ in Laplace domain. G_m and G_s are the transfer functions of the master and the slave, respectively.

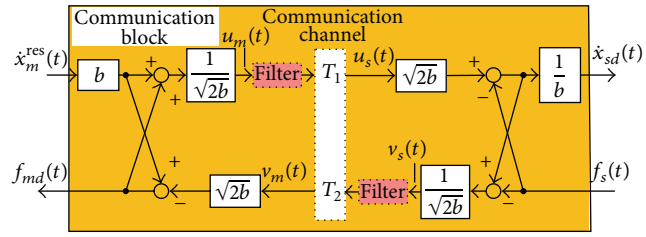

Figure 2: The arithmetic of wave variable.

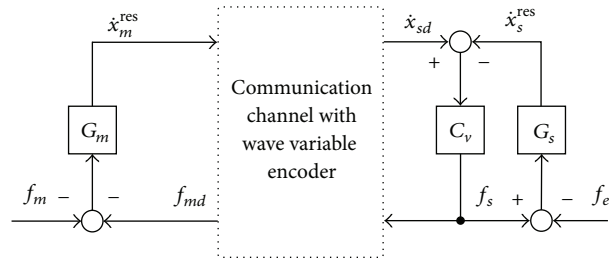

Figure 3: Original wave variable application.

2.3.2. Kinesthetic Force-Based (KFB) Wave Variable. For this application approach, the force effect in the wave variable encoder is directly designed as the environment force, which realizes the direct force reflection as follows [26]:

$$f_s(t) = f_e(t). \tag{10}$$

The structure of this KFB method is described in Figure 4. The difference between the two methods is the design of the force source in wave variable encoding. Although this design does not influence the passivity of communication block with wave transmission, it influences the passivity of the slave part and also the robust stability of the overall system. This problem is analyzed in the next section.

3. Passivity and Stability

This section gives out the relationship between the human force and master motion and the relationship between the environment force and slave motion by human and environment impedances. Then, the stability of both the original and

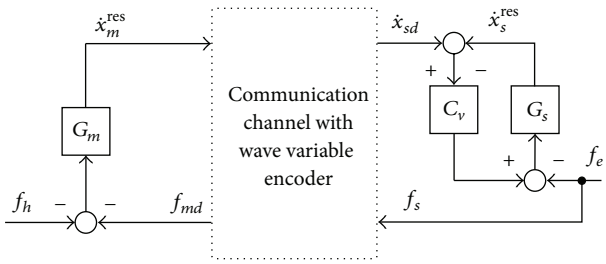

Figure 4: Kinesthetic force-based wave variable.

KFB wave variable applications is analyzed. It is pointed out that the latter one is not stable for some situations of high frequency and hard environment.

3.1. Relationship between Passivity and Force Source Design. The passivity of a two-port network can be judged by the scattering matrix $\mathbf{S}(s)$ that is defined as

$$\mathbf{S}(s) = \begin{bmatrix} 1 & 0 \\ 0 & -1 \end{bmatrix} [\mathbf{H}(s) - I] [\mathbf{H}(s) + I]^{-1}, \tag{11}$$

where $\mathbf{H}(s)$ is the Laplace transformation of the hybrid matrix in (1). There is following theorem.

Theorem 1 (see [21]). *A system is passive if and only if its scattering matrix satisfies the following condition:*

$$\sup_{\forall\omega>0} \lambda^{1/2} [\mathbf{S}^*(\omega j) \mathbf{S}(\omega j)] \leq 1. \tag{12}$$

The relationship between the passivity and the design of force source is investigated using this theorem.

In the original wave variable, the force source that participates in encoding the wave variable is designed as the control force of the slave robot. The two-port network of the slave robot is shown as Figure 5(a). According to this figure, the hybrid matrix in frequency domain $\mathbf{H}(s)$ is calculated as follows:

$$\mathbf{H}(s) = \begin{bmatrix} \dfrac{C_v(s)}{1 + C_v(s) G_s(s)} & \dfrac{C_v(s) G(s)}{1 + C_v(s) G_s(s)} \\ -\dfrac{C_v(s) G(s)}{1 + C_v(s) G_s(s)} & \dfrac{s}{1 + C_v(s) G_s(s)} \end{bmatrix}. \tag{13}$$

In the situation of KFB wave variable, the force source is designed as the environment force as shown in Figure 5(b). Correspondingly, the hybrid matrix is calculated as follows:

$$\mathbf{H}(s) = \begin{bmatrix} 0 & 1 \\ -\dfrac{C_v(s) G(s)}{1 + C_v(s) G_s(s)} & \dfrac{s}{1 + C_v(s) G_s(s)} \end{bmatrix}. \tag{14}$$

Then, the passivity can be investigated by substituting the hybrid matrices into (11) and calculating the eigenvalue in (12) for the passivity judgement of specific design.

In practice, velocity controller $C_v(s)$ is usually designed as a PI controller. For linear motor driven 1-DOF (degree-of-freedom) robot, the transfer function of the slave robot $G_s(s)$ is a nominal model that is an integration element as $G_s(s) = 1/(M_s s)$, where M_s is the inertial mass. In practice, the dynamics can be guaranteed by using disturbance observer (DOB) based robust internal loop control [28, 29]. Therefore, the nominal model of the robot is available in the analysis. For the robot used in the experiment of this paper, the parameter M_s is unity. The left part of the passivity condition, the inequality (12), is calculated and plotted as shown in Figure 6 with different gains of the controller $C_v(s)$.

Obviously, the passivity condition (12) is satisfied in the original wave variable design. However, the design of the KFB wave variable does not guarantee the passivity of the two-port model of the slave robot. This discloses that the force source cannot be designed arbitrarily. The broken passivity of the slave two-port model can not guarantee the robust stability of the whole system under communication delay between the master and the slave.

3.2. Stability of Overall System under Time Delay

3.2.1. Relationship between Force and Motion. To analyze the stability of the whole system, the relationship between force and motion is discussed first of all. In a human-machine interaction-like system, the bilateral teleoperation, the human force, and the environment force relate to the motion of the master and the slave robots through the human and the environment impedances. Considering the spring-damping impedance models [30], this relationship is described as follows:

$$\begin{aligned} F_h &= K_h \left(X_m^{res} - X_h^{des}\right) + D_h s X_m^{res} = Z_h X_m^{res} - K_h X_h^{des}, \\ F_e &= K_e \left(X_s^{res} - X_e^{int}\right) + D_e s X_s^{res} = Z_e X_s^{res} - K_e X_e^{int}, \end{aligned} \tag{15}$$

where K_h, D_h, K_e, and D_e are human stiffness, human damping, environment stiffness, and environment damping, respectively. F_h, F_e, X_m^{res}, and X_s^{res} are the Laplace transformations of f_h, f_e, x_m^{res}, and x_s^{res}, respectively. X_h^{des} is the desired position by human. X_e^{int} is the initial position of environment. $Z_h = K_h + D_h s$ and $Z_e = K_e + D_e s$ denote the human and environment impedances, respectively.

Without losing generality, X_e^{int} can be assumed as zero. Then, the only input value is X_h^{des}, and the outputs are X_m^{res} and X_s^{res} for the bilateral teleoperation system. Also without losing generality, the input X_h^{des} can be seen as zero when the stability is considered for the control system itself.

3.2.2. The Situation of Original Wave Variable. The wave inverse transmission (6) can be rewritten in the frequency domain expressions as follows:

$$\begin{aligned} F_{md} &= F_s e^{-T_2 s} Q(s) + b\left(s X_m^{res} - s X_{sd} e^{-T_2 s} Q(s)\right), \\ s X_{sd} &= s X_m^{res} e^{-T_1 s} Q(s) + \frac{1}{b}\left(F_{md} e^{-T_1 s} Q(s) - F_s\right). \end{aligned} \tag{16}$$

Here, $Q(s)$ is the wave domain filter. In the situation of the original wave variable method, there is no wave domain filter

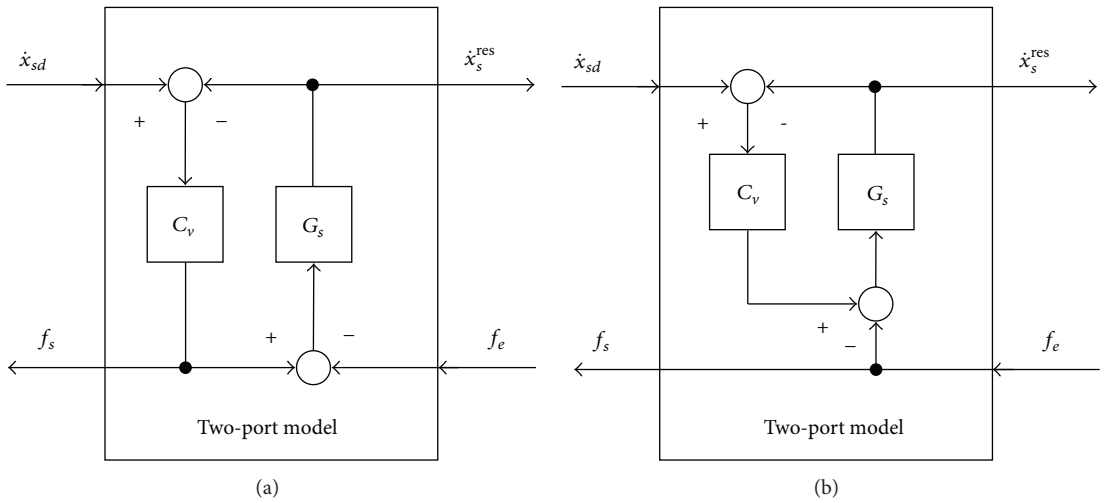

Figure 5: The two-port model of two different designs: (a) original wave variable; (b) KFB wave variable.

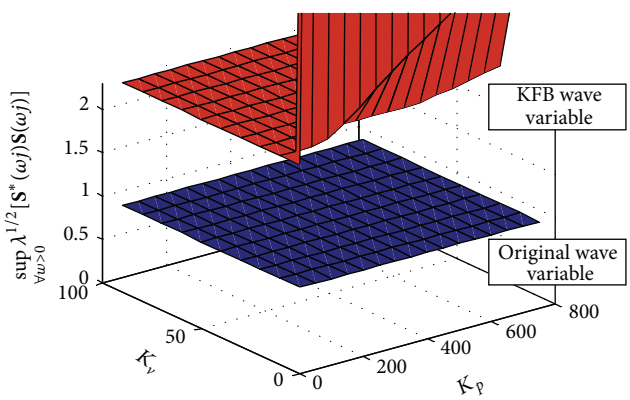

Figure 6: The passivity judgement.

in the sense of $Q(s) = 1$. Besides, the control relationship of the following obtained according to Figure 3:

$$G_m^{-1} s X_m^{res} = -F_h - F_{md},$$
$$G_s^{-1} s X_s^{res} = F_s - F_e. \tag{17}$$

Considering the dynamics of the human operator and the environment, the characteristic equation of the overall system can be calculated as (18) considering $Q(s) = 1$ according to (16) and (17):

$$\left(G_m^{-1}s + bs + Z_h\right)\left(\frac{C_v + b}{b}G_s^{-1}s + sC_v + \frac{C_v + b}{b}Z_e\right) - \left(\frac{bs - G_m^{-1}s}{b}C_v - \frac{C_v}{b}Z_h\right) \times \left(bs + \frac{b - C_v}{C_v}G_s^{-1}s - \frac{C_v - b}{C_v}Z_e\right)e^{-(T_1+T_2)s} = 0. \tag{18}$$

In fact, (18) is also the characteristic equation of the unit feedback system of $S_1(s)S_2(s)e^{-(T_1+T_2)s}$. $S_1(s)$ and $S_2(s)$ are described as follows:

$$S_1(s) = \left(\frac{bs - G_m^{-1}s}{b}C_v - \frac{C_v}{b}Z_h\right) \times \left(bs + \frac{b - C_v}{C_v}G_s^{-1}s - \frac{C_v - b}{C_v}Z_e\right),$$
$$S_2(s) = \left[\left(G_m^{-1}s + bs + Z_h\right) \times \left(\frac{C_v + b}{b}G_s^{-1}s + sC_v + \frac{C_v + b}{b}Z_e\right)\right]^{-1}. \tag{19}$$

Therefore, the stability of the system in Figure 3 is equivalent to the unit feedback system of $S_1(s)S_2(s)e^{-(T_1+T_2)s}$.

If $S_1(s)$ and $S_2(s)$ are L_2 stable, according to the small gain theorem, to make the system stable under arbitrary time delay in the signal transmission, which is the target of wave variable method, the following equation should be satisfied:

$$\left\|S_1(\omega j)S_2(\omega j)e^{-(T_1+T_2)\omega j}\right\|_\infty < 1. \tag{20}$$

By substituting (19) into (20), to make the system stable under any time delay, the following equation should be satisfied:

$$\sup_{\forall\omega>0}\left|\frac{(G_m^{-1}s - bs + Z_h)[\alpha G_s^{-1}s - bsC_v + \alpha Z_e]}{(G_m^{-1}s + bs + Z_h)[\beta G_s^{-1}s + bsC_v + \beta Z_e]}\right|_{s=j\omega} < 1, \tag{21}$$

where $\alpha = C_v - b$ and $\beta = C_v + b$.

The dynamics of the master robot is the same as the slave one, which is $G_m = 1/(M_m s)$, where M_m is the inertial mass of the master robot. In order to verify the stability of

such a system, quantitative analysis can be implemented. The employed parameters in the quantitative analysis are shown in Table 1.

The situation of great environment stiffness, $K_e = 10^6$ N/m, denotes that the environment is a hard object and $K_e = 10^{-6}$ depicts the free motion. The parameters are designed for the experimental devices in Section 4. Such designed K_p and K_v make the control of slave robot have the unity damping to avoid oscillation. The wave impedance b is designed as a great value to reduce the oscillation of system responses [31]. In the quantitative analysis, it is assumed that the human operator does not apply any effect on the system to consider the stability of only the controlled robots. The values of damping of the environment and the human operator simulate the viscous friction in both the two robots. According to Figure 7, the values of $|S_1||S_2|$ are less than one. The system is stable for either free motion or hard contact under any time delay in whole frequency domain. According to the above subsection, the design of the force source in the wave variable guarantees the passivity of the two-port model of slave. The passivity of the overall system is then guaranteed. The system performs strong robustness against the time delay in the signal transmission.

3.2.3. The Situation of KFB Wave Variable. Following the same line of above analysis, the KFB wave variable method is also analyzed, which has different design on the force source.

According to (20), condition (22) should be satisfied to make the system have robustness against any time delay:

$$\sup_{\forall\omega>0}\left|\frac{(G_m^{-1}-bs+Z_h)[bsG_s^{-1}+bsC_v+(bs-C_v)Z_e]}{(G_m^{-1}+bs+Z_h)[bsG_s^{-1}+bsC_v+(bs+C_v)Z_e]}\right|_{s=j\omega}<1. \tag{22}$$

The quantitative analysis is also implemented. With the same parameters in Table 1, the values of $|S_1||S_2|$ are shown in Figure 8. According to the result, (22) is not satisfied in the situation of hard contact. Because the passivity is broken in the two-port model of the slave, the stability of overall system is also not guaranteed in the presence of time delay. It is proved that the design of force source influences the robust stability of the overall system. The design of the force source should make any two-port model be passive in the system.

In fact, direct application of the KFB wave variable approach was not implemented in past works. There always exists a wave domain filter in the transmission line as shown in Figure 2. However, it is not clear enough what is the most important effect and how to design the wave domain filter. With the filter, the values of $|S_1||S_2|$ are calculated as shown in Figure 9. The first-order filter $g/(s+g)$ is employed. The cutoff frequency g is set as 550.0 rad/s and 31.4 rad/s, respectively. According to the results, the wave domain filter reduces the values of $|S_1||S_2|$. In practice, the wave domain filter strengthens the robust stability of overall system in the presence of time delay. If the design of force source breaks the stability of overall system, wave domain filter can make up for this problem only when the cutoff frequency is appropriate. The analysis process in this paper is quite necessary in the design of a wave variable based bilateral control system. The analysis does not only show the stability of overall system, but also provides a reference to design the system parameters for some newly proposed wave variable based system.

Table 1: Parameters for stability analysis.

Parameters	Mark	Value
Master mass	M_m	1.0 (kg)
Slave mass	M_S	1.0 (kg)
Position gain	K_p	400.0 (s^{-2})
Velocity gain	K_v	40.0 (s^{-1})
Wave impedance	b	50.0
Environment damping	D_e	2.0 (Nm/s)
Human damping	D_h	2.0 (Nm/s)
Human stiffness	K_h	10^{-6} (N/m)

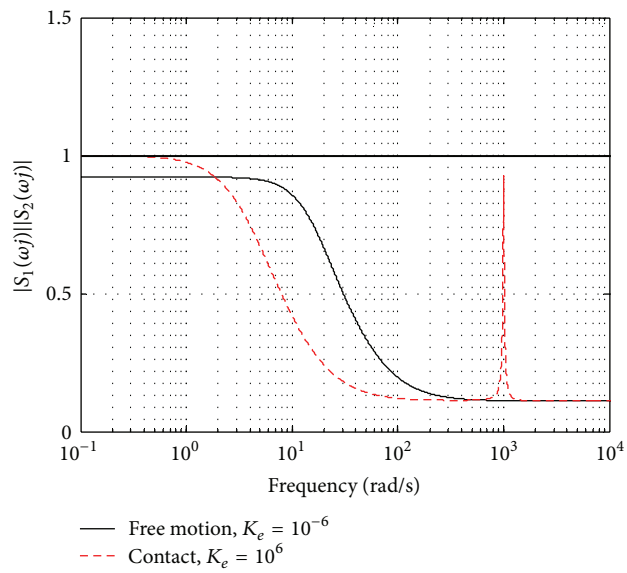

Figure 7: The stability of the overall system with the original wave variable.

4. Experiments

The experiments are implemented to prove above analyses in this paper. In Section 4.1, the experimental setup is illustrated. Then, the experimental results are shown in Section 4.2.

4.1. Experimental Setup. In the experiments, two single DOF robots are utilized as the master and the slave, respectively. The structure and devices of experimental system are shown in Figure 10. The original wave variable based system and the KFB wave variable method are both implemented by programming in Linux RTAI. Wide bandwidth sensorless force measurement is realized by the reaction force observer (RFOB) [32]. An aluminium cube is used as a hard environment that is put in the side of slave.

An internal loop robust controller, the disturbance observer, is employed to compensate model uncertainties and guarantee that the dynamics of the robots performs as the

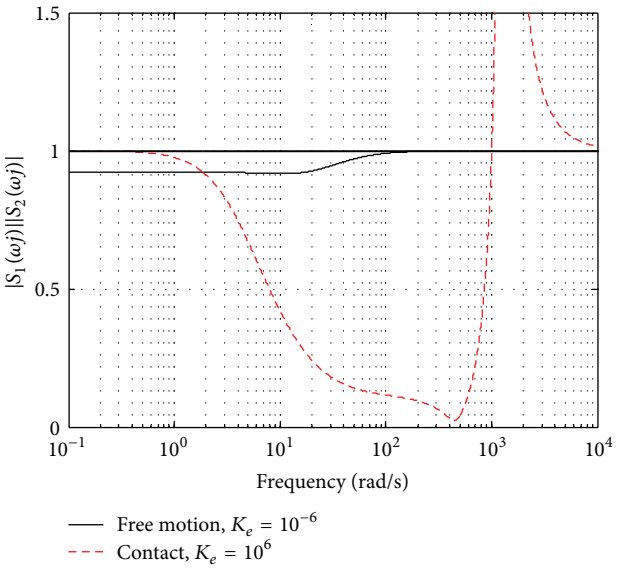

Figure 8: The stability of the overall system with the KFB wave variable.

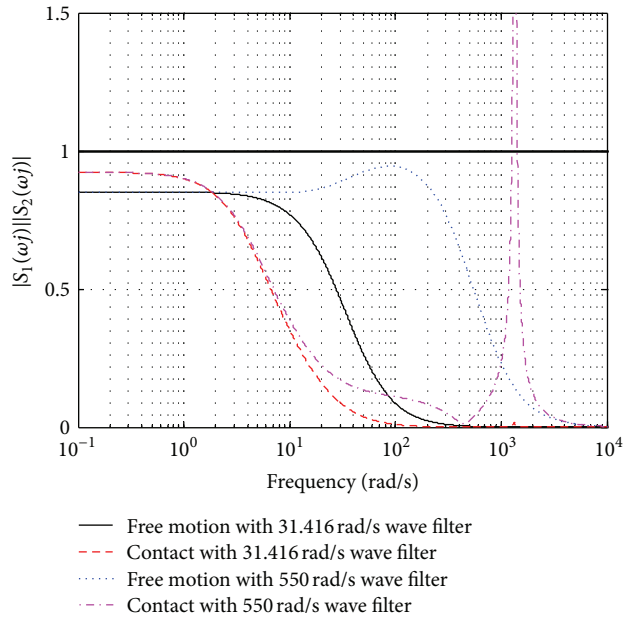

Figure 9: The stability of the overall system with the KFB wave variable and wave domain filters.

one in the analysis [33]. The structure of the internal loop is illustrated in Figure 11. The equivalent disturbance that contains the external disturbances and dynamics uncertainties are compensated within the bandwidth of the DOB. g_{dis} is the cutoff frequency. Greater g_{dis} means stronger robustness against the equivalent disturbance. In practice, major influence of the disturbances and uncertainties is in the low frequency domain. Therefore, with the DOB, the dynamics of the robot is guaranteed to be similar to the model that is used in the analysis. Then, the wave variable based approach is verified with little influence of other factors.

The experiments are composed of 4 cases. Case 1 is the situation of original wave variable based control. Case 2 is the situation of KFB wave variable based control without the wave domain filter. Case 3 and Case 4 are the KFB wave variable based system with the wave domain filter. The cutoff frequency of the filter is set highly in Case 3 as 550 rad/s and lowly in Case 4 as 31.416 rad/s. All the results are plotted into figures with x_m^{res}, x_s^{res}, f_h, and $-f_e$. The experimental parameters are shown in Table 2. Here, the cutoff frequencies of RFOB and DOB are smaller in Case 2 to extend the working time because the system is seriously instable in this case according to the above analysis.

4.2. Experimental Results. Figure 12 illustrates the position and force responses of the original wave variable based control system that corresponds to Case 1. It can be found that the system is stable for both free motion and contact operation even with the round-trip time delay of 1000 ms.

Figure 13 illustrates the results of KFB wave variable based control system that corresponds to Case 2. Without the wave domain filter, the system is unstable, especially when contact occurs. The force responses are obviously emanative. At about 3.3 s, the system stops for protection. This is in agreement with the theoretical analysis.

Table 2: Experimental parameters.

Parameters	Case 1	Case 2	Case 3	Case 4
Wave impedance b	50.0	50.0	50.0	50.0
Position gain K_p (s^{-2})	400.0	400.0	400.0	400.0
Velocity gain K_v (s^{-2})	40.0	40.0	40.0	40.0
Cutoff frequency of DOB (rad/s)	500.0	50.0	500.0	500.0
Cutoff frequency of RFOB (rad/s)	500.0	50.0	500.0	500.0
Cutoff frequency of wave filter (rad/s)	—	—	550.0	31.416
Time delay (ms)	$T_1 = T_2 =$ 500	$T_1 = T_2 =$ 500	$T_1 = T_2 =$ 500	$T_1 = T_2 =$ 500

Figure 14 illustrates the results of KFB wave variable approach with the wave domain filter that corresponds to Case 3. Although there is the wave filter, the system is also unstable, especially when contact occurs according to Figure 8. The theoretical analysis shows that the system stability is not guaranteed if the cutoff frequency of this filter is not appropriately designed. The experimental results prove the analysis.

Finally, the results of Case 4 are shown in Figure 15. The system is stable when the cutoff frequency of the wave domain filter is small enough for the KFB based control. Compared with the original wave variable method, the design of KFB wave variable deduces the oscillation of the slave robot in the

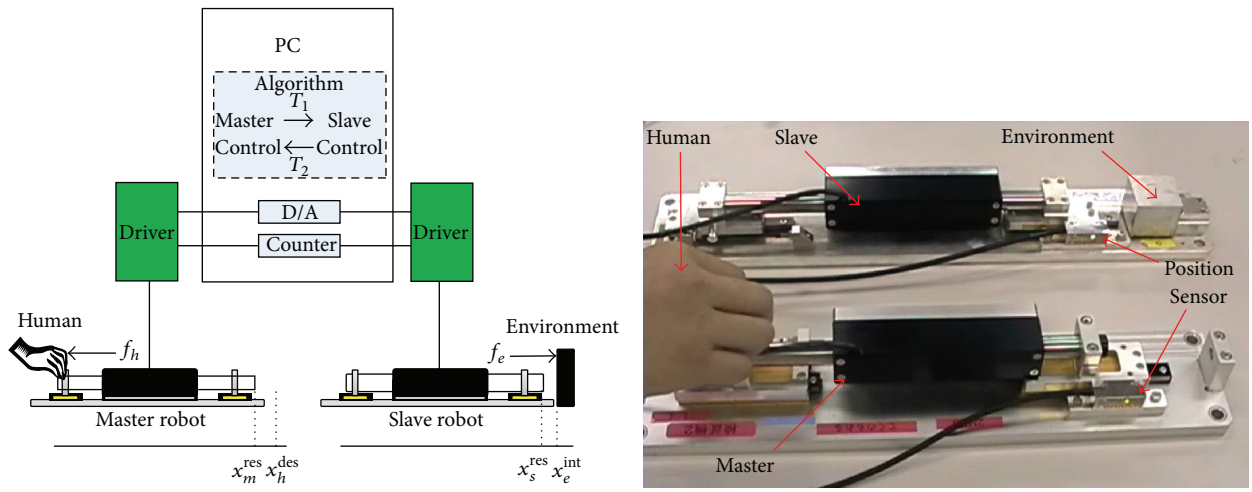

(a) Structure of experimental setup

(b) The experimental setup

Figure 10: The experimental setup.

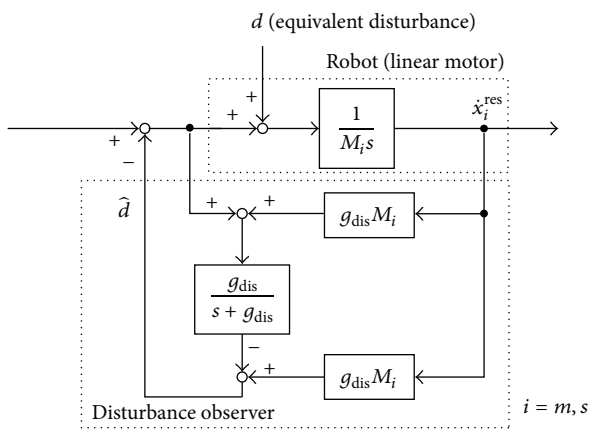

Figure 11: The structure of DOB based internal loop robust control.

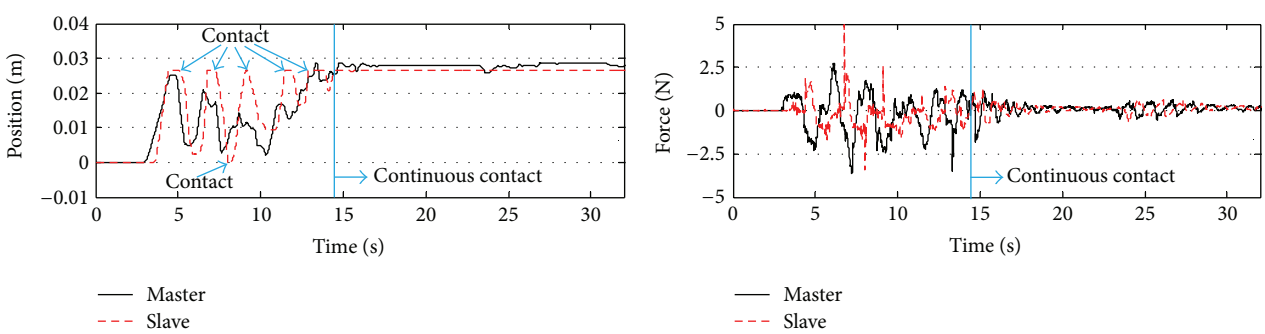

(a)

(b)

Figure 12: Experimental results of original wave variable application method.

state of free motion. The experimental results illustrated the place of improvement by the KFB wave variable and proved the correctness of the analysis process in this paper.

According to the analysis and the experiment, the following results are proved. Firstly, the design of force source in wave variable influences the stability of overall system. Secondly, the analysis process proposed in this paper helps researchers to judge the robust stability of bilateral system against time delay. If the system is unstable, the wave domain filters strengthen the stability. The proposed analysis process

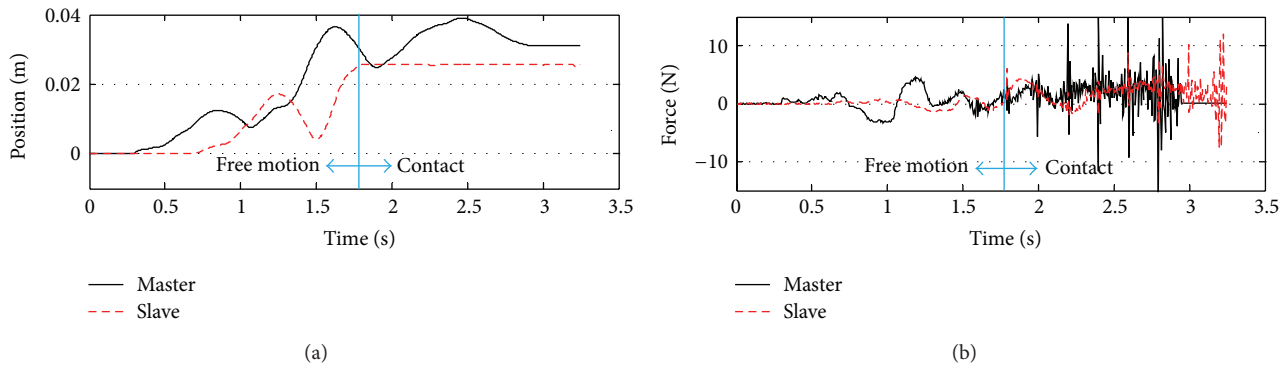

Figure 13: Experimental results of KFB wave variable method without wave domain filter.

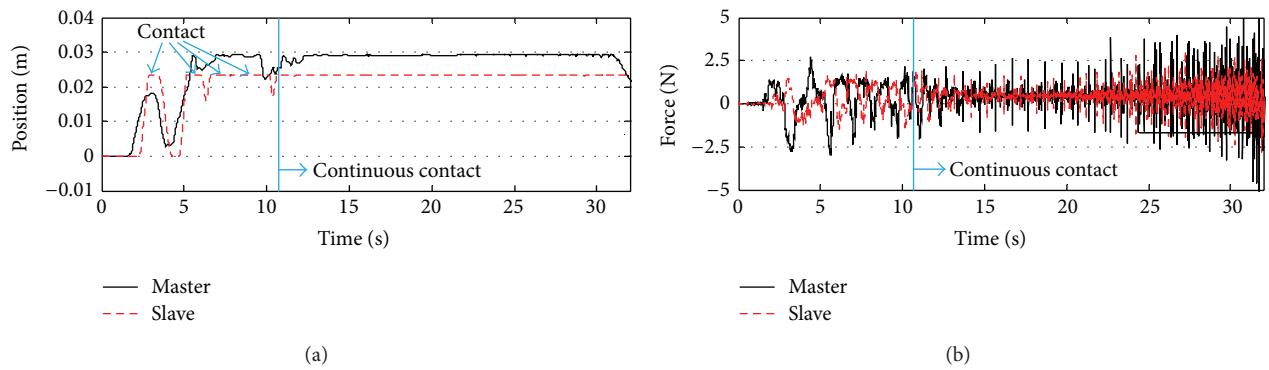

Figure 14: Experimental results of KFB wave variable method with wave domain filter of 550 rad/s cutoff frequency.

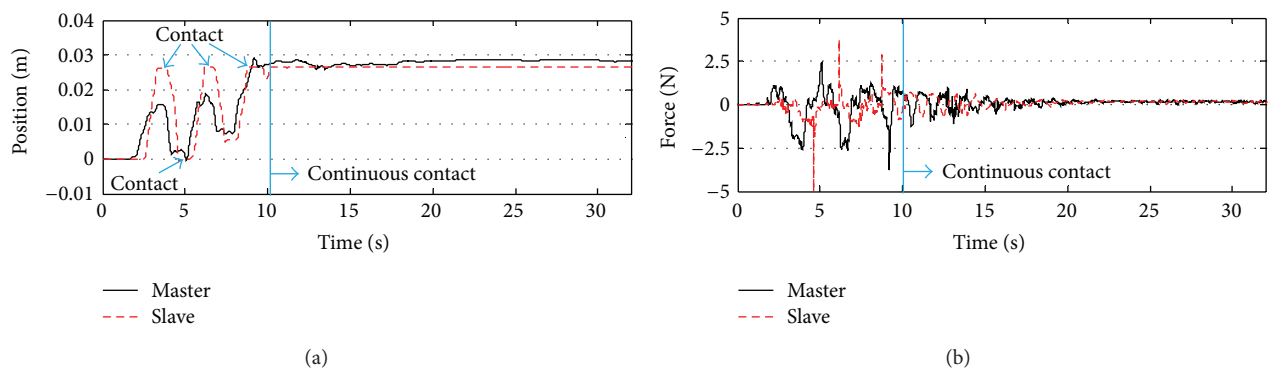

Figure 15: Experimental results of KFB wave variable method with wave domain filter of 31.416 rad/s cutoff frequency.

is useful in the design of the cutoff frequency of the wave domain filters.

5. Conclusion

This paper focused on the problem of stability caused by the design of the force source in encoding the wave variable in the delayed bilateral control system. The influence of the force source design is analyzed for the original wave variable based system and the kinesthetic force-based wave variable method specifically.

It is pointed that the design of the force source may destroy the stability of the two-port network in slave and then break the robust stability of the control system. The overall bilateral control structure is considered including the human and the environment impedances in frequency domain. Analysis illustrates that appropriately designed wave variable based system has robust stability against any time delay. However, this stability is broken if the design of the force source is not appropriate in encoding the wave variable. In the unstable situation, adding a wave domain filter improves the robust stability. The analysis in this paper

clearly illustrates the reason and provides a reference for the design of the wave domain filter.

Experimental results in practical system prove the analyses. This paper is helpful to understand the remarkable problem on the design of the force source in wave variable based bilateral control.

Conflict of Interests

The authors declare that there is no conflict of interests regarding the publication of this paper.

Acknowledgments

This work was supported in part by the National Science Foundation of China under Grant 61304032, in part by the Science and Technology Development Program of Jilin Province under Grant 20130522156JH, and in part by CIOMP Knowledge Innovation Program under Grant Y2CX1SS123. The authors also thank Professor Kouhei Ohnishi in Keio University, Japan, who provided the experimental devices and gave a lot of beneficial suggestions on this research.

References

[1] A. El Saddik, "The potential of haptics technologies," *IEEE Instrumentation and Measurement Magazine*, vol. 10, no. 1, pp. 10–17, 2007.

[2] J. Bae, W. Zhang, and M. Tomizuka, "Network-based rehabilitation system for improved mobility and tele-rehabilitation," *IEEE Transactions on Control Systems Technology*, vol. 21, no. 5, pp. 1980–1987, 2013.

[3] Y. Ye and P. X. Liu, "Improving haptic feedback fidelity in wave-variable-based teleoperation orientated to telemedical applications," *IEEE Transactions on Instrumentation and Measurement*, vol. 58, no. 8, pp. 2847–2855, 2009.

[4] D. Tian, D. Yashiro, and K. Ohnishi, "Wireless haptic communication under varying delay by switching-channel bilateral control with energy monitor," *IEEE/ASME Transactions on Mechatronics*, vol. 17, no. 3, pp. 488–498, 2012.

[5] Y. Yokokohji and T. Yoshikawa, "Bilateral control of master-slave manipulators for ideal kinesthetic coupling—formulation and experiment," *IEEE Transactions on Robotics and Automation*, vol. 10, no. 5, pp. 605–619, 1994.

[6] E. Delgado, M. Díaz-Cacho, and A. Barreiro, "Stability of teleoperation systems for time-varying delays by neutral LMI techniques," *Mathematical Problems in Engineering*, vol. 2012, Article ID 467629, 17 pages, 2012.

[7] F. Hashemzadeh, I. Hassanzadeh, M. Tavakoli, and G. Alizadeh, "A new method for bilateral teleoperation passivity under varying time delays," *Mathematical Problems in Engineering*, vol. 2012, Article ID 792057, 19 pages, 2012.

[8] C.-L. Lin, C.-H. Chen, and H.-C. Huang, "Stabilizing control of networks with uncertain time varying communication delays," *Control Engineering Practice*, vol. 16, no. 1, pp. 56–66, 2008.

[9] Z. Shuai, H. Zhang, J. Wang et al., "Combined AFS and DYC control of four-wheel-independent-drive electric vehicles over CAN network with time-varying delays," *IEEE Transactions on Vehicular Technology*, 2013.

[10] H. Zhang, Y. Shi, and J. Wang, "Observer-based tracking controller design for networked predictive control systems with uncertain Markov delays," *International Journal of Control*, vol. 86, no. 10, pp. 1824–1836, 2013.

[11] H. Zhang, Y. Shi, and M. Liu, "H_∞ step tracking control for networked discrete-time nonlinear systems with integral and predictive actions," *IEEE Transactions on Industrial Informatics*, vol. 9, no. 1, pp. 337–345, 2013.

[12] H. Zhang, Y. Shi, and A. S. Mehr, "Robust static output feedback control and remote PID design for networked motor systems," *IEEE Transactions on Industrial Electronics*, vol. 58, no. 12, pp. 5396–5405, 2011.

[13] H. Zhang, Y. Shi, and A. S. Mehr, "Robust weighted Hinf; Filtering for networked systems with intermittent measurements of multiple sensors," *International Journal of Adaptive Control and Signal Processing*, vol. 25, no. 4, pp. 313–330, 2011.

[14] K. Natori, T. Tsuji, K. Ohnishi, A. Hace, and K. Jezernik, "Robust bilateral control with internet communication," in *Proceedings of the 30th Annual Conference of IEEE Industrial Electronics Society (IECON '04)*, pp. 2321–2326, Busan, Republic of Korea, November 2004.

[15] K. Natori and K. Ohnishi, "Time delay compensation in bilateral teleoperation systems," in *Proceedings of the IEEE International Conference on Mechatronics (ICM '06)*, pp. 601–606, Budapest, Hungary, July 2006.

[16] N. Iiyama, K. Natori, and K. Ohnishi, "Bilateral teleoperation under time-varying communication time delay considering contact with environment," *Electronics and Communications in Japan*, vol. 92, no. 7, pp. 38–46, 2009.

[17] K. Natori, T. Tsuji, K. Ohnishi, A. Hace, and K. Jezernik, "Time-delay compensation by communication disturbance observer for bilateral teleoperation under time-varying delay," *IEEE Transactions on Industrial Electronics*, vol. 57, no. 3, pp. 1050–1062, 2010.

[18] A. Suzuki and K. Ohnishi, "Performance conditioning of time delayed bilateral teleoperation system by scaling down compensation value of communication disturbance observer," in *Proceedings of the 11th IEEE International Workshop on Advanced Motion Control (AMC '10)*, pp. 524–529, Nagaoka, Japan, March 2010.

[19] A. Shahdi and S. Sirouspour, "Adaptive/robust control for time-delay teleoperation," *IEEE Transactions on Robotics*, vol. 25, no. 1, pp. 196–205, 2009.

[20] N. Chopra, M. W. Spong, and R. Lozano, "Synchronization of bilateral teleoperators with time delay," *Automatica*, vol. 44, no. 8, pp. 2142–2148, 2008.

[21] R. J. Anderson and M. W. Spong, "Bilateral control of teleoperators with time delay," *IEEE Transactions on Automatic Control*, vol. 34, no. 5, pp. 494–501, 1989.

[22] G. Niemeyer and J.-J. E. Slotine, "Stable adaptive teleoperation," *IEEE Journal of Oceanic Engineering*, vol. 16, no. 1, pp. 152–162, 1991.

[23] S. Munir and W. J. Book, "Internet-based teleoperation using wave variables with prediction," *IEEE/ASME Transactions on Mechatronics*, vol. 7, no. 2, pp. 124–133, 2002.

[24] G. Niemeyer and J.-J. E. Slotine, "Telemanipulation with time delays," *International Journal of Robotics Research*, vol. 23, no. 9, pp. 873–890, 2004.

[25] N. A. Tanner and G. Niemeyer, "High-frequency acceleration feedback in wave variable telerobotics," *IEEE/ASME Transactions on Mechatronics*, vol. 11, no. 2, pp. 119–127, 2006.

[26] A. Aziminejad, M. Tavakoli, R. V. Patel, and M. Moallem, "Stability and performance in delayed bilateral teleoperation: theory and experiments," *Control Engineering Practice*, vol. 16, no. 11, pp. 1329–1343, 2008.

[27] A. Aziminejad, M. Tavakoli, R. V. Patel, and M. Moallem, "Transparent time-delayed bilateral teleoperation using wave variables," *IEEE Transactions on Control Systems Technology*, vol. 16, no. 3, pp. 548–555, 2008.

[28] S. Katsura, Y. Matsumoto, and K. Ohnishi, "Realization of "law of action and reaction" by multilateral control," *IEEE Transactions on Industrial Electronics*, vol. 52, no. 5, pp. 1196–1205, 2005.

[29] D. Tian, D. Yashiro, and K. Ohnishi, "Improving transparency of bilateral control system by sliding mode assist disturbance observer," *IEEJ Transactions on Electrical and Electronic Engineering*, vol. 8, no. 3, pp. 277–283, 2013.

[30] D. Tian, D. Yashiro, and K. Ohnishi, "Haptic transmission by weighting control under time-varying communication delay," *IET Control Theory & Applications*, vol. 6, no. 3, pp. 420–429, 2012.

[31] K. Kawashima, K. Tadano, G. Sankaranarayanan, and B. Hannaford, "Bilateral teleoperation with time delay using modified wave variables," in *Proceedings of the IEEE/RSJ International Conference on Intelligent Robots and Systems (IROS '08)*, pp. 424–429, Nice, France, September 2008.

[32] T. Murakami, F. Yu, and K. Ohnishi, "Torque sensorless control in multidegree-of-freedom manipulator," *IEEE Transactions on Industrial Electronics*, vol. 40, no. 2, pp. 259–265, 1993.

[33] K. Ohnishi, M. Shibata, and T. Murakami, "Motion control for advanced mechatronics," *IEEE/ASME Transactions on Mechatronics*, vol. 1, no. 1, pp. 56–67, 1996.

Hindawi Publishing Corporation
Mathematical Problems in Engineering
Volume 2013, Article ID 758961, 13 pages
http://dx.doi.org/10.1155/2013/758961

Research Article

Experimental Study on Communication Delay of Powertrain System of Plug-In Hybrid Electric Vehicles

Dafang Wang,[1] Bowen Yang,[1] Cheng Zhu,[2] Ji Qi,[1] and Geliang Ni[1]

[1] *School of Automotive Engineering, Harbin Institute of Technology, Weihai 264209, China*
[2] *China Automotive Technology & Research Center, Tianjin 300300, China*

Correspondence should be addressed to Dafang Wang; wdflcjl@163.com

Received 9 September 2013; Revised 16 October 2013; Accepted 16 October 2013

Academic Editor: Hui Zhang

In order to contrast and analyze the real-time performance of the powertrain system of a plug-in hybrid electric vehicle, a mathematical model of the system delay is established under the circumstances that the transmission adopts the CAN (controller area network) protocol and the TTCAN (time-triggered CAN) protocol, respectively, and the interior of the controller adopts the foreground-background mode and the OSEK mode respectively. In addition, an experimental platform is developed to test communication delays of messages under 4 different implementation models. The 4 models are testing under the CAN protocol while the controller interior adopts the foreground-background mode; testing under the CAN protocol while the controller interior adopts the OSEK mode; testing under the TTCAN protocol while the controller interior adopts the foreground-background mode, and testing under the TTCAN protocol while the controller interior adopts the OSEK mode. The theoretical and testing results indicate that the communication delay of the OSEK mode is a little longer than the one of the foreground-background mode. Moreover, compared with the CAN protocol, the periodic message has a better real-time performance under the TTCAN protocol, while the nonperiodic message has a worse one.

1. Introduction

The controlling and managing system of a plug-in hybrid electric vehicle controls the main assemblies through bus and makes full use and coordination of advantages of each part, so that the vehicle can get the best operating condition. The system adopts network-based control mode, which affects the real-time performance. References [1–5] analyze the relationship between network-induced delays and system performance, introducing network-induced delay in the system modeling, considering the network-induced delays and random data-missing occurrence, analyzing the problem of stability control under different network-induced latency, and pointing out that it is necessary to consider network-induced delays in the choice of control algorithms. The controlling and managing system of the plug-in hybrid electric vehicle is a typical distributed real-time control system. Calculation delay of the controller interior and arbitration and transmission delay during the network communication process have a significant effect on the performance of the system. Nowadays, the mainstream bus of the vehicle distributed real-time control system is CAN bus, while the TTCAN bus is adopted in some condition asking for a high-quality real-time performance. The controller interior mainly adopts the foreground-background mode and the OSEK mode.

The delay of the bus communication can be divided into 4 parts: generating delay, queue delay, transmission, and receiving delay [6]. According to the influencing factors, the delay can be divided into two parts. The first one is on-line delay, which includes queuing delay and transmission delay. This sort of delay is related to the process of data transmitting on the network. Concretely, it is related to the priority setting of data, the type of communication network, and the protocol. The second one is on-chip delay, which includes generating delay and receiving delay. This sort of delay is related to the behaviors in controller nodes. Specifically, it is related to hardware indexes like the operating frequency and the software indexes such as the realization of the control algorithm and the task priority setting of the controller.

On the aspect of the on-line delay of CAN bus, [7–13] put forward the worst transmission delay and the queue delay models aimed at periodic massages. The queue delay models built by the abovementioned references are the same, while the transmission delay models are a little different. Reference [14] presents a buffered estimation method aimed at the system-on-chip (SoC) based on a priority-ranked queuing model and builds a buffered queuing model. The queue is an M/G/1 queue with several different client levels and nonpreemptive arbitration. A mathematical model of average waiting time is deduced, which can provide some reference value for us to build the average waiting-time model of the nonperiodic message on CAN bus. However, there is no actual test of the delay in [14]. References [15, 16] assume that the arrival of message accords with Poisson process and take the transmission process of CAN message as an M/G/1 queuing process to be analyzed. A mathematical model of average delay of message is deduced.

On the aspect of the on-line delay of TTCAN bus, [17, 18] develop a TTCAN experimental platform which can realize the sending and receiving of massages on LEVEL1 which is stipulated by the TTCAN protocol. To periodic messages, the delay time of CAN and TTCAN bus is contrasted and analyzed through measurement. It is pointed out that the real-time performance of periodic messages transmitting on the TTCAN bus cannot be influenced by other nodes, which means that the real-time property of the network is improved. Reference [12] sends nonperiodic messages through arbitration windows. Assuming that the generating moments of nonperiodic messages accord with uniform distribution and then considering the effects of monopolized windows and free windows, a mathematical expectation model for on-line delays of nonperiodic messages with TTCAN protocol is established. The average delays of messages with different IDs are tested through experiments. After contrasting and analyzing the measured and theoretical values as well as the delay time of nonperiodic messages under CAN and TTCAN modes, it is pointed out that TTCAN protocol degrades real-time performance of the nonperiodic messages.

Most of the studies on the vehicular network delay have paid attention to the on-line delay, while they have ignored the on-chip delay [8–12, 15–18]. They point out that the on-chip delay can be neglected for the delay of the vehicular network. If aiming at the message adopted the CAN protocol, meanwhile the processing speed of the chip is fast and the sending-and-receiving priority level of the CAN message is high, the statement can be tenable. But the on-chip delay cannot be ignored when these conditions are not satisfied. At the same time, if adopting the TTCAN protocol, the task scheduling inside the nodes need to match up with the TTCAN task window; otherwise, it will cause the exacerbation of the delay of the TTCAN message.

On the aspect of the on-chip delay based on the foreground-background mode, [8] thinks that the generating delay of messages is permanent without considering the preemption of multiple interrupts in nodes. It is stressed that the receiving delay firstly depends on the receiving mode being roll-polling mode or interrupt trigger mode and secondly depends on the multiple interrupt scheduling methods in nodes. A mathematical model of receiving delay is given out, but there is no measured delay data.

And for the analysis on the aspect of the on-chip delay based on the OSEK mode, aiming at general static embedded real-time operating system, [19, 20] point out that the RM scheduling algorithm is the best scheduling algorithm, and the schedulable rules of the RM arithmetic are given as well. References [21, 22] discuss the burden of microcontroller caused by the embedded kernel and give out the cost time of alarming, triggering tasks, scheduling tasks, and terminating tasks in the OSEK mode. Meanwhile, the worst responding time of fixed priority/first-in-first-out (FP/FIFO) scheduling policy in the OSEK mode is given, separately adopting the preemptive and nonpreemptive mechanisms. And the difference of theoretical responding time is contrasted and analyzed in the condition of considering and not considering the burdens of microcontroller caused by embedded kernel of OSEK. The difference between measured and theoretical responding time is also contrasted, taking the burdens of microcontroller caused by embedded kernel of OSEK into consideration. Then, the necessity of considering the burdens of microcontroller caused by embedded kernel of OSEK is pointed out. References [23, 24] consider that the use of OSEK model can improve the efficiency of the transplant and achieve the reuse of software modules. However, the burden added to the MCU caused by the OSEK system is not taken into consideration.

In this paper, the delay characteristic of the vehicular distributed real-time control system is analyzed, including the on-line delay and the on-chip delay. To finally achieve a better performance of the system, the overall delay model which adopts the different on-chip mechanisms and the different networking protocols is analyzed, and the cooperation of the on-chip scheduling and the network scheduling is also taken into consideration.

2. The Powertrain Network of Plug-In Hybrid Electric Vehicles

2.1. Topology Structure of the Powertrain System. The power comes from three parts: vehicle engines and power units in an APU system, power battery pack, and plug-in charging system. However, the actual power for the running vehicle is mainly supplied by the APU system and the vehicle-mounted power battery pack. The composition of the plug-in controlling system is shown in Figure 1.

In Figure 1, the light-color segments represent signal transmission, including the figure signals, analog signals, and messages on the CAN bus, while the dark-color segments represent driving connections, including high-voltage signals and mechanical connection signals. Powertrain system network is connected with CAN bus, and the transmission rate is 250 Kbits/s. The powertrain CAN network includes 5 nodes which are vehicle controller, motor controller, variable-speed controller, battery controlling system, and APU controller. In the test, they can be realized by the 5 nodes in the network hardware nodes system correspondingly in the experimental platform testing the CAN communication delay. To the driver

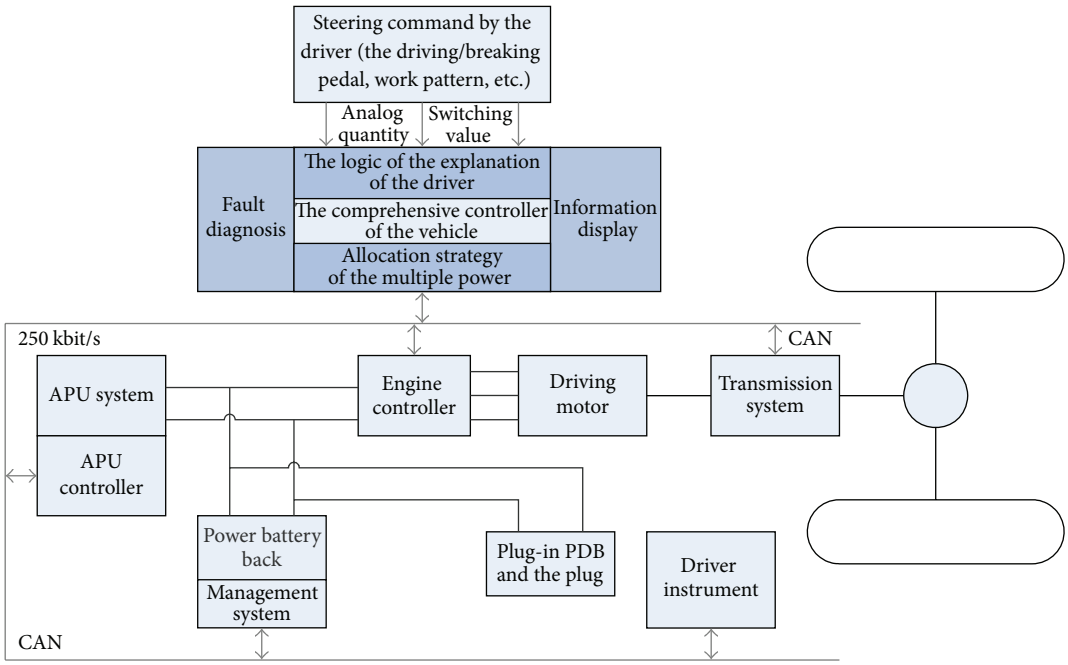

Figure 1: Composition of the plug-in controlling system.

Table 1: Message sending conditions of each node of powertrain.

Sending node	Message	Sending rate (ms)	Receiving node	Message content
Vehicle controller	ID06	10	Motor controller	Motor controls parameter
	ID10	40	APU controller	APU controls parameter
	ID15	80	All of the nodes	Condition of the vehicle controller
	ID03	Nonperiodic	All of the nodes	Vehicle is giving an alarm
Motor controller	ID07	10	Vehicle controller	Motor working parameter
	ID12	40	All of the nodes	Motor working condition
	ID01	Nonperiodic	All of the nodes	Motor is giving an alarm
Variable speed controller	ID08	20	All of the nodes	Transmission working parameter
	ID11	40	All of the nodes	Transmission working condition
	ID02	Nonperiodic	All of the nodes	Transmission is giving an alarm
Battery management system	ID09	20	Vehicle controller	Battery pack working parameter
	ID16~44	80	Message display	Battery pack is collection points message
	ID04	Nonperiodic	All of the nodes	Battery system is giving an alarm
APU controller	ID13	40	All of the nodes	APU working parameter
	ID14	80	All of the nodes	APU working condition
	ID05	Nonperiodic	All of the nodes	APU is giving an alarm

instrument node in Figure 1, the node does not belong to the powertrain part, but the node is in the powertrain network in the real vehicle to function on monitoring and display. The node only receives messages from the network, but it does not send messages through the network. It can be realized by the upper computer nodes in the experimental platform testing the CAN communication delay, and the purpose here is to monitor the time parameter of the network message transmission.

2.2. Definition of Parameter Groups of Each Node in the Powertrain. The powertrain system of a plug-in hybrid electric vehicle consists of 5 nodes, and the setting conditions of parameter groups of each node are given out in Table 1.

According to Table 1, the powertrain CAN network transmits 44 messages with different IDs, and the priorities of messages are the same with the numbers, which means that the priority of the message ID01 is the highest and the priority of the message ID44 is the lowest. The messages include 39

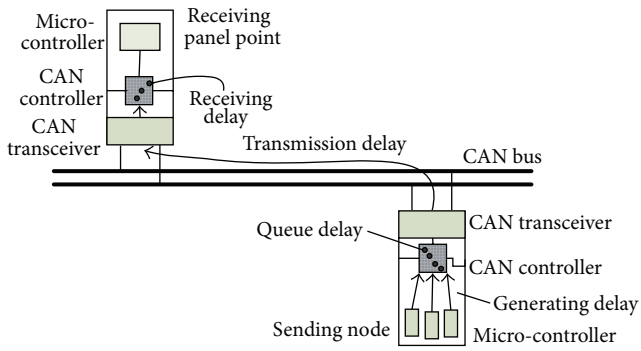

Figure 2: Communication delay model.

periodic messages, and the longest sending period among them is 80 ms, while the shortest is 10 ms. There are also 5 nonperiodic messages whose generating process is assumed to be a Poisson process.

3. Theoretical Model of Communication Delay

The bus adopts the CAN transmission and TTCAN protocol, and the interior of controller nodes adopts the foreground-background mode and the OSEK mode, respectively, to realize the total communication delay of the powertrain distributed real-time controlling system of a plug-in hybrid electric vehicle under these 4 working conditions. Considering the specific application to be a passenger car, the vehicle communication should be corresponding to protocol SAEJ1939. Therefore, the massage form is defined as expanding frame form.

3.1. Composition of Communication Delay. Aiming at the distributed real-time controlling system based on the CAN bus, [7] gives out the composition of the communication delay of point-to-point messages, which is shown in Figure 2.

The communication delay of the bus can be divided into 4 parts, which are generating delay, queue delay, transmission delay, and receiving delay [6].

The generating delay: the period from the moment of microcontroller that sends node receiving the request from the same node to the moment of writing the prepared data into the sending cache queue of the CAN controller.

The queue delay: the period from the moment of massage entering the sending cache queue of the CAN controller to the moment of the massage obtaining controlling right of the bus.

The transmission delay is the period from the moment of massage occupying the bus to the moment of massage leaving the bus.

The receiving delay is the period from the moment of massage leaving the bus to providing the effective data to the microcontroller that receives nodes.

To describe it easier, this paper divided the communication delay into two parts: on-line delay which includes queue delay and transmission delay and on-chip delay which includes generating delay and receiving delay.

3.2. Mathematical Model of Communication Delay

3.2.1. The Model of the On-Line Delay. For the periodic message, the queue delay could be expressed with an iteration formula as follows:

$$t_m^{n+1} = \sum_{\forall j \in hp(m)} \left[\frac{t_m^n + J_j + \tau_{\text{bit}}}{T_j} \right] c_j + \sum_{j=1}^{N} \frac{c_j^2}{2T_j}. \quad (1)$$

In the previous formula, n represents the iteration. When $t_m^{n+1} = t_m^n$, the iteration is convergence, and the result value is supposed to be the average queue delay. $hp(m)$ is the gather of message frames whose priority is higher than m. T_j is the transmission period of the periodic message frame j. J_j is the maximum error of message frame js period. c_j is the transmission delay of the message frame j. c_j is the time needed to transmit a bit on the transmission media.

The transmission delay of message m is c_m, and the transmission delay of the expending message frame is expressed as follows:

$$c_m = \left(67 + 8s_m + \left\lceil \frac{\lfloor (54 + 8s_m)/4 \rfloor}{2} \right\rceil \right) \tau_{\text{bit}} + \rho_{\text{cons}}. \quad (2)$$

In the previous formula, s_m is the number of bytes contained by the message m data field and is an integer between 0 and 8. ρ_{cons} is a constant related to the electrical specification of the bus physical medium.

The average queue delay and transmission delay are independent of each other, and the average on-line delay is the sum of the two:

$$T_m = t_m + c_m. \quad (3)$$

In the previous formula, T_m is the average on-line delay.

Substituting (1) and (2) into (3), we can acquire that

$$\begin{aligned} T_m = &\sum_{\forall j \in hp(m)} \left[\frac{t_m + J_j + \tau_{\text{bit}}}{T_j} \right] c_j + \sum_{j=1}^{N} \frac{c_j^2}{2T_j} \\ &+ \left(67 + 8s_m + \left\lceil \frac{\lfloor (54 + 8s_m)/4 \rfloor}{2} \right\rceil \right) \tau_{\text{bit}} + \rho_{\text{cons}}. \end{aligned} \quad (4)$$

To the nonperiodic messages, according to the priorities ranking from high to low, the highest-priority message is called type 1 message; the second high-priority message is called type 2 message, and so on, while the lowest-priority message is called type n message.

Firstly, consider type 1 message, which means the problem of the average queue delay of messages with the highest-priority.

When a type 1 message requests to transmit on the bus, its average waiting time $\overline{W_{q1}}$ is

$$\overline{W_{q1}} = \overline{W^e} = \sum_{i=1}^{n} \frac{\lambda_i E\left(\chi_i^2\right)}{2}. \quad (5)$$

In the previous formula, $\overline{W_{q1}}$ represents the average waiting time of the type 1 message, which means the period from the moment of requesting to transmit to the moment of occupying the bus. $\overline{W^e}$ is the average remaining time of the massage that is transmitted currently when type 1 message arrives. n represents the amount of the message types. λ_i is the requesting rate of type i message. χ_i represents the transmission time of type i message and is a random variable.

Then, consider the problem of the average queue delay of type i messages.

When a type i message requests to transmit on the bus, its average waiting time $\overline{W_{qi}}$ is

$$\overline{W_{qi}} = \frac{\overline{W_{q(i-1)}}\left(1 - \sum_{j=1}^{i-2} \rho_j + \rho_{i-1}\right)}{\left(1 - \sum_{j=1}^{i-1} \rho_j\right)}. \quad (6)$$

In the previous formula, $\rho = \lambda/\mu$, λ is a parameter of the Poisson process and μ is the reciprocal of the average servicing time.

Then, consider the transmission delay; the on-line delay of the message is

$$\overline{W_i} = c_m + \overline{W_{qi}}. \quad (7)$$

What is different from the analysis of on-line delay of the periodic CAN messages is that every periodic TTCAN message transmits in the appointed exclusive-time window, ensuring that the bus is free when each periodic massage gets triggered by scheduling the overall time. Therefore, the queue delay of the periodic message will not exist any longer. As a result, under the TTCAN protocol, the on-line delay of the periodic message is just transmission delay. Substituting $t_m = 0$ into (3), the mathematical model of the average on-line delay of the periodic TTCAN message can be acquired, and is shown as follow:

$$T_m = \left(67 + 8s_m + \left\lceil \frac{\lfloor (54 + 8s_m)/4 \rfloor}{2} \right\rceil\right)\tau_{\text{bit}} + \rho_{\text{cons}}. \quad (8)$$

Nonperiodic TTCAN messages are all assumed to be scheduled in the arbitration time window. Based on the analysis of average on-line delay of the CAN nonperiodic message, the effects of exclusive-time window and free-time window are taken into consideration. When the nonperiodic message m generates in a certain exclusive-time window i, it could only be sent when it is delayed to a following certain arbitration time window.

Set the number of the exclusive-time windows (or the free-time windows) within the average arriving period of nonperiodic massages to be K and the length of the time window to be h. In that way, the average delay caused by the nonperiodic messages which are affected by the exclusive-time window (or the free-time window) is supposed to be

$$G_m = \sum_{i=1}^{K} \frac{(L_i + c_m)^2 \left(1 - e^{-\lambda h}\right)}{(2 \times h)}. \quad (9)$$

In the previous formula, L_i represents the time length of the exclusive-time window (or the free-time window) i.

According to (9) and (7), the average on-line delay formula based on the queue theory should be

$$\overline{W_i} = \frac{1}{\mu_i} + \overline{W_{qi}} + G_m. \quad (10)$$

3.2.2. On-Chip Delay Model. In the node of the controller, the average performing time of the task can be expressed as follows:

$$r_i = e_i + \sum_{\forall j \in hp(i)} \left\lceil \frac{r_i}{P_j} \right\rceil e_j \quad (11)$$

In the previous formula, r_i is the average performing time of task i, $hp(i)$ is the set of the tasks whose priorities are higher than those of task i, e_i is the performing time of task T_i, and P_i is the period of task T_i. The first part on the right side of (11) means the performing time when there is only task, and the second part means the disturbing time caused by the performing of the task with a higher priority.

The generating delay of messages means the time needed from the moment of sending node requesting to generate message to the moment of writing the generated message into the sending cache of bus controller, which means the period from the moment that the message sends the task to the moment that the task is finished in the node. Message receiving delay means the time needed from the moment that the message leaves from the bus to the moment that the carried data is provided to the target task of receiving nodes, which means the period from the moment that the message receives the task to the moment that the task is finished in the node.

4. Experimental Study of Communication Delay

4.1. Experiment Environment

4.1.1. Basic Experiment Environment. The bus adopts the CAN and TTCAN transmission protocols, respectively, and interior of the controller nodes adopts the foreground-background mode and the OSEK mode, respectively. The overall communication delay of the powertrain distributed real-time controlling system of a plug-in hybrid electric vehicle under these four working conditions is analyzed. The specific experiment environment is expressed as follows.

The bus baud rate of the communication delay testing platform is set to be 250 Kbit/s, and the expanding data frame form is adopted to write communication programs of the 5 nodes shown in Figure 1. In order to simplify the analysis process, assumptions of the node program of the vehicle controller are put forward as follows.

(1) The program is divided into 5 tasks, which is used for realizing the transmission of 3 periodic messages and 1 nonperiodic message as well as the receiving of messages.

(2) The controlling strategy related to each task is finished inside the task.

Table 2: The individual performing time of tasks under the foreground-background mode.

Description of tasks	Performing time (ms)
Sending message ID03	0.0132
Sending message ID06	0.0352
Sending message ID10	0.0272
Sending message ID15	0.0162
Message receiving	0.0142

Table 3: The individual performing time of tasks under the OSEK mode.

Description of tasks	Performing time (ms)
Sending message ID03	0.0292
Sending message ID06	0.0512
Sending message ID10	0.0432
Sending message ID15	0.0322
Message receiving	0.0302

(3) The priority of the receiving tasks of messages in the node is the highest, and the priority of tasks sending from the message equals the priority of the message.

Table 2 gives out the measured performing time of the 5 tasks of the vehicle controller nodes under the foreground-background mode.

Table 3 gives out the measured performing time of the 5 tasks of the vehicle controller nodes under the OSEK mode.

According to Tables 2 and 3, for the same task, the performing time under the OSEK mode is longer than that under the foreground-background mode, which is related to the task scheduling structure inside the OSEK system. And this indicates that load to microcontroller in the OSEK mode is larger than that in the foreground-background mode.

4.1.2. The Establishment and the Schedulable Analysis of the TTCAN Matrix Period. When the transmission protocol adopts the TTCAN mode, the matrix period, the basic period, and the width of the time window which means the transmission column width in the matrix period should be determined.

Firstly, assume that the matrix includes P lines and Q columns. The transmission column width of a column must guarantee the transmission of a package of whole messages, and, for the expanding frame message, the width is supposed to be

$$T_{\mathrm{CW}j} = \max_{M_{0,j}}^{M_{P,j}} \left[\left(67 + 8s_m + \left\lfloor \frac{54 + 8s_m}{4} \right\rfloor \right) \tau_{\mathrm{bit}} + \rho_{\mathrm{cons}} \right]. \quad (12)$$

In the previous formula, $T_{\mathrm{CW}j}$ is the transmission column width of the column j, and $M_{i,j}$ is the line i column j of the matrix period.

Length of the basic period is usually set as the greatest common divisor of all message periods, while the length of the matrix period is usually set as the least common multiple of all message periods. The calculated matrix period needs a schedulable analysis in order to explain whether the matrix period is enough for scheduling all of the messages or not. Reference [25] puts forward a sort of scheduling algorithm based on the AL (average loading) without considering the effects of nonperiodic messages. Modify the algorithm, and then give out an AL scheduling algorithm which considers periodic messages and nonperiodic messages at the same time.

In advance, N is defined to be the number of periodic messages, periodic is set to be $T = \{T_1, T_2, \ldots, T_M\}$, and M is defined to be the number of the periods. The number of the message whose periodic is T_i among them is n_i, $1 \le i \le M$. V is the number of nonperiodic messages. It is defined that the reaching process of nonperiodic messages is accorded with a Poisson process whose average rate is λ. Then,

$$N = \sum_{i=1}^{M} n_i. \quad (13)$$

Let the width of each column in the matrix period be the same, and the width T_{CW} is

$$T_{\mathrm{CW}} > \max_{j=1}^{Q} \left(T_{\mathrm{CW}j} \right). \quad (14)$$

Let the basic period be the greatest common divisor (GCD) of the period:

$$T_{\mathrm{BC}} = \mathrm{GCD}\left(T_1, T_2, \ldots, T_M \right). \quad (15)$$

Let the matrix period be the lowest common multiple (LCM) of the period:

$$T_{\mathrm{MC}} = \mathrm{LCM}\left(T_1, T_2, \ldots, T_M \right). \quad (16)$$

The ratio k_i of the message period and the basic period is

$$k_i = \frac{T_i}{T_{\mathrm{BC}}}. \quad (17)$$

The number of the basic periods N_{BC} is

$$N_{\mathrm{BC}} = \frac{T_{\mathrm{MC}}}{T_{\mathrm{BC}}}. \quad (18)$$

The number of the time window needed in a basic period is

$$S_i = S_{i-1} + \left\lceil \frac{n_i}{k_i} \right\rceil + \lceil V \lambda T_{\mathrm{BC}} \rceil. \quad (19)$$

Let S_0 be equal to 0; the largest message number which could be transmitted in a basic period is

$$\gamma_{\max} = \frac{\left(T_{\mathrm{BC}} - T_{\mathrm{RM}} \right)}{T_{\mathrm{CW}}}. \quad (20)$$

In the previous formula, T_{RM} is the length of the time window of referential message.

If the schedulable condition is satisfied:

$$S_M \le \gamma_{\max}, \quad (21)$$

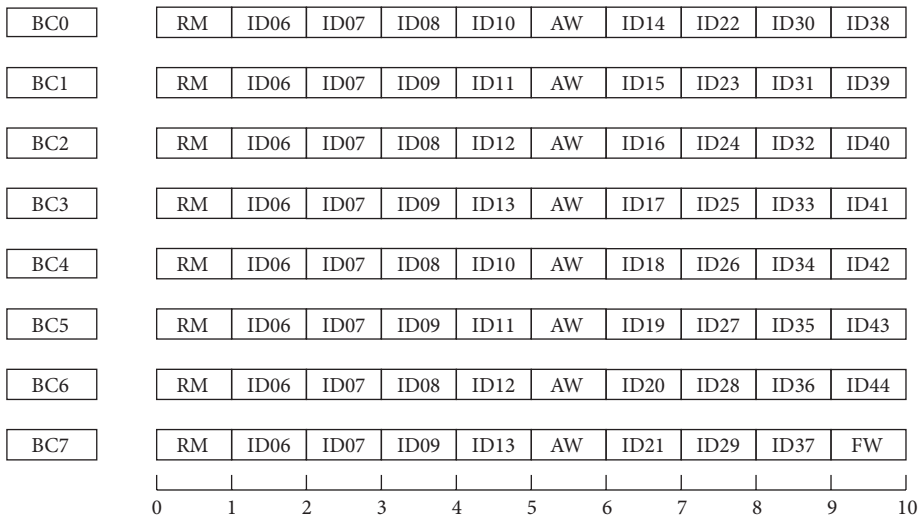

Figure 3: The matrix period of the plug-in powertrain of the TTCAN protocol.

then we can reach a conclusion that the message can be scheduled. According to this, the qualified matrix period can be established.

For the messages sent by each node of the powertrain of a plug-in hybrid electric vehicle which is defined in Table 1, according to (12), $T_{\mathrm{CW}j} = 0.64$ can be get and then substitute it to (14), and $T_{\mathrm{CW}} = 1$. According to (15), $T_{\mathrm{BC}} = 10$, and, according to (16), $T_{\mathrm{MC}} = 80$. According to (18), $N_{\mathrm{BC}} = 8$, and, according to (19), $S_4 = 9$. Let $T_{\mathrm{RM}} = 1$, according to (20), $\gamma_{\max} = 9$. Therefore, the conditions of (21) are met, and then a conclusion can be reached that the message can be scheduled, and the matrix period established is shown in Figure 3.

In Figure 3, AW stands for the arbitration window, and FW stands for the free window. The matrix period includes 8 basic periods, and the length of each basic period is 10 ms, so the length of the matrix period is 80 ms. Moreover, the width of each column is the same, which is 1 ms. Nonperiodic messages ID1~ID5 are transmitted in the arbitration window.

4.1.3. The On-Chip and On-Line Combined Scheduling of the Periodic Message under the TTCAN Mode. For the periodic message, the transmission under the TTCAN mode needs the cooperation of the interior scheduling of the node and the window scheduling on the bus.

The periodic message F is sent from window $M_{i,j}$ of the matrix period, that is, when the message is sent from line i column j of the matrix period. The beginning moment of window $M_{i,j}$ is defined as $I_{M_{i,j}}$; then, inside the node, the best beginning moment I_{T_F} of task T_F that is, sending periodic message F is defined, which means the phase of task T_F. It is shown as follows:

$$I_{T_F} = I_{M_{i,j}} - r_{T_F p}. \tag{22}$$

In the previous formula, $r_{T_F p}$ is the worst performing time of task T_F.

The cooperation of the trigger phase of the sending task and the transmission window of the corresponding message on the bus can be realized by the overall time stamp provided by the reference message. According to the trigger phase T_F defined by (22), on one hand, it could guarantee that the data could be written into the cache before the sending window of the periodic message F reaching; on the other hand, it could guarantee that the data written in the sending cache are the newest data.

4.2. Testing Results. Then, the tests of the communication delay of the powertrain of a plug-in hybrid electric vehicle are conducted in 4 working conditions separately, which are the following: testing under the CAN communication protocol while the controller interior adopts the foreground-background mode; testing under the CAN communication protocol while the controller interior adopts the OSEK mode; testing under the TTCAN communication protocol while the controller interior adopts the foreground-background mode; testing under the TTCAN communication protocol while the controller interior adopts the OSEK mode.

4.2.1. The Testing Results of Communication Delay under the Foreground-Background Mode with the CAN Protocol. Under the foreground-background mode, 3 timer interruptions control the sending of 3 periodic CAN messages, an exterior triggered interruption controls the sending of a nonperiodic CAN message, and a CAN receiving interruption controls the real-time receiving of the CAN message. Figure 4 gives out the communication delay of the nonperiodic message, and Figure 5 gives out the communication delays of the 3 periodic messages under this mode. The communication delay is the delay summation of the four parts including generating, queue, transmission, and receiving.

Table 4: The comparison of the measured and theoretical communication delays of the message of the vehicle controller node under foreground-background mode with the CAN protocol.

Message ID	Measured average communication delay (ms)	Theoretical average communication delay (ms)	Average communication delay error	Maximum measured communication delay (ms)
ID03	0.75585	0.73658	−2.62%	1.4599
ID06	0.73184	0.75523	3.10%	1.4097
ID10	0.80478	0.77407	−3.97%	2.3594
ID15	0.79332	0.78634	−0.89%	3.9359

Table 5: The comparison of the measured and theoretical communication delays of the message of the vehicle controller node under OSEK mode with the CAN protocol.

Message ID	Measured average communication delay (ms)	Theoretical average communication delay (ms)	Average communication delay error	Maximum measured communication delay (ms)
ID03	0.76043	0.7692	1.14%	1.6344
ID06	0.76505	0.78827	2.95%	1.6427
ID10	0.86326	0.80728	−6.93%	2.1817
ID15	0.88312	0.81935	−7.78%	3.878

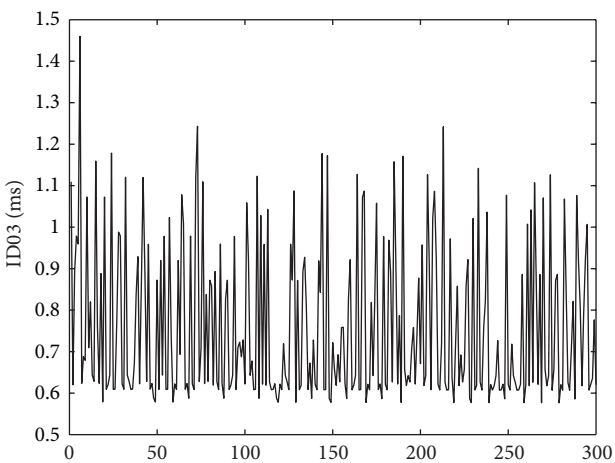

Figure 4: The communication delay of the nonperiodic message under the foreground-background mode with CAN protocol.

According to Figures 4 and 5, the average communication delay of each ID message can be acquired after the statistic analysis, which is shown in Table 4.

4.2.2. The Testing Results of Communication Delay under the OSEK Mode with the CAN Protocol. Under the OSEK mode, the sending and receiving of the message are directly controlled by OSEK tasks. The communication delay of nonperiodic messages is shown in Figure 6, and the communication delays of the 3 periodic messages are shown in Figure 7.

According to Figures 6 and 7, the average communication delay of each ID message can be acquired after the statistic analysis, which is shown in Table 5.

4.2.3. The Testing Results of Communication Delay under the Foreground-Background Mode with the TTCAN Protocol. Figure 8 gives out the communicationdelay of the nonperiodic message, and Figure 9 gives out the communication delays of 3 periodic messages.

For the communication delay of the periodic message shown in Figure 9, the sending and receiving delay parts are only disturbed by the sending task of the nonperiodic message inside the node, while the other periodic tasks and the receiving tasks are all finished inside their own region, which have no effect on the sending of periodic messages.

According to Figures 8 and 9, the average communication delay of each ID message can be acquired after the statistic analysis, which is shown in Table 6.

4.2.4. The Testing Results of Communication Delay under the OSEK Mode with the TTCAN Protocol. Under the OSEK mode, the sending and receiving of the message are directly controlled by OSEK tasks. Figure 10 gives out the communication delay of the nonperiodic message, and Figure 11 gives out the communication delay of the 3 periodic messages.

According to Figures 10 and 11, the average communication delay of each ID message can be acquired after the statistic analysis, which is shown in Table 7.

4.3. The Data Analysis of the Communication Delay. The following analysis results can be acquired according to Tables 4 to 7.

(1) According to the measured transmission process of messages, the matrix period and the schedulable analysis proposed in Section 4.1.2 are verified to be true. The schedule of messages can be finished.

(2) Under all kinds of the working conditions and modes, the theoretical and the measured results are approaches. The maximal error is just −7.78%, which indicates that the theoretical model is reasonable.

(3) Under the CAN protocol, for the same message no matter it is periodic or nonperiodic, the average communication delay under the OSEK mode is longer

Table 6: The comparison of the measured and theoretical communication delays of the message of the vehicle controller node under foreground-background mode with the TTCAN protocol.

Message ID	Measured average communication delay (ms)	Theoretical average communication delay (ms)	Average communication delay error	Maximum measured communication delay (ms)
ID03	5.2397	5.1803	−1.15%	15.317
ID06	0.6094	0.6174	1.30%	0.6173
ID10	0.6014	0.6094	1.31%	0.6093
ID15	0.5904	0.5984	1.34%	0.5983

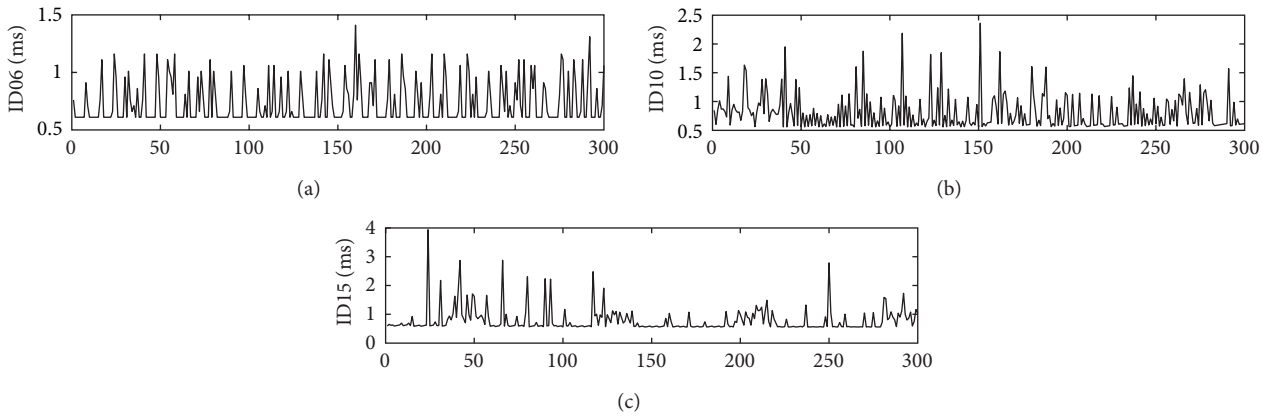

Figure 5: The communication delay of the periodic message under the foreground-background mode with CAN protocol.

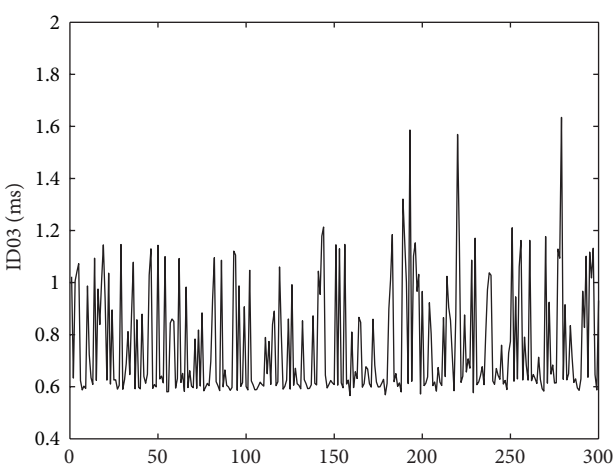

Figure 6: The communication delay of the nonperiodic message of the vehicle controller node under the OSEK mode with the CAN protocol.

than the one under the foreground-background mode. The reason is that the generating delay and the receiving delay (on-chip delay) under the OSEK mode are longer than the ones under the foreground-background mode.

(4) Under the CAN protocol, the longest communication delay of each message under the OSEK mode is not consistently longer than the longest communication delay under the foreground-background mode, which means that the longest communication delay has more randomness than the average communication delay.

(5) Under the TTCAN protocol, for the same message no matter it is periodic or nonperiodic, the communication delay under the OSEK mode is longer than the one under the foreground-background mode. The reason is that the generating delay and the receiving delay (on-chip delay) under the OSEK mode are longer than the ones under the foreground-background mode.

(6) For the periodic message, no matter it is the foreground-background mode or the OSEK mode, the communication delay under the TTCAN protocol is shorter than the one under the CAN protocol. It is mainly because the queue delay of the communication delay under the TTCAN protocol is 0, which makes the integral communication delay decline.

(7) For the nonperiodic message, no matter it is the foreground-background mode or the OSEK mode, the communication delay under the TTCAN protocol is much longer than the one under the CAN protocol. It is mainly because only arbitration window in the network bandwidth allows the sending of the nonperiodic message under the TTCAN protocol. As a result, the exclusive window and the free window enlarge the queue delay of the nonperiodic message and delay the transmission of the nonperiodic message, which causes the increase of the communication delay of nonperiodic messages.

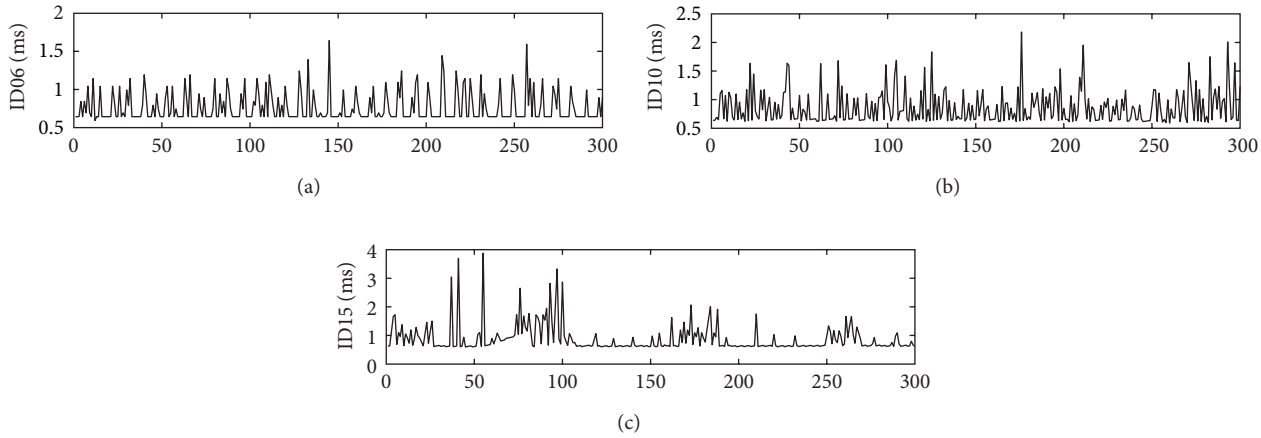

Figure 7: The communication delay of the periodic message of the vehicle controller node under the OSEK mode with the CAN protocol.

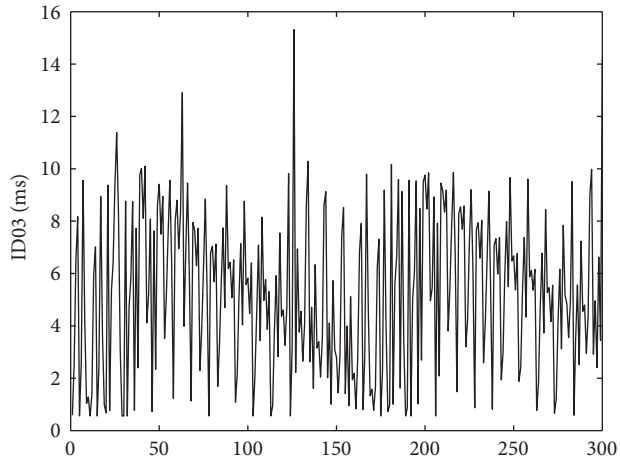

Figure 8: The communication delay of the nonperiodic message of the vehicle controller node under the foreground-background mode with the TTCAN protocol.

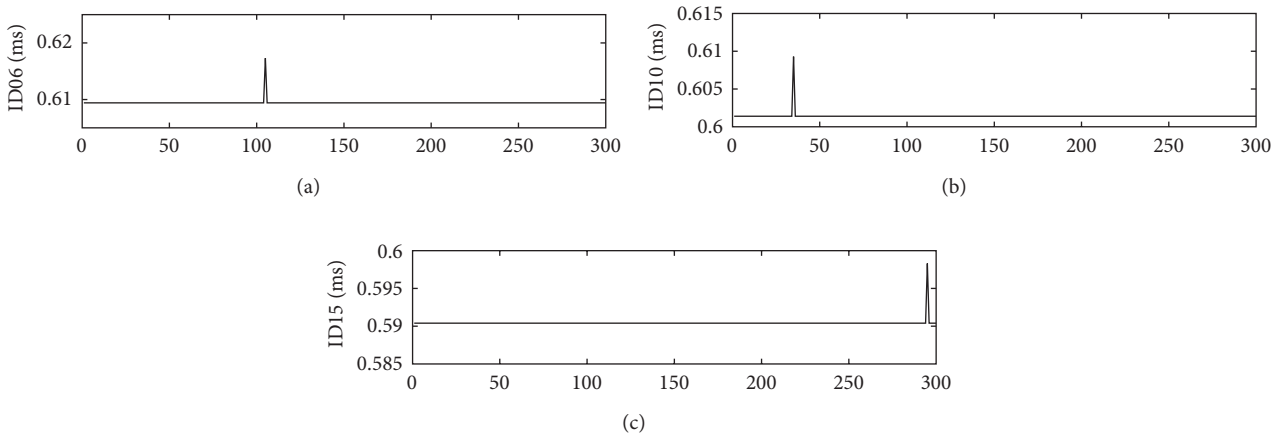

Figure 9: The communication delay of the periodic message of the vehicle controller node under foreground-background mode with the TTCAN protocol.

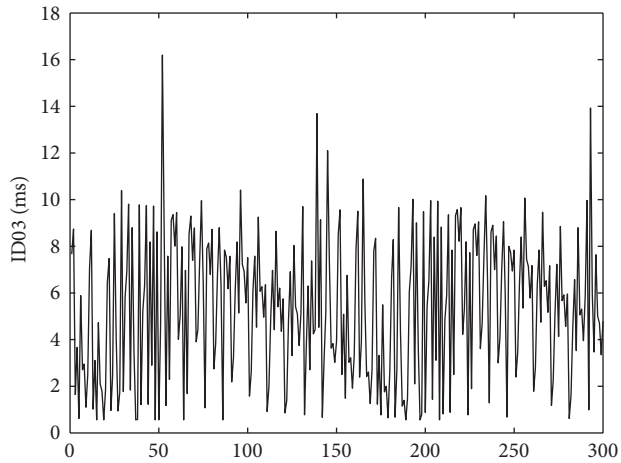

Figure 10: The communication delay of the nonperiodic message of the vehicle controller node under OSEK mode with the TTCAN protocol.

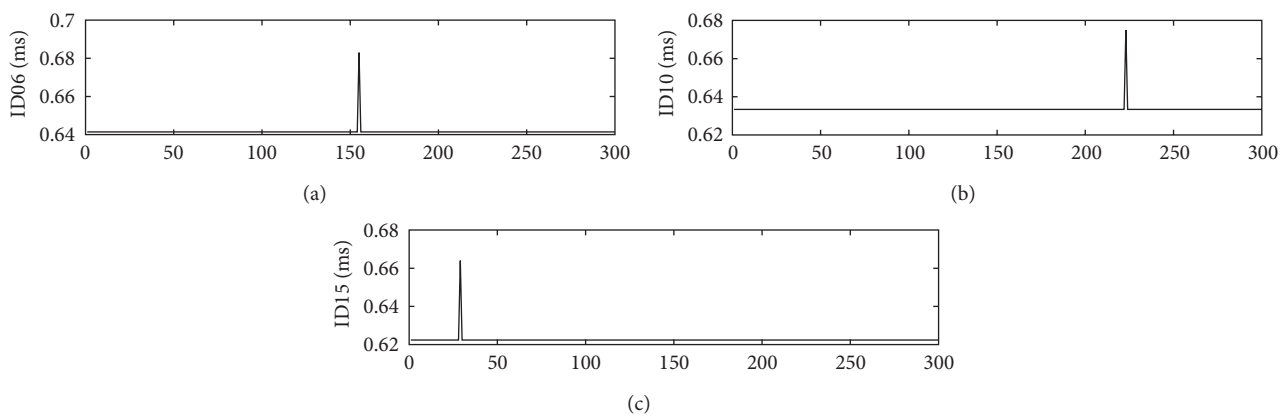

Figure 11: The communication delay of the periodic message of the vehicle controller node under OSEK mode with the TTCAN protocol.

The analysis results above are acquired under the conditions that the periodic message and the nonperiodic message are transmitted in the network at the same time and that the working conditions of the sending delay and the receiving delay inside the node under the foreground-background mode and the OSEK mode are considered at the same time.

5. Conclusion

Regarding the powertrain network system of a plug-in hybrid electric vehicle as the studying target, the communication delay of the message is tested. Firstly, the topological structure and the definition of the parameter set of each node of the powertrain system of this plug-in hybrid electric vehicle are given out. The bus is established adopting the CAN protocol and the TTCAN protocol, respectively, and the delay model of the foreground-background mode and the OSEK mode systems are adopted inside the node. The schedulable rules under the TTCAN protocol based on the average loading arithmetic which takes the periodic message and the nonperiodic one into consideration at the same time are established. According to the rules, the matrix period of message transmission in the powertrain system of a plug-in hybrid electric vehicle is established as well. Through the measured message transmission process, it could be acquired that the matrix period is enough to finish the schedule of messages, verifying the accuracy of the scheduling algorithm. The on-chip and on-line united scheduling problem of the periodic message under the TTCAN mode is analyzed, and the best on-chip phase of the sending task of the periodic message is defined. Then, the communication delay of the message is tested under the foreground-background mode and the OSEK mode, using the CAN and TTCAN as the transmission protocol, respectively. In the 4 working conditions above, after analyzing the test data, it could be concluded that the communication delay time of the OSEK mode is a little longer than the one of the foreground-background mode in the same condition. The real-time performance of the periodic message under the TTCAN protocol is better than the one under the CAN protocol, while the real-time performance of the nonperiodic message is worse than the one under the CAN protocol. The data of the measured average communication delay is very similar to

Table 7: The comparison of the measured and theoretical communication delays of the message of the vehicle controller node under OSEK mode with the TTCAN protocol.

Message ID	Measured average communication delay (ms)	Theoretical average communication delay (ms)	Average communication delay error	Maximum measured communication delay (ms)
ID03	5.3449	5.213	−2.53%	16.198
ID06	0.6414	0.6494	1.23%	0.6830
ID10	0.6334	0.6414	1.25%	0.6334
ID15	0.6224	0.6304	1.27%	0.6640

the theoretical one, and the maximal error is just −7.78%, which means that the theoretical model is reliable.

Conflict of Interests

The authors declare that there is no conflict of interests regarding the publication of this paper.

Acknowledgments

This work is sponsored by the Aerospace Support Technology Fund (2013-HT-HGD09), the National Laboratory for Electric Vehicles Foundations (NELEV-2013-004), Shandong Province Outstanding Young Scientists Research Award Funds (BS2012NJ001), and Beijing Science and Technology Project (Z121100005612001).

References

[1] Z. Shuai, H. Zhang, J. Wang, J. Li, and M. Ouyang, "Combined AFS and DYC control of four-wheel-independent-drive electric vehicles over CAN network with time-varying delays," *IEEE Transactions on Vehicular Technology*, 2013.

[2] H. Zhang, Y. Shi, and J. Wang, "Observer-based tracking controller design for networked predictive control systems with uncertain Markov delays," *International Journal of Control*, vol. 86, no. 10, pp. 1824–1836, 2013.

[3] H. Zhang, Y. Shi, and M. X. Liu, "H_∞ step tracking control for networked discrete-time nonlinear systems with integral and predictive actions," *IEEE Transactions on Industrial Informatics*, vol. 9, no. 1, pp. 337–345, 2013.

[4] H. Zhang, Y. Shi, and A. Saadat Mehr, "Robust static output feedback control and remote PID design for networked motor systems," *IEEE Transactions on Industrial Electronics*, vol. 58, no. 12, pp. 5396–5405, 2011.

[5] H. Zhang, Y. Shi, and A. S. Mehr, "Robust weighted Hinf; Filtering for networked systems with intermittent measurements of multiple sensors," *International Journal of Adaptive Control and Signal Processing*, vol. 25, no. 4, pp. 313–330, 2011.

[6] K. Tindell, A. Burns, and A. J. Wellings, "Analysis of hard real-time communications," *Real-Time Systems*, vol. 9, no. 2, pp. 147–171, 1995.

[7] J. M. Jeon, D. W. Kim, H. S. Kim, Y. J. Cho, and B. H. Lee, "An analysis of network-based control system using CAN(controller area network) protocol," in *Proceedings of the IEEE International Conference on Robotics & Automation*, pp. 3577–3581, Seoul, Korea, May 2001.

[8] Z.-J. Wu, M.-Q. Hu, J.-Y. Zheng, and Y.-S. Du, "Study on the delay of CAN bus at the process level of substation," *Automation of Electric Power Systems*, vol. 29, no. 11, pp. 34–39, 2005.

[9] L. Yabo, Z. Junzhi, and L. Qingchun, "An analysis on real-time capability of CAN networks for hybrid electric vehicle," *Automotive Engineering*, vol. 27, no. 1, pp. 16–19, 2005.

[10] J.-B. Wang and B.-G. Xu, "Analysis and online evaluation of CAN message real-time performance," *Control and Decision*, vol. 22, no. 4, pp. 448–452, 2007.

[11] S. Hasnaoui, O. Kallel, R. Kbaier, and S. B. Ahmed, "An implementation of a proposed modification of CAN protocol on CAN fieldbus controller component for supporting a dynamic priority policy," in *Proceedings of the 38th IAS Annual Meeting. Conference Record of the Industry Applications Conference*, pp. 23–31, October 2003.

[12] J. Li, Y. Zhu, and G. Tian, "Response time analysis for CAN and TTCAN communications," *Journal of Tsinghua University*, vol. 46, no. 2, pp. 261–265, 2006.

[13] D. Heffernan and A. Bohannon, "Real-time design in a distributed control network application layer environment," *IEE Proceedings*, vol. 148, no. 5, pp. 149–155, 2001.

[14] W. Xufan and Y. Jun, "Queuing network based model for bus buffer estimation," *Journal of Applied Sciences*, vol. 24, no. 1, pp. 45–49, 2006.

[15] S. Jiugen, *Real-time study of NCS [Ph.D. thesis]*, University of Science and Technology of China, Hefei, China, 2003.

[16] S. Jiugen and Z. Peiren, "The study of CAN networks application in real-time system," *Journal of University of Science and Technology of China*, vol. 35, no. 2, pp. 196–201, 2005.

[17] W. Huan and W. Lifang, "A research on the real-time analysis," *High Technology Letters*, vol. 16, no. 8, pp. 830–883, 2006.

[18] W. Huan, *The study of TTCAN bus tech in electric vehicle [Ph.D. thesis]*, Chinese Academy of Sciences, Beijing, China, 2006.

[19] C. M. Krishna and K. G. Shin, *Real-Time Systems*, Tsinghua University Press, Beijing, China, 2001.

[20] C. M. Krishna and K. G. Shin, *Real-Time Systems*, Dai Qionghai Transactions, Tsinghua University Press, Beijing, China, 2004.

[21] F. Bimbard and L. George, "On the conception of an autonomous and modular robot based on an Event Driven OSEK System with deterministic real-time behavior," in *Proceedings of the International Conference on Autonomic and Autonomous Systems*, July 2006.

[22] F. Bimbard and L. George, "FP/FIFO feasibility conditions with kernel overheads for periodic tasks on an event driven OSEK system," in *Proceedings of the 9th IEEE International Symposium on Object-Oriented Real-Time Distributed Computing (ISORC '06)*, pp. 566–574, April 2006.

[23] Y. Jianfeng, Z. Wenhua, H. Wenhua, and S. Qianjun, "Development of automotive ECU using RTOS in compliance with

OSEK/VDX standard," *Automotive Engineering*, vol. 26, no. 2, pp. 210–213, 2004.

[24] C.-W. Liu, S.-Y. Wang, and Q. Yang, "Study of high pressure common rail fuel injection system based on OSEKWorks platform," *Chinese Internal Combustion Engine Engineering*, vol. 25, no. 4, pp. 28–31, 2004.

[25] W. Cao, T. Zhang, Y. Liu, and Y. Wang, "Design and analysis on scheduling of messages in automotive control system based on TTCAN," *Transactions of the Chinese Society of Agricultural Machinery*, vol. 38, no. 12, pp. 41–44, 2007.

Hindawi Publishing Corporation
Mathematical Problems in Engineering
Volume 2013, Article ID 410864, 7 pages
http://dx.doi.org/10.1155/2013/410864

Research Article

Optimal Slip Ratio Based Fuzzy Control of Acceleration Slip Regulation for Four-Wheel Independent Driving Electric Vehicles

Guodong Yin,[1,2] Shanbao Wang,[1] and Xianjian Jin[1]

[1] *School of Mechanical Engineering, Southeast University, Nanjing 211189, China*
[2] *State Key Laboratory of Mechanical Transmission, Chongqing University, Chongqing 400044, China*

Correspondence should be addressed to Guodong Yin; ygd@seu.edu.cn

Received 26 September 2013; Accepted 27 October 2013

Academic Editor: Hui Zhang

To improve the driving performance and the stability of the electric vehicle, a novel acceleration slip regulation (ASR) algorithm based on fuzzy logic control strategy is proposed for four-wheel independent driving (4WID) electric vehicles. In the algorithm, angular acceleration and slip rate based fuzzy controller of acceleration slip regulation are designed to maintain the wheel slip within the optimal range by adjusting the motor torque dynamically. In order to evaluate the performance of the algorithm, the models of the main components related to the ASR of the four-wheel independent driving electric vehicle are built in MATLAB/SIMULINK. The simulations show that the driving stability and the safety of the electric vehicle are improved for fuzzy logic control compared with the conventional PID control.

1. Introduction

The demand for more environmentally friendly and fuel efficient vehicles has been increased in response to growing concerns about a clean environment and saving energy. Pure electric vehicle stands out with its superior zero emission performance; it has emerged as a viable solution to meet those requirements [1, 2]. Therefore, the research on electric vehicle is important.

A 4WID electric vehicle employs four in-wheel (or hub) motors to drive the four wheels, and the torque and driving mode of each wheel can be controlled independently. As one of the most popular active safety systems of vehicles, acceleration slip regulation (ASR) is widely used in 4WID electric vehicles nowadays to improve the vehicle's acceleration performance [3–6]. The basic principle of ASR is to control the slip rate of driving wheels within the range of the optimal slip rate. The research on ASR is conducted using the sliding mode variable structure control system, the PID control, and the optimal control separately [7–11]. Based on the threshold angular acceleration and adhesion rate, an antiskid fuzzy logic controller was designed, and the simulation results show that the fuzzy controller can effectively keep the slip rate in a reasonable range [12–15].

In this paper, a fuzzy logic control strategy of acceleration slip regulation based on angular acceleration and slip rate is proposed to maintain the wheel slip within the optimal range by adjusting the motor torque dynamically. The simulation results show that the fuzzy controller effectively prevents driving wheel slipping and reduces the slip rate.

2. Vehicle Dynamic Model

A quarter dynamics vehicle model is established as follows.

2.1. The Wheel Dynamic Model. The dynamic differential equations for the calculation of longitudinal motion of the vehicle are described as follows [16]:

$$\begin{aligned} m\dot{u} &= F_d - F_f \\ j_\omega \dot{\omega}_i &= T_i - F_d R + F_{zi} f R \\ F_d &= \mu_i(\lambda) F_{zi}. \end{aligned} \tag{1}$$

Considering the longitudinal acceleration and lateral acceleration of the vehicle, the normal load expression for each wheel could be written as

$$F_{z(fl,fr)} = \left(\frac{1}{2}Mg \pm Ma_y\frac{h}{d_f}\right)\frac{l_r}{l} - \frac{1}{2}Ma_x\frac{h}{l}$$
$$F_{z(rl,rr)} = \left(\frac{1}{2}Mg \pm Ma_y\frac{h}{d_r}\right)\frac{l_f}{l} + \frac{1}{2}Ma_x\frac{h}{l}, \quad (2)$$

where i is fl, fr, rl, rr; M, m, u are the vehicle mass, a quarter of the mass vehicle, and vehicle velocity, respectively, F_f is the driving resistance; F_d is the driving force; j_ω is the wheel inertia; ω_i is the wheel rotational speed of ith wheel; T_i is the driving torque of ith in-wheel motor; f, μ_i, F_{zi} are the coefficient of rolling friction, friction coefficient of ith wheel, and normal force of ith tire, respectively (Figure 1).

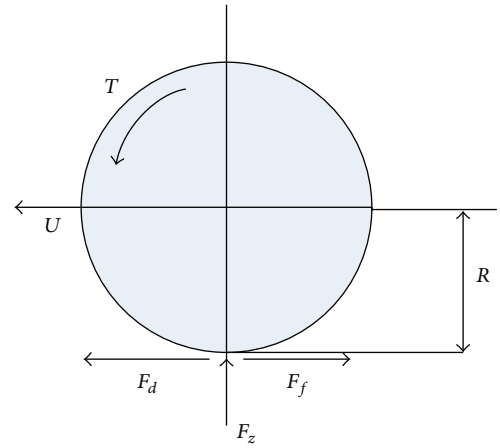

Figure 1: A quarter vehicle dynamic model.

2.2. Slip Ratio.

$$\lambda_i = \frac{R\omega_i - u_i}{R\omega_i} \quad \text{(driving)}$$
$$\lambda_i = \frac{u_i - R\omega_i}{u_i} \quad \text{(braking)}, \quad (3)$$

where λ_i is the lip ratio of ith tire and u_i is the center speed of ith wheel.

2.3. Model of In-Wheel Motor. In this paper, the mathematical model of permanent magnet synchronous in-wheel motor can be expressed as follows:

$$u_d = ri_d + \frac{d\psi_d}{dt} - \omega_s\psi_q,$$
$$u_q = ri_q + \frac{d\psi_q}{dt} + \omega_s\psi_d, \quad (4)$$

where $\psi_d = L_d i_d + M_{afd} i_f$, $\psi_q = L_q i_q$, $\omega_s = p\omega_r$; u_d, u_q are d- and q-axis stator voltages, respectively; i_d, i_q are d- and q-axis stator currents, respectively; ψ_d, ψ_q are d- and q-axis flux linkage, respectively; L_q, L_d are d- and q-axis stator inductances respectively; r is stator resistance.

Meanwhile, motor torque equation is defined as

$$T_e = \frac{3}{2}p\left[\psi_{fd}i_q + \left(L_d - L_q\right)i_d i_q\right] \quad (5)$$

Motion equation:

$$\frac{d\omega_r}{dt} = \frac{1}{J}\left[T_e - B\omega_r - T_l\right] \quad (6)$$

where B is damping coefficient, J is rotational inertia, T_l is load torque, and p is number of pole pairs.

We take i_q, ω_r as state variables with motor control, $i_d = 0$. The state equations of permanent magnet synchronous motor (PMSM) can be represented as follows:

$$\begin{bmatrix}\dot{x}_1\\ \dot{x}_2\end{bmatrix} = \begin{bmatrix}\frac{-r}{L_q} & \frac{-p\psi_{fd}}{L_q}\\ \frac{3}{2J}p\psi_{fd} & \frac{-B}{J}\end{bmatrix}\begin{bmatrix}x_1\\ x_2\end{bmatrix} + \begin{bmatrix}\frac{1}{L_q} & 0\\ 0 & \frac{-1}{J}\end{bmatrix}\begin{bmatrix}u\\ T_l\end{bmatrix}. \quad (7)$$

The control input variables are u and T_l, and the output variables are i_q and ω_r.

3. Control Algorithm of ASR

It is easy to lead wheel excessive slip for the driving of four-wheel drive electric vehicle on the low adherent surfaces, and the excessive slip of wheel affects the stability and safety of vehicle. Wheel angular acceleration increases rapidly in the process of excessive slip, which cause slip ratio to increase quickly and driving force to decrease. In this paper, a fuzzy controller of acceleration slip regulation based on angular acceleration and slip rate is designed, and the wheel slip rate will be controlled in a reasonable range.

3.1. Threshold Angular Acceleration. Ignoring the rolling resistance and wind resistance, the relationship between wheel angular acceleration α, torque T_i, and slip ratio λ can be described by as the following formulas:

$$\dot{\lambda} = \frac{-\dot{u}\omega R + \dot{\omega}uR}{\omega^2 R^2} = \frac{\left[j_\omega + (1-\lambda)mR^2\right]\alpha - T_i}{\omega m R^2},$$
$$\alpha = \dot{\omega} = \frac{T_i}{j_\omega + mR^2(1-\lambda)} + \frac{\omega m R^2\dot{\lambda}}{j_\omega + mR^2(1-\lambda)}. \quad (8)$$

If slip rate λ increases slowly, $\dot{\lambda} \approx 0$. Wheel angular acceleration can be represented as follows:

$$\alpha = \frac{T_i}{j_\omega + mR^2(1-\lambda)}. \quad (9)$$

With the increase of slip rate, angular acceleration is always greater than this value in fact. During the process of control, angular acceleration only needs to be close to this value. According to the automobile theory, when the wheel goes into slip state during driving, wheel angular acceleration and slip ratio will increase rapidly. Therefore the angular acceleration reflects whether the vehicle is in a state of slip to some extent.

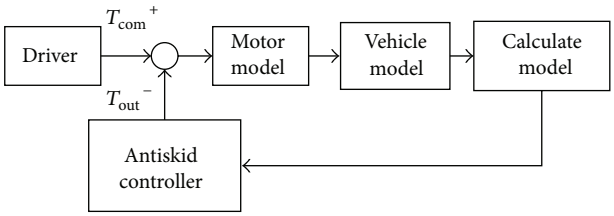

FIGURE 2: The block diagram of ASR control.

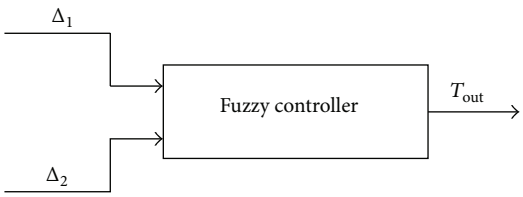

FIGURE 3: The block diagram of fuzzy controller.

TABLE 1: Fuzzy rules.

T_{out}	$\Delta_1 = \alpha - \alpha_p$						
	NB	NM	NS	ZO	PS	PM	PB
$\Delta_2 = \lambda - \lambda_{opt}$							
NS	ZO	ZO	ZO	ZO	ZO	ZO	ZO
ZO	ZO	ZO	ZO	ZO	ZO	PS	PS
PS	ZO	ZO	ZO	ZO	PS	PM	PM
PM	ZO	ZO	PS	PS	PM	PB	PB
PB	ZO	PS	PM	PM	PB	PB	PB

The control aim for ASR is to make slip ratio near optimal slip ratio and to obtain high driving force. The angular acceleration threshold value can be described as follows:

$$\alpha_p = \frac{T_i}{j_\omega + mR^2\left(1 - \lambda_{opt}\right)}. \tag{10}$$

3.2. The Optimal Slip Ratio. In this paper, two optimal slip ratios are considered. The optimal slip ratios of front wheel and rear wheel are 0.2 and 0.16, respectively.

3.3. The Antiskid Control Structure of 4WID EV. The electric vehicle rapidly accelerates under the instruction of drivers, and antiskid controller properly regulates four torques of the motor according to the current motion state of vehicle to maintain the slip rate of wheel in a reasonable range.

As shown in Figure 2, the electric vehicle generates torque T_{com} according to driver's instructions. Antiskid controller generates T_{out} according to the current state of vehicle. The command torque of the motor is the difference between the T_{com} and T_{out}.

4. Antiskid Controller

It is clear that the increasing slip ratio can increase the driving force between the road and the tire by virtue of an increase of friction coefficient, but further increase of slip will reduce driving force and induce an unstable acceleration of the wheel. Therefore, if the slip ratio is bigger than the optimal slip ratio λ_{opt}, the driving force will be diminished drastically. An antiskid controller is designed to maintain the wheel slip within the optimal range by adjusting the motor torque dynamically.

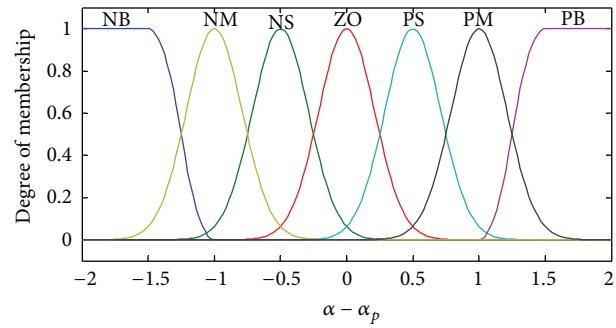

FIGURE 4: Difference between actual angular acceleration and threshold angular acceleration; $\Delta_1 = \alpha - \alpha_p$.

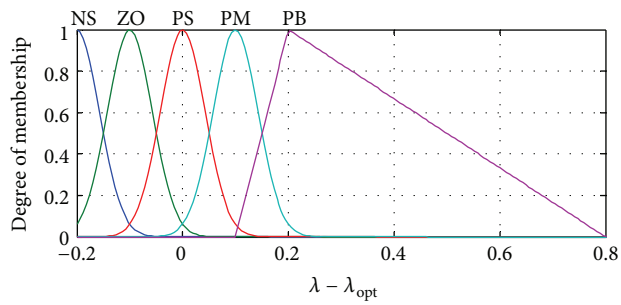

FIGURE 5: Difference between actual slip and optimal slip, $\Delta_2 = \lambda - \lambda_{opt}$.

4.1. Fuzzy Antiskid Controller. In this paper, a fuzzy antiskid controller is designed according to the principle of fuzzy control. The fuzzy controller has two input signals, and two inputs are the difference between actual slip ratio and threshold slip ratio and the difference between actual angular acceleration and threshold angular acceleration. Fuzzy antiskid controller block diagram is described as in Figure 3.

The input signals are shown in Figure 3; $\Delta_1 = \alpha - \alpha_p$ and $\Delta_2 = \lambda - \lambda_{opt}$. The controller generates one output T_{out} according to the input current value and the fuzzy rules. The value can reduce torque of the motor and thus reduce the driving wheel slip rate.

According to the theoretical derivation and practical experience, membership functions of inputs and output are shown in Figures 4, 5, and 6. The Δ_1 and the T_{out} are divided into seven fuzzy subsets:[NB, NM, NS, ZO, PS,PM, PB], and the Δ_2 is divided into five fuzzy subsets: [NS, ZO, PS, PM, PB].

The Mamdani methods and gravity center method are used to perform the fuzzy logic calculation and defuzzy identification in this paper. Table 1 shows the rule base for the fuzzy antiskid controller.

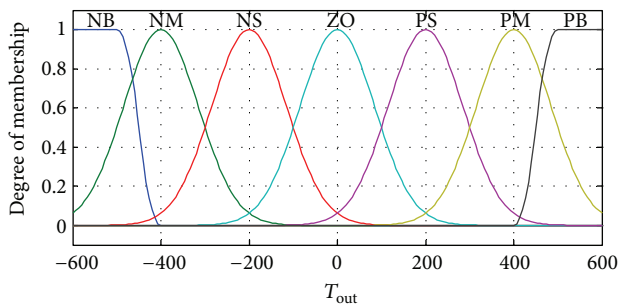

FIGURE 6: The output of fuzzy controller, T_{out}.

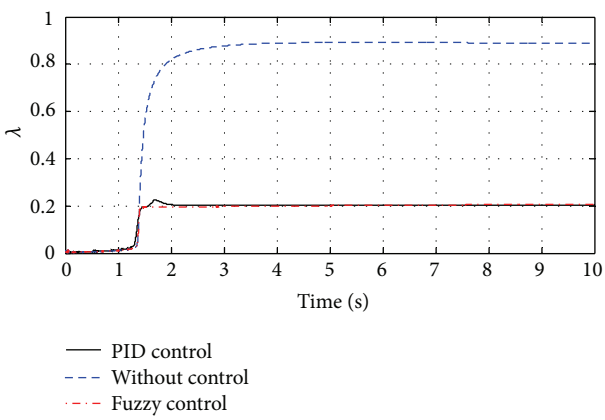

FIGURE 7: The slip of front wheel.

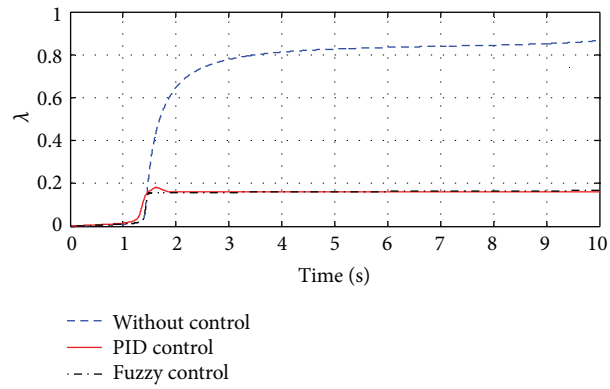

FIGURE 8: The slip of rear wheel.

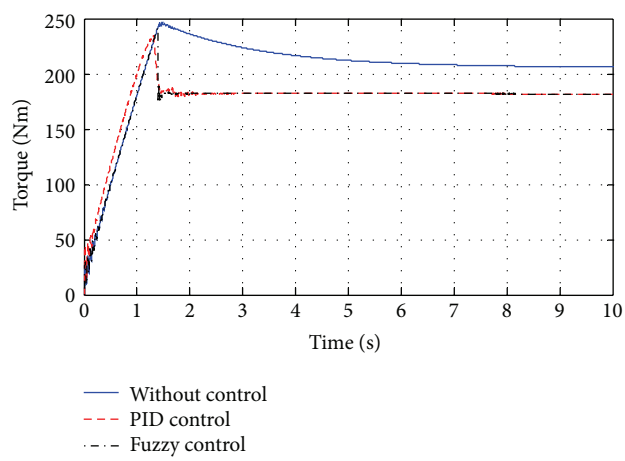

FIGURE 9: The motor torque of front wheel.

The output of fuzzy antiskid controller is determined by considering the difference between actual slip ratio and optimal slip ratio and the difference between actual angular acceleration and threshold angular acceleration. If the actual angular acceleration is less than the threshold angular acceleration, it shows that driving wheel adhesion is in a good condition. Meanwhile, if the output variable of controller is zero, the fuzzy controller does not reduce the torque out of drive motor. If the actual angular acceleration is larger than the threshold angular acceleration, it shows that the drive wheel is in a state of slip. Fuzzy controller decides the output variable according to the current value of slip ratio. The output variable of fuzzy controller can reduce output torque of motor and reduce the slip rate of drive wheel.

4.2. PID Controller. In this paper, a PID antiskid controller is designed to compare the effect of fuzzy controller and PID controller. The main design intent for this antiskid controller is to maintain actual slip near a reference value. The input of PID controller is the error of signal $\Delta\lambda = \lambda - \lambda_{opt}$, and the output can be represented as follows:

$$T_{outpid}(t) = K_p \Delta\lambda(t) + K_i \int \Delta\lambda(t)\, dt + K_d \frac{d\Delta\lambda(t)}{dt}, \quad (11)$$

where K_p, K_i, and K_d are the proportional gains, the integral coefficient, and the differential coefficient, respectively.

5. Simulation Results and Analysis

The simulation platform is built in MATLAB/SIMULINK and CarSim to evaluate the performance of the proposed antiskid controller. The 4WID full-vehicle dynamics model is established in CarSim including front and rear suspension, steering, body tires, and other systems. The antiskid controller and motor model are established in MATLAB/SIMULINK. Two kinds of road surface conditions are established to observe the effect of the fuzzy controller and PID controller.

5.1. The First Test Condition. The electric vehicle rapidly accelerates at an initial speed of 5 km/h. In this simulation the tire-road friction coefficient (TRFC) is set to 0.2. The acceleration command from driver is so large that the vehicle begins to slip on the low adhesion road. The simulation results are shown as in Figures 7 and 8.

The slip ratios of front wheel and rear wheel are shown in Figure 7 and Figure 8. The vehicle runs on the low friction coefficient road. The slip rate of front wheel reaches 0.9 quickly without antiskid controller. Under effect of the fuzzy antiskid controller, the slip rate of front wheel and rear wheel are close to optimal slip ratio 0.2 and 0.16, respectively. Both

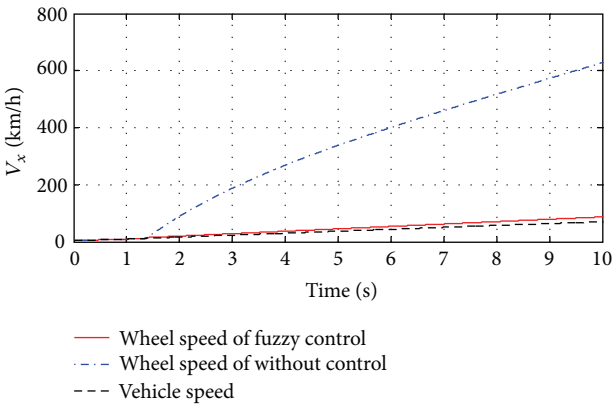

Figure 10: Comparison of speed for front wheel.

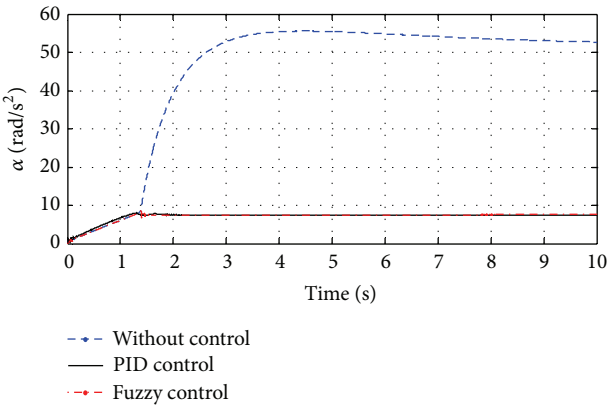

Figure 11: The actual angular acceleration for front wheel.

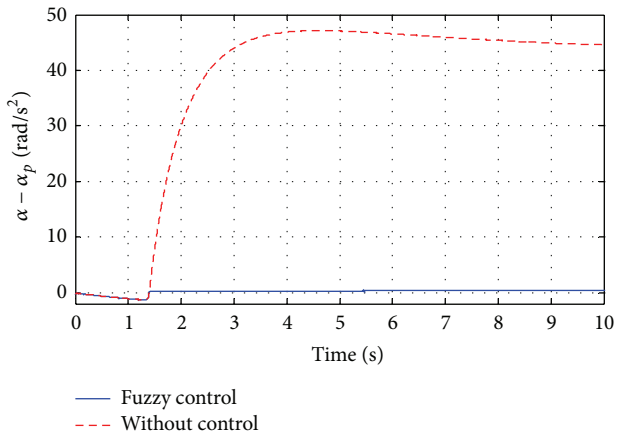

Figure 12: Difference between actual angular acceleration and threshold angular acceleration.

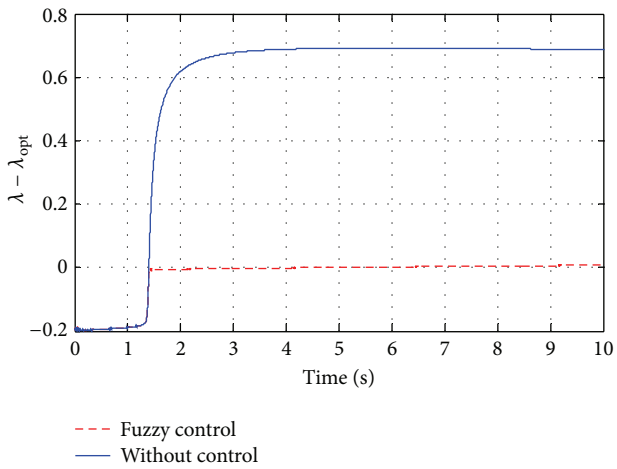

Figure 13: Difference between actual slip ratio and optimal slip ratio.

of fuzzy controller and PID controllers can reduce the slip and improve the stability of the electric vehicle. However, the control performance of the proposed fuzzy controller is better than that of the conventional PID controller.

As shown in Figure 9, both of fuzzy controller and PID controller can reduce motor torque of front wheel. Finally, the motor torques are the same in different control methods. In addition, the wheel angular velocity is shown in Figure 10, and the fuzzy antiskid controller can effectively reduce the wheel angular velocity.

As shown in Figure 11, both of fuzzy controller and PID controller can reduce actual angular acceleration for front wheel.

As shown in Figure 12, the difference between actual angular acceleration and threshold angular acceleration raises rapidly without antiskid controller. Under the effect of fuzzy antiskid controller, the difference between actual angular acceleration and threshold angular acceleration is close to zero. The threshold angular acceleration is effective to reduce actual angular acceleration.

As shown in Figure 13, The difference between actual slip ratio and threshold slip ratio reaches 0.7 rapidly without antiskid controller. Under the effect of fuzzy antiskid controller, the actual slip ratio is close to optimal slip.

5.2. The Second Test Condition. The electric vehicle rapidly accelerates at an initial speed of 20 km/h. The steering angle of front wheel is 5 degree. In this simulation the TRFC was set to 0.2. The acceleration command from driver is so large that the vehicle begins to slip on the low adhesion road. The simulation results are shown in Figure 14.

As shown in Figure 14, The slip rate of front wheel reaches 0.85 quickly without antiskid controller. Under effect of the antiskid controller, the slip rate of front wheel is close to optimal slip ratio 0.2.

The lateral acceleration of vehicle is shown in Figure 15. It can be seen from the figure that the lateral acceleration of vehicle under the effect of antiskid controller is bigger than that of lacking antiskid controller before 8 second. The vehicle begins to spin after 8 second, so the lateral acceleration of without controller is bigger than that of using controller. Both the fuzzy antiskid controller and PID antiskid controllers can enhance the lateral stability and safety of electric vehicle.

As shown in Figure 16, with the effect of fuzzy antiskid controller, the difference between actual angular acceleration and threshold angular acceleration is close to zero. The fuzzy

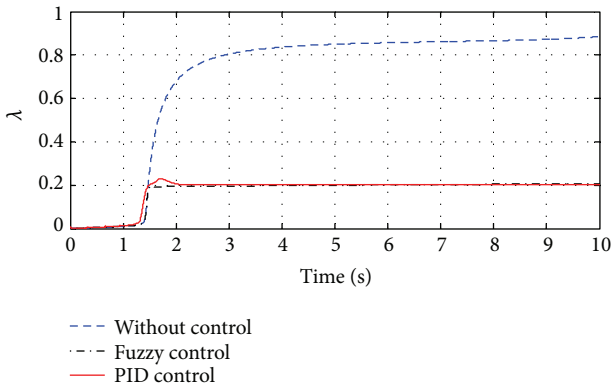

Figure 14: The slip of front wheel.

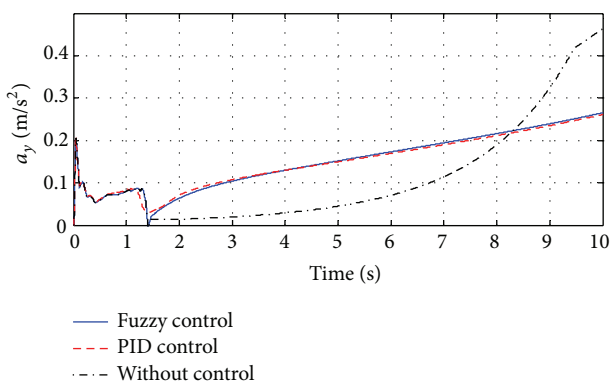

Figure 15: The lateral acceleration of vehicle.

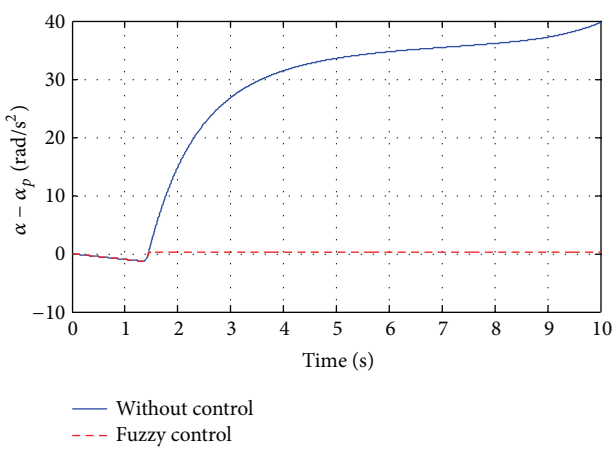

Figure 16: Difference between actual angular acceleration and threshold angular acceleration.

antiskid controller is effective to reduce actual angular acceleration.

The yaw rate of vehicle is shown in Figure 17. Under the effect of fuzzy controller, the yaw rate of vehicle maintains steadiness at 0.018 rad/s while the yaw rate of vehicle without fuzzy controller raises quickly. Figure 17 shows that fuzzy antiskid controller can improve lateral stability of electric vehicle to a certain degree on ice road.

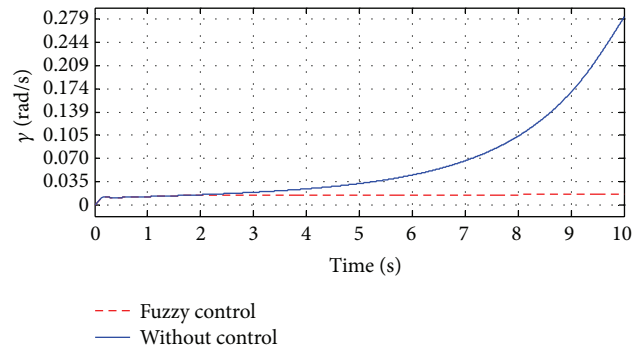

Figure 17: The yaw rate of vehicle.

6. Conclusions

In the paper, the antiskid fuzzy logic controller for four-wheel independent driving electric vehicles is proposed based on threshold angular acceleration and optimal slip rate. The simulation results show that fuzzy slip rate controller can effectively reduce the slip ratio. It can enhance the driving performance, the maneuverability, and stability of four-wheel independent driving electric vehicle.

Acknowledgments

This research was supported by the National Science Foundation of China (51105074, 51205058) and the Foundation of State Key Laboratory of Mechanical Transmission (SKLMT-KFKT-201206).

References

[1] L. Keqiang, "Automotive technology development trends and countermeasures of China," *Automotive Engineering*, vol. 31, no. 11, pp. 1005–1016, 2009.

[2] G. Chunlin, Z. Zijian, W. Li et al., "Prospects and key factors analysis of electric vehicles development," *Automotive Engineering*, vol. 34, no. 9, pp. 852–858, 2012.

[3] G. Yin, N. Chen, and P. Li, "Improving handling stability performance of four-wheel steering vehicle via μ-synthesis robust control," *IEEE Transactions on Vehicular Technology*, vol. 56, no. 5, pp. 2432–2439, 2007.

[4] Z. Shuai, H. Zhang, J. Wang, J. Li, and M. Ouyang, "Combined AFS and DYC control of four-wheel-independent-drive electric vehicles over can network with time-varying delays," *IEEE Transactions on Vehicular Technology*, 2013.

[5] L. Gang, Z. Changfu, Z. Qiang et al., "Acceleration slip regulation control of 4WID electric vehicles based on fuzzy road identification," *Journal of South China University of Technology*, vol. 40, no. 12, pp. 99–104, 2012.

[6] J. Deur, D. Pavković, G. Burgio, and D. Hrovat, "A model-based traction control strategy non-reliant on wheel slip information," *Vehicle System Dynamics*, vol. 49, no. 8, pp. 1245–1265, 2011.

[7] D. Yin, S. Oh, and Y. Hori, "A novel traction control for EV based on maximum transmissible torque estimation," *IEEE Transactions on Industrial Electronics*, vol. 56, no. 6, pp. 2086–2094, 2009.

[8] M. Yoshimura and H. Fujimoto, "Driving torque control method for electric vehicle with in-wheel motors," *IEEJ Transactions on Industry Applications*, vol. 131, no. 5, pp. 721–728, 2011.

[9] H. Zhang, Y. Shi, and J. Wang, "Observer-based tracking controller design for networked predictive control systems with uncertain Markov delays," *International Journal of Control*, vol. 86, no. 10, pp. 1824–1836, 2013.

[10] R. De Castro, R. Esteves Araújo, and D. Freitas, "Wheel slip control of EVS based on sliding mode technique with conditional integrators," *IEEE Transactions on Industrial Electronics*, vol. 60, no. 8, pp. 3256–3271, 2013.

[11] H. Zhang, Y. Shi, and A. Saadat Mehr, "Robust static output feedback control and remote PID design for networked motor systems," *IEEE Transactions on Industrial Electronics*, vol. 58, no. 12, pp. 5396–5405, 2011.

[12] D. Zhiqiang, *Fuzzy control of acceleration slip regulation for electric vehicles with in-wheel motors [M.S. thesis]*, Tongji University, Shanghai, China, 2006.

[13] H. Zhang, Y. Shi, and M. Liu, "H_∞ step tracking control for networked discrete-time nonlinear systems with integral and predictive actions," *IEEE Transactions on Industrial Informatics*, vol. 9, no. 1, pp. 337–345, 2013.

[14] Y. Jiantao, *Adhesion control method based on nonlinear control for four-wheel drive electric vehicle [M.S. thesis]*, Tongji University, Shanghai, China, 2008.

[15] H. Zhang, Y. Shi, and A. Saadat Mehr, "On H_∞ filtering for discrete-time takagi-sugeno fuzzy systems," *IEEE Transactions on Fuzzy Systems*, vol. 20, no. 2, pp. 396–401, 2012.

[16] N. Zhao and B.-M. Ge, "H_∞ robust control of permanent magnet synchronous motor used in electric vehicle," *Electric Machines and Control*, vol. 11, no. 5, pp. 462–466, 2007.

Hindawi Publishing Corporation
Mathematical Problems in Engineering
Volume 2013, Article ID 708261, 11 pages
http://dx.doi.org/10.1155/2013/708261

Research Article

Global Optimal Energy Management Strategy Research for a Plug-In Series-Parallel Hybrid Electric Bus by Using Dynamic Programming

Hongwen He, Henglu Tang, and Ximing Wang

National Engineering Laboratory for Electric Vehicles, Beijing Institute of Technology, Beijing 100081, China

Correspondence should be addressed to Hongwen He; hwhebit@bit.edu.cn

Received 3 August 2013; Revised 5 October 2013; Accepted 5 October 2013

Academic Editor: Hui Zhang

Energy management strategy influences the power performance and fuel economy of plug-in hybrid electric vehicles greatly. To explore the fuel-saving potential of a plug-in hybrid electric bus (PHEB), this paper searched the global optimal energy management strategy using dynamic programming (DP) algorithm. Firstly, the simplified backward model of the PHEB was built which is necessary for DP algorithm. Then the torque and speed of engine and the torque of motor were selected as the control variables, and the battery state of charge (SOC) was selected as the state variables. The DP solution procedure was listed, and the way was presented to find all possible control variables at every state of each stage in detail. Finally, the appropriate SOC increment is determined after quantizing the state variables, and then the optimal control of long driving distance of a specific driving cycle is replaced with the optimal control of one driving cycle, which reduces the computational time significantly and keeps the precision at the same time. The simulation results show that the fuel economy of the PEHB with the optimal energy management strategy is improved by 53.7% compared with that of the conventional bus, which can be a benchmark for the assessment of other control strategies.

1. Introduction

In recent years, the problems of energy shortage and environmental pollution have greatly promoted the development of electric vehicles (EVs). Among the EVs, the pure electric vehicles (PEVs) run with zero emissions and renewable electricity, but their disadvantages, such as the short operation range, high battery price, and long battery charging time, have limited the user's acceptability. The hybrid electric vehicles (HEVs) have longer operation range and higher performance than PEVs, but the electricity that keeps the battery state of charge (SOC) in a narrow window is still from the onboard fossil fuel [1, 2]. While the plug-in hybrid electric vehicle (PHEVs), with larger battery capacity, can run a long pure electric mileage and make full use of the cheap power from gird, hence it is more competitive than EVs and charge sustainable HEVs [3].

The energy management strategy is one of the key factors that influence the fuel economy and power performance of the PHEVs. In the PHEVs, in order to make full use of the electricity energy stored in batteries, it is preferred that the battery energy drops to its minimum when the vehicle arrives at the destination. Therefore the energy management strategy becomes more complicated than that of the HEVs. Similar to HEVs, the energy management strategies in PHEVs can be usually classified into two categories: rule-based control strategies and optimization-based control strategies [4]. The main idea of rule-based control strategies is to make each component work in efficient area individually [5–7]. The reference [2] put forward a PHEV rule-based control strategy after considering the all-electric range and charge depletion range operations. The reference [5] proposed a PEHV rule-based energy management strategy by using the ADVISOR. The rule-based control strategies are simple and easy to implement, but they cannot safeguard the systematic optimization and cannot fully exploit the advantages of PHEVs.

The optimization-based control strategies include global optimization and real-time optimization. The real-time optimization realizes a local optimum step by step real timely

and loses the potential to get a global optimum. The adaptive control is a good example of real-time optimization, and the H∞ control theory is powerful in adaptive control [8–11]. The global optimization finds an optimal solution for the whole process, which is suitable for energy management issues of the PHEB with regular driving cycle. For example, dynamic programming (DP) algorithm, which is effective to solve the constrained and nonlinear optimization problems, is selected to realize a global optimization of energy management for HEVs [12]. The reference [12] studied an optimal energy management of a parallel HEV with the known driving cycle using DP algorithm. The reference [13] built the driving cycle model using traffic information with the help of intelligent transportation systems and utilized the DP algorithm to study the global energy management optimization of a parallel plug-in hybrid electric sport utility vehicle (SUV). The reference [14] presented a way on how to implement the DP algorithm in the optimization of HEVs and carried out a global optimization with Toyota Prius as an example. The reference [15] determined an optimal energy management law for a two-clutch single-shaft parallel HEV by using optimization software, named KOALA. By comparisons, the DP algorithm has been proved to be powerful and effective in the global optimization of control strategies in HEVs. In this paper, a global optimization of the energy management strategy for a plug-in series-parallel hybrid bus (PHEB) is explored, and the battery energy state control is specially considered and discussed. The PHEB model was built in Section 2 and the global optimization problem with DP algorithm was put forward in Section 3. The DP numerical computation method was discussed and put forward in Section 4 and the simulation results were given in Section 5. Section 6 gives the main conclusions.

2. Plug-In Series-Parallel Hybrid Electric Bus Modeling

2.1. Plug-In Series-Parallel Hybrid Electric Bus Configuration. Figure 1 shows a schematic view of the PHEB powertrain, which includes a diesel engine, an integrated starter generator (ISG) motor, and a main drive motor. The ISG is connected to engine through a torsion damper. There is an on-off mode clutch between the ISG motor and the main drive motor. The PHEB works in parallel mode or engine-only mode when the mode clutch is in "ON" condition, and the diesel engine, ISG motor, and main drive motor drive the wheel mechanically. While the PHEB works in its series mode or all-electric mode when the mode clutch is in "OFF" condition, the main drive motor drives the wheels directly, and the diesel engine drives the ISG motor to generate electricity or not according to the battery state of charge. The main specific parameters of the PHEB are listed in Table 1.

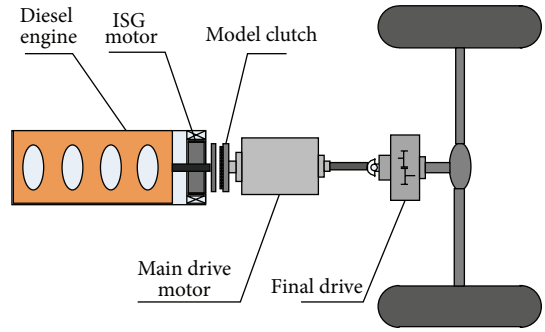

Figure 1: The plug-in series-parallel hybrid electric bus powertrain configuration.

Table 1: Main specific parameters of the plug-in series-parallel hybrid electric bus powertrain.

Diesel engine	
Maximum power (kW)	147
Maximum torque (Nm)	730
ISG motor	
Maximum power (kW)	55
Maximum torque (Nm)	500
Drive motor	
Maximum power (kW)	166
Maximum torque (Nm)	2080
Battery	
Capacity (Ah)	60
Voltage (V)	580
Final drive ratio	6.17
Curb weight (kg)	12500
Gross weight (kg)	18000
Air resistance coefficient	0.55
Frontal area (m^2)	6.6
Tire dynamic radius (mm)	473

2.2. Plug-In Series-Parallel Hybrid Electric Bus Simulation Models. There are two modeling methods in PHEV simulations. One is forward modeling, which is more accurate but with heavier computational burden, and is always used to test the vehicle dynamic performance and drivability. The other one is the backward modeling, which is calculated with fixed time steps ignoring the dynamics of the powertrain components and usually is used to evaluate the vehicle fuel economy [16]. Since the global optimization is based on the fixed driving cycle and the DP problem is solved backward from the terminal of the driving cycle, we built the facing-backward simulation models as follows.

The diesel engine is modeled as a 3-dimension look-up table, where the inputs are the engine torque and speed and the output is the fuel consumption rate, as shown in Figure 2. The fuel consumption efficiency map is based on the experimental data.

The ISG motor is modeled as a 3-dimension look-up table based on the experimental efficiency map as shown in

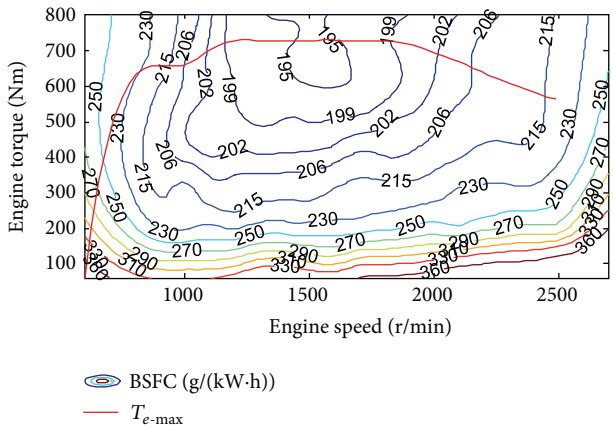

FIGURE 2: The fuel consumption efficiency map of the diesel engine.

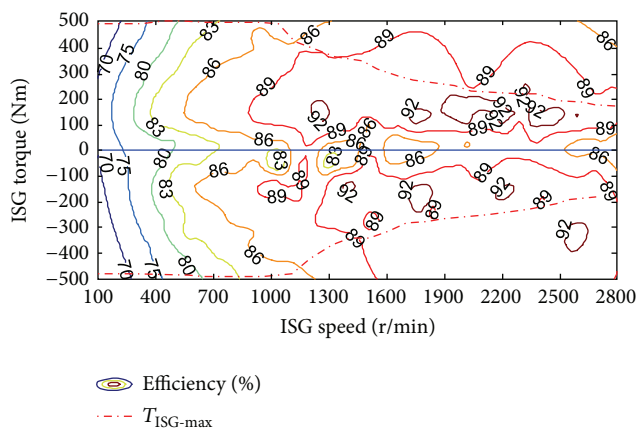

FIGURE 3: The ISG efficiency map.

Figure 3. Due to the limit of battery power, the output torque of ISG T_{ISG} is described as follows:

$$T_{\text{ISG}} = \begin{cases} \min\left(T_{\text{ISG\_req}}, T_{\text{ISG\_dis\_max}}(n_{\text{ISG}}), \right. \\ \qquad \left. T_{\text{ISG\_bat\_dis\_max}}(n_{\text{ISG}}, \text{SOC})\right), & T_{\text{ISG\_req}} \geq 0 \\ \max\left(T_{\text{ISG\_req}}, T_{\text{ISG\_chg\_max}}(n_{\text{ISG}}), \right. \\ \qquad \left. T_{\text{ISG\_bat\_chg\_max}}(n_{\text{ISG}}, \text{SOC})\right), & T_{\text{ISG\_req}} < 0, \end{cases} \tag{1}$$

where $T_{\text{ISG\_req}}$ is the required ISG torque, n_{ISG} is the ISG speed, SOC is the battery state of charge (SOC), $T_{\text{ISG\_dis\_max}}$ and $T_{\text{ISG\_chg\_max}}$ are the maximum ISG torque when driving and generating, respectively, and $T_{\text{ISG\_bat\_chg\_max}}$ and $T_{\text{ISG\_bat\_dis\_max}}$ are the torque limits due to battery current limits in the charging and discharging modes, which are functions of ISG speed and torque.

The main drive motor is modeled as a 3-dimension look-up table based on the experimental efficiency map as shown

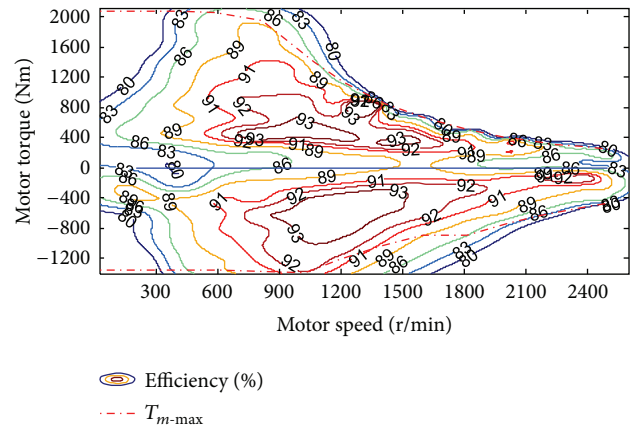

FIGURE 4: The efficiency map of the main drive motor.

in Figure 4. Due to the limit of battery power, the output torque of the main drive motor T_m is as follows:

$$T_m = \begin{cases} \min\left(T_{m\text{\_req}}, T_{m\text{\_dis\_max}}(n_m), \right. \\ \qquad \left. T_{m\text{\_bat\_dis\_max}}(n_m, \text{SOC})\right) & T_{m\text{\_req}} \geq 0 \\ \max\left(T_{m\text{\_req}}, T_{m\text{\_chg\_max}}(n_m), \right. \\ \qquad \left. T_{m\text{\_bat\_chg\_max}}(n_m, \text{SOC})\right), & T_{m\text{\_req}} < 0, \end{cases} \tag{2}$$

where $T_{m\text{\_req}}$ is the required torque of the main drive motor, n_m is the speed of the main drive motor, $T_{m\text{\_dis\_max}}$ and $T_{m\text{\_chg\_max}}$ are the maximum torque when driving and regenerative braking, respectively, and $T_{m\text{\_bat\_chg\_max}}$ and $T_{m\text{\_bat\_dis\_max}}$ are the torque limits due to battery current limits when charging and discharging, respectively, which are the functions of the main drive motor speed and torque.

The static equivalent circuit battery model described in [12] is used. The model inputs are the speed and torque of ISG and main drive motor, the model output is the battery SOC, which is calculated by (3)

$$\begin{aligned} \text{SOC}(k+1) = \text{SOC}(k) \\ - \Big(V_{\text{oc}} - \big(V_{\text{oc}}^2 - 4(R_{\text{int}} + R_t) \\ \times \big(T_m \cdot n_m \cdot \eta_m^{-\text{sgn}(T_m)} \\ + T_{\text{ISG}} \cdot n_{\text{ISG}} \cdot \eta_{\text{ISG}}^{-\text{sgn}(T_{\text{ISG}})}\big)\big)^{1/2}\Big) \\ \times \left(2(R_{\text{int}} + R_t) \cdot Q_b\right)^{-1}, \end{aligned} \tag{3}$$

where R_{int} is the internal resistance, V_{oc} is the open-circuit voltage, R_{int} and V_{oc} are the function of SOC, Q_b is the maximum battery capacity, R_t is the terminal resistance, η_m and η_{ISG} are the efficiencies of the main drive motor and ISG accordingly, and k denotes the calculation step in discretization way.

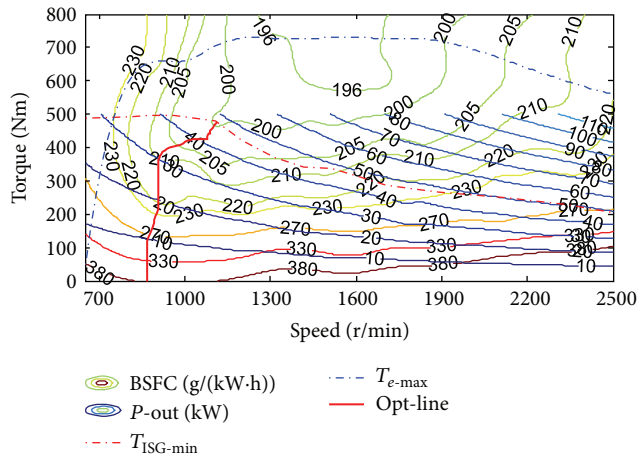

FIGURE 5: Engine-ISG fuel consumption map.

The mode clutch works in three conditions: disengaged, where clutch = 0; engaged, where clutch = 1; and half-engaged, where 0 < clutch < 1. The transition duration is very small, less than the time interval of the sample point of the driving cycle, so only two working conditions are considered in the dynamic optimization. If clutch = 1, the torque of engine and ISG motor can be delivered to final drive completely. If clutch = 0, only the main drive motor drives the vehicle.

When the PHEB works in series hybrid mode, taking the efficiency of engine and ISG into consideration, the minimum fuel consumption curve can be found as shown in Figure 5. For each required P_{ISG}, only the points on the minimum fuel consumption line are considered.

The time interval is set to 1 second. Assuming that the torques of the engine, main drive motor, and ISG remain constant in one time interval, we can calculate the vehicle dynamics as

$$v_v(k+1) = v_v(k) + \frac{1}{\delta M}\left(\frac{T_{\text{req}}(k)\cdot i_o\cdot\eta}{r_d} - \frac{v_v(k)}{|v_v(k)|}\left(F_f + F_a(v_v(k))\right)\right), \tag{4}$$

where T_{req} is the total required torque as the input of the final drive, η is the mechanical powertrain efficiency, i_o is the final drive ratio, v_v is the vehicle speed, r_d is the dynamic tire radius, δM is the effective mass of the vehicle, and F_a and F_f are aerodynamic drag force and rolling resistance force, respectively.

According to (4), we can get the T_{req} as the driving cycle is known in advance. For the PHEB powertrain, the relationship between T_{req} and the powertrain components can be expressed as

$$T_{\text{req}}(k) = T_e(k) + T_{\text{ISG}}(k) + T_m(k) + \frac{T_b(k)}{i_o}, \tag{5}$$

where T_b is the hydraulic brake torque and T_e is the engine torque.

3. Global Optimal Energy Management Strategy Modeling

For PHEB, DP aims to find the control of each stage to minimize the cost function over the whole driving cycles. The control variables and state variables are determined before DP problem is formulated. The state variables, including vehicle speed v_v and SOC, reflect the operating state of the system. As the driving cycle and the vehicle speed v_v in every stage are known, SOC is chosen as the state variable. There are many control variables in the PHEB such as engine torque T_e, engine speed n_e, motor torque T_m, ISG torque T_{ISG}, and hydraulic brake torque T_b, but only three of them are independent. Here the n_e, T_e, and T_m are chosen as the independent control variables.

In the discrete-time format, the PHEB system can be expressed as

$$x(k+1) = f(x(k), u(k)), \tag{6}$$

where $x(k)$ and $u(k)$ are state vector and control vector, respectively.

For PHEB, the price of electricity is very low compared with that of diesel when used to drive the same distance [13], so we focus our research on minimizing the fuel consumption. The cost function is built as follows:

$$J = \sum_{k=0}^{N-1} L(x(k), u(k)) = \sum_{k=0}^{N-1} \text{fuel}(k), \tag{7}$$

where N is the duration of the driving cycle, and L is the instantaneous cost; fuel denotes the diesel consumption.

If the SOC drops below the lower limit, the battery will not supply electricity to the main drive motor. To avoid the condition that the engine cannot supply the required torque, another cost function should be considered besides (7) then the cost function rewrites as follows:

$$J = \sum_{k=0}^{N-1} L(x(k), u(k)) = \sum_{k=0}^{N-1}\left[\text{fuel}(k) + \alpha\left(T_{\text{req}}(k) - T_e(k) - T_{\text{ISG}}(k) - T_m(k) - \frac{T_b(k)}{i_o}\right)^2\right], \tag{8}$$

where α is a positive weighting factor.

Constrains (5) and (9) are necessary to ensure a smooth operation of the engine, ISG, main drive motor, and batteries

during the optimization. Consider

$$\begin{aligned}
n_{e\text{-min}} &\le n_e(k) \le n_{e\text{-max}},\\
T_{e\text{-min}}(n_e(k)) &\le T_e(k) \le T_{e\text{-max}}(n_e(k)),\\
T_{\text{ISG-min}}(n_{\text{ISG}}(k), \text{SOC}(k)) &\le T_{\text{ISG}}(k)\\
&\le T_{\text{ISG-max}}(n_{\text{ISG}}(k), \text{SOC}(k)),\\
T_{m\text{-min}}(n_m(k), \text{SOC}(k)) &\le T_m(k)\\
&\le T_{m\text{-max}}(n_m(k), \text{SOC}(k)),\\
\text{SOC}_{\min} &\le \text{SOC}(k) \le \text{SOC}_{\max},\\
n_m(k) = n_e(k) &= n_{\text{ISG}}(k) \quad \text{if clutch} = 1,\\
n_e(k) &= n_{\text{ISG}}(k) \quad \text{if clutch} = 0,\\
T_e(k) + T_{\text{ISG}}(k) &= 0 \quad \text{if clutch} = 0.
\end{aligned} \tag{9}$$

4. A Numerical Computation for the DP Problem

Based on Bellman's Principle of Optimization, the global optimization problem can be solved by dealing with a sequence of subproblems of optimization backward from the terminal of the driving cycle [17, 18]. Then the DP problem can be described by the recursive equation (10)-(11). The subproblem for $(N-1)$ step is

$$J^*_{N-1}(x(N-1)) = \min_{u(N-1)} [L(x(N-1), u(N-1))]. \tag{10}$$

For step k $(0 \le k < N-1)$, the subproblem is

$$J^*_k(x(k)) = \min_{u(k)} [L(x(k), u(k)) + J^*_{k+1}(x(k+1))], \tag{11}$$

where $J^*_k(x(k))$ is the optimal cost-to-go function at state $x(k)$ from stage k to the end of the driving cycle and $x(k+1)$ is the state in stage $k+1$ after the control $u(k)$ is applied to state $x(k)$ at stage k according to (6).

4.1. Solving the DP Problem Backward. The recursive equation (10)-(11) is solved backward, and quantization and interpolation are needed to solve the equation. The continuous state SOC is discretized into finite grids first, and the number of discretized state S is

$$S = \frac{(\text{SOC}_{\max} - \text{SOC}_{\min})}{\delta\text{SOC}}, \tag{12}$$

where δSOC is the increment of the discretized SOC and $\text{SOC}_{\max}$ and $\text{SOC}_{\min}$ are upper and lower constrains of SOC.

Then find all possible control solutions at every state of each stage. The function $J^*_k(x(k))$ at every grid points of SOC is evaluated, and $J^*_{k+1}(x(k+1))$ is evaluated by interpolation if the calculated value of admissible SOC_{k+1} in (3) does not fall exactly on grid points. The way of interpolation is shown in [13]. The procedure of solving the DP problem backward

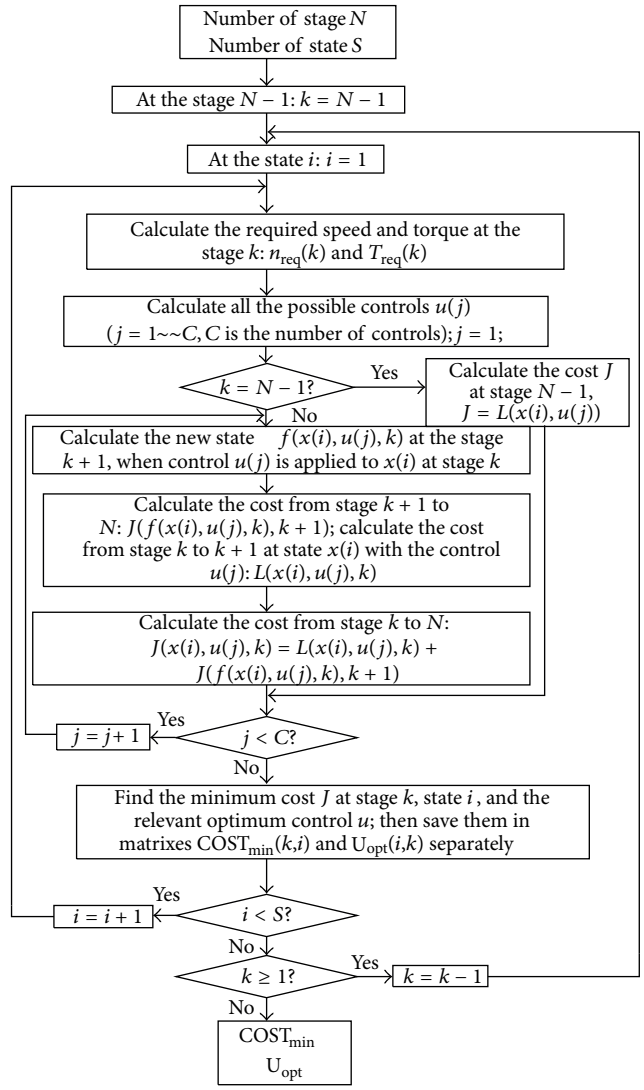

Figure 6: The flow chart of solving the DP problem backward.

is shown in Figure 6, where the required speed n_{req} is the same as driving cycle and required torque is determined by inversely solving vehicle dynamic model as shown in (4).

4.1.1. To Find All Possible Control Solutions. It is very important to find all possible control solutions in the procedure of solving the DP problems backward. The possible control solutions are the possible combination of the discrete torque of the components in each state of the driving cycle which meets the torque need of the vehicle. The number of the control solutions influences the accuracy of the optimization greatly, and the way to search for all the control solutions influences the computational burden significantly. To get a compromise, here we find the possible working modes of the PHEB first, and then we find all possible control solutions in every mode; finally we get all the control solutions at every grid point of SOC.

The PHEB works in many modes, such as engine-only mode, battery electric (EV) mode, engine-ISG parallel mode,

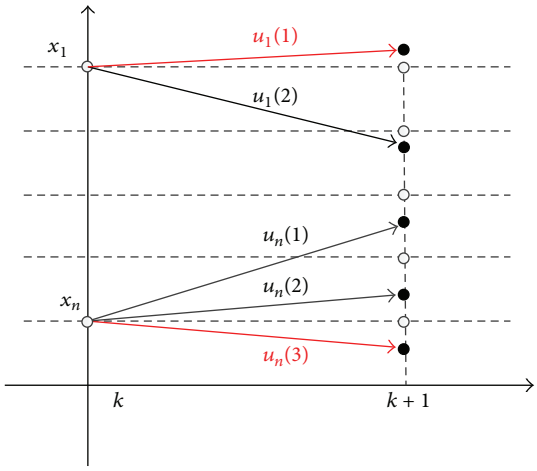

FIGURE 7: Schematic diagram of state transformation with control variables.

engine-motor parallel mode, and series mode. The ISG is used as a starter and generator and will not drive the bus directly. Only when the torque required by the vehicle exceeds the maximum torque that can be provided by the main drive motor and engine together, the ISG will provide the remaining torque.

According to (6), the state variables in the $x(k+1)$ may exceed the range of SOC, as shown in Figure 7, where the state at stage $k+1$ exceeds the range of SOC with the control variables $u_1(1)$ and $u_n(3)$. To avoid this situation, the control variables should be limited. We divide SOC into three areas: $\mathrm{SOC}_{\max} \geq \mathrm{SOC} \geq \mathrm{SOC}_{\mathrm{high}}$, $\mathrm{SOC}_{\min} \leq \mathrm{SOC} \leq \mathrm{SOC}_{\mathrm{low}}$, and $\mathrm{SOC}_{\mathrm{low}} < \mathrm{SOC} < \mathrm{SOC}_{\mathrm{high}}$. The initial SOC and terminal SOC are usually in the area $\mathrm{SOC}_{\mathrm{low}} < \mathrm{SOC} < \mathrm{SOC}_{\mathrm{high}}$.

(A) When the SOC is higher than high limit $\mathrm{SOC}_{\mathrm{high}}$, the motor drives the bus without regenerative braking. Only when the torque required by the vehicle exceeds the maximum torque that can be provided by drive motor, ISG will supply positive torque to drive the bus. If more driving power is required, the engine comes to work to supply the remaining torque.

(B) When the SOC drops below the low limit $\mathrm{SOC}_{\mathrm{low}}$, the battery will not supply electric energy any more. According to the required torque and required speed areas of final drive shown in Figure 8, the PHEB works in different modes as listed in Table 2. The blue line in Figure 8 represents the maximum output torque of the motor with the power supplied by engine, ISG, when PHEB works in series mode.

(C) If $\mathrm{SOC}_{\mathrm{low}} < \mathrm{SOC} < \mathrm{SOC}_{\mathrm{high}}$, the torque that can be supplied by the powertrain components is shown in Figure 9. The possible working modes are shown in Table 3.

If the PHEB works in series mode, discretize the minimum fuel consumption curve into finite points, and the engine/ISG works on these points. If the PHEB works in engine-motor parallel mode, such as the PHEV which works

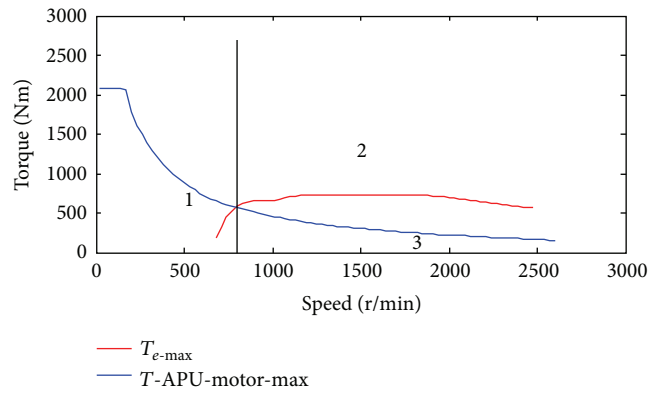

FIGURE 8: The required speed and torque of the final drive when $\mathrm{SOC} < \mathrm{SOC}_{\mathrm{low}}$.

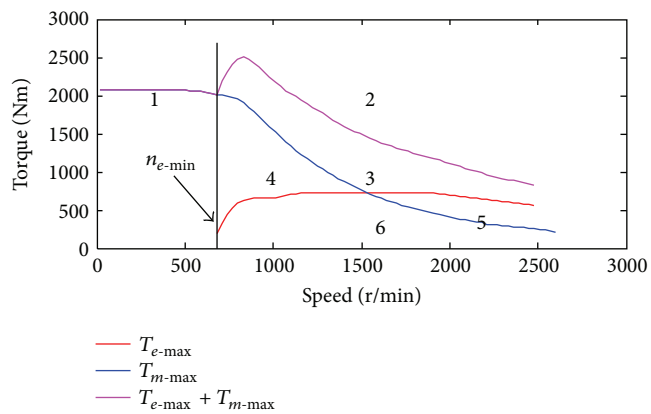

FIGURE 9: The required speed and torque of final drive when $\mathrm{SOC}_{\mathrm{low}} < \mathrm{SOC} < \mathrm{SOC}_{\mathrm{high}}$.

on area 3 in Figure 9, the flow chart to find all possible controls is shown in Figure 10(a). If the PHEB works in the same mode on areas 4, 5, and 6 in Figure 9, the initial condition of T_e is set to be T_{req}. If the PHEB works in engine-ISG parallel mode, the way to find the possible controls is shown in Figure 10(b).

4.2. To Find the Optimal Control Path Forward. The optimal controls at every state point of every stage are obtained by solving the DP problem backward; if the initial SOC is specified, the optimal control path will be found forward. The interpolation is also needed to find the optimal control path as shown in Figure 11. If the optimal control at stage k is u_k, the optimal control u_{k+1} at stage $k+1$ is got through interpolation between the controls $u_{k+1}(i)$ and $u_{k+1}(i+1)$, which are the optimal controls at state grid points $x(i)$ and $x(i+1)$, respectively, at stage $k+1$.

5. Simulation Results

For the PHEB, it is reasonable to make full use of the battery energy. Considering the health and the efficiency of the battery, the low level, the high level, and the initial SOCs were

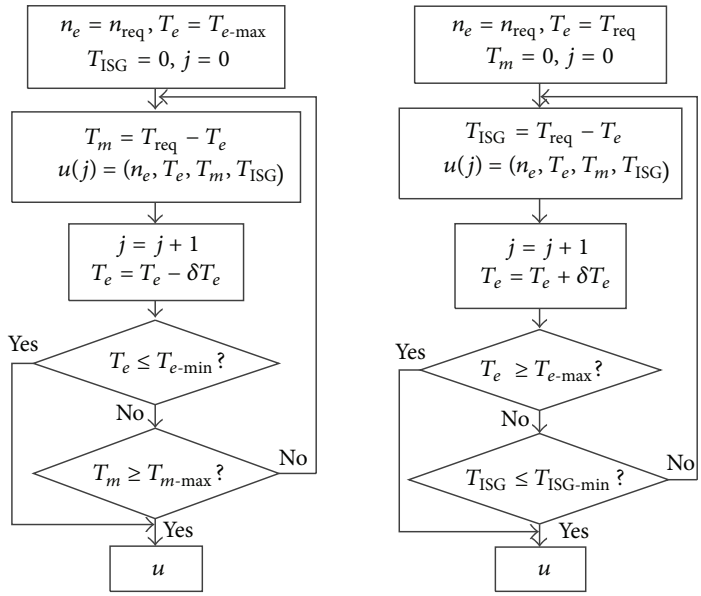

(a) For engine-motor parallel mode (b) For engine-ISG parallel mode

Figure 10: The way to find possible control solutions.

Table 2: Working modes when SOC < SOC_{low}.

The required speed and torque areas of the final drive in Figure 8	PHEB possible working mode	Remarks
1	Series mode	Engine/ISG works in maximum power point
2	Engine-only mode	Engine only drives the PHEB
3	Engine-ISG parallel mode	Engine drives the PHEB, and the ISG generates as much electric energy as possible to charge the battery

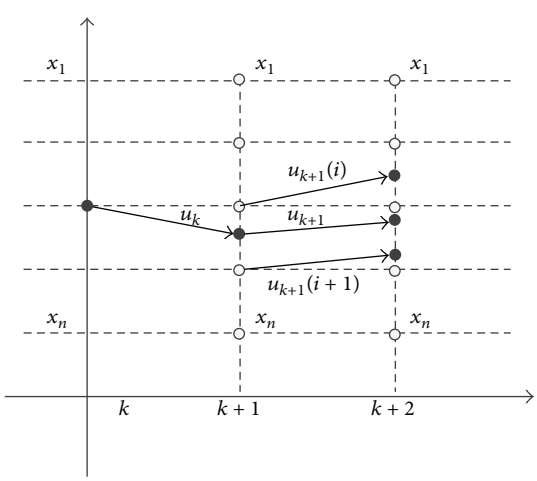

Figure 11: The schematic diagram of interpolation.

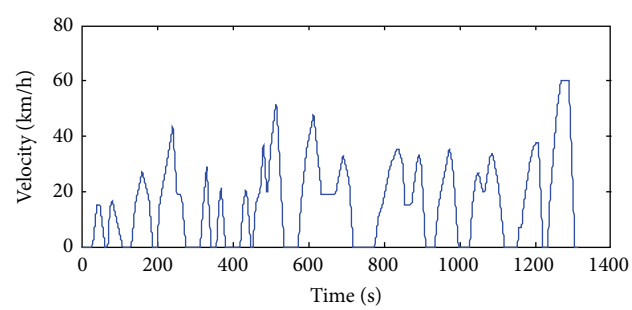

Figure 12: The profile for one CTUDC driving cycle.

selected to be 0.3, 0.8, and 0.6, respectively. The driving cycle is the Chinese typical urban drive cycle (CTUDC) as shown in Figure 12. The total distance of one CTUDC is 5.897 km, and the duration of one CTUDC is 1314 seconds.

The battery capacity of PHEB is much higher than that of HEVs, and the PHEB drives with the mode of one day one charge, so the PHEB would drive for many consecutive driving cycles. To show the energy distribution between the engine, ISG, and main drive motor, the model is simulated with the input of 15 consecutive CTUDC cycles. The increment of discretized SOC, δSOC, is selected to be 0.001, the increment of engine torque δT_e is selected to be 5 Nm, the weighting factor α is selected to be 100, and the PHEB weight of simulation is set to be the gross weight.

Figure 13 shows the simulation result of SOC under the DP optimal control for 15 consecutive CTUDC cycles.

Table 3: Possible PHEB modes when $SOC_{low} < SOC < SOC_{high}$.

Required torque and speed areas of final drive	PHEB possible working modes	Remarks
1	EV mode, series mode	If the motor cannot supply sufficient torque, the ISG motor will provide the remaining torque
2	Engine-ISG-motor parallel mode	The required torque of final drive exceeds the maximum torque provided by engine and motor together, and ISG motor provides remaining torque
3	Engine-motor parallel mode	None
4	EV mode, series mode, engine-motor parallel mode	None
5	engine-ISG parallel mode, engine-motor parallel mode, engine-only mode	None
6	Engine-only mode, EV mode, engine-ISG parallel mode, engine-motor parallel mode, series mode	None

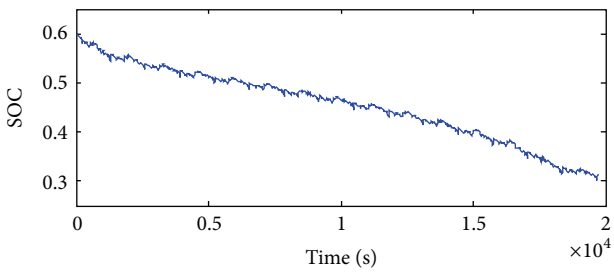

Figure 13: The SOC simulation result for 15 CTUDC cycles.

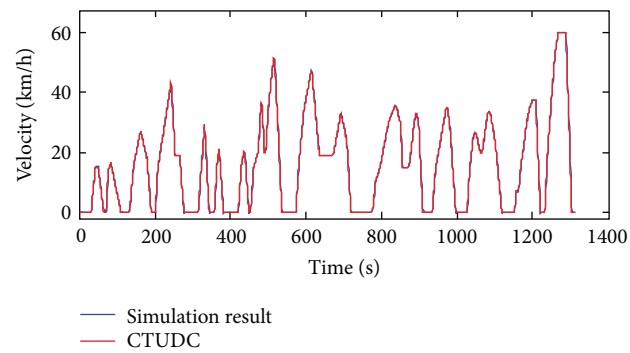

Figure 14: Velocity comparison between simulation and CTUDC cycle.

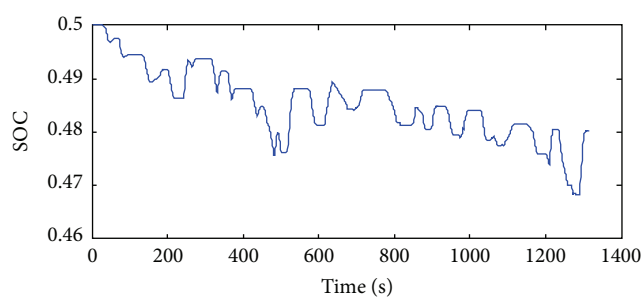

Figure 15: The SOC simulation result for one CTUDC cycle.

The SOC decreased to 0.314 when the bus reached the destination. Because of the regenerative braking at the end of the cycle, the terminal SOC is a little higher than the low level, but it is still very close to the low level, so the bus can make full use of the battery energy with the optimal control.

The SOC decreases evenly from the initial SOC to the low level of the SOC. When the optimal control was applied to the 15 consecutive CTUDC cycles, the SOC reduction would be 0.02 for one cycle on average. To relieve the heavy computational burden, the optimal control for one CTUDC cycle can be used as the optimal control for 15 consecutive CTUDC driving cycles through restricting the initial SOC and terminal SOC. The initial SOC and desired terminal SOC are selected to be 0.5 and 0.48, respectively. To ensure that the SOC at final time is the desired value, an additional terminal constrain on SOC needs to be imposed and the cost function would be

$$\begin{aligned} J &= \sum_{k=0}^{N-1} L(x(k), u(k)) \\ &= \sum_{k=0}^{N-1} \left[\text{fuel}(k) + \alpha \left(T_{\text{req}}(k) - T_e(k) - T_{\text{ISG}}(k) \right.\right. \\ &\qquad \left.\left. - T_m(k) - \frac{T_b(k)}{i_o} \right)^2 \right] \\ &\quad + \beta \left(\text{SOC}(N) - \text{SOC}_f \right)^2, \end{aligned} \tag{13}$$

where β is positive weighting factor and SOC_f is the desired SOC at the end of driving cycle.

The increment of SOC, δSOC, is selected to be 0.001, the increment of engine torque δT_e is selected to be 5 Nm, and the weighting factors α and β are selected to be 100 and 1×10^7, respectively. The difference between simulation result of velocity and desired vehicle velocity is very small as shown in Figure 14. Figure 15 shows the simulation result of SOC with the optimal control for one driving cycle, and the terminal SOC turned out to be 0.4804, which is very close to the desired value.

Table 4: The simulation results for different driving cycles.

Number of driving cycle	15	1
Distance (km)	88.46	5.897
Initial SOC	0.6	0.5
Terminal SOC	0.314	0.4804
Electric energy consumption (kWh)	9.95	0.682
Fuel consumption (L)	17.44	1.174
Fuel consumption per 100 km (L/100 km)	19.72	19.90
Computation time (s)	50220.8	2643.2

The simulation results for 15 consecutive driving cycles and one driving cycle are shown in Table 4. The fuel consumption per 100 km of 15 driving cycles is 19.72 L, and the fuel consumption per 100 km of one driving cycle with restricted terminal SOC is 19.90 L. The fuel consumption per 100 km increased by 0.91%, while the computation time decreased by 94.7%. Considering that the internal resistance of the battery is a function of SOC, the optimal control of one driving cycle with restricted terminal SOC is applied to the simulation for 15 consecutive driving cycles, and the simulation result is shown in Table 5.

With the optimal control for one driving cycle, the fuel consumption per 100 km increased by 0.91% and the electric energy consumption increased by 3.2%, but the terminal SOC is still higher than the low level. The computation time of solving DP problem to find the optimal control decreased significantly, so it is feasible to find the optimal controls for consecutive driving cycles by solving the DP problem for one driving cycle with restricted initial SOC and terminal SOC.

The state increment δSOC in (12) also influences the accuracy of the optimization. If the δSOC is smaller, the quantized search area will be larger, hence the computational burden will be heavier. To study the tradeoff between accuracy of the optimization and computation time, δSOC is selected to be 0.0005, 0.001, and 0.005, respectively. The SOC simulation results are shown in Figure 16. The terminal SOC dropped to 0.4802, 0.4804, and 0.4806, respectively, which are very close to the desired value. When δSOC is selected to be 0.001, the curve of SOC is very similar to the curve when δSOC is selected to be 0.0005.

The fuel consumption and computation time results are summarized in Table 6. Compared with the results when δSOC is 0.0005, the fuel consumption increased by 0.61% and the computation time decreased by 53.9% when δSOC is 0.001, while the fuel consumption increased by 7.03% and the computation time decreased by 91.0% when δSOC is 0.005. Considering the tradeoff between fuel consumption and computation time, it is feasible to set δSOC to be 0.001. And the simulation results in this case are shown in Figure 17.

The output torque of the PHEB components is shown in Figure 17. It can be seen that the ISG seldom works as a generator to charge the battery, and most of the negative power is from regenerative braking. If the ISG works as a generator, there are engine efficiency losses, ISG efficiency losses, main drive motor efficiency losses, and battery efficiency losses, hence the system is ineffective, so in most cases the optimal control strategy based on DP avoids the situation when the ISG works as a generator. At the end of the cycle, to force the terminal SOC to be the desired value, the ISG supplied negative power to charge the battery.

The working modes of the PHEB is shown in Figure 18, where mode = 0 means that the bus stops and no powertrain components is working; mode = −1 means regenerative

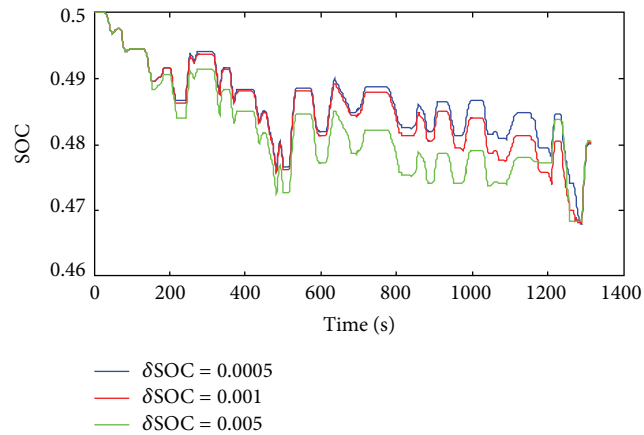

Figure 16: The SOC simulation results with different δSOCs.

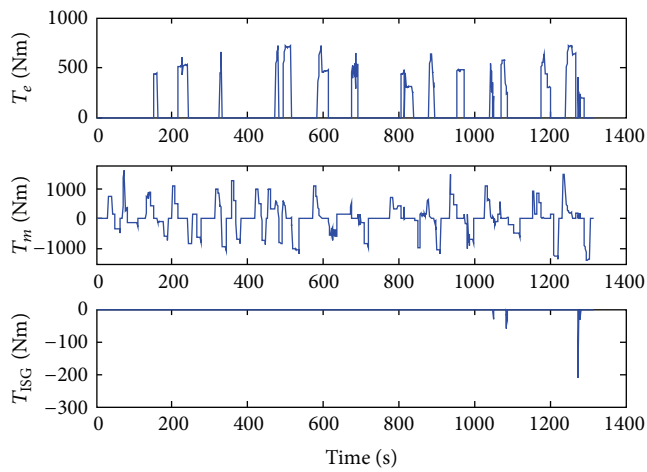

Figure 17: The simulation results with DP optimal control when δSOC is 0.001.

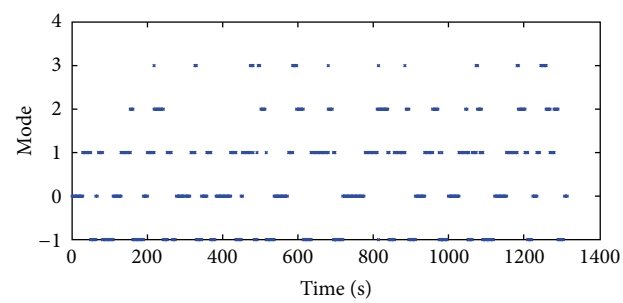

Figure 18: The PHEB working modes under optimal control strategy.

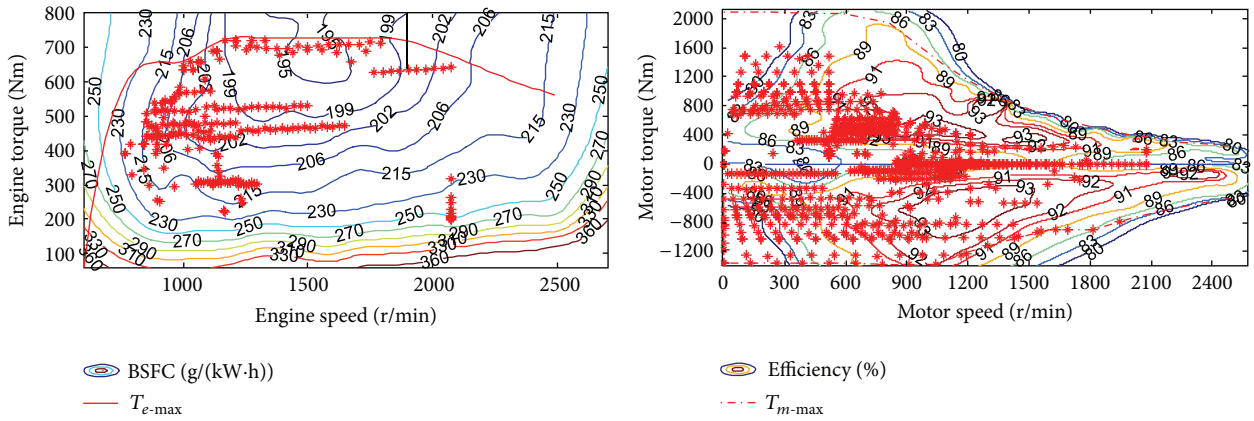

(a) engine (b) motor

Figure 19: Working areas of the components.

Table 5: Simulation results for different control strategies.

Control strategy	Number of driving cycle	Initial SOC	Terminal SOC	Electric energy consumption (kWh)	Fuel consumption (L)	Fuel consumption per 100 km (L/100 km)
DP optimal control for 15 consecutive cycles	15	0.6	0.314	9.95	17.44	19.72
DP optimal control for one cycle with restricted initial and terminal SOCs	15	0.6	0.305	10.27	17.603	19.90

Table 6: Simulation result of fuel consumption and computation time.

δSOC	0.0005	0.001	0.005
Fuel consumption per 100 km (L/100 km)	19.78	19.90	21.17
Computation time (s)	5733.4	2643.2	517.4

braking mode, mode = 1 means EV mode, mode = 2 means engine-only mode, mode = 3 means parallel mode, and mode = 4 means series mode. It can be seen that the system does not work in series mode in case of the low efficiency.

When the PHEB works in full load condition and the load rate of engine is high, the engine can work in high efficiency area without need of the load regulation of ISG, so the ISG seldom supplies negative torque. The working points of engine and main drive motor are shown in Figure 19. It shows that the engine works in high efficiency areas in most cases. The main drive motor drives the bus alone when the vehicle speed is low. The engine works if the vehicle required speed is high and the main drive motor supplies the remaining torque to maintain the engine working in high efficiency. The ISG seldom works under the optimal control based on DP, but it does not mean that the ISG is useless, because the energy control strategy of the PHEB is based on rules in reality, the driving distance is not a fixed value, and the ISG is needed to charge the battery to maintain the SOC level. There is no standard PHEB fuel consumption for rule-based energy management control strategy, and the PHEB may consume more fuel than traditional bus if the control rule parameters were not properly designed. So we made a comparison of the fuel consumption between the PHEB with optimized control strategy and the prototype conventional diesel bus. The results show that the experimented fuel consumption of the prototype conventional diesel bus is 43 L/100 km in CTUDC driving cycle, and the fuel consumption of the optimized PHEB is 19.90 L/100 km, with additional electricity consumption of 11.61 kWh/100 km, the fuel consumption decreased by 53.7%. The optimal control based on DP can improve fuel economy significantly. It should be noted that the fuel consumption results given by the optimal control based on DP are maximum potential gains, and they cannot be reached in a real vehicle, because the entire driving cycle is known in advance, and neither comfort constraints nor highly dynamic phenomena are taken into account [15].

6. Conclusions

It is very complicated to determine the energy management strategy for a series-parallel PHEB, and the dynamic programming is a powerful tool to get global optimization results. The backward simulation model of the series-parallel PHEB was built. Then, to explore the potential of fuel economy, the dynamic programming algorithm is utilized to

realize an optimal control on a known-in-advance driving cycle. The procedure of DP for the series-parallel powertrain topology is introduced in detail. An appropriate method is proposed to improve the computational efficiency which can reduce the computation burden greatly and keep the precision of DP.

The simulation results show that with the global optimal control, the battery SOC can reach its lower limit at the end of the cycle, which means that the bus can make full of the battery energy. Meanwhile, the ISG seldom works in generation mode under given cycle and SOC interval, which avoids the inefficient situation. It is proved that the optimal control based on DP can reduce the fuel consumption greatly.

The drawback of optimal control based on DP is that the driving cycle should be known in advance, and the computational burden is still very heavy, so it is difficult to be applied in a real vehicle. In the further study, a near-optimal control law will be extracted according to the global optimization results.

Conflict of Interests

The authors declare that there is no conflict of interests regarding the publication of this paper.

Acknowledgments

This work was supported by the National High Technology Research and Development Program of China (2011AA11A228, 2012AA111603, and 2011AA11A290) in part, the International Cooperation Research Program of Chinese Ministry of Science and Technology (2011DFB70020) in part, and the Program for New Century Excellent Talents in University (NCET-11-0785) in part. The authors would also like to thank the reviewers for their corrections and helpful suggestions.

References

[1] M. Ehsani, Y. Gao, and A. Emadi, *Modern Electric, Hybrid Electric, and Fuel Cell Vehicles: Fundamentals, Theory, and Design*, CRC Press, New York, NY, USA, 2009.

[2] Y. Gao and M. Ehsani, "Design and control methodology of plug-in hybrid electric vehicles," *IEEE Transactions on Industrial Electronics*, vol. 57, no. 2, pp. 633–640, 2010.

[3] C. H. Stephan and J. Sullivan, "Environmental and energy implications of plug-in hybrid-electric vehicles," *Environmental Science and Technology*, vol. 42, no. 4, pp. 1185–1190, 2008.

[4] S. G. Wirasingha and A. Emadi, "Classification and review of control strategies for plug-in hybrid electric vehicles," *IEEE Transactions on Vehicular Technology*, vol. 60, no. 1, pp. 111–122, 2011.

[5] H. Banvait, S. Anwar, and Y. Chen, "A rule-based energy management strategy for plugin hybrid electric vehicle (PHEV)," in *Proceedings of the American Control Conference (ACC '09)*, pp. 3938–3943, St. Louis, Mo, USA, June 2009.

[6] N. J. Schouten, M. A. Salman, and N. A. Kheir, "Fuzzy logic control for parallel hybrid vehicles," *IEEE Transactions on Control Systems Technology*, vol. 10, no. 3, pp. 460–468, 2002.

[7] P. Pisu and G. Rizzoni, "A comparative study of supervisory control strategies for hybrid electric vehicles," *IEEE Transactions on Control Systems Technology*, vol. 15, no. 3, pp. 506–518, 2007.

[8] H. Zhang, Y. Shi, and M. Liu, "H_∞step tracking control for networked discrete-time nonlinear systems with integral and predictive actions," *IEEE Transactions on Industrial Informatics*, vol. 9, no. 1, pp. 337–345, 2013.

[9] H. Zhang, Y. Shi, and A. S. Mehr, "Robust H_∞PID control for multivariable networked control systems with disturbance/noise attenuation," *International Journal of Robust and Nonlinear Control*, vol. 22, no. 2, pp. 183–204, 2012.

[10] H. Zhang, Y. Shi, and A. S. Mehr, "Robust weighted H_∞filtering for networked systems with intermittent measurements of multiple sensors," *International Journal of Adaptive Control and Signal Processing*, vol. 25, no. 4, pp. 313–330, 2011.

[11] H. Zhang, Y. Shi, and A. S. Mehr, "Robust static output feedback control and remote PID design for networked motor systems," *IEEE Transactions on Industrial Electronics*, vol. 58, no. 12, pp. 5396–5405, 2011.

[12] C.-C. Lin, H. Peng, J. W. Grizzle, and J.-M. Kang, "Power management strategy for a parallel hybrid electric truck," *IEEE Transactions on Control Systems Technology*, vol. 11, no. 6, pp. 839–849, 2003.

[13] Q. Gong, Y. Li, and Z.-R. Peng, "Trip-based optimal power management of plug-in hybrid electric vehicles," *IEEE Transactions on Vehicular Technology*, vol. 57, no. 6, pp. 3393–3401, 2008.

[14] W. Wang and S. M. Lukic, "Dynamic programming technique in hybrid electric vehicle optimization," in *Proceedings of the IEEE International Electric Vehicle Conference*, pp. 4–8, Greenville, SC, USA, March 2012.

[15] J. Scordia, M. Desbois-Renaudin, R. Trigui, B. Jeanneret, F. Badin, and C. Plasse, "Global optimisation of energy management laws in hybrid vehicles using dynamic programming," *International Journal of Vehicle Design*, vol. 39, no. 4, pp. 349–367, 2005.

[16] W. Zheng, *Reseach on power train parameter matching method and control strategy for hybrid electric vehicle [Ph.D. thesis]*, Harbin Institute of Technology, Harbin, China, 2010.

[17] Y. Zou, S. J. Hou, and E. L. Han, "Dynamic programming-based energy management strategy optimization for hybrid electric commercial vehicle," *Automotive Engineering*, vol. 34, no. 8, pp. 663–668, 2012.

[18] R. Bellman, *Dynamic Programming*, Princeton University Press, Princeton, NJ, USA, 1957.

Hindawi Publishing Corporation
Mathematical Problems in Engineering
Volume 2013, Article ID 637621, 10 pages
http://dx.doi.org/10.1155/2013/637621

Research Article

Modeling and Analysis of Online Delay of Nonperiodic CAN Message

Dafang Wang,[1] Bowen Yang,[1] Yi Jin,[2] Ji Qi,[1] and Nannan Li[1]

[1] *School of Automotive Engineering, Harbin Institute of Technology, Weihai 264209, China*
[2] *Academy of Armored Forces Engineering, Beijing 100000, China*

Correspondence should be addressed to Dafang Wang; wdflcjl@163.com

Received 3 September 2013; Accepted 11 October 2013

Academic Editor: Hui Zhang

In order to analyze the online communication delay of nonperiodic CAN message, the mathematical model of average on-line delay is established based on M/G/1 queuing theory and an experimental platform is designed to analyze the delay of CAN communication, with which the on-line delays of messages with a different ID are tested at different load ratios. The results show that the model is very close to the actual situation indicating the high accuracy of the model. In the results, for the same message, the average and maximum online delays both increase with the raise of load ratio. At the same load ratio, the maximum on-line delay increases with the decrease of the message priority, and the average on-line delay remains almost unchanged.

1. Introduction

The vehicle distributed real-time control system is a specific application of distributed real-time control system, which is a closed-loop feedback control system consisting of a sensor, a controller, and an actuator on a real-time network. Its network medium is generally shared by several control loops which is obviously different from the traditional mode. This type of networked control mode is superior to the traditional point-to-point centralized control mode, because of its sharing of information resources, much decrease of connecting wiring harness, digitization and modularization of control assembly and components, and being easier to expand and maintain as well as high efficiency, reliability, and flexibility, and so forth [1–9]. On the other hand, the use of networked control impacts on system performance. References [10–14] analyze the relationship between network-induced delays and system performance, introducing network-induced delay in the system modeling, considering the network-induced delays and random data missing occurrence, analyzing the problem of stability control under a different network-induced latency, pointing out that it is necessary to consider network-induced delays in the choice of control algorithms.

In the network control system, apart from the transmission of the time-triggered periodic message, the event-triggered nonperiodic message is suggested to be taken into account. The generation of nonperiodic message is not related to time and as a result its transmission delay cannot be analyzed according to the transmission mode of periodic message. Nonperiodic message generally is not the regular input and output information in the network control system. Its generating frequency is much lower than the periodic one. If this type of message is sent as periodic message, the load of the network will get greatly increased. However, this type of message is usually some detection data of the system, like the warning message. Therefore, the request for the reliability and real-time performance is much higher than the periodic one. For example, considering the warning signal of the battery in the monitoring system of an electric vehicle, the sensor sends a binary warning signal when the battery breaks down. If this message could not be sent to the monitoring center in time, the consequence caused is more serious than the transmission problems caused by regular controlling information (like rotate speed, electricity, etc.). Therefore, there is a high necessity to analyze the transmission delay of nonperiodic message.

Nowadays, the mainstream bus of the vehicle distributed real-time control system is Controller Area Network (CAN) bus. The delay of CAN communication can be divided into four parts: generating delay, queue delay, transmission delay, and receiving delay [15]. Considering that the queue delay and transmission delay are related to the process of message transferring on the bus, these two parts should be defined as on-line delays. In order to obtain the communication delay of nonperiodic CAN message, two problems need to be figured out. First of all, what kinds of laws are the generating process of nonperiodic message consistent with? Secondly, what characteristics dose the queue process possess when the nonperiodic message with specific generating laws transmits on the CAN network? Scholars around the world have already done some research work on the communication delay of nonperiodic CAN message [15–32].

References [15–19] take the nonperiodic message as periodic one and consider the minimum value of interval time between two transmissions of the message frame as its period. References [20–23] utilize a dynamic priority strategy to enhance the real-time performance of nonperiodic message. Reference [24] adopts the time-triggered mode and analyzes the scheduling and real-time problems of CAN. Reference [25] builds an experimental platform for analyzing the real-time performance of CAN. Reference [26] assumes that the occurrence of error frame accords with Poisson process and analyzes the influence on network-induced delays caused by error frames; nevertheless, there is only theoretical analysis but no experimental data. Reference [27] analyzes the waiting time and the length of the queue of messages applying the M/M/1 queuing process but does not provide corresponding experimental data. References [28, 29] do not differentiate between periodic and nonperiodic messages and uniformly adopt an M/G/1 queuing process to establish the mathematical model of average delay. Reference [30] puts forward a buffered estimation method aimed at the System on Chip (SoC) based on a priority-ranked queuing model and builds a buffered queuing model. The queue is an M/G/1 queue with several different client levels and non-preemptive arbitration. A mathematical model of average waiting time is deduced, which can provide some reference value for us to build the average waiting time model of the nonperiodic message on CAN bus.

In this paper, a mathematical model of average on-line delay of nonperiodic message is built using the queuing theory. Moreover, on-line delays of messages with different priorities at different load ratios are tested separately. After analyzing and contrasting the measured and theoretical values, basic characteristics and laws of the on-line delay of nonperiodic CAN message are acquired.

2. Basic Introductions about Online Delay of Nonperiodic CAN Message Modeling

2.1. Markov Process and Poisson Process. In classical mechanics, the track at a given moment t can be solved using the state at some moment $t_0 < t$ without knowing the state before moment t_0. Such principle can be adopted in systems following probability rules but not decisive rules, which means when the state of the process at moment $t = t_0$ is known, the state at moment t ($t > t_0$) dose not correlate with the state before moment $t = t_0$. Such feature that there is no relationship between "future" and "past" with the knowledge of "present" is called Markov property or nonaftereffect property. A process possessing this property is usually called a Markov process.

A Markov process is an important type of random process in both theory and in practical applications. It is widely applied in network simulation [31].

As for a Markov process, the following definitions should be given.

A random process $\{X(t), t \in T\}$ is present; if considering any n moments t_i of the parameters, $i = 1, 2, \ldots, n$, $t_1 < t_2 < \cdots < t_n$,

$$\begin{aligned} P\{X(t_n) < x_n \mid X(t_1) = x_1, \\ X(t_2) = x_2, \ldots, X(t_{n-1}) = x_{n-1}\} \\ = P\{X(t_n) < x_n \mid X(t_{n-1}) = x_{n-1}\} \end{aligned} \tag{1}$$

then this random process $\{X(t), t \in T\}$ can be called a Markov process. The property shown by expression (1) is named Markov property or nonaftereffect property.

The value of $X(t)$ in the Markov process $\{X(t), t \in T\}$ is called state. $X(t) = x$ means that the process is in a state x at a moment t, and the whole value set in the process

$$E = \{x : X(t) = x, t \in T\} \tag{2}$$

is called state space. If both the parameter set T and the state space E are discrete Markov processes, it can be called a Markov chain.

A Poisson process is defined as follows.

If the counting process $\{N(t), t \geq 0\}$ that takes nonnegative integer value meets the following conditions:

(1) $N(0) = 0$;

(2) having independent increment;

(3) for any $0 \leq s < t$, $N(t) - N(s)$ is accorded with the Poisson distribution whose parameter is $\lambda(t - s)$,

$$P\{N(t) - N(s) = k\} = \frac{[\lambda(t-s)]^k}{k!} e^{-\lambda(t-s)}, \quad k = 0, 1, 2, \ldots, \tag{3}$$

Then the random process $\{N(t), t \geq 0\}$ is called a (homogeneous) Poisson process whose parameter (or average ratio, intensity) is λ.

The following processes are typical cases of Poisson process. During the time interval $[0, t)$.

(1) The number of customers arriving at a supermarket $N(t)$.

(2) The number of machines breaking down in a workshop $N(t)$.

(3) The number of error codes in a communication system $N(t)$.

Suppose $N(t)$ to be the number of times of event happening during the interval $[0,t)$, $\{N(t), t \geq 0\}$ to be a Poisson process with a parameter λ and $\tau_1, \tau_2, \ldots, \tau_n$ to be the moment of the event happening the 1st, 2nd, ..., n time. t_k represents the waiting time until the event happens the k time, and T_k $(k \geq 1)$ represents the separation distance between the $k-1$ and the k appearance,

$$T_k = \tau_k - \tau_{k-1}, \quad k = 1, 2, \ldots, n, \ \tau_0 = 0. \tag{4}$$

As can be proved, the variables in the interval sequence $\{T_n, n = 1, 2, \ldots, n\}$ are all independent and identically distributed random variables, which are changed by exponential distribution with a parameter λ,

$$p_t = P\{T_n = t\} = \begin{cases} \lambda e^{-\lambda t} & t \geq 0 \\ 0 & t < 0 \end{cases} \quad \lambda > 0. \tag{5}$$

2.2. Queuing and Serving Process. Queuing is a common phenomenon in our daily life. For example, people queue up to wait for buses when on and off duty and customers line up to shop in the stores. Obviously, the queue consists of two parties. One party asks for getting service and the other party tries to provide service. The people or things (like equipments) that require service are generally called customers and the service staff or service agency that provide service is called service staff or service counter. Then the customers and the service counter form a queuing and serving system, which can also be called a stochastic service system.

A queuing system is determined by many conditions. While for the sake of simplicity, 3~5 English letters with diagonal lines between them are usually used to indicate a queuing system. The first letter represents the distribution pattern of input variables, the second one represents the distribution pattern of the service time, the third one represents the number of service counter, and the forth one represents the capacity of service system. Sometimes a fifth letter may be used to represent the customer number in the customer source. M/M/1 means that the input process is a Poisson current, the service time follows a negative exponential distribution, and the system has only one service counter. The M/M/1 queuing and serving system has a quite good Markov property at any moment. M/G/1 means that the input process is a Poisson current, the service time is independent and follows a probability distribution, and the system has only one service counter, whereas M/G/1 queuing and serving system has the Markov property only at some special random moments but not any moment. These random moments are called regeneration points which means that the system restarts since the moment. Utilizing regeneration points, a common queuing and serving system can be turned into a Markov chain and get solved with relevant methods. This kind of method is called imbedding Markov chain approach [32].

In an M/G/1 queuing and serving process, the customers arrive in Poisson current whose parameter is λ $(\lambda > 0)$, which means the sequence $\{T_i, i \geq 1\}$ showing interval time of adjacent arrival is independent and is accorded with negative exponential distribution.

The sequence $\{\chi_i, i \geq 1\}$ of the service time that customers need is independent and follows a general distribution $G(t), t \geq 0$, and $0 < 1/\mu = \int_0^\infty t dG(t)$ is taken as the average service time. There is only one service counter in the system. When a customer arrives, he can accept service at once if the counter is free. Otherwise, he should wait in line and accept service according to the arrival order. He leaves the new system as soon as the service ends. In addition, the arrival process and the service process are still independent of each other.

Set $N(t)$ to be the number of customers in the system (the queue length) at the moment t. In an M/G/1 queuing system, considering that the service time follows a general distribution, the service for a customer who is accepting his service at an optional moment t could be unfinished. Because the remaining service time distribution does not have the no-memory property any more since the moment t, the queue length $\{N(t), t \geq 0\}$ does not have Markov property consequently. However, if N_n^+ is set to be the number of the customers left in the system when the customer n finishes his service and leaves, which means the rest queue length, $n \geq 1$, it can be proved that the sequence $\{N_n^+, n \geq 1\}$ is a Markov chain and should be called an imbedding Markov chain of the queue length process $\{N(t), t \geq 0\}$. It can also be proved that the necessary and sufficient condition of the chain $\{N_n^+, n \geq 1\}$ being positive recurrence is $\rho = \lambda/\mu < 1$. When the chain $\{N_n^+, n \geq 1\}$ is positive recurrence, it is acknowledged that the sequence $\{N_n^+, n \geq 1\}$ owns the only stationary distribution,

$$p_j^+ = \lim_{n \to \infty} P\left(N_n^+ = j\right) > 0, \quad j = 0, 1, 2, \ldots. \tag{6}$$

As can be proved, when $\rho < 1$, the limit of the n-step transition probability of the imbedding Markov chain always exists and is a positive value which does not depend on the initial state. That is to say, it is a stationary distribution. When $\rho \geq 1$, no matter how large the positive integer m is, the probability of the number of customers left in the system $\leq m$ as the customer n finishes his service and leaves is always tending to 0 $(n \to \infty)$. This indicates that the queue will get longer and longer and the system cannot reach a statistical balance. In an M/G/1 queuing system, if $\rho = \lambda/\mu < 1$, then the generating function of the stationary distribution p_j^+, $j \geq 0$ is

$$P^+(z) = \frac{(1-\rho)(1-z)\, g(\lambda(1-z))}{g(\lambda(1-z)) - z}, \quad |z| < 1. \tag{7}$$

Thereinto, $g(\lambda(1-z)) = \int_0^\infty e^{-\lambda(1-z)t} dG(t)$.

Assume that customers get served according to the first-come-first-serve (FCFS) rule and set $W_q(t)$ and $W(t)$ to represent the waiting and stay time distribution under the statistical balance; the inverse Laplace transforms of them are

$$\begin{aligned} w_q(s) &= \int_0^\infty e^{-st}\, dW_q(t), \\ w(s) &= \int_0^\infty e^{-st}\, dW(t). \end{aligned} \tag{8}$$

Then the specific expressions of $w_q(s)$ and $w(s)$ in an M/G/1 queuing system are deduced under the condition $\rho < 1$.

Apparently, under a statistical balance, the number of customers left in the system as a customer finishes his service and leaves equals the number of customers reaching the system during his stay, which means

$$\begin{aligned} p_j^+ &= P\left(j \text{ customers arrive during his stay}\right) \\ &= \int_0^\infty \frac{(\lambda t)^j}{j!} e^{-\lambda t} dW(t), \quad j = 0, 1, 2, \ldots. \end{aligned} \tag{9}$$

Therefore,

$$\begin{aligned} P^+(z) &= \sum_{j=0}^{\infty} z^j p_j^+ = \int_0^\infty e^{-\lambda t} \sum_{j=0}^{\infty} \frac{(\lambda t z)^j}{j!} dW(t) \\ &= \int_0^\infty e^{-\lambda(1-z)t} dW(t) = w(\lambda(1-z)). \end{aligned} \tag{10}$$

According to the formula (7) and (10), it can be deduced that

$$\frac{(1-\rho)(1-z)\, g(\lambda(1-z))}{g(\lambda(1-z)) - z} = w(\lambda(1-z)). \tag{11}$$

Set $s = \lambda(1-z)$ and the following expression can be obtained:

$$w(s) = \frac{s(1-\rho)\, g(s)}{s - \lambda[1 - g(s)]}. \tag{12}$$

The stay time W equals waiting time W_q plus service time χ, which means $W = W_q + \chi$. Moreover, W_q and χ are independent of each other. Therefore,

$$w(s) = w_q(s) \cdot g(s). \tag{13}$$

According to the formula (12) and (13), the following expression can be obtained:

$$w_q(s) = \frac{s(1-\rho)}{s - \lambda[1 - g(s)]}. \tag{14}$$

Based on the formula (14), utilize the inverse Laplace transform,

$$W_q(t) = \sum_{n=0}^{\infty} (1-\rho)\, \rho^n \widehat{G}^{(n)}(t), \quad t \geq 0. \tag{15}$$

Thereinto, $\widehat{G}(t) = \mu \int_0^t [1 - G(x)] dx$ represents the equilibrium distribution of service time $G(t)$, and $\widehat{G}^{(n)}(t)$ is the n-fold convolution of $\widehat{G}(t)$, $n \geq 1$.

According to the formula (15), under the condition $\rho < 1$, the average waiting time of the M/G/1 system is supposed to be

$$\overline{W}_q = \frac{\lambda E\left[\chi^2\right]}{2(1-\rho)}. \tag{16}$$

Thereinto, χ represents the random variable of service time.

Formula (16) expresses the average waiting time deduced under the FCFS rules which can be divided into two parts,

$$\overline{W}_q = \rho \overline{W}_q + \frac{\lambda E\left[\chi^2\right]}{2}. \tag{17}$$

Apparently, the first part on the right side of the equal sign in the formula (17) means the waiting time of customers existing in the queue when a new customer arrives, and the second part represents the current customer's average rest service time when a new customer arrives. Under the FCFS rules, it can be deduced that when a new customer arrives, the current customer's rest service time is supposed to be

$$\overline{W}_e = \frac{\lambda E\left[\chi^2\right]}{2}. \tag{18}$$

Because the average stay time equals average waiting time plus average service time, the average stay time is

$$\overline{W} = \frac{1}{\mu} + \frac{\lambda E\left[\chi^2\right]}{2(1-\rho)}. \tag{19}$$

3. Modeling for Online Delay of Nonperiodic CAN Message

The average on-line delay time of nonperiodic message in a CAN bus system can be figured out with the knowledge of queuing theory. The CAN bus communication system is taken as a queuing and serving system. Each node that sends information frame is the generation source of information. According to the analysis in Section 2 as well as some relevant introductions in [28, 30], the nonperiodic message's generation process on each node is a Poisson process. The intervals of the node's request correspond to the customers' arrival intervals, the transmission time of the bus after node's request corresponds to the service time in queuing theory, and the CAN bus corresponds to a service staff. As a result, the system can be described to be a queuing model which is shown in Figure 1, and n nodes can be taken as the arrival sequence of n customers.

The features of the queuing model include the following ones.

(1) n arriving currents in the queuing model share one public queue and the queue network is open loop.

(2) Customers have grade identification and the priorities are $1, 2, \ldots, n$ from high to low. The service mechanism adopts non-preemptive discrimination with priorities.

(3) The arrivals of customers are all Poisson arrivals, and the speed of the arrivals are $\lambda_1, \lambda_2, \ldots, \lambda_n$.

(4) To enhance the adaptability of the model, it is assumed that the service time follows a general random distribution. The average service time for customers in different levels is $1/\mu_1, 1/\mu_2, \ldots, 1/\mu_n$.

In conclusion, the response time model for nonperiodic messages in a CAN bus system can be taken as a non-preemptive priority M/G/1 queue.

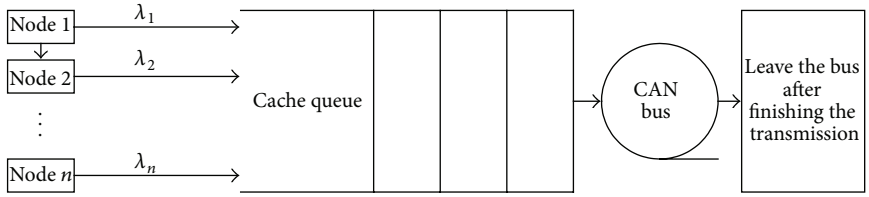

Figure 1: CAN bus queuing and serving model.

Meanwhile, the following instructions for message transmitting in CAN bus are put forward.

(1) For real-time information, there is no local queuing delay, which means that there is no sending buffer for the message with the same ID.

(2) Considering the transmission process of the protocol frame with the priority i and the uniqueness of identifier of CAN protocol frame, and there are no local queues, the time from a CAN message's reaching the network queue to getting sent successfully consists of two parts. One part is called blocking time that represents the remaining transmission time of the message who is getting transmitted as the frame arrives at the network. Another part is the interference time of the protocol frames with higher priority reaching the network during this period of time.

(3) According to the message priority, the message with the highest priority is called class 1 message and the one with a higher priority is called class 2 message. And so on, the message with the lowest priority should be class n message.

Firstly, considering class 1 message, which means the average queue delay problems of highest priority messages.

When a class 1 message requests to pass the bus and transmit, its average waiting time $\overline{W_{q1}}$ is expressed as follows.

(1) When a message requests to transmit, the remaining transmission time of the messages (regardless of its priority class) who are transmitting through the bus is supposed to be

$$\overline{W_{q1}} = \overline{W^e}. \tag{20}$$

Thereinto, $\overline{W_{q1}}$ represents the average waiting time of the class 1 message which means the time quantum from requesting for transmission to taking the bus and $\overline{W^e}$ represents the average remaining time of the messages who are transmitting when the class 1 message reaches.

According to the formula (18), the average remaining service time of the current customer is supposed to be

$$\overline{W^e} = \sum_{i=1}^{n} \frac{\lambda_i E\left(\chi_i^2\right)}{2}. \tag{21}$$

Thereinto, n represents the sum of message categories, λ_i represents the request speed of class i message, and χ_i represents the transmission time of class i message which is a random variable.

Then, take class 2 message into consideration, which means the average queue delay problems of higher priority messages.

When a class 2 message requests to pass the bus to transmit, its average waiting time $\overline{W_{q2}}$ is expressed as follows.

(1) $\overline{W^e}$ is the remaining time of the messages (regardless of its priority class) who are taking the bus to transmit when the message requests for transmission.

(2) The total transmission time of class 1 messages in the queue before the message's arrival $\overline{W_2^b}$ is supposed to be

$$\overline{W_2^b} = \frac{\lambda_1 \overline{W_{q1}}}{\mu_1} = \rho_1 \overline{W_{q1}}. \tag{22}$$

(3) The total transmission time of class 1 messages that reach during the message's waiting period $\overline{W_2^a}$ is supposed to be

$$\overline{W_2^a} = \frac{\lambda_1 \overline{W_{q2}}}{\mu_1} = \rho_1 \overline{W_{q2}}. \tag{23}$$

According to the formula (20), (22), and (23), it can be deduced that the waiting time of class 2 message $\overline{W_{q2}}$ is to be

$$\begin{aligned} \overline{W_{q2}} &= \overline{W^e} + \overline{W_2^b} + \overline{W_2^a} \\ &= \overline{W_{q1}} + \rho_1 \overline{W_{q1}} + \rho_1 \overline{W_{q2}}, \\ \overline{W_{q2}} &= \frac{\overline{W_{q1}}\left(1+\rho_1\right)}{\left(1-\rho_1\right)}. \end{aligned} \tag{24}$$

Finally, consider the average queue delay problem of the class i message.

When a class i message requests to transmit through the bus, its average waiting time $\overline{W_{qi}}$ is derived in the following possibilities:

(1) $\overline{W^e}$ is the remaining time of the messages (regardless of its priority class) who are taking the bus to transmit when the message requests for transmission.

(2) Before the mentioned class i message arrives, the total transmission time of messages with priorities higher than i is defined as $\overline{W_i^b}$:

$$\overline{W_i^b} = \sum_{j=1}^{i-1} \frac{\lambda_j \overline{W_{qj}}}{\mu_j} = \sum_{j=1}^{i-1} \rho_j \overline{W_{qj}}. \tag{25}$$

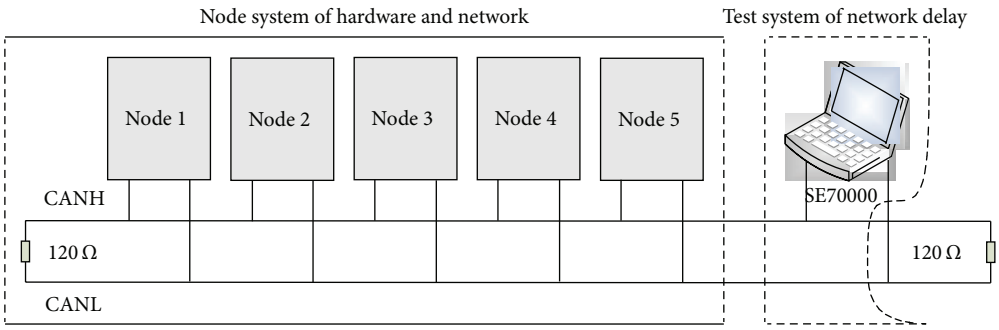

Figure 2: The experimental platform for testing the communication delay of CAN message.

(3) During the waiting period of the mentioned class i message, the total transmission time of the arriving messages whose priorities are higher than i, is defined as $\overline{W_i^a}$:

$$\overline{W_i^a} = \sum_{j=1}^{i-1} \frac{\lambda_j \overline{W_{qi}}}{\mu_j} = \sum_{j=1}^{i-1} \rho_j \overline{W_{qi}}. \tag{26}$$

According to the formulas (25), and (26), it can be deduced that the waiting time of class i message $\overline{W_{qi}}$ is to be

$$\begin{aligned} \overline{W_{qi}} &= \overline{W^e} + \overline{W_i^b} + \overline{W_i^a} \\ &= \overline{W^e} + \sum_{j=1}^{i-1} \rho_j \overline{W_{qj}} + \sum_{j=1}^{i-1} \rho_j \overline{W_{qi}}, \\ \overline{W_{qi}} &= \frac{\overline{W_{q(i-1)}} \left(1 - \sum_{j=1}^{i-2} \rho_j + \rho_{i-1}\right)}{\left(1 - \sum_{j=1}^{i-1} \rho_j\right)}. \end{aligned} \tag{27}$$

Then consider the transmission delay of messages, the online delay is supposed to be

$$\overline{W_i} = \frac{1}{\mu_i} + \overline{W_{qi}} \tag{28}$$

which is corresponding to the customer's average sojourn time in the queuing theory. In this paper, extended data frame is adopted. The first part of the right side of formula (28) can be computed according to the following expression:

$$\frac{1}{\mu_i} = \left(67 + 8s_m + \left\lceil \frac{\lfloor (54 + 8s_m)/4 \rfloor}{2} \right\rceil\right) \tau_{\text{bit}} + \rho_{\text{cons}}. \tag{29}$$

Thereinto, s_m represents the byte numbers included in the data field of message m, which should be an integer between 0 and 8. All eight bytes of data field are used in the paper, so the value should be 8. ρ_{cons} represents a constant related to electrical specifications of physical media of a bus and the value for per meter length of shielded twisted-pair cable could be 5 ns. τ_{bit} represents the time that is needed for a data bit to transmit on the transmission medium. The Baud rate of the network in this paper is 250 kbit/s, so the value for τ_{bit} should be 4 μs.

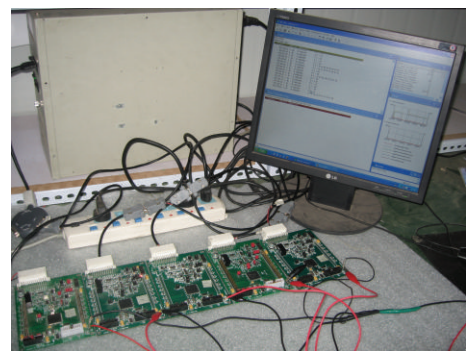

Figure 3: Using the experimental platform to test communication delay of CAN.

4. Testing Analysis of Communication Delay of Nonperiodic CAN Message

The trigger process of actual working conditions are simulated under the circumstance of taking the external event trigger mode as the trigger mode of nonperiodic CAN messages. The specific way to carry out is described concisely. Firstly, a pulse signal whose interval is an index distribution with a parameter λ is built. Then the pulse signal is plussed to the external interrupt interface of the singlechip and trigger CAN messages according to the level of fluctuation of the interface. Finally, the communication delay of nonperiodic CAN message at different load ratios is analyzed by changing the value of parameter λ.

4.1. Topological Structure Design of Test Platform. In order to test and verify the above-mentioned mathematical model for online delay during the process of periodic messages transmitting in the bus, an experimental platform is developed and designed to test the communication delay of CAN message, which is shown in Figure 2. Meanwhile, Figure 3 is a real photograph of using the experimental platform.

The experimental platform consists of computer network node system and network-induced delays testing system. The node system is made up of 5 CAN controller nodes. All nodes are designed by ourselves and the structures are exactly the same. The testing system is used to track the sending and receiving process of CAN message. The system uses a CAN

Table 1: Partial data that is monitored by network-induced delays testing system at a load ratio 13.33%.

ID	Receiving moment (ms)	ID	Receiving moment (ms)
0x11111115	20,736.30	0x11111111	20,791.45
0x11111114	20,739.95	0x11111114	20,793.95
0x11111111	20,744.25	0x11111111	20,801.05
0x11111112	20,756.50	0x11111114	20,802.75
0x11111111	20,758.65	0x11111112	20,803.35
0x11111114	20,765.55	0x11111114	20,804.75
0x11111115	20,767.10	0x11111113	20,808.45
0x11111114	20,770.75	0x11111114	20,818.35
0x11111111	20,776.25	0x11111114	20,819.95
0x11111112	20,787.70	0x11111113	20,832.05

network analyzer SE70000 from company NEC to finish the test, with which the sending and receiving process of message, recording the sending and receiving moment of message, recording the message ID, and counting the average and peak load ratio of the bus and some other functions can be realized.

4.2. Testing Results of Online Delay at Different Load Ratios. The test and analysis is carried out on the experimental platform for testing communication delay of CAN message which is shown in Figure 2. The on-line delays of messages with a different ID at different load ratios are tested in an actual communication process and are compared with the theory model for on-line delay which is built in Section 3.

4.2.1. Testing Results of Online Delay at a Load Ratio 13.33%. The load ratio being 13.33% is measured by SE70000. Under such working condition, the data of network part measured in real time is shown in Table 1.

Every actual receiving moment of message with a different ID is obtained. Apparently, the difference between two receiving moments of the same message is the actual receiving interval. The difference between the actual receiving interval and the actual trigger interval is the queue delay in the transmission process. The transmission delay in the transmission process of message with different ID can be tested with an oscilloscope. The sum of the measured transmission delay and the queue delay should be the on-line delay of message. The measured on-line delays data of messages with a different ID at a load ratio 13.33% are shown in Figure 4. The abscissa of the figure represents the sending times of message. 300 sets of data are tested totally, which means that the message with a same ID transmits for 300 times. And the ordinate represents the on-line delay size of transmission process with a different ID. After statistics and analysis, the average on-line delays of messages with different ID are acquired as well, which are shown in Table 2.

In Table 2, the theoretical average on-line delay is computed according to the formula (28). As can be seen in Table 2, the maximal difference value between the theoretical value and the measured value is 5.38%, which indicates that the theoretical average on-line delay model is practicable and has a high accuracy.

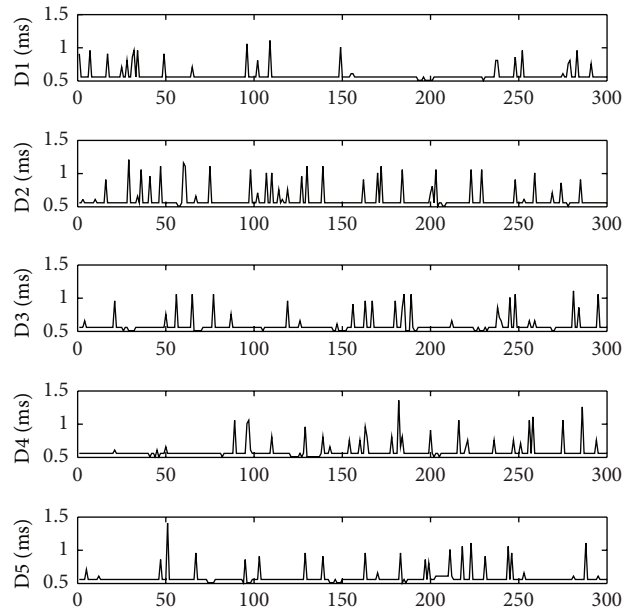

Figure 4: Measured on-line delays of messages with a different ID at a load ratio 13.33%.

Table 2: Comparison between the measured and theoretical average on-line delay value at a load ratio 13.33%.

ID	Measured average online delay (ms)	Theoretical average online delay (ms)	Difference
0x11111111	0.58267	0.60833	4.22%
0x11111112	0.6035	0.61069	1.18%
0x11111113	0.58467	0.61326	4.66%
0x11111114	0.58767	0.61607	4.61%
0x11111115	0.58583	0.61915	5.38%

4.2.2. Testing Results of Online Delay at a Load Ratio 27.64%. The measured on-line delays data of messages with a different ID at a load ratio 27.64% are shown in Figure 5. After statistics and analysis, the average on-line delays are acquired as well, which are shown in Table 3.

In Table 3, the theoretical average on-line delay is computed according to the formula (28). As can be seen in Table 3, the maximal difference value between the theoretical value and the measured value is 7.89%, which indicates that the theoretical average on-line delay model is practicable and has a high accuracy.

4.2.3. Testing Results of Online Delay at a Load Ratio 37.92%. The measured on-line delays data of messages with a different ID at a load ratio 37.92% are shown in Figure 6. After statistics and analysis, the average on-line delays are acquired as well, which are shown in Table 4.

In Table 4, the theoretical average on-line delay is computed according to the formula (28). As can be seen in Table 3,

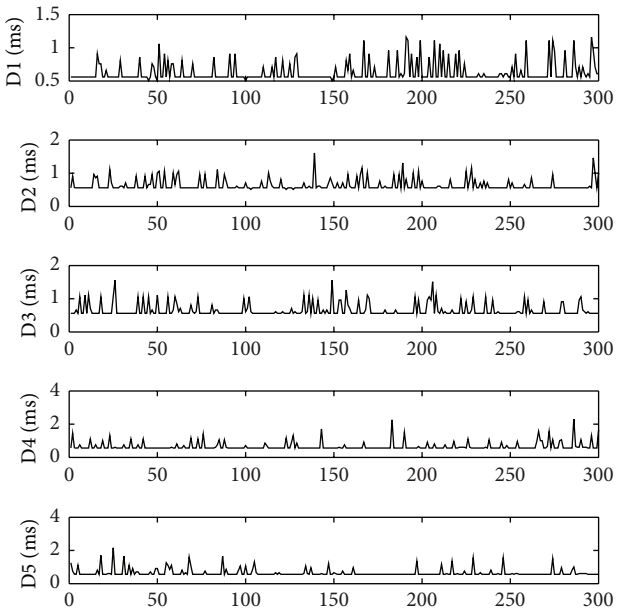

Figure 5: Measured on-line delays of messages with a different ID at a load ratio 27.64%.

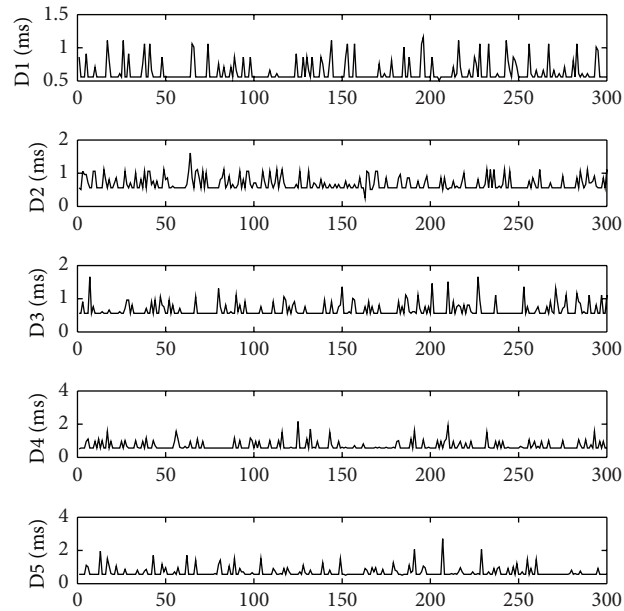

Figure 6: Measured on-line delays of messages with a different ID at a load ratio 37.92%.

Table 3: Comparison between the measured and theoretical average on-line delay value at a load ratio 27.64%.

ID	Measured average online delay (ms)	Theoretical average online delay (ms)	Difference
0x11111111	0.62733	0.64866	3.29%
0x11111112	0.63633	0.65837	3.35%
0x11111113	0.64967	0.66995	3.03%
0x11111114	0.654	0.68391	4.37%
0x11111115	0.64567	0.70095	7.89%

Table 4: Comparison between the measured and theoretical average on-line delay value at a load ratio 37.92%.

ID	Measured average online delay (ms)	Theoretical average online delay (ms)	Difference
0x11111111	0.63083	0.68898	8.44%
0x11111112	0.6805	0.71152	4.36%
0x11111113	0.66217	0.741	10.64%
0x11111114	0.68333	0.7806	12.46%
0x11111115	0.681	0.83556	18.50%

the maximal difference value between the theoretical value and the measured value is 18.50%, which indicates that the theoretical average on-line delay model is practicable and has a high accuracy.

4.3. Analysis for Testing Data of On-Line Delay. Charts are drawn to show the measured average and maximal values of on-line delays of messages at different load ratios based on Tables 2 to 4 and Figures 4 to 6, which are shown in Figures 7 and 8.

The analysis results are given based on Tables 2 to 4 and Figures 7 to 8.

(1) The average on-line delay values calculated with the mathematical model is very close to the measured ones for the messages with all priorities at three kinds of load ratios. The maximal error is 18.50%, indicating that the theoretical model is reasonable.

(2) For the same message, the measured average and maximal on-line delays are both increasing with the increase of load and reaching speed, which means that it conforms to the law that on-line delay increases when the load increases.

(3) To the same load, the priority has little impact on the average on-line delay. This phenomenon indicates that the queue delay for nonperiodic message comes from no arbitration delay mostly, which is in line with the characteristic of small trigger probability in the same phase position for nonperiodic message.

(4) The on-line delay of message consists of queue delay and transmission delay. For the extended frame message whose data field is 8 bytes, the length of a single frame is generally the same and the difference of transmission delay is small. Queue delay consists of arbitration delay and no arbitration delay. The arbitration delay means the delay of the message with a lower priority caused by the one with a higher priority when two messages are sent simultaneously, which includes the arbitration delay in the nodes and the one on the bus. The arbitration delay is related to the message priorities. The no-arbitration delay is a delay for the message frame because of there having been other message frames transmitting on

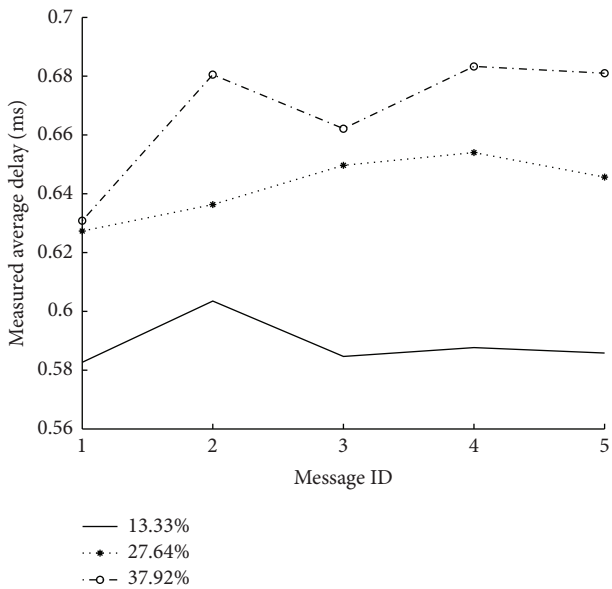

Figure 7: Average on-line delays of messages with a different ID at different load ratios.

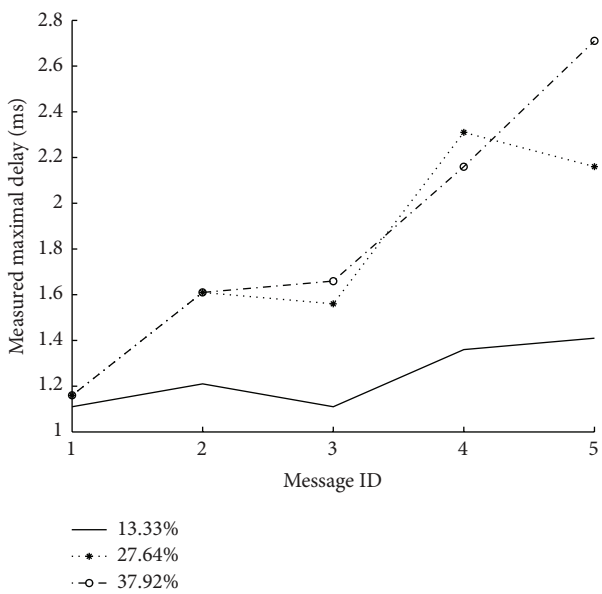

Figure 8: Maximal on-line delays of messages with a different ID at different load ratios.

the bus (no matter the priority of the message is high or low). The no-arbitration delay is independent of the message priorities. At a low load ratio, the probability for several messages triggering at a same phase position is extremely small. That is to say, priority has little influence on the maximal on-line delay value. While at a high load ratio, the probability for several messages triggering at the same phase position increases, which is to say, priority has a large influence on the maximal on-line delay value. Therefore, the priority affects the maximal on-line delay value a little at a low load ratio but a lot at a high load ratio. This result indicates that the probability of messages with a different ID getting triggered at the same time increases with the increase of load, which results in the message with a high priority getting arbitration and then reducing the on-line delay.

(5) In a few cases, the on-line delay of the message with a higher priority is higher than that with a lower priority at the same load ratio. This is because the transmission cycle is different for each message. Then the collision chance of some higher priority message is great, making the no-arbitration delay of higher priority message high.

(6) In a few cases, for the same message, the maximal on-line delay decreases with the increase of the load ratio. That is because the probability of collision is related to message's transmission interval and transmission phase. The increase of the load does not guarantee more collision chances of multiple messages at the same time. Consequently, the condition of low on-line delay at a high load ratio for a message could happen.

(7) The average on-line delay can reflect the trend of load ratio affecting on-line delay better than the maximal one.

5. Conclusion

In this paper, a Poisson process is adopted to simulate the reaching process of nonperiodic message in vehicle network system and a mathematical model is built to analyze the average on-line delay of nonperiodic real-time CAN message based on queuing theory. In addition, the reliability of the model is tested and verified with the measured data. For the messages with each priority at different load ratios, the values of average on-line delays which are computed by the mathematical model are very close to the measured values. That is to say, the theoretical model is quite reasonable. To the same message, the measured average and maximal on-line delays are both increasing with the increase of load and reaching speed, which means that it conforms to the law that on-line delay increases when the load increases. To the same load, the priority has little impact on the average on-line delay. This phenomenon indicates that the queue delay for nonperiodic message comes from no arbitration delay mostly, which is in line with the characteristic of small trigger probability in the same phase position for nonperiodic message. The priority affects the maximal on-line delay value a little at a low load ratio but a lot at a high load ratio. This result indicates that the probability of the messages with a different ID getting triggered at the same time increases with the increase of load ratio, which results in the message with a low priority losing arbitration and then increasing the on-line delay.

Conflict of Interests

The authors declare that there is no conflict of interests regarding the publication of this article.

Acknowledgments

This work is sponsored by the Aerospace Support Technology Fund (2013-HT-HGD09), the National Laboratory for Electric Vehicles Foundations (NELEV-2013-004), Shandong Province Outstanding Young Scientists Research Award Funds (BS2012NJ001), and Beijing Science and Technology Project (Z121100005612001).

References

[1] A. S. Tanenbaum and M. van Steen, *Distributed Systems: Principles and Paradigms*, Tsinghua University Press, Beijing, China, 2004.

[2] C. M. Krishna and K. G. Shin, *Real-Time Systems*, Tsinghua University Press, Beijing, China, 2001.

[3] C. M. Krishna and K. G. Shin, *Real-Time Systems*, Tsinghua University Press, Beijing, China, 2004.

[4] J. M. Jeon, D. W. Kim, H. S. Kim, Y. J. Cho, and B. H. Lee, "An analysis of network-based control system using CAN (controller area network) protocol," in *Proceedings of the IEEE International Conference on Robotics and Automation (ICRA '01)*, pp. 3577–3581, Seoul, Republic of Korea, May 2001.

[5] D. Heffernan and A. Bohannon, "Real-time design in a distributed control network application layer environment," *IEE Proceedings: Software*, vol. 148, no. 5, pp. 149–155, 2001.

[6] Y. Wang and Z.-Q. Long, "Analysis of real time ability of message transmission based on CAN systems," *Journal of Tianjin Polytechnic University*, vol. 24, no. 2, pp. 43–46, 2005.

[7] Y. Zhong, Z. Zhong, Q. Yu, and Z. Zeng, "A research on a general protocol for CAN bus in electric vehicles," *Automotive Engineering*, vol. 28, no. 5, pp. 423–438, 2006.

[8] Y. Li, J. Zhang, and Q. Lu, "An analysis on real-time capability of CAN networks for hybrid electric vehicle," *Automotive Engineering*, vol. 27, no. 1, pp. 16–19, 2005.

[9] J.-B. Wang and B.-G. Xu, "Analysis and online evaluation of CAN message real-time performance," *Control and Decision*, vol. 22, no. 4, pp. 448–452, 2007.

[10] Z. Shuai, H. Zhang, J. Wang, J. Li, and M. Ouyang, "Combined AFS and DYC control of four-wheel-independent-drive electric vehicles over CAN network with time-varying delays," *IEEE Transactions on Vehicular Technology*, 2013.

[11] H. Zhang, Y. Shi, and J. Wang, "Observer-based tracking controller design for networked predictive control systems with uncertain Markov delays," *International Journal of Control*, vol. 86, no. 10, pp. 1824–1836, 2013.

[12] H. Zhang, Y. Shi, and M. X. Liu, "H_∞ step tracking control for networked discrete-time nonlinear systems with integral and predictive actions," *IEEE Transactions on Industrial Informatics*, vol. 9, no. 1, pp. 337–345, 2013.

[13] H. Zhang, Y. Shi, and A. Saadat Mehr, "Robust static output feedback control and remote PID design for networked motor systems," *IEEE Transactions on Industrial Electronics*, vol. 58, no. 12, pp. 5396–5405, 2011.

[14] H. Zhang, Y. Shi, and A. Saadat Mehr, "Robust weighted H_∞ filtering for networked systems with intermittent measurements of multiple sensors," *International Journal of Adaptive Control and Signal Processing*, vol. 25, no. 4, pp. 313–330, 2011.

[15] K. Tindell, A. Burns, and A. J. Wellings, "Analysis of hard real-time communications," *Real-Time Systems*, vol. 9, no. 2, pp. 147–171, 1995.

[16] J. Li, Y. Zhu, and G. Tian, "Response time analysis for CAN and TTCAN communications," *Journal of Tsinghua University*, vol. 46, no. 2, pp. 261–265, 2006.

[17] K. M. Zuberi and K. G. Shin, "Non-preemptive scheduling of messages on controller area network for real-time control applications," in *Proceedings of the IEEE Real-Time Technology and Applications Symposium*, pp. 240–249, Chicago, Ill, USA, May 1995.

[18] K. Tindell, A. Burns, and A. J. Wellings, "Calculating controller area network (CAN) message response times," *Control Engineering Practice*, vol. 3, no. 8, pp. 1163–1169, 1995.

[19] J. Tian, Y. Huang, L. Wang, and G. Li, "Application of fixed priority schedule algorithm in CAN bus," *Computer Engineering*, vol. 32, no. 23, pp. 94–96, 2006.

[20] L. Xue, "The dynamic priority assigning mechanism and non-RT data exchange on CAN field-bus," *Computer Engineering and Applications*, vol. 12, pp. 33–35, 1999.

[21] S. Hasnaoui, O. Kallel, R. Kbaier, and S. Ben Ahmed, "An implementation of a proposed modification of CAN protocol on CAN fieldbus controller component for supporting a dynamic priority policy," in *Proceedings of the IEEE Industry Applications Conference*, pp. 23–31, Salt Lake City, Utah, USA, October 2003.

[22] J. Shi, P. Liu, and P. Zhang, "On the real-time performance of CAN data transfer and its applications," *Information and Control*, vol. 33, no. 3, pp. 342–346, 2004.

[23] H.-S. Choi and J.-M. Lee, "A dynamic precedence queue mechanism to assign efficient bandwidth in CAN networks," in *Proceedings of the IEEE/ASME International Conference on Advanced Intelligent Mechatronics (AIM '05)*, pp. 1354–1359, Monterey, Calif, USA, July 2005.

[24] W. Lu, L. Liu, and Y. Wang, "Study and performance analysis of TT- FPS based on CAN bus," *Engineering Science*, vol. 8, no. 5, pp. 45–48, 2006.

[25] L. Wang, X. Tang, and C. Zhou, "Research and application of in-vehicle CAN bus evaluation platform," *Chinese High Technology Letters*, vol. 15, no. 1, pp. 58–61, 2005.

[26] Z.-J. Wu, M.-Q. Hu, J.-Y. Zheng, and Y.-S. Du, "Study on the delay of CAN bus at the process level of substation," *Automation of Electric Power Systems*, vol. 29, no. 11, pp. 34–39, 2005.

[27] Z. Xie and J. Guo, "Priority allotment and time delay analysis of CAN bus line in underground mine," *Coal Science and Technology*, vol. 32, no. 11, pp. 32–34, 2004.

[28] J. Shi, *Real-time study of NCS*, University of Science and Technology of China, Hefei, China, 2003.

[29] J. Shi and P. Zhang, "The study of CAN networks application in real-time system," *Journal of University of Science and Technology of China*, vol. 35, no. 2, pp. 196–201, 2005.

[30] X. Wu and J. Yang, "Queuing network based model for bus buffer estimation," *Journal of Applied Sciences*, vol. 24, no. 1, pp. 45–49, 2006.

[31] L. Chen and Q. Zhu, *Stochastic Processes and Its Applications*, Higher Education Press, Beijing, China, 2003.

[32] Y. Tang and X. Tang, *Queuing Theory Basis and Applications*, University of Electronic Science and Technology of China Press, Chengdu, China, 2000.

Hindawi Publishing Corporation
Mathematical Problems in Engineering
Volume 2013, Article ID 940936, 11 pages
http://dx.doi.org/10.1155/2013/940936

Research Article

Peak Power Demand and Energy Consumption Reduction Strategies for Trains under Moving Block Signalling System

Qing Gu,[1] Tao Tang,[1] Fang Cao,[1] Hamid Reza Karimi,[2] and Yongduan Song[1,3]

[1] *State Key Laboratory of Rail Traffic Control and Safety, Beijing Jiaotong University, Beijing 100044, China*
[2] *Department of Engineering, Faculty of Engineering and Science, University of Agder, 4898 Grimstad, Norway*
[3] *School of Automation, Chongqing University, Chongqing 400044, China*

Correspondence should be addressed to Yongduan Song; ydsong@bjtu.edu.cn

Received 16 July 2013; Accepted 24 September 2013

Academic Editor: Xinjie Zhang

In the moving block signalling (MBS) system where the tracking target point of the following train is moving forward with its leading train, overload of the substations occurs when a dense queue of trains starts (or restarts) in very close distance interval. This is the peak power demand problem. Several methods have been attempted in the literature to deal with this problem through changing train's operation strategies. However, most existing approaches reduce the service quality. In this paper, two novel approaches—"Service Headway Braking" (SHB) and "Extending Stopping Distance Interval" (ESDI)—are proposed according to available and unavailable extra station dwell times, respectively. In these two methods, the restarting times of the trains are staggered and traction periods are reduced, which lead to the reduction of peak power demand and energy consumption. Energy efficient control switching points are seen as the decision parameters. Nonlinear programming method is used to model the process. Simulation results indicate that, compared with ARL, peak power demands are reduced by 40% and 20% by applying SHB and ESDI without any arrival time delay, respectively. At the same time, energy consumptions are also reduced by 77% and 50% by applying SHB and ESDI, respectively.

1. Introduction

Moving block signalling (MBS) [1] was proposed a few decades ago to reduce headway among successive trains in a track line. Theoretically, two successive trains are separated by a short distance, which is equivalent to the braking distance of the following train from its current speed, as well as a safety margin. This distance can be changed with the limit for the given operating speed and train characteristics, such as train length and braking rate. In MBS, when a leading train stops for a long time, the following trains will stop at the tail of the leading train. When this leading train restarts, the following trains will start almost simultaneously. It could cause synchronization of the peak demand of trains and increases the total peak power demand significantly, which is highly energy consumed and may lead to overload of the nearby substations. How to reduce peak power demand is called "Peak Demand Reduction" (PDR) problem.

This problem could be solved by improving the infrastructure or the train operation strategies. Energy storage system (ESS) is a very important component in modern railway power supply system. Advanced control and manufacturing technology improve the stability, capacity, and weight of ESS [2–5], which makes it suitable to be equipped in the substations or in trains. It could store the regenerative braking energy and assist the main power source during train's acceleration period. However, it is costly to equip ESS since the whole system needs a large number of them, for example, in urban railway system, nearly each of the stations or trains needs an ESS. At the same time, the cost of maintenance for ESS is also huge, especially when the frequency of acceleration\braking is high (which means the high frequency of charge and discharge and leads to life time reduction). Furthermore, it is inconvenient to be adopted by existing lines since the reconstruction project is costly and complex. Therefore, changing train operation strategies is a more convenient and economical way to reduce peak power demand.

There are two kinds of traditional PDR techniques based on changing operation strategies; one is called starting time

delay (STD), which introduces a starting time delay to each of the following trains. Under this category, there are two specific techniques called single STD and grade STD. The difference between them is the introduced starting time delay to each of the following trains, which are the same in single STD technique but different in grade STD (showing a deceasing trend). The other one is called acceleration rate limit (ARL), which means the acceleration of the following trains is limited to a certain extent (or different extents). Under this category, there are two specific techniques called single ARL and grade ARL. The difference between them is the limited acceleration rate to each of the following trains, which are the same in ARL technique but different in grade ARL (showing a deceasing trend). In addition to the above techniques, there is also a PDR technique called coordinated PDR. It is a combination of the STD and ARL techniques with feeding the regenerated power of decelerating trains to accelerating trains in the same queue, by coordinating the movement of queued trains.

Takeuchi and his colleagues discussed these techniques in [6–8]. Simulation results show that the graded ARL technique has the best performance in reducing peak power demand among single STD, grade STD, single ARL, grade ARL, and coordinated PDR techniques. In the traditional techniques, time delay is introduced and quality of service is degraded. Ho and Wong [9] use an expert system to help the operators for decision making, and it focuses on the balance between time delay and peak power demand. In [10], by braking and powering the trains simultaneously, Albrecht proposed a way to reduce the peak energy consumption and maximize the regenerative energy. Chen and his colleagues [11] proposed a method to minimize the peak energy consumption by adjusting the train dwell times at each station in MRT systems. Kim et al. [12] developed a mixed integer programming model to minimize the peak power energy demand that occurs when trains are running simultaneously, and the basic principle of the method is the same with STD. All of the methods proposed in [6–12] are implemented after the trains' restarting, by adjusting the timetable or driving strategy.

Although the existing techniques can reduce peak power demand at different degrees, they increase the travel time between the successive stations and decrease the service quality. And the energy consumption is increased since there are more traction periods.

In this paper, in order to reduce peak power demand and energy consumption, we first analyze the reasons of the formation of the peak power demand, and, then, two novel approaches are proposed based on the main reasons with considering the energy efficient driving strategies. One is for available extra station dwell time, named Service Headway Braking (SHB), and the other one is for unavailable extra station dwell time, named Extending Stopping Distance Interval (ESDI). Both of them are real-time adjustment methods and can be implemented before the leading train's restarting. Therefore, there is no need to change timetable. Considering energy saving driving strategy could be seen as a kind of driving mode switching process [13–16]; a nonlinear programming model is contributed and the simulation results show that, compared with the best traditional PDR techniques, both of these two methods could reduce the peak power demand and energy consumption without any arrival time delay increasing. And when the available extra station dwell time is the same as the unavailable extra station dwell time, SHB performs better than ESDI since more peak power and energy consumption could be reduced.

2. Tracking Dynamics and Peak Power Demand in MBS

2.1. Tracking Model in MBS. Under MBS, the tracking target point of the following train moves forward continuously as the leading train travels. The instantaneous distance $L_z(t)$ of two successive trains is calculated as

$$L_z(t) = S_{\text{leading}}(t) - S_{\text{following}}(t), \tag{1}$$

where $S_{\text{leading}}(t)$ is the position of the leading train's head and $S_{\text{following}}(t)$ is the position of the following train's head.

The distance between two successive trains must be larger than the safety margin at any moment even if the leading train comes to a sudden halt, so we have

$$L_z(t) \geq L_{\text{safe}} + L_t + \frac{V_{\text{following}}(t)^2}{2b}, \tag{2}$$

where L_t is the length of the train, L_{safe} is the length of safety margin, $V_{\text{following}}(t)$ is the instantaneous speed of the following train, and b is deceleration rate.

Based on (1) and (2), the relation between the leading train and following train should satisfy

$$S_{\text{leading}}(t) \geq L_{\text{safe}} + L_t + S_{\text{following}}(t) + \frac{V_{\text{following}}(t)^2}{2b}, \tag{3}$$

which implies that the instantaneous speed and position of the following train should satisfy

$$V_{\text{following}}(t) \leq \sqrt{2 \times b \times \left(S_{\text{leading}}(t) - S_{\text{following}}(t) - L_{\text{safe}} - L_t\right)}, \tag{4}$$

$$S_{\text{following}}(t) \leq S_{\text{leading}}(t) - L_{\text{safe}} - L_t - \frac{V_{\text{following}}(t)^2}{2b}. \tag{5}$$

2.2. Reasons of the Formation of Peak Power Demand. The reason of the formation of the peak power demand is the restarting of the dense queue, and the reasons for the formation of the dense queue are listed as follows.

(1) Features of moving block signaling system. (Two trains will start simultaneously if the distance interval between them is $L_{\text{safe}} + L_t$.)

(2) Extra dwell time in station.

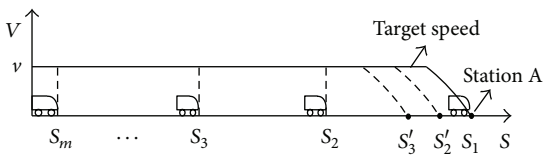

Figure 1: Formation of dense queue.

There are two kinds of extra station dwell time: one is available and the other is unavailable. In daily railway operation, there may be some exceptions, such as a passenger may be caught in the door of the train or a short-term surge in passenger flow (i.e., passenger flow increases sharply after a football match). In these circumstances, adjusting the whole timetable is not convenient, because the circumstances only exit in a short period. In this case, the operator will arrange the train to stop a little longer and this extra station dwell time is available. However, if a train is broken in a station and we are not sure how long we need to fix it, in this situation, the extra station dwell time is unavailable.

Based on the analysis above, it is known that peak power demand could be reduced by avoiding the dense queue. In order to achieve this goal, we first analyze the relation between extra station dwell time and the number of delayed trains.

2.3. Station Delay Propagation. Generally speaking, each train has a required dwell time at a station. If a train stops longer than the required dwell time, we call the extra time as *delay time*. In this section, we focus on the relation between the *delay time* and the number of delayed trains. In MBS, the *delay time* may impact the following trains and cause a dense queue. Figure 1 shows the formation of the dense queue.

As it is shown in Figure 1, there are m trains in the track. Train 1 stops at station A. The position of station A is S_1. For each train, the dwell time is T_{dwell}. The target speeds of the trains are the same and constant. According to the normal condition, each train arrives at station A and stops for T_{dwell} and then starts to run.

When train 1 starts, the positions of following trains are S_i, $i = 2, 3, \ldots, m$. The tracking time (the running time of the ith train running from S_i to S_{i-1}) between two successive trains is $\Delta t_{\text{tracking}}$; it is also the scheduled departure time interval. However, the following trains may become a dense queue if train A does not run immediately after T_{dwell}. Defining T_{delay} is the *delay time* of the leading train after T_{dwell} and n is the number of the delayed trains caused by T_{delay}. Based on (5), train i which is delayed should stop at point S_i'; in other words, S_i' is the stop position of train i in the dense queue:

$$S_i' = S_{i-1} - L_{\text{safe}} - L_t. \tag{6}$$

Let Δt_i be the running time in which train i arrived at S_i'. Based on (2), we have $S_1 - S_2' = L_t + L_{\text{safe}}$, $S_1 - S_3' = 2(L_t + L_{\text{safe}})$, $S_1 - S_4' = 3(L_t + L_{\text{safe}}), \ldots, S_1 - S_n' = (n-1)(L_t + L_{\text{safe}})$, and $\Delta t_2 = \Delta t_{\text{tracking}} - T_{\text{dwell}} - ((L_t + L_{\text{safe}})/v)$, $\Delta t_3 = 2 \times \Delta t_{\text{tracking}} - T_{\text{dwell}} - 2 \times ((L_t + L_{\text{safe}})/v), \ldots, \Delta t_n = (n-1) \times \Delta t_{\text{tracking}} - T_{\text{dwell}} - (n-1) \times ((L_t + L_{\text{safe}})/v)$.

Letting $T_{\text{delay}} \geq \Delta t_n$, we have

$$\begin{aligned} &T_{\text{delay}} \\ &\quad \geq (n-1)\,\Delta t_{\text{tracking}} - T_{\text{dwell}} - (n-1) \times \frac{L_t + L_{\text{safe}}}{v}; \end{aligned} \tag{7}$$

then the number of delayed trains should satisfy

$$n \leq \frac{T_{\text{delay}} + T_{\text{dwell}}}{\Delta t_{\text{tracking}} - \left(\left(L_t + L_{\text{safe}}\right)/v\right)} + 1. \tag{8}$$

2.4. Peak Power Demand Calculation. The power demand of the ith train P_i is calculated by

$$P_i = F_i(v) \times v_i, \tag{9}$$

where $F_i(v)$ is the traction force of the ith train and v_i is the speed of the ith train after restarting.

The peak power demand of the ith train $P_{i-\text{peak}}$ is calculated by

$$P_{i-\text{peak}} = \max\{P_i\}, \tag{10}$$

where $F_i(t)$ is the traction force of the ith train and $v_i(t)$ is the highest speed of the ith train after restarting.

The total peak power demand of all delayed following trains $P_{\text{total}}(t)$ is calculated by

$$P_{\text{total}} = \sum_{i=1}^{n} P_{i-\text{peak}}, \tag{11}$$

where n is the number of delayed following trains.

2.5. Energy Efficient Control Switching Points. Because there are more traction periods, traditional PRD techniques cause energy consumption increasing. Energy conservation is the research interest in many fields [17, 18], especially in rail transport [13–16]. Therefore, it would be better to reduce peak power demand and energy consumption at the same time. Train operation is a switching process; the operation modes are switching among traction, braking, and coasting (with no traction and braking force). There are lots of researches on switching system [19–21]. For optimal control of switching system, we could apply the methodologies proposed in [22, 23]. However, the computation complexity will be a big problem when we adopt the technologies above. In this paper, we first apply Pontryagin maximum principle to find the discrete optimal control modes and then treat the control switching speed as the decision parameters to obtain a reference trajectory.

For electric traction systems, the motion equations of train have the following forms:

$$\begin{aligned} \frac{dv(x)}{dx} &= \frac{u_f f(v) - u_b b(v) - r(v)}{v(x)}, \\ \frac{dt(x)}{dx} &= \frac{1}{v(x)}, \end{aligned} \tag{12}$$

where x is the position of the train, $v(x)$ is the speed of the train at position x, $t(x)$ is the time at which the train is located at the position x, u_f is the relative traction force, $f(v)$ is the specific maximum traction force per mass unit, u_b is the relative braking force, $b(v)$ is the specific maximum braking force per mass unit, and $r(v)$ is the specific basic resistance.

Note that the basic resistance $r(v)$ is usually given by Davis equation:

$$r(v) = a_1 v^2 + a_2 v + a_3, \tag{13}$$

where a_1, a_2, and a_3 are regression coefficients obtained by fitting test data to the Davis equation. a_3 accounts for air resistance. a_1, a_2 account for mass and mechanical resistance. And $r(v)$ has following characteristics:

$$r'(v) > 0, \qquad r''(v) \geq 0. \tag{14}$$

The energy efficient operation problem is modeled as follows:

$$\begin{aligned} &\min J = \int_0^X u_f f(v)\, dx \\ &\text{s.t. } 0 \leq u_f \leq 1,\ 0 \leq u_b \leq 1, \\ &\qquad v \leq V(x), \end{aligned} \tag{15}$$

where J is the specific mechanical work of the traction force, $V(x)$ is the speed limit. The boundary conditions are

$$\begin{aligned} x(0) &= x_0, \qquad x(T) = x_T, \\ v(0) &= v_0, \qquad v(T) = v_T. \end{aligned} \tag{16}$$

By applying Pontryagin maximum principle to solve the problem as specified in (15) with constraints (16), the optimal solution should maximize the Hamiltonian function:

$$\begin{aligned} H = {} & \frac{p_1}{v}\left(u_f f(v) - u_b b(v) - r(v)\right) \\ & + \frac{p_2}{v} - u_f f(v), \end{aligned} \tag{17}$$

where p_1 should satisfy the differential equation:

$$\frac{dp_1}{dx} = -\frac{\partial H}{\partial v}. \tag{18}$$

It is easy to prove that the Hamiltonian reaches the maximum with respect to u_f and u_b. And there are five energy efficient control modes as follows.

(i) Full power ($u_f = 1, u_b = 0$) if $(p_1/v) < 0$.

(ii) Partial power ($u_f \in (0,1), u_b = 0$) if $(p_1/v) = 0$.

(iii) No power and no braking ($u_f = 0, u_b = 0$) if $0 < (p_1/v) < 1$.

(iv) Partial braking ($u_f = 0, u_b \in (0,1)$) if $(p_1/v) = 1$.

(v) Full braking ($u_f = 0, u_b = 1$) if $(p_1/v) > 1$.

They could be seen as four possible driving phases, which are

(i) acceleration with full power;

(ii) speed holding with partial power or braking;

(iii) coasting with no power and braking;

(iv) braking with full braking.

Based on the above analysis, it is seen that the energy saving strategy relies on these optimal controls. Train energy saving driving process is the process of switching from an optimal control to another, and the switching sequence is acceleration, speed holding, coasting, and braking.

Then, the optimal control switching speeds and running phases duration are treated as decision parameters. The energy and power can be expressed by these decision parameters. The power demand is used as the objective function of a nonlinear programming problem. The constraints include running time and distance. In actual train operation, maximum power and braking cannot be applied by considering the ride comfort. Instead, a service acceleration/braking rate is applied. Therefore, by solving the nonlinear programming model, a reference trajectory leading to less power and energy consumption can be obtained.

3. Peak Demand Reduction Techniques

3.1. Service Headway Braking Strategy. Based on the analysis above, we know the restarting of the dense queue in a small area leads to peak power demand and both of the two traditional PDR techniques are carried out after the formation of the dense queue. In this section, we propose a novel operation strategy to reduce the peak power by avoiding the formation of a dense queue based on the available extra station dwell time. In the following parts, we use *reaccelerate* to indicate train accelerates from a nonzero initial speed and restart to indicate train starts from 0 m/s.

3.1.1. SHB Strategy Analysis. Figure 3 shows the new operation strategy; the leading train stops at station A and the position is S_1. The black thick solid line is calculated by (2), and we call it braking curve in this paper. Under normal circumstance, the following train should brake when it touches the brake curve. However, if the leading train starts to run when the following train touches braking curve, the following train will not brake but reaccelerate. Therefore, in the new strategy, if the following train touches the braking curve when the leading train starts to run, and the speed at this moment is not 0 m/s, the moment in which each train reaches the peak power demand can be staggered. Meanwhile, since the following trains brake at first, they will not stop too to cause a dense queue. By these two reasons, the total peak power demand can be reduced. Based on the analysis above and considered the energy saving operation process, a new operation strategy is proposed as follows.

As shown in Figure 2(a), the target speed of the trains in the track is v_1; the leading train has an extra dwell time, which is T_{delay}. If T_{delay} is long enough to cause a dense queue with n trains, then, after T_{dwell}, let train i ($i = 2, 3, \ldots, n$) brake with service braking deceleration b to v_{i2} (the position at this time

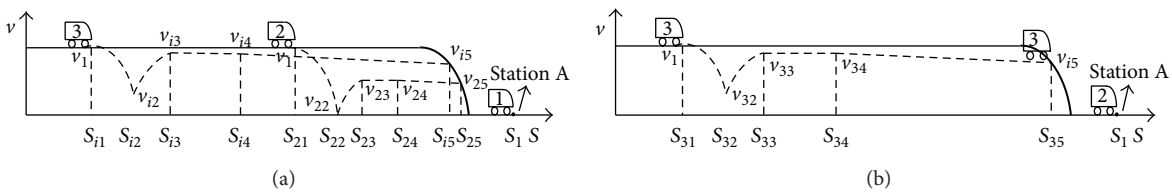

Figure 2: (a) Following trains' SHB driving curves after train 1 stops for T_{dwell}. (b) The position of train 3 when train 2 starts to move.

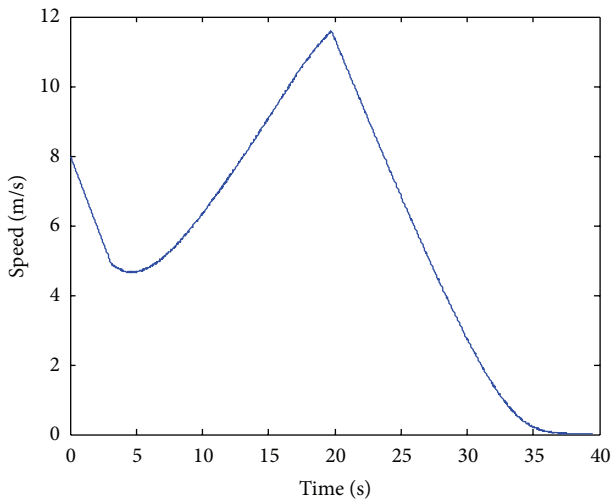

Figure 3: V-T profile of the following train starts form the braking profile.

is S_{i2}); if $v_{i2} = 0$, then it stops at S_{i2} for Δt_{i2}, then accelerates to v_{i3} with service acceleration a (the position at this time is S_{i3}), and then runs with v_{i4}, ($v_{i4} = v_{i3}$) for Δt_{i4} to S_{i4}; after that it reduces traction force and keeps the train moving with a constant deceleration b' to v_{i5} (the position at this time is S_{i5}, v_{i5} and S_{i5} are a pair of points in the braking curve). At this time, train *i-1* restarts, therefore, train *i*starts to track train *i-1* according to the moving block tracking distance interval until arrives at station A.

Figure 2(b) shows the position of train 3 when train 2 starts to move from station A. It is observed that train 3 will reaccelerate from the braking curve (S_{35}) to arrive at station A (S_1); we use T_{tt} to represent this time period and all of the delayed following trains need this time period to arrive at station A after their leading train's restarting. In this circumstance, for train 2, the running time between S_{21} and S_{25} is T_{delay}; for train 3, the running time between S_{31} and S_{35} is $T_{\text{delay}} + T_{\text{dwell}} + T_{tt}$; ...; for train i, the running time between S_{i1} and S_{i5} is $T_{\text{delay}} + (i-2) \times (T_{\text{dwell}} + T_{tt})$.

In order to obtain T_{tt}, a simulation is done as follows: $L_t = 140\,(\text{m})$, $L_{\text{safe}} = 50\,(\text{m})$. The leading train stops at station A where the position is 400 (m): $S_{\text{leading}}(0) = 400\,(\text{m})$. Let the following train start from the point in braking curve; the speed and position of the following train is calculated by (4) or (5); the results are shown in Table 1.

From Table 1, we can see that the arrival times of following trains seem constant when they reaccelerate from the braking curve. In order to show the trend of this tracing process, Figure 3 gives the V-T profile when the reaccelerating speed and position are 8 m/s and 178 (m).

Table 1: Running time of following train.

$S_{\text{leading}}(0)$ (m)	$V_{\text{following}}(0)$ (m/s)	$S_{\text{following}}(0)$ (m)	Running time of the following train arrives at station A (s)
400	16	82	40.26
400	12	138	39.82
400	8	178	39.5
400	4	202	39.42
400	0	210	39.38

Based on the analysis above, the whole strategy is consisting of 6 steps, braking, waiting, traction, speed holding, coasting, and finally tracking the front train. The indexes of them are $1, 2, \ldots, 6$.

It is worth noting that this operation strategy is energy efficient, because the duration of some steps may be 0 based on an appropriate target function. For example, if we get $v_{i2} = v_{i3} = v_{i4} > 0$ based on a certain target function, there will be no traction process before reaccelerating and the train will brake and coast until reaccelerating.

In this new strategy, all the following trains brake at first; therefore, they will not stop too to cause a dense queue; at the same time, the other trains are coasting when one train reaccelerates, so the reaccelerating times of the following trains are staggered. Therefore the peak power demand is avoided.

3.1.2. Model of SHB. In this section, we formulate the mathematical model of the operation process. For train i, define t_{ij} ($j = 1, 2, \ldots, 5$) as the starting time of each step; ΔS_{ij} ($j = 1, 2, \ldots, 5$) and ΔT_{ij} ($j = 1, 2, \ldots, 5$) are the running distance and time of each step, respectively. In order to stagger the reaccelerating times of the following trains, we should take an appropriate value to v_{i5}. Because if $v_{i5} = 0$, the successive two trains will reaccelerate simultaneously again and peak power demand cannot be reduced. On the contrary, if v_{i5} is close to v_1, the effect of energy saving will be reduced. Therefore, we recommend $v_1 > v_{i5} \geq v_1/2$. At the same time, for train i, the total running time and distance should satisfy the following equations:

$$\sum_{j=1}^{5} \Delta T_{ij} = T_{\text{delay}} + (i-2) \times \left(T_{\text{dwell}} + T_{tt}\right), \tag{19}$$

$$\sum_{j=1}^{5} \Delta S_{ij} = S_1 - S_{i1} - L_{\text{safe}} - L_t. \tag{20}$$

Since the traction phase is highly energy consumed and power supported, we minimize the peak power. Therefore, based on the analysis above, the problem could be seen as a constrained nonlinear programming problem as follows:

$$\min f = \sum_{i=1}^{n} p_i\left(v_{i3}\right) \tag{21}$$

$$\begin{aligned}
\text{s.t. } & v_{i2} - v_{i3} \le 0, \\
& v_{i5} - v_{i4} \le 0, \\
& -v_{ij}, -\Delta T_{ij} \le 0, \\
& \frac{v_1}{2} \le v_{i5} < v_1, \\
& \sum_{j=1}^{5} \Delta T_{ij} = T_{\text{delay}} + (i-2) \times \left(T_{\text{dwell}} + T_{tt}\right), \\
& \sum_{j=1}^{5} \Delta S_{ij} = S_1 - S_{i1} - L_{\text{safe}} - L_t,
\end{aligned} \tag{22}$$

where

$$\begin{aligned}
\sum_{j=1}^{5} \Delta T_{ij} &= \frac{v_{i2} - v_1}{b} + \Delta T_{i2} + \frac{v_{i3} - v_{i2}}{a} \\
&\quad + \Delta T_{i4} + \frac{v_{i5} - v_{i4}}{b'}, \\
\sum_{j=1}^{5} \Delta S_{ij} + L_b &= \frac{v_{i2}^2 - v_1^2}{2 \times b} + \frac{v_{i3}^2 - v_{i2}^2}{2 \times a} \\
&\quad + \Delta T_{i4} \times v_{i4} + \frac{v_{i5}^2 - v_{i4}^2}{2 \times b'} + \frac{v_{i5}^2}{2 \times |b|},
\end{aligned} \tag{23}$$

where α, β are penalty factors, $\alpha, \beta > 0$; a, b are service acceleration and deceleration of the train; b' is a very small deceleration; i is the index of the delayed following trains $i = 2, \ldots, n$; j is the index of operation steps, $j = 1, 2, \ldots, 6$; v_{ij} is the starting speed of each step for train i; S_1 is the position of the leading train (the leading train); S_{i1} is the position of the ith following train; ΔS_{ij} is the running distance of the jth step for train i; ΔT_{ij} is the duration of of the jth step for train i; L_{ib} is the braking distance if train i brakes from v_{i5}; T_{dwell} is the scheduled station dwell time; T_{tt} is the tracking time in which train i tracks train *i-1* from S_{i5} to S_1.

During the running process of successive following trains, the time interval among them is $T_{\text{dwell}}+T_{tt}$. When train i starts to move from S_{i2}, the distance between train i and train *i-1* is shortest; at this time, the speed of train i is larger than $v_1/2$ and the distance interval between them is at least $(T_{\text{dwell}} + T_{tt}) \times v_1/2$; according to the general condition in mass transit system, $T_{\text{dwell}} = 10\,\text{s}$, $L_{\text{safe}} = 50\,\text{m}$, $L_t = 140\,\text{m}$, $\text{MAX}(v_1) = 20\,\text{m/s}$, $b = 1\,\text{m/s}^2$, it is easy to know that $(T_{\text{dwell}}+T_{tt})\times v_1/2 > L_{\text{safe}}+L_t+(v_1/2)^2/2b$; this is satisfied by (3). Therefore, it is no need to consider the distance constraint shown in (3) between successive following trains in (22) again.

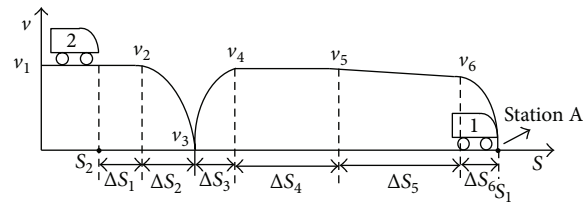

Figure 4: Operation strategy of ESDI.

3.2. Extending Stopping Distance Interval Strategy. The previous section shows SHB strategy; it could reduce the peak power demand if the *delay time* is available. In this section, we will show a strategy which could reduce the peak power demand by decreasing the density of the dense queue. By adopting this strategy, the peak power demand could be reduced if the extra station dwell time is unavailable. Because, in the same T_{delay}, the longer the stopping distance interval of the following trains, the lower densities of the stopped train queue. Therefore, when they restart, the peak power demands are reduced.

3.2.1. ESDI Strategy Analysis. According to the analysis in Section 3.1.1, it can be seen that no matter the train reaccelerates from which point in the braking curve, T_{tt} is nearly the same. Based on T_{tt}, we can extend the stopping distance interval of the following trains to reduce the density of the dense queue. The new operation strategy is proposed as follows.

Figure 4 shows the new operation strategy. The operation process of the following trains when the leading train dose does not move after T_{dwell} could be divided into 6 steps, speed holding, braking, traction, speed holding, coasting, and braking to stop. Define t_i $(i = 1, 2 \ldots, 6)$ as the starting time of each step, $v_1 = v_2$, and $v_3 = 0$, $v_4 = v_5$; define the running time and distance of each step as ΔT_i and ΔS_i $(i = 1, 2, \ldots, 6)$, respectively. When the leading train has an extra dwell time, each of following trains will run according to these 6 steps. Define *MI* as the traveling distance during T_{tt} (*MI* is also stopping distance interval) for the following trains. During this process, the running time of steps 3 to 6 should be equal to T_{tt}.

In this new strategy, the stopping distance interval of the following trains is increased, so the density of the queue is decreased, and the peak power demand is reduced.

3.2.2. Model of ESDI. In this section, we formulate the mathematic model of the operation process. According to the last section, it is known that we know that the stopping intervals of the trains are extended in the new operation strategy; therefore, peak power demand can be reduced when the trains restart. Define *MI* as the stopping interval of two successive trains; we have

$$\begin{aligned}
MI &= \sum_{i=3}^{6} \Delta S_i \\
&= \frac{v_4^2}{2 \times a} + v_4 \times \Delta T_4 + \frac{\left(v_6^2 - v_5^2\right)}{2 \times b'} + \frac{v_6^2}{2 \times |b|}.
\end{aligned} \tag{24}$$

In order to grantee the feasibility of the new operation strategy, if leading train stops at the station, after T_{dwell}, the distance between the first following and the leading train should satisfy the following equation:

$$MI \leq S_{\text{tracking}} - T_{\text{dwell}} \times v_1, \tag{25}$$

where S_{tracking} is the second train's position when the leading train stops at station, and it is calculated by

$$S_{\text{tracking}} = \left(T_{\text{traking}} - \frac{v_1}{|b|}\right) \times v_1 + \frac{v_1^2}{2 \times |b|}. \tag{26}$$

Since the traction phase is highly energy consumed and power supported, we minimize the peak power. Based on the analysis above, we use nonlinear programming to model the problem as follows:

$$\begin{aligned} &\min f = p(v_4), \\ &\text{s.t. } v_3 - v_2 \leq 0, \\ &\quad v_6 - v_5 \leq 0, \\ &\quad MI \leq S_{\text{tracking}} - T_{\text{dwell}} \times v_1, \\ &\quad (T_{\text{dwell}} + \Delta T_1) \times v_1 + \frac{v_1^2}{2 \times |b|} + \sum_{i=3}^{6} \Delta S_i = S_2 - S_1, \\ &\quad \sum_{i=3}^{6} \Delta T_i - T_{tt} = 0, \end{aligned} \tag{27}$$

where α, β are penalty factors, $\alpha > 0$; a, b are service acceleration and deceleration of the train; v_i is the starting speed of step i; S_1 is the position of the leading train (the leading train); S_2 is the position of the following train; S_{tracking} is the second train's position when the leading train stops at station; T_{dwell} is the scheduled station dwell time.

4. Simulation and Discussion

In this section, a simulation is used to test and verify the new strategies. The length of train (L_t) is 140 m, safety margin (L_{safe}) is 50 m, service tracking headway is 120 seconds, dwell time (T_{dwell}) is 10 seconds, target speed (v_1) is 16 m/s, service acceleration rate (a) is 1 m/s^2, service braking deceleration rate (b) is 1 m/s^2, and position of station A is 3710 m (S_1 = 3710).

In order to choose b', we analyze the practical data of coasting phase from Dalian Fast Track [24]. Because the speed in coasting phase declines very slowly, so the profile of speed time could be seen as a straight line and the slope of the line is the deceleration rate of coasting phase. We use least-square procedure to fit the speed-time date sectional and the results are shown in Table 2.

From Table 2, it is clear that the higher the coasting starting speed, the greater the deceleration. In order to supply a small traction force to keep the train moving in a constant deceleration b', we choose $b' = 0.01$ m/s^2 as appropriate.

Table 2: Measured value of coasting data.

Speed range (km/h)	Slop (m/s^2)	Average error (m)
37–31	−0.0147	0.0227
41-40	−0.0125	0.0361
43-42	−0.0147	0.0364
54–48	−0.0213	0.0236
60-59	−0.0237	0.0296
62-61	−0.0210	0.0301
79–75	−0.0315	0.0237

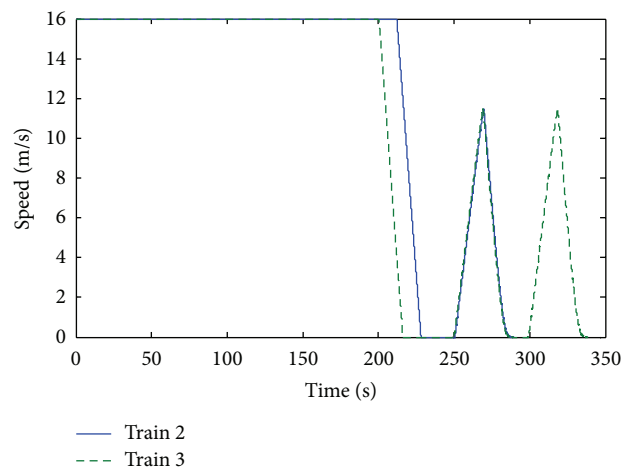

Figure 5: V-T profile without PDR technique.

4.1. Service Headway Braking Strategy. If T_{delay} is 250 seconds, according to (8), 3 trains will be delayed (including the leading train). Because we choose $v_{\text{ref}} = 8$, therefore, $T_{tt} = 38.5$ is selected from Table 1. Based on (21)-(22), we have

$$\begin{aligned} &v_{22} = 0, \quad v_{23} = 9.57, \quad v_{25} = 8, \quad \Delta t_{24} = 0, \\ &v_{32} = 13.043, \quad v_{33} = 13.043, \\ &v_{35} = 10.08, \quad \Delta t_{34} = 0. \end{aligned} \tag{28}$$

Figures 9 and 10 and Table 3 show the simulation results.

In order to show the peak power demand without any PDR technique and compare it with the performance of traditional PDR technique, Figures 5–8 are given. According to Figures 5 and 6, we can see that the two following trains are starting simultaneously from 250 s; the peak power demand is 25.1 kw/t. The arrival times of train 2 and train 3 are 289.38 s and 338.76 s, respectively.

Figures 7 and 8 show the performance of graded ARL technique. The acceleration of train 2 and train 3 is 0.5 m/s^2 and 0.3 m/s^2. By applying different acceleration, the peak power demand is reduced to 22.07 kw/t. However, the time delay is increased. The arrival times of train 2 and train 3 are 297.78 s and 400.36 s, respectively. That means the arrival times of the two trains are 8.4 s and 61.6 s later than their times without PDR techniques, respectively.

The performance of applying SHB technique is shown from Figures 9 and 10. As can be seen, train 2 has a waiting

Table 3: Comparison of the graded ARL and SHB techniques.

	Arrival time of train 2 (s)	Arrival time of train 3 (s)	Peak power demand (kw/t)	Energy consumption (kw·h)	Stopping time before arrival (s)	
					Train 2	Train 3
Non-PDR	289.38	338.76	25.1	15.9137	130	43.75
Graded ARL	297.78	400.36	22.07	46.3402	130	43.75
SHB	289.5	339.16	13.42	10.5016	65.66	0

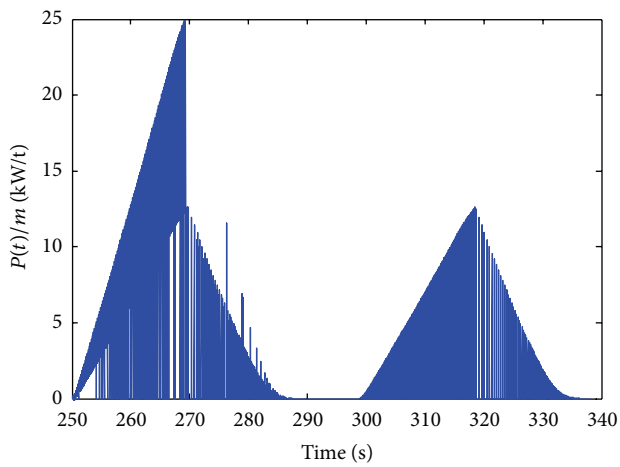

Figure 6: Peak power demand profile without PDR technique.

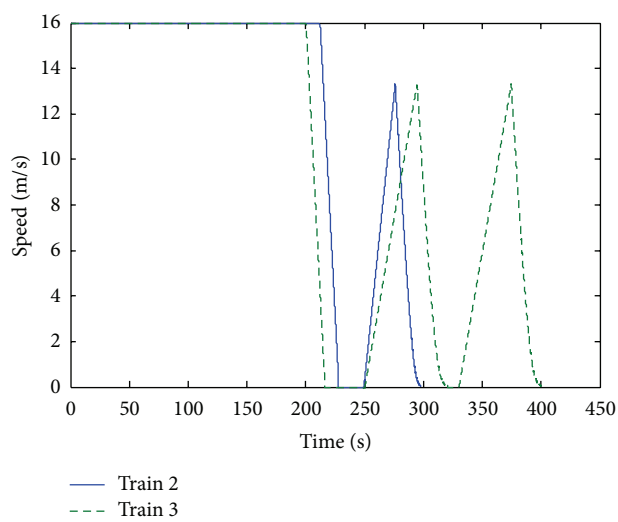

Figure 7: V-T profile with graded ARL technique.

time 65.66 s at the position of 2048 m and then restarting at 81.66 s. At this time, train 3 is coasting; therefore, there is no peak power in this time. The two trains restart with different speeds in different time points, which can be seen form the red and blue circles in Figure 9. That means the reaccelerating times of the two trains are staggered. Furthermore, the two trains reaccelerate with nonzero initial speeds, which means the reacceleration periods are reduced. Therefore, the peak power demand is reduced to 13.42 kw/t. According to Figure 9, the two trains have no speed holding phases, and

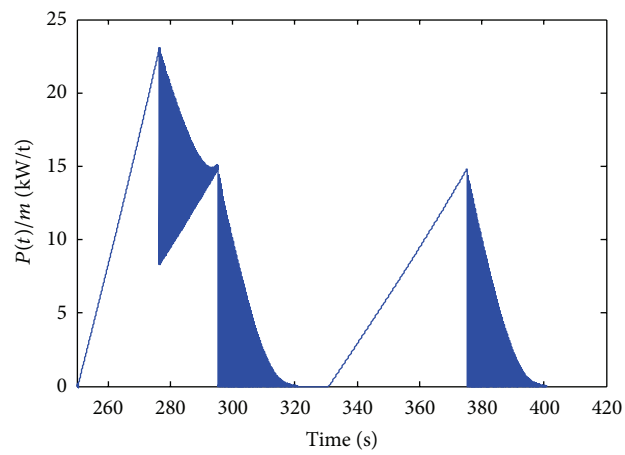

Figure 8: Peak power demand profile with graded ARL technique.

train 3 has no traction phases before step 6. Therefore, the energy consumption is reduced. The arrival times of train 2 and train 3 are 289.5 s and 339.16 s, respectively.

Table 3 shows the result data of the simulation. Graded ARL technique can reduce the peak power demand; however, the arrival times of the two trains are delayed significantly. SHB technique has great advantages. According to Table 3, the delay times of the two trains are very short; at the same time, the energy consumption is also reduced to a low level, even less than value without any PDR technique. In addition, the stopping times before arrival of the two trains are reduced to 65.66 and 0, respectively.

4.2. Extending Stopping Distance Interval Strategy. According to Section 3.1.2, we choose $T_{tt} = 40$ s; when the leading train stops at the station and dose not start to run after T_{dwell}, based on (27), we have

$$v_4 = v_5 = 16, \qquad v_6 = 15.92, \qquad \Delta T_4 = 0. \tag{29}$$

If the extra dwell time is 250 seconds, in graded ARL, 3 trains will be delayed (including the leading train) according to (8). And the length of the dense queue is 380 m. The performance of graded ARL technique can be seen in Figure 5.

In ESDI, based on (24) the stopping distance interval for the following trains (MI) is 383.68 m. Based on (8), 2 trains (besides the leading train) will be delayed. However, the length of the dense queue is 767.36 m. In the same time period and distance area with graded ARL technique, we calculate the peak power demand, and the performance is shown in Figures 11 and 12.

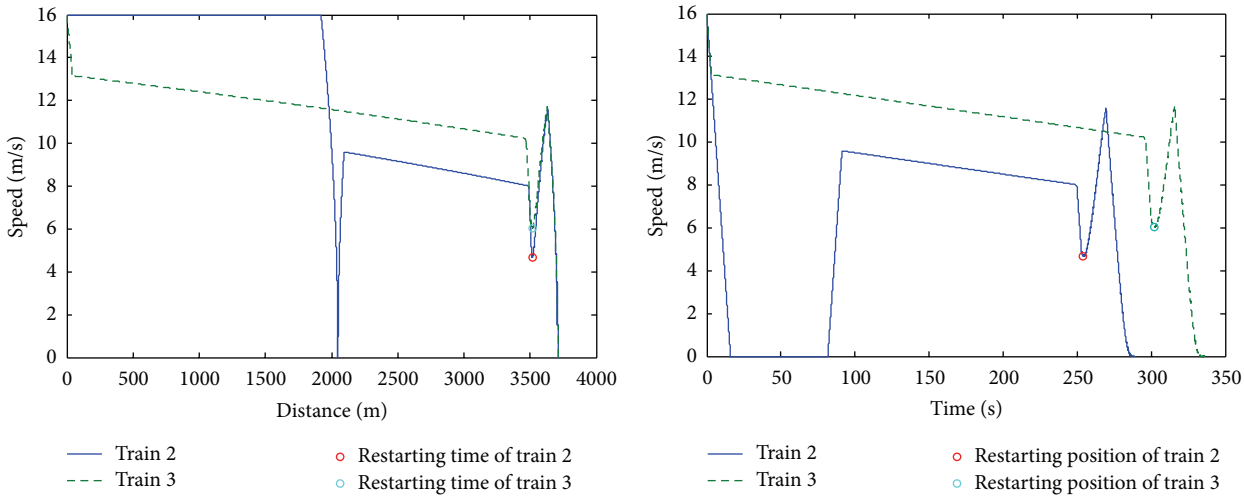

Figure 9: V-S and V-T profiles with SHB technique.

Table 4: Comparison the PDR techniques.

	Arrival time of train 2 (s)	Arrival time of train 3 (s)	Peak power demand (kw/t)	Energy consumption (kw·h)	Stopping time before arrival (s)	
					Train 2	Train 3
Non-PDR	289.38	338.76	25.1	15.9137	130	43.75
Graded ARL	297.78	400.36	22.07	46.3402	130	43.75
SHB	289.5	339.16	13.42	10.5016	65.66	0
ESDI	290	340	18.18	22.86	153.98	57.96

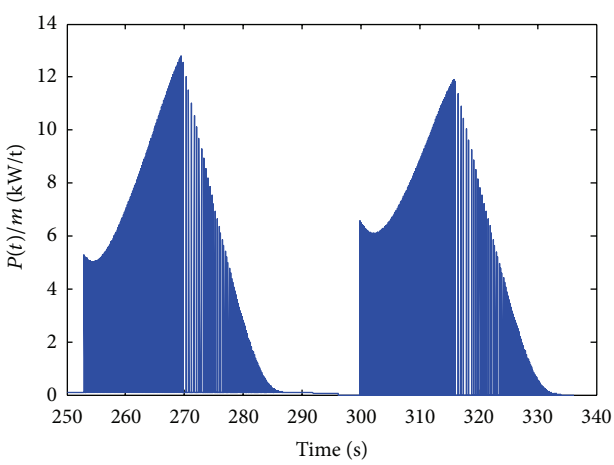

Figure 10: Peak power demand profile with SHB technique.

As we see, using ESDI technique, the arrival times of the following two trains are almost the same as their times with no PDR technique. Without any PDR technique, the stopping distance interval is 190 m, so the dense queue caused by the extra station time (250 s) is 380 m. The peak power demand after 250 s within 380 m is 25.1 kw/t. In ESDI strategy, stopping distance interval is extended to 383.86 m, which is two times longer than the distance in ARL. That is to say, the restarting position of train 2 belongs to the nearby substation. Thus the power demands by train 2 and train 3 are not afforded by the same substation. Therefore, the peak power demand after 250 s within 380 m is reduced to 18.18 kw/t. Compared with non-PDR technique, the peak power demand is reduced by 18%. In ESDI, train 2 has a stopping time 153.98 s at the position of 2944.6 m. Train 3 has a stopping time 57.96 s at the position of 3328.32 m. Compared with non-PDR technique, the stopping time before arrival is increased by 18%.

According to above analysis, we can see that the new strategy reduces peak power demand by sacrificing the stopping time before arrival. However, the advantages of ESDI are still obvious, because it is more efficient on energy saving; it can reduce energy consumption by 50% compared with graded ARL technique.

From Table 4, it is seen that, although the arrival times of trains when applying SHB and the arrival times of trains when applying ESDI are the same, SHB reduces more peak power demand and energy consumption, which means SHB performs than ESDI when the available and unavailable extra station dwell times are the same.

5. Conclusion

Peak power demand reduction strategies are discussed in this paper. The reasons of peak power demand problem are analyzed deeply and two main reasons are given.

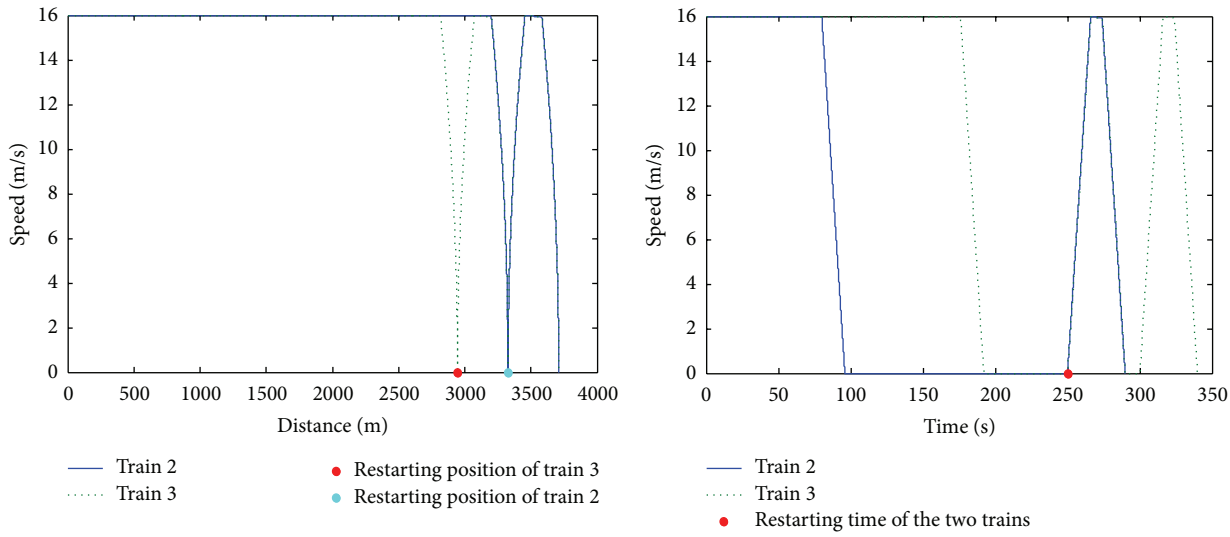

Figure 11: V-S and V-T profiles with ESDI technique.

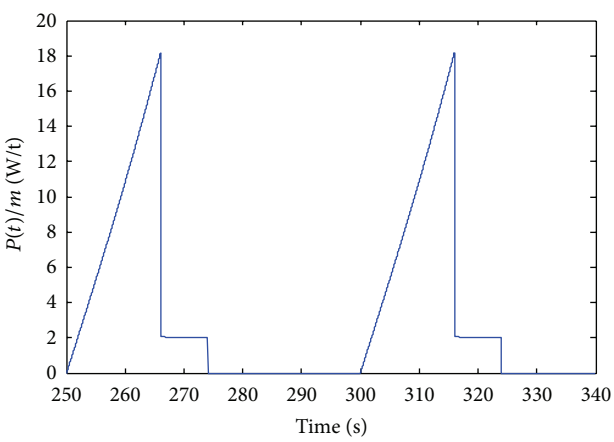

Figure 12: Peak power demand profile with ESDI technique.

Based on the reasons and according to different situations, two new peak demand reduction techniques are proposed. One is Service Headway Braking (SHB) strategy, which is used to reduce peak power demand when the extra station dwell time is available. The other is Extending Stopping Distance Interval (ESDI) strategy, which is used to reduce peak power demand when the extra station dwell time is unavailable. Nonlinear programming approach is introduced to model the operation strategy. The simulation results show that, compared with the best traditional PDR techniques, SHB can reduce 40% of peak power demand and 77% of energy consumption without increasing the arrival time delay. ESDI can reduce 20% of peak power demand and 50% of energy consumption without increasing the arrival time delay. Therefore, SHB has a better performance than ESDI when the available and unavailable extra station dwell times are the same. The basic principle of the two strategies is to avoid the formation of the dense queue. Therefore, both of the two strategies are implemented before the formulation of the dense queue.

Conflict of Interests

The authors declare that there is no conflict of interests.

Acknowledgments

This work was supported by the National High Technology Research and Development Program of China (no. 2011AA110502) and the National Natural Science Foundation of China (no. 61134001).

References

[1] L. V. Pearson, *Moving block railway signalling [Ph.D. thesis]*, Loughborough University of Technology, Loughborough, UK, 1973.

[2] T. Chaiyatham and I. Ngamroo, "Optimal fuzzy gain scheduling of PID controller of superconducting magnetic energy storage for power system stabilization," *International Journal of Innovative Computing, Information and Control*, vol. 9, no. 2, pp. 651–666, 2013.

[3] D. Iannuzzi, E. Pagano, and P. Tricoli, "The use of energy storage systems for supporting the voltage needs of urban and suburban railway contact lines," *Energies*, vol. 6, pp. 1802–1820, 2013.

[4] H. Lee, S. Jung, Y. Cho, H. Jung, H. Kim, and G. Jang, "Peak power reduction and energy efficiency improvement with the superconducting flywheel energy storage in electric railway system," *Physica C*, vol. 494, pp. 246–249, 2013.

[5] Y. Arai, H. Seino, K. Yoshizawa, and K. Nagashima, "Development of superconducting magnetic bearing with superconducting coil and bulk superconductor for flywheel energy storage system," *Physica C*, vol. 494, pp. 250–254, 2013.

[6] H. Takeuchi, C. J. Goodman, and S. Sone, "Peak demand reduction techniques when starting under Moving Block Signalling,"

in *Proceedings of the International Conference on Developments in Mass Transit Systems*, pp. 280–285, April 1998.

[7] H. Takeuchi and C. J. Goodman, "Simulation study of peak demand reduction strategies when starting under moving block signalling," in *Proceedings of the 5th International Conference on Computer Aided Design, Manufacture and Operation in the Railway and other Advanced Mass Transit Systems*, pp. 187–196, August 1996.

[8] H. Takeuchi, C. J. Goodman, and S. Sone, "Moving block signalling dynamics: performance measures and re-starting queued electric trains," *IEE Proceedings*, vol. 150, no. 4, pp. 483–492, 2003.

[9] T. K. Ho and K. K. Wong, "Peak power demand reduction under moving block signalling using an expert system," *IEE Proceedings*, vol. 150, no. 4, pp. 471–482, 2003.

[10] T. Albrecht, "Reducing power peaks and energy consumption in rail transit systems by simultaneous train running time control," *Advances in Transport*, vol. 15, pp. 885–894, 2004.

[11] J.-F. Chen, R.-L. Lin, and Y.-C. Liu, "Optimization of an MRT train schedule: reducing maximum traction power by using genetic algorithms," *IEEE Transactions on Power Systems*, vol. 20, no. 3, pp. 1366–1372, 2005.

[12] K. M. Kim, S.-M. Oh, and M. Han, "A mathematical approach for reducing the maximum traction energy: the case of Korean MRT trains," in *Proceedings of the International MultiConference of Engineers and Computer Scientists (IMECS '10)*, pp. 2169–2173, March 2010.

[13] K. K. Wong and T. K. Ho, "Dynamic coast control of train movement with genetic algorithm," *International Journal of Systems Science*, vol. 35, no. 13-14, pp. 835–846, 2004.

[14] P. G. Howlett, P. J. Pudney, and X. Vu, "Local energy minimization in optimal train control," *Automatica*, vol. 45, no. 11, pp. 2692–2698, 2009.

[15] R. Liu and I. M. Golovitcher, "Energy-efficient operation of rail vehicles," *Transportation Research A*, vol. 37, no. 10, pp. 917–932, 2003.

[16] E. Khmelnitsky, "On an optimal control problem of train operation," *IEEE Transactions on Automatic Control*, vol. 45, no. 7, pp. 1257–1266, 2000.

[17] Y. Zhang, S. F. Jin, and W. Y. Yue, "An enhanced energy saving strategy for an active DRX in LTE wireless networks," *International Journal of Innovative Computing, Information and Control*, vol. 9, no. 11, pp. 4373–4387, 2013.

[18] S. Ali and D. Kim, "Energy conservation and comfort management in building environment," *International Journal of Innovative Computing, Information and Control*, vol. 9, no. 6, pp. 2229–2244, 2013.

[19] Z. Wu, M. Cui, P. Shi, and H. Karimi, "Stability of stochastic nonlinear systems with controlled state-dependent switching," *IEEE Transactions on Automatic Control*, vol. 58, no. 8, pp. 1904–1918, 2013.

[20] R. Wang, P. Shi, Z. Wu, and Y. Sun, "Stabilization of switched delay systems with polytopic uncertainties under asynchronous switching," *Journal of the Franklin Institute*, vol. 350, no. 8, pp. 2028–2043, 2013.

[21] R. Wang, Z.-G. Wu, and P. Shi, "Dynamic output feedback control for a class of switched delay systems under asynchronous switching," *Information Sciences*, vol. 225, pp. 72–80, 2013.

[22] X. Xu and P. J. Antsaklis, "Optimal control of switched systems based on parameterization of the switching instants," *IEEE Transactions on Automatic Control*, vol. 49, no. 1, pp. 2–16, 2004.

[23] S. C. Bengea and R. A. DeCarlo, "Optimal control of switching systems," *Automatica*, vol. 41, no. 1, pp. 11–27, 2005.

[24] Z. Y. Yu, "Train operation experimental report in Dalian fast track," Tech. Rep., Beijing Jiaotong University.

Hindawi Publishing Corporation
Mathematical Problems in Engineering
Volume 2013, Article ID 749689, 9 pages
http://dx.doi.org/10.1155/2013/749689

Research Article

Spatial Path Following for AUVs Using Adaptive Neural Network Controllers

Jiajia Zhou, Zhaodong Tang, Honghan Zhang, and Jianfang Jiao

College of Automation, Harbin Engineering University, Harbin 150001, China

Correspondence should be addressed to Zhaodong Tang; bsa323@163.com

Received 18 August 2013; Accepted 8 October 2013

Academic Editor: Hamid Reza Karimi

The spatial path following control problem of autonomous underwater vehicles (AUVs) is addressed in this paper. In order to realize AUVs' spatial path following control under systemic variations and ocean current, three adaptive neural network controllers which are based on the Lyapunov stability theorem are introduced to estimate uncertain parameters of the vehicle's model and unknown current disturbances. These controllers are designed to guarantee that all the error states in the path following system are asymptotically stable. Simulation results demonstrated that the proposed controller was effective in reducing the path following error and was robust against the disturbances caused by vehicle's uncertainty and ocean currents.

1. Introduction

The research of AUV has been a hot topic in recent years with the development of marine robotics. Voluminous literature, for example [1–3], has been presented on the subject of designing path following controllers for AUVs. In order to design an automatic path following control system for AUVs, several problems must be solved. Among them the most difficult and challenging is that AUV's dynamics are highly nonlinear and the hydrodynamic coefficients of vehicles are difficult to be accurately estimated a priori since the variations of these coefficients with different operating conditions. In addition to vehicle dynamics, Caharija et al. [4] pointed out that the sea currents affect the vehicles significantly which are the lack of actuation in sway. As a universal phenomenon, the single AUV's spatial path following problem is a basis for formation coordinated control of multiple AUVs [5, 6].

Hereinabove, it is shown that modelling inaccuracy is primary difficult to achieve oriented results. The data driven fault diagnosis and process monitoring methods based on input and output data could be an effective way in real-time implementation where the physical model is hard to obtain [7–9]. And when it comes to system uncertainty, robust control could be used to attenuate disturbances in a relatively suboptimal extent. For example, load disturbance in the modelling of vehicles could be restricted to a satisfied expectation using the robust H_∞ PID controller [10]. Compared with robust control theory, adaptive strategy is an effective method of dealing with optimal control problems in vehicle control systems [11, 12]. Wang et al. [13] designed an adaptive PID controller for the path tracking system. From the simulation results, it was known that the proposed controller could not satisfy the tracking characteristics during automation performance. Based on Lyapunov stability theory and backstepping, Lapierre and Soetanto [14] proposed a path following controller for the motion control system of an AUV. It was demonstrated that the control characteristics of this kind of controller was relied on the accuracy of the hydrodynamic model. Chen and Wang [15] presented an adaptive control law with a parameter projection mechanism to track the desired vehicle longitudinal motion in the presence of tire-road friction coefficient uncertainties and actively injected braking excitation signals. The simulation results demonstrated that the proposed method was valuable for autonomous vehicle systems. A parameter-dependent adaptive H_∞ controller was constructed in [16] to guarantee robust asymptotic stability of the linear parameter-varying systems. And numerical examples were carried out to verify the effective impact on the attenuation in system disturbance. Li et al. [17] found an adaptive controller using a new

neural network model, which was effective to improve the control precision by 30% in the case of system with random disturbance. To compensate the uncertainties in robot control systems, the radial basis functional (RBF) neural network was introduced to enhance system stability and transient performance [18].

In this paper, we propose an adaptive neural network control method for spatial path following control of an AUV. Three lightly interacting subsystems are introduced to fulfil this mission. RBF neural network (NN) is introduced to estimate unknown terms including inaccuracies of the vehicle. Adaptive laws are chosen to guarantee optimal estimation of the weight of NN to make the approximation more accurate. The control performance of the closed-loop systems are guaranteed by appropriately choosing the design parameters. Based on the Lyapunov stability theorem, the proposed controllers are designed to guarantee all the error states in the subcontrol systems which are asymptotically stable.

The paper is organized as follows. Section 2 formulates the vehicle dynamics for an underactuated AUV in the six-degree-of-freedom (6-DOF) form. Section 3 develops three adaptive neural network controllers to solve the path following problem with uncertain dynamics and external disturbance, such as sea currents. The proposed controllers' stability is analysed by Lyapunov theory in this section. The simulation results using the proposed controllers are illustrated in Section 4. Finally, Section 5 contains the main conclusions and describes some problems that warrant further investigation.

2. Problem Formulation

2.1. Vehicle Dynamics. The dynamic model of the AUV in the three dimensional space is described in this section. See details in Bian et al. [19]. The vehicle which we studied in this paper measures 7.45 × 2.32 × 1.97 m. It is equipped with two main thrusters for propulsion, which are mounted symmetrically about its longitudinal axis in the horizontal plane. A cruciform tail including two different control surfaces is fixed right behind the thrusters to provide an enlarged torque around the transverse axis in the body fixed frame, which is helpful in enhancing the ability of spatial path following control. This vehicle is underactuated for the lack of propellers about its normal axis and transverse axis. The maximum designed speed of the vehicle with respect to the water is 3.08 m/s approximately. An outline of the vehicle with respect to the earth-fixed coordinate and body-fixed coordinate is shown in Figure 1.

According to the criteria underwater vehicle motion model in Fossen [20], this 6-DOF model can be described as follows.

Dynamic equation:

$$\mathbf{M}\dot{\boldsymbol{\nu}} + \mathbf{C}(\boldsymbol{\nu})\boldsymbol{\nu} + \mathbf{D}(\boldsymbol{\nu})\boldsymbol{\nu} = \boldsymbol{\tau}. \tag{1}$$

Kinematic equation:

$$\dot{\boldsymbol{\eta}} = \mathbf{J}(\boldsymbol{\eta})\boldsymbol{\nu}, \tag{2}$$

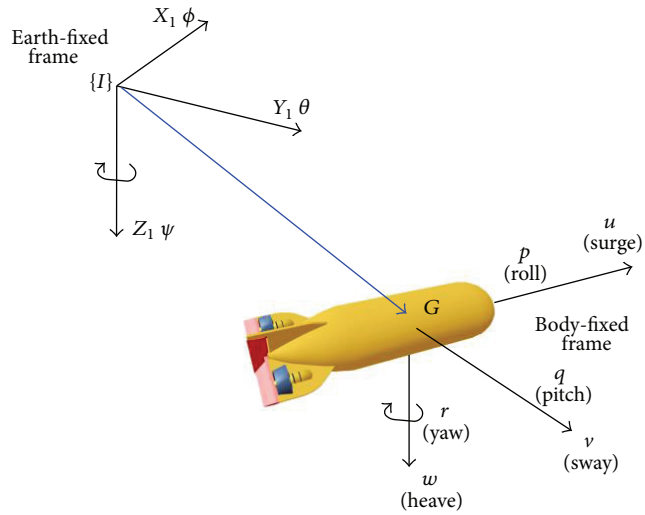

Figure 1: Employed coordinate frame systems.

where $\boldsymbol{\eta} = [\boldsymbol{\eta}_1, \boldsymbol{\eta}_2]^T$, $\boldsymbol{\nu} = [\boldsymbol{\nu}_1, \boldsymbol{\nu}_2]^T$, $\boldsymbol{\eta}_1 = [x, y, z]^T$, $\boldsymbol{\eta}_2 = [\varphi, \theta, \phi]^T$, $\boldsymbol{\nu}_1 = [u, v, w]^T$, and $\boldsymbol{\nu}_2 = [p, q, r]^T$.

The symbols φ, θ, ϕ, p, q, and r denote the roll, pitch, and yaw angles and velocities, respectively; x, y, z, u, v, and w are the surge, sway, and heave displacements and velocities, respectively. The matrix $\mathbf{J}(\boldsymbol{\eta}) = \operatorname{diag}\{\mathbf{J}_1(\boldsymbol{\eta}_2), \mathbf{J}_2(\boldsymbol{\eta}_2)\}$ is the transformation matrix from the body-fixed coordinated frame to the earth-fixed coordinated frame; $\mathbf{M} = \mathbf{M}^T > 0$ is the mass and inertia matrix; $\mathbf{C}(\boldsymbol{\nu})$ is the Coriolis and centripetal matrix; $\mathbf{D}(\boldsymbol{\nu})$ is the damping matrix; $\boldsymbol{\tau}$ is the control input, including force and moments generated by propellers and hydroplanes.

2.2. Spatial Path Following. Spatial path following problems of AUV can be solved by a dynamic task and a geometric task, whose objectives are to make the vehicle sail at an expected speed and move to the proposed three-dimensional path.

The former process of path following problem can be briefly stated as follows. Given a spatial path Γ, the goal is to design some feedback control law which yields the control forces for the vehicle's thrusters so that its centre of mass would converge asymptotically to a desired path by forcing its speed to track a desired speed assignment. The latter one can be described as below: considering the AUV depicted in Figure 2, where P is an arbitrary point on the path and Q denotes its centre of mass. The objective is to design the controllers which force the vehicle's position to converge to the desired path by driving the course angle and depth to converge to desired ones.

3. Controller Design

The objective is to realize the path following for AUVs in three dimensions. Consider Healey and Lienard [21], and according to practical operational applications in AUVs, the 6-DOF nonlinear equations of motion can be separated into three lightly interacting subsystems, including diving,

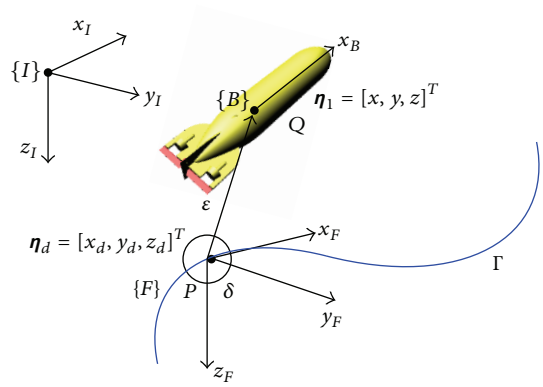

Figure 2: Spatial path following control problem.

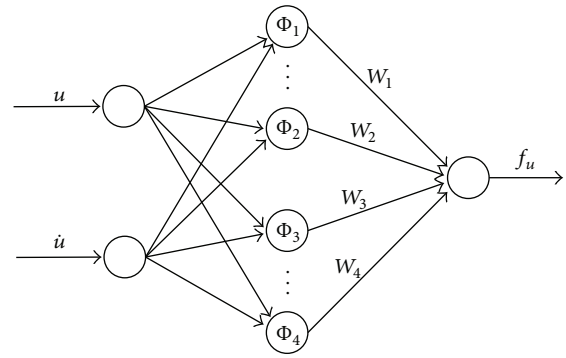

Figure 3: Diagram of RBF neural network for identification.

steering, and speed control. Our research will focus on dealing with the problem of spatial path following through the three subsystems.

3.1. Speed Control. For control design purposes, the interactions from the other degrees of freedom is neglected; the speed control model could be given by

$$\dot{u} = \frac{1}{(m - X_{\dot{u}})}\left[X_{uu}u^2 + X_{\text{prop}} + d_u\right], \tag{3}$$

where $X_{\dot{u}}$ and X_{uu} are dimensional hydrodynamic coefficients in surge; X_{prop} is thrusters' force; d_u represents modelling inaccuracies and external disturbances.

Define

$$f_u = X_{uu}u^2 + d_u. \tag{4}$$

Then, (4) can be rewritten as

$$\dot{u} = \frac{1}{(m - X_{\dot{u}})}\left(X_{\text{prop}} + f_u\right), \tag{5}$$

where X_{prop} is the forward force generated by the two main thrusters.

To deal with the uncertain terms, a RBF NN is chosen to estimate f_u which is described as

$$f_u = W_u^* \Phi_u + \varepsilon_u, \tag{6}$$

where W_u^* is an optimized weight estimation of the neural network; Φ_u is the basis function; ε_u is its estimation error. An identification diagram of the RBF neural network is shown in Figure 3.

Assume

$$X_{\text{prop}} = -\widehat{W}_u \Phi_u - k_u u, \tag{7}$$

where $k_u > 0$; $\widehat{W}_u$ is the weight estimation of the neural network.

Choose a Lyapunov function

$$V_u = \frac{1}{2}u^2 + \frac{1}{2}\widetilde{W}_u^2, \tag{8}$$

where $\widetilde{W}_u = W_u - \widehat{W}_u$.

Equation (8)'s derivative can be calculated as

$$\begin{aligned}\dot{V}_u &= u\dot{u} + \widetilde{W}_u\dot{\widetilde{W}}_u = u\dot{u} + \widetilde{W}_u\dot{\widetilde{W}}_u \\ &= u\left[\frac{X_{uu}u^2}{(m - X_{\dot{u}})} + \frac{X_{\text{prop}}}{(m - X_{\dot{u}})} + \frac{d_u}{(m - X_{\dot{u}})}\right] + \widetilde{W}_u\dot{\widetilde{W}}_u \\ &= \frac{u}{(m - X_{\dot{u}})}\left[X_{uu}u^2 + X_{\text{prop}} + d_u\right] + \widetilde{W}_u\dot{\widetilde{W}}_u \\ &= \frac{u}{(m - X_{\dot{u}})}\left[W_u\Phi_u + \varepsilon_u + X_{\text{prop}}\right] + \widetilde{W}_u\dot{\widetilde{W}}_u.\end{aligned} \tag{9}$$

Combined with (7) and (9),

$$\begin{aligned}\dot{V}_u &= \frac{u}{(m - X_{\dot{u}})}\left[W_u\Phi_u + \varepsilon_u - \widehat{W}_u\Phi_u - k_u u\right] + \widetilde{W}_u\dot{\widetilde{W}}_u \\ &= \frac{u\widetilde{W}_u\Phi_u}{(m - X_{\dot{u}})} + \frac{u\varepsilon_u}{(m - X_{\dot{u}})} - \frac{k_u u^2}{(m - X_{\dot{u}})} + \widetilde{W}_u\dot{\widetilde{W}}_u.\end{aligned} \tag{10}$$

An adaptive law is designed as follows:

$$\dot{\widetilde{W}}_u = \dot{\widehat{W}}_u = -\frac{u\Phi_u}{(m - X_{\dot{u}})} + \lambda\left(\widehat{W}_u - W_{u0}\right), \tag{11}$$

where $\lambda_u > 0$; W_{u0} is the initial weight value of the neural network. Then (9) can be changed as

$$\begin{aligned}\dot{V}_u &= \frac{u\varepsilon_u}{(m - X_{\dot{u}})} - \frac{k_u u^2}{(m - X_{\dot{u}})} + \widetilde{W}_u\left(\frac{u\Phi_u}{(m - X_{\dot{u}})} + \dot{\widetilde{W}}_u\right) \\ &= \frac{u\varepsilon_u}{(m - X_{\dot{u}})} - \frac{k_u u^2}{(m - X_{\dot{u}})} + \widetilde{W}_u\lambda_u\left(\widehat{W}_u - W_{u0}\right).\end{aligned} \tag{12}$$

Because ε is small enough, $|u| < 3.1$ m/s, $m - X_{\dot{u}} \gg 0$, and $(u/(m - X_{\dot{u}}))\varepsilon$ can be considered as small positive constant.

In (12),

$$\begin{aligned}&\widetilde{W}_u\lambda_u\left(\widehat{W}_u - W_{u0}\right) \\ &\quad = \widetilde{W}_u\widehat{W}_u\lambda_u - \widetilde{W}_u W_{u0}\lambda_u \\ &\quad = -\frac{\lambda_u}{2}\left\|\widetilde{W}_u\right\|_F^2 - \frac{\lambda}{2}\left\|\widehat{W}_u - W_{u0}\right\|_F^2 \\ &\qquad + \frac{\lambda_u}{2}\left\|W_u - W_{u0}\right\|_F^2.\end{aligned} \tag{13}$$

Based on Lyapunov stability theorem, it is provided that if one of the inequations in (14) is true, (15) would come true which guarantees the speed error converge to a small neighbourhood zero domain.

$$\frac{\lambda_u}{2}\left\|\widetilde{W}_u\right\|_F^2 \geq \frac{\lambda_u}{2}\left\|W_u - W_{u0}\right\|_F^2,$$
$$\frac{\lambda_u}{2}\left\|\widehat{W}_u - W_{u0}\right\|_F^2 \geq \frac{\lambda_u}{2}\left\|W_u - W_{u0}\right\|_F^2, \tag{14}$$

$$\dot{V}_u \leq -\gamma_u V_u + \sigma_u, \tag{15}$$

where $\gamma_u > 0$; σ_u is a small positive constant.

3.2. Diving Control. Consider the vehicle dynamics referred in Silvestre and Pascoal [22], and for the sake of diving control design, it is defined as follows:

$$\begin{aligned} dz &= -u_0(\theta - \sin\theta) + (u_0 - u)\sin\theta \\ &\quad + w\cos\theta, \\ b &= \left(I_y - \frac{1}{2}\rho L^5 M'_{\dot{q}}\right)^{-1}, \\ f_q &= b\left[\frac{1}{2}\rho L^5 M'_{q|q|} q|q| + \frac{1}{2}\rho L^4 M'_{uq} uq \right. \\ &\quad \left. + \frac{1}{2}\rho L^3 M'_{uu} u^2\right], \\ M_{Ty} &= \frac{1}{2}\rho L^3 M'_{\delta s} u^2 \delta_s. \end{aligned} \tag{16}$$

If the surge speed is $u = u_0$, the depth control model can be simplified as

$$\begin{aligned} \dot{z} &= -u_0\theta + dz, \\ \dot{\theta} &= q, \\ \dot{q} &= f_q + bM_{Ty}, \\ Y &= z. \end{aligned} \tag{17}$$

To be convenient for controller design, (17) can be rewritten as

$$\begin{bmatrix} \dot{\varsigma}_1 \\ \dot{\varsigma}_2 \\ \dot{\varsigma}_3 \\ Y \end{bmatrix} = \begin{bmatrix} \varsigma_2 + d\varsigma_1 \\ \varsigma_3 \\ -u_0 f_q + \left(-u_0 b M_{Ty}\right) \\ \varsigma_1 \end{bmatrix} = \begin{bmatrix} f(\varsigma_1, \varsigma_2) \\ f_2(\varsigma_3) \\ f_3 - b' M_{Ty} \\ \varsigma_1 \end{bmatrix}, \tag{18}$$

where $\varsigma = [\varsigma_1, \varsigma_2, \varsigma_3]^T = [z, -u_0\theta, -u_0 q]^T$.

In this section the backstepping techniques are adopted based on iterative methodology, where a virtual control input is introduced to ensure that the diving error can be converged to zero. And based on the Lyapunov stability theorem, an adaptive neural network controller is designed to guarantee that all the error states in the diving control system are asymptotically stable.

From (18), a more simplified pure-feedback form is shown as follows:

$$\begin{bmatrix} \dot{\varsigma}_1 \\ \dot{\varsigma}_2 \\ \dot{\varsigma}_3 \end{bmatrix} = \begin{bmatrix} f(\varsigma_1, \varsigma_2) \\ f_2(\varsigma_3) \\ f_3 - b' M_{Ty} \end{bmatrix}. \tag{19}$$

Step 1. Given a desired depth ς_{d1}, the depth error is described as

$$\begin{aligned} \dot{Z}_1 &= \varsigma_1 - \varsigma_{d1} \\ &= f_1(\varsigma_1, \varsigma_2, u) - \dot{\varsigma}_{d1}. \end{aligned} \tag{20}$$

Define a virtual control variable:

$$v_1 = -\varsigma_{d1} + K_1 \dot{Z}_1. \tag{21}$$

From $\partial v_1/\partial \varsigma_2 = 0$, we can know

$$\frac{\partial\left[f_1(\varsigma_1, \varsigma_2, u) + v_1\right]}{\partial \varsigma_2} > \varepsilon > 0. \tag{22}$$

When we take ς_2 as the input of the virtual control variable, there must exist a $\varsigma_2 = \alpha_1^*(\varsigma_1, v_1, u)$ satisfying

$$f_1(\varsigma_1, \alpha_1^*, u) + v_1 = 0. \tag{23}$$

Referring to the mean value theorem of Lagrange, γ_1 $(0 < \gamma_1 < 1)$ can be found which yields

$$f_1(\varsigma_1, \varsigma_2, u) = f_1(\varsigma_1, \alpha_1^*, u) + \gamma_1(\varsigma_2, \alpha_1^*), \tag{24}$$

where $\gamma_1 := g_1(\varsigma_1, \varsigma_{2\gamma_1}, u)$, $\varsigma_{2\gamma_1} = \gamma_1\varsigma_2 + (1 - \gamma_1)\alpha_1^*$.

Combined with (21) and (24), (20) can be rewritten as

$$\dot{Z}_1 = -K_1 Z_1 + \gamma_1(\varsigma_2 - \alpha_1^*). \tag{25}$$

Then α_1^* can be estimated by RBF neural network as follows:

$$\alpha_1^* = W^{*T}\Phi(Z_1) + \varepsilon. \tag{26}$$

Consider $Z_2 = \varsigma_2 - \alpha_1$ and $\alpha_1 = -c_1 Z_1 + \widehat{W}^T\Phi(Z_1)$, where $\widehat{W}$ is to be the estimation of W^*. Then (25) becomes

$$\begin{aligned} \dot{Z}_1 &= -K_1 Z_1 + \gamma_1(Z_2 + \alpha_1 - \alpha_1^*) \\ &= -K_1 Z_1 + \gamma_1\left[Z_2 - c_1 Z_1 + \widetilde{W}^T\Phi(Z_1) - \varepsilon\right], \end{aligned} \tag{27}$$

where $\widetilde{W} = \widehat{W} - W^*$.

Choose a Lyapunov function:

$$V_1 = \frac{1}{2\gamma_1} Z_1^2 + \frac{1}{2}\widetilde{W}^T \Gamma_1 \widetilde{W}. \tag{28}$$

The derivative of (28) can be calculated as

$$\dot{V}_1 = -\frac{K_1}{\gamma_1}Z_1^2 + Z_1Z_2 - c_1Z_1^2 - \frac{\gamma_1}{2\gamma_1^2}Z_1^2 - Z_1\varepsilon + \widetilde{W}^T\Phi(Z_1)Z_1 + \widetilde{W}^T\Gamma_1\widetilde{W}. \tag{29}$$

With the adaptive law,

$$\dot{\widehat{W}} = \left[-\Phi(Z_1)Z_1 - \sigma_1\left(\widehat{W}\right)\right]\cdot\Gamma_1, \tag{30}$$

where σ is a small positive constant.

Step 2. Consider

$$Z_2 = \varsigma_2 - \alpha_1 \Longrightarrow \dot{Z}_2 = f_2(\varsigma_3) = \varsigma_3. \tag{31}$$

It is assumed that

$$\alpha_2 = -Z_1 - c_2Z_2 + \alpha_1^*. \tag{32}$$

Choose another Lyapunov function:

$$V_2 = V_1 + \frac{1}{2}Z_2^2. \tag{33}$$

The derivative of (33) can be calculated as

$$\dot{V}_2 = -\frac{K_1}{\gamma_1}Z_1^2 - c_1Z_1^2 - \frac{\sigma\left\|\widetilde{W}\right\|^2}{2} + \frac{\sigma\left\|W^*\right\|^2}{2} + \frac{\varepsilon^2}{4c_1} - c_2Z_2^2 + Z_2Z_3. \tag{34}$$

Step 3. Define $\varsigma_3 = Z_3 - \alpha_2$.

It can be calculated as

$$\dot{Z}_3 = f_q - b'M_{Ty} - \dot{\alpha}_2. \tag{35}$$

And, we can obtain

$$M_{Ty}^* = -Z_2 - c_3Z_3 - \frac{1}{b'}\left(\dot{\alpha}_2 - f_q\right). \tag{36}$$

Then the unknown term $(1/b')f_q$ can be estimated by RBF NN, and the ideal optimal control law can be written as

$$M_{Ty}^* = -Z_2 - c_3Z_3 + W_2^*\Phi(Z_3) - \frac{\dot{\alpha}_2}{b'} + \varepsilon_2. \tag{37}$$

Finally, we obtain the actual control input:

$$M_{Ty} = -Z_2 - c_3Z_3 - \frac{\dot{\alpha}_2}{b'} + \widehat{W}_2\Phi(Z_3). \tag{38}$$

From (35)–(37), it can be derived that

$$\dot{Z}_3 = -K_3Z_3 - b'\left[-Z_2 - c_3Z_3 - \frac{\dot{\alpha}_2}{b'} + \widetilde{W}_2^T\Phi(Z_3) - \varepsilon_2\right]. \tag{39}$$

Consider a Lyapunov function:

$$V_3 = V_2 - \frac{1}{2b'}Z_3^2 + \frac{1}{2}\widetilde{W}_2^T\Gamma_2\widetilde{W}_2. \tag{40}$$

We can obtain its derivative

$$\dot{V}_3 = V_2 - Z_2Z_3 - c_3Z_3^2 + \widetilde{W}_2\Phi(Z_3)Z_3 + \widetilde{W}_2^T\Gamma_2\dot{\widehat{W}}_2, \tag{41}$$

where $\dot{\widehat{W}}_2 = \Gamma_2[-\Phi(Z_3)Z_3 - \sigma_3\widehat{W}_2]$ and $\sigma_3 > 0$.

As what we did in Step 1, (41) can be calculated as

$$\dot{V}_3 < -\sum_{j=1}^{3}c_{j0}^*Z_j^2 - \sum_{j=1}^{3}\frac{\sigma_j\left\|\widehat{W}_j\right\|}{2} + \sum_{j=1}^{3}\frac{\sigma_j\left\|W_j^*\right\|}{2} + \sum_{j=1}^{3}\frac{\varepsilon_j}{2}, \tag{42}$$

where $c_{30}^* := c_{30} > 0$.

Consider the Lyapunov stability theorem, it can be concluded that all the signals in the diving control system are bounded. Furthermore, the output tracking error of the system will converge to a small neighbourhood zero domain by appropriately choosing control parameters.

3.3. Guidance Law and Steering Control

3.3.1. Line-of-Sight Guidance. Referring to Fossen [20] and Oh and Sun [23], we briefly introduce Line-of-Sight guidance law in this section for path following in the horizontal plane and discuss its application for straight lines and circular arcs.

Calculate the angle between the proposed path and the north of earth-fixed coordinate in Figure 4:

$$\alpha_k := \arctan 2\left(\eta_{k+1} - \eta_k, \xi_{k+1} - \xi_k\right) \in [-\pi, \pi]. \tag{43}$$

Considering the cross track error $e_\gamma(t)$ and a look-ahead distance Δ, the desired course angle for the steering control system can be computed as

$$\gamma_d = \alpha_k + \arctan\left(\frac{-e_\gamma}{\Delta}\right) = \alpha_k + \gamma_e, \tag{44}$$

where $\Delta = nL$ ($n = 2\sim5$).

When it comes to the circular arcs in Figure 5, we can obtain the guidance law just as (44) in form.

3.3.2. Steering Controller Design. Referring to the vehicle dynamics in horizontal plane in [24] and considering the advantage of steering controller design, we define

$$X_1 = \psi, \qquad X_2 = \dot{\psi}. \tag{45}$$

The kinetics model of the AUV in horizontal plane can be simplified as

$$\begin{bmatrix}\dot{X}_1\\ \dot{X}_2\\ Y_\psi\end{bmatrix} = \begin{bmatrix}X_2\\ f_\psi(v) + b_\psi\delta_r + d_\psi\\ X_1\end{bmatrix}, \tag{46}$$

where $v := g_\psi(u, v, r)$ includes the nonlinear terms with u, v, and r in the steering equation; d_ψ is the disturbance satisfied with $|d_\psi| \le \varepsilon_0$, $\varepsilon_0 > 0$.

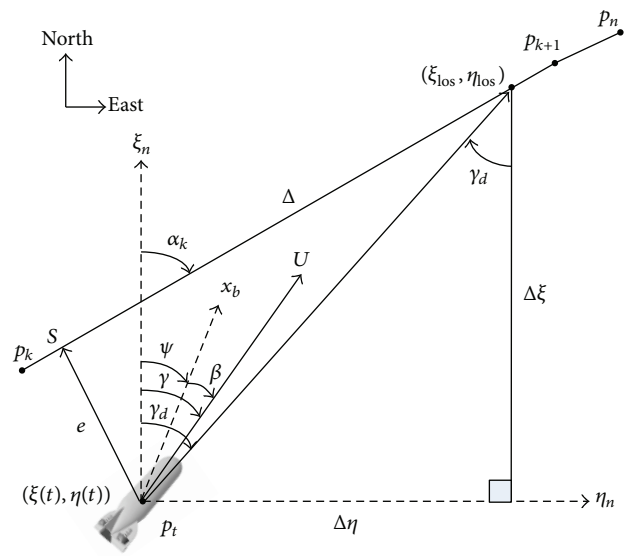

Figure 4: Principle of LOS guidance for straight line.

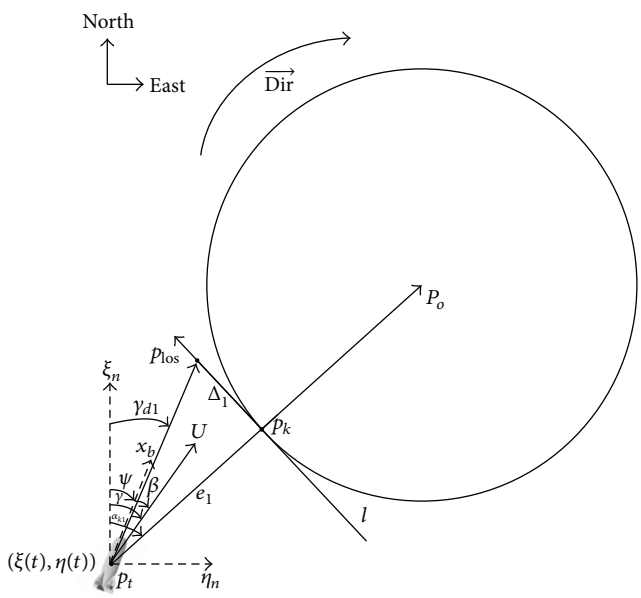

Figure 5: Principle of LOS guidance for circular arc.

Consider a heading track error:

$$e_\psi = Y_\psi - Y_{\psi d}, \tag{47}$$

where the desired course angle $\gamma_d = Y_{\psi d}$.

Choose $K \in R$ which makes (48) a stabilized system:

$$h(s) = s + K. \tag{48}$$

Then the derivative of the steering error system can be written as follows:

$$\dot{e}_\psi = \mathbf{A}e_\psi + \mathbf{B}\left[f_\psi(v) + b_\psi\tau - \ddot{Y}_{\psi d} + \mathbf{K}e_\psi + d_\psi\right], \tag{49}$$

where $A = -K$ and $B = 1$.

Then we can find $P > 0$ and $Q \geq 0$ which make the following Lyapunov stable equation solvable:

$$A^T P + PA = -Q. \tag{50}$$

On the assumption that $f_\psi(v)$ and b_ψ are known and $d_\psi = 0$, a linear controller can be obtained as (51) using pole-assignment method:

$$u_\psi = -b_\psi^{-1}\left(f_\psi(v) - \ddot{Y}_{\psi d} + \mathbf{K}e_\psi\right). \tag{51}$$

Combined with (46), we can find

$$\dot{e}_\psi + \mathbf{K}e_\psi = 0. \tag{52}$$

For K is chosen appropriately according to (48), it can be derived that $\lim_{t\to\infty} e_\psi(t) = 0$.

In fact, $f_\psi(v)$ and b_ψ are uncertain, and d_ψ does exist. To deal with the uncertain terms, a RBF NN is chosen to estimate $f_\psi(v)$:

$$f_\psi(v) = W^*\Phi(v) + \varepsilon_\psi, \tag{53}$$

where W^* is an optimized weight estimation of the neural network; $\Phi(v)$ is a vector of Gaussian function $\Phi(v) = \exp(\|v - c_0\|^2/b_0{}^2)$, $c_0 \in R$ is its centre, and b_0 is the width of the basis function.

If the weight estimation of neural network $\widehat{W}$ is uniformly bounded, a positive constant w can be found, which satisfies $\|\widehat{W}\| < w_0$.

For ε_ψ is the estimation error of the RBF NN, then

$$f_\psi(v) - \widehat{f}_\psi(v) = \varepsilon_\psi. \tag{54}$$

Meanwhile, consider a weight error for the RBF NN:

$$\widetilde{W} = W^* - \widehat{W}. \tag{55}$$

Combined with (49), (54), and (55), it can be calculated as

$$\begin{aligned}\dot{e}_\psi &= Ae_\psi + B\Big[\widehat{f}_\psi(v) + \widehat{b}_\psi\delta_r - \ddot{Y}_{\psi d} + Ke_\psi \\ &\quad + \left(f_\psi(v) - \widehat{f}_\psi(v)\right) \\ &\quad + \left(b_\psi - \widehat{b}_\psi\right)\delta_r + d_\psi(t)\Big] \\ &= Ae_\psi + B\Big[\widehat{f}_\psi(v) + \widehat{b}_\psi\delta_r - \dot{Y}_{\psi d} + Ke_\psi \\ &\quad + \Delta f_\psi + \widetilde{W}\phi(v) + \widetilde{b}_\psi\delta_r + d_\psi\Big].\end{aligned} \tag{56}$$

In order to compensate for estimation error and current disturbance as shown in (56), a virtual control input described as (17) is introduced as

$$\nu = -\kappa\frac{B^T Pe_\psi}{\left\|B^T Pe_\psi\right\| + \lambda_\psi}, \tag{57}$$

where $\kappa = P + \varepsilon_\psi$ and $\kappa \geq |\Delta f_\psi| + |d_\psi|$; λ_ψ is a small positive constant.

Herein, (56) can be rewritten as follows:

$$\dot{e}_\psi = Ae_\psi + B\left[\Delta f_\psi + \widetilde{W}\phi(\xi) + \widetilde{b}_\psi \tau_\psi + d_\psi + \nu\right]. \quad (58)$$

Introduce adaptive laws:

$$\dot{\widehat{W}} = \gamma_1 \Phi(\xi) BPe_\psi, \qquad \dot{\widehat{b}}_\psi = \gamma_2 \tau_\psi BPe_\psi, \quad (59)$$

where γ_1 and γ_2 are positive constants.

To deal with the problem of stability, a Lyapunov function (60) is chosen to guarantee the proposed adaptive NN controller satisfying that the signals in the steering control system are bounded:

$$V_\psi = \frac{1}{2}Pe_\psi^2 + \frac{1}{2\gamma_1}\widetilde{W}^2 + \frac{1}{2\gamma_2}\widetilde{b}_\psi^2. \quad (60)$$

The differentiation of (60) can be calculated as

$$\begin{aligned}\dot{V}_\psi &= e_\psi \dot{e}_\psi P + \frac{1}{\gamma_1}\widetilde{W}\dot{\widetilde{W}} + \frac{1}{\gamma_2}\widetilde{b}_\psi \dot{\widetilde{b}}_\psi \\ &= e_\psi PB\left(\Delta f_\psi + d_\psi + \widetilde{W}\phi(\upsilon) + \widetilde{b}_\psi \delta_s + \nu\right) \\ &\quad + \frac{1}{\gamma_1}\widetilde{W}\dot{\widetilde{W}} + \frac{1}{\gamma_2}\widetilde{b}_\psi \dot{\widetilde{b}}_\psi.\end{aligned} \quad (61)$$

With a combination of (59) and (61), it can be derived that

$$\dot{V}_\psi = e_\psi PB\left(\Delta f_\psi + d_\psi + \nu\right). \quad (62)$$

Moreover, because

$$\begin{aligned}&e_\psi^T PB\left(\Delta f_\psi + d_\psi + \nu\right) \\ &\quad \le \left\|B^T Pe_\psi\right\|\left(\left\|\Delta f_\psi\right\| + \left\|d_\psi\right\|\right) + e_\psi^T PB\nu \\ &\quad = \left\|B^T Pe_\psi\right\|\left(\left\|\Delta f_\psi\right\| + \left\|d_\psi\right\|\right) - \kappa\frac{\left(B^T Pe_\psi\right)^2}{\left\|B^T Pe_\psi\right\| + \lambda_\psi} \\ &\quad \le \left\|B^T Pe_\psi\right\|\left(\left\|\Delta f_\psi\right\| + \left\|d_\psi\right\|\right) - \kappa\frac{\left\|B^T Pe_\psi\right\|^2}{\left\|B^T Pe_\psi\right\| + \lambda_\psi}\end{aligned} \quad (63)$$

and $\|B^T Pe_\psi\|^2/(\|B^T Pe_\psi\| + \lambda_\psi) > \|B^T Pe_\psi\| - \lambda_\psi$ are true, (62) can be calculated as

$$\dot{V}_\psi \le \left\|B^T Qe_\psi\right\|\left(\left\|\Delta f_\psi\right\| + \left\|d_\psi\right\| - \kappa\left\|B^T Pe_\psi\right\| - \lambda_\psi\right). \quad (64)$$

It is known that $\kappa \ge |\Delta f_\psi| + |d_\psi|$; then we can obtain

$$\dot{V}_\psi \le -\kappa\lambda_\psi \le 0. \quad (65)$$

Similar to the derivation of diving controller, it can be concluded that all the signals in the steering control system are bounded. Furthermore, the output tracking error of the system will converge to a small neighbourhood zero domain by appropriately choosing control parameters.

Finally, the control input can be given by

$$u_\psi = -\widehat{b}_\psi^{-1}\left(\widehat{f}_\psi(\upsilon) - \dot{Y}_{\psi d} + \mathbf{K}e_\psi - \nu\right). \quad (66)$$

4. Simulation Results

In order to validate the proposed controller, it is assessed in the C/C++ simulation environment with a full nonlinear model for the designed vehicle. It is assumed that the states of the system are updated with a period of $T = 0.1$ s (seconds). Considering jacket healthy state detection which is a regular task for offshore platform, a spiral three-dimensional path is programmed to complete the detection job. In order to fulfil this mission successfully, the control objective is going to achieve a high tracking precision with the proposed control method.

Two simulations are carried out to demonstrate the advantage of the proposed method, including path following conditions without sea current and undersea current, where the unvarying current is set to be heading east with 0.25 m/s. The vehicle is initially rest at a random position $(x, y, z) = (0\,\text{m}, 35\,\text{m}, 0.5\,\text{m})$ with an unspecified attitude $(\varphi, \theta, \psi) = (0^\circ, 0^\circ, 90^\circ)$. The desired forward speed is 1.8 m/s. The gains and parameters for the adaptive neural network speed controller are $\lambda_u = 1.2$, $k_u = 2.5$, and $\gamma_u = 1.8$, while the ANN steering controller's initial values are set as follows: $c_1 = 5$, $c_2 = 12$, $c_3 = 10$, $b = 3.8386e - 005$, $\Gamma_1 = \Gamma_2 = \text{diag}\{1.5\}$, and $\sigma_1 = \sigma_3 = 0.5$. The parameters for the diving control system are chosen as $K = 2.8$, $\lambda_\psi = 0.1$, $\gamma_1 = 2$, and $\gamma_2 = 1.5$. And the initial weights of RBF NN for the three subsystems are chosen as zero.

Figures 6–9 show the simulation results for spatial path following between different ocean circumstances. It is shown that the proposed mission under disturbance of current or not could be achieved by the designed adaptive neural network controllers. It is clear that the proposed method is suitable to follow the spatial path with a random position and attitude, which is very practical in jacket healthy state detection mission.

Figure 6 is the response of spatial path following under different circumstances in three-dimensional space, where S means the start point and E is the end of the mission. We can see that the performances in the two simulations are good in general. It can be seen that the two tracks are identical with the same initial values for controllers' compensation to the uncertain dynamics and ocean current.

From Figure 7, it is shown that the position track errors during the jacket detection missions are gradually converged to zero. Combined with Figures 7 and 8, we can clearly see that although the overshoots have a little increase at the 67th second and the 54th one, which indicate the presence of ocean current in the process, the errors decrease to zero very quickly using the proposed controllers, which was designed to guarantee the errors in the spatial path following systems to be restricted to a small value gradually. In the meanwhile, when it is compared to the surge speed responses under different circumstances in Figure 9, it is evident that the fluctuant speed is the primary reason responsible for the overshoots in the spatial path following.

The simulation results obtained illustrate that the proposed methodology is effective and reduces the path following errors. Moreover, it is relatively simple to apply this proposed control in simulation.

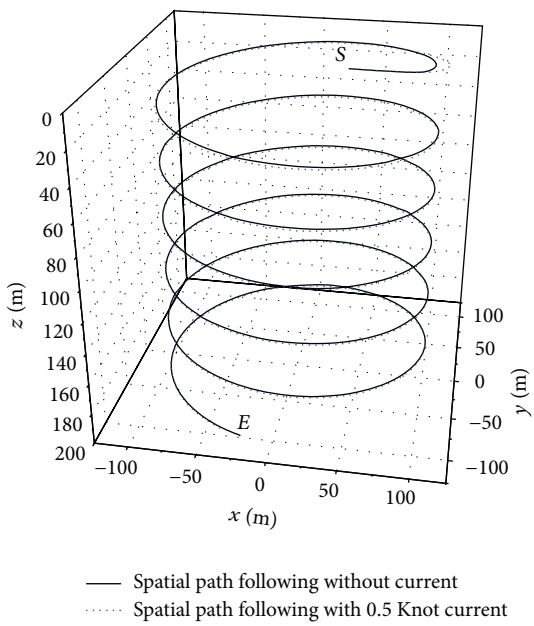

Figure 6: Spatial path following under different circumstances.

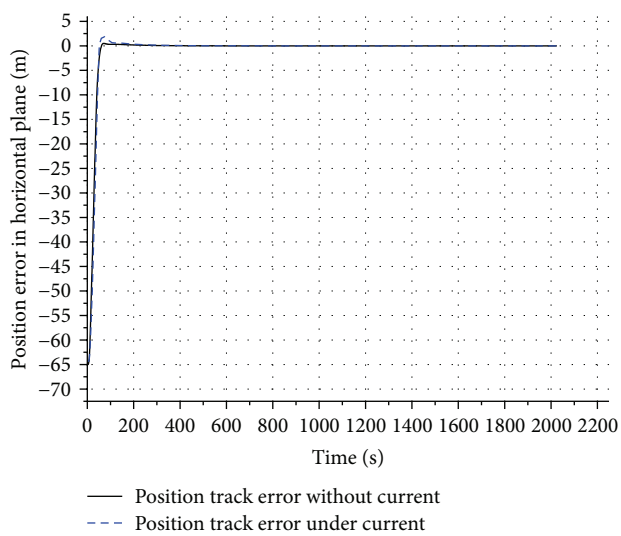

Figure 7: Position track errors in the horizontal plane.

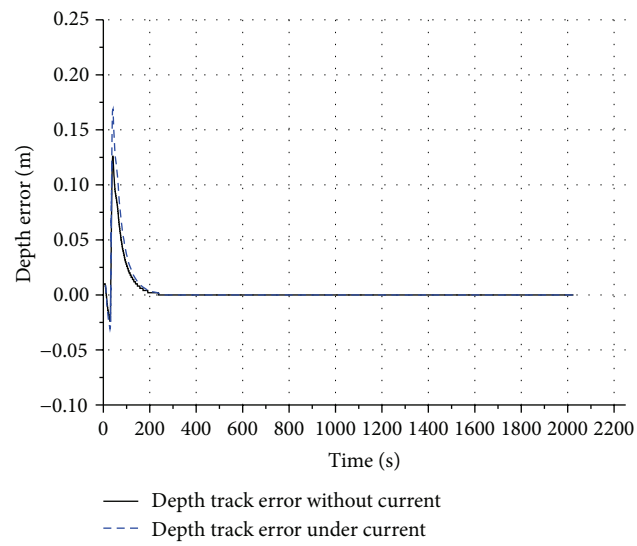

Figure 8: Depth track errors in the vertical plane.

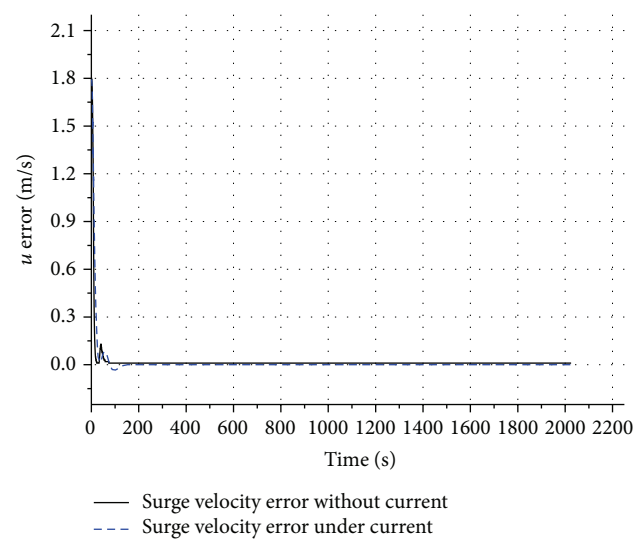

Figure 9: Surge speed errors under different circumstances.

5. Conclusions

The objective of this paper was to accurately follow a given path in the presence of systemic variations and ocean current. On one hand, three lightly interacting subsystems, including diving, steering, and speed control, were proposed to simplify the controller design for the spatial path following with 6-DOF nonlinear equations. On the other hand, those three controllers were designed to guarantee that all the error states in the spatial path following system were asymptotically stable by using adaptive neural network method. The simulation results illustrated that the proposed methodology was effective and attenuated the path following error under current. Future work will address the problems of path following under more common spatial curves. The problem of external disturbance about varying sea currents also warrants further research.

Acknowledgments

This work was supported by the Fundamental Research Funds for the Central Universities, under Grant HEUCF041330; the Fundamental Research Funds for the Central Universities of key laboratory's open key; the National Natural Science Foundation of China, under Grant 51309067/E091002. And the authors also would like to thank the editor and three reviewers for their helpful comments.

References

[1] P. Encarnação and A. Pascoal, "3D path following for autonomous underwater vehicle," in *Proceedings of the 39th IEEE Confernce on Decision and Control*, pp. 2977–2982, Sydney, Australia, December 2000.

[2] L. Lapierre and B. Jouvencel, "Robust nonlinear path-following control of an AUV," *IEEE Journal of Oceanic Engineering*, vol. 33, no. 2, pp. 89–102, 2008.

[3] H. M. Jia, L. J. Zhang, X. Q. Bian et al., "A nonlinear bottom-following controller for underactuated autonomous under water vehicles," *Journal of Central South University*, vol. 19, pp. 1240–1248, 2012.

[4] W. Caharija, K. Y. Pettersen, J. T. Gravdahl, and E. Borhaug, "Path following of underactuated autonomous underwater vehicles in the presence of ocean currents," in *Proceedings of the 51th IEEE Conference on Decision and Control*, pp. 528–535, Maui, Hawaii, USA, 2012.

[5] Y. Tang, H. J. Gao, W. Zou et al., "Distributed synchronization in networks of agent systems with nonlinearities and random switchings," *IEEE Transactions on Cybernetics*, vol. 43, no. 1, pp. 358–370, 2013.

[6] Y. Tang, H. J. Gao, J. Kurths et al., "Evolutionary pinning control and its application in UAV coordination," *IEEE Transactions on Industrial Informatics*, vol. 8, no. 4, pp. 828–838, 2012.

[7] S. Yin, S. Ding, and H. Luo, "Real-time implementation of fault tolerant control system with performance optimization," *IEEE Transactions on Industrial Electronics*, vol. 61, no. 5, pp. 2402–2411, 2013.

[8] S. Yin, S. Ding, A. Haghani et al., "A comparison study of basic data-driven fault diagnosis and process monitoring methods on the benchmark Tennessee Eastman process," *Journal of Process Control*, vol. 22, no. 9, pp. 567–1581, 2012.

[9] S. Yin, S. X. Ding, A. H. A. Sari, and H. Hao, "Data-driven monitoring for stochastic systems and its application on batch process," *International Journal of Systems Science*, vol. 44, no. 7, pp. 1366–1376, 2013.

[10] H. Zhang, Y. Shi, and A. S. Mehr, "Robust H_∞ PID control for networked control systems with acceptable noise rejection," in *Proceedings of the American Control Conference (ACC '10)*, pp. 1356–1361, Marriott Waterfront, Baltimore, Md, USA, July 2010.

[11] S. Yin, X. Yang, and H. R. Karimi, "Data-driven adaptive observer for fault diagnosis," *Mathematical Problems in Engineering*, vol. 2012, Article ID 832836, 21 pages, 2012.

[12] Y. Tang and W. K. Wong, "Distributed synchronization of coupled neural networks via randomly occurring control," *IEEE Transactions on Neural Networks and Learning Systems*, vol. 24, no. 3, pp. 435–447, 2013.

[13] B. Wang, Y. M. Su, L. Wan, and Y. Sun, "Adaptive PID control system for an autonomous underwater vehicle," *High Technology Letters*, vol. 17, no. 1, pp. 7–12, 2011.

[14] L. Lapierre and D. Soetanto, "Nonlinear path-following control of an AUV," *Ocean Engineering*, vol. 34, no. 11-12, pp. 1734–1744, 2007.

[15] Y. Chen and J. M. Wang, "Adaptive vehicle speed control with input injections for longitudinal motion independent road frictional condition estimation," *IEEE Transactions on Vehicular Technology*, vol. 60, no. 3, pp. 839–848, 2011.

[16] H. R. Karimi, "Parameter-dependent adaptive H∞ control design for a class of linear parameter-varying systems using polynomially parameter-dependent quadratic functions," *Proceedings of the Institution of Mechanical Engineers I*, vol. 221, no. 4, pp. 589–600, 2007.

[17] X. H. Li, F. Xu, J. H. Zhang et al., "A multilayer feed forward small-world neural network controller and its application on electrohydraulic actuation system," *Journal of Applied Mathematics*, vol. 2013, Article ID 872790, 8 pages, 2013.

[18] S. H. Wen, J. Y. Yuan, and J. H. Zhu, "Radial basis functional link network and Hamilton Jacobi Issacs for force/position control in robotic manipulation," *Mathematical Problems in Engineering*, vol. 2012, Article ID 568796, 10 pages, 2012.

[19] X. Q. Bian, C. H. Mou, Z. P. Yan, and H. Wang, "Formation coordinated control for multi-AUV based on spatial curve path tracking," in *Proceedings of the MTS/IEEE Kona Conference (OCEANS '11)*, Waikoloa, Hawaii, USA, September 2011.

[20] T. I. Fossen, *Handbook of Marine Craft Hydrodynamics and Motion Control*, John Wiley & Sons, New York, NY, USA, 2011.

[21] A. J. Healey and D. Lienard, "Multivariable sliding mode control for autonomous diving and steering of unmanned underwater vehicles," *IEEE Journal of Oceanic Engineering*, vol. 18, no. 3, pp. 327–339, 1993.

[22] C. Silvestre and A. Pascoal, "Depth control of the INFANTE AUV using gain-scheduled reduced order output feedback," *Control Engineering Practice*, vol. 15, no. 7, pp. 883–895, 2007.

[23] S.-R. Oh and J. Sun, "Path following of underactuated marine surface vessels using line-of-sight based model predictive control," *Ocean Engineering*, vol. 37, no. 2-3, pp. 289–295, 2010.

[24] C. Silvestre and A. Pascoal, "Control of the INFANTE AUV using gain scheduled static output feedback," *Control Engineering Practice*, vol. 12, no. 12, pp. 1501–1509, 2004.

Hindawi Publishing Corporation
Mathematical Problems in Engineering
Volume 2013, Article ID 439515, 9 pages
http://dx.doi.org/10.1155/2013/439515

Research Article

Dynamic Ride Height Adjusting Controller of ECAS Vehicle with Random Road Disturbances

Xing Xu, Long Chen, Liqin Sun, and Xiaodong Sun

School of Automotive and Traffic Engineering, Jiangsu University, Zhenjiang 212013, China

Correspondence should be addressed to Xing Xu; xuxing@mail.ujs.edu.cn

Received 20 August 2013; Accepted 24 September 2013

Academic Editor: Hui Zhang

The ride height control system is greatly affected by the random road excitation during the ride height adjusting of the driving condition. The structure of ride height adjusting system is first analyzed, and then the mathematical model of the ride height adjusting system with the random disturbance is established as a stochastic nonlinear system. This system is decoupled using the differential geometry theory and stabilized using the Variable Structure Control (VSC) technique. The designed ride height control system converges in probability to be asymptotically stable in the sliding motion band, and the desired control law is solved to ensure the stable adjustment of the ride height system. Simulation results show that the proposed stochastic VSC method is effective for the dynamic adjusting of the ride height. Finally, the semiphysical rig test illustrates the applicability of the proposed scheme.

1. Introduction

Ride height adjustment is one of the advantages for Electronically Controlled Air Suspension (ECAS) [1, 2]. The height adjustment, which contains the aerothermodynamics and vehicle dynamic processes of variable mass system, is accomplished by charging/discharging gas into/from air spring. The ECU of the ride height adjusting system can automatically regulate the ride height (maintaining or switching the ride height of the vehicle) to improve the performance of the suspension, according to the different driving states.

In the past several years, the study of ride height adjusting system attracted the attention of researchers all over the world. A prototype self-leveling active suspension system for road vehicles is presented to analyze the characteristic of the system [3]. In fact, the adjustment of the ride height system, which belongs to multidomain dynamics, is a process where the energy of the compressed air is converted to potential energy of vehicle sprung mass. Since the ride height adjusting system includes the continuous dynamic system state and the discrete logic state of the height mode switch, a novel approach for the verification of hybrid systems based on linear and mixed-integer linear programming for the electronic height control was proposed [4, 5]. Then, the ride height control system based on the model was designed. A multibody dynamic model of an air suspension vehicle by using Lagrange's method was built, and a ride height simulation under the condition of a step input using PID and PD control strategy was performed [6]. Some advanced control algorithms were also used to improve the adjusting performance of the ride height system. Chen et al. used the combined PID and VSC method to control the Hydro-Pneumatic Suspension, which could eliminate the oscillation and improve the control accuracy of the ride height system [7]. Yu et al. studied the fuzzy control of the ride height system, and the proposed control system has good robustness for the case of the changed structure parameters [8]. Yang et al. further studied the charging/discharging gas system of ECAS, designed the inductance integral height measuring system for real-time tracking information of ride height, and tried to improve the stability of the ride height adjustment system by adopting gearshift integral PID/PWM algorithm [9–11]. Feng and Du adopted the Fuzzy/PWM algorithm on the electronic controlled air suspension of semitrailer based on a quarter-car model, and then the phenomenon of overshoot and oscillation can be overcome effectively [12]. Kim and Lee used a sliding mode control algorithm to improve the tracking accuracy of the control and to overcome nonlinearities and uncertainties in the air suspension system [13]. However, the dynamic adjusting, especially the stability

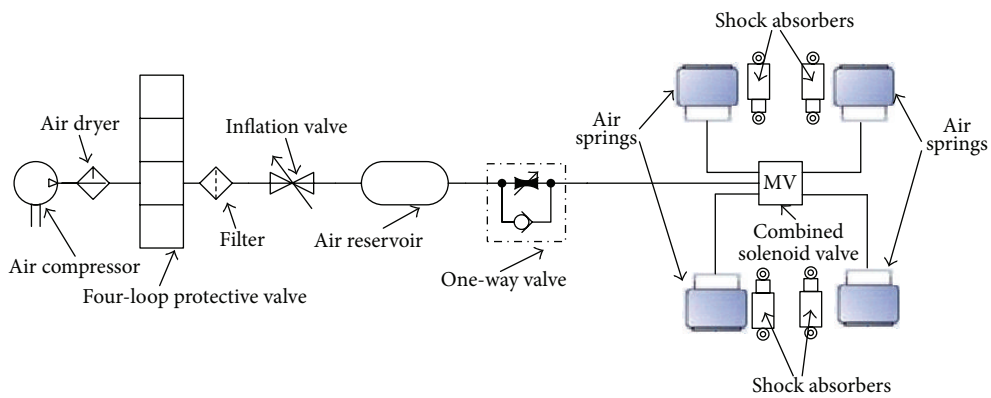

Figure 1: Pneumatic scheme of the ride height system for full vehicle.

control with respect to the random disturbances, has little research, but we can find some theories to apply the nonlinear system with disturbances [14, 15]. According to the characteristics of the nonlinear stochastic adjustment system, the ride height control system is designed by using the stochastic VSC technique in the present paper. The stochastic VSC law is solved by the stabilization in a certain probability, and this may achieve the stable adjustment of the dynamic ride height.

This paper is organized as follows. In Section 2, the ride height adjusting system is described. In Section 3, the dynamic model with random disturbances is built. In Section 4, we design a stochastic variable structure controller to achieve the stable adjusting of ride height, and the simulating results of comparing the algorithm proposed in this paper with PID algorithm are carried out. Experimental results show the effectiveness of the proposed method, as shown in Section 5. Conclusions are provided in Section 6.

2. Structure of Ride Height Adjusting System

The structure of ECAS system is shown in Figure 1. The high pressure air in air springs is exchanged with air reservoir or the atmosphere, which can lead to the state changing of ride height adjusting system. Thus, the considered system is characterized by pneumatic and mechanical coupling.

To further demonstrate the working principle of ride height adjusting system, a quarter ride height system model is used to describe the changing process of the ride height, as shown in Figure 2. Supposing that the sprung mass of suspension is a centralized mass M, the displacement of the sprung mass is changed by charging/discharging compressed air, and the ride height is adjusted to satisfy the vehicle driving performance. In the charging process, air from the air reservoir is supplied into the air spring through the pipeline as shown in Figure 2(a). In the discharging process, air from the air spring is released into the atmosphere through the pipeline as shown in Figure 2(b). In the practical application, the volume change rate and effective area of a diaphragm air spring are constant, and the height of the diaphragm air spring is similar to a piston motion of engine. Therefore, we can see that the characteristics of air springs and compressed gas lead to the nonlinearity of the ride height adjustment system. Additionally, the ride height adjustment system is disturbed by the road excitation when the vehicle was driven at different road conditions and speeds.

3. Mathematical Model of Ride Height Adjusting System with Random Disturbances

The random disturbance caused by irregularities of the road surface is filtered by the tire system, and it can be unified into the random change of suspension deflection [16]. The ride height adjusting system includes the processes of variable mass thermodynamics and vehicle dynamics, and a quarter-vehicle mathematical model is shown as [17]

$$\begin{aligned} m_s\ddot{Z}_s &= \left(P_3 - P_a\right) A_e - m_s g \\ &\quad - \left(C_3^{(1)}\dot{Z}_s + C_3^{(2)}\dot{Z}_s^2 + C_3^{(3)}\dot{Z}_s^3\right) - k_s\omega, \\ V_3\dot{P}_3 &= -\kappa P_3 \Delta V \dot{Z}_s + \kappa R T_3 q_m, \\ V_3 &= V_{30} + \Delta V Z_s, \end{aligned} \tag{1}$$

where m_s is the sprung mass; Z_s is the absolute displacement of sprung mass; P_3 is the internal absolute pressure of air spring; P_a is the atmospheric pressure; A_e is the effective area of air spring; g is the acceleration of gravity; $C_3^{(i)}$, $i = 1, 2, 3$ are one-degree term, quadratic term, and three-degree term of damping, respectively; k_s is the interference coefficient, relating to the character parameters of tire, air spring, and shock absorber; ω is the Gauss white noise with mean value of zero, relating to the irregularity of road surface and vehicle speed; κ is the adiabatic coefficient; q_m is the mass flow rate of inflow gas (or the outflow gas, which is negative); T_3 is the internal temperature of air spring; V_3 is the volume of air spring (subscript 0 stands for the initial volume of air spring), and ΔV is the volume change rate of air spring.

Choose the state variable of ride height tracking system as $X = \left[X_1 \;\; X_2 \;\; X_3\right]^T = \left[Z_s \;\; \dot{Z}_s \;\; P_3\right]^T$; that is, X_1, X_2, and X_3,

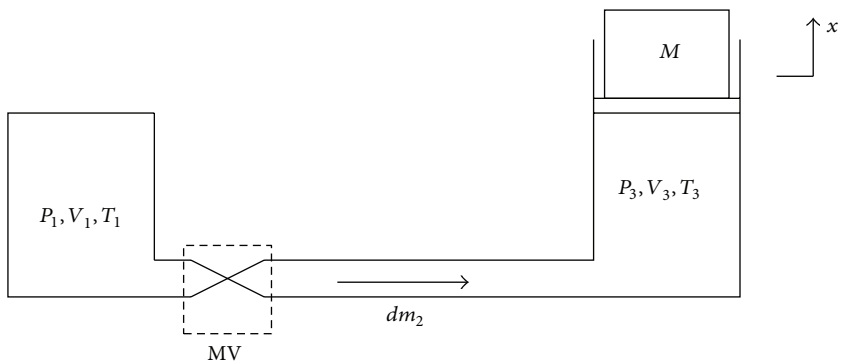

(a) Charging compressed air into air spring

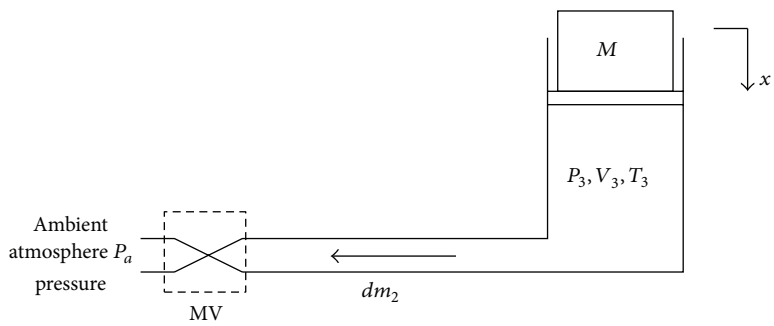

(b) Discharging compressed air from air spring

Figure 2: Structure of ride height adjustment for a quarter vehicle.

separately, are the ride height, the rate of ride height changing, and the pressure of air spring, so we can rewrite (1) as

$$\dot{X} = f(X) + g(X)u + q(X)\omega, \qquad y = h(X) = X_1, \tag{2}$$

where

$$f(X) = \begin{bmatrix} X_2 \\ \dfrac{1}{m_s}\left[X_2^3(X_3 - P_a)A_e - m_s g - \left(C_3^{(1)}X_2 + C_3^{(2)}X_2^2 C_3^{(3)}X_2^3\right)\right] \\ -\dfrac{\kappa \Delta V X_2}{V_{30} + \Delta V X_1}X_3, \end{bmatrix},$$

$$g(X) = \begin{bmatrix} 0 \\ 0 \\ \dfrac{\kappa R T_3}{V_{30} + \Delta V X_1} \end{bmatrix}, \qquad q(X) = \begin{bmatrix} 0 \\ -\dfrac{k_s}{m_s} \\ 0 \end{bmatrix}, \tag{3}$$

and the control input u is the air mass flow rate q_m.

4. Ride Height Adjusting System via Stochastic VSC Algorithm

4.1. Disturbance Decoupling of Dynamic Ride Height Adjusting System. For Lie derivative $L_q h(X) = 0$ and $L_q L_f h(X) = (-k_S/m_s) \neq 0$, the interference characteristic index ν is 2 [18, 19]. According to the differential geometry theory and $L_g L_f h(X) = L_g h(X) = 0$, $L_f h(X) = X_2$, and $L_f^2 h(X) = X_3$, (2) can be decoupled as

$$\dot{X} = \begin{bmatrix} L_f h(X) + L_g h(X)u + L_q h(X)\omega \\ L_f^2 h(X) + L_g L_f h(X)u + L_q L_f h(X)\omega \\ L_f^3 h(X) + L_g L_f^2 h(X)u + L_q L_f^2 h(X)\omega \end{bmatrix} = \begin{bmatrix} X_2 \\ X_3 + L_q L_f h(X)\omega \\ L_f^3 h(X) + L_g L_f^2 h(X)u + L_q L_f^2 h(X)\omega \end{bmatrix}, \tag{4}$$

where $L_q L_f^2 h(X) = C_3^{(1)} + 2\,C_3^{(2)}\,X_2 + 3\,C_3^{(3)}\,{X_2}^2 k_s/{m_s}^2$.

4.2. Variable Structure Control Approach to Design the Ride Height Adjusting System. The nonlinearity of the suspension system is composed of air spring and shock absorber, and the disturbance caused by road irregularity is the main characteristic of ride height adjusting system. VSC algorithm can obtain a perfect robustness to the interference and perturbation of the system [20] and will be proposed in

this paper. The control input function $u(t)$ is solved by defining the switching function vector $s(t)$. Considering (4), the decoupled system is

$$\dot{X} = \begin{bmatrix} X_2 \\ X_3 \\ L_f^3 h(X) \end{bmatrix} + \begin{bmatrix} 0 \\ 0 \\ L_g L_f^2 h(X) \end{bmatrix} u + \begin{bmatrix} 0 \\ L_q L_f h(X) \\ L_q L_f^2 h(X) \end{bmatrix} \omega. \tag{5}$$

The height adjusting system belongs to a single-input nonlinear system. Let $a(x) = L_f^3 h(X)$, $b(x) = L_g L_f^2 h(X)$, $\Gamma(X) = \begin{bmatrix} 0 \\ L_q L_f h(X) \\ L_q L_f^2 h(X) \end{bmatrix}$. Then, (5) is defined as $\dot{X} = f(X) + g(X)u + q(X)\omega$. Because the mean value of the normal white noise ω is zero and is relative to the Wiener process [21], (5) is a typically Itô-type stochastic system [22]. It is obvious that the ride height system cannot be globally controlled in the bandwidth region with 100% of total probability. So, the stochastic VSC input $u(t)$ may ensure that the sliding mode of the system could be controlled by a certain probability $1-\delta < 100\%$. We define that the switching function $s(t)$ must be controlled in a determined region by a certain probability, and it helps to solve the control law. The target equation can be represented as

$$P\{|s(t)| \le \mu\} = 1 - \delta. \tag{6}$$

If (6) is satisfied, the Itô-type stochastic system is asymptotically stable as a certain probability at the new balance point, and the control law of VSC input can be solved according to the above.

Firstly, define $e_1 = X_1 - X_d$, $e_2 = \dot{X}_1 - \dot{X}_d$, $e_3 = \ddot{X}_1 - \ddot{X}_d$, switching function $s(t) = c\begin{bmatrix} e_1 \\ e_2 \\ e_3 \end{bmatrix}$, and tracking height X_d, and substituting these into (5) yields

$$\dot{e} = \begin{bmatrix} X_2 \\ X_3 \\ a(x) \end{bmatrix} + \begin{bmatrix} 0 \\ 0 \\ b(x) \end{bmatrix} u + \Gamma(X)\omega. \tag{7}$$

The part 1.2-Variable Structure Control Strategy in literature [23] can be extended to the nonlinear stochastic system. To get the control law of the ride height adjusting system, we define $m_s = E\{s(t)|X(t)\}$ and $\bar{v} = c\Gamma\omega$. Noting that the variance of ω is σ^2, we can see that $\bar{v}$ is a Gaussian procedure with zero mean and variance $(c\Gamma)^2\sigma^2$. At the same time, the variance can be appropriately identified according to the deflection of suspension. The control law can be solved according to three conditions of the switching function.

(1) Consider $s(t) > \theta^{-1}W$, where θ $(0 < \theta < 1)$ is the regulating parameter of the switching function and W is defined by the equation $\int_{-W}^{W}(1/\sqrt{2\pi}\,\bar{\sigma})\exp(-x^2/2\bar{\sigma}^2)\,dx = 1-\varepsilon$. The equation $\int_{-\theta s(t)}^{\theta s(t)}(1/\sqrt{2\pi}\,\bar{\sigma})\exp(-(x-m^2)/2\bar{\sigma}^2)dx = 1-\varepsilon$ has two solutions of $m_1^+(t)$ and $m_2^+(t)$ which satisfy $m_1^+(t) < m_2^+(t)$; then the control law is

$$u(t) = u^+(t) \in b^{-1}(x)\left[-a(x) - c_1e_2 - c_2e_3 + m_1^+(t)(t,x), \right. \\ \left. -a(x) - c_1e_2 - c_2e_3 + m_2^+(t)(t,x)\right]. \tag{8}$$

(2) Consider $s(t) < -\theta^{-1}W$. The equation $\int_{\theta s(t)}^{-\theta s(t)}(1/\sqrt{2\pi}\,\bar{\sigma})\times \exp(-(x-m)^2/2\bar{\sigma}^2)dx = 1-\varepsilon$ has only two solutions of $m_1^-(t)$ and $m_2^-(t)$ which satisfy $m_1^-(t) < m_2^-(t)$; then the control law is

$$u(t) = u^-(t) \in b^{-1}(x)\left[-a(x) - c_1e_2 - c_2e_3 + m_1^-(t)(t,x), \right. \\ \left. -a(x) - c_1e_2 - c_2e_3 + m_2^-(t)(t,x)\right]. \tag{9}$$

(3) Consider $|s(t)| < \theta^{-1}W$:

$$u(t) = u_{eq}(t) = b^{-1}(x)\left[-a(x) - c_1e_2 - c_2e_3\right]. \tag{10}$$

The ideal design objective is that the confidence interval $1-\varepsilon$ is as large as possible, and the bandwidth $\theta^{-1}W_c$ of sliding motion is as small as possible, but these conditions are contradictory. The parameter of ε and the sliding motion band can be determined in the practical application.

4.3. Simulation of Dynamic Ride Height Control System. Control strategies such as stochastic VSC and PID control were compared by means of computational simulations with the help of the software MATLAB/Simulink. Simulation results were conducted to validate the accuracy and effectiveness of the proposed control algorithm. The simulation model consists of the variable mass thermodynamics system model of air spring, the quarter vehicle model, and the controller, as shown in Figure 3. The program of control algorithm is realized by using S-function, and this may be coded to make dSPACE controller acquaint (see Section 5). Since the disturbance magnitude is determined by the irregularity of road surface and the vehicle speed, the road model is built by the integral white-noise as shown in Figure 4, and the disturbance data may be the equipment of road simulator by format changing. Taking B level typical road and the speed 50 km/h as example, the disturbance magnitude is calculated after a low-pass filter of the tire and suspension damping, as shown in Figure 5.

For the comparison of stochastic VSC and PID control algorithm, the same adjusting time needs to be ensured, and the control parameters of K_P for PID [24, 25] and c_1 for VSC are predetermined according to the height adjusting time. Table 1 shows the major parameters of the ride height adjusting system used in the simulation. The ride height adjustment of ECAS has three switchmodes of "High Mode," "Normal Mode," and "Low Mode" in this study. "Normal Mode" is the normal ride height, and other modes are applied in special conditions. The height changing distance between "Normal Mode" and "High Mode" is 20 mm, and the height changing distance between "Normal Mode" and "Low Mode"

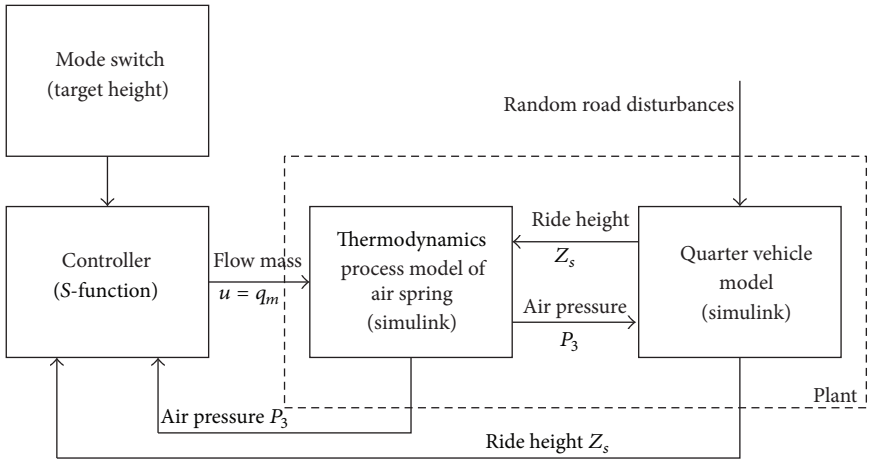

Figure 3: Simulation scheme.

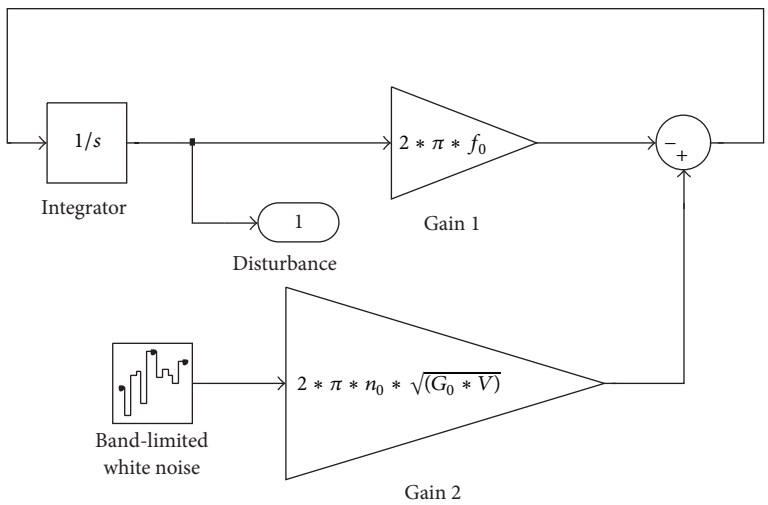

Figure 4: Road simulink model based on the integral white-noise.

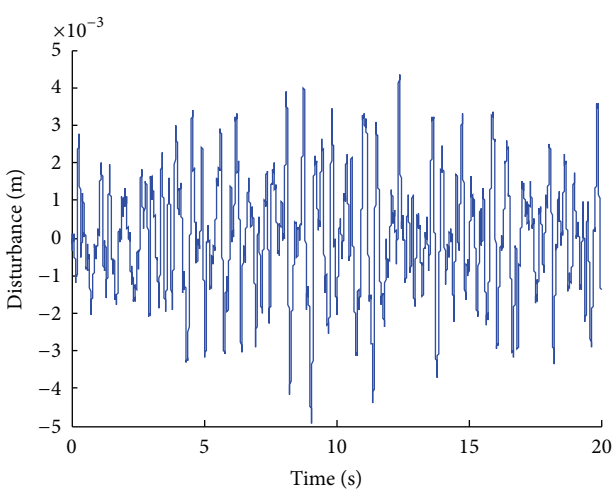

Figure 5: Disturbance magnitude of the B level typical road and the speed 50 km/h.

Table 1: Values of the ride height adjusting system parameters.

Parameters	Value
Sprung mass M (kg)	1074
First degree term of damping coefficient $C_3^{(1)}$ (N·s/m)	8832
Quadratic term of damping coefficient $C_3^{(2)}$ ((N·s/m)^2)	6245
Third degree term of damping coefficient $C_3^{(3)}$ ((N·s/m)^3)	−1568
Effective area A_e (m^2)	0.019
Volume changing rate ΔV (m^3/m)	0.025
Initial effective volume V_{30} (m^3)	0.0048
Volume of air reservoir V_1 (m^3)	0.06
Pressure of air reservoir P_1 (MPa)	1.0

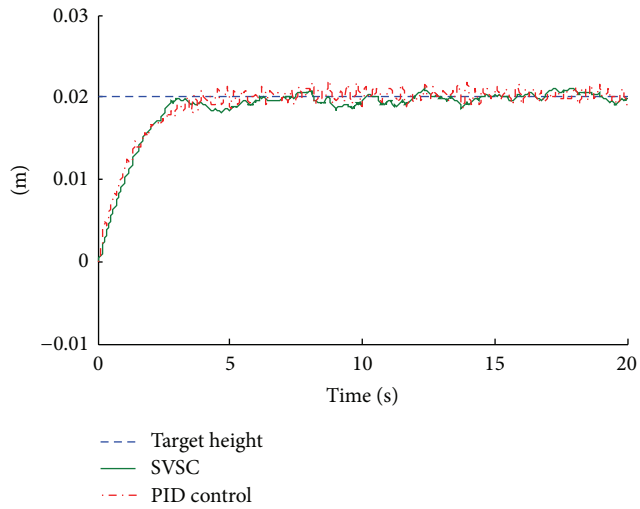

Figure 6: Lifting of the ride height.

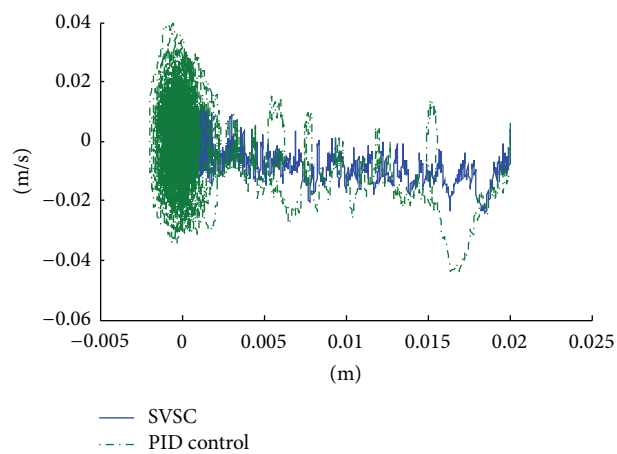

Figure 7: Lifting trajectory of height errors.

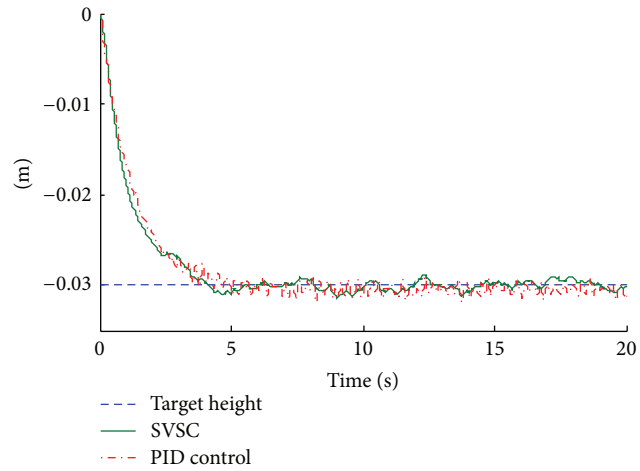

Figure 8: Lowering of the ride height.

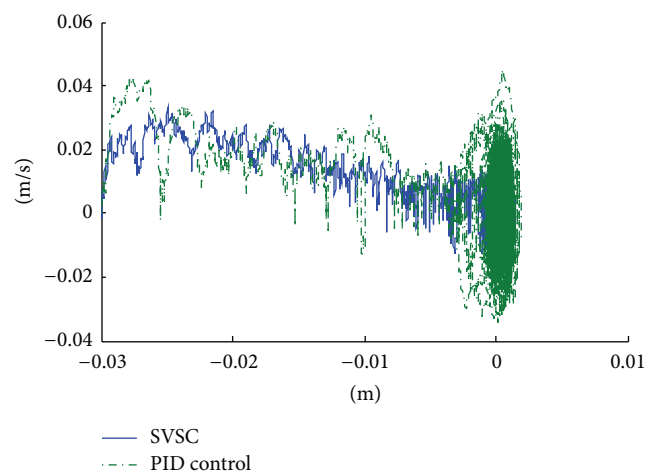

Figure 9: Lowing trajectory of height errors.

is 30 mm. So, we choose the control parameters $K_P = 0.8$, $K_I = 0.2$, and $K_D = 0.5$ for PID control and $c_1 = 15$ and $c_2 = 10$ for VSC.

The experimental results are obtained by applying the stochastic VSC and PID control techniques. Figures 6 and 7 show the results of the ride height lifting condition for the simulations. With the same adjusting time 4 s of both control methods, we can see from Figure 6 that the standard deviation using VSC technique is 3.4 mm, and the one using PID control technique is 3.6 mm. Figures 8 and 9 show the results of the ride height lowing condition for the simulations. By using the same analyzing method, it is observed from Figure 8 that the standard deviation using VSC technique is 4.8 mm and the one using PID control technique is 5.2 mm, under the same adjusting time 5 s of both control methods. Moreover, it is known from the trajectory of height errors in Figures 7 and 9 that the adjusting process of VSC system is more stable. Therefore, the simulation results show that the controller can greatly improve the adjusting stability and the system oscillation by using the stochastic VSC technique. Some performance comparison is shown in Table 2.

5. Test and Validation

The actual adjusting test was conducted with a semiphysical rig equipped with a ride height control system, where the full character was equivalent to six coil springs. Payload of the ride height system can be changed by increasing or decreasing the amount of the iron-sand bags. Random road disturbances created by the simulink model were input into the system of the Digital Hydraulic Servo Test Machine of INSTRON 8800. Meanwhile, the proposed stochastic VSC algorithm was programmed by means of Matlab/Simulink and directly downloaded into the dSPACE/RapidPro platform. In addition, a compressor was used to supply the high pressure air for the ride height system. In current testing applications, the control input calculated by stochastic SVC technique is the mass flow rate u, but the ON-OFF solenoid valve has just two states which cannot continuously adjust the mass flow rate.

Table 2: Performance index comparison of VSC and PID technique.

Performance index	SVSC		PID	
	Lifting	Lowering	Lifting	Lowering
Height deviation (mm)	3.4	4.8	3.6	5.2
Acceleration amplitude of vehicle body (m/s^2)	5.61	5.63	5.96	6.24
Acceleration of vehicle body r.m.s (m/s^2)	1.08	1.09	1.14	1.17
Height adjusting time (s)	4	5	4	5

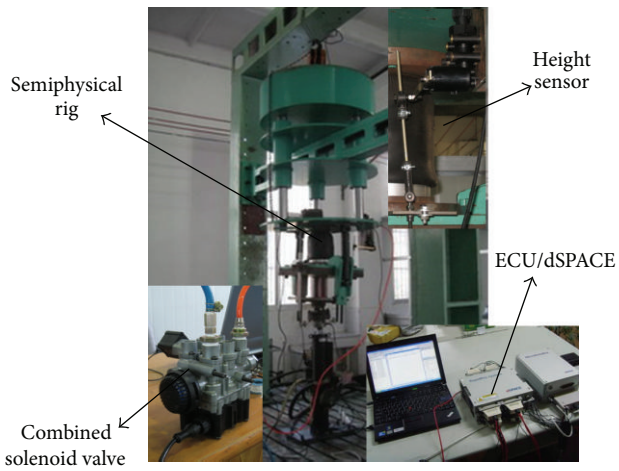

Figure 10: Testing rig of the ride height adjustment system.

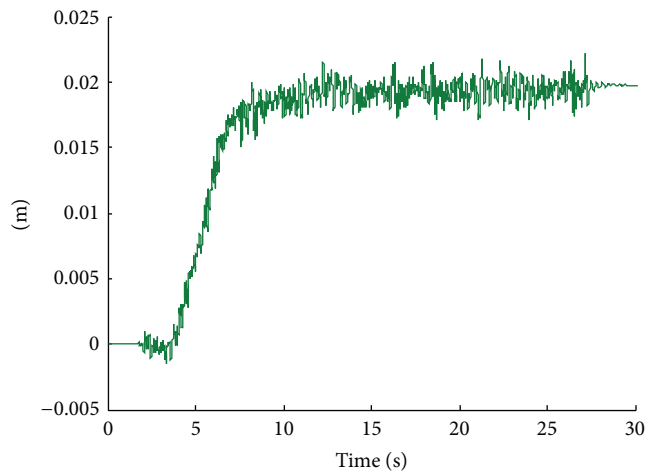

Figure 11: Height lifting testing.

So, the average mass flow rate during 0.062 seconds of the pulse period is controlled by the PWM duty cycle. Since the response speed of solenoid valve is limited, a working dead-zone of solenoid valve should be no less than 0.025 seconds. In addition, the solenoid valve for charging and discharging the compressed gas does not allow opening simultaneously which can reduce energy consumption. Figure 10 shows the configuration of the semi-physical rig test platform. The pressure of air spring is measured by an installed pressure sensor, and the ride height changing is measured by an installed height sensor.

Figures 11, 12, 13, and 14 show the testing results for the proposed control system. The adjusting time of both height lifting and lowering is over 5 s, because the route loss of the pipeline, the pressure decreasing of the air reservoir, and the saturation of control input jointly contribute to the more adjusting time than that of simulations. Nevertheless, the whole height adjusting process has no significant overshoot, and the proposed control system can stably switch the height mode and weaken the effect of disturbances. This result shows the robustness of the proposed controller.

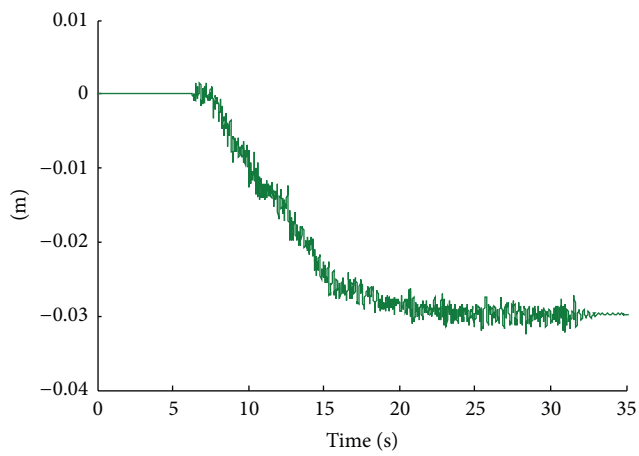

Figure 12: Height lowering testing.

6. Conclusions

This paper focuses on the ride height control system under the random road disturbances. The nonlinear model of ride height system, which contains the aerothermodynamics and vehicle dynamic processes, is established. On the basis of the present simulations and test, the following conclusion can be made.

(i) The ride height adjusting system is modeled as an Itô-type stochastic nonlinear system. Zero stability of the ride adjusting system will not be obtained by the control algorithm. The control law is obtained by using Gauss normal distribution in a certain probability, which can be carried out to weaken the random disturbance of the road irregularities.

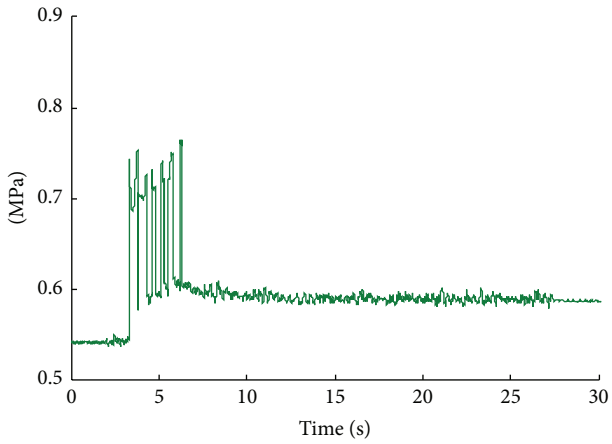

Figure 13: Pressure changing of air spring of ride height lifting with random disturbances.

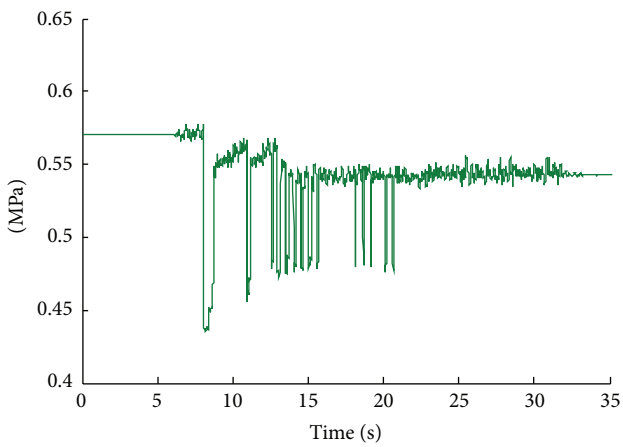

Figure 14: Pressure changing of air spring of ride height lowering with random disturbances.

(ii) Under the same adjusting time, the proposed controller and PID controller both can achieve the same height accuracy, but the proposed controller has a better ride performance than that of the PID controller during the height adjusting process, which shows that the proposed controller is suitable for the current system.

(iii) Rig tests show that the proposed control method is feasible and can satisfy the stability performance of the ride height adjusting system.

Conflict of Interests

No conflict of interests exists in the submission of this paper, and the paper is approved by all authors for publication.

Disclosure

The authors would like to declare that the work described was an original research that has not been published previously and is not under consideration for publication elsewhere, in whole or in part.

Acknowledgments

This study was supported by the National Natural Science Foundation of China under Grant no. 51105177, the Research Fund for the Doctoral Program of the Higher Education of China under Grant no. 20113227120015, the Natural Science Foundation of Jiangsu Province under Grant no. BK20131255, the Scientific Research Foundation for Advanced Talents, Jiangsu University under Grant no. 11JDG047, and the Hunan Provincial Natural Science Foundation of China under Grant 12JJ6036. Xing Xu gratefully acknowledges these support agencies. The authors also wish to extend their sincere acknowledgments to the anonymous reviewers for providing many invaluable references and suggestions.

References

[1] J. Youn, I. Park, and M. Sunwoo, "Heuristic resource allocation and scheduling method for distributed automotive control systems," *International Journal of Automotive TechNology*, vol. 14, no. 4, pp. 611–624, 2013.

[2] M. Hirose, S. Matsushige, S. Buma, and K. Kamiya, "TOYOTA electronic modulated air suspension system for the 1986 soarer," *IEEE Transactions on Industrial Electronics and Control Instrumentation*, vol. 35, no. 2, pp. 193–200, 1988.

[3] A. W. Burton, A. J. Truscott, and P. E. Wellstead, "Analysis, modelling and control of an advanced automotive self-levelling suspension system," *IEE Proceedings: Control Theory and Applications*, vol. 142, no. 2, pp. 129–139, 1995.

[4] A. Bemporad and M. Morari, "Verification of hybrid systems via mathematical programming," in *Hybrid Systems: Computation and Control, No*, vol. 1569, pp. 31–45, 1999.

[5] Z. B. Shuai, H. Zhang, J. M. Wang, J. Q. Li, and M. G. Ouyang, "Combined AFS and DYC control of four-wheel-independent-drive electric vehicles over CAN network with time-varying delays," *IEEE Transactions on Vehicular Technology*, 2013.

[6] Y. Song, "Study on ride height PID control technology of air suspension vehicle," *Journal of Hubei Automotive Industries Institute*, vol. 21, no. 2, pp. 1–4, 2007.

[7] Z. Chen, D. Jin, G. Ma, X. Huang, and L. Zhao, "Simulation of variable structure control strategy in combination with PID for vehicle body height," *Journal of Tsinghua University*, vol. 39, no. 8, pp. 72–75, 1999.

[8] W. B. Yu, L. Z. Zhang, and N. Li, "Study of the fuzzy control of air suspension of vehicle height system," *Electronic Instrumentation Customer*, vol. 13, no. 2, pp. 6–8, 2006.

[9] Q. Y. Yang, *Research on Matching and Inflation/Deflating of Suspension System in ECAS-Bus*, Jiangsu University, Zhenjiang, China, 2008.

[10] X. Xu, Z. Chen, L. Quan, Z. Li, and K. Zhou, "Real-time tracking of ride height for bus with electronically controlled air suspension," *Journal of Mechanical Engineering*, vol. 47, no. 2, pp. 136–141, 2011.

[11] X. Xu, Z. Z. Chen, and Z. X. Li, "Investigation on modeling and control of body height adjustment for bus with electrically controlled air suspension," *Automobile Technology*, no. 11, pp. 42–46, 2009.

[12] Y. Y. Feng and Q. G. Du, "Investigation on body height adjustment for semi-trailer with electrically controlled air suspension and design of fuzzy/PWM controller," *Science Technology and Engineering*, vol. 32, no. 10, pp. 7974–7979, 2010.

[13] H. Kim and H. Lee, "Height and leveling control of automotive air suspension system using sliding mode approach," *IEEE Transactions on Vehicular Technology*, vol. 60, no. 5, pp. 2027–2041, 2011.

[14] H. Zhang, Y. Shi, and M. X. Liu, "H_∞ step tracking control for networked discrete-time nonlinear systems with integral and predictive actions," *IEEE Transactions on Industrial Informatics*, vol. 9, no. 1, pp. 337–345, 2013.

[15] H. Zhang and Y. Shi, "Observer-based H_∞ feedback control for arbitrarily time-varying discrete-time systems with intermittent measurements and input constraints," *Journal of Dynamic Systems, Measurement, and Control*, vol. 134, no. 6, Article ID 061008, 12 pages, 2012.

[16] H. Zhang, Y. Shi, and A. Saadat Mehr, "Robust non-fragile dynamic vibration absorbers with uncertain factors," *Journal of Sound and Vibration*, vol. 330, no. 4, pp. 559–566, 2011.

[17] X. Xu, *Study on Control of Ride Height Nonlinear System for Bus with ECAS*, Jiangsu University, Zhenjiang, China, 2010.

[18] M. Riccardo and T. Patrizio, *Design of Nonlinear System-Adaptive and Robust Control of Differential Geometry*, Publishing House of Electronics Industry, Beijing, China, 2006.

[19] H. Zhang, Y. Shi, and A. S. Mehr, "Robust H_∞ PID control for multivariable networked control systems with disturbance/noise attenuation," *International Journal of Robust and Nonlinear Control*, vol. 22, no. 2, pp. 183–204, 2012.

[20] P. Wilfrid and P. B. Jean, *Sliding Mode Control in Engineer*, Marcel Dekker, New York, NY, USA, 2002.

[21] B. T. Wu, Q. S. Li, and Y. W. Yang, *Stochastic Processes and Stochastic Differential Equations*, University of Electronic Science and Technology of China Press, Chengdu, China, 1994.

[22] H. Zhang, Y. Shi, and B. X. Mu, "Optimal H_∞-based linear-quadratic regulator tracking control for discrete-time Takagi-Sugeno fuzzy systems with preview actions," *Journal of Dynamic Systems, Measurement, and Control*, vol. 135, no. 4, Article ID 044501, 5 pages, 2013.

[23] F. Zheng, M. A. Cheng, and W. B. Gao, "Incomplete state information variable structure control of stochastic systems," *Acta Aeronautica et Astronautica Sinica*, vol. 15, no. 7, pp. 870–876, 1994.

[24] K. J. Åström and T. Hägglund, "Revisiting the Ziegler-Nichols step response method for PID control," *Journal of Process Control*, vol. 14, no. 6, pp. 635–650, 2004.

[25] H. Zhang, Y. Shi, and A. Saadat Mehr, "Robust static output feedback control and remote PID design for networked motor systems," *IEEE Transactions on Industrial Electronics*, vol. 58, no. 12, pp. 5396–5405, 2011.

Hindawi Publishing Corporation
Mathematical Problems in Engineering
Volume 2013, Article ID 208753, 9 pages
http://dx.doi.org/10.1155/2013/208753

Research Article

A Study on Control Strategy of Regenerative Braking in the Hydraulic Hybrid Vehicle Based on ECE Regulations

Tao Liu, Jincheng Zheng, Yongmao Su, and Jinghui Zhao

School of Automobile Engineering, Harbin Institute of Technology, Weihai 264209, China

Correspondence should be addressed to Jincheng Zheng; zhengjincheng.com@163.com

Received 1 July 2013; Revised 19 August 2013; Accepted 27 August 2013

Academic Editor: Hui Zhang

This paper establishes a mathematic model of composite braking in the hydraulic hybrid vehicle and analyzes the constraint condition of parallel regenerative braking control algorithm. Based on regenerative braking system character and ECE (Economic Commission of Europe) regulations, it introduces the control strategy of regenerative braking in parallel hydraulic hybrid vehicle (PHHV). Finally, the paper establishes the backward simulation model of the hydraulic hybrid vehicle in Matlab/simulink and makes a simulation analysis of the control strategy of regenerative braking. The results show that this strategy can equip the hydraulic hybrid vehicle with strong brake energy recovery power in typical urban drive state.

1. Introduction

Regenerative braking is an important technology of the hybrid vehicles that appeals to very strong research interests all over the world [1–5]. Research on control strategy is one of most important topics of regenerative braking and can be roughly categorized into two types according to the propose of research. One is to enhance the braking performance and driving comfort. The other is to improve the regenerative efficiency and to save resources. Almost the present research concentrates on regenerative braking in many of electric vehicles (EV), hybrid electric vehicles (HEV), and plug-in hybrid electric vehicles. A mass of solutions in regenerative braking system control have been carried out. For example, Kim et al. [6] and Peng et al. [7] put forward two regenerative braking strategies based on the fuzzy control to pursue high regenerative efficiency and good braking performance. The simulation results indicated that both regenerative braking control strategies could increase the fuel economy for HEV and improve vehicle stability. Oh et al. [8], Jo et al. [9], Zhang et al. [10], Moreno et al. [11], and others have carried out research studies in this field as well. Nevertheless, pieces of the literature devoted to hydraulic hybrid vehicle (HHV) are relatively scarce. Wu et al. [12] proposed a strategy for passenger cars based on dividing the accumulator volume into two parts, one for regeneration and the other for road-decoupling. Hui et al. [13] presented a fuzzy torque control strategy based on vehicle load changes for real-time controlling the energy distribution in PHHV. Though they proposed a methodology of braking to improve the fuel economy in a typical urban cycle, the braking characteristics were not investigated deeply. What is more, the efficiency of brake energy recovery and the distribution of braking force were not considered and optimized at all. The design of regenerative braking strategy in HHV remains a problem yet. Compared with electrified vehicles, HHV has some advantage, particularly for vehicles containing hydraulic equipment on board [14]. For instance, hydraulic accumulator is of higher power density and ability to accept the high rates and high frequencies of charging and discharging [15]. Besides, the service life of a hydraulic accumulator as the storage is more than a battery. Therefore, HHV has a greater potential than electrified vehicles, and the research on that makes much sense. Generally, there are two types of hydraulic hybrid systems: parallel hydraulic hybrid vehicle (PHHV) and series hydraulic hybrid vehicle (SHHV). PHHV uses a traditional mechanical drive train with hydraulic pump/motor unit inline between the transmission and axle [16]. The configuration of PHHV is simpler than that of SHHV and easier to be refitted. Therefore, PHHV occupies large proportion of HHV at home and abroad.

However, it is hard for PHHV driven by rear wheel to obtain a good braking stability as well as an effective regenerative energy recovery. One reason for this phenomenon is that the rear wheel is easy for locking when the hydraulic regenerative braking force is exerted on the back axle. Therefore, when the hydraulic braking force is strong enough, the back-axle utilization adhesion curves may surpass the constraint of ECE (Economic Commission of Europe) regulations, resulting in the premature rear lock and decline in the utilization adhesion coefficient. To cope with this situation, the paper puts forward the control strategy of regenerative braking in the parallel composite braking system, which consists of the conventional fictional braking system and hydraulic regenerative braking system. The control strategy is revised according to the external character of the parallel composite braking system and ECE regulations. The simulation results demonstrate its effectiveness in improving the brake energy recovery in typical urban drive state.

2. Configuration of PHHV

This rear-wheel-drive hydraulic hybrid vehicle, shown in Figure 1, consists primarily of an internal combustion engine, a high pressure accumulator, low pressure reservoir, and a variable displacement hydraulic pump/motor unit. The primary power source is the same diesel engine used in the conventional vehicle. The transmission, propeller shaft, and the differential and driving shaft are the same as those in the conventional vehicle. The hydraulic pump/motor is coupled with the propeller shaft via a torque coupler [17, 18]. The basic parameters of the parallel hydraulic hybrid vehicle studied in this paper are as shown in Table 1.

During deceleration, the hydraulic pump/motor decelerates the vehicle while operating as a pump to capture the energy normally lost to friction brakes in a conventional vehicle. Also, when the vehicle brake is applied, the hydraulic pump/motor uses the braking energy to charge the hydraulic fluid from a low pressure hydraulic accumulator into a high-pressure accumulator, increasing the pressure of the nitrogen gas in the high pressure accumulator. The high pressure hydraulic fluid is used by the hydraulic pump/motor unit to generate torque during the next vehicle launch and acceleration [19–21]. It is designed and sized to capture braking energy from normal, moderate braking events and is supplemented by friction brakes for aggressive braking.

Ignoring the vehicle rolling resistance moment, the front wheel braking force F_{f1} and the rear wheel braking force F_{f2} are given by the following, respectively:

$$F_{f1} = \frac{\varphi\left(Gb + m\left(du/dt\right)h_g - \left(C_D A u^2/21.15\right)h_g\right)}{L}, \tag{1}$$

$$F_{f2} = \frac{\varphi\left(Ga - m\left(du/dt\right)h_g + \left(C_D A u^2/21.15\right)h_g\right)}{L}, \tag{2}$$

where φ is the adhesion coefficient between tire and road surface, G is the vehicle gravity (N), m is the vehicle quality (kg), a is the distance from vehicle center of gravity to front axle center line (m), b is the distance from vehicle center of gravity to rear axle center line (m), L is wheel base (m), h_g is the height of the center of gravity (m), C_D is the air resistance coefficient, A is the frontal area (m^2), u and is the vehicle speed (m/s).

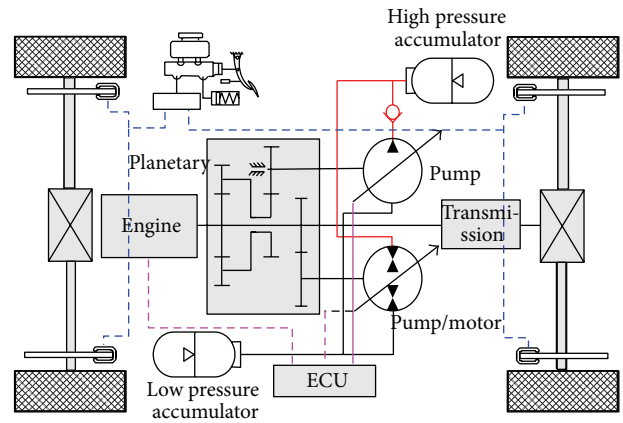

Figure 1: Configuration of PHHV.

Table 1: Basic parameters of PHHV.

Name	Parameter
Wheel radius	0.28 m
Maximum weight	1795 kg
Complete vehicle kerb mass	865 kg
Final drive axle ratio	4.129
Volume of the hydraulic accumulator	25 L
Filling pressure of the hydraulic accumulator	12 MPa
Maximum working pressure of the hydraulic accumulator	31 MPa
Minimum working pressure of the hydraulic accumulator	15 MPa
Torque coupler gear ratio	1.3
Hydraulic pump/motor capacity	A4VG56/56 mL/r

3. Design of Parallel Regenerative Braking Control Algorithm

During the composite braking, the brake severity is usually set at 0.1~0.7. After this phase, the regenerative braking force on the rear wheel, will rise, which will raise the utilization adhesion coefficient of the rear wheel whereas that of the front wheel goes down. As a result, the utilization adhesion coefficient on the rear wheel tends to surpass the constraint of ECE regulations, while the front wheel tends to be safer, with the possibility of lock being lowered in a further way.

In order to ensure the vehicle braking performance, ECE regulations demand the following: when the adhesion

coefficient φ is between 0.2 and 0.8, the braking severity is $z \geq 0.1 + 0.7(\varphi - 0.2)$; thus, the following is gained:

$$F_{xb2} \leq \frac{z + 0.04}{0.7} \frac{\left(a - zh_g\right) G}{L}, \qquad F_{xb1} = Gz - F_{xb2}. \tag{3}$$

As shown in Figure 2, the maximum rear wheel braking force curves are depicted in the wheel braking force distribution diagram, where line OC denotes line β, over which the ideal wheel braking force distribution line I lies. The vehicle synchronization adhesion coefficient is 0.75. The regulations can be satisfied with the ignorance of the regenerative braking system character. Line AB in the figure denotes the composite braking phase when the energy can be recovered to the largest degree, and OA is the biggest braking force during the pure regenerative braking. In order to prevent the premature lock of rear wheels during massive braking ($z > 0.7$) of the vehicle, the right boundary line goes down along with the line r where brake severity is 0.7, as is shown in Figure 2 as line BC.

In the composite braking phase shown in Figure 2, the braking force on front and rear wheels is as follows:

$$F_{xb2} = K\left(F_{xb1} + 0.115G\right) \quad \left(0.1 < z < z_{\mathrm{B}}\right),$$
$$F_{xb2} = \frac{-0.7h_g}{L + 0.7h_g} F_{xb1} + \frac{0.7Gb}{L + 0.7h_g} \quad \left(z_{\mathrm{B}} \leq z \leq 0.7\right), \tag{4}$$

where z_{B} is brake severity corresponding to point B, K is slope of line AB.

Here $K = 1.1407$, $z_{\mathrm{B}} = 0.45$. After the revise according to points A and C, the limit values of braking severity z are 0.127 and 0.715. The regenerative braking force $F_{\mathrm{p/m}}$ can be gained by the regenerative braking control algorithm:

$$F_{\mathrm{p/m}} = \begin{cases} \dfrac{T_{\mathrm{p/m}}}{r} = Gz, & z \leq 0.127, \\ Gz - \dfrac{G\left(z - 0.115K\right)}{\left(1 + K\right)\beta}, & 0.127 < z \leq z_{\mathrm{B}}, \\ Gz - \dfrac{Gz\left(L + 0.7h_g\right) - 0.7Ga}{L\beta}, & z_{\mathrm{B}} < z < 0.715. \end{cases} \tag{5}$$

After the concrete parameters of the hydraulic hybrid vehicle are input into the above equations, the relation in conditions of different brake severity and hydraulic accumulator pressure between regenerative braking system character and the algorithm distribution results is gained, which is depicted in Figure 3. As is shown in the figure, when hydraulic accumulator pressure is relatively lower and the brake severity $z \leq 0.1$ and $z \geq 0.5$, the regenerative braking distribution result is that the demanded regenerative braking force is lower than regenerative braking system character, proving that the regenerative braking power of the system has not been fully performed. In the phase of $0.1 < z < 0.5$, the regenerative braking power is far from the requirements of the algorithm. Therefore, it is necessary to add character constraint of the regenerative braking system.

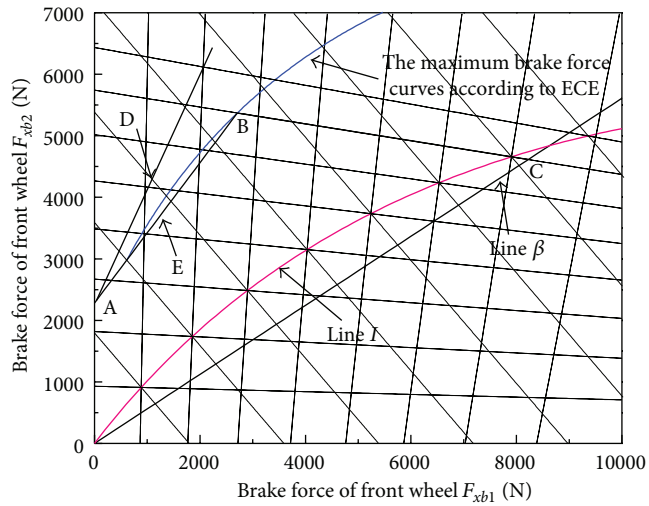

Figure 2: Brake force distribution curves of PHHV.

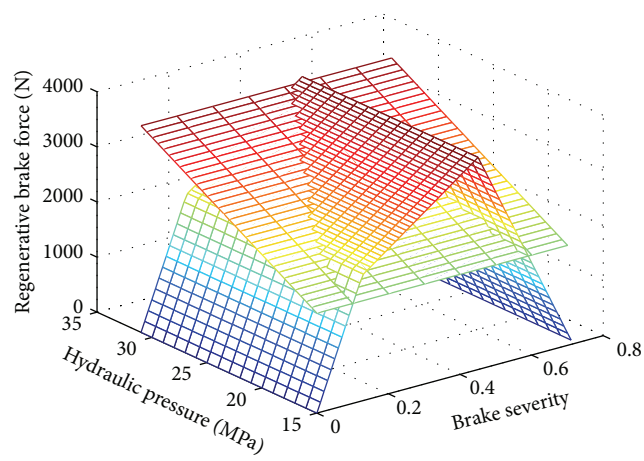

Figure 3: Relation between regenerative braking system character and algorithm distribution results.

4. The Parallel Regenerative Braking Control Algorithm Based on Regenerative Braking System Character and ECE Regulations

The regenerative braking force is linearly related with hydraulic accumulator pressure. Therefore, the basic thought of control algorithm is that before the distribution of each time the maximum braking power $F_{\mathrm{p/m\_max}}$ of the regenerative braking system is confirmed according to the driving speed and hydraulic accumulator pressure; the pure regenerative braking is adopted when the total braking force demand F_{bd} corresponding to braking severity z meets the condition of $F_{\mathrm{bd}} < F_{\mathrm{p/m\_max}}$; otherwise, the composite braking is adopted. In the process of composite braking, the regenerative braking force will be preferential for use, and the frictional braking force will supplement the rest. The detailed process of algorithm distribution is as follows.

(1) According to target brake severity, the total braking force demand is calculated as $F_{\mathrm{bd}} = Gz$. The maximum regenerative braking power $F_{\mathrm{p/m\_max}}$ at the moment of the hydraulic pump/motor is gained by referring to the pressure phenomena of the accumulator.

(2) If $F_{\mathrm{p/m\_max}} \geq F_{\mathrm{bd}}$, the braking force will be fully provided by the hydraulic pump/motor, when $F_{\mathrm{p/m}} = F_{\mathrm{bd}}$ and both the front wheel frictional braking force F_f and the rear F_r will be 0.

(3) If $F_{\mathrm{p/m\_max}} < F_{\mathrm{bd}}$, the frictional braking force on front and rear wheels goes up along with line β, when the regenerative braking force is $F_{\mathrm{p/m}} = F_{\mathrm{p/m\_max}}$, the frictional braking force on rear wheels is $F_r = (1-\beta)(F_{\mathrm{bd}}-F_{\mathrm{p/m\_max}})$, and the hydraulic braking force on front wheels is $F_f = \beta(F_{\mathrm{bd}} - F_{\mathrm{p/m\_max}})$. Therefore, the regenerative braking force during braking can be gained and is shown in Figure 4, while the simultaneous simulation results of front and rear axle utilization coefficients are in Figure 5.

According to Figures 4 and 5, as the algorithm ensures the maximum regenerative braking power in the first place, the braking force distribution surpasses the constraint of ECE regulations, resulting in the necessity of adding ECE regulations constraints into the algorithm. After the calculation, the relation between the maximum limiting line of ECE regulations to rear wheel braking force and the front-rear force distribution line in the phase of the maximum algorithm regenerative braking force is shown in Figure 2.

It can be seen from Figure 2 that line AD which denotes the basic algorithm distribution is beyond ECE regulations. Thereby, taking point D, for example, the distribution results should be revised onto the point E intersected by ECE line and the corresponding equal-braking-severity line. The detailed revise algorithm is as follows.

(1) The regenerative braking power $F_{\mathrm{p/m\_max}}$ should be gained from pressure phenomena of hydraulic accumulator by referring to the target brake severity z and the total braking force demand F_{bd}.

(2) If $F_{\mathrm{p/m\_max}} \geq F_{\mathrm{bd}}$, from the following equations

$$\begin{aligned} F_{xb2} &= K\left(F_{xb1} + 0.115G\right) \\ 0 &= Gz - F_{xb1}, \end{aligned} \tag{6}$$

$F_{xb2} = F_{xb2\mathrm{A}}$ can be gained, where $F_{xb2\mathrm{A}}$ denotes the rear wheel braking force corresponding to point A.

If $F_{\mathrm{p/m\_max}} \leq F_{xb2\mathrm{A}}$, the braking force will be completely provided by regenerative braking, when the regenerative braking moment is $T_{\mathrm{p/m}} = F_{\mathrm{bd}}/r$ and the front wheel frictional braking force F_f and the rear F_r are both 0, which should be revised otherwise. The detail is as follows.

If $0 < z \leq 0.127$, the regenerative braking moment is $T_{\mathrm{p/m}} = F_{\mathrm{bd}}/r$ and both the front frictional braking force F_f and the rear F_r are 0.

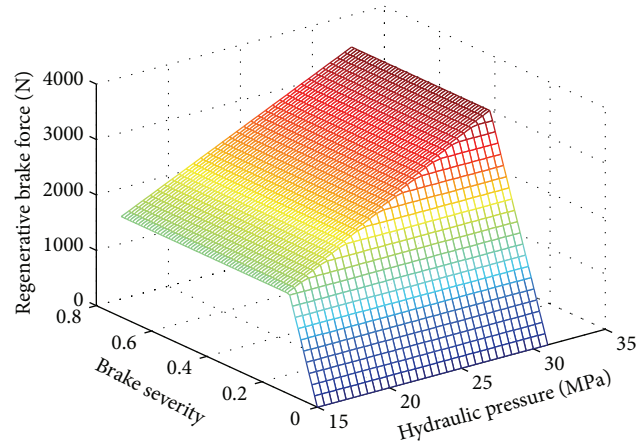

Figure 4: The results of the algorithm allocation based on the constrained regenerative braking system.

If $0.127 < z \leq 0.2$,

$$\begin{aligned} F_{xb2} &= K\left(F_{xb1} + 0.115G\right), \\ F_f &= F_{xb1} = Gz - F_{xb2}, \\ F_f &= \frac{\beta}{1-\beta}F_r, \\ F_m &= F_{\mathrm{bd}} - F_r - F_f. \end{aligned} \tag{7}$$

If $0.2 < z \leq 0.45$,

$$\begin{aligned} F_{xb2} &= \frac{z+0.04}{0.7}\frac{\left(a - zh_g\right)G}{L}, \\ F_f &= F_{xb1} = Gz - F_{xb2}, \\ F_f &= \frac{\beta}{1-\beta}F_r, \\ F_m &= F_{\mathrm{bd}} - F_r - F_f. \end{aligned} \tag{8}$$

If $0.45 < z \leq 0.715$,

$$\begin{aligned} F_{xb2} &= -\frac{0.7h_g}{L+0.7h_g}F_{xb1} + \frac{0.7Ga}{L+0.7h_g}, \\ F_f &= F_{xb1} = Gz - F_{xb2}, \\ F_f &= \frac{\beta}{1-\beta}F_r, \\ F_m &= F_{\mathrm{bd}} - F_r - F_f. \end{aligned} \tag{9}$$

(3) If $F_{\mathrm{p/m\_max}} < F_{\mathrm{bd}}$, the predistributed front-rear wheel frictional braking force rises along line β. The regenerative braking force is $F_{\mathrm{p/m}} = F_{\mathrm{p/m\_max}}$, while the rear wheel frictional braking force is $F_r = (1-\beta)(F_{\mathrm{bd}} - F_{\mathrm{p/m\_max}})$ and the front is $F_f = \beta(F_{\mathrm{bd}} - F_{\mathrm{p/m\_max}})$.

If $0 < z \leq 0.127$, the regenerative braking force is $F_m = F_{\max}$, while the rear wheel frictional braking force is $F_r = (1-\beta)(F_{\mathrm{bd}} - F_{\mathrm{p/m\_max}})$ and the front is $F_f = \beta(F_{\mathrm{bd}} - F_{\mathrm{p/m\_max}})$.

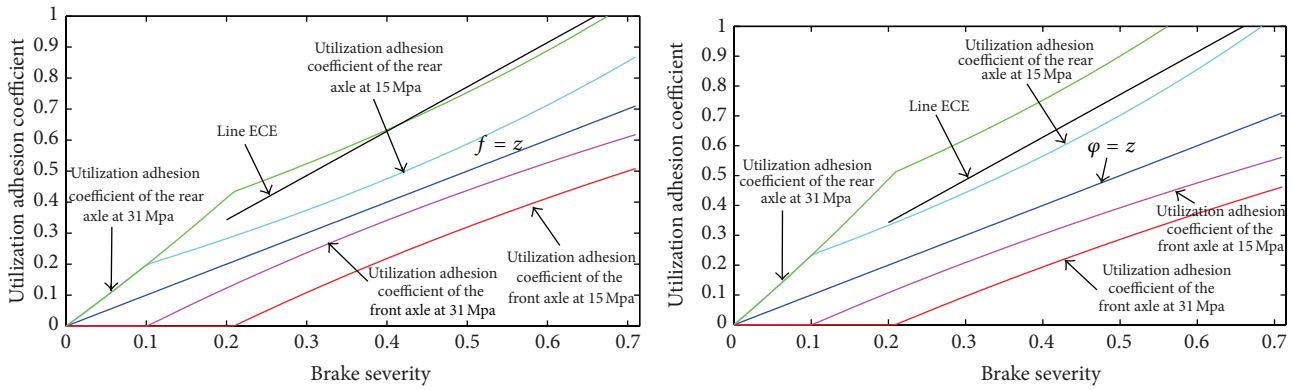

(a) Full load (b) Empty load

Figure 5: Simulation results of front and rear axle utilization coefficients.

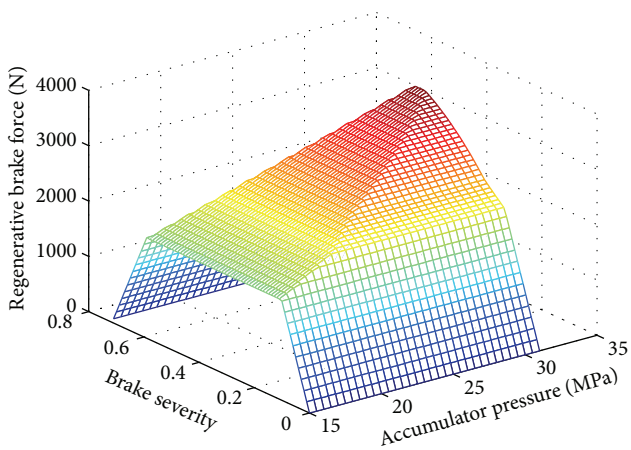

Figure 6: The results of braking force distribution revised according to ECE regulations.

If $0.127 < z \leq 0.2$, from the equations

$$F_{xb2} = K\left(F_{xb1} + 0.115G\right),$$
$$F_{xb1} = Gz - F_{xb2}, \tag{10}$$

$F_{xb1} = F_{xb1\mathrm{E}}$ can be gained, where $F_{xb1\mathrm{E}}$ denotes the front wheel braking force corresponding to point E. If the predistribution result is $F_f > F_{xb1\mathrm{E}}$, the revise is not necessary, while this is needed otherwise. The revise results are as follows

$$F_{xb2} = K\left(F_{xb1} + 0.115G\right),$$
$$F_f = F_{xb1} = Gz - F_{xb2},$$
$$F_f = \frac{\beta}{1-\beta}F_r, \tag{11}$$
$$F_{\mathrm{p/m}} = F_{\mathrm{bd}} - F_r - F_f.$$

If $0.2 < z \leq 0.45$, from the equations

$$F_{xb2} = \frac{z + 0.04}{0.7}\frac{\left(a - zh_g\right)G}{L},$$
$$F_f = F_{xb1} = Gz - F_{xb2}, \tag{12}$$

$F_{xb1} = F_{xb1\mathrm{E}}$ can be gained, where $F_{xb1\mathrm{E}}$ denotes the front wheel braking force corresponding to point E. If the predistribution result is $F_f > F_{xb1\mathrm{E}}$, the revise is not necessary, while this is needed otherwise. The revise results are as follows

$$F_{xb2} = \frac{z + 0.04}{0.7}\frac{\left(a - zh_g\right)G}{L},$$
$$F_f = F_{xb1} = Gz - F_{xb2},$$
$$F_f = \frac{\beta}{1-\beta}F_r, \tag{13}$$
$$F_{\mathrm{p/m}} = F_{\mathrm{bd}} - F_r - F_f.$$

If $0.45 < z \leq 0.715$, from the equations

$$F_{xb2} = \frac{-0.7h_g}{L + 0.7h_g}F_{xb1} + \frac{0.7Ga}{L + 0.7h_g},$$
$$F_f = F_{xb1} = Gz - F_{xb2}, \tag{14}$$

$F_{xb1} = F_{xb1\mathrm{E}}$ can be gained, where $F_{xb1\mathrm{E}}$ denotes the front wheel braking force corresponding to point E. If the predistribution result is $F_f > F_{xb1\mathrm{E}}$, the revise is not necessary, while this is needed otherwise. The revise results are as follows

$$F_{xb2} = \frac{-0.7h_g}{L + 0.7h_g}F_{xb1} + \frac{0.7Ga}{L + 0.7h_g},$$
$$F_f = F_{xb1} = Gz - F_{xb2},$$
$$F_f = \frac{\beta}{1-\beta}F_r, \tag{15}$$
$$F_{\mathrm{p/m}} = F_{\mathrm{bd}} - F_r - F_f.$$

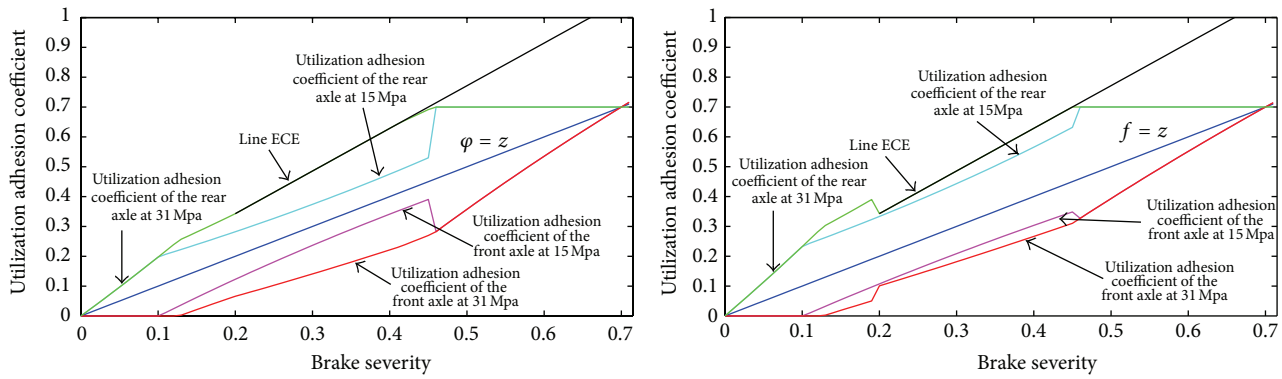

(a) Full load (b) Empty load

Figure 7: Simulation results of revised front and rear axle utilization coefficients.

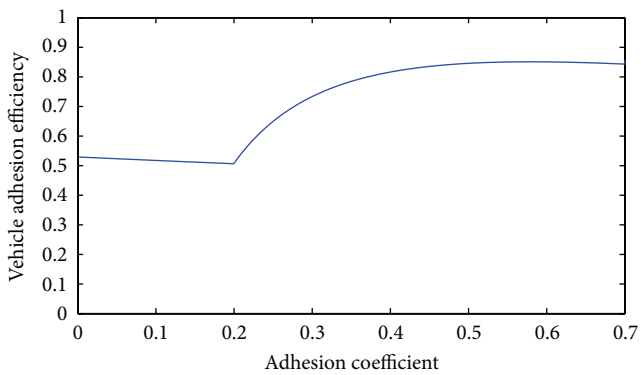

Figure 8: The vehicle adhesion efficiency based on parallel regenerative braking.

The results of braking force distribution revised according to ECE regulations are shown in Figure 6, and the utilization adhesion coefficient curves are shown in Figure 7.

The comparisons between Figures 4 and 6 as well as Figures 5 and 7 show that the revised zone is relatively large and the distribution results after revise can satisfy the requirements of both regenerative braking system and ECE regulations.

According to Figure 2 which tells the distribution phenomena, on the condition of the remaining braking force ratio β, ECE regulation limits can be easily exceeded if the parallel regenerative braking control algorithm without revise by ECE is adopted, aiming to fully perform the regenerative braking power. Although the braking force distribution results revised according to ECE regulations meet the requirement of the regulations, the braking energy recovery efficiency is affected, however, resulting in the necessity of rematch to the braking force ratio β to improve the safety and energy recovery efficiency of hydraulic hybrid vehicles.

According to Figure 7, in order to recover the braking energy to the largest degree, the rear axle will be preferentially exerted on regenerative braking force; thus, the utilization adhesion coefficient on the rear axle is above that of the front. Therefore, the rear wheels will lock every time before the front ones, which is a dangerous condition. Hence, the hybrid vehicle driven by rear wheels must be equipped with ABS (antilock brake system), which controls the performance of regenerative braking system. At the same time, however, the vehicle adhesion efficiency should satisfy the requirement of regulations of $\varepsilon \geq 0.75$.

The vehicle adhesion efficiency when braking is depicted in Figure 8. When the vehicle brakes on the road with extralow adhesion coefficient (below 0.3 in the figure), the adhesion efficiency will be $\varepsilon < 0.75$. Therefore, if the road adhesion coefficient is lower than 0.3, the parallel composite braking system will checkout the information about the road adhesion phenomenon though ABS and the regenerative braking system controller, and then it stops exerting regenerative braking force at the right time.

5. Simulation Research

Vehicle control model is the core of control strategy. Based on the requirement of driving cycle, the total torques are distributed among engine, hydraulic accumulator, hydraulic pump/motor, and the friction brake system reasonably. Vehicle control model consists of regenerative braking system, energy release system, and active stamping system, as shown in Figure 9.

Based on the algorithm above, the model of braking force distribution on hydraulic hybrid vehicles is set up in Matlab/Simulink and shown in Figure 10.

In order to verify the rationality and validity of the regenerative braking strategy discussed in this chapter, the parallel regenerative braking control strategy is adopted, and 1015, NYCC, and UDDS drive states are chosen to make the simulation study of brake energy recovery. After the road being set with high adhesion coefficient, the simulation results are achieved and shown in Table 2. Meanwhile the results of the evaluation of driving cycles with strategy of the ADVISOR in [22] are cited and shown in Table 3.

According to Table 2, the control strategy of regenerative braking in the hydraulic hybrid vehicle discussed in this

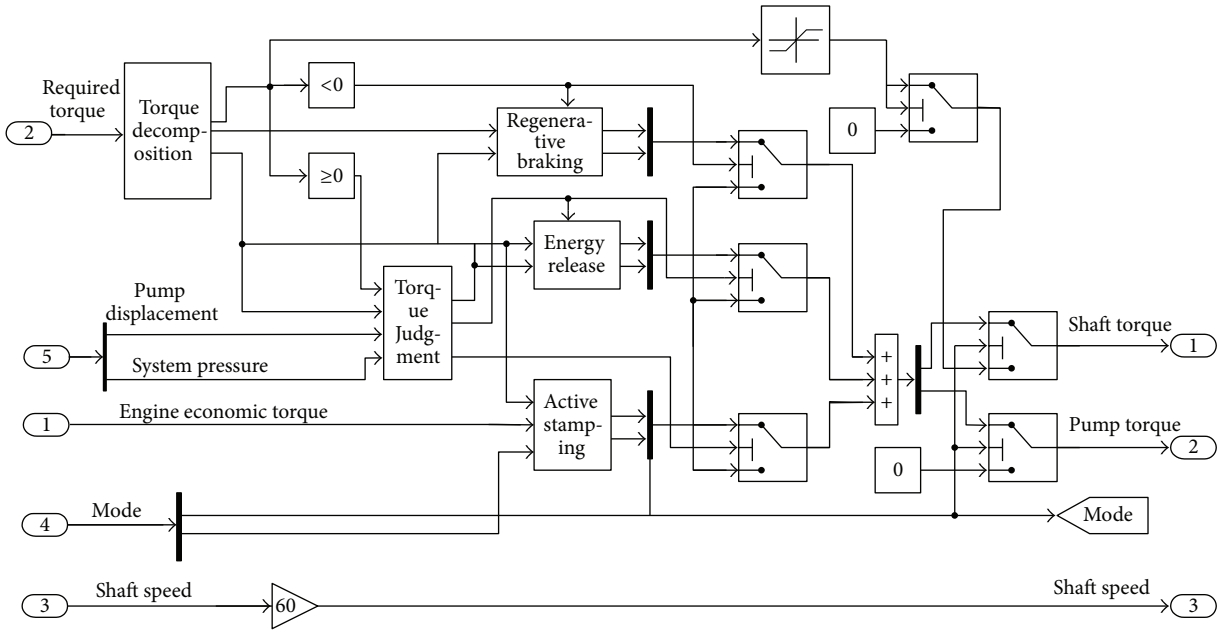

Figure 9: Top-level diagram of vehicle control model.

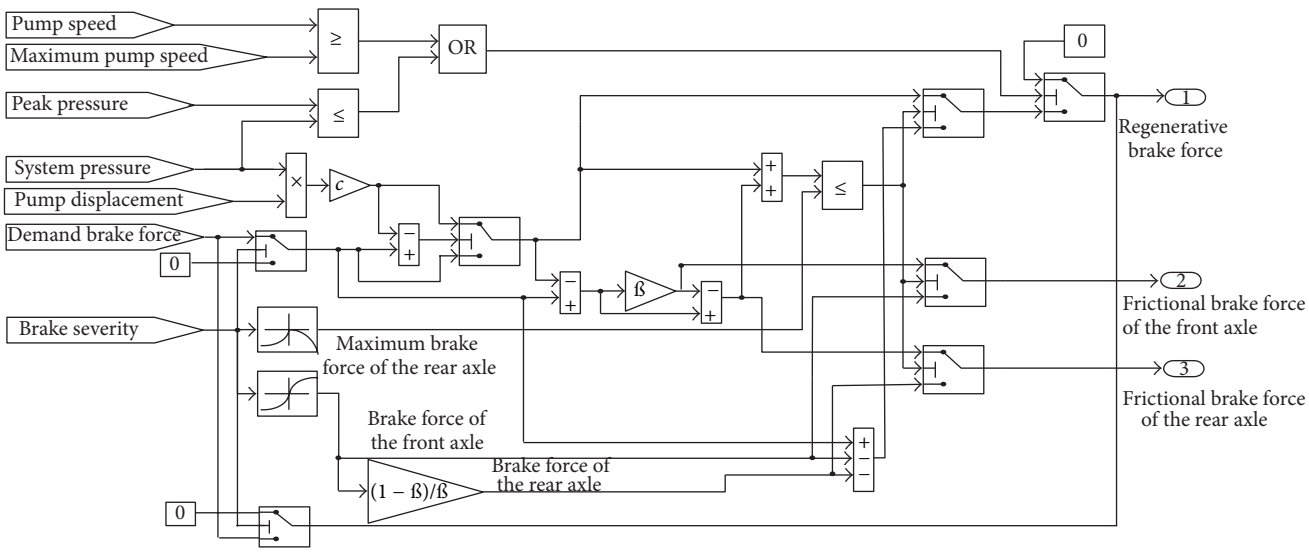

Figure 10: Model of braking force distribution of parallel regenerative braking.

paper can achieve the brake energy recovery to the largest degree based on the brake security. The brake energy recovery efficiency in 1015, NYCC, and UDDS is, respectively, 73.5% 75.25%, and 60.60%.

Compare the results in Table 2 with those in Table 3; it is not hard to find that the control strategy of regenerative braking in the hydraulic hybrid vehicle discussed in this paper can achieve more brake energy recovery than the strategy of the ADVISOR cited in [22].

6. Conclusions

Based on the higher power density and lower energy density of the hydraulic accumulator as well as the characteristics of the urban state, this paper puts forward the control algorithm of parallel composite braking in the hydraulic hybrid vehicle driven by rear wheels. By means of revise, the composite braking was controlled just within the requirements of ECE regulations. Therefore, based on the ensured brake security,

Table 2: The results of brake energy recovery rate in different drive states with the proposed strategy.

Drive state	Average acceleration a_{avg} (m·s^{-2})	Brake severity $z \leq 0.1$ (%)	Brake energy E_r (kWh)	Brake energy recovery rate ε_r (%)
1015	0.57/−0.65	96.2	0.2256	73.5
NYCC	0.62/−0.61	75.5	0.04	75.25
UDDS	0.51/−0.58	74.5	2.731	60.60

Table 3: The results of the evaluation of driving cycles with strategy of the ADVISOR.

Drive state	Traveling distance (Km)	Brake energy (kJ)	Regenerative braking efficient (kJ)	Brake energy recovery rate (%)
1015	4.2	660	367	56
NYCC	1.9	614	302	49
UDDS	12	1856	1017	55

the algorithm designed can enlarge the regenerative braking ratio to the utmost in the phase of composite braking, improving the brake energy recovery power of the vehicle at the end.

Acknowledgments

This work was supported by National Natural Science Foundation of China and Natural Science Foundation of Shandong Province under Contracts no. 50875054 and no. ZR2009FL002.

References

[1] W. Gunselman, "Technologies for increased energy efficiency in railway systems," in *Proceedings of the 11th European Conference on Power Electronics and Applications*, pp. 1–10, 2005.

[2] K. Son, S. Noh, K. Kwon, J. Choi, and E. K. Lee, "Line voltage regulation of urban transit systems using supercapacitors," in *Proceedings of the IEEE 6th International Power Electronics and Motion Control Conference (IPEMC '09)*, pp. 933–938, May 2009.

[3] K. Matsuda, H. Ko, and M. Miyatake, "Train operation minimizing energy consumption in dc electric railway with onboard energy storage device," in *Power Supply, Energy Management and Catenary Problems Part A*, pp. 45–54, WIT Press, Southampton, UK, 2010.

[4] T. Konishi, H. Morimoto, T. Aihara, and M. Tsutakawa, "Fixed energy storage technology applied for DC Electrified railway," *IEEJ Transactions on Electrical and Electronic Engineering*, vol. 5, no. 3, pp. 270–277, 2010.

[5] M. Ogasa, "Application of energy storage technologies for electric railway vehicles-examples with hybrid electric railway vehicles," *IEEJ Transactions on Electrical and Electronic Engineering*, vol. 5, no. 3, pp. 304–311, 2010.

[6] D. Kim, S. Hwang, and H. Kim, "Vehicle stability enhancement of four-wheel-drive hybrid electric vehicle using rear motor control," *IEEE Transactions on Vehicular Technology*, vol. 57, no. 2, pp. 727–735, 2008.

[7] D. Peng, Y. Zhang, C. L. Yin, and J. W. Zhang, "Combined control of a regenerative braking and antilock braking system for hybrid electric vehicles," *International Journal of Automotive Technology*, vol. 9, no. 6, pp. 749–757, 2008.

[8] K. Oh, D. Kim, T. Kim, C. Kim, and H. Kim, "Operation algorithm for a parallel hybrid electric vehicle with a relatively small electric motor," *KSME International Journal*, vol. 18, no. 1, pp. 30–36, 2004.

[9] C. Jo, J. Ko, H. Yeo, T. Yeo, S. Hwang, and H. Kim, "Cooperative regenerative braking control algorithm for an automatic-transmission-based hybrid electric vehicle during a downshift," *Proceedings of the Institution of Mechanical Engineers, Part D: Journal of Automobile Engineering*, vol. 226, no. 4, pp. 457–467, 2012.

[10] J. Zhang, C. Lv, J. Gou, and D. Kong, "Cooperative control of regenerative braking and hydraulic braking of an electrified passenger car," *Proceedings of the Institution of Mechanical Engineers, Part D: Journal of Automobile Engineering*, vol. 226, no. 10, pp. 1289–1302, 2012.

[11] J. Moreno, M. E. Ortúzar, and J. W. Dixon, "Energy-management system for a hybrid electric vehicle, using ultracapacitors and neural networks," *IEEE Transactions on Industrial Electronics*, vol. 53, no. 2, pp. 614–623, 2006.

[12] P. Wu, N. Luo, F. J. Fronczak, and N. H. Beachley, "Fuel economy and operating characteristics of a hydropneumatic energy storage automobile," SAE Paper 851678, 1985.

[13] S. Hui, J. Ji-hai, and W. Xin, "Torque control strategy for a parallel hydraulic hybrid vehicle," *Journal of Terramechanics*, vol. 46, no. 6, pp. 259–265, 2009.

[14] A. Taghavipour, M. S. Foumani, and M. Boroushaki, "Implementation of an optimal control strategy for a hydraulic hybrid vehicle using CMAC and RBF networks," *Scientia Iranica*, vol. 19, no. 2, pp. 327–334, 2012.

[15] S. Hui, "Multi-objective optimization for hydraulic hybrid vehicle based on adaptive simulated annealing genetic algorithm," *Engineering Applications of Artificial Intelligence*, vol. 23, no. 1, pp. 27–33, 2010.

[16] R. Ramakrishnan, S. S. Hiremath, and M. Singaperumal, "Theoretical investigations on the effect of system parameters in series hydraulic hybrid system with hydrostatic regenerative braking," *Journal of Mechanical Science and Technology*, vol. 26, no. 5, pp. 1321–1331, 2012.

[17] R. P. Kepner, "Hydraulic power assist—a demonstration of hydraulic hybrid vehicle regenerative braking in a road vehicle application," SAE Paper 2002-01-3128, 2002.

[18] T. Liu, J. Jiang, and H. Sun, "Investigation to simulation of regenerative braking for parallel hydraulic hybrid vehicles,"

in *Proceedings of the International Conference on Measuring Technology and Mechatronics Automation (ICMTMA '09)*, pp. 242–245, April 2009.

[19] Y. J. Kim and Z. Filipi, "Simulation study of a series hydraulic hybrid propulsion system for a light truck," SAE Paper 2007-01-4151, 2007.

[20] R. P. Kepner, "Hydraulic power assist—a demonstration of hydraulic hybrid vehicle regenerative braking in a road vehicle application," SAE Paper 2002-01-3128.

[21] M. Paul and S. Jacek, "Development and simulation of a hydraulic-hybrid powertrain for use in commercial heavy vehicles," SAE Paper 2003-01-3370.

[22] L. Chu, M. Shang, Y. Fang, J. Guo, and F. Zhou, "Braking force distribution strategy for HEV based on braking strength," in *Proceedings of the International Conference on Measuring Technology and Mechatronics Automation (ICMTMA '10)*, pp. 759–764, March 2010.

Hindawi Publishing Corporation
Mathematical Problems in Engineering
Volume 2013, Article ID 283528, 9 pages
http://dx.doi.org/10.1155/2013/283528

Research Article

Adaptive Real-Time Estimation on Road Disturbances Properties Considering Load Variation via Vehicle Vertical Dynamics

Wuhui Yu,[1] Xinjie Zhang,[1,2,3] Konghui Guo,[1,2] Hamid Reza Karimi,[4] Fangwu Ma,[3] and Fumiao Zheng[1]

[1] *State Key Laboratory of Automotive Simulation and Control, Jilin University, Changchun, Jilin 130022, China*
[2] *State Key Laboratory of Advanced Design and Manufacture for Vehicle Body, Hunan University, Changsha, Hunan 410082, China*
[3] *Zhejiang Geely Automobile Research Institute CO. L.t.d, Hangzhou 311228, China*
[4] *Department of Engineering, Faculty of Engineering and Science, University of Agder, 4898 Grimstad, Norway*

Correspondence should be addressed to Xinjie Zhang; xjzhang5885@gmail.com

Received 27 August 2013; Accepted 12 September 2013

Academic Editor: Hui Zhang

Vehicle dynamics are directly dependent on tire-road contact forces and torques which are themselves dependent on the wheels' load and tire-road friction characteristics. An acquisition of the road disturbance property is essential for the enhancement of vehicle suspension control systems. This paper focuses on designing an adaptive real-time road profile estimation observer considering load variation via vehicle vertical dynamics. Firstly, a road profile estimator based on a linear Kalman filter is proposed, which has great advantages on vehicle online control. Secondly, to minimize the estimation errors, an online identification system based on the Recursive Least-Squares Estimation is applied to estimate sprung mass, which is used to refresh the system matrix of the adaptive observer to improve the road estimation efficiency. Last, for mining road category from the estimated various road profile sequencse, a road categorizer considering road frequency and amplitude simultaneously is approached and its efficiency is validated via numerical simulations, in which the road condition is categorized into six special ranges, and this road detection strategy can provide the suspension control system with a better compromise for the vehicle ride comfort, handling, and safety performance.

1. Introduction

The road properties have significant impact on vehicle performance because vehicle dynamics are directly dependent on tire-road contact forces and torques. Road roughness is a broad term that incorporates everything from potholes and cracks to the random deviations that exist in a profile. The analysis and estimation of a road surface are hot and challenging topics, and the researches related to road disturbances have been presented, which can be classified into three categories: road measurement, road modeling, and road estimation. Each of these categories is reviewed briefly in the sequel.

Road Measurement. It mainly focuses on measuring the road profile accurately for road serviceability, survey, and road maintenance. There are primarily three methods in use internationally. The first category consists of profilometers and profilographs [1–4]. These are manually directed and/or trailer towed mechanisms that directly contact the pavement under evaluation, such as the longitudinal profile analyser (LPA). The second category is inertial profilers such as the Mays Meter [5] and the GMP (general motor profilometer) [6], in which a vehicle mounted accelerometer is applied to collect data while traveling at normal speed conditions. González et al. also developed a road roughness estimator by the use of acceleration measurement [7]. Furthermore, Ngwangwa et al. reconstructed road defects and road roughness classification using vehicle responses with artificial neural networks simulation [8]. The third category, equipped with a laser (ultrasonic) transceiver [9], is more accurate but very expensive.

Road Modeling. It mainly focuses on providing road input source to the virtual vehicle simulation system or the Four-Post Test Rig for vehicle ride analysis. In 1970s, the PSD (power spectral density) function was used by Whitehouse and Archard [10] and Shinozuka and Jan [11] to investigate the road roughness. In 1993, Cebon proposed a method based on the IFFT (inverse fast fourier transform) to discretize PSD, which is a simple, fast, and convenient tool for generating road surfaces [12, 13]. In 1995, the contemporary international standard ISO 8608 [14] dealt with road roughness assumes, due to classification of roads into different classes according to their unevenness, equal intensity of road unevenness in the whole range of wavelengths and a general form of the fitted PSD were given. A method based on linear filtering (autoregressive and moving average method or ARMA modelling) was proposed by Yoshimura in 1998 [14], which has a smaller calculation, and a faster simulation speed, but its precision is not very well. Pazooki et al. [15], in 2007, summarized different stochastic models of parallel road tracks and evaluated their accuracy by comparing the difference of the measured parallel tracks and the synthetic parallel tracks. In 2012, Hassan and Evans [16] developed a comprehensive off-road vehicle ride dynamics model considering a random roughness model of the two parallel tracks.

Road Estimation. It mainly focuses on providing real-time rough road estimation for vehicle online control system. Since road input directly affects vehicle vertical suspension dynamics, the availability of suspension sensors such as accelerator and suspension deflection sensor provide an excellent opportunity for road input estimation. Fialho and Balas developed a road adaptive active suspension using linear parameter varying gain-scheduling [17], in which the road estimation results are applied to the suspension control system to achieve a better balance between ride and handling performance. A new simultaneous input and state estimation algorithm were developed based on the idea of achieving minimum mean square error and minimum error variance [18]. Two stable SISE algorithms were developed based on the minimum variance unbiased estimation technique [19]. A Takagi-Sugeno Fuzzy observer was built for estimating both vehicle dynamics and road geometry [20]. Vehicle sideslip and roll parameters are estimated in presence of the road bank angle and the road curvature as unknown inputs. But it is still not completely ready to be tested in experimental studies since the vehicle speed, parameters variations, and sensor noise are not considered. If the systems are subject to parameter uncertainties, the approaches proposed in [21–23] can be employed. Our previous study [24, 25] also shows the great potential in the enhancement of suspension performance by adopting road estimation in the suspension control system, even though the road estimation algorithm is very simple (just using the statistic value of the accelerator or suspension deflection sensor measurement to classify the road). Recently, a real-time estimation method based on Kalman filter is proposed to estimate the road profile, and experimental results show the accuracy and the potential of the estimation process [26]. But in this research, the vehicle sprung mass change due to vehicle load variation is not considered, which may attenuate the robustness. Imine and Delanne developed a sliding mode observer to estimate the road profiles, which is hard for real-time implementation since a 16 degrees of freedom (DOF) full car model is too complex to be applied online [27, 28].

This paper focuses on developing a road estimation system for an online vehicle control system, which is limited by some important practical requirements. It should, for instance, be:

simple enough to run in real time despite onboard processing limitations;

reliable enough to operate successfully despite instrumentation failures;

robust to variations in vehicle dynamics;

fast enough to detect the road input changes when a car is driven on road;

easy to incorporate into a control strategy.

With these requirements in mind, the objective of this research has three steps: (1) to develop a road estimator for satisfying the above 5 practical requirements; (2) to obtain vehicle sprung mass online to minimize the road profile estimation errors; (3) and to classify the estimated road profile into several categories according to the main control strategy. The proposed method uses measurements from available sensors: accelerometers and suspension deflection sensors. For simplicity reasons, a quarter-car vehicle model is considered. The estimation process consisting of three blocks is shown in Figure 1.

The first block serves to calculate vehicle sprung mass online from sensor measurements, while the second block contains a Kalman filter that uses the result of the first block as a system parameter adjustor in order to improve robustness of the road estimation system. The third block serves to categorize the estimated road profile elevation into specific types.

The rest of the paper is organized as follows. Section 2 describes a road input state estimator based on a linear Kalman filter. Section 3 presents an online sprung mass estimator based on the Recursive Least-Squares Estimation. In Section 4, a novel road categorizer is proposed, and it is validated via numerical simulations. And, the paper is concluded in Section 5.

2. Road Profile Estimator

2.1. 2-DOF Quarter-Car Model. To implement the Kalman filter method, a suitable vehicle model must be developed. In order to describe the vertical dynamics of a vehicle which runs on an uneven road with a constant speed, a 2-DOF quarter-car model is represented in Figure 2. The quarter-car model does not consider the pitch and roll motions. Despite its simplicity, it captures the most basic feature of the vertical model of the vehicle [29]. We assume that wheels are rolling

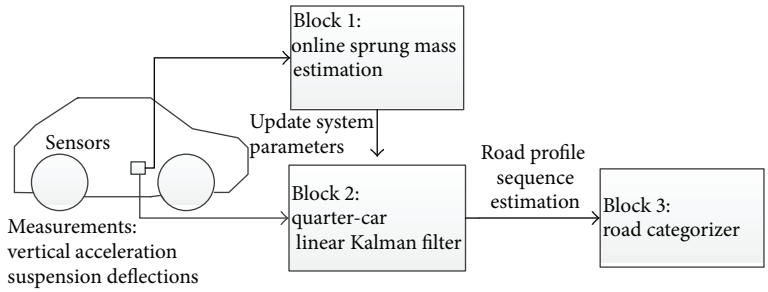

Figure 1: Road estimation process.

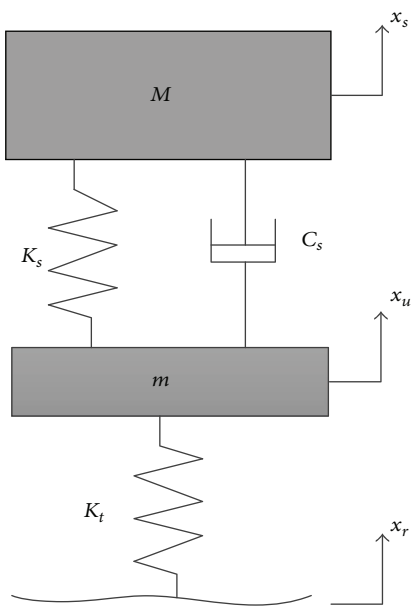

Figure 2: A quarter-car model.

without slip or contact loss. Equations (1) and (2) represent the vehicle body and the wheel motion, respectively:

$$m\ddot{x}_u - C_s(\dot{x}_s - \dot{x}_u) - K_s(x_s - x_u) + K_t(x_u - x_r) = 0, \quad (1)$$

$$M\ddot{x}_s + C_s(\dot{x}_s - \dot{x}_u) + K_s(x_s - x_u) = 0, \quad (2)$$

where M and m are, respectively, the sprung mass and the unsprung mass of a quarter car, K_s represents the suspension stiffness, K_t represents the tire vertical stiffness, C_s is the damper damping coefficient, x_s is the sprung mass position, x_u is the unsprung mass position, and x_r is the road input.

2.2. Kalman Filter for Road Input Estimation. The road input x_r is an estimated signal and it should be a part of the system states. Hence, in this paper, state variables for the quarter car are presented as follows:

$$\begin{aligned} &x_1 = x_s, \qquad x_2 = \dot{x}_s, \qquad x_3 = x_u, \\ &x_4 = \dot{x}_u, \qquad x_5 = x_r, \qquad x_6 = \dot{x}_r. \end{aligned} \quad (3)$$

And the road roughness profile applied in the estimation observer satisfies the following equation [30]:

$$\ddot{x}_r + a_2\dot{x}_r + a_1 x_r = 0, \quad (4)$$

where a_1 and a_2 are constant real numbers. The modified quarter car has to be stable in order to provide useful result; this implies that the real parts of the eigenvalues associated with (4) have to be negative, and consequently x_r converges to zero based on the selection of the constants a_1 and a_2. However, since x_r represents the road profile input, it should contain as much road input information as possible. In other words, x_r should be damped as slowly as possible, which will affect the stability of (4). Therefore, there is a trade-off between system stability and road input information integrity. In this paper, a_1 and a_2 are set to 20, which are close to two times of the quarter-car tire hop frequency, is sufficient to keep (4) stable [30]. The quarter car state equations can be written as follows:

$$\begin{aligned} x_{k+1} &= A_k x_k + \upsilon_k, \\ y_k &= H_k x_k + \omega_k, \end{aligned} \quad (5)$$

where $x_k = (x_{1,k}\ x_{2,k}\ x_{3,k}\ x_{4,k}\ x_{5,k}\ x_{6,k})^T$ is a state vector; $y_k = ((x_{1,k} - x_{3,k})x_{1,k}\ \ \ddot{x}_{1,k})^T$ is an observer vector, where $x_{1,k} - x_{3,k}$ is a suspension deflection measured by sensor; $x_{1,k}$ is a vehicle body position calculated by a twice numerical integration (trapezoidal method) of the filtered vertical acceleration signal; $\ddot{x}_{1,k}$ is a filtered vertical acceleration. υ_k and ω_k are the process and measurement noise vector, respectively, assumed to be white, zero mean, and uncorrelated.

Evolution and observation constant matrices are given as

$$A = E + \Delta t \begin{pmatrix} 0 & 1 & 0 & 0 & 0 & 0 \\ -\frac{Kt}{M} & -\frac{Cs}{M} & \frac{Kt}{M} & -\frac{Cs}{M} & 0 & 0 \\ 0 & 0 & 0 & 1 & 0 & 0 \\ \frac{Ks}{m} & \frac{Cs}{m} & -\frac{Ks+Ku}{m} & -\frac{Cs}{m} & \frac{Ku}{m} & 0 \\ 0 & 0 & 0 & 0 & 0 & 1 \\ 0 & 0 & 0 & 0 & -20 & -20 \end{pmatrix},$$

$$H = \begin{pmatrix} 1 & 0 & -1 & 0 & 0 & 0 \\ -\frac{Kt}{M} & -\frac{Cs}{M} & \frac{Kt}{M} & \frac{Cs}{M} & 0 & 0 \\ 1 & 0 & 0 & 0 & 0 & 0 \end{pmatrix}, \quad (6)$$

Table 1: Quarter-car model parameter.

Δt	Sampling period	5 ms
M	Vehicle sprung mass	320 kg
K_s	Suspension stiffness	20.8 kN/m
m	Unsprung mass	40 kg
K_t	Tire vertical stiffness	235 kN/m
C_s	Suspension damping	1.5 kN·s/m

where E is the identity matrix and Δt is the sampling period. And it is easy to verify that the observability matrix O is full rank:

$$O = \left(H \quad HG \quad HG^2 \quad HG^3 \quad HG^4 \quad HG^5\right)^T. \tag{7}$$

A standard Kalman filter formulation is used for the velocity estimation [31, 32]. The time update and measurement update equations of the filter are constructed as follows:

$$\begin{gathered}
\text{time update} \\
\{\hat{x}^-\}_k = [A]\{\hat{x}\}_{k-1} + [B]\,u_{k-1}, \\
[P^-]_k = [A]\,[P]_{k-1}[A]^T + [Q], \\
\text{measurement update} \\
[K]_k = [P^-]_k[H]^T\left([H]\,[P^-]_k[H]^T + [R]\right)^{-1}, \\
\{\hat{x}\}_k = \{\hat{x}^-\}_k + [K]_k\left(\{y\}_k - [H]\,\{\hat{x}^-\}_k\right), \\
[P]_k = \left([I] - [K]_k\,[H]\right)[P^-]_k,
\end{gathered} \tag{8}$$

where Q is a process noise covariance matrix, R is a measurement noise covariance matrix, P is an estimation of error covariance matrix, K is a Kalman gain, and $\hat{x}$ is an estimated state vector. The process and measurement noise variables υ_k and ω_k determine how much should the process model and the measurements should be trusted by the filter.

2.3. Simulation Setup. This paper presents simulations of the quarter-car system as shown in Figure 2 with parameters tabulated in Table 1.

Two types of road inputs were used during experimental and simulation analysis. One input is a trigonal bump with 40 mm height and 400 mm length shown in Figure 3; another input is a random road input modeled based on the inverse Fourier transform as Figure 4.

Figure 5 to Figure 8 show a comparison between the actual and the estimated road profile height. In Figures 5 and 7, the vehicle passes the bump at a constant speed of 15 km/h and 45 km/h, respectively. In Figures 6 and 8, the vehicle runs on a random road, and the speed is 30 km/h and 60 km/h, respectively. The simulation results show that, in the random road input or the low speed bump input condition, the road estimator is very efficient, while in the condition of passing the bump with a relatively high speed, as shown in Figure 7, the estimation result is not very well. This is induced by the road model defined in (4). In fact, the road model applied in the proposed estimation observer should make a compromise between system stability and the integrity of road input information. We want to keep the system stable sacrificing the integrity of road input information in this research. And this strategy decreases the road estimator performance in an impulse input condition. The higher the vehicle speed is, the sharper the road input in time domain will be and the worse the road estimator will be. But its negative effect is acceptable since most drivers will reduce the vehicle speed when they run over a bump.

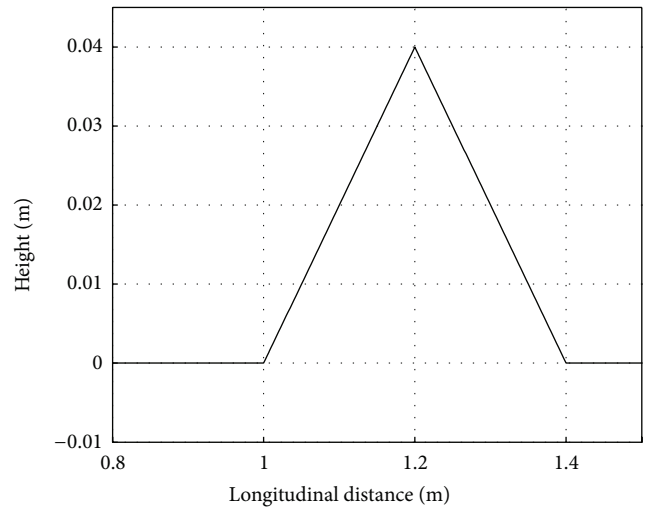

Figure 3: Bump road input.

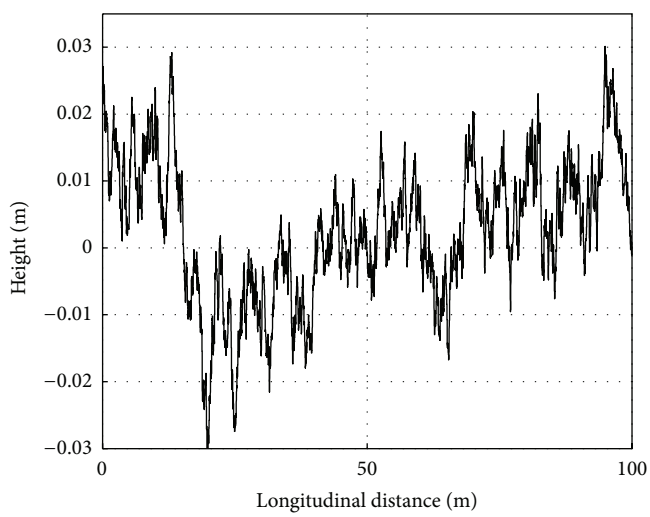

Figure 4: Random road input.

3. Sprung Mass Estimation

The road estimation method presented afore is based on a hypothesis that the vehicle system parameters in Table 1 are known and invariable. But in a real vehicle control system, it is not easy to obtain the sprung mass of the equivalent 2-DOF model, because of the nonlinear properties of the suspension system and the weight distribution variation on

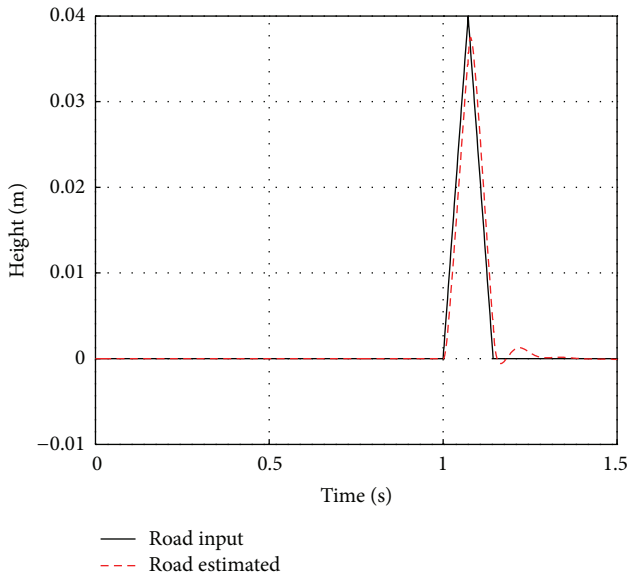

Figure 5: Bump input estimation (15 km/h).

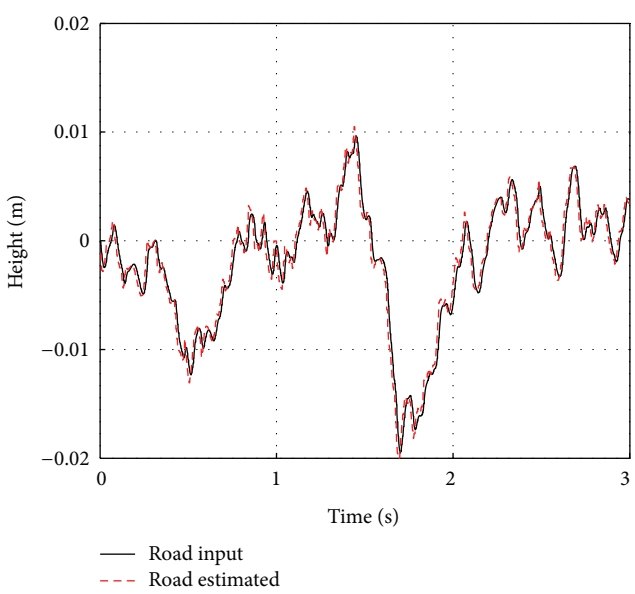

Figure 6: Random road estimation (30 km/h).

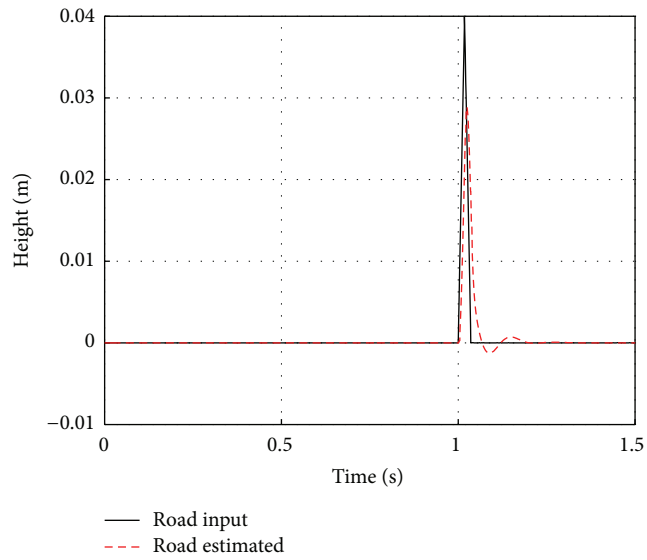

Figure 7: Bump input estimation (45 km/h).

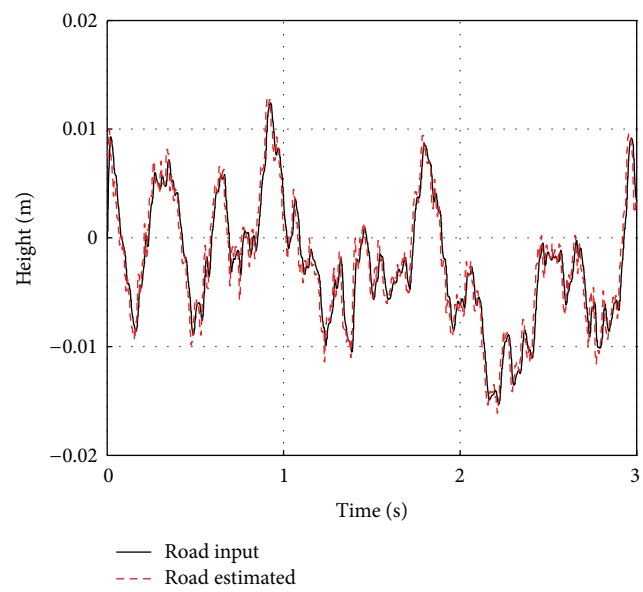

Figure 8: Random road estimation (60 km/h).

different driving conditions. What is more, the sprung mass varies greatly between empty and full loaded, especially for a commercial vehicle. All these factors will induce a significant sprung mass change and, then, attenuate the efficiency of the road estimation system. As shown in Figure 9, 20% sprung mass error will induce an obvious road estimation error. Consequently, it is necessary to estimate the sprung mass online for improving the efficiency of road estimation.

3.1. Solution Formulation. With setting $y = -K_s(x_s - x_u)$, $\theta = [M,\ C_s]^T$, and $\psi^T = [\ddot{x}_s, \dot{x}_s - \dot{x}_u]$, (2) can be written as

$$y = \psi^T \cdot \theta. \tag{9}$$

The vehicle sprung mass and suspension damping coefficient are estimated simultaneously via the Recursive Least-Squares Estimation. The Recursive Least-Squares Estimation procedures are given as follows:

$$\widehat{\theta}_{N+1} = \widehat{\theta}_N + K_{N+1}\left(y_{N+1} - \psi_{N+1}^T \widehat{\theta}_N\right), \tag{10}$$

$$K_{N+1} = \frac{P_N \psi_{N+1}}{1 + \psi_{N+1}^T P_N \psi_{N+1}}, \tag{11}$$

$$\begin{aligned} P_{N+1} &= P_N - \frac{P_N \psi_{N+1} \psi_{N+1}^T P_N}{1 + \psi_{N+1}^T P_N \psi_{N+1}} \\ &= \left(I - K_{N+1} \psi_{N+1}^T\right) P_N, \end{aligned} \tag{12}$$

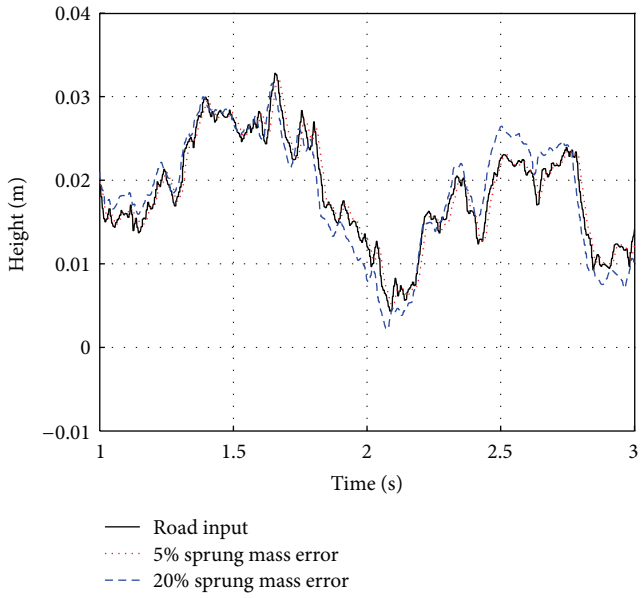

Figure 9: Road estimation on different sprung mass errors.

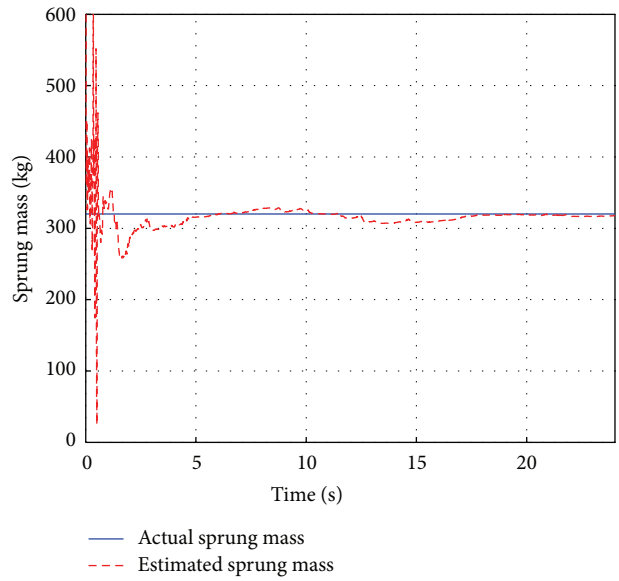

Figure 10: Sprung mass estimation.

where P is a symmetric covariance matrix (2×2) and $\widehat{\theta}_N$ is the Least-Squares estimation of θ; the calculation order is described as follows.

Calculate K_1 by $\widehat{\theta}_0$ and P_0 according to (11) first; then, update the value of y_1 and ψ_1^T; and then, calculate $\widehat{\theta}_1$ and P_1 according to (10) and (12), respectively; last, recursive the mentioned steps in order until the error reaches the standard. As for the initial values, $\widehat{\theta}_0$ and P_0, they can be calculated by the Least-Squares Estimation.

3.2. Simulation. Here, the vehicle system model parameters are from Table 1; the road profile defined in Figure 4 is selected as a vertical road input and the vehicle runs with a constant speed of 20 km/h. The estimation result is shown in Figure 10, which demonstrates the estimation result converges at an acceptable region (the error is less than 5%) after 2.5 s and then shows great efficiency after 20 s. Generally, the vehicle load is a constant during a vehicle start-stop period and the convergence time for sprung mass estimation is usually far less than a vehicle start-stop period. The sprung mass estimation is a little bit time-consuming, but it is not a big issue. For example, the original sprung mass is set in normal load condition. The road estimation block will be triggered once the vehicle has been started and the vehicle velocity is greater than 10 km/h; it will obtain the sprung mass (the error is less than 5%) in 2.5 s after the road estimation block is triggered, and the sprung mass will be refreshed. And then the sprung mass will be updated in every 2.5 s until it is stable (the change is less than 1%) or the estimation time is more than 40 s.

4. Road Categorizer

In the previous sections, the road estimator performs very well in a quarter-car system. However, does this estimator have the same performance applied to an actual car online system? It cannot be denied that the estimated result, in an actual car online system, will be worse than expectation due to the effect of wheel radius, wheel contact area, and the noise signals in the control system. What is more, the estimated road profile cannot be applied to the control strategy directly since these road sequences are estimated by postestimation, which produces an unavoidable time delay. However, in many vehicle control systems, such as active/semiactive suspension system, obtaining the primary road category information is effective [33]. Hence, it is necessary to develop a road categorizer to distinguish the road category for the main control strategy. But the most common road classification methods, estimating the road PSD (power spectral density) or the road RMS (root mean square), are not enough effective for an online control system, because these methods need to compute plenty of road height values which will consume a lot of estimation time, and this time lag usually cannot be neglected in a real-time control system.

In fact, most onboard suspension control systems, only require the mainly frequency or amplitude information of road input. In [33, 34], a road-frequency adaptive suspension is proposed, where the road surface is classified by the frequency properties according to the fact that [0–4 Hz] is the car-body frequency region and [4–8 Hz] is the human-body frequency region. [8–12 Hz] is the wheel frequency region and [12–∞ Hz] is the harshness frequency region. Bastow et al. also categorize the road profile into four grades, which defined a very good surface with amplitudes under 5 mm, medium-quality roads with amplitudes less than 13 mm, poor-quality roads with amplitudes less than 25 mm, and off-road with the amplitudes often exceeding 25 mm [35]. However, it is a challenging issue to design a proper filter to avoid some unimportant long waves without any phase delay, as shown in Figure 4; the road waves are not fluctuating along the horizontal plane due to the effect of some long waves

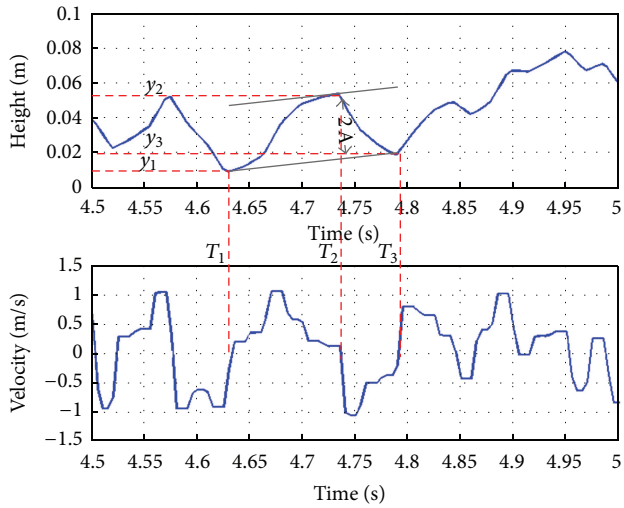

FIGURE 11: Road amplitude estimation method.

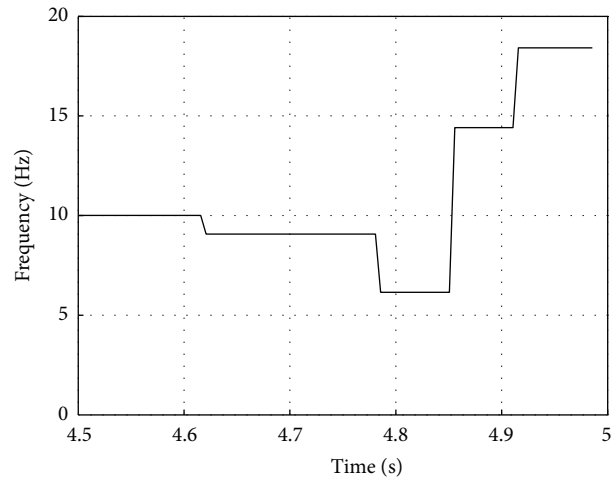

FIGURE 12: Road frequency estimation.

which has small contribution on the vehicle vertical dynamic; consequently, we should estimate the road input frequency and amplitude avoiding the unimportant long waves. In the other hand, the road categorizer only depending on the road frequency or the road amplitude does not work very well always. And the suspension control strategy should consider the road frequency and amplitude simultaneously in some case, such that a car runs on a road twice with different speed or a car runs on different road (ISO Class A and ISO Class C) with same speed. It will be much better if the road categorizer considers road frequency and amplitude simultaneously. Hence, a novel road categorizing method considering road frequency and amplitude simultaneously is proposed in the following paragraph.

For road frequency estimation, refer to the article [34], a first-order zero-crossing algorithm is applied, with the road velocity state $\dot{x}_r$ being the input, to identify the frequency components of road disturbances. The frequency estimation result of Figure 11 is shown in Figure 12, and the current estimation value is actually the last circle's frequency.

As for road amplitude analysis, road velocity state $\dot{x}_r$ does not contain the amplitude information, but the road amplitude estimation only via x_0 is very difficult, since some of the significant road waves are not fluctuating along the horizontal plane. As shown in Figure 11, the value of "A" is one of the main amplitudes values, which is the amplitude of the wave with dominant frequency, should be estimated.

In the sequel, a novel road amplitude estimation method is proposed as shown in Figure 11, where, T_1, T_2, and T_3, used to detect each complete cycle, are the three attached times when first-order zero-crossing of the road velocity sequence happens; y_1, y_2, and y_3 are the three road height values in the times T_1, T_2, T_3, respectively. Then the road amplitude "A" can be simply calculated as (13), where T_1, T_3 are used to detect the troughs of a circle and T_2 used to detect the peak of a circles are the distance between the point (T_2, y_2) to the

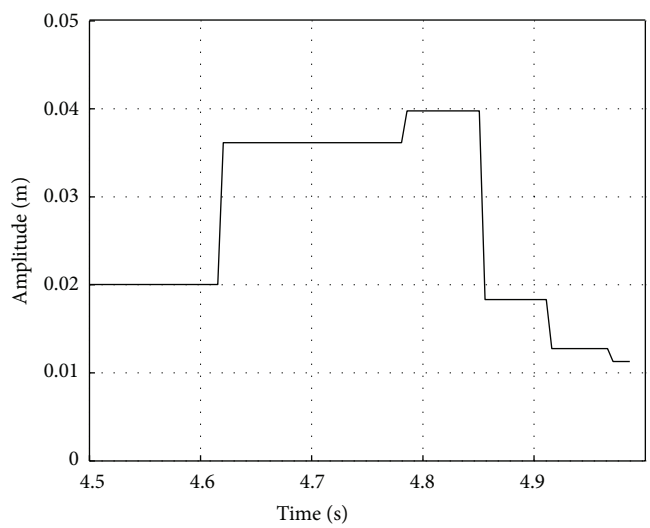

FIGURE 13: Road amplitude estimation.

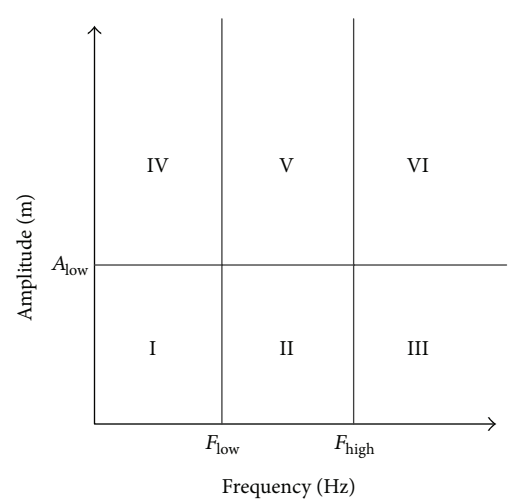

FIGURE 14: Road detection strategy.

Table 2: Suspension mode selection based on road condition.

Range	Driving condition	Suspension control objective
I and II	Good road surface with medium or low speed, mostly on an urban driving condition	Improve the vehicle ride performance
III	Expressway driving condition	Improve the road holding
IV	Bad road with low speed	Limit the low frequency body motion
V and VI	Poor-quality road surface with medium-high speed and the impulse road input	Attenuate the impact feeling

line going through the points (T_1, y_1), (T_3, y_3); is two times of the amplitude A; in this paper, an approximate algorithm is used as follows:

$$A = \begin{cases} \frac{1}{2}\left|y_2 - \left(y_1 + \frac{T_2 - T_1}{T_3 - T_1}(y_3 - y_1)\right)\right| & \text{if } y_3 \geq y_1, \\ \frac{1}{2}\left|y_2 - \left(y_3 + \frac{T_3 - T_2}{T_3 - T_1}(y_1 - y_3)\right)\right| & \text{if } y_3 < y_1. \end{cases} \quad (13)$$

The amplitude estimation result is shown in Figure 13; even though the algorithm is running in real time, the estimation result still has a complete cycle time lag.

As road frequency and amplitude estimation can be achieved, a road categorizer special for a semiactive suspension control system can be designed, as shown in Figure 14. A certain type of road can be detected by judging the amplitude and frequency of the estimated road profile into the specific range (I–VI), where the suggestion values of A_{low}, F_{low}, and F_{high} are 10 mm, 4 Hz, and 8 Hz, respectively. The suspension mode selection based on the road condition in specific range (I–VI) is detailed in Table 2. Ranges I and II are the medium-low frequency and low amplitude areas, corresponding to good road surface with medium-low speed, mostly on an urban driving condition. In this case, the suspension system should be turned to soft mode to improve the vehicle ride performance. Range III is the high frequency and low amplitude area, corresponding to the expressway driving condition, in which more attention should be paid to the tire deflection, and a relative hard mode suspension system should be regulated to achieve better road holding for driving safety. Range IV is the low frequency and high amplitude area corresponding to a bad road with low speed, which is very common for an off-road. In this condition, limiting the low frequency body motion should be a key objective. Ranges V and VI correspond to poor-quality road surface with medium-high speed and the impulse road input. In these cases, the suspension system should be adjusted to attenuate the impact feeling.

5. Conclusions

An acquisition of road disturbances property is essential for the enhancement of suspensions control systems. This paper presented a method to estimate the road profile elevation based on Kalman filter. To minimize the estimation errors, an online identification system based on Recursive Least-Squares Estimation is adopted to estimate sprung mass in real time, which is applied to refresh the system matrix of the adaptive observer. And a novel road categorizer considering road frequency and amplitude simultaneously is approached to classify various road profile sequence for suspension control system. The main conclusions are as follows.

(1) A road profile estimator based on linear Kalman filter is proposed, which has great advantages on practical online vehicle control.

(2) An online sprung mass estimator is proposed, which demonstrates the estimation result converges at an acceptable region (the error is less than 5%) after 2.5 s and then shows great efficiency after 20 s. With this online sprung mass estimator, the accuracy road estimation result can be improved greatly.

(3) A novel road amplitude estimation method is proposed. And the road condition is categorized into six special ranges according to the road frequency and amplitude estimation result simultaneously, which can provide the suspension control system with a better trade-off for the ride comfort, handling, and safety performance.

Conflict of Interests

The authors declare that there is no conflict of interests regarding the publication of this paper.

Acknowledgments

Special thanks are due to the Open Research Fund Program of the State Key Laboratory of Advanced Design and Manufacturing for Vehicle Body (31115028), the China Postdoctoral Science Foundation (2012M520028), the National Natural Science Foundation of China (51205155), and the National Basic Research Program of China (973 Program) (2011CB711201) for supporting authors' research.

References

[1] R. P. Barre, R. T. Forbes, and S. Andrews, "The measurement and analysis of road surface roughness," Motor Industry Research Association Report, 1970.

[2] M. W. Sayers, T. D. Gillespie, and W. D. O. Paterson, "Guidelines for conducting and calibrating road roughness measurements," World Bank Technical Paper Number 46, 1986.

[3] ISO 8608, *Mechanical Vibration Road Surface Profiles Reporting of Measured Data*, International Standards Organization, 1995.

[4] "Standard test Method for measuring road roughness by static rod and level method," *Annual Book of ASTM Standards*, vol. 4, pp. 750–755, 1996.

[5] "Standard test method for measuring longitudinal profile of traveled surfaces with an accelerometer: established inertial

profiling Reference," *Annual Book of ASTM Standards*, no. 4, pp. 702–706, 1996.

[6] E. B. Splanger and W. J. Kelly, "Road profilometer method for measuring road profile," General Motors Research Publication GMR-452, 1964.

[7] A. González, E. J. O'Brien, Y.-Y. Li, and K. Cashell, "The use of vehicle acceleration measurements to estimate road roughness," *Vehicle System Dynamics*, vol. 46, no. 6, pp. 483–499, 2008.

[8] H. M. Ngwangwa, P. S. Heyns, F. J. J. Labuschagne, and G. K. Kululanga, "Reconstruction of road defects and road roughness classification using vehicle responses with artificial neural networks simulation," *Journal of Terramechanics*, vol. 47, no. 2, pp. 97–111, 2010.

[9] R. McCann and S. Nguyen, "System identification for a model-based observer of a road roughness profiler," in *Proceedings of IEEE Region 5 Technical Conference (TPS '07)*, pp. 336–343, April 2007.

[10] D. J. Whitehouse and J. F. Archard, "The properties of random surfaces of significance in their contact," *Proceedings of the Royal Society of London. Series A*, vol. 316, pp. 97–121, 1970.

[11] M. Shinozuka and C.-M. Jan, "Digital simulation of random processes and its applications," *Journal of Sound and Vibration*, vol. 25, no. 1, pp. 111–128, 1972.

[12] D. Cebon, *Interaction between Heavy Vehicles and Roads*, Society of Automotive Engineers, 1993.

[13] J.-J. Wu, "Simulation of rough surfaces with FFT," *Tribology International*, vol. 33, no. 1, pp. 47–58, 2000.

[14] T. Yoshimura, "A semi-active suspension of passenger cars using fuzzy reasoning and the field testing," *International Journal of Vehicle Design*, vol. 19, no. 2, pp. 150–166, 1998.

[15] A. Pazooki, S. Rakheja, and D. Cao, "Modeling and validation of off-road vehicle ride dynamics," *Mechanical Systems and Signal Processing*, vol. 28, pp. 679–695, 2012.

[16] R. Hassan and R. Evans, "Road roughness characteristics in car and truck wheel tracks," *International Journal of Pavement Engineering*, pp. 1–10, 2012.

[17] I. Fialho and G. J. Balas, "Road adaptive active suspension design using linear parameter-varying gain-scheduling," *IEEE Transactions on Control Systems Technology*, vol. 10, no. 1, pp. 43–54, 2002.

[18] H. Fang, Y. Shi, and J. Yi, "A new algorithm for simultaneous input and state estimation," in *Proceedings of the American Control Conference (ACC 08)*, pp. 2421–2426, Seattle, Wash, USA, June 2008.

[19] H. Fang, Y. Shi, and J. Yi, "On stable simultaneous input and state estimation for discrete-time linear systems," *International Journal of Adaptive Control and Signal Processing*, vol. 25, no. 8, pp. 671–686, 2011.

[20] H. Dahmani, M. Chadli, A. Rabhi, and A. El Hajjaji, "Vehicle dynamics and road geometry estimation using a Takagi-Sugeno fuzzy observer with unknown inputs," in *Proceedings of IEEE Intelligent Vehicles Symposium (IV '11)*, pp. 272–277, Baden-Baden, Germany, June 2011.

[21] H. Zhang, Y. Shi, and A. Saadat Mehr, "Robust static output feedback control and remote PID design for networked motor systems," *IEEE Transactions on Industrial Electronics*, vol. 58, no. 12, pp. 5396–5405, 2011.

[22] H. Zhang, Y. Shi, and A. S. Mehr, "Robust H_∞ PID control for multivariable networked control systems with disturbance/noise attenuation," *International Journal of Robust and Nonlinear Control*, vol. 22, no. 2, pp. 183–204, 2012.

[23] H. Zhang, Y. Shi, A. Saadat Mehr, and H. Huang, "Robust FIR equalization for time-varying communication channels with intermittent observations via an LMI approach," *Signal Processing*, vol. 91, no. 7, pp. 1651–1658, 2011.

[24] K. H. Guo and W. H. Yu, "Semi-active suspension adaptive control strategy," *Journal of Hunan University (Natural Sciences)*, no. 40, pp. 39–44, 2013.

[25] X. J. Zhang and W. H. Yu, "Semi-active suspension adaptive control strategy based on hybrid control," in *FISITA World Automotive Congress*, 2012.

[26] M. Doumiati, A. Victorino, A. Charara, and D. Lechner, "Estimation of road profile for vehicle dynamics motion: experimental validation," in *Proceedings of the American Control Conference (ACC '11)*, pp. 5237–5242, San Francisco, Calif, USA, July 2011.

[27] H. Imine, Y. Delanne, and N. K. M'Sirdi, "Road profile input estimation in vehicle dynamics simulation," *Vehicle System Dynamics*, vol. 44, no. 4, pp. 285–303, 2006.

[28] H. Imine, Y. Delanne, and N. K. M'Sirdi, "Road profile inputs for evaluation of the loads on the wheels," *Vehicle System Dynamics*, vol. 43, pp. 359–369, 2005.

[29] M. M. Elmadany and Z. S. Abduljabbar, "Linear quadratic Gaussian control of a quarter-car suspension," *Vehicle System Dynamics*, vol. 32, no. 6, pp. 479–497, 1999.

[30] S. Nguyen, *System Identification for a Model Based Observer Road Roughness Profiler*, University of Arkansas, 2006.

[31] W. Greg and B. Gary, *An Introduction to the Kalman Filter*, Department of Computer Science, University of North California at Chapel Hill, 2006.

[32] R. E. Kalman, "A newapproach to linear filtering and prediction problems," *Transactions of the ASME-Journal of Basic Engineering*, no. 82, pp. 35–45, 1960.

[33] J. Lu, "A frequency-adaptive multi-objective suspension control strategy," *Journal of Dynamic Systems, Measurement and Control*, vol. 126, no. 3, pp. 700–707, 2004.

[34] L. H. Nguyen, K.-S. Hong, and S. Park, "Road-frequency adaptive control for semi-active suspension systems," *International Journal of Control, Automation and Systems*, vol. 8, no. 5, pp. 1029–1038, 2010.

[35] D. Bastow, G. Howard, and J. P. Whitehead, *Car Suspension and Handling*, SAE International, Warrendale, Pa, USA, 4th edition, 2004.

Hindawi Publishing Corporation
Mathematical Problems in Engineering
Volume 2013, Article ID 986584, 12 pages
http://dx.doi.org/10.1155/2013/986584

Research Article

A Frequency Compensation Algorithm of Four-Wheel Coherence Random Road

Jun Feng,[1] Xinjie Zhang,[1,2,3] Konghui Guo,[1,2] Fangwu Ma,[3] and Hamid Reza Karimi[4]

[1] *State Key Laboratory of Automotive Simulation and Control, Jilin University, Changchun, Jilin 130022, China*
[2] *State Key Laboratory of Advanced Design and Manufacture for Vehicle Body, Hunan University, Changsha, Hunan 410082, China*
[3] *Zhejiang Geely Automobile Research Institute Co. Ltd., Hangzhou 311228, China*
[4] *Department of Engineering, Faculty of Engineering and Science, University of Agder, 4898 Grimstad, Norway*

Correspondence should be addressed to Xinjie Zhang; xjzhang5885@gmail.com

Received 28 July 2013; Revised 15 August 2013; Accepted 15 August 2013

Academic Editor: Hui Zhang

The road surface roughness is the main source of kinematic excitation of a moving vehicle, which has an important influence on vehicle performance. In recent decades, random road models have been widely studied, and a four-wheel random road time domain model is usually generated based on the correlation of the four-wheel input, in which a coherence function is used to describe the coherence of the road input between the left and right wheels usually. However, during our research, there are some conditions that show that the road PSD (power spectral density) of one wheel is smaller than the other one on the same axle. Actually, it is caused by the uncorrelation between the left- and right-wheel road surface roughness. Hence, a frequency compensation algorithm is proposed to correct the deviation of the PSD of the road input between two wheels on the same axle, and it is installed in a 7-DOF vehicle dynamic study. The simulation result demonstrates the applicability of the proposed algorithm such that two-wheel road input deviation compensation has an important influence on vehicle performances, and it can be used for a control system installed in the vehicle to compensate road roughness for damper tuning in the future.

1. Introduction

The road surface roughness is the main source of kinematic excitation of a moving vehicle, which has an important influence on ride comfort, ride safety, vehicle maneuverability, driver's and occupants' comfort, and vehicle dynamic load [1–3]. Measurements of road surface roughness data are preferably done with laser/inertial high-speed profilometers, and modern laser/inertial road profilometers can record several parallel profiles simultaneously typically [4]. However, they are very expensive, inconvenient to use, susceptible to external factors, and so forth. And at the same period, the road surface roughness models have been widely investigated and applied in vehicle dynamics research. An accurate driving dynamics simulation of a vehicle on a road section is only possible if these input models are accurate themselves [5], and scholars have been focusing on the random road surface excitation simulation and reconstruction. The road surface roughness, as a stochastic process, is generally described by a PSD (power spectral density) function in a frequency domain, and, in engineering practice, it is regarded as a zero-mean stationary (or isotropic) and ergodic Gaussian process. In 1970s, the PSD function was used by Whitehouse [6] and Shinozuka [7] to investigate the road roughness. In 1993, Cebon [8] proposed a method based on the IFFT (Inverse Fast Fourier Transform) to discretize PSD which is a simple, fast, and convenient tool for generating road surfaces [2, 9]. In 1993, Grigoriu [10] proposed a method based on the harmony superposition to simulate stationary random processes. The harmony superposition method has an exact theory foundation and is suitable for arbitrarily stated spectral features. But it is rather time consuming and has an increasing demand on computer storage as a large set of trigonometric terms has to be calculated in a simulation procedure. In 1995, the contemporary international standard ISO 8608 [11] dealt with road roughness assumption, due to classification of roads into different classes according to their unevenness, equal intensity of road unevenness in the whole

range of wavelengths, and a general form of the fitted PSD was given. A method based on linear filtering (auto-regressive and moving average methods or ARMA modelling) was proposed by Yoshimura in 1998 [12], which has a smaller calculation, and a faster simulation speed, but its precision is not very well. Bogsjö [13], in 2007, summarized different stochastic models of parallel road tracks and evaluated their accuracy by comparing the difference of the measured parallel tracks and the synthetic parallel tracks. In the same year, Ambrož proposed a system for measuring road section parameters that can be used in driving dynamics simulations. In 2012, Pazooki et al. [14] developed a comprehensive offroad vehicle ride dynamics model considering a random roughness model of the two parallel tracks. Hassan and Evans [15] collected the road longitudinal profile data of a car and truck wheel tracks and then investigated the differences of their surface roughness characteristics, which showed that the HATI (heavy articulated truck index) lane average values of a truck wheel tracks are higher than car wheel tracks. Three new road profile models [16] are proposed by Bogsjö et al. in 2012, which were compared with the classical road surface road model, and five different models were fitted to eight measured road surfaces and their accuracy and efficiency were studied.

Generally, for some researches and publications about random road surface reconstruction, a single-wheel road time domain model is established via the inverse Fourier transform, and a four-wheel road time domain model is generated based on the correlation of the four-wheel input, in which there is a time delay between the front and rear axle and the space is correlated between the left and right wheel is [17]. However, during our research, there are some conditions show that the road roughness amplitude and the road PSD of one wheel is smaller than the other one on the same axle, in other words, there is a deviation between two tracks on the same axle. Also, in 1980s, Heath [18, 19] pointed out that the method used for the calculation of the cross-spectrum from experimental sampled data is inaccurate at high wavenumbers. Pazooki et al. [14] considered the uncorrelated component between the left and right wheels when working on modeling and validation of an off-road vehicle ride dynamics. In fact, the deviation between two tracks on the same axle has an important influence on vehicle performances. Hence, the deviation for two-wheel road input and its influence on a vehicle dynamics behavior is undertaken in this paper, and a PSD frequency compensation algorithm is proposed to improve the accuracy of the road input reconstruction.

In this paper, single-wheel and a four-wheel road time domain model is established via the Inverse Fourier Transform, and the deviation between the two wheels road PSDs on the same axle is studied firstly. Secondly, a road frequency compensation algorithm is proposed to correct the deviation of the two-wheel road PSDs on the same axle and it is installed in a road time domain model, and then it is studied via simulation and compared with ISO 8608. Finally, the road frequency compensation algorithm is applied on a 7-DOF vehicle dynamic study.

2. Power Spectral Density of the Road Surface Roughness

The road surface roughness is usually described in terms of the PSD of the road displacement amplitudes [20–22], and the road spectral density depends on the road itself (roughness and wave number/distribution). According to ISO 8608, road roughness level is classified from A to H, and a general form of the fitted PSD is given as follows:

$$G_q(n) = G_q(n_0) \cdot \left(\frac{n}{n_0}\right)^{-W}, \tag{1}$$

where n is the spatial frequency (m^{-1}), n_0 is the reference spatial frequency ($n_0 = 0.1\,\mathrm{m}^{-1}$), $G_q(n)$ is the spatial PSD ($\mathrm{m}^2/\mathrm{m}^{-1}$), $G_q(n_0)$ is the spatial PSD at the reference spatial frequency ($\mathrm{m}^2/\mathrm{m}^{-1}$), W is undulation exponent, and the undulation exponents are given with values in the range from 1.8 to 3.3.

The general expression for the relationship between the vehicle speed V (m/s), the spatial frequency f (Hz), and the temporal frequency $G_q(f)$ (m^2/Hz) are presented in

$$\begin{gathered} f = V \cdot n, \\ G_q(f) = \frac{1}{V} \cdot G_q(n) = G_q(n_0) \cdot n_0^W \cdot \frac{V^{W-1}}{f^W}. \end{gathered} \tag{2}$$

Taking statistical analysis of the road surface into account, the spatial frequency n ranges from 0.011 to 2.83 m^{-1}, at the commonly speed (10–30 m/s), it can guarantee the temporal frequency f ranges from 0.33 to 28.3 Hz, which considers the natural frequencies of the sprung mass and unsprung mass effectively.

3. Single-Wheel Road Time Domain Model

Discrete PSD in temporal frequency domain is required to simulate road surface in time domain, which can be obtained by

$$G_q(f_k) = \begin{cases} 0, & k = 1, 2, \ldots, N_l, \\ G_q(n_0)\, n_0^W \dfrac{V^{W-1}}{f_k^W}, & k = N_l + 1, N_l + 2, \ldots, N_u + 1, \\ 0, & k = N_u + 2, N_u + 3, \ldots, N, \end{cases} \tag{3}$$

where $G_q(f_k)$ is the discrete PSD in temporal frequency domain, and N_l is the lower limit of the spatial frequency, N_u is the upper limit of the spatial frequency.

According to the Fourier transform, the relationship between the discrete PSD in temporal frequency domain

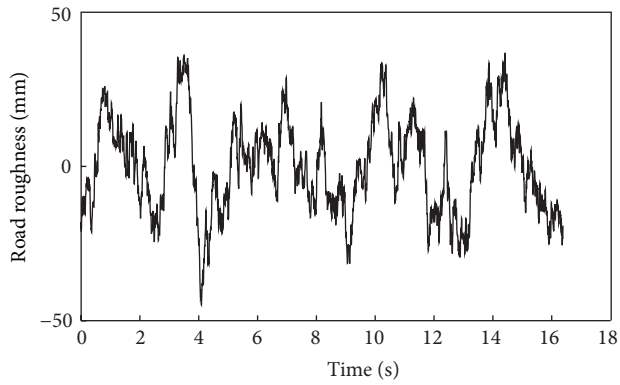

Figure 1: Single-wheel road surface time domain signal (C-level road, 70 Km/h).

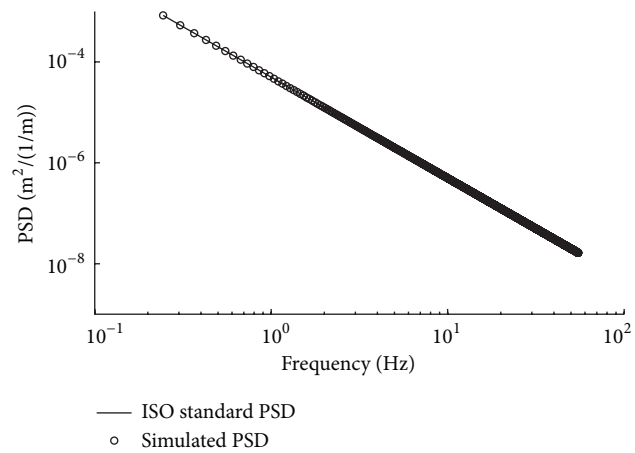

Figure 2: Comparison of the road PSD simulated with the ISO 8608 standard.

and the corresponding spectral amplitude can be obtained as follows:

$$|Q(k)| = N\sqrt{\frac{\Delta f}{2}G_q(f_k)}, \quad \Delta f = \frac{1}{T} \tag{4}$$

$$Q(k) = |Q(k)| \cdot e^{j\phi_k}, \tag{5}$$

where $Q(k)$ is the road random excitation spectrum, T is the sampling time, $|Q(k)|$ is the corresponding spectral amplitude, j is the imaginary unit, and ϕ_k is a uniformly distributed random variable ranged from 0 to 2π, $k = 1, 2, \ldots, N$.

Then, road roughness random excitation signal can be obtained by the inverse Fourier transform of the complex sequences $Q(k)$ $(k = 1, 2, 3, \ldots, N)$:

$$x(n) = \frac{1}{N}\sum_{k=1}^{N} Q(k)\, e^{j(2\pi/N)nk}, \quad k = 1, 2, \ldots, N. \tag{6}$$

A single-wheel C-level road surface time domain signal is shown in Figure 1, in which the vehicle speed is 70 km/h. A comparison of the road PSD simulated with the ISO 8608 standard is shown in Figure 2, which shows that the road PSD simulated can match the ISO C-level road very well. In a word, the inverse Fourier transform method for a single-wheel road time domain model is accurate.

4. Four-Wheel Road Time Domain Model

A four-wheel vehicle is subjected to excitations due to road roughness on the left and right wheel paths. Hence, to describe the excitations we need a stochastic model of parallel road tracks. The model should describe the variation within each track and the covariation between the tracks [23]. A four-wheel road time domain model is usually generated based on the correlation of the four-wheel road input, in which there is a time delay between the front and rear axle and the space is correlated between the left and right wheels. And, a four-wheel road surface domain model is established based on the following two assumptions.

(1) The wheel tracks of the vehicle front axle and rear axle are equal, and the vehicle keeps in a straight line with a constant speed.

(2) The statistical properties of the road profiles at left and right tires are the same, in other words, the auto-power spectral density of the road profiles at left and right tires is the same and equal to the standard.

While the left and right tracks are usually statistically equivalent, the actual profiles are not identical. Generally, the difference between the left and right tracks brings a roll disturbance. However, the information regarding this roll disturbance is not included in the PSD of the individual wheel paths. Hence, in addition to the PSD, it is appropriate to study the coherence function. The statistical properties of road roughness between the left and right wheels are usually described by a cross-power spectral density function or a coherence function [24–26]. Surprisingly, the coherence functions of all roads (smooth motorways, main roads, paved country roads, gravel roads, etc.) are very similar [27]. And the coherence function is described by

$$\operatorname{coh}(n) = \frac{|G_{xy}(n)|}{\sqrt{G_{xx}(n)\cdot G_{yy}(n)}}, \tag{7}$$

where $G_{xx}(n)$ and $G_{yy}(n)$ are the auto-spectral densities of the individual tracks (m^2/m^{-1}), and $G_{xy}(n)$ is the associated cross-spectral density (m^2/m^{-1}), B is the wheel track (m), and n is the spatial frequency (m^{-1}).

The measurement data yield a coherence function which drops from a high value at $n = 0$ to a very small value at high-frequency band [28], and the range is from 0 to 1. When $\operatorname{coh}(n) = 0$, the left- and right-wheel road roughness is completely uncorrelated, while the left- and right-wheel road roughness is perfectly correlated if $\operatorname{coh}(n) = 1$. Robson [29] pointed out that the coherence function depends on the

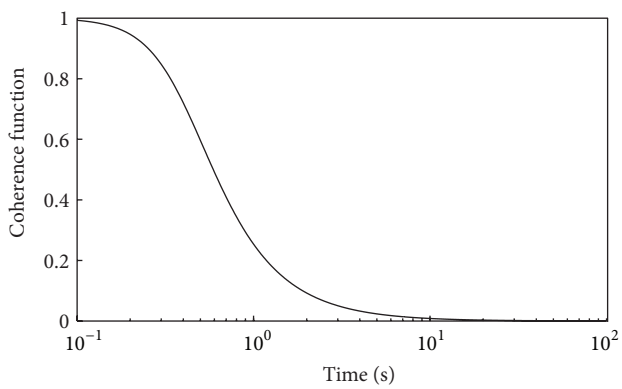

Figure 3: The coherence function of the left and right track under C-level road.

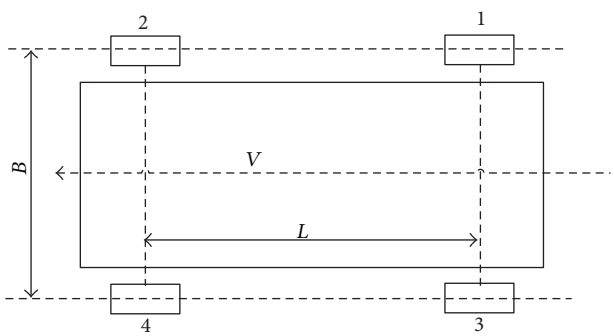

Figure 4: A top view of four-wheel vehicle.

wheel track and spatial frequency. The coherence function was described by Ammon [30] as

$$\operatorname{coh}(n, B) = \left[1 + \left(\frac{nB^{\varepsilon}}{n_q}\right)^{\partial}\right]^{-q}, \tag{8}$$

where the inflection point and the slope of the inflection point are determined by the parameters n_q and q, which can be fitted by experimental data. ε is the density of the coherence function between different tracks and ∂ is the frequency index. The coherence function of the left and right tracks under C-level road is shown in Figure 3.

Previously the single-wheel road time domain model and coherence function have been introduced, then a four-wheel road time domain model will be discussed as follows. A top view of four-wheel vehicle is shown in Figure 4, and the spectrum matrix of four-wheel road input is described in

$$\begin{aligned}\left[G_q(f)\right] &= \begin{bmatrix} G_{11} & G_{12} & G_{13} & G_{14} \\ G_{21} & G_{22} & G_{23} & G_{24} \\ G_{31} & G_{32} & G_{33} & G_{34} \\ G_{41} & G_{42} & G_{43} & G_{44} \end{bmatrix} \\ &= \begin{bmatrix} G_{11} & G_{11}e^{-j2\pi f\tau} & G_{13} & G_{13}e^{-j2\pi f\tau} \\ G_{11}e^{j2\pi f\tau} & G_{11} & G_{13}e^{j2\pi f\tau} & G_{13} \\ G_{13}^{*} & G_{13}^{*}e^{-j2\pi f\tau} & G_{33} & G_{33}e^{-j2\pi f\tau} \\ G_{13}^{*}e^{j2\pi f\tau} & G_{13}^{*} & G_{33}e^{j2\pi f\tau} & G_{33} \end{bmatrix},\end{aligned} \tag{9}$$

where G_{ij} $(i \neq j)$ $(i, j = 1, 2, 3, 4)$ is the cross-power spectral density, G_{ij} $(i = j)$ is the auto-power spectral density, G_{ij}^{*} is the complex conjugate matrix of G_{ij}, and τ is the time delay of front- and rear-wheel road input, which can be expressed as

$$\tau = \frac{L}{V}, \tag{10}$$

where L is the wheelbase (m) and V is the vehicle speed (m/s). $G_{13}(f)$ can be obtained by

$$\begin{aligned}G_{13}(f) &= \left|G_{13}(f)\right| e^{j\phi_{13}(f)} \\ &= \sqrt{G_{11}(f) \cdot G_{33}(f)} \cdot \operatorname{coh}(f) \cdot e^{j\phi_{13}(f)},\end{aligned} \tag{11}$$

where $\phi_{13}(f)$ is the phase difference of road PSD of the left- and right-front wheel. According to measured pavements, the phase differences of road PSD of the left- and right-front wheel are approximately 0; at this point, the impacts on vehicle performance are negligible; thus, it is assumed that $\phi_{13}(f) = 0$ in this paper. Therefore, (11) and (9) can be rewritten as

$$\begin{gathered}G_{13}(f) = \left|G_{13}(f)\right| e^{j\phi_{13}(f)} = \sqrt{G_{11}(f) \cdot G_{33}(f)} \cdot \operatorname{coh}(f), \\ \left[G_q(f)\right] = G_q(f) \begin{bmatrix} 1 & e^{-j2\pi f\tau} & \operatorname{coh}(f) & \operatorname{coh}(f)\, e^{-j2\pi f\tau} \\ e^{j2\pi f\tau} & 1 & \operatorname{coh}(f)\, e^{j2\pi f\tau} & \operatorname{coh}(f) \\ \operatorname{coh}(f) & \operatorname{coh}(f)\, e^{-j2\pi f\tau} & 1 & e^{-j2\pi f\tau} \\ \operatorname{coh}(f)\, e^{j2\pi f\tau} & \operatorname{coh}(f) & e^{j2\pi f\tau} & 1 \end{bmatrix}.\end{gathered} \tag{12}$$

Then, the road spectrum relationship between the left and right wheels can be obtained as follows:

$$Q_3(f) = Q_1(f) \operatorname{coh}(f). \tag{13}$$

And the road spectrum relationship between the front and rear wheels can be obtained as follows:

$$Q_2(f) = Q_1(f)\, e^{-j2\pi f\tau}. \tag{14}$$

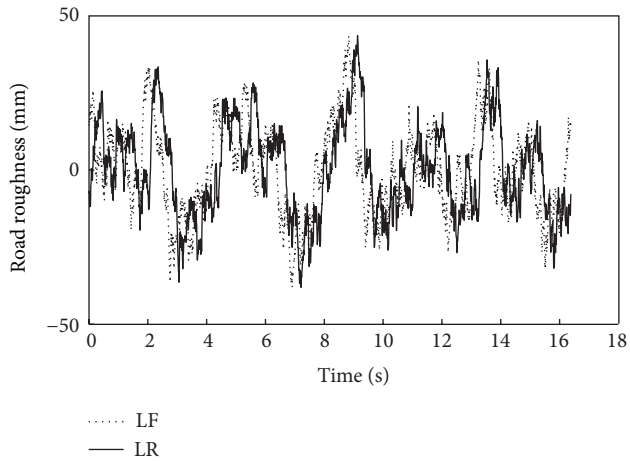

Figure 5: Comparison of left-front wheel (LF) with left-rear wheel (LR) time domain signal.

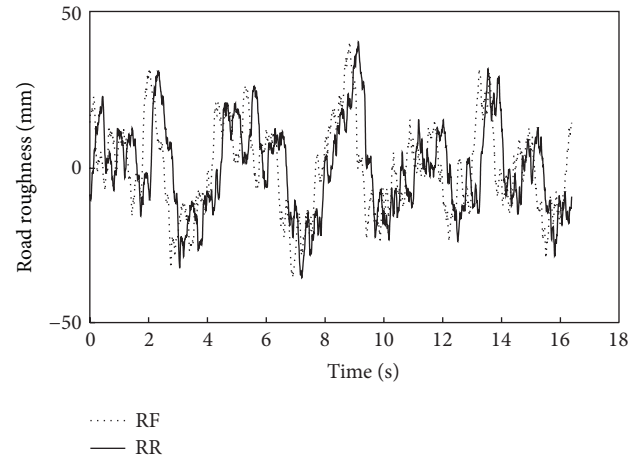

Figure 6: Comparison of right-front wheel (RF) with right-rear wheel (RR) time domain signal.

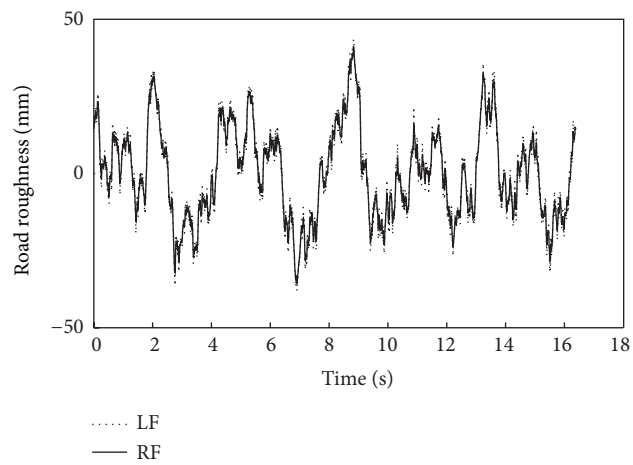

Figure 7: Comparison of left-front wheel (LF) with right-front wheel (RF) time domain signal.

So far a four-wheel time domain model can be obtained via the following steps.

(1) Road roughness level $G_q(n_0)$, the vehicle speed V, the coherence function $\mathrm{coh}(f)$, the lower limit of the spatial frequency N_l, and the upper limit of the spatial frequency N_u are known as initial conditions.

(2) The spectrum of left-front wheel road roughness $Q_1(k)$ can be obtained analogous to the method of generating single-wheel road random excitation spectrum.

(3) The road random excitation spectrum of other wheels $Q_2(k)$ and $Q_4(k)$ can be obtained from (15)–(17), and there is a time delay between the left-front road input $Q_1(k)$ and the left-rear road input $Q_3(k)$. The $Q_2(k)$ and $Q_4(k)$ are obtained via a coherence function between the left and right wheels:

$$Q_2(k) = Q_1(k)\, e^{-j2\pi f_k \tau}, \tag{15}$$

$$Q_3(k) = Q_1(k)\, \mathrm{coh}(k), \tag{16}$$

$$Q_4(k) = Q_3(k)\, e^{-j2\pi f_k \tau} = Q_1(k)\, \mathrm{coh}(k)\, e^{-j2\pi f_k \tau}. \tag{17}$$

(4) The corresponding road roughness random excitation signals can be obtained by the inverse Fourier transform of the complex sequences $Q_i(k)$ $(i = 1, 2, 3, 4)$,

$$x_i(n) = \frac{1}{N}\sum_{k=1}^{N} Q_i(k)\, e^{j(2\pi/N)nk}, \quad n = 1, 2, \ldots, N. \tag{18}$$

5. Simulation Results

The results indicated in this section include the simulation of the road surfaces discussed in the previous section. And a four-wheel road surface time domain signal for a class C random road at the speed of 70 Km/h is shown in Figures 5–7.

Figure 5 shows a comparison of the road time domain signal between the left-front wheel (LF) and the left-rear wheel (LR), and the comparison of the road time domain signal between the right-front wheel (RF) and the right-rear wheel (RR) is shown in Figure 6. It can be found obviously that there is time delay between front-wheel and rear-wheel time domain signals, which is exactly equal to the L/V (see (10)). Figure 8 is a comparison of the road PSDs simulated with the ISO 8608 standards. Figures 8(a) and 8(c) demonstrate that the road PSD of the front and rear wheels is consistent with the ISO 8608 standard values, which proves that the Inverse Fourier Transform is accurate to generate the front- and rear-wheel time domain signals. However, from Figure 7, we can see that the amplitude of right-front wheel (RF) is smaller than left-front wheel (LF) time domain signal; simultaneously, there is a deviation $\Delta G_q(f)$ between the road PSD of the left and right wheels from the beginning of midfrequency band in Figures 8(b) and 8(d), and the deviation increases with the frequency increasing. In other words, the road PSD of the right wheel is smaller than the

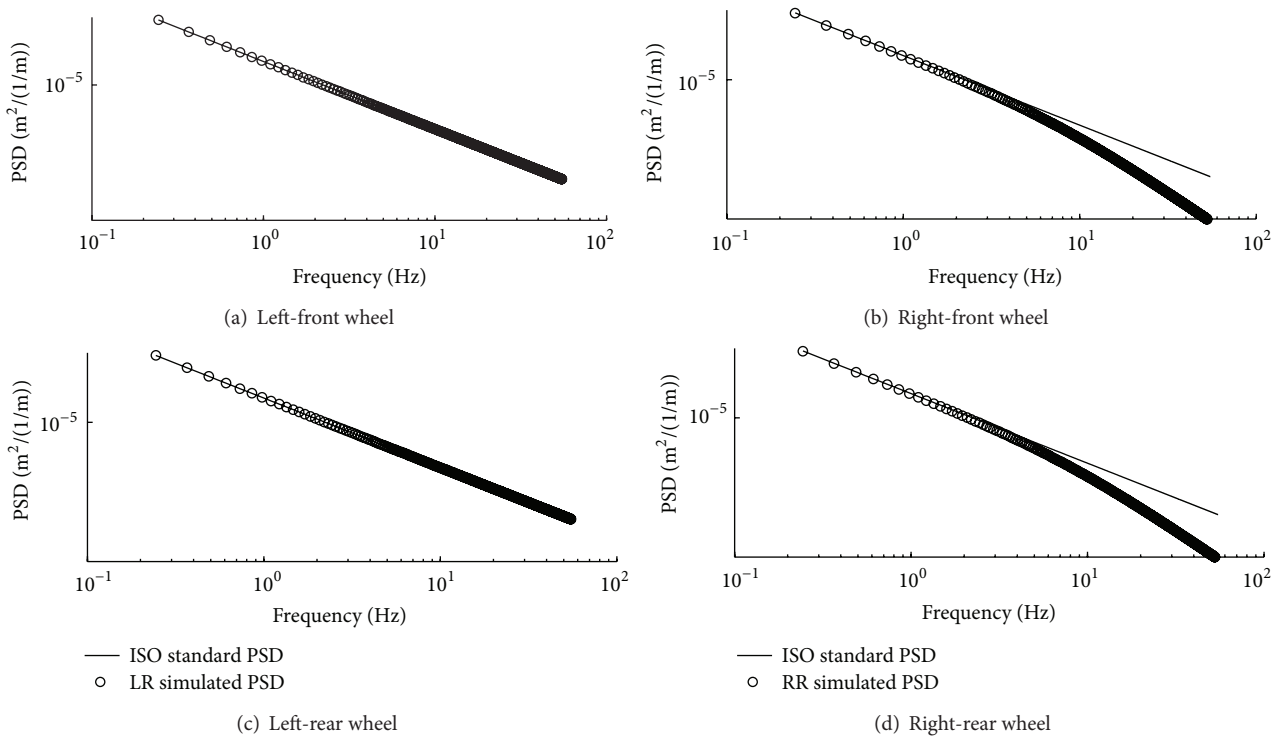

(a) Left-front wheel (b) Right-front wheel

(c) Left-rear wheel (d) Right-rear wheel

Figure 8: Comparison of the road PSDs simulated with the ISO 8608 standards.

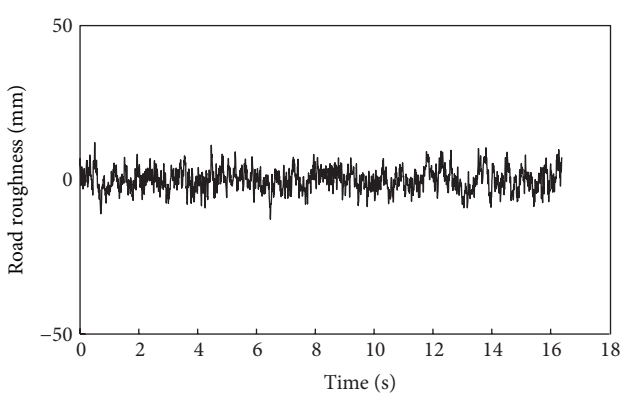

Figure 9: The smaller time domain signal generated based on the deviation $\Delta G_q(f)$.

road PSD of the left wheel on the same axle that is consistent with the ISO 8608 standard value, which can be described by

$$\Delta G_q(f) = G_q(f) - G_{q\text{simu}}(f), \tag{19}$$

where $G_q(f)$ is the standard PSD values, $G_{q\text{simu}}(f)$ is the simulated PSD values, and $\Delta G_q(f)$ is the deviation between the road PSD of the left wheel (consistent with the standard) and right wheel.

In addition, the right-wheel time domain signal cannot be obtained when $\text{coh}(f)$ is 0, which only considers the correlation of the left- and right-wheel road roughness, while ignoring the uncorrelation of the left- and right-wheel road roughness. Since the value of coherence function is between 0 and 1 and it is near 0 at high-frequency band, according to (16) and (17), it can be found that the reasons for the deviation are mainly from the coherence function. Hence, the compensation of the right-wheel time domain signal will be presented in the sequel.

6. Correction of Four-Wheel Road Time Domain Model

From the above, we know that there is a deviation $\Delta G_q(f)$ between the road PSD of left and right wheels since the uncorrelation of the left- and right-wheel road roughness is ignored. Hence, considering the uncorrelation of the left and right wheel road roughness, a new road spectrum relationship between the left and right wheels can be described by,

$$Q_3'(f) = Q_1(f)\,\text{coh}(f) + \Delta Q(f), \tag{20}$$

where, $\Delta Q(f)$ reflects the uncorrelation of the left- and right-wheel road roughness, which can be obtained by $\Delta G_q(f)$ based on (4) and (5). A compensation using time domain signal is generated via the inverse Fourier transform of $\Delta Q(f)$ by using new random sequence numbers, which is shown in Figure 9.

A new right-wheel time domain signal can be obtained by compensating the time domain deviation signal. A comparison of left-front wheel with right-front wheel time domain-compensated signal is shown in Figure 10, and it can be found that the amplitude of right-front wheel (RF) and left-front wheel (LR) time domain signals are the same approximately.

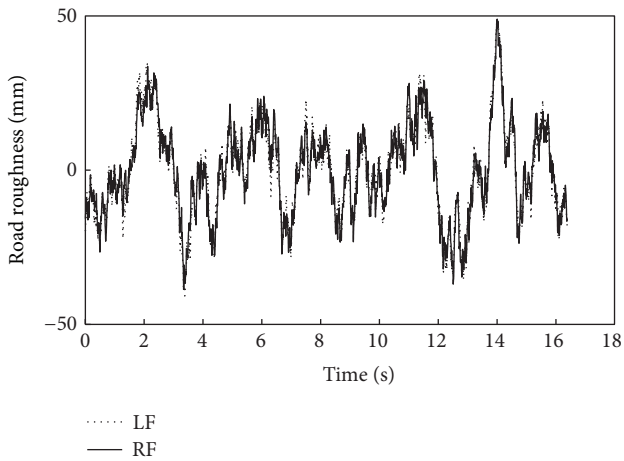

Figure 10: Comparison of left-front wheel (LF) with right-front wheel (RF) time domain signal after compensating.

Then, the new road PSDs of the four wheels can be obtained via Fourier transform, which is shown in Figure 11. It shows that the new road PSDs simulated can match ISO 8608 standards very well. In a word, this frequency compensation algorithm for a four-wheel road time domain model is accurate.

In addition, for the limit case, the method is also applicable. When coh(f) is 0, the left- and right-wheel time domain signals are completely uncorrelated, and a comparison of left-front wheel with left-rear wheel time domain signals is shown in Figure 12. It illustrates that the right-front wheel (RF) and left-front wheel (LR) time domain signals are completely uncorrelated, which correspond with the definition of the correlation function. Figure 13 shows the comparison of the road PSDs simulated with the ISO 8608 standards. Obviously, the new road PSDs simulated can match ISO 8608 standards very well.

When coh(f) is 1, the left- and right-wheel road roughness are perfectly correlated, and a comparison of the left-front wheel with the left-rear wheel time domain signals is shown in Figure 14. It illustrates that the right-front wheel (RF) and left-front wheel (LR) time domain signals are completely the same, which correspond with the definition of the correlation function. Figure 15 shows the comparison of the road PSDs simulated with the ISO 8608 standards. Obviously, the new road PSDs simulated can also match ISO 8608 standards very well. In summary, this frequency compensation algorithm for a four-wheel road time domain model is accurate.

The frequency compensation algorithm can also be used to correct the four-wheel surface time domain models generated by other methods when there is a deviation between the road PSDs simulated and the ISO 8608 standards.

7. Analysis on Vehicle Dynamic Behavior

Since the road surface irregularities are the main source of excitation to the vehicle system, to analyze the vehicle dynamic behavior more accurately, a suitable representation of these irregularities is required, which is shown in Figure 16.

A comparison of vehicle dynamic behavior w/o (with or without) compensation will be presented as follows. Firstly, a 7-DOF vertical vehicle model is shown in Figure 17, which considers the vertical motion, pitch and roll of the sprung mass, and the four vertical motions of four unsprung masses.

Each corner of the vehicle is identified with $\{i, j\}$ index, where $i = \{l, r\}$ holds for left/right and $j = \{f, r\}$ for front/rear. These corners (i.e., positions and velocities of the dynamical part) are described as

$$\begin{aligned}
z_{fl} &= z - \alpha l_f + \beta w - z_{tfl},\\
z_{fr} &= z - \alpha l_f - \beta w - z_{tfr},\\
z_{rl} &= z + \alpha l_r + \beta w - z_{trl},\\
z_{rr} &= z + \alpha l_r - \beta w - z_{trr},\\
\dot{z}_{fl} &= \dot{z} - \dot{\alpha} l_f + \dot{\beta} w - \dot{z}_{tfl},\\
\dot{z}_{fr} &= \dot{z} - \dot{\alpha} l_f - \dot{\beta} w - \dot{z}_{tfr},\\
\dot{z}_{rl} &= \dot{z} + \dot{\alpha} l_r + \dot{\beta} w - \dot{z}_{trl},\\
\dot{z}_{rr} &= \dot{z} + \dot{\alpha} l_r - \dot{\beta} w - \dot{z}_{trr},
\end{aligned} \tag{21}$$

where z is the center of the sprung mass, α (resp. β) is the pitch (resp. roll) angle of the sprung mass around y-axis (resp. x-axis) at the center of sprung mass. l_f, l_r, and w define the vehicle geometrical properties (as shown in Figure 17).

The full vehicle model, as depicted on Figure 17, is given by the following motion equations:

$$\begin{aligned}
m_{tfl}\ddot{z}_{tfl} + k_{tfl}\left(z_{tfl} - z_{fl}\right) - F_{sfl} - F_{dfl} &= 0,\\
m_{tfr}\ddot{z}_{tfr} + k_{tfr}\left(z_{tfr} - z_{fr}\right) - F_{sfr} - F_{dfr} &= 0,\\
m_{trl}\ddot{z}_{trl} + k_{trl}\left(z_{trl} - z_{rl}\right) - F_{srl} - F_{drl} &= 0,\\
m_{trr}\ddot{z}_{trr} + k_{trr}\left(z_{trr} - z_{rr}\right) - F_{srr} - F_{drr} &= 0,\\
\sum m\ddot{z} + F_{sij} + F_{dij} &= 0,\\
\sum I_\alpha \ddot{\alpha} - F_{sfj} l_f + F_{srj} l_r - F_{dfj} l_f + F_{drj} l_r &= 0,\\
\sum I_\beta \ddot{\beta} + wF_{sil} - wF_{sir} + wF_{dil} - wF_{dir} &= 0,
\end{aligned} \tag{22}$$

where m and m_{tij} denote the sprung and unsprung mass, respectively. The moment of inertia about the x-axis (resp. y-axis) of the vehicle sprung mass is denoted as I_β (resp. I_α). F_{sij} and F_{dij} are spring force and damper force, respectively, which can be described by

$$F_{sij} = k_{sij} z_{ij}, \qquad F_{dij} = c_{ij}\dot{z}_{ij}, \tag{23}$$

where k_{sij} and c_{ij} are spring stiffness and damping coefficient, respectively.

Then, the full vehicle model can be established by Matlab/Simulink, and the outputs include the weighted RMS

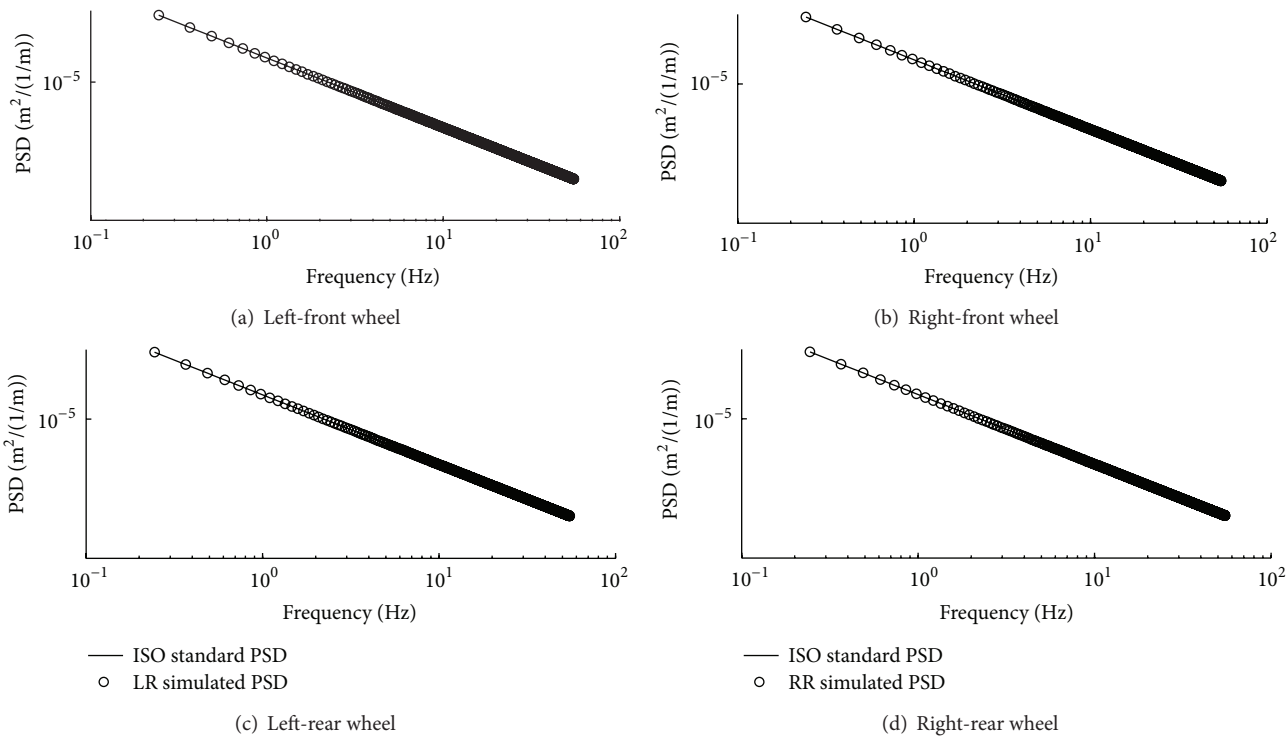

(a) Left-front wheel (b) Right-front wheel

(c) Left-rear wheel (d) Right-rear wheel

Figure 11: Comparison of the new road PSDs of the four wheels simulated with the ISO 8608 standards.

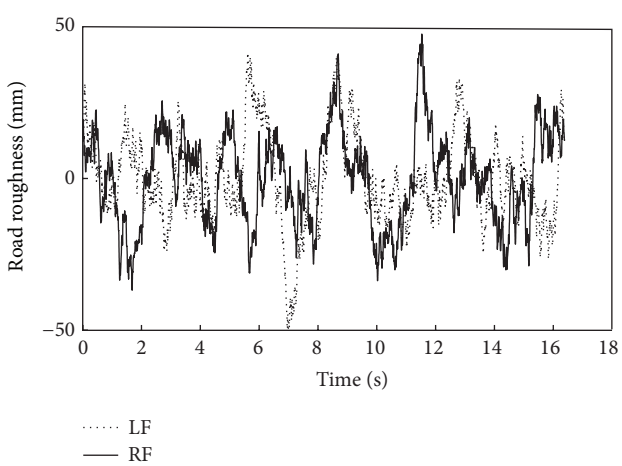

Figure 12: Comparison of left-front wheel (LF) with left-rear wheel (LR) time domain signal when coh(f) is 0.

(root mean square) of acceleration (Ac_rms, m/s^2), the roll angle RMS (β_rms), the pitch angle RMS (α_rms), and the tire vertical force RMS (Ft_FL_rms, Ft_FR_rms, Ft_RL_rms, Ft_RR_rms, N).

In this paper, the frequency compensation algorithm is installed in the road input for a sedan model to illustrate the sedan's behavior. The parameters of a C-class sedan are shown in Table 1. Simulation results run over a C-level road surface with the speed of 70 Km/h tabulated in Table 2. And the frequency compensation algorithm can also be installed in the other vehicle runs on a random road.

Table 1: Parameters of the C-class sedan.

Symbol	Description	Unit	Value
m	Vehicle sprung mass	kg	2110
m_{fl}	Front/left unsprung mass	kg	58.3
m_{fr}	Front/right unsprung mass	kg	58.3
m_{rl}	Rear/left unsprung mass	kg	63.3
m_{rr}	Rear/right unsprung mass	kg	63.3
k_{tfl}	Front/left vertical tyre stiffness	N/m	235000
k_{tfr}	Front/right vertical tyre stiffness	N/m	235000
k_{trl}	Rear/left vertical tyre stiffness	N/m	235000
k_{trr}	Rear/right vertical tyre stiffness	N/m	235000
k_{sfl}	Front/left spring stiffness	N/m	27500
k_{sfr}	Front/right spring stiffness	N/m	27500
k_{srl}	Rear/left spring stiffness	N/m	31300
k_{srr}	Rear/right spring stiffness	N/m	31300
l_f	Distance between front-axle/c.o.g. G	m	1.455
l_r	Distance between rear-axle/c.o.g. G	m	1.515
w	Wheel track	m	1.610
I_β	Sprung mass roll moment of inertia	kg·m^2	710.1
I_α	Sprung mass pitch moment of inertia	kg·m^2	3668.5

In this analysis, the road input of left-front tire is set as a baseline, then the right-front road input is obtained via a coherence function w/o a compensation, and the rear road

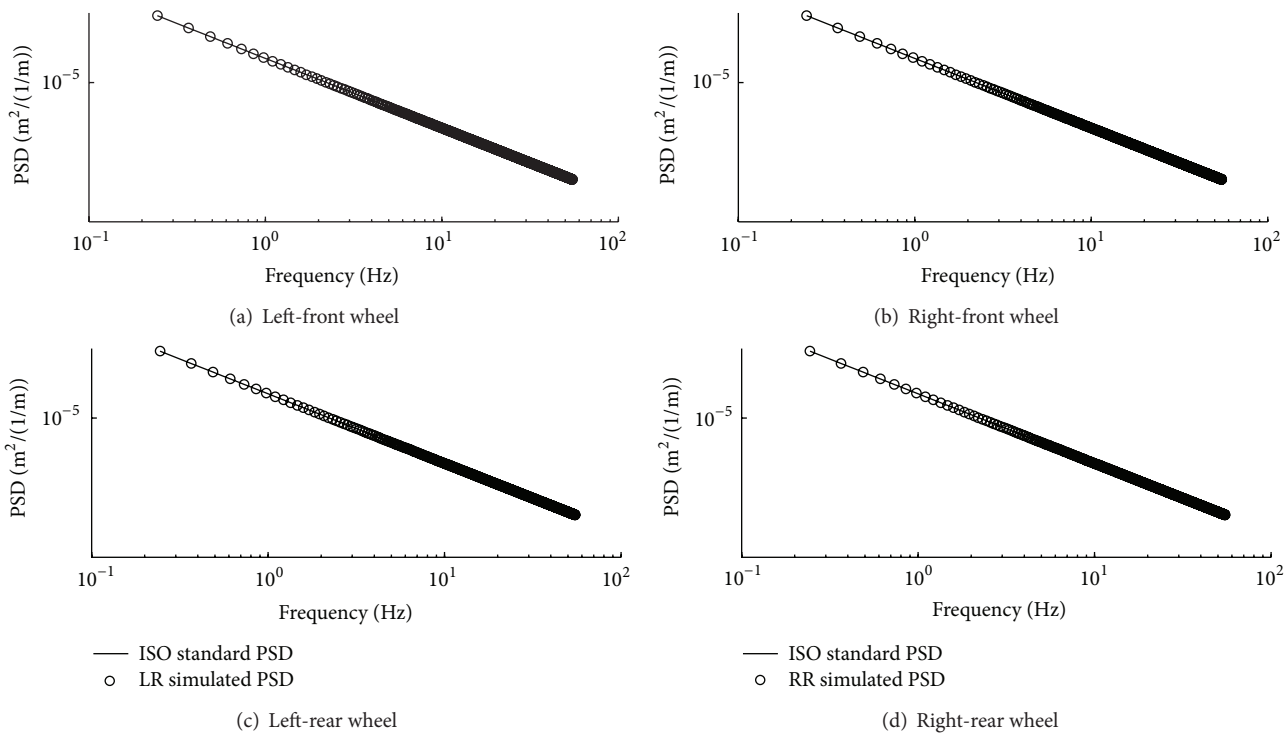

(a) Left-front wheel (b) Right-front wheel

(c) Left-rear wheel (d) Right-rear wheel

Figure 13: Comparison of the road PSDs simulated with the ISO 8608 standards when coh(f) is 0.

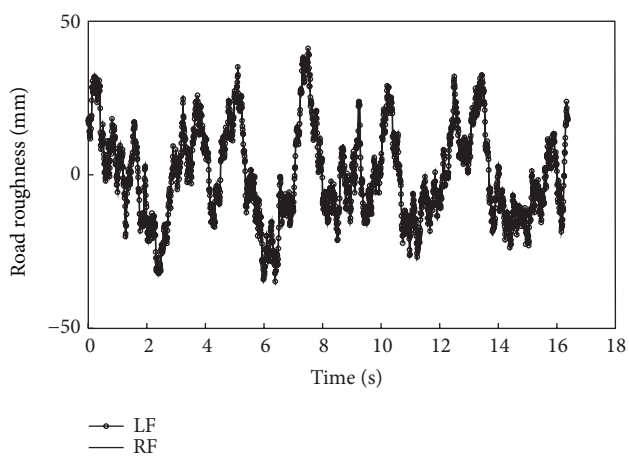

Figure 14: Comparison of left-front wheel (LF) with left-rear wheel (LR) time domain signal when coh(f) is 1.

Table 2: Simulation results.

Results	Without compensation	With compensation	Difference
Ac_rms	0.3638	0.4081	10.8%
α_rms	0.0062	0.0062	0
β_rms	$9.10e-4$	0.0017	46.4%
Ft_FL_rms	$1.0115e+3$	$1.0162e+3$	0.5%
Ft_FR_rms	$0.6824e+3$	$1.0100e+3$	32.7%
Ft_RL_rms	$1.0514e+3$	$1.0566e+3$	0.5%
Ft_RR_rms	$0.7190e+3$	$1.0534e+3$	31.4%

input has a time delay dependent on the wheel base and vehicle speed. Table 2 shows that the α_rms, Ft_FL_rms, and Ft_RL_rms without compensation are almost equal to the values with compensation since the PSDs of the left-side road input are the same, while the Ac_rms, β_rms, Ft_FR_rms, and Ft_RR_rms without compensation are significant smaller than the values with compensation, which is precisely caused by the previously mentioned deviation, since there is a deviation between the road PSDs of the two wheels on the same axle, which is the main reason that the acceleration RMS, the roll angle RMS, the RMS of tire vertical force of the right-front and right-rear wheels without compensation are smaller than the values with compensation. Hence, the deviation of the PSD of the road input between two wheels on the same axle has an important influence on vehicle performances, which illustrates the importance of the frequency compensation algorithm proposed, which can be used for a control system installed in the vehicle to compensate road roughness for damper tuning in the future.

8. Conclusions

The road surface roughness has an important influence on ride comfort, ride safety, vehicle maneuverability, driver's and occupants' comfort, and vehicle dynamic load. In recent decades, random road models have been widely studied, and a four-wheel random road time domain model is usually generated based on the correlation of the four-wheel input, in

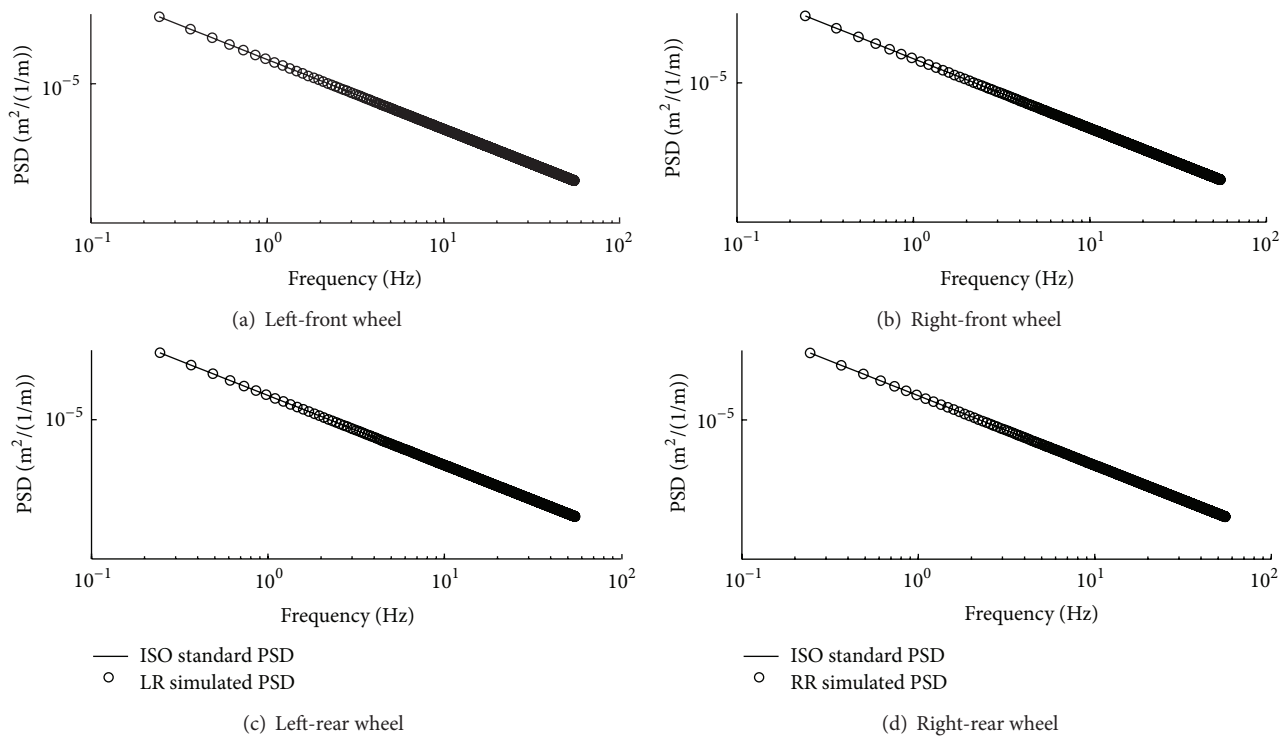

Figure 15: Comparison of the road PSDs simulated with the ISO 8608 standards when coh(f) is 1.

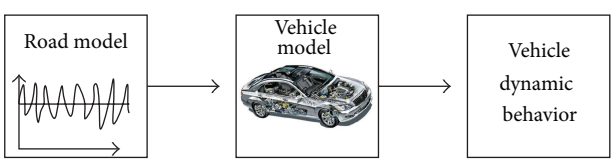

Figure 16: Analysis on the vehicle dynamic behavior.

which a coherence function is used to describe the coherence of the road input between the left and right wheels usually. Generally, the value of coherence function is between 0 and 1, and it is near 0 at high-frequency band. As a result, the road roughness amplitude and the road PSD of one track will be smaller than the other one on the same axle; actually, it is caused by the uncorrelation between the left- and right-wheel road surface roughness. Hence, a frequency compensation algorithm is proposed to correct the deviation of the PSD of the road input between two wheels on the same axle, and it is installed in a 7-DOF vehicle dynamic study. The main conclusions can be drawn from the current study as follows.

(1) It is simple and accurate to generate a single-wheel time signal model by using the inverse Fourier transform method.

(2) With the Inverse Fourier Transform method via coherence function, the road PSDs of the front and rear wheels are consistent with the standard values; however, there is a deviation between the two-wheel road PSDs on the same axle. The coherence function value is between 0 and 1, and it is near 0 at high-frequency band. As a result, the road roughness amplitude and the road PSD of one track will be smaller than the other one on the same axle.

(3) A road frequency compensation algorithm is proposed to correct the deviation of the two wheels road PSDs on the same axle, and it is installed in a road time domain model. The simulation results showed that the road PSDs with frequency compensation are consistent with the ISO 8608 standard values, which demonstrates that the proposed algorithm is correct, especially, for some limit case such as the left and right wheel road input are completely uncorrelated or perfectly correlated.

(4) The vehicle dynamic behavior with road frequency compensation show that the deviation compensation of two wheels on the same axle has an important influence on vehicle performances, which should be considered in the vehicle dynamic studies and the road frequency compensation can be used for a control system installed in the vehicle to compensate road roughness for damper tuning in the future.

Acknowledgments

Special thanks are due to the Open Research Fund Program of the State Key Laboratory of Advanced Design and Manufacturing for Vehicle Body (31115028), the China Postdoctoral Science Foundation (2012M520028), the National Natural Science Foundation of China (51205155), and the

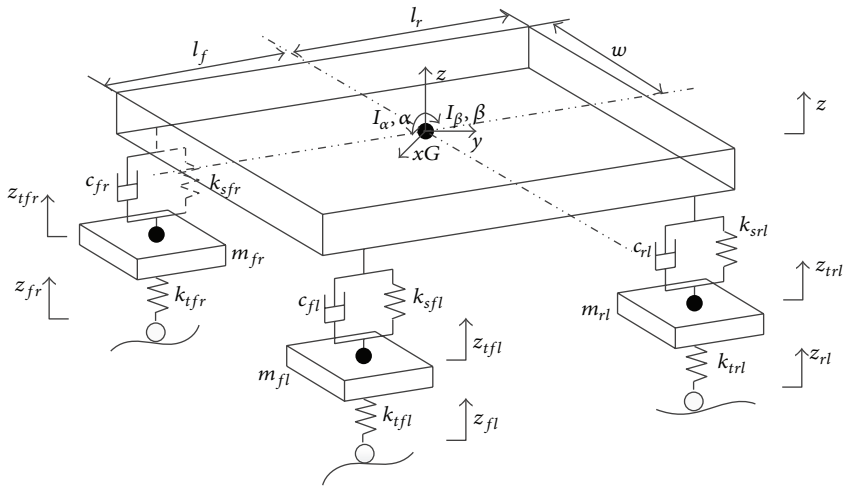

Figure 17: 7 DOF full vehicle model.

National Basic Research Program of China (973 Program) (2011CB711201) for supporting authors' research.

References

[1] P. Múčka, "Road waviness and the dynamic tyre force," *International Journal of Vehicle Design*, vol. 36, no. 2-3, pp. 216–232, 2004.

[2] Z. Yonglin and Z. Jiafan, "Numerical simulation of stochastic road process using white noise filtration," *Mechanical Systems and Signal Processing*, vol. 20, no. 2, pp. 363–372, 2006.

[3] K. Ahlin, J. Granlund, and F. Lindström, "Comparing road profiles with vehicle perceived roughness," *International Journal of Vehicle Design*, vol. 36, no. 2-3, pp. 270–286, 2004.

[4] S. M. Karamihas and M. W. Sayers, *The Little Book of Profiling*, University of Michigan, Ann Arbor, Mich, USA, 1998.

[5] M. Ambrož, G. Šušteršič, and I. Prebil, "Creating models of road sections and their use in driving dynamics simulations," *Vehicle System Dynamics*, vol. 45, no. 10, pp. 911–924, 2007.

[6] D. J. Whitehouse and J. F. Archard, "The properties of random surfaces of significance in their contact," *Proceedings of the Royal Society of London A*, vol. 316, pp. 97–121, 1970.

[7] M. Shinozuka and C.-M. Jan, "Digital simulation of random processes and its applications," *Journal of Sound and Vibration*, vol. 25, no. 1, pp. 111–128, 1972.

[8] D. Cebon, *Interaction between Heavy Vehicles and Roads*, vol. 951, Society of Automotive Engineers, 1993.

[9] J.-J. Wu, "Simulation of rough surfaces with FFT," *Tribology International*, vol. 33, no. 1, pp. 47–58, 2000.

[10] M. Grigoriu, "On the spectral representation method in simulation," *Probabilistic Engineering Mechanics*, vol. 8, no. 2, pp. 75–90, 1993.

[11] ISO, *Mechanical Vibration-Road Surface Profiles-Reporting of Measured Data*, International Organization for Standardization, 1995.

[12] T. Yoshimura, "A semi-active suspension of passenger cars using fuzzy reasoning and the field testing," *International Journal of Vehicle Design*, vol. 19, no. 2, pp. 150–166, 1998.

[13] K. Bogsjö, "Evaluation of stochastic models of parallel road tracks," *Probabilistic Engineering Mechanics*, vol. 22, no. 4, pp. 362–370, 2007.

[14] A. Pazooki, S. Rakheja, and D. Cao, "Modeling and validation of off-road vehicle ride dynamics," *Mechanical Systems and Signal Processing*, vol. 28, pp. 679–695, 2012.

[15] R. Hassan and R. Evans, "Road roughness characteristics in car and truck wheel tracks," *International Journal of Pavement Engineering*, 2012.

[16] K. Bogsjö, K. Podgórski, and I. Rychlik, "Models for road surface roughness," *Vehicle System Dynamics*, vol. 50, no. 5, pp. 725–747, 2012.

[17] S. A. Hassan and O. S. Lashine, "Identification of road surface qualities for linear and non-linear vehicle modeling," in *Proceedings of the 20th International Modal Analysis Conference (IMAC '02)*, pp. 318–323, Society for Experimental Mechanics, 2002.

[18] A. N. Heath, "Application of the isotropic road roughness assumption," *Journal of Sound and Vibration*, vol. 115, no. 1, pp. 131–144, 1987.

[19] A. N. Heath, "Evaluation of the isotropic road roughness assumption," *Vehicle System Dynamics*, vol. 17, supplement 1, pp. 157–160, 1988.

[20] D. Cebon and D. E. Newland, "The artificial generation of road surface topography by the inverse FFT method," *Vehicle System Dynamics*, vol. 12, no. 1–3, pp. 160–165, 1983.

[21] C. J. Dodds, "The laboratory simulation of vehicle service stress," *Journal of Engineering for Industry*, vol. 96, no. 2, pp. 391–398, 1974.

[22] D. Cebon and D. E. Newlan, "The artificial generation of road surface topography by the inverse FFT method," in *Proceedings of the 8th IAVSD-Symposium on the Dynamics of Vehicles on Roads and Tracks*, pp. 29–42, Swets and Zeitlinger, Cambridge, Mass, USA, 1983.

[23] C. J. Dodds and J. D. Robson, "The description of road roughness," *Journal of Sound and Vibration*, vol. 31, no. 2, pp. 175–183, 1973.

[24] K. M. A. Kamash and J. D. Robson, "Implications of isotropy in random surfaces," *Journal of Sound and Vibration*, vol. 54, no. 1, pp. 131–145, 1977.

[25] K. M. A. Kamash and J. D. Robson, "The application of isotropy in road surface modelling," *Journal of Sound and Vibration*, vol. 57, no. 1, pp. 89–100, 1978.

[26] G. C. Carter, "Coherence and time delay estimation," *Proceedings of the IEEE*, vol. 75, no. 2, pp. 236–255, 1987.

[27] K. Bogsjö, "Coherence of road roughness in left and right wheelpath," *Vehicle System Dynamics*, vol. 46, supplement 1, pp. 599–609, 2008.

[28] R. Hongbin, C. Sizhong, and W. Zhicheng, "Model of excitation of random road profile in time domain for a vehicle with four wheels," in *Proceedings of the International Conference on Mechatronic Science, Electric Engineering and Computer (MEC '11)*, pp. 2332–2335, Jilin, China, August 2011.

[29] J. D. Robson, "Road surface description and vehicle response," *International Journal of Vehicle Design*, vol. 1, no. 1, pp. 25–35, 1979.

[30] D. Ammon, "Problems in road surface modelling," *Vehicle System Dynamics*, vol. 20, pp. 28–41, 1992.

Hindawi Publishing Corporation
Mathematical Problems in Engineering
Volume 2013, Article ID 598489, 12 pages
http://dx.doi.org/10.1155/2013/598489

Research Article

Finite Frequency Vibration Control for Polytopic Active Suspensions via Dynamic Output Feedback

Yifu Zhang,[1] Gongdai Liu,[2] Pinchao Wang,[2] and Hamid Reza Karimi[3]

[1] *Research Institute of Intelligent Control and Systems, Harbin Institute of Technology, Harbin 150001, China*
[2] *School of Astronautics, Harbin Institute of Technology, Harbin 150001, China*
[3] *Department of Engineering, Faculty of Engineering and Science, University of Agder, N-4898 Grimstad, Norway*

Correspondence should be addressed to Yifu Zhang; yifu.zhang19@gmail.com

Received 18 June 2013; Accepted 25 July 2013

Academic Editor: Hui Zhang

This paper presents a disturbance attenuation strategy for active suspension systems with frequency band constraints, where dynamic output feedback control is employed in consideration that not all the state variables can be measured on-line. In view of the fact that human are sensitive to the virbation between 4–8 Hz in vertical direction, the H_∞ control based on generalized Kalman-Yakubovich-Popov (KYP) lemma is developed in this specific frequency, in order to achieve the targeted disturbance attenuation. Moreover, practical constraints required in active suspension design are guaranteed in the whole time domain. At the end of the paper, the outstanding performance of the system using finite frequency approach is confirmed by simulation.

1. Introduction

By reason of rough road conditions, passengers in the car are often in a vibration environment which negatively impacts the comfort, mental, and physical health of them, and suspensions are crucial to attenuate the disturbance transferred to passengers [1–3]. Hence, various approaches various approaches have been developed that aim to enhance suspensions' performance such as adaptive control [4], robust control [5, 6], and fuzzy control [7]. Generally speaking, there are three types of suspensions: passive, semiactive, and active suspensions. Compared with the other two kinds of suspensions, active suspensions have a greater potential to improve ride comfort and to guarantee the ride safety due to the existence of active actuator.

There are three performance requirements for active suspension systems. One is the ride comfort, which requires isolation of vibration from road; another one is handling performance mainly described by road holding, which restricts the hop of wheel in order to ensure continuous contact of wheels to road; the last one is the sprung displacement which limits the suspension stroke within an allowable band.

However, these requirements are usually conflicting. For instance, a large suspension displacement may exist if a better rider comfort performance is required . A variety of control strategies have been applied to cope with this conflict [8–12]. In particular, because the H_∞ norm index can measure the vibration attenuation performance of system appropriately [13], many suspension problems are considered by H_∞ control theory [14–22]. In this paper, the handling performance and the suspension stroke are regarded as constraints, and the ride comfort is deemed as the main index to optimize.

Although various control strategies have been applied to promote ride comfort performance of suspension systems, few of them notice the fact that due to the human body structure and other factors people are more sensitive to disturbances in 4–8 Hz than other frequency in vertical direction (ISO2361). Therefore, it is considerable to develop a finite frequency strategy to reduce the negative effect caused by disturbances in 4–8 Hz. The generalized Kalman-Yakubovich-Popov (KYP) lemma, which has been used to solve practical problems [23, 24], is applied to achieve the finite frequency control to active suspensions.

It should be mentioned that the parameters of passengers including model for suspension system could vary due to the mass change of passengers, so how to guarantee the performance of suspension with varying parameters is worth discussing. Meanwhile, considering that the mass of passengers

can be accessed on line, in this paper, the suspension model is described as a polytope, and then a parameter-dependent control law is proposed to assure the above performance requirements, which can also reach a lower conservativeness than control law based on quadratic stability and constant parameter feedback at the same time. In addition, though state feedback may attain a superior performance compared with static output feedback, measuring some states may bring burden to the systems. Thusly, constructing dynamic output feedback is desirable, which can achieve a relative enhanced performance and meanwhile reduce state-measuring sensors.

The paper is organized as follows. In Section 2 the state-space model for quarter car suspension is presented. In Section 3 the theorems which can be used to design the dynamic feedback controller are illustrated. The simulation is presented in Section 4, and the conclusion is in Section 5.

Notation. For a matrix P, P^T, P^*, P^{-1}, P^{-T}, and $P^{\perp}$ stand for its transpose, conjugate transpose, inverse, transposed inverse, and orthogonal complement, respectively; $\mathrm{sym}(P)$ denotes $P+P^T$. $P>0$ $(P<0)$ means that matrix P is positive (negative) definite. For a matrix, $\{\cdot\}_i$ stands for the ith line of the matrix. $\|G(j\omega)\|_\infty$ stands for the H_∞ norm of transfer function matrix G. For matrices P and Q, $P\otimes Q$ means the Kronecker product. In symmetric block matrices or complex matrix expressions, we use an asterisk $(*)$ to represent a term that is induced by symmetry.

2. Quarter Car Suspension Model

The model of a quarter car suspension is shown in Figure 1. m_s and m_u stand for sprung and unsprung mass, respectively. z_s, z_u, and z_r denote the sprung, unsprung displacement, and disturbance displacement from the road, respectively. k_s, k_t, c_s, and c_t are the stiffnesses and dampings of the suspension system, respectively. The input of the controller is denoted by u.

Based on the law of Newton, the motion equation of suspension can be denoted as

$$\begin{aligned} &m_s\ddot{z}_s(t)+c_s\left[\dot{z}_s(t)-\dot{z}_u(t)\right]+k_s\left[z_s(t)-z_u(t)\right]=u(t),\\ &m_u\ddot{z}_u(t)-c_s\left[\dot{z}_s(t)-\dot{z}_u(t)\right]-k_s\left[z_s(t)-z_u(t)\right]\\ &\qquad+k_t\left[z_u(t)-z_r(t)\right]-c_t\left[\dot{z}_r(t)-\dot{z}_u(t)\right]=-u(t). \end{aligned} \tag{1}$$

Define the following state variables and the disturbance input:

$$\begin{aligned} &\xi_1(t)=z_s(t)-z_u(t), \qquad \xi_2(t)=z_u(t)-z_r(t),\\ &\xi_3(t)=\dot{z}_s(t), \qquad \xi_4(t)=\dot{z}_u(t), \qquad w(t)=\dot{z}_r(t). \end{aligned} \tag{2}$$

Then (1) is equivalent to

$$\dot{\xi}(t)=A(m_s)\xi(t)+B(m_s)u(t)+B_1(m_s)w(t), \tag{3}$$

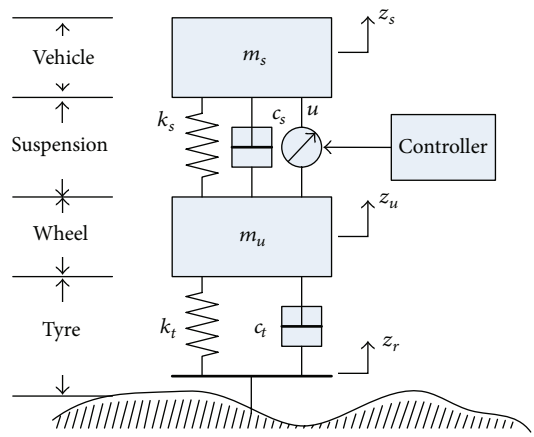

Figure 1: The quarter car model.

where

$$\begin{aligned} &\xi(t)=\left[\xi_1(t)\,\xi_2(t)\,\xi_3(t)\,\xi_4(t)\right]^T,\\ &A(m_s)=\begin{bmatrix} 0 & 0 & 1 & -1\\ 0 & 0 & 0 & 1\\ -\dfrac{k_s}{m_s} & 0 & -\dfrac{c_s}{m_s} & \dfrac{c_s}{m_s}\\ \dfrac{k_s}{m_u} & -\dfrac{k_t}{m_u} & \dfrac{c_s}{m_u} & -\dfrac{c_s+c_t}{m_u} \end{bmatrix},\\ &B(m_s)=\begin{bmatrix} 0 & 0 & \dfrac{1}{m_s} & \dfrac{-1}{m_u} \end{bmatrix}^T,\\ &B_1(m_s)=\begin{bmatrix} 0 & -1 & 0 & \dfrac{c_t}{m_u} \end{bmatrix}^T. \end{aligned} \tag{4}$$

Define

$$z_{o1}(t)=\ddot{z}_s(t), \tag{5}$$

which reflects the acceleration of m_s that contains the body mass of passengers and seat. In the design of control law for suspension system, body acceleration is the main index that needs to be optimized.

The handling performance requires continuous contact of wheel to road, which means that the suspension system needs to guarantee that dynamic tire load is less than static load, namely,

$$k_t\left(z_u(t)-z_r(t)\right)<\left(m_s+m_u\right)g. \tag{6}$$

The stroke of the suspension could not be so large that it may exceed the maximum, which can be formulated as

$$\left|z_s(t)-z_u(t)\right|<z_{\max}. \tag{7}$$

The state space expression is described integrally as

$$\begin{aligned} &\dot{\xi}(t)=A(m_s)\xi(t)+B(m_s)u(t)+B_1w(t),\\ &z_{o1}(t)=C_1(m_s)\xi(t)+D_1(m_s)u(t),\\ &z_{o2}(t)=C_2(m_s)\xi(t),\\ &y(t)=C\xi(t), \end{aligned} \tag{8}$$

where A, B, and B_1 are same with the definition in (4), and

$$C_1(m_s) = \begin{bmatrix} -\frac{k_s}{m_s} & 0 & -\frac{c_s}{m_s} & \frac{c_s}{m_s} \end{bmatrix},$$
$$C_2(m_s) = \begin{bmatrix} \frac{1}{z_{\max}} & 0 & 0 & 0 \\ 0 & \frac{k_t}{(m_s g + m_u g)} & 0 & 0 \end{bmatrix},$$
$$D_1(m_s) = \frac{1}{m_s},$$
$$C = \begin{bmatrix} 1 & 0 & 0 & 0 \\ 0 & 1 & 0 & 0 \\ 0 & 0 & 1 & 0 \end{bmatrix}. \tag{9}$$

$z_{o1}(t)$ reflects the acceleration output of m_s; $z_{o2}(t)$ represents for the relative (normalized) constraints output; $y(t)$ stands for the output of measurable states.

The parameter-varying model is depicted as the following polytopic form:

$$(A(m_s), B(m_s), B_1(m_s), C_1(m_s), C_2(m_s), D_1(m_s)) = \sum_{i=1}^{2} \lambda_i (A_i, B_i, B_{1i}, C_{1i}, C_{2i}, D_{1i}), \tag{10}$$

where

$$\begin{aligned} &(A_1, B_1, B_{11}, C_{11}, C_{21}, D_{11}) \\ &\quad = (A(m_{s\max}), B(m_{s\max}), B_1(m_{s\max}), \\ &\qquad C_1(m_{s\max}), C_2(m_{s\max}), D_1(m_{s\max})), \\ &(A_2, B_2, B_{12}, C_{12}, C_{22}, D_{12}) \\ &\quad = (A(m_{s\min}), B(m_{s\min}), B_1(m_{s\min}), \\ &\qquad C_1(m_{s\min}), C_2(m_{s\min}), D_1(m_{s\min})), \\ &\lambda_1 = \frac{1/m_s - 1/m_{s\min}}{1/m_{s\max} - 1/m_{s\min}}, \\ &\lambda_2 = \frac{1/m_{s\max} - 1/m_s}{1/m_{s\max} - 1/m_{s\min}}, \end{aligned} \tag{11}$$

and $m_{s\max}$, $m_{s\min}$ stand for the maximum and minimum of m_s, respectively.

The form of dynamic output feedback controller is described as

$$\begin{aligned} \dot{\eta}(t) &= A_K(m_s)\eta(t) + B_K(m_s)y(t), \\ u(t) &= C_K(m_s)\eta(t) + D_K(m_s)y(t). \end{aligned} \tag{12}$$

Substituting (12) into (8), we get

$$\begin{aligned} \dot{x}(t) &= \overline{A}(m_s)x(t) + \overline{B}(m_s)w(t), \\ z_{o1}(t) &= \overline{C_1}(m_s)x(t), \\ z_{o2}(t) &= \overline{C_2}(m_s)x(t), \end{aligned} \tag{13}$$

where

$$\begin{aligned} x(t) &= \begin{bmatrix} \xi(t) \\ \eta(t) \end{bmatrix}, \\ \overline{A}(m_s) &= \begin{bmatrix} A(m_s) + B(m_s)D_K(m_s)C & B(m_s)C_K(m_s) \\ B_K(m_s)C & A_K(m_s) \end{bmatrix}, \\ \overline{B}(m_s) &= \begin{bmatrix} B_1(m_s) \\ 0 \end{bmatrix}, \\ \overline{C_1}(m_s) &= [C_1(m_s) + D_1(m_s)D_K(m_s)C \quad D_1(m_s)C_K(m_s)], \\ \overline{C_2}(m_s) &= [C_2(m_s) \quad 0]. \end{aligned} \tag{14}$$

Denote

$$G(j\omega) = \overline{C_1}(m_s)\left(j\omega I - \overline{A}(m_s)\right)^{-1}\overline{B}(m_s), \tag{15}$$

as the transfer function from $w(t)$ to $z_{o1}(t)$.

The H_∞ norm of transfer function matrix G is applied to depict the ride comfort performance of suspension system, which is defined as

$$\|G(j\omega)\|_\infty = \sup_{0 \notin w \in L_2[0,+\infty)} \frac{\|z_{o2}\|_{L_2}}{\|w\|_{L_2}}, \tag{16}$$

where

$$\begin{aligned} \|z_{o2}\|_{L_2} &= \left(\int_0^{+\infty} \|z_{o2}(t)\|^2 dt\right)^{1/2}, \\ \|w\|_{L_2} &= \left(\int_0^{+\infty} \|w(t)\|^2 dt\right)^{1/2}. \end{aligned} \tag{17}$$

The control target is summarized as follows.

For a certain γ, design a dynamic output feedback in the form of (12) which satisfies

(I) The closed loop system is asymptotically stable.

(II) The finite frequency (from ω_1 to ω_2) H_∞ norm from road disturbance to vehicle acceleration is less than γ. namely,

$$\|G(j\omega)\|_{\omega_1<\omega<\omega_2\infty} < \gamma. \tag{18}$$

(III) The relative constraint responses shown in the following can be satisfied as long as the disturbance energy is less than the maximum of the 2-norm of disturbance input denoted as $w_{\max}$. that is,

$$\left|\{z_{o2}(t)\}_k\right| < 1, \quad k = 1, 2. \tag{19}$$

3. Dynamic Output Feedback Controller Design for Polytopic Suspension System

In this section, we will derive three theorems for the design of output feedback controller that satisfies (19) and one theorem of full frequency controller used for comparison.

3.1. Finite Frequency Design

Theorem 1. *For the given parameters $\gamma, \eta, \rho > 0$, if there exist symmetric matrices $P(m_s)$, positive definite symmetric matrices $P_S(m_s)$, $Q(m_s)$, and general matrix $W(m_s)$ satisfying*

$$\begin{bmatrix} -\operatorname{sym}(W(m_s)) & -W^T(m_s)\overline{A}(m_s)+P_S(m_s) & -W^T(m_s) & -W^T(m_s)\overline{B}(m_s) \\ * & -P_S(m_s) & 0 & 0 \\ * & * & -P_S(m_s) & 0 \\ * & * & * & -\eta I \end{bmatrix} < 0, \tag{20}$$

$$\begin{bmatrix} \Omega_1 & \Omega_2 \\ * & \Omega_3 \end{bmatrix} < 0, \tag{21}$$

$$\begin{bmatrix} -I & \sqrt{\rho}\left\{\overline{C}_2(m_s)\right\}_k \\ * & -P_S(m_s) \end{bmatrix} < 0, \quad k = 1, 2, \tag{22}$$

where

$$\begin{gathered} \Omega_1 = \begin{bmatrix} -\omega_1\omega_2 Q(m_s) - \operatorname{sym}\left(\overline{A}^T(m_s)W(m_s)\right) & P(m_s) - j\omega_c Q(m_s) + W^T(m_s) \\ P(m_s) + j\omega_c Q(m_s) + W(m_s) & -Q(m_s) \end{bmatrix}, \\ \Omega_2 = \begin{bmatrix} -W^T(m_s)\overline{B}(m_s) & \overline{C}_1^T(m_s) \\ 0 & 0 \end{bmatrix}, \\ \Omega_3 = \begin{bmatrix} -\gamma^2 I & 0 \\ 0 & -I \end{bmatrix}, \\ \omega_c = \frac{(\omega_1+\omega_2)}{2}, \end{gathered} \tag{23}$$

then a dynamic output feedback controller exists, which satisfies the requirements of (I), (II) and (III) with $w_{\max} = \rho/\eta$.

Proof. By using Schur complement, inequality (20) is equivalent to

$$\begin{bmatrix} \Gamma & -W^T(m_s)\overline{A}(m_s)+P_S(m_s) \\ * & -P_S(m_s) \end{bmatrix} < 0, \tag{24}$$

where

$$\begin{aligned} \Gamma = {} & \frac{1}{\eta}W^T(m_s)\overline{B}(m_s)\overline{B}^T(m_s)W(m_s) \\ & + W^T(m_s)P_S^{-1}(m_s)W(m_s) + \operatorname{sym}(W(m_s)). \end{aligned} \tag{25}$$

Multiplying (24) by $\operatorname{diag}\{-W^{-T}(m_s), P_S^{-T}(m_s)\}$ from the left side and by $\operatorname{diag}\{-W^{-1}(m_s), P_S^{-1}(m_s)\}$ from the right side, respectively, we obtain

$$\begin{bmatrix} \frac{1}{\eta}\overline{B}(m_s)\overline{B}^T(m_s) + P_S^{-1}(m_s) - \operatorname{sym}(L(m_s)) & \overline{A}(m_s)P_S^{-1}(m_s) + L^T(m_s) \\ * & -P_S^{-1}(m_s) \end{bmatrix} < 0, \tag{26}$$

where $L = -W^{-1}$.

Applying reciprocal projection theorem (see Appendix A) and choosing $S^T(m_s) = \overline{A}(m_s)P_S^{-1}(m_s)$, $\Psi(m_s) = (1/\eta)\overline{B}(m_s)\overline{B}^T(m_s)$, inequality (26) is equivalent to

$$\overline{A}(m_s)P_S^{-1}(m_s) + P_S^{-1}(m_s)\overline{A}^T(m_s) + \frac{1}{\eta}\overline{B}(m_s)\overline{B}^T(m_s) < 0. \tag{27}$$

Multiplying the above inequality from both the left and the right sides by $P_S(m_s)$, we get

$$\begin{aligned} &P_S(m_s)\overline{A}(m_s) + \overline{A}^T(m_s)P_S(m_s) \\ &\quad + \frac{1}{\eta}P_S(m_s)\overline{B}(m_s)\overline{B}^T(m_s)P_S(m_s) < 0, \end{aligned} \tag{28}$$

which guarantees

$$P_S(m_s)\overline{A}(m_s) + \overline{A}^T(m_s)P_S(m_s) < 0, \tag{29}$$

obviously. From the standard Lyapunov theory for continuous-time linear system, the closed-loop system (13) is asymptotically stable with $w(t) = 0$.

By substitution, inequality (21) is equivalent to

$$\begin{aligned} &[I \;\; F_B(m_s)]\,\Omega(m_s)\,[I \;\; F_B(m_s)]^T \\ &\quad + \operatorname{sym}(F_A(m_s)W(m_s)R) < 0, \end{aligned} \tag{30}$$

where

$$\begin{gathered} F_A(m_s) = \begin{bmatrix} -\overline{A}^T(m_s) \\ I \\ -\overline{B}^T(m_s) \end{bmatrix}, \qquad F_B(m_s) = \begin{bmatrix} \overline{C}_1^T(m_s) \\ 0 \\ 0 \end{bmatrix}, \\ R = [I \;\; 0 \;\; 0], \\ \Omega(m_s) = T\begin{bmatrix} \Phi\otimes P_s(m_s) + \Psi\otimes Q(m_s) & 0 \\ 0 & \Pi \end{bmatrix}T^T, \\ \Pi = \begin{bmatrix} I & 0 \\ 0 & -\gamma^2 I \end{bmatrix}, \qquad \Phi = \begin{bmatrix} 0 & 1 \\ 1 & 0 \end{bmatrix}, \\ \Psi = \begin{bmatrix} -1 & j\omega_c \\ -j\omega_c & -\omega_1\omega_2 \end{bmatrix}, \qquad T = \begin{bmatrix} 0 & I & 0 & 0 \\ I & 0 & 0 & 0 \\ 0 & 0 & 0 & I \\ 0 & 0 & I & 0 \end{bmatrix}. \end{gathered} \tag{31}$$

Based on projection lemma (see Appendix A), inequality (30) is equivalent to

$$F_A^{\perp}(m_s)[I \;\; F_B(m_s)]\,\Omega(m_s)\,[I \;\; F_B(m_s)]^T(F_A^{\perp}(m_s))^T < 0, \tag{32}$$

$$(R^T)^{\perp}[I \;\; F_B(m_s)]\,\Omega(m_s)\,[I \;\; F_B(m_s)]^T(R^{T\perp})^T < 0. \tag{33}$$

Noting that inequality (33) is eternal establishment, we just need to consider inequality (32), which is equivalent to

$$F^T(m_s)\,\Omega(m_s)\,F(m_s) < 0, \tag{34}$$

where

$$F(m_s) = \begin{bmatrix} I & \overline{A}^T(m_s) & 0 & \overline{C}_1^T(m_s) \\ 0 & \overline{B}^T(m_s) & I & 0 \end{bmatrix}^T. \tag{35}$$

Rewrite inequality (34) as

$$\begin{aligned} &\begin{bmatrix} \overline{A}(m_s) & \overline{B}(m_s) \\ I & 0 \\ \overline{C}_1(m_s) & 0 \\ 0 & I \end{bmatrix}^T \begin{bmatrix} \Phi\otimes P(m_s) + \Psi\otimes Q(m_s) & 0 \\ 0 & \Pi \end{bmatrix} \\ &\quad\times \begin{bmatrix} \overline{A}(m_s) & \overline{B}(m_s) \\ I & 0 \\ \overline{C}_1(m_s) & 0 \\ 0 & I \end{bmatrix} < 0, \end{aligned} \tag{36}$$

and then we obtain

$$\begin{aligned} &\begin{bmatrix} \overline{A}(m_s) & \overline{B}(m_s) \\ I & 0 \end{bmatrix}^T (\Phi\otimes P(m_s) + \Psi\otimes Q(m_s)) \\ &\quad\times \begin{bmatrix} \overline{A}(m_s) & \overline{B}(m_s) \\ I & 0 \end{bmatrix} + \begin{bmatrix} \overline{C}_1(m_s) & 0 \\ 0 & I \end{bmatrix}^T \\ &\quad\times \Pi \begin{bmatrix} \overline{C}_1(m_s) & 0 \\ 0 & I \end{bmatrix} < 0. \end{aligned} \tag{37}$$

Applying generalized KYP lemma (see Appendix A), we get

$$\Xi^*\Pi\Xi < 0, \qquad \omega_1 < \omega < \omega_2, \tag{38}$$

where

$$\Xi = \begin{bmatrix} \overline{C}_1(m_s) & 0 \\ 0 & I \end{bmatrix}\begin{bmatrix} (j\omega I - (\overline{A}(m_s))^{-1}\overline{B}(m_s) \\ I \end{bmatrix}, \tag{39}$$

namely,

$$\sup_{\omega_1<\omega<\omega_2} \|G(j\omega)\|_\infty < \gamma. \tag{40}$$

Select

$$V(t) = x^T(t)P_S(m_s)x(t) \tag{41}$$

as the Lyapunov function, we obtain

$$\begin{aligned} \dot{V}(t) &= 2x^T(t)P_S(m_s)\overline{A}(m_s)x(t) \\ &\quad + 2x^T(t)P_S(m_s)\overline{B}(m_s)w(t). \end{aligned} \tag{42}$$

Applying the following inequality

$$\begin{aligned} &2x^T(t)P_S(m_s)\overline{B}(m_s)w(t) \\ &\quad\le \frac{1}{\eta}x^T(t)P_s(m_s)\overline{B}(m_s)\overline{B}^T(m_s)P_S(m_s)(x)t \\ &\quad + \eta w^T(t)w(t), \quad \forall\eta > 0, \end{aligned} \tag{43}$$

and (28) to (42), we get

$$\dot{V}(t) \le \eta w^T(t) w(t). \tag{44}$$

Integrate (44) from 0 to t:

$$V(t) - V(0) \le \eta \int_0^t w^T(t) w(t)\, dt = \eta \|w(t)\|_2 \le \eta w_{\max}. \tag{45}$$

Substituting (41) into (45) with $V(0) = 0$, we get

$$x^T(t) P_S(m_s) x(t) \le V(0) + \eta w_{\max} = \rho, \tag{46}$$

which is equivalent to

$$\overline{x}^T(t) \overline{x}(t) \le \rho, \tag{47}$$

where $\overline{x}(t) = P_S^{1/2}(m_s)x(t)$.

Noting that

$$\begin{aligned} &\max \left|\{z_{o2}(t)\}_k\right|^2 \\ &\quad = \max \left\| \overline{x}^T(t) P_S^{-1/2}(m_s) \left\{\overline{C}_2(m_s)\right\}_k^T \right. \\ &\qquad \left. \times \left\{\overline{C}_2(m_s)\right\}_k P_S^{-1/2}(m_s) \overline{x}(t) \right\|_2 \\ &\quad \le \rho \theta_{\max} \left(P_S^{-1/2}(m_s) \left\{\overline{C}_2(m_s)\right\}_k^T \left\{\overline{C}_2(m_s)\right\}_k P_S^{-1/2}(m_s) \right), \end{aligned} \tag{48}$$

where $\theta_{\max}$ stands for the maximum eigenvalue, we can therefore guarantee constraints mentioned in (19) as long as

$$\rho P_S^{-1/2}(m_s) \{C_2(m_s)\}_k^T \{C_2(m_s)\}_k P_S^{-1/2}(m_s) < I, \tag{49}$$

which is equivalent to (22) by applying Schur complement. □

Before giving a convex expression which can be solved by LMI Toolbox, we firstly perform transformation to inequalities (20), (21), and (22).

Decompose matrix $W(m_s)$ for convenience in the following form:

$$\begin{aligned} W(m_s) &= \begin{bmatrix} X(m_s) & Y(m_s) \\ U(m_s) & V(m_s) \end{bmatrix}, \\ W^{-1}(m_s) &= \begin{bmatrix} M(m_s) & G(m_s) \\ H(m_s) & L(m_s) \end{bmatrix}. \end{aligned} \tag{50}$$

According to the literature [25], we assume that both $U(m_s)$ and $H(m_s)$ are invertible without loss of generality.

Denote

$$\Delta(m_s) = \begin{bmatrix} I & M(m_s) \\ 0 & H(m_s) \end{bmatrix}, \tag{51}$$

and perform the congruence transformation to inequalities (20), (21), and (22) by

$$\begin{aligned} J_1(m_s) &= \operatorname{diag}\left\{\Delta^T(m_s), \Delta^T(m_s), \Delta^T(m_s), I\right\}, \\ J_2(m_s) &= \operatorname{diag}\left\{\Delta^T(m_s), \Delta^T(m_s), I, I\right\}, \\ J_3(m_s) &= \operatorname{diag}\left\{I, \Delta^T(m_s)\right\}, \end{aligned} \tag{52}$$

respectively.

Denote

$$\begin{aligned} \widehat{Q}(m_s) &= \Delta^T(m_s) Q(m_s) \Delta(m_s), \\ \widehat{P}(m_s) &= \Delta^T(m_s) P(m_s) \Delta(m_s), \\ \widehat{P}_S(m_s) &= \Delta^T(m_s) P_S(m_s) \Delta(m_s), \\ \widehat{A}(m_s) &= \Delta^T(m_s) W^T(m_s) \overline{A}(m_s) \Delta(m_s) \\ &= \begin{bmatrix} X^T(m_s) A(m_s) + \widehat{B}_K(m_s) C & \widehat{A}_K(m_s) \\ A(m_s) + B(m_s) \widehat{D}_K(m_s) C & A(m_s) M(m_s) + B(m_s) \widehat{C}_K(m_s) \end{bmatrix}, \\ \widehat{B}(m_s) &= \Delta^T(m_s) W^T(m_s) \overline{B}(m_s) \\ &= \begin{bmatrix} X^T(m_s) B_1(m_s) \\ B_1(m_s) \end{bmatrix}, \\ \widehat{C}_1(m_s) &= \overline{C_1}(m_s) \Delta(m_s) \\ &= \left[C_1(m_s) + D_1(m_s) \widehat{D}_K(m_s) C \quad C_1(m_s) M(m_s) + D_1(m_s) \widehat{C}_K(m_s) \right], \\ \widehat{C}_2(m_s) &= \overline{C}_2(m_s) \Delta(m_s) = \left[C_2(m_s) \quad C_2(m_s) M(m_s) \right], \end{aligned}$$

$$\widehat{W}(m_s) = \Delta^T(m_s) W(m_s) \Delta(m_s) = \begin{bmatrix} X^T(m_s) & Z(m_s) \\ I & M(m_s) \end{bmatrix}, \tag{53}$$

then we get the following theorem.

Theorem 2. *For the given parameters $\gamma, \eta, \rho > 0$, if there exist symmetric matrix $\widehat{P}(m_s)$, positive definite symmetric matrices $\widehat{P}_S(m_s)$, $\widehat{Q}(m_s)$, and general matrices $\widehat{A}_K(m_s)$, $\widehat{B}_K(m_s)$, $\widehat{C}_K(m_s)$, $\widehat{D}_K(m_s)$, $\widehat{W}(m_s)$, $M(m_s)$, $X(m_s)$, $Z(m_s)$ satisfying*

$$\begin{bmatrix} \operatorname{sym}\left(\widehat{W}(m_s)\right) & -\widehat{A}(m_s) + \widehat{P}_S(m_s) & -\widehat{W}^T(m_s) & -\widehat{B}(m_s) \\ * & -\widehat{P}_S(m_s) & 0 & 0 \\ * & * & -\widehat{P}_S(m_s) & 0 \\ * & * & * & -\eta I \end{bmatrix} < 0, \tag{54}$$

$$\begin{bmatrix} -\omega_1\omega_2\widehat{Q}(m_s) - \operatorname{sym}\left(\widehat{A}(m_s)\right) & \widehat{P}(m_s) - j\omega_c\widehat{Q}(m_s) + \widehat{W}^T(m_s) & -\widehat{B}(m_s) & \widehat{C}_1^T(m_s) \\ \widehat{P}(m_s) + j\omega_c\widehat{Q}(m_s) + \widehat{W}(m_s) & -\widehat{Q}(m_s) & 0 & 0 \\ -\widehat{B}^T(m_s) & 0 & -\gamma^2 I & 0 \\ \widehat{C}_1(m_s) & 0 & 0 & -I \end{bmatrix} < 0, \tag{55}$$

$$\begin{bmatrix} -I & \sqrt{\rho}\left\{\widehat{C}_2(m_s)\right\}_k \\ * & -\widehat{P}_S(m_s) \end{bmatrix} < 0, \quad k = 1, 2, \tag{56}$$

then a dynamic output feedback controller exists, which satisfies the requirements of (I), (II) and (III) with $w_{\max} = \rho/\eta$.

The corresponding controller in the form of (12) can be given by

$$\begin{aligned} D_K(m_s) &= \widehat{D}_K(m_s), \\ C_K(m_s) &= \left(\widehat{C}_K(m_s) - D_K(m_s) CM(m_s)\right) H^{-1}(m_s), \\ B_K(m_s) &= U^{-T}(m_s)\left(\widehat{B}_K(m_s) - X^T(m_s) B(m_s) D_K(m_s)\right), \\ A_K(m_s) &= U^{-T}(m_s)\left[\widehat{A}_K(m_s) - X^T(m_s) A(m_s) M(m_s) \right. \\ &\quad - X^T(m_s) B(m_s) D_K(m_s) CM(m_s) \\ &\quad - U^T(m_s) B_K(m_s) CM(m_s) \\ &\quad \left. - X^T(m_s) B(m_s) C_K(m_s) H(m_s)\right] \\ &\quad \times H^{-1}(m_s). \end{aligned} \tag{57}$$

Though a parameter-dependent controller can be designed via Theorem 2, it is difficult to obtain targeted matrices in real time as m_s varies. Therefore, we give a tractable LMI-based theorem as follows.

Theorem 3. *For the given parameters γ, η, and $\rho > 0$, if there exist symmetric matrix $\widehat{P}_i$, positive definite symmetric matrices $\widehat{P}_{Si}, \widehat{Q}_i$, and general matrices $\widehat{A}_{Ki}, \widehat{B}_{Ki}, \widehat{C}_{Ki}, \widehat{D}_{Ki}, \widehat{W}_i, M_i, X_i, Z_i$ $(i = 1, 2)$, satisfying*

$$\begin{bmatrix} J_1 & J_2 \\ * & J_3 \end{bmatrix} < 0, \quad 1 \le i \le j \le 2, \tag{58}$$

$$\begin{bmatrix} K_1 + jK_2 & K_3 \\ * & K_4 \end{bmatrix} < 0, \quad 1 \le i \le j \le 2, \tag{59}$$

$$\begin{bmatrix} -I & \sqrt{\rho}\left\{\widehat{C}_{2ij} + \widehat{C}_{2ji}\right\}_k \\ * & -\widehat{P}_{Si} - \widehat{P}_{Sj} \end{bmatrix} < 0, \quad k = 1, 2;\ 1 \le i \le j \le 2, \tag{60}$$

where

$$J_1 = \begin{bmatrix} \operatorname{sym}\left(\widehat{W}_i + \widehat{W}_j\right) & -\widehat{A}_{ij} - \widehat{A}_{ji} + \widehat{P}_{Si} + \widehat{P}_{Sj} \\ * & -\widehat{P}_{Si} - \widehat{P}_{Sj} \end{bmatrix},$$

$$J_2 = \begin{bmatrix} -\widehat{W}_i^T - \widehat{W}_j^T & -\widehat{B}_{ij} - \widehat{B}_{ji} \\ 0 & 0 \end{bmatrix},$$

$$J_3 = \begin{bmatrix} -\widehat{P}_{Si} - \widehat{P}_{Sj} & 0 \\ * & -2\eta I \end{bmatrix},$$

$$K_1 = \begin{bmatrix} -\omega_1\omega_2\left(\widehat{Q}_i + \widehat{Q}_j\right) - \operatorname{sym}\left(\widehat{A}_{ij} + \widehat{A}_{ji}\right) & \widehat{P}_i + \widehat{P}_j + \widehat{W}_i^T + \widehat{W}_j^T \\ \widehat{P}_i + \widehat{P}_j + \widehat{W}_i + \widehat{W}_j & -\widehat{Q}_i - \widehat{Q}_j \end{bmatrix},$$

$$K_2 = \begin{bmatrix} 0 & -\omega_c\left(\widehat{Q}_i + \widehat{Q}_j\right) \\ \omega_c\left(\widehat{Q}_i + \widehat{Q}_j\right) & 0 \end{bmatrix},$$

$$K_3 = \begin{bmatrix} -\widehat{B}_{ij} - \widehat{B}_{ji} & \widehat{C}_{1ij}^T + \widehat{C}_{1ji}^T \\ 0 & 0 \end{bmatrix},$$

$$K_4 = \begin{bmatrix} -2\gamma^2 I & 0 \\ 0 & -2I \end{bmatrix},$$

$$\widehat{A}_{ij} = \begin{bmatrix} X_i^T A_j + \widehat{B}_{Ki} C & \widehat{A}_{Ki} \\ A_i + B_i \widehat{D}_{Kj} C & A_i M_j + B_i \widehat{C}_{Kj} \end{bmatrix},$$

$$\widehat{B}_{ij} = \begin{bmatrix} X_i^T B_{1j} \\ B_{1i} \end{bmatrix},$$

$$\widehat{C}_{1ij} = \left[C_{1i} + D_{1i} \widehat{D}_{Kj} C \quad C_{1i} M_j + D_{1i} \widehat{C}_{Kj} \right],$$

$$\widehat{C}_{2ij} = \left[C_{2i} \quad C_{2i} M_j \right],$$

$$\widehat{W}_i = \begin{bmatrix} X_i^T & Z_i \\ I & M_i \end{bmatrix}, \tag{61}$$

then a dynamic output feedback controller exists, which satisfies the requirements of (I), (II) and (III) with $w_{\max} = \rho/\eta$.

The corresponding controller in the form of (12) *can be given by*

$$D_K(m_s) = \widehat{D}_K(m_s),$$

$$C_K(m_s) = \left(\widehat{C}_K(m_s) - D_K(m_s) CM(m_s) \right) H^{-1}(m_s),$$

$$B_K(m_s) = U^{-T}(m_s) \left(\widehat{B}_K(m_s) - X^T(m_s) B(m_s) D_K(m_s) \right),$$

$$\begin{aligned} A_K(m_s) = U^{-T}(m_s) \big[& \widehat{A}_K(m_s) - X^T(m_s) A(m_s) M(m_s) \\ & - X^T(m_s) B(m_s) D_K(m_s) CM(m_s) \\ & - U^T(m_s) B_K(m_s) CM(m_s) \\ & - X^T(m_s) B(m_s) C_K(m_s) H(m_s) \big] \\ & \times H^{-1}(m_s), \end{aligned} \tag{62}$$

where

$$\begin{aligned} & \left(\widehat{A}_K(m_s), \widehat{B}_K(m_s), \widehat{C}_K(m_s), \right. \\ & \left. \widehat{D}_K(m_s), M(m_s), X(m_s), Z(m_s) \right) \\ & = \sum_{i=1}^{2} \lambda_i \left(\widehat{A}_{Ki}, \widehat{B}_{Ki}, \widehat{C}_{Ki}, \widehat{D}_{Ki}, M_i, X_i, Z_i \right), \end{aligned} \tag{63}$$

and λ_i $(i = 1, 2)$ *can be calculated by* (11).

Proof. we just prove that inequality (58) is sufficient to inequality (54) for simplicity.

Denote

$$\Psi(m_s) = \begin{bmatrix} \operatorname{sym}\left(\widehat{W}(m_s)\right) & -\widehat{A}(m_s) + \widehat{P}_S(m_s) & -\widehat{W}^T(m_s) & -\widehat{B}(m_s) \\ * & -\widehat{P}_S(m_s) & 0 & 0 \\ * & * & -\widehat{P}(m_s) & 0 \\ * & * & * & -\eta I \end{bmatrix}, \tag{64}$$

which stands for the left of inequality (54).

Inequality (58) is equivalent to

$$\begin{aligned} & \Psi_{ij} + \Psi_{ji} < 0, \quad 1 \le i < j \le 2, \\ & \Psi_{ii} < 0, \quad i = 1, 2, \end{aligned} \tag{65}$$

where

$$\Psi_{ij} = \begin{bmatrix} \operatorname{sym}\left(\widehat{W}_i\right) & -\widehat{A}_{ij} + \widehat{P}_{Si} & -\widehat{W}_i^T & -\widehat{B}_{ij} \\ * & -\widehat{P}_{Si} & 0 & 0 \\ * & * & -\widehat{P}_{Si} & 0 \\ * & * & * & -\eta I \end{bmatrix}, \quad 1 \le i \le j \le 2. \tag{66}$$

Assume that

$$\begin{aligned} & \left(\widehat{A}_K(m_s), \widehat{B}_K(m_s), \widehat{C}_K(m_s), \right. \\ & \left. \widehat{D}_K(m_s), M(m_s), X(m_s), Z(m_s) \right) \\ & = \sum_{i=1}^{2} \lambda_i \left(\widehat{A}_{Ki}, \widehat{B}_{Ki}, \widehat{C}_{Ki}, \widehat{D}_{Ki}, M_i, X_i, Z_i \right), \end{aligned} \tag{67}$$

and then we get

$$\Psi(m_s) = \sum_{i=1}^{2} \sum_{j=1}^{2} \lambda_i \lambda_j \Psi_{ij} = \sum_{i=1}^{2} \lambda_i^2 \Psi_{ii} + \lambda_1 \lambda_2 \left(\Psi_{12} + \Psi_{21} \right), \tag{68}$$

which is negative definite by inequality (65), that is,

$$\Psi(m_s) < 0. \tag{69}$$

□

Remark 4. $U(m_s)$, $H(m_s)$ should be chosen to meet the definition, that is,

$$U^T(m_s) H(m_s) = Z(m_s) - X^T(m_s) M(m_s). \tag{70}$$

However, the value of $U(m_s)$ and $H(m_s)$ can be chosen variously for the given $Z(m_s)$, $H(m_s)$, and $M(m_s)$. In this paper, we use the singular value decomposition approach.

Remark 5. Based on [26], for real matrices S_1 and S_2, $S_1 + jS_2 < 0$ is equivalent to $\begin{bmatrix} S_1 & S_2 \\ -S_2 & S_1 \end{bmatrix} < 0$. Thusly, (59) can be converted into real matrix inequality by defining

$$S_1 = \begin{bmatrix} K_1 & K_3 \\ * & K_4 \end{bmatrix}, \qquad S_2 = \begin{bmatrix} K_2 & 0 \\ 0 & 0 \end{bmatrix}. \tag{71}$$

Remark 6. The matrices of dynamic output feedback controller $A_K(m_s)$, $B_K(m_s)$, $C_K(m_s)$, $D_K(m_s)$, and Lyapunov matrix $P_S(m_s)$ are dependent nonlinearly on parameter m_s. For instance, as can be seen in the above deduction, matrix $D_K(m_s)$ in Theorem 3 can be formulated as

$$\begin{aligned} D_K(m_s) = \widehat{D}_K(m_s) &= \sum_{i=1}^{2} \lambda_i \widehat{D}_{Ki} = \lambda_1 \widehat{D}_{K1} + \lambda_2 \widehat{D}_{K2} \\ &= \frac{1/m_s - 1/m_{s\min}}{1/m_{s\max} - 1/m_{s\min}} \widehat{D}_{K1} \\ &\quad + \frac{1/m_{s\max} - 1/m_s}{1/m_{s\max} - 1/m_{s\min}} \widehat{D}_{K2}, \end{aligned} \tag{72}$$

where $\widehat{D}_{K1}$ and $\widehat{D}_{K2}$ are the corresponding matrix solutions of LMIs in Theorem 3, and the value of matrix $D_K(m_s)$ may vary with the change of m_s.

Remark 7. Inequalities from (58) to (60) can be simplified from 12 LMIs to 4 LMIs if the following matrix variables are chosen as $\widehat{P}_1 = \widehat{P}_2$, $\widehat{P}_{S1} = \widehat{P}_{S2}$, $\widehat{Q}_1 = \widehat{Q}_2$, $\widehat{A}_{K1} = \widehat{A}_{K2}$, $\widehat{B}_{K1} = \widehat{B}_{K2}$, $\widehat{C}_{K1} = \widehat{C}_{K2}$, $\widehat{D}_{K1} = \widehat{D}_{K2}$, $\widehat{W}_1 = \widehat{W}_2$, $M_1 = M_2$, $X_1 = X_2$, and $Z_1 = Z_2$. However, this simplification will keep the matrices for the designed controller constant for all m_s, and an invariant Lyapunov function, rather than a parameter-dependent one, has to be used for the whole domain, which will bring a larger conservativeness than Theorem 3.

3.2. Full Frequency Design. Based on the theorem of [27], we formulate Theorem 8 without proof for simplicity.

Theorem 8. *For the given parameter $\gamma > 0$, if there exist positive definite symmetric matrices Y_{Ci}, X_{Ci} and general matrices $\widehat{A}_{Ci}, \widehat{B}_{Ci}, \widehat{C}_{Ci}, \widehat{D}_{Ci}$, $(i = 1, 2)$, satisfying*

$$\begin{bmatrix} \operatorname{sym}\left(\overline{A}_{eij} + \overline{A}_{eji}\right) & \overline{B}_{eij} & \overline{C}_{e1ij}^T + \overline{C}_{e1ji}^T \\ * & -2\gamma^2 I & 0 \\ * & * & -2I \end{bmatrix} < 0, \quad 1 \le i \le j \le 2, \tag{73}$$

$$\begin{bmatrix} -2I & \sqrt{\rho}\left\{\overline{C}_{e2ij} + \overline{C}_{e2ji}\right\}_k \\ * & -\overline{P}_{Ci} - \widehat{P}_{Cj} \end{bmatrix} < 0, \quad k = 1, 2;\ 1 \le i \le j \le 2, \tag{74}$$

where

$$\begin{aligned} \overline{A}_{eij} &= \begin{bmatrix} A_i X_{Cj} + B_i \widehat{C}_{Cj} & A_i + B_i \widehat{D}_{Cj} C \\ \widehat{A}_{Ci} & Y_{Ci} A_j + \widehat{B}_{Ci} C \end{bmatrix}, \\ \overline{B}_{eij} &= \begin{bmatrix} B_{1i} \\ Y_{Ci} B_{1j} \end{bmatrix}, \\ \overline{C}_{e1ij} &= \left[C_{1i} X_{Cj} + D_{1i} \widehat{C}_{Cj} \quad C_{1i} + D_{1i} \widehat{D}_{Cj} C\right], \\ \overline{C}_{e2ij} &= \left[C_{2i} X_{Cj} \quad C_{2i}\right], \\ \overline{P}_{C_i} &= \begin{bmatrix} X_{Ci} & I \\ I & Y_{Ci} \end{bmatrix}, \end{aligned} \tag{75}$$

then a dynamic output feedback controller exists, which satisfies (I) and (III), and $\|G(j\omega)\|_\infty < \gamma$ with $w_{\max} = \rho/\eta$.

The corresponding controller in the form of (12) *can be given by*

$$D_K(m_s) = \widehat{D}_C(m_s), \tag{76}$$

$$C_K(m_s) = \left(\widehat{C}_C(m_s) - \widehat{D}_C(m_s) C X_C(m_s)\right) M_C^{-T}(m_s), \tag{77}$$

$$B_K(m_s) = N_C^{-1}(m_s)\left(\widehat{B}_C(m_s) - Y_C(m_s) B(m_s) \widehat{D}_C(m_s)\right), \tag{78}$$

$$\begin{aligned} A_K(m_s) &= N_C^{-1}(m_s)\left[\widehat{A}_C(m_s) - Y_C(m_s) A(m_s) X_C(m_s) \right. \\ &\quad - Y_C(m_s) B(m_s) \widehat{D}_C(m_s) C X_C(m_s) \\ &\quad - N_C(m_s) B_K(m_s) C X_C(m_s) \\ &\quad \left. - Y_C(m_s) B(m_s) C_K(m_s) M_C^T\right] \\ &\quad \times M_C^{-T}(m_s), \end{aligned} \tag{79}$$

where

$$\begin{aligned} &\left(\widehat{A}_C(m_s), \widehat{B}_C(m_s), \widehat{C}_C(m_s), \widehat{D}_C(m_s), X_C(m_s), Y_C(m_s)\right) \\ &\quad = \sum_{i=1}^{2} \lambda_i \left(\widehat{A}_{Ci}, \widehat{B}_{Ci}, \widehat{C}_{Ci}, \widehat{D}_{Ci}, X_{Ci}, Y_{Ci}\right), \end{aligned} \tag{80}$$

and λ_i $(i = 1, 2)$ can be calculated by (11).

The same approach mentioned in Remark 4 is used to obtain the value of $N_C(m_s)$ and $M_C(m_s)$, which should meet the following equation:

$$N_C(m_s) M_C^T(m_s) = I - Y_C(m_s) X_C(m_s). \tag{81}$$

4. A Design Example

In this section, we will show how to apply the above theorems to design finite frequency controller and full frequency controller for a specific suspension system. The parameter for the suspension is shown in Table 1.

We first choose the following parameters: $\rho = 1$, $\eta = 10000$, $z_{\max} = 0.1$ m, $\omega_1 = 8\pi$rad/s, and $\omega_2 = 16\pi$rad/s. Then, the matrices in (12) can be calculated by applying Theorem 3

Table 1: The model parameters of active suspensions.

k_s	k_t	c_s	c_t	$m_{s\max}$	$m_{s\min}$	m_s	m_u
18 kN/m	200 kN/m	1 kN/m	10 N/m	384 kg	254 kg	320 kg	40 kg

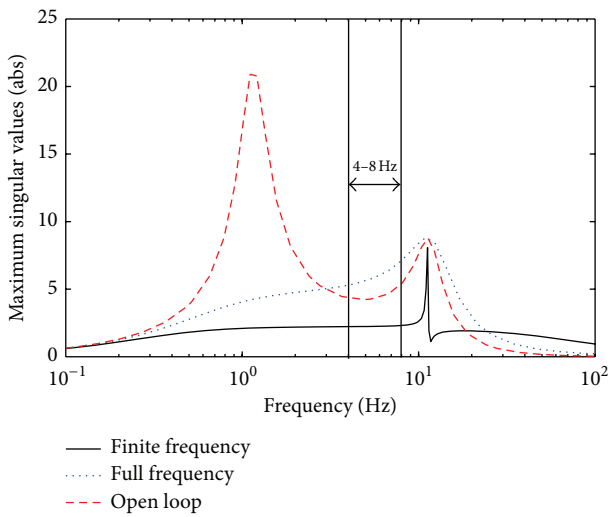

Figure 2: The curves of maximum singular values.

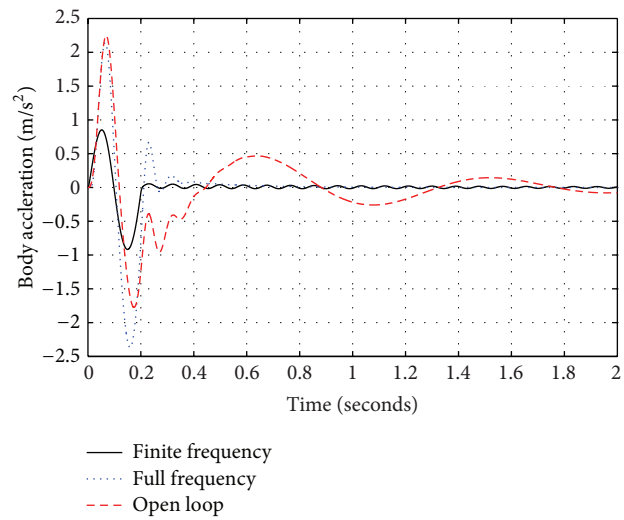

Figure 3: The time response of body acceleration.

and Remark 7 for finite frequency controller and Theorem 8 for full frequency controller (shown in Appendix B) with the least guaranteed H_∞ performances $\gamma = 2.54$ for Theorem 3, $\gamma = 2.73$ for Remark 6, and $\gamma = 10.98$ for Theorem 8.

Then, the curves of maximum singular values of systems using open-loop, finite frequency (parameter-dependent), and full frequency controllers are shown in Figure 2. Compared with the other two curves (the open-loop system and the system with full frequency controller), the system with finite frequency controller has the least H_∞ norm of the three systems in 4–8 Hz, which indicates that the finite frequency controller has a better effect on the attenuation of targeted frequency disturbance.

In order to examine the performance of finite frequency controller, we assume that the disturbance is in the form of

$$w(t) = \begin{cases} A\sin(2\pi f t) & t \in [0, T] \\ 0 & t \notin [0, T], \end{cases} \tag{82}$$

where A, f stand for the amplitude and the frequency of disturbance, respectively, and $T = 1/f$.

Suppose that A is 0.4 m and f is 5 Hz, and then the body acceleration and the relative constraints responses to this disturbance are shown in Figures 3, 4, and 5, respectively.

It is obvious that the body acceleration response for finite frequency controller decreases faster with respect to time than the other two controllers, and at the same time, both the relative dynamic tire load response and relative suspension stroke response are within the allowable range, which satisfy requirement (III), namely, $|\{z_{o2}(t)\}_k| < 1$, $k = 1, 2$.

5. Conclusion

In this paper, we manage to design a dynamic output feedback controller for active suspensions with practical

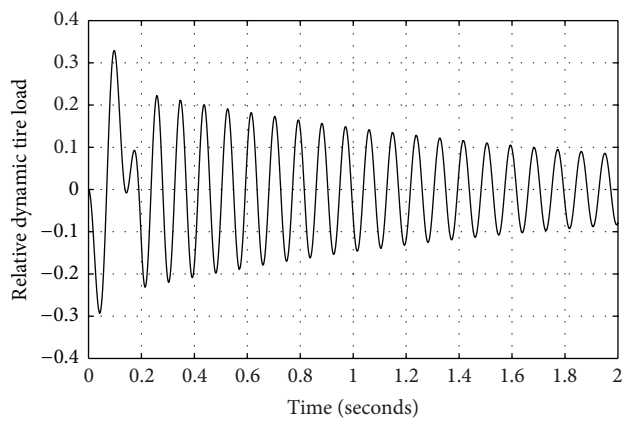

Figure 4: The time response of relative dynamic tire load.

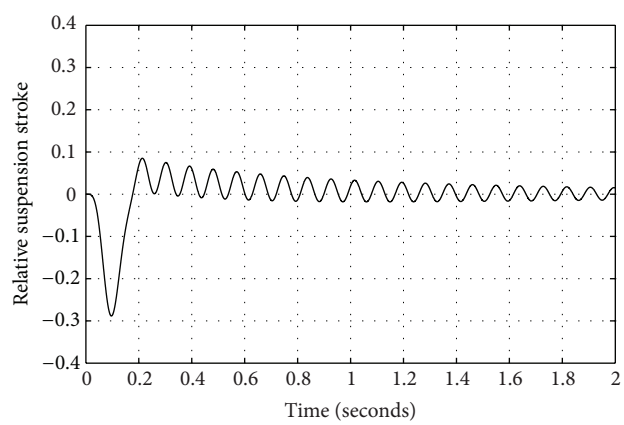

Figure 5: The time response of relative suspension stroke.

constraints included. This controller particularly diminishes disturbance at 4–8 Hz, which is the frequency sensitive band for human. Besides, for the reason that the controller is a parameter-dependent one, it has a smaller conservativeness than controller designed on the basis of quadratic stability and constant parameter feedback. The excellent performance of the closed-loop system with finite frequency controller has been demonstrated by simulation.

Appendices

A. Related Lemmas

Lemma A.1 (generalized KYP lemma [28]). *Let matrices Θ, F, Φ, and Ψ be given, Denote by N_ω the null space of $T_\omega F$, where $T_\omega = [I \quad -j\omega I]$. The inequality*

$$N_\omega^* \Theta N_\omega < 0, \qquad \omega \in [\omega_1 \quad \omega_2] \tag{A.1}$$

holds, if and only if, there exist $P, Q > 0$ such that

$$F^* (\Phi \otimes P + \Psi \otimes Q) F < 0, \tag{A.2}$$

where

$$\Phi = \begin{bmatrix} 0 & 1 \\ 1 & 0 \end{bmatrix}, \qquad \Psi = \begin{bmatrix} -1 & j\omega_c \\ -j\omega_c & -\omega_1\omega_2 \end{bmatrix}, \tag{A.3}$$

with $\omega_c = (\omega_1 + \omega_2)/2$.

Lemma A.2 (projection lemma [25]). *Let Γ, Λ, and Θ be given, there exists a matrix satisfying*

$$\text{sym}\ (\Gamma\Lambda\Theta) + \Theta < 0, \tag{A.4}$$

if and only if, the following two conditions hold:

$$\Gamma^\perp \Theta (\Gamma^\perp)^T < 0, \qquad (\Lambda^T)^\perp \Theta \left((\Lambda^T)^\perp \right)^T < 0. \tag{A.5}$$

Lemma A.3 (reciprocal projection lemma [25]). *Let P be any given positive definite matrix. The following statements are equivalent.*

(1) $\Psi + S + S^T < 0$.

(2) *The LMI problem*

$$\begin{bmatrix} \Psi + P - [W_s] & S^T + W^T \\ * & -P \end{bmatrix} < 0 \tag{A.6}$$

is feasible with respect to X.

B. Controller Matrices

The parameter matrices of the dynamic output feedback controller for Theorem 3:

$$A_K = \begin{bmatrix} -14.821 & -0.12731 & -1.1424 & 0.00255 \\ -228.44 & -136.92 & 13.701 & 0.02030 \\ 2038.1 & 151.59 & -21.603 & -0.47598 \\ 2.4991 \times 10^9 & -7.4319 \times 10^7 & 4.2012 \times 10^6 & -1.0171 \times 10^6 \end{bmatrix},$$

$$B_K = \begin{bmatrix} 99.943 & 109.08 & 44.969 \\ -3170.6 & -2956.8 & -891.61 \\ -632.00 & 1156.4 & -1125.8 \\ -1.0944 \times 10^8 & -1.8461 \times 10^9 & -7.9445 \times 10^7 \end{bmatrix}, \tag{B.1}$$

$$C_K = [3814.4 \quad -686.19 \quad 1758.9 \quad 3.5961],$$

$$D_K = [-1.8676 \times 10^5 \quad -2.0429 \times 10^5 \quad -86675].$$

The parameter matrices of the dynamic output feedback controller for Theorem 8:

$$A_K = \begin{bmatrix} -12.734 & 26.225 & 21.367 & -0.31502 \\ -36.286 & 14.954 & 36.984 & 0.69500 \\ -111.01 & -84.507 & -65.487 & -0.0771 \\ -45995 & -42118 & -29117 & -1623.6 \end{bmatrix},$$

$$B_K = \begin{bmatrix} -793.37 & -56.495 & -136.30 \\ 1770.9 & 122.15 & 113.03 \\ -90.855 & 3448.7 & -802.39 \\ 6.4417 \times 10^5 & 7.1058 \times 10^6 & -2.7515 \times 10^5 \end{bmatrix},$$

$$C_K = [518.19 \quad -604.03 \quad -590.41 \quad 10.015],$$

$$D_K = [25422 \quad 1720.8 \quad 2609.8]. \tag{B.2}$$

References

[1] D. Hrovat, "Survey of advanced suspension developments and related optimal control applications," *Automatica*, vol. 33, no. 10, pp. 1781–1817, 1997.

[2] W. Sun, H. Gao, and O. Kaynak, "Adaptive backstepping control for active suspension systems with hard constraints," *IEEE Transactions on Mechatronics*, vol. 18, pp. 1072–1079, 2013.

[3] W. Sun, H. Gao, and B. Yao, "Adaptive robust vibration control of full-car active suspensions with electrohydraulic actuators," *IEEE Transactions on Control Systems Technology*, 2013.

[4] I. Fialho and G. J. Balas, "Road adaptive active suspension design using linear parameter-varying gain-scheduling," *IEEE Transactions on Control Systems Technology*, vol. 10, no. 1, pp. 43–54, 2002.

[5] H. Zhang, Y. Shi, and A. Saadat Mehr, "Robust static output feedback control and remote PID design for networked motor systems," *IEEE Transactions on Industrial Electronics*, vol. 58, no. 12, pp. 5396–5405, 2011.

[6] H. Zhang, Y. Shi, and A. Saadat Mehr, "Robust non-fragile dynamic vibration absorbers with uncertain factors," *Journal of Sound and Vibration*, vol. 330, no. 4, pp. 559–566, 2011.

[7] M. Yu, S. B. Choi, X. M. Dong, and C. R. Liao, "Fuzzy neural network control for vehicle stability utilizing magnetorheological suspension system," *Journal of Intelligent Material Systems and Structures*, vol. 20, no. 4, pp. 457–466, 2009.

[8] D. E. Williams and W. M. Haddad, "Active suspension control to improve vehicle ride and handling," *Vehicle System Dynamics*, vol. 28, no. 1, pp. 1–24, 1997.

[9] A. G. Ulsoy, D. Hrovat, and T. Tseng, "Stability robustness of LQ and LQG active suspensions," *Journal of Dynamic Systems, Measurement and Control, Transactions of the ASME*, vol. 116, no. 1, pp. 123–131, 1994.

[10] W. Sun, H. Gao Sr., and O. Kaynak, "Finite frequency H_∞ control for vehicle active suspension systems," *IEEE Transactions on Control Systems Technology*, vol. 19, no. 2, pp. 416–422, 2011.

[11] W. Sun, J. Li, Y. Zhao, and H. Gao, "Vibration control for active seat suspension systems via dynamic output feedback with limited frequency characteristic," *Mechatronics*, vol. 21, no. 1, pp. 250–260, 2011.

[12] H. Chen and K.-H. Guo, "Constrained H_∞ control of active suspensions: an LMI approach," *IEEE Transactions on Control Systems Technology*, vol. 13, no. 3, pp. 412–421, 2005.

[13] H. R. Karimi, N. Luo, M. Zapateiro, and L. Zhang, "H_∞ control design for building structures under seismic motion with wireless communication," *International Journal of Innovative Computing, Information and Control*, vol. 7, no. 9, pp. 5269–5284, 2011.

[14] H. Chen, Z.-Y. Liu, and P.-Y. Sun, "Application of constrained H_∞ control to active suspension systems on half-car models," *Journal of Dynamic Systems, Measurement and Control, Transactions of the ASME*, vol. 127, no. 3, pp. 345–354, 2005.

[15] H. Du, J. Lam, and K. Y. Sze, "Non-fragile output feedback H_∞ vehicle suspension control using genetic algorithm," *Engineering Applications of Artificial Intelligence*, vol. 16, no. 7-8, pp. 667–680, 2003.

[16] M. Yamashita, K. Fujimori, K. Hayakawa, and H. Kimura, "Application of H_∞ control to active suspension systems," *Automatica*, vol. 30, no. 11, pp. 1717–1729, 1994.

[17] H. Zhang, Y. Shi, and M. Liu, "H_∞ step tracking control for networked discrete-time nonlinear systems with integral and predictive actions," *IEEE Transactions on Industrial Informatics*, vol. 9, pp. 337–345, 2013.

[18] M. C. Smith and F.-C. Wang, "Controller parameterization for disturbance response decoupling: application to vehicle active suspension control," *IEEE Transactions on Control Systems Technology*, vol. 10, no. 3, pp. 393–407, 2002.

[19] W. Sun, Y. Zhao, J. Li, L. Zhang, and H. Gao, "Active suspension control with frequency band constraints and actuator input delay," *IEEE Transactions on Industrial Electronics*, vol. 59, no. 1, pp. 530–537, 2012.

[20] W. Sun, Z. Zhao, and H. Gao, "Saturated adaptive robust control of active suspension systems," *IEEE Transactions on Industrial Electronics*, vol. 60, pp. 3889–3896, 2013.

[21] H. Gao, J. Lam, and C. Wang, "Multi-objective control of vehicle active suspension systems via load-dependent controllers," *Journal of Sound and Vibration*, vol. 290, no. 3-5, pp. 654–675, 2006.

[22] D. Sammier, O. Sename, and L. Dugard, "Skyhook and H_∞ control of semi-active suspensions: some practical aspects," *Vehicle System Dynamics*, vol. 39, no. 4, pp. 279–308, 2003.

[23] T. Iwasaki, S. Hara, and H. Yamauchi, "Dynamical system design from a control perspective: finite frequency positive-realness approach," *IEEE Transactions on Automatic Control*, vol. 48, no. 8, pp. 1337–1354, 2003.

[24] B. Hencey and A. G. Alleyne, "A KYP lemma for LMI regions," *IEEE Transactions on Automatic Control*, vol. 52, no. 10, pp. 1926–1930, 2007.

[25] P. Apkarian, H. D. Tuan, and J. Bernussou, "Continuous-time analysis, eigenstructure assignment, and H_2 synthesis with enhanced linear matrix inequalities (LMI) characterizations," *IEEE Transactions on Automatic Control*, vol. 46, no. 12, pp. 1941–1946, 2001.

[26] P. Gahinet, A. Nemirovskii, A. Laub, and M. Chilali, *LMI Control Toolbox Users Guide*, The Math. Works, Natick, Mass, USA, 1995.

[27] C. Scherer, P. Gahinet, and M. Chilali, "Multiobjective output-feedback control via LMI optimization," *IEEE Transactions on Automatic Control*, vol. 42, no. 7, pp. 896–911, 1997.

[28] J. Collado, R. Lozano, and R. Johansson, "On Kalman-Yakubovich-Popov Lemma for stabilizable systems," *IEEE Transactions on Automatic Control*, vol. 46, no. 7, pp. 1089–1093, 2001.